Contemporary Cardiology
Series Editor: Peter P. Toth

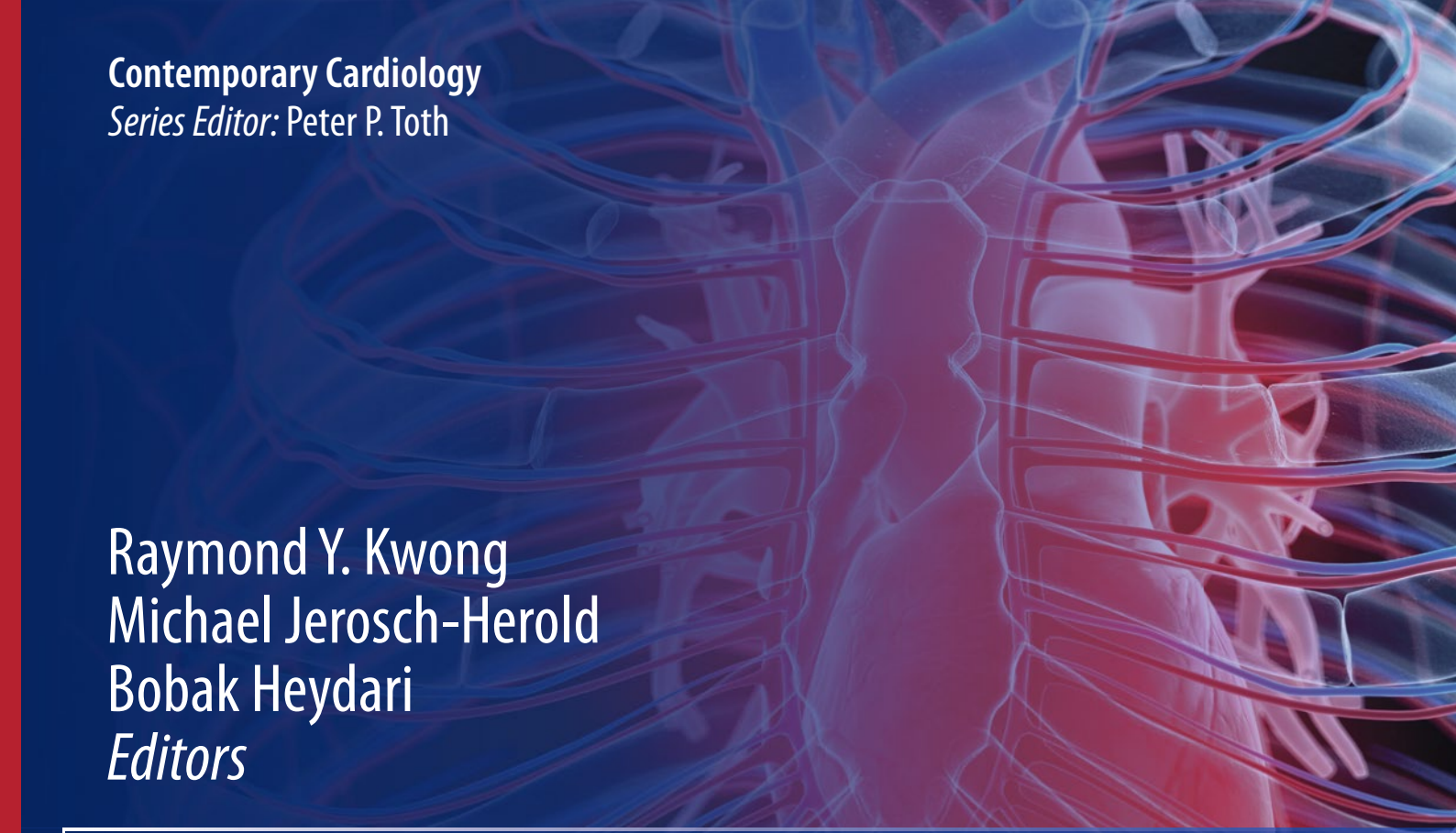

Raymond Y. Kwong
Michael Jerosch-Herold
Bobak Heydari
Editors

Cardiovascular Magnetic Resonance Imaging

Second Edition

EXTRAS ONLINE

Humana Press

Contemporary Cardiology

Series Editor:

Peter P. Toth
Ciccarone Center for the Prevention of Cardiovascular Disease
Johns Hopkins University School of Medicine
Baltimore, Maryland
USA

For more than a decade, cardiologists have relied on the Contemporary Cardiology series to provide them with forefront medical references on all aspects of cardiology. Each title is carefully crafted by world-renown cardiologists who comprehensively cover the most important topics in this rapidly advancing field. With more than 75 titles in print covering everything from diabetes and cardiovascular disease to the management of acute coronary syndromes, the Contemporary Cardiology series has become the leading reference source for the practice of cardiac care.

More information about this series at http://www.springer.com/series/7677

Raymond Y. Kwong
Michael Jerosch-Herold
Bobak Heydari
Editors

Cardiovascular Magnetic Resonance Imaging

Second Edition

Humana Press

Editors
Raymond Y. Kwong
Cardiovascular Division
Harvard Medical School
Brigham and Women's Hospital
Boston, MA
USA

Michael Jerosch-Herold
Department of Radiology
Harvard Medical School
Brigham and Women's Hospital
Boston, MA
USA

Bobak Heydari
Department of Cardiac Sciences
University of Calgary
Calgary, AB
Canada

ISSN 2196-8969 ISSN 2196-8977 (electronic)
Contemporary Cardiology
ISBN 978-1-4939-8839-6 ISBN 978-1-4939-8841-9 (eBook)
https://doi.org/10.1007/978-1-4939-8841-9

Library of Congress Control Number: 2018966145

This Springer imprint is published by the registered company Springer Science+Business Media, LLC part of Springer Nature
The registered company address is: 233 Spring Street, New York, NY 10013, U.S.A

Foreword

Imaging is the bread-and-butter of cardiology. In fact, almost all patients with heart disease will have some form of imaging at some point. Non-invasive cardiac imaging is a fantastic innovation story that began a century ago with the chest X-ray, greatly accelerated in the 1960s with the development of nuclear cardiology and echocardiography, complementing invasive cath lab-based imaging methods. However, cardiac imaging had seen nothing like the massive step change in non-invasive techniques that has occurred over the past 20 years, made possible by major advances in computing power, hardware design, and, most importantly, the great work of a new generation of highly innovative technical and clinical researchers who have massively changed the boundaries of the field. Cardiac MRI (CMR) and cardiac CT have been at the forefront of this exciting development. However, what sets CMR apart from all other non-invasive imaging contenders is its enormous versatility. By manipulating the MRI signal in various forms, we can image and quantify almost every aspect of cardiac physiology and pathophysiology, enabling highly reproducible assessment of, amongst many other aspects, cardiac anatomy, function, perfusion, inflammation, viability, oxygenation, and metabolism. To just give one striking example, I can remember a time when our best hope to diagnose myocarditis was taking a cardiac biopsy, which samples a tiny fraction of subendocardial myocardium. Now modern CMR techniques have become an established test for diagnosing this condition, enabling the assessment of the severity and extent of inflammation for the entire heart, as well as monitoring of its recovery.

As a consequence of these new capabilities and a very active research community, the worldwide growth in CMR centres and numbers of patient scans performed has been substantial; an enormous body of knowledge on the role of CMR has been accumulated, and a major new subspecialty for both cardiologists and radiologists has come into existence. With such opportunity and activity arises the need for systematic, balanced reference sources of knowledge in the field. Many different CMR methods and approaches have been developed, and there is also a major need for standardisation amongst different vendors and field strengths. There is also still a challenging disconnect between the available education in CMR and the needs of practicing CMR clinicians worldwide.

It is in this important context that the second edition of *Cardiovascular Magnetic Resonance Imaging* is making a major contribution to this rapidly growing field. Kwong, Jerosch-Herold, and Heydari are international leaders in CMR who have consistently been at the forefront of both clinical research and new method development in CMR over the past two decades. For the second edition of their classic textbook on CMR, they have assembled an outstanding cadre of leaders in the field as contributors. Indeed, the author list comprises over 60 experts from diverse disciplines including biomedical engineering, clinical cardiology, radiology, and MR physics.

In 25 chapters, this scholarly textbook systematically covers all relevant aspects of cardiac MR theory, methods, and clinical practice. Each chapter is clearly structured and is extensively referenced, including the latest publications and developments in the field, but with a clear focus on those methods that are clinically validated. The text is supported throughout the book by extensive illustrations, which are of the highest quality. Overall, the authors have created a textbook that is much greater than the sum of its parts, which will serve both the novice and the

experienced CMR clinician as a comprehensive yet easily accessible source of knowledge and reference in their daily practice.

This is the second edition of this remarkable textbook. In this new edition, the most recent applications of CMR, such as its use for preparation for electrophysiological ablative treatment of arrhythmias, targeted molecular MR imaging, and the growing use of T1 mapping methods, have been incorporated as additional chapters. Following the positive response to the first edition, a larger book print size has enhanced readability.

For all these reasons, this second edition of *Cardiovascular Magnetic Resonance Imaging* will become an important resource for CMR specialists, providing essential guidance for their daily clinical practice. I congratulate the editors and authors for creating this fantastic textbook and hope that many of us in the field will take advantage to learn from its wisdom for many years to come.

Stefan Neubauer, MD, FRCP, FACC, FMedSci
Head, Division of Cardiovascular Medicine, University of Oxford, Oxford, UK
Director, Oxford Centre for Clinical Magnetic Resonance Research, Oxford, UK

Preface

Since the successful invention three decades ago of the first magnetic resonance imaging (MRI) system by Damadian et al. for cancer diagnosis, the medical use of MRI has become an essential component in the diagnosis and management of patients with a wide range of diseases. Extensive hardware and software advances have surmounted initial obstacles in imaging a rapidly beating heart and allowed imagers to apply MRI techniques to patients with cardiovascular pathology. Over the past years, cardiovascular MRI has become the gold standard in assessment of cardiac structure and function, and an indispensable tool in many routine clinical cardiac diagnoses with the advantage of not only providing structural but a multitude of functional and physiologic information that are adjunctive or superior to conventional imaging tools.

The second edition of *Cardiovascular Magnetic Resonance Imaging* comprises the efforts of a team of international authors from different disciplines who contributed a broad range of expertise to the current field of cardiovascular MRI. Throughout the production of this book, the emphasis has been on comprehensive, scientifically accurate, and clear explanations of the many components of this rapidly advancing field. We aim to maintain a balance between technical foundations, cardiac physiology, clinical validation, and available prognostic implications to enhance the educational value of this reference textbook. Radiologists, cardiologists, internists, physicists, and residents and fellows with interests in cardiovascular MRI may benefit from the range of materials presented.

While plenty remains to be explored to unleash the full potential of magnetic resonance technology in imaging the heart, the field of cardiovascular MRI has experienced steady growth with balanced emphases in both technical improvement and clinical application. The chapters in MRI pulse sequence techniques and MRI physics in the second edition of *Cardiovascular Magnetic Resonance Imaging* are intended to serve as practical introductory resources to help our readers overcome the starting challenges in this field. On the other hand, many of the other chapters provide in-depth discussion of advanced clinical and research applications to suit the readership of advanced cardiac MRI practitioners or investigators. Such a wide scope of presented knowledge in this field could not have been possible without the vast expertise of our 60 authors.

Since the publication of the first edition of this book, there have been extensive advancements in cardiovascular MRI techniques, the establishment of novel MRI biomarkers, and ongoing active areas of exciting research that hold tremendous future potential. The second edition of *Cardiovascular Magnetic Resonance Imaging* summarises this new knowledge both from clinical and physics perspectives by updating core chapters and adding new chapters that cover essential topics that have made rapid progress, such as T1 and T2 mapping, assessment of myocardial strain, interventional MRI, atrial fibrosis evaluation for radiofrequency ablation, quantitative stress perfusion, and 4D flow imaging. Similar to the last version, this edition contains a large collection of images and movies to provide visual context and enhance the reading experience of the book.

We wish to express our appreciation to the editors at Springer for the opportunity to undertake this project and for their outstanding help and support in bringing the second edition of *Cardiovascular Magnetic Resonance Imaging* to fruition. We hope you will enjoy reading this book.

Raymond Y. Kwong — Boston, MA, USA
Michael Jerosch-Herold — Boston, MA, USA
Bobak Heydari — Calgary, AB, Canada

Contents

Contributors

Ayaz Aghayev Brigham and Women's Hospital, Harvard Medical School, Department of Radiology, Boston, MA, USA

Mehmet Akçakaya Department of Medicine (Cardiovascular Division), Beth Israel Deaconess Medical Center and Harvard Medical School, Boston, MA, USA

Department of Electrical and Computer Engineering, University of Minnesota, Minneapolis, MN, USA

Center for Magnetic Resonance Research, University of Minnesota, Minneapolis, MN, USA

Marcelo E. Andia Radiology Department, School of Medicine, Pontificia Universidad Catolica de Chile, Santiago, Chile

Andrew E. Arai National Institutes of Health, National Heart, Lung and Blood Institute, Bethesda, MD, USA

Leon Axel NYU School of Medicine, NYU Langone Medical Center, Departments of Radiology, Medicine, and Neuroscience and Physiology, New York, NY, USA

David A. Bluemke NIH Clinical Center, Department of Radiology and Imaging Sciences, Bethesda, MD, USA

René M. Botnar Division of Imaging Sciences and Biomedical Engineering, King's College London, St Thomas' Hospital, London, UK

The British Heart Foundation Centre of Excellence, Cardiovascular Division, King's College London, London, UK

Lawrence M. Boxt Department of Radiology, Englewood Hospital Medical Center, Englewood, NJ, USA

Peter Caravan Massachusetts General Hospital, Harvard Medical School, Martinos Center for Biomedical Imaging, Charlestown, MA, USA

Kevin Duffy Cardiovascular Medicine Division, Department of Medicine, Perelman School of Medicine, University of Pennsylvania, Philadelphia, PA, USA

Ana Paula de Faria State University of Campinas, Faculty of Medical Science, University Hospital, Department of Pharmacology, Campinas, Brazil

Victor A. Ferrari Cardiovascular Medicine Division, Department of Medicine, Perelman School of Medicine, University of Pennsylvania, Philadelphia, PA, USA

Otávio Rizzi Coelho-Filho State University of Campinas, Faculty of Medical Science, University Hospital, Department of Medicine, Campinas, Brazil

Patrycja Z. Galazka Non-invasive Cardiovascular Imaging, Cardiovascular Division, Department of Medicine and Department of Radiology, Brigham and Women's Hospital, Harvard Medical School, Boston, MA, USA

Tal Geva Department of Cardiology, Boston Children's Hospital, Boston, MA, USA
Department of Pediatrics, Harvard Medical School, Boston, MA, USA

Henry R. Halperin Johns Hopkins Hospital, Department of Medicine, Baltimore, MD, USA

Yuchi Han Cardiovascular Medicine Division, Department of Medicine, Perelman School of Medicine, University of Pennsylvania, Philadelphia, PA, USA

Markus Henningsson Division of Imaging Sciences and Biomedical Engineering, King's College London, St Thomas' Hospital, London, UK

Li-Yueh Hsu National Institutes of Health, National Heart, Lung and Blood Institute, Bethesda, MD, USA

Masaki Ishida Mie University Hospital, Department of Radiology, Tsu, Japan

Michael Jerosch-Herold Brigham and Women's Hospital, Harvard Medical School, Boston, MA, USA

Christopher M. Kramer Departments of Radiology and Medicine, University of Virginia Health System, Charlottesville, VA, USA

Raymond Y. Kwong, M.D., M.P.H. Non-invasive Cardiovascular Imaging, Cardiovascular Division, Department of Medicine, Brigham and Women's Hospital, Harvard Medical School, Boston, MA, USA

Sara Lacerda Division of Imaging Sciences and Biomedical Engineering, King's College London, St Thomas' Hospital, London, UK

Robert J. Lederman Cardiovascular, Division of Intramural Research, National Heart, Lung, and Blood Institute, National Institutes of Health, Bethesda, MD, USA

Martin J. Lipton Department of Radiology, Pritzker School of Medicine, University of Chicago, Chicago, IL, USA

Marcus R. Makowski Department of Radiology, Institut für Radiologie, Berlin, Germany

Michael Markl Northwestern University Feinberg School of Medicine, Department of Radiology and Biomedical Engineering, Chicago, IL, USA

Nassir Marrouche University of Utah School of Medicine, Comprehensive Arrhythmia Research and Management Center, Salt Lake City, UT, USA

Rodrigo Modolo State University of Campinas, Faculty of Medical Science, University Hospital, Department of Internal Medicine, Campinas, Brazil

Róisín B. Morgan Non-invasive Cardiovascular Imaging, Cardiovascular Division, Department of Medicine, Brigham and Women's Hospital, Harvard Medical School, Boston, MA, USA

David J. Murphy Non-invasive Cardiovascular Imaging, Radiology Division, Department of Radiology, Brigham and Women's Hospital, Boston, MA, USA

Leenhapong Navaravong Bangkok Heart Hospital, Bangkok, Thailand
UnityPoint Clinic – Cardiology, Iowa Methodist Medical Center, Des Moines, IA, USA

Saman Nazarian Johns Hopkins Hospital, Department of Medicine, Baltimore, MD, USA

Reza Nezafat Department of Medicine (Cardiovascular Division), Beth Israel Deaconess Medical Center and Harvard Medical School, Boston, MA, USA

Alkystis Phinikaridou Division of Imaging Sciences and Biomedical Engineering, King's College London, St Thomas' Hospital, London, UK

Begoña Lavin-Plaza Division of Imaging Sciences and Biomedical Engineering, King's College London, St Thomas' Hospital, London, UK

Andrew J. Powell Department of Cardiology, Boston Children's Hospital, Boston, MA, USA
Department of Pediatrics, Harvard Medical School, Boston, MA, USA

Ashwin Prakash Department of Cardiology, Boston Children's Hospital, Boston, MA, USA
Department of Pediatrics, Harvard Medical School, Boston, MA, USA

Subha V. Raman The Ohio State University Wexner Medical Center, Department of Internal Medicine/Cardiovascular Medicine, Columbus, OH, USA

Rahul H. Rathod Department of Cardiology, Boston Children's Hospital, Boston, MA, USA
Department of Pediatrics, Harvard Medical School, Boston, MA, USA

Toby Rogers Cardiovascular, National Institutes of Health, National Heart, Lung, and Blood Institute, Bethesda, MD, USA

Hajime Sakuma Mie University Hospital, Department of Radiology, Tsu, Japan

Michael Salerno Departments of Medicine, Radiology, and Biomedical Engineering, University of Virginia Health System, Charlottesville, VA, USA

Jeanette Schulz-Menger Working Group on Cardiovascular Magnetic Resonance, Experimental and Clinical Research Center-a joint cooperation between the Charité Medical Faculty and the Max-Delbrück Center for Molecular Medicine, Berlin, Germany
HELIOS Klinikum Berlin-Buch, Department of Cardiology and Nephrology, Berlin, Germany

Ravi Teja Seethamraju Department of MR/R&D, Siemens Healthcare, Boston, MA, USA

Thiago Quinaglia A. C. Silva State University of Campinas, Faculty of Medical Science, University Hospital, Department of Medicine, Campinas, Brazil

David E. Sosnovik Massachusetts General Hospital, Harvard Medical School, Martinos Center for Biomedical Imaging, Charlestown, MA, USA

Michael L. Steigner Brigham and Women's Hospital, Harvard Medical School, Department of Radiology, Boston, MA, USA

Rolf Symons NIH Clinical Center, Department of Radiology and Imaging Sciences, Bethesda, MD, USA

Maxine Tang Department of Medicine (Cardiovascular Division), Beth Israel Deaconess Medical Center and Harvard Medical School, Boston, MA, USA

Servet Tatli Department of Radiology, Lehigh Valley Health Network, Allentown, PA, USA

Madalina Alexandra Toms NYU School of Medicine, NYU Langone Medical Center, Department of Radiology, New York, NY, USA

Ralf Wassmuth Working Group on Cardiovascular Magnetic Resonance, Experimental and Clinical Research Center-a joint cooperation between the Charité Medical Faculty and the Max-Delbrück Center for Molecular Medicine, Berlin, Germany
Internal Medicine and Cardiology Department, Oberhavel-Kliniken Hennigsdorf, Hennigsdorf, Germany

Walter R. Witschey Department of Radiology, Perelman School of Medicine, University of Pennsylvania, Philadelphia, PA, USA

E. Kent Yucel Tufts Medical Center, Department of Radiology, Boston, MA, USA

Karolina M. Zareba The Ohio State University Wexner Medical Center, Department of Internal Medicine/Cardiovascular Medicine, Columbus, OH, USA

Cardiac Magnetic Resonance Imaging Physics

1

Mehmet Akçakaya, Maxine Tang, and Reza Nezafat

Introduction

In this chapter, we will introduce the basics of cardiovascular magnetic resonance (CMR). We will describe the physics of magnetic resonance imaging (MRI), including how the magnetization is generated and manipulated and what T_1, T_2, and T_2* relaxation processes mean. We will then study how to encode a tissue using magnetization, so that spatial information about the tissue can be used to generate an image. We will then study the basics of image formation and fast imaging techniques. We will conclude with a brief overview some of the existing CMR pulse sequences.

MRI Physics

Magnetic resonance (MR) depends on the interaction between an external magnetic field and the intrinsic angular momentum, or spin, of a nucleus of interest. A nucleus has an electrical charge and a spin, and thus its magnetic moment interacts with a magnetic field, as long as both its atomic number (i.e., the number of protons) and atomic weight (i.e., the number of protons and neutrons) are not even. Among the many nuclei that have spin, hydrogen nucleus made up of a proton (i.e., ^{1}H nucleus) is a natural candidate for imaging the body. The human body contains tissues composed primarily of water and fat, both of which contain hydrogen. Thus, we will concentrate on the use of MR for imaging of hydrogen atoms in the body.

M. Akçakaya
Department of Medicine (Cardiovascular Division), Beth Israel Deaconess Medical Center and Harvard Medical School, Boston, MA, USA

Department of Electrical and Computer Engineering, University of Minnesota, Minneapolis, MN, USA

Center for Magnetic Resonance Research, University of Minnesota, Minneapolis, MN, USA
e-mail: akcakaya@umn.edu

M. Tang · R. Nezafat (✉)
Department of Medicine (Cardiovascular Division), Beth Israel Deaconess Medical Center and Harvard Medical School, Boston, MA, USA
e-mail: rnezafat@bidmc.harvard.edu

Magnetization

MR measurements are made on a collection of hydrogen atoms rather than individual atoms. Thus, we will consider the behavior of a collection of hydrogen atoms. In the absence of a magnetic field, in a tissue containing hydrogen atoms, each proton has a spin of equal magnitude but in a random direction (Fig. 1.1). Thus, a vector addition of these spins leads to a zero sum or no net magnetization. However, if the tissue is placed within a strong magnetic field (called B_0), the hydrogen atoms tend to align with this applied magnetic field, resulting in a net magnetization, denoted by the magnetization vector M. A larger magnetic field creates greater alignment of the hydrogen protons. As a result of the interaction of the B_0 field and the magnetic moment of the positively charged hydrogen nucleus, the individual protons begin to rotate, or precess, around the axis of the B_0 field. The rate or frequency of the precession is a fundamental property of the nucleus and is proportional to the strength of the magnetic field as characterized by the Larmor equation:

$$\varpi = \gamma B / (2\pi), \tag{1.1}$$

where ϖ is the precessional frequency in hertz (Hz), γ is a constant for the nucleus referred to as the gyromagnetic ratio, and B is the magnetic field strength in tesla (T). For the hydrogen atom, $\gamma/(2\pi) = 42.58 \times 10^6$ Hz/T. Thus, at 1.5 T field strength, $\varpi_0 = 63.87 \times 10^6$ Hz or approximately 64 MHz (in the same range as FM radio signals).

As we will discuss later, the Larmor equation is fundamental to CMR imaging. In order to generate an image, the magnetic field B is varied for different spatial locations, thus

R. Y. Kwong et al. (eds.), *Cardiovascular Magnetic Resonance Imaging*, Contemporary Cardiology,
https://doi.org/10.1007/978-1-4939-8841-9_1

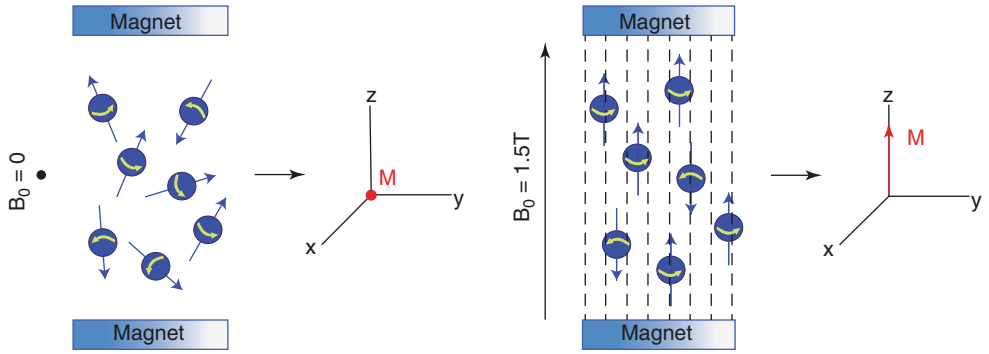

Fig. 1.1 In the absence of a magnetic field, the hydrogen atoms in a tissue have a spin of equal magnitude but in a random direction. A vector addition of these spins results in a zero sum, i.e., no net magnetization, M. If the tissue is a placed within a strong magnetic field, B_0, the hydrogen atoms align with this magnetic field, resulting in a non-zero magnetization vector, M. A larger magnetic field creates greater alignment of the hydrogen protons

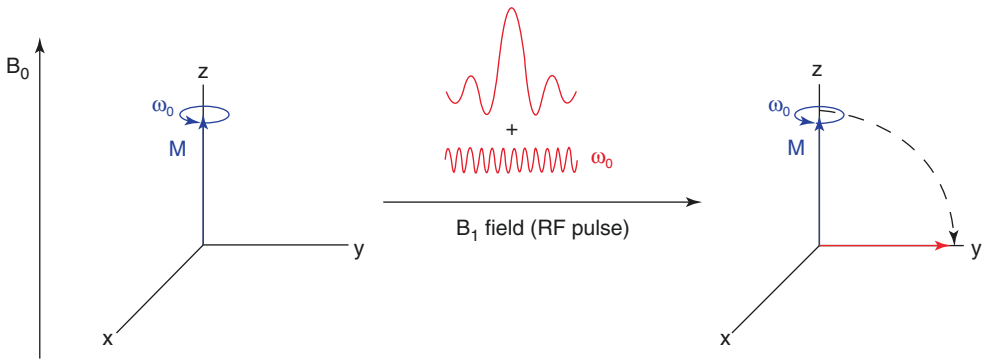

Fig. 1.2 When the hydrogen protons are in the presence of the B_0 field only, they precess around the axis of the B_0 field, denoted by the z-axis. The precession around the B_0 field is in an incoherent fashion, creating no net magnetization in the transverse (x-y) plane. If a B_1 magnetic field is applied, the magnetization vector M is effectively rotated into the transverse plane. A 90° pulse that rotates the magnetization vector M fully into the transverse plane is depicted. The angle of rotation depends on the strength of the B_1 field and the duration of the RF pulse

ensuring different tissue location precesses at different frequencies. These frequencies are then measured to create an MR image [1]. We next discuss, how these measurements are performed, for the simplest case when $B = B_0$.

RF Excitation

The detection of signal in MRI relies on an energy transfer principle. The ^{1}H protons in the patient are first "excited" with a pulse of energy at the Larmor frequency. This energy is absorbed and subsequently re-emitted, which is measured as the signal.

The energy to excite the ^{1}H protons is applied using a radiofrequency (RF) pulse with central frequency at $\varpi_0 = \gamma B_0/(2\pi)$, specified by its corresponding (less powerful) magnetic field B_1. The B_1 field is applied perpendicular to the main magnetic field so that energy can be transferred to the protons and the magnetization vector M can be rotated out of equilibrium and away from the B_0 direction. As discussed previously, in the presence of the B_0 field, the hydrogen protons precess around the axis of the B_0 field, typically denoted as the z-axis (parallel to the B_0 field). The precession around the B_0 field is in an incoherent fashion, creating no net magnetization in the transverse (x-y) plane. Following the application of the B_1 field, net magnetization is created in the transverse plane. The B_1 field effectively rotates the magnetization vector M into the transverse plane, where the angle of rotation (or correspondingly the net magnetization in the transverse plane) is dependent on the strength of the B_1 field and the duration of the RF pulse. For instance, a 90° pulse rotates the magnetization vector M fully into the transverse plane (Fig. 1.2).

When the B_1 field is turned off, the ^{1}H protons will tend to go back to the equilibrium by aligning with the B_0 field. During this process, energy is emitted at frequency ϖ_0. Furthermore, the net magnetization precesses about B_0. If a loop of wire is placed perpendicular to the transverse plane, these rotating magnetization vectors will induce a voltage by Faraday's law of induction. This induced voltage is called the free induction decay (FID) signal and is the MR signal that is measured for the creation of the image. The loop of wire, where the voltage is induced, is referred to as a receiver coil,

since it "receives" the MR signal. In CMR, a phased array of receiver coils is typically used, consisting of 5 or more elements (32 or as many as 128 elements may be used). This coil array is placed on the chest and back of the patient, and these multiple coil elements are used for improved signal-to-noise ratio or fast imaging techniques, as we will discuss.

Relaxation

Relaxation describes the process by which the magnetization vector goes back to equilibrium after the RF excitation has been turned off. The return of the magnetization vector in the longitudinal (z) direction is characterized by T_1 relaxation, also referred to as spin-lattice relaxation. The decay of the magnetization vector component in the transverse (x-y) plane is characterized by the T_2 relaxation, or the spin-spin relaxation.

T_1 Relaxation

After the application of a 90° RF pulse, all the magnetization, M_0, is in the transverse plane, resulting in a longitudinal magnetization (M_z) of 0. Once the RF pulse is turned off, the magnetization returns to the original M_0 value in an exponential growth process (Fig. 1.3):

$$M_z(t) = M_0\left(1 - e^{-t/T_1}\right), \tag{1.2}$$

where t is the time after the RF pulse. Thus, T_1 is the time it takes for the longitudinal magnetization to grow back to 63% of its original value after a 90° RF pulse. Also note that in this experiment, the magnetization grows back to 95% of its original value after three T_1 periods and 99% after five T_1 periods.

T_1 relaxation is referred to as spin-lattice relaxation, since the energy transfer is from the excited nuclei (spins) and their surroundings (lattice), and not to another nucleus. This energy is transferred to the lattice through molecular motion with a frequency that "matches" the resonant frequency. Thus, T_1 times depend on the particular tissue. Furthermore, at lower resonant frequencies (i.e., lower B_0), the probability of a molecular motion matching the resonant frequency is higher. Therefore, at lower field strengths, the spin-lattice energy transfer happens more readily, and T_1 is shorter. In the context of CMR, T_1 of the myocardium is around 1100 ms and 1200 ms at 1.5 T and 3.0 T, respectively; and T_1 of blood is around 1600 ms, etc. [2].

T_2 Relaxation

T_2 relaxation characterizes the decay of the transverse magnetization. After the application of a 90° RF pulse, all the magnetization is in the transverse plane, resulting in a transverse magnetization (M_{xy}) equal to M_0. Once the RF pulse is turned off, the transverse magnetization decays to 0 in an exponential process:

$$M_{xy}(t) = M_0 e^{-t/T_2}, \tag{1.3}$$

where t is the time after the RF pulse. Thus, T_2 is the time it takes for the transverse magnetization to decay to 37% of its original value.

T_2 relaxation depends on the process of spin-spin relaxation (Fig. 1.4). After the application of the RF pulse, and the rotation of the magnetization to the transverse plane, the transverse magnetization is coherent with a resonant frequency around ϖ_0. As time elapses, the nuclei (spins) start to transfer energy to nearby nuclei. These interactions lead to rotations and vibrations, causing the broadening of the resonant frequencies on the microscopic level. Macroscopically, this leads to the loss of the coherence of the transverse magnetization, also referred to as "dephasing." Eventually, the phases are dis-

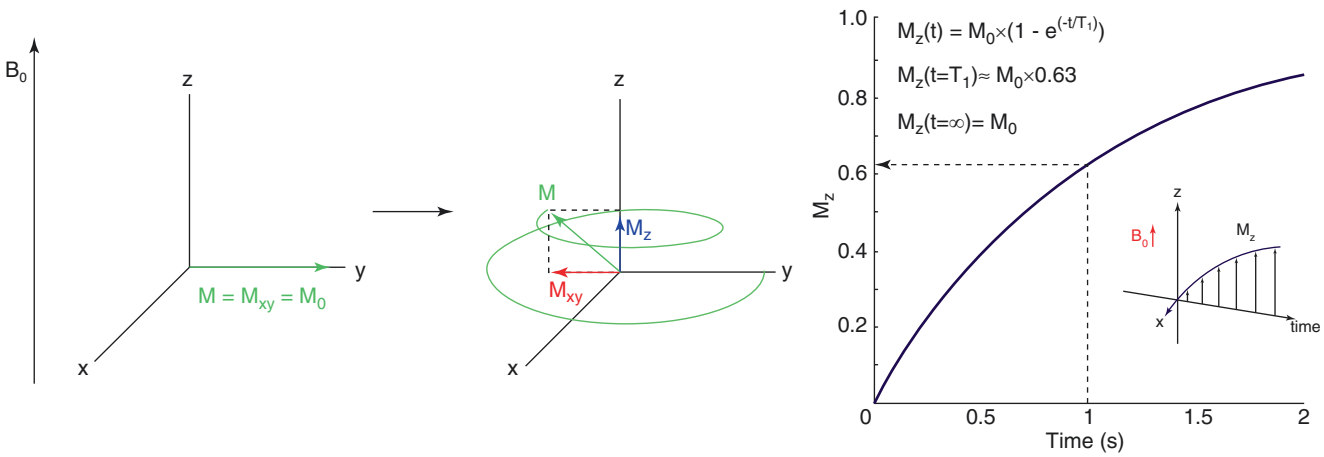

Fig. 1.3 T_1 relaxation is an exponential growth process that characterizes how the magnetization returns to its original M_0 value once the RF pulse is turned off. Specifically, T_1 is the time it takes for the longitudinal magnetization to grow back to 63% of its original value after a 90° RF pulse

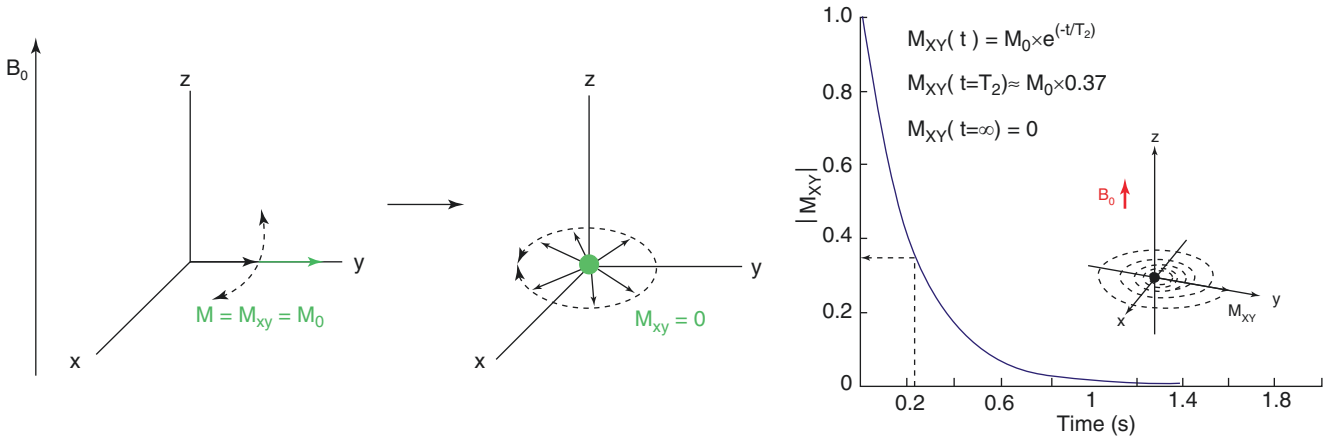

Fig. 1.4 T_2 relaxation is an exponential decay process that characterizes how the transverse magnetization decays to 0 as a result of spin-spin relaxation. While the transverse magnetization is coherent after the application of the RF pulse, as time elapses, the nuclei (spins) start to transfer energy to nearby nuclei. These interactions lead to rotations and vibrations, causing the broadening of the resonant frequencies on the microscopic level, leading to loss of coherence at the macroscopic level

ordered, creating no net magnetization. This dephasing process is irreversible. In general the dependence of T_2 on the field strength is not readily described as in T_1 relaxation.

Additional dephasing may occur due to nonuniformity in the main field B_0 or magnetic susceptibility in adjacent tissues. Both these effects will lead to different resonant frequencies that vary throughout the sample. These so-called "off-resonance" spins decrease the net transverse magnetization. Relaxation due to these effects, as well as the spin-spin T_2 relaxation, is referred to as T_2* decay. Thus $T_2^* \leq T_2$. While the spin-spin T_2 relaxation is irreversible, the additional effects leading to T_2* relaxation may be reversed, as we will discuss in Spin Echo Sequences subsection.

Spatial Encoding of the Image

In the previous section, we described how MR signal is measured using the voltage induced by the magnetic field. In order to generate the image, we first vary the magnetic field based on spatial locations, using magnetic field gradients. This creates a FID signal that is dependent on the spatially varying magnetic field. The next principle is to change the spatially varying field multiple times (through changing the magnetic field gradients) to create multiple FID signals with different spatial encoding. Then, these FID signals can be used to generate the image, as we will discuss in detail.

Gradients

Magnetic field gradients are the means to create spatial encoding in MRI. These are used in conjunction with the static magnetic field B_0 and typically lead to less than 1 % variation in the total magnetic field. Gradient coils are coils within the magnetic field that affect the magnetic field in the z-direction (B_z). By varying the gradients in x-, y-, and z-directions with gradient strengths G_x, G_y, and G_z, we create a magnetic field that changes linearly with the spatial location within the magnet:

$$B_z(x,,y,,z) = B_0 + G_x \cdot x + G_y \cdot y + G_z \cdot z, \qquad (1.4)$$

where the units of gradient strengths are typically in millitesla per meter ($mT \bullet m^{-1}$). This varying magnetic field leads to different precession frequencies for different locations, given by the Larmor equation in Eq. (1.1):

$$\varpi(x,,y,,z) = \frac{\gamma}{2\pi}\left(B_0 + G_x \cdot x + G_y \cdot y + G_z \cdot z\right). \qquad (1.5)$$

Thus protons at different spatial locations resonate at different frequencies depending on their location. By changing the gradient strength and repeating the measurements, we get information about that spatial location at a different frequency. We next discuss how an image is generated by repeating this process sufficiently many times. This process of taking a sequence of measurements with different spatial frequency information is also the reason for the relatively slow imaging time of MRI compared to other imaging modalities.

Slice Selection (Encoding in Z)

The first step for spatially localizing the signal in MRI is to localize the signal in one of the directions (which is taken as the z-direction without loss of generality). This is done by using the B_1 field to excite the protons in a selected slice, covering a subsection of the z-coordinates. The slice selec-

tion process has multiple components. First, a (slice selection) gradient is applied in the z-direction, causing the nuclei to precess at different frequencies, $\varpi(z) = \gamma/2\pi(B_0 + G_z \cdot z)$, based on their locations in z. In conjunction with this gradient, a frequency-selective RF pulse is applied, which excites a particular location and a particular slice thickness (Fig. 1.5).

The frequency-selective RF pulse is used to excite spins within a certain range of frequencies, specified by its central frequency (i.e., the location) and its bandwidth (i.e., the slice thickness), which is usually in the 1000–2000 Hz range. This is typically achieved by using a pulse shape called the "sinc" function:

$$B_1(t) = B_1 \cdot \frac{\sin(\pi t / T)}{\pi t / T}, \qquad (1.6)$$

where B_1 is the strength of the magnetic field and T is chosen to excite a band of frequencies, whose bandwidth corresponds to 1/T. Using such an RF pulse, only a slice (whose thickness is determined by the bandwidth) containing nuclei whose precessional frequencies are within that range is excited. The rest of the nuclei are unaffected since their precessional frequencies are not within the range of the RF pulse. The slice thickness can be varied by changing the gradient strength, G_z. High values of G_z lead to rapid changes of the precessional frequencies with spatial location, leading to smaller slice thicknesses.

We note that due to the finite value of slice thickness, nuclei within the same slice experience different gradient strengths. Thus at the end of the RF excitation, there is a variation of the phase of the spins within the slice, i.e., the spins are not all in phase. Thus, typically a "rephasing" gradient is applied following the slice selection process, which has the opposite magnitude and half the duration of the slice selection gradient (Fig. 1.6).

The rephasing gradient has an area (defined as the product of the magnitude of the gradient and its duration) that is half of the area of the slice selection gradient. This enforces the phases of the spins after the slice selection and rephasing process to match the phases of the spins before the application of any gradients.

In CMR, for the special case when no z gradient is utilized, the whole volume is excited, corresponding to an infinite slice thickness. This is referred to as a nonselective RF excitation and is used in most CMR pulses for contrast preparation.

While we have concentrated on the z-direction, in practice, multiple gradients may be turned on at the same time to specify a particular slice orientation. The slices acquired this way are oblique slices and are commonly used in CMR, though the principles of frequency-selective RF excitation remain the same.

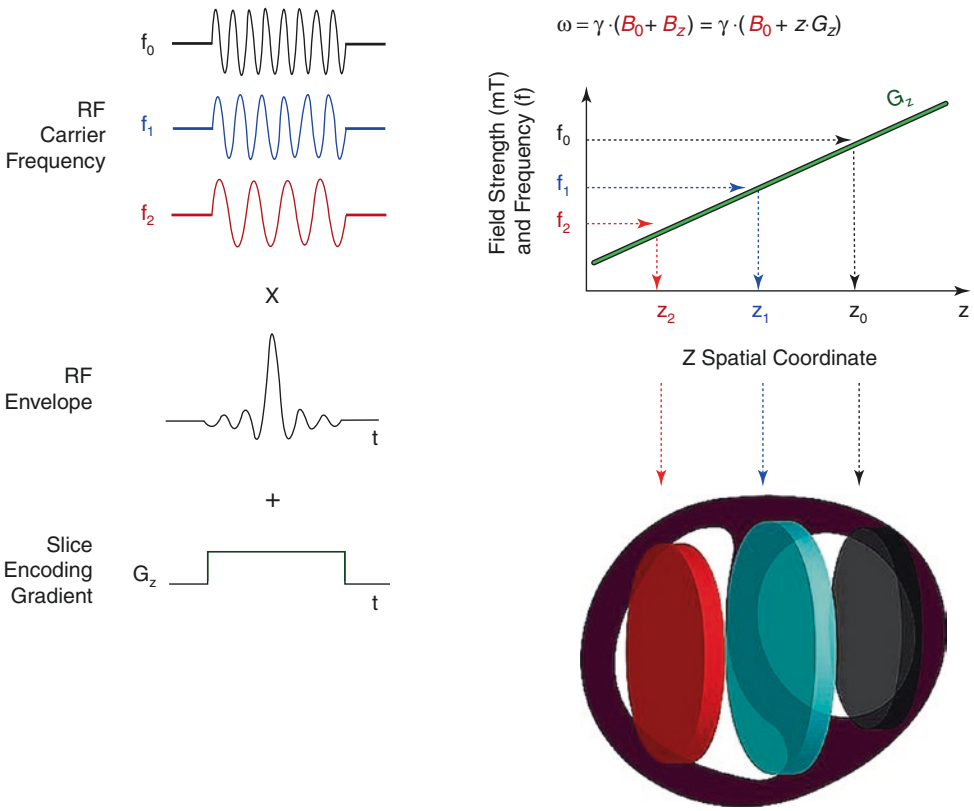

Fig. 1.5 In the slice selection process, a gradient is applied in the z-direction, causing the nuclei to precess at different frequencies, based on their locations in z. In conjunction with this gradient, a frequency-selective RF pulse is applied, which excites a particular location and a particular slice thickness. The frequency-selective RF pulse is used to excite spins within a certain range of frequencies, specified by its central frequency (i.e., the location) and its bandwidth (i.e., the slice thickness)

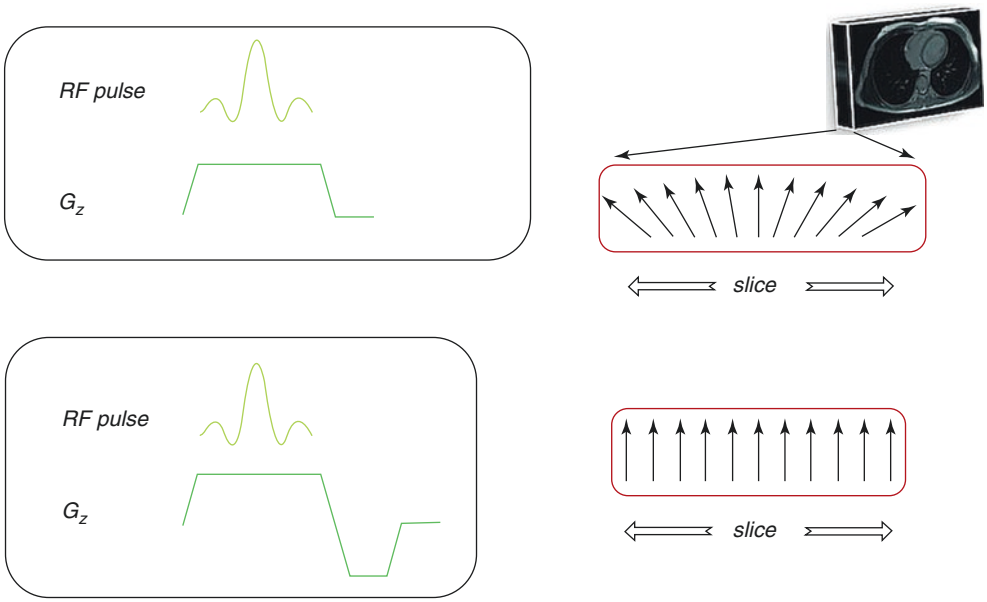

Fig. 1.6 Due to the non-zero slice thickness, nuclei within the same slice experience different gradient strengths, resulting in a variation of the spins within the slice that may lead to dephasing. Thus, a "rephasing" gradient is applied following the slice selection process, which has the opposite magnitude and half the duration of the slice selection gradient, enforcing the phases of the spins to match the phases of the spins before the application of any gradients

Frequency Encoding (Encoding in X)

Frequency encoding (or readout) concerns the portion during which the FID signal is detected. By turning on a gradient in the x-direction (without loss of generality) during the readout, the protons precess at different frequencies based on their spatial location in the x-direction. The signal that is being readout then becomes a superposition of these frequencies. As we will see, these different frequencies have a direct correspondence with the number of spins at a particular location through a relationship called the Fourier transform. Thus, frequency encoding essentially allows for localization of protons in the x-direction (Fig. 1.7).

We note that the FID signal, which is recorded during the readout, is a continuous signal in time. However, prior to storage and processing, this data is digitized by a process called "sampling." The Nyquist sampling theorem states that a continuous signal can be reconstructed from its uniformly spaced samples if the samples are taken at a rate that is twice the bandwidth of the signal. The bandwidth here is specified by the user as the receiver bandwidth, and the total range of frequencies in the image in the x-direction is twice this bandwidth. The user also specifies the field of view in the readout direction (FOV_x). Thus if N_x samples are taken, the resolution per pixel is given as $\Delta x = FOV_x / N_x$, whose units are in millimeters/pixel. Alternatively, one can look at the resolution in frequency, in units of Hz/pixel, as the total range of frequencies in the image divided by N_x.

Phase Encoding (Encoding in Y)

The spatial encoding in the remaining direction (y-direction) is achieved by a process called phase encoding, which is based on the fact that precision of nuclei is periodic. The phase-encoding step is performed after slice selection and prior to frequency encoding. After the slice has been selected, and G_z has been turned off, all the protons in the slice are precessing at frequency ϖ_0. When G_y is turned on, protons start to precess at different frequencies based on their y-locations according to $\varpi(z) = \gamma/2\pi(B_0 + G_y \cdot y)$. When G_y is turned off, the precession returns to its original frequency ϖ_0. But the differences in frequencies during the time G_y has been on are reflected as differences in phase. The amount of phase shift depends, in addition to the location along the y-direction, on the strength of the gradient, G_y, as well as its duration (Fig. 1.8).

Similar to the frequency encoding, a number of phase encodings are acquired to characterize the localization of protons in the y-direction. Thus N_y phase encodings are performed for a field of view of FOV_y, and the resolution per pixel is given as $\Delta y = FOV_y / N_y$. Unlike frequency encoding, which provides the localization in x-direction with one measurement, phase encoding is performed over N_y separate measurements. This leads to the slow acquisition time, since the entire frequency encoding is collected for each of these N_y phase encodings. The spatial localization in y-direction is achieved by varying the strength of G_y at each phase encoding, leading to a different phase accumulation. For instance, the first phase-encoding measurement may be taken with $G_y = 0$, leading to no phase difference in the y-direction, the next one with a small G_y, followed by doubling G_y, and so on. When the frequency encoding is performed following the phase-encoding process, x and y localization information are encoded together.

We finally note that the slice excitation, phase encoding, and frequency encoding are the basic building blocks of a two-dimensional acquisition. For three-dimensional acquisition, instead of one fixed slice excitation, one also performs phase encoding in the z-direction, taking N_y measurements

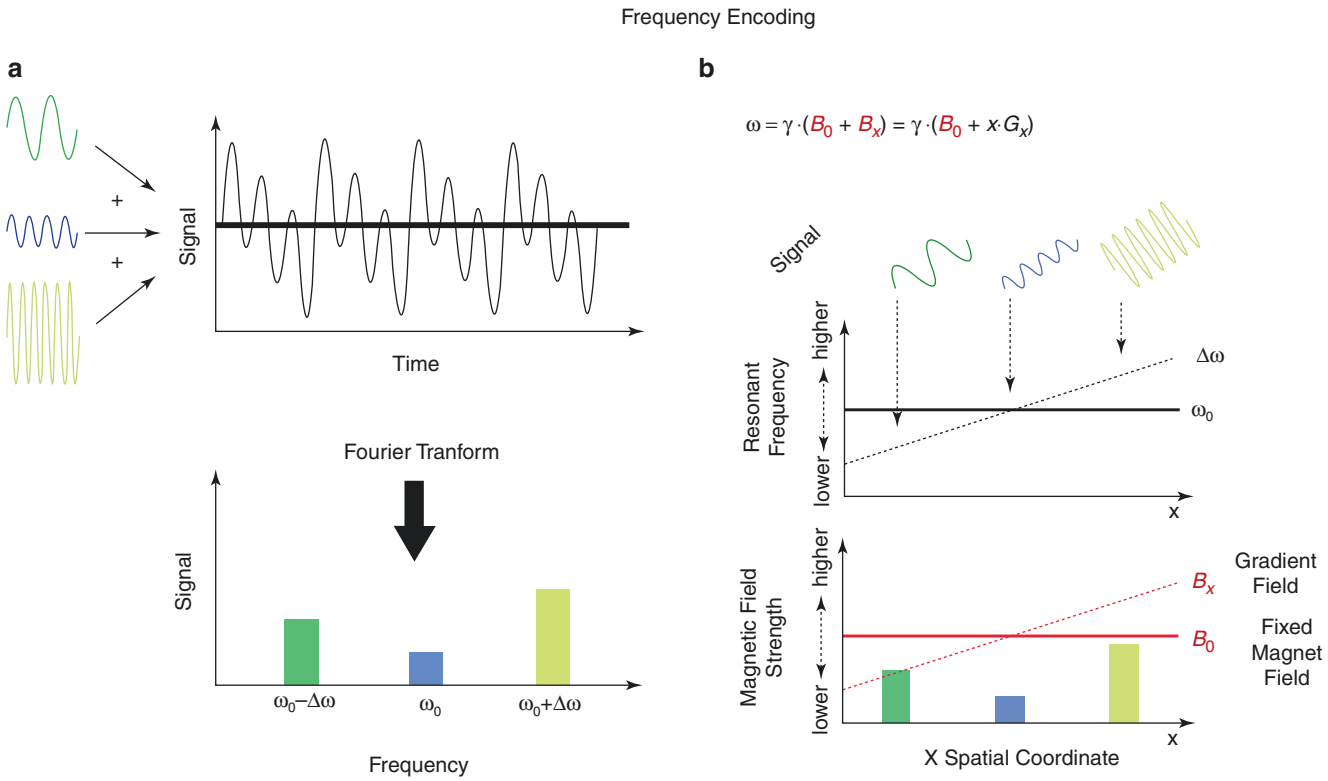

Fig. 1.7 When the gradient in the x-direction is turned on during the readout, the protons precess at different frequencies based on their spatial location in the x-direction. The signal that is being readout then becomes a superposition of these frequencies. Thus, frequency encoding essentially allows for localization of protons in the x-direction

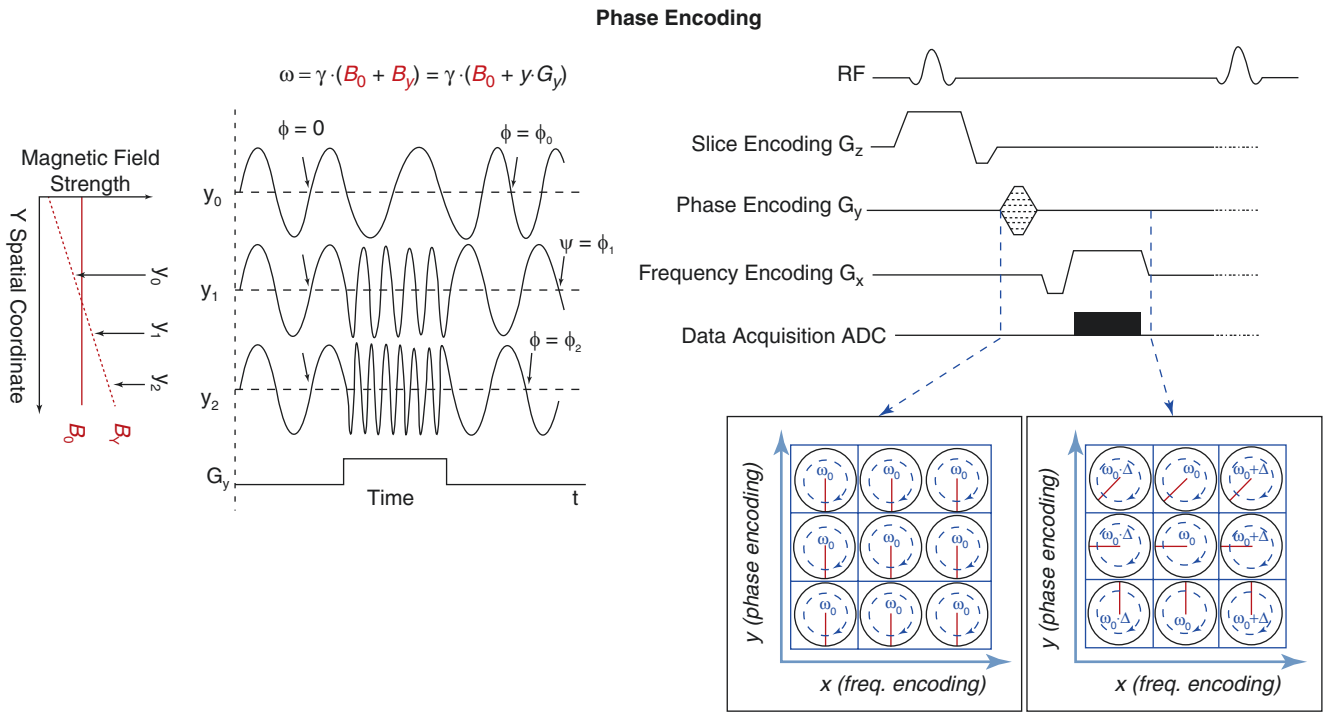

Fig. 1.8 The spatial encoding in the y-direction is achieved by phase encoding, which is performed after slice selection and prior to frequency encoding. After the slice selection, all the protons in the slice are precessing at frequency. When the y gradient, G_y, is turned on, protons start to precess at different frequencies based on their y-locations. When G_y is turned off, the precession returns to its original frequency, but the differences in frequencies during the time G_y has been on are reflected as differences in phase. The amount of phase shift depends on the strength of the gradient, G_y, as well as its duration

in y-direction and N_z measurements in z-direction, for a total of $N_y \bullet N_z$ measurements, which lengthens the scan duration accordingly.

K-Space and Image Formation

Raw K-Space Data, the Fourier Transform, and Image Formation

As we saw, each of the MRI measurements taken during a scan includes information from all the spins, encoded based on their spatial locations. These data can be viewed as points in k-space (Fig. 1.9). k-space corresponds to the spatial frequency content of the image, which is also mathematically represented as the Fourier transform of the image data. For a two-dimensional acquisition, the point (c_x, k_y) in the k-space corresponds to the acquired signal determined by the x and y gradients as:

$$k_x = \gamma\left(G_x \cdot t_x\right)$$
$$k_y = \gamma\left(G_y \cdot t_y\right), \tag{1.7}$$

where t_x and t_y are the cumulative durations in which the x and y gradients have been active, respectively. As k_x and k_y depict spatial frequencies, they have units of Hz/m.

The k-space formalism allows us to view different MRI readouts as a "traversal" across the k-space. Each phase-encoding step corresponds to a move along the k_y-axis (the y-axis of the two-dimensional k-space) to a desired value depending on the strength of G_y and duration of t_y. Then all the desired k_x points at this k_y location (or the k-space line) are acquired during the frequency-encoding step. At the subsequent phase-encoding step, a k-space line for another k_y value is acquired. This process is repeated until the k-space grid is filled (including both the positive and negative values for a given maximum frequency) (See Fig. 1.10).

Once the k-space is filled, the image is generated by applying a mathematical tool called Fourier transform on the k-space data (Fig. 1.11). Fourier transform is an operation that allows an image to be decomposed into its spatial frequency content or vice versa. Thus, once the k-space is filled, i.e., contains all the necessary spatial frequency content, the underlying image is generated using the Fourier transform. In particular, if all the acquired k-space points are uniformly separated (i.e., they lie on a Cartesian grid), a computationally efficient version of the Fourier transform, called the fast Fourier transform, can be used, significantly reducing the processing time to generate an image.

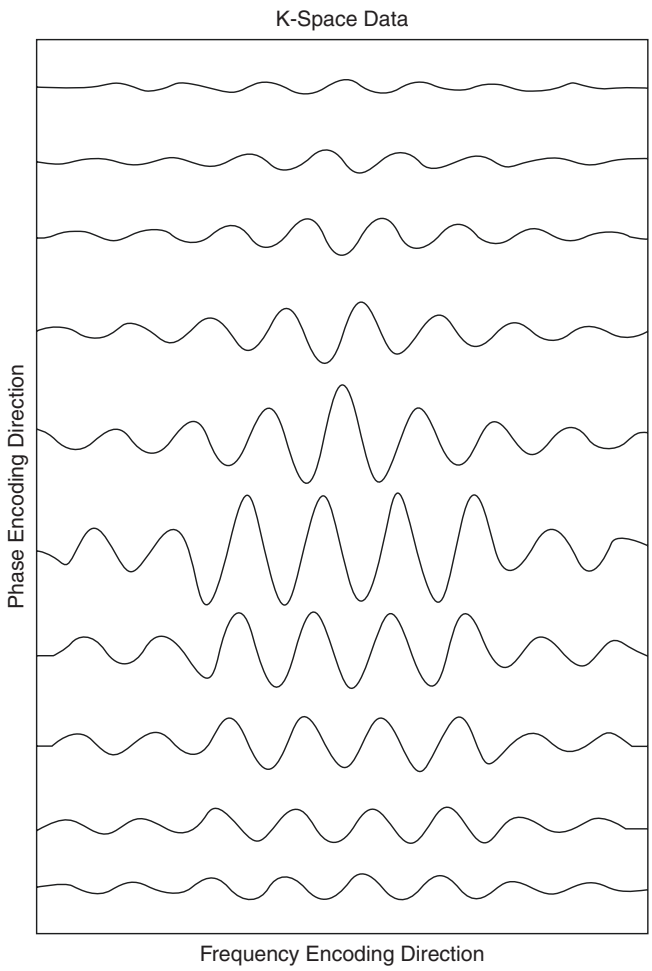

Fig. 1.9 MRI measurements taken during a scan includes information from all the spins, encoded based on their spatial locations. The signal that is being read out then becomes a combination of frequencies dependent on the spatial locations. These data can be viewed as part of the k-space, which represents the spatial frequency domain

K-Space Sampling and Imaging Parameters

In the previous subsection, we viewed MRI measurements as points acquired in the k-space. More rigorously, since the k-space is the space of spatial frequency content of an image, it is continuous by nature and not discretized to points. Thus, the MRI measurements correspond to sampling of the continuous k-space. When this process works and how it is affected by the imaging parameters can be explained by the Nyquist sampling theorem.

According to the Nyquist sampling theorem, the k-space needs to be sampled in a way such that the samples are uniformly spaced with a distance determined by its field of view (or equivalently its spatial extent) and covering the range of spatial frequencies required for a specified spatial resolution. All these requirements are satisfied by creating a Cartesian grid on which points are spaced with a distance Δk_x (or Δk_y in the y-direction) and the k-space is sampled between spa-

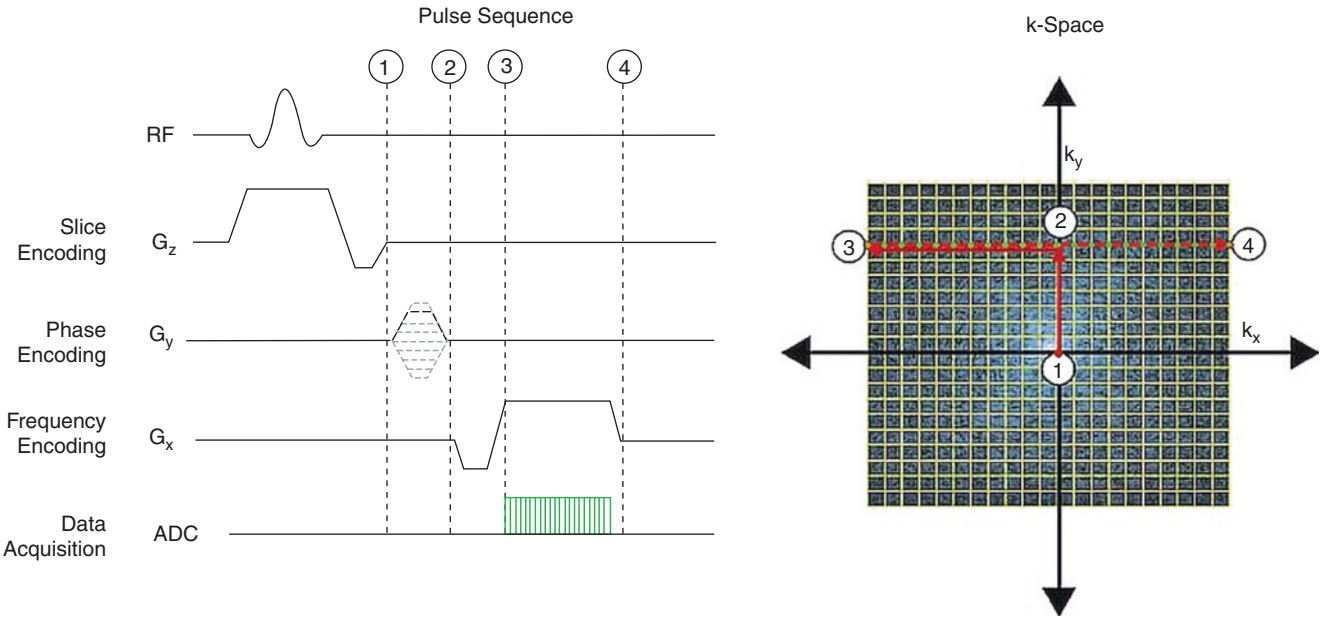

Fig. 1.10 The k-space formalism allows us to view different MRI readouts as a "traversal" in the k-space. The phase-encoding step corresponds to a move along the k_y-axis (the y-axis of the two-dimensional k-space) to a desired value depending on the strength and duration of G_y as depicted in Step 2. Then all the desired k_x points at this k_y location (or the k-space line) are acquired during the frequency-encoding step, as described in Steps 3 and 4. At the subsequent phase-encoding step, a k-space line for another k_y value is acquired

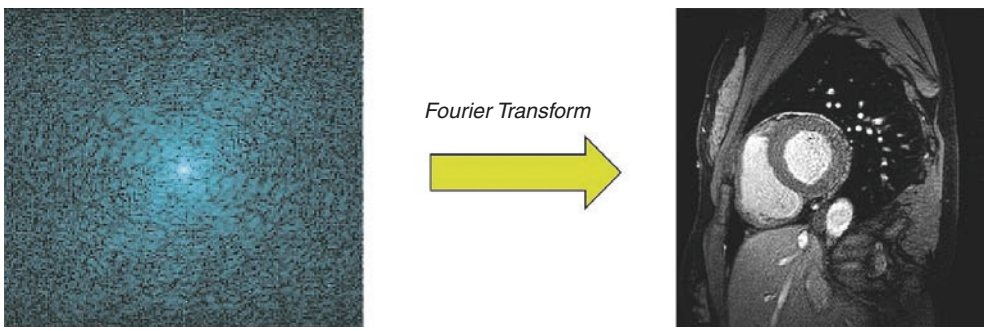

Fig. 1.11 Once the k-space is filled, the image is generated by applying a mathematical tool called Fourier transform on the k-space data. Fourier transform is an operation that allows an image to be decomposed into its spatial frequency content or vice versa

tial frequencies $-k_x^{max}$ and k_x^{max} (or $-k_y^{max}$ and k_y^{max} in the y-direction), where

$$\Delta k_x = \frac{1}{FOV_x}, \qquad \Delta k_y = \frac{1}{FOV_y}, \qquad k_x^{max} = \frac{1}{\Delta x}, \qquad k_y^{max} = \frac{1}{\Delta y} \tag{1.8}$$

with Δx and Δy the specified spatial resolutions per pixel in x and y-directions, respectively. Hence each k-space measurement in such an acquisition corresponds to a point on this Cartesian grid. In most CMR exams, Δx is chosen to be equal to Δy, while FOV_x and FOV_y are adjusted for the appropriate coverage. In terms of the description we used in the previous section, N_x and N_y, the number of frequency and phase encodings, respectively (or the number of pixels in x and y-directions, respectively), represents the number of samples acquired in the k-space along the k_x and k_y directions, respectively, with $N_x = FOV_x/\Delta x$ and $N_y = FOV_y/\Delta y$ (and for a three-dimensional acquisition $N_z = FOV_z/\Delta z$) (See Fig. 1.12).

We also note that in reality, the underlying image has an infinitely fine spatial resolution, but the user specifies the resolution required for the CMR exam. Thus, the same scan can be repeated with a 2 mm resolution or a 1 mm resolution, with the latter providing finer spatial details. However, that also means k_y^{max} is higher, implying a higher number of phase encodings N_y for the same field of view, which results in a (twice) longer scan time. In CMR, the trade-off between the resolution, field of view, and scan time needs to be carefully optimized, since we also need to compensate for respiratory and cardiac motions. Hence, methods for reducing scan time without creating significant artifacts are highly desirable in CMR fast imaging.

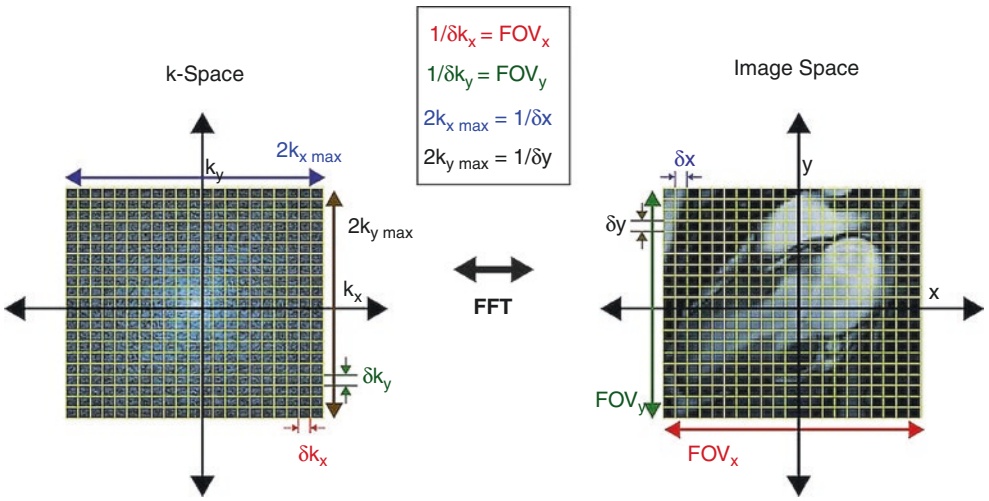

Fig. 1.12 For a fully sampled Cartesian acquisition, the k-space is sampled uniformly on a Cartesian grid, on which points are spaced with a distance Δk_x (or Δk_y in the y-direction) and the k-space is sampled between spatial frequencies $-k_x^{max}$ and k_x^{max} (or $-k_y^{max}$ and k_y^{max} in the y-direction). These values are related to the field of view and resolution in the spatial domain, as follows: $\Delta k_x = 1/FOV_x$ (and $\Delta k_y = 1/FOV_y$) and $k_x^{max} = 1/\Delta x$ (and $k_y^{max} = 1/\Delta y$), where Δx and Δy are the spatial resolutions in x and y-directions, respectively. Hence each k-space measurement in such an acquisition corresponds to a point on this Cartesian grid

Partial Fourier Imaging

The underlying hypothesis for partial Fourier imaging to reduce the number of acquired phase-encode lines, N_y, relies on the Hermitian symmetry property of the Fourier transform and thus the k-space. For real images, the k-space point at (k_x, k_y) has the same real and negative imaginary component as the point at $(-k_x, -k_y)$. Thus for a real image, acquiring only positive k_y values suffices, since the negative ones can be filled by the Hermitian symmetry [3]. In reality, the underlying image is not real. However, this symmetry can be well-approximated using reconstruction techniques that utilize a few additional negative k_y lines (usually 60–65% of the k-space is acquired). This allows the reconstruction of an image with a given field of view and spatial resolution but less phase-encode lines and thus less scan time. The disadvantages of partial Fourier techniques are a loss of signal-to-noise ratio due to the reduced number of measurements and the limited acceleration in scan time.

Parallel Imaging

Parallel imaging is the clinically most widely used method for reducing the imaging time in CMR. This technique uses the information among the multiple receivers in phased array coils. Each element of a phased array coil acquires its own k-space, which can be used to produce a coil image. Each of these coil images is a spatially modulated version of the underlying image. In parallel imaging, part of the k-space is acquired in each coil, but this spatial modulation information from each of the coils is used to generate a final image. In clinically available implementations, for an acceleration rate of R, every R^{th} k_y line is sampled. This translates to a reduction of FOV_y by a factor of R. Then the missing k-space information is filled by processing either in the image domain or in the k-space itself.

SENSE (sensitivity encoding) is an image domain-based approach for parallel imaging [4–6]. In this method, for each partially sampled k-space, the corresponding coil image is calculated. An acceleration rate of R by sampling very R^{th} line in the k-space results in a foldover artifact in the image domain. For instance, for R = 2, the top half of the image is folded back onto the bottom part (assuming the y-direction lies in this direction). Since each coil "sees" differently modulated views of the underlying image, each of these aliased images is different based on how the coils affect the underlying image. This latter information, called the coil sensitivities, can be acquired from a separate (or interleaved) calibration scan. Using the coil sensitivities and the multiple different aliased coil images, the final image can be "unfolded" to remove the foldover artifacts. Thus, this technique produces one final image combining all the information from the multiple receiver coils.

The second group of techniques relies on processing in the k-space. The main idea is that the missing k-space lines can be estimated using a weighted combination of the acquired data, where the weights are chosen based on the coil sensitivities. This forms the basis of the first parallel imaging technique, SMASH [7–9]. Improvements to SMASH have been proposed so that the coil sensitivities do not need to be calculated from a separate acquisition. Instead the combination weights are estimated in the same scan. In GRAPPA, these weights are estimated using autocalibration

data from a few additional lines acquired without any gaps in the central part of the k-space [10]. These techniques produce one image per each coil element after the reconstruction stage, which are then combined to generate the final image displayed to the user.

Theoretically, the acceleration rate is less than or equal to the number of coil elements. In reality, the acceleration rates are always less than the number of coil elements. In CMR, commonly a 2-fold acceleration is achieved with 5-channel cardiac coils, and a 4-fold acceleration is achieved with 32-channel cardiac coils. Parallel imaging leads to a loss of signal-to-noise ratio due to the reduced number of measurements but also is due to the coil geometry. Since coils have overlapping coverage in terms of their receiver characteristics, based on the placement of coils and the acceleration rates, there are local variations in the signal-to-noise ratio. This can be analytically characterized by evaluating the geometry factor (or g-factor).

Non-Cartesian Trajectories

So far we have concentrated on k-space sampling using a Cartesian grid. However, it is possible to traverse the k-space in non-Cartesian trajectories by using different combinations and durations of x and y gradients. Two types of non-Cartesian trajectories are clinically available in CMR: radial [11–14] and spiral [15–20] (Fig. 1.13). In both these trajectories, the distinction between phase- and frequency-encoding directions is not made unlike Cartesian imaging.

In radial imaging, coordinated gradient switching in both in-plane (x and y) directions occurs between readouts. The readout is then performed along a straight line going through the center of k-space. Each readout is then rotated by a predefined angle, leading to a k-space trajectory reminiscent of computed tomography. Historically, radial imaging was used in the very first MRI images. Radial imaging has advantages: (1) Angular undersampling by sampling every R^{th} angle leads to incoherent spreading of aliasing artifacts, unlike the Cartesian undersampling used in parallel imaging that leads to distinct foldover artifacts. Thus, faster acquisitions are possible using angular undersampling. (2) Each radial readout goes through the center of k-space, which leads to motion insensitivity, since motion is averaged out by the oversampling of this central region. However, the reconstruction of radial is more complicated than Cartesian imaging, since the fast Fourier transform cannot be used. Typically, the radial data is "re-gridded" onto a Cartesian grid and then processed, which leads to longer reconstruction time. Due to the nature of the radial imaging, more k-space readouts are required to sample the edges of k-space at the same rate as Cartesian imaging. Since this imaging technique is often used for fast

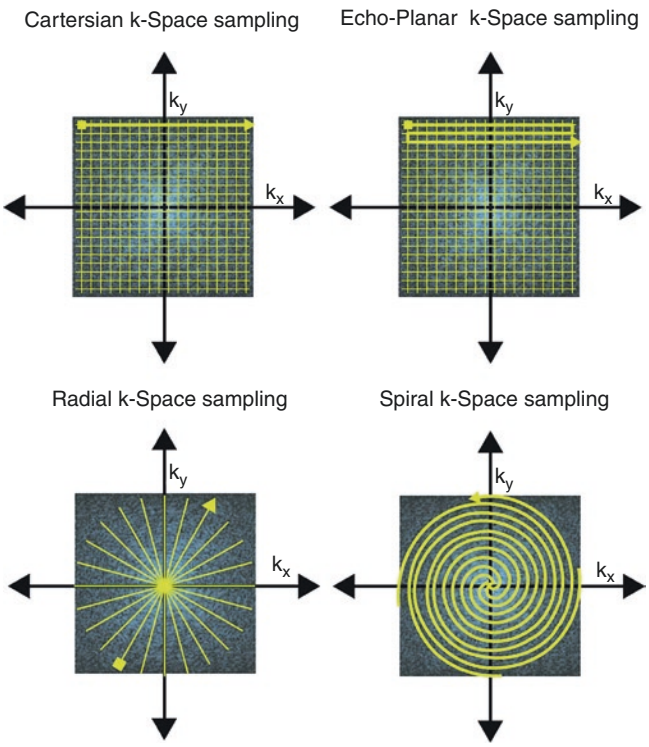

Fig. 1.13 K-space traversals, other than the standard Cartesian k-space sampling, are possible in MRI. In (18) k-space sampling, multiple k-space lines are read out after a single RF excitation. In non-Cartesian trajectories, such as radial and spiral imaging, the G_x and G_y gradients are manipulated simultaneously to allow for the traversal of the k-space off the Cartesian grid

imaging, the edges of the k-space are not finely sampled, which may lead to blurring artifacts.

In spiral imaging, more data is collected after a single RF pulse, by sampling the k-space in a spiral pattern (in k_x-k_y plane). Often, more than one spiral interleaf is required to sample the k-space sufficiently. Spiral imaging has high SNR efficiency and more efficient filling of k-space. It is also well-suited for fast imaging, since the aliasing artifacts associated with undersampling are incoherent. However, due to the long readouts, errors can accumulate making spiral imaging susceptible to off-resonance effects, chemical shifts, and trajectory errors, which may lead to blurring artifacts. Reconstruction of spiral imaging also requires similar processing as radial imaging.

Compressed Sensing

Compressed sensing (CS) is as an alternative fast imaging technique that exploits the compressibility of MR images [21, 22]. In addition to compressibility, CS requires an undersampling pattern that leads to incoherent aliasing artifacts. This can be achieved by random undersampling of k-space data in the phase-encode direction(s) for Cartesian

acquisitions or by undersampling radial and spiral trajectories. CS reconstruction removes incoherent aliasing artifacts by an iterative reconstruction that alternates between enforcing consistency with acquired data and removal of artifacts using compressibility. Information from multiple receiver coils can be incorporated into data consistency to enhance this technique in a manner similar to parallel imaging. CS has advantages: (1) The achievable acceleration rates are not limited by the number of coil elements, and (2) due to the use of compressibility, its noise properties are more favorable than parallel imaging. However, CS reconstruction is computationally expensive. Furthermore, during the reconstruction, parameters need to be set to give a certain weight to the compressibility of data. In cases when this weight is too high, or in case the compressibility assumes a model that mismatches the underlying data, this may lead to blurring artifacts. There has been a trend to learn the compressibility information from the data, which has been shown to improve the reconstruction quality. This technique is not widely clinically available.

CMR Pulse Sequences

Pulse sequences provide the means to obtain an MR image and contain the hardware instructions (types of radiofrequency pulses, timing of gradients, etc.). These instructions are specified by the operator using parameters, such as field of view or other parameters that we will see. The ranges of parameters for these values are limited by implementation (e.g., the duration of the RF pulse) or scanner hardware (e.g., maximum gradient amplitude) or physiological considerations (e.g., heart rate).

In order to specify the steps performed by the MR scanner hardware, pulse sequence diagrams are commonly utilized. Pulse sequence diagrams provide a schematic representation of these steps across time (specified in the left-right direction). In its most basic form, four lines are required to represent the RF transmitter and gradients in the slice, phase, and readout directions. Analog-to-digital conversion may also be included on a fifth line. If a particular component is not utilized at a given time, it is represented by a flat (zero) line. The exact timings, gradient amplitudes, and other details are often not included in such diagrams that are meant to provide an overview of the pulse sequence.

Spin Echo Sequences

Spin echo sequences aim to reverse some of the T_2* dephasing caused by B_0 field inhomogeneity, as mentioned in the Relaxation subsection. It consists of a 90° RF pulse, followed by a delay of duration t, and a 180° RF pulse, followed by a second time delay of t. The initial pulse rotates the magnetization into the transverse plane. During the first delay of t, proton dephasing follows a T_2* relaxation process. Then the 180° RF pulse reverses the phases of the protons. After a duration of t, the protons rephase and gain their coherence in the transverse plane. This creates a *spin echo*, which is detected at the receiver coils (see Fig. 1.14). The process is analogous to runners of different speeds starting at the same point. After running for a duration of t, they will be at different positions (out of phase). If, at this point, they turn around (180° RF pulse), and run for a time of t in the opposite direction, they will end up at the same starting location together.

For a given slice, multiple excitations are performed to acquire the full k-space with appropriate gradient encoding. The time between subsequent excitation RF pulses is called the repetition time (TR). The time from the excitation RF pulse to the spin echo is called the echo time (TE). Both TR and TE can be specified by the operator. In a spin echo sequence, a short TR and short TE leads to a T_1 weighting, whereas a longer TR and long TE lead to T_2 weighting. If all the images are acquired after full magnetization recovery (approximately $5T_1$ values), this leads to a long TR (~6–8 s for CMR), leading to a slow data collection process.

A variant of the spin echo sequence is the fast spin echo (FSE) or turbo spin echo sequence (TSE), which is important for CMR applications. In this technique, multiple 180° RF pulses are applied following a single RF excitation pulse for a given slice. When these 180° pulses are spaced a duration of 2 t apart, they create spin echoes that are t away from each 180° pulse. A different phase-encoding gradient is applied between each 180° pulse, providing multiple k_y lines to be acquired after a single RF excitation (Fig. 1.14b). For CMR, typically 16–64 echoes (called an echo train) are collected following a single RF excitation. The acquisition of such data still requires a large amount of time, which is a main disadvantage. Thus, this method is typically utilized in phases of the cardiac cycle with limited motion, such as diastole. FSE/TSE has high signal-to-noise ratio and inherent T_2 contrast. Furthermore, since the central k-space line is important in determining the overall contrast, by acquiring this line at a specific time after the RF pulse (called the effective TE), one can get a desired T_2 weighting (with longer effective TE creating more T_2 contrast). These techniques are used in CMR for tissue characterization and to depict the vascular wall and adjacent tissues.

Gradient Echo Sequences

Gradient echo sequences use a gradient reversal for refocusing the protons, in contrast to the 180° pulse in spin echo sequences. The use of gradients creates dephasing of protons. By applying a gradient of the same duration but oppo-

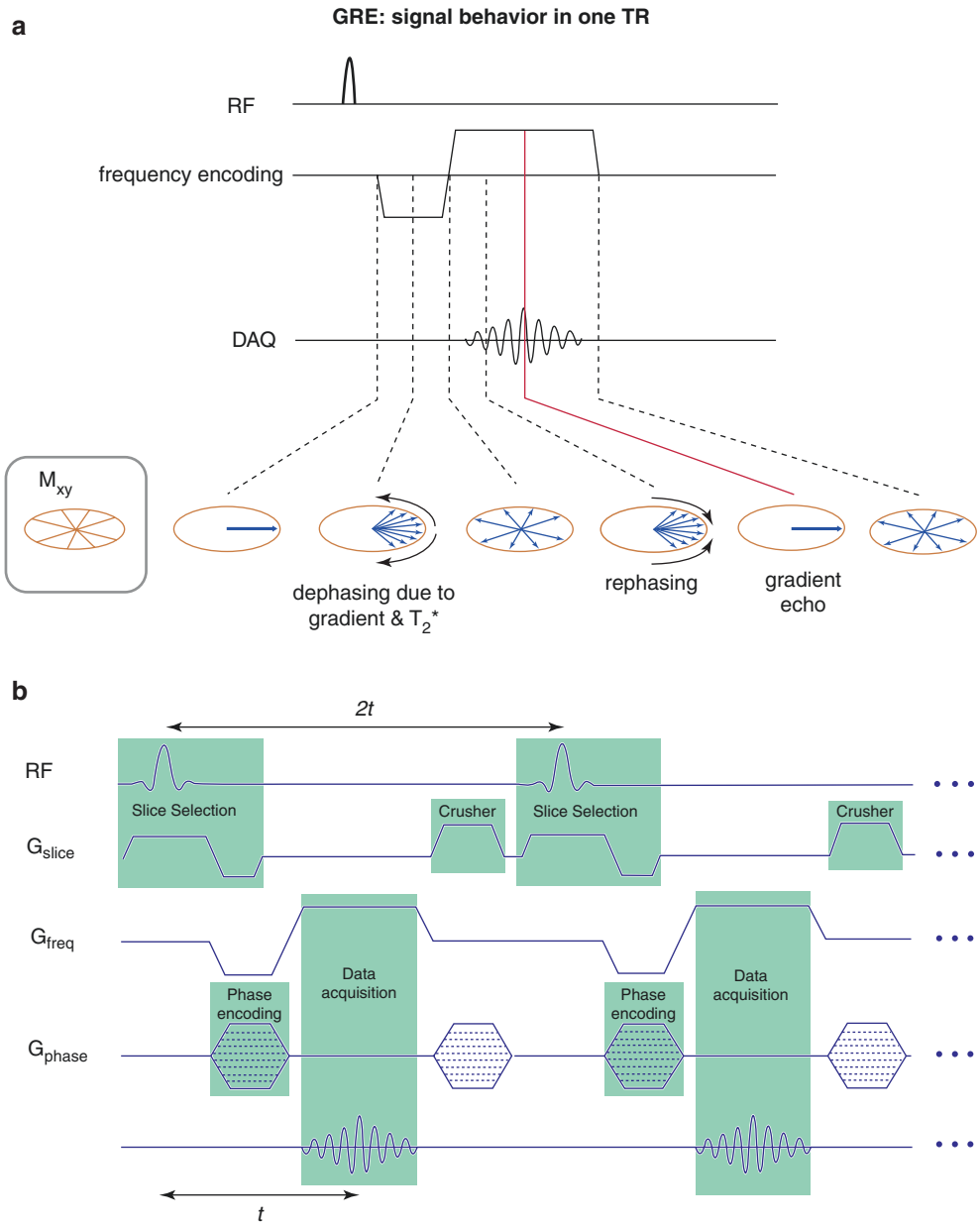

Fig. 1.14 (**a**) Gradient echo sequences use a gradient reversal for refocusing the protons. The use of gradients creates dephasing of protons in the transverse plane. By applying a gradient of the same duration but opposite magnitude, this dephasing can be reversed, creating a gradient echo. Note that gradient echo images have a T_2* weighting, determined by the echo time. (**b**) Gradient-recalled echo (GRE) sequence is commonly used in CMR. Following the acquisition of the FID signal, GRE uses a crusher or spoiler gradient to dephase the remaining transverse magnetization. Hence, only the longitudinal magnetization at this point corresponds to the FID signal after the next excitation pulse (in other words for every TR). Spoiling is performed by high-amplitude gradient pulses to remove the coherence of the transverse magnetization. An acquisition with a symmetric echo is depicted, where the gradient echo is generated at t and the repetition time is 2 t

site magnitude, this dephasing can be reversed, creating a gradient echo. Unlike spin echo imaging, gradient echo images have a T_2* weighting, determined by the TE. If the TE is very short (TE < 3 ms), this decay is within an acceptable range [23]. The incentive for using gradient echo imaging in CMR is that it allows for imaging with a very short TR. For a short TR, one cannot use the 180° pulse of spin echo sequences for refocusing.

Gradient-Recalled Echo

In gradient echo imaging, to image with a short TR, the initial RF pulse is not a 90° pulse but a pulse with a smaller *flip angle*, α. These small flip angles improve signal-to-noise ratio in gradient echo imaging. The intuitive explanation for this phenomenon is that with a large α, although more signal is on the transverse plane, the longitudinal magnetization is small and does not recover within a short TR, leading to a much smaller signal for subsequent echoes. Lower α reduces the detectable signal but allows for more longitudinal magnetization to be preserved for subsequent echoes. In CMR, α in the range of 5–25° is commonly used for gradient echo imaging.

One of the most commonly used gradient echo imaging techniques in CMR is the gradient-recalled echo (GRE) sequence. Following the acquisition of the gradient echo signal, GRE uses a crusher or spoiler gradient to dephase the remaining transverse magnetization. Hence, only the longitudinal magnetization at this point corresponds to the FID

signal after the next excitation pulse (in other words for every TR). Spoiling is performed by high-amplitude gradient pulses to remove the coherence of the transverse magnetization. As described previously, GRE images have T_2* weighting, but for the TE used in CMR (1–3 ms), this is often negligible. Thus, the main weighting comes from the T_1 regrowth during the TR and the transverse component of magnetization following the RF pulse with flip angle α, creating a T_1 weighting. Compared to spin echo imaging, GRE imaging has lower overall signal level due to short TR and small α, and it is more sensitive to metal implants due to the T_2* effects. We also note that in other MRI applications, different TR and TE combinations may be used to generate proton density-weighted images (long TR, short TE), T_2*-weighted images (long TR, long TE) or T_1-weighted images (short TR and short TE), although the last one is the one commonly used in CMR.

Balanced Steady-State Free Precession

Balanced steady-state free precession (bSSFP) is a gradient echo sequence, which is related to the GRE sequence but has a fundamental difference in the way the transverse magnetization is utilized. bSSFP sequences use a TR shorter than the T_1 and T_2 relaxation times. Unlike GRE sequences, in a bSSFP sequences, spins are rephased in all directions (x, y, z) to zero phase after the acquisition in each TR (i.e., *balanced*), and no spoilers or crushers are utilized. This allows for the spins to be coherent, and the transverse magnetization is reused in the next TR instead of being spoiled (Fig. 1.15). Also by choosing TR shorter than T_2, the transverse signal does not dephase completely. Then the spins are flipped around the y-axis by applying RF pulses with alternating phases to reuse the transverse and longitudinal magnetization at every TR. The flip angles are typically chosen in the range of 45–75° for the TR used in CMR, in order to allow for sufficient transverse components.

In CMR, this process is used to create an echo after the RF pulse, which has a contrast weighting that depends on both T_1 and T_2 (see Fig. 1.16 for images showing GRE vs. SSFP) [24]. Before imaging, this process of refocusing the transverse and longitudinal magnetization is applied multiple times until the magnetization reaches a steady-state value both in longitudinal and transverse components.

bSSFP sequences are used for imaging ventricular function in almost all CMR sequences at 1.5 T. Since this technique relies on rephasing of the magnetization, off-resonance and field inhomogeneity effects are important, as they may lead to dephasing of the magnetization. Thus, application of bSSFP techniques at higher field strengths (e.g., 3 T or 7 T) is challenging due to off-resonance artifacts and at the very least requires careful B_0 shimming.

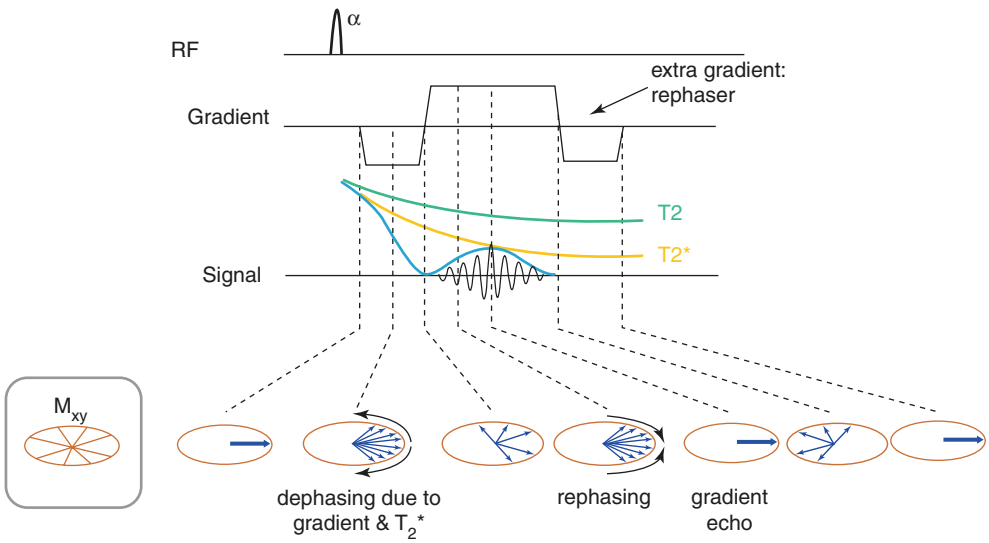

Fig. 1.15 Balanced steady-state free precession (bSSFP) sequence is a gradient echo sequence that begins similarly to the GRE sequence but uses a symmetric rephasing gradient after signal acquisition. The rephasing gradient creates a coherent transverse magnetization that can be used in the next repetition (TR). Because the transverse magnetization is recovered, no spoiler gradient is used, unlike in GRE

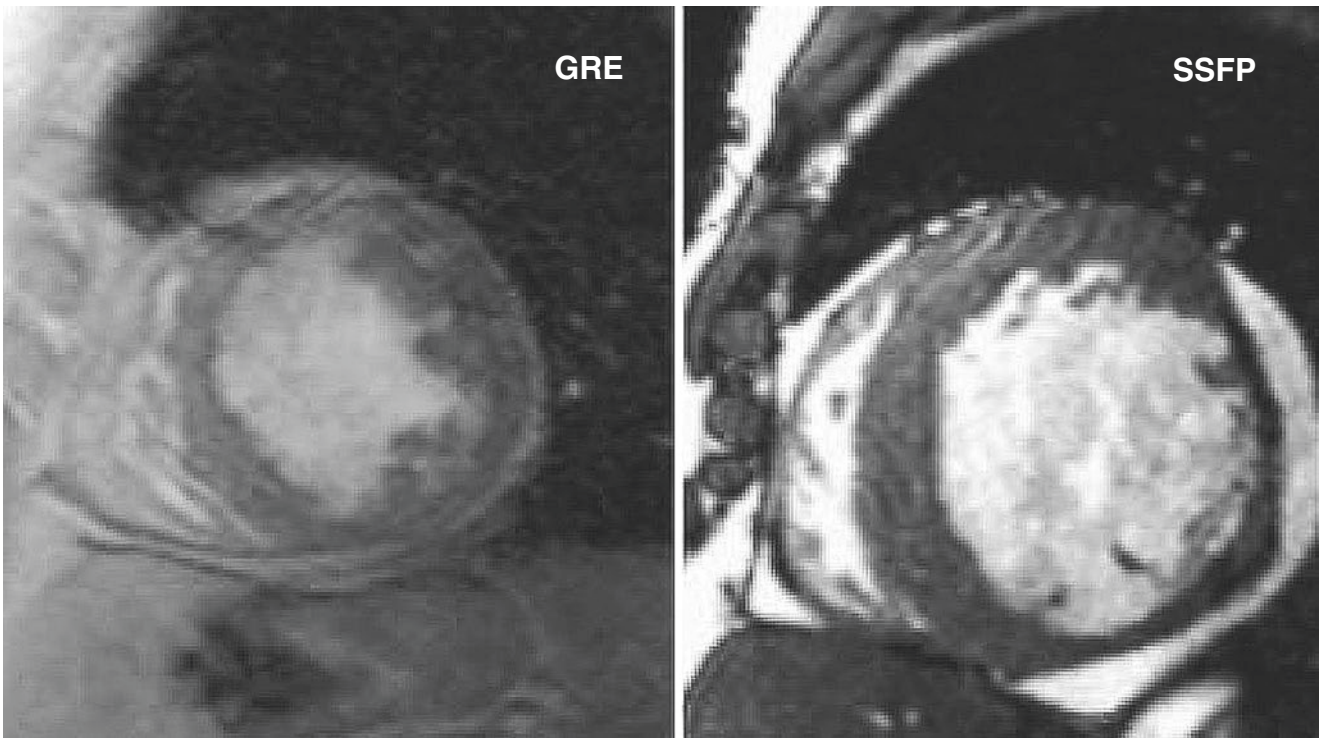

Fig. 1.16 Unlike GRE sequences, in a balanced steady-state free precession (bSSFP) sequence, spins are rephrased in all directions (x, y, z) to zero phase after the acquisition in each TR (i.e., balanced), and no spoilers or crushers are utilized. Thus, the spins are allowed to be coherent, and the transverse magnetization is reused in the next TR instead of being spoiled. In CMR, this process is used to create an echo after the RF pulse, which has a contrast weighting that depends on both T_1 and T_2, as opposed to the T_1-weighted CMR images using GRE

References

1. Lauterbur PC. Image formation by induced local interactions. Examples employing nuclear magnetic resonance. Clin Orthop Relat Res. 1973;1989(244):3–6.
2. Sharma P, Socolow J, Patel S, Pettigrew RI, Oshinski JN. Effect of Gd-DTPA-BMA on blood and myocardial T1 at 1.5T and 3T in humans. J Magn Reson Imaging. 2006;23(3):323–30.
3. MacFall JR, Pelc NJ, Vavrek RM. Correction of spatially dependent phase shifts for partial Fourier imaging. Magn Reson Imaging. 1988;6(2):143–55.
4. Hunold P, Maderwald S, Ladd ME, Jellus V, Barkhausen J. Parallel acquisition techniques in cardiac cine magnetic resonance imaging using TrueFISP sequences: comparison of image quality and artifacts. J Magn Reson Imaging. 2004;20(3):506–11.
5. Tsao J, Boesiger P, Pruessmann KP. K-t BLAST and k-t SENSE: dynamic MRI with high frame rate exploiting spatiotemporal correlations. Magn Reson Med. 2003;50(5):1031–42.
6. Pruessmann KP, Weiger M, Scheidegger MB, Boesiger P. SENSE: sensitivity encoding for fast MRI. Magn Reson Med. 1999;42(5):952–62.
7. Bydder M, Larkman DJ, Hajnal JV. Generalized SMASH imaging. Magn Reson Med. 2002;47(1):160–70.
8. Hutchinson M, Raff U. Fast MRI data acquisition using multiple detectors. Magn Reson Med. 1988;6(1):87–91.
9. Sodickson DK, Manning WJ. Simultaneous acquisition of spatial harmonics (SMASH): fast imaging with radiofrequency coil arrays. Magn Reson Med. 1997;38(4):591–603.
10. Griswold MA, Jakob PM, Heidemann RM, et al. Generalized autocalibrating partially parallel acquisitions (GRAPPA). Magn Reson Med. 2002;47(6):1202–10.
11. Barger AV, Grist TM, Block WF, Mistretta CA. Single breath-hold 3D contrast-enhanced method for assessment of cardiac function. Magn Reson Med. 2000;44(6):821–4.
12. Peters DC, Ennis DB, McVeigh ER. High-resolution MRI of cardiac function with projection reconstruction and steady-state free precession. Magn Reson Med. 2002;48(1):82–8.
13. Larson AC, White RD, Laub G, McVeigh ER, Li D, Simonetti OP. Self-gated cardiac cine MRI. Magn Reson Med. 2004;51(1):93–102.
14. Bi X, Park J, Larson AC, Zhang Q, Simonetti O, Li D. Contrast-enhanced 4D radial coronary artery imaging at 3.0 T within a single breath-hold. Magn Reson Med. 2005;54(2):470–5.
15. Meyer CH, Pauly JM, Macovski A, Nishimura DG. Simultaneous spatial and spectral selective excitation. Magn Reson Med. 1990;15(2):287–304.
16. Meyer CH, Hu BS, Nishimura DG, Macovski A. Fast spiral coronary artery imaging. Magn Reson Med. 1992;28(2):202–13.

17. Bornert P, Stuber M, Botnar RM, et al. Direct comparison of 3D spiral vs. Cartesian gradient-echo coronary magnetic resonance angiography. Magn Reson Med. 2001;46(4):789–94.
18. Nayak KS, Pauly JM, Yang PC, Hu BS, Meyer CH, Nishimura DG. Real-time interactive coronary MRA. Magn Reson Med. 2001;46(3):430–5.
19. Hardy CJ, Zhao L, Zong X, Saranathan M, Yucel EK. Coronary MR angiography: respiratory motion correction with BACSPIN. J Magn Reson Imaging. 2003;17(2):170–6.
20. Yang PC, Meyer CH, Terashima M, et al. Spiral magnetic resonance coronary angiography with rapid real-time localization. J Am Coll Cardiol. 2003;41(7):1134–41.
21. Block KT, Uecker M, Frahm J. Undersampled radial MRI with multiple coils. Iterative image reconstruction using a total variation constraint. Magn Reson Med. 2007;57(6):1086–98.
22. Lustig M, Donoho DL, Pauly JM. Sparse MRI: The application of compressed sensing for rapid MR imaging. Magn Reson Med. 2007;58(6):1182–95.
23. Haase A, Matthaei D, Hanicke W, Frahm J. Dynamic digital subtraction imaging using fast low-angle shot MR movie sequence. Radiology. 1986;160(2):537–41.
24. Scheffler K, Lehnhardt S. Principles and applications of balanced SSFP techniques. Eur Radiol. 2003;13(11):2409–18.

Clinical Cardiac Magnetic Resonance Imaging Techniques

2

Leon Axel and Madalina Alexandra Toms

General Overview of Imaging Indications and Techniques

Cardiac magnetic resonance imaging (CMRI) has many potential advantages over conventional cardiac imaging techniques. These include a lack of ionizing radiation, free choice of imaging planes, the capability for tissue characterization, qualitative and quantitative evaluation of the motion of both the blood and the myocardium, and assessment of regional perfusion. These capabilities have been realized through the implementation of many MRI techniques, which have many associated imaging options. While this range of options to choose from when performing a cardiac MRI examination can be daunting, it provides a great deal of flexibility that can be used to tailor the examination to the patient and the particular clinical question to be addressed.

Some of the current clinical indications of cardiac MRI are summarized in Table 2.1.

Optimal performance of a clinical cardiac MRI examination depends on appropriate choices of the imaging methods to be employed and of the corresponding values of the technical parameters of these methods. While there are particular considerations involved in setting up different specific imaging methods, and specific implementations by different manufacturers may differ, there are some considerations and trade-offs that are common to almost all MRI methods. In particular, there are trade-offs to be considered related to the finite amount of time that is available for performing the examination, due to both time pressure from clinical demand for use of the MRI system by other patients and the limited capacity of the patient to remain still within the system. In addition, if the patient is unstable, the examination should be kept as short as possible, consistent with answering the clinical question, due to the difficulty of fully monitoring and supporting patients inside the MRI system. The limited time available for data acquisition often leads to the need to choose between using that time for optimizing spatial resolution and field of view and optimizing temporal resolution.

Table 2.1 CMRI protocols used for the various indications. The protocols for questions related to congenital heart disease are tailored to the lesion and the individual clinical scenario and therefore vary substantially. Protocols contain different specific combinations of imaging techniques and vary slightly with respect to slice positioning, depending on the indication and structures to be assessed

Indications	Protocol
Acute coronary syndrome including acute MI	Acute MI
Suspected myocardial ischemia	Adenosine stress perfusion
Suspected or known ARVC/D	ARVC/ARVD
Suspected or known congenital heart disease	Congenital
Rule out or rule in coronary anomaly or proximal coronary artery stenosis	Coronary angiography
Rule out or rule in inducible myocardial ischemia	Dobutamine stress function
Assessment of myocardial viability and scarring, suspected or known cardiomyopathy	Viability (fibrosis)
Suspected acute or chronic myocarditis, rule out active myocarditis	Inflammation
Assessment of volumes, mass, and global and/or regional LV function.	Ventricular function and morphology
Rule out or rule in pericardial disease	Pericardium
Pulmonary vein anatomy pre- or post-atrial ablation procedures	Pulmonary venography
Suspected or known valvular disease	Valvular
Suspected or known aortic disease	3D aortography
Suspected or known myocardial iron overload	T2*

L. Axel (✉)
NYU School of Medicine, NYU Langone Medical Center, Departments of Radiology, Medicine, and Neuroscience and Physiology, New York, NY, USA
e-mail: leon.axel@nyumc.org

M. A. Toms
NYU School of Medicine, NYU Langone Medical Center, Department of Radiology, New York, NY, USA
e-mail: madalina.toms@nyumc.org

R. Y. Kwong et al. (eds.), *Cardiovascular Magnetic Resonance Imaging*, Contemporary Cardiology,
https://doi.org/10.1007/978-1-4939-8841-9_2

Optimizing spatial resolution, in turn, often comes at the cost of diminished signal-to-noise ratio (SNR), leading to another trade-off to be considered.

A cardiac MRI examination typically consists of the acquisition a fairly standard set of images with common methods and in common orientations, supplemented with "optional" imaging that is particularly useful for the specific clinical condition in question. Ideally, the examination should be monitored by a physician who can help choose these optional imaging methods as well as optimize the choice of imaging parameters. They can also modify the examination as needed to better evaluate any unexpected findings that may show up during the acquisition of the "standard" images. A standard cardiac MRI examination will start with initial screening of the patient and setting up of cardiac gating (and possible intravenous access for contrast administration). This will be followed by MRI with initial quick "scout" localizing images and a stack of relatively rapid "survey" images through the chest (in one or more orientations) to get an initial overview of the heart and the associated intrathoracic anatomy. After identifying the location of the axes of the ventricles in three dimensions, basic static and cine images will be acquired of the heart in standard short- and long-axis orientations, as well as various optional images, as indicated by the specific clinical questions. In this chapter, we will present a systematic approach to the performance of a clinical cardiac MRI examination, focusing on some of the associated technical considerations, with a basic review of some of the relevant imaging physics. Other chapters will present more details on the imaging methods themselves and their applications to specific clinical conditions.

Basic Physics Review

MRI is based on the phenomenon of nuclear magnetic resonance (NMR). Certain kinds of atomic nuclei ("spins"), in particular, including hydrogen, exhibit a collective magnetization (M) when placed in a strong magnetic field (B0). This magnetization is aligned with the external polarizing field at equilibrium. While not readily detectable in its equilibrium state, the nuclear magnetization can be caused to be rotated away from this equilibrium orientation ("excited") by application of a weaker oscillating magnetic field (B1) (typically in the radio-frequency (RF) range) at a specific resonance frequency (the Larmor frequency), which is proportional to the strength of the polarizing field and characteristic of the particular kind of nucleus. The strength and duration of the exciting RF magnetic field determine the resulting orientation of the nuclear magnetization. The net magnetization M is decomposed into two orthogonal components: longitudinal (Mz, oriented along B0) and transverse (Mxy, oriented perpendicular to B0). The transverse magnetization (Mxy) rotates around B0 ("precesses") and can generate a measurable signal in a suitable external receiver coil. The longitudinal magnetization (Mz) is stationary and does not directly contribute to the detected signal; however, any longitudinal magnetization must be tipped into the transverse plane by a radio-frequency pulse in order to produce a measurable signal. The change of the orientation of the nuclear magnetization produced by the exciting RF pulse can be set to be any desired amount, from 0° to 180°. In the case of a 180° pulse, no new transverse magnetization will be produced, but any initial longitudinal magnetization along the main magnetic field will wind up oriented in the opposite direction (i.e., it will be inverted or "negative").

Immediately after the exciting magnetic field (B1) is turned off, the net magnetization M starts to return to its equilibrium state, a process known as relaxation. Two distinct kinds of relaxation processes will happen simultaneously:

1. Longitudinal relaxation refers to the recovery of the component of the nuclear magnetization along the axis of the B0 field to its original value at equilibrium. This relaxation is characterized by a characteristic exponential time constant, T1; this will depend on the specific state of the tissue but is typically on the order of a second for myocardial tissue.
2. Transverse relaxation refers to the decay of the component of the nuclear magnetization perpendicular to the axis of the B0 field (and the decay of its associated signal). This process is by necessity faster than the longitudinal relaxation, and thus the signal typically decays away long before the spin system returns to its equilibrium. Two factors contribute to loss of the signal: intrinsic relaxation, characterized by a tissue state-dependent characteristic exponential time constant, T2, and extrinsic relaxation, due to local magnetic field inhomogeneities resulting in loss of phase coherence between signal from different nuclei within an imaged region, characterized by a shorter apparent exponential time constant, T2*.

If there is a short delay between consecutive RF excitations, there will be incomplete recovery of the longitudinal magnetization between excitations for regions with longer T1 times and thus a relative decrease in their signal ("T1 weighting"). If there is a delay between the times of excitation and the detection of the signal, there will be a greater decay of the transverse magnetization in the regions with shorter T2 times and a relative decrease in their signal ("T2 weighting"). In the absence of T1 and T2 effects (short signal detection delays and long waits between excitations), there will still be a regional dependence of the relative signal on the local amount of signal-producing nuclei ("proton-density weighting"). (This is discussed further below.) The relaxation times of tissues can be altered by the administration of exogenous contrast agents, which are typically stable chelated forms of gadolinium. These contrast agents shorten the relaxation times of the tissues to which they are distributed.

The apparent loss of signal due to local B0 field inhomogeneity can be transiently recovered as an "echo." In the case of fixed local field inhomogeneities, e.g., due to the presence of magnetically different materials such as air, metal, or

iron deposition [1], use of suitable additional RF excitation pulses can produce a transient refocusing of the signal ("spin echoes") that allows the transient recovery of the signal to the strength determined by the intrinsic T2 time. In the case of field inhomogeneities produced by the gradient magnetic fields used in imaging (see below), reversal of the gradient fields can produce a transient refocusing of the signal ("gradient echoes"); in this case, the echo signal will only recover to the strength determined by the local T2* time. When rapidly repeated RF excitation pulses are used, with inter-pulse intervals (TR) that are short compared to both T1 and T2, there can be a steady state set up, in which there is some refocusing of signal from the residual transverse magnetization remaining from prior excitation, which is added to the signal from the longitudinal magnetization that recovered between the excitations, "steady-state free precession" (SSFP). The signal detected will thus depend on both the T1 and T2 times, with stronger signal from regions with longer T2 time but weaker signal from those with longer T1 times, with a net signal that depends on the local ratio of T2/T1. In SSFP imaging, there is typically use of an alternating direction of the RF excitations, with an associated partial magnetization transfer from transverse to longitudinal components and vice versa. However, there are thus two different kinds of steady state that can be set up, depending on the local B0 field strength (i.e., the off-resonance shift), one in which the RF pulses and magnetization alternate in phase together and another in which they are opposite in phase. At the boundaries between these regions, there may be no net refocusing, seen as corresponding dark bands in the image.

In clinical practice, gradient-echo images are used for 2D or 3D T1-weighted imaging with and without gadolinium contrast agents, such as for MR angiography or contrast-enhanced cardiac imaging, and for flow-sensitive imaging and cardiac contractility studies. Spin-echo images are usually reserved for T2-weighted imaging and for the assessment of anatomic structures, including the heart and vessel walls. SSFP imaging is the "workhorse" method used for cardiovascular cine imaging.

Magnetic Resonance Imaging

The signal from the magnetic resonance phenomenon is typically in the radio-frequency range and thus cannot be simply focused or collimated like the signals used in other kinds of cardiovascular imaging. Rather, we use the principle that the local signal frequency is dependent on the strength of the local magnetic field. Thus, through the use of supplementary "gradient" magnetic fields, applied after the signal excitation, we can encode position information in the detected signals; this information can be decoded by the system computer during the image reconstruction process. Similarly, we can use gradient magnetic fields during the excitation process to select the regions to be excited, e.g., for selection of the location of the imaged slice or slab of slices. A field gradient is a magnetic field added to B0, with a strength that varies linearly with the position along a pre-defined gradient direction and whose strength is under computer control. The MR imaging system typically has three sets of gradient coils, one along each nominal axis ("X, Y, and Z"), with each by itself producing a magnetic field gradient in the respective direction; these can be flexibly combined to produce any net desired gradient field in space.

In conventional 2D MR imaging, spatial localization of the detected signal for image reconstruction is achieved in three steps. First, slice-selective gradients are used so that only a user-specified thin slice of tissue is excited and emits signal. Then, to localize signal within a given slice, two sets of gradients are used: frequency-encoding gradients are applied during the signal detection, and phase-encoding gradients are applied at some time between the RF excitation and the signal detection. The slice selection gradient is applied during the RF excitation only. However, an additional gradient pulse of opposite polarity is then applied to refocus any dephasing of the excited spins that may have arisen across the thickness of the slice during the excitation process. The frequency-encoding gradient is used to localize the source of signals along the corresponding direction. The magnetic field gradient is applied during the detection of the signal; the local variation of the magnetic field causes a corresponding variation of the frequency of the emitted signal. The gradient thus effectively encodes the location of a proton along the frequency-encoded direction by the frequency of its signal. Again, an additional gradient pulse of opposite polarity is applied prior to signal detection, to refocus any dephasing of the excited spins that may arise along this direction during the detection process. To convert the signal, detected over time, to the equivalent set of frequencies, we use the mathematical operation known as the Fourier transform, which can be efficiently carried out in the image reconstruction computer. The raw signal data can be considered as acquired in a "k-space" dimension, which is equivalent to the Fourier transform of the image.

The remaining ("phase-encoding") gradients are used to reconstruct the remaining dimension in the image. Although they are only applied between the times of excitation and signal detection, they produce a persistent regular spatial variation of the phase of the signals received from spins along the corresponding direction in the image; the "wavelength" of the spatial variation of the phase is proportional to the strength of the phase-encoding gradient used in a particular excitation-detection sequence. This phase variation results in modulation of the net-detected signal, due to interference of the signals from different positions along the corresponding direction. By repeating a series of signal acquisitions with a suitable set of different such phase-encoding gradient pulses, we can build up enough data to reconstruct the corresponding signal distribution along that direction; again we use the Fourier transform to carry out this image reconstruction from the raw data. While the process of acquiring

the gradient-encoded raw data needed for image (position) reconstruction is very rapid, the phase-encoded data is relatively time-consuming to acquire, as each such data point requires a separate phase-encoded signal acquisition. While the frequency-encoded data are acquired in real time, and so any part of the object that extends beyond the boundaries of the reconstructed field of view (FOV) can be simply filtered out electronically, the phase-encoded data are not acquired in real time, and thus any part of the object extending beyond the reconstructed FOV will be subject to aliasing or "wrap-around" artifact, and will appear on the other side of the image, as if it were folded over.

For extending this approach to full 3D imaging, we can perform selective excitation of the volume to be covered by a stack of reconstructed slices. Then spatial localization within this volume is performed by detecting the signal using one frequency-encoding gradient during the signal detection, as for 2D imaging, and two sets of phase-encoding gradients applied prior to signal detection, aligned along the other two orthogonal directions in the imaged volume. Again, the Fourier transform is employed for the reconstruction of the corresponding image dimensions from the raw data set. There will now be the potential for aliasing artifact along both of the phase-encoded directions in the reconstructed images.

The MR imaging system consists of several components:

1. Main magnet (usually superconducting) and shim coils. In the superconducting magnet, there is no resistance to current flowing through the wires, so the magnetic field stays "on" with no added energy needed. The main magnetic field is not perfectly homogenous. The inhomogeneity of a field is typically described in parts per million (ppm) for a predefined volume in the center of the magnet (e.g., 5 ppm for a spherical phantom with radius of 10 cm). Shimming refers to the use of additional magnet coils (or suitably placed small pieces of metal) to improve the field homogeneity.
2. Transmitting coils emit the radio-frequency pulses that generate the B1 field. RF excitation can be performed by a set of coils, referred to as body coils, within the main structure of the magnet, or by a separate coil or coils positioned directly over the region of interest.
3. Receiving coils are used to detect the magnetic signal produced by the excited spins. A variety of coils can be used to receive signals. For optimal cardiovascular images, surface coils which are positioned closer to the body, such as a phased-array coil, are usually preferred over circumferential volume coils. Typical cardiovascular phased-array coils have 4–8 elements per array and 2 arrays, one positioned anteriorly over the chest and the other posteriorly under the back.
4. Gradient coils are used primarily for spatial localization of the signal. Three pairs of coils are used to generate field gradients in the x, y, and z directions. The amplitude of a magnetic field created by a pair of gradient coils depends on the amount of electrical current passing through each coil. There are also special gradient amplifiers used to generate the associated strong pulses of current.
5. Radio-frequency (RF) electronics – used both for the generation of the strong B1 fields used for excitation of the spins and for detection and amplification of the weak resulting signals.
6. Computers are used both for control of the RF and gradient pulse generation (and of the other aspects of the system, such as patient table movement) and for reconstruction and display of the resulting images.

Cardiovascular MRI

Flow Effects in MRI Flow can affect signals (and thus corresponding image brightness) in MRI in a variety of ways. In the case of T1-weighted imaging, blood, with its relatively long T1 relaxation time, would be expected to have a relatively low signal, due to its loss of magnetization ("saturation") by rapidly repeated excitations. However, in the presence of flow through the imaging region, this saturated blood can be replaced by more fully magnetized blood from upstream, resulting in increased signal intensity ("flow-related enhancement"). With additional excitation pulses placed to saturate the signal from the upstream blood, we can further manipulate the brightness of the blood image, as discussed futher below. In the case of T2-weighted imaging, with relatively long delays between the initial excitation pulse and subsequent refocusing pulse, motion of initially excited blood out of the plane of the refocusing pulse can result in decreased signal intensity. While it may not be visible in conventional magnitude images, motion of blood between the pairs of gradient pulses used to correct for gradient-induced dephasing can result in a net phase shift of the signal; this is the basis of phase-based velocity imaging methods (discussed below).

"Real-Time" Cardiac Imaging

A major difference of cardiovascular MRI from MRI of other systems is the intrinsic motion of the structures of interest. To avoid degradation of the images by this motion, we can try to acquire the images rapidly enough to "freeze" the motion ("real-time" imaging). However, rapidly acquiring real-time sequences generally requires a trade-off between achievable spatial and temporal resolution and signal-to-noise ratio (SNR) that may result in image degradation. Currently, dynamic parallel imaging methods can be used to achieve moderate acceleration rates of 2–3(R) using coil arrays (as is described in more detail elsewhere in this book); compressed sensing (CS) is an alternative promising method to accelerate image acquisition [2].

However, the spatiotemporal resolution that can be achieved within one heartbeat or less (for real-time imaging) is still limited.

Even with these limitations, such real-time cine-MRI is often preferred over segmented acquisitions (see below) in patients with breath-holding difficulties or arrhythmia, which may lead to severe image degradation with conventional cine imaging. In this case, a run of imaging acquisition spanning several heartbeats is typically acquired at each location of interest. Real-time image acquisition can also be used to acquire information on dynamic variability of cardiac morphology and function, for example, with respiratory-induced changes in the heart, such as in constrictive pericarditis.

Cardiac Gating

While cardiovascular MR images can be acquired rapidly with "real-time" approaches, there are significant limitations in the temporal and spatial resolution of the resulting images. Thus, synchronization of the imaging with the cardiac cycle ("gating") is an essential component of most cardiac MRI, in order to overcome blurring of images caused by myocardial contraction and flow effects from pulsatile blood. Gating allows accurate assessment of cardiac structure and function, by synchronizing image acquisitions with the cardiac cycle, and it allows the use of k-space segmentation to improve imaging, by permitting the combining of data acquired from multiple cardiac cycles. The most effective form of cardiac gating is electrocardiographic gating, where imaging is triggered by detection of the QRS complex (corresponding to the beginning of the ventricular contraction; the P-wave is not reliably detectable in MRI) in a three- or four-lead electrocardiogram (ECG) from (MRI-compatible) electrodes positioned on the chest wall. Multiple "segments" of k-space data that will be used to make up a single MR image (of a given cardiac phase) can be acquired within a user-specifiable interval, centered at the same point within the cardiac cycle, over a series of sequential heartbeats; this serves to eliminate blurring due to cardiac motion within the single image (Fig. 2.1) [3, 4], as long as the heartbeats are sufficiently similar to each other and there is negligible respiratory motion during the data acquisition. The set of images spanning a cardiac cycle can then be displayed in a cine mode as a sort of synthetic heartbeat (although the actual imaging data were acquired over multiple heartbeats).

A satisfactory ECG signal for gating must be obtained before scanning is commenced, in order to create optimal diagnostic images, and time spent in achieving this is well rewarded in image quality. The skin may need to be shaved or cleaned to ensure that ECG electrodes are in good electrical contact with it. Lead placement is another important part of obtaining a reliable ECG trace, and this does not mirror standard diagnostic ECG positions for the limb leads (so that the resulting waveforms do not necessarily resemble standard monitor signals). Leads should generally be closely spaced, in order to minimize potentially interfering voltage differences between them induced by blood flow when the patient is placed within the magnet (see below), which can distort the ECG signal and lead to unreliable gating. Optimal lead position also varies depending on the location, orientation, and size of each individual's heart and may need to be individually adjusted. The goal is to obtain a well-defined and relatively high-amplitude QRS complex, while the patient is in the magnet, where the R upstroke of ventricular depolarization is significantly larger than the T wave of the cardiac cycle, so that image triggering will occur consistently at the same point within the cycle. For safety reasons, the ECG leads should not be allowed to form loops, due to risk of burns from the induction of a current in the leads by the strong RF power used in MR imaging; in addition, only specific MRI-compatible leads should be used, to minimize the risk of burns.

Furthermore, care should be taken to recheck the ECG signal once the patient has entered the bore of the magnet, as interference from voltages produced by the flow of the blood in the strong magnetic field (the "magnetohydrodynamic" effect) can

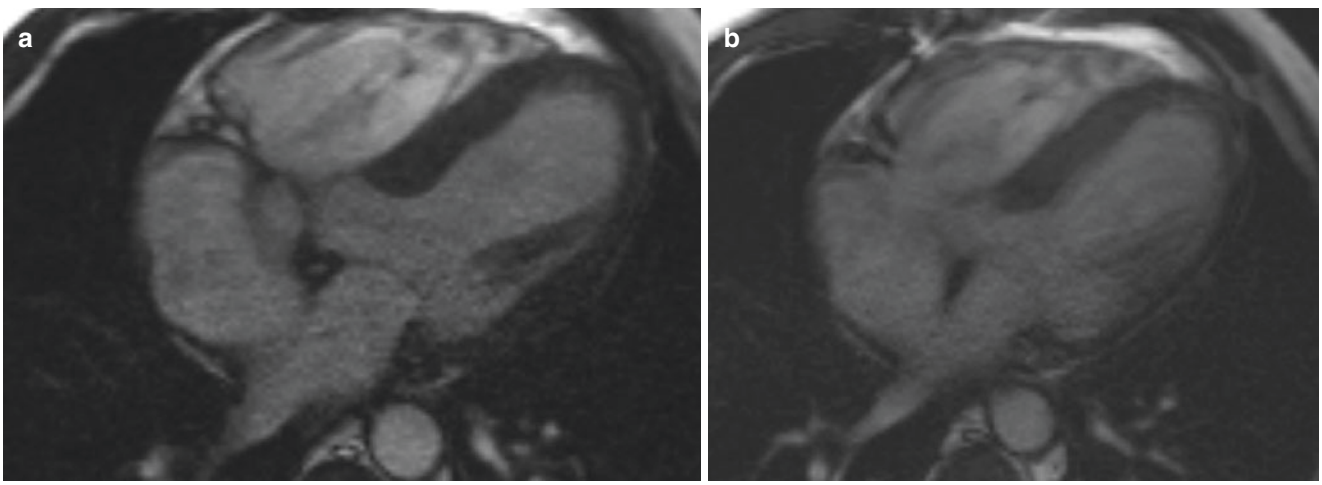

Fig. 2.1 (**a**) Gradient-echo FLASH image with cardiac gating; (**b**) without gating. (**a**) True SSFP (steady-state free precession) image with cardiac gating. (**b**) True SSFP (steady-state free precession) image without cardiac gating

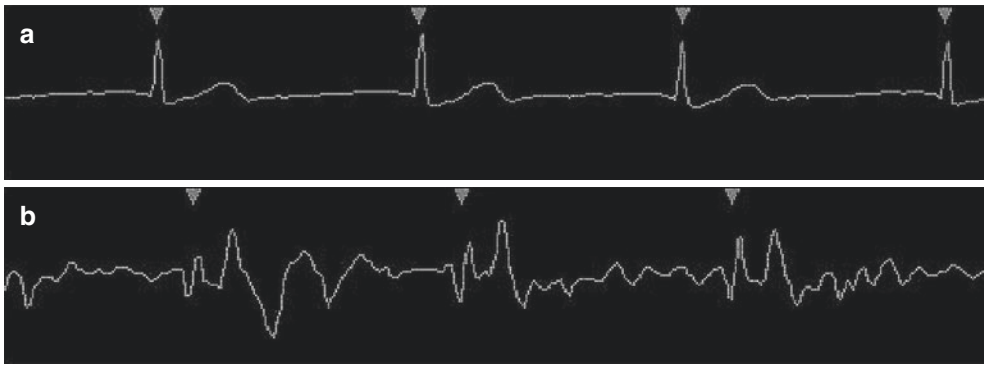

Fig. 2.2 (**a**) ECG signal acquired outside the bore of the magnet, showing detection of the QRS complexes; (**b**) ECG signal acquired from the same subject within the bore of the magnet, demonstrating distortion of the signal, with more prominent apparent T waves (with successful QRS detection in this case, despite the interference)

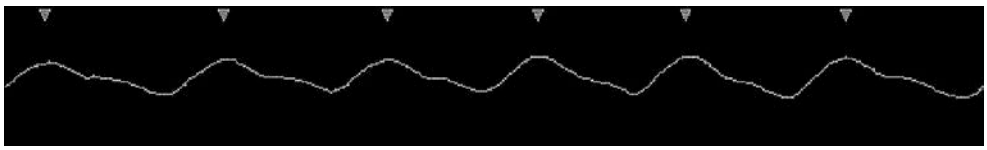

Fig. 2.3 Signal from a peripheral pulse monitor, with demonstration of triggering with each pulse cycle

distort the signal obtained (see Fig. 2.2) so that the R wave may no longer be clearly defined, even if it looked very clear while the patient was outside the bore. This effect becomes more pronounced at higher field strengths, as the weak physiologic ECG voltage (in the order of 1 mV or less) is forced to contend with proportionally stronger flow-induced voltages. Another potential source of interference with the ECG in MRI is the magnetic gradient pulses used in imaging, which may induce voltages in the leads associated with the rapid switching of the fields. The position of the ECG monitoring electrodes may need to be empirically readjusted until an adequate ECG signal is detected while the patient is in the bore of the system. Again, reliable gating is essential for optimal cardiovascular MR imaging.

Another potential problem that may be encountered with ECG gating in MRI is inappropriate triggering from voltage peaks produced by RF pulses during the examination. The current use of fiber-optic transmission of ECG signals significantly reduces artifacts from radio-frequency pulses [5] and gradient pulses, by keeping the conducting components of the ECG system short. One way of overcoming inappropriate triggering is "vectorcardiography" [6], where the QRS complex is identified by the monitoring equipment not only by its timing and magnitude but also in a "three-dimensional" voltage vector orientation, such that any electrical signals with a different vector to the desired QRS complex will be ignored, even if they have a relatively larger magnitude.

Arrhythmias may lead to inadequate or inappropriate triggering if the imaging software does not consistently recognize the R wave, and they can lead to image blurring and artifacts due to inconsistent anatomical configuration of the heart if there is a substantial variation in the R-R interval (and associated degrees of ventricular filling). Multiple image acquisitions that are averaged (referred to as multiple "averages") may help to reduce some image artifacts if an arrhythmia is present but will still leave residual blurring. If there is a significant cardiac arrhythmia, an arrhythmia rejection setting can be selected, in which cardiac cycles with R-R interval durations that fall outside a range specified by the operator are not used for image acquisition. However, this will tend to increase overall acquisition time, which can be problematic in the setting of a breath-hold sequence; some arrhythmias (e.g., atrial fibrillation) may still leave significant R-R variability even with successful rejection of heartbeats outside the acceptance window. Low-voltage ECG traces (e.g., related to body habitus, COPD, or large effusions) may also lead to inadequate or inconsistent triggering.

Peripheral triggering, which uses a signal derived from MRI-compatible optical fingertip pulse monitors, provides a less preferred but often adequate alternative, if a satisfactory ECG signal cannot be obtained (Fig. 2.3). Associated images may be significantly more blurred than with ECG gating, as triggering from the peak of the peripheral pulse wave signal is delayed in relation to the R wave of the cardiac QRS complex, making the imaging more vulnerable to any R-R interval variation.

Another potential alternative to the ECG is the use of "wireless" gating or "self-gating," where periodic changes of the MR signal during the cardiac cycle from the beating heart itself can be used as information to synchronize the MRI data acquisition with the cardiac cycle, thus allowing acquisition of a crisp image without the need for electrodes and leads; however, this is not yet used in current routine clinical practice.

Cardiac-synchronized MRI data acquisition can use either "prospective" gating or "retrospective" gating. In prospective gating, the detection of the QRS complex triggers the start of repeated acquisition of segments of imaging data within each cardiac cycle (see below), synchronized with the timing of the QRS complex, with the total data acquisition typically

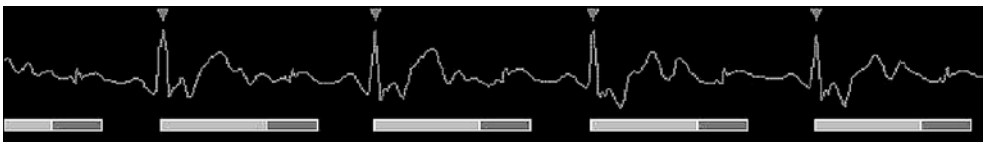

Fig. 2.4 Prospective ECG gating, with image acquisition commencing after triggering from the R wave and terminating before the end of each cardiac cycle

spread over several cardiac cycles, in each of which different data segments are acquired (see Fig. 2.4) [7]; this imaging data is then reconstructed as a set of corresponding image frames over the (synthetic) cardiac cycle. In retrospective gating, there is continuous asynchronous acquisition of segments of imaging data acquisition over several cardiac cycles, with updating of the data segments to be acquired with each successive QRS detection; post-processing with suitable data interpolation onto a "standard" cardiac cycle leads to image reconstruction of effective image frames at multiple time points (phases) in the cardiac cycle, with the number of phases per cardiac cycle predetermined by the operator, based on the heart rate and the rate of data acquisition [8].

Prospective gating generally leads to better temporal resolution images than retrospective gating (other factors being equal); however, the data acquisition time may be longer. A portion at the end of each cardiac cycle is lost, as data acquisition is generally suspended near the end of diastole, to await the onset of the next QRS complex, and thus the end portion of the cardiac cycle (usually ~50–100 ms) is not sampled, in order to allow for potential variation in the length of each R-R interval. In addition, there may be a short (user-selectable) interval delay (trigger delay) between recognizing the R wave and commencing data acquisition. As there is a period of the cardiac cycle in prospective gating where the signal is not being acquired, there is the tendency for tissues to recover some magnetization during this period, which may cause the first image acquired after triggering to be brighter than the remaining images; this can be a relative disadvantage for cine images performed to assess ventricular wall motion. "Dummy" excitation pulses can be used during this period to prevent this magnetization recovery and keep the signal strength more uniform. Assessment of cardiac volumes and function can also be affected by the method of ECG gating, with lower ejection fractions generally being calculated with prospective versus retrospective ECG gating, as some portions of the cardiac cycle (including the peak effects of the atrial component of ventricular filling) are not imaged [9].

Retrospective gating leads to more temporal blurring, as there is interpolation onto a set number of equally spaced phases for image reconstruction each cardiac cycle, despite possible differences in the actual duration of each R-R interval. However, it is generally a more robust technique than prospective gating, with the advantages that it has more uniform signal intensity in time (due to no interruption of the train of excitation pulses) and it can be used to image the whole cardiac cycle (due to no need to stop image data acquisition before the end of diastole to wait for the next QRS detection); thus, it is particularly useful for cine imaging of function, where a smooth transition between cardiac cycles is preferable for assessing regional and global wall motion. However, in the presence of arrhythmias with significant R-R variation, the usual use of uniform interpolation of the data from each acquired cardiac cycle onto a "standard" cycle can lead to additional artifacts in the reconstructed images; in this case, retrospective-gated imaging may provide better image reconstructions.

Segmentation of the k-space data acquisition for cardiac MRI begins with considering the full set of raw data (lines in "k-space"), or phase-encoding steps, which must be acquired in order to reconstruct a complete image. These can be grouped into separate segments, with each such segment, containing an operator-specified number of phase-encoding steps, treated as if they were all acquired at the same time in the cardiac cycle; a different set of such segmented data is acquired repeatedly in each cardiac cycle. Such sets of data segments are acquired at approximately the same time point in each consecutive cycle, over multiple heartbeats, until sufficient raw phase-encoded data lines are obtained to reconstruct the images. Such segments of raw data can be used to make either serial images at a single location, reconstructed over different phases of the cardiac cycle (single slice, multiple phase), as with cine imaging for assessment of wall motion. Alternatively, they can be used for reconstructing multiple static images, with each obtained for a different slice and a single phase for each slice in the cardiac cycle (multiple slices, single phase), as is useful for assessment of myocardial scar tissue on delayed-enhancement images. With improving MR technology, stronger gradients have enabled faster imaging, and it is now also possible to acquire multiple imaging slices or sections over different phases of the cardiac cycle (multiple section, multiple phase) [10].

As with many factors in MRI, there is a trade-off between spatial and temporal resolution and field of view. The overall acquisition time is generally to be kept as short as possible, as this is vital for breath-holding sequences. Higher-spatial resolution images will require a larger number of phase-encoding steps and subsequently a larger number of phase-encoded k-space lines (referred to as "views") per segment

for the same total image data acquisition time. This will lead to a decrease in temporal resolution, as more time within the cardiac cycle is taken to acquire each segment (and to reconstruct each resulting image frame). As the R-R interval is finite, only a limited number of segments can be acquired within each cycle, and in the context of cine imaging, the number of cardiac phases that can be independently imaged (without "view sharing") will be decreased. If more phases of the cardiac cycle are to be acquired and reconstructed in the same overall acquisition time, then the number of phase-encoding steps per frame will need to be decreased, at the cost of decreased spatial resolution or decreased field of view.

Patient heart rate is also an important factor. In patients with slower heart rates, if the number of views per segment is kept low for high temporal resolution, acquisition times may extend beyond a reasonably achievable breath-hold, as the same number of heartbeats (with their R-R intervals) is still required to acquire enough data for an image. In order to keep total acquisition time low, the options in a bradycardic patient are either to increase the number of views obtained in each segment, at the cost of temporal resolution, or to decrease the number of views used to make up each image, decreasing spatial resolution or field of view. For higher heart rates, we can decrease the number of views per segment to achieve imaging of a comparable number of phases per cardiac cycle in a comparable total imaging time. Similarly, we can speed up the process of acquiring data covering the heart by interleaving acquisitions at multiple levels but at the cost of decreased temporal sampling or increased imaging (and breath-holding) time.

One method of improving the effective temporal resolution (or temporal sampling rate) in gated cardiac MR images is to use view sharing [11]. With this technique, some "views" (phase encoded data sets) from one segment are combined with views from the next segment to create a new, intermediate cardiac phase image. For example, with single-section multiple-phase imaging, if there are ten segments in a cardiac cycle of 800 ms (disregarding time for arrhythmia rejection and triggering with prospective gating), each with eight views per segment, with each view having a TR of 10 ms, then the sequence has a temporal resolution of 8×10 ms = 80 ms and 800 ms/10 ms = 10 phases per cardiac cycle. Using view sharing, the last four views of one segment could be combined with the first four views of the next segment to create new intermediate phases between each existing phase. This would improve the nominal effective temporal resolution of the sequence, even though in reality, the same number of views is being acquired whether or not view sharing is being used, and the true temporal resolution remains the same. However, the number of reconstructed phases within a cardiac cycle would be increased, with a potential for a "smoother" cine display.

Cine Imaging

The ability of MR imaging methods to synchronize the image data acquisition with the cardiac cycle (as described above) permits reconstruction of high-quality movies ("cine" imaging) of the different phases of the cardiac cycle, even though the imaging data may be acquired over the course of multiple cardiac cycles. This is, of course, dependent on the cardiac cycles being reasonably consistent with each other, which may not be the case in the presence of cardiac arrhythmias or breathing.

Cine imaging can be readily implemented with gradient-echo imaging (e.g., "fast low-angle shot," or FLASH, imaging); this can be gated either retrospectively or prospectively. The blood in cardiac chambers and vessel lumens generally appears bright in cine gradient-echo imaging due to the flow-related enhancement effects described above. Note that the amount of this flow-related enhancement can depend on the orientation of the images: for short-axis cine imaging with gradient echoes, the flow is primarily perpendicular to the image plane, leading to a prominent and consistently bright image of the blood within the cardiac chambers and vessel lumens, while with long-axis cine imaging, the presence of a significant component of within-plane flow can lead to less of a bright-blood effect in the images. Also, note that through-plane motion of the heart wall itself may similarly lead to a noticeable amount of phasic variation in the apparent brightness of the myocardium. The strength of the signal from the relatively stationary tissues depends on the amount of their magnetic saturation (due to the repeated excitation pulses they experience); this, in turn, depends on both the strength of the pulses (the size of the "flip angle") and the time between the pulses (TR). With increasing size of the flip angle used in rapid gradient-echo imaging, there is initially an increase in signal, due to more excitation being produced, but this will then be offset by the greater saturation effects of further increases in the flip angle, leading to an optimum flip angle for maximum signal strength at given values of TR and T1 (the "Ernst angle"). This signal dependence on flip angle has a fairly broad maximum; flip angles on the order of 25° or so generally work well for cine imaging with gradient echoes, and higher angles may be needed if cine imaging is performed after contrast administration. The echo time, TE, is generally kept as short as possible in gradient-echo cine imaging, in order to keep the imaging as fast as possible. The signal from fat and water will evolve different phases between the time of their initial excitation and the time of their signal detection, due to the difference of their resonance frequencies. Thus, depending on the value of TE, fat and water may be in phase or out of phase in the final image, leading to corresponding different appearances of the interfaces between fat and water, due to volume averaging of their signals (e.g., at the boundaries of the epicardial fat with the

epicardium or the pericardium), even though the phase itself is not directly displayed in the conventional MR images.

As the hardware of MRI systems has gotten faster and more stable, the use of SSFP imaging approaches for cine imaging has become more popular. As the achieving of a steady state in SSFP relies on maintaining a continuous stream of excitation pulses, cine imaging with SSFP is generally used with retrospective gating only. The bright signal from blood in SSFP cine imaging depends primarily on the relaxation times of blood rather than on its motion, as described above, leading to a more consistent bright-blood appearance independent of image orientation or blood flow patterns. However, the interference with achieving the steady state when the blood is flowing in an inhomogeneous magnetic field (such as may be created by metal from surgical procedures, such as valve prostheses, or even from the inhomogeneous structure of the patient themselves, particularly at high magnetic field strengths) can lead to significant image artifacts from the blood. In such cases, by adjusting the frequency of the RF transmitter, we may be able to minimize the artifacts or to change their location so that they do not interfere with the image of a structure of interest (Fig. 2.5); ideally the magnet field would be "reshimmed" on the patient to improve the homogeneity of the field. Another limitation of SSFP imaging at higher magnetic fields is the associated heating (SAR) that the rapidly repeated excitation pulses it uses can create.

A useful variant of cine imaging for use with motion evaluation is to combine it with magnetization tagging, e.g., produced with spatial modulation of magnetization (SPAMM) [12] (Fig. 2.6). In tagged MRI, localized perturbations are created in the magnetization of the body, which appear in subsequent images as dark marks that move with the underlying tissue. Thus, we can follow the motion of otherwise indistinguishable portions of the heart wall, e.g., to permit direct observation of aspects of the motion such as circumferential or longitudinal shortening that would otherwise be essentially invisible. In tagged MRI, the persistence of the tags is limited by the T1 relaxation time of the myocardium. The saturation effects of the imaging excitation pulses can also lead to fading of the tags, so that the excitation flip angle is generally decreased in tagged cine imaging, in order to minimize the fading effects of the imaging on the tags. The longer T1 relaxation times at higher field strengths tend to lead to better tag persistence at these fields.

Respiratory Motion

Aside from cardiac motion, respiratory motion is another important cause of image blurring and "ghosting" artifact in the phase-encoding direction (Fig. 2.7). The largest amount of respiratory motion is generally in the cranio-caudal direction, but there is also a degree of anterior-posterior and transverse motion of the diaphragm. This, in turn, changes the position and shape of the heart with respiratory phase, with a motion of approximately 1 cm in the cranio-caudal direction reported in the literature [13].

There are several ways of combating respiratory motion in clinical practice. The most widely used in standard cardiac sequences is breath-holding by the patient during image acquisition. While this can potentially eliminate respiratory motion, the length of each acquisition is limited by the individual's breath-holding capability, which in the elderly or debilitated may mean very brief acquisition times of less than 10 s; other subjects may be unable to follow breathing instructions. In addition, there may be a variation in the degree of breath-holding with each breath, leading to changes in position of the heart and potential misregistration artifact if a series of contiguous images (such as a stack of slices through the heart) is being acquired over sequential breath-holds [14]. There may even be variations in diaphragm position ("drifting") during a single breath-hold. Imaging with breath-holding at end-tidal expiration is one technique that can be used to reduce variability in diaphragm position between and within breath-holds, as it is a relatively reproducible condition [15]. However, this practice may not be feasible in patients with limited respiratory reserve, who are generally more comfortable holding their breath near end-inspiration.

Alternatively, if the patient is unable to comply with breath-holding instructions, increasing the number of averages used to construct an image has been used to improve signal-to-noise ratio (SNR) and reduce "ghosting" (but not blurring) respiratory motion artifacts [16]. However, this increases overall scan time, and there are now more sophisticated methods of minimizing respiratory motion artifact that may be preferred.

Respiratory gating can be performed, with monitoring of respiratory motion during data acquisition. This can be implemented with either acquisition during a consistent part of the respiratory phase (typically the end-expiratory phase) or post-processing of continuously acquired data, with rejection of data that was acquired outside a specified respiratory window before image reconstruction. This may involve the use of a bellows or other strain gauge, which is comprised of a mechanical sensor which is physically wrapped around the patient's chest to monitor chest wall motion, which provides a crude reflection of respiratory motion.

A respiratory "navigator" pulse sequence provides an alternative method of gating, which directly tracks diaphragmatic motion. This is based on the selective acquisition of signal from a column of material centered on the moving diaphragm, which is positioned so as to be perpendicular to its interface with the lung and parallel to its direction of motion [17]. The column excitation is commonly achieved by the intersection of consecutive slice-selective planar excitations with intersecting 90° and 180° excitations. Detecting

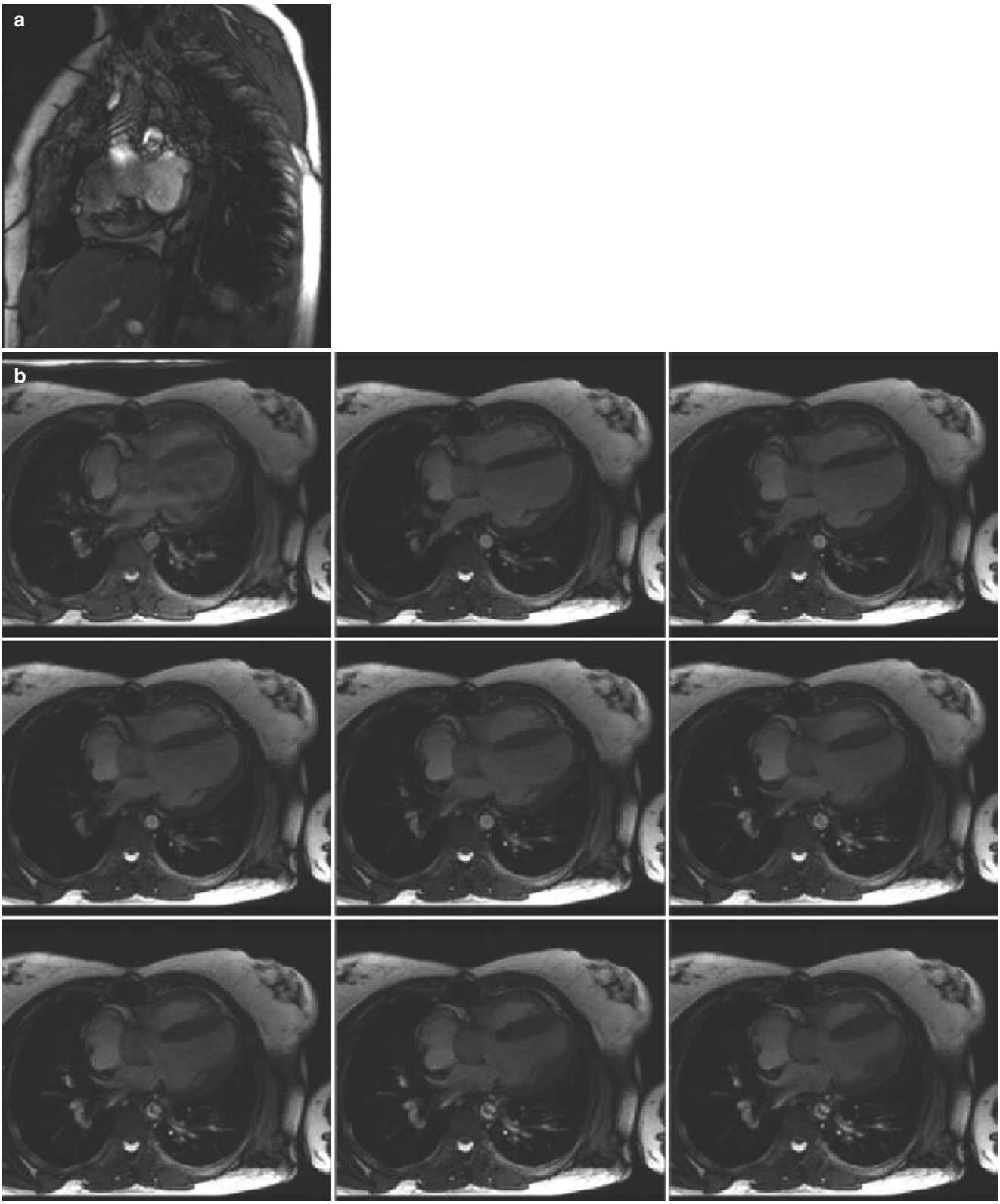

Fig. 2.5 (**a**) Artifact from magnetic field inhomogeneity in a SSFP sequence performed at 3 Tesla; (**b**) "Frequency scout," where images are obtained with small adjustments in the frequency of the RF transmitter in order to find the most suitable frequency

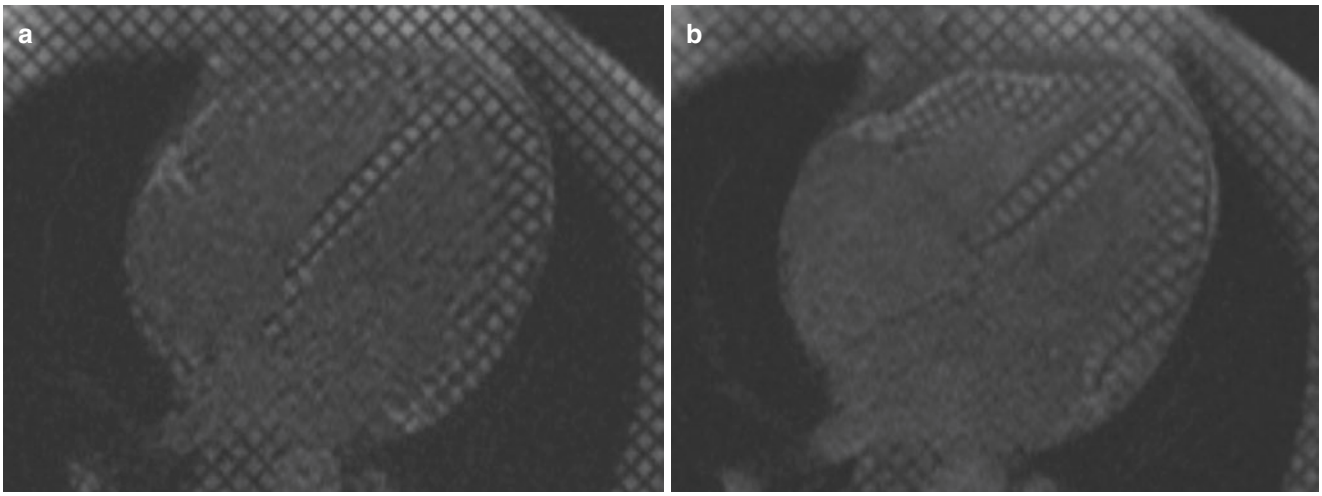

Fig. 2.6 Four-chamber view with magnetization tagging created at end-diastole, allowing for more accurate depiction of intramural wall motion during cine imaging (**a**) early systole; (**b**) end-systole

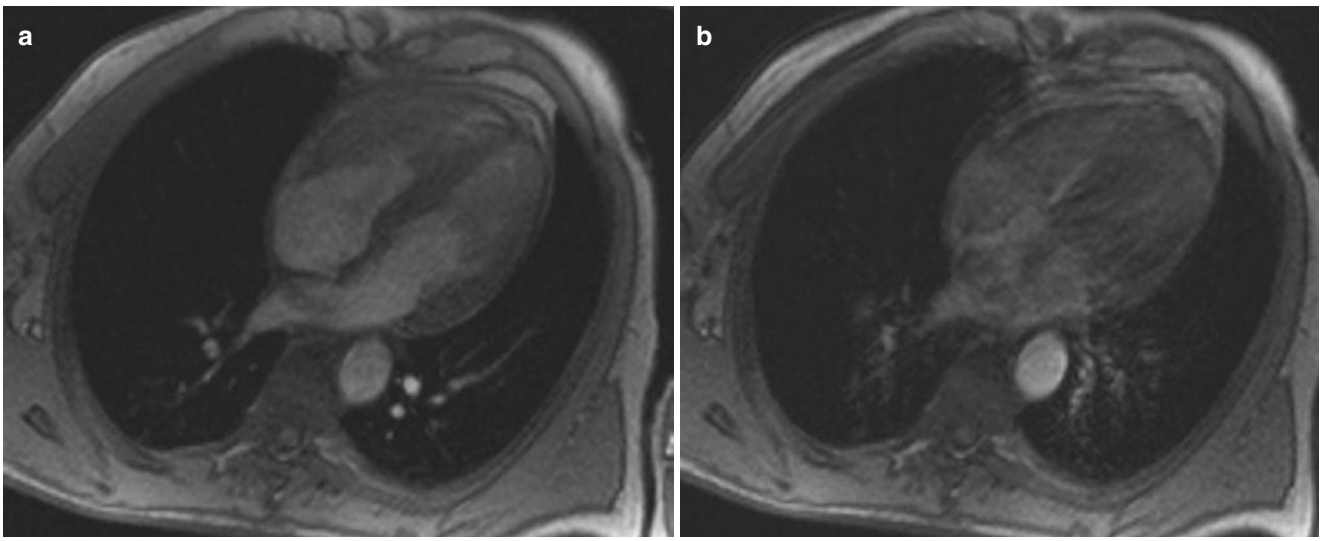

Fig. 2.7 (**a**) Breath-hold gradient-echo FLASH image; (**b**) same image acquired with free breathing

the echoes obtained from the navigator column with a readout gradient oriented along the column can provide a rapid and accurate 1-d depiction of the moving edge. Acquiring these navigator echoes during the imaging sequence allows for continuous monitoring of diaphragmatic motion during data acquisition. This information can then be used in one of two ways: (1) with the patient free-breathing and with data acquisition triggered by a set navigator acceptance window and (2) using a multiple breath-hold technique, with signal from the navigator column fed back to the patient so that he/she can hold their breath at the same diaphragmatic position every respiratory cycle. While the second technique has potential advantages in decreasing acquisition time, in practice, the need for additional patient training and reliance on their breath-holding capabilities generally means that there is no effective gain in time over the free-breathing navigator technique [18].

With the free-breathing technique, very little patient cooperation is required. The main disadvantage compared with breath-holding is the overall increase in scan time, but for sequences where the image data acquisition time is beyond that achievable in a breath-hold (e.g., high-resolution coronary MRA), use of a navigator free-breathing technique is clearly advantageous. As with ECG gating, this synchronization may be either retrospective or prospective, with data acquisition triggered only when the diaphragm position falls within a defined navigator acceptance window.

There are several important components when planning a navigator-dependent sequence. The first is appropriate positioning of the navigator excitation column or columns, as this

will determine the amount of diaphragmatic motion detected. Sachs and colleagues reported better image quality with the use of three orthogonal navigator columns; however, this was at the expense of increased scan time [19]. Regardless of the number of navigator columns used, these must be positioned over a diaphragmatic edge, where the edge will move along the column during the respiratory cycle. Columns are typically positioned to intersect the right dome of the diaphragm (away from the heart). Care must be taken to ensure that the columns (and the slice-selective excitations used to produce them) do not extend into a region of interest, as signal loss from the navigator pulse excitation will interfere with visualization of any affected tissue (Fig. 2.8). The column cross-section should be small, in order to improve edge detection of the curved diaphragm.

Once the column positions are set, a "scout" sequence of column excitations is performed to assess the patient's diaphragmatic excursion over a series of respirations, and a 2D histogram can then be obtained summarizing the relative frequencies with which different levels of the patient's diaphragm are measured over time (Fig. 2.9).

The navigator acceptance window is then selected based on the appearance of the histogram. The acceptance window is centered on the highest point of the diaphragm, which occurs at end expiration, where there is a short period of relative diaphragmatic immobility. The width of the acceptance window is typically of the order of 4–5 mm, with wider windows leading to improved scanning efficiency (with acceptance of a larger portion of the respiratory cycle) but with increased image blurring and conversely for narrower windows. One problem inherent to the free-breathing navigator technique is respiratory drift, where diaphragmatic position may alter over time, as a patient becomes more relaxed or agitated. This may cause the edge of the diaphragm to progressively move out of the navigator acceptance window with successive respirations, such that there is the potential for little or no triggering of data acquisition throughout the respiratory cycle. Again, as with many facets of MRI, there is a trade-off between the narrowness of the acceptance window and overall acquisition time.

The application of correction factors in the navigator sequence may help to improve its accuracy and improve scan efficiency. Real-time prospective slice following attempts to correct for motion of the heart, through tracking of the diaphragm. This is complicated by the different amounts of motion encountered in different locations of the heart during the respiratory cycle, with relatively less motion occurring at the base of the heart compared with its inferior surface. Use of slice-following technique can allow the use of a wider acquisition window without significant loss of image quality and, with greater acceptance during each respiratory cycle, allows for faster overall scan time [20]. However, the necessary correction factors are specific to the individual and therefore may require an initial preparatory sequence to determine the degree of motion of a patient's heart at different respiratory phases [21]. Retrospective motion correction post-processing techniques are now also being realized [22].

Another form of respiratory gating which has been described is utilizing the ECG variations that can be encountered with each respiratory cycle to provide information

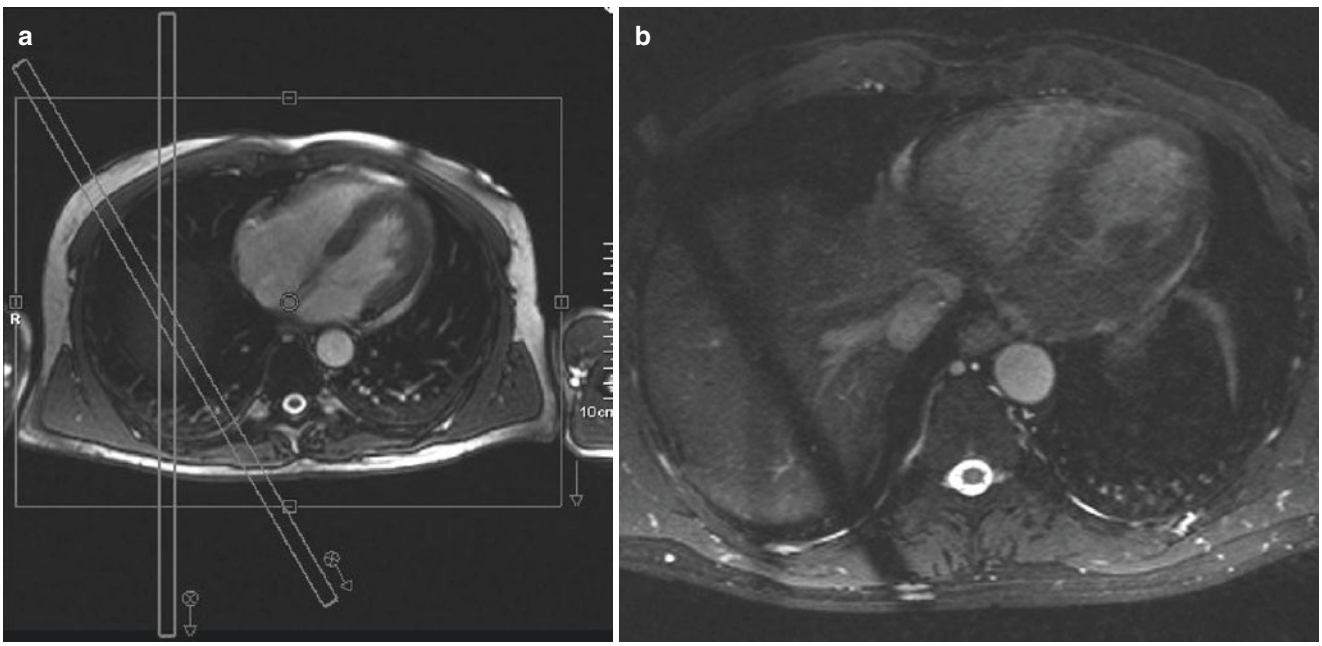

Fig. 2.8 (**a**) Navigator column placement (defined by the intersection of two separate columns) with graphic prescription, at the dome of the right hemidiaphragm; (**b**) loss of signal in the image at the sites from which navigator echoes are obtained

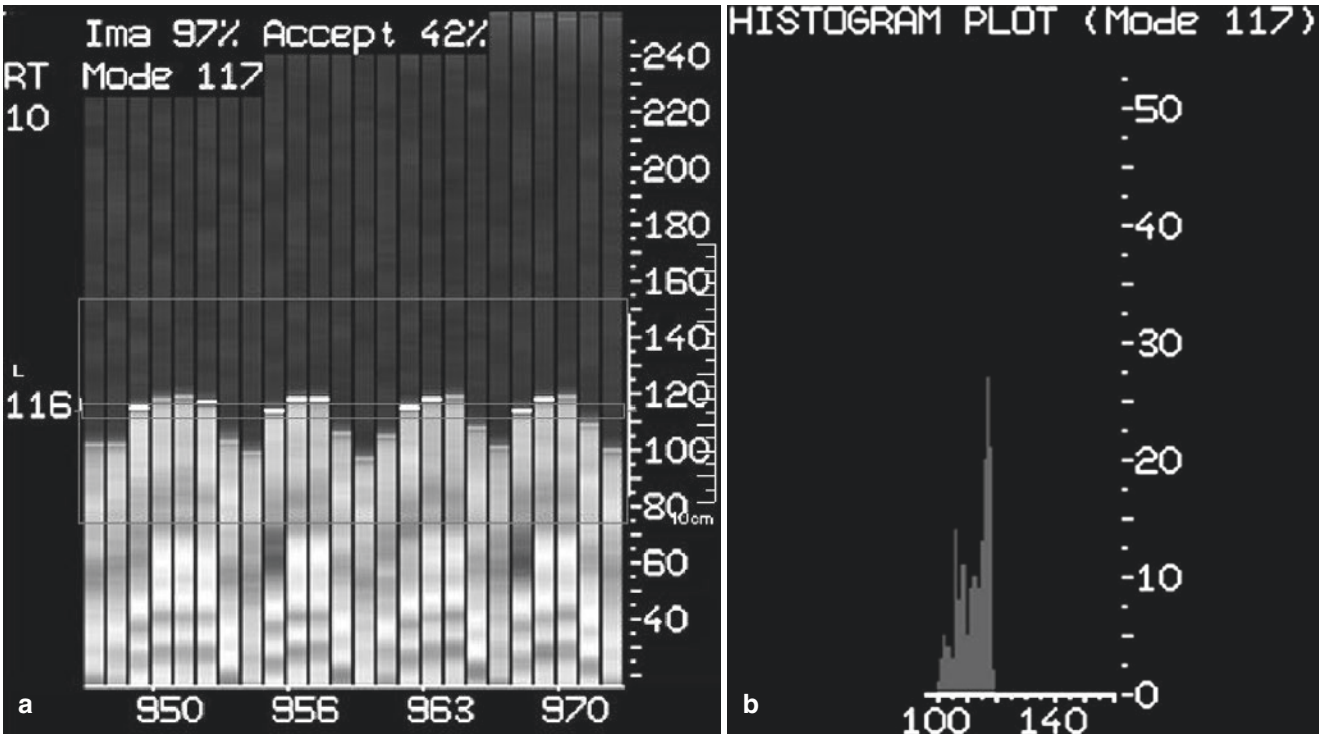

Fig. 2.9 (**a**) Graph depicting diaphragm position in the y-axis and time in the x-axis with use of a respiratory navigator. (**b**) Histogram summarizing the frequency of diaphragm positions during a navigator-dependent sequence

about respiratory phase [23]. However, this is not used in current clinical practice. Alternatively, the signal variations resulting from respiratory motion can potentially be used for "self-gating" [24].

Image Positioning

Unlike standard views of the thorax, which can be oriented in the axial, sagittal, or coronal planes, cardiac MR images are generally obtained along the long and short axes of the heart. The ability to obtain views in any orientation, without the limitations imposed by needing to find an adequate window for insonation, is one of the main strengths of MRI over echocardiography. Similar to echocardiography, views in the left ventricular short-axis, horizontal ("four-chamber") and vertical ("two-chamber") long axes, and through the left ventricular outflow tract ("three-chamber") are typically obtained in a routine cardiac MR study and allow ready assessment of cardiac chamber morphology and function. These standard views can be easily obtained with knowledge of basic cardiac anatomy.

Multi-planar scout images are initially obtained, to ensure that the heart and left ventricle, in particular, are well centered within the imaging field of view, for optimal visualization. From these images, a stack of breath-hold axial images can be obtained (Fig. 2.10). In general, the imaging system allows for directly specifying image locations to be acquired, relative to structures displayed in prior images, using interactive graphics overlays ("graphic prescription").

These form the basis for setting up image locations along the cardiac axes and also provide an overview of the thorax, potentially displaying associated or incidental pathology. A vertical long-axis or two-chamber scout view can then be obtained by prescribing it from a selected initial axial view depicting the left atrium, mitral valve, and left ventricle and then obtaining a single image perpendicular to this one that passes through the estimated plane of the left ventricular apex (Fig. 2.11a). From this two-chamber scout, a horizontal long-axis or four-chamber scout view that includes the left ventricular (LV) axis can then be obtained, again by acquiring a similar image, perpendicular to the two-chamber view, that passes through the mitral valve, and the estimated position of the left ventricular apex (Fig. 2.11b) A short stack of short-axis scout views (spanning rom the apex to the origins of the great vessels) can then be acquired orthogonal to both the two-chamber and four-chamber scout views at the level of the left and right ventricular bases (Fig. 2.11c).

True two-chamber, four-chamber, three-chamber, and short-axis views of the heart can then be obtained from this series of planning images: a true four-chamber view can be acquired by prescribing an image perpendicular to a short-axis view through the ventricular bases, which is also perpendicular to the interventricular septum and is below the level of the aortic valve (Fig. 2.12a). A two-chamber view can be acquired by prescribing an image plane bisecting the mitral valve and the left ventricular apex on the four-chamber view

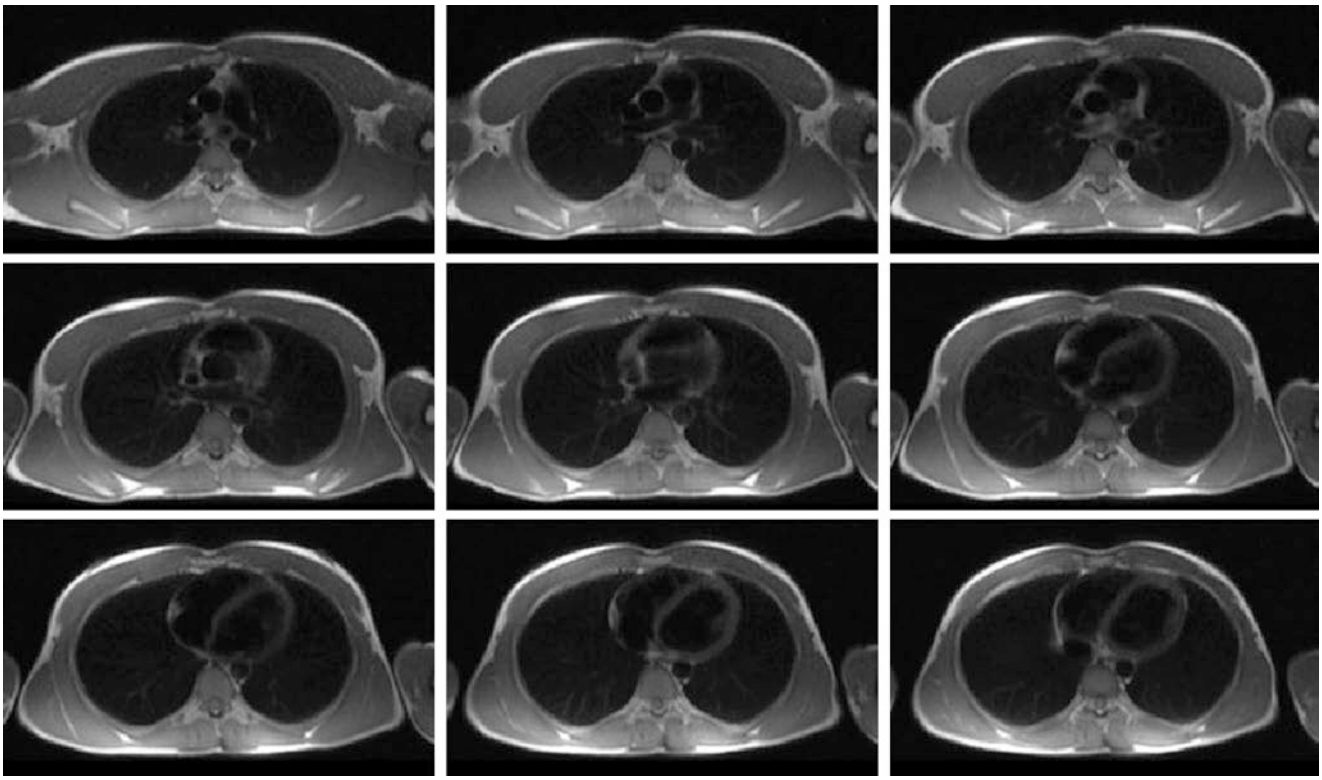

Fig. 2.10 Axial double inversion-recovery SSFP images (see below) for overview of the chest and further image planning

(Fig. 2.12b), and a three-chamber view can be prescribed from a scout short-axis view that is parallel to the left ventricular outflow tract (Fig. 2.12c). Alternatively, two-, three-,and four-chamber views can be prescribed from a mid-ventricular level short-axis scout image, with scan planes centered on the center of the left ventricle, with each scan plane separated from the other two by approximately 60°.

Various different imaging sequences, including cine imaging for assessment of cardiac motion and function, or delayed contrast-enhanced images for assessment of myocardial scar tissue, can then be acquired using the same image positions as these initial cine images. This is vital for correlating areas of structural and functional abnormality and allows for sequential comparisons for patients who undergo multiple studies during the course of their management.

Aside from selecting appropriate positioning of images along the orientation of the cardiac axes, care must be taken to select an appropriate field of view to balance the demands of adequate spatial resolution with acquisition time. The phase-encoding direction should be placed along the direction in the plane where the patient's diameter is shortest, which for most patients is in the anterior-posterior direction when obtaining sagittal or axial views; this can be interactively adjusted while prescribing the image location. This allows a reduction in the number of phase-encoding steps, with a subsequent saving in scan time, which is particularly important for breath-hold sequences. However, if the number of phase-encoding steps is decreased too much, aliasing or "wrap" of structures outside the chosen field of view will occur in this direction. This could potentially obscure the region of interest (Fig. 2.13).

The orientation and position of the field of view are also important factors to consider in order to minimize aliasing. Orientation of the phase-encoding direction should typically be parallel to the orientation of the shortest direction across the chest wall in prescribing images. Every effort should be made to have the structure of interest well-centered in the image, such that peripheral structures remain within the prescribed region. This is particularly important in sequences where parallel imaging is used, which are more sensitive to aliasing, and where the associated artifacts will often appear in the center of the images obtained [25].

Aside from the standard cardiac views described above, there may be additional or alternative views acquired for specific indications. For example, cardiac MRI is commonly used if arrhythmogenic right ventricular dysplasia/cardiomyopathy (ARVD/C) is suspected. Dedicated high-resolution images targeting the right ventricular wall are required if ARVD/C is to be identified or definitively excluded. Images should be obtained as perpendicular as possible to the anterior and inferior portions of the right ventricular free wall, as it is thin and not well visualized if obliquely intersecting views are acquired. These can be planned from scout sagittal images through the right ventricle (Fig. 2.14). The

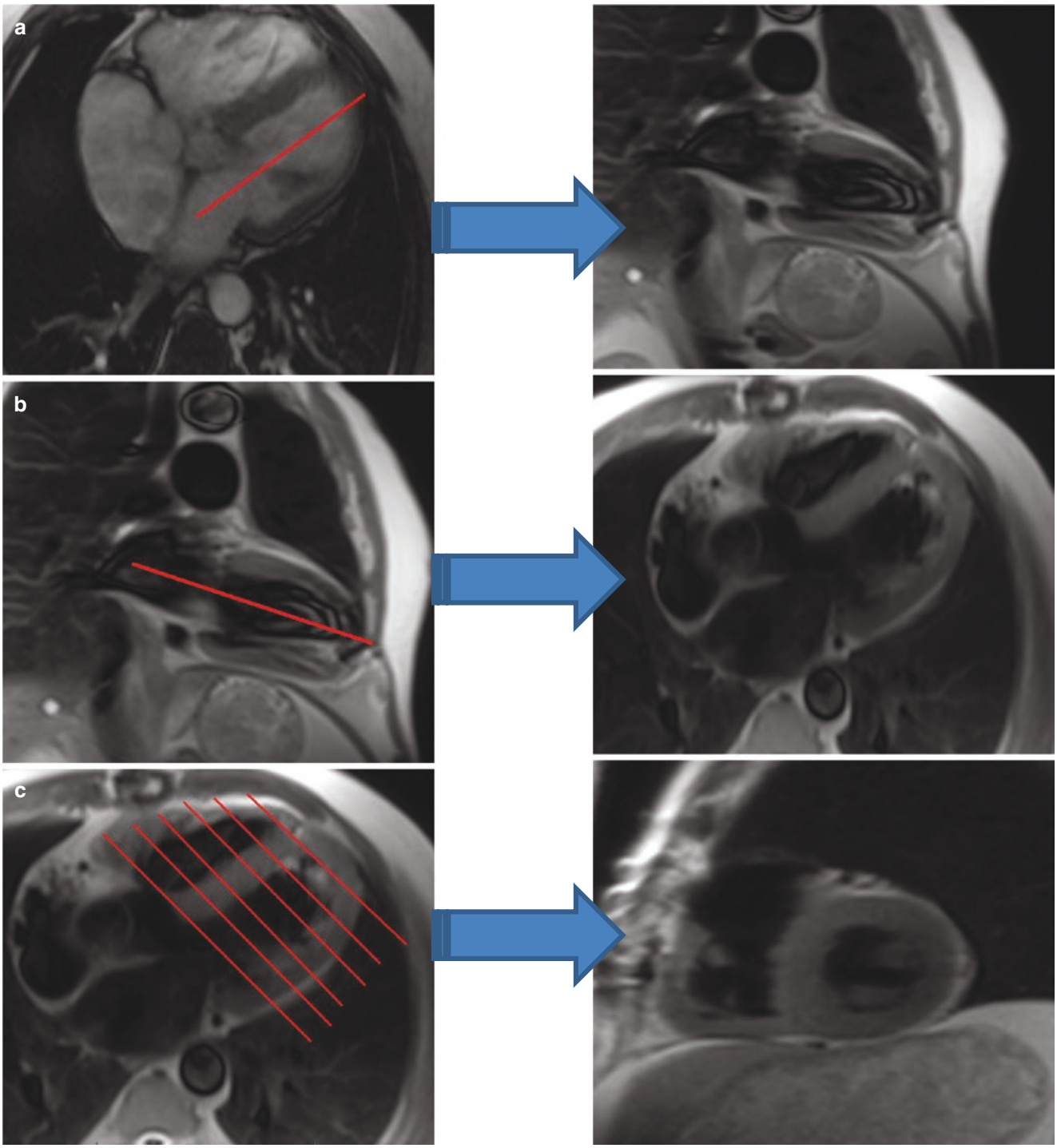

Fig. 2.11 Setup and acquired "scout" images to determine true cardiac axes. (**a**) Near two-chamber scout, acquired by perpendicular prescription from the axial; (**b**) near four-chamber scout, acquired by perpendicular prescription from the two-chamber image; (**c**) short -axis image scout stack through the ventricular bases, acquired by perpendicular prescription from the four-chamber scout image

structure and function of the right ventricle is measured well by the same stack of parallel, contiguous short-axis imaging planes that are used for assessment of the LV. These image planes can be prescribed from a horizontal long-axis view to contain parallel planes extending from the tricuspid-mitral valve plane to the LV apex. Additional useful RV-specific scan planes include (1) a RV two-chamber view, prescribed similarly to the LV from the four-chamber view; (2) a three-chamber view that intersects the tricuspid and pulmonary valves and the RV apex for imaging the RV inflow-outflow

tract; (3) an RV outflow plane, which can be prescribed from the RV 3-chamber view as a plane parallel to the conus arteriosus and the pulmonary trunk; and (4) a short-axis slice through the pulmonary valve, prescribed perpendicular to the RV outflow plane.

Another important indication for cardiac MRI is for the evaluation or follow-up of congenital heart disease. Supplementary views may commonly be required, due to atypical anatomy in these patients. For example, a view oriented appropriately to the interatrial septum may be useful in the assessment of atrial septal defect or patent foramen ovale. It is also often important in the setting of congenital heart disease to evaluate views of the right ventricular outflow tract, which can be obtained by systematically acquiring orthogonal long-axis views beginning with a long-axis view through the right ventricle.

3D contrast-enhanced MR angiography is useful for the evaluation of the aorta and pulmonary arteries. It is also highly effective for the assessment of collateral vessels or shunts, with the use of rapid sequential time-resolved short TE and low-flip-angle gradient-echo imaging [26]. We can similarly use initial scout images to prescribe images that are aligned with or perpendicular to specific desired vascular structures. There is again a trade-off between maximal anatomic coverage and minimal acquisition time, and this is an important consideration in choosing the plane of coverage of the 3D slab. If the aorta is the focus of the study, an oblique sagittal plane parallel to the orientation of the aortic arch is recommended (Fig. 2.15). If the pulmonary arterial system requires assessment, for example, in the evaluation of main or branch pulmonary artery stenosis, a coronal plane will generally provide maximal anatomic coverage.

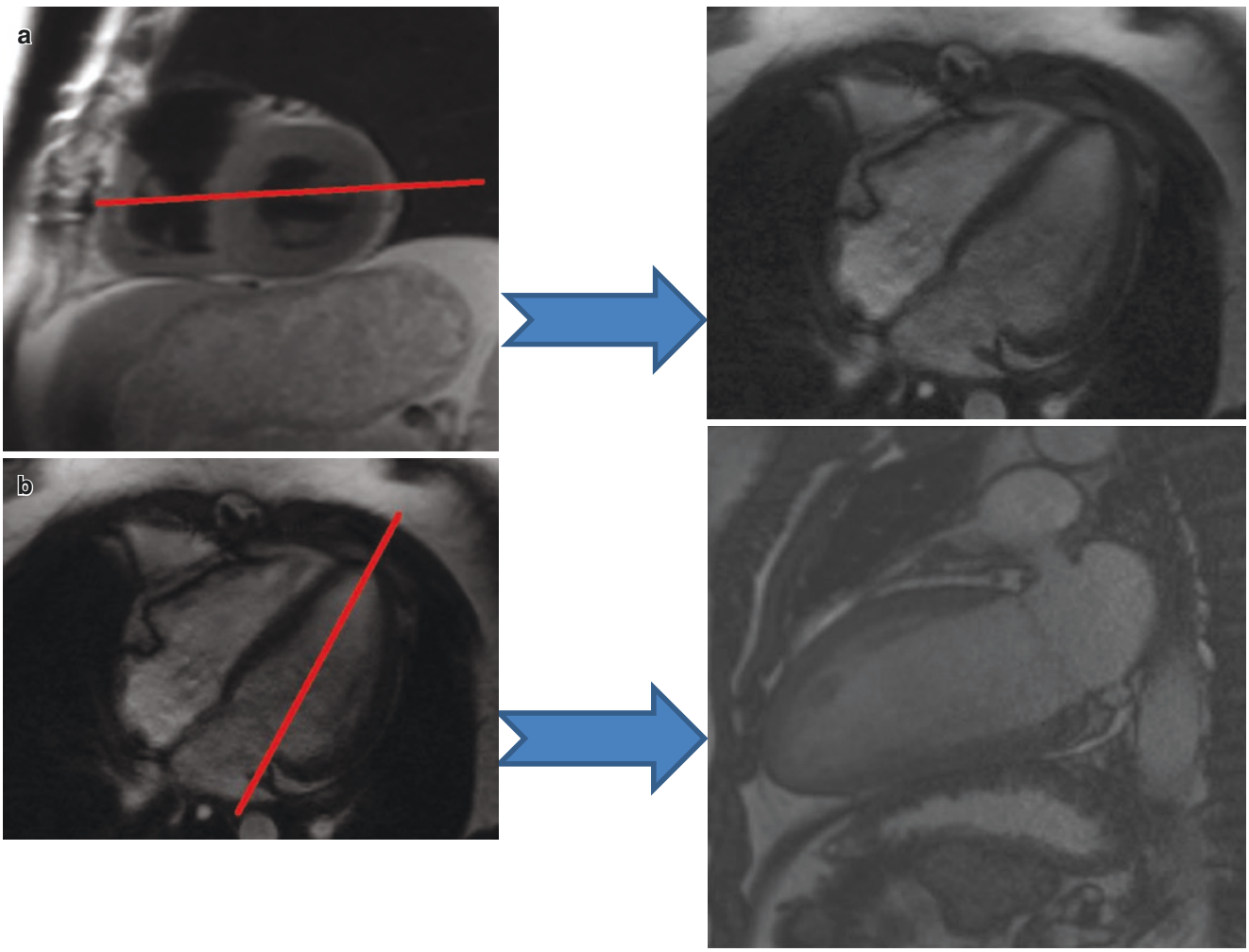

Fig. 2.12 Setup and images obtained along the true cardiac axes. (**a**) Four-chamber cine view, acquired by perpendicular prescription from the axial image to its left; (**b**) two-chamber cine view, acquired by perpendicular prescription from the four-chamber image to its left; (**c**) perpendicular prescription from the short-axis scout images for three-chamber view; (**d**) three-chamber cine view, acquired from short-axis prescription; (**e**) perpendicular prescription from the true four-chamber cine image for short-axis views; (**f**) short-axis cine view, acquired from the four-chamber cine prescription

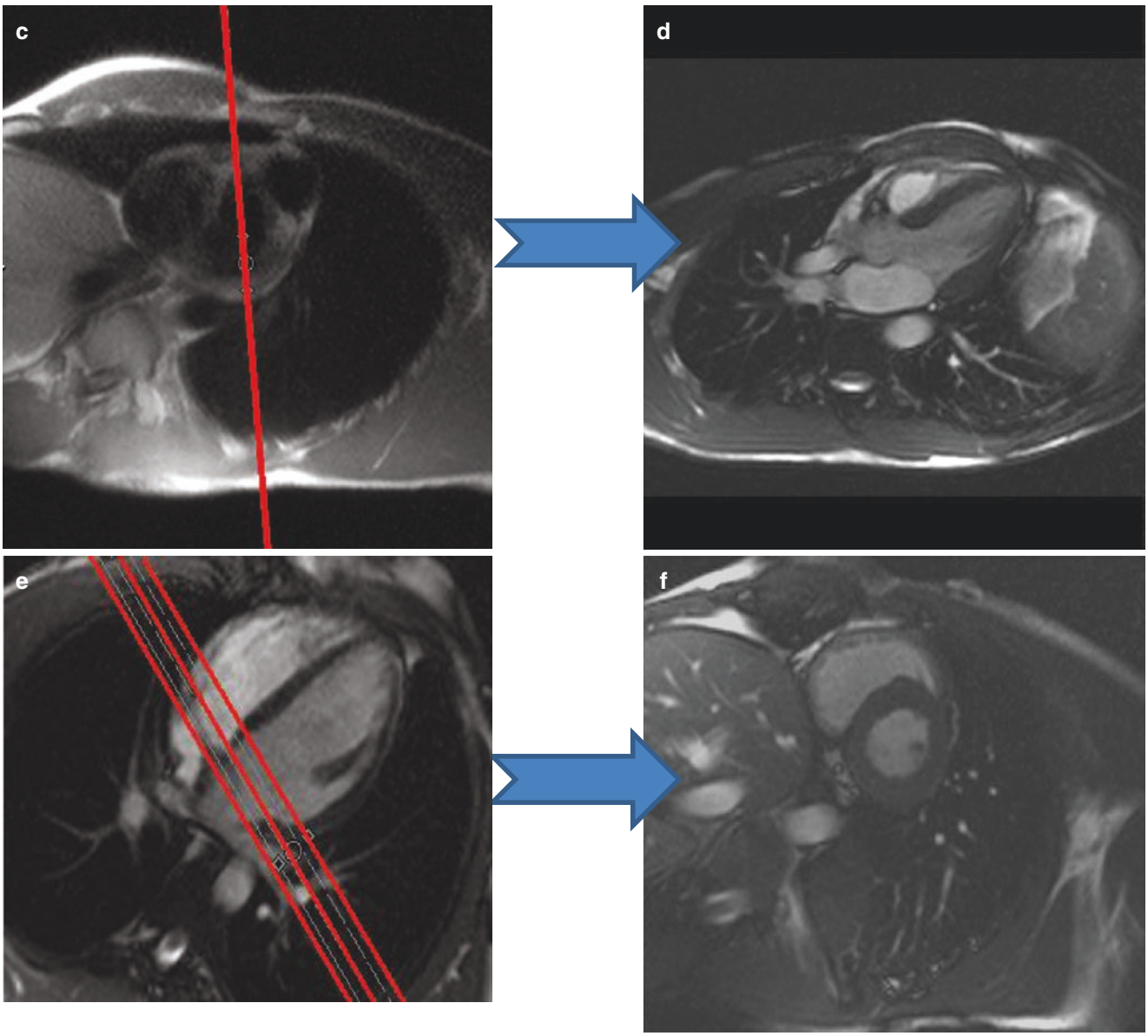

Fig. 2.12 (continued)

PD, T1, and T2 Weighting: Tissue Characteristics and Contrast Agents

The amount of signal detected by a receiver coil will dictate the brightness of the voxel in a MR image. T1 relaxation time, T2 relaxation time, and proton-density are MR tissue properties which can be affected by different tissue states. We can design MRI pulse sequences that are sensitized to these properties, to different degrees. Altered tissue properties will then be reflected in the corresponding local brightness of the resulting MR images, to different extents, depending on the pulse sequence designs.

The relative contributions of the T1 and T2 relaxation times to the image contrast depend on the specific imaging method employed and the choice of the relevant imaging variable values, particularly the time between consecutive excitations (the "repetition time," TR) and the time between the excitation and the detection of the signal as a gradient or spin echo (the "echo time," TE). In general, the shorter the TR time, the less time there will be for recovery of the magnetization between excitations, so that regions with shorter T1 values (e.g., fat or contrast-enhanced blood) will tend to appear relatively brighter ("T1 weighting"). Similarly, the longer the TE time, the more time there will be for decay of the signal before its detection, so that regions with longer T2 values (e.g., fluid or edematous tissue) will tend to appear relatively brighter ("T2 weighting"). In the case of imaging approaches employing a train of repeated spin echoes (e.g., generated with multiple 180° refocusing

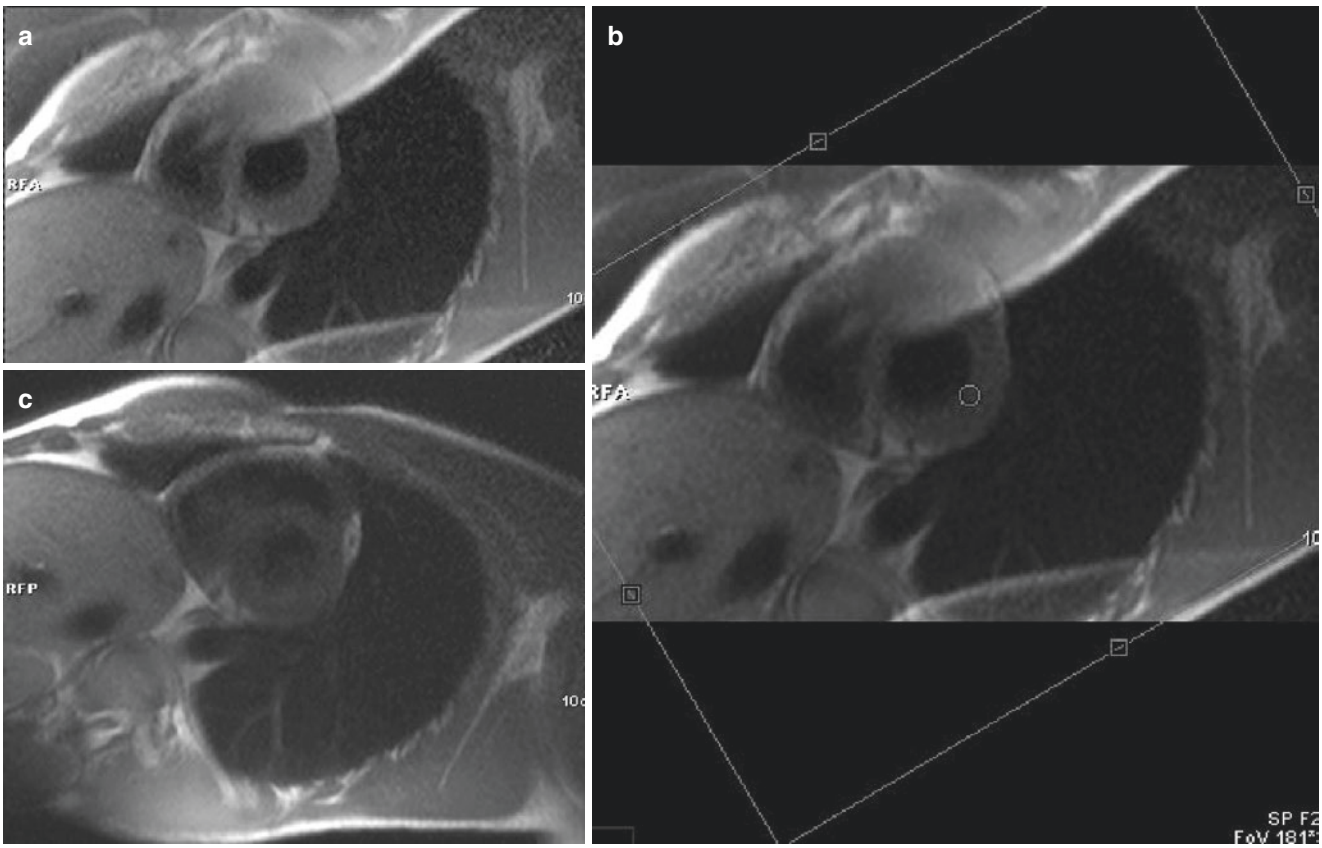

Fig. 2.13 (**a**) Aliasing with "folding" of chest wall into the region of interest; (**b**) demonstrating how angling the prescribed scan field of view to follow the chest wall can prevent peripheral structures from aliasing; (**c**) elimination of aliasing image from a after adjusting orientation of field of view

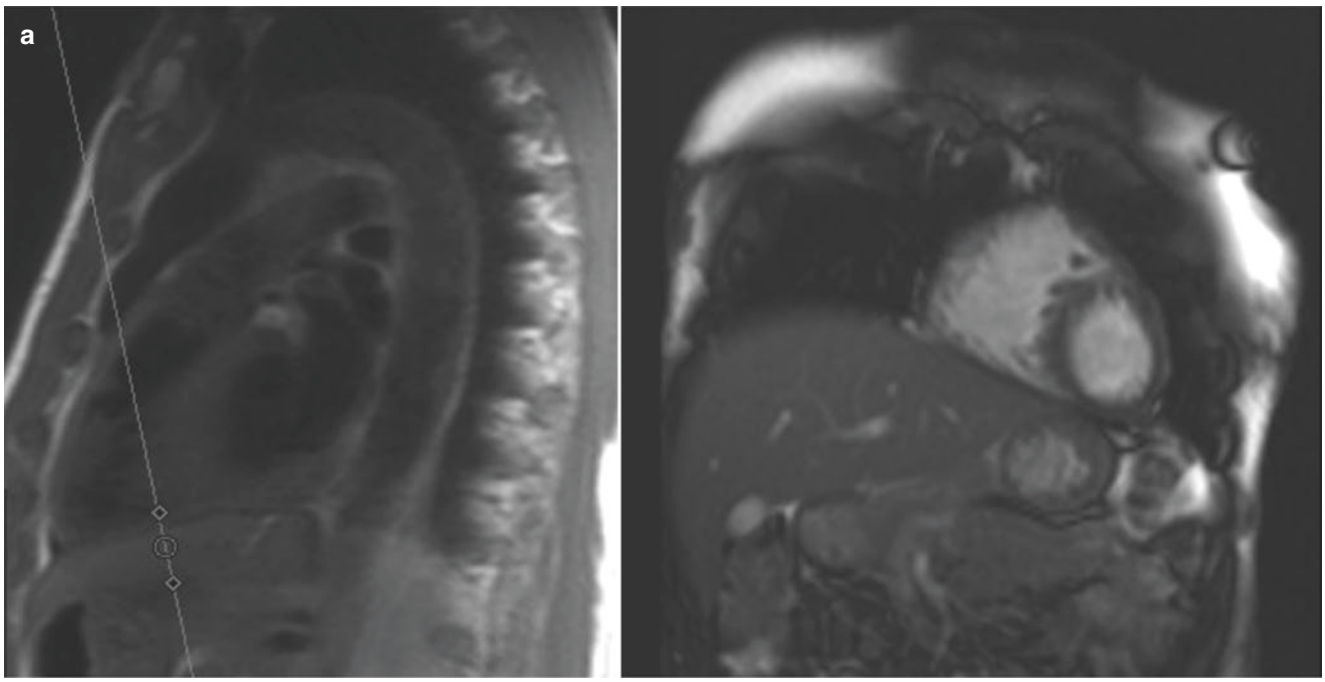

Fig. 2.14 (**a-c**) Examples of images perpendicular to the right ventricular wall, demonstrating their planning

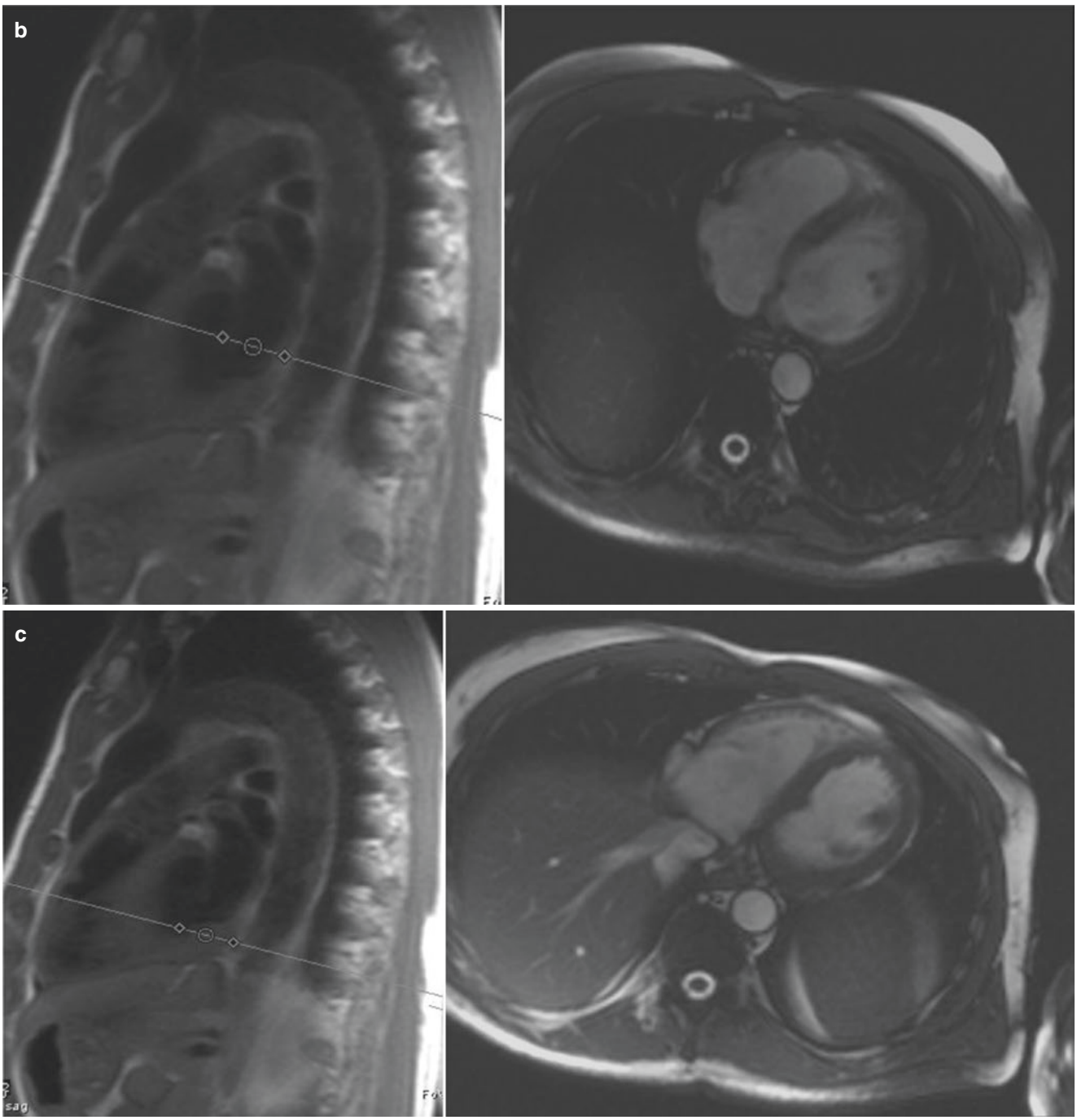

Fig. 2.14 (continued)

excitations after an initial 90° excitation), the effective TE time is the time after the initial excitation when the imaging data near the center of "k-space" are acquired. If the heart rate is rapid, it may be necessary to set up the T2-weighted imaging sequence so that the excitations skip alternate heartbeats, in order that the potentially competing effects of T1 weighting can be minimized. Note that in the case of gradient-echo imaging, local magnetic field inhomogeneities (e.g., due to local iron deposition) can lead to incomplete refocusing of the echo and resultant signal loss ("T2* weighting"); this can thus cause darkening in images of hemochromatosis or in the region of old hematomas. Also note that motion between initial excitation and refocusing pulses can lead to decreased signal in the spin-echo imaging methods (due to their spatial localization, as described above for blood flow), so that pericardial effusions, for example, may not appear as bright as might be expected in T2-weighted imaging.

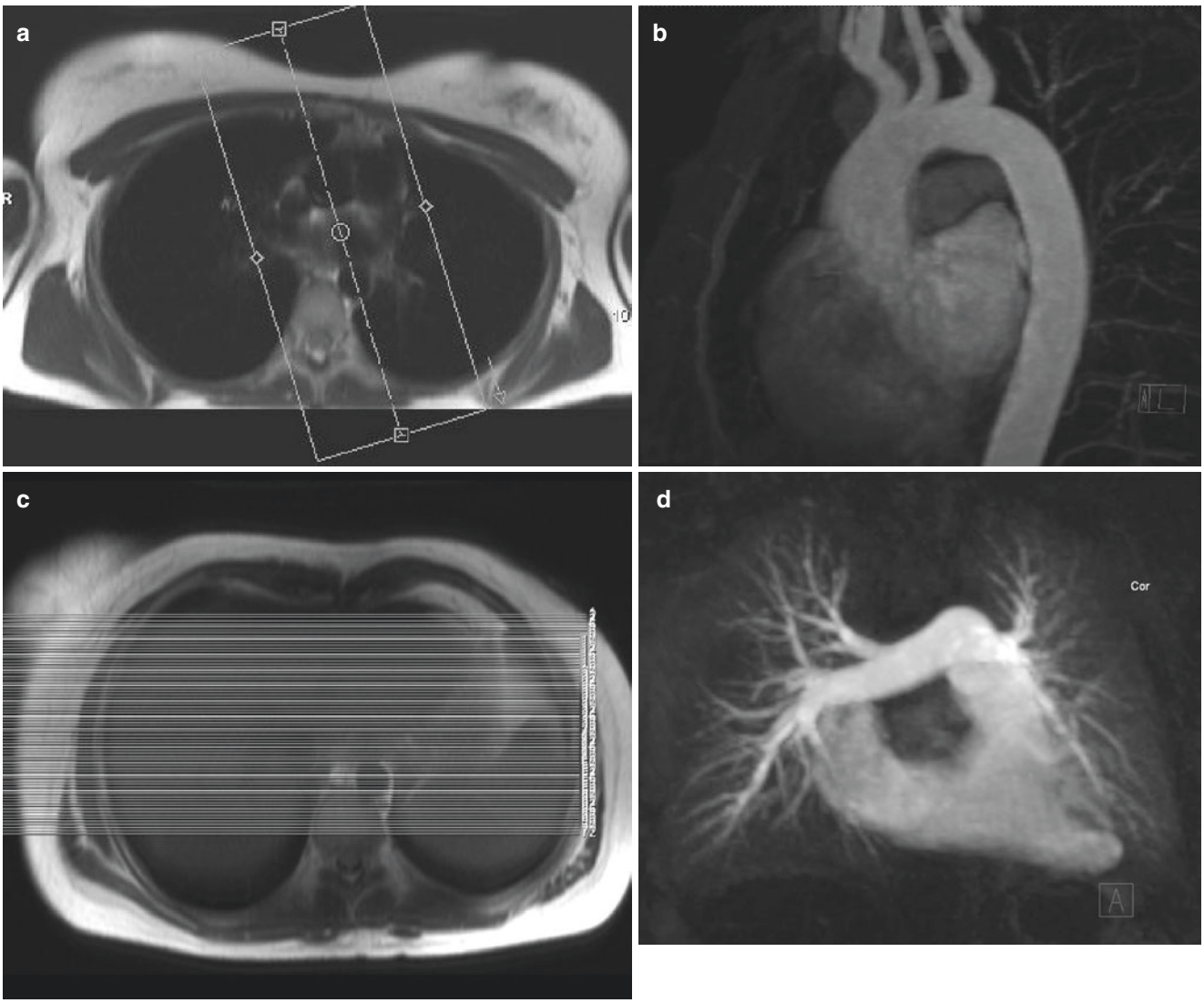

Fig. 2.15 (**a**) Oblique sagittal 3D field of view for MRA targeting the aortic arch, prescribed from an axial HASTE image; (**b**) subtracted maximal intensity projection (MIP) images obtained from the MRA slab depicted; (**c**) prescribing image location from true axial HASTE image for pulmonary MRA; (**d**) subtracted MIP image acquired in the pulmonary arterial phase

An alternative way to create T1 weighting is to use an initial "inversion" excitation pulse to invert the longitudinal magnetization prior to the signal excitation ("inversion-recovery" imaging). In the time interval between the inversion pulse and the excitation pulse, the initially inverted magnetization will recover back toward its equilibrium state, oriented along the main magnetic field, crossing through a state of zero magnetization along the way. The resulting signal produced by the excitation pulse will depend on the duration of the delay between the inversion pulse and the excitation pulse. If the delay is long compared to the T1 relaxation time, the signal will be close to that which would have been produced without the inversion pulse; if the delay is such that the excitation pulse is applied close to the time when the magnetization is passing through zero, the signal will be very small (the image will be dark). On the other hand, if the delay is so short that the magnetization is still negative, there will again be signal produced but with an opposite phase; with conventional magnitude imaging, this will result in a brighter signal again, but with more specialized "phase-sensitive" imaging methods, we can detect the difference between regions with negative and positive magnetization.

The characteristic short T1 value of fat leads to it tending to have a bright appearance in MRI, which typically has a fair amount of effective T1 weighting. This can be helpful, e.g., to help delineate the bright pericardial fat from the lower signal of the adjacent pericardium or the myocardium. However, if it is desired to suppress the signal from fat, there are two approaches that can be used. In one approach, a short-time inversion-recovery (STIR) sequence is used for imaging, with the inver-

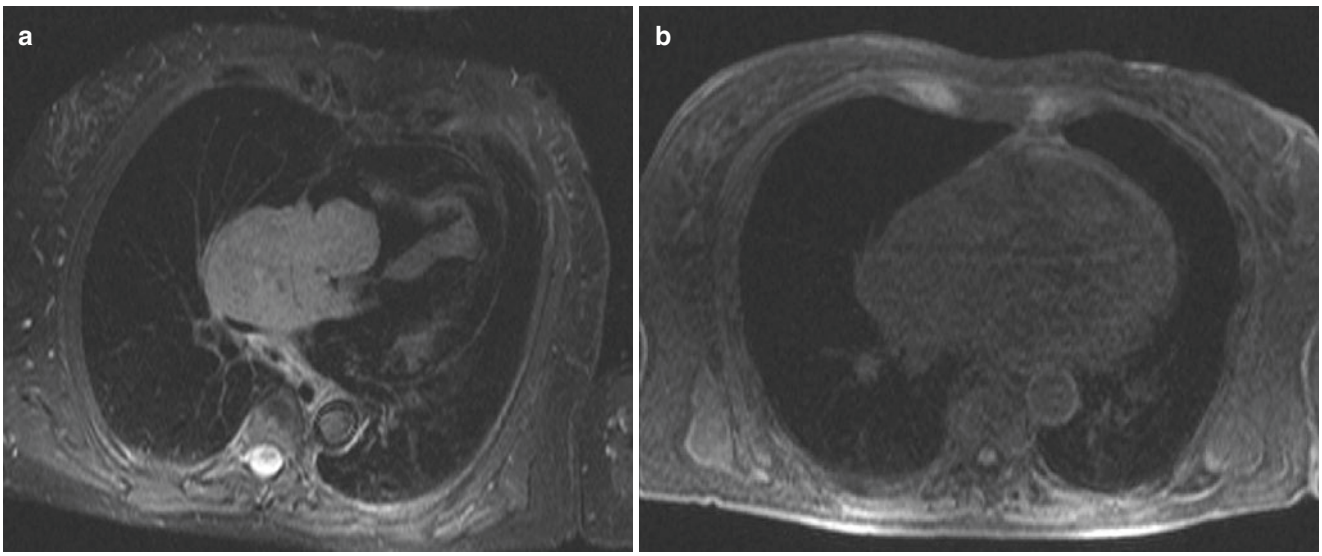

Fig. 2.16 (**a**) Short tau inversion-recovery image; note the large bilobed enhancing mass within the right atrium, with extension through to the pericardium, due to non-Hodgkin's lymphoma. (**b**) Frequency-selective fat-saturated 3D gradient-echo T1-weighted sequence, demonstrating how we can inadvertently create an isointense appearance of mass with surroundings with poor choice of imaging parameter values

sion time kept short, so that the recovering fat magnetization is approximately nulled (and it thus will appear dark) at the time of excitation for image data acquisition, while longer T1 tissues will still have a significant amount of magnetization and will appear relatively brighter. Even though the magnetization of the other tissues with longer T1 values will actually be negative, this will not affect their appearance in conventional MR imaging displays, which only display the magnitude of the local signal. While this approach to fat suppression is fairly robust, it is not specific to fat, as other regions with similar short T1 values will also have their magnetization nulled by the inversion pulse. A more specific approach to fat suppression is to use a frequency-selective saturation pulse, tuned to the resonance frequency of the fat (which differs by about 3.5 parts per million from that of water) to null the magnetization of fat. When followed immediately by an excitation pulse for imaging data acquisition, this will result in effective nulling of the signal from fat. This is particularly useful for verifying the fat content of masses such as lipomas. However, note that in the presence of magnetic field inhomogeneity, the local resonance frequency of fat will vary correspondingly, so that a frequency-selective pulse that effectively suppresses fat in one region may fail to do so in another or may even result in water saturation [27] (Fig. 2.16).

T2*-Weighted Spoiled Gradient Echo

T2* weighting with spoiled gradient-echo pulse sequences is achieved by increasing the TR and TE to relatively long values. As the T2* values for tissues are shorter than the T2 values, the echo times chosen to achieve T2* weighting with gradient echo are also much shorter than the echo times required to achieve T2 weighting with spin-echo sequences. With T2*-weighted gradient-echo imaging, the image contrast can be strongly influenced by the presence of magnetic susceptibility effects; this can be used to detect the presence of iron, for example, where there is hemorrhage or iron loading of tissue. The local value of T2* can be calculated from the loss of signal observed with longer TE times; this is related to the degree of iron deposition in hemochromatosis.

Bright Blood and Dark Blood Imaging

A striking aspect of cardiac MRI is that blood can appear either bright or dark in the images, depending on how they were acquired. This is largely due to the different effects of motion on the MR signal with different signal acquisition methods (including "time-of-flight" and phase-shift effects) [28], although the distinctive relaxation times of blood can also play a role, particularly in "steady-state free precession" (SSFP) or contrast agent-enhanced imaging. These effects can be exploited to produce useful image contrast between the blood and the heart wall and can even provide qualitative or quantitative assessment of flow.

When imaging with rapid T1-weighted gradient-echo imaging (e.g., "FLASH"), the blood can appear relatively bright compared to the adjacent stationary tissue. This is due to the replacement between consecutive excitations of the partially magnetically saturated blood left in the slice being imaged from the last excitation. This more magnetized blood produces a stronger signal and appears relatively bright in the images, as compared to the more stationary heart wall, which does not get such replenishment of its magnetization; this has been called "flow-related enhancement." Note that through-plane motion of the heart wall can actually produce a noticeable alteration of the signal from the heart wall itself during the cardiac cycle, although the relatively slower

motion of the wall leads to less signal enhancement than that seen for the blood. Also note that when imaging a thick slab of tissue with gradient-echo imaging techniques, the flow-related enhancement may only be apparent in blood vessels near the entrance side of the slab, as the blood may get repeatedly excited (and thus partially saturated) as it flows deeper into the slab.

"Time-of-flight" (TOF) technique uses 2D and 3D gradient-echo sequences and relies on flow-related enhancement to produce a "bright-blood" effect in the images, without the need to use exogenous contrast material. The goals of TOF imaging are generally to produce high spatial resolution images, where flow-related enhancement is maximized, flow-related dephasing is minimized, and background tissue is suppressed. Flowing blood enters the slice fully magnetized and generates high signal following the RF pulse. This creates bright signal in vessels with flowing blood, relative to dark background of the stationary tissue. To maximize flow-related enhancement, the imaging slices are positioned perpendicular to the direction of blood flow. Any inflow of unsaturated protons will produce increased signal. Therefore, both arteries and veins are bright. A spatially selective saturation band (see below) is usually applied upstream to saturate venous signal when MR arteriography is desired. Flow compensation, together with reduced TE and small voxel size (high spatial resolution), can help to reduce overestimation of stenosis. 3D TOF has higher spatial resolution and is less susceptible to turbulent flow than 2D TOF, but it is also less sensitive to slow flow.

When imaging the heart with spin echoes produced by 90° and 180° spatially selective radio-frequency (RF) excitations, motion of the blood between the two excitations can lead to a decreased signal from the blood, as it needs to experience both RF pulses in order to produce the signal. This tendency to darkening of the blood in spin-echo imaging, due to motion, can be enhanced by adding extra pulses to decrease the magnetization of the inflowing blood. This "black-blood" appearance can also be readily achieved by applying two 180° pulses in rapid succession ("double inversion-recovery"). The first inversion pulse is nonselective, to produce effective inversion of the magnetization of everything within the RF coil; the next is a selective 180° pulse centered at the location of the slice to be imaged, which is used to effectively restore the magnetization of the stationary tissues within the slice to their starting condition. If we then wait for the magnetization of the blood in the inverted regions to pass through a zero magnetization state (on their way back toward their equilibrium magnetization state) before imaging, those blood-filled structures in which blood which has been replaced by blood from outside of the slice will appear black.

Motion of excited spins along magnetic field gradients, such as those used in MRI can result in the signal from the moving spins acquiring a phase shift relative to the signal from adjacent stationary spins. Although the phase information is not directly displayed in conventional MRI, it can still affect the displayed magnitude. For example, if there is a strong shearing spatial gradient of velocity (and its associated phase) in a given region, there can be interference between the different phases within a voxel and a resulting loss of the net local signal from the blood. In addition, if there is unsteady flow, as in turbulence associated with a jet, the associated fluctuations in the signal phase can lead to a local loss of image intensity. Both of these effects can lead to a darkening of the image of the blood in "bright-blood" imaging of abnormal flows, such as those associated with stenosis.

When using SSFP imaging methods, the blood can produce a strong signal independent of its motion, due to its relaxation time properties, and thus it will typically appear bright in the MR images. In SSFP, rapidly repeated excitations produce an increased signal by setting up a steady-state condition where the magnetization is refocused between each excitation. This can happen even off the resonance frequency, but there may be a different steady-state setup that depends on the amount of the frequency offset. In particular, there are two different sorts of steady states that can be set up, depending on the amount of frequency offset: one where the signal is in phase with the exciting RF pulses and one where it has an opposite phase. The net signal produced in SSFP thus depends on both the T2 relaxation time, through the amount of magnetization remaining in the interval between pulses, that can be refocused, and the T1 relaxation time, through the amount of recovery of the longitudinal magnetization in the interval between pulses, which can be excited. In blood (and other fluids), the high ratio of the T2 to the T1 relaxation times results in a strong signal with SSFP. The phase of the resulting signal depends on the local field strength. However, when the local magnetic field strength varies with position such that the flowing blood is carried from an area with one phase into an area with the opposite phase, the steady state will be interrupted, and the resulting fluctuations in the blood signal can cause local signal loss and artifacts that can propagate into other areas of the image. To reduce the effects of this artifact, we can adjust the homogeneity of the magnetic field ("shimming"), or we can simply try to adjust the resonance frequency, to change the location of the artifact.

Another way that blood can appear bright in the image is due to shortening of the T1 relaxation time by injection of an MRI contrast agent, which will lead to increased signal in the presence of T1 weighting in the imaging method. If a 3D volume is rapidly and repeatedly imaged after the injection of a bolus of contrast agent (producing T1 weighting), the blood vessels with high concentrations of the agent at the time of image acquisition will appear bright. If the image acquisition is fast enough, the delay after the injection can be adjusted so

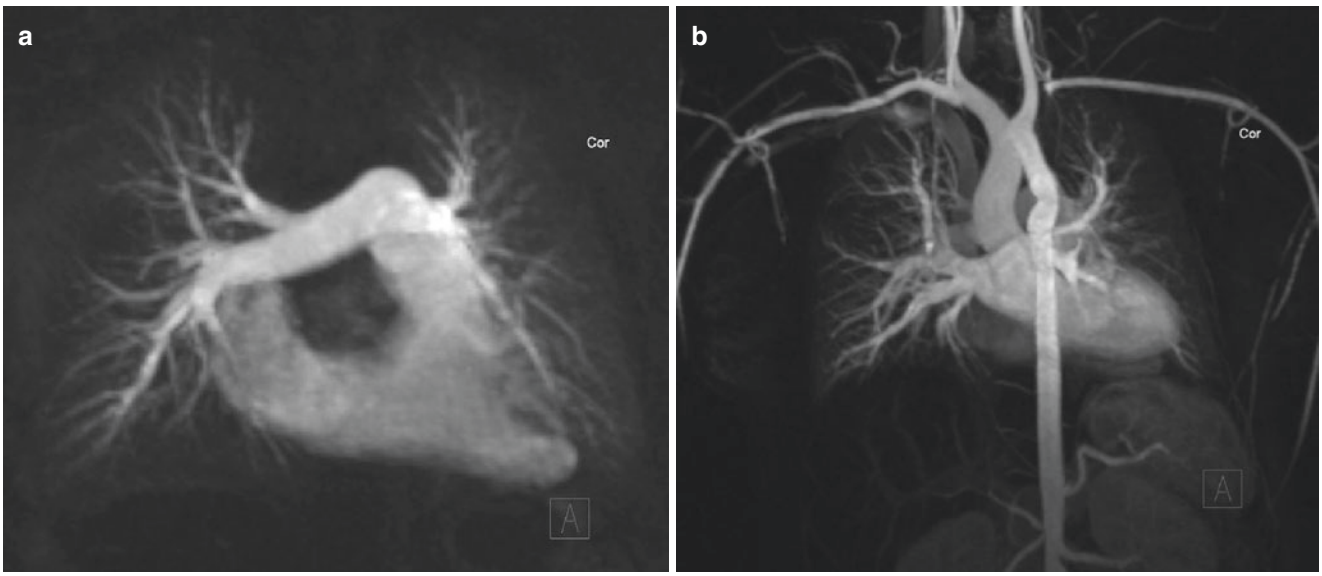

Fig. 2.17 Sequential 3D T1-weighted images acquired after a single injection of contrast, rendered as "maximum intensity projection" (MIP) images after an appropriate timing delay in order to obtain: (**a**) pulmonary arterial phase and (**b**) systemic arterial phase. Note abnormal kinking of the proximal descending aorta in this patient, whose status is post-aortic coarctation repair. The left subclavian artery is also occluded from prior surgery

as to have prominent enhancement of only a desired portion of the vascular tree, e.g., arteries vs. veins or pulmonary vs. systemic vessels (Fig. 2.17).

Choosing the timing of this delay can be aided by acquiring a rapid series of sequential images of a representative vessel after the injection of a small test bolus of the agent, often called a "timing run," to detect the time of the arrival of the bolus in the vessel of interest after the injection (Fig. 2.18). The bright vessel images in the imaged region can then be processed with a suitable computer program to produce a synthetic angiographic display of the vessels from any desired point of view (an "MRA"), e.g., with "maximum intensity projection" (MIP) or "volume-rendered technique" (VRT). Issues related to MRA will be discussed in more detail in other chapters in this book.

There are three principal approaches to the modification of the image contrast. Firstly, RF preparation ("conditioning") pulses (such as inversion and fat-saturation pulses) may be added to "prepare" the magnetization in imaging pulse sequences, prior to the signal readout with RF excitation pulses. A second method of modifying the MR contrast is through the intravenous administration of an exogenous contrast agent, as above. The third contrast mechanism consists of motion-sensitive imaging, with various potential mechanisms used to have signal reflect differences in motion (e.g., between flow blood and vessel wall or to encode flow velocities). Whereas for most of the MR techniques one only uses images where the MR image pixel intensity reflects the magnitude of MR signal ("magnitude images"), for phase-contrast flow-velocity imaging, one also uses images that reflect the phase of the signal, which is made to reflect the flow or motion velocity at that location. These flow-based contrast modification methods will be discussed further, below.

Inversion and Saturation "Conditioning" Pulses

Saturation of the magnetization with suitable conditioning pulses can be used to suppress the signal from specific tissues and thus alter their appearance in images. These tissues are initially excited by a 90° RF pulse, and their magnetization is thus tipped into the transverse plane. Subsequently, a dephasing gradient pulse is used to spread the phases of any resulting signal from an imaged tissue element ("voxel"), so that there is no net-detected signal (the signal has been "crushed"), and therefore it can no longer contribute to imaging. As there is initially no longitudinal magnetization remaining in the tissue, no signal will result from an immediately following RF excitation pulse. This suppressive effect of the preconditioning RF pulse will go away when the tissue recovers its longitudinal magnetization, which will depend on its T1 relaxation time. The effect of the saturation pulse can be made to be spatially defined (with spatially selective excitation) or tissue-selective (e.g., with frequency-selective fat saturation).

There are many applications that use saturation pulses, including the following:

1. In time-of-flight applications (TOF), spatially selective saturation pulses can be applied on one side of the region to be imaged, and thus used to suppress signal from protons flowing into the imaged slice from the asymmetrically saturated direction (such as venous blood), thereby

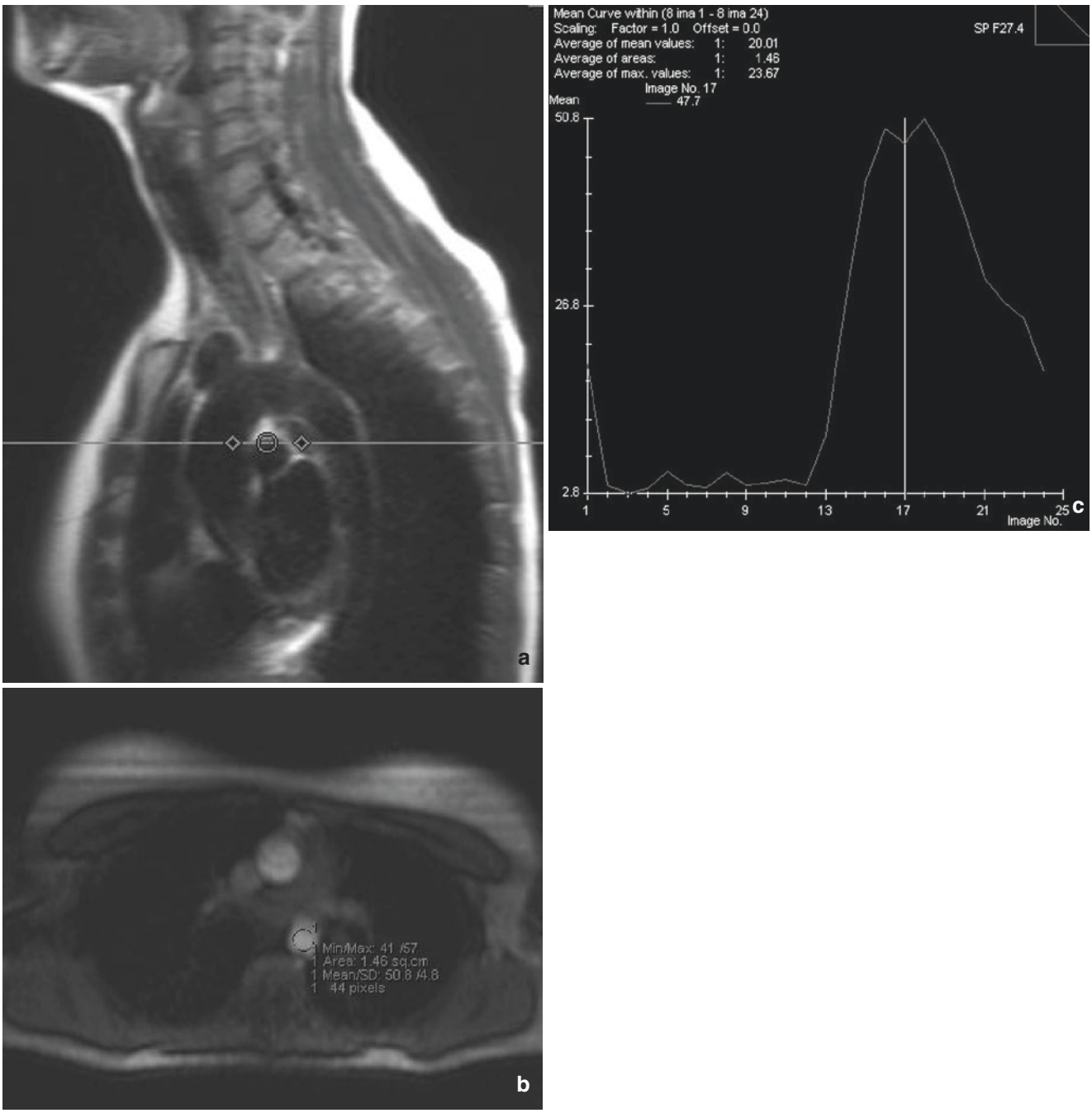

Fig. 2.18 (**a**) Planning image for timing run imaging of single slice, acquired sequentially after bolus injection of a small amount of intravenous contrast agent; (**b**) example of image acquired during the timing run, with region of interest placed over the descending aorta; (**c**) graphical depiction of signal intensity within the region of interest over time after the contrast agent bolus injection, allowing for selection of the appropriate timing delay when signal intensity within the thoracic aorta is maximal (if a thoracic aorta MRA is desired)

enabling selective imaging of the arterial protons [6]. This can also be used to show reversal of the usual direction of flow, e.g., with subclavian steal [6].

2. Spatially selective saturation of regions outside the region of interest can be used to avoid some undesired imaging artifacts, such as wrap around by structures outside the field of view or motion artifacts from blood or CSF.
3. Frequency-selective saturation can be used for selectively modifying the signal from fat or water, which have intrinsic resonance frequencies that differ by a few parts per million. For example, we can selectively produce saturation of the tissue fat by applying a frequency-selective saturation pulse sequence at the beginning of the pulse sequence, consisting of a 90° RF prepulse, applied at the

resonance frequency of fat, which is immediately followed by a dephasing "crusher" gradient pulse. This results in selective depletion of the magnetization of the fat component of the tissue, so that only the water protons will contribute significantly to subsequent image formation until the fat magnetization recovers. Note that this signal saturation effect will go away with the recovery of the fat longitudinal magnetization over time. Also note that the magnetic field over the region being imaged must be uniform enough that a given frequency of the saturation pulse will correspond to the local resonance frequency of fat over the region of interest, in order to reliably saturate all of the fat tissue.

Inversion-recovery imaging refers to the use of inversion conditioning pulses to selectively suppress the signal from certain tissues, based on their T1 magnetization recovery times; the resulting change in their longitudinal magnetization will result in alteration of the signal produced by a subsequent RF excitation pulse. A typical inversion-recovery sequence first applies a 180° RF prepulse. At a specific "null point" during the subsequent recovery of the longitudinal magnetization (depending on its T1 value), a given tissue would have little or no longitudinal magnetization and thus would produce little or no signal in response to an excitation RF pulse; it would thus appear dark in the resulting image. The timing of the null point will depend on the T1 value of a specific tissue. The time between the 180° inversion prepulse and the subsequent RF excitation is referred to as the "inversion time." For spin-echo and gradient-echo imaging, the RF excitation pulse is applied at an inversion time which can be adjusted to achieve tissue nulling of a selected tissue. The inversion-recovery technique affects all protons in the image. Note that in the setting of an inhomogeneous magnetic field (e.g., with some metal in the region), the nominal inversion pulse may not be equally effective over the whole region, with resulting spatial variation in the resulting imaged signal suppression, even with a uniform underlying tissue. Also note that with conventional magnitude imaging, the signal from a region of very incomplete magnetization recovery, with longitudinal magnetization that is still negative (i.e., with a longer T1 value), may still appear to be relatively bright in the image, as we cannot distinguish the signal from regions with positive or negative magnetizations. However, it is possible to modify the imaging method to allow distinguishing the sign of the magnetization ("phase-sensitive IR imaging") in the resulting images, which both extends the dynamic range of the imaging and resolves possible ambiguity of the images, as regions with negative magnetization can now be rendered as darker than those with more fully recovered positive magnetization.

We can also use "short-time inversion-recovery" (STIR) imaging to achieve fat suppression, as an alternative to the frequency-selective saturation approach described above [29]. In this case, we take advantage of the fact that fat tends to have a T1 value that is typically fairly uniform but shorter than that of most water-containing tissues. Thus, applying an inversion pulse and waiting for an inversion time that is appropriate for nulling the fat T1 value will result in a dark appearance of the fat. Note, however, that any water-containing tissues that happened to have similar short T1 values would also be nulled in the image, so that this is not really chemically selective imaging.

Another application of inversion-recovery imaging is its use in the production of images with dark blood, through the use of "double inversion-recovery dark blood imaging" [30]. In this approach to dark blood imaging, we use a pair of preliminary inversion pulses: first, a nonselective inversion pulse, which inverts the magnetization in the whole 3D region being imaged, and then an immediately following spatially selective re-inversion pulse, which restores the longitudinal magnetization of the region to be subsequently imaged back to its initial state (but which leaves the magnetization in the rest of the region still inverted). If we then wait for an inversion time that will result in the blood that was initially inverted in becoming nulled, then any blood entering the imaged region from the "singly inverted" region outside the imaged slice during the inversion interval will appear dark in the resulting image. Note that in regions of very slow flow, the blood may not be fully exchanged during the inversion time, resulting in residual signal in that region that must not be mistaken for thrombus or abnormal adjacent tissue.

Gadolinium-Based Contrast Agents

In addition to the application to MRA described above, the gadolinium-based contrast agents are also used in two of the key CMR applications for the imaging of ischemic heart disease: myocardial perfusion imaging and late gadolinium enhancement (LGE) imaging. Both of these techniques combine the use of preparation pulses and the administration of a Gd-based contrast agent to achieve T1-weighted images. As the associated issues of contrast agent dosing and safety concerns will be discussed further in other chapters in this book, we will not consider them further here.

As mentioned above, the bolus injection of MRI contrast agents can be used to transiently increase the signal from the blood and of the signal from the regions to which they get delivered by the blood. The transient increase in brightness of blood vessels produced by a contrast agent bolus can be used for the production of 3D MRA images, as discussed a little further below, while the transient increase in tissue brightness produced by a the first passage of a contrast agent bolus can be used to assess the relative perfusion of the tissue through corresponding alterations in the relative delivery

of contrast agent to the tissue. Slightly delayed imaging of the tissue after the bolus injection can be used to assess for inflammation or other sources of increased early enhancement, while longer delayed imaging of enhancement can be used to bring out areas of tissue infarction, inflammation, or scarring [31].

In performing 3D MRA studies with contrast agents, there are typically several steps we take. First, we acquire scout volumetric images of the region we plan to image, to check that the image position we have specified will cover the region we are interested in imaging, without any interference by image aliasing of other regions outside it. Note that the strong T1-weighting of the imaging methods employed usually results in relatively poor SNR of these initial scout images, prior to the injection of contrast agent, which can make the image location planning somewhat challenging. As described earlier, a "timing run" may be performed, with rapid sequence imaging of the target vessel after injection of a small test bolus of the contrast agent, in order to find out how long the bolus will take to arrive after injection; this can be used in setting the delay between injection and the start of image data acquisition. The effective time within the image acquisition when the imaging is most sensitive to the contrast agent effects (the "center of k-space") can also be taken into account in choosing the timing of the imaging. Just prior to the acquisition of the contrast-enhanced images, a non-contrast image data set may be acquired for use in subtracting out the images of the baseline-unenhanced structures (assuming good spatial registration between the two data sets). The contrast dose for the MRA acquisition is adjusted for the patient's size, and the duration of the injection is adjusted to be suitable for the duration of the data acquisition. The contrast agent bolus injection is followed by injection of a bolus of normal saline, to flush the remaining contrast agent out of injection line and the peripheral veins. Acquisition of the dynamic contrast-enhanced data sets is typically performed in multiple passes, to permit assessment of the sequential phases of the enhancement of different structures (e.g., pulmonary and systemic or arterial and venous vessels), as well as to allow for possible unexpected variations in the timing of the optimal enhancement phase of the structures of interest. After acquisition of the 3D-enhanced images (and any optional subtraction of pre-enhancement images), manufacturer-supplied or third-party image processing programs will be used to interactively explore the data sets and to reconstruct MRA images of the structures of interest for display or archiving.

For MRI studies of perfusion, we again use initial scout images to make sure that the region of interest will be covered adequately (Fig. 2.19). Again, the SNR of these pre-contrast scout images will generally be relatively poor, making the image location planning somewhat challenging. In perfusion imaging, we typically try to acquire multiple images of the heart within each heartbeat, over multiple heartbeats, with the image acquisitions interleaved at multiple locations within the heart. The number of locations that can be monitored in this way will depend on the heart rate and the speed of the imaging. T1 sensitization of the imaging, in order to bring out the arrival of the contrast agent bolus, is typically achieved by the application of a saturation pulse at the start of each image acquisition. For quantitative studies of perfusion, it may be necessary to take extra steps to ensure accurate saturation throughout the region of interest [32]. The rate of the contrast bolus injection will be limited by the size and location of the intravenous cannula used for the injection but is typically on the order of 5 ml/s for 2 s; injecting for longer times does not yield much improvement in the level of tissue enhancement achieved. The contrast agent bolus is immediately followed by a saline bolus, as for MRA studies. The patient is instructed to hold their breath during the image acquisitions for as long as they can and then to breathe quietly, so as to minimize the respiratory effect.

The early phase of enhancement of tissue after injection of a contrast bolus is related to the "vascularity" of the tissue and reflects a combination of the delivery of the contrast agent to the tissue by the blood flow, the fractional blood volume of the tissue, and the leakiness of the microcirculation permitting extravascular exchange of the contrast agent. For example, inflammation associated with infectious processes may show prominent early enhancement, as may vascular areas of tumors.

Imaging of the late phase of contrast enhancement of tissue after injection of a contrast agent bolus ("late enhancement") can be used to bring out areas of abnormal accumulation of contrast agent in an expanded extracellular space, e.g., due to effective increased or prolonged retention of the contrast agent in local areas of fibrosis, such as in healed infarcts. Such areas of relative accumulation of contrast agent in the myocardium can be made more prominent in the images by using inversion-recovery imaging to effectively null the signal from the normal myocardium, so that the shorter local T1 times resulting from increased contrast agent accumulation, e.g., in areas of fibrosis, will result in corresponding brighter relative signals [33]. In choosing the time for performing delayed-enhancement imaging, there must be a long enough delay for the contrast agent differences between the abnormal and normal myocardium to develop, while it must be short enough for there to still be sufficient contrast agent left in the abnormal region to show up in the images; a time on the order of 10–15 min after the injection of the contrast agent generally works out well. The optimal inversion time to be used for nulling the signal from the normal myocardium will depend on the particular contrast dose and delay time used and on the physiology of the individual patient and must be empirically adjusted for each study. One way to adjust this parameter

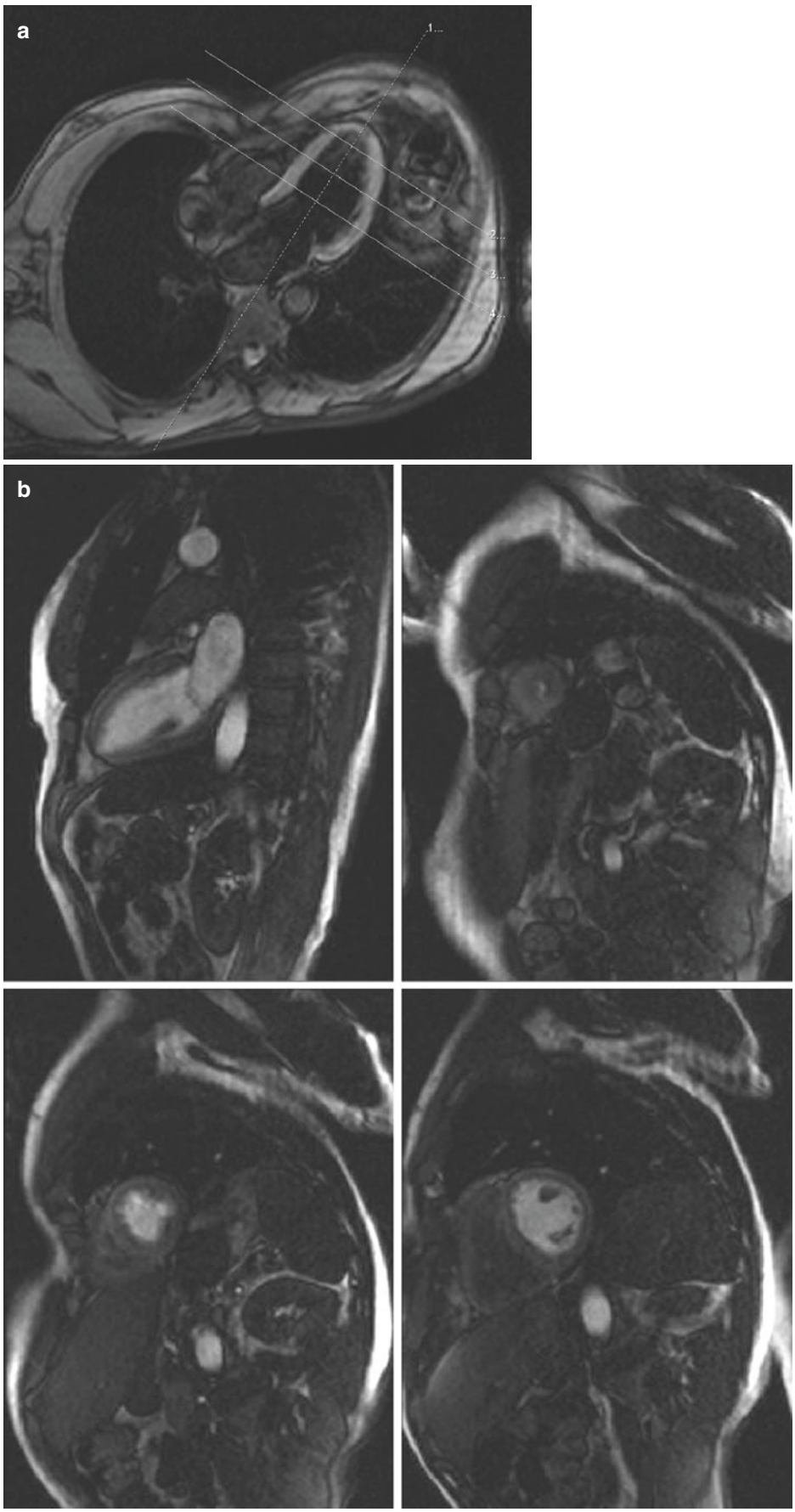

Fig. 2.19 (**a**) Initial planning image for first-pass perfusion sequence; (**b**) selection of image planes to be acquired. In this example, three short-axis views and one long-axis two-chamber view are repeatedly obtained in rapid succession with the dynamic injection of intravenous gadolinium. (**c**) The sequence of selected image frames depicts initial blood pool phase (RV cavity followed by LV cavity enhancement) followed by enhancement of the myocardium. Hypoperfusion of a segment of myocardium may indicate the presence of ischemia or infarction

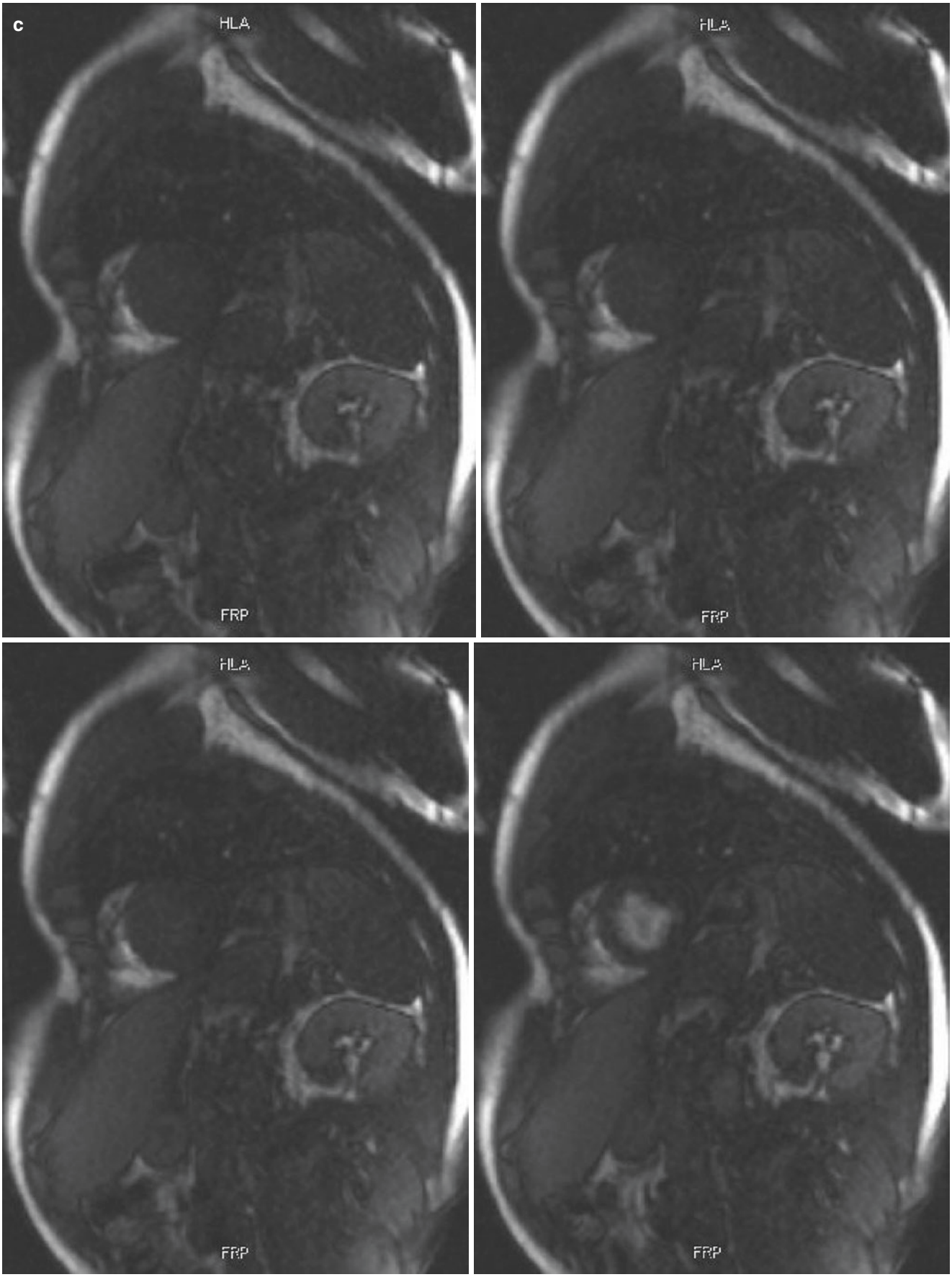

Fig. 2.19 (continued)

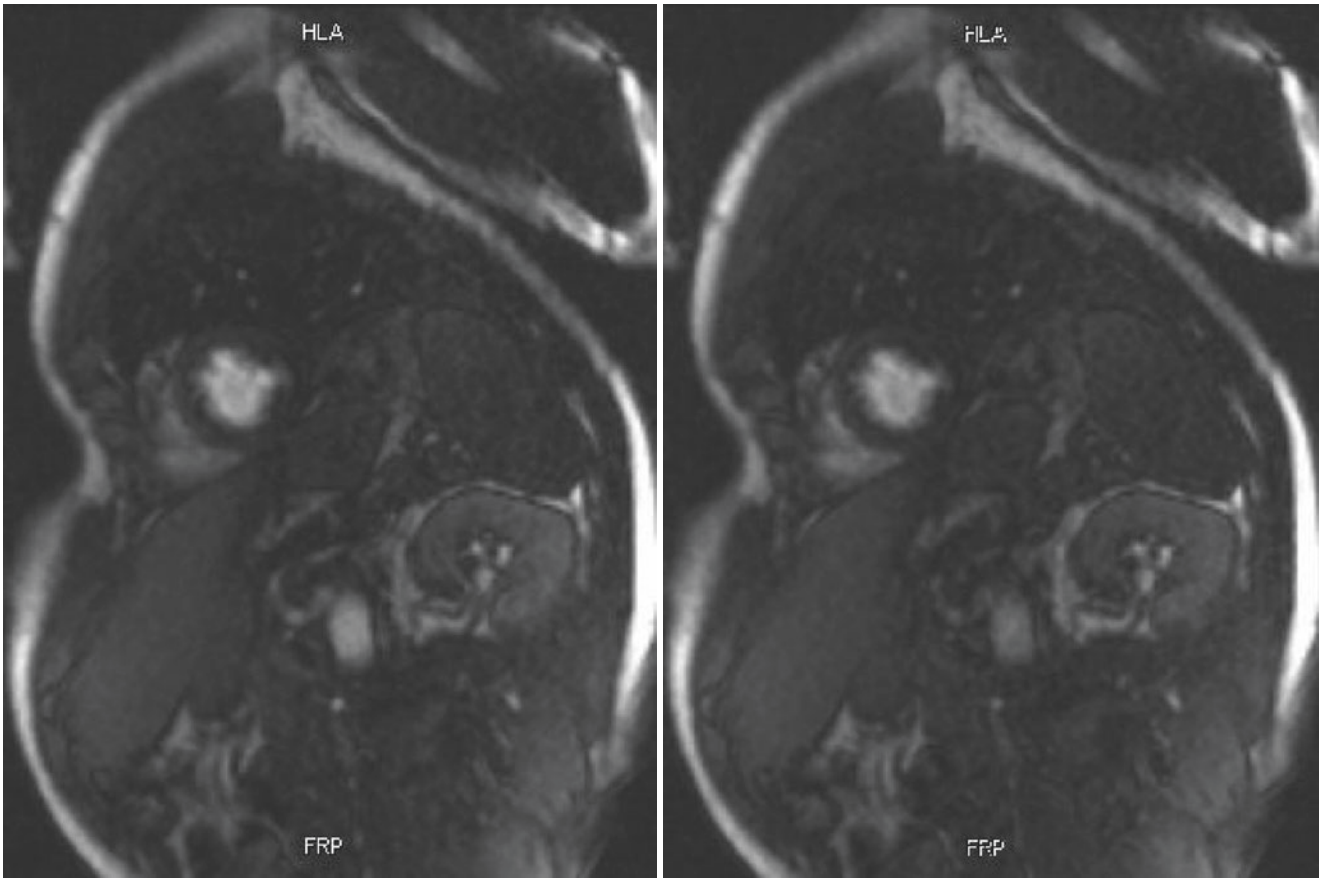

Fig. 2.19 (continued)

is to perform a modified cine imaging, with an inversion conditioning pulse applied at the start of each cardiac cycle (a "T1 scout" image set), so that each reconstructed cardiac phase corresponds to a different inversion time, and then look for the time of the cardiac cycle phase that best nulls the normal myocardium (Fig. 2.20). Note that the imaging itself will affect the effective T1 recovery process, so that the best value to choose for the actual imaging inversion time may still need to be adjusted from this time. A modified IR imaging method, which collects enough additional data to permit a phase-sensitive image reconstruction, can reduce the need to precisely choose the right value of the IR time to null the myocardium [34], as mentioned above. An additional consideration in delayed-enhancement imaging is the choice of whether to perform a rapid 3D (or stacked 2D) image acquisition, which can be repeated in different image orientations to best evaluate different portions of the myocardium, or to acquire serial "segmented" single 2D images, which can have better temporal and spatial resolution but at the cost of longer image acquisition times. In the setting of arrhythmias or respiratory motion, the resulting image artifacts may diminish the added value of the segmented images. A useful compromise is to routinely acquire the 3D image sets in multiple orientations, adding acquisition of individual higher-quality 2D images of any areas of question.

Phase Contrast

Another useful variant of cine imaging is to use the motion-induced phase shifts that can arise in MRI, as described above, to directly image the local velocities in vascular and cardiac structures [35]. This is generally accomplished through the addition of bipolar pairs of gradient pulses, whose net effect will be to leave stationary spins unchanged but which will result in a change in the phase of the signal from spins moving along the direction of the gradient. This phase change can be measured with suitable modified image reconstruction methods. The magnitude of the resulting phase shift will be proportional to the distance moved along the gradient during the interval between the pair of pulses and will also depend on the strength of the gradient pulses. The phase shift in each location can thus be used to create an image of the corresponding velocity at each location in the conventional magnitude image (Fig. 2.21). In performing such "phase-contrast" imaging of velocity, there are some choices that must be made by the operator. First, as only one

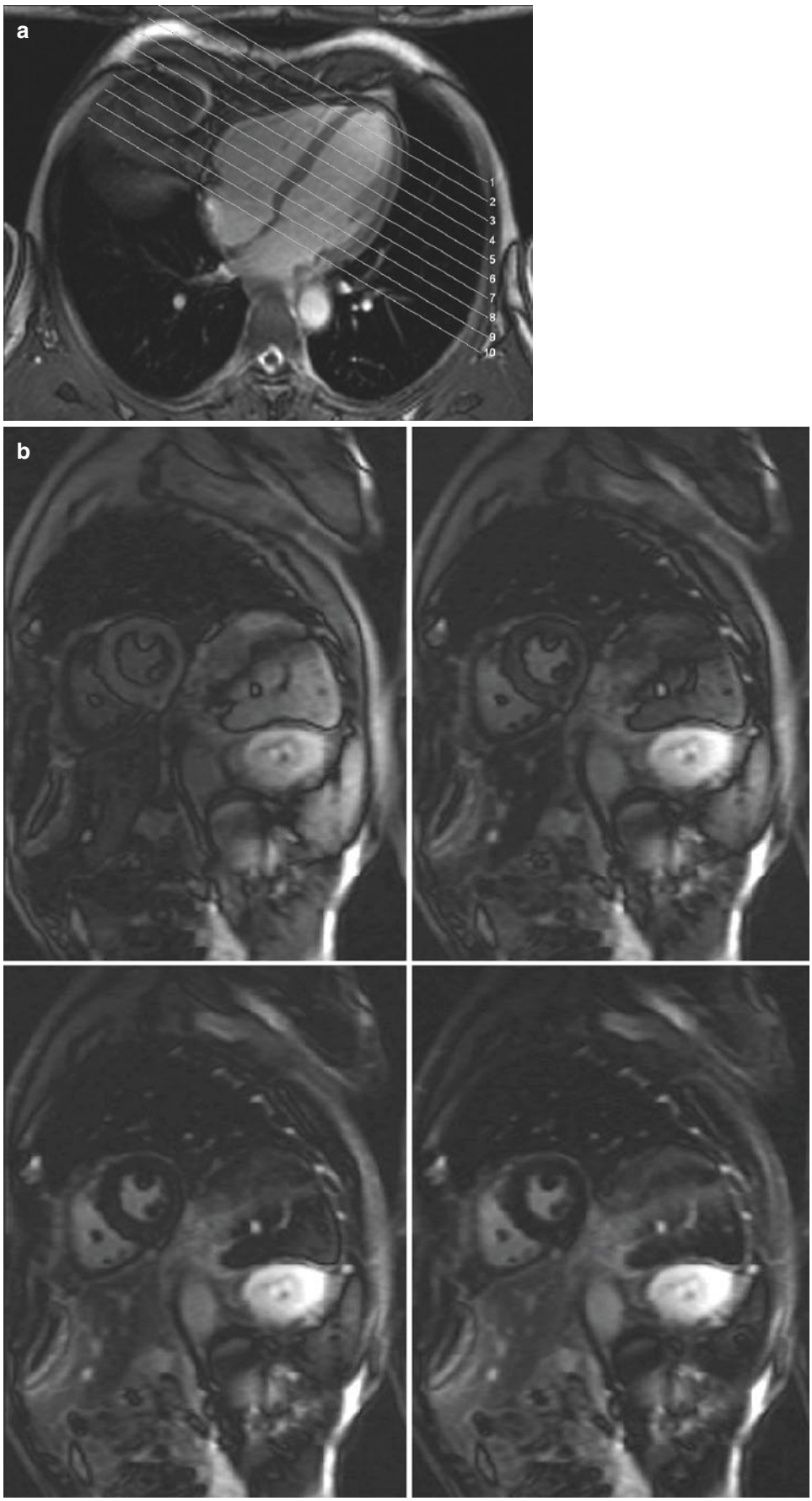

Fig. 2.20 Example of acquisition of a stacked set of 2D late-enhancement images along the ventricular short axis: (**a**) planning the image locations; (**b**) choosing the inversion time from a set of "T1 scout" images (only selected images shown); (**c**) final stack of acquired images

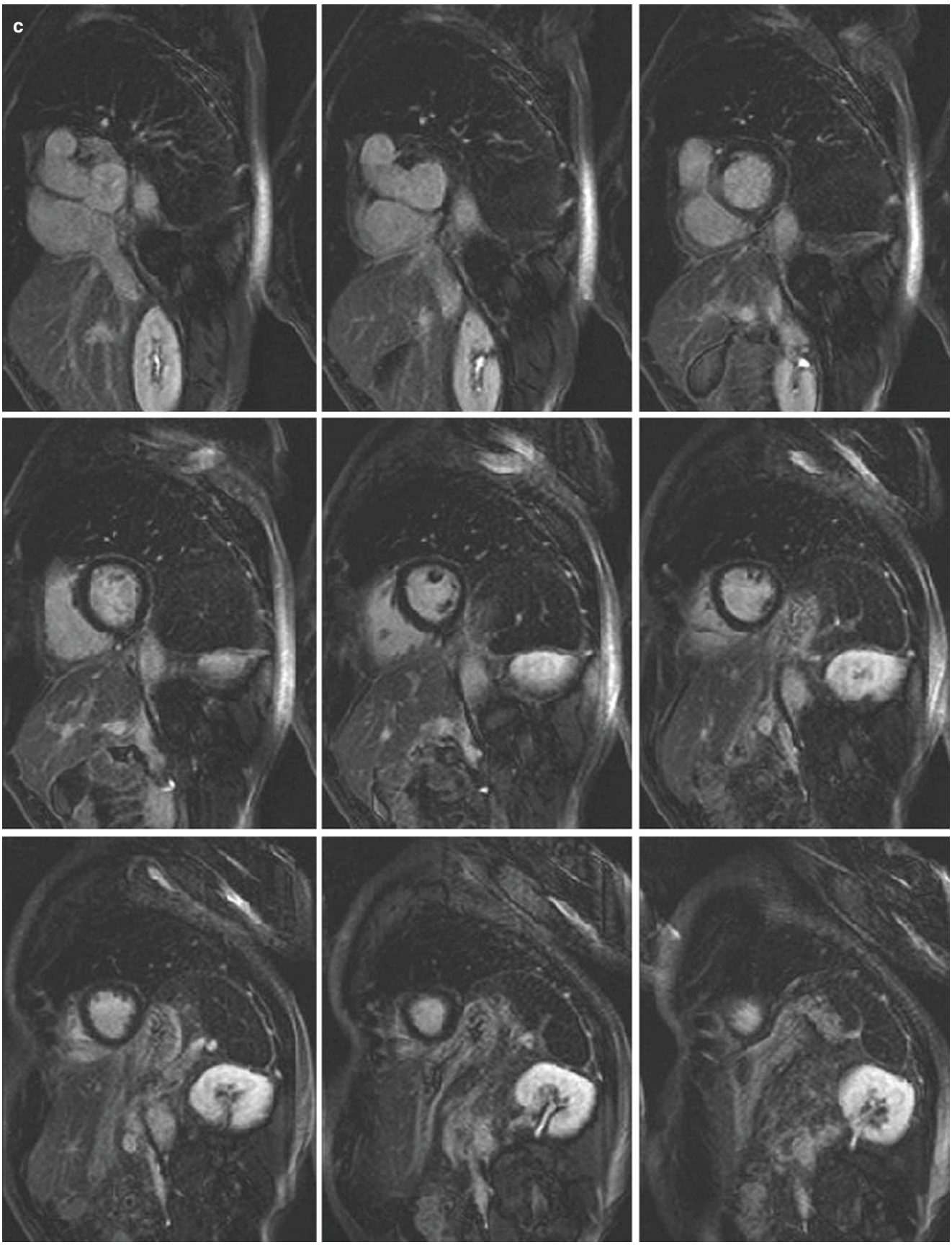

Fig. 2.20 (continued)

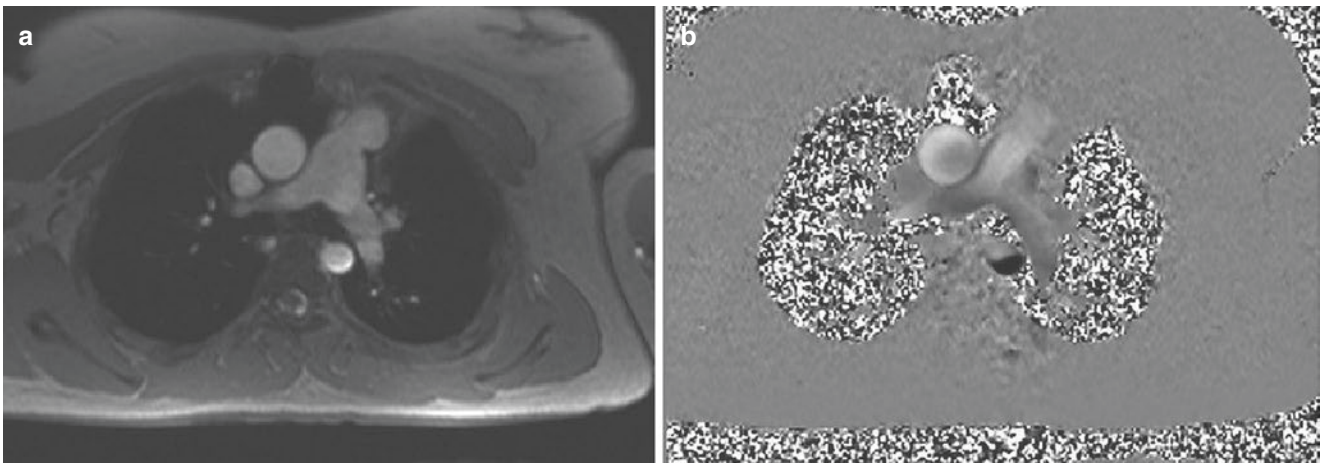

Fig. 2.21 (**a**) Magnitude (for anatomic correlation) and (**b**) corresponding phase-contrast velocity images, demonstrating through-plane flow through the ascending and descending aorta, which is oriented in opposite directions (and hence displayed with different image intensity). Note the nonuniform distribution of the velocities across the vessel lumens. A through-plane component of the flow in the adjacent right pulmonary artery is also evident

spatial component of velocity can be measured at a time, the component to be measured must be chosen. This is typically chosen to be the component perpendicular to the imaging plane, as this is most useful for flow volume calculations. Correspondingly, when studying volume flows, the imaging plane itself is generally optimally chosen to be perpendicular to the axis of the vessel lumen of interest. We can readily prescribe these slice locations from other images of the vessels of interest, analogously to the prescription of different cardiac chamber images described above. If measurements of more velocity components are desired, this will require additional image acquisitions (and correspondingly more imaging time). While the acquisition of multiple velocity components can be interleaved to improve spatial registration of the data, this cannot be used to reduce the imaging time, except at the cost of reduced temporal or spatial resolution. Another imaging parameter choice that must be made is the value of the velocity encoding value ("VENC"). This is the velocity for which the corresponding phase shift will be +/− 180°. Greater velocities, leading to greater phase shifts than this, will be indistinguishable ("aliased") from velocities with smaller magnitudes and possibly opposite sign. While a VENC on the order of 150 cm/s should suffice for capturing most normal arterial flows, the higher velocities that can be found in abnormal flows, e.g., related to accelerations through areas of stenosis, can require the use of higher VENC values. On the other hand, when studying slower flows, the use of lower values of VENC can improve the accuracy of the measurements. Thus, the VENC values may need to be adjusted on an individual patient basis, according to the particular clinical scenario. An important caveat that must be noted is that there can frequently be some residual baseline errors in the calculated velocities, related to imperfect behavior of the actual gradient pulses, which can produce inaccuracies in the corresponding calculated flows and flow volumes. We can approximately compensate for these errors by referencing the velocities to measurements made in adjacent stationary tissue ("baseline correction"), but this is still subject to some uncertainty, as the resulting reference values may vary with the position where they are measured. As with conventional cine imaging, there are compromises that must be made between the competing demands of spatial, temporal, and velocity resolution. It should be noted here that phase-contrast imaging requires for each phase-encoding step two TR periods to encode the differential effect of flow velocity in the phase of the signal, i.e., eliminate from the phase of the signal any background variation of the signal phase (e.g., from field inhomogeneities). With standard cine imaging, we only need one TR for each phase-encoding step. If everything else remains unchanged, phase-contrast cine imaging requires twice as long acquisition times (and breath-hold durations if required) compared to standard cine imaging. If we are willing to restrict our spatial resolution or field of view, we can potentially increase the temporal resolution enough to study pulse waves traveling along vessels, or increase the imaging rate enough to follow the dynamic response of flows to transient perturbations, such as respiratory maneuvers.

While phase-contrast imaging methods are primarily used to study the velocity of flowing blood, analogous to Doppler ultrasound (but without any limitations on the direction of the velocity measurement), they can also be used to study the velocity of the heart muscle (analogous to tissue Doppler studies). This can provide an alternative to tagged approaches for studying regional cardiac function.

There are various relative advantages and disadvantages of these different approaches, and the methods for their application to clinical questions are still being developed and evaluated.

Conclusion

In summary, there are many options for choosing particular technical methods of imaging in CMR, which can be used to optimally address different clinical questions. The great flexibility of imaging that this provides is a real strength of CMR, compared to other imaging methods. Other new imaging methods that are currently under development promise to further expand the capabilities of CMR and to increase its clinical utility.

Acknowledgment Adam Schwartz helped with the selection and preparation of images for the figures.

References

1. Ridgway JP. Cardiovascular magnetic resonance physics for clinicians: part I. J Cardiovasc Magn Reson. 2010;12:71.
2. Feng L, Otazo R, Srichai MB, Lim RP, Sodickson DK, Kim D. Highly-accelerated real-time cine MRI using compressed sensing and parallel imaging with cardiac motion constrained reconstruction. Magn Reson Med. 2013;70(1):64–74.
3. Atkinson DJ, Edelman RR. Cineangiography of the heart in a single breath hold with a segmented turboFLASH sequence. Radiology. 1991;178:357–60.
4. Edelman RR, Manning WJ, Burstein D, Paulin S. Coronary arteries: breath-hold MR angiography. Radiology. 1991;181:641–3.
5. Felblinger J, Lehmann C, Boesch C. Electrocardiogram acquisition during MR examinations for patient monitoring and sequence triggering. Magn Reson Med. 1994;32:523–9.
6. Fischer SE, Wickline SA, Lorenz CH. Novel real-time R-wave detection algorithm based on the vectorcardiogram for accurate gated magnetic resonance acquisitions. Magn Reson Med. 1999;42:361–70.
7. Boxerman JL, Mosher TJ, McVeigh ER, Atalar E, Lima JA, Bluemke DA. Advanced MR imaging techniques for evaluation of the heart and great vessels. Radiographics. 1998;18:543–64.
8. Lenz GW, Haacke EM, White RD. Retrospective gating: a review of technical aspects and future directions. Magn Reson Imaging. 1989;7:445–55.
9. Sievers B, Addo M, Kirchberg S, Bakan A, John-Puthenveettil B, et al. How much are atrial volumes and ejection fractions assessed by cardiac magnetic resonance imaging influenced by the ECG gating method? J Cardiovasc Magn Reson. 2005;7:587–93.
10. Lee VS, Resnick D, Bundy JM, Simonetti OP, Lee P, Weinreb JC. Cardiac function: MR evaluation in one breath hold with real-time true fast imaging with steady-state precession. Radiology. 2002;222:835–42.
11. Foo TK, Bernstein MA, Aisen AM, Hernandez RJ, Collick BD, Bernstein T. Improved ejection fraction and flow velocity estimates with use of view sharing and uniform repetition time excitation with fast cardiac techniques. Radiology. 1995;195:471–8.
12. Axel L, Montillo A, Kim D. Tagged magnetic resonance imaging of the heart: a survey. Med Image Anal. 2005;9:376–93.
13. Danias PG, Stuber M, Botnar RM, Kissinger KV, Edelman RR, Manning WJ. Relationship between motion of coronary arteries and diaphragm during free breathing: lessons from real-time MR imaging. AJR Am J Roentgenol. 1999;172:1061–5.
14. Holland AE, Goldfarb JW, Edelman RR. Diaphragmatic and cardiac motion during suspended breathing: preliminary experience and implications for breath-hold MR imaging. Radiology. 1998;209:483–9.
15. Plathow C, Ley S, Zaporozhan J, Schöbinger M, Gruenig E, Puderbach M, et al. Assessment of reproducibility and stability of different breath-hold maneuvres by dynamic MRI: comparison between healthy adults and patients with pulmonary hypertension. Eur Radiol. 2006;16(1):173–9. Epub 2005 Jun 21
16. Haacke EM, Patrick JL. Reducing motion artifacts in two-dimensional Fourier transform imaging. Magn Reson Imaging. 1986;4:359–76.
17. Ehman RL, Felmlee JP. Adaptive technique for high-definition MR imaging of moving structures. Radiology. 1989;173:255–63.
18. Taylor AM, Keegan J, Jhooti P, Gatehouse PD, Firmin DN, Pennell DJ. Differences between normal subjects and patients with coronary artery disease for three different MR coronary angiography respiratory suppression techniques. J Magn Reson Imaging. 1999;9:786–93.
19. Sachs TS, Meyer CH, Pauly JM, Hu BS, Nishimura DG, Macovski A. The real-time interactive 3-D-DVA for robust coronary MRA. IEEE Trans Med Imaging. 2000;19:73–9.
20. Danias PG, McConnell MV, Khasgiwala VC, Chuang ML, Edelman RR, Manning WJ. Prospective navigator correction of image position for coronary MR angiography. Radiology. 1997;203:733–6.
21. Taylor AM, Keegan J, Jhooti P, Firmin DN, Pennell DJ. Calculation of a subject-specific adaptive motion-correction factor for improved real-time navigator echo-gated magnetic resonance coronary angiography. J Cardiovasc Magn Reson. 1999;1:131–8.
22. Wang Y, Ehman RL. Retrospective adaptive motion correction for navigator-gated 3D coronary MR angiography. J Magn Reson Imaging. 2000;11:208–14.
23. Felblinger J, Boesch C. Amplitude demodulation of the electrocardiogram signal (ECG) for respiration monitoring and compensation during MR examinations. Magn Reson Med. 1997;38:129–36.
24. Larson AC, White RD, Laub G, McVeigh ER, Li D, Simonetti OP. Self gated cardiac cine MRI. Magn Reson Med. 2004;51(1):93–102.
25. Goldfarb JW. The SENSE ghost: field-of-view restrictions for SENSE imaging. J Magn Reson Imaging. 2004;20:1046–51.
26. Finn JP, Baskaran V, Carr JC, McCarthy RM, Pereles FS, et al. Thorax: low-dose contrast-enhanced three-dimensional MR angiography with subsecond temporal resolution – initial results. Radiology. 2002;224:896–904.
27. Axel L, Kolman L, Charafeddine R, Hwang SN, Stolpen AH. Origin of a signal intensity loss artifact in fat-saturation MR imaging. Radiology. 2000;217:911–5.
28. Axel L. Blood flow effects in magnetic resonance imaging. AJR Am J Roentgenol. 1984;143:1157–66.
29. Nakats M, Hatabu H, Itoh H, Morikawa K, Miki Y, Kasagi K, et al. Comparison of short inversion time inversion recovery (STIR) and fat-saturated (chemsat) techniques for background fat intensity suppression in cervical and thoracic MR imaging. J Magn Reson Imaging. 2000;11:56–60.
30. Edelman RR, Chien D, Kim D. Fast selective black blood MR imaging. Radiology. 1991;181:655–60.
31. Kim RJ, Wu E, Rafael A, Chen E-L, Parker MA, Simonetti O, et al. The use of contrast enhanced MRI to identify reversible myocardial dysfunction. N Engl J Med. 2000;343(20):1445–53.

32. Kim D, Cernicanu A, Axel L. B(0) and B(1)-insensitive uniform T(1)-weighting for quantitative, first-pass myocardial perfusion magnetic resonance imaging. Magn Reson Med. 2005;54:1423–9.
33. Simonetti OP, Kim RJ, Fieno DS, Hillenbrand HB, Wu E, Bundy JM, et al. An improved MR imaging technique for the visualization of myocardial infarction. Radiology. 2001;218:215–23.
34. Kellman P, Arai AE, McVeigh ER, Aletras AH. Phase-sensitive inversion recovery for detecting myocardial infarction using gadolinium-delayed hyperenhancement. Magn Reson Med. 2002;47:372–83.
35. Srichai MB, Lim RP, Wong S, Lee VS. Cardiovascular applications of phase-contrast MRI. AJR Am J Roentgenol. 2009;192(3):662–75.

Anatomy of the Heart and Great Arteries

3

Lawrence M. Boxt and Martin J. Lipton

Introduction

Magnetic resonance imaging (MRI) techniques produce high spatial, contrast, and temporal resolution image data for evaluation of cardiac and great vessel anatomy, regional tissue characterization, vascular blood flow, cardiac chamber filling and contraction, regional myocardial dynamics, and myocardial perfusion. MRI produces series of tomographic images of the heart and great arteries in arbitrary section, allowing tailoring of an examination to address a specific clinical problem, or a systematic analysis of cardiac structure and physiologic function. Identifying a specific abnormality is based upon recognizing variance between the instant image data at hand and an expected normal appearance of the heart and great arteries.

In this chapter, we will describe the anatomy of the heart and great arteries as demonstrated on magnetic resonance imaging. Anatomy, as portrayed by MRI significantly differs from that observed in the dissection lab or operating room. On MRI we view these structures in tomographic section. That is, rather than viewing the entire organ, and its relationship with surrounding organs, we view the heart in slices. The analogy of echocardiographic imaging is quite appropriate for MR examination of the heart. In other words, the MR scanner produces images of sections of the heart and great vessels, which may be interpreted in order to recognize normal structure, differentiate normal from abnormal, and begin the process of morphologic diagnosis. MR diagnosis is based upon visualization of a series of images, each obtained in prescribed standardized, or arbitrary anatomic section. By analysis of left-to-right, anterior-to-posterior, and superior-to-inferior relationships among adjacent structures, we create a three-dimensional image of these organs in our mind. By recognizing the variance between what we expect and what we see, we begin to acquire a sense of what is abnormal. To identify an abnormality, one must first recognize the normal. It is the purpose of this chapter to describe the anatomy of the heart and great vessels and demonstrate the appearance of these structures on MR examination.

Cardiac MRI (CMR) complements echocardiographic study and, in those individuals in whom adequate echo windows cannot be obtained, has become the imaging modality of choice. Clinical indications for the performance of CMR [1, 2] as well as its interpretation [3] have significantly increased diffusion of CMR into the clinical workplace.

Pericardium

The heart is contained within the middle mediastinum by the pericardium. The visceral pericardium is adherent to the ventricular myocardium and cannot be visually separated from the epicardial fat. The parietal pericardium may be identified as a paper-thin high signal intensity surface surrounding the heart and great arteries (Figs. 3.1, 3.2, and 3.3). On the left side of the heart, the pericardium attaches on the superior aspect of the main pulmonary artery. On the right, the ascending aorta is enveloped approximately up to the level of the azygos vein. Recesses (potential spaces) in the pericardium are typically found anterior to the ascending aorta and medial to the main pulmonary artery (the anterior aortic recess), between the ascending aorta and transverse right pulmonary artery (the superior pericardial recess), and around the entry of the pulmonary veins to the left atrium. Visualization of the parietal pericardium depends upon the presence and extent of low-density fatty deposition in the pericardial fat pad and middle mediastinum.

L. M. Boxt (✉)
Department of Radiology, Englewood Hospital Medical Center, Englewood, NJ, USA

M. J. Lipton
Department of Radiology, Pritzker School of Medicine, University of Chicago, Chicago, IL, USA

R. Y. Kwong et al. (eds.), *Cardiovascular Magnetic Resonance Imaging*, Contemporary Cardiology,
https://doi.org/10.1007/978-1-4939-8841-9_3

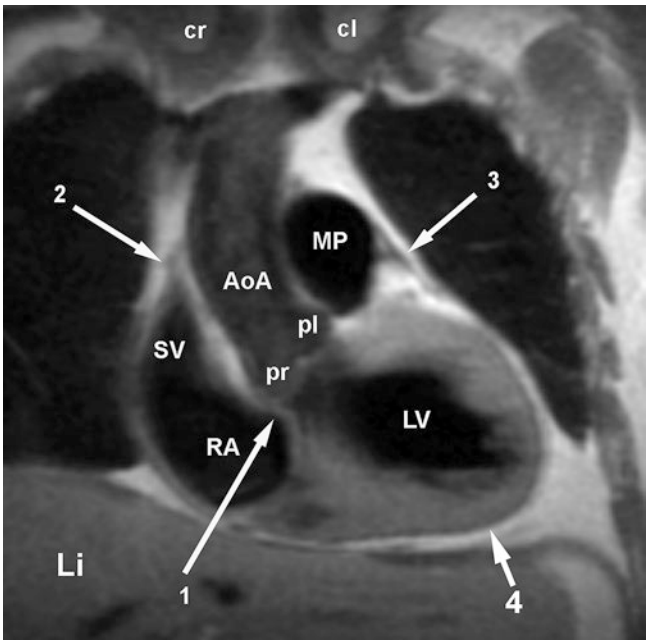

Fig. 3.1 Coronal double inversion recovery image from a 50-year-old woman, obtained through the right (cr) and left (cl) clavicular heads, and posterior right (pr) and posterior left (pl) aortic sinuses of Valsalva. The subaortic interventricular septum includes the atrioventricular septum (arrow 1) between the right atrium (RA) and left ventricle (LV). The entry of the superior vena cava (SV) into the RA is posterior to the orifice of the right atrial appendage (not visualized). The pericardium attaches along the ascending aorta (AoA) on the right heart border (arrow 2) and on the pulmonary artery (arrow 3) on the left. The low signal pericardial space (arrow 4) continues along the diaphragmatic surface of the heart. The liver (Li) and stomach (St) are labeled

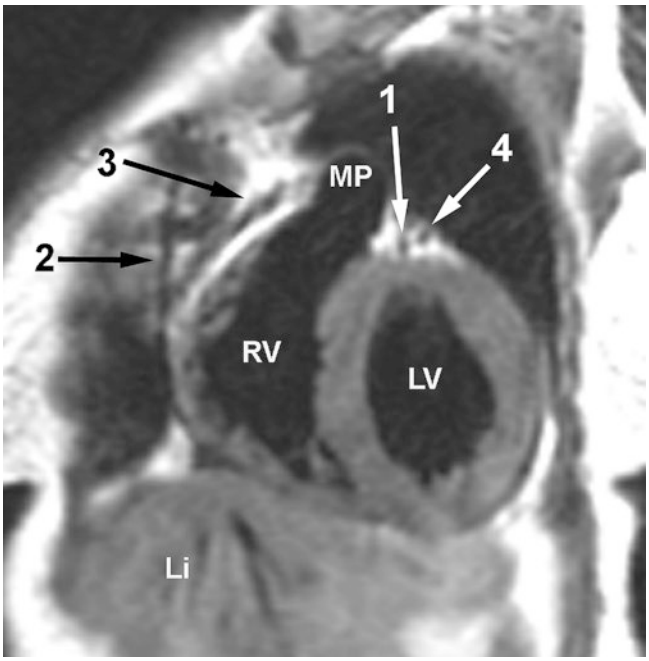

Fig. 3.2 Left anterior oblique (LAO) sagittal double inversion recovery image from a 60-year-old woman. The anterior, trabeculated right ventricle (RV) lies immediately behind the right internal mammary artery (arrow 2). Notice how the pericardium (arrow 3) attaches on the top of the main pulmonary artery (MP). Embedded within the epicardial fat above the left ventricular (LV) myocardium, the anterior descending (arrow 1) and circumflex (arrow 4) coronary arteries have split from the left main coronary artery (not seen)

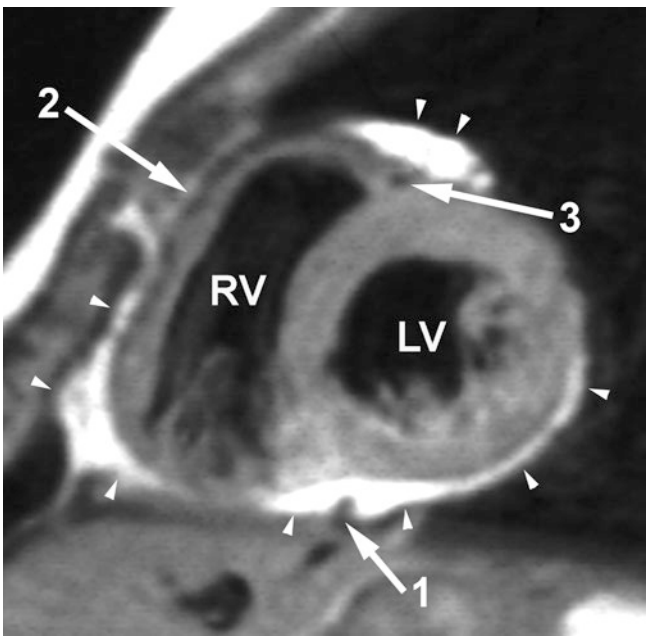

Fig. 3.3 Short axis double inversion recovery image from a 25-year-old man. Notice how high signal intensity fat surrounds the heart (arrowheads). Right ventricular (RV) free wall myocardium can be separated from the pericardial fat by the pencil-thin pericardial space (arrow 2). The anterior descending artery (arrow 3) is viewed in cross section as a signal void along the superior aspect of the interventricular septum. The posterior descending coronary artery is seen in cross section as a signal void within the epicardial fat along the inferior aspect of the interventricular septum (arrow 1)

Aorta

The aorta is attached to the heart by the annulus fibrosis. The annulus supports the aortic valve and is part of a fibrous skeleton which supports the mitral and pulmonary valves as well. The aortic annulus lies nearly in the center of the heart, just oblique to the plane of the cardiac short axis (Figs. 3.1, 3.4, and 3.5). The thoracic aorta is divided into a series of segments. The bulbous aortae or bulbous portion of the aorta lies between the aortic annulus and the tubular portion of the aorta. Arterial wall thickness is a particularly useful indicator of the presence of atherosclerotic change [4–6]. In the thoracic aorta, average wall thickness in women is less than in men (2.11 versus 2.32 mm, $p = 0.028$ [7]). Wall thickness varies from location to location [8] and increases with age at examination and ethnicity [7, 9]. Accurate measurement of aortic wall signal intensity is limited by radial aortic pulsatory motion as well as limited spatial resolution of the MR scanner itself. Thus, a "normal" range of signal is difficult to define. However, comparison of an unenhanced segment of the aorta with itself 5-to-10 min after intravenous contrast administration (so-called delayed hyperenhancement) may have value in assessing mural aortic disease [10, 11].

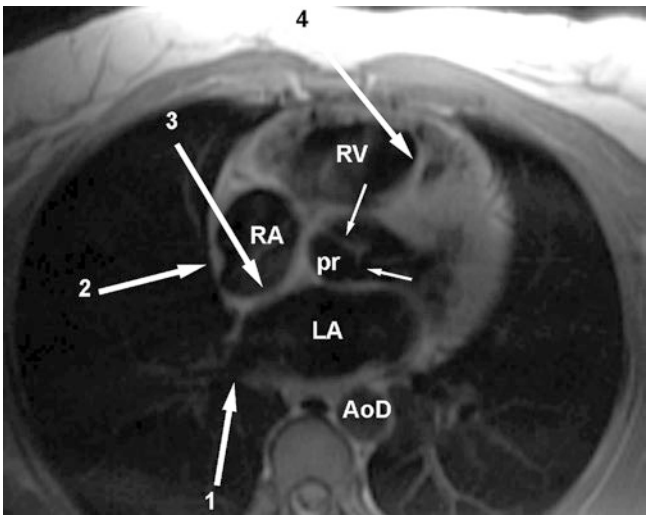

Fig. 3.4 Axial double inversion recovery image from a 45-year-old woman. The right ventricle (RV) lies anteriorly. Myocardial trabeculation between the interventricular septum and right ventricular free wall (arrow 4) is identified. Within the sinus portion of the aorta, the posterior right aortic sinus of Valsalva (pr) and aortic valvular commissures (small arrows) are evident. The right (RA) and left (LA) atria are separated, at this level, by the secundum interatrial septum (arrow 3). The crista terminalis appears as focal thickening of the RA wall (arrow 2). The right lower lobe pulmonary vein (arrow 1) is just entering the LA

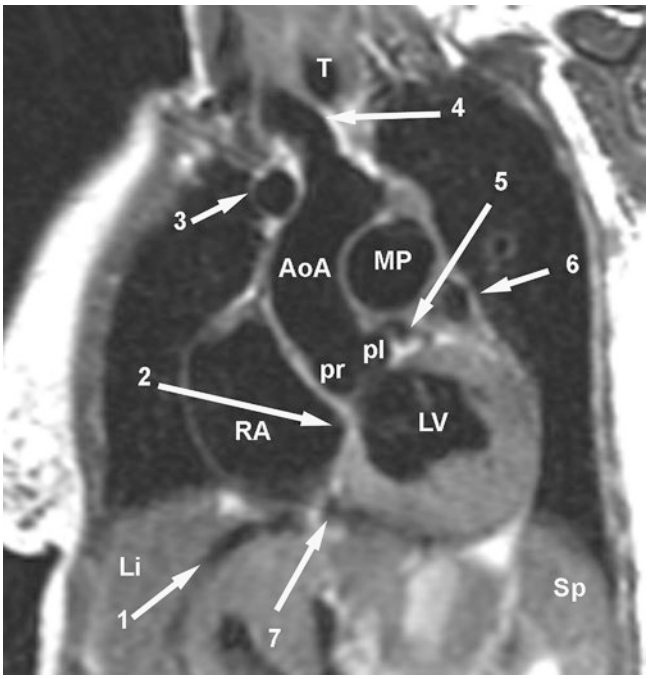

Fig. 3.5 Left anterior oblique (LAO) sagittal double inversion recovery image from a 60-year-old woman, through the sinus portion of the aorta. The left main and proximal left anterior descending coronary arteries (arrow 5) arise from the posterior left aortic sinus of Valsalva (pl). Immediately inferior to the posterior right sinus is the atrioventricular septum, separating the right atrium (RA) from the left ventricle (LV). An hepatic vein (arrow 1) passes through the liver (Li) toward the diaphragmatic surface of the RA, lateral to coronary sinus (arrow 7), seen in cross section embedded within the fat of the inferior portion of the posterior atrioventricular ring. The liver (Li) and spleen (Sp) are labeled

Aortic caliber increases with age [12] and median aortic caliber is greater in men than women. However, care must be taken to measure aortic caliber at precise locations, and orthogonal to the axis of the aortic segment under investigation. MR technique [13] affects caliber measurement. Motion blurring affects inter-observer variability non-ECG-gated MR angiography and can be reduced by application of navigator-type respiratory and ECG gating.

Standard anatomic levels for measurement of aortic caliber (Fig. 3.6) include the annulus, within the sinus portion, at the sino-tubular junction, and the widest ascending aortic segment (usually at the level of the transverse right pulmonary artery). Omniplanar acquisition by MRI allows acquisition in imaging planes orthogonal to the anatomic section under investigation, i.e., in the sagittal and coronal oblique planes for evaluation of the annulus and sino-tubular junction, and coronal left ventricular outflow tract pane for intrasinus and ascending aortic measurement.

Measurement of aortic caliber by MRI compares favorably with measurement obtained using echocardiographic technique [14–21] and multidetector computed tomography [18, 22, 23] and is considered by some to be the "gold standard" for this purpose. Aortic caliber as determined by CMR in large series of healthy men and women provides the basis for reference standards for caliber at specific locations on the aorta [24, 25]. Caliber measurements of the aortic root and ascending aorta in healthy adults are presented in Tables 3.1, 3.2, and 3.3.

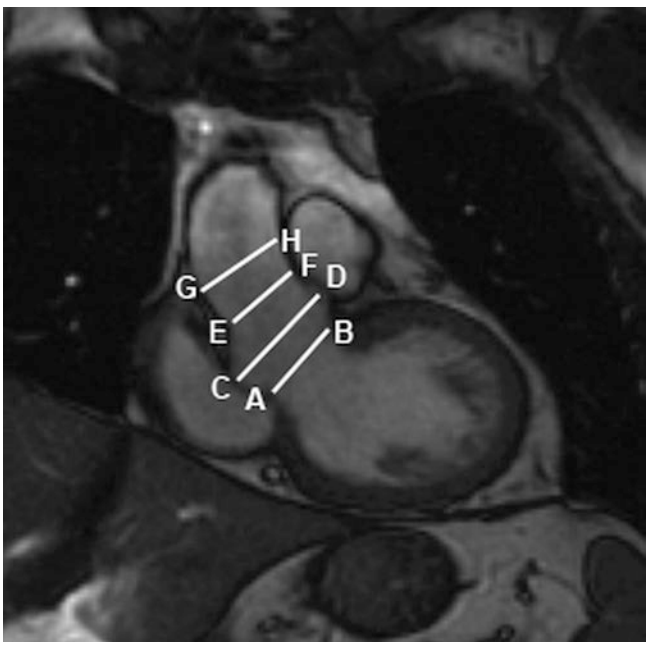

Fig. 3.6 Diastolic gradient echo acquisition in coronal left ventricular outflow tract section. Measurement of aortic caliber is typically obtained at the level of the aortic annulus (line AB), within the greatest dimension of the sinus portion (line CD), at the sino-tubular junction (line EF), and the ascending aorta (line GH)

Table 3.1 Aortic caliber indexed to anatomic level. Data given as mean ± SD, range as ±2 SD

Anatomic level	Imaging plane	Diastolic caliber, mm	Range, mm	Systolic caliber, mm	Range, mm
		Women, age = 49.2 ± 16.6 years			
Annulus	Sag LVOT	19.9 ± 1.9	16–24	21.0 ± 2.1	17–25
	Cor LVOT	23.0 ± 2.1	19–27	23.0 ± 2.0	19–27
Sinuses	Cor LVOT	30.2 ± 3.2	24–37	31.2 ± 3.1	25–37
Sino-tubular junction	Sag LVOT	23.8 ± 3.1	18–30	25.3 ± 2.8	20–31
	Cor LVOT	30.2 ± 3.2	24–37	31.2 ± 3.1	25–37
		Men, age = 49.3 ± 17.2 years			
Annulus	Sag LVOT	22.2 ± 2.4	17–27	22.4 ± 2.1	18–27
	Cor LVOT	26.2 ± 2.3	22–31	25.7 ± 2.1	22–30
Sinuses	Cor LVOT	34.1 ± 4.3	26–43	35.3 ± 4.0	27–43
Sino-tubular junction	Sag LVOT	25.4 ± 3.9	18–33	27.3 ± 3.9	21–34
	Cor LVOT	34.1 ± 4.3	26–43	35.3 ± 4.0	27–43

From [23]

Table 3.2 Aortic caliber indexed by gender

Age category, years	*N*	Median caliber, mm/M^2	Range, mm	*N*	Median caliber, mm/M^2	Range, mm
		Women (non-indexed to BSA)			**Men (non-indexed to BSA)**	
45–54	416	28.8	17.8–37.7	345	31.6	25.2–44.6
55–64	232	30.1	23.7–40.5	229	32.8	24.4–49.8
65–74	157	30.6	24.2–40.0	139	34.2	27.8–43.9
75–84	37	31.1	26.7–37.2	57	34.7	27.7–43.5
		Women (indexed to BSA)			**Men (indexed to BSA)**	
45–54	416	16.7	11.2–23.4	345	15.9	11.6–22.3
55–64	232	17.6	12.8–25.8	229	16.8	12.6–24.3
65–74	157	18.1	13.0–26.7	139	17.8	12.8–25.1
75–84	37	19.7	15.3–28.8	57	18.6	14.7–23.6

From [28]

Table 3.3 Aortic caliber indexed to body habitus. Range is ±2 SD

Caliber, mm	Average	Range	Average	Range	Average	Range
Body habitus	Normal		Overweight		Obese	
	Women					
Annulus	20.6	17.4–23.8	21.7	18.4–25.0	21.5	17.2–25.8
Sinuses	27.5	21.9–33.1	28	21.8–34.2	27.5	21.3–33.7
S-T junction	21.6	16.6–26.6	22.3	17.0–27.6	22.1	15.9–28.3
Ascending Ao	24.7	17.8–31.6	26.5	19.3–33.7	26.6	18.8–23.2
Descending Ao	18.5	14.6–22.4	19.2	14.8–23.6	19.6	16.5–23.2
	Men					
Annulus	23.9	18.6–29.2	24.3	18.9–29.7	25.6	20.4–30.8
Sinuses	31.9	24.3–39.5	32.8	25.2–40.4	33.3	24.3–42.3
S-T junction	24.4	18.2–30.6	25.7	16.7–34.7	26.2	18.9–33.5
Ascending Ao	26.0	18.7–33.3	27.4	18.9–35.9	28.5	23.1–33.9
Descending Ao	20.1	14.7–25.5	20.9	15.6–26.2	22.2	16.3–28.1

From [24]

The high temporal resolution of cine MRI acquisition allows determination of aortic caliber at both ventricular end systole and end diastole (Fig. 3.7). The change in caliber reflects material properties of the aortic wall, thus providing a means of measuring aortic "stiffness." These caliber measurements, when paired with aortic pressure measurements, may be used to calculate aortic compliance (i.e., change in caliber with increasing pressure), and "elastance," the reciprocal return to normal caliber upon removal of the distending arterial pressure [26, 27]. Results from the Multi-Ethnic Study of Atherosclerosis (MESA) showed positive correlation between aortic wall thickness and increasing age [9], as well as decreasing aortic distensibility with increasing age [28].

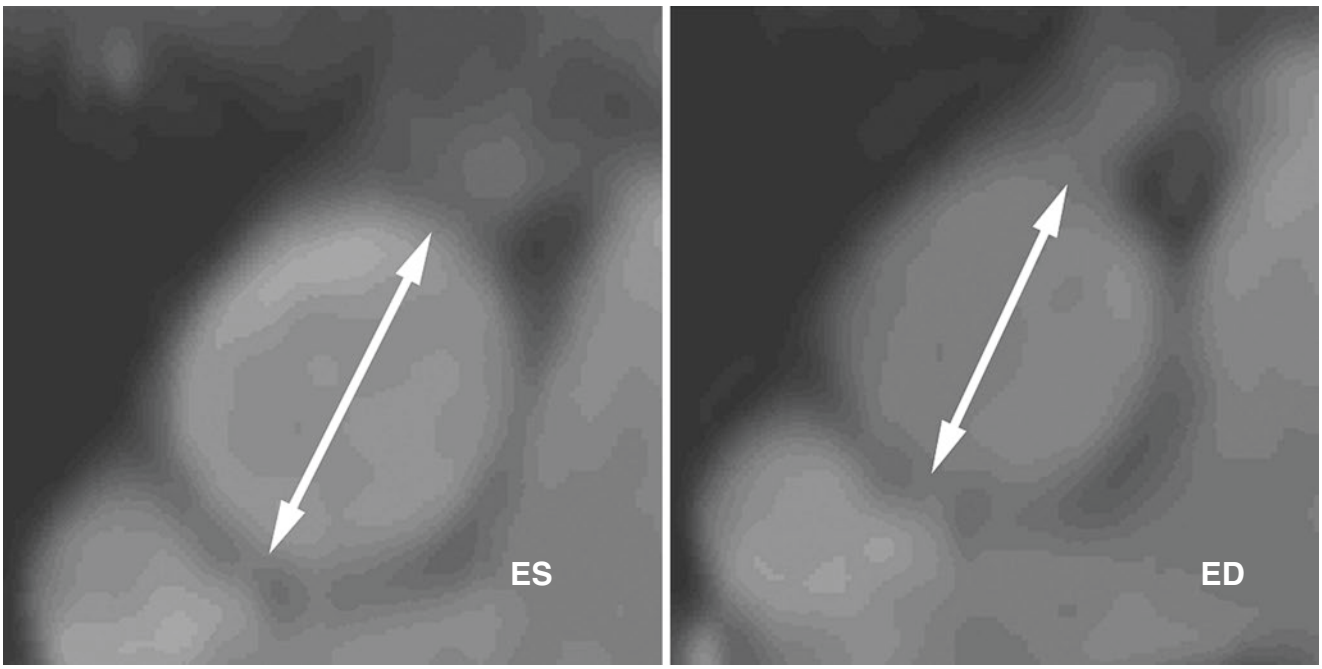

Fig. 3.7 Oblique axial gradient echo acquisition through the ascending aorta obtained at end systole (ES) and end diastole (ED). Notice the difference in aortic diameter (double headed arrows) and area with left ventricular contraction

A systolic pulse wave front propagating through the aorta increases aortic caliber as it passes. Pathologic processes that reduce elastic arterial recoil (such as preclinical atherosclerosis) limit wall distensibility and increase propagation velocity of the pulse wave through the aorta. Velocity encoded MRI allows accurate measurement of blood flow velocity in large arteries and may be utilized to assess such pathologic changes [29–31].

The axis of the most proximal portion of the ascending aorta points slightly anteriorly and toward the right. As the aorta ascends, it continues to be directed slightly toward the right and anteriorly, displacing the superior vena cava toward the right. Thus, in coronal section, the right lateral wall of the ascending aorta gently curves toward the right, and in the sagittal section, curves anteriorly (Figs. 3.1, 3.5, 3.6, 3.8, 3.9, 3.10, 3.11, 3.12, 3.13, 3.14, 3.15, 3.16, and 3.17). The aorta returns to the midline by the level of the body of the second right costal cartilage. As the aorta continues its ascent, it curves dorsally and toward the left to form the aortic arch. Although the total length of the ascending aorta averages 5–5.5 cm, body habitus, diaphragm position, and chest conformation all have influence on its appearance. The aortic arch lies almost entirely behind the manubrium of the sternum (Fig. 3.18). It is not contained within the pericardium. The plane of the aortic arch lies in an off sagittal left anterior oblique plane (Fig. 3.19). The origins of the three major aortic branches, the innominate, left common carotid, and left subclavian arteries, are slightly ventral to the vertex of the

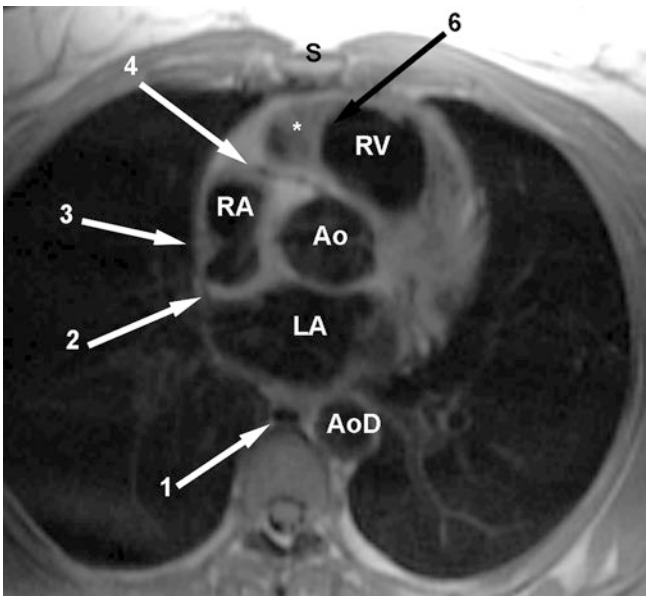

Fig. 3.8 Axial double inversion recovery image from a 45-year-old woman. Within the aortic root (Ao), the origin and proximal course of the right coronary artery (arrow 4) is evident. The left atrium (LA) lies between the Ao and descending aorta (AoD). The right (RA) and left (LA) atria are separated at this level by the sinus venosus portion of the interatrial septum (arrow 2). Along the lateral aspect of the RA, the high signal intensity crista terminalis (arrow 3) may be visualized. The right ventricle (RV) lies behind the sternum (S) and is again apparently segregated into two portions (*) by a myocardial trabeculation (arrow 6). The azygos vein (arrow 1) anddescending thoracic aorta (AoD) are labeled

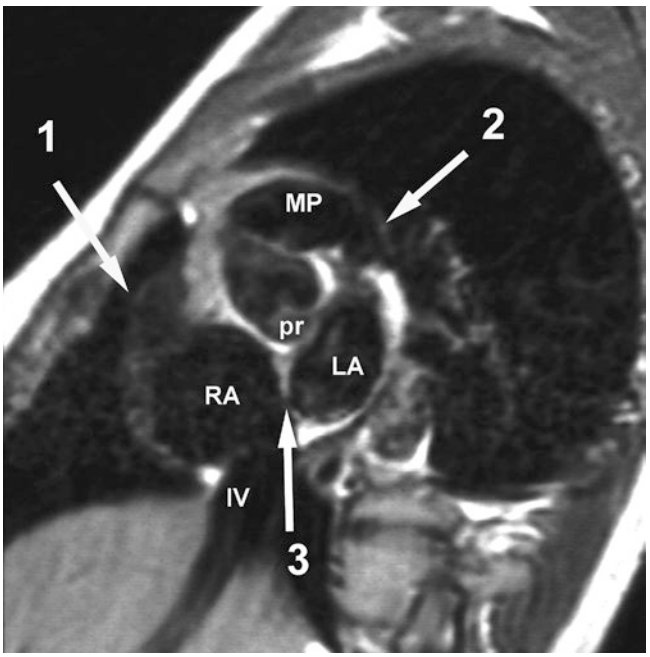

Fig. 3.9 Short axis double inversion recovery image from a 25-year-old man through the posterior right aortic sinus of Valsalva (pr). In this section, the right atrial appendage (arrow 1) lies directly anterior to the aorta, and the left atrial appendage (arrow 2) is at the same level as the distal main pulmonary artery (MP). Notice the relationship of the pr with the left (LA) and right (RA) atria, and the superior interatrial septum. In this plane, the inferior vena cava (IV) is seen entering the RA

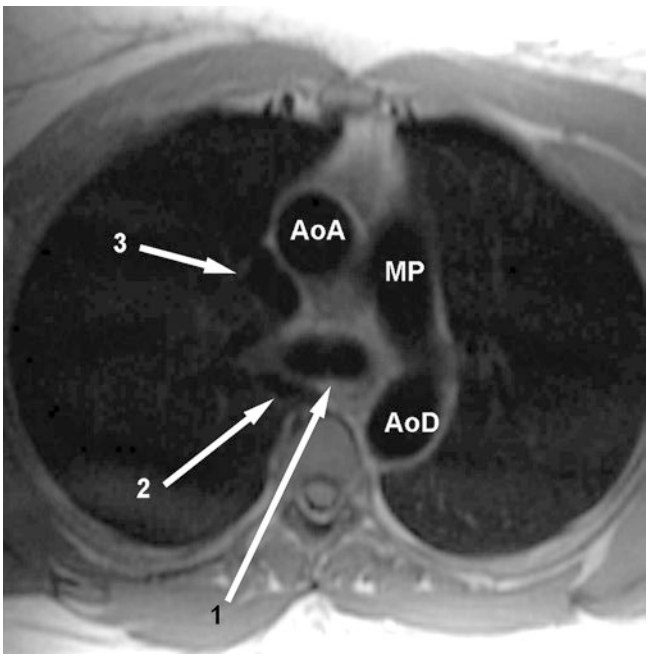

Fig. 3.11 Axial double inversion recovery image from a 45-year-old woman, at the level of the carina (arrow 1). The ascending (AoA) and descending (AoD) aorta are labeled. The body of the main pulmonary artery (MP) passes toward the AoD to become the left pulmonary artery. At this level, the azygos vein (arrow 2) can be seen moving toward the right to pass over the right hilum. The superior vena cava (arrow 3) lies toward the right and posterior to the AoA

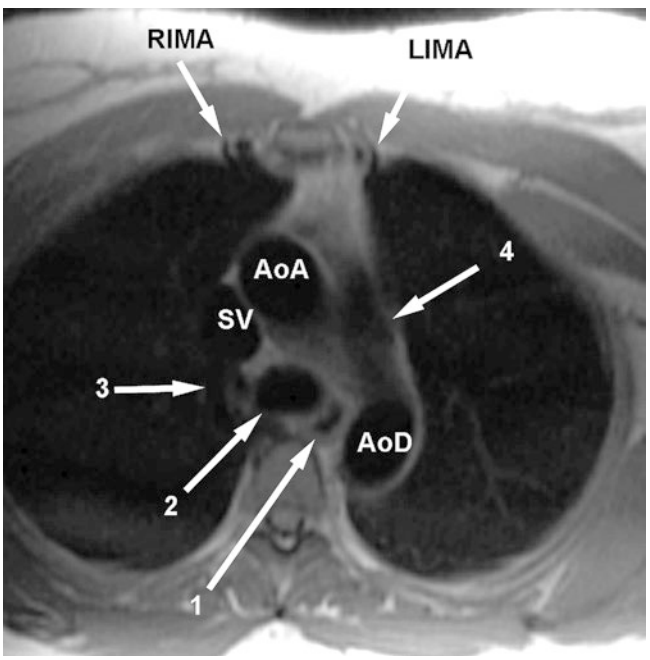

Fig. 3.10 Axial double inversion recovery image from a 45-year-old woman. The ascending (AoA) and descending (AoD) aorta are identified. The top of the main pulmonary artery (arrow 4) is now coming into view. Both the right (RIMA) and left (LIMA) internal mammary arteries have reached the anterior chest wall, just to the right, and left of midline, respectively. At this level, the azygos vein (arrow 3) is passing over the right hilum to drain into the posterior aspect of the superior vena cava (SV). The trachea (arrow 2) and esophagus (arrow 1) are labeled

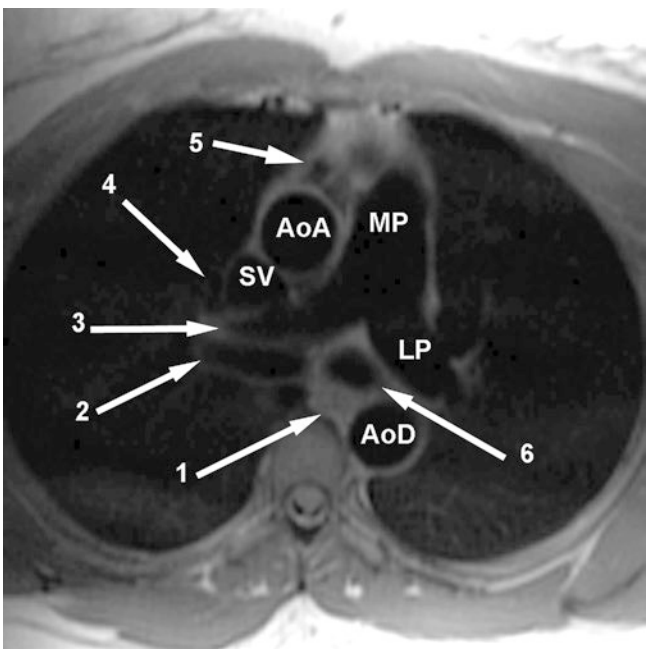

Fig. 3.12 Axial double inversion recovery image from a 45-year-old woman, at the level of the pulmonary artery bifurcation. The main (MP) pulmonary artery continues as the left (LP) pulmonary artery; the right pulmonary artery (arrow 3) passes behind the ascending aorta (AoA) and superior vena cava (SV) to the right hilum. Note that the right pulmonary artery is anterior to the right bronchus (arrow 2); the LP is just about to cross over the top of the left bronchus (arrow 6). The right upper lobe pulmonary vein (arrow 4) lies anterior to the right pulmonary artery. At this anatomic level, the ascending aorta (AoA) has become enveloped by the pericardium; an anterior pericardial space (arrow 5) is apparent

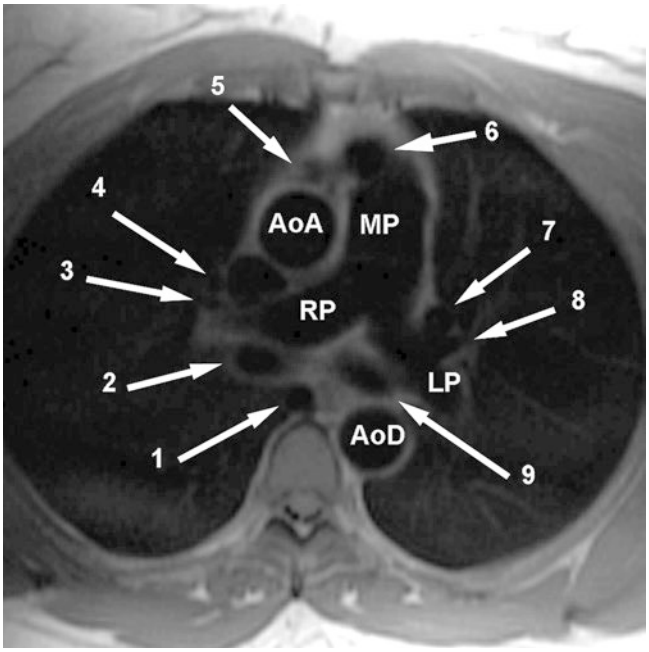

Fig. 3.13 Axial double inversion recovery image from a 45-year-old woman. The superior aspect of the right ventricular outflow (arrow 6) is now apparent. The left pulmonary artery (LP) has crossed the left bronchus (arrow 9) to enter the left hilum. Note that the left upper lobe pulmonary vein (arrow 7) is anterior to the left upper lobe pulmonary artery (arrow 8). The right pulmonary artery (RP) lies anterior to the right bronchus (arrow 2). The right upper lobe pulmonary vein (arrow 4) lies anterior to the right upper lobe pulmonary artery (arrow 3). Immediately anterior to the ascending aorta (AoA) is the anterior pericardial space (arrow 5). The azygos vein (arrow 1) is labeled

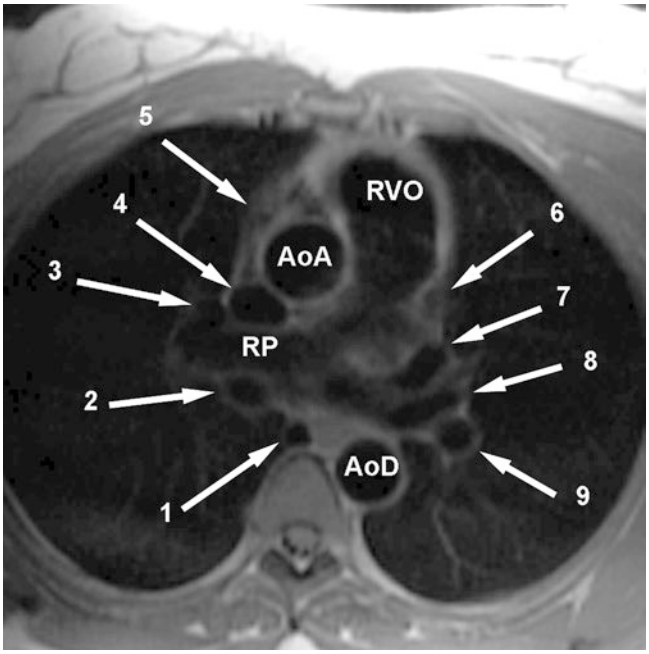

Fig. 3.14 Axial double inversion recovery image from a 45-year-old woman. The left-sided right ventricular outflow tract (RVO) lies anterior to the ascending aorta (AoA). At this level, we begin to see the tip of the left (arrow 6) and the right (arrow 5) atrial appendages. The right atrial appendage lies anterior to the AoA. The left atrial appendage lies anterior to the left upper lobe pulmonary vein (arrow 7) and artery (arrow 8). The descending left pulmonary artery (arrow 9) lies anterior and to the left of the descending aorta (AoD). The right upper lobe pulmonary vein (arrow 3) lies adjacent to the superior vena cava (arrow 4) and anterior to the right pulmonary artery (RP). The RP lies anterior to the right bronchus (arrow 2). The azygos vein (arrow 1) is identified

arch (Figs. 3.5, 3.19, 3.20, 3.21, 3.22, and 3.23). The innominate artery originates from the arch and takes a slightly rightward course anterior to the midline trachea before dividing into the right common carotid and right subclavian arteries. The left common carotid artery originates slightly dorsal and to the left of the innominate, dorsal and to the left of the trachea. The origin of the left subclavian artery is from the dorsal aspect of the aortic arch. It takes an almost vertical course from the aorta toward the thoracic outlet, and then turns toward the left and pulmonary apex. The aortic arch is usually left-sided, mildly displacing the trachea toward the right (Figs. 3.10, 3.18, 3.21, 3.22, 3.23, 3.24, and 3.25). No controlled reference data is available for measurement of the aortic arch; however, in one series of 66 adults (aged 44.1 ± 19.1 years), mean aortic arch caliber of the proximal arch was 29.3 ± 5.5 mm, and mean caliber of the distal arch was 24.9 ± 4.6 mm [32]. The ligamentum arteriosum (the remnant of the ductus arteriosus) is attached to the inferior aspect of the arch, just beyond the origin of the left subclavian artery. The proximal descending thoracic aorta lies to the left of the spine (Figs. 3.4, 3.8, 3.10, 3.11, 3.12, 3.13, 3.14, and 3.15). As it travels from cephalad to caudad in the posterior mediastinum, it comes to lie near the midline (Figs. 3.26 and 3.27). After the origin of the left subclavian artery, the descending thoracic aorta tapers gradually before entering the aortic hiatus. Descending aortic caliber in different adult populations is shown in Table 3.3.

The (usually) three bronchial arteries originate from the ventral aspect of descending aorta, between the levels of T5 and T6. Paired intercostal arteries originate from the dorsal aspect of the aorta, between the 3rd and 11th intercostal spaces.

Superior Vena Cava

Immediately cephalad to the aortic arch, the left subclavian vein is joined by the left internal jugular vein to form the left innominate vein (Figs. 3.17 and 3.18). The left innominate vein crosses from left to right just anterior to the aortic arch and proximal innominate artery (Fig. 3.19) to join the confluence of the right subclavian and internal jugular veins, forming the superior vena cava (SVC), to the right of the aorta (Figs. 3.1, 3.10, 3.12, and 3.14). The SVC passes behind the

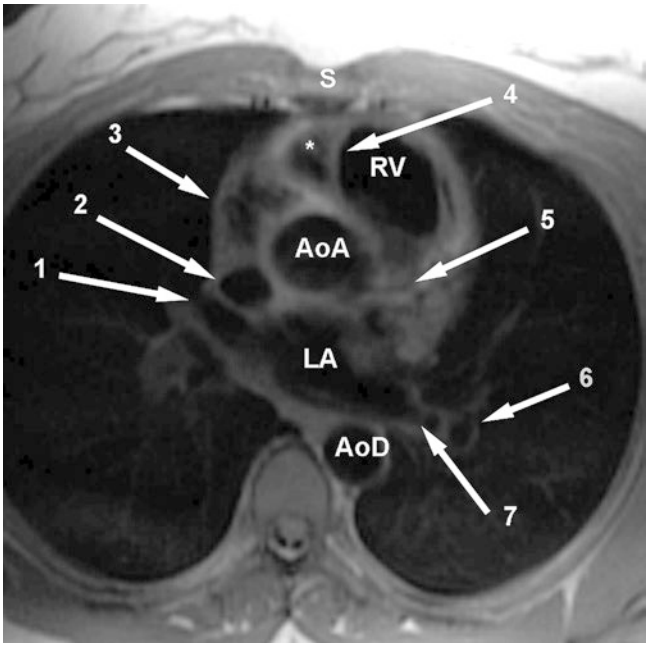

Fig. 3.15 Axial double inversion recovery image from a 45-year-old woman. The left atrium (LA) lies between the proximal ascending aorta (AoA) and descending aorta (AoD). At this level, the proximal left anterior descending coronary artery (arrow 5) is visualized. The right upper lobe pulmonary vein (arrow 1) drains into the LA behind the superior vena cava (arrow 2); the left lower lobe vein (arrow 7) empties into the LA from anterior to the descending aorta (AoD). The left lower lobe pulmonary artery (arrow 6) lies lateral and posterior to the lower lobe vein. Note the trabecular appearance of the right atrial appendage (arrow 3) as it wraps around the anterior aspect of the AoA. The sinus portion of the right ventricle (RV) lies anteriorly, immediately behind the body of the sternum (S). A myocardial trabeculation (arrow 4) extends from the interventricular septum to the right ventricular free wall, apparently isolating a medial portion of the RV chamber (*)

right sternal margin to enter the pericardium at the level of the second costal cartilage. The SVC receives the azygous vein just above the right upper lobe bronchus (Figs. 3.28, 3.29, 3.30, and 3.31). As the superior cava passes through the mediastinum to drain into the right atrium, it passes from anterior to posterior to the ascending aorta, entering the right atrium at the level of the third costal cartilage. The SVC drains into the right atrium just posterior to the orifice of the right atrial appendage and slightly anterior to the entrance of the inferior vena cava (Figs. 3.14, 3.21, and 3.26). The posterior wall of the SVC, as it enters the right atrium, is the sinus venosus portion of the interatrial septum and separates the SVC from the left atrium (Fig. 3.4).

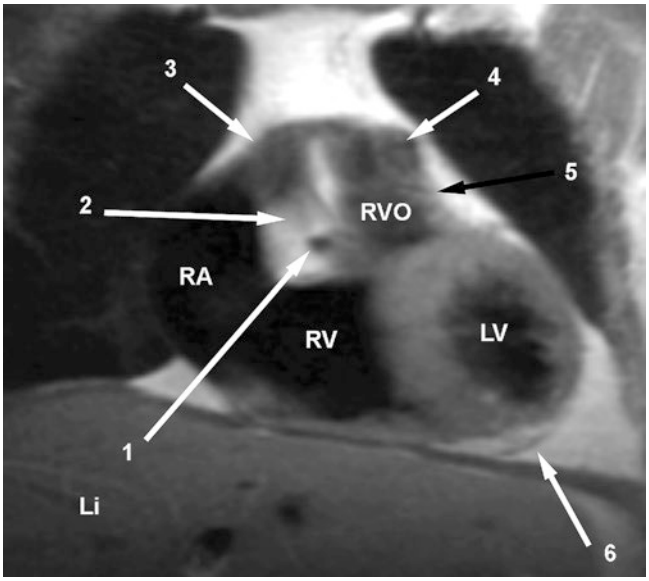

Fig. 3.16 Coronal double inversion recovery image from a 50-year-old woman through the origin of the right coronary artery (arrow 1). Still within the right atrium (RA) and right ventricle (RV), we visualize more of the left ventricle (LV). The superior and medial-most aspect of the right atrial appendage (arrow 3) lies anterior to the faintly visualized anterior aspect of the ascending aorta (arrow 2). The right ventricular outflow (RVO) extends posterior to the right ventricular sinus (RV), separated by the infundibulum. The pulmonary artery sinuses of Valsalva (arrow 4) are supported by the pulmonary valve (arrow 5). Inferoapical pericardium is marked (arrow 6)

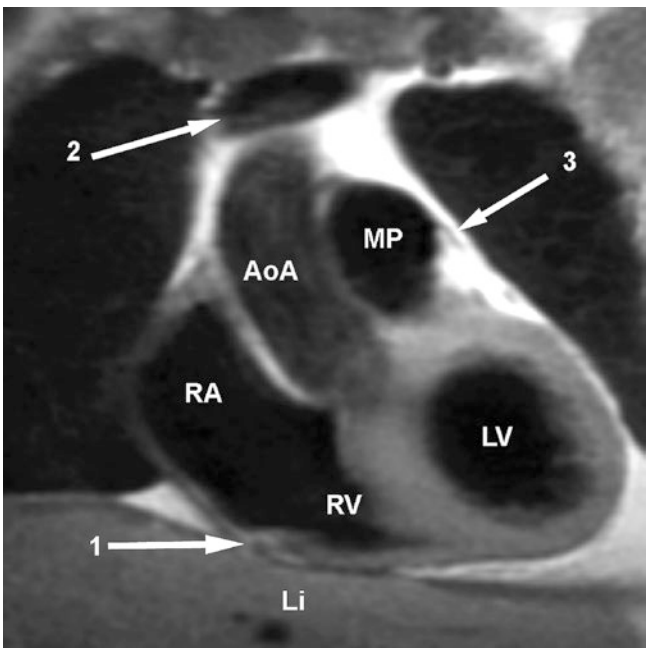

Fig. 3.17 Coronal double inversion recovery image from a 50-year-old woman. The left innominate vein (arrow 2) passes from left-to-right, and superior-to-inferior, cephalad to the top of the ascending aorta (AoA) . The distal right coronary artery (arrow 1) is viewed in cross section as it passes into the underside of the anterior atrioventricular ring, between the right atrium (RA) and inflow portion of the right ventricle (RV). The pericardium on the left side of the heart (arrow 3) is seen attaching to the top of the main pulmonary artery (MP). In this normal individual abdominal situs solitus is indicated by the right-sided liver (Li)

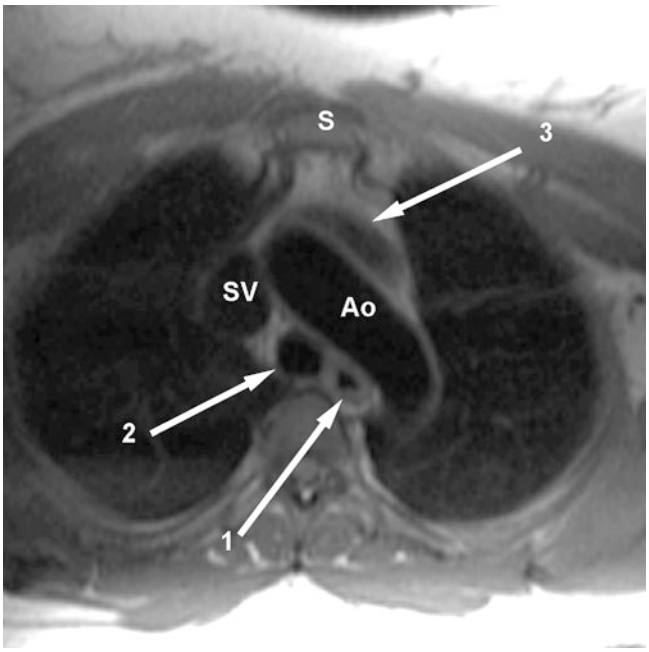

Fig. 3.18 Axial double inversion recovery image from a 45-year-old woman. The aortic arch (Ao) runs anteriorly-to-posteriorly and right-to-left, passing anterior to the air-filled (muscular) esophagus (arrow 1) and trachea (arrow 2). At this level, the left innominate vein (arrow 3) has not joined with the right innominate vein to for the superior vena cava (SV)

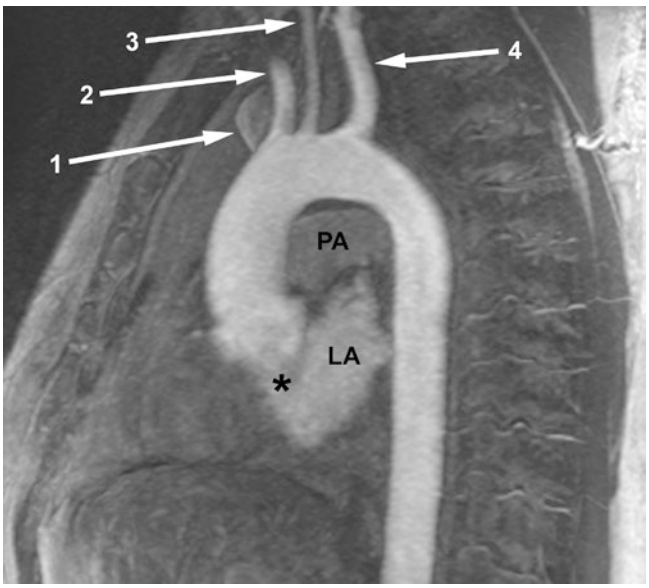

Fig. 3.19 Thick section maximum intensity projection image reconstructed in left anterior oblique sagittal section from a contrast enhanced magnetic resonance aortagram in a 45-year-old man. The main pulmonary artery (PA) is faintly opacified. The left atrium (LA) and left ventricular outflow (*) are better opacified. The innominate vein (arrow 1) passes directly anterior to the innominate artery (arrow 2). The left common carotid (arrow 3) and left subclavian (arrow 4) arteries arise prior to the descent of the aorta through the chest

Fig. 3.20 Left anterior oblique (LAO) sagittal double inversion recovery image from a 60-year-old woman through the ascending aorta (AoA) . In this section, the right atrial appendage (RAA) is anterior to the AoA and superior to the inflow portion of the right ventricle (RV). Before joining the right innominate vein (arrow 2) to form the superior vena cava, the left innominate vein (arrow 3) passes anterior to the left common carotid artery (arrow 4). Inferior and toward the left from the main pulmonary artery (MP), the tip of the left atrial appendage (arrow 5) can be seen. Note the left ventricular papillary muscles (arrows 6 and 7). The spleen (Sp) and intrahepatic (Li) inferior vena cava (arrow 1) are labeled

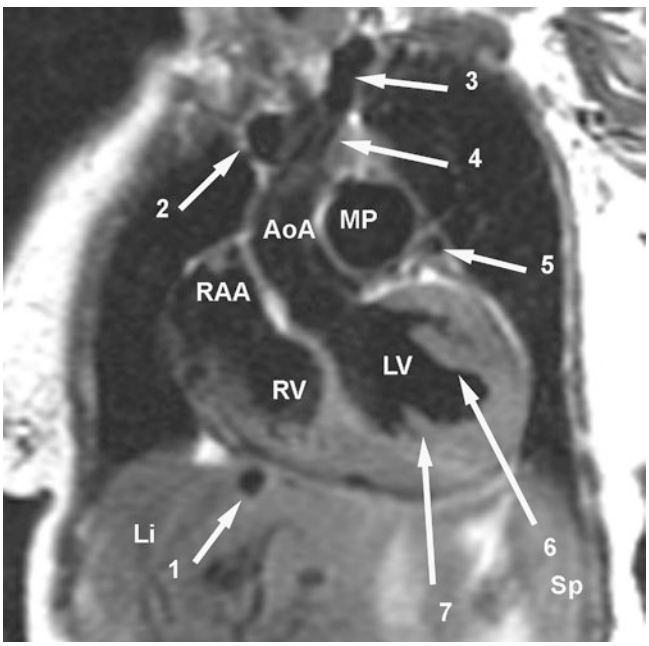

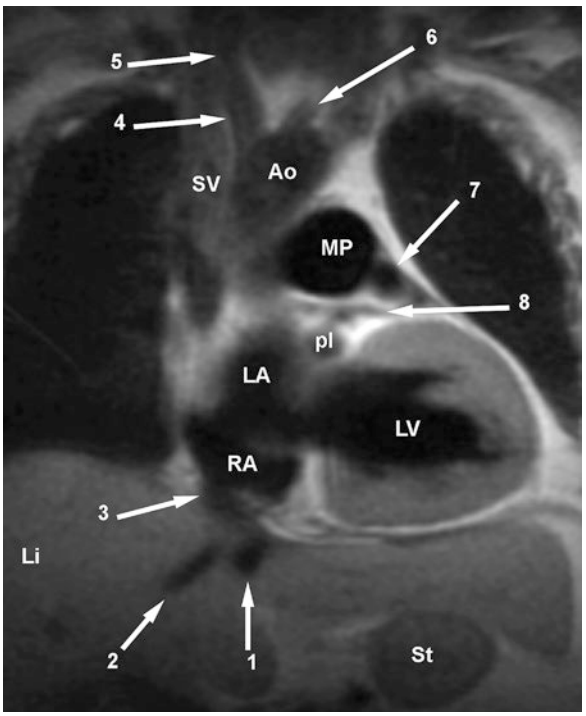

Fig. 3.21 Coronal double inversion recovery image from a 50-year-old woman. An hepatic vein (arrow 2) approaches the intrahepatic inferior vena cava (arrow 1). The suprahepatic inferior vena cava (arrow 3) is seen entering the posterior aspect of the right atrium (RA). The left atrium (LA) lies cephalad, posterior and medial to the RA, communicating with the left ventricle (LV) across the mitral valve (not visualized). The left main coronary artery (arrow 8) is seen originating from the posterior left aortic sinus of Valsalva (pl). The superior vena cava (SV) is posterior to the ascending aorta (not visualized), and within the same tomographic plane as the aortic arch (Ao). The innominate (arrow 4), right common carotid (arrow 5), and origin of the left common carotid (arrow 6) arteries are visualized, The finger-like left atrial appendage (arrow 7) is viewed in cross section, just inferior and to the left of the main pulmonary artery (MP). The liver (Li) and stomach (St) are labelled

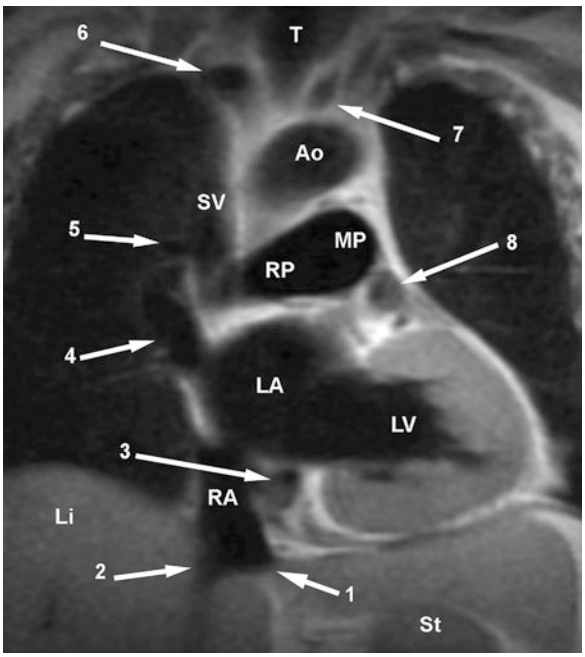

Fig. 3.22 Coronal double inversion recovery image from a 50-year-old woman. An hepatic vein (arrow 2) drains into the suprahepatic inferior vena cava (arrow 1), which enters the right atrium (RA) lateral and inferior to the coronary sinus (arrow 3). The coronary sinus (arrow 3) lies to the right of the fat in the posterior atrioventricular ring, beneath the left atrium (LA). The right upper lobe pulmonary vein (arrow 4) drains into the LA anterior to the right hilum. The azygos arch (arrow 5) can be seen draining to the posterior aspect of the superior vena cava (SV). The proximal-most right subclavian artery (arrow 6) can be seen immediately after its origin from the innominate artery. A segment of the left common carotid artery (arrow 7) lies to the left of the cervical trachea (T). The right pulmonary artery (RP) arises from the main pulmonary artery (MP), and then courses from superior-to-inferior and left-to-right along the roof of the LA to pass behind the SV. The body of the left atrial appendage (arrow 8) is contained by pericardium and lies just above the fat of the posterior atrioventricular ring. The liver (Li) and stomach (St) are labelled

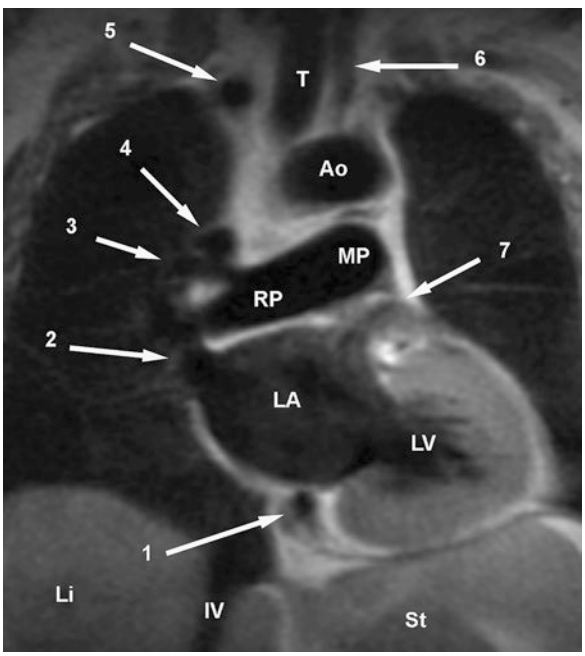

Fig. 3.23 Coronal double inversion recovery image from a 50-year-old woman through the origin of the right upper lobe pulmonary artery (arrow 3). The right pulmonary artery continues the left-to-right and cephalad-to-caudad course along the roof of the left atrium (LA). The right upper lobe pulmonary vein (arrow 2) drains into the LA just anterior to the right pulmonary artery. The azygos arch (arrow 4) is seen in cross section as it passes over the right hilum. The proximal right subclavian artery (arrow 5) is viewed in cross section as it passes toward the right shoulder; the left common carotid artery (arrow 6) lies to the left of the trachea (T). The mid left-heart border forming (collapsed) left atrial appendage (arrow 7) is seen draining into the left atrium. The roof of the coronary sinus (arrow 1) is formed by the floor of the LA. The inferior left-heart border is formed by the left ventricular (LV) myocardium. The liver (Li) and stomach (St) are labeled

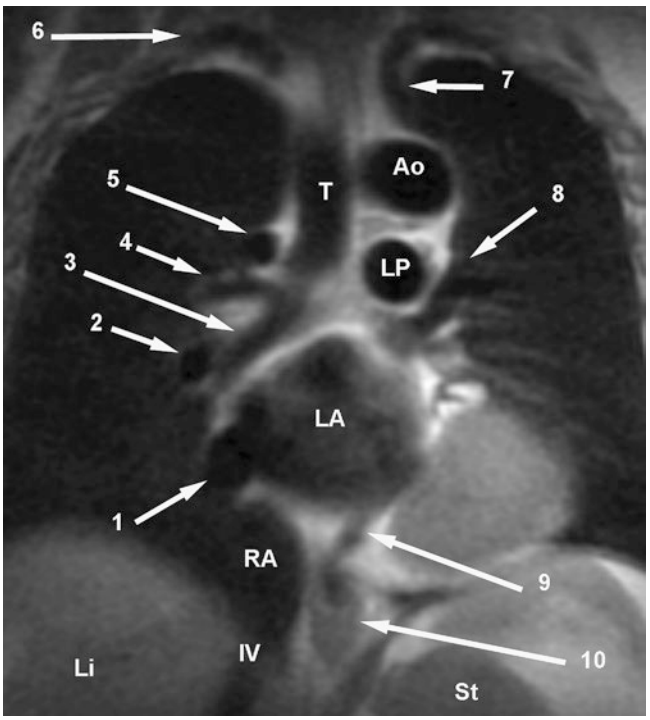

Fig. 3.24 Coronal double inversion recovery image from a 50-year-old woman through the origin of the right bronchus (arrow 3) from the trachea (T). The aortic arch (Ao) lies to the left of the T. The course of the right (arrow 6) and left (arrow 7) subclavian arteries over their respective pulmonary apices is well seen. The left upper lobe pulmonary vein (arrow 8) drains to the left of the left pulmonary artery (LP) before it enters the left atrium (LA). The right lower lobe pulmonary vein (arrow 1) is seen draining to the inferior aspect of the LA. The right hilum is well-demonstrated. The azygos arch (arrow 5) passes over the right upper lobe bronchus (arrow 4) at the level of the right bronchial origin. Incidentally, notice the short course from the tracheal bifurcation to the origin of the right upper lobe bronchus. The right hilar pulmonary artery (arrow 2) is no greater in caliber than its adjacent right bronchus. Embedded within the fat of the posterior atrioventricular ring, the coronary sinus (arrow 9) has not yet entered the right atrium (RA). Immediately proximal to the diaphragmatic hiatus, the distal esophagus (arrow 10) has not yet connected with the stomach (St). The liver (Li) and intrahepatic inferior vena cava (IV) are labeled

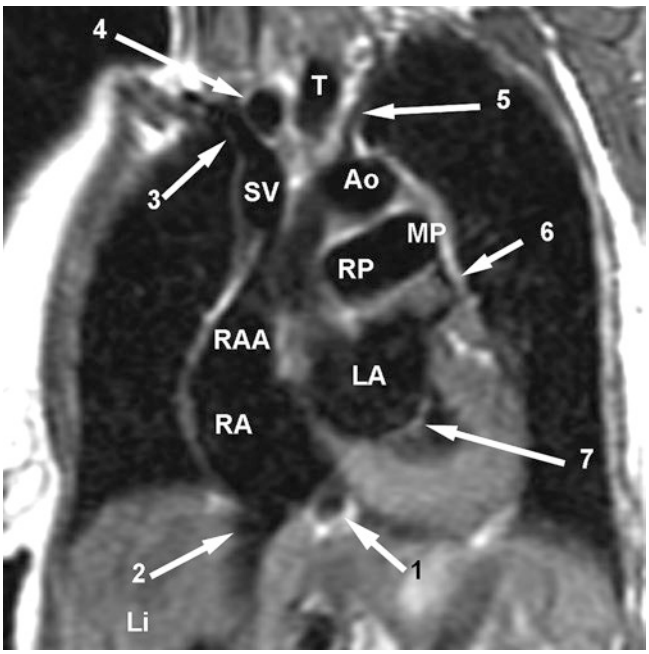

Fig. 3.25 Left anterior oblique (LAO) sagittal double inversion recovery image from a 60-year-old woman. In this section, the proximal right pulmonary artery (RP) is seen arising from the main pulmonary artery (MP), passing inferiorly and toward the right, over the roof of the left atrium (LA). Immediately inferior to the MP, turbulence within the mouth of the left atrial appendage (arrow 6) is seen. At this same level, the mouth of the right atrial appendage (RAA) is viewed as well. Notice the left-to-right relationship between the LA and the right atrium (RA). The coronary sinus (arrow 1) to the right of the fat of the posterior atrioventricular ring lies medial and slightly superior to the entry of the inferior vena cava (arrow 2) into the RA. The right innominate vein (arrow 3), which lies to the right of the innominate artery (arrow 4) has joined the left innominate vein (not viewed) to form the superior vena cava (SV). The origin and proximal portion of the left vertebral artery (arrow 5) is seen. The mitral valve (arrow 7) and liver (Li) are labeled

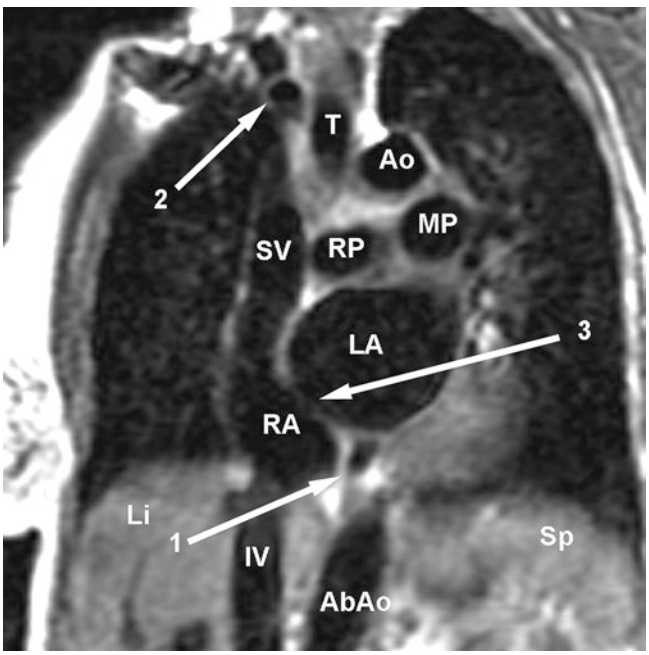

Fig. 3.26 Left anterior oblique (LAO) sagittal double inversion recovery image from a 60-year-old woman. The secundum interatrial septum (arrow 3) separates the left (LA) from right (RA) atrium. Inferior to the LA, the coronary sinus (arrow 1) runs in the posterior atrioventricular ring, medial to the entry of the inferior vena cava (IV) into the RA. The superior vena cava (SV) lies in the same plane as the transverse right pulmonary artery (RP). Just to the right of the midline trachea (T), the origin of the right subclavian artery (arrow 2) is viewed in cross section. The abdominal aorta (AbAo) lies to the left of the intrahepatic (Li) IV. The spleen (Sp) is labeled

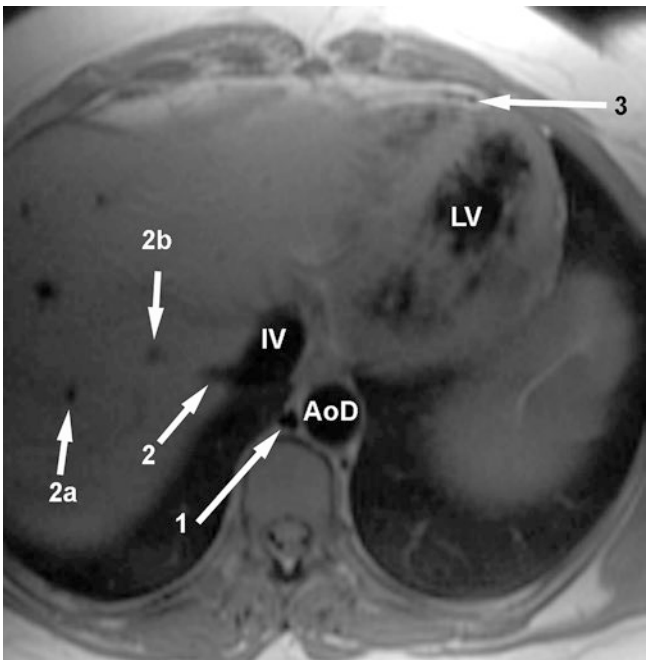

Fig. 3.27 Axial double inversion recovery image from a 45-year-old woman. The inferior aspect of the left ventricular cavity (LV) is seen. Below the diaphragm, a right hepatic vein (arrow 2) is seen entering the inferior vena cava (IV). In addition, other segmental hepatic veins (arrows 2a and 2b) are viewed. Note the signal void of the pericardial space (arrow 3) sandwiched between the epicardial and pericardial fat layers. The azygos vein (arrow 1) and descending thoracic aorta (AoD) are labeled

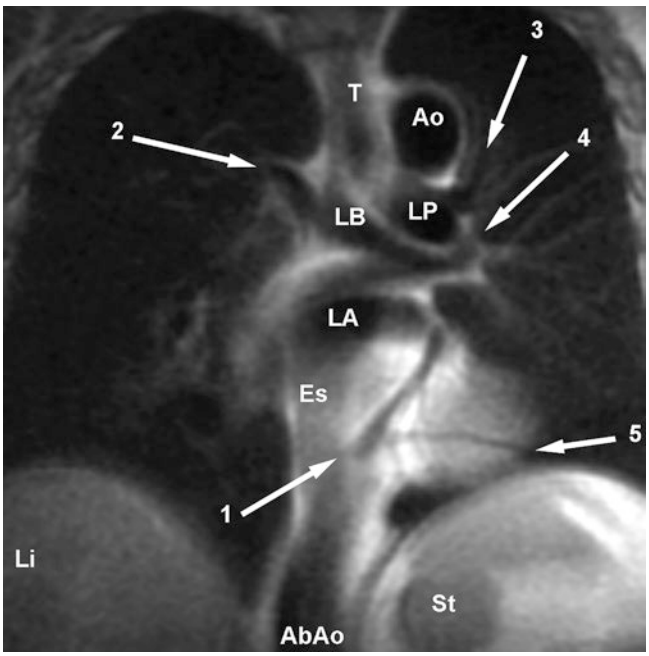

Fig. 3.28 Coronal double inversion recovery image from a 50-year-old woman. The morphologic left lung is characterized by the passage of the left pulmonary artery (LP) over the left bronchus (LB). Notice the long course the LB takes before giving the left upper lobe bronchus (arrow 4). Arising from the LP, the left upper lobe pulmonary artery (arrow 3) courses parallel to the Ao. The trachea (T) lies to the right of the aortic arch (Ao). Passing obliquely within the high signal intensity fat of the posterior atrioventricular ring, the coronary sinus (arrow 1) is joined by an inferior cardiac vein (arrow 5) passing along the epicardium of the posterior left ventricular wall. Along the right cardiac border, the azygos arch (arrow 2) is seen curving from a paraspinal position laterally to begin to arch over the right hilum. The intermediate intensity band formed by the anterior aspect of the esophagus (Es) shares the tomographic section containing the back wall of the left atrium (LA). Lumbar spine lordosis pushes the abdominal aorta (AbAo) anteriorly. The liver (Li) and stomach (St) are labeled

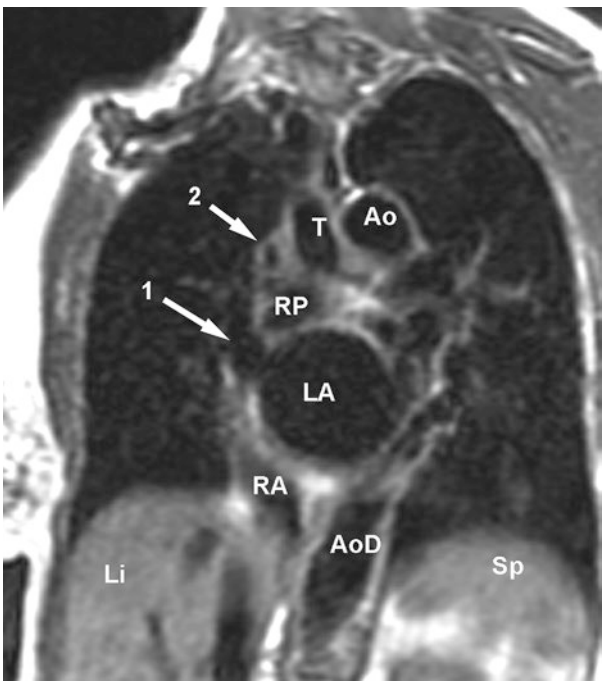

Fig. 3.29 Left anterior oblique (LAO) sagittal double inversion recovery image from a 60-year-old woman. The left-sided aortic arch (Ao) displaces the trachea (T) to the right. The right upper lobe pulmonary vein (arrow 1) is seen draining into the left atrium (LA) immediately anterior to the right pulmonary artery (RP) passage over the LA toward the right hilum. Seen in cross section, the azygos vein (arrow 2) arches over the right hilum prior to drainage into the superior vena cava (not seen). The right-heart border forming right atrium (RA) lies inferior and toward the right with respect to the LA and lower descending thoracic aorta (AoD). The liver (Li) and spleen (Sp) are labeled

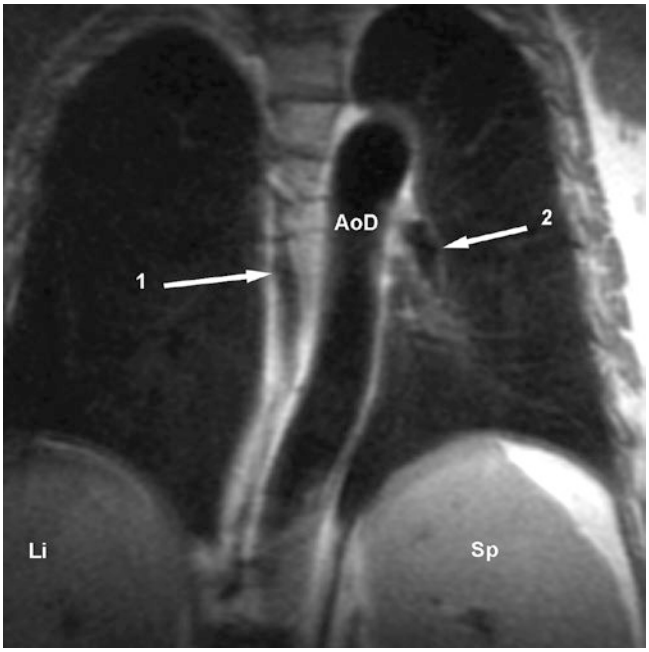

Fig. 3.30 Left anterior oblique (LAO) sagittal double inversion recovery image from a 60-year-old woman. The azygos vein (arrow 1) ascends just to the right of the descending thoracic aorta (AoD). The posterior aspect of the descending left pulmonary artery (arrow 2), liver (Li), and spleen (Sp) are labeled

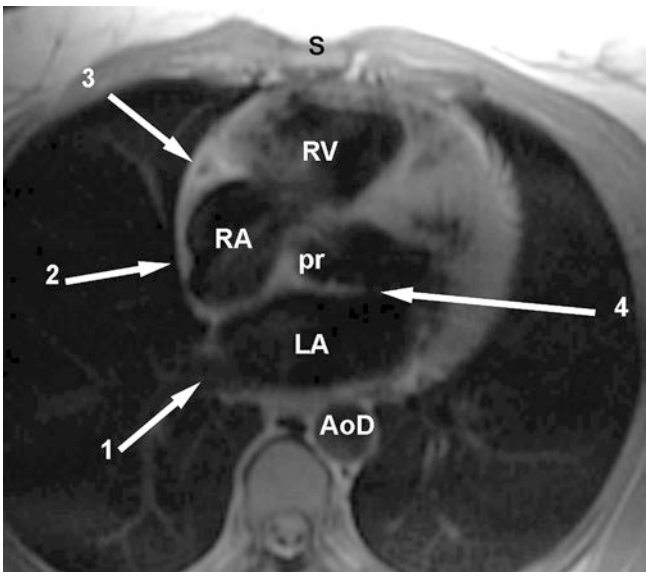

Fig. 3.31 Axial double inversion recovery image from a 45-year-old woman. The anterior right ventricle (RV) lies behind the sternum (S). The right coronary artery can be seen in cross section, traveling within the fat of the anterior atrioventricular ring (arrow 3). The crista terminalis (arrow 2) is seen as a high signal intensity object along the lateral wall of the right atrium (RA). The right lower lobe pulmonary vein is seen entering the left atrium (LA). Notice how the anterior mitral leaflet (arrow 4) is continuous with the aortic annulus and posterior right aortic sinus of Valsalva (pr). The descending aorta is labeled

Right Atrium

The crista terminalis, the remnant of the vein of the sinus venosus (Figs. 3.4 and 3.8) segregates the right atrial (RA) cavity into an anterior trabeculated portion, and a smooth-walled posterior portion. The lateral RA wall is very thin; the distance between the cavity of the RA and the outer lateral border of the heart should be no greater than 3 mm. Increased thickening usually means a pericardial effusion or pericardial thickening. The right atrial appendage (RAA) is a broad-based, triangular structure, contained within the pericardium, which extends from about the middle of the heart obliquely around the ascending aorta (Figs. 3.1, 3.9, 3.13, 3.14, 3.15, 3.20, and 3.25). Collapsed when RA pressure and volume are normal, the pectinate muscles characteristically seen in the RA anterior to the crista terminalis tend to prevent its collapse. When enlarged, the pectinate muscles of the RAA appear as intracavitary filling defects, analogous to ventricular myocardial bundles in the right ventricle (Figs. 3.12, 3.13, 3.14, and 3.15). Currently, there is no consensus in the literature regarding acquisition and analysis methodology for CMR evaluation of right atrial size and volume.

The coronary sinus extends from the confluence of the great cardiac vein, between the LA and left ventricle in the posterior atrioventricular ring, and then passes beneath the left atrium to the diaphragmatic surface of the heart to drain into the RA medial and slightly superior to the entry of the IVC (Figs. 3.5, 3.22, 3.23, 3.25, 3.26, and 3.28). The eustacian valve separates these two structures. The suprahepatic portion of the inferior vena cava (IVC) usually receives the hepatic veins before draining into the heart. Occasionally, the hepatic veins drain directly into the floor of the RA.

The interatrial septum separates the left from right atrium (Figs. 3.4, 3.9, 3.21, 3.22, 3.24, 3.25, 3.26, and 3.29). It forms a curved surface, usually bowing toward the right atrium. Normal thinning in the region of the foramen ovale may be seen; this change in septal thickness is exaggerated in individuals with extra fat deposits around the heart, and elsewhere. The right atrium should appear nearly the same size as the left atrium. Measurement of right atrial size is less difficult than estimation of right atrial volume. Nevertheless, right atrial enlargement is associated with clockwise cardiac rotation.

The tricuspid valve resides within the anterior atrioventricular ring, immediately subjacent to the right coronary artery. The plane of the valve annulus is nearly sagittal and may therefore be visualized in axial section. The septal and anterior leaflets appear as long filling defects attached to the AV ring, and connected to the right ventricular free wall and septum by very fine chordae, and papillary muscles of varying size.

Right Ventricle

The right ventricle resides immediately posterior to the sternum, more or less in the midline (Figs. 3.2, 3.3, 3.4, 3.8, 3.15, 3.16, 3.17, 3.20, 3.32, 3.33, 3.34, and 3.35). Unless hypertrophied, the right ventricular free wall myocardium is only about 2 to 3 mm in thickness, and difficult to visualize. The shape of the RV can be surmised by visualizing the ventricle as the sum of the axial sections obtained during CMR or CT examination. From the level of the pulmonary valve, moving caudad, the shape of the ventricle changes. The right ventricular outflow tract is round in shape, surrounded by the ventricular infundibulum (Figs. 3.2, 3.14, 3.16, 3.36, and 3.37), and lies to the patient's left. Moving in a caudad direction, the chamber increases in size, assuming a triangular shape, the base formed by the AV ring, and the apex at the intersection of the free wall and interventricular septum.

The unusual shape of the right ventricle lends itself to quantitative analysis of cine-MR imagery. Planimetry of the epicardial and endocardial borders of images obtained at end diastole and end systole provide the basis for evaluation of right ventricular volume and assessment of right ventricular function. Acquisition of the entire cardiac mass provides a complete data set, obviating the need for making any geometric assumptions about the unusual geometry of the ventricle. Right ventricular end diastolic volume is calculated by multiplying slice thickness by the sum of the end diastolic endocardial area of all slices containing the right ventricular cavity; similarly, end systolic volume is the sum of the end systolic slice areas. Right ventricular stroke

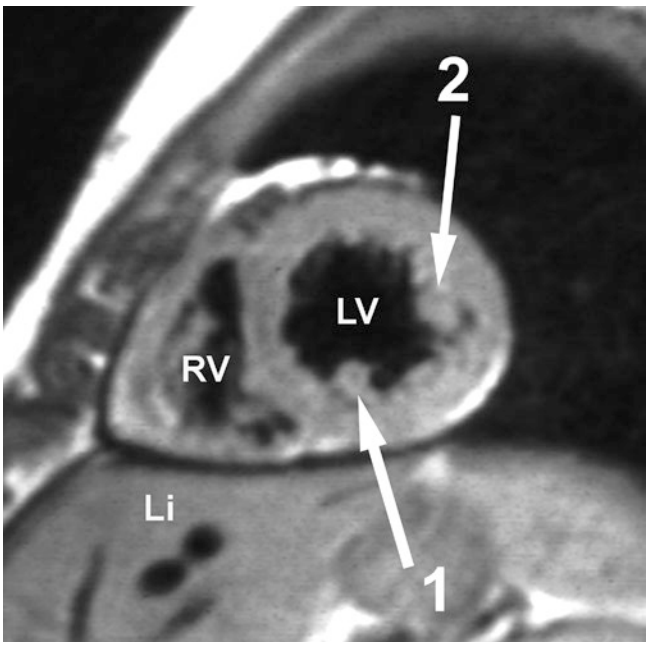

Fig. 3.33 Systolic short axis double inversion recovery image from a 25-year-old man through the base of the left ventricular (LV) papillary muscles (arrows 1 and 2). Notice how the right ventricular (RV) chamber extends slightly inferior to the LV chamber. The liver (Li) is labeled

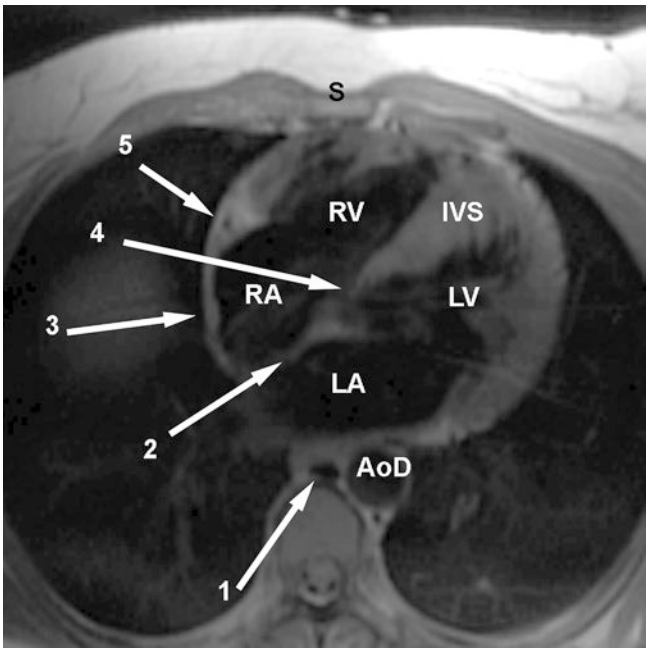

Fig. 3.32 Axial double inversion recovery image from a 45-year-old woman. The right (RV) and left (LV) ventricles share the interventricular septum. The anterior aspect of the septum is muscular (IVS). The posterior aspect of the septum contains the membranous portion (arrow 4), immediately inferior to the aortic valve. At this level, the primum interatrial septum (arrow 2) forms the medial aspect of the interatrial septum between the right (RA) and left (LA) atria. The crista terminalis (arrow 3), right coronary artery in cross section (arrow 5), azygos vein (arrow 1), and sternum (S) are labeled

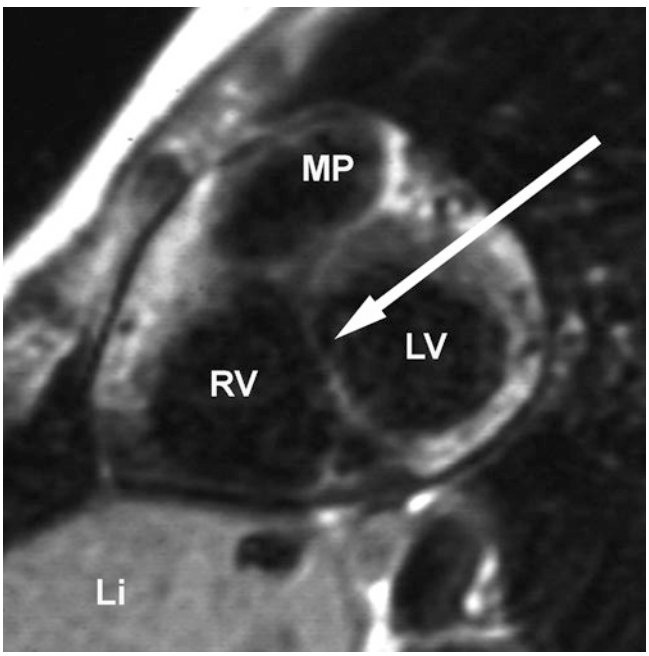

Fig. 3.34 Short axis double inversion recovery image from a 25-year-old man through the posterior interventricular septum (arrow). The main pulmonary artery (MP) begins to course from the top of the right ventricle (RV) over the top of the left ventricle (LV). The liver (Li) is labeled

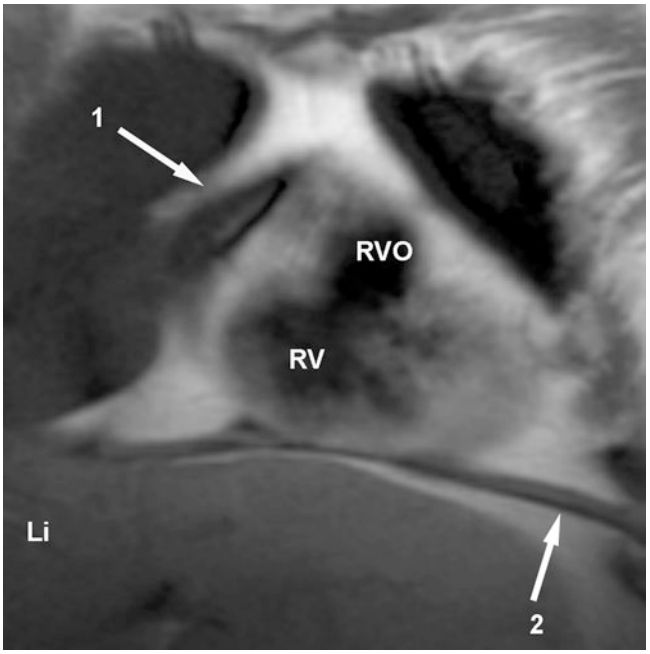

Fig. 3.35 Coronal double inversion recovery image from a 50-year-old woman, obtained immediately posterior to the sternum. The sinus (RV) and outflow (RVO) portions of the right ventricle occupy the retrosternal space. The anterior tip of the triangular-shaped right atrial appendage (arrow 1) is not heart-border forming. A small portion of the left diaphragm (arrow 2) is seen. The liver (Li) is labeled

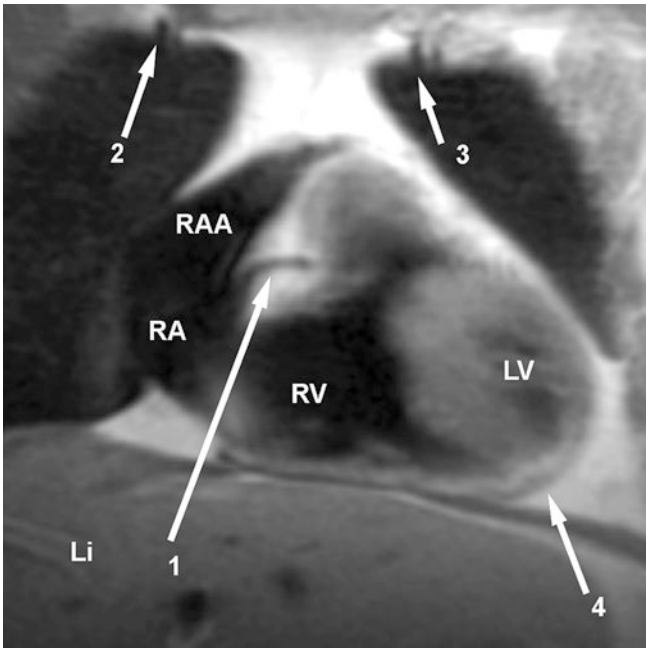

Fig. 3.36 Coronal double inversion recovery image from a 50-year-old woman. The cavity of the right-heart border forming right atrium (RA), the broad-based and triangular-shaped right atrial appendage (RAA), and the inflow portion of the right ventricle (RV) occupy the anterior of the heart. Here only a small portion of the left ventricular (LV) cavity is visualized. The pericardial space (arrow 4) just inferior to the cardiac apex is characterized by low-signal fluid and pericardium separating high-signal fat. The right coronary artery (arrow 1) is seen passing toward the right within the fat of the right atrioventricular ring. The right (arrow 2) and left (arrow 3) internal mammary arteries are visualized passing over the thoracic apices toward the anterior chest wall. The liver (Li) is labeled

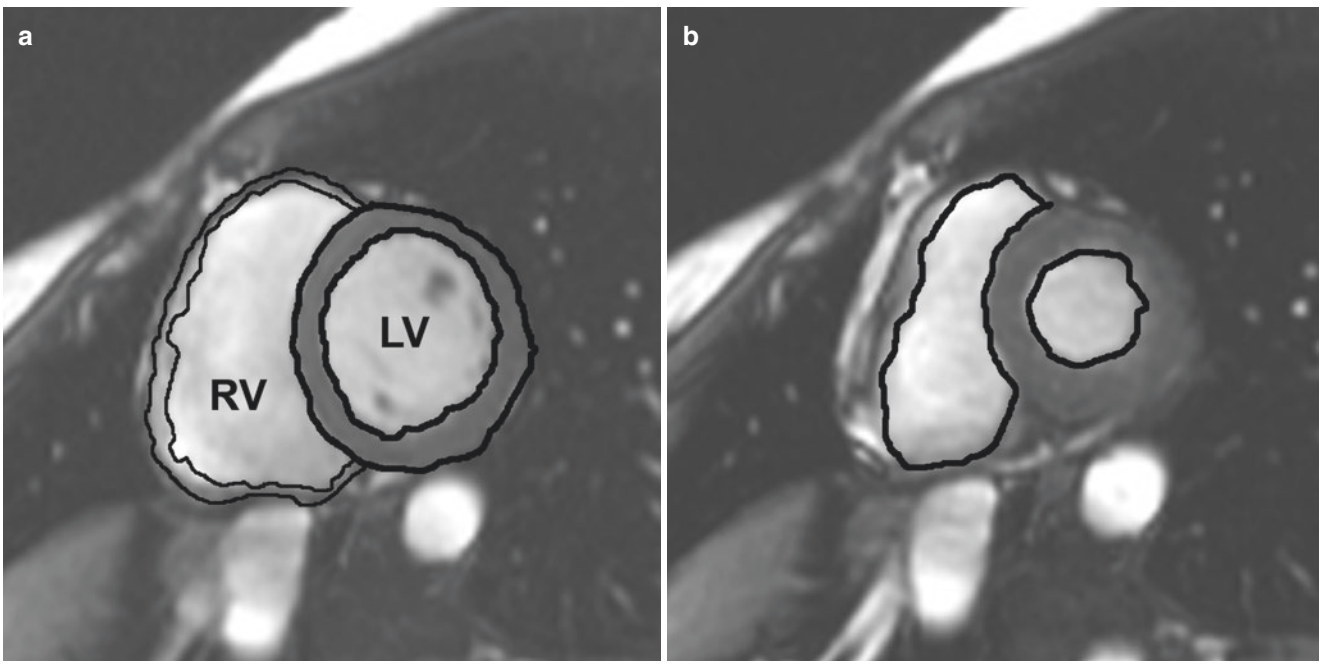

Fig. 3.37 Normal short axis gradient echo images obtained from a 52-year-old woman. (**a**) End diastolic image. The right (RV) and left (LV) ventricular endocardial and epicardial borders have been hand-traced. (**b**) End systolic image demonstrating hand tracing of the endocardial borders

volume is the difference between end diastolic and end systolic volume, and ejection fraction is the stroke volume indexed to (i.e., divided by) the end diastolic volume (Fig. 3.38). CMR is considered to be the "gold standard" for quantitating right ventricular function [33, 34] (Table 3.4).

Right ventricular mass may be difficult to calculate because of the unusually heavy trabeculation of the right ventricular myocardium. The area of ventricular myocardium at end diastole is the difference between the areas of the epicardial right ventricular contour and the endocardial border. Myocardial mass is the myocardial volume (slice area times slice thickness summed over the entire ventricle) times the specific gravity of myocardium, 1.05 g/ml. By convention, choosing to assign intracavitary trabeculations and the papillary muscles to the myocardial wall and assignment of the interventricular septum to the left ventricle produce reliable estimation of right ventricular mass (Table 3.4).

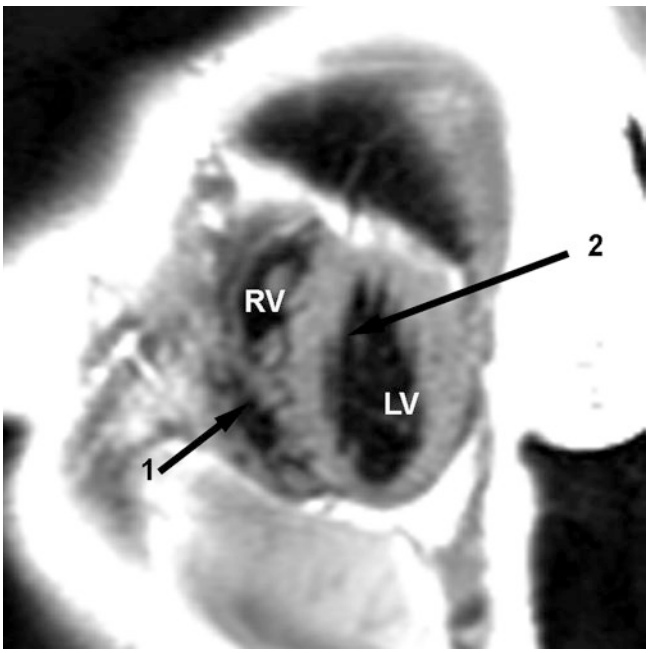

Fig. 3.38 Left anterior oblique (LAO) sagittal double inversion recovery image from a 60-year-old woman. The anterior right ventricle (RV) and posterior left ventricle (LV) both share the interventricular septum. Notice how the RV side of the septum (arrow 1) is markedly trabeculated, and the LV side (arrow 2) is relatively smooth

The tricuspid valve is separated from the pulmonary valve by the right ventricular infundibulum. The right ventricular surface of the interventricular septum is irregular (Figs. 3.2, 3.4, 3.34, and 3.39). Although the septomarginal trabeculation may not always be identified, papillary muscles extending from it to the tricuspid valve leaflets are commonplace. Numerous muscle bundles extend from the interventricular septum across the RV chamber to the free wall (Figs. 3.4, 3.8, and 3.15). The inferior-most of these is the moderator band, which carries the conducting bundle.

The interventricular septum normally bows toward the right ventricle (Figs. 3.2, 3.3, 3.16, 3.17, 3.34, and 3.39), so that in short axis reconstruction, the left ventricle appears as a doughnut and the left ventricular cavity as the hole (Figs. 3.3, 3.34, and 3.38). The RV in short axis section appears as an appendage to the left ventricle, extending from slightly inferior to the inferior-most aspect of the interventricular septum, RV outflow tract and pulmonary valve, which resides superior to the LV (Figs. 3.2, 3.3, 3.8, 3.14, 3.16, 3.17, and 3.35).

Pulmonary Artery

The pulmonary valve lies slightly out of the axial plane, so may appear elongated in conventional axial acquisition (Figs. 3.12, 3.13, 3.14, and 3.16). The main pulmonary artery (PA) is supported by the pulmonary annulus and passes posteriorly as it ascends within the pericardium. The caliber of the main pulmonary artery should be about the caliber of the ascending aorta at this anatomic level. Estimation of main pulmonary artery caliber by MRI in healthy adults [35, 36] compares favorably with caliber measurements obtained from computed tomography.

Table 3.4 Right ventricular volume and mass

	Women				Men			
	<60y		≥60y		<60y		≥60y	
Parameter	Mean ± SD	Range	Mean ± SD	Range	Mean ± SD	Range	Mean ± SD	Range
RVEDV, ml	133 ± 22	89–177	114 ± 22	70–158	169 ± 25	119–219	153 ± 25	103–203
RVEDVI, ml/M^2	78 ± 9	60–96	60 ± 9	48–84	87 ± 12	63–111	77 ± 12	53–101
RVESV, ml	49 ± 13	23–75	35 ± 13	9–61	62 ± 15	32–92	48 ± 5	18–78
RVESVI, ml/M^2	28 ± 7	14–42	20 ± 7	6–34	32 ± 7	18–46	24 ± 7	10–38
RVSV, ml	85 ± 13	59–111	80 ± 13	54–106	107 ± 17	73–141	105 ± 17	71–139
RVSVI, ml/M^2	50 ± 6	38–62	46 ± 6	34–58	55 ± 8	39–71	53 ± 8	37–69
RVEF, %	64 ± 6	52–76	70 ± 6	58–82	64 ± 7	50–78	69 ± 7	55–83
RVM, g	50 ± 11	28–72	44 ± 1	22–66	68 ± 14	40–96	63 ± 14	35–91
RVMI, g/M^2	30 ± 5	20–40	25 ± 5	15–35	35 ± 7	21–49	32 ± 7	18–46

From [34]

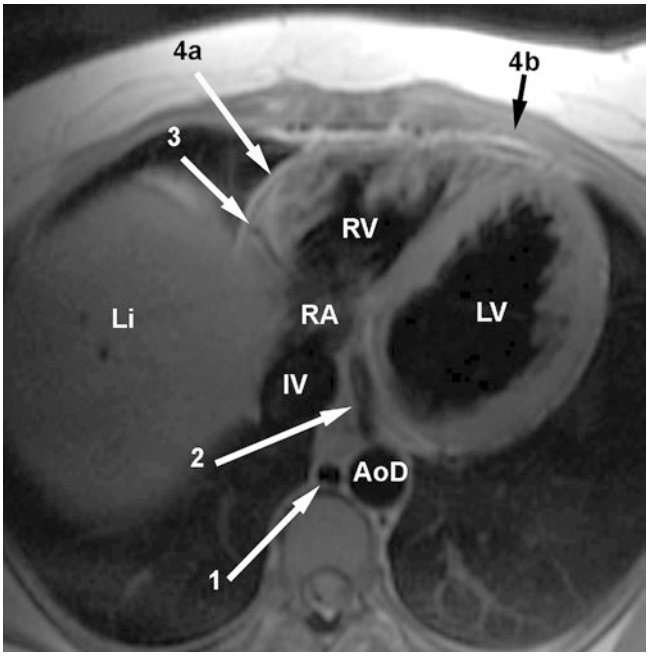

Fig. 3.39 Axial double inversion recovery image from a 45-year-old woman. The signal of the right hemi-diaphragm and liver (Li) fill most of the right chest. The right (RV) and left (LV) ventricles are separated by the muscular interventricular septum. At this level, the right coronary artery (arrow 3) has turned along the inferior aspect of the anterior atrioventricular ring. The coronary sinus (arrow 2) runs to the right of the fat of the posterior atrioventricular ring, beneath the left atrium (not visualized), and immediately medial to the LV. The inferior vena cava (IV) has passed through the Li and is just entering the posterior aspect of the RA. Note the pencil-thin signal void of the pericardial space (arrows 4a and 4b) between the high signal of the epicardial and pericardial fat. The azygos vein (arrow 1) and descending thoracic aorta (AoD) are labeled

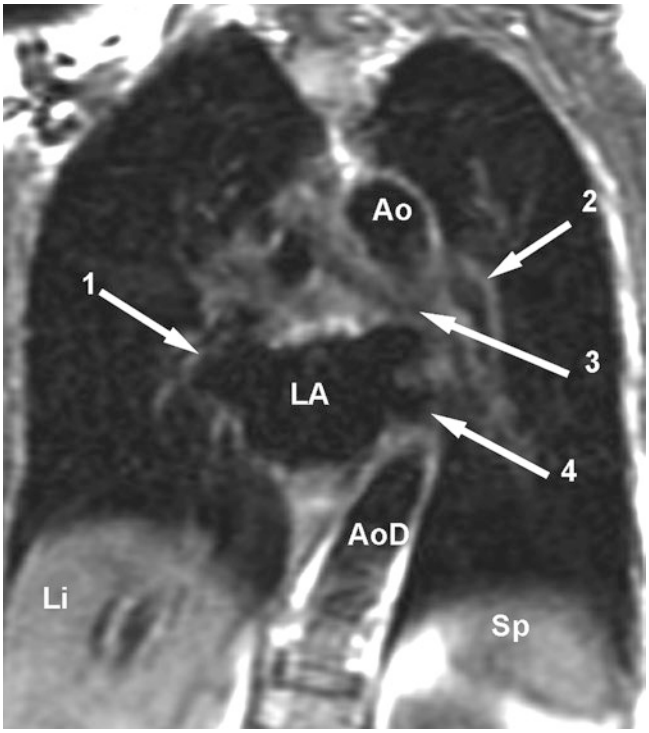

Fig. 3.40 Left anterior oblique (LAO) sagittal double inversion recovery image from a 60-year-old woman through the distal aortic arch (Ao) and posterior aspect of the left atrium (LA). The right upper lobe pulmonary vein (arrow 1) is seen draining into the LA. The left pulmonary artery (arrow 2) lies superior and posterior to the distal left bronchus (arrow 3). The left lower lobe pulmonary vein (arrow 4) drains into the LA immediately anterior to the descending aorta (AoD), which has not yet entered the abdomen. Liver (Li) and spleen (Sp) are labeled

The left pulmonary artery is the extension of the main PA coursing above the left atrium (Figs. 3.12, 3.24, and 3.28). When the PA crosses the left bronchus, it becomes the left PA (Figs. 3.12, 3.13, 3.24, 3.28, and 3.30). The right PA originates from the underside of the main PA and passes along the roof of the left atrium, posterior to the ascending aorta and superior vena cava, to enter the right hilum (Figs. 3.12, 3.13, 3.14, 3.22, 3.23, 3.25, 3.26, and 3.29). The pericardium is reflected over the top of the main PA (Figs. 3.1, 3.2, 3.17, and 3.25).

Pulmonary Veins

The upper lobe pulmonary veins lie anterior to their respective pulmonary arteries (Figs. 3.13, 3.14, 3.15, 3.22, 3.23, 3.24, 3.28, 3.29, and 3.40). As the left upper lobe vein courses inferiorly, it passes in front of the left PA and enters the left atrium immediately posterior to the orifice of the left atrial appendage (Figs. 3.14, 3.23, and 3.24). The right upper lobe vein lies anterior to the right pulmonary artery. It passes from anterior to posterior and inferiorly to enter the left atrium immediately posterior to the entrance of the superior vena cava into the right atrium (Figs. 3.12, 3.13, 3.14, 3.15, 3.22, 3.23, 3.24, and 3.29). The left lower lobe pulmonary vein always courses in a caudad direction directly anterior to the descending thoracic aorta before entering the posterior left aspect of the left atrium (Figs. 3.15 and 3.40). The right lower lobe vein drains to the right posterior inferior aspect of the left atrium (Figs. 3.4 and 3.15).

Left Atrium

The left atrium lies posterior, superior, and toward the left with respect to the right atrium (Figs. 3.4, 3.8, 3.9, 3.15, 3.24, 3.26, 3.29, 3.32, 3.33, and 3.41). The two atria share the interatrial septum, which forms an oblique surface between the two. The interatrial septum normally thins in the region of the foramen ovale. The left atrium is just about the same size as the right atrium. The inner surface of the LA is bald smooth. The confluence of the left upper lobe pulmo-

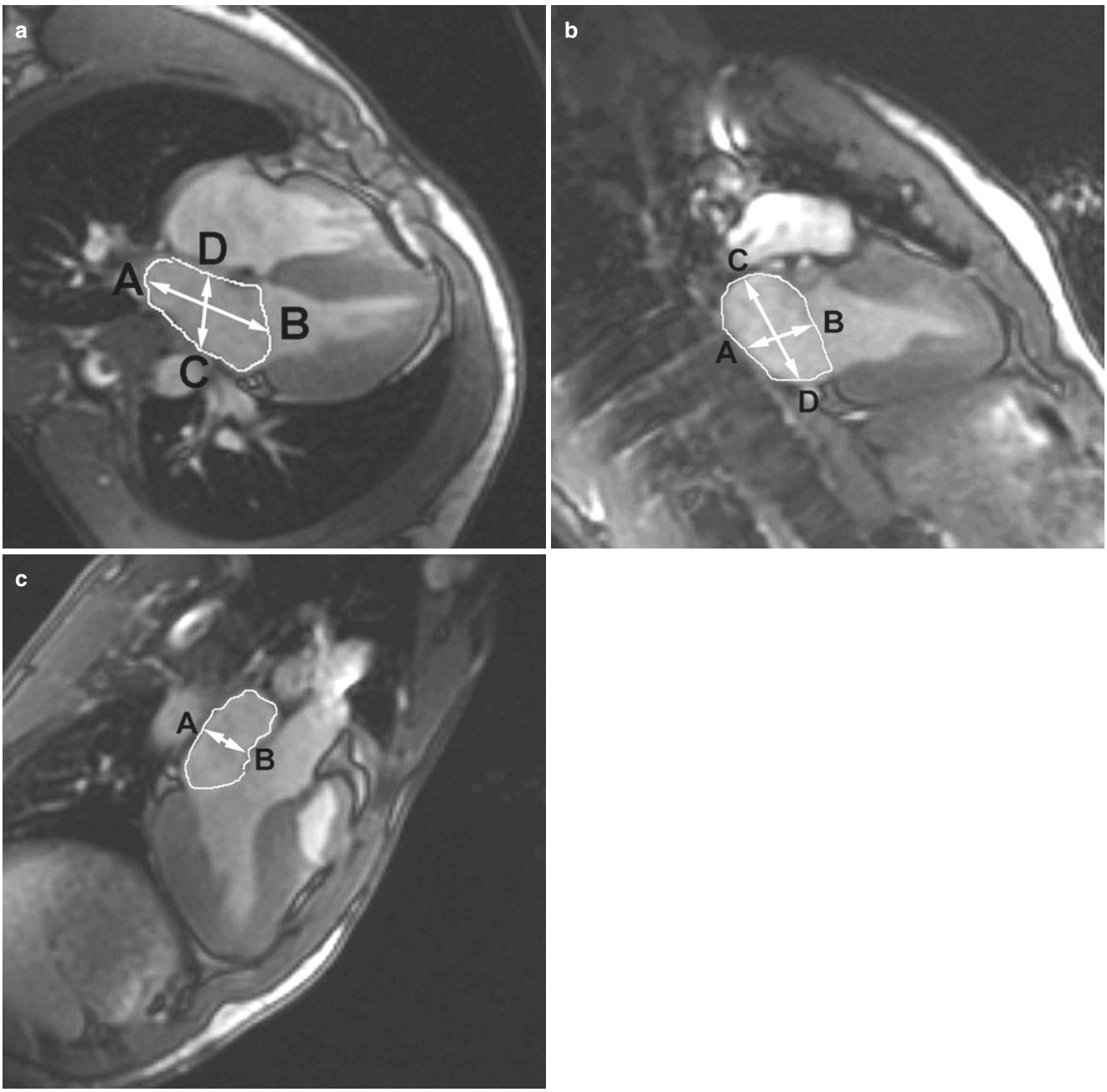

Fig. 3.41 Calculation of left atrial volume. (**a**) Systolic 4 chamber view displaying planimetered area (dotted line) and longitudinal (double headed arrow AB) and transverse (double headed arrow CD) atrial 4 chamber dimension. (**b**) Systolic 2 chamber view demonstrating hand planimetered area of the left atrium (dotted line) and longitudinal (double headed arrow AB) and transverse (double headed arrow CD) diameters. (**c**) Planimetered left atrial area (dotted line) and anteroposterior diameter (double headed arrow AB) in a 3 chamber view

nary vein and orifice of the left atrial appendage is a redundant endothelium, which may appear to be thickened in its medial-most aspect. The left atrial appendage is long and finger-like (Figs. 3.5, 3.20, 3.21, and 3.22). Analogous to the right atrial appendage, it contains pectinate musculature. However, these myocardial trabeculations are always smaller in caliber than those of the RAA and almost never cross from one face of the appendage to the other. The LAA runs from caudad to cephalad, around the left aspect of the heart, below the level of the pulmonary valve.

Tomographic left atrial visualization by 2-D echocardiography allows measurement of maximal linear dimension in arbitrary section. However, the atrium is neither symmetric in shape nor uniform in the manner it enlarges. Thus, geometric assumptions for single dimensional analysis may not accurately assess instant volume or change in volume in

pathologic states. More accurate assessment of the left atrium is obtained by utilizing measurement of multiple linear dimensions and direct 3D echocardiographic technique. Steady-state free precession (cine) MR evaluation of left atrial volume, presuming no geometric assumption, is obtained using Simpson's Rule by summing tomographic sectional area over the entire organ. MR estimation of left atrial volume (Fig. 3.41) is the "gold standard" for assessing atrial size and function [33, 37, 38]. Reference values for left atrial dimensions and volume (Table 3.5) are typically greater than that obtained by standard echocardiographic methods and demonstrate increased volume associated with increasing body surface and patient age. The left atrial wall is thin; there are no reference standards for determination of a pathologically thickened wall. However, the appearance of delayed hyperintensity of the wall after intravenous contrast administration is a sensitive means of detecting focal pathologic processes, including fibrosis, commonly associated with failed radiofrequency atrial fibrillation ablation therapy [39–42].

The mitral valve lies within the posterior atrioventricular ring, immediately subjacent to the circumflex coronary artery (Figs. 3.25 and 3.32). Fibrous continuity between the anterior mitral leaflet and the aortic annulus is demonstrated on axial acquisition (Figs. 3.4 and 3.32).

Left Ventricle

The left ventricle lies posterior and to the left with respect to the RV; the inflow of the left ventricle lies to the left of the inflow to the right ventricle (Figs. 3.2, 3.3, 3.4, 3.16, 3.17, 3.20, 3.32, 3.33, 3.34, 3.36, 3.37, 3.38, and 3.39). The left ventricular myocardium is nearly uniform in thickness (1 cm at end diastole). However, in axial acquisition, the posterior LV wall may appear thicker than the septal or apical myocardium (or vice versa) (Figs. 3.4, 3.27, 3.32, 3.38, and 3.39) because it has been cut obliquely with respect to its internal axis. Although some trabecular myocardial filling defects may be identified within the ventricular cavity, the LV is characterized by its smooth walls and two large papillary muscles (Figs. 3.20 and 3.33). These always originate from the posterior wall of the ventricle. The plane of the interventricular septum is directed anterior to the coronal plane and inferiorly toward the left hip. It normally bows toward the RV (Figs. 3.2, 3.3, 3.33, 3.34, 3.37, 3.38, and 3.42). The aortic valve shares the fibrous trigone of the heart and is, as previously described, in continuity with the anterior mitral leaflet (Fig. 3.31).

The posterior AV ring also contains the coronary sinus (Figs. 3.22, 3.23, 3.24, 3.25, 3.26, 3.28, and 3.39). This vein lies anterior to the circumflex artery, and passes around the ring between the LA and LV, to run beneath the LA prior to its drainage into the RA. Before entering the RA, is receives other venous tributaries, which run along the epicardial surface of the heart.

Left ventricular myocardium exhibits intermediate, homogeneous signal intensity when viewed using conventional gradient echo acquisition techniques. Upon intravenous administration of gadolinium-based contrast agents, the signal increases as the contrast agent rapidly redistributes into the extracellular space and then returns to baseline signal after the contrast passed out of the myocardium (Fig. 3.42). Areas of non-enhancement reflect regional hypoperfusion and myocardial ischemia. Imagery obtained several minutes

Table 3.5 Left atrial dimensions and volume

	All individuals		Women		Men	
	Mean ± SD	Range	Mean ± SD	Range	Mean ± SD	Range
Volume, ml	73 ± 14.9	44–102	68 ± 14.9	42–95	77 ± 14.9	48–107
Volume index, ml/M^2	40 ± 6.7	27–53	40 ± 6.7	27–52	39 ± 6.7	26–53
4 Ch area, cm^2	21 ± 3.7	14–28	20 ± 3.7	14–27	22 ± 3.7	14–30
4 Ch area index, cm^2/M^2	12 ± 1.8	8–15	12 ± 1.8	8–15	11 ± 1.8	7–15
4 Ch longitudinal diameter, cm	5.7 ± 0.7	4.3–7.0	5.5 ± 0.7	4.1–6.9	5.9 ± 0.7	4.5–7.2
4 Ch longitudinal diameter index, cm/M^2	3.1 ± 0.4	2.3–3.9	3.2 ± 0.4	2.4–4.1	3.0 ± 0.4	2.3–3.7
4 Ch transverse diameter, cm	4.1 ± 0.5	3.0–5.1	4.1 ± 0.5	3.0–5.1	4.1 ± 0.5	3.0–5.2
4 Ch transverse diameter index, cm/M^2	2.2 ± 0.3	1.6–2.8	2.4 ± 0.3	1.8–3.0	2.1 ± 0.3	1.5–2.8
2 chamber area, cm^2	20 ± 4.7	11–29	19 ± 4.7	10–28	21 ± 4.7	12–31
2 chamber area index, cm^2/M^2	11 ± 2.4	6–16	11 ± 2.4	6–16	11 ± 2.4	6–15
2 chamber longitudinal diameter, cm	4.9 ± 0.7	3.4–6.3	4.6 ± 0.7	3.1–6.0	5.0 ± 0.7	3.6–6.4
2 chamber longitudinal diameter index	2.6 ± 0.4	1.9–3.2	2.7 ± 0.4	1.2–4.1	2.5 ± 0.4	1.8–3.2
2 chamber transverse diameter, cm	4.6 ± 0.5	3.6–5.6	4.4 ± 0.5	3.4–5.5	4.6 ± 0.5	3.7–5.5
2 chamber transverse diameter index, cm^2/M^2	2.5 ± 0.2	2.0–2.9	2.6 ± 0.2	1.5–3.6	2.3 ± 0.2	1.9–2.8
3 chamber area, cm^2	18 ± 3.6	11–25	17 ± 1.8	11–24	19 ± 3.6	13–26
3 chamber area index, cm^2/M^2	10 ± 1.8	6–13	10 ± 1.8	7–13	10 ± 1.8	6–13
3 chamber AP diameter, cm	3.2 ± 0.5	2.2–4.2	3.1 ± 0.5	2.1–4.1	3.3 ± 0.5	2.3–4.2
3 chamber diameter index, cm^2/M^2	1.7 ± 0.3	1.2–2.3	1.8 ± 0.3	1.3–2.3	1.7 ± 0.3	0.7–2.6

From [38]

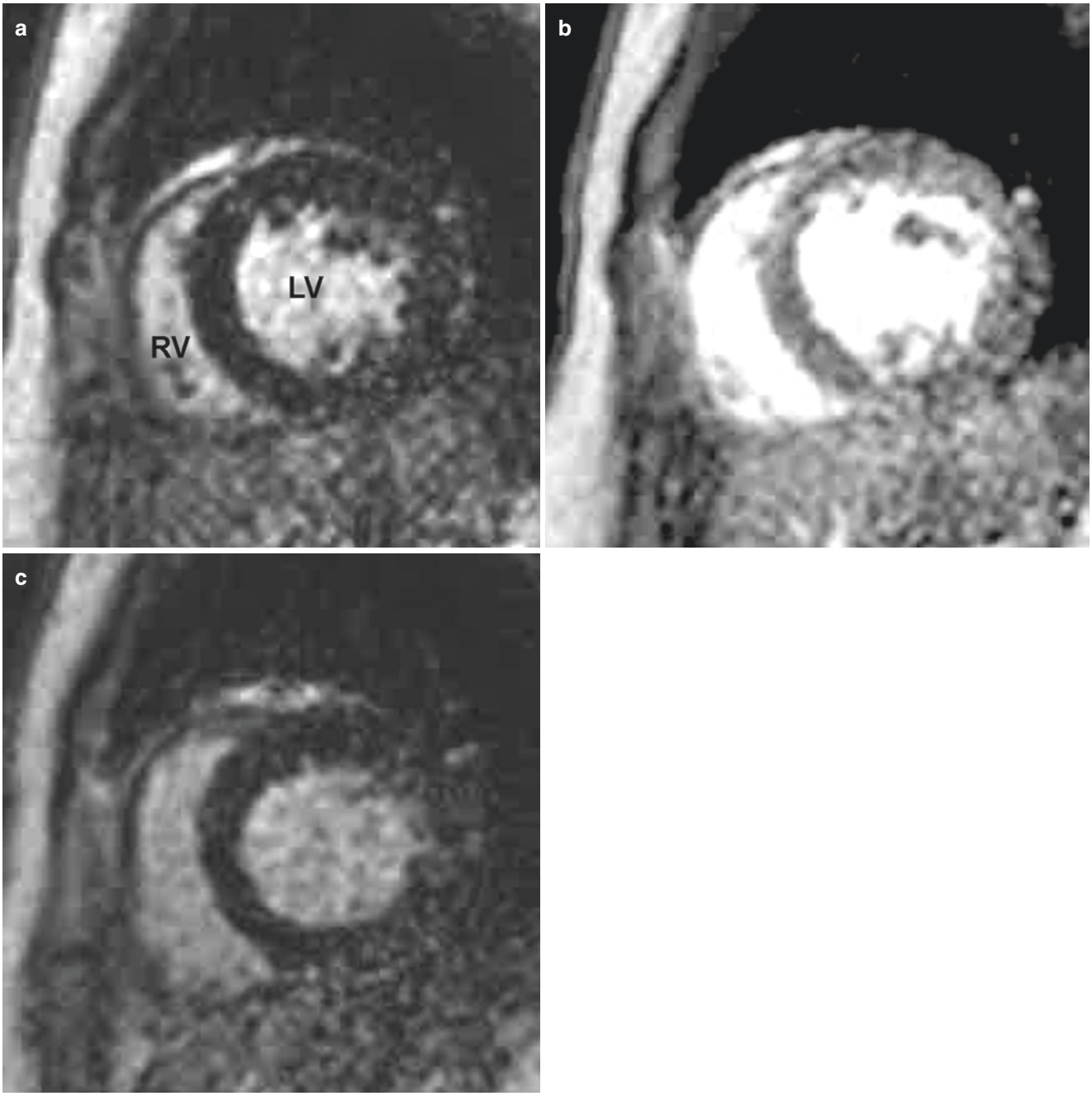

Fig. 3.42 Short axis gradient echo acquisition immediately after rapid intravenous administration of 10 ml Gd-DTPA. (**a**) Contrast has passed the pulmonary bed and now opacifies both the right (RV) and left (LV) ventricles. The ventricular myocardium is not enhanced. (**b**) Two seconds later, the ventricular myocardium and all other tissues enhance. (**c**) Ten minutes after intravenous contrast administration, the ventricular myocardium has returned to baseline signal intensity

after intravenous contrast administration (performed with the application of appropriate nulling pulses to minimize the inherent signal of myocardium) demonstrates "delayed hyperenhancement" in segments of abnormal myocardium. Although the exact mechanism of this process is not completely understood, this abnormal signal probably reflects delayed wash-in and washout kinetics of nonviable tissue and differing volumes of gadolinium distribution in viable and nonviable regions [43–45]. The clinical utility of this technique is discussed in much greater detail in a later chapter of this book.

CMR is the "gold standard" for quantitative analysis of the left ventricle and its' function. ECG-gated tomographic acquisition in the cardiac short axis provides a series of images obtained at regular intervals within the cardiac cycle, from which ventricular volume and myocardial mass may be

precisely calculated. In a manner analogous to that for right ventricular analysis, both end diastolic and end systolic images of the left ventricle are obtained, and the epicardial and endocardial borders of each are planimetered (Fig. 3.37). The difference between the area of the end diastolic epicardial and endocardial borders is the myocardial slice area. This value times slice thickness is the slice myocardial volume. Slice myocardial volume summed over the whole left ventricle is the total myocardial volume. Myocardial volume multiplied by the specific gravity of ventricular myocardium yields the left ventricular mass. Similarly, the end diastolic volume is obtained by summing the product of the area of the slice endocardial border and slice thickness; end systolic volume is obtained by summing the product of the area of the slice endocardial border and slice thickness from end systolic images. In this manner, left ventricular end diastolic and end systolic volume may be calculated. Reference values for left ventricular volume and mass (Table 3.6) are available [33, 34].

Coronary Arteries

The aortic valve divides the aortic bulb into the three sinuses of Valsalva, named by their anatomic location. The anterior aortic sinus lies anteriorly, between the right atrial appendage and right ventricular outflow (Figs. 3.16, 3.43, 3.44, 3.45, and 3.46). There are two posterior sinuses. The posterior right sinus is the inferior-most sinus, lying above the atrioventricular septum and between the right and left atria (Figs. 3.1, 3.4, 3.5, 3.9, 3.31, 3.43, and 3.46). This is also referred to as the "non-coronary sinus"; it provides the origin of no coronary artery. The posterior left sinus is the most superior in position, lying directly anterior to the left atrium (Figs. 3.1, 3.5, 3.21, 3.43, 3.44, and 3.45). The coronary arteries originate from the aorta, immediately above the sinuses, and below the sinotubular ridge, a transition in caliber between the sinuses and the tubular portion of the aorta. The left main coronary artery originates from the posterior left sinus. It usually arises from the upper third of the sinus and takes a slightly cephalad and leftward course toward the epicardium. It then dips below the left atrial appendage and heads back toward the posterior atrioventricular ring to become the circumflex artery (Figs. 3.5, 3.15, 3.21, 3.44, and 3.45). The circumflex artery passes through the posterior atrioventricular ring, giving marginal branches along the posterior wall of the left ventricle (Figs. 3.2, 3.5, 3.44, and 3.45). Prior to the passage of the left

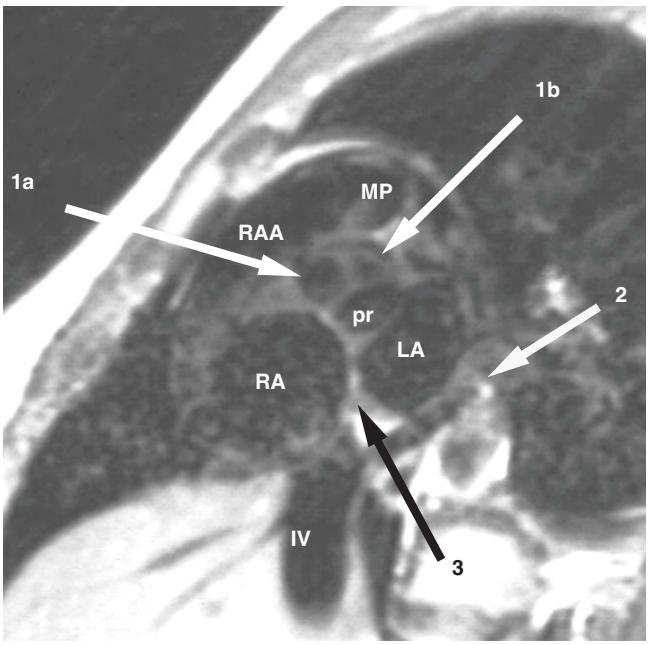

Fig. 3.43 Short axis double inversion recovery image from a 25-year-old man through the aortic valve. The anterior (arrow 1a), posterior left (arrow 1b), and posterior right (pr) aortic sinuses of Valsalva are labeled. The coronary sinus (arrow 2) passes beneath the left atrium (LA) within the posterior atrioventricular ring toward the right atrium (RA). The right atrial appendage (RAA) lies anterior to the aortic root. The suprahepatic inferior vena cava (IV) drains into the posterior aspect of the RA lateral to the drainage of the coronary sinus. Fatty infiltration of the interatrial septum (arrow 3) enhances its appearance

Table 3.6 Left ventricular volume and mass

	Women				Men			
	<60y		≥60y		<60y		≥60y	
Parameter	Mean ± SD	Range	Mean ± SD	Range	Mean ± SD	Range	Mean ± SD	Range
LVEDV, ml	132 ± 21	90–174	120 ± 21	78–162	161 ± 21	119–203	148 ± 21	106–190
LVEDVI, ml/M^2	78 ± 8.7	61–95	69 ± 8.7	52–86	82 ± 9	64–100	76 ± 9	58–94
LVESV, ml	44 ± 9.5	25–63	38 ± 9.5	19–57	55 ± 11	33–77	48 ± 11	26–70
LVESVI, ml/M^2	26 ± 4.7	17–35	22 ± 4.7	13–31	28 ± 5.5	17–39	25 ± 5.5	14–36
LVSV, ml	88 ± 14	60–116	82 ± 14	54–110	106 ± 14	78–134	100 ± 14	72–128
LVSVI, ml/M^2	52 ± 6.2	40–64	47.5 ± 6.2	35–60	52 ± 6.1	43–67	52 ± 6.1	40–64
LVEF, %	67 ± 4.6	58–76	69 ± 4.6	60–78	66 ± 4.5	57–75	68 ± 4.5	59–77
LVM, g	106 ± 18	70–142	110 ± 18	74–146	147 ± 20	107–187	145 ± 20	105–185
LVMI, g/M^2	62 ± 7.5	47–77	63 ± 7.5	48–78	74 ± 8.5	57–91	73 ± 8.5	56–90

From [34]

main artery beneath the left atrial appendage, the left anterior descending artery arises from the left main. The left anterior descending artery passes behind the right ventricular outflow and along the top of the interventricular septum toward the cardiac apex (Figs. 3.2, 3.3, 3.5, 3.15, 3.21, 3.44, and 3.45). The right coronary artery originates from the upper portion of the anterior sinus of Valsalva. It takes an abrupt turn toward the right, beneath the right atrial appendage, to enter the epicardial fat of the anterior atrioventricular ring. It then passes within the ring, between the bodies of the right atrium and ventricle, toward the cardiac crux, the intersection of the atrioventricular rings and interventricular septum, along the diaphragmatic surface of the heart (Figs. 3.8, 3.16, 3.32, 3.36, 3.39, 3.44, 3.45, and 3.46). The posterior descending artery perfuses the inferior interventricular septum and may act as an important collateral bed in patients with atherosclerotic

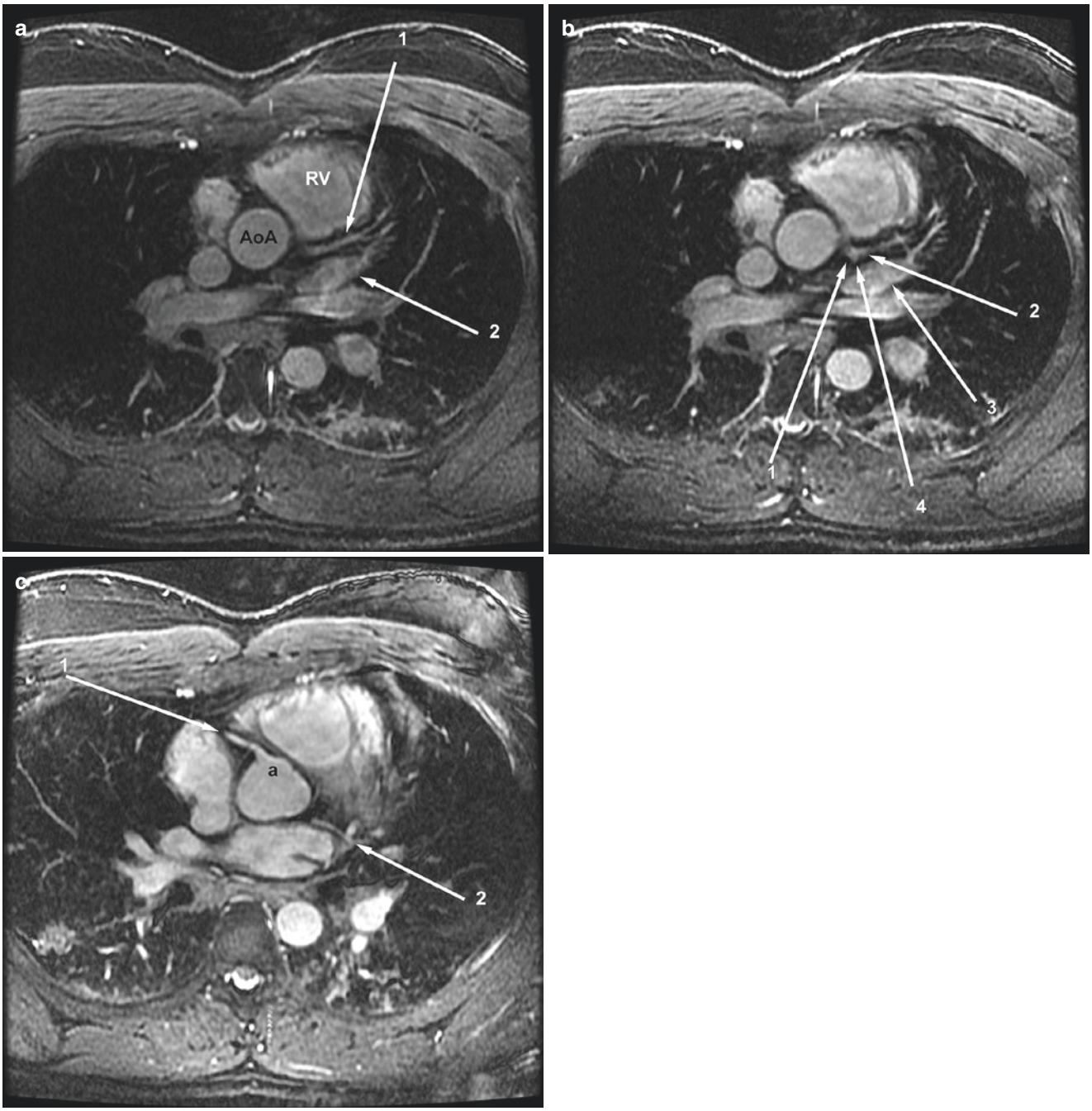

Fig. 3.44 Axial fat saturated contrast-enhanced gradient echo acquisitions from a 45-year-old woman. (**a**) Anterior descending coronary artery (arrow 1) passes along the top of the interventricular septum, between the right ventricle (RV) and left atrial appendage (arrow 2). The ascending aorta (AoA) is labeled. (**b**) Image obtained 3 mm inferior to A. The origins of the left anterior descending (arrow 2), and circumflex (arrow 4) coronary arteries from the left main artery (arrow 1) are visualized. The circumflex is cut off, as it moves out of plane, inferior to the left atrial appendage (arrow 3). (**c**) Image obtained 3 mm inferior to **b**. The proximal circumflex artery (arrow 2) passes beneath the left atrial appendage to enter the posterior atrioventricular ring. At this level, the origin and proximal right coronary artery (arrow 1) is seen arising from the anterior aortic sinus of Valsalva (a)

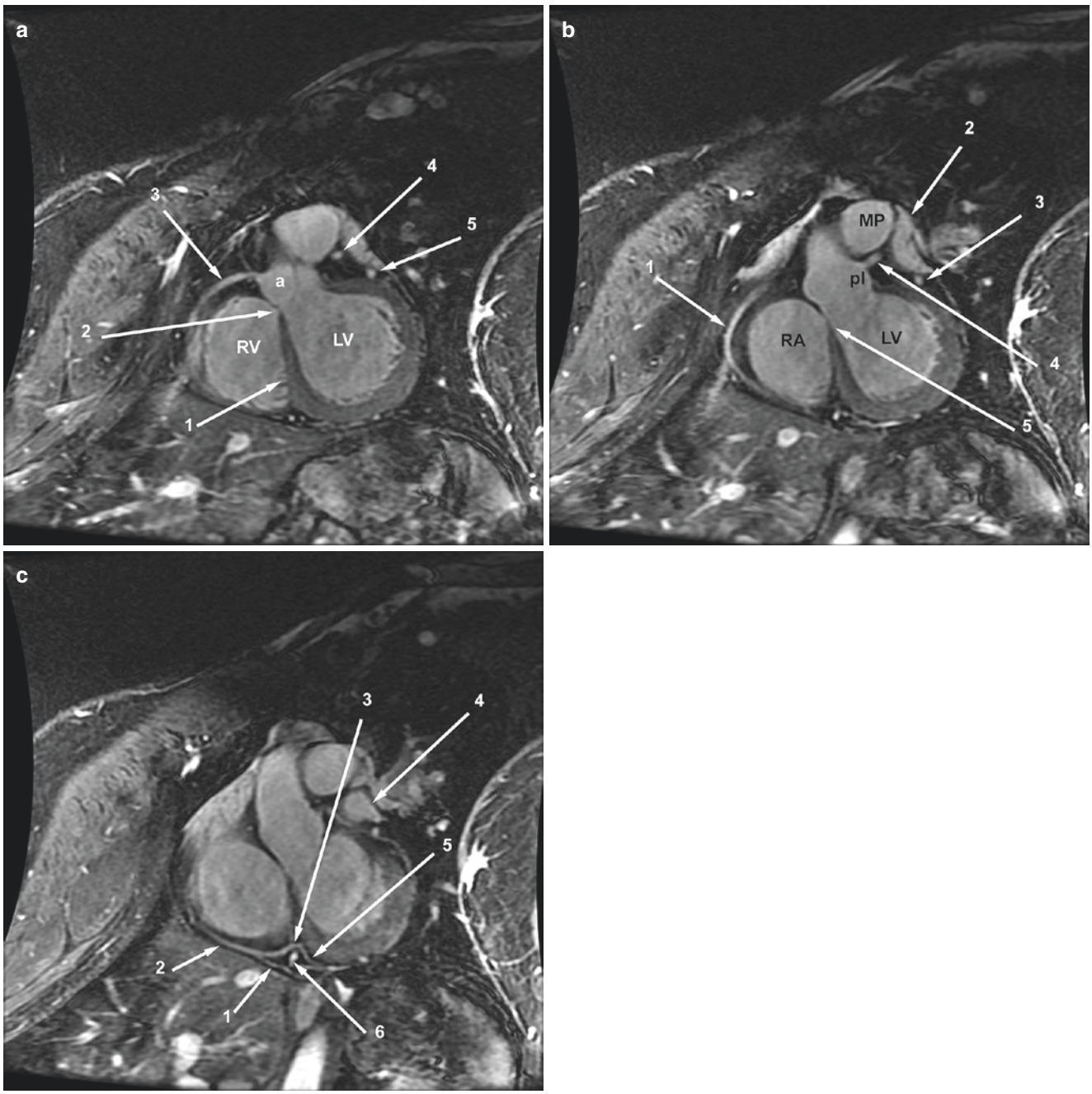

Fig. 3.45 Left anterior oblique (LAO) sagittal fat saturated contrast-enhanced gradient echo acquisitions. (**a**) After the right coronary artery (arrow 3) originates from the anterior aortic sinus of Valsalva (a), it passes into the signal void of the fat within the anterior atrioventricular ring. The membranous (arrow 2) and muscular (arrow 1) interventricular septum separates the right (RV) from left (LV) ventricles. Portions of the distal left main (arrow 4) and proximal circumflex (arrow 5) arteries are labeled. (**b**) Left anterior oblique (LAO) sagittal fat saturated contrast-enhanced gradient echo acquisition 4 mm to the left of figure **a**. The mid-right coronary artery (arrow 1) passes through the saturated fat of the anterior atrioventricular ring. Originating from the posterior left aortic sinus of Valsalva (pl), the left main coronary artery (arrow 4) passes behind the main pulmonary artery (MP) toward the left atrial appendage (arrow 2). The proximal circumflex artery (arrow 3) is seen beneath the left atrial appendage. The atrioventricular septum (arrow 5) separates the left ventricle (LV) from the medial portion of the right atrium (RA). (**c**) Left anterior oblique (LAO) sagittal fat saturated contrast-enhanced gradient echo acquisition 4 mm to the left of figure **b**. The distal right coronary artery (arrow 2) is seen passing around the inferior aspect of the anterior atrioventricular ring. In the posterior aspect of the ring, the distal right coronary artery (arrow 3) passes over the coronary sinus (arrow 6) and continues in the posterior atrioventricular ring as the posterior left ventricular branch (arrow 5). Immediately prior to passing over the coronary sinus, the posterior descending coronary artery (arrow 1) arises. The left atrial appendage (arrow 4) is labeled

Fig. 3.46 Short axis fat saturated contrast-enhanced gradient echo acquisitions from the patient in figures 3.44 and 3.45. In this section through the aortic root, the origin of the right coronary artery (arrow 1) is seen entering the anterior atrioventricular ring. Note the relationship among the posterior right aortic sinus of Valsalva (pr), the left atrium (LA), and right atrium (RA). The proximal left main coronary artery (arrow 2) is seen beneath the proximal main pulmonary artery (MP). The coronary sinus (arrow 3) is seen entering the posterior aspect of the RA

heart disease. In 85% of individuals, the posterior descending artery arises from the distal right coronary artery; this is called a right dominant circulation (Fig. 3.45c).

References

1. Pennell DJ, Sechtem UP, Higgins CB, Manning WJ, Pohost GM, Rademakers FE, et al. Clinical indications for cardiovascular magnetic resonance (CMR): Consensus panel report. J Cardiovasc Magn Reson. 2004;6(4):727–65.
2. Hundley WG, Bluemke DA, Finn JP, Flamm SD, Fogel MA, Friedrich MG, et al. ACCF/ACR/AHA/NASCI/SCMR 2010 Expert consensus document on cardiovascular magnetic resonance. J Am Coll Cardiol. 2010;55(23):2614–62.
3. Schulz-Menger J, Bluemke DA, Bremerich J, Flamm SD, Fogel MA, Friedrich MG, et al. Standardized image interpretation and post processing in cardiovascular magnetic resonance: Society for Cardiovascular Magnetic Resonance (SCMR) Board of Trustees Task Force on Standardized Post Processing. J Cardiovasc Magn Reson. 2013;15:35–54.
4. Bots ML, Hoes AW, Koudstaal PJ, Hofman A, Grobbee DE. Common carotid intima-media thickness and risk of stroke and myocardial infarction: the Rotterdam Study. Circulation. 1997;96(5):1432–7.
5. Chambless LE, Heiss G, Folsom AR, Rosamond W, Szklo M, Sharrett AR, et al. Association of coronary heart disease incidence with carotid arterial wall thickness and major risk factors: the Atherosclerosis Risk in Communities (ARIC) Study. Am J Epidemiol. 1997;146(5):483–94.
6. O'Leary DH, Polak JF, Kronmal RA, Manolio TA, Burke GL, Wolfson SK Jr. Carotid-artery intima and media thickness as a risk factor for myocardial infarction and stroke in older adults: cardiovascular risk study. N Engl J Med. 1999;340(1):14–22.
7. Li AE, Kamel I, Rando F, Anderson M, Kumbasar B, Lima JA, et al. Using MRI to assess aortic wall thickness in the Multiethnic Study of Atherosclerosis: distribution by race, sex, and age. Am J Roentgenol. 2004;182(3):593–7.
8. Mensel B, Quadrat A, Schneider T, Kühn JP, Dörr M, Völzke H, et al. MRI-based determination of reference values of thoracic aortic wall thickness in a general population. Eur Radiol. 2014;24(9):2038–44.
9. Malayeri AA, Natori S, Bahrami H, Bertoni AG, Kronmal R, Lima JA, et al. Relation of aortic wall thickness and distensibility to cardiovascular risk factors (from the Multi-Ethnic Study of Atherosclerosis [MESA]). Am J Cardiol. 2008;102(4):491–6.
10. Desai MY, Stone JH, Foo TK, Hellmann DB, Lima JA, Bluemke DA. Delayed contrast-enhanced MRI of the aortic wall in Takayasu's arteritis: Initial experience. Am J Roentgenol. 2005;184(6):1427–31.
11. Kato Y, Terashima M, Ohigashi H, Tezuka D, Ashikaga T, Hirao K, et al. Vessel wall inflammation of Takayasu arteritis detected by contrast-enhanced magnetic resonance imaging: Association with disease distribution and activity. PLoS One. 2015;10(12):e0145855.
12. Mensel B, Heßelbarth L, Wenzel M, Kühn JP, Dörr M, Völzke H, et al. Thoracic and abdominal aortic diameters in a general population: MRI-based reference values and association with age and cardiovascular risk factors. Eur Radiol. 2016;26(4):969–78.
13. Potthast S, Mitsumori L, Stanescu LA, Richardson ML, Branch K, Dubinsky TJ, et al. Measuring aortic diameter with different MR techniques: Comparison of three-dimensional (3D) navigated steady-state free-precession (SSFP), 3D contrast-enhanced magnetic resonance angiography (CE-MRA), 2D T2 black blood, and 2D cine SSFP. J Magn Reson Imaging. 2010;31(1):177–84.
14. Pontone G, Andreini D, Bartorelli AL, Bertella E, Mushtaq S, Gripari P, et al. Comparison of accuracy of aortic root annulus assessment with cardiac magnetic resonance versus echocardiography and multidetector computed tomography in patients referred for transcatheter aortic valve implantation. Am J Cardiol. 2013;112(11):1790–9.
15. Hiratzka LF, Bakris GL, Beckman JA, Bersin RM, Carr VF, Casey DE Jr, et al. 2010 ACCF/AHA/AATS/ACR/ASA/SCA/SCAI/SIR,STS/SVM Guidelines for the diagnosis and management of patients with thoracic aortic disease. J Am Coll Cardiol. 2010;55(14):e27–e129.
16. Ostberg JE, Brookes JA, McCarthy C, Halcox J, Conway GS. A comparison of echocardiography and magnetic resonance imaging in cardiovascular screening of adults with Turner syndrome. J Clin Endocrinol Metab. 2004;89(12):5966–71.
17. Bannas P, Rybczynski M, Sheikhzadeh S, von Kodolitsch Y, Derlin T, Yamamura J, et al. Comparison of cine-MRI and transthoracic echocardiography for the assessment of aortic root diameters in patients with suspected Marfan syndrome. Fortschr Röntgenstr. 2015;187(11):1022–8.
18. Jabbour A, Ismail TF, Moat N, Gulati A, Roussin I, Alpendurada F, et al. Multimodality imaging in transcatheter aortic valve implantation and post-procedural aortic regurgitation. J Am Coll Cardiol. 2011;58(21):2165–73.
19. Friedman BJ, Waters J, Kwan OL, DeMaria AN. Comparison of magnetic resonance imaging and echocardiography in determination of cardiac dimensions in normal subjects. J Am Coll Cardiol. 1985;5(6):1369–76.

20. Paelinck BP, Van Herck PL, Rodrigus I, Claeys MJ, Laborde JC, Parizel PM, et al. Comparison of magnetic resonance imaging of aortic valve stenosis and aortic root to multimodality imaging for selection of transcatheter aortic valve implantation candidates. Am J Cardiol. 2011;108(1):92–8.
21. Goldstein SA, Evangelista A, Abbara S, Arai A, Asch FM, Badano LP, et al. Multimodality imaging of diseases of the thoracic aorta in adults: from the American Society of Echocardiography and the European Association of Cardiovascular Imaging. J Am Soc Echocardiogr. 2015;28(2):119–82.
22. Tsang W, Bateman MG, Weinert L, Pellegrini G, Mor-Avi V, Sugeng L, et al. Accuracy of aortic annular measurements obtained from three-dimensional echocardiography, CT and MRI: human in vitro and in vivo studies. Heart. 2012;98(15):1146–52.
23. Burman ED, Keegan J, Kilner PJ. Aortic root measurement by cardiovascular magnetic resonance. Circ Cardiovasc Imaging. 2008;1:104–13.
24. Davis AE, Lewandowski AJ, Holloway CJ, Ntusi NAB, Banerjee R, Nethononda R, et al. Observational study of regional aortic size referenced to body size: production of a cardiovascular magnetic resonance nomogram. J Cardiovasc Magn Reson. 2014;16:9.
25. Kaiser T, Kellenberger CJ, Albisetti M, Bergsträsser E, Valsangiacomo Buechel ER. Normal values for aortic diameters in children and adolesents—assessment in vivo with contrast-enhanced CMR-angiography. J Cardiovasc Magn Reson. 2008;10:56.
26. Cavalcante JL, Lima JAC, Redheuil A, Al-Mallah MH. Aortic stiffness. J Am Coll Cardiol. 2011;57(14):1511–22.
27. Herment A, Kachenoura N, Lefort M, Bensalah M, Dogui A, Frouin F, et al. Automated segmentation of the aorta from phase contrast MR images: validation against expert tracing in healthy volunteers and in patients with a dilated aorta. J Magn Reson Imaging. 2010;31(4):881–8.
28. Turkbey EB, Jain A, Johnson C, Redheuil A, Arai AE, Gomes AS, et al. Determinants and normal values of ascending aortic diameter by age, gender, and race/ethnicity in the Multi-Ethnic Study of Atherosclerosis (MESA). J Magn Reson Imaging. 2014;39(2):360–8.
29. Grotenhuis HB, Westenberg JJ, Steendijk P, van der Geest RJ, Ottenkamp J, Bax JJ, et al. Validation and reproducibility of aortic pulse wave velocity as assessed with velocity-encoded MRI. J Magn Reson Imaging. 2009;30(3):521–6.
30. Wentland AL, Grist TM, Wieben O. Review of MRI-based measurements of pulse wave velocity: a biomarker of arterial stiffness. Cardiovasc Diagn Ther. 2014;4(2):193–206.
31. Voges I, Jerosch-Herold M, Hedderich J, Pardun E, Hart C, Gabbert DD, et al. Normal values of aortic dimensions, distensibility, and pulse wave velocity in children and young adults: a cross-sectional study. J Cardiovasc Magn Reson. 2012;14:77–90.
32. Garcier J-M, Petitcolin V, Filaire M, Mofid R, Azarnouch K, Ravel A, et al. Normal diameter of the thoracic aorta in adults: a magnetic resonance imaging study. Surg Radiol Anat. 2003;25(3):322–9.
33. Hudsmith LE, Petersen SE, Francis JM, Robson MD, Neubauer S, et al. Normal human left and right ventricular and left atrial dimensions using steady state free precession magnetic resonance imaging. J Cardiovasc Magn Reson. 2005;7(5):775–82.
34. Kawel-Boehm N, Maceira A, Valsangiacomo-Buechel ER, Vogel-Claussen J, Turkbey EB, Williams R, et al. Normal values for cardiovascular magnetic resonance in adults and children. J Cardiovasc Magn Reson. 2015;17:20–62.
35. Boerrigter B, Mauritz G-J, Marcus JT, Helderman F, Postmus PE, Westerhof N, et al. Progressive dilatation of the main pulmonary artery is a characteristic of pulmonary arterial hypertension and is not related to changes in pressure. Chest. 2010;138(6):1395–401.
36. Paz R, Mohiaddin RH, Longmore DB. Magnetic resonance assessment of the pulmonary arterial trunk anatomy, flow, pulsatility and distensibility. Eur Heart J. 1993;14(11):1524–30.
37. Rodevand O, Bjornerheim R, Ljosland M, Maehle J, Smith HJ, Ihlen H. Left atrial volumes assessed by three- and two-dimensional echocardiography compared to MRI estimates. Int J Card Imaging. 1999;15(5):397–410.
38. Maceira AM, Cosin-Sales J, Roughton M, Prasad SK, Pennell DJ. Reference left atrial dimensions and volumes by steady state free precession cardiovascular magnetic resonance. J Cardiovasc Magn Reson. 2010;12:65–75.
39. Dickfeld T, Kato R, Zviman M, Lai S, Meininger G, Lardo AC, et al. Characterization of radiofrequency ablation lesions with gadolinium-enhanced cardiovascular magnetic resonance imaging. J Am Coll Cardiol. 2006;47(2):370–8.
40. Peters DC, Wylie JV, Hauser TH, Kissinger KV, Botnar RM, Essebag V, et al. Detection of pulmonary vein and left atrial scar after catheter ablation with three-dimensional navigator-gated delayed enhancement MR imaging: initial experience. Radiology. 2007;243(3):690–5.
41. Oakes RS, Badger TJ, Kholmovski EG, Akoum N, Burgon NS, Fish EN, et al. Detection and quantification of left atrial structural remodeling with delayed-enhancement magnetic resonance imaging in patients with atrial fibrillation. Circulation. 2009;119(113):1758–67.
42. Seitz J, Horvilleur J, Lacotte J, et al. Correlation between AF substrate ablation difficulty and left atrial fibrosis quantified by delayed-enhancement cardiac magnetic resonance. Pacing Clin Electrophysiol. 2011;34(10):1267–77.
43. Lima JA, Judd RM, Bazille A, Schulman SP, Atalar E, Zerhouni EA, et al. Regional heterogeniety of human myocardial infarcts demonstrated by contrast-enhanced MRI: potential mechanisms. Circulation. 1995;92(5):1117–25.
44. Kim RJ, Chen EL, Lima JA, Judd RM, et al. Myocardial Gd-DTPA kinetics determine MRI contrast enhancement and reflect the extent and severity of myocardial injury after acute reperfused infarction. Circulation. 1996;94(12):3318–26.
45. Flacke SJ, Fischer SE, Lorenz CH. Measurement of the gadopentetate dimeglumine partion coefficient in human myocardium in vivo: normal distribution and elevation in acute and chronic infarction. Radiology. 2001;218(3):703–10.

Normal Left and Right Ventricular Volume and Function

4

Ralf Wassmuth and Jeanette Schulz-Menger

Introduction

In patients with heart disease, quantification of left and right ventricular size and function is important for prognosis [1, 2]. Cardiac magnetic resonance imaging is the gold standard for left ventricular volume and mass. It offers high signal-to-noise ratio independent from acoustic window or obesity. The reproducibility is excellent due to outstanding endocardial border definition and standardized imaging planes independent from the operator. Spatial resolution is high, while temporal resolution is satisfactory. Images can be obtained free of contrast or radiation and are therefore well suited for regular follow-up.

Typically the assessment of left ventricular (LV) slice and function represents the initial module within a CMR protocol after scout or localizer images have been acquired to define the position of the heart [3]. Cine loops might even be acquired after contrast administration, although this will diminish the excellent contrast between bright blood and dark myocardium. Increasing the flip angle can compensate for this effect to a certain extent.

Electronic Supplementary Material The online version of this chapter (https://doi.org/10.1007/978-1-4939-8841-9_4) contains supplementary material, which is available to authorized users.

R. Wassmuth (✉)
Working Group on Cardiovascular Magnetic Resonance, Experimental and Clinical Research Center-a joint cooperation between the Charité Medical Faculty and the Max-Delbrück Center for Molecular Medicine, Berlin, Germany

Internal Medicine and Cardiology Department, Oberhavel-Kliniken Hennigsdorf, Hennigsdorf, Germany

J. Schulz-Menger
Working Group on Cardiovascular Magnetic Resonance, Experimental and Clinical Research Center-a joint cooperation between the Charité Medical Faculty and the Max-Delbrück Center for Molecular Medicine, Berlin, Germany

HELIOS Klinikum Berlin-Buch, Department of Cardiology and Nephrology, Berlin, Germany

Sequences

The standard approach to measure LV volume and function includes steady-state free precession (SSFP) gradient echo sequences (depending on the vendor platform also known as TrueFISP, FIESTA, or balanced FFE) [4], with one slice acquired during a breath-hold of about 10–15 heartbeats. During each cardiac cycle, a portion of the data is recorded and later fused to form an averaged movie of ventricular contraction. Unlike echocardiography, CMR is currently not a real-time technique in clinical routine, but near-real-time or real-time methods are increasingly available.

Both fat and fluid appear bright on SSFP images; therefore, the differentiation of epicardial fat and pericardial fluid can sometimes be difficult. Additional T_2-weighted images, delineating fluid as bright signal, or late enhancement images, depicting fluid as dark signal, might help. Alternatively, more technically demanding ways in differentiating fat from water have been proposed [5, 6].

Higher field strengths offer the possibility to spend the signal gain in cutting down scan time. On the other hand, SSFP images may suffer from more artifacts at 3 T than at 1.5 T.

Positioning

Cardiac imaging requires precise and reproducible angulation of the imaging planes along the cardiac axes. Therefore, a double-oblique orientation has to be established. The long axis of the heart usually deviates about 40° left from a true sagittal axis and 40° downward from the axial plane. It is important to ensure that the long axis obtained truly hits the apex as any deviation will result in major foreshortening of all further measurements. Most centers use fast scout images for axial slices through the heart, followed by a vertical long axis through the apex and the middle of the mitral valve. Based on this, the true long axis can be acquired. A stack of

R. Y. Kwong et al. (eds.), *Cardiovascular Magnetic Resonance Imaging*, Contemporary Cardiology,
https://doi.org/10.1007/978-1-4939-8841-9_4

short-axis slices aligns rectangular to the true long axis parallel to the mitral valve plane.

Slice Orientation and Coverage

Full coverage of the LV with contiguous short-axis slices is the gold standard approach for quantification for LV size and mass (Fig. 4.1, Video 4.1). It does not require any geometrical assumptions and represents complete volumetric coverage. Kramer et al. suggested a slice thickness of 6–8 mm with 4–2 mm gap in their updated protocol recommendations in 2013 [3].

The definition of the most basal slice with its impact on EDV and EF poses a problem for reproducibility [7]. To shorten scan time but ensure reproducibility, Messroghli et al. proposed a "three-out-of-five" approach for the assessment of regional function, prescribing five short-axis slices but obtaining only three of them [8].

Multi-planar volumetric measurements surpass biplanar measurements in accuracy and reproducibility regardless of whether echo or CMR is concerned [9]. Still, for most non-scientific routine studies regarding normal or close to normal ventricles in a high-throughput setting, the acquisition of one mid-ventricular short-axis plus three long-axis loops (four-chamber view, two-chamber view, three-chamber view; Fig. 4.2a–c and Video 4.2a–c) may be considered for the assessment of LV size and systolic function. The choice of protocol also depends on the capability and the speed of the scanner. Meanwhile, most of the scanners allow for 3D coverage of the whole left ventricle in 3–4 min..

Friedrich et al. compared biplanar long axis with multiple short-axis measurements and found good overall agreement between two-dimensional and three-dimensional measurements, although EF was overestimated by biplanar long-axis measurements. Biplanar long-axis measurements were less sensitive to detect LV dilation [10, 11]. If LV dilation or considerable remodeling is present or high reproducibility for follow-up is required, a complete stack of short-axis images is required.

Electrocardiogram Trigger

Most CMR sequences require a robust electrocardiogram (ECG) trigger to run properly [12]. Vector ECG has been found less vulnerable to artifacts from the magnetic field [13, 14]. Alternatively, a pulse trigger can be used for cine imaging. However, it will change the order of cardiac phases within the cine loop due to the delay of the peripheral pulse wave. Retrospective triggering is the method of choice as it includes late diastole for better coverage of atrial filling [15]. Prospective triggering underestimates true end-diastolic volume (EDV) and ejection fraction (EF) [15–17]. Considerable variations in the R-R interval and arrhythmias can compromise image quality; however, many patients with atrial fibrillation but sufficient rate control can be

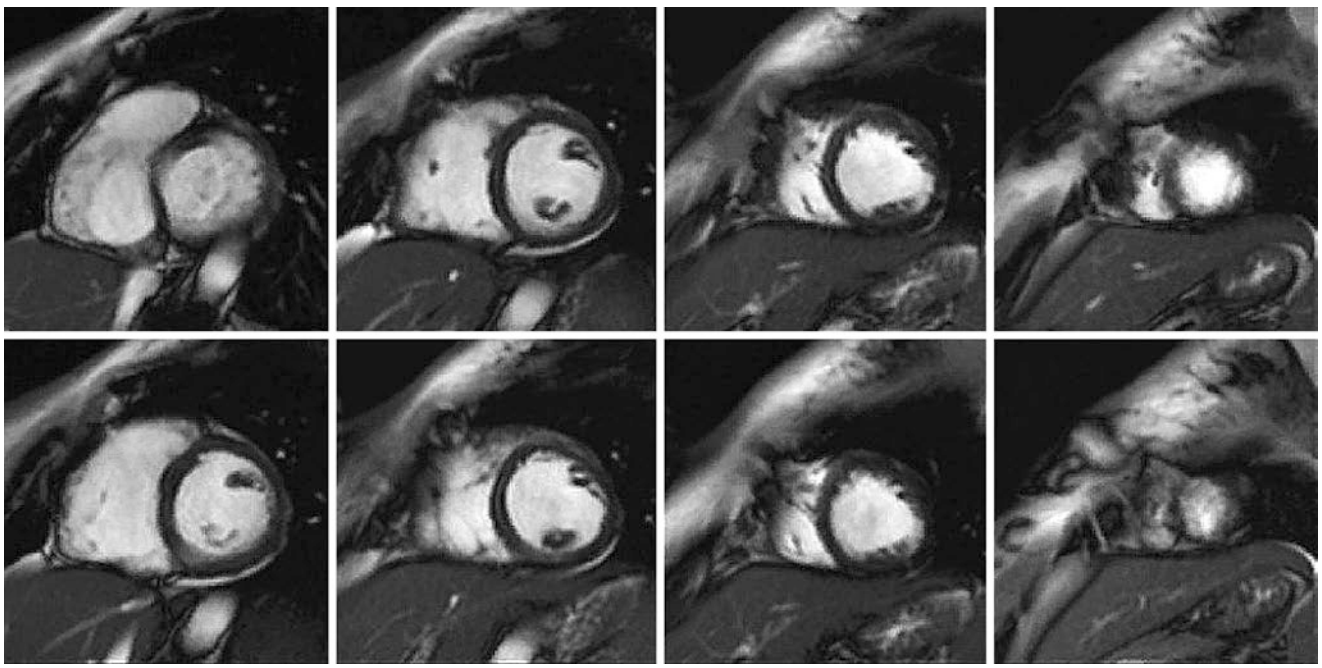

Fig. 4.1 Stack of diastolic short-axis images from the base (top left) to the apex (bottom right) of the left ventricle. In the most basal slice (top left), the anteroseptal thinning indicates the transition into the LV outflow tract. In this case obtaining one more slice on each side at the base and the apex would have been a better choice. Even the right ventricle might be assessed on these images. However, some users might prefer axial slices for better definition of the tricuspid valve plane

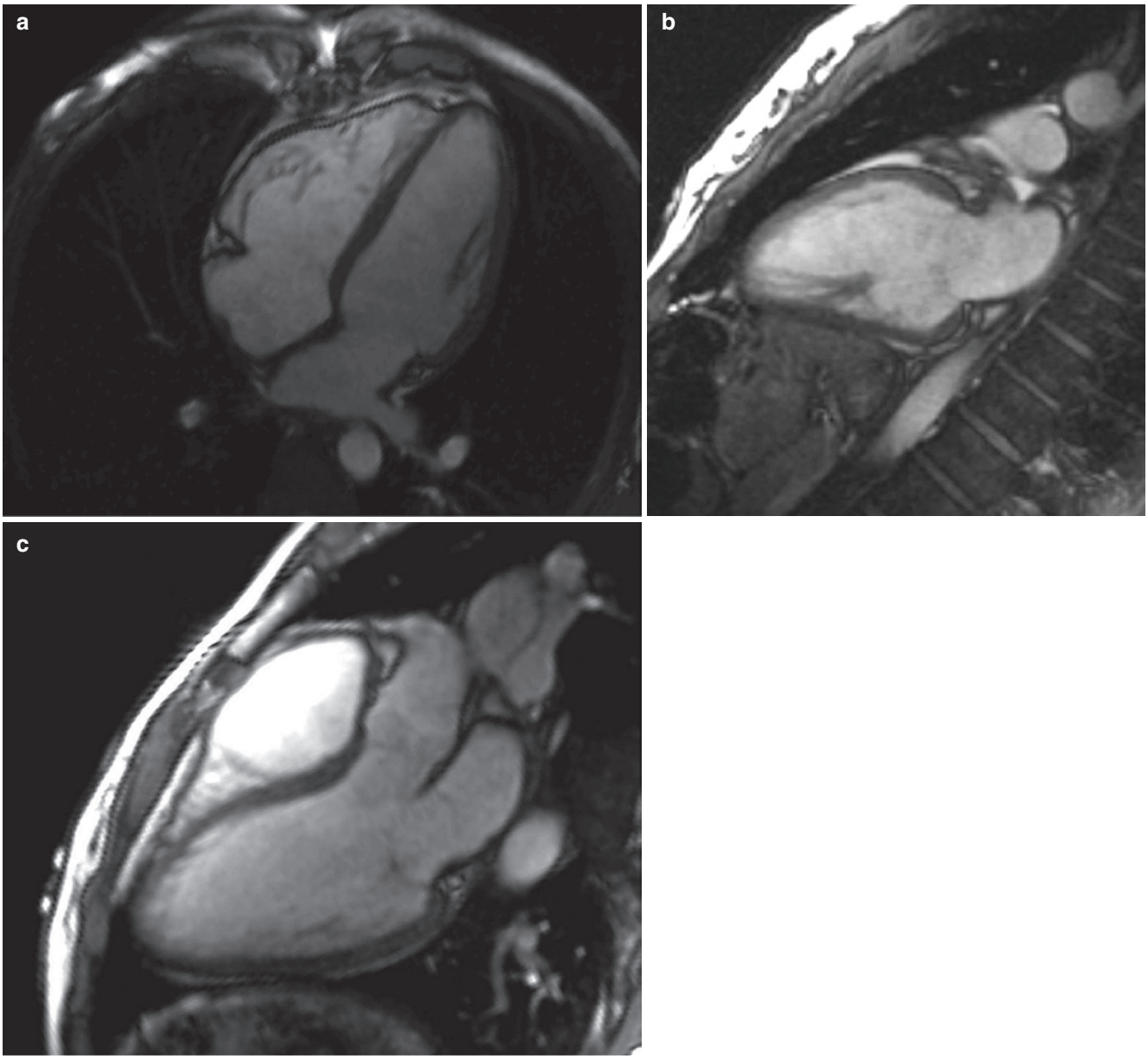

Fig. 4.2 **(a)** Diastolic frame of a four-chamber-view steady-state free precession cine loop. All four cardiac chambers, the descending aorta, and a left pulmonary vein are depicted. **(b)** Diastolic frame of a two-chamber-view steady-state free precession cine loop. The left atrium and the left ventricle are depicted. **(c)** Diastolic frame of a three-chamber-view steady-state free precession cine loop. The left atrium, the aortic root, and the left ventricle are depicted. Parts of the right ventricle are also visible

scanned with good results. Future approaches include self-gated [18] or non-gated image acquisition.

Resolution

The product of repetition time and numbers of *k*-space lines acquired determines the temporal resolution in cine imaging. With lower temporal resolution, it is less likely to correctly determine true systole; therefore, EF will be underestimated. Decreasing spatial resolution also results in underestimation of EF because of partial volume effect, but to a smaller extent. Typical spatial resolution in a routine scan using SSFP sequences is about 1.5 mm/pixel. This will result in about 5 pixels across the ventricular wall given a wall thickness of 10 mm. We recommend a high temporal resolution of 45 ms or less with a spatial resolution of 1.5 mm/pixel [19].

Fast Imaging

Various techniques are already in use to shorten scan time, including view sharing and parallel imaging. By these methods, more than one slice can be acquired per breath-hold. However, this increment in speed comes with a loss in spatial resolution and signal-to-noise ratio.

In dynamic imaging like cine or perfusion, modern acceleration techniques take advantage of the redundancy of information throughout the cardiac cycle [20]. From phase to phase, there is little extra information. This enables limited data acquisition (undersampling) and extrapolation. Recently, the concept of "compressed sensing (CS)" has arrived in the clinical arena. Vincenti et al. acquired a complete stack of short-axis images plus certain long axes in one breath-hold and achieved similar results as a standard cine protocol [21].

Great Vessels

The aortic root should be assessed with ECG-triggered SSFP cine loops, as it rapidly moves throughout the cardiac cycle. For the aortic root, more specifically oriented views can be obtained perpendicular to the basic three-chamber view. The sinus of Valsalva and the sinotubular junction are of importance for a comprehensive assessment of the aorta. The ascending aorta and aortic arch can be better delineated with 3D CMR angiography. Details have been described in guidelines for multimodality imaging of the thoracic aorta endorsed by all major imaging societies [22].

The right ventricular outflow tract and the pulmonary artery are of interest in patients with pulmonary hypertension and congenital heart disease. Burman et al. provided reference values in normal volunteers for comparison [23].

Pulmonary veins usually are depicted with a 3D angiography covering the whole left atrium. Their anatomy is important before pulmonary venous isolation.

Measurements and Evaluation

All major hardware vendors deliver evaluation software for ventricular function analysis. Moreover several platform-independent third-party software solutions offer dedicated and easy-to-use quantification tools. They allow for semi-automatic contour tracking resulting in less variability than planning of the slice position itself [24]. For most routine studies regarding normal or close-to-normal ventricles, we consider quantification of two or three long-axis loops sufficient for analysis. This can be done in a few minutes [11]. However, users have to be aware that biplanar or triplanar assessment always relies on geometrical assumptions and can never offer the same accuracy as full volumetric coverage [25]. For grossly abnormal hearts or for precise follow-up, a stack of short-axis images is required. Based on a mid-ventricular short-axis image, the phase representing the minimal volume should be selected for systole and the phase with maximal volume for end-diastole. Contijoch et al. demonstrated that end-diastole should be chosen manually instead of automatically, selecting the first or last phase after the ECG trigger signal to avoid significant deviation in end-diastolic volume [26]. In case of postsystolic shortening, the end-systolic phase might better be chosen according to the aortic valve closure than to minimal volume.

In the absence of sinus rhythm, LV quantification should be applied with great caution. The standard cine loop is based on multiple heartbeats. The incorrect assignment of end-systole can induce inconsiderable deviation from true volumes and ejection fraction. In those cases real-time techniques might provide an alternative.

It is still a matter of debate whether to include papillary muscles into myocardial mass (to be preferred theoretically for better accuracy) or to include it into left ventricular cavity volume (faster and easier from a practical standpoint for automatic quantification and for better reproducibility and precision). Large portions of the myocardial wall have a trabecular structure. Even if myocardium looks uniform on conventional CMR images, autopsy studies and experimental high-resolution CMR [27] reveal the trabecular structure of myocardium. In a study by Chuang et al., trabeculations and papillary muscles accounted for 28% of myocardial mass [28]. In validation studies comparing CMR to ex vivo hearts including papillary muscles into myocardium resulted in better agreement [29, 30]. However, manual contouring of trabeculations and papillary muscles still is tedious and cumbersome work despite all the comfortable software available [31]. Miller et al. compared in a recent study in 50 patients "simplified" vs. "detailed" contouring, i.e., exclusion or inclusion of papillary muscles and trabeculations into myocardial mass [25]. Simplified contouring significantly underestimated myocardial mass and EF [25]. Therefore, the SCMR stated in their 2013 recommendations that ideally papillary muscles should be assigned to myocardial mass [32]. Still, it is considered acceptable to include them into cavity volume, if necessary, for practical reasons. Alternatively, automatic threshold methods are available automatically including complex trabecular structures into myocardial mass. They offer higher reproducibility (i.e., precision) but less accuracy than manual contouring of trabeculations [25, 33]. Users should refer to normal values using the same method and specifically state in their report which method of quantification they use [32].

There is consensus that in long-axis measurements, the papillary muscle should be excluded from the wall to avoid overestimation of ventricular mass [10, 34].

Basal descend: In short-axis evaluation, the most basal slice has to be defined in a consistent manner. Including or excluding the basal slice will introduce a large variation in EDV and LV mass [7]. Correct definition of the basal slice can have a larger impact on LV mass than the inclusion or exclusion of papillary muscles [25]. The ventricular myocardium in the most basal slice often looks like a horseshoe instead of a completely closed ring. It has been proposed to include a slice if 50% of the myocardial ring is visible [35]. The SCMR has endorsed this rule in their 2013 recommendations [32]. Care has to be taken to start with a corresponding basal systolic slice. Because of the longitudinal shortening of the heart, the number of systolic slices will often be one or two less than in diastole.

Ejection fraction (EF), although widely used, is not an ideal parameter to describe systolic function [36, 37]. There is a considerable amount of data confirming its prognostic value, if it is markedly reduced [1]. However, it overestimates the impact of radial function and underestimates longitudinal function. Due to myocardial fiber orientation, impairment of longitudinal contraction is an early step in many diseases. Therefore EF is not a sensitive marker for early, subtle damage, e.g., after cardiotoxic chemotherapy [38]. Strain imaging has gained considerable enthusiasm in the echo world. Global longitudinal strain has proven to be a stable and clinical meaningful parameter that is more sensitive than EF in many clinical scenarios [37]. CMR is able to calculate strain [39] and elucidate LV twisting and torsion patterns [40], but so far it is rarely part of routine imaging.

Left Atrium

Left atrial size increases due to pressure or volume overload. In diastolic dysfunction, left atrial (LA) size increases as a result of ventricular resistance to filling. Therefore, LA volume is prognostically important after myocardial infarction [41, 42] and in dilated cardiomyopathy [43] and in atrial fibrillation [44]. Aortic and mitral valve stenosis increase left atrial pressure. In mitral regurgitation atrial volume overload induces left atrial enlargement. A comprehensive study of a patient with heart failure should therefore include a quantitative measurement at least of the left atrium [45].

Various approaches have been proposed for assessment of LA volume. Biplanar estimation of LA volume is quick and better than simple area or diameter [46] but depends on geometric assumptions in the same way as 2D echocardiography does and underestimates true LA volume [47]. Still, a recent consensus document by European imaging and arrhythmia experts endorses biplanar LA measurements based on the area-length method or the disc formula as standard approach for management of atrial fibrillation [44].

Beyond biplanar measurement CMR can depict the left atrium in short-axis images simply extending a stack of left ventricular short-axis images. This volumetric assessment outperforms biplanar estimation in reproducibility [48]. Dedicated reference values for CMR-based LA dimensions are available [47, 48]. The 2013 SCMR protocol update and the guidelines for post-processing do not recommend any specific approach for left atrial quantification [3, 32].

Due to limited penetration into the depth of the left atrium, 2D echocardiography tends to underestimate LA volume compared to CMR or CT [45, 49–51].

CMR can quantify the various components of left atrial function (emptying reservoir, conduit function) [52], but this is still a matter of research.

Right Ventricle

In contrast to echocardiography and ventriculography, MRI offers full insight into right ventricular (RV) anatomy and function in any orientation. Its complex anatomy, smaller wall thickness, and abundance of trabecular structures have precluded easy quantification like that available for the LV. Reproducibility is therefore lower than for the LV [53].

There is still no consensus about the optimal slice orientation in RV imaging. Many users favor short-axis imaging as this is often available anyway for LV measurements. However, LV short axis does not equal RV short axis [54]. Moreover, it may be difficult to define the proximal and distal end of the RV, that is, the tricuspid valve plane and the infundibulum. Obtaining an axial stack of cine loops for the RV is accepted alternative, as indicated by the SCMR recommendations [32]. Axial orientation might improve reproducibility of RV quantification [54]. In patients suspicious for arrhythmogenic right ventricular cardiomyopathy, both short-axis and axial RV images might be recommended [55]. Even in normal volunteers, regional RV contraction patterns might appear abnormal to the inexperienced investigator; therefore, regional wall motion abnormalities should be interpreted with great caution.

The tricuspid valve plane is better defined in long-axis slices. Therefore RV long axes depicting the tricuspid valve (Fig. 4.3, Video 4.3) and the RV outflow tract should be added.

For ease of quantification, trabeculations are most often ignored and assigned to the RV cavity. Animal experiments demonstrated good agreement between SSFP-based CMR measurements of RV mass compared to ex vivo data [56]. Altmayer et al. suggested to assess RV myocardial mass in systole. Their systolic measurements of RV mass in sheep and human beings were faster and had better reproducibility than diastolic measurements [57].

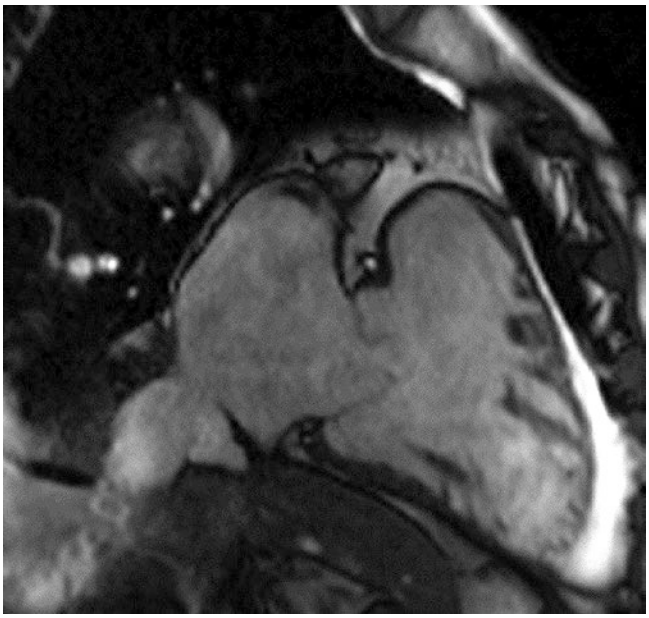

Fig. 4.3 Long axis of the right ventricle, which might be called two-chamber view of the right ventricle depicting the right ventricle. The tricuspid valve and the right atrium. This image orientation is based on four-chamber view cutting through the right ventricular apex and the center of the tricuspid valve

Right Atrium

Pulmonary hypertension, either due to pulmonary disease or left heart failure, finally results in right atrial (RA) dilatation. Therefore assessment of RA size and function is particularly important in patients with pulmonary hypertension. RA size and RA function are of prognostic value in pulmonary hypertension [58, 59]. In addition RA imaging is important before and during RA electrophysiological interventions [60]. Recently, Maceira et al. published RA reference values [61]. They included the right atrial appendage and excluded the cava veins. This should be taken into account when applying their data. Within their study Maceira compared complete volumetric short-axis assessment with a biplanar approach. A biplanar estimation with RA volume = 3.08 × (2C area) + 3.36 × (4C area) − 44.4 resulted in an excellent correlation with true RA volume (R^2 = 0.895) despite underestimation. This was better than using the mono-planar area-length method [61].

Diastolic Function

A considerable amount of patients do suffer from severe heart failure despite normal systolic function [62]. Many of them have a history of hypertension and LV hypertrophy. Due to difficulties in elucidating the exact mechanism, the term "heart failure with preserved ejection fraction" has been introduced [63]. Frequently diastolic function is impaired in those patients.

Assessment of diastolic function is not included in most routine CMR protocols. Replication of echo parameters is often felt unsatisfactory as these echo parameters themselves appear less than optimal due to overlap, pseudonormalization, and limited specificity. One of the basic problems is that diastology is a matter of pressure over volume, whereas pressure cannot directly be measured neither by echocardiography nor CMR.

Several approaches have been proposed:

Time-Volume Curves

Contouring the LV cavity not only at end-diastole and end-systole but throughout the cardiac cycle results in time-volume curves. Temporal resolution has to be high enough [64] to calculate an E/A ratio corresponding to echocardiography, peak filling rate, and time to peak filling based on the curves. These parameters have been used, e.g., for intervention studies in obesity [65, 66]. However it is time-consuming work that is valuable for scientific studies but less suited for daily routine. Higher temporal resolution, as desired, means even more frames to analyze. LV time-volume curves might also be based on a biplanar model, which reduces image acquisition and evaluation time [66]. Automatic contouring can reduce evaluation time with the drawbacks in accuracy discussed earlier [67]. To further reduce expenditure in scan time and evaluation, Okyama et al. suggested to analyze fractional area change instead of volume and one diastolic time point only (30% of diastole) instead of all early diastolic frames [68].

LV Lengthening Velocity

Corresponding to the echocardiographic E´, CMR allows for measurement of the early diastolic longitudinal lengthening velocity [66].

Transmitral Flow

Using phase-contrast measurements at the mitral valve plane, CMR can replicate E/A ratios known from echocardiography [69]. The Leiden group measured transmitral inflow into the left ventricle in a three-dimensional way. In addition, they included mitral valve tracking during the cardiac cycle and could demonstrate the superiority of 3D flow data compared to 2D measurements [70].

Left Atrial Function

Left atrial enlargement alone is a long-term marker of diastolic impairment, as mentioned earlier. In addition, the assessment of LA function has been used to characterize diastolic function. Farzaneh-Far et al. measured atrial volumes on a biplanar basis. Left atrial passive emptying fraction was defined as the difference of maximal LA volume and volume before atrial contraction divided by maximal volume. They measured atrial function under dobutamine stress. The failure to augment atrial passive emptying under stress was associated with worse outcome and might represent a surrogate for diastolic dysfunction [52].

Normal Values

Several sets of normal values have been published for CMR [71–75]. Normal values are not absolute numbers but should be indexed to body size. Most often, indexing to body surface area is recommended [32]. However, indexing to body surface area is not satisfactory, as it reduces sensitivity for slight abnormalities in obese subjects. Ideally, dimensions are indexed for fat-free (lean) body mass [76–78], but this is cumbersome and not realistic for clinical routine. Data from the Framingham offspring study confirm that ejection fraction tends to be higher in females than in males. Moreover LV mass and size decrease with age [78, 79].

When referring to any normal values, users should be aware of the details and analyze their data in the same way the reference data have been analyzed.

Professional athletes have to be evaluated separately as they often show results outside the normal range for the general population, including a mildly increased LV end-diastolic volume and mildly decreased EF [80].

Comparison to Other Modalities

CMR has been extensively validated against the traditional imaging modalities as well as against animal models and autopsy studies [29]. It has been accepted as the gold standard for LV mass and all cardiac volumes. The excellent reproducibility of CMR measurements [81] results in fewer patients required to detect true differences in LV parameters compared to echocardiography [82]. Therefore, CMR is the method of choice to conduct scientific studies of changes in LV parameters as the sample size decreases significantly [83, 84].

Compared to CMR echocardiography offers higher temporal resolution than CMR. Therefore endocardial border detection is often suboptimal. This contributes to higher test-to-test variability in addition to a higher dependency on individual operators. On the other hand, there is more experience with diastolic and strain measurements. Cardiac computed tomography involves radiation and requires iodinated contrast injection. It has its strengths mainly in depicting the coronary arteries. Due to lower temporal resolution, it is less suited for dynamic studies of cardiac function. In addition, functional studies would require full radiation throughout the cardiac cycle that is otherwise not applied.

Marwick nicely compared the advantages and disadvantages of the various imaging modalities in assessing systolic LV function [37].

Outlook

The heart failure epidemic [85, 86] will ensure persisting demand for noninvasive assessment of cardiac function. Future technical improvements in computer speed and coil development will allow for CMR imaging of cardiac function in even shorter scan times with increasing temporal and spatial resolution. A comprehensive CMR protocol including cine, scar, and coronary imaging might only last 5 min [87]. Real-time or near-real-time scanning will result in better image quality we used today with standard sequences.

References

1. Raymond I, Mehlsen J, Pedersen F, Dimsits J, Jacobsen J, Hildebrandt PR. The prognosis of impaired left ventricular systolic function and heart failure in a middle-aged and elderly population in an urban population segment of Copenhagen. Eur J Heart Fail. 2004;6(5):653–61.
2. Solomon SD, Zelenkofske S, McMurray JJ, Finn PV, Velazquez E, Ertl G, et al. Sudden death in patients with myocardial infarction and left ventricular dysfunction, heart failure, or both. N Engl J Med. 2005;352(25):2581–8.
3. Kramer CM, Barkhausen J, Flamm SD, Kim RJ, Nagel E. Standardized cardiovascular magnetic resonance (CMR) protocols 2013 update. J Cardiovasc Magn Reson. 2013;15:91.
4. Carr JC, Simonetti O, Bundy J, Li D, Pereles S, Finn JP. Cine MR angiography of the heart with segmented true fast imaging with steady-state precession. Radiology. 2001;219(3):828–34.
5. Reeder SB, Markl M, Yu H, Hellinger JC, Herfkens RJ, Pelc NJ. Cardiac CINE imaging with IDEAL water-fat separation and steady-state free precession. J Magn Reson Imaging. 2005;22(1):44–52.
6. Kellman P, Hernando D, Shah S, Zuehlsdorff S, Jerecic R, Mancini C, et al. Multiecho dixon fat and water separation method for detecting fibrofatty infiltration in the myocardium. Magn Reson Med. 2009;61(1):215–21.
7. Marcus JT, Gotte MJ, DeWaal LK, Stam MR, Van der Geest RJ, Heethaar RM, et al. The influence of through-plane motion on left ventricular volumes measured by magnetic resonance imaging: implications for image acquisition and analysis. J Cardiovasc Magn Reson. 1999;1(1):1–6.
8. Messroghli DR, Bainbridge GJ, Alfakih K, Jones TR, Plein S, Ridgway JP, et al. Assessment of regional left ventricular function:

accuracy and reproducibility of positioning standard short-axis sections in cardiac MR imaging. Radiology. 2005;235(1):229–36.
9. Chuang ML, Hibberd MG, Salton CJ, Beaudin RA, Riley MF, Parker RA, et al. Importance of imaging method over imaging modality in noninvasive determination of left ventricular volumes and ejection fraction: assessment by two- and three-dimensional echocardiography and magnetic resonance imaging. J Am Coll Cardiol. 2000;35(2):477–84.
10. Friedrich MG, Schulz-Menger J, Strohm O, Dick AJ, Dietz R. The diagnostic impact of 2D- versus 3D-left ventricular volumetry by MRI in patients with suspected heart failure. MAGMA. 2000;11(1–2):16–9.
11. Childs H, Ma L, Ma M, Clarke J, Cocker M, Green J, et al. Comparison of long and short axis quantification of left ventricular volume parameters by cardiovascular magnetic resonance, with ex-vivo validation. J Cardiovasc Magn Reson. 2011;13:40.
12. Gatehouse PD, Firmin DN. The cardiovascular magnetic resonance machine: hardware and software requirements. Herz. 2000;25(4):317–30.
13. Fischer SE, Wickline SA, Lorenz CH. Novel real-time R-wave detection algorithm based on the vectorcardiogram for accurate gated magnetic resonance acquisitions. Magn Reson Med. 1999;42(2):361–70.
14. Chia JM, Fischer SE, Wickline SA, Lorenz CH. Performance of QRS detection for cardiac magnetic resonance imaging with a novel vectorcardiographic triggering method. J Magn Reson Imaging. 2000;12(5):678–88.
15. Feinstein JA, Epstein FH, Arai AE, Foo TK, Hartley MR, Balaban RS, et al. Using cardiac phase to order reconstruction (CAPTOR): a method to improve diastolic images. J Magn Reson Imaging. 1997;7(5):794–8.
16. Kunz RP, Oellig F, Krummenauer F, Oberholzer K, Romaneehsen B, Vomweg TW, et al. Assessment of left ventricular function by breath-hold cine MR imaging: comparison of different steady-state free precession sequences. J Magn Reson Imaging. 2005;21(2):140–8.
17. Sievers B, Addo M, Kirchberg S, Bakan A, John-Puthenveettil B, Franken U, et al. Impact of the ECG gating method on ventricular volumes and ejection fractions assessed by cardiovascular magnetic resonance imaging. J Cardiovasc Magn Reson. 2005;7(2):441–6.
18. Manka R, Buehrer M, Boesiger P, Fleck E, Kozerke S. Performance of simultaneous cardiac-respiratory self-gated three-dimensional MR imaging of the heart: initial experience. Radiology. 2010;255(3):909–16.
19. Miller S, Simonetti OP, Carr J, Kramer U, Finn JP. MR imaging of the heart with cine true fast imaging with steady-state precession: influence of spatial and temporal resolutions on left ventricular functional parameters. Radiology. 2002;223(1):263–9.
20. Tsao J, Kozerke S. MRI temporal acceleration techniques. J Magn Reson Imaging. 2012;36(3):543–60.
21. Vincenti G, Monney P, Chaptinel J, Rutz T, Coppo S, Zenge MO, et al. Compressed sensing single-breath-hold CMR for fast quantification of LV function, volumes, and mass. JACC Cardiovasc Imaging. 2014;7(9):882–92.
22. Goldstein SA, Evangelista A, Abbara S, Arai A, Asch FM, Badano LP, et al. Multimodality imaging of diseases of the thoracic aorta in adults: from the American Society of Echocardiography and the European Association of Cardiovascular Imaging: endorsed by the Society of Cardiovascular Computed Tomography and Society for Cardiovascular Magnetic Resonance. J Am Soc Echocardiogr. 2015;28(2):119–82.
23. Burman ED, Keegan J, Kilner PJ. Pulmonary artery diameters, cross sectional areas and area changes measured by cine cardiovascular magnetic resonance in healthy volunteers. J Cardiovasc Magn Reson. 2016;18(1):12.
24. Danilouchkine MG, Westenberg JJ, Lelieveldt BP, Reiber JH. Accuracy of short-axis cardiac MRI automatically derived from scout acquisitions in free-breathing and breath-holding modes. MAGMA. 2005;18(1):7–18.
25. Miller CA, Jordan P, Borg A, Argyle R, Clark D, Pearce K, et al. Quantification of left ventricular indices from SSFP cine imaging: impact of real-world variability in analysis methodology and utility of geometric modeling. J Magn Reson Imaging. 2013;37(5):1213–22.
26. Contijoch F, Witschey WR, Rogers K, Gorman J 3rd, Gorman RC, Ferrari V, et al. Impact of end-diastolic and end-systolic phase selection in the volumetric evaluation of cardiac MRI. J Magn Reson Imaging. 2016;43(3):585–93.
27. Peters DC, Ennis DB, McVeigh ER. High-resolution MRI of cardiac function with projection reconstruction and steady-state free precession. Magn Reson Med. 2002;48(1):82–8.
28. Chuang ML, Gona P, Hautvast GL, Salton CJ, Blease SJ, Yeon SB, et al. Correlation of trabeculae and papillary muscles with clinical and cardiac characteristics and impact on CMR measures of LV anatomy and function. JACC Cardiovasc Imaging. 2012;5(11):1115–23.
29. Francois CJ, Fieno DS, Shors SM, Finn JP. Left ventricular mass: manual and automatic segmentation of true FISP and FLASH cine MR images in dogs and pigs. Radiology. 2004;230(2):389–95.
30. Fieno DS, Jaffe WC, Simonetti OP, Judd RM, Finn JP. TrueFISP: assessment of accuracy for measurement of left ventricular mass in an animal model. J Magn Reson Imaging. 2002;15(5):526–31.
31. Patel AR, Mor-Avi V. Are trabeculae and papillary muscles an integral part of cardiac anatomy: or annoying features to exclude while tracing endocardial boundaries? JACC Cardiovasc Imaging. 2012;5(11):1124–6.
32. Schulz-Menger J, Bluemke DA, Bremerich J, Flamm SD, Fogel MA, Friedrich MG, et al. Standardized image interpretation and post processing in cardiovascular magnetic resonance: Society for Cardiovascular Magnetic Resonance (SCMR) board of trustees task force on standardized post processing. J Cardiovasc Magn Reson. 2013;15:35.
33. Souto M, Masip LR, Couto M, Suarez-Cuenca JJ, Martinez A, Tahoces PG, et al. Quantification of right and left ventricular function in cardiac MR imaging: comparison of semiautomatic and manual segmentation algorithms. Diagnostics (Basel). 2013;3(2):271–82.
34. Bloomer TN, Plein S, Radjenovic A, Higgins DM, Jones TR, Ridgway JP, et al. Cine MRI using steady state free precession in the radial long axis orientation is a fast accurate method for obtaining volumetric data of the left ventricle. J Magn Reson Imaging. 2001;14(6):685–92.
35. Alfakih K, Reid S, Jones T, Sivananthan M. Assessment of ventricular function and mass by cardiac magnetic resonance imaging. Eur Radiol. 2004;14(10):1813–22.
36. Cikes M, Solomon SD. Beyond ejection fraction: an integrative approach for assessment of cardiac structure and function in heart failure. Eur Heart J. 2016;37(21):1642–50.
37. Marwick TH. Methods used for the assessment of LV systolic function: common currency or tower of Babel? Heart. 2013;99(15):1078–86.
38. Ewer MS, Lenihan DJ. Left ventricular ejection fraction and cardiotoxicity: is our ear really to the ground? J Clin Oncol. 2008;26(8):1201–3.
39. Mordi I, Bezerra H, Carrick D, Tzemos N. The combined incremental prognostic value of LVEF, late gadolinium enhancement, and global circumferential strain assessed by CMR. JACC Cardiovasc Imaging. 2015;8(5):540–9.
40. Young AA, Cowan BR. Evaluation of left ventricular torsion by cardiovascular magnetic resonance. J Cardiovasc Magn Reson. 2012;14:49.
41. Moller JE, Hillis GS, Oh JK, Seward JB, Reeder GS, Wright RS, et al. Left atrial volume: a powerful predictor of survival after acute myocardial infarction. Circulation. 2003;107(17):2207–12.

42. Beinart R, Boyko V, Schwammenthal E, Kuperstein R, Sagie A, Hod H, et al. Long-term prognostic significance of left atrial volume in acute myocardial infarction. J Am Coll Cardiol. 2004;44(2):327–34.
43. Rossi A, Cicoira M, Zanolla L, Sandrini R, Golia G, Zardini P, et al. Determinants and prognostic value of left atrial volume in patients with dilated cardiomyopathy. J Am Coll Cardiol. 2002;40(8):1425.
44. Donal E, Lip GY, Galderisi M, Goette A, Shah D, Marwan M, et al. EACVI/EHRA Expert Consensus Document on the role of multi-modality imaging for the evaluation of patients with atrial fibrillation. Eur Heart J Cardiovasc Imaging. 2016;17(4):355–83.
45. Abhayaratna WP, Seward JB, Appleton CP, Douglas PS, Oh JK, Tajik AJ, et al. Left atrial size: physiologic determinants and clinical applications. J Am Coll Cardiol. 2006;47(12):2357–63.
46. Tsang TS, Abhayaratna WP, Barnes ME, Miyasaka Y, Gersh BJ, Bailey KR, et al. Prediction of cardiovascular outcomes with left atrial size: is volume superior to area or diameter? J Am Coll Cardiol. 2006;47(5):1018–23.
47. Maceira AM, Cosin-Sales J, Roughton M, Prasad SK, Pennell DJ. Reference left atrial dimensions and volumes by steady state free precession cardiovascular magnetic resonance. J Cardiovasc Magn Reson. 2010;12:65.
48. Hudsmith LE, Cheng AS, Tyler DJ, Shirodaria C, Lee J, Petersen SE, et al. Assessment of left atrial volumes at 1.5 Tesla and 3 Tesla using FLASH and SSFP cine imaging. J Cardiovasc Magn Reson. 2007;9(4):673–9.
49. Agner BF, Kuhl JT, Linde JJ, Kofoed KF, Akeson P, Rasmussen BV, et al. Assessment of left atrial volume and function in patients with permanent atrial fibrillation: comparison of cardiac magnetic resonance imaging, 320-slice multi-detector computed tomography, and transthoracic echocardiography. Eur Heart J Cardiovasc Imaging. 2014;15(5):532–40.
50. Kuhl JT, Lonborg J, Fuchs A, Andersen MJ, Vejlstrup N, Kelbaek H, et al. Assessment of left atrial volume and function: a comparative study between echocardiography, magnetic resonance imaging and multi slice computed tomography. Int J Cardiovasc Imaging. 2012;28(5):1061–71.
51. Whitlock M, Garg A, Gelow J, Jacobson T, Broberg C. Comparison of left and right atrial volume by echocardiography versus cardiac magnetic resonance imaging using the area-length method. Am J Cardiol. 2010;106(9):1345–50.
52. Farzaneh-Far A, Ariyarajah V, Shenoy C, Dorval JF, Kaminski M, Curillova Z, et al. Left atrial passive emptying function during dobutamine stress MR imaging is a predictor of cardiac events in patients with suspected myocardial ischemia. JACC Cardiovasc Imaging. 2011;4(4):378–88.
53. Grothues F, Moon JC, Bellenger NG, Smith GS, Klein HU, Pennell DJ. Interstudy reproducibility of right ventricular volumes, function, and mass with cardiovascular magnetic resonance. Am Heart J. 2004;147(2):218–23.
54. Alfakih K, Plein S, Bloomer T, Jones T, Ridgway J, Sivananthan M. Comparison of right ventricular volume measurements between axial and short axis orientation using steady-state free precession magnetic resonance imaging. J Magn Reson Imaging. 2003;18(1):25–32.
55. Tandri H, Calkins H. MR and CT imaging of arrhythmogenic cardiomyopathy. Card Electrophysiol Clin. 2011;3(2):269–80.
56. Shors SM, Fung CW, Francois CJ, Finn JP, Fieno DS. Accurate quantification of right ventricular mass at MR imaging by using cine true fast imaging with steady-state precession: study in dogs. Radiology. 2004;230(2):383–8.
57. Altmayer SP, Teeuwen LA, Gorman RC, Han Y. RV mass measurement at end-systole: improved accuracy, reproducibility, and reduced segmentation time. J Magn Reson Imaging. 2015;42(5):1291–6.
58. Sato T, Tsujino I, Ohira H, Oyama-Manabe N, Ito YM, Yamada A, et al. Right atrial volume and reservoir function are novel independent predictors of clinical worsening in patients with pulmonary hypertension. J Heart Lung Transplant. 2015;34(3):414–23.
59. Darsaklis K, Dickson ME, Cornwell W 3rd, Ayers CR, Torres F, Chin KM, et al. Right atrial emptying fraction non-invasively predicts mortality in pulmonary hypertension. Int J Cardiovasc Imaging. 2016;32(7):1121–30.
60. Faletra FF, Muzzarelli S, Dequarti MC, Murzilli R, Bellu R, Ho SY. Imaging-based right-atrial anatomy by computed tomography, magnetic resonance imaging, and three-dimensional transoesophageal echocardiography: correlations with anatomic specimens. Eur Heart J Cardiovasc Imaging. 2013;14(12):1123–31.
61. Maceira AM, Cosin-Sales J, Roughton M, Prasad SK, Pennell DJ. Reference right atrial dimensions and volume estimation by steady state free precession cardiovascular magnetic resonance. J Cardiovasc Magn Reson. 2013;15:29.
62. Gandhi SK, Powers JC, Nomeir AM, Fowle K, Kitzman DW, Rankin KM, et al. The pathogenesis of acute pulmonary edema associated with hypertension. N Engl J Med. 2001;344(1):17–22.
63. Senni M, Paulus WJ, Gavazzi A, Fraser AG, Diez J, Solomon SD, et al. New strategies for heart failure with preserved ejection fraction: the importance of targeted therapies for heart failure phenotypes. Eur Heart J. 2014;35(40):2797–815.
64. Krishnamurthy R, Pednekar A, Cheong B, Muthupillai R. High temporal resolution SSFP cine MRI for estimation of left ventricular diastolic parameters. J Magn Reson Imaging. 2010;31(4):872–80.
65. Rider OJ, Francis JM, Ali MK, Petersen SE, Robinson M, Robson MD, et al. Beneficial cardiovascular effects of bariatric surgical and dietary weight loss in obesity. J Am Coll Cardiol. 2009;54(8):718–26.
66. Utz W, Engeli S, Haufe S, Kast P, Hermsdorf M, Wiesner S, et al. Myocardial steatosis, cardiac remodelling and fitness in insulin-sensitive and insulin-resistant obese women. Heart. 2011;97(19):1585–9.
67. Mendoza DD, Codella NC, Wang Y, Prince MR, Sethi S, Manoushagian SJ, et al. Impact of diastolic dysfunction severity on global left ventricular volumetric filling – assessment by automated segmentation of routine cine cardiovascular magnetic resonance. J Cardiovasc Magn Reson. 2010;12:46.
68. Okayama S, Nakano T, Uemura S, Fujimoto S, Somekawa S, Watanabe M, et al. Evaluation of left ventricular diastolic function by fractional area change using cine cardiovascular magnetic resonance: a feasibility study. J Cardiovasc Magn Reson. 2013;15:87.
69. Bollache E, Redheuil A, Clement-Guinaudeau S, Defrance C, Perdrix L, Ladouceur M, et al. Automated left ventricular diastolic function evaluation from phase-contrast cardiovascular magnetic resonance and comparison with Doppler echocardiography. J Cardiovasc Magn Reson. 2010;12:63.
70. Brandts A, Bertini M, van Dijk EJ, Delgado V, Marsan NA, van der Geest RJ, et al. Left ventricular diastolic function assessment from three-dimensional three-directional velocity-encoded MRI with retrospective valve tracking. J Magn Reson Imaging. 2011;33(2):312–9.
71. Alfakih K, Plein S, Thiele H, Jones T, Ridgway JP, Sivananthan MU. Normal human left and right ventricular dimensions for MRI as assessed by turbo gradient echo and steady-state free precession imaging sequences. J Magn Reson Imaging. 2003;17(3):323–9.
72. Grebe O, Kestler HA, Merkle N, Wohrle J, Kochs M, Hoher M, et al. Assessment of left ventricular function with steady-state-free-precession magnetic resonance imaging. Reference values and a comparison to left ventriculography. Z Kardiol. 2004;93(9):686–95.
73. Hudsmith LE, Petersen SE, Francis JM, Robson MD, Neubauer S. Normal human left and right ventricular and left atrial dimensions using steady state free precession magnetic resonance imaging. J Cardiovasc Magn Reson. 2005;7(5):775–82.
74. Maceira AM, Prasad SK, Khan M, Pennell DJ. Normalized left ventricular systolic and diastolic function by steady state free pre-

cession cardiovascular magnetic resonance. J Cardiovasc Magn Reson. 2006;8(3):417–26.
75. Natori S, Lai S, Finn JP, Gomes AS, Hundley WG, Jerosch-Herold M, et al. Cardiovascular function in multi-ethnic study of atherosclerosis: normal values by age, sex, and ethnicity. AJR Am J Roentgenol. 2006;186(6 Suppl 2):S357–65.
76. George KP, Birch KM, Pennell DJ, Myerson SG. Magnetic-resonance-imaging-derived indices for the normalization of left ventricular morphology by body size. Magn Reson Imaging. 2009;27(2):207–13.
77. Dewey FE, Rosenthal D, Murphy DJ Jr, Froelicher VF, Ashley EA. Does size matter? Clinical applications of scaling cardiac size and function for body size. Circulation. 2008;117(17):2279–87.
78. Yeon SB, Salton CJ, Gona P, Chuang ML, Blease SJ, Han Y, et al. Impact of age, sex, and indexation method on MR left ventricular reference values in the Framingham Heart Study offspring cohort. J Magn Reson Imaging. 2015;41(4):1038–45.
79. Chuang ML, Gona P, Hautvast GL, Salton CJ, Breeuwer M, O'Donnell CJ, et al. CMR reference values for left ventricular volumes, mass, and ejection fraction using computer-aided analysis: the Framingham Heart Study. J Magn Reson Imaging. 2014;39(4):895–900.
80. Abergel E, Chatellier G, Hagege AA, Oblak A, Linhart A, Ducardonnet A, et al. Serial left ventricular adaptations in world-class professional cyclists: implications for disease screening and follow-up. J Am Coll Cardiol. 2004;44(1):144–9.
81. Danilouchkine MG, Westenberg JJ, de Roos A, Reiber JH, Lelieveldt BP. Operator induced variability in cardiovascular MR: left ventricular measurements and their reproducibility. J Cardiovasc Magn Reson. 2005;7(2):447–57.
82. Grothues F, Smith GC, Moon JC, Bellenger NG, Collins P, Klein HU, et al. Comparison of interstudy reproducibility of cardiovascular magnetic resonance with two-dimensional echocardiography in normal subjects and in patients with heart failure or left ventricular hypertrophy. Am J Cardiol. 2002;90(1):29–34.
83. Bellenger NG, Davies LC, Francis JM, Coats AJ, Pennell DJ. Reduction in sample size for studies of remodeling in heart failure by the use of cardiovascular magnetic resonance. J Cardiovasc Magn Reson. 2000;2(4):271–8.
84. Strohm O, Schulz-Menger J, Pilz B, Osterziel KJ, Dietz R, Friedrich MG. Measurement of left ventricular dimensions and function in patients with dilated cardiomyopathy. J Magn Reson Imaging. 2001;13(3):367–71.
85. Redfield MM. Heart failure – an epidemic of uncertain proportions. N Engl J Med. 2002;347(18):1442–4.
86. Bleumink GS, Knetsch AM, Sturkenboom MC, Straus SM, Hofman A, Deckers JW, et al. Quantifying the heart failure epidemic: prevalence, incidence rate, lifetime risk and prognosis of heart failure The Rotterdam Study. Eur Heart J. 2004;25(18):1614–9.
87. Xu J, Kim D, Otazo R, Srichai MB, Lim RP, Axel L, et al. Towards a five-minute comprehensive cardiac MR examination using highly accelerated parallel imaging with a 32-element coil array: feasibility and initial comparative evaluation. J Magn Reson Imaging. 2013;38(1):180–8.

Regional Myocardial Strain and Function: From Novel Techniques to Clinical Applications

5

Yuchi Han, Walter R. Witschey, Kevin Duffy, and Victor A. Ferrari

Introduction

CMR allows for a highly accurate description of segmental wall motion and quantitation of contractile function. The excellent contrast between the endocardium and blood pool improves measurement of wall thickness, end-diastolic and end-systolic volumes, and LV ejection fraction using steady-state free precession (SSFP) images. Advancement in 3D echocardiography techniques has improved upon limitations of geometric assumption, but additional limitations regarding imaging windows and endocardial definition persist. Computed tomography (CT) has emerged as a new tool to evaluate cardiac function, but the radiation risk and low temporal resolution hamper its value in assessing regional function. CMR has been the noninvasive method of choice for the evaluation of regional myocardial movement since myocardial tagging was invented almost 30 years ago. A number of developments and improvements on the technique have taken place to improve image resolution, quality, three-dimensional image acquisition, and scan time. The purpose of this chapter is to describe the methods and clinical applications of these techniques for assessment of segmental ventricular function.

Y. Han (✉) · K. Duffy · V. A. Ferrari
Cardiovascular Medicine Division, Department of Medicine, Perelman School of Medicine, University of Pennsylvania, Philadelphia, PA, USA
e-mail: yuchi.han@uphs.upenn.edu

W. R. Witschey
Department of Radiology, Perelman School of Medicine, University of Pennsylvania, Philadelphia, PA, USA

Methods and Techniques

Motion Quantification

Analysis of cardiac motion is closely related to engineering principles of continuum mechanics. Many aspects of motion (kinematics) are well beyond the scope of this chapter, and there are many excellent books [1] and reviews [2] on this topic. The discussion here is limited to brief definitions of quantitative motion parameters, such as displacement, strain, and torsion.

From the viewpoint of kinematics, the heart is a continuous material, and its behavior is the summative property of many cardiac myocytes, their extracellular space, and nearby vascular space. This assumption is valid because the MRI spatial scale (voxel volume ~ 1–40 mm^3) is much larger than the microscopic scale. The initial position of cardiac muscle at end-diastole is the reference configuration, and different positions during the cardiac cycle are the deformed configurations. The displacement is the distance and direction of tissue motion between the reference and deformed configuration, and the displacement field is a description of all tissue displacements.

The displacement field is also a spatial map that provides useful information about regional myocardial health. Ischemic tissue may have reduced displacement in regions of impaired contractile function. One shortcoming of the displacement field technique is that it reports both regional and global translation and rotation. Global and regional displacement in opposite directions would be incorrectly interpreted as impaired function without first accounting for global displacement.

Myocardial strain is a parameter derived from displacement that simplifies the analysis of myocardial motion. The concept is that myocardium will undergo local stretching, shortening, or shearing as it transitions from reference

R. Y. Kwong et al. (eds.), *Cardiovascular Magnetic Resonance Imaging*, Contemporary Cardiology,
https://doi.org/10.1007/978-1-4939-8841-9_5

to deformed configurations. Strain quantifies local motion without the influence of confounding global motion. Unlike tissue displacement, which is an absolute quantity, strain may be defined in several ways. For instance, Cauchy strain is a dimensionless quantity defined as the ratio of displacement to a reference length and is expressed as a percentage.

The myocardial displacement is a 3D vector quantity with components u_R, u_C, and u_L, where the subscripts R, C, and L refer to local radial, circumferential, and longitudinal wall coordinates. The Green-Lagrange strain is a tensor quantity (a 3 × 3 matrix)

$$E = \begin{bmatrix} e_{RR} & e_{RC} & e_{RL} \\ e_{CR} & e_{CC} & e_{CL} \\ e_{LR} & e_{LC} & e_{LL} \end{bmatrix},$$

where the diagonal elements quantify stretch or shrink and off-diagonal elements measure shear. Strain could also be reported with respect to the local fiber orientation, also called the principal strain, a diagonal tensor

$$E = \begin{bmatrix} e_{11} & & \\ & e_{22} & \\ & & e_{33} \end{bmatrix}.$$

The velocity and strain rate are the time rate of change of displacement and strain, respectively.

CMR Motion Imaging: Strain and Displacement

Normal myocardial architecture consists of ventricular myocytes organized in helical layers of fiber bundles with a preferential transmural orientation [3–5]. The maximum principal strain e_{11} is presumed to correspond to the myocardial fiber orientation. As will be discussed further, both displacement and strain are readily obtained from tagged MRI and displacement encoding of stimulated echoes (DENSE) MRI techniques.

Magnetic resonance imaging offers multiple advantages to radio-opaque marker [6, 7] or ultrasonic transducer (sonomicrometry) [8, 9] motion tracking for cardiovascular applications, including its noninvasive nature, a closely packed displacement field, and 3D spatial coverage. Numerous MRI methods have been introduced to quantitatively assess regional myocardial function, and the scope of topics is broad, so we refer interested readers to more detailed reviews of MRI methodology [2, 10, 11] and image analysis [10]. This section will focus mainly on tagging, displacement encoding (DENSE), strain encoded (SENC), velocity mapping, and feature tracking MRI techniques.

Myocardial Tagging

Myocardial tagging refers to MR imaging techniques that generate noninvasive deformable lines or grids to track myocardial motion. The imaging sequence employs magnetization preparation for grid encoding followed by cine MRI to monitor grid deformation [12, 13]. Spatial modulation of magnetization (SPAMM) [13] uses a radiofrequency pulse pair and magnetic field gradient to generate deformable lines in one dimension, although multidimensional tags allow for 2D or 3D motion field imaging [14].

Computer vision algorithms extract grid deformation and produce closely packed displacement fields using optical flow [14–16], image registration [17], deformable models, splines [18, 19], and Gabor filters [20]. The displacement field spatial resolution is determined by tag grid density and is larger than the pixel resolution, although most algorithms produce dense displacement fields at native image resolution [14]. To improve upon magnitude image-based motion detection, frequency domain detection, called harmonic phase (HARP) imaging, extracts motion from cardiac phase [21–24].

Validation studies have been performed with sonomicrometry [25, 26] and in vitro systems [27, 28]. Sonomicrometry exhibited reduced circumferential shortening compared to tagging, suggesting that the transducers impaired local function [26].

There are several limitations to myocardial tagging techniques. Tag persistence is associated with myocardial water spin relaxation (T_1 and T_2) and cine pulse sequence parameters. Muscle T_1 is approximately 1 s at 1.5 T, and tags are known to fade in the middle and late diastolic cardiac phases, although it is possible to prolong tag persistence with increased T_1 at a higher magnetic field strength or with complementary [29] (Fig. 5.1) or cascaded [30] SPAMM.

DENSE Imaging

DENSE performs displacement encoding by using a pair of magnetic field gradients separated by a mixing period to spatially encode displacement as MR signal phase information [31]. DENSE displays motion information by regional vectors with motion direction and length representing the magnitude of motion. DENSE provides excellent myocardial border definition since it is based on a black blood sequence and is highly reproducible and quantitatively equivalent to myocardial tagging sequences in in vivo experiments (Fig. 5.2) [32].

SENC Imaging

SENC is a newer variation of the tagging technique. In some ways, it is similar to DENSE as its basis is a stimu-

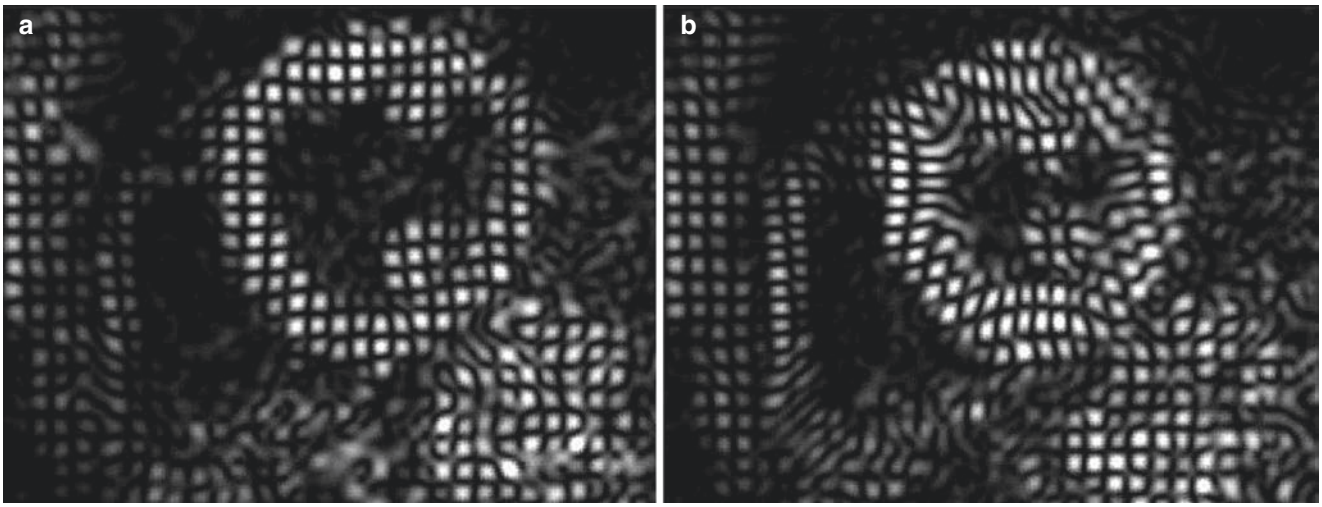

Fig. 5.1 CSPAMM tagging of a subject at end-diastole (**a**) and at end-systole (**b**). Well-adapted CSPAMM sequences provide excellent persistence of tagging into diastole with high spatial and temporal resolution

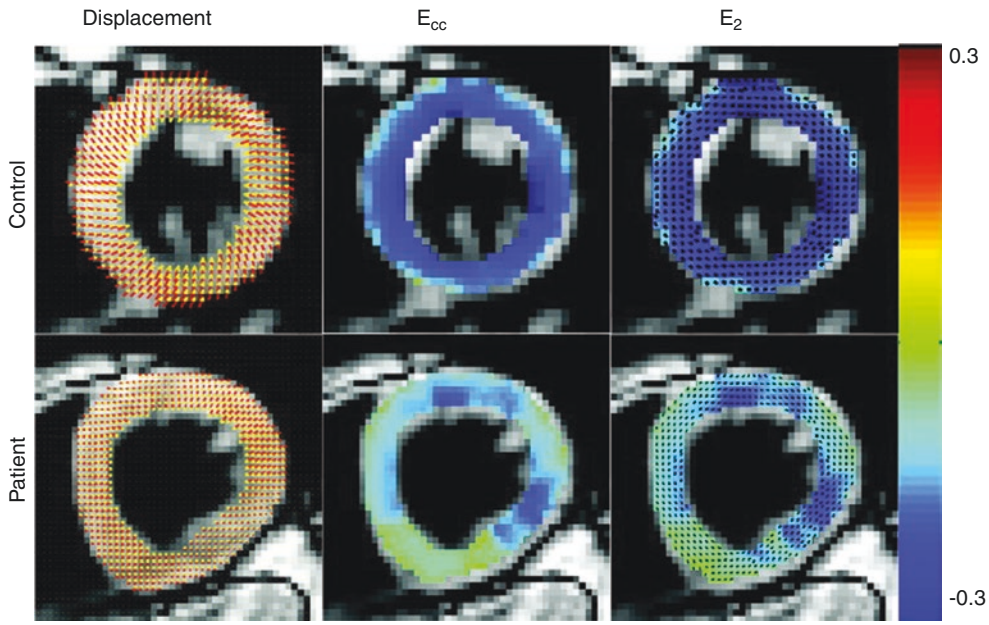

Fig. 5.2 Representative end-systolic (left column) displacement, (middle column) E_{cc}, and (right column) E_2 field maps of a control, as well as those of a 49-year-old male patient with nonischemic cardiomyopathy and ejection fraction of 45%. These examples demonstrate the sensitivity of fast cine DENSE MRI to detect regional variation in contractile function. Compared to the control subject, the patient exhibited considerably lower displacement and magnitude of E_{cc} and E_2 (Reprinted from Feng et al. [32], with permission from John Wiley and Sons)

lated echo acquisition mode pulse sequence, but in contrast to DENSE, the strain information is contained in the magnitude rather than phase images and has the advantages of measuring high-resolution strain with simple post-processing. In contrast to conventional tagging, SENC is applied in the through-plane direction by creating a stack of magnetization-saturated planes that lie inside and parallel to the image plane and therefore obtains a through-plane strain map. SENC has been validated against conventional tagging and has been shown to be accurate and reproducible (Fig. 5.3) [33].

Velocity Encoding

Velocity mapping uses a bipolar magnetic field gradient to encode velocity as MR signal phase information [34, 35]. The maximum encoded velocity, v_{enc}, is set to account for peak anticipated tissue velocity to prevent aliasing. Long acquisition times have hampered clinical application and require prospective respiratory gating to mitigate breathing motion artifacts. New image acquisition and reconstruction strategies may reduce total scan times. Self-gating has been used to derive motion information directly from under-sam-

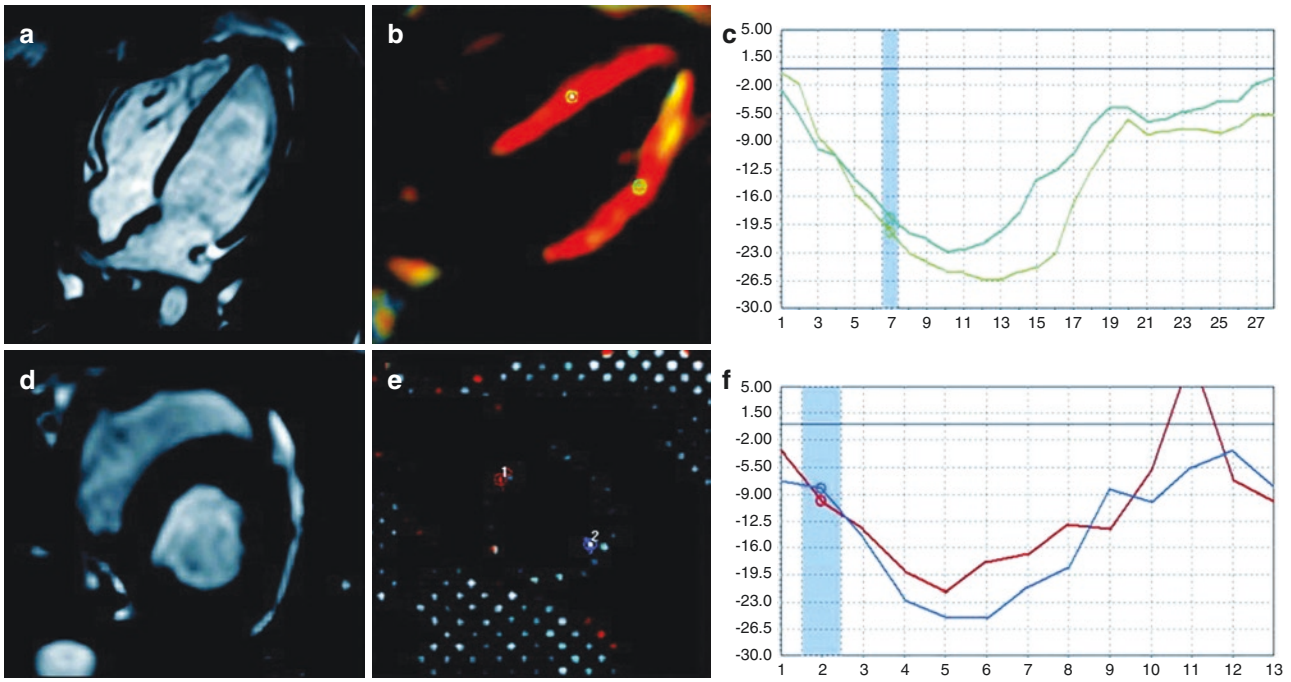

Fig. 5.3 Strain measurements obtained by SENC and MR tagging. (**a**) CINE image (four-chamber view) of a healthy volunteer. (**b**) Color-coded functional SENC image in the same plane orientation. Maximum contraction is illustrated in red. (**c**) The circumferential strain results obtained by SENC. (**d**) CINE image (short-axis view) of the same healthy volunteer. (**e**) Color-coded MR tagging image in the same plane orientation as the short-axis slice (midventricular) for comparison of circumferential strain obtained by MR tagging to SENC imaging as SENC is a technique that uses tag surfaces that are parallel—not orthogonal—to the image plane. (**f**) The circumferential strain results calculated by MR tagging (Reprinted from Neizel et al. [33], with permission from John Wiley and Sons)

pled MR images [36] and may improve scan efficiency and image quality.

Feature Tracking

MR feature tracking (FT) (Fig. 5.4) [37] infers quantitative motion parameters directly from myocardial tissue features, such as contours, trabeculations, and other distinctive cardiac anatomy, with computer vision [38, 39]. Rapid clinical adoption is now possible since several commercial software packages are now available, motion is quantified from cine SSFP images, and no additional MR pulse sequences are required.

Validation studies showed close correlation between FT and tagging using HARP analysis in normal subjects, in Duchenne muscular dystrophy population [40], and in pediatric cancer survivors [41]. Circumferential (e_{CC}) and radial (e_{RR}) LV strain appear to be most reproducible [42]. Radial strain was reported to have the best sensitivity and specificity for detection of postinfarction scar [43]. Reproducibility and strain values from FT algorithms are also reduced when derived from post contrast injection cine images [44].

Feature tracking algorithms are currently not standardized, so discrepancies between software have been reported [45]. Incorporation of myocardial incompressibility constraints may potentially improve robustness and preserve physiologic conditions [46]. Large-scale adoption of this technique and establishing cutoffs to guide clinical practice are hampered by lack of standardization in sequence parameters and analytic tools, but the potential utility of FT continues to expand.

Clinical Applications

Normal Regional Function

The accurate assessment of regional LV function has been improved greatly with myocardial tissue tagging. Lima et al. [25] showed in an animal model that CMR with tissue tagging allows accurate assessment of systolic wall thickening, with good correlation to invasive methods using sonomicrometers. The strongest correlation between MR imaging and percent systolic wall thickening by sonomicrometer crystals is achieved by using the three-dimensional volume element approach, by accounting for obliquity between the image plane and the left ventricular wall.

In the normal human LV, there is transmural heterogeneity of circumferential shortening with endocardial segments > mid wall > epicardial segments and longitudinal heterogeneity of circumferential shortening with apical segments > basal segments [47]. There are also patterns of regional heterogeneity of myocardial contraction and relaxation that

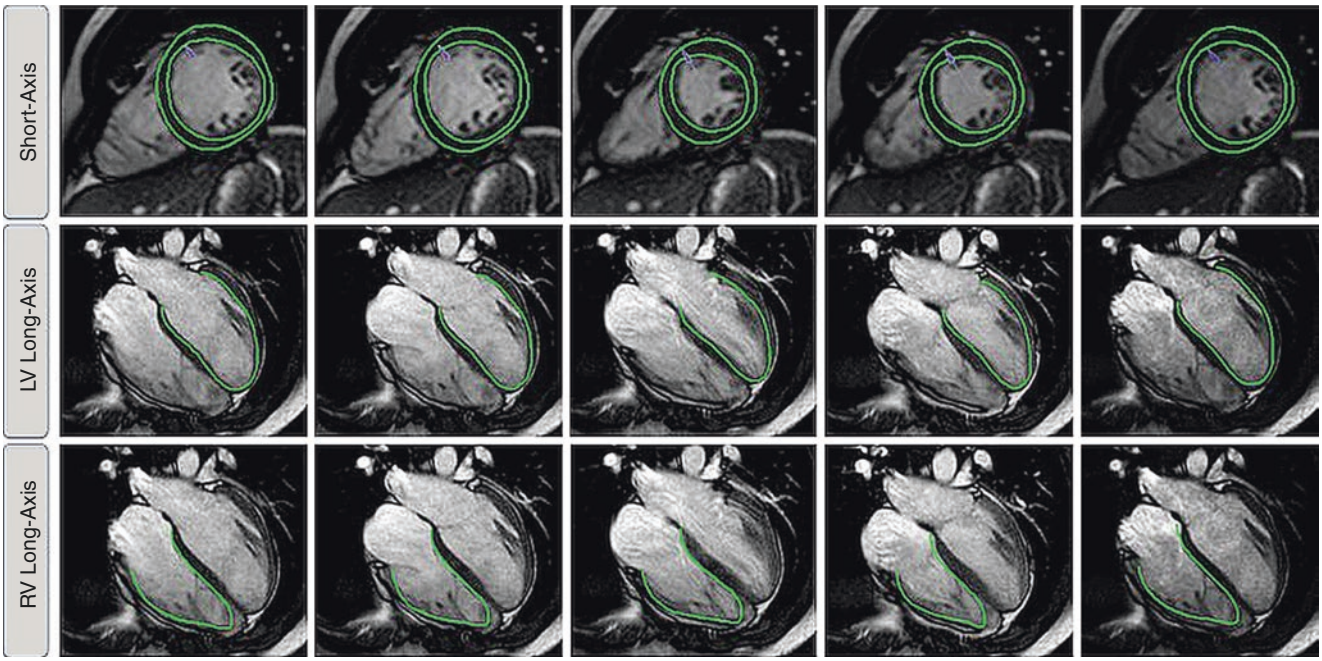

Fig. 5.4 Feature tracking in short-axis and long-axis orientation**.** The figure shows a representative example of the tracking in short-axis and long-axis orientation of the left ventricle (LV) and the right ventricle (RV) (Reprinted from Schuster et al. [37])

occur with aging resulting in increased apical systolic rotation and reduced apical relaxation [48, 49].

CMR has been the gold standard to evaluate the right ventricular (RV) volume and function. The RV myocardial contraction pattern is more difficult to describe as compared to the LV due to its complex shape and its very thin wall, which makes strain analysis more challenging. For the left ventricle, a 2D tag grid can be used to track intersection points within the myocardial wall; however, the RV is too thin for this to be practical. Instead, investigators have used either 1D tags or bidirectional tags with tracking of the intersection of the tag lines with the mid wall of the RV, rather than tracking intersection points of grid lines. New techniques such as SENC are able to provide higher-resolution strain analysis of the RV [50].

For normal RV regional function, increasing regional short-axis shortening from the RV outflow tract to the RV apex has been described using 1D, 2D tagging and SENC [50–52]. Longitudinal contraction is found to be greater at the apex and base, with a decrease in mid-ventricular segments by SENC [50]. The apex also appears to reach peak shortening earlier than mid-ventricular and basal segments [50].

Myocardial Ischemia

Using myocardial tagging in a radial orientation, Azhari and Denisova demonstrated that subendocardial dysfunction was the best discriminant of ischemia [53, 54]. The analysis of wall motion abnormalities with dobutamine stress echocardiography is an established method for detection of myocardial ischemia. CMR has been combined with stress modalities for the evaluation of CAD. Dobutamine CMR with tagging has been shown to detect significantly more new wall motion abnormalities than cine imaging alone in a study of 207 patients with known or suspected CAD [55]. Similarly, combining SENC with dobutamine CMR, Korosoglou et al. demonstrated the incremental value of strain by detecting a significantly larger number of patients with ischemia as compared to wall motion analysis alone [56]. SENC also has been shown to improve the diagnostic accuracy in detecting myocardial ischemia during dobutamine stress at an intermediate dose as compared to cine imaging, using quantitative coronary angiography as the standard of reference [57]. In a study using adenosine triphosphate (ATP) to induce perfusion abnormalities in ischemic segments, circumferential strain by tagging was shown to decrease in ischemic segments, as opposed to nonischemic segments, where circumferential strain increased compared to resting images [58].

Myocardial Infarction

CMR is also an especially good tool for the detection and quantification of myocardial infarction (MI). Infarction is a heterogeneous process involving predominantly the endocardium in smaller infarcts or can be more transmural in more substantial infarcts. An MI can result in multiple

patchy areas of necrosis surrounded by viable myocardium. CMR with tissue tagging can highlight areas of infarction and can also assess the effects of infarction on the non-infarcted regions of the ventricle. Circumferential and longitudinal strains are decreased not only in the infarcted areas but also in the remote zones in patients with reperfused anteroapical infarction [59]. This study also showed increases in the radius of curvature of the ventricular walls in both the infarcted and remote zones. A similar study [60] using tagged CMR and two-dimensional finite element analysis early after anteroapical infarction clearly demonstrated decreased wall strain and reorientation of the short-axis vector of myocardial contraction away from the centroid of the left ventricle. Early after infarction remote zone hyperfunction was seen, indicating a possible compensatory increase in function remote from the infarcted area. Average short- and long-axis strain values decreased to approximately 25% of normal in infarcted regions. A third study [61] demonstrated similar findings of decreased deformation not only in anteroapical MI but also in infarcts of all coronary distributions. Together, these findings imply an increase in segmental wall stress in regions distant from large infarcts resulting in globally decreased function and frequently leading to a post-MI chronic cardiomyopathy.

Microvascular obstruction (MO) is an important predictor of unfavorable remodeling after MI by preventing adequate healing early after myocardial infarction. This phenomenon is also referred to as a "no-reflow" territory as seen after angioplasty of acute infarcts fail to return adequate flow to a vessel. A canine infarct model has been used to explore the relationship of the extent of MO and its effect on regional and global function [62]. Animals with a greater extent of MO had a significantly greater risk of developing unfavorable remodeling within 10 days of infarction as assessed by CMR functional imaging. Myocardial strain decreased significantly in the infarcted regions, and the greater the area of MO within the infarct, the greater the decrease in myocardial strain. Not only was strain decreased in infarcted areas but also in regions adjacent to the infarct with normal perfusion.

Peak systolic circumferential strain measured by SENC is able to differentiate non-transmural from transmural infarcted myocardium with high sensitivity and specificity correlating well with tagging in acute MI [63].

Viability

Assessment of viability is important in the management of ischemic heart disease because revascularization of dysfunctional but viable myocardium can improve function and survival. Traditionally, viability can be assessed through the evaluation of mechanical function (dobutamine echocardiography) or perfusion and metabolism (SPECT and PET). CMR has been developed to also evaluate mechanical function (dobutamine CMR +/− tagging) or perfusion and metabolism (contrast CMR and spectroscopic analysis) in addition to delayed enhancement to assess myocardial viability.

Low-dose dobutamine echocardiography is an established method for the detection of viability. As with dobutamine echocardiography, dobutamine CMR can similarly detect increased function in dysfunctional but viable myocardium. When compared to PET, dobutamine CMR correlates well, with a sensitivity of 88% and a specificity of 87% [64]. Sayad et al. described quantitation of left ventricular wall thickening using CMR with myocardial tagging in patients with segmental wall abnormalities at rest [65]. Each subject underwent CMR scanning with low-dose dobutamine infusion (up to 10 μg/kg/min) at baseline and 4–8 weeks after revascularization. Using CMR with tagging, resting end-diastolic and end-systolic wall thicknesses in abnormal segments at rest were compared with those measured at peak dobutamine and again after revascularization. It was found that end-systolic wall thickness after low-dose dobutamine infusion predicted improvement in segmental function after revascularization. Alternatively, segments with a resting end-systolic wall thickness of <7 mm did not improve after revascularization [65]. 3D myocardial strain analysis using tagging with low-dose dobutamine can also be used to differentiate viable from nonviable myocardium. While at rest, circumferential strain was decreased compared to controls in both the viable and nonviable segments. When compared with resting images, dobutamine stress imaging resulted in an increase in circumferential strain in the viable segments and no change in the nonviable segments [66].

Dobutamine CMR with myocardial tagging can also be used in the setting of revascularized acute myocardial infarction to predict recovery of function. Geskin et al. performed tagged dobutamine CMR studies in 20 patients within an average of 4 days after infarction with revascularization [67]. At approximately 8 weeks, a CMR without dobutamine was performed to assess for recovery of function. Those patients with a normal intramyocardial circumferential segment shortening on the initial study had greater recovery of function on the follow-up CMR.

Hypertrophic Cardiomyopathy

Hypertrophic cardiomyopathy (HCM), an autosomal dominant genetic disease caused by a defect in one of a number of genes of the sarcomere, is characterized by left ventricular hypertrophy and myofibrillar disarray. There are many morphological variants, and frequently the pattern of hypertrophy is asymmetrical. Histologically, patients often have patchy areas of fibrosis, which may be visualized as areas of delayed enhancement [68].

To further characterize contractile function in HCM, Young et al. [69] performed a strain analysis on 2D SPAMM tagging CMR images from 7 HCM and 12 normal volunteers. A 3D finite element model was used to associate the short-axis and long-axis data. On a regional level, strain analysis revealed that circumferential shortening was reduced in the entire septum and most other regions in the HCM patients when compared to the normal controls. While contractile function was reduced, left ventricular torsion in the HCM group was increased by approximately 5° [69].

Similarly, Kramer et al. [70] found prominent regional heterogeneity using 2D tagging in cardiac function in 10 HCM patients with a predominant pattern of asymmetric septal hypertrophy vs. normal subjects. While circumferential shortening was less in the septal, inferior, and anterior walls, it was not significantly different in the lateral wall. At all short-axis levels, circumferential shortening was decreased in HCM, and longitudinal shortening was markedly reduced at the basal septum [70]. A number of reports also describe the association of decreased myocardial strain with areas of delayed enhancement using tagging [71] or feature tracking [72].

Not surprisingly, diastolic function is also abnormal in HCM. Ennis et al. [73] studied eight patients with HCM and found that, in addition to decreased systolic strain, regional diastolic strain was reduced as well. The patients had decreased early diastolic strain rates, indicative of a prolonged early filling phase. The strain rate was then seen to increase during mid-diastole, signifying a continued slow filling phase and abnormal relaxation throughout diastole.

On many levels, HCM appears to be a heterogeneous process, with regional variability in the degree of wall thickness, the pattern of delayed enhancement, and contractile function.

Pressure Overload Left Ventricular Hypertrophy

Patients often develop concentric left ventricular hypertrophy (LVH) as a result of disorders associated with elevated afterload, such as systemic hypertension or aortic stenosis. Compensatory hypertrophy may also lead to contractile dysfunction. Palmon et al. [74] studied 30 patients with hypertension and concentric LVH using SPAMM tagging to more accurately quantitate regional contractile function. Circumferential and longitudinal shortening was depressed by approximately 5–10% when compared to normal volunteers. Unlike the normal volunteers, patients with hypertensive LVH had regional variability with the greatest circumferential shortening occurring in the lateral wall and the least shortening occurring inferiorly.

Patients with concentric LVH and preserved systolic function in large cohort studies such as MESA (Multi-Ethnic Study of Atherosclerosis) were evaluated with CMR. Rosen et al. [75] analyzed tagged CMR studies in 441 such patients with the HARP analysis method and found that, as with previous smaller trials, left ventricular systolic strain was decreased. This reduction in strain had regional variability with a more pronounced effect in the LAD distribution. In another analysis of the MESA patients, Edvardsen et al. [76] studied 218 patients with concentric LVH and found no difference in systolic strain between the LVH patients and the normal controls but found a noticeable difference in diastolic function where the LVH patients had significantly reduced regional diastolic strain rates signifying a more prolonged and slower diastolic relaxation.

Dilated Cardiomyopathy

In the endocardium, both fiber and cross-fiber shortening are greatly reduced in dilated cardiomyopathy (DCM) [77]. Myocardial strain analysis has allowed assessment of mechanical dyssynchrony in DCM which is a key predictor for responsiveness to LV pacing [78]. Regional heterogeneity has been demonstrated in DCM using tagging with the anteroseptum and inferoseptum as most affected segments and the inferolateral wall as the least affected segments as compared to normal [79, 80]. A great majority but not all patients with LBBB demonstrate systolic lengthening in the septum shown by myocardial tagging and consequently greater dyssynchrony compared to non-LBBB patients [81]. There is a decrease in systolic torsion magnitude in DCM in addition to discontinuing counter-clock rotation of the apex before end-systole [82].

Valvular Heart Disease

While the heart valves may be evaluated by CMR through direct visualization of the leaflets and quantification of regurgitation volume through phase contrast methods, the impact of ventricular remodeling with abnormal loading conditions can be best evaluated by CMR.

In the pressure overloaded state of severe aortic stenosis, there are contractile abnormalities as with hypertensive heart disease. Stuber et al. [83] reported in patients with aortic stenosis that torsion was significantly increased and diastole was delayed, as indicated by late peak diastolic untwisting. Similar results were reported by Nagel et al. [84] showing that maximal systolic torsion was increased in the aortic stenosis patients (from 8° to 14°) and that diastolic untwisting was delayed and prolonged. The abnormal pathologic changes associated with the high afterload state of aortic stenosis can actually be reversed, as demonstrated by Sandstede et al. [85] in their study of 12 patients with aortic

stenosis who underwent aortic valve replacement. Compared with eight healthy volunteers, the aortic stenosis patients prior to valve replacement had significantly higher torsion (25° compared to 14°). One year after surgery, the apical torsion had normalized to 16°.

Aortic regurgitation (AR), due to the increased volume and pressure load on the left ventricle, leads to left ventricular dilatation and eccentric hypertrophy. Optimal timing for surgery can be difficult to determine, as patients may remain relatively asymptomatic even as their left ventricle becomes markedly abnormal. The quantification of regional left ventricular function using tagged CMR could potentially detect subtle changes in myocardial function, which could herald the need to replace the aortic valve prior to the development of irreversible LV dysfunction. However, the results of myocardial strain in chronic AR patients are less than useful. Ungacta et al. [86] studied six patients with chronic severe aortic insufficiency using tagging pre and post AVR and showed no difference in various contractile parameters such as global circumferential shortening or radial thickening compared to controls. The postsurgery study 5 months later also showed no significant difference in overall circumferential shortening or radial thickening despite a decrease in LV volume and a return to a more normal ventricular geometry as compared to controls. On a regional basis, however, posterior wall strain was reduced [86]. In a later study of 14 chronic AR patients, [87] the pre-surgery strain was not different compared to controls. At 28 ± 11 months of follow-up post AVR, 3D minimum principal, longitudinal, and circumferential strain were decreased as compared to controls.

Severe mitral regurgitation (MR) can result in abnormal myocardial contractile function, despite having normal global parameters such as ejection fraction. Mankad et al. [88] studied regional strain in seven patients with severe mitral regurgitation before surgery and again approximately 8 weeks after surgery. Prior to surgery, maximum strain (similar to radial thickening) was increased compared to normal and became even greater after surgery. Prior to surgery, minimum strain (comparable to circumferential shortening) was decreased compared to normal and further declined after surgery. Heterogeneity of myocardial longitudinal and circumferential strains are also demonstrated in chronic MR, shown as decreased strain in the LV septum and increased strain in the LV lateral wall in 15 patients with asymptomatic chronic severe MR [89].

Pericardial Disease

The pericardium can be well visualized with CMR, despite having an average thickness of 1.5–2 mm [90]. Differentiating between constrictive pericarditis and restrictive cardiomyopathy can often be difficult; CMR adds additional information in these cases. In addition to more clearly defining the anatomic structure of the pericardium through standard cine CMR imaging, tagged CMR allows the interpreter to discern whether the pericardium is adhered to the heart [91]. In normal hearts, the pericardium and the underlying heart move independently, where the underlying myocardium twists and the overlying pericardium does not (a relative "sliding" motion of the visceral and parietal pericardium). This can be visualized by using 1D- or 2D-tagged CMR. At end-diastole the tag lines cross both the pericardium and myocardium, and with systole, the visceral pericardial/myocardial tags move together and become displaced relative to the parietal pericardium and its tags in normal hearts. In cases of constriction, since the parietal pericardium is often adhered to the underlying visceral pericardium/myocardium, no sliding motion occurs, and the parietal pericardial tags remain aligned, and move and deform with, the visceral pericardium/myocardium and the associated tag lines. It is important to remember that constriction is a complex diagnosis and that the presence of pericardial adhesion(s) alone is not pathognomonic for the diagnosis.

Right Ventricular Function

The ability to accurately assess global and regional right ventricular (RV) function is very valuable in the study of diseases affecting the RV such as pulmonary hypertension, congenital heart disease, and arrhythmogenic RV dysplasia/cardiomyopathy (ARVD/C).

Fayad et al. [51] showed that in normal patients, RV regional shortening was not uniform, and in the pulmonary hypertension patients, both short- and long-axis regional shortening was decreased, most prominently in the RV outflow tract and the basal septum. In 21 patients with pulmonary arterial hypertension (PAH), high temporal resolution (14 ms) tagging MRI was performed, and Marcus et al. showed that there is left-to-right delay caused by lengthening of the duration of RV shortening, which is correlated with leftward septal bowing and decreased LV filling [92]. Voeller et al. further investigated RV strain change as a response to mild pressure overload versus severe pressure overload before the occurrence of RV dilation in a canine model [93]. They demonstrated that in mild RV pressure overload, there was no change in RV strain or function as compared to severe RV pressure overload, where there was a significant decrease in RV circumferential strain, with RV filling became dependent on the RV conduit function [93].

Bomma et al. [94] studied global and regional right and left ventricular function in patients with ARVD/C and found that global RV systolic function was reduced and RV volumes were increased in these patients as compared to controls. Both of these findings were more pronounced

toward the base of the RV. Tandri et al. [95] performed assessment of regional RV function in 20 patients with idiopathic right ventricular outflow tract (RVOT) tachycardia and found no difference in global and regional parameters as compared to controls. These results argue against the hypothesis that RVOT tachycardia may be an early form of ARVD/C.

In congenital heart disease, tagged CMR may provide a more quantitative approach to assessment of ventricular function that could permit more precise titration of medications or choice of surgical approaches based on long-term functional measures [96]. In a recent report of 372 patients with repaired tetralogy of Fallot, LV circumferential strain and RV longitudinal strain using feature tracking from cine images emerged as predictors of adverse outcome, independent of QRS duration, ejection fraction, ventricular volumes, New York Heart Association class, and peak oxygen uptake [97].

Conclusions

CMR methods are powerful tools for noninvasive assessment of regional left and right ventricular function. As modern cardiovascular care involves more difficult decision-making, the need exists for a greater understanding of the complex three-dimensional contractile patterns of both ventricles. An integrated knowledge of the effects of through-plane motion, torsional displacement, and strain measurements independent of incident ultrasound beam angle are only a few of the advances that modern CMR techniques have provided. The clinical applications for these methods continue to expand. Evaluation of cardiomyopathies, myocardial viability, ventricular remodeling, and assessment of patients for resynchronization therapy are examples of disorders where CMR has elucidated a new understanding of the mechanisms underlying these processes. More rapid acquisition and analysis methods, some of which are nearing clinical use, will further expand the clinical utility of these tools. The emergence of feature tracking techniques on cine CMR holds the potential to rapidly advance the application of myocardial regional assessment in heart diseases.

References

1. Holzapfel G. Nonlinear solid mechanics: a continuum approach for engineering. Chichester: Wiley; 2000.
2. Simpson RM, Keegan J, Firmin DN. MR assessment of regional myocardial mechanics. J Magn Reson Imaging. 2013;37(3):576–99.
3. Streeter DD Jr, Spotnitz HM, Patel DP, Ross J Jr, Sonnenblick EH. Fiber orientation in the canine left ventricle during diastole and systole. Circ Res. 1969;24(3):339–47.
4. LeGrice IJ, Smaill BH, Chai LZ, Edgar SG, Gavin JB, Hunter PJ. Laminar structure of the heart: ventricular myocyte arrangement and connective tissue architecture in the dog. Am J Phys. 1995;269(2 Pt 2):H571–82.
5. Schmid P, Jaermann T, Boesiger P, Niederer PF, Lunkenheimer PP, Cryer CW, et al. Ventricular myocardial architecture as visualised in postmortem swine hearts using magnetic resonance diffusion tensor imaging. Eur J Cardiothorac Surg. 2005;27(3):468–72.
6. Ingels NB Jr, Daughters GT 2nd, Stinson EB, Alderman EL, Miller DC. Three-dimensional left ventricular midwall dynamics in the transplanted human heart. Circulation. 1990;81(6):1837–48.
7. Arts T, Hunter WC, Douglas AS, Muijtjens AM, Corsel JW, Reneman RS. Macroscopic three-dimensional motion patterns of the left ventricle. Adv Exp Med Biol. 1993;346:383–92.
8. Ratcliffe MB, Gupta KB, Streicher JT, Savage EB, Bogen DK, Edmunds LH Jr. Use of sonomicrometry and multidimensional scaling to determine the three-dimensional coordinates of multiple cardiac locations: feasibility and initial implementation. IEEE Trans Biomed Eng. 1995;42(6):587–98.
9. Gorman JH 3rd, Gupta KB, Streicher JT, Gorman RC, Jackson BM, Ratcliffe MB, et al. Dynamic three-dimensional imaging of the mitral valve and left ventricle by rapid sonomicrometry array localization. J Thorac Cardiovasc Surg. 1996;112(3):712–26.
10. Wang H, Amini AA. Cardiac motion and deformation recovery from MRI: a review. IEEE Trans Med Imaging. 2012;31(2):487–503.
11. Ibrahim E-SH. Myocardial tagging by cardiovascular magnetic resonance: evolution of techniques – pulse sequences, analysis algorithms, and applications. J Cardiovasc Magn Reson. 2011;13:36.
12. Zerhouni EA, Parish DM, Rogers WJ, Yang A, Shapiro EP. Human heart: tagging with MR imaging – a method for noninvasive assessment of myocardial motion. Radiology. 1988;169(1):59–63.
13. Axel L, Dougherty L. MR imaging of motion with spatial modulation of magnetization. Radiology. 1989;171(3):841–5.
14. Xu C, Pilla JJ, Isaac G, Gorman JH 3rd, Blom AS, Gorman RC, et al. Deformation analysis of 3D tagged cardiac images using an optical flow method. J Cardiovasc Magn Reson. 2010;12:19.
15. Prince JL, McVeigh ER. Motion estimation from tagged MR image sequences. IEEE Trans Med Imaging. 1992;11(2):238–49.
16. Gupta SN, Prince J. On variable brightness optical flow for tagged MRI. Information Processing in Medical Imaging. 1995. p. 323–34.
17. Chandrashekara R, Mohiaddin RH, Rueckert D. Analysis of 3-D myocardial motion in tagged MR images using nonrigid image registration. IEEE Trans Med Imaging. 2004;23(10):1245–50.
18. Kerwin WS, Prince JL. Cardiac material markers from tagged MR images. Med Image Anal. 1998;2(4):339–53.
19. Amini AA, Chen Y, Elayyadi M, Radeva P. Tag surface reconstruction and tracking of myocardial beads from SPAMM-MRI with parametric B-spline surfaces. IEEE Trans Med Imaging. 2001;20(2):94–103.
20. Chen T, Wang X, Chung S, Metaxas D, Axel L. Automated 3D motion tracking using Gabor filter bank, robust point matching, and deformable models. IEEE Trans Med Imaging. 2010;29(1):1–11.
21. Osman NF, Kerwin WS, McVeigh ER, Prince JL. Cardiac motion tracking using CINE harmonic phase (HARP) magnetic resonance imaging. Magn Reson Med. 1999;42(6):1048–60.
22. Osman NF, McVeigh ER, Prince JL. Imaging heart motion using harmonic phase MRI. IEEE Trans Med Imaging. 2000;19(3):186–202.
23. Sampath S, Prince JL. Automatic 3D tracking of cardiac material markers using slice-following and harmonic-phase MRI. Magn Reson Imaging. 2007;25(2):197–208.
24. Arts T, Prinzen FW, Delhaas T, Milles JR, Rossi AC, Clarysse P. Mapping displacement and deformation of the heart with local sine-wave modeling. IEEE Trans Med Imaging. 2010;29(5):1114–23.
25. Lima JA, Jeremy R, Guier W, Bouton S, Zerhouni EA, McVeigh E, et al. Accurate systolic wall thickening by nuclear magnetic

resonance imaging with tissue tagging: correlation with sonomicrometers in normal and ischemic myocardium. J Am Coll Cardiol. 1993;21(7):1741–51.
26. Yeon SB, Reichek N, Tallant BA, Lima JA, Calhoun LP, Clark NR, et al. Validation of in vivo myocardial strain measurement by magnetic resonance tagging with sonomicrometry. J Am Coll Cardiol. 2001;38(2):555–61.
27. Young AA, Axel L, Dougherty L, Bogen DK, Parenteau CS. Validation of tagging with MR imaging to estimate material deformation. Radiology. 1993;188(1):101–8.
28. Moore CC, Reeder SB, McVeigh ER. Tagged MR imaging in a deforming phantom: photographic validation. Radiology. 1994;190(3):765–9.
29. Fischer SE, McKinnon GC, Maier SE, Boesiger P. Improved myocardial tagging contrast. Magn Reson Med. 1993;30(2):191–200.
30. Park J, Metaxas DN, Axel L, Yuan Q, Blom AS. Cascaded MRI-SPAMM for LV motion analysis during a whole cardiac cycle. Int J Med Inform. 1999;55(2):117–26.
31. Aletras AH, Ding S, Balaban RS, Wen H. DENSE: displacement encoding with stimulated echoes in cardiac functional MRI. J Magn Reson. 1999;137(1):247–52.
32. Feng L, Donnino R, Babb J, Axel L, Kim D. Numerical and in vivo validation of fast cine displacement-encoded with stimulated echoes (DENSE) MRI for quantification of regional cardiac function. Magn Reson Med. 2009;62(3):682–90.
33. Neizel M, Lossnitzer D, Korosoglou G, Schaufele T, Lewien A, Steen H, et al. Strain-encoded (SENC) magnetic resonance imaging to evaluate regional heterogeneity of myocardial strain in healthy volunteers: comparison with conventional tagging. J Magn Reson Imaging. 2009;29(1):99–105.
34. Bryant DJ, Payne JA, Firmin DN, Longmore DB. Measurement of flow with NMR imaging using a gradient pulse and phase difference technique. J Comput Assist Tomogr. 1984;8(4):588–93.
35. Pelc LR, Sayre J, Yun K, Castro LJ, Herfkens RJ, Miller DC, et al. Evaluation of myocardial motion tracking with cine-phase contrast magnetic resonance imaging. Investig Radiol. 1994;29(12):1038–42.
36. Paul J, Wundrak S, Bernhardt P, Rottbauer W, Neumann H, Rasche V. Self-gated tissue phase mapping using golden angle radial sparse SENSE. Magn Reson Med. 2016;75(2):789–800.
37. Schuster A, Kutty S, Padiyath A, Parish V, Gribben P, Danford DA, et al. Cardiovascular magnetic resonance myocardial feature tracking detects quantitative wall motion during dobutamine stress. J Cardiovasc Magn Reson. 2011;13:58.
38. Veress A, Weiss J, Rabbitt R, Lee J, Gullberg J. Measurement of 3D left ventricular strains during diastole using image warping and untagged MRI images. IEEE Comput Cardiol. 2001:165–8.
39. Sinusas AJ, Papademetris X, Constable RT, Dione DP, Slade MD, Shi P, et al. Quantification of 3-D regional myocardial deformation: shape-based analysis of magnetic resonance images. Am J Physiol Heart Circ Physiol. 2001;281(2):H698–714.
40. Hor KN, Gottliebson WM, Carson C, Wash E, Cnota J, Fleck R, et al. Comparison of magnetic resonance feature tracking for strain calculation with harmonic phase imaging analysis. JACC Cardiovasc Imaging. 2010;3(2):144–51.
41. Lu JC, Connelly JA, Zhao L, Agarwal PP, Dorfman AL. Strain measurement by cardiovascular magnetic resonance in pediatric cancer survivors: validation of feature tracking against harmonic phase imaging. Pediatr Radiol. 2014;44(9):1070–6.
42. Morton G, Schuster A, Jogiya R, Kutty S, Beerbaum P, Nagel E. Inter-study reproducibility of cardiovascular magnetic resonance myocardial feature tracking. J Cardiovasc Magn Reson. 2012;14:43.
43. Maret E, Todt T, Brudin L, Nylander E, Swahn E, Ohlsson JL, et al. Functional measurements based on feature tracking of cine magnetic resonance images identify left ventricular segments with myocardial scar. Cardiovasc Ultrasound. 2009;7:53.
44. Kuetting DL, Dabir D, Homsi R, Sprinkart AM, Luetkens J, Schild HH, et al. The effects of extracellular contrast agent (Gadobutrol) on the precision and reproducibility of cardiovascular magnetic resonance feature tracking. J Cardiovasc Magn Reson. 2016;18(1):30.
45. Schuster A, Stahnke VC, Unterberg-Buchwald C, Kowallick JT, Lamata P, Steinmetz M, et al. Cardiovascular magnetic resonance feature-tracking assessment of myocardial mechanics: Intervendor agreement and considerations regarding reproducibility. Clin Radiol. 2015;70(9):989–98.
46. Bistoquet A, Oshinski J, Skrinjar O. Left ventricular deformation recovery from cine MRI using an incompressible model. IEEE Trans Med Imaging. 2007;26(9):1136–53.
47. Clark NR, Reichek N, Bergey P, Hoffman EA, Brownson D, Palmon L, et al. Circumferential myocardial shortening in the normal human left ventricle. Assessment by magnetic resonance imaging using spatial modulation of magnetization. Circulation. 1991;84(1):67–74.
48. Fonseca CG, Oxenham HC, Cowan BR, Occleshaw CJ, Young AA. Aging alters patterns of regional nonuniformity in LV strain relaxation: a 3-D MR tissue tagging study. Am J Physiol Heart Circ Physiol. 2003;285(2):H621–30.
49. Oxenham HC, Young AA, Cowan BR, Gentles TL, Occleshaw CJ, Fonseca CG, et al. Age-related changes in myocardial relaxation using three-dimensional tagged magnetic resonance imaging. J Cardiovasc Magn Reson. 2003;5(3):421–30.
50. Hamdan A, Thouet T, Kelle S, Paetsch I, Gebker R, Wellnhofer E, et al. Regional right ventricular function and timing of contraction in healthy volunteers evaluated by strain-encoded MRI. J Magn Reson Imaging. 2008;28(6):1379–85.
51. Fayad ZA, Ferrari VA, Kraitchman DL, Young AA, Palevsky HI, Bloomgarden DC, et al. Right ventricular regional function using MR tagging: normals versus chronic pulmonary hypertension. Magn Reson Med. 1998;39(1):116–23.
52. Klein SS, Graham TP Jr, Lorenz CH. Noninvasive delineation of normal right ventricular contractile motion with magnetic resonance imaging myocardial tagging. Ann Biomed Eng. 1998;26(5):756–63.
53. Azhari H, Weiss JL, Rogers WJ, Siu CO, Shapiro EP. A noninvasive comparative study of myocardial strains in ischemic canine hearts using tagged MRI in 3-D. Am J Phys. 1995;268(5 Pt 2):H1918–26.
54. Denisova O, Shapiro EP, Weiss JL, Azhari H. Localization of ischemia in canine hearts using tagged rotated long axis MR images, endocardial surface stretch and wall thickening. Magn Reson Imaging. 1997;15(9):1037–43.
55. Kuijpers D, Ho KY, van Dijkman PR, Vliegenthart R, Oudkerk M. Dobutamine cardiovascular magnetic resonance for the detection of myocardial ischemia with the use of myocardial tagging. Circulation. 2003;107(12):1592–7.
56. Korosoglou G, Lossnitzer D, Schellberg D, Lewien A, Wochele A, Schaeufele T, et al. Strain-encoded cardiac MRI as an adjunct for dobutamine stress testing: incremental value to conventional wall motion analysis. Circ Cardiovasc Imaging. 2009;2(2):132–40.
57. Korosoglou G, Lehrke S, Wochele A, Hoerig B, Lossnitzer D, Steen H, et al. Strain-encoded CMR for the detection of inducible ischemia during intermediate stress. JACC Cardiovasc Imaging. 2010;3(4):361–71.
58. Kido T, Nagao M, Kurata A, Miyagawa M, Ogimoto A, Mochizuki T. Stress/rest circumferential strain in non-ischemia, ischemia, and infarction – quantification by 3 Tesla tagged magnetic resonance imaging. Circ J. 2013;77(5):1235–41.
59. Bogaert J, Bosmans H, Maes A, Suetens P, Marchal G, Rademakers FE. Remote myocardial dysfunction after acute anterior myocardial infarction: impact of left ventricular shape on regional function: a

magnetic resonance myocardial tagging study. J Am Coll Cardiol. 2000;35(6):1525–34.
60. Marcus JT, Gotte MJ, Van Rossum AC, Kuijer JP, Heethaar RM, Axel L, et al. Myocardial function in infarcted and remote regions early after infarction in man: assessment by magnetic resonance tagging and strain analysis. Magn Reson Med. 1997;38(5):803–10.
61. Gotte MJ, van Rossum AC, Marcus JT, Kuijer JP, Axel L, Visser CA. Recognition of infarct localization by specific changes in intramural myocardial mechanics. Am Heart J. 1999;138(6 Pt 1):1038–45.
62. Gerber BL, Rochitte CE, Melin JA, McVeigh ER, Bluemke DA, Wu KC, et al. Microvascular obstruction and left ventricular remodeling early after acute myocardial infarction. Circulation. 2000;101(23):2734–41.
63. Neizel M, Lossnitzer D, Korosoglou G, Schaufele T, Peykarjou H, Steen H, et al. Strain-encoded MRI for evaluation of left ventricular function and transmurality in acute myocardial infarction. Circ Cardiovasc Imaging. 2009;2(2):116–22.
64. Baer FM, Voth E, Schneider CA, Theissen P, Schicha H, Sechtem U. Comparison of low-dose dobutamine-gradient-echo magnetic resonance imaging and positron emission tomography with [18F] fluorodeoxyglucose in patients with chronic coronary artery disease. A functional and morphological approach to the detection of residual myocardial viability. Circulation. 1995;91(4):1006–15.
65. Sayad DE, Willett DL, Hundley WG, Grayburn PA, Peshock RM. Dobutamine magnetic resonance imaging with myocardial tagging quantitatively predicts improvement in regional function after revascularization. Am J Cardiol. 1998;82(9):1149–51. A10
66. Bree D, Wollmuth JR, Cupps BP, Krock MD, Howells A, Rogers J, et al. Low-dose dobutamine tissue-tagged magnetic resonance imaging with 3-dimensional strain analysis allows assessment of myocardial viability in patients with ischemic cardiomyopathy. Circulation. 2006;114(1 Suppl):I33–6.
67. Geskin G, Kramer CM, Rogers WJ, Theobald TM, Pakstis D, Hu YL, et al. Quantitative assessment of myocardial viability after infarction by dobutamine magnetic resonance tagging. Circulation. 1998;98(3):217–23.
68. Choudhury L, Mahrholdt H, Wagner A, Choi KM, Elliott MD, Klocke FJ, et al. Myocardial scarring in asymptomatic or mildly symptomatic patients with hypertrophic cardiomyopathy. J Am Coll Cardiol. 2002;40(12):2156–64.
69. Young AA, Kramer CM, Ferrari VA, Axel L, Reichek N. Three-dimensional left ventricular deformation in hypertrophic cardiomyopathy. Circulation. 1994;90(2):854–67.
70. Kramer CM, Reichek N, Ferrari VA, Theobald T, Dawson J, Axel L. Regional heterogeneity of function in hypertrophic cardiomyopathy. Circulation. 1994;90(1):186–94.
71. Kim YJ, Choi BW, Hur J, Lee HJ, Seo JS, Kim TH, et al. Delayed enhancement in hypertrophic cardiomyopathy: comparison with myocardial tagging MRI. J Magn Reson Imaging. 2008;27(5):1054–60.
72. Bogarapu S, Puchalski MD, Everitt MD, Williams RV, Weng HY, Menon SC. Novel cardiac magnetic resonance feature tracking (CMR-FT) analysis for detection of myocardial fibrosis in pediatric hypertrophic cardiomyopathy. Pediatr Cardiol. 2016;37(4):663–73.
73. Ennis DB, Epstein FH, Kellman P, Fananapazir L, McVeigh ER, Arai AE. Assessment of regional systolic and diastolic dysfunction in familial hypertrophic cardiomyopathy using MR tagging. Magn Reson Med. 2003;50(3):638–42.
74. Palmon LC, Reichek N, Yeon SB, Clark NR, Brownson D, Hoffman E, et al. Intramural myocardial shortening in hypertensive left ventricular hypertrophy with normal pump function. Circulation. 1994;89(1):122–31.
75. Rosen BD, Edvardsen T, Lai S, Castillo E, Pan L, Jerosch-Herold M, et al. Left ventricular concentric remodeling is associated with decreased global and regional systolic function: the Multi-Ethnic Study of Atherosclerosis [see comment]. Circulation. 2005;112(7):984–91.
76. Edvardsen T, Rosen BD, Pan L, Jerosch-Herold M, Lai S, Hundley WG, et al. Regional diastolic dysfunction in individuals with left ventricular hypertrophy measured by tagged magnetic resonance imaging – the Multi-Ethnic Study of Atherosclerosis (MESA). Am Heart J. 2006;151(1):109–14.
77. MacGowan GA, Shapiro EP, Azhari H, Siu CO, Hees PS, Hutchins GM, et al. Noninvasive measurement of shortening in the fiber and cross-fiber directions in the normal human left ventricle and in idiopathic dilated cardiomyopathy. Circulation. 1997;96(2):535–41.
78. Nelson GS, Curry CW, Wyman BT, Kramer A, Declerck J, Talbot M, et al. Predictors of systolic augmentation from left ventricular preexcitation in patients with dilated cardiomyopathy and intraventricular conduction delay. Circulation. 2000;101(23):2703–9.
79. Young AA, Dokos S, Powell KA, Sturm B, McCulloch AD, Starling RC, et al. Regional heterogeneity of function in nonischemic dilated cardiomyopathy. Cardiovasc Res. 2001;49(2):308–18.
80. Joseph S, Moazami N, Cupps BP, Howells A, Craddock H, Ewald G, et al. Magnetic resonance imaging-based multiparametric systolic strain analysis and regional contractile heterogeneity in patients with dilated cardiomyopathy. J Heart Lung Transplant. 2009;28(4):388–94.
81. Han Y, Chan J, Haber I, Peters DC, Zimetbaum PJ, Manning WJ, et al. Circumferential myocardial strain in cardiomyopathy with and without left bundle branch block. J Cardiovasc Magn Reson. 2010;12:2.
82. Kanzaki H, Nakatani S, Yamada N, Urayama S, Miyatake K, Kitakaze M. Impaired systolic torsion in dilated cardiomyopathy: reversal of apical rotation at mid-systole characterized with magnetic resonance tagging method. Basic Res Cardiol. 2006;101(6):465–70.
83. Stuber M, Scheidegger MB, Fischer SE, Nagel E, Steinemann F, Hess OM, et al. Alterations in the local myocardial motion pattern in patients suffering from pressure overload due to aortic stenosis. Circulation. 1999;100(4):361–8.
84. Nagel E, Stuber M, Burkhard B, Fischer SE, Scheidegger MB, Boesiger P, et al. Cardiac rotation and relaxation in patients with aortic valve stenosis [see comment]. Eur Heart J. 2000;21(7):582–9.
85. Sandstede JJW, Johnson T, Harre K, Beer M, Hofmann S, Pabst T, et al. Cardiac systolic rotation and contraction before and after valve replacement for aortic stenosis: a myocardial tagging study using MR imaging. AJR Am J Roentgenol. 2002;178(4):953–8.
86. Ungacta FF, Davila-Roman VG, Moulton MJ, Cupps BP, Moustakidis P, Fishman DS, et al. MRI-radiofrequency tissue tagging in patients with aortic insufficiency before and after operation. Ann Thorac Surg. 1998;65(4):943–50.
87. Pomerantz BJ, Wollmuth JR, Krock MD, Cupps BP, Moustakidis P, Kouchoukos NT, et al. Myocardial systolic strain is decreased after aortic valve replacement in patients with aortic insufficiency. Ann Thorac Surg. 2005;80(6):2186–92.
88. Mankad R, McCreery CJ, Rogers WJ Jr, Weichmann RJ, Savage EB, Reichek N, et al. Regional myocardial strain before and after mitral valve repair for severe mitral regurgitation. J Cardiovasc Magn Reson. 2001;3(3):257–66.
89. Maniar HS, Brady BD, Lee U, Cupps BP, Kar J, Wallace KM, et al. Early left ventricular regional contractile impairment in chronic mitral regurgitation occurs in a consistent, heterogeneous pattern. J Thorac Cardiovasc Surg. 2014;148(4):1694–9.
90. Bogaert J, Maes A, Van De WF, Bosmans H, Herregods MC, Nuyts J, et al. Functional recovery of subepicardial myocardial tissue in transmural myocardial infarction after successful reperfusion: an important contribution to the improvement of regional and global left ventricular function. Circulation. 1999;99(1):36–43.
91. Kojima S, Yamada N, Goto Y. Diagnosis of constrictive pericarditis by tagged cine magnetic resonance imaging. N Engl J Med. 1999;341(5):373–4.

92. Marcus JT, Gan CT, Zwanenburg JJ, Boonstra A, Allaart CP, Gotte MJ, et al. Interventricular mechanical asynchrony in pulmonary arterial hypertension: left-to-right delay in peak shortening is related to right ventricular overload and left ventricular underfilling. J Am Coll Cardiol. 2008;51(7):750–7.
93. Voeller RK, Aziz A, Maniar HS, Ufere NN, Taggar AK, Bernabe NJ Jr, et al. Differential modulation of right ventricular strain and right atrial mechanics in mild vs. severe pressure overload. Am J Physiol Heart Circ Physiol. 2011;301(6):H2362–71.
94. Bomma C, Dalal D, Tandri H, Prakasa K, Nasir K, Roguin A, et al. Regional differences in systolic and diastolic function in arrhythmogenic right ventricular dysplasia/cardiomyopathy using magnetic resonance imaging. Am J Cardiol. 2005;95(12):1507–11.
95. Tandri H, Bluemke DA, Ferrari VA, Bomma C, Nasir K, Rutberg J, et al. Findings on magnetic resonance imaging of idiopathic right ventricular outflow tachycardia. Am J Cardiol. 2004;94(11):1441–5.
96. Menteer J, Weinberg PM, Fogel MA. Quantifying regional right ventricular function in tetralogy of Fallot. J Cardiovasc Magn Reson. 2005;7(5):753–61.
97. Orwat S, Diller GP, Kempny A, Radke R, Peters B, Kuhne T, et al. Myocardial deformation parameters predict outcome in patients with repaired tetralogy of Fallot. Heart. 2016;102(3):209–15.

Techniques for MR Myocardial Perfusion Imaging

6

Michael Jerosch-Herold

Introduction

Outside the field of MRI, most techniques for myocardial perfusion imaging rely on the detection of injected tracers to assess myocardial blood flow and detect ischemia. Examples are tracers that emit gamma rays for single-photon emission tomography or tracers that scatter ultrasound waves, such as injected gas-filled bubbles. With MRI, blood-borne contrast agents can be used to assess myocardial perfusion. The presence of the contrast agent in tissue is detected through its effects on the local T1 and T2 relaxation times of 1H nuclei. An alternative approach for assessing myocardial perfusion without using an exogenous contrast agent relies on selectively "labeling" 1H spins and detecting the signal changes that are induced by tissue blood flow carrying "labeled" 1H spins in or out of an image slice. Though the absence on contrast agents makes arterial spin labeling an attractive proposition, its use is limited by the relatively small signal changes that need to be detected for quantifying myocardial perfusion. This chapter will focus foremost on contrast-enhanced perfusion imaging, as it remains the most widely used approach for myocardial perfusion imaging.

A paramagnetic contrast agent alters the T1 and T2/ T2* relaxation properties of 1H nuclei in its vicinity. If a contrast agent is injected as a bolus, then the relaxation properties of the blood and myocardial tissue vary with time and reflect the passage of the blood-borne contrast. The detection of the transit of the contrast agent through the coronary perfusion bed therefore relies on the use of MR pulse sequences that are sensitive to particular relaxation properties, either the transverse or the longitudinal relaxation with characteristic time constants, T2/ T2* and T1, respectively. For the heart, the preference for T1-weighted over T2*-weighted perfusion imaging is based on several factors: (1) T1-weighted perfusion imaging gives rise to positive signal enhancement during the first pass, rather than signal loss, and results in well-delineated cardiac structures during the first pass of the contrast bolus. The relatively large vascular volume in the myocardium compared to perfusion beds in other organs, and the relatively rapid leakage of many gadolinium-based contrast agents into the interstitial space result in sufficient T1-based contrast-to-noise during the first pass of a contrast agent. (2) T_2*-weighted perfusion imaging generally requires relatively long echo-times compared to T1-weighted techniques, and is therefore more sensitive than T_1-weighted imaging to susceptibility artifacts (e.g., from the bolus of contrast in the LV cavity during its first pass through the heart), magnetic field inhomogeneities, and flow or motion. T2*-weighted techniques are almost never used today for cardiac perfusion imaging.

An important limitation of MR cardiac perfusion imaging has been the incomplete spatial coverage of the heart, which is increasingly being overcome by imaging acceleration techniques. Imaging acceleration techniques are today crucial for enabling more complete coverage of the heart in cardiac perfusion studies. A substantial portion of this chapter will therefore be dedicated to imaging acceleration techniques for cardiac perfusion imaging.

Pulse Sequence Techniques

Pulse sequence techniques for myocardial perfusion imaging are generally designed to give a strongly T1-weighted signal. T1 weighting (and only a weak dependence on T2 or T2*) is achieved in myocardial perfusion imaging by preceding the image read-out by a magnetization preparation, either in the form of a magnetization inversion or a magnetization saturation. A magnetization preparation allows to tune the T1-weighting to the range of T1 times that occur during the first pass of a contrast bolus, compared to primarily relying on the repetition time (TR) and flip angle in the image read-out.

M. Jerosch-Herold (✉)
Brigham and Women's Hospital, Harvard Medical School, Boston, MA, USA
e-mail: mjerosch-herold@bwh.harvard.edu

R. Y. Kwong et al. (eds.), *Cardiovascular Magnetic Resonance Imaging*, Contemporary Cardiology,
https://doi.org/10.1007/978-1-4939-8841-9_6

The image acquisition needs to be performed as rapidly as possible, and for this reason, a magnetization preparation is combined with a "single-shot" image read-out. The term "single shot" refers here to performing all image encoding steps in rapid succession (i.e., with short echo and repetition times) as a single block after a magnetization preparation. Various forms of image read-out are being used, depending on field strength and MRI scanner hardware (e.g., speed of gradient system). Common choices are gradient-echo imaging with or without steady-state free precession and using different forms of k-space trajectories, echo-planar imaging, and hybrids of these techniques.

Figure 6.1a shows images acquired in a patient during the first pass of a contrast agent bolus (0.03 mmol per kg body weight of Gd-DTPA) with a T1-weighted imaging gradient-echo fast low-angle single-shot (FLASH) technique with saturation preparation. Contrast enhancement is highest in the ventricular cavities, typically by a factor 4–5 compared to the myocardium when extracellular contrast agents are used. The curves in Fig. 6.1b show how the signal intensity changes during the course of the contrast transit, in myocardial regions and in the left ventricular blood pool.

With magnetization-prepared T_1-weighted perfusion imaging, the T1 weighting is effectively determined by the time interval between saturation or inversion preparation and the read-out of the low spatial frequencies (i.e., central k-space lines) during image acquisition. For the saturation-recovery preparation, the delay time before the beginning of the image read-out is generally only 10–20 ms, when a linear phase-encoding order is used for the image read-out, i.e., the time between the beginning of the image read-out and the acquisition of the central k-space lines gives additional time for saturation recovery. For an inversion recovery, one often needs to have a longer delay ("inversion time" TI) between inversion pulse and image read-out so that the signal intensity is close to null before contrast administration.

Figure 6.2 shows a comparison of the dependence of the FLASH signal on R1 (=1/T1) for three different forms of T1 weighting, namely, image acquisition without a magnetization preparation, and with a saturation recovery or inversion recovery preparations, respectively. (It is assumed that a couple of images were already acquired with a repetition rate corresponding to the heart rate, for reasons that will be clarified below.) The signal intensity was expressed as percentage

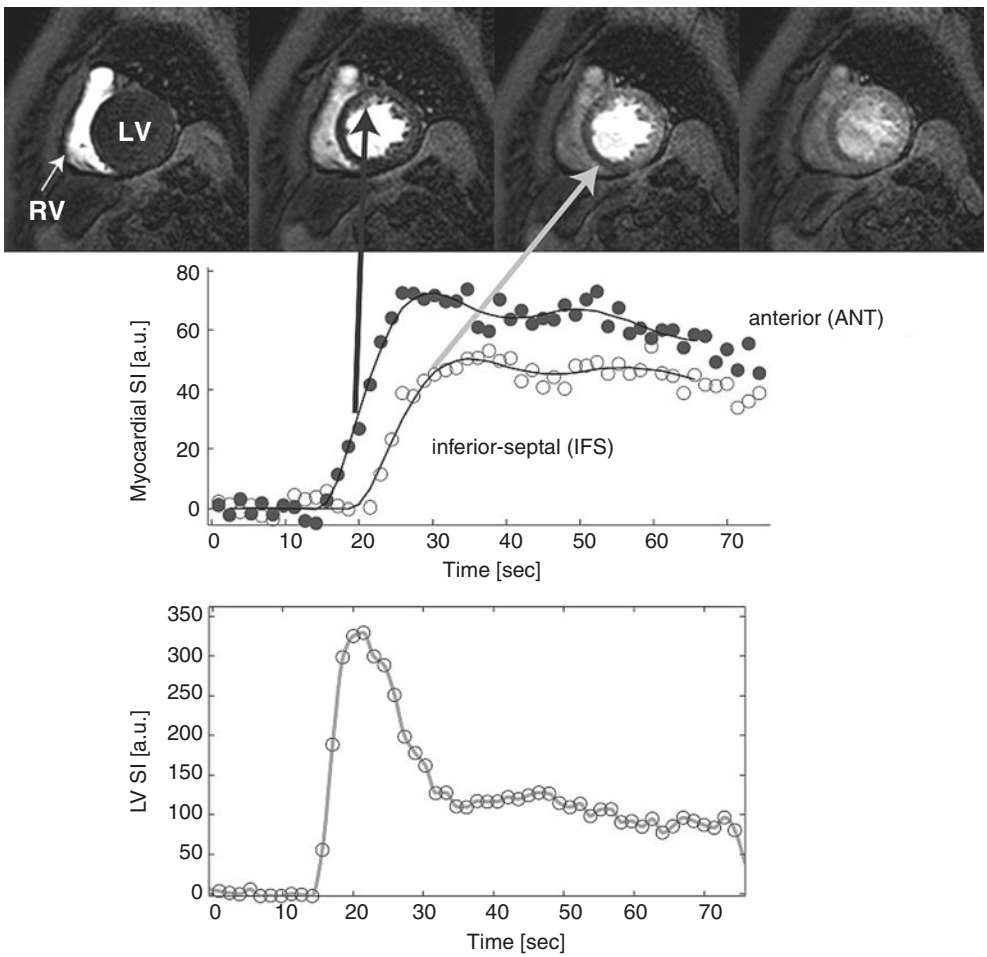

Fig. 6.1 The top row shows a subset of images collected in a patient during the first pass of an IV injected bolus of Gd-DTPA contrast (0.03 mmol/kg) on a 3 T scanner (Philips Intera) with a parallel imaging acceleration factor of 1.8. Contrast enhancement is first observed in the right ventricular (RV) cavity, then in the left ventricular (LV) cavity, and followed by myocardial contrast enhancement. This particular patient had a perfusion deficit in the inferior septum. Two signal intensity curves are shown in graph**,** which give the average signal intensity in an anterior and inferior septal myocardial sector in each acquired image. The SI curve for the inferior septal sector shows delayed contrast uptake, with a slower rate of enhancement and lower peak enhancement, than in the anterior sector

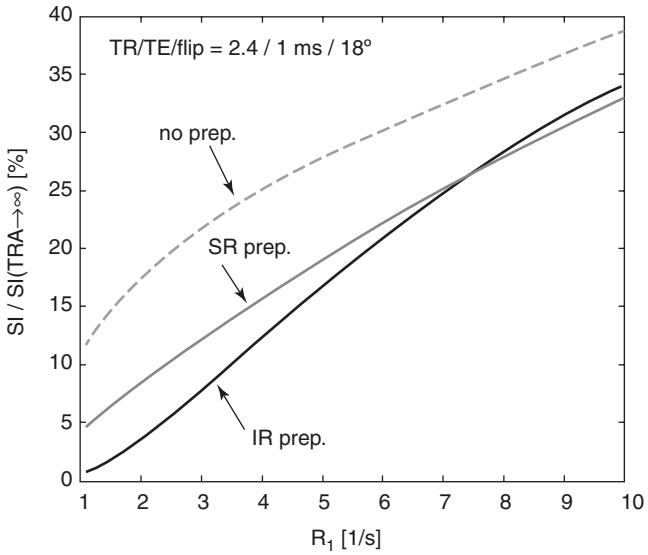

Fig. 6.2 The signal intensity measured with a fast gradient-echo read-out (TR/TE/flip = 2.4/1 ms/18°; 80 phase-encoding steps with linear ordering) was simulated for a range of R1 values and for three different acquisition schemes, with an inversion recovery (SR) preparation, an inversion recovery (IR) preparation, and without any magnetization preparation before the FLASH read-out. The range of R1 values corresponds roughly to R1 changes in the LV cavity that occur with the transit of a bolus of Gd-DTPA contrast at a dosage of 0.05 mmol per kg of body weight. The IR preparation gives the largest dynamic range for the SI changes, while the dynamic range is smallest when no magnetization preparation is used, and in this latter case, the relation between SI and R1 also deviates markedly from a linear relationship. TRA-time for repetition of image acquisitions; TR-time for repetition of radio-frequency pulses in image read-out; TE: time to echo

of the equilibrium signal intensity (i.e. the signal intensity when the time for repetition of image acquisitions becomes very long, or TRA →∞). The lowest R1 value in the graph (1 s^{-1}) is in the vicinity of the "native" T1 of the blood and myocardium, i.e., before any administration of a contrast agent. With a bolus of ~0.1 mmol of Gd-DTPA per kg of body weight, R1 can peak at values as high as 10–15 s^{-1} in the ventricular blood pool [1]. Over the range of R1 values from ~1 s^{-1} to 10 s^{-1}, a fast low-angle gradient-echo read-out with inversion recovery preparation shows the largest dynamic range for signal intensity (SI) changes, followed by the same type of image read-out with saturation recovery preparation, and finally the image read-out without any magnetization preparation. The pre-contrast signal is here lowest with the IR preparation, leading to high-contrast enhancement, defined as percent signal intensity increase during transit of a contrast bolus, relative to the pre-contrast signal. Visual perceptibility increases with the grayscale dynamic range. Percent contrast enhancement relative to the pre-contrast signal is often used as a metric to assess perceptibility of contrast enhancement in perfusion studies.

While the T1 rate constant (1/T1) in the blood is linearly proportional to the concentration of contrast agent, a similar approximately linear relationship between signal intensity (SI) and R1 or tracer concentration can be achieved with T1-weighted imaging only over a limited range of contrast concentrations. The linearity range can be tuned by adjusting the time after saturation (TS; time between saturation pulse and read-out of central k-space lines) or inversion (TI). A very short TS will result in a wider range of R1 values over which the relation of SI vs. R1 is approximately linear. But a wider linear range also implies that for a given change in R1, the resulting SI change is smaller, because the dynamic range has an upper limit that is set by the proton density-weighted SI. If we refer to the ratio of the change (Δ) in SI, for a given change of ΔR1 (ΔSI/(ΔR1) as R1 sensitivity, then a lower R1 sensitivity of the signal means that areas with reduced myocardial blood flow may be more difficult to detect, relative to normally perfused myocardium. Maintaining linearity for the signal changes during the first pass of the contrast agent has to be balanced against the requirement of good sensitivity for detection of hypoperfusion.

Although saturation of the magnetization reduces the T1 sensitivity compared to an inversion pulse, it has the distinct advantage that the T1 weighting is independent of any previous "history" of the 1H magnetization – the longitudinal magnetization component is nulled by the SR preparation. Myocardial perfusion imaging is in generally ECG-gated. As shown in Fig. 6.3, the magnetization does not fully recover between applications of the magnetization preparation for normal heart rates, because T1 is of the same order of magnitude as the duration of the cardiac cycle. With an IR preparation, the degree of magnetization inversion will depend on the degree to which the magnetization recovered in a previous heart interval, and this introduces a dependence of the signal intensity on heart rate. Fluctuations of the signal intensity are introduced by heart rate irregularities. This type of heart rate-dependent fluctuations can be avoided by using a magnetization saturation preparation [2]. Use of the saturation recovery preparation also lends itself well to use in multi-slice perfusion imaging [3] as illustrated in Fig. 6.4. Omission of the magnetization preparation results in poorer contrast enhancement, compared to the use of an IR or SR magnetization preparation, and is therefore rarely used for myocardial perfusion imaging.

Perfusion Imaging with Steady-State Free Precession

During gradient-echo imaging, the gradient pulses applied for slice selection, phase encoding, and gradient-echo generation and read-out result in a position-dependent phase of the transverse magnetization, which can be reversed by applying additional gradient pulses to refocus the transverse magnetization before the next radio-frequency pulse. Balancing the areas under the positive and negative gradient waveform lobes during each repetition interval (TR), combined with toggling of the radio-frequency excitation pulses between positive and

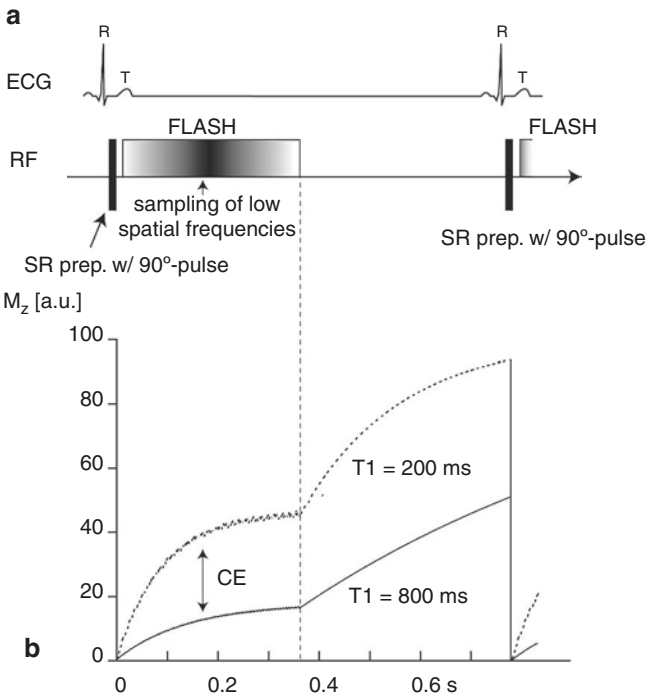

Fig. 6.3 (**a**) Illustrates a pulse sequence with a saturation recovery (SR) magnetization preparation applied after detection of the R wave on the ECG, followed by a fast, low-angle (single-) shot (FLASH) gradient-echo image acquisition with linear phase-encoding order. (**b**) Shows the evolution of the longitudinal magnetization after a saturation recovery magnetization preparation, followed by a fast gradient-echo read-out, and a period of undisturbed relaxation recovery. The rapid application of radio-frequency pulses during the image read-out alters the shape of the relaxation recovery, giving rise to a shorter effective T1* relaxation time constant, than for the undisturbed relaxation recovery. With a linear phase-encoding order, the overall image contrast, set by the timing for reading out low spatial frequencies ("low k-space"), corresponds approximately to the signal acquired in the middle of the image acquisition. The vertical line labeled "CE" shows the differences in signal for T1 = 200 ms and T1 = 800 ms at this midpoint of the image read-out. An advantage of the SR preparation is independence of contrast enhancement (CE), from the duration of the period of undisturbed relaxation, or the heart rate, as the longitudinal magnetization is reset to zero before each image read-out

negative flip angles (±α), results in steady-state free precession with minimal "spoiling" of transverse magnetization, except due to T2/T2* relaxation and off-resonance shifts. Most importantly, one overcomes the limitation of the Ernst angle and can use higher flip angles (α) than feasible with spoiled gradient-echo imaging to achieve a higher signal-to-noise ratio. A preparation consisting of a radio-frequency pulse with flip angle α/2 preceding by TR/2, the subsequent string of ±α-pulses with repetition time (TR) for the image acquisition, helps to attain the steady state more efficiently at the beginning of the image read-out. Fast imaging with steady-state precession (SSFP) produces a signal with weighting proportional to T2/T1 at a fixed flip angle: the SSFP signal increases with T2 and with 1/T1. It is therefore feasible to use SSFP for T1-weighted imaging of contrast enhancement. A limitation of SSFP is its susceptibility to produce dark banding on images. These dark bands are centered at off-resonance frequency shifts with a resultant phase shift over a repetition time (TR) equal to π/2, i.e., where the RF pulse at the end of a TR period will not transform transverse magnetization into longitudinal magnetization. The effect can be mitigated by shortening TR such that the phase shifts building up during a repetition time (TR) are considerably less than π/2 within the field of view or over the heart. For cardiac perfusion imaging, the appearance of banding artifacts can be exacerbated by the passage of a contrast bolus through the cardiac chambers, which can cause frequency shifts depending on how much the blood is loaded with gadolinium contrast. The effect can lead to measurable frequency shifts on the order of 50–100 Hz, with standard contrast dosages [4]. At field strengths of 3 Tesla and higher, SSFP read-outs generally lead to unacceptable image artifacts during bolus transit, and gradient-echo techniques are used predominantly without SSFP for perfusion imaging at 3 T or higher field strengths.

Perfusion Imaging Artifacts

Perfusion image artifacts, and in particular one type of artifact that occurs at the endocardial border in the form of a "dark rim," can significantly impair the diagnostic performance of myocardial perfusion imaging. The dark-rim artifact (DRA) has acquired particular notoriety because it can be mistaken for a narrow zone with reduced blood flow in the endocardial layer and lead to false-positive diagnosis of hypoperfusion. The origin of DRAs remains somewhat controversial as there are at least two competing mechanisms that can give rise to DRAs. One is tied to the limited number of Fourier-encoding steps that are performed during image acquisition, a limitation that applies in particular to the phase-encoding direction. Fourier reconstruction gives rise to an artifact at anatomical borders with sharp changes in signal intensity (e.g., between the LV blood pool and myocardium during the first pass of contrast), which manifests itself as an undershoot at the foot and an overshoot of the *reconstructed* signal at the top of a steplike signal change. This artifact is known as Gibbs ringing, in honor of the nineteenth-century American physicist Josiah Willard Gibbs who described its occurence as a result of Fourier reconstruction of a signal. In the case of myocardial perfusion imaging, such a sharp steplike jump in signal intensity occurs during peak contrast enhancement in the left ventricular cavity and before the myocardium has undergone appreciable contrast enhancement. The undershoot of the reconstructed signal at the LV cavity border can manifest itself as a "dark rim," and this artifact is most prominent at a border perpendicular to the phase-encoding direction, as the sampling density in the

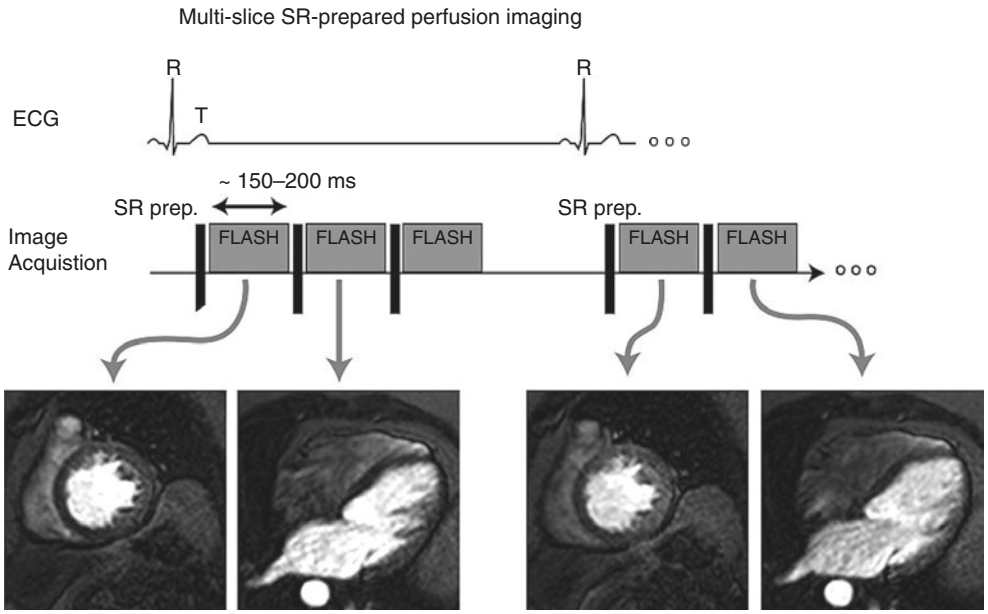

Fig. 6.4 The pulse sequence technique illustrated in Fig. 6.3 can easily be generalized to a multi-slice technique, as shown in this diagram. The saturation recovery (SR) preparation generally does only take 10–15 ms and can therefore be repeated for each slice, although it should preferably be slice non-selective, to avoid alteration of the T1 contrast in the blood pool due to inflow of "unprepared" spins. The image read-out, chosen in the above diagram to be a fast low-angle single-shot (FLASH) acquisition, can be replaced by different image read-out modules such as echo-planar acquisitions or spiral scanning. Nevertheless the FLASH read-out is one of the more robust approaches, allowing application over a relatively wide range of magnetic field strengths. Of note in the FLASH images in the bottom row is the absence of any banding artifacts despite intersecting slice planes, which is a benefit of the SR preparation, repeated here for each slice before acquiring the respective image

read-out direction is generally higher. (The under- and overshoot are of similar magnitude, but relative to the high signal intensity in the blood pool, the overshoot is not noticeable.)

DRAs may not be entirely due to Gibb's ringing and also be caused by intra-voxel dephasing of the magnetization at anatomical borders separating regions with different magnetic susceptibilities. What both possible mechanisms have in common is that they will tend to become more pronounced as one increases the injected contrast dosage. Intra-voxel dephasing will also tend to be more prominent when the voxel dimension in a given direction is larger, and therefore the preferential appearance of the dark-rim artifact perpendicular to the phase-encoding direction cannot be used as proof that it, rather than Gibbs ringing, is the culprit.

For perfusion imaging based on Cartesian k-space trajectories (i.e., parallel lines of data points are acquired in k-space), one can try to increase the number of phase encodings to reduce the appearance or prominence of DRAs. With the SSFP techniques, the appearance of subendocardial black "banding" artifacts during wash-in of contrast into the LV cavity is more frequently observed than with spoiled gradient-echo imaging, though with SSFP imaging, one generally can achieve higher in-plane resolution which makes the DRA less prominent. Switching to non-Cartesian k-space trajectories, like the one used for radial or spiral imaging, may be a more effective strategy to avoid DRAs [5].

Arterial Input Sampling

For a quantitative assessment of myocardial perfusion, one has to take into consideration the characteristics of the contrast agent injection. The kinetics of the transit of the contrast bolus through the LV cavity determines the rate of myocardial contrast enhancement. The myocardial contrast enhancement can be modeled as linear response to the arterial input of contrast, if the signal intensity in both the myocardial tissue and the blood pool changes linearly with contrast concentration. For the quantification of myocardial perfusion, one therefore needs to measure both the myocardial response and the arterial input [6].

Sampling of the arterial input is mostly performed in the LV cavity, simply because the cavity is always visible on views used for myocardial perfusion imaging, be they short or long axis views. In our experience, it is best to sample the arterial input in the LV near the base of the heart, i.e., close to the aortic outflow. In the LV cavity, the contrast enhancement is an order of magnitude higher than in the myocardium. Any saturation of the signal enhancement at higher-contrast agent concentrations is most likely to be observed in the blood pool and results in a "distorted" measurement of the arterial input. Signal saturation can be avoided by using low-contrast agent dosages on the order of 0.03–0.04 mmol per kg of body weight with fast gradient-

echo sequences (e.g., TR/TE/flip ~ 2 ms/1 ms/15–20° at 1.5 Tesla). Using low-contrast dosages decreases the myocardial contrast enhancement, and peak contrast-to-noise is in many respects the limiting factor in myocardial perfusion studies. Therefore new approaches are being sought to combine accurate arterial input sampling with optimal myocardial contrast enhancement.

Due to the relatively large dimensions of the cavity, it is in principle feasible to acquire images at low spatial resolution to sample the arterial input with a T1 weighting that minimizes signal saturation effects in the blood pool. Acquisition of low-resolution images for the sole purpose of sampling the arterial input allows one to use a very short time after saturation (TS) or time after inversion (TI) which extends the range of contrast concentrations over which the signal intensity changes approximately linearly with contrast concentration [7, 8]. Furthermore, if the arterial input is sampled with low spatial resolution, then the time penalty for acquiring additional images of the arterial input is within acceptable limits and approximately ~50 ms. This method of measuring the arterial input with a different T1 weighting than used for myocardial imaging is referred to as "dual-contrast" technique and is illustrated in Fig. 6.5.

An interesting variation on this approach was proposed by Köstler et al., for radial imaging [9]. In radial imaging low spatial frequencies are over-sampled, because the center of the spatial frequency space is traversed during each radial trajectory. One can exploit this to calculate low-resolution images, sufficient to depict the LV cavity, for multiple delays (TIs) after the initial magnetization preparation (e.g., a saturation pulse), and estimate R1 (i.e., 1/T1), which is linearly proportional to contrast concentration.

It should be mentioned that whatever magnetization preparation is used for T_1 weighting, it should at least, for the purpose of sampling the arterial input, be non-slice selective, to avoid that blood flow in the ventricular cavity sweeps the prepared magnetization out of the slice during the image read-out, which would undo the effects of the magnetization preparation. Also for the myocardium, a non-slice-selective magnetization preparation renders the signal intensity more insensitive to through-plane motion.

An alternative to arterial input sampling with the dual-contrast technique is the dual-bolus injection technique [10]. A small contrast dosage and a several-fold higher contrast dosage are injected consecutively, so that the contrast enhancement in the LV cavity and in the myocardium can be sampled separately under optimal conditions. With the assumption of hemodynamic stability, and by using equal injection volumes but different contrast agent dilutions, it is possible to use a scaled replica of the arterial input in the LV cavity, measured with the lower dosage bolus injection, to analyze the contrast enhancement in the myocardium, observed with a later higher-contrast agent dosage injection.

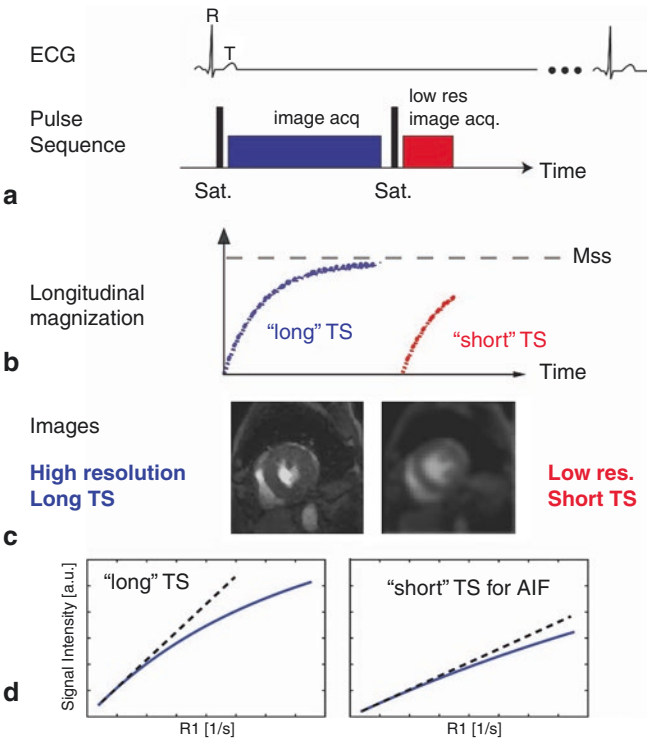

Fig. 6.5 (**a**) The dual-contrast perfusion imaging technique for quantitative perfusion imaging with separate sampling of the arterial input uses a pulse sequence with two types of image acquisition that are tuned to myocardial imaging (blue) and imaging of the contrast enhancement in the blood pool (red), respectively. For both image acquisitions, one uses a saturation pulse ("Sat.") for T1 weighting, but the images for blood pool imaging have a 2–3 times lower resolution and shorter acquisition time, which allows to have relatively short times after saturation (TS). Myocardial images are acquired for multiple slices, while the low-resolution blood pool images are generally only obtained for only one slice. The evolution of the longitudinal magnetization is shown for both cases in (**b**). The effective signal intensity in the image corresponds to the signal halfway during image acquisition when a linear phase-encoding order is used, and for the blood pool images, the resulting TS is much shorter than for the myocardial images. Representative images for analysis of myocardial and blood pool enhancements are shown in (**c**) and illustrate the difference in spatial resolution. This type of acquisition scheme results in smaller signal enhancement for the same change in R1 for the low-resolution images of the arterial input (AIF) with short TS, compared to the higher resolution images for analysis of myocardial enhancement (**d**). For the contrast concentrations in the blood pool, this means that the "AIF images" suffer from little signal saturation and allow more accurate sampling of the AIF, compared to using the "myocardial" images for AIF sampling

Recirculation of contrast after the first injection of the small dosage contrast bolus should be negligible when the second bolus is injected, which is easily attained by using widely different dilution ratios for the two injections (e.g., equivalent to 0.005 mmol/kg and 0.1 mmol/kg of Gd-DTPA), even if both injections are performed within 20–30 s of each other. The set-up of the injections for the dual-bolus technique requires some care, with the time between injections set to approximately 25 s [11].

Ultrafast Imaging Techniques

Besides the rather simple and robust approach of fast gradient-echo imaging, there are faster methods such as echo-planar imaging (EPI) [12], which can be used for very fast image acquisition in dynamic studies. Both techniques sample data in k-space on a Cartesian grid, but with single-shot (2D) echo-planar imaging, all signal samples are acquired after a single radio-frequency pulse excitation by using small gradient "notch" pulses to advance in the phase-encoding direction between the read-out of gradient echoes. This is in contrast to GRE imaging where only a single line of phase-encoded data ("k-space" line) is acquired after each radio-frequency excitation. With EPI the effective echo time that determines the T2* weighting is now set by the time between the radio-frequency excitation and the acquisition of the central k-space lines. (Though the nominal echo time, defined as the time from the RF excitation to the acquisition of the central phase-encoded line, may be quite short, the effective echo time is considerably longer and represents a weighted average of TEs for k-space lines.) Effective echo times for EPI or spiral imaging are not as short as for gradient-echo imaging. For this and other reasons, in cardiac perfusion imaging the acquisition of k-space lines after RF excitation is broken into segments to reduce the effective echo time and minimize artifacts from motion and field inhomogeneities [13]. These so-called hybrid EPI techniques have been successfully applied for myocardial perfusion imaging at lower field strengths and yield a higher signal-to-noise ratio than FLASH techniques [14].

Non-Cartesian K-Space Trajectories

Over the last decade, the use of non-Cartesian grid trajectories for k-space data sampling during signal acquisition, such as radial and spiral trajectories, has been shown to provide several advantages over Cartesian sampling, such as isotropic resolution in the image plane and the near or complete absence of dark-rim artifacts [5]. Another important advantage of radial and spiral imaging is tied to the development of iterative reconstruction algorithms which made it feasible to reduce the k-space sampling density (e.g., angular undersampling by reducing the number of projections acquired in a radial scan) in the outer regions of k-space below the Nyquist limit without leading to the types of "streaking" artifacts that would be observed with the more established forms of non-iterative projection reconstruction (Radon transform or Fourier transform after regridding of the k-space data onto a Cartesian grid). Iterative reconstruction is based on the idea that the reconstructed images should be as *consistent* as possible with the acquired data. The difference between the k-space data *predicted* from a reconstructed image and the *acquired* k-space data is reduced in successive iteration steps. Still, these techniques are not without significant challenges: when to stop the iterations and the size of the changes in the image values with each iteration step are important parameters for fine-tuning this type of reconstruction, and there may not be a "recipe" that works under all circumstances. Furthermore, iterative reconstruction is computationally quite demanding because image reconstruction is repeated for each iteration step, and each image reconstruction itself typically requires relatively time-consuming regridding of the data, something which is completely avoided with Cartesian k-space trajectories that allow direct application of the fast Fourier transform (FFT). Specialized computer hardware, as used in graphic cards with large numbers of computation units, can reduce the reconstruction time to levels where it amounts to a few minutes for myocardial perfusion studies, rather than an order of magnitude longer. Spiral imaging can suffer from image blurring due to off-resonance effects, which can nevertheless be corrected by generating a low-resolution field map [15].

Initial clinical evaluation of multi-slice ECG-gated 2D spiral perfusion imaging demonstrated high SNR, minimal imaging blurring, and no DRA, and all these factors seem to have contributed to high diagnostic accuracy for the detection of coronary artery disease [16]. With radial perfusion imaging, the angular undersampling has been pushed to a degree where it becomes feasible to continuously acquire data without ECG-gating and use relatively short reconstruction windows of 160 ms to generate cardiac-phase-resolved images [17]. Overall, non-Cartesian sampling appears to hold considerable promise for speeding up myocardial perfusion imaging without degrading image quality, and for reducing the appearance of artifacts that can be mistaken for perfusion defects.

Imaging Acceleration for Perfusion MRI

So-called parallel imaging techniques were originally introduced for pulse sequences with Cartesian k-space trajectories [18, 19]. Parallel imaging refers to the simultaneous use of multiple coils, each with its own receiver channel, to reduce the number of phase-encoding steps, while preserving spatial resolution. A conceptual illustration is shown in Fig. 6.6. The algorithms for reconstruction of the undersampled images can operate on the sensitivity-encoded images calculated for the individual coil elements (SENSE) [19, 20] or on the k-space data (simultaneous acquisition of spatial harmonics – SMASH) [18]. In the latter case, the spatial sensitivity profiles of the coils are used to synthesize during reconstruction the missing phase-encoded lines of data as linear combinations of the lines acquired through different

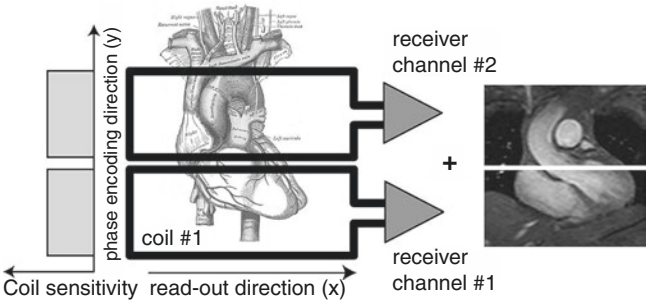

Fig. 6.6 A simplified scheme for parallel imaging is shown in this conceptual illustration with the simplifying assumption that the sensitivity profiles of two coil elements in a linear array do not overlap. The field of view in the phase-encoding direction can be halved, and two images for this reduced field of view are acquired over separate receiver channels. The two images can be combined into an image for a full field of view. In the more general case that the coil sensitivity profiles do overlap, a full field of view image can still be reconstructed by determining the coil sensitivity profiles and using this information to eliminate fold-over. Parallel imaging algorithms can either be applied to the images (e.g., SENSE) or to the spatial frequency data (e.g., SMASH)

coils/receiver channels. Alternatively, for SENSE, one first reconstructs for each coil/receiver channel the images from the under-sampled sets of k-space data (i.e., corresponding to a FOV reduction equivalent to the acceleration factor) and then "unaliases" the images by use of the coil-sensitivity matrices. Both of these approaches are suitable for reconstruction of myocardial perfusion images acquired with parallel-imaging acceleration.

Compared to the case where the full number of phase encodings is carried out, the higher image acquisition speed is achieved at the price of a reduced signal-to-noise ratio, which drops at least by a factor equal to the square root of the speed-up factor, but is also dependent on the properties of the coil array. As myocardial perfusion imaging is noticeably limited by the attainable signal-to-noise, the advantages of parallel imaging methods are limited by the need to maintain a minimally acceptable signal-to-noise ratio. In practical terms this means that parallel-imaging speed-up factors higher than x 2–3 are rarely used.

Spatiotemporal Sampling and Acceleration

Dynamic studies of contrast enhancement involve spatial sampling for the acquisition of each image and temporal sampling to detect signal intensity changes. For myocardial perfusion imaging, the temporal sampling frequency should equal the heart rate, in particular for perfusion studies during pharmacological stress or vasodilation. The image acquisition is repeated for every R-to-R interval in an ECG-gated acquisition. As shown by Kroll et al., adequate temporal sampling should be maximized, even at the expense of the signal-to-noise ratio, to optimize the quantitative assessment of myocardial perfusion [21]. With multi-slice 2D acquisitions of 200 ms per slice, contrast enhancement is sampled in 3–5 slices at baseline and 2–3 slices during hyperemia. With a temporal resolution equal to a heartbeat duration, it is generally not feasible to image the entire heart without resorting to parallel imaging techniques or other methods that allow a reduction of the image acquisition time.

Spatial and temporal sampling during a myocardial perfusion study entails a significant amount of *data redundancy*: images of the same anatomical region are acquired repeatedly while contrast enhancement takes place. It is possible to reduce the spatial sampling requirements and take advantage of spatiotemporal redundancy in dynamic imaging studies. Without any other adjustments, a halving of the field of view would speed up the image acquisition by a factor of two but also cause aliasing. Madore et al. described an elegant framework, called unaliasing by Fourier encoding the overlaps using the temporal dimension (UNFOLD), for separating aliased from non-aliased image components in dynamic studies [22–24]. Essentially, the approach involves halving the number of phase encodings for each image and alternately acquiring only the even- and odd-numbered phase-encoding steps. If one were to reconstruct these images by Fourier transformation, one would observe that the aliased image components would flip sides when images reconstructed from even- and odd-numbered phase encodings are compared, while the unaliased image component would remain stationary. The aliased components in the images are now a function of image number or time and vary at a frequency that corresponds to half the image acquisition frequency. (This suggests a generalization of the point spread function, which defines the aliasing characteristics, from the spatial domain to a 2D space-frequency domain, a concept to which we will return below.) The aliased image components can be removed by filtering of the temporal frequency spectrum at each pixel location. A simplified version of such an approach is shown in Fig. 6.7. This approach assumes that there is no contrast enhancement in the aliased portion of the image or that the highest temporal frequency of contrast enhancement is less than half of the frequency at which the aliased image components are being modulated by alternating the phase-encoding pattern. The UNFOLD approach has been applied by Di Bella in myocardial perfusion studies [25] and was found to work well if the patient holds her/his breath, as respiratory motion interferes with UNFOLD.

An elegant approach for spatiotemporal acceleration was introduced by Breuer et al. [26] to demonstrate that "controlled aliasing in parallel imaging results in higher acceleration" (CAIPIRINHA) for multi-slice imaging. The CAIPIRINHA technique, not unlike UNFOLD, applies a phase modulation scheme to untangle image aliasing from simultaneously excited slices, in this case by phase cycling of the RF pulses.

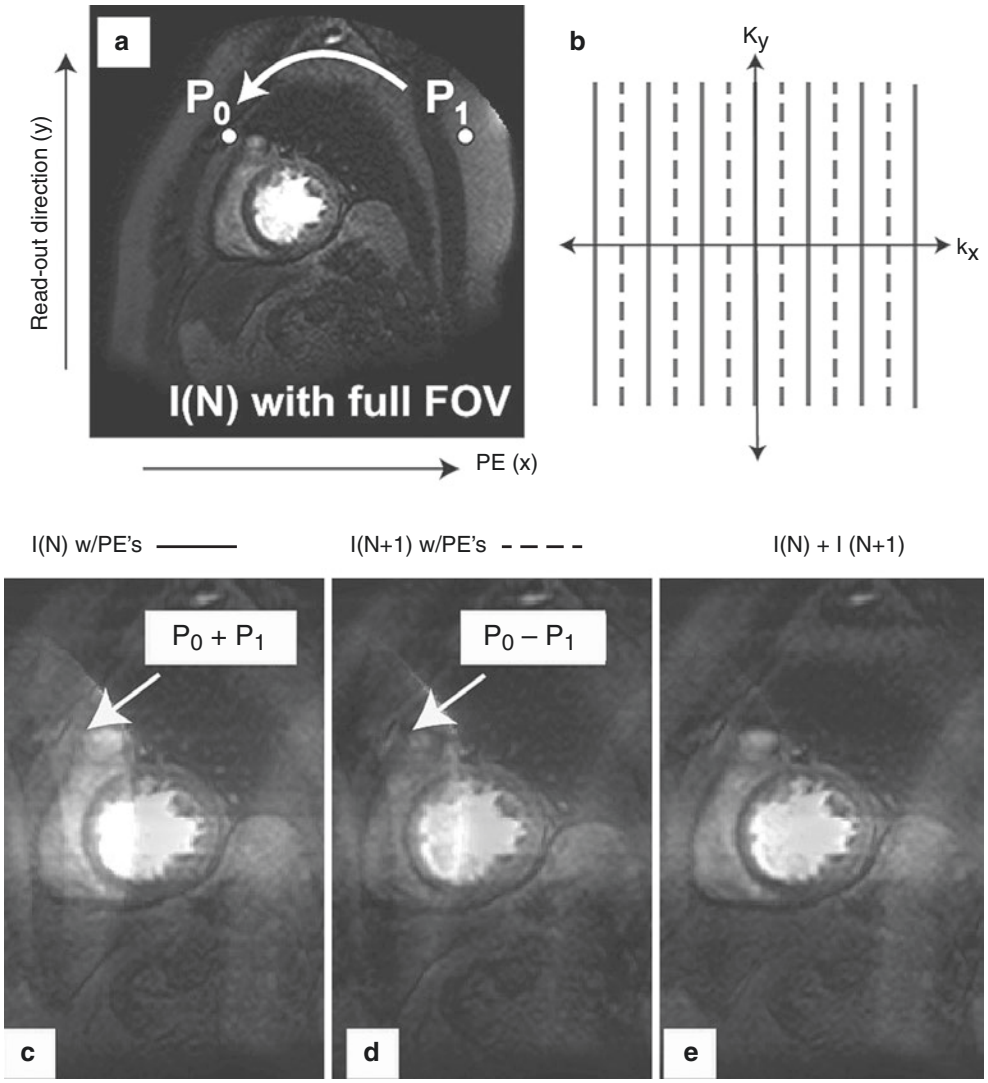

Fig. 6.7 Unaliasing by Fourier encoding the overlaps using the temporal dimension (UNFOLD) can be applied in dynamic studies by interleaving the phase encodings for acquisition of consecutive images. The interleaved phase encodings are shown as solid and dashed lines in (**a**). The full field of view image in (**b**) was acquired by performing all phase encodings (dashed and solid lines) for the image acquisition, while the consecutive images in (**c**) and (**d**) were acquired with only one subset of the phase encodings, which means that the field of view in the phase-encoding direction is halved, giving rise to fold-over artifacts. The relative shift of the phase encodings means that the fold-over artifacts are modulated in this case by a factor of +/− 1 for the fold-over on the left and −/+ for the fold-over on the right. This temporal modulation can be used to eliminate the fold-over by temporal filtering. To illustrate the basic concept, the image in (**e**) was obtained as complex sum of the images from (**c**) and (**d**), which eliminates the fold-over artifact on the left of the image

UNFOLD provided the impetus to develop much faster spatiotemporal acceleration techniques, such as k-t BLAST, k-t SENSE, and most recently k-t PCA (PCA – principal component analysis). These techniques exploit even more than UNFOLD the high spatiotemporal redundancy in dynamic perfusion studies. Figure 6.8 shows how the sampling pattern changes with k-t acceleration from a Cartesian to a sheared grid pattern. Such data sampling on a sheared grid gives rise, as expected, to aliasing, if each image is reconstructed from the acquired under-sampled data by conventional Fourier transformation. The aliasing pattern in the images varies between images at a frequency defined by the "degree" of shearing of the k-space sampling pattern. The effect of lattice undersampling (i.e., sampling on a sparse sheared grid instead of the denser Cartesian grid defined by the field of view and image resolution) can be described by a point spread function (PSF) in x-f space, where x stands for the spatial location along the phase-encoding direction and "f" for frequency. An example is shown in Fig. 6.8, which illustrates how the sheared sampling grid gives rise to a PSF that has, in addition to a lobe at the origin of x-f space, further lobes that describe the aliasing pattern.

To avoid aliasing k-t acceleration techniques like k-t BLAST, use "training data," in the form of low-resolution

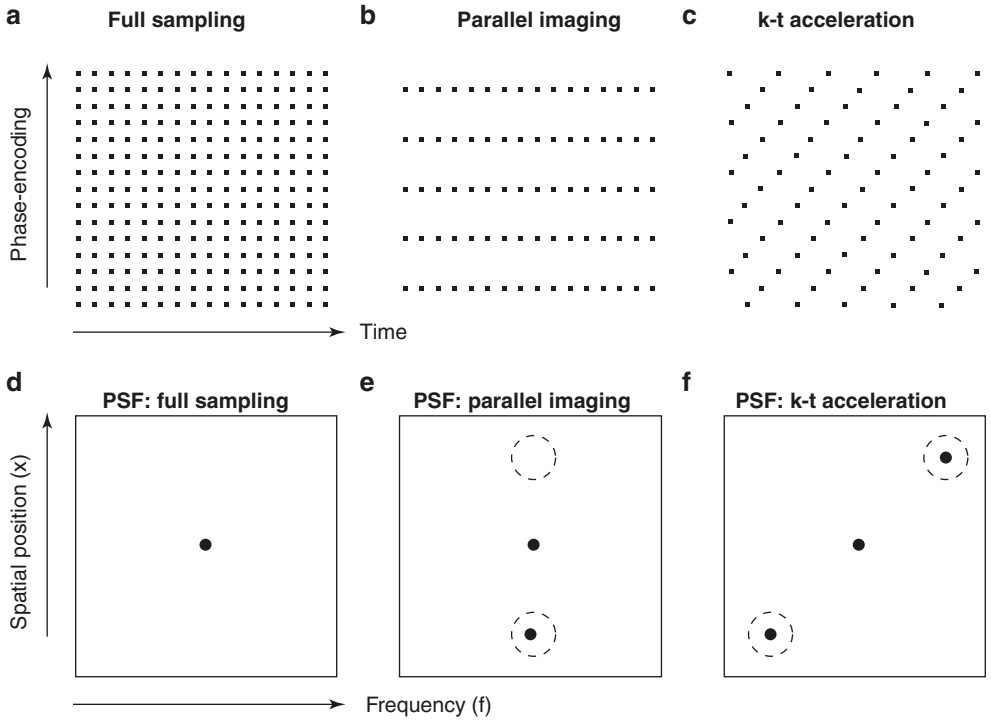

Fig. 6.8 The upper row (**a–c**) shows k-space sampling patterns for myocardial perfusion imaging, where the vertical axis denotes the phase-encoding direction, and the horizontal axis is the time domain for dynamic imaging. (**a**) Full sampling of k-space for each image, (**b**) sampling of the same subset of phase-encoded lines for acceleration by parallel imaging with multiple coils, and (**c**) a periodically varying subsampling pattern (period of 4) with the appearance of sheared grid for k-t acceleration. The lower row shows point spread functions (PSF) for these k-space sampling patterns. The PSF describes how a point source is mapped into an image by the image acquisition. The panels (**d–f**) show a generalization of the point spread function to a domain x-f, where f denotes a frequency axis that is the complement to time in dynamic imaging and x is a coordinate in the spatial domain (e.g., phase-encoding direction). With full k-space sampling, the PSF has only a single peak at the origin in the x-f domain, resulting in an image without aliasing artifacts. With parallel imaging with x 3 acceleration, (**b**) one produces two additional peaks (highlighted with dashed circles) in the phase-encoding direction which describe the aliasing, which has to be removed by using coil-sensitivity maps. The advantage of k-t acceleration (same acceleration factor as with parallel imaging in (**e**)) is that the peaks describing the aliasing get pushed away from the vertical line through the origin when aliasing is the same for all images (**b**) and shifted to locations along the frequency axis that correspond to the repetition time for the k-space sampling pattern. This allows higher acceleration factors and facilitates the removal of aliased components in the reconstructed images, e.g., through temporal low-pass filtering as done with UNFOLD. Furthermore, sparse k-t sampling patterns can be combined with parallel imaging acceleration to achieve multiplicative effects for image acceleration factors

images for reconstruction of images from all acquired data – we will refer to them as "full-resolution" images. For example, the central part of k-space is acquired for all images to obtain such a low-resolution "training set" in parallel with the sampling on a sheared grid outside the central region. For the reconstruction of the "full-resolution" images, one generates for each location along the phase-encoding direction a frequency spectrum of the temporal changes of the signal intensity, i.e., one generates so-called x-f maps. In dynamic imaging, only parts of the acquired images may show some variation with time, which leads to sparse signal representation in x-f space. An adaptive filter-based reconstruction technique is then applied to reconstruct the "full-resolution" images. It is referred to as adaptive, because it uses an estimate of the local signal content for each point in x-f space, based on the training data. This works well as long as the x-f maps from the training data are relatively sparse. Respiratory motion during a first pass study can compromise the performance of k-t acceleration techniques, because peaks in the x-f maps are broadened by respiratory motion, which makes it more difficult to avoid aliasing effects [27]. Further improvements and higher acceleration factors are possible by combining k-t acceleration techniques with parallel imaging (i.e., parallel acquisition with multiple coils) giving rise to techniques such as k-t SENSE.

The k-t PCA algorithm represents a further advance in spatiotemporal acceleration. Principal component analysis of the training data is used to transform the x-f data to a more suitable "basis" with principal components replacing the f-coordinate – it is somewhat akin to using data compression. This results in a map with fewer and better separated peaks, which is helpful for unaliasing. With the k-t PCA method, it became possible to achieve acceleration factors as high as x 5–10 for CMR perfusion imaging with whole-heart cover-

age, using ten short axis slices [28]. Post-processing in spatiotemporal acceleration techniques can have an effect similar to low-pass filtering in the time domain and cause temporal blurring. This should be kept in mind as it may effectively result in a bias to *underestimate* perfusion.

None of the aforementioned imaging acceleration methods defy the Nyquist limit to the same degree as compressive sensing. Compressive sensing is based on the recognition that some signals, which can be represented in a "sparse form" by certain forms of signal encoding, can be reconstructed from a low number of random or pseudorandom samples of such encoding steps. For example, in magnetic resonance spectroscopy, we may only observe a few isolated peaks in the spectrum. In this case the Fourier-transformed signal giving the spectrum is a suitable encoding for compressive sensing. "Compressive sensing" would then amount to taking a random, relatively small number of signal data samples from the free induction decay of the signal and using the "a priori" knowledge that the spectrum is sparse to achieve an artifact-free reconstruction from the sparse set of random data samples. (The reconstruction of the spectrum would not be performed by Fourier transform, as is usually done, but instead by solving a constrained optimization problem, e.g., using the constraint that the spectrum is sparse.) The above example of the NMR spectrum is construed because for the acquisition of a free induction decay, we do not save time by only taking a random sample of signal points. A more relevant application is when compressive sampling is used to acquire an image with only a (pseudorandom) subset of phase encodings. It is in this latter form that compressive sensing has been applied in MRI for sparse sampling and image reconstruction.

Based on the concepts of compressive sensing, spatiotemporal acceleration has been further enhanced with methods like k-t SPARSE [29, 30]. One important change compared to k-t SENSE is the introduction of pseudorandom k-t sampling for k-t SPARSE to generate incoherent artifacts.

3D Perfusion Imaging

3D whole-heart perfusion imaging has been a long-standing goal for CMR, not the least because it is the standard for nuclear perfusion imaging. CMR offers higher spatial resolution compared to nuclear imaging, but combining this with 3D, or whole-heart multi-slice coverage, of the heart has been a challenge. The advances in CMR imaging acceleration over the last decade have brought 3D cardiac perfusion imaging within reach. Whether 3D myocardial perfusion imaging by CMR should be considered as the "holy-grail" remains debatable, as a 3D image acquisition imposes specific constraints for coping with cardiac motion, compared with a 2D multi-slice approach. Other aspects, such as high spatial resolution for detection of endo- to epicardial perfusion gradients, may be equally important for diagnostic performance as whole-heart coverage. The trade-offs for balancing these different aims and requirements remain to be evaluated in parallel with the technical advancements.

3D imaging, and hence 3D myocardial perfusion imaging, has the advantage that the signal-to-noise ratio is significantly higher than for its 2D counterpart, specifically by a factor given by the square root of the number of partitions used for sampling in the "partition-encoding" direction, i.e., the direction equivalent to the slice-encoding direction in multi-slice 2D imaging. With 3D cardiac perfusion, image acquisition has to be limited to diastole to avoid motion artifacts and blurring, while with the 2D equivalent, the images for different slice locations can be acquired over the entire cycle. The k-space sampling trajectories applied for 2D perfusion imaging (Cartesian, spiral, or radial) can also be used in 3D perfusion imaging for 2D planes of k-space, while for the third direction, one uses standard Fourier encoding. For example, with radial sampling, one can acquire a stack of 2D radial trajectories (also called a "stack of stars"), so that the volume of k-space being sampled forms a cylinder. Alternatively, it is possible to perform full 3D radial sampling, but this is only feasible for 3D perfusion imaging with vast undersampling and is rarely used for 3D CMR perfusion imaging.

Practical Recommendations

The table below (Table 6.1) summarizes what are arguably settings that establish a good starting point for perfusion studies with fast, multi-slice T1-weighted gradient-echo techniques.

Myocardial Perfusion Imaging at High Magnetic Field Strengths

Magnetic field strengths higher than 1.5 Tesla can be both a blessing and a bane for myocardial perfusion imaging. Use of higher field strengths is expected to result in better signal-to-noise and contrast-to-noise than at lower field strengths. Unfortunately techniques such as gradient-echo imaging with steady-state free precession do not work well at high field strengths (≥3 T), potentially depriving one of using a significant advance in MR sequence techniques made during the last couple of years. Myocardial perfusion studies with the same technique applied at 1.5 Tesla and 3 Tesla confirmed that the increase in field strength brings a significant improvement in signal-to-noise and contrast-to-noise [31, 32]. The contrast-to-noise improvement may not only be due

Table 6.1 Perfusion study settings

Parameter	Setting	Considerations
Spatial resolution	<2.5 mm in-plane resolution	Dark-rim artifacts more prominent with poor resolution in phase-encoding direction
Temporal resolution	Equal to R-to-R duration	Period of myocardial contrast enhancement is relatively brief and most sensitive to blood flow level
Slice thickness	<10 mm	Thin slices (<6 mm) often given unacceptable signal-to-noise, and through-plane motion renders it meaningless to use very thin slices
Parallel imaging	Parallel-imaging acceleration x 2; spatiotemporal acceleration can be much higher	For example, with k-t PCA speed-up factors of 5–8 have been achieved
Flip angle	15–20° for fast gradient-echo imaging	Assume here a TR/TE on the order of 2 ms and 1 ms, respectively. It is helpful to estimate the Ernst angle for the particular combination of TR and TE
Echo time (TE)	As short as feasible; ~1–2 ms recommended	Dark-rim, or susceptibility artifacts, and also motion artifacts at high heart rates are more likely with longer echo times
Receiver bandwidth	400–800 Hz/pixel for fast GRE	With SSFP can be 1000 Hz/pixel or higher
T1 weighting	Saturation recovery preparation	Inversion recovery gives stronger T1 weighting but renders signal susceptible to heart rate variations
Contrast administration	Bolus injection, preferably with power injector at 3–5 ml/s for 0.5 mmol/ml dilution of Gd-DTPA	A slow infusion of contrast will lead to a loss of sensitivity for assessing blood flow
Through-plane motion correction	Breath-holding during first pass through LV	In most cases patient can only hold breath during initial contrast enhancement

to higher signal-to-noise but also to the increase of myocardial T1s when moving from 1.5 Tesla to higher field strengths.

Signal Analysis and Post-processing

With ^{1}H MRI the presence of contrast agent is deduced from the reduction of the ^{1}H relaxation time constants and the increase of the ^{1}H signal intensity, if the signal is predominantly T_1-weighted. Water is a freely diffusible tracer, and although the contrast agent may be confined to the intravascular or extracellular space, the ^{1}H nuclei interacting with the paramagnetic contrast agent complexes may move back and forth between spaces permeated by contrast agent and inaccessible to contrast agent, respectively. This process of water exchange can lead to an overestimation of the distribution volume for the contrast agent – the ^{1}H nuclei carry the effect of the contrast agent to spaces inaccessible to the contrast agent itself [33]. The process of water exchange on T1 measurements was carefully investigated a few decades ago, but the repercussions of the theory of water exchange on perfusion MRI have often been ignored with some notable exceptions [33, 34]. Springer and Li recently developed a comprehensive theory that weds the theory of water exchange with the Kety-Schmidt model [34].

The effects of water exchange can be considered at the stage of the pulse sequence optimization or during post-processing of the data. For the former, the work of Donahue [33, 35, 36] showed that the effects of water exchange can be minimized by using flip angles well above the Ernst angle in spoiled gradient-echo imaging. Suppressing the effects of water exchange then allows to neglect those effects at the post-processing stage. Alternatively, one can incorporate the effects of water exchange into the tracer kinetic analysis, as shown by Springer and Li [34, 37], though this may complicate the task of modeling myocardial enhancement.

Spin-Labeling Techniques in the Heart

Water can be used in perfusion studies as an endogenous contrast agent. To do this requires alteration of the state of ^{1}H nuclei with sharp spatial definition, and observing the flux of these prepared ^{1}H nuclei into adjacent tissue [38–40]. The experiments are typically run in a difference mode to subtract the background signal from stationary ^{1}H nuclei. Alteration of the state of ^{1}H nuclei typically consists in applying a spatially selective inversion pulse. The same acquisition is then repeated with a non-slice-selective inversion pulse, and the difference signal is proportional to the number of ^{1}H nuclei that have moved into or out of the slice being imaged. The slice should be thin enough so that a detectable change of the magnetization can result from ^{1}H flux within less than a time on the order of T1, T1 being the “lifetime” of the altered magnetization state.

The spin-labeling technique does not appear to be mature enough yet for routine clinical application. Spin-labeling depends on a relatively accurate direct or indirect quantification of T1 differences, because the inflow of labeled spins produces small change of T1, which is proportional to the blood flow [41].

Interestingly, the errors for estimating myocardial blood flow, with either contrast-enhanced techniques or spin labeling, have a reciprocal dependence on the level of blood flow. Previous studies have shown that the confidence bands for estimating blood flow increase in proportion to blood flow or the perfusion reserve [42]. With spin-labeling, the accuracy of estimating blood flow increases with blood flow, because the proportion of labeled spins entering a slice is directly proportional to flow [41]. It was therefore fortuitous that some of the first validation studies of the spin-labeling technique were made in rodents, where myocardial blood flows even at baseline are 3–5 times higher than in humans.

Conclusions

Technical developments in the field of CMR perfusion imaging continue at a vigorous pace, with the overall goals of achieving complete heart coverage, avoid image artifacts, and facilitate the quantification of myocardial perfusion. This exposition has focused on some tried and robust approaches, while also offering an outlook on promising new developments. It appears fair to state that with CMR, much room is left to exhaust the full potential of myocardial perfusion imaging, but at the same time, the currently available techniques are already more than adequate for clinical studies.

References

1. Bellamy DD, Pereira RS, McKenzie CA, Prato FS, Drost DJ, et al. Gd-DTPA bolus tracking in the myocardium using T1 fast acquisition relaxation mapping (T1 FARM). Magn Reson Med. 2001;46(3):555–64.
2. Tsekos NV, Zhang Y, Merkle H, Wilke N, Jerosch-Herold M, et al. Fast anatomical imaging of the heart and assessment of myocardial perfusion with arrhythmia insensitive magnetization preparation. Magn Reson Med. 1995;34(4):530–6.
3. Wilke N, Jerosch-Herold M, Wang Y, Huang Y, Christensen BV, Stillman AE, et al. Myocardial perfusion reserve: assessment with multisection, quantitative, first-pass MR imaging. Radiology. 1997;204(2):373–84.
4. Ferreira P, Gatehouse P, Bucciarelli-Ducci C, Wage R, Firmin D. Measurement of myocardial frequency offsets during first pass of a gadolinium-based contrast agent in perfusion studies. Magn Reson Med. 2008;60(4):860–70.
5. Salerno M, Sica CT, Kramer CM, Meyer CH. Optimization of spiral-based pulse sequences for first-pass myocardial perfusion imaging. Magn Reson Med. 2011;65(6):1602–10.
6. Jerosch-Herold M, Seethamraju RT, Swingen CM, Wilke NM, Stillman AE. Analysis of myocardial perfusion MRI. J Magn Reson Imaging. 2004;19(6):758–70.
7. Gatehouse PD, Elkington AG, Ablitt NA, Yang GZ, Pennell DJ, Firmin DN. Accurate assessment of the arterial input function during high-dose myocardial perfusion cardiovascular magnetic resonance. J Magn Reson Imaging. 2004;20(1):39–45.
8. Kim D, Cernicanu A, Axel L. Multi-slice, first-pass myocardial perfusion MRI with undistorted arterial input function and higher myocardial enhancement at 3 T. Paper presented at: Scientific Sessions of the International Society of Magnetic Resonance in Medicine (ISMRM); May 11, 2005; Miami Beach, FL.
9. Köstler H, Ritter C, Baunach D, Beer M, Larson AC, Simonetti O, et al. Determination of the arterial input function in high dose radial myocardial perfusion imaging. Paper presented at: Scientific Sessions of the International Society of Magnetic Resonance in Medicine, 2005; Miami Beach, FL.
10. Christian TF, Rettmann DW, Aletras AH, Liao SL, Taylor JL, et al. Absolute myocardial perfusion in canines measured by using dual-bolus first-pass MR imaging. Radiology. 2004;232(3):677–84.
11. Ishida M, Schuster A, Morton G, Chiribiri A, Hussain S, Paul M, et al. Development of a universal dual-bolus injection scheme for the quantitative assessment of myocardial perfusion cardiovascular magnetic resonance. J Cardiovasc Magn Reson. 2011;13:28.
12. Edelman RR, Li W. Contrast-enhanced echo-planar MR imaging of myocardial perfusion: preliminary study in humans. Radiology. 1994;190(3):771–7.
13. Epstein FH, London JF, Peters DC, Goncalves LM, Agyeman K, Taylor J, et al. Multislice first-pass cardiac perfusion MRI: validation in a model of myocardial infarction. Magn Reson Med. 2002;47(3):482–91.
14. Elkington AG, Gatehouse PD, Cannell TM, Moon JC, Prasad SK, et al. Comparison of hybrid echo-planar imaging and FLASH myocardial perfusion cardiovascular MR imaging. Radiology. 2005;235(1):237–43.
15. Chen W, Meyer CH. Semiautomatic off-resonance correction in spiral imaging. Magn Reson Med. 2008;59(5):1212–9.
16. Salerno M, Taylor A, Yang Y, Kuruvilla S, Ragosta M, et al. Adenosine stress cardiovascular magnetic resonance with variable-density spiral pulse sequences accurately detects coronary artery disease: initial clinical evaluation. Circ Cardiovasc Imaging. 2014;7(4):639–46.
17. Chen D, Sharif B, Bi X, Wei J, Thomson LE, Bairey Merz CN, et al. Quantification of myocardial blood flow using non-electrocardiogram-triggered MRI with three-slice coverage. Magn Reson Med. 2016;75(5):2112–20.
18. Sodickson DK, Manning WJ. Simultaneous acquisition of spatial harmonics (SMASH): fast imaging with radiofrequency coil arrays. Magn Reson Med. 1997;38(4):591–603.
19. Pruessmann KP, Weiger M, Scheidegger MB, Boesiger P. SENSE: sensitivity encoding for fast MRI. Magn Reson Med. 1999;42(5):952–62.
20. Pruessmann KP, Weiger M, Boesiger P. Sensitivity encoded cardiac MRI. J Cardiovasc Magn Reson. 2001;3(1):1–9.
21. Kroll K, Wilke N, Jerosch-Herold M, Wang Y, Zhang Y, Bache RJ, Bassingthwaighte JB. Accuracy of modeling of regional myocardial flows from residue functions of an intravascular indicator. Am J Physiol. 1996;40:H1643–55.
22. Madore B. Using UNFOLD to remove artifacts in parallel imaging and in partial-Fourier imaging. Magn Reson Med. 2002;48(3):493–501.
23. Madore B. UNFOLD-SENSE: a parallel MRI method with self-calibration and artifact suppression. Magn Reson Med. 2004;52(2):310–20.
24. Madore B, Glover GH, Pelc NJ. Unaliasing by fourier-encoding the overlaps using the temporal dimension (UNFOLD), applied to cardiac imaging and fMRI. Magn Reson Med. 1999;42(5):813–28.

25. Di Bella EV, Wu YJ, Alexander AL, Parker DL, Green D, McGann CJ. Comparison of temporal filtering methods for dynamic contrast MRI myocardial perfusion studies. Magn Reson Med. 2003;49(5):895–902.
26. Breuer FA, Blaimer M, Heidemann RM, Mueller MF, Griswold MA, Jakob PM. Controlled aliasing in parallel imaging results in higher acceleration (CAIPIRINHA) for multi-slice imaging. Magn Reson Med. 2005;53(3):684–91.
27. Otazo R, Kim D, Axel L, Sodickson DK. Combination of compressed sensing and parallel imaging for highly accelerated first-pass cardiac perfusion MRI. Magn Reson Med. 2010;64(3):767–76.
28. Vitanis V, Manka R, Giese D, Pedersen H, Plein S, et al. High resolution three-dimensional cardiac perfusion imaging using compartment-based k-t principal component analysis. Magn Reson Med. 2011;65(2):575–87.
29. Pawar K, Egan GF, Zhang J. Accelerating k-t sparse using k-space aliasing for dynamic MRI imaging. Conf Proc IEEE Eng Med Biol Soc. 2013;2013:2619–23.
30. Usman M, Prieto C, Schaeffter T, Batchelor PG. k-t Group sparse: a method for accelerating dynamic MRI. Magn Reson Med. 2011;66(4):1163–76.
31. Araoz PA, Glockner JF, McGee KP, Potter DD Jr, Valeti VU, et al. 3 Tesla MR imaging provides improved contrast in first-pass myocardial perfusion imaging over a range of gadolinium doses. J Cardiovasc Magn Reson. 2005;7(3):559–64.
32. Cheng AS, Pegg TJ, Karamitsos TD, Searle N, Jerosch-Herold M, Choudhury RP, Banning AP, Neubauer S, Robson MD, Selvanayagam JB. Cardiovascular magnetic resonance perfusion imaging at 3-tesla for the detection of coronary artery disease: a comparison with 1.5-tesla. J Am Coll Cardiol. 2007;49(25):2440–9.
33. Donahue KM, Weisskoff RM, Chesler DA, Kwong KK, Bogdanov AA Jr, et al. Improving MR quantification of regional blood volume with intravascular T1 contrast agents: accuracy, precision, and water exchange. Magn Reson Med. 1996;36(6):858–67.
34. Li X, Huang W, Yankeelov TE, Tudorica A, Rooney WD, Springer CS Jr. Shutter-speed analysis of contrast reagent bolus-tracking data: preliminary observations in benign and malignant breast disease. Magn Reson Med. 2005;53(3):724–9.
35. Donahue KM, Burstein D. Proton exchange rates in myocardial tissue with Gd-DTPA administration. New York; 1993.
36. Donahue KM, Weisskoff RM, Burstein D. Water diffusion and exchange as they influence contrast enhancement. J Magn Reson Imaging. 1997;7(1):102–10.
37. Landis CS, Li X, Telang FW, Coderre JA, Micca PL, Rooney WD, et al. Determination of the MRI contrast agent concentration time course in vivo following bolus injection: effect of equilibrium transcytolemmal water exchange. Magn Reson Med. 2000;44(4):563–74.
38. Wacker CM, Fidler F, Dueren C, Hirn S, Jakob PM, Ertl G, et al. Quantitative assessment of myocardial perfusion with a spin-labeling technique: preliminary results in patients with coronary artery disease. J Magn Reson Imaging. 2003;18(5):555–60.
39. Waller C, Kahler E, Hiller KH, Hu K, Nahrendorf M, Voll S, et al. Myocardial perfusion and intracapillary blood volume in rats at rest and with coronary dilatation: MR imaging in vivo with use of a spin-labeling technique. Radiology. 2000;215(1):189–97.
40. Reeder SB, Atalay MK, McVeigh ER, Zerhouni EA, Forder JR. Quantitative cardiac perfusion: a noninvasive spin-labeling method that exploits coronary vessel geometry. Radiology. 1996;200(1):177–84.
41. Zhang H, Shea SM, Park V, Li D, Woodard PK, Gropler RJ, Zheng J. Accurate myocardial T1 measurements: toward quantification of myocardial blood flow with arterial spin labeling. Magn Reson Med. 2005;53(5):1135–42.
42. Klocke FJ, Simonetti OP, Judd RM, Kim RJ, Harris KR, Hedjbeli S, et al. Limits of detection of regional differences in vasodilated flow in viable myocardium by first-pass magnetic resonance perfusion imaging. Circulation. 2001;104(20):2412–6.

Techniques in the Assessment of Cardiovascular Blood Flow and Velocity

7

Michael Markl

Introduction

Since its original description in the 1980s [1–4], phase-contrast (PC) MRI has seen broad clinical acceptance for the visualization and quantitative evaluation of blood flow in the heart, aorta, and large vessels [5–7]. Further developments of phase-contrast techniques have allowed for the acquisition of a time-resolved (CINE), three-dimensional (3D) PC-MRI with three-directional velocity encoding which is often referred to as "4D flow MRI." This chapter will introduce the fundamental physics principles underlying flow quantification with PC-MRI, describe the interpretation of results for clinical application, and provide an introduction to recent advanced in PC-MRI such as real-time flow imaging and 4D flow MRI and their potential applications.

Phase-contrast (PC) MRI (also sometimes termed "flow-sensitive MRI" or "MR velocity mapping") takes advantage of the direct relationship between blood flow velocity and the phase of the MR signal that is acquired during a MRI measurement. The underlying principles have been known and applied over several decades [1–3, 5, 8, 9]. The mapping of just the component of time-resolved velocity-directed perpendicularly through a 2D plane is widely used for clinical measurements of volume flow [10–13]. This approach allows measurements of forward, regurgitant, and shunt flows in congenital and acquired heart disease [14–17], and measurements of jet velocity in aortic valve disease or in stenotic vascular regions such as aortic coarctation.

M. Markl (✉)
Northwestern University Feinberg School of Medicine, Department of Radiology and Biomedical Engineering, Chicago, IL, USA
e-mail: mmarkl@northwestern.edu

Principles and Techniques of Velocity Encoding

Most MR sequences demonstrate sensitivity to flow and motion, which can lead to artifacts in many applications. The intrinsic motion sensitivity of MRI, however, can be used to image vessels as in phase-contrast MR angiography but also to quantify blood flow and motion of tissue. Using appropriate (bipolar) velocity encoding gradients, flow- or motion-dependent phase effects can be used to encode the underlying blood flow velocity directly into the MR signal phase. Two acquisitions with different velocity encoding sensitivities are used to eliminate the unwanted background phase variation from the images: if the acquisitions use opposite polarity velocity encoding sensitivities, then one can simply calculate the phase difference for the signals from the two acquisitions to obtain a phase that is independent from the background phase, and proportional to the velocity in each voxel. Alternatively one acquisition can be velocity insensitive [5, 13, 18]. Subtraction of phase images from the two acquisitions removes background phase effects. The signal intensities in the resulting phase difference images are directly related to the blood flow velocity and can thus be used to visualize and quantify blood flow (phase-contrast principle). It is important to note that only the velocity component along the direction of the bipolar flow encoding gradient contributes to the phase of the MR signal and only a single velocity direction can be encoded with an individual measurement. A brief mathematical description of the fundamental principles of PC-MRI is given in the Appendix.

For cardiovascular applications, the 2D PC data is acquired over multiple cardiac cycles using ECG-gated CINE imaging to measure time-resolved pulsatile blood flow as illustrated in Fig. 7.1 [3, 5, 9, 13]. Since the MR acquisition is not sufficiently fast to measure all required data during a single heartbeat, the periodic flow is assessed by reconstructing images from data acquired over several cardiac cycles. For each heartbeat and time frame, only a subset

R. Y. Kwong et al. (eds.), *Cardiovascular Magnetic Resonance Imaging*, Contemporary Cardiology,
https://doi.org/10.1007/978-1-4939-8841-9_7

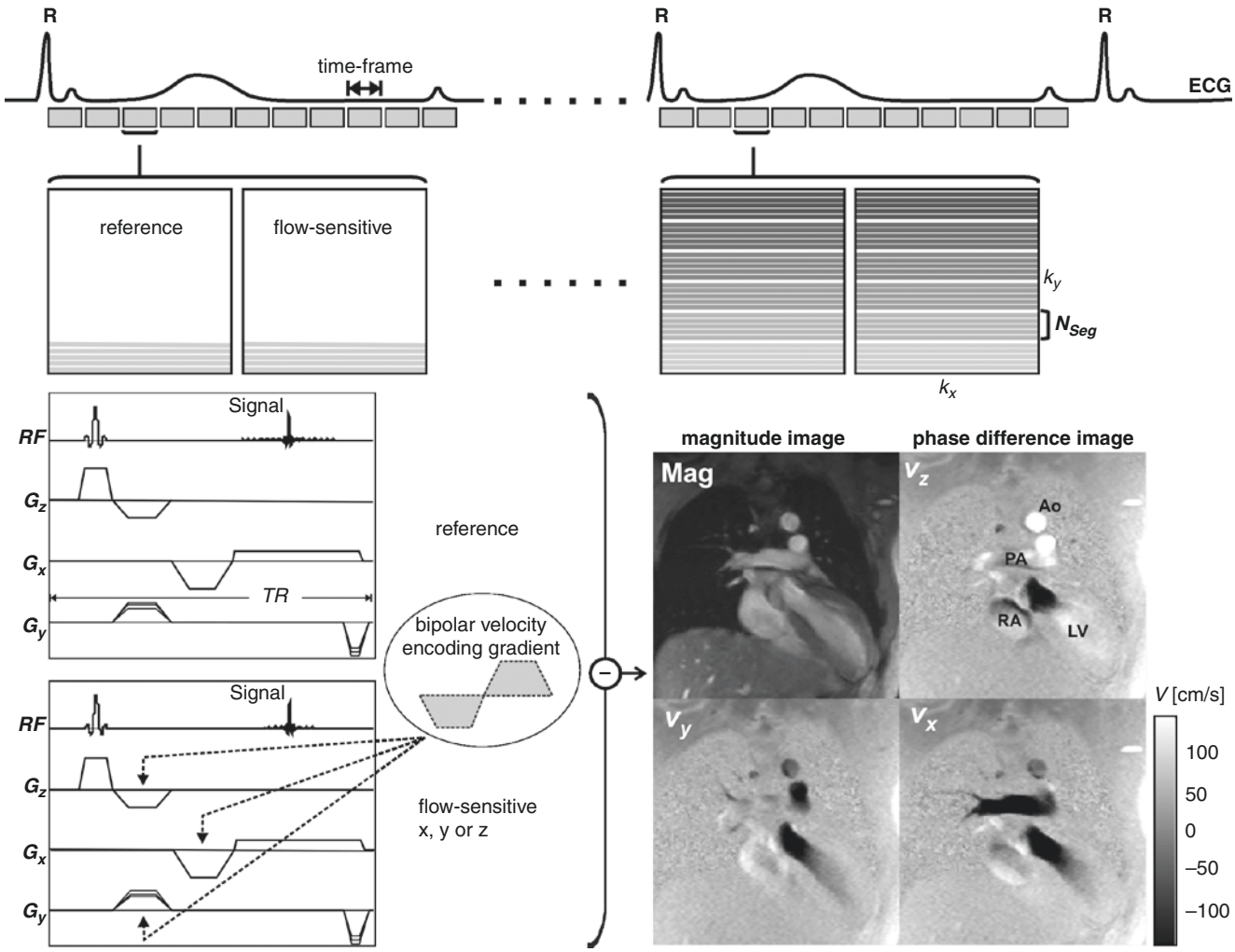

Fig. 7.1 Standard 2D CINE PC-MRI with one-directional velocity encoding along the y or z direction. Reference and velocity sensitive scan (added bipolar velocity encoding gradient) are acquired in direct succession. The subtraction of both data sets provides phase difference images which contain quantitative blood flow velocities as shown for blood flow in the heart. The bipolar velocity encoding gradient can be placed either along the z, y, or x direction to measure blood flow velocities v_z, v_y, or v_x based on the selection by the user. The amplitude and duration of the velocity encoding gradient determines the velocity sensitivity (venc) of the PC acquisition. Due to time constraints, the MR data cannot be acquired during a single heartbeat, and PC data are collected over several cardiac cycles. The measurement is synchronized with the cardiac cycle using an ECG-gated k-space segmented data acquisition. For each heartbeat and time frame, only a subset (N_{Seg}) of all required (N_y) phase encoding steps are measured (k-space segmentation). The procedure is repeated until the full raw data set is acquired and time-resolved (CINE) images can be derived depicting the dynamics of pulsatile through-plane flow. The selection of the number of phase encoding lines N_{Seg} determines the temporal resolution (time to collect data for a single time frame $\Delta t = 2$ TR N_{Seg}) and a total scan time $T_{acq} = N_y/N_{Seg}\, T_{CC}$ of the phase-contrast CINE acquisition (T_{CC} = duration of one cardiac cycle). For a typical TR on the order of 5–10 ms and N_{Seg} = 3–4, measurements can be performed during breath holding and with temporal resolutions of 30–80 ms. LV left ventricle, RA right atrium, PA pulmonary artery, Ao aorta

(N_{Seg}) of all required (N_y) phase encoding steps are measured (k-space segmentation principle). The procedure is repeated for a different k-space subset until the full raw data set is acquired for all time frames. Data acquisition typically includes single-direction velocity measurement, in most cases orthogonal to the 2D imaging slice (through-plane encoding). For single-direction velocity encoding, two raw data lines have to be acquired for each phase encoding step (reference scan + flow-sensitive acquisition). For a given repetition time TR and cardiac period of T_{ECG}, different imaging protocols can be constructed based on a trade-off between temporal resolution (Δt), spatial resolution (N_y phase encoding lines per slice), and total acquisition time T_{acq}. The selection of the number of phase encoding lines N_{Seg} then determines the temporal resolution $\Delta t = 2\ TR\ N_{Seg}$ and a total scan time $T_{acq} = N_y/N_{Seg}\, T_{ECG}$ of the phase-contrast CINE acquisition. Typical measurement parameters (spatial resolution, 1.5–2.5 mm; temporal resolution, 30–60 ms; slice thickness, 5–8 mm) permit the acquisition of 2D CINE PC data during a 10–20 s breath-hold period.

While most application of 2D CINE PC-MRI use through-plane velocity encoding, typical MRI protocols allow for the selection of in-plane flow encoding along the x or y direction of the imaging plane. While trough-plane encoding is predominantly employed for the quantification of volume flow and peak velocities, in-plane encoding can be useful for the visualization of the location and extent of stenotic flow jets to guide plane placement for subsequent assessment of peak velocity and pressure gradient estimation.

Following image reconstruction, 2D CINE PC-MRI yields a series of anatomical (magnitude) and flow velocity (phase difference) images that represent the temporal changes of morphology and blood flow over the cardiac cycle. As a result, time-resolved (CINE) images can be derived depicting the dynamics of periodic physiological processes during the cardiac cycle as shown in Fig. 7.2. (See Table 7.1.)

Table 7.1 Description of image series typically reconstructed from 2D CINE PC-MRI with single-direction velocity encoding. Example images for through-plane velocity encoding are shown in Fig. 7.2

2D PC image series	Interpretation
Magnitude	Cardiovascular anatomy, signal intensity = MR signal amplitude averaged over two scans used for single-direction velocity encoding
Complex difference	Flow-encoded magnitude image, signal intensity = absolute value of encoded velocity, no information on flow direction (e.g., velocities—100 cm/s and + 100 cm/s have identical pixel intensity)
Phase difference	Blood flow velocity, signal intensity represents the local velocities along the encoding direction (e.g., through plane)

PC-MRI and Velocity Encoding Sensitivity (venc)

An important (user-defined) PC-MRI parameter is the velocity encoding sensitivity (venc), which represents the maximum flow velocity that can be acquired. As shown in Fig. 7.3, when the underlying velocity exceeds the acquisition setting for venc, velocity aliasing can occur which is typically visible as a sudden change from high to low velocity within a region of flow. If aliasing artifacts are present, accurate flow visualization and quantification may be compromised unless antialiasing correction can be successfully performed [19]. Alternatively, the venc can be increased, and the acquisition is repeated to avoid aliasing. It is important to note, however, that velocity noise σ_ϕ is directly related to the venc [5] and is

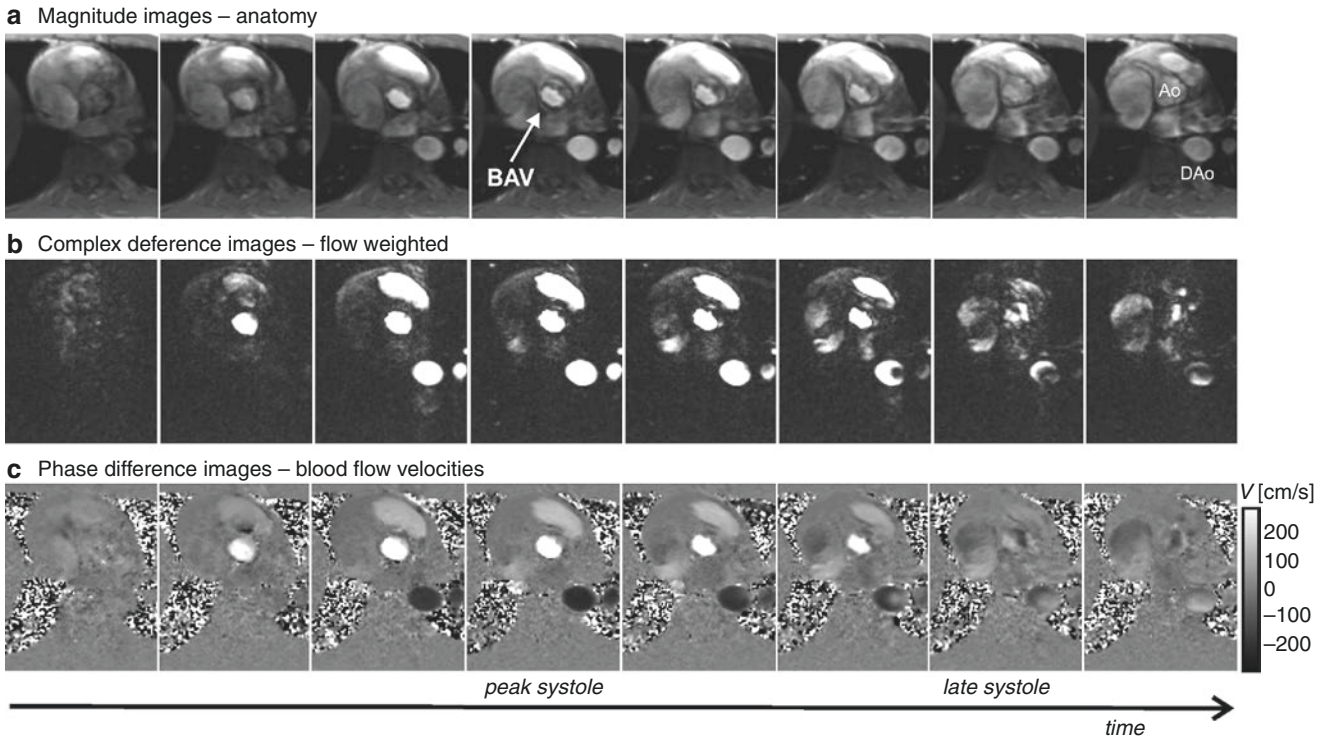

Fig. 7.2 2D CINE PC-MRI with through-plane velocity encoding (bipolar encoding gradient along the slice direction) in a patient with a bicuspid aortic valve (BAV). **a**–**c** show images that are typically reconstructed from a 2D CINE PC-MRI acquisition including time-resolved anatomical data (**a**), flow-weighted data (**b**), and phase difference images (**c**). Not that the gray scale intensity for the phase-contrast images characterizes the motion direction: the ascending aorta at the level of the BAV (Ao) appears white due to the positive blood flow direction (flow foot to head), whereas the descending aorta (DAo) appears black encoding to (negative) flow in the opposite direction (head to foot). Flow quantification revealed elevated peak systolic velocity in close to 2.5 m/s in this BAV patient. A more detailed description of the different image reconstructions (magnitude, flow weighted, phase difference) is provided in Table 7.1

inversely related to the signal-to-noise ratio (SNR) in the corresponding magnitude images ($\sigma_\phi \sim 1/\mathrm{SNR}$) and can be estimated by

$$\sigma_v = \frac{\sqrt{2}}{\pi}\frac{\mathrm{venc}}{\mathrm{SNR}}$$

Therefore, selecting a high venc may alleviate the issue of velocity aliasing but will also increase the level of velocity noise in flow velocity images. As a result, the venc should ideally be selected as high as needed to avoid aliasing but as low as possible to reduce velocity noise. As a general rule, to capture the best image quality, the chosen venc should represent the physiological velocity of the vessel of interest and be adapted to the measurement of interest and present hemodynamic conditions. Typical settings for venc are 150–200 cm/s in the thoracic aorta, 250–400 cm/s in the aorta with aortic stenosis or coarctation, 100–150 cm/s for intracardiac flow, and 50–80 cm/s in large vessels of the venous system. If a large imaging volume with various vessels is examined, there may be no optimal venc setting, and the value has to be chosen in accordance to the clinical question.

Phase Offset Errors and Corrections

There are multiple sources of phase offset errors in PC and 4D flow MRI that can degrade image quality and impair measurements by introducing inaccuracies in flow quantification. The most commonly encountered inaccuracies include phase offset errors due to eddy currents [20], Maxwell terms [21], and gradient field nonlinearity [22]. A detailed description and discussion of these sources of phase offset errors are beyond the scope of this review article. Nonetheless, it is important to apply appropriate correction strategies to compensate for these potential sources of error before further processing of the data for 3D visualization or flow quantification. While correction for Maxwell terms and gradient field nonlinearity can be performed during image reconstruction (without the need for user interaction), eddy current correction cannot easily be automated and has to be integrated into the data analysis workflow.

The most commonly employed strategy for eddy current correction is based on the methodology presented by Walker et al. in 1993 [20]. The approach is based on thresh-holding to identify regions with static tissue. These regions are then used to estimate eddy current induced linearly varying phase offset errors, which are subsequently subtracted from the entire image. An alternative strategy requires the scanning of a large spherical (static) phantom directly after the 4D flow scan with identical imaging parameters followed by the subtraction of the resulting phase difference images from the in vivo 4D flow data. However, the long scan time and logistics needed to perform the additional 4D flow phantom scan make this option less desirable, and image-based correction is most often used. Unfortunately, no unified strategies, algorithms, or software across different MR system vendors and 4D flow MRI applications exist. Nevertheless, studies have shown that 4D flow MRI can be reliably used for 3D visualization and flow quantification if appropriate correction strategies such as proposed by Walker et al. [20] are employed.

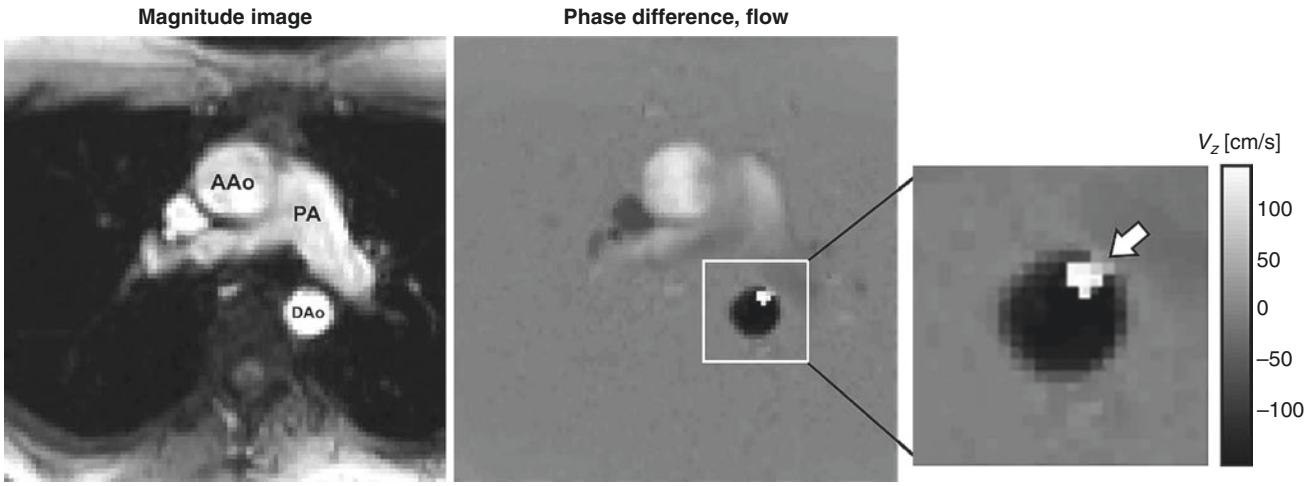

Fig. 7.3 Typical appearance of velocity aliasing in through plane-encoded blood flow velocities measurements in the ascending (AAo) and descending (DAo) aorta and the pulmonary artery (PA). Regions in the descending aorta with systolic blood flow velocities exceeding the predefined velocity sensitivity (venc) lead to in mis-encoding of blood flow and a phase wraparound in the phase-difference images (right, white arrow). Lower blood flow velocities in the ascending aorta (i.e., <venc) results in un-aliased and more homogenous depiction of through-plane flow

Applications of 2D CINE PC-MRI

Flow Quantification

Applications of 2D CINE PC-MRI include the assessment of left ventricular performance (e.g., cardiac output), regurgitation volumes in case of valve insufficiency, or evaluation of peak velocities in stenotic regions (e.g., aortic coarctation). In this context, quantification of blood flow using 2D CINE PC-MRI has been widely employed in a number of clinical applications such as heart valve disease or for the assessment of atrial and ventricular shunts [10–17]. Data analysis typically includes the semiautomatic segmentation of the vascular lumen or region of interest. Once the lumen boundaries have been defined, relevant parameters such as volume flow, peak systolic velocity, or retrograde fraction can be quantified. Figure 7.4 illustrates flow analysis and quantification in the ascending aorta of a healthy subject.

Q_P/Q_S Ratio

In the clinical setting of cardiovascular MRI, two-dimensional PC imaging planes transecting the aorta and main pulmonary artery are commonly used representing the aortic (Q_S) and pulmonary (Q_P) flow. The ratio Q_P/Q_S (normal adults 1.05, range 0.98–1.07; normal children, mean 0.99, range 0.85–1) [23, 24] can be significantly altered in the presence of a right-to-left ($Q_P/Q_S > 1$) [14, 25] or left-to-right ($Q_P/Q_S < 1$) shunts such as atrial-septal or ventricular-septal defects [23, 26].

Stenosis Quantification and Estimation of Pressure Gradients

In patients with vessel stenosis or narrowing such as aortic coarctation, a imaging plane along the long-axis of the vessel with in-plane flow encoding along the main flow direction enables identification of the location of the flow acceleration indicative of stenosis of varying degrees [27, 28]. Subsequently, 2D PC acquisitions are performed proximal to, at, and distal to the stenosis to obtain a sense of the hemodynamic significance of the stenosis to determine the systolic peak velocity v_{sys}. Similar to direct trans-stenotic pressure measurements invasively acquired by catheter placement and comparable to echocardiographic estimation, systolic pressure gradients can be estimated following the modified Bernoulli equation, $\Delta P = 4(v_{sys}^2)$, to assess stenosis severity [28].

Assessment of Cardiac Valve Function

Currently, PC-MRI is only accepted as a second-line diagnostic tool in ACC/AHA guidelines for diagnosis of valvular stenosis or regurgitation [29]. Measurements desired to ana-

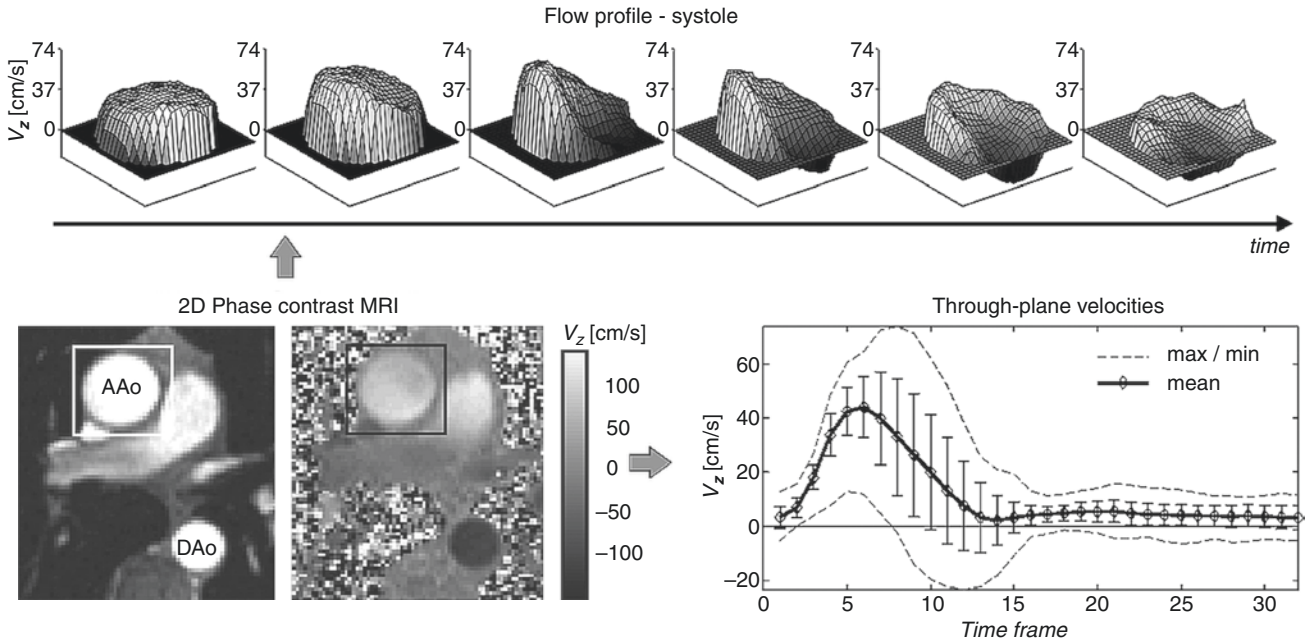

Fig. 7.4 Blood flow quantification based on 2D CINE PC-MRI with through-plane velocity encoding located in the proximal ascending aorta (AAo) just above the aortic valve. Delineation of vessel boundaries permits the calculation of mean, max, and min blood flow velocities (lower right) which can be used to calculate average and peak flow rates. Additional visualization of systolic through-plane flow profiles (top) provides detailed insights into the temporal evolution of the spatial distribution of blood flow velocities

lyze stenosis severity and regurgitant volumes via flow and velocity measurements are not trivial due to the cardiac and associated valvular motion as well as the presence of turbulent and accelerated flow. Furthermore, motion-adapted imaging strategies [30] or short TE techniques [31] are to date not routinely available on clinical scanners.

Nevertheless, 2D CINE PC-MRI has been evaluated and clinically correlated with ultrasound measurements using orifice area, flow, and velocity to estimate disease severity [32–35]. While ultrasound remains the widely accepted reference standard, a MR-based valve evaluation can allow for a comprehensive work-up during any cardiac MR scan. Regurgitant volumes and fractions can be readily assessed in the absence of shunts. Figure 7.5 illustrates the use of 2D CINE PC-MRI with in-plane velocity encoding for the identification of a regurgitate jet flow in the left ventricular outflow tract in a patient with aortic insufficiency. In addition to high blood flow velocities during systolic, in-plane flow encoding clearly reveals a diastolic flow jet associated with accelerated and reverse flow through the incompletely closed valve. Once such stenotic jets have been identified, a second 2D CINE PC-MRI scan with through-plane velocity encoding orthogonal to the flow jet direction can be used to quantify the regurgitant flow fraction. It should be noted that flow assessment in such cases can be complicated by the developing turbulence and associated dephasing and displacement error, the often eccentric stenotic jet, and the need to carefully align the acquisition plane with its direction.

Advanced Techniques

A number of more advanced and promising flow MR imaging techniques have been reported, which allow a more comprehensive emulation of blood flow characteristics. A selection of advanced techniques includes:

- Real-time phase-contrast MRI for the evaluation of flow changes on short time scales [36, 37]
- Fourier or Bayesian multipoint velocity encoding to encode flow velocities as a separate dimension and assess sub-voxel velocity distributions [38–40]
- 4D flow MRI for the comprehensive analysis of complex time-resolved 3D blood flow characteristics [41–43]
- Direct encoding of the acceleration component of blood flow [44, 45]

In the following, the basic principles and potential application for two emerging techniques, real-time flow imaging and 4D flow MRI, are presented.

Real-Time Flow Imaging

For certain subjects, e.g., patients with congestive heart failure and shortness of breath, the length of the breath-holding period required to collect 2D CINE PC-MRI data may not be tolerable. Several real-time MR acquisition strategies have recently been developed for real-time cardiovascular flow imaging [46–48]. To achieve sufficiently high frame rates needed for real-time flow acquisitions, the 2D PC-MRI pulse sequence combines fast data readout modules (such as echo planar imaging, EPI) with parallel acceleration in the temporal direction. In addition, a modified phase-contrast reconstruction algorithm, shared velocity encoding, has been employed to enhance temporal update rates [49, 50]. Shared velocity encoding is used to further improve temporal resolution based on the concept to share sets of full k-space data between adjacent frames and doubles the effective frame rate.

A number of studies have demonstrated the feasibility of real-time flow imaging for the visualization and quantification of blood flow without the need for ECG gating and

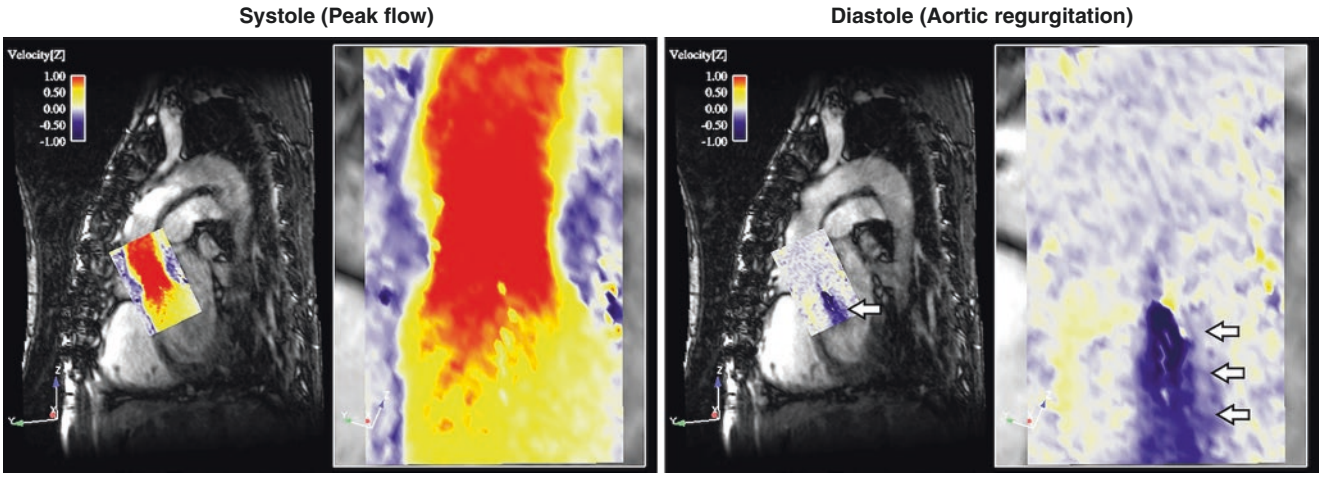

Fig. 7.5 Color-coded in-plane velocity for a patient with aortic insufficiency overlaid onto the simultaneously acquired anatomical (magnitude) images. The systolic and diastolic time frames show in-plane blood flow velocities normal to the aortic valve. A diastolic velocity jet indicating incomplete valve closure and complex regurgitant blood flow (white arrows) is clearly visible during diastole

breath holding [49, 51–56]. Studies have shown that real-time flow imaging can quantify accentuated and discordant respirophasic changes in flow velocities or response of blood flow to psychosocial stress that cannot be identified noninvasively with standard 2D CINE PC-MRI [52, 55]. As an example, Fig. 7.6 illustrates the application of real-time flow imaging for the quantification of left atrial blood flow in patients with atrial fibrillation. In addition, real-time flow imaging with in-plane velocity encoding and color coding of velocities similar to Doppler ultrasounds can be employed to provide an intuitive visualization (real-time color-flow movies) of, e.g., intracardiac flow, carotid flow, and proximal coronary flow [54].

4D Flow MRI

Further developments of PC-MRI techniques have allowed for the acquisition of time-resolved (CINE), three-dimensional (3D) PC-MRI data with three-directional velocity encoding which is often referred to as "4D flow MRI"(also termed "flow-sensitive 4D MRI," "time-resolved 3D velocity mapping," or "4D velocity mapping"). In contrast to standard 2D CINE PC-MRI which allows for the evaluation of blood flow in a single user selected 2D slice, 4D flow MRI can provide information on the temporal and spatial evolution of 3D blood flow with full volumetric coverage of any cardiac or vascular region of interest [42, 43, 57, 58]. The technique is based on prospectively or retrospectively ECG-gated 3D PC-MRI using three-directional velocity encoding [42, 59]. For application on the thorax and abdomen such as the heart, aorta, main pulmonary arteries, or the liver vasculature, respiratory control by bellows, self-gating techniques, or navigator gating of the diaphragm motions is used to minimize breathing artifacts.

Recent technical developments, including highly undersampled radial 4D flow techniques (PC-VIPR) [60–64] and highly accelerated 4D flow methods (kt-GRAPPA [65–68], kt-PCA [69–71], compressed sensing [72–74]), have resulted in reasonable overall scan times, e.g., 8–12 min for 4D flow MRI of the aorta and 10–15 min for whole heart coverage. As a result, the application of 4D flow MRI in a clinical setting has become more feasible. Within these scan time constraints, typical imaging parameters for thoracic 4D flow MRI applications are summarized below:

- Thoracic aorta: spatial resolution = (2.0–2.5)mm^3, temporal resolution = 35–50 ms, velocity sensitivity (venc) = 150–300 cm/s, total scan time: 5–8 min
- Heart: spatial resolution = (2.5–3.0)mm^3, temporal resolution = 35–45 ms, velocity sensitivity (venc) = 100–120 cm/s, total scan time: 6–12 min

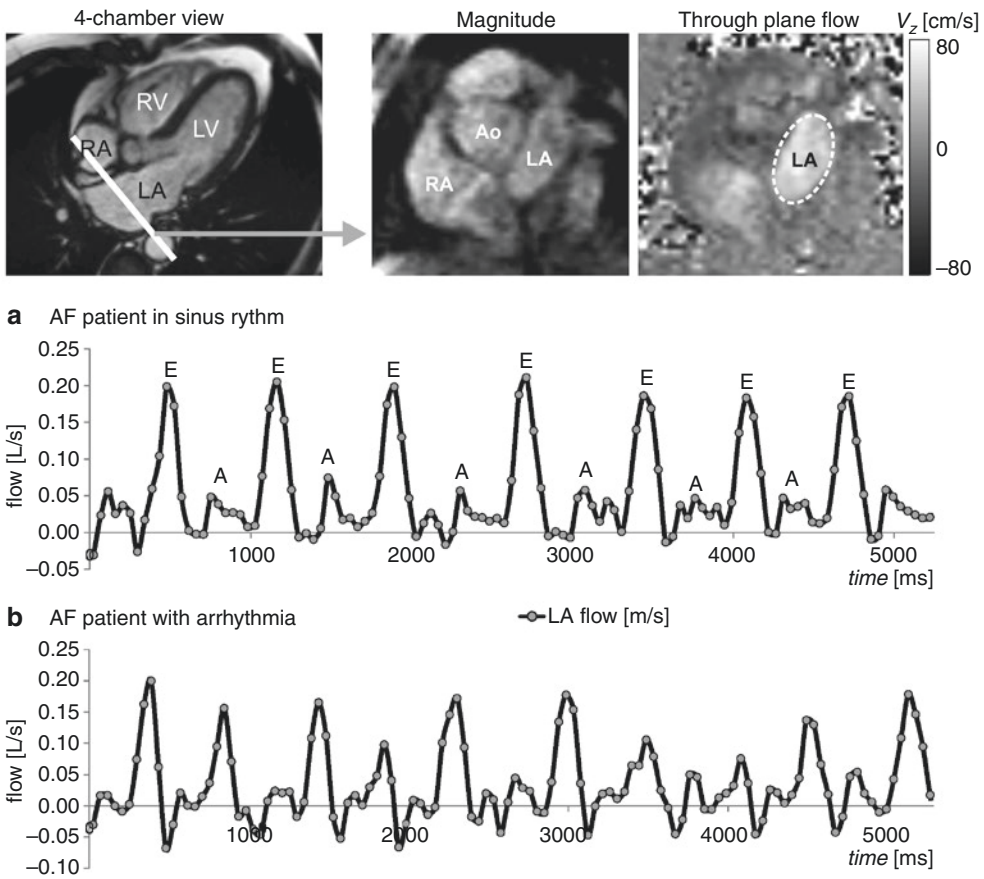

Fig. 7.6 Real-time flow curves at mid-atrial short axis level over multiple heartbeats in two patients with atrial fibrillation in sinus rhythm (**a**) and with arrhythmia (**b**) during the MRI scan. The flow-time curves show beat-to-beat flow dynamics over multiple heartbeats with an effective frame rate of 50 ms. Note the marked beat-to-beat variability of flow-time curves in the patient with arrhythmia

The nature of the 4D flow data (three spatial dimensions, three blood flow velocity directions and time) points toward its ability to provide 3D visualization and quantification of cardiovascular hemodynamics. Three-dimensional blood flow visualization (streamlines/pathlines) permits the depiction of complex flow patterns and changes in cardiovascular hemodynamic associated with cardiovascular disease [75–77]. Three-dimensional streamlines are instantaneous traces which run parallel to the direction of the measured blood flow velocity field (Fig. 7.7b). Time-resolved 3D pathlines utilize the full 4D (3D and time) information and can be used to visualize the spatiotemporal dynamics of pulsatile 3D blood flow patterns. Both streamlines and pathlines are often color coded to display the local absolute blood flow velocity. The anatomic and velocity information of the 4D flow data can additionally be used to derive a 3D phase-contrast angiogram (3D PC-MRA), which can be combined with 3D blood flow visualization to guide anatomic orientation and analysis plane placement for flow quantification (see Fig. 7.7).

A particular advantage of 4D flow MRI over 2D CINE PC-MRI is related to the possibility for retrospective selection of territories at any location inside the 3D data volume to perform post hoc quantification of blood flow parameters such as total flow, peak velocity, or regurgitant fraction [59, 78–81]. Four-dimensional flow MRI offers a single and easy method to prescribe the data acquisition (3D volume covering entire cardiovascular region of interest), instead of multiple 2D planes for flow analysis with standard 2D PC-MRI. Two-dimensional planes are time-consuming and difficult to position in cases with complex vascular architecture (e.g., congenital heart disease, liver vasculature), often requiring multiple acquisitions. Moreover, the combination of 3D blood flow visualization with flow quantification enables a comprehensive evaluation of the impact of cardiovascular pathologies on global and local changes in cardiac or vascular hemodynamics [82–88].

A growing number of patient studies have demonstrated the potential of 4D flow MRI for improved characterization of cardiovascular disease. Previously reported results include the application of 4D flow MRI for the analysis of 3D blood flow in the heart [80, 82, 89–93], atria [94, 95] and heart valves [83, 96–98], the thoracic [7, 84, 85, 98–104] and abdominal aorta [105], the main pulmonary vessels [62, 106–108], carotid arteries [72, 109–111], large intracranial arteries and veins [112–116], the arterial and portal venous systems of the liver [61–63, 117, 118], peripheral arteries [119], and renal arteries [120–122].

A number of studies have shown that localized alterations in cardiac and vascular anatomy such as a mild ascending aortic aneurysms or moderate valve disease can result in extensive alterations of local blood flow patterns. Such findings indicate a potentially important role for the comprehensive analysis of hemodynamic changes based on 4D flow MRI rather than relying on simple anatomical parameters (vessel diameters, stenosis grade, etc.). However, the predic-

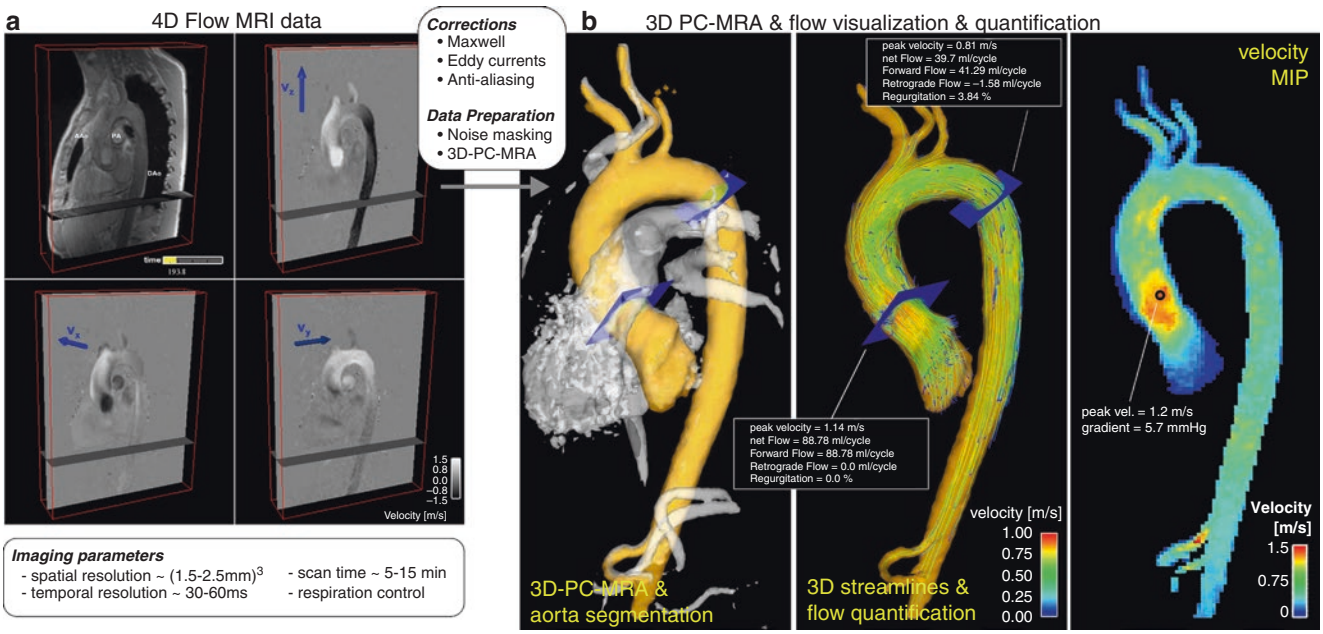

Fig. 7.7 Acquisition of 4D flow MRI data (**a**) and visualization and quantification of 3D hemodynamics (**b**) in the aorta of a healthy subject. The 4D flow data comprises information along all three spatial dimension and three velocity directions and time in the cardiac cycle. A 3D phase-contrast angiogram (**b**, iso-surface rendering of the aorta) can be calculated from 4D flow MRI data to aid visualization and placement of analysis planes for retrospective flow quantification. Calculation of a systolic maximum intensity projection (MIP, right) provides a quick and easily analyzable overview over systolic velocity distribution

tive and diagnostic value of the analyzed flow patterns and quantitative parameters are still limited. The presently available data does not (yet) allow prognostic statements, and larger trials including follow-up MR examinations before and after therapy or during the progression of disease are needed to evaluate the clinical value 4D flow MRI.

In addition to long acquisition times, another limitation of 4D flow MRI is related to the complex and often time-consuming post acquisition data analysis. 4D flow MRI can also provide the opportunity to improve upon current clinical hemodynamic assessments by deriving additional metrics of cardiovascular hemodynamics. A number of groups have shown that 4D flow MRI can be used to derive advanced hemodynamic measures such as wall shear stress [123–125], pressure difference [120, 126–128], pulse wave velocity [129, 130], turbulent kinetic energy, and others [131, 132] for an improved characterization of cardiovascular disease beyond simple measures of flow. More automated methods for flow visualization and retrospective quantification would thus be helpful for applications within a clinical workflow. New software tools and algorithms need to be developed, for example, to define standardized analysis planes in routinely acquired 4D velocity data.

In summary, 4D flow MRI has great potential for the detailed visualization of complex flow patterns associated with healthy and pathologically altered hemodynamics. The method allows for the evaluation of a large body of hemodynamic parameters (flow, WSS, pressure difference maps, turbulent kinetic energy, energy loss, etc.) that can be derived from the 4D flow data. Initial reports on the clinical application of these parameters are promising. It is still unclear, however, which parameters are most suitable for the evaluation of different types of cardiovascular pathologies. Longitudinal studies are thus warranted to investigate the predictive value of novel 4D flow hemodynamic parameters and their utility to complement existing clinical risk stratification and therapy management strategies.

Appendix: MR Signal Phase and Velocity Encoding

Changes in the MR signal induced by blood flow can be derived from the precession of spins in local magnetic fields. The measurement of MR signal phase allows for motion quantification of moving spins in the blood. The time evolution of the MR signal phase of the transversal magnetization of an object at the location $r(t)$ can be derived from the spatial-dependent Larmor frequency

$$\omega_L\left(\vec{r},t\right)=\gamma\left(B_0+\Delta B_0\left(\vec{r}\right)+\vec{r}\left(t\right)\vec{G}\left(t\right)\right) \tag{7.1}$$

where B_0 denotes the static main magnetic field, ΔB_0 reflects contributions by local field inhomogeneities, and $G(t)$ is the time-dependent magnetic field gradient. The resulting signal phase ϕ acquired at echo time TE can be derived by integrating the Larmor equation resulting in

$$\phi\left(\vec{r},\mathrm{TE}\right)=\phi_0\left(\vec{r}\right)+\gamma\int_{t_0}^{\mathrm{TE}}\vec{G}\left(t\right)\vec{r}\left(t\right)dt \tag{7.2}$$

where the initial signal phase and the effects of field inhomogeneities are combined in the spatially dependent and typically unknown background phase ϕ_0(r). To evaluate the effect of blood flow on the signal phase, the spatial location of a moving object or flowing spins can be approximated in first order as $\vec{r}\left(t\right)=\vec{r}_0+\vec{v}t$ with constant velocity v, i.e., it is implied that tissue motion or blood flow does not change fast with respect to the temporal footprint (TE) of the data acquisition. Equation (7.2) then simplifies to

$$\begin{aligned}\phi\left(\vec{r},\mathrm{TE}\right)&=\phi_0\left(\vec{r}\right)+\gamma\vec{r}_0\int_{t_0}^{\mathrm{TE}}\vec{G}\left(t\right)dt+\gamma\vec{v}\int_{t_0}^{\mathrm{TE}}\vec{G}\left(t\right)tdt\\&=\phi_0\left(\vec{r}\right)+\gamma\vec{r}_0\vec{M}_0+\gamma\vec{v}\vec{M}_1\end{aligned} \tag{7.3}$$

In addition to the background phase $\phi_0(r)$, the signal phase measured at TE is determined by the 0th and first order gradient moments M_0 and M_1. For PC-MRI, a bipolar gradient is typically used in order to quantify velocities, i.e., two gradients with identical amplitude G and duration Δt but with opposite polarity. For a bipolar gradient as depicted in Fig. 7.8, the symmetry of this gradient scheme results in a vanishing 0th gradient moment $M_0 = 0$ and a first gradient moment given by $M_1 = -G\Delta t^2$.

As a result, stationary spins no longer contribute to the signal phase, and Eq. (7.3) reduces to

$$\phi\left(\vec{r},\mathrm{TE}\right)=\phi_0\left(\vec{r}\right)+\gamma\vec{v}\vec{M}_1 \tag{7.4}$$

The remaining non-zero first gradient moment M_1 thus determines the velocity-induced signal phase, and flowing spins experience a contribution in the signal phase which is proportional to the velocity v of the moving spins as illustrated in Fig. 7.8. The flow-induced phase in Eq. 7.4 can be controlled by adjusting the first gradient moment M_1 by varying gradient duration Δt or amplitude G which determines the velocity sensitivity venc. However, the measured signal phase $\phi(r, \mathrm{TE})$ is still offset by the unknown background phase $\phi_0(r)$. By subtracting the phase $\phi_{ref}(r, \mathrm{TE})$ of an additionally performed reference scan, the background phase can be eliminated. The resulting phase difference $\Delta\phi = \phi - \phi_{\mathrm{ref}}$ finally yields the velocities of the moving spins:

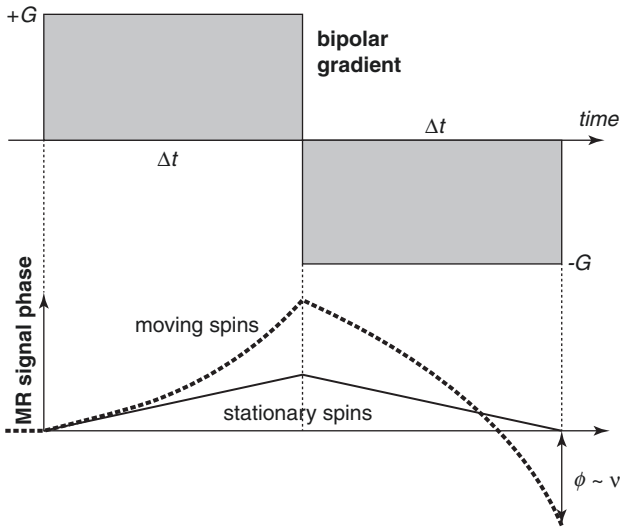

Fig. 7.8 Bipolar velocity encoding gradient and temporal evolution of the MR signal phase for stationary spins and an object moving with a constant flow velocity *v*

$$\vec{v} = \frac{\Delta\phi}{\gamma \Delta \vec{M}_1} \tag{7.5}$$

The calculated phase difference $\Delta\phi$ reflects changes in the MR signal phase associated with the motion component along the direction of the velocity encoding gradient. By adding a bipolar gradient to the MR pulse sequence along the read, phase, or slice direction and by subtracting a reference measurement without encoding gradient, flow or motion along each individual direction can be directly quantified.

References

1. Moran PR. A flow velocity zeugmatographic interlace for nmr imaging in humans. Magn Reson Imaging. 1982;1:197–203.
2. Bryant DJ, Payne JA, Firmin DN, Longmore DB. Measurement of flow with nmr imaging using a gradient pulse and phase difference technique. J Comput Assist Tomogr. 1984;8:588–93.
3. Nayler GL, Firmin DN, Longmore DB. Blood flow imaging by cine magnetic resonance. J Comput Assist Tomogr. 1986;10:715–22.
4. Firmin DN, Nayler GL, Klipstein RH, Underwood SR, Rees RS, Longmore DB. In vivo validation of MR velocity imaging. J Comput Assist Tomogr. 1987;11:751–6.
5. Pelc NJ, Herfkens RJ, Shimakawa A, Enzmann DR. Phase contrast cine magnetic resonance imaging. Magn Reson Q. 1991;7:229–54.
6. Kilner PJ, Yang GZ, Mohiaddin RH, Firmin DN, Longmore DB. Helical and retrograde secondary flow patterns in the aortic arch studied by three-directional magnetic resonance velocity mapping. Circulation. 1993;88:2235–47.
7. Kvitting JP, Ebbers T, Wigstrom L, Engvall J, Olin CL, Bolger AF. Flow patterns in the aortic root and the aorta studied with time-resolved, 3-dimensional, phase-contrast magnetic resonance imaging: implications for aortic valve-sparing surgery. J Thorac Cardiovasc Surg. 2004;127:1602–7.
8. Van Dijk P. Direct cardiac nmr imaging of heart wall and blood flow velocity. J Comput Assist Tomogr. 1984;171:429–36.
9. Mohiaddin RH, Pennell DJ. MR blood flow measurement. Clinical application in the heart and circulation. Cardiol Clin. 1998;16:161–87.
10. Atkinson DJ, Edelman RR. Cineangiography of the heart in a single breath hold with a segmented turboflash sequence. Radiology. 1991;178:357–60.
11. Pelc NJ, Bernstein MA, Shimakawa A, Glover GH. Encoding strategies for three-direction phase-contrast MR imaging of flow. J Magn Reson Imaging. 1991;1:405–13.
12. Thomsen C, Cortsen M, Sondergaard L, Henriksen O, Stahlberg F. A segmented k-space velocity mapping protocol for quantification of renal artery blood flow during breath-holding. J Magn Reson Imaging. 1995;5:393–401.
13. Chai P, Mohiaddin R. How we perform cardiovascular magnetic resonance flow assessment using phase-contrast velocity mapping. J Cardiovasc Magn Reson. 2005;7:705–16.
14. Beerbaum P, Korperich H, Barth P, Esdorn H, Gieseke J, Meyer H. Noninvasive quantification of left-to-right shunt in pediatric patients: phase-contrast cine magnetic resonance imaging compared with invasive oximetry. Circulation. 2001;103:2476–82.
15. Didier D. Assessment of valve disease: qualitative and quantitative. Magn Reson Imaging Clin N Am. 2003;11:115–34, vii
16. Gatehouse PD, Keegan J, Crowe LA, Masood S, Mohiaddin RH, Kreitner KF, Firmin DN. Applications of phase-contrast flow and velocity imaging in cardiovascular MRI. Eur Radiol. 2005;15:2172–84.
17. Underwood SR, Firmin DN, Rees RS, Longmore DB. Magnetic resonance velocity mapping. Clin Phys Physiol Meas. 1990;11:37–43.
18. Bernstein MA, Shimakawa A, Pelc NJ. Minimizing te in moment-nulled or flow-encoded two- and three-dimensional gradient-echo imaging. J Magn Reson Imaging. 1992;2:583–8.
19. Bock J, Kreher BW, Hennig J, Markl M. Optimized pre-processing of time-resolved 2d and 3d phase contrast MRI data. In: 15th Annual Meeting of ISMRM. 2007.
20. Walker PG, Cranney GB, Scheidegger MB, Waseleski G, Pohost GM, Yoganathan AP. Semiautomated method for noise reduction and background phase error correction in MR phase velocity data. J Magn Reson Imaging. 1993;3:521–30.
21. Bernstein MA, Zhou XJ, Polzin JA, King KF, Ganin A, Pelc NJ, Glover GH. Concomitant gradient terms in phase contrast MR: analysis and correction. Magn Reson Med. 1998;39:300–8.
22. Markl M, Bammer R, Alley MT, Elkins CJ, Draney MT, Barnett A, et al. Generalized reconstruction of phase contrast MRI: analysis and correction of the effect of gradient field distortions. Magn Reson Med. 2003;50:791–801.
23. Arheden H, Holmqvist C, Thilen U, Hanseus K, Bjorkhem G, Pahlm O, et al. Left-to-right cardiac shunts: comparison of measurements obtained with MR velocity mapping and with radionuclide angiography. Radiology. 1999;211:453–8.
24. Powell AJ, Maier SE, Chung T, Geva T. Phase-velocity cine magnetic resonance imaging measurement of pulsatile blood flow in children and young adults: in vitro and in vivo validation. Pediatr Cardiol. 2000;21:104–10.
25. Beerbaum P, Korperich H, Gieseke J, Barth P, Peuster M, Meyer H. Rapid left-to-right shunt quantification in children by phase-contrast magnetic resonance imaging combined with sensitivity encoding (sense). Circulation. 2003;108:1355–61.
26. Iversen K, Jensen AS, Jensen TV, Vejlstrup NG, Sondergaard L. Combination therapy with bosentan and sildenafil in eisenmenger syndrome: a randomized, placebo-controlled, double-blinded trial. Eur Heart J. 2010;31:1124–31.
27. Mohiaddin RH, Kilner PJ, Rees S, Longmore DB. Magnetic resonance volume flow and jet velocity mapping in aortic coarctation. J Am Coll Cardiol. 1993;22:1515–21.

28. Kilner PJ, Firmin DN, Rees RS, Martinez J, Pennell DJ, Mohiaddin RH, Underwood SR, Longmore DB. Valve and great vessel stenosis: assessment with MR jet velocity mapping. Radiology. 1991;178:229–35.
29. Doherty JU, Kort S, Mehran R, Schoenhagen P, Soman P. ACC/AATS/AHA/ASE/ASNC/HRS/SCAI/SCCT/SCMR/STS. Appropriate Use Criteria for Multimodality Imaging in Valvular Heart Disease: A Report of the American College of Cardiology Appropriate Use Criteria Task Force, American Association for Thoracic Surgery, American Heart Association, American Society of Echocardiography, American Society of Nuclear Cardiology, Heart Rhythm Society, Society for Cardiovascular Angiography and Interventions, Society of Cardiovascular Computed Tomography, Society for Cardiovascular Magnetic Resonance, and Society of Thoracic Surgeons. J Am Coll Cardiol. 2017;70:1647–72.
30. Kozerke S, Schwitter J, Pedersen EM, Boesiger P. Aortic and mitral regurgitation: quantification using moving slice velocity mapping. J Magn Reson Imaging. 2001;14:106–12.
31. O'Brien KR, Myerson SG, Cowan BR, Young AA, Robson MD. Phase contrast ultrashort te: a more reliable technique for measurement of high-velocity turbulent stenotic jets. Magn Reson Med. 2009;62:626–36.
32. Altiok E, Frick M, Meyer CG, Al Ateah G, Napp A, Kirschfink A, et al. Comparison of two- and three-dimensional transthoracic echocardiography to cardiac magnetic resonance imaging for assessment of paravalvular regurgitation after transcatheter aortic valve implantation. Am J Cardiol. 2014;113:1859–66.
33. Cawley PJ, Hamilton-Craig C, Owens DS, Krieger EV, Strugnell WE, Mitsumori L, et al. Prospective comparison of valve regurgitation quantitation by cardiac magnetic resonance imaging and transthoracic echocardiography. Circ Cardiovasc Imaging. 2013;6:48–57.
34. Chan KM, Wage R, Symmonds K, Rahman-Haley S, Mohiaddin RH, Firmin DN, et al. Towards comprehensive assessment of mitral regurgitation using cardiovascular magnetic resonance. J Cardiovasc Magn Reson. 2008;10:61.
35. Dall'Armellina E, Hamilton CA, Hundley WG. Assessment of blood flow and valvular heart disease using phase-contrast cardiovascular magnetic resonance. Echocardiography. 2007;24:207–16.
36. Nayak KS, Pauly JM, Kerr AB, Hu BS, Nishimura DG. Real-time color flow MRI. Magn Reson Med. 2000;43:251–8.
37. Joseph AA, Merboldt KD, Voit D, Zhang S, Uecker M, et al. Real-time phase-contrast MRI of cardiovascular blood flow using undersampled radial fast low-angle shot and nonlinear inverse reconstruction. NMR Biomed. 2012;25:917–24.
38. Dumoulin CL, Souza SP, Hardy CJ, Ash SA. Quantitative measurement of blood flow using cylindrically localized fourier velocity encoding. Magnet Reson Med. 1991;21:242–50.
39. Macgowan CK, Kellenberger CJ, Detsky JS, Roman K, Yoo SJ. Real-time fourier velocity encoding: an in vivo evaluation. J Magn Reson Imaging. 2005;21:297–304.
40. Binter C, Knobloch V, Manka R, Sigfridsson A, Kozerke S. Bayesian multipoint velocity encoding for concurrent flow and turbulence mapping. Magn Reson Med. 2013;69:1337–45.
41. Markl M, Frydrychowicz A, Kozerke S, Hope M, Wieben O. 4d flow MRI. J Magnet Reson Imaging. 2012;36:1015–36.
42. Markl M, Kilner PJ, Ebbers T. Comprehensive 4d velocity mapping of the heart and great vessels by cardiovascular magnetic resonance. J Cardiovasc Magn Reson. 2011;13:7.
43. Wigstrom L, Sjoqvist L, Wranne B. Temporally resolved 3d phase-contrast imaging. Magn Reson Med. 1996;36:800–3.
44. Tasu JP, Jolivet O, Mousseaux E, Delouche A, Diebold B, Bittoun J. Acceleration mapping by fourier acceleration-encoding: in vitro study and initial results in the great thoracic vessels. Magn Reson Med. 1997;38:110–6.
45. Barker AJ, Staehle F, Bock J, Jung BA, Markl M. Analysis of complex cardiovascular flow with three-component acceleration-encoded MRI. Magn Reson Med. 2012;67:50–61.
46. Zhang S, Uecker M, Voit D, Merboldt KD, Frahm J. Real-time cardiovascular magnetic resonance at high temporal resolution: radial flash with nonlinear inverse reconstruction. J Cardiovasc Magn Reson. 2010;12:39.
47. Nayak KS, Hu BS. The future of real-time cardiac magnetic resonance imaging. Curr Cardiol Rep. 2005;7:45–51.
48. Kowalik GT, Steeden JA, Pandya B, Odille F, Atkinson D, et al. Real-time flow with fast gpu reconstruction for continuous assessment of cardiac output. J Magn Reson Imaging. 2012;36:1477–82.
49. Lin HY, Bender JA, Ding Y, Chung YC, Hinton AM, Pennell ML, et al. Shared velocity encoding: a method to improve the temporal resolution of phase-contrast velocity measurements. Magn Reson Med. 2012;68:703–10.
50. Kellman P, Epstein FH, McVeigh ER. Adaptive sensitivity encoding incorporating temporal filtering (tsense). Magn Reson Med. 2001;45:846–52.
51. Fasshauer M, Joseph AA, Kowallick JT, Unterberg-Buchwald C, Merboldt KD, Voit D, et al. Real-time phase-contrast flow MRI of haemodynamic changes in the ascending aorta and superior vena cava during mueller manoeuvre. Clin Radiol. 2014;69:1066–71.
52. Jones A, Steeden JA, Pruessner JC, Deanfield JE, Taylor AM, Muthurangu V. Detailed assessment of the hemodynamic response to psychosocial stress using real-time MRI. J Magn Reson Imaging. 2011;33:448–54.
53. Joseph A, Kowallick JT, Merboldt KD, Voit D, Schaetz S, Zhang S, et al. Real-time flow MRI of the aorta at a resolution of 40 msec. J Magn Reson Imaging. 2014;40:206–13.
54. Liu CY, Varadarajan P, Pohost GM, Nayak KS. Real-time color-flow MRI at 3 t using variable-density spiral phase contrast. Magn Reson Imaging. 2008;26:661–6.
55. Thavendiranathan P, Verhaert D, Walls MC, Bender JA, Rajagopalan S, Chung YC, et al. Simultaneous right and left heart real-time, free-breathing CMR flow quantification identifies constrictive physiology. JACC Cardiovasc Imaging. 2012;5:15–24.
56. Thompson RB, McVeigh ER. Real-time volumetric flow measurements with complex-difference MRI. Magn Reson Med. 2003;50:1248–55.
57. Frydrychowicz A, Francois CJ, Turski PA. Four-dimensional phase contrast magnetic resonance angiography: potential clinical applications. Eur J Radiol. 2011;80:24–35.
58. Hope MD, Sedlic T, Dyverfeldt P. Cardiothoracic magnetic resonance flow imaging. J Thorac Imaging. 2013;28:217–30.
59. Wigstrom L, Sjoqvist L, Wranne B. Temporally resolved 3d phase-contrast imaging. Magn Reson Med. 1996;36:800–3.
60. Wentland AL, Wieben O, Francois CJ, Boncyk C, Munoz Del Rio A, Johnson KM, et al. Aortic pulse wave velocity measurements with undersampled 4d flow-sensitive MRI: comparison with 2d and algorithm determination. J Magn Reson Imaging. 2013;37:853–9.
61. Roldan-Alzate A, Frydrychowicz A, Niespodzany E, Landgraf BR, Johnson KM, et al. In vivo validation of 4d flow MRI for assessing the hemodynamics of portal hypertension. J Magn Reson Imaging. 2013;37:1100–8.
62. Francois CJ, Srinivasan S, Schiebler ML, Reeder SB, Niespodzany E, Landgraf BR, et al. 4d cardiovascular magnetic resonance velocity mapping of alterations of right heart flow patterns and main pulmonary artery hemodynamics in tetralogy of fallot. J Cardiovasc Magn Reson. 2012;14:16.
63. Frydrychowicz A, Landgraf BR, Niespodzany E, Verma RW, Roldan-Alzate A, Johnson KM, et al. Four-dimensional velocity mapping of the hepatic and splanchnic vasculature with radial sampling at 3 tesla: a feasibility study in portal hypertension. J Magn Reson Imaging. 2011;34:577.

64. Johnson KM, Lum DP, Turski PA, Block WF, Mistretta CA, Wieben O. Improved 3d phase contrast MRI with off-resonance corrected dual echo vipr. Magn Reson Med. 2008;60:1329–36.
65. Schnell S, Markl M, Entezari P, Mahadewia RJ, Semaan E, Stankovic Z, et al. K-t GRAPPA accelerated four-dimensional flow MRI in the aorta: effect on scan time, image quality, and quantification of flow and wall shear stress. Magn Reson Med. 2014;72:522–33.
66. Stalder AF, Dong Z, Yang Q, Bock J, Hennig J, Markl M, Li K. Four-dimensional flow-sensitive MRI of the thoracic aorta: 12- versus 32-channel coil arrays. J Magn Reson Imaging. 2012;35:190–5.
67. Jung B, Honal M, Ullmann P, Hennig J, Markl M. Highly k-t-space-accelerated phase-contrast MRI. Magn Reson Med. 2008;60:1169–77.
68. Huang F, Akao J, Vijayakumar S, Duensing GR, Limkeman M. K-t GRAPPA: a k-space implementation for dynamic MRI with high reduction factor. Magn Reson Med. 2005;54:1172–84.
69. Knobloch V, Boesiger P, Kozerke S. Sparsity transform k-t principal component analysis for accelerating cine three-dimensional flow measurements. Magn Reson Med. 2013;70:53–63.
70. Giese D, Schaeffter T, Kozerke S. Highly undersampled phase-contrast flow measurements using compartment-based k-t principal component analysis. Magn Reson Med. 2013;69:434–43.
71. Pedersen H, Kozerke S, Ringgaard S, Nehrke K, Kim WY. K-t PCA: temporally constrained k-t blast reconstruction using principal component analysis. Magn Reson Med. 2009;62:706–16.
72. Tao Y, Rilling G, Davies M, Marshall I. Carotid blood flow measurement accelerated by compressed sensing: validation in healthy volunteers. Magn Reson Imaging. 2013;31:1485–91.
73. Tariq U, Hsiao A, Alley M, Zhang T, Lustig M, Vasanawala SS. Venous and arterial flow quantification are equally accurate and precise with parallel imaging compressed sensing 4d phase contrast MRI. J Magn Reson Imaging. 2013;37:1419–26.
74. Hsiao A, Lustig M, Alley MT, Murphy MJ, Vasanawala SS. Evaluation of valvular insufficiency and shunts with parallel-imaging compressed-sensing 4d phase-contrast MR imaging with stereoscopic 3d velocity-fusion volume-rendered visualization. Radiology. 2012;265:87–95.
75. Buonocore MH. Visualizing blood flow patterns using streamlines, arrows, and particle paths. Magn Reson Med. 1998;40:210–26.
76. Rodriguez Munoz D, Markl M, Moya Mur JL, Barker A, Fernandez-Golfin C, et al. Intracardiac flow visualization: current status and future directions. Eur Heart J Cardiovasc Imaging. 2013;14:1029–38.
77. Unterhinninghofen R, Ley S, Ley-Zaporozhan J, von Tengg-Kobligk H, Bock M, Kauczor HU, et al. Concepts for visualization of multidirectional phase-contrast MRI of the heart and large thoracic vessels. Acad Radiol. 2008;15:361–9.
78. Bogren HG, Mohiaddin RH, Yang GZ, Kilner PJ, Firmin DN. Magnetic resonance velocity vector mapping of blood flow in thoracic aortic aneurysms and grafts. J Thorac Cardiovasc Surg. 1995;110:704–14.
79. Markl M, Chan FP, Alley MT, Wedding KL, Draney MT, Elkins CJ, et al. Time-resolved three-dimensional phase-contrast MRI. J Magn Reson Imaging. 2003;17:499–506.
80. Roes SD, Hammer S, van der Geest RJ, Marsan NA, Bax JJ, Lamb HJ, et al. Flow assessment through four heart valves simultaneously using 3-dimensional 3-directional velocity-encoded magnetic resonance imaging with retrospective valve tracking in healthy volunteers and patients with valvular regurgitation. Investig Radiol. 2009;44:669–75.
81. Valverde I, Simpson J, Schaeffter T, Beerbaum P. 4d phase-contrast flow cardiovascular magnetic resonance: comprehensive quantification and visualization of flow dynamics in atrial septal defect and partial anomalous pulmonary venous return. Pediatr Cardiol. 2010;31:1244–8.
82. Wigstrom L, Ebbers T, Fyrenius A, Karlsson M, Engvall J, Wranne B, Bolger AF. Particle trace visualization of intracardiac flow using time-resolved 3d phase contrast MRI. Magn Reson Med. 1999;41:793–9.
83. Kozerke S, Hasenkam JM, Pedersen EM, Boesiger P. Visualization of flow patterns distal to aortic valve prostheses in humans using a fast approach for cine 3d velocity mapping. J Magn Reson Imaging. 2001;13:690–8.
84. Bogren HG, Buonocore MH, Valente RJ. Four-dimensional magnetic resonance velocity mapping of blood flow patterns in the aorta in patients with atherosclerotic coronary artery disease compared to age-matched normal subjects. J Magn Reson Imaging. 2004;19:417–27.
85. Markl M, Draney MT, Miller DC, Levin JM, Williamson EE, Pelc NJ, et al. Time-resolved three-dimensional magnetic resonance velocity mapping of aortic flow in healthy volunteers and patients after valve-sparing aortic root replacement. J Thorac Cardiovasc Surg. 2005;130:456–63.
86. Frydrychowicz A, Harloff A, Jung B, Zaitsev M, Weigang E, Bley TA, et al. Time-resolved, 3-dimensional magnetic resonance flow analysis at 3 t: visualization of normal and pathological aortic vascular hemodynamics. J Comput Assist Tomogr. 2007;31:9–15.
87. Hope MD, Meadows AK, Hope TA, Ordovas KG, Saloner D, Reddy GP, et al. Clinical evaluation of aortic coarctation with 4d flow MR imaging. J Magn Reson Imaging. 2010;31:711–8.
88. Markl M, Geiger J, Arnold R, Stroh A, Damjanovic D, et al. Comprehensive 4-dimensional magnetic resonance flow analysis after successful heart transplantation resolves controversial intraoperative findings and reveals complex hemodynamic alterations. Circulation. 2011;123:e381–3.
89. Kilner PJ, Yang GZ, Wilkes AJ, Mohiaddin RH, Firmin DN, Yacoub MH. Asymmetric redirection of flow through the heart. Nature. 2000;404:759–61.
90. Bolger AF, Heiberg E, Karlsson M, Wigstrom L, Engvall J, Sigfridsson A, et al. Transit of blood flow through the human left ventricle mapped by cardiovascular magnetic resonance. J Cardiovasc Magn Reson. 2007;9:741–7.
91. Uribe S, Beerbaum P, Sorensen TS, Rasmusson A, Razavi R, Schaeffter T. Four-dimensional (4d) flow of the whole heart and great vessels using real-time respiratory self-gating. Magn Reson Med. 2009;62:984–92.
92. Eriksson J, Carlhall CJ, Dyverfeldt P, Engvall J, Bolger AF, Ebbers T. Semi-automatic quantification of 4d left ventricular blood flow. J Cardiovasc Magn Reson. 2010;12:9.
93. Toger J, Carlsson M, Soderlind G, Arheden H, Heiberg E. Volume tracking: a new method for quantitative assessment and visualization of intracardiac blood flow from three-dimensional, time-resolved, three-component magnetic resonance velocity mapping. BMC Med Imaging. 2011;11:10.
94. Fluckiger JU, Goldberger JJ, Lee DC, Ng J, Lee R, Goyal A, Markl M. Left atrial flow velocity distribution and flow coherence using four-dimensional flow MRI: a pilot study investigating the impact of age and pre- and postintervention atrial fibrillation on atrial hemodynamics. J Magn Reson Imaging. 2013;38:580–7.
95. Fyrenius A, Wigstrom L, Ebbers T, Karlsson M, Engvall J, Bolger AF. Three dimensional flow in the human left atrium. Heart. 2001;86:448–55.
96. Westenberg JJ, Roes SD, Ajmone Marsan N, Binnendijk NM, Doornbos J, Bax JJ, et al. Mitral valve and tricuspid valve blood flow: accurate quantification with 3d velocity-encoded MR imaging with retrospective valve tracking. Radiology. 2008;249:792–800.
97. Kvitting JP, Dyverfeldt P, Sigfridsson A, Franzen S, Wigstrom L, et al. In vitro assessment of flow patterns and turbulence intensity in prosthetic heart valves using generalized phase-contrast MRI. J Magn Reson Imaging. 2010;31:1075–80.
98. Hope MD, Hope TA, Crook SE, Ordovas KG, Urbania TH, et al. 4d flow CMR in assessment of valve-related ascending aortic disease. JACC Cardiovasc Imaging. 2011;4:781–7.

99. Bogren HG, Buonocore MH. 4d magnetic resonance velocity mapping of blood flow patterns in the aorta in young vs. elderly normal subjects. J Magn Reson Imaging. 1999;10:861–9.
100. Hope MD, Hope TA, Meadows AK, Ordovas KG, Urbania TH, et al. Bicuspid aortic valve: four-dimensional MR evaluation of ascending aortic systolic flow patterns. Radiology. 2010;255:53–61.
101. Frydrychowicz A, Markl M, Hirtler D, Harloff A, Schlensak C, Geiger J, et al. Aortic hemodynamics in patients with and without repair of aortic coarctation: in vivo analysis by 4d flow-sensitive magnetic resonance imaging. Investig Radiol. 2011;46:317–25.
102. Barker AJ, Markl M, Burk J, Lorenz R, Bock J, Bauer S, et al. Bicuspid aortic valve is associated with altered wall shear stress in the ascending aorta. Circ Cardiovasc Imaging. 2012;5:457–66.
103. Burk J, Blanke P, Stankovic Z, Barker A, Russe M, Geiger J, et al. Evaluation of 3d blood flow patterns and wall shear stress in the normal and dilated thoracic aorta using flow-sensitive 4d CMR. J Cardiovasc Magn Reson. 2012;14:84.
104. Geiger J, Arnold R, Herzer L, Hirtler D, Stankovic Z, Russe M, et al. Aortic wall shear stress in marfan syndrome. Magn Reson Med. 2013;70:1137–44.
105. Wentland AL, Grist TM, Wieben O. Repeatability and internal consistency of abdominal 2d and 4d phase contrast MR flow measurements. Acad Radiol. 2013;20:699–704.
106. Reiter G, Reiter U, Kovacs G, Kainz B, Schmidt K, Maier R, et al. Magnetic resonance-derived 3-dimensional blood flow patterns in the main pulmonary artery as a marker of pulmonary hypertension and a measure of elevated mean pulmonary arterial pressure. Cir Cardiovasc Imaging. 2008;1:23–30.
107. Geiger J, Markl M, Jung B, Grohmann J, Stiller B, et al. 4d-mr flow analysis in patients after repair for tetralogy of fallot. Eur Radiol. 2011;21:1651–7.
108. Bachler P, Pinochet N, Sotelo J, Crelier G, Irarrazaval P, et al. Assessment of normal flow patterns in the pulmonary circulation by using 4d magnetic resonance velocity mapping. Magn Reson Imaging. 2013;31:178–88.
109. Harloff A, Albrecht F, Spreer J, Stalder A, Bock J, Frydrychowicz A, et al. 3d blood flow characteristics in the carotid artery bifurcation assessed by flow-sensitive 4d MRI at 3t. Magn Reson Med. 2009;61:65–74.
110. Markl M, Wegent F, Zech T, Bauer S, Strecker C, Schumacher M, et al. In vivo wall shear stress distribution in the carotid artery: effect of bifurcation geometry, internal carotid artery stenosis, and recanalization therapy. Circ Cardiovasc Imaging. 2010;3:647–55.
111. Meckel S, Leitner L, Bonati LH, Santini F, Schubert T, Stalder AF, et al. Intracranial artery velocity measurement using 4d pc MRI at 3 t: comparison with transcranial ultrasound techniques and 2d pc MRI. Neuroradiology. 2013;55:389–98.
112. Bammer R, Hope TA, Aksoy M, Alley MT. Time-resolved 3d quantitative flow MRI of the major intracranial vessels: initial experience and comparative evaluation at 1.5t and 3.0t in combination with parallel imaging. Magn Reson Med. 2007;57:127–40.
113. Wetzel S, Meckel S, Frydrychowicz A, Bonati L, Radue EW, Scheffler K, et al. In vivo assessment and visualization of intracranial arterial hemodynamics with flow-sensitized 4d MR imaging at 3t. AJNR Am J Neuroradiol. 2007;28:433–8.
114. Boussel L, Rayz V, Martin A, Acevedo-Bolton G, Lawton MT, Higashida R, et al. Phase-contrast magnetic resonance imaging measurements in intracranial aneurysms in vivo of flow patterns, velocity fields, and wall shear stress: comparison with computational fluid dynamics. Magn Reson Med. 2009;61:409–17.
115. Isoda H, Ohkura Y, Kosugi T, Hirano M, Takeda H, Hiramatsu H, et al. In vivo hemodynamic analysis of intracranial aneurysms obtained by magnetic resonance fluid dynamics (mrfd) based on time-resolved three-dimensional phase-contrast MRI. Neuroradiology. 2010;52:921–8.
116. van Ooij P, Guedon A, Poelma C, Schneiders J, Rutten MC, Marquering HA, et al. Complex flow patterns in a real-size intracranial aneurysm phantom: phase contrast MRI compared with particle image velocimetry and computational fluid dynamics. NMR Biomed. 2012;25(1):14–26.
117. Stankovic Z, Csatari Z, Deibert P, Euringer W, Blanke P, Kreisel W, et al. Normal and altered three-dimensional portal venous hemodynamics in patients with liver cirrhosis. Radiology. 2012;262:862–73.
118. Stankovic Z, Csatari Z, Deibert P, Euringer W, Jung B, Kreisel W, et al. A feasibility study to evaluate splanchnic arterial and venous hemodynamics by flow-sensitive 4d MRI compared with doppler ultrasound in patients with cirrhosis and controls. Eur J Gastroenterol Hepatol. 2013;25:669–75.
119. Frydrychowicz A, Winterer JT, Zaitsev M, Jung B, Hennig J, et al. Visualization of iliac and proximal femoral artery hemodynamics using time-resolved 3d phase contrast MRI at 3t. J Magn Reson Imaging. 2007;25:1085–92.
120. Lum DP, Johnson KM, Paul RK, Turk AS, Consigny DW, Grinde JR, et al. Transstenotic pressure gradients: measurement in swine – retrospectively ecg-gated 3d phase-contrast MR angiography versus endovascular pressure-sensing guidewires. Radiology. 2007;245:751–60.
121. Bley TA, Johnson KM, Francois CJ, Reeder SB, Schiebler ML, Landgraf BR, et al. Noninvasive assessment of transstenotic pressure gradients in porcine renal artery stenoses by using vastly undersampled phase-contrast MR angiography. Radiology. 2011;261:266–73.
122. Francois CJ, Lum DP, Johnson KM, Landgraf BR, Bley TA, Reeder SB, et al. Renal arteries: isotropic, high-spatial-resolution, unenhanced MR angiography with three-dimensional radial phase contrast. Radiology. 2011;258:254–60.
123. Stalder AF, Russe MF, Frydrychowicz A, Bock J, Hennig J, Markl M. Quantitative 2d and 3d phase contrast MRI: optimized analysis of blood flow and vessel wall parameters. Magn Reson Med. 2008;60:1218–31.
124. Markl M, Wallis W, Harloff A. Reproducibility of flow and wall shear stress analysis using flow-sensitive four-dimensional MRI. J Magn Reson Imaging. 2011;33:988–94.
125. Oshinski JN, Curtin JL, Loth F. Mean-average wall shear stress measurements in the common carotid artery. J Cardiovasc Magn Reson. 2006;8:717–22.
126. Tyszka JM, Laidlaw DH, Asa JW, Silverman JM. Three-dimensional, time-resolved (4d) relative pressure mapping using magnetic resonance imaging. J Magn Reson Imaging. 2000;12:321–9.
127. Ebbers T, Wigstrom L, Bolger AF, Engvall J, Karlsson M. Estimation of relative cardiovascular pressures using time-resolved three-dimensional phase contrast MRI. Magn Reson Med. 2001;45:872–9.
128. Bock J, Frydrychowicz A, Lorenz R, Hirtler D, Barker AJ, Johnson KM, et al. In vivo noninvasive 4d pressure difference mapping in the human aorta: phantom comparison and application in healthy volunteers and patients. Magn Reson Med. 2011;66:1079–88.
129. Bolster BD Jr, Atalar E, Hardy CJ, McVeigh ER. Accuracy of arterial pulse-wave velocity measurement using MR. J Magn Reson Imaging. 1998;8:878–88.
130. Markl M, Wallis W, Brendecke S, Simon J, Frydrychowicz A, Harloff A. Estimation of global aortic pulse wave velocity by flow-sensitive 4d MRI. Magn Reson Med. 2010;63:1575–82.
131. Dyverfeldt P, Sigfridsson A, Kvitting JP, Ebbers T. Quantification of intravoxel velocity standard deviation and turbulence intensity by generalizing phase-contrast MRI. Magn Reson Med. 2006;56:850–8.
132. Dyverfeldt P, Gardhagen R, Sigfridsson A, Karlsson M, Ebbers T. On MRI turbulence quantification. Magn Reson Imaging. 2009;27:913–22.

Contrast Agents in Cardiovascular Magnetic Resonance Imaging

8

David J. Murphy and Raymond Y. Kwong

Introduction

The inception of the era of magnetic resonance imaging (MRI) has transformed modern cardiovascular imaging. Since Damadian et al. manufactured the first whole-body MRI machine capable of imaging the human body in 1977 [1], continued advances in MRI technology have placed it at the forefront of noninvasive cardiovascular imaging. MRI provides reproducible, multi-parametric, multi-planar two-dimensional (2D), and three-dimensional (3D) imaging with high temporal and spatial resolution. MRI has an advantage over other noninvasive cardiovascular imaging modalities, as it does not expose the patient to ionizing radiation. It offers excellent soft tissue contrast, which can be further enhanced by the use of paramagnetic MR contrast agents, improving both the signal-to-noise (SNR) and contrast-to-noise (CNR) ratios.

General Considerations in MRI Contrast

Image Contrast

One of the principal advantages of MRI over other diagnostic imaging modalities is its superior soft tissue contrast. Image contrast in MRI refers to relative differences in signal intensity (SI) between different tissues, allowing for their differentiation by the reader on the MR image. Contrast exists between different tissues due to differences in proton density (the number of "MRI visible" protons per unit volume), inflow phenomena, susceptibility, and the tissue relaxation time. MRI pulse sequences are designed to emphasize these differences in signal intensity in order to provide images of diagnostic quality.

T1 and T2 Tissue Relaxation

When the human body is placed in the MRI magnet, protons in the body will precess in the strong magnetic field. The protons will align in the longitudinal direction of the external magnetic field (B_0). Each proton has a longitudinal vector pointing either with the external field (low-energy protons) or against the field (high-energy protons). Due to the small excess amount of low-energy protons, the resultant vector is a steady longitudinal magnetization along the direction of B_0, the magnitude of which is proportional to the strength of the external magnetic field, measured in teslas (T). There is no resultant vector in the transverse direction, as the individual protons point in random directions, canceling each other out. When an external radiofrequency (RF) pulse is applied, this has two effects. Some of the protons are excited to the high-energy state, pointing against the longitudinal magnetic field, and the spins get in phase in the transverse plane. This results in an overall reduction in the longitudinal magnetization vector, and an increased horizontal magnetization vector. Once the RF pulse is turned off, the higher-energy protons lose their energy and flip back to their low-energy orientation along the direction of B_0. This process, by which high-energy spins dissipate their energy and transform back to the lower-energy state, is called T1 or spin-lattice relaxation. This transfer occurs when a tissue encounters a magnetic field fluctuating close to its Larmor frequency, which is in turn dependent of the strength of B_0. The T1 relaxation time depends on the net transfer of energy from the spin to its surrounding environment ("lattice"), hence the term spin-lattice relaxation. As spin-lattice relaxation occurs, the longitudinal magnetization

D. J. Murphy
Non-invasive Cardiovascular Imaging, Radiology Division, Department of Radiology, Brigham and Women's Hospital, Boston, MA, USA

R. Y. Kwong (✉)
Non-invasive Cardiovascular Imaging, Cardiovascular Division, Department of Medicine, Brigham and Women's Hospital, Harvard Medical School, Boston, MA, USA
e-mail: rykwong@bwh.harvard.edu

R. Y. Kwong et al. (eds.), *Cardiovascular Magnetic Resonance Imaging*, Contemporary Cardiology,
https://doi.org/10.1007/978-1-4939-8841-9_8

component recovers in an exponential fashion. T1 is the length of time it takes for the longitudinal magnetization of a tissue to recover to 63% of its original value. T1 times vary between different tissues and among tissues in different magnetic field strengths, providing tissue contrast. Tissues with shorter T1 times have higher SI on T1-weighted images following each RF pulse.

After application of the RF pulse, the spins precess in phase in the transverse plane, resulting in an overall net transverse magnetization vector. Small local differences in the local magnetic field strength cause the spins to rotate at a slightly different rate, driving them out of phase. This process is called T2 or "spin-spin" relaxation. The transverse magnetization component of a tissue decays in an exponential fashion to its original zero value. The T2 value for a given tissue is the length of time it takes to reduce the magnetization by 63% of its peak value. T2 relaxation time is strongly influenced by the local tissue environment. Inhomogeneities in the local magnetic field (B1) drive faster local spin dephasing, resulting in a faster decay of transverse signal, referred to as T2* relaxation.

Relaxivity

MRI contrast agents improve image contrast by shortening tissue T1 and T2 relaxation times. Paramagnetic contrast agents shorten T1 and T2 relaxation times of water protons in their immediate surroundings, creating a locally increased magnetic field strength. This change in the local magnetic field strength results in increased local field inhomogeneities, driving the shortening of T1 and T2 relaxation. The resultant increased SI on T1-weighted images provides the basis behind the use of contrast agents in MR. The degree to which a contrast agent shortens T1 and T2 is referred to as relaxivity. This is the inverse of T1 and T2 and is expressed as R1 (s^{-1}) and R2 (s^{-1}), respectively. The increase in R1 or R2 after administration of a given concentration of contrast medium (C, mmol/L) is the relaxivity constant of that agent, denoted as r1 ($mM^{-1}\ s^{-1}$) and r2 ($mM^{-1}\ s^{-1}$), respectively.

$$R1 = 1/T1 = r1 \times C$$

$$R2 = 1/T2 = r2 \times C$$

As the concentration of the contrast agent (C) increases, this increases relaxivity, thus shortening T1, resulting in higher SI on T1-weighted imaging. This does not come without consequences though; T2 is also shortened resulting in lower SI on all MR images, including those with T1 weighting.

Paramagnetic Metals

Paramagnetic metals function as effective MR contrast agents due to their ability to add to the local magnetic field. They shorten both T1 and T2 relaxation times, but it is the former effect that is the most useful in clinical imaging, increasing SI on T1-weighted images. All of the lanthanide (rare-earth) metals with unpaired electrons have potential to be paramagnetic agents; however, most of these agents are not suitable for clinical MRI due to their unmatched metal spin relaxation time and Larmor frequency [2]. Those rare-earth metals with suitable characteristics for MRI include gadolinium (Gd^{3+}), manganese (Mn^{2+}), iron (Fe^{3+}), and dysprosium (Dy^{3+}) [3]. Initial studies in the 1980s explored the use of manganese (Mn^{2+}) [4] and iron (Fe^{3+}) [5]-based contrast agents, before a German group, led by Weinmann et al., demonstrated that gadolinium (Gd^{3+}) was an effective paramagnetic ion in terms of T1 relaxivity [6, 7].

Gadolinium

Gadolinium does not produce MRI signal by itself; it achieves this by altering the surrounding magnetic field. The Gd^{3+} ion has seven unpaired electrons, each of which contributes to a strong magnetic moment, and an unusually strong hydrogen-proton spin-lattice relaxation effect. This makes it an ideal paramagnetic contrast agent. The magnetic moment (μ) of each unpaired electron is over 600 times greater than that of a proton [8]. The T1 relaxation time is proportional to the square of the magnetic moment (μ^2); the presence of Gd^{3+} causes protons nearby to relax a million times faster than usual, resulting in increased T1 SI. The Gd^{3+} ion itself is highly toxic; therefore, they are chelated with organic ligands to create gadolinium-based contrast agents (GBCAs) that can be used safely in clinical imaging.

The performance of a contrast agent is highly dependent on its concentration and its relaxivity constant, a numerical expression of the extent to which it shortens T1 and T2 relaxation times in a given magnetic field strength. The relationship between signal intensity and gadolinium concentration is however not linear. At higher concentrations, its T2 shortening effect can overcome the T1 shortening causing signal loss, even in T1-weighted images. This is the main reason why MRI SI is not directly proportional to the concentration of gadolinium, and why beyond a certain concentration, signal loss can occur. This effect can be observed in routine clinical practice as localized signal loss in areas with high gadolinium concentrations, such as in the urinary bladder, renal collecting systems, and the veins adjacent to the injection site.

Super-Paramagnetic Agents

Super-paramagnetic agents are another group of rare-earth metals that can be used as MR contrast agents. They form a significantly larger magnetic moment than the paramagnetic agents such as gadolinium. This larger magnetic moment has a substantially greater effect on shortening T2 rather than T1

relaxation times, causing areas of reduced SI on T2-weighted imaging. These agents are made of an iron oxide core or iron/manganese composite, covered in a polymer matrix.

Gadolinium-Based Contrast Agents (GBCAs)

Basic Structure

All of the gadolinium-based contrast agents (GBCAs) contain the paramagnetic gadolinium ion, Gd^{3+}. It is complexed with a ligand or chelator to protect against the potential toxic effects of the free Gd^{3+} ion. The free Gd^{3+} ion is highly toxic and can competitively inhibit calcium (Ca^{2+}) ions, which can adversely affect enzyme activity and voltage-gated calcium channels [9]. The presence of a chelator protects the endogenous tissue from interacting with the toxic Gd^{3+} ions and allows the agent to be excreted from the body without undergoing significant biotransformation. In order to prevent dissociation of free Gd^{3+} ions from the GBCA in vivo, the chelator must be powerful [10]. The presence of the chelator does hinder the paramagnetic effect of the Gd^{3+} ions, reducing the overall relaxivity of GBCAs [11]. Despite the presence of a chelator, no GBCA is completely resistant to dissociation of free Gd^{3+} ions. It is important, therefore, that GBCAs are rapidly cleared from the body after injection and imaging to prevent accumulation of a potentially toxic agent. Currently available GBCAs are largely cleared by either renal or hepatobiliary excretion, depending on the individual agent.

There are currently nine available GBCAs licensed by the European Medicines Agency (EMA) and the Food and Drug Administration (FDA) in the USA for clinical use. The properties of the common GBCAs are summarized in Table 8.1. These different agents can be classified according to their chemical structure. The chelating ligands are either linear or macrocyclic in structure, and the overall GBCA structure is either ionic (possessing a charge) or nonionic (neutral). In the linear agents, the ligand wraps around the Gd^{3+} ion, but does not completely enclose it. The macrocyclic agents consist of a chelator, which completely surrounds the Gd^{3+} ion in a cage-like structure. The latter agents demonstrate greater stability in vivo than the linear agents, with little (if any) free Gd^{3+} ion dissociation, even in patients with significant renal impairment [12]. The Gd^{3+} ion has nine coordination sites; eight are used as bonds between the Gd^{3+} ion and its chelator, with the single remaining site of importance in the GBCA's primary function as a paramagnetic agent and its interaction with surrounding water molecules [13]. The ionic linear GBCAs (gadopentetate dimeglumine (Gd-DTPA), gadoxetate disodium (Gd-EOB-DTPA), gadofosveset trisodium (Gd-DTPA-DO3A)) each have an overall negative charge due to five ionic carboxylic oxygen-binding atoms (each with one negative charge) and three neutral amino nitrogen atoms binding with the Gd^{3+} ion. This overall negative charge is neutralized by the addition of either a sugar amine with a positive charge (meglumine) or sodium (Na^{+}) ion. The nonionic linear GBCA (gadodiamide (GD-DTBA-BMA), gadoversetamide (Gd-DTPA-BMEA)) ligands bind the Gd^{3+} ion with three carboxylic oxygen-binding atoms, two nonionic carboxylic oxygen-binding atoms, and three neutral amino nitrogen atoms. This results in no overall charge, but the bind between the Gd^{3+} ion and chelator is weaker than in the linear ionic compounds, decreasing the stability of the linear nonionic compounds.

The macrocylic GBCAs are derived from a macrocyclic polyamino ring, with a greater inherent stability compared with their linear counterparts. The macrocyclic GBCAs can be divided into ionic and nonionic agents, based on the number of ionic carboxylic oxygen atoms in the chelator; those with more than three will have an overall negative charge. Both the ionic macrocyclic GBCA (gadoterate meglumine (Gd-DOTA)) and nonionic GBCAs (gadobutrol (Gd-BT-DO3A), gadoteridol (Gd-HP-DO3A)) are inherently stable. The nonionic macrocyclic GBCAs have a lower osmolality and viscosity than the ionic macrocyclic agents [13].

Stability

The stability of GBCAs can be described with reference to the concepts of thermodynamic and kinetic stability. Thermodynamic stability is the energy required to break the bonds between the Gd^{3+} ion and its chelator, resulting in release of the free Gd^{3+} ion. Kinetic stability is the rate at which this dissociation occurs. These properties depend on a number of factors, including the inherent structure of the agent (macrocyclic vs linear, strength of ionic bonds present) and the surrounding environment (temperature and pH). For clinically available GBCAs, the ligand structure, be it macrocyclic or linear, is the most important variable in determining dissociation kinetics. This is due to the requirement for multiple bonds to be simultaneously broken for the Gd^{3+} ion to break free from a macrocyclic ligand, whereas the Gd^{3+} ion can break free from the linear ligands one bond at a time, akin to opening a zip on an item of clothing. This results in the macrocyclic agents having a higher kinetic stability compared to their linear counterparts [14]. In addition, linear GBCAs are more susceptible to competitive reactions between endogenous cations, such as copper (Cu^{2+}) and zinc (Zn^{2+}), and the ligand resulting in Gd^{3+} dissociation [15]. The dissociation half-life of GBCAs are reported as kinetic stability in acidic conditions (pH 1.0), because the dissociation rates at physiological conditions (pH 7.4) are too slow to accurately measure [10, 16].

Osmolality

The majority of GBCAs are formulated at 0.5 M (mol/L). This allows for rapid administration, and by consequence they are somewhat hyperosmolar relative to plasma. Agents

Table 8.1 Summary table of gadolinium-based contrast agent's properties [8]

Class	Charge	Chemical name	Abbreviation	Trade name	Concentration (mol/L)	Relaxivity (L/mmol s) (3T in plasma)	Osmolality (mOsm/kg H20,37 C)	Excretion	Conditional complex stability, log K_{cond}	NSF risk
Linear	Nonionic	Gadodiamide	Gd-DTPA-BMA	OmniScan *(GE Healthcare)*	0.5	4.0	789	Renal	14.9	High
		Gadoversetamide	Gd-DTPA-BMEA	OptiMARK *(Mallinckrodt)*	0.5	4.5	1110	Renal	15.0	High
	Ionic	Gadopentetate dimeglumine	Gd-DTPA	Magnevist *(Bayer)*	0.5	3.7	1960	Renal	18.4	High
		Gadobenate dimeglumine	Gd-BOPTA	MultiHance *(Bracco)*	0.5	5.5	1970	Renal (95%) HPB (5%)	18.4	Intermediate
		Gadoxetate disodium	Gd-EOB-DTPA	Primovist Eovist *(Bayer)*	0.25	6.2	688	Renal (50%) HPB (50%)	18.7	Intermediate
		Gadofosveset trisodium	Gd-DTPA-DO3A	Ablavar *(Lantheus)*	0.25	9.9	825	Renal (95%) HPB (5%)	18.9	Intermediate
Macrocyclic	Nonionic	Gadobutrol	Gd-BT-DO3A	Gadovist Gadavist *(Bayer)*	1.0	5.0	1603	Renal	15.5	Low
		Gadoteridol	Gd-HP-DO3A	ProHance *(Bracco)*	0.5	3.7	630	Renal	17.2	Low
	Ionic	Gadoterate meglumine	Gd-DOTA	Dotarem *(Guerbet)*	0.5	3.5	1350	Renal	19.3	Low

Reprinted from Lohrke et al. [8]

with lower osmolality have improved dose tolerance, which is useful when administering rapid boluses via a power injector. GBCAs with higher osmolality can be problematic in cases of extravasation and can result in local soft tissue necrosis [17, 18].

Biodistribution and Elimination

The distribution of the various GBCAs throughout the body after administration differs for each agent and is referred to as biodistribution. After intravenous injection, GBCAs first enter the bloodstream. From here, the majority of GBCAs diffuse into the interstitial space (space between cells) from the capillaries, rapidly reaching equilibrium between the intravascular and interstitial compartments. Collectively, these two compartments make up the extracellular compartment. In addition, the GBCA molecules may be taken up by cells in specific organs (liver and kidney) according to their chemical structure; this occurs by both active uptake and passive diffusion. This varying biodistribution of GBCAs allows us to group them accordingly into extracellular, intracellular, tissue-specific and blood pool/intravascular agents [19]. For the majority of commercially available GBCAs, there is no intracellular distribution, except for varying hepatocyte uptake for certain agents (gadoxetate disodium/gadoxetic acid and gadobenate dimeglumine) [20]. In cardiovascular imaging, we focus mainly on the extracellular and intravascular agents, as there are currently no commercially available intracellular GBCAs for cardiovascular purposes.

Localization of Cardiovascular GBCAs

The clinical benefit of administering contrast agents relies on our ability to localize the agent within a given body compartment. This can be achieved by altering a number of different MRI parameters. After injection of a bolus of contrast agent into a peripheral vein, it travels through the pulmonary circulation first and then into the arterial system. The rapid acquisition of images while the contrast agent is in the arterial system is the cornerstone behind magnetic resonance angiography (MRA). Figure 8.1 shows examples of MRA that use different contrast agents. There are a number of methods that can be employed to appropriately time MRA imaging. One of these methods is the test bolus method. This involves administering 1–2 ml of contrast and acquiring a series of rapid 2D images of the vessel in question to determine optimum imaging time. The diagnostic MRA is then performed using the temporal information garnered from the test bolus. Fluoroscopic triggering is another commonly used technique; this consists of administering the full bolus of contrast and simultaneously obtaining rapid, fluoroscopic-like images of the area of interest. When the bolus is visually detected within the vessel, the operator can trigger the MRA acquisition. As the contrast bolus enters the venous circulation, it begins to redistribute from the intravascular into the extravascular interstitial space, eventually reaching equilibrium. The proportion of the contrast bolus that leaves the blood pool is inversely related to its avidity of plasma protein binding.

Extracellular Fluid GBCAs

The majority of GBCAs in routine clinical use are extracellular fluid (ECF) agents. After injection, they initially distribute in the intravascular space, before rapidly diffusing across the vascular membranes into the interstitial space, establishing equilibrium. By using specific pulse sequence parameters, it is possible to image the contrast media in arterial, venous, and equilibrium phases. The arterial phase is the time between contrast arrival in the arterial region of interest and venous filling. The timing of the arterial phase is highly dependent on the patient's cardiac output but is usually between 15 s and 25 s. As the contrast fills the venous system, it diffuses rapidly into the interstitial space across the vascular membranes. The equilibrium, or steady-state, phase occurs after approximately 10 min, as the GBCA concentration reaches equilibrium between the intravascular and interstitial compartments. Tissues with large interstitial spaces and/or leakier capillaries will concentrate more GBCA in this phase, leading to increased SI in these regions during steady-state phase imaging. Figure 8.2 shows examples of cardiac late gadolinium enhancement images using different contrast agents.

ECF GBCAs quickly distribute to the extracellular space after injection and are excreted via glomerular filtration, with a terminal half-life for plasma elimination of 90 min for subjects without renal impairment [11, 19]. As these compounds are exclusively excreted via the kidneys, their rate of elimination slows down in patients with impaired renal function, with a strong correlation between the blood elimination half-life of the agent and creatinine clearance [21, 22].

Binding of GBCA to a protein or other larger molecular structure can slow down the tumbling rate, increasing the relaxivity of the agent. Gadobenate dimeglumine (Gd-BOPTA) and gadoxetate disodium (Gd-EOB-DTPA) both exhibit weak plasma protein binding (approximately 10%) to the presence of an aromatic ring. This weak plasma protein binding helps increase relaxivity compared to the other ECF GBCAs [20, 23, 24]. This plasma protein interaction does not impact significantly on renal clearance rates, and the nature of the plasma protein interaction is too weak and transient for them to act as blood pool agents [19].

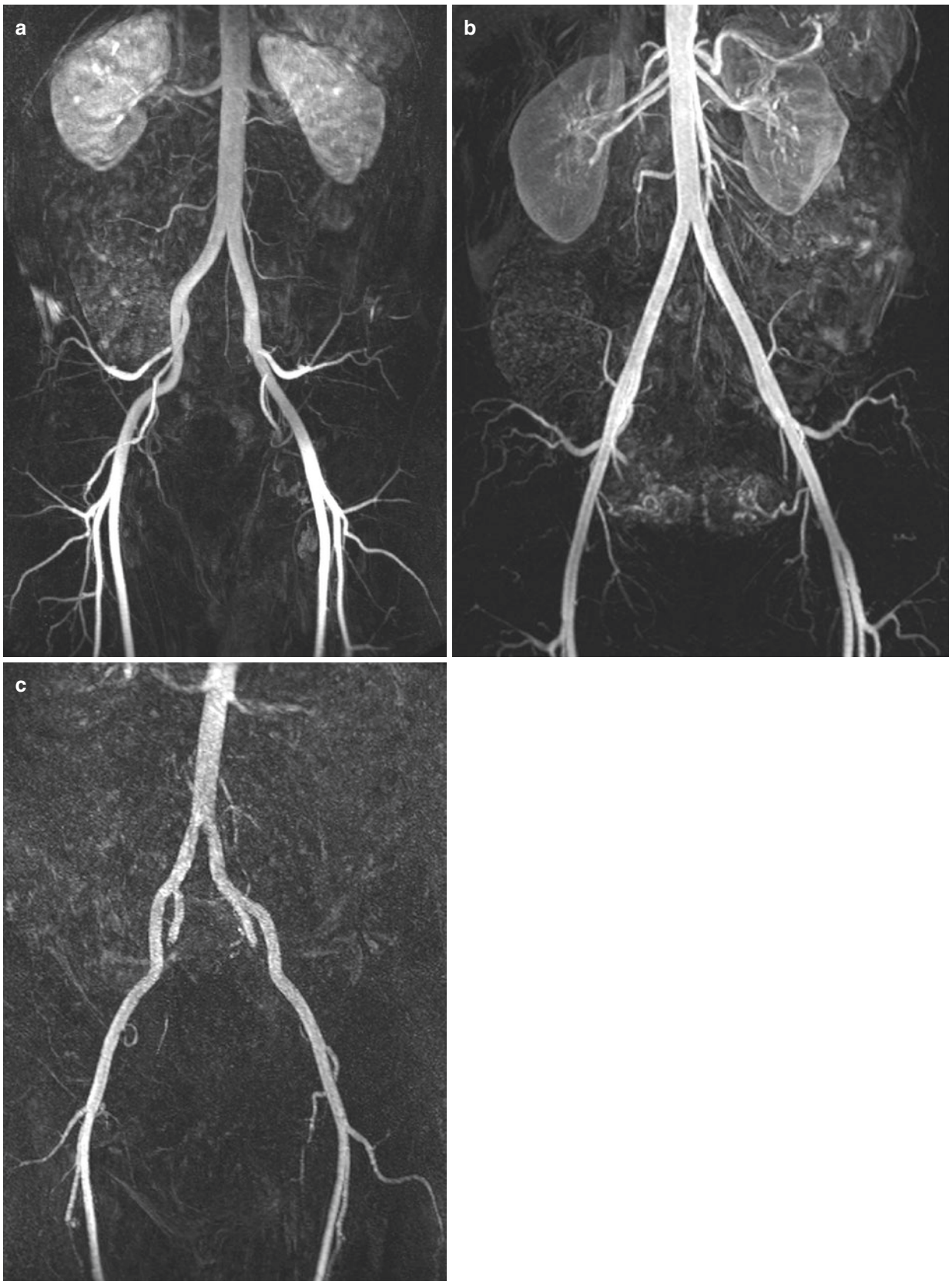

Fig. 8.1 Coronal, arterial phase subtraction maximum intensity projection (MIP) MRA images of the abdomen and pelvis with different contrast agents. (**a**) Macrocyclic ionic GBCA gadoterate meglumine (Dotarem). (**b**) Linear ionic GBCA gadobenate dimeglumine (MultiHance). (**c**) USPIO agent ferumoxytol (Feraheme) in a patient with chronic renal failure. Note that multihance-enhanced images enhanced the vascular lumen substantially stronger than Dotarem given its higher relaxitivity. For patients with renal failure who cannot receive GBCAs, ferumoxytol is a viable option as a intravascular contrast agent using T1 weighted MRA methods

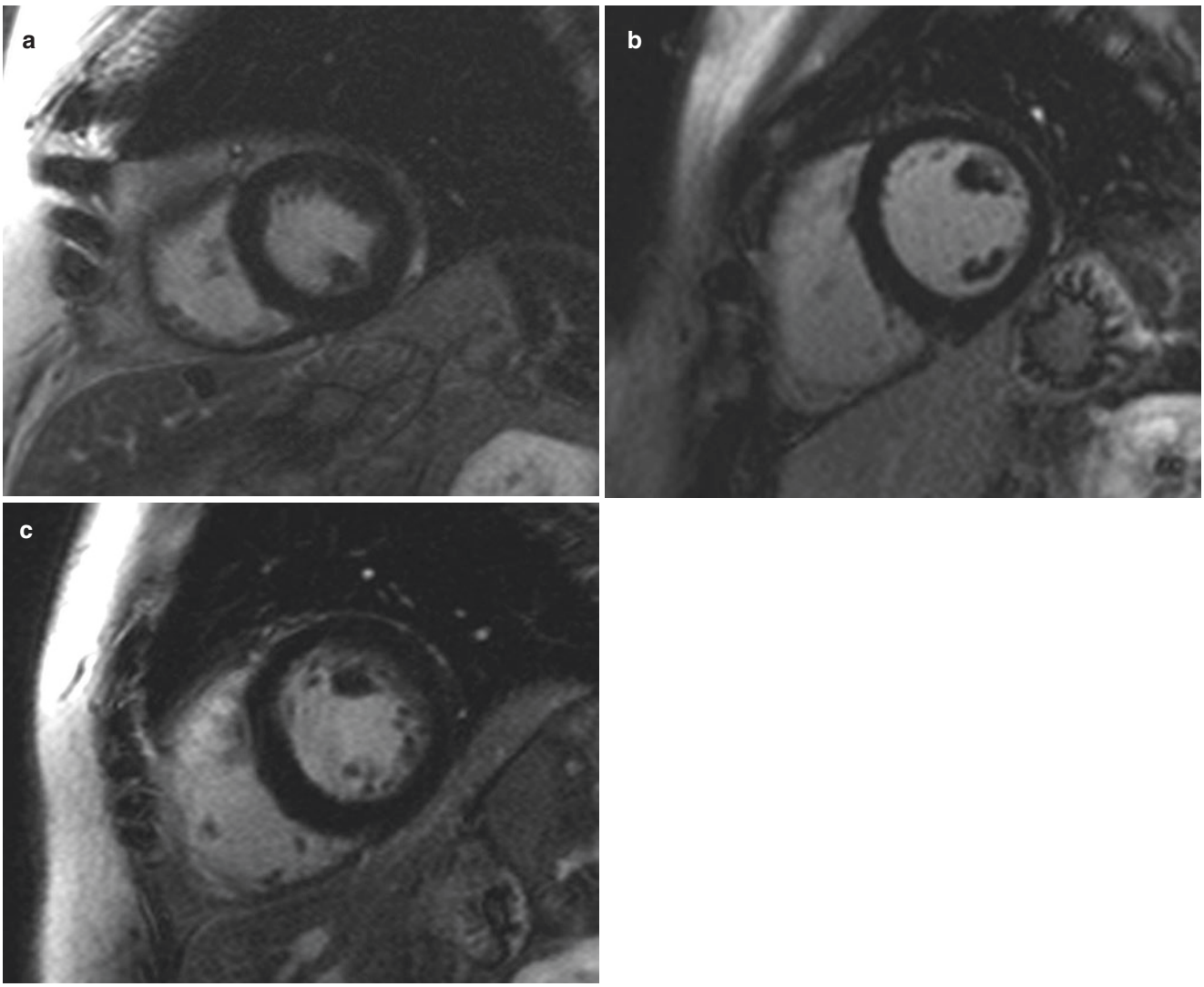

Fig. 8.2 Cardiac MRI short-axis mid-left ventricle late gadolinium enhancement images with different GBCAs. (**a**) Linear ionic GBCA gadopentetate dimeglumine (Magnevist). (**b**) Liner ionic GBCA gadobenate dimeglumine (MultiHance). (**c**) Macrocyclic ionic GBCA gadoterate meglumine (Dotarem). Note that on average multihance can provide higher signal-to-noise LGE images, but tissue enhancement may be affected by high protein-binding and it not be consistent with less protein-bound GBCAs

Intravascular GBCA

Gadofosveset trisodium (Gd-DTPA-DO3A/MS-325) is currently the only intravascular GBCA licensed by the FDA. It was licensed by the European Medicines Agency for distribution in the European Union (EU) in 2005 but was voluntarily withdrawn from commercial use in the EU by the manufacturer in 2011. It is a linear ionic agent, which binds strongly to albumin, limiting its diffusion into the extravascular space [25, 26]. Its strong albumin binding is due to a lipophilic albumin-binding group (biphenylcyclohexyl) on the chelate. The fraction of the agent that binds to plasma albumin depends on both the concentrations of albumin and of the agent itself. The overall effect of this is an increase in plasma relaxivity compared with the extracellular fluid GBCAs. The increased blood SI is appreciable on T1-weighted images up to 4 h post administration [27], with a serum half-life of 2–3 h [28]. Gadofosveset is predominantly renally excreted, but there is a small component (approximately 5%) of biliary excretion [29]. It is not completely confined to the blood pool, with a small proportion diffusing into the interstitial space. Due to its relatively high proportion of albumin binding, it is excreted slower than other GBCAs, with a terminal plasma half-life of 16.5 h in patients with normal renal function, with slower excretion in patients with renal impairment [30]. It has a high kinetic stability compared with the other linear GBCAs, with in vitro testing showing stability two to three times that of Gd-DPTA [31].

GBCA-Related Imaging Artifacts

Localized signal loss is one of the commonly observed artifacts associated with GBCA use. This primarily occurs in areas of high concentration of the agent and is caused by T2-shortening effect. In areas of high GBCA concentration, the T2 relaxation time is shortened to such an extent that it is less than the echo time (TE), resulting in localized signal loss, even on T1-weighted imaging. This effect can be observed in extravascular locations of high GBCA concentration, such as the renal collecting systems and urinary bladder. It can be relevant in cardiovascular imaging when performing venous extremity imaging, particularly of the upper limb, where injection of the limb in question should be avoided, where possible.

During first-pass imaging with GBCAs, the bolus increases the magnetic field within the capillaries. Tissues with a high capillary density experience a greater local change in magnetic field, creating a gradient in the local magnetic field between the capillaries and adjacent tissue. This gradient increases local field (B_1) inhomogeneity, increasing tissue T2*, causing signal loss on susceptibility-weighted imaging. This T2* effect can be used in clinical myocardial perfusion MR [32, 33].

Future GBCAs

There are several novel GBCAs currently under investigation for possible clinical use. Among them are agents with substantially higher longitudinal relaxivity than those currently commercially available. Increased relaxivity would allow for less GBCA to be used, which may help improve patient safety. GBCAs increase relaxation by creating a local fluctuating magnetic field. The T1 relaxivity of GBCAs depends in part on the number of water molecules bound directly to the Gd^{3+} complex. The GBCA complex tumbles in a solution, creating a fluctuating magnetic field, inducing local proton relaxation. The tumbling rate is described by the characteristic rotational time, τ_R [34]. The molecular size, complex rigidity, and affinity of protein binding all affect the τ_R of the agent. Increasing the rotational correlation time (i.e., slowing the tumbling rate) will increase relaxivity. This can be achieved by making larger molecules, with more protein binding. A number of new agents are being trialed, bound to molecules such as albumin, dextran, and other macromolecules, with up to five times the relaxivity of current approved GBCAs [35]. There is a trade-off with this increase in molecule, as it can limit their distribution throughout the body. This may prove to be advantageous in vascular MRI, but is not desirable for a CMR contrast agent.

GBCA Adverse Reactions

Allergic-Like Reactions

Adverse reactions to GBCA administration are rare. These can manifest as non-allergic reactions (headache, fatigue, nausea, vomiting, taste disturbance) or allergic-like reactions. Although these adverse reactions can appear allergic in phenotype, their precise mechanism at a cellular level is poorly understood. They do not demonstrate the classic immunoglobulin (IgE)-mediated response typically seen in type 1 hypersensitivity reactions; however, they do manifest clinically as allergic-type reactions [36]. They can be classified as either mild, moderate, or severe according to the clinical severity [37]. Mild reactions manifest as mild pruritus, hives, and limited cutaneous edema. Moderate reactions have more prominent symptoms, such as diffuse erythema and pruritus with stable vital signs. Severe reactions to GBCA are rare and can manifest as respiratory distress, bronchospasm,

hypotension, and anaphylaxis and can ultimately lead to cardiac arrest. The incidence of minor adverse reactions is similar across all the currently available GBCAs [38–40]. A retrospective review of over 150,000 GBCA administrations reported an overall reaction rate of 5.9 per 10,000 injections, 78% of which were classed as mild; the overall rate of severe reactions was 1 per 40,000 GBCA injection [38]. The reported overall frequency of allergic-like reactions to GBCAs of 0.04–0.07% [38, 41] is less than the approximate rate of 1.5% reported for iodinated contrast media used in CT and invasive angiography [42].

Risk factors for allergic-type reactions include asthma, prior allergic-type reaction to contrast media, and prior allergic reaction to substances other than contrast media. Most mild reactions resolve without any treatment, requiring only a period of observation before safe discharge from the radiology department. Anaphylaxis to GBCAs is rare but does occur; a review of the FDA's adverse event reporting system from 1988 to 2012 found 614 reported cases of anaphylaxis associated with GBCAs [43]. Pharmacological therapy for mild reactions consists of oral antihistamine therapy, with steroids and bronchodilators required for more serious reactions [44]. In the rare case of a serious or anaphylactic reaction, prompt treatment with epinephrine is lifesaving.

Most patients who develop an allergic-like reaction after GBCA injection are not precluded from receiving them again in the future. A recurrence rate of allergic-like reactions of approximately 30% was reported on one series of over 140,000 GBCA administrations [45]. This risk of recurrence is reflected in international guidelines. The American College of Radiology (ACR) and the United Kingdom Royal College of Radiologists (RCR) recommend the use of steroid and antihistamine premedication for patients with a history of a moderate or severe reaction prior to readministration [37, 46]. Even with appropriate premedication, breakthrough allergic reactions can occur [47]. There is currently no evidence that steroid and antihistamine premedication reduce the risk of severe contrast reactions. Therefore, the decision to administer GBCA to a patient with a documented history of a severe reaction or anaphylaxis to GBCAs should be made on a case-by-case basis, after an individualized risk-benefit analysis.

Extravasation

Extravasations occur when the contrast media escapes from the venous lumen into the interstitial space during contrast injection. The incidence of contrast media extravasation can be reduced by a number of simple steps. Intravenous cannulas should be checked that they are appropriate for use prior to contrast administration by the use of a saline flush. The use of a 20-gauge or larger cannula in an antecubital or other large forearm vein is recommended when flow rates of 3 ml/s or higher are required, and flow rates should not exceed 1.5 ml/s in 22-gauge catheters, or those placed in peripheral locations, such as in the hands [37]. A test injection may be performed when using a power injector, which is commonly used in cardiovascular imaging.

Treatment is usually conservative, involving elevation of the affected limb and application of a warm or cold compress. Severe complications include compartment syndrome, skin ulceration, and tissue necrosis. Most patients respond to conservative measures, with a surgical consultation reserved for those who have progressive pain, altered sensation, skin ulceration, skin blistering, or reduced capillary refill [44]. The risk of tissue damage is greater with the higher osmolar GBCAs [17]. Overall though, the risk of tissue loss is less than with iodinated contrast used in CT, due to its relative lower osmolarity and also due to the lower volumes of contrast media typically used in cardiovascular MRI compared with CT.

Nephrogenic Systemic Fibrosis (NSF)

Nephrogenic systemic fibrosis (NSF) is an acquired fibrosing condition characterized by thickening, induration, and tightening of the skin with subcutaneous edema. It may be locally confined to the skin or may have systemic involvement affecting the lungs, skeletal muscle, heart, pericardium, and kidneys [48]. It is a serious condition, which can be fatal. The skin thickening and tethering are associated with increased pigmentation, often beginning in the lower extremities before progressing cranially [49]. Diagnosis can be difficult, requiring a detailed dermatological examination, combined with light microscopy of skin punch biopsy. A combined clinic-pathological diagnostic scoring system has been developed by the NSF registry in New Haven (CT, USA) to aid in the evaluation of suspected cases of NSF [50]. The typical features of NSF are listed in Table 8.2.

Table 8.2 Clinical features of nephrogenic systemic fibrosis [50]

System	Clinical feature
Skin	Symmetric, bilateral fibrotic indurated papules, plaques, or subcutaneous nodules Subcutaneous edema may give rise to a peau d'orange pattern Commonly involves lower and upper limbs Trunk less frequently affected Head typically spared
Musculoskeletal	Muscle induration and joint contractures can be seen with severe disease
Eyes	Asymptomatic yellowish scleral plaques are common
Viscera	Visceral fibrosis can affect the lungs, diaphragm, myocardium, pericardium, pleura, and dura mater

NSF can occur as a late reaction in patients with severe chronic or acute renal failure after GBCA exposure. The association between this progressive fibrosing condition and GBCA exposure was first described in 2006 [51]. Prior to this, GBCAs had been routinely administered to patients with renal impairment and dialysis patients, patients in whom iodinated contrast is relatively contraindicated. Following the initial reports, the FDA issued a "black box" warning on the use of GBCAs in patients with severe renal impairment [52], followed by a similar warning from the EMA [53]. Clinical manifestations of NSF usually occur within 12 weeks of GBCA administration [50], but some series report delayed onset of symptoms of up to 3 years [54]. This latency period may be even longer in selected cases, with one case report of a 10-year interval between GBCA exposure and NSF presentation [55].

The risk of NSF post GBCA exposure depends on three factors: the patient's renal function, the type of GBCA used, and the dose administered [56]. Of these, renal function is the most important risk factor. The risk is greatest in patients on renal dialysis, in patients with stage 5 chronic kidney disease (GFR < 30 ml/min) not on dialysis, and in patients with acute kidney injury (AKI). The risk is dependent on the severity of renal dysfunction, regardless of its etiology or duration [54]. One retrospective study found an incidence of NSF of 18% in patients with stage 5 chronic kidney disease (CKD) post gadodiamide administration [57]. In contrast, the risk of NSF is lower in patients with CKD stages 1–4 [57, 58].

The type of GBCA used greatly influences the risk of developing NSF. Almost all of the reported cases of NSF have been reported after exposure to gadodiamide, gadoversetamide, or gadopentetate dimeglumine. A comprehensive review of the 1395 cases of NSF reported up to 2014 found that 76.2% of cases had exposure to gadodiamide, 40.1% to gadopentetate dimeglumine, and 7.3% to gadoversetamide [59]. Both the FDA and EMA classify these three GBCAs as high-risk agents in terms of NSF risk [56]. Gadodiamide has the most amount of reported cases of NSF, with a three- to sevenfold higher risk than other GBCAs in patients with renal impairment [60]. In vulnerable patients, the dose of GBCA administered is a contributing factor in the risk of developing NSF. A retrospective analysis of 300 patients who received gadodiamide found an increased incidence of NSF in patients with renal impairment that received twice the regular dose (0.2 mmol/kg), compared with patients who received a standard dose (0.1 mmol/kg) [61].

The differential NSF risk among the licensed GBCAs is due mainly to differences in their chemical structure. As described in earlier sections, the macrocyclic agents offer better protection of the toxic Gd^{3+} ions than their linear counterparts. Among the linear agents, the nonionic compounds have the weakest binding between the ligand and the Gd^{3+} ion, due to the reduced number of binding carboxyl groups. These linear nonionic compounds are the least stable agents and thus have the highest NSF risk.

The exact mechanism by which NSF occurs has not yet been fully elucidated. One theory is that Gd^{3+} is caused to dissociate from the GBCA compound by the binding of endogenous cations in plasma, such as Fe^{3+}, Zn^{2+}, Cu^{2+}, and Ca^{2+}, to the chelating ligand. This process is called transmetallation. Supporting this theory are several studies demonstrating alterations in serum levels of these endogenous elements following GBCA exposure [62–64]. Zinc is the main cation that displaces Gd^{3+}, due to its high blood concentrations. The transmetallation process occurs preferably in patients with renal impairment due to the increase in elimination half-life of the GBCA. In patients with normal renal function, this is approximately 90 min and can be prolonged to over 24 h in patients with advanced renal impairment.

Free Gd^{3+} ions, once released from the chelator through this process, bind to endogenous anions, particularly phosphate (PO_4^-). The resulting complexes between gadolinium ions and endogenous anions form insoluble salts, which precipitate and deposit in tissues. These salts are then engulfed by circulation macrophages, which release multiple proinflammatory and profibrotic cytokines. These in turn attract circulating fibrocytes, which begin to synthesize and deposit a fibrotic extracellular matrix [49, 56, 65]. This excess of fibrotic tissue manifests clinically as the dermal and visceral fibrosis that characterizes NSF.

Several different therapies have been trialed for NSF, such as plasmapheresis, phototherapy, and monoclonal antibodies, but no agents have to date proved curative [56]. Restoration of normal renal function is the only strategy which has been proven to halt NSF progression, and cure has been reported in patients post recovery from AKI and following successful renal transplantation [66].

With these limitations in NSF treatment, the emphasis is on prevention. This depends on appropriate GBCA use, namely, in terms of the choice of agent, dose of agent, and patient selection. Patients with CKD 4 and 5, patients on dialysis (hemodialysis and peritoneal dialysis), and patients with AKI have the highest risk for developing NSF. Patients with CKD 3 (eGFR 30–59 ml/min) are at a lower risk, and there are no cases to date of NSF reported in patients with an eGFR >60 ml/min [67]. Almost all confirmed cases of NSF followed exposure to a linear nonionic GBCA.

Once at-risk patients are identified, strategies to prevent NSF include performing MRI without GBCA, performing an alternative imaging modality, and delaying the examination until renal function improves. If performing an MRI with GBCA is deemed essential, then an agent with a low NSF risk (macrocyclic agents) should be used, at the lowest dose possible in order to obtain diagnostic image quality. No cases of NSF were reported in reviews of almost 400 patients on dialysis who received either gadoterate or gadoteridol, both macrocyclic GBCAs [68, 69]. Performing hemodialysis post GBCA exposure in vulnerable patients cannot reverse fibrotic tissue formation, but it can remove the contrast agent [70]. If it is to

be performed, one suggested regimen is to start hemodialysis within 2 h of GBCA exposure and to perform several additional sessions over subsequent consecutive days [71]. There is no current recommendation for patients on peritoneal dialysis.

Since the link between NSF and GBCAs was established in the mid-2000s, the number of reported cases has reduced dramatically with the prudent use of GBCAs in at-risk patients. It has not been completely eliminated, however, and continued vigilance is necessary.

Gadolinium Deposition in Patients with Normal Renal Function

It was widely believed up until the recent few years that GBCAs were completely eliminated from the body in patients with normal renal function. However, there is emerging data demonstrating tissue gadolinium accumulation in patients with normal renal function post GBCA exposure [65]. This deposition had been demonstrated in studies of postmortem neuronal tissue, with the greatest accumulation reported in the dentate nucleus, with lesser amounts detected in the thalamus, dentate, pons, and globus pallidus [72]. The neuronal deposition can be associated with dose-dependent increased SI on non-contrast T1-weighted sequences, most marked in the dentate nucleus in the cerebellum and in the globus pallidus [73]. As described with NSF risk, the rates of brain deposition appear to correlate with the stability of the GBCA used. The agent most associated with neuronal deposition is the linear nonionic GBCA gadodiamide [74]. The more stable macrocyclic agents have, in general, not been associated with significant increases in cerebral T1 SI [75]. The macrocyclic GBCAs, however, do not seem to be completely without risk, with brain deposition reported following exposure to the macrocyclic nonionic agent gadobutrol [73]. This suggests that the risk of brain deposition cannot be solely evaluated based solely on GBCA ligand-structure morphology. The only GBCA which has not yet been associated with either increased cerebral T1 signal or pathological neuronal deposition is the macrocyclic ionic agent gadoterate meglumine [76].

Gadolinium accumulation has also been reported in the bone and skin in patients with normal renal function at the time of GBCA exposure [77, 78]. Darrah et al. found evidence of gadolinium deposition in femoral head bone samples collected at the time of total hip replacement, up to 8 years after GBCA exposure [79]. It is unclear yet whether the accumulated gadolinium represents free or chelated Gd^{3+}; however, the greater concentrations of tissue deposition associated with the less stable GBCAs (linear nonionic) suggest the deposition is predominantly free Gd^{3+}. The known toxic effects of free Gd^{3+} result from either its ability to compete competitively with Ca^{2+} or its insolubility at physiologic pH, causing it to precipitate as an insoluble salt causing local macrophage activation, as previously described.

The clinical significance and long-term effects, if any, of the tissue gadolinium accumulation observed in patients with normal renal function are not yet clear. All GBCAs probably deposit in vivo to some degree, but at present it is only the weaker linear chelates that have been definitively linked to a meaningful disease in NSF. It is likely that the amount of gadolinium tissue deposition strongly influences the development of a definite clinical entity. No definitive clinical syndrome resulting from this gadolinium deposition has yet been isolated, but it is under investigation by the FDA [80]. Its ultimate significance is yet to be determined.

GBCAs and Sickle Cell Disease

The administration of GBCAs to patients with sickle cell disease has previously been an issue of controversy. In vitro studies have demonstrated that deoxygenated red blood cells align perpendicular to the magnetic field [81]. It has thus been suggested that the increased magnetic moments associated with the administration of a paramagnetic contrast agent may increase the proportional perpendicular alignment, precipitating a vaso-occlusive crisis. Despite this, there have been no documented cases of vaso-occlusive or hemolytic complications related to GBCAs to date [82]. The use of GBCAs in cardiovascular MRI for patients with sickle cell disease does not appear to be associated with increased frequency of adverse events.

GBCAs and Pregnancy

Pregnant women and breastfeeding mothers are a special population group with regard to GBCA exposure. There is little data on GBCA administration in pregnancy and uncertainty as to whether GBCAs can enter the fetal circulation via the placenta. Given the recent reports of gadolinium tissue deposition, the advice in current guidelines against administering GBCAs in pregnancy in the absence of a very strong clinical indication are prudent. When imaging lactating mothers, one of the more stable macrocyclic agents should be used, and breastfeeding should be stopped for 24 h post contrast administration to limit possible infant exposure. To date, there have been no reported cases of adverse events occurring in infants that are breastfeeding after maternal GBCA exposure, but a cautious approach should be taken given the infant's immature renal system.

GBCAs and the Environment

In the past number of years, there have been increasing reports of the detection of anthropogenic (pollutant) rare-earth metals

in surface water. Chief among them has been the detection of anthropogenic gadolinium in surface and drinking water [83–86]. The cause of this is felt to be largely due to the use of GBCAs in medical imaging, and some of the highest concentrations are to be found near to medical facilities [83]. The concentrations that have been found in the ecosystem are well below those that could be harmful to the aquatic ecosystem. To date, there have been no adverse outcomes reported from the presence of trace anthropogenic gadolinium in drinking water, but this is under continued surveillance by the environmental regulatory agencies.

Non-gadolinium-Based Cardiovascular MR Contrast Agents

Iron Oxide Nanoparticles

Iron oxide nanoparticles (ION) have been investigated over the last two decades as potential alternative MRI contrast agents. Below a certain particle size, they exhibit superparamagnetic properties, strongly reducing T1, T2, and T2* relaxation times. They differ from paramagnetic agents in that they only exhibit magnetization when in the presence of an external magnetic field. Structurally they consist of a magnetic iron oxide core, covered in a nonmagnetic polymer coating. The coating is crucial for making the agent soluble and usually consists of the polysaccharide dextran or a derivative. After intravenous administration, they disperse in the blood pool. They do not undergo renal excretion; rather, they are taken up by monocytes/macrophages and are incorporated in the reticuloendothelial system [87]. They can be classified according to their size into superparamagnetic iron oxide particles (SPIO) measuring 50–250 nm and ultra-small SPIO (USPIO) measuring 20–50 nm. USPIOs cause a strong reduction in T1, T2, and T2* relaxation times. This results in significant signal loss on T2-weighted images, but it does also significantly shorten T1 relaxation, allowing its use as a positive contrast agent with T1-weighted imaging.

Ferumoxytol

Ferumoxytol is an USPIO agent that has been under investigation as an MR contrast agent for over a decade [88]. It has been approved by the FDA as a therapeutic preparation for the treatment of iron-deficient anemia in patients with chronic kidney disease [89]. Its use as an MR contrast agent is currently off-label. Given the risks outlined of using GBCAs in patients with severe renal dysfunction, ferumoxytol has emerged as an attractive alternative.

Due to its relatively small size (approximately 30 nm), carbohydrate coating and neutral charge ferumoxytol have a prolonged intravascular time of 12–15 h, allowing for a long vascular imaging window [87, 90]. As a USPIO agent, it undergoes phagocytosis by macrophages after a delay, concentrating it in areas of increased inflammation. This unique property allows for the identification of pathological areas of inflammation [91].

Intravenous iron is associated with a risk of anaphylaxis and hypotension. Ferumoxytol was specifically designed to minimize the risk of a severe adverse reaction; nevertheless, serious adverse reactions do occur. The reported rates of anaphylaxis with its therapeutic use ranges from 0.02% to 1.3% [92]. In 2015, the FDA issued a black box warning on the use of ferumoxytol, with 79 cases of anaphylaxis reported after approximately 1.2 million therapeutic doses [93]. The mechanism of this reaction is felt to be due to bioactive-free iron causing mast cell degranulation [94]. The overall risk of serious adverse events appears similar to that of iodinated contrast media, and higher than GBCAs, although the latter comparison is mitigated somewhat by its superior safety profile in patients with renal impairment.

Typical imaging doses of ferumoxytol are usually 1.5–4 mg/kg, diluted with normal saline at a ratio of 1 part ferumoxytol to 4 parts saline [88, 90, 92]. This is significantly less than the therapeutic dose for treating anemia of 1020 mg, approximately 14.6 mg/kg for a 70 kg adult. For vascular MRI, injection rates of 2 ml/s are commonly used, followed by a saline chaser [90]. MR image SI may be altered by ferumoxytol for days to months after administration, be it for therapeutic or diagnostic purposes. This allows for the use of slower, high-resolution 3D MRA techniques [95]. High injection rates have been associated with signal loss artifact on T1-weighted images during arterial phase imaging which can mimic thrombus, likely due to T2*-shortening effects of concentrated ferumoxytol [96].

Ferumoxytol has a number of potential applications in cardiovascular imaging. It has been successfully used in aortic and peripheral vascular imaging, with potential applications in coronary artery MRA and cardiac MRI [90, 97]. Studies in patients with myocardial infarction suggest that ferumoxytol may be useful in estimating the size of the infarct up to 96 h after administration due to its increase macrophage uptake in infarcted myocardium, manifesting as signal loss on T2-weighted imaging [98, 99].

Other Iron Oxide Agents

Aside from ferumoxytol, a number of other USPIOs have been investigated as potential MR contrast agents. Ferumoxtran-10 is an USPIO agent with similar properties to ferumoxytol with a dextran polymer coating [87]. It was extensively investigated as a potential cardiovascular MR contrast agent in clinical studies but was discontinued in 2010. The carboxydetran-covered agent ferucarbotran (Resovist), a SPIO agent, was previously approved for use in

liver imaging and was investigated as a potential CMR contrast agent before it was discontinued from clinical use in 2009 [87]. Recently, there has been interest in another group of IONs that are even smaller than USPIOs, called very small SPIOs (VSPIO) with a size <20 nm, although these agents are still at the experimental phase [100]. The ability of USPIOs enhanced MRI to detect inflammatory processes associated with a range of cardiovascular pathology is an exciting prospect, with a number of potential clinical applications.

Manganese-Based Contrast Agents

Manganese (Mn2+) is an essential element of human diet and a paramagnetic lanthanide metal. It has five unpaired electrons, which accounts for its powerful paramagnetic properties, shortening both T1 and T2 relaxation times considerably. It is toxic in its free form and is thus chelated onto a ligand for clinical use. Mangafodipir trisodium (Telescan, GE healthcare, Milwaukee, WI) is the commercially available manganese-based contrast agent, consisting of the manganese ion chelated to dipyridol diphosphate. T1-shortening effects predominate at lower concentrations, with T2-shortening effects predominating at higher concentrations. It is taken up by hepatocytes and predominantly excreted via the biliary system, a feature which is taken advantage of in its principal application in hepatic MRI [101]. Mangafodipir trisodium was investigated as a potential MR contrast agent for first-pass myocardial perfusion imaging, but has not been widely adopted in clinical practice.

Other manganese-based contrast agents are currently under investigation as potential cardiovascular MR contrast agents. Manganese chloride is one such agent, with potential as an intracellular contrast agent [102]. Free manganese ions act as calcium analogues, are taken up into myocardial cells via voltage-gated calcium channels, and are then retained in myocyte mitochondria. This intracellular uptake potentially allows for the detection of infarcted myocardium with accuracy [102]. There are concerns about the use of manganese as an intracellular contrast agent at high doses due to the possibility of inducing acute heart failure. An initial study on humans has demonstrated safety of magnesium chloride as a cardiac MR contrast agent when used at a small dose [102]. Further clinical studies, however, are required if it is to become a clinically useful contrast agent for cardiovascular imaging.

Clinical Applications

Magnetic Resonance Angiography (MRA)

Contrast-enhanced magnetic resonance angiography (CE-MRA) techniques provide excellent angiographic images without radiation. Modern MRA techniques, such as centric k-space filling and parallel imaging, allow for arterial phase imaging without venous contamination with excellent SNR and CNR. In terms of contrast agents used in MRA, GBCAs predominate, with recent interest in the use of ferumoxytol in selected patients. GBCAs with high relaxivity that remain within the blood pool are the most attractive from an image quality point of view. However, safety considerations, such as NSF risk and brain deposition, must also be taken into account when choosing a GBCA for MRA. The linear ionic GBCA gadobenate dimeglumine is still the most commonly used contrast agent in CE-MRA. Although it is not an intravascular agent, it does have a higher degree of protein binding than the majority of the other GBCAs and has a relatively higher relaxivity. Gadobenate dimeglumine provides diagnostic MRA quality compared with the traditional vascular imaging gold standard, invasive digital subtraction angiography (DSA) [103].

The approval of the first predominantly intravascular GBCA, the linear ionic agent gadofosveset trisodium was much heralded due to its high relaxivity and high protein binding. Its added diagnostic benefit above that of the ECF GBCAs, however, has not proved to be universally accepted. Since its initial approval by the EMA in 2007, it has since been withdrawn from the EU for commercial reasons. Several direct comparisons with gadobenate dimeglumine have not revealed a significant improvement in arterial phase image quality [104–106]. Gadofosveset trisodium does offer an advantage over the extracellular GBCAs in intravascular SI in equilibrium phase imaging performed more than 15 min postinjection [107].

Concerns over the safety of GBCAs are important when choosing an agent for MRA. Both gadobenate dimeglumine and gadofosveset trisodium are linear ionic agents, placing them in the intermediate risk category for the development of NSF in susceptible patients. The recent discovery of cerebral gadolinium deposition in patients with normal renal function is also of concern, although the clinical significance of this phenomenon is yet to be determined. The currently available GBCA with the most favorable risk profile in terms of NSF and cerebral deposition is the macrocyclic ionic agent gadoterate meglumine. This agent has inferior protein binding and relaxivity compared with some of the other GBCAs, but this is somewhat offset by its safety profile. Its macrocyclic, ionic structure renders it a highly stable GBCA. There have to date been no reported cases of NSF with this agent, even in patient with severe renal dysfunction [108, 109], and it is also the only GBCA in which cerebral deposition has not been demonstrated [76]. In patients whom GBCA administration is not desirable, the USPIO agent ferumoxytol has recently emerged as a viable alternative, providing diagnostic quality MRA images, although concerns do exist about its risk of hypersensitivity reaction.

Cardiac Magnetic Resonance (CMR)

One of the major advantages of CMR as an imaging modality is its ability to distinguish damaged from normal myocardium. The use of MR contrast is crucial to this. As described before, extracellular GBCAs rapidly dissociate into the extracellular space after intravenous administration, before slowly washing out again. The increased extracellular space found in areas of infarcted or edematous myocardium results in accumulation of ECF GBCA, manifesting as increased SI on T1-weighted imaging relative to normal myocardium. This helps differentiate normal from damaged myocardium and is the basis behind the use of late gadolinium enhancement (LGE) imaging, performed 10–20 min after GBCA administration. LGE imaging is a fast, robust, reproducible method of determining myocardial viability in patients with reduced left ventricular function and can predict the likelihood of recovery in contractile function post revascularization [110, 111]. To achieve good LGE imaging, it is preferable to use a GBCA that is not highly protein-bound, allowing it to freely dissociate into the extracellular space. This is the converse of the features desirable in a CE-MRA agent. To assess for myocardial viability, the ideal contrast agent would be one that is taken up by myocardial myocytes, but there are no such commercially available MR contrast agents. The linear ionic GBCA gadopentete dimeglumine was traditionally the most commonly used agent, usually at a dose of 0.15–0.2 mmol/kg. There are safety concerns about this agent, and the other linear GBCAs, primarily due to the risk of NSF. As a result, many institutions have switched to using macrocyclic agents GBCAs in CMR, such as gadobutrol and gadoterate meglumine at a dose of 0.1–0.15 mmol/kg, without a significant deterioration in diagnostic image quality [112].

Aside from LGE imaging, the assessment of myocardial perfusion in patients with suspected coronary artery disease is the other major reason to use contrast in CMR. In myocardial perfusion imaging (MPI), the increase in myocardial SI during the first pass of a GBCA bolus through the myocardial microcirculation correlates with coronary blood flow, with significant CAD manifesting as segmental areas of hypoperfusion in a typical coronary arterial distribution [113, 114]. This can be performed both at rest and after administration of a pharmacological vasodilator stress agent such as adenosine or regadenason. Quantitative myocardial perfusion techniques are now available, allowing more accurate assessment of myocardial blood flow [115].

Conclusion

The use of contrast in clinical cardiovascular MRI is crucial in improving the ability to make accurate diagnoses. Advances in MR technology bring exciting new possibilities for the use of contrast media in cardiovascular MR, but continued vigilance is required to ensure the highest standards of patient safety.

References

1. Damadian R, Goldsmith M, Minkoff L. NMR in cancer: XVI. FONAR image of the live human body. Physiol Chem Phys. 1977;9(1):97–100, 108.
2. Shokrollahi H. Contrast agents for MRI. Mater Sci Eng C Mater Biol Appl. 2013;33(8):4485–97.
3. Bottrill M, Kwok L, Long NJ. Lanthanides in magnetic resonance imaging. Chem Soc Rev. 2006;35(6):557–71.
4. Brady TJ, Goldman MR, Pykett IL, Buonanno FS, Kistler JP, Newhouse JH, et al. Proton nuclear magnetic resonance imaging of regionally ischemic canine hearts: effect of paramagnetic proton signal enhancement. Radiology. 1982;44(2):343–7.
5. Young IR, Clarke GJ, Bailes DR, Pennock JM, Doyle FH, Bydder GM. Enhancement of relaxation rate with paramagnetic contrast agents in NMR imaging. J Comput Tomogr. 1981;5(6):543–7.
6. Weinmann HJ, Brasch RC, Press WR, Wesbey GE. Characteristics of gadolinium-DTPA complex: a potential NMR contrast agent. Am J Roentgenol. 1984;142(3):619–24.
7. Laniado M, Weinmann HJ, Schörner W, Felix R, Speck U. First use of GdDTPA/dimeglumine in man. Physiol Chem Phys Med NMR. 1984;16(2):157–65.
8. Lohrke J, Frenzel T, Endrikat J, Alves FC, Grist TM, Law M, et al. 25 years of contrast-enhanced MRI: developments, current challenges and future perspectives. Adv Ther. 2016;33(1):1–28.
9. Sherry AD, Caravan P, Lenkinski RE. Primer on gadolinium chemistry. J Magn Reson Imaging. 2009;30(6):1240–8.
10. Port M, Idée J-M, Medina C, Robic C, Sabatou M, Corot C. Efficiency, thermodynamic and kinetic stability of marketed gadolinium chelates and their possible clinical consequences: a critical review. Biometals. 2008;21(4):469–90.
11. Oksendal AN, Hals PA. Biodistribution and toxicity of MR imaging contrast media. J Magn Reson Imaging. 1993;3(1):157–65.
12. Frenzel T, Lengsfeld P, Schirmer H, Hütter J, Weinmann H-J. Stability of gadolinium-based magnetic resonance imaging contrast agents in human serum at 37 degrees C. Investig Radiol. 2008;43(12):817–28.
13. Hao D, Ai T, Goerner F, Hu X, Runge VM, Tweedle M. MRI contrast agents: basic chemistry and safety. J Magn Reson Imaging. 2012;36(5):1060–71.
14. Laurent S, Elst LV, Muller RN. Comparative study of the physicochemical properties of six clinical low molecular weight gadolinium contrast agents. Contrast Media Mol Imaging. 2006;1(3):128–37.
15. Tweedle MF, Hagan JJ, Kumar K, Mantha S, Chang CA. Reaction of gadolinium chelates with endogenously available ions. Magn Reson Imaging. 1991;9(3):409–15.
16. Schmitt-Willich H. Stability of linear and macrocyclic gadolinium based contrast agents. Br J Radiol. 2007;80(955):581–2.
17. Runge VM, Dickey KM, Williams NM, Peng X. Local tissue toxicity in response to extravascular extravasation of magnetic resonance contrast media. Investig Radiol. 2002;37(7):393–8.
18. Rose TA, Choi JW. Intravenous imaging contrast media complications: the basics that every clinician needs to know. Am J Med. 2015;128(9):943–9.
19. Aime S, Caravan P. Biodistribution of gadolinium-based contrast agents, including gadolinium deposition. J Magn Reson Imaging. 2009;30(6):1259–67.
20. Seale MK, Catalano OA, Saini S, Hahn PF, Sahani DV. Hepatobiliary-specific MR contrast agents: role in imaging the liver and biliary tree. Radiographics. 2009;29(6):1725–48.

21. Tombach B, Bremer C, Reimer P, Schaefer RM, Ebert W, Geens V, et al. Pharmacokinetics of 1M gadobutrol in patients with chronic renal failure. Investig Radiol. 2000;35(1):35–40.
22. Schuhmann-Giampieri G, Krestin G. Pharmacokinetics of Gd-DTPA in patients with chronic renal failure. Investig Radiol. 1991;26(11):975–9.
23. de Haën C, Cabrini M, Akhnana L, Ratti D, Calabi L, Gozzini L. Gadobenate dimeglumine 0.5 M solution for injection (MultiHance) pharmaceutical formulation and physicochemical properties of a new magnetic resonance imaging contrast medium. J Comput Assist Tomogr. 1999;23(Suppl 1):S161–8.
24. Huppertz A, Balzer T, Blakeborough A, Breuer J, Giovagnoni A, Heinz-Peer G, et al. Improved detection of focal liver lesions at MR imaging: multicenter comparison of gadoxetic acid-enhanced MR images with intraoperative findings. Radiology. 2004;230(1):266–75.
25. Caravan P, Cloutier NJ, Greenfield MT, McDermid SA, Dunham SU, Bulte JWM, et al. The interaction of MS-325 with human serum albumin and its effect on proton relaxation rates. J Am Chem Soc. 2002;124(12):3152–62.
26. Lauffer RB, Parmelee DJ, Dunham SU, Ouellet HS, Dolan RP, Witte S, et al. MS-325: albumin-targeted contrast agent for MR angiography. Radiology. 1998;2:529–38.
27. Grist TM, Korosec FR, Peters DC, Witte S, Walovitch RC, Dolan RP, et al. Steady-state and dynamic MR angiography with MS-325: initial experience in humans. Radiology. 1998;207(2):539–44.
28. Parmelee DJ, Walovitch RC, Ouellet HS, Lauffer RB. Preclinical evaluation of the pharmacokinetics, biodistribution, and elimination of MS-325, a blood pool agent for magnetic resonance imaging. Investig Radiol. 1997;32(12):741–7.
29. Sabach AS, Bruno M, Kim D, Mulholland T, Lee L, Kaura S, et al. Gadofosveset trisodium: abdominal and peripheral vascular applications. Am J Roentgenol. 2013;200(6):1378–86.
30. Spanakis M, Marias K. In silico evaluation of gadofosveset pharmacokinetics in different population groups using the Simcyp simulator platform. In Silico Pharmacol. 2014 Dec;2(1):1–9.
31. Caravan P, Comuzzi C, Crooks W, McMurry TJ, Choppin GR, Woulfe SR. Thermodynamic stability and kinetic inertness of MS-325, a new blood pool agent for magnetic resonance imaging. Inorg Chem. 2001;40(9):2170–6.
32. Wendland MF, Saeed M, Masui T, Derugin N, Higgins CB. First pass of an MR susceptibility contrast agent through normal and ischemic heart: gradient-recalled echo-planar imaging. J Magn Reson Imaging. 1993;3(5):755–60.
33. Sakuma H, O'Sullivan M, Lucas J, Wendland MF, Saeed M, Dulce MC, et al. Effect of magnetic susceptibility contrast medium on myocardial signal intensity with fast gradient-recalled echo and spin-echo MR imaging: initial experience in humans. Radiology. 1994;190(1):161–6.
34. Dumas S, Jacques V, Sun W-C, Troughton JS, Welch JT, Chasse JM, et al. High relaxivity magnetic resonance imaging contrast agents. Part 1. Impact of single donor atom substitution on relaxivity of serum albumin-bound gadolinium complexes. Investig Radiol. 2010;45(10):600–12.
35. Varga-Szemes A, Kiss P, Rab A, Suranyi P, Lenkey Z, Simor T, et al. In vitro Longitudinal Relaxivity Profile of Gd(ABE-DTTA), an investigational magnetic resonance imaging contrast agent. Radiographics. 2016;11(2):e0149260.
36. Brockow K, Ring J. Anaphylaxis to radiographic contrast media. Curr Opin Allergy Clin Immunol. 2011;11(4):326–31.
37. American College of Radiology (ACR). ACR Committee on Drugs and Contrast Media. ACR Manual on Contrast Media Version 10.1 2015. Available from: http://www.acr.org/~/media/37D84428BF1D4E1B9A3A2918DA9E27A3.pdf. Last accessed 26 Feb 2017.
38. Prince MR, Zhang H, Zou Z, Staron RB, Brill PW. Incidence of immediate gadolinium contrast media reactions. Am J Roentgenol. 2011;196(2):W138–43.
39. Dillman JR, Ellis JH, Cohan RH, Strouse PJ, Jan SC. Frequency and severity of acute allergic-like reactions to gadolinium-containing i.v. contrast media in children and adults. Am J Roentgenol. 2007;189(6):1533–8.
40. Aran S, Shaqdan KW, Abujudeh HH. Adverse allergic reactions to linear ionic gadolinium-based contrast agents: experience with 194, 400 injections. Clin Radiol. 2015;70(5):466–75.
41. Bruder O, Schneider S, Pilz G, van Rossum AC, Schwitter J, Nothnagel D, et al. Update on acute adverse reactions to gadolinium based contrast agents in cardiovascular MR. large multinational and multi-ethnical population experience with 37788 patients from the EuroCMR registry. J Cardiovasc Magn Reson. 2015;17:58.
42. Palkowitsch PK, Bostelmann S, Lengsfeld P. Safety and tolerability of iopromide intravascular use: a pooled analysis of three non-interventional studies in 132,012 patients. Acta Radiol. 2014;55(6):707–14.
43. Raisch DW, Garg V, Arabyat R, Shen X, Edwards BJ, Miller FH, et al. Anaphylaxis associated with gadolinium-based contrast agents: data from the Food and Drug Administration's adverse event reporting system and review of case reports in the literature. Expert Opin Drug Saf. 2014;13(1):15–23.
44. Beckett KR, Moriarity AK, Langer JM. Safe use of contrast media: what the radiologist needs to know. Radiographics. 2015;35(6):1738–50.
45. Jung J-W, Kang H-R, Kim M-H, Lee W, Min K-U, Han M-H, et al. Immediate hypersensitivity reaction to gadolinium-based MR contrast media. Radiology. 2012;264(2):414–22.
46. The Royal College of Radiologists. Standards for intravascular contrast agent administration to adult patients. 3rd ed. London: Royal College of Radiologists; 2015. p. 1–22. Available from: https://www.rcr.ac.uk/sites/default/files/Intravasc_contrast_web.pdf. Last accessed 26 Feb 2017.
47. Jingu A, Fukuda J, Taketomi-Takahashi A, Tsushima Y. Breakthrough reactions of iodinated and gadolinium contrast media after oral steroid premedication protocol. BMC Med Imaging. 2014;14:34.
48. Kribben A, Witzke O, Hillen U, Barkhausen J, Daul AE, Erbel R. Nephrogenic systemic fibrosis: pathogenesis, diagnosis, and therapy. J Am Coll Cardiol. 2009;53(18):1621–8.
49. Thomsen HS. Nephrogenic systemic fibrosis: a serious adverse reaction to gadolinium – 1997–2006–2016. Part 1. Acta Radiol. 2016;57(5):515–20.
50. Girardi M, Kay J, Elston DM, Leboit PE, Abu-Alfa A, Cowper SE. Nephrogenic systemic fibrosis: clinicopathological definition and workup recommendations. J Am Acad Dermatol. 2011;65(6):1095–7.
51. Grobner T. Gadolinium – a specific trigger for the development of nephrogenic fibrosing dermopathy and nephrogenic systemic fibrosis? Nephrol Dial Transplant. 2006;21(4):1104–8.
52. U.S. Food and Drug Administration. A Public Health Advisory. Gadolinium-containingcontrastagentsformagneticresonanceimaging (MRI). 2006. Available from: http://www.fda.gov/Drugs/DrugSafety/PostmarketDrugSafetyInformationforPatientsandProviders/DrugSafetyInformationforHeathcareProfessionals/PublicHealthAdvisories/ucm053112.htm. Last accessed 26 Feb 2017.
53. European Medicines Agency. Vasovist and nephrogenic systemic fibrosis (NSF). 2009. Available from: http://www.ema.europa.eu/ema/index.jsp?curl=pages/news_and_events/news/2009/11/news_detail_000418.jsp&mid=WC0b01ac058004d5c1. Last accessed 26 Feb 2017.
54. Abujudeh HH, Kaewlai R, Kagan A, Chibnik LB, Nazarian RM, High WA, et al. Nephrogenic systemic fibrosis after gadopentetate

dimeglumine exposure: case series of 36 patients. Radiology. 2009;253(1):81–9.
55. Larson KN, Gagnon AL, Darling MD, Patterson JW, Cropley TG. Nephrogenic systemic fibrosis manifesting a decade after exposure to gadolinium. JAMA Dermatol. 2015;151(10):1117–20.
56. Daftari Besheli L, Aran S, Shaqdan K, Kay J, Abujudeh H. Current status of nephrogenic systemic fibrosis. Clin Radiol. 2014;69(7):661–8.
57. Rydahl C, Thomsen HS, Marckmann P. High prevalence of nephrogenic systemic fibrosis in chronic renal failure patients exposed to gadodiamide, a gadolinium-containing magnetic resonance contrast agent. Investig Radiol. 2008;43(2):141–4.
58. Shabana WM, Cohan RH, Ellis JH, Hussain HK, Francis IR, Su LD, et al. Nephrogenic systemic fibrosis: a report of 29 cases. Am J Roentgenol. 2008 Mar;190(3):736–41.
59. Edwards BJ, Laumann AE, Nardone B, Miller FH, Restaino J, Raisch DW, et al. Advancing pharmacovigilance through academic-legal collaboration: the case of gadolinium-based contrast agents and nephrogenic systemic fibrosis-a research on adverse drug events and reports (RADAR) report. Br J Radiol. 2014;87(1042):20140307.
60. Thomsen HS, Marckmann P. Extracellular Gd-CA: differences in prevalence of NSF. Eur J Radiol. 2008;66(2):180–3.
61. Broome DR, Girguis MS, Baron PW, Cottrell AC, Kjellin I, Kirk GA. Gadodiamide-associated nephrogenic systemic fibrosis: why radiologists should be concerned. Am J Roentgenol. 2007;188(2):586–92.
62. Swaminathan S, Horn TD, Pellowski D, Abul-Ezz S, Bornhorst JA, Viswamitra S, et al. Nephrogenic systemic fibrosis, gadolinium, and iron mobilization. N Engl J Med. 2007;357(7):720–2.
63. Kimura J, Ishiguchi T, Matsuda J, Ohno R, Nakamura A, Kamei S, et al. Human comparative study of zinc and copper excretion via urine after administration of magnetic resonance imaging contrast agents. Radiat Med. 2005;23(5):322–6.
64. High WA, Ayers RA, Chandler J, Zito G, Cowper SE. Gadolinium is detectable within the tissue of patients with nephrogenic systemic fibrosis. J Am Acad Dermatol. 2007;56(1):21–6.
65. Rogosnitzky M, Branch S. Gadolinium-based contrast agent toxicity: a review of known and proposed mechanisms. Biometals. 2016;29(3):365–76.
66. Cuffy MC, Singh M, Formica R, Simmons E, Abu Alfa AK, Carlson K, et al. Renal transplantation for nephrogenic systemic fibrosis: a case report and review of the literature. Nephrol Dial Transplant. 2011;26(3):1099–101.
67. Thomsen HS. Nephrogenic systemic fibrosis: a serious adverse reaction to gadolinium – 1997–2006–2016. Part 2. Acta Radiol. 2016;57(6):643–8.
68. Reilly RF. Risk for nephrogenic systemic fibrosis with gadoteridol (ProHance) in patients who are on long-term hemodialysis. Am Heart J. 2008;3(3):747–51.
69. Amet S, Launay-Vacher V, Clément O, Frances C, Tricotel A, Stengel B, et al. Incidence of nephrogenic systemic fibrosis in patients undergoing dialysis after contrast-enhanced magnetic resonance imaging with gadolinium-based contrast agents: the prospective Fibrose Nephrogénique Systémique study. Investig Radiol. 2014;49(2):109–15.
70. Khawaja AZ, Cassidy DB, Shakarchi Al J, McGrogan DG, Inston NG, Jones RG. Revisiting the risks of MRI with gadolinium based contrast agents-review of literature and guidelines. Insights Imaging. 2015;6(5):553–8.
71. European Society of Urogenital Radiology (ESUR). ESUR Contrast Media Safety Committee. ESUR Guidelines on Contrast Media 9.0. 2014. Available from: http://www.esur.org/esur-guidelines/. Last accessed 26 Feb 2017.
72. McDonald RJ, McDonald JS, Kallmes DF, Jentoft ME, Murray DL, Thielen KR, et al. Intracranial gadolinium deposition after contrast-enhanced MR imaging. Radiology. 2015;275(3):772–82.
73. Stojanov DA, Aracki-Trenkic A, Vojinovic S, Benedeto-Stojanov D, Ljubisavljevic S. Increasing signal intensity within the dentate nucleus and globus pallidus on unenhanced T1W magnetic resonance images in patients with relapsing-remitting multiple sclerosis: correlation with cumulative dose of a macrocyclic gadolinium-based contrast agent, gadobutrol. Eur Radiol. 2016;26(3):807–15.
74. Ramalho J, Semelka RC, Ramalho M, Nunes RH, AlObaidy M, Castillo M. Gadolinium-based contrast agent accumulation and toxicity: an update. Am J Neuroradiol. 2016;37(7):1192–8.
75. Kanda T, Osawa M, Oba H, Toyoda K, Kotoku J, Haruyama T, et al. High signal intensity in dentate nucleus on unenhanced T1-weighted MR images: association with linear versus macrocyclic gadolinium chelate administration. Radiology. 2015;275(3):803–9.
76. Robert P, Lehericy S, Grand S, Violas X, Fretellier N, Idée J-M, et al. T1-weighted Hypersignal in the deep cerebellar nuclei after repeated administrations of gadolinium-based contrast agents in healthy rats: difference between linear and macrocyclic agents. Investig Radiol. 2015;50(8):473–80.
77. Murata N, Gonzalez-Cuyar LF, Murata K, Fligner C, Dills R, Hippe D, et al. Macrocyclic and other non-group 1 gadolinium contrast agents deposit low levels of gadolinium in brain and bone tissue: preliminary results from 9 patients with normal renal function. Investig Radiol. 2016;51(7):447–53.
78. Roberts DR, Lindhorst SM, Welsh CT, Maravilla KR, Herring MN, Braun KA, et al. High levels of gadolinium deposition in the skin of a patient with normal renal function. Investig Radiol. 2016;51(5):280–9.
79. Darrah TH, Prutsman-Pfeiffer JJ, Poreda RJ, Ellen Campbell M, Hauschka PV, Hannigan RE. Incorporation of excess gadolinium into human bone from medical contrast agents. Metallomics. 2009;1(6):479–88.
80. Food and Drug Administration (FDA). FDA Drug Safety Communication (2015) FDA evaluating the risk of brain deposits with repeated use of gadolinium-based contrast agents for magnetic resonance imaging (MRI). Available from: http://www.fda.gov/Drugs/DrugSafety/ucm455386.htm. Last accessed 26 Feb 2017.
81. Brody AS, Sorette MP, Gooding CA, Listerud J, Clark MR, Mentzer WC, et al. AUR memorial Award. Induced alignment of flowing sickle erythrocytes in a magnetic field. A preliminary report. Investig Radiol. 1985;20(6):560–6.
82. Dillman JR, Ellis JH, Cohan RH, Caoili EM, Hussain HK, Campbell AD, et al. Safety of gadolinium-based contrast material in sickle cell disease. J Magn Reson Imaging. 2011;34(4):917–20.
83. Hatje V, Bruland KW, Flegal AR. Increases in anthropogenic gadolinium anomalies and rare earth element concentrations in San Francisco Bay over a 20 year record. Environ Sci Technol. 2016;50(8):4159–68.
84. Rabiet M, Brissaud F, Seidel JL, Pistre S, Elbaz-Poulichet F. Positive gadolinium anomalies in wastewater treatment plant effluents and aquatic environment in the Hérault watershed (South France). Chemosphere. 2009;75(8):1057–64.
85. Kulaksız S, Bau M. Rare earth elements in the Rhine River, Germany: first case of anthropogenic lanthanum as a dissolved microcontaminant in the hydrosphere. Environ Int. 2011;37(5):973–9.
86. Telgmann L, Wehe CA, Birka M, Künnemeyer J, Nowak S, Sperling M, et al. Speciation and isotope dilution analysis of gadolinium-based contrast agents in wastewater. Environ Sci Technol. 2012;46(21):11929–36.
87. Bietenbeck M, Florian A, Sechtem U, Yilmaz A. The diagnostic value of iron oxide nanoparticles for imaging of myocardial inflammation – quo vadis? J Cardiovasc Magn Reson. 2015;17:54.

88. Prince MR, Zhang HL, Chabra SG, Jacobs P, Wang Y. A pilot investigation of new superparamagnetic iron oxide (ferumoxytol) as a contrast agent for cardiovascular MRI. J Xray Sci Technol. 2003;11(4):231–40.
89. Lu M, Cohen MH, Rieves D, Pazdur R. FDA report: Ferumoxytol for intravenous iron therapy in adult patients with chronic kidney disease. Am J Hematol. 2010;85(5):315–9.
90. Hope MD, Hope TA, Zhu C, Faraji F, Haraldsson H, Ordovas KG, et al. Vascular imaging with Ferumoxytol as a contrast agent. Am J Roentgenol. 2015;205(3):W366–73.
91. Gkagkanasiou M, Ploussi A, Gazouli M, Efstathopoulos EP. USPIO-enhanced MRI neuroimaging: a review. J Neuroimaging. 2016;26(2):161–8.
92. Vasanawala SS, Nguyen K-L, Hope MD, Bridges MD, Hope TA, Reeder SB, et al. Safety and technique of ferumoxytol administration for MRI. Magn Reson Med. 2016;75(5):2107–11.
93. Food and Drug Administration (FDA). FDA Drug Safety Communication: FDA strengthens warnings and changes prescribing instructions to decrease the risk of serious allergic reactions with anemia drug Feraheme (ferumoxytol) 2015. Available from: http://www.fda.gov/Drugs/DrugSafety/ucm440138.htm. Last accessed 26 Feb 2017.
94. Bircher AJ, Auerbach M. Hypersensitivity from intravenous iron products. Immunol Allergy Clin North Am. 2014;34(3):707–23.
95. Mukundan S, Steigner ML, Hsiao L-L, Malek SK, Tullius SG, Chin MS, et al. Ferumoxytol-enhanced magnetic resonance imaging in late-stage CKD. Am J Kidney Dis. 2016;67(6):984–8.
96. Fananapazir G, Marin D, Suhocki PV, Kim CY, Bashir MR. Vascular artifact mimicking thrombosis on MR imaging using ferumoxytol as a contrast agent in abdominal vascular assessment. J Vasc Interv Radiol. 2014;25(6):969–76.
97. Hanneman K, Kino A, Cheng JY, Alley MT, Vasanawala SS. Assessment of the precision and reproducibility of ventricular volume, function, and mass measurements with ferumoxytol-enhanced 4D flow MRI. J Magn Reson Imaging. 2016;44(2):383–92.
98. Yilmaz A, Dengler MA, van der Kuip H, Yildiz H, Rösch S, Klumpp S, et al. Imaging of myocardial infarction using ultrasmall superparamagnetic iron oxide nanoparticles: a human study using a multi-parametric cardiovascular magnetic resonance imaging approach. Eur Heart J. 2013;34(6):462–75.
99. Alam SR, Shah ASV, Richards J, Lang NN, Barnes G, Joshi N, et al. Ultrasmall superparamagnetic particles of iron oxide in patients with acute myocardial infarction: early clinical experience. Circ Cardiovasc Imaging. 2012;5(5):559–65.
100. Alam SR, Stirrat C, Richards J, Mirsadraee S, Semple SIK, Tse G, et al. Vascular and plaque imaging with ultrasmall superparamagnetic particles of iron oxide. J Cardiovasc Magn Reson. 2015;17:83.
101. Burke C, Alexander Grant L, Goh V, Griffin N. The role of hepatocyte-specific contrast agents in hepatobiliary magnetic resonance imaging. Semin Ultrasound CT MR. 2013;34(1):44–53.
102. Fernandes JL, Storey P, da Silva JA, de Figueiredo GS, Kalaf JM, Coelho OR. Preliminary assessment of cardiac short term safety and efficacy of manganese chloride for cardiovascular magnetic resonance in humans. J Cardiovasc Magn Reson. 2011;13:6.
103. Thurnher S, Miller S, Schneider G, Ballarati C, Bongartz G, Herborn CU, et al. Diagnostic performance of gadobenate dimeglumine enhanced MR angiography of the iliofemoral and calf arteries: a large-scale multicenter trial. Am J Roentgenol. 2007;189(5):1223–37.
104. Camren GP, Wilson GJ, Bamra VR, Nguyen KQ, Hippe DS, Maki JH. A comparison between gadofosveset trisodium and gadobenate dimeglumine for steady state MRA of the thoracic vasculature. Biomed Res Int. 2014;2014:Article ID 625614, 6 pages.
105. Christie A, Chandramohan S, Roditi G. Comprehensive MRA of the lower limbs including high-resolution extended-phase infra-inguinal imaging with gadobenate dimeglumine: initial experience with inter-individual comparison to the blood-pool contrast agent gadofosveset trisodium. Clin Radiol. 2013;68(2):125–30.
106. Frydrychowicz A, Russe MF, Bock J, Stalder AF, Bley TA, Harloff A, et al. Comparison of gadofosveset trisodium and gadobenate dimeglumine during time-resolved thoracic MR angiography at 3T. Acad Radiol. 2010;17(11):1394–400.
107. Erb-Eigner K, Taupitz M, Asbach P. Equilibrium-phase MR angiography: comparison of unspecific extracellular and protein-binding gadolinium-based contrast media with respect to image quality. Contrast Media Mol Imaging. 2016;11(1):71–6.
108. Deray G, Rouviere O, Bacigalupo L, Maes B, Hannedouche T, Vrtovsnik F, et al. Safety of meglumine gadoterate (Gd-DOTA)-enhanced MRI compared to unenhanced MRI in patients with chronic kidney disease (RESCUE study). Eur Radiol. 2013;23(5):1250–9.
109. Ishiguchi T, Takahashi S. Safety of gadoterate meglumine (Gd-DOTA) as a contrast agent for magnetic resonance imaging: results of a post-marketing surveillance study in Japan. Drugs R D. 2010;10(3):133–45.
110. Kim RJ, Wu E, Rafael A, Chen EL, Parker MA, Simonetti O, et al. The use of contrast-enhanced magnetic resonance imaging to identify reversible myocardial dysfunction. N Engl J Med. 2000;343(20):1445–53.
111. Jerosch-Herold M, Kwong RY. Magnetic resonance imaging in the assessment of ventricular remodeling and viability. Radiographics. 2008;5(1):5–10.
112. Rudolph A, Messroghli D, Knobelsdorff-Brenkenhoff von F, Traber J, Schüler J, Wassmuth R, et al. Prospective, randomized comparison of gadopentetate and gadobutrol to assess chronic myocardial infarction applying cardiovascular magnetic resonance. BMC Med Imaging. 2015;15:55.
113. Heydari B, Jerosch-Herold M, Kwong RY. Assessment of myocardial ischemia with cardiovascular magnetic resonance. Prog Cardiovasc Dis. 2011;54(3):191–203.
114. Nagel E, Klein C, Paetsch I, Hettwer S, Schnackenburg B, Wegscheider K, et al. Magnetic resonance perfusion measurements for the noninvasive detection of coronary artery disease. Circulation. 2003;108(4):432–7.
115. Heydari B, Kwong RY, Jerosch-Herold M. Technical advances and clinical applications of quantitative myocardial blood flow imaging with cardiac MRI. Prog Cardiovasc Dis. 2015;57(6):615–22.

Safety and Monitoring for Cardiac Magnetic Resonance Imaging

9

Rolf Symons, Saman Nazarian, Henry R. Halperin, and David A. Bluemke

Introduction

Cardiovascular magnetic resonance imaging (MRI) has become the modality of choice in the evaluation and treatment of cardiovascular disorders. Cardiac MRI allows for a comprehensive noninvasive assessment of cardiovascular anatomy and physiology with unsurpassed soft tissue resolution and multi-planar imaging capability without the need for ionizing radiation. Cardiac MRI is a safe imaging modality without any side effects in the vast majority of patients. However, with the growing number of patients with higher acuity of disease referred to cardiac MRI, some specific safety and monitoring issues should be addressed.

First, the number of patients treated with permanently or temporarily implanted cardiovascular devices with potential electromagnetic interaction with the MRI environment is increasing. Familiarity with each device class and its potential for electromagnetic interaction is essential for radiologists and cardiologists performing cardiac MRI. There is a remarkable and ever-increasing variety of implanted medical devices, which have the potential for interaction with the powerful main and gradient magnetic fields imposed by the MRI scanner as well as the radio-frequency (RF) energy that is deposited in the patient. Therefore, the risk associated with implanted ferromagnetic devices may be lower in magnets with lower field strengths relative to high field units.

Second, the (repeated) use of gadolinium-based contrast agents (GBCAs) in cardiac MRI, especially in patients with reduced kidney function, is associated with rare though significant side effects. The most important and potentially fatal side effect is nephrogenic systemic fibrosis (NSF) which involves fibrosis of the skin and internal organs and is believed to be caused by prolonged tissue exposure to GBCAs in patients with reduced kidney function. Another only recently reported possible adverse effect involves gadolinium deposition in the brain of patients who received multiple doses of GBCAs. To date, no adverse health effects of gadolinium deposition in the brain have been identified, though further research is warranted and preventive recommendations should be adopted. Prevention of these adverse reactions involves identification of patients at risk, risk-benefit evaluation of the need for contrast administration in cardiac MRI, understanding the risks associated with different types of GBCAs, and considerations of alternative methods of diagnostic imaging (e.g., computed tomography or ultrasound) relative to MRI.

Finally, safety issues of cardiac MRI in pregnant or lactating women include possible adverse biological effects of the magnetic fields, RF energy deposition, acoustic noise, or fetal exposure to GBCAs. While there is to date no indication that CMR during pregnancy has produced deleterious effects in humans, data is limited and additional investigations are warranted to fully characterize the risks associated with CMR in pregnant patients. Cardiac MRI can generally be used on pregnant patients if other forms of diagnostic imaging are inadequate or would require exposure to ionizing radiation.

Because of the wide range of circumstances encountered in the MRI suite, the descriptions that follow should not be construed as recommendations that are appropriate for all patients. The reader is encouraged to consult dedicated handbooks or websites dedicated to MRI safety (e.g., www.mri-safety.com) that provide more specific information regarding specific safety concerns. The final decision to perform MRI is frequently made by considering the potential benefit of MRI relative to the associated risks.

R. Symons · D. A. Bluemke (✉)
NIH Clinical Center, Department of Radiology and Imaging Sciences, Bethesda, MD, USA
e-mail: rolf.symons@nih.gov; david.bluemke@nih.gov

S. Nazarian · H. R. Halperin
Johns Hopkins Hospital, Department of Medicine, Baltimore, MD, USA
e-mail: snazarian@jhmi.edu; hhalper@jhmi.edu

R. Y. Kwong et al. (eds.), *Cardiovascular Magnetic Resonance Imaging*, Contemporary Cardiology,
https://doi.org/10.1007/978-1-4939-8841-9_9

Patient Condition and Monitoring

As the indications for cardiovascular MRI expand, patients with higher acuity of disease and increased dependence on monitoring and intervention are referred for MRI. Patients with cardiovascular disease are often referred for imaging in the setting of arrhythmias, hypotension, myocardial ischemia, or congestive heart failure. Contrast administration, prolonged supine imaging, and interaction with implantable or temporary devices may lead to changes in patient condition during the MRI examination. Appropriate monitoring with continuous electrocardiogram (ECG) telemetry, pulse oximetry, non-invasive blood pressure, and a well-rehearsed plan for monitoring of patient symptoms and treatment are essential for all cardiac MRI studies. To perform MRI safely, some devices may have to be disabled, and patient monitoring is limited. To increase safety, steps need to be taken to replace the disabled function.

Potential for Interaction with Implanted Devices

Ferromagnetic materials in a magnetic field are subject to force and torque. The potential for movement of an implanted device in the MRI environment depends on the magnetic field strength, ferromagnetic properties of the material, the implant distance from the magnet bore, and the stability of the implant [1].

The RF and pulsed-gradient magnetic fields in the MRI environment may induce electrical currents in leads and other ferromagnetic wires within the field. Implant length (vs. the RF wavelength) and conformations such as loops favor improved transition of energy to the implanted device. RF pulses may also lead to implant heating and tissue damage at the device-tissue interface.

Sophisticated electronic implants, such as those in neurostimulators, pacemakers, and implantable cardioverter defibrillators (ICDs), have the potential for receiving electromagnetic interference in the MRI environment, resulting in programming changes or loss of function.

Patient Screening

Given the potential risks listed, it is essential to conduct a systematic review of the patient's condition, implanted devices, and safety for MRI. At our institution, all patients are asked to review, answer, and sign a safety questionnaire (Fig. 9.1). A time-out is the last step immediately before starting the MRI to perform a final check to make sure the correct patient undergoes the correct MRI procedure. The latest data regarding the MRI safety of devices commonly used in cardiovascular patients are reviewed here.

Devices with Potential for Interaction with Magnetic Resonance Imaging

ECG Leads

Metallic telemetry leads used routinely for patient monitoring can induce artifacts and may heat in the MRI environment, resulting in skin burns. Specially designed non-ferromagnetic ECG leads and filtered monitoring systems have been designed for the MRI environment up to 1.5 T (e.g., S/5 MRI Monitor, Datex-Ohmeda, Finland; http://www.gehealthcare.fi/kliiniset_jarjestelmat/hoitoalueet/perioperatiivinenhoito/potilasvalvonta/fi_FI/iMMMRI/_files/7678416549760295 9/default/MRI_8004924.pdf). Such systems also offer continuous SpO_2 monitoring, which in our experience is an invaluable tool for monitoring of the cardiac rhythm, especially when the ECG signal, despite filtering, becomes unreadable in the setting of specific MRI pulse sequences.

Sternal Wires

Sternal wires used for closure after thoracotomy procedures are typically made of stainless steel, which is minimally ferromagnetic. Animal studies have suggested the safety of MRI in this setting [2]. Over the course of 15 years in a large acute care hospital setting, one patient had chest discomfort that was classified as "possibly" related to sternal wires; the MRI in this case was discontinued, with resolution of symptoms and no further complications. However, sternal wires, similar to any other metallic implant, typically induce susceptibility artifacts in the immediate area and may limit imaging of the anterior right ventricle [3].

Epicardial Wires

Temporary epicardial pacing wires are routinely cut short at the skin and left in place after cardiac surgery. There are reports of safe performance of MRI in patients with such retained temporary wires [4, 5]. Permanent epicardial pacing leads and patches placed at cardiac surgery, however, have more ferromagnetic materials and are prone to heating in the MRI environment. Unlike endovascular leads, these devices are not cooled by the blood pool, and in experimental models up to 20 °C of heating has been observed [6]. For this reason, at our institution, we do not scan patients with permanent

epicardial leads and patches. Temporary epicardial wires are removed prior to MRI whenever possible.

Prosthetic Valves, Annuloplasty Rings, and Transcatheter Valves

Ex vivo studies of a variety of current prosthetic valves and annuloplasty rings, including the mechanical St. Jude, Bjork-Shiley, and Carbo-Medics and bioprosthetic (with metal struts) such as the Hancock, have shown minimal torque and heating (<0.8 °C) at 1.5 T and with specific absorption rates limited to 1.1 W/kg [7–9]. Artifact size correlated with the amount of metal in the device and was exaggerated on gradient echo pulse sequences.

Shellock also evaluated prosthetic valve and annuloplasty ring safety at 3 T, revealing minor magnetic field interactions [10]. Studies to determine the force required to cause partial or total detachment of a heart valve prosthesis in patients with degenerative valvular disease have found that forces significantly higher than those induced at 4.7 T would be required to pull a suture through the valve annulus tissue [11].

The only prosthetic valves previously thought to have potential for experiencing enough force and torque to cause clinically concerning problems were the Star-Edwards pre-6000 series prostheses. Deflection measurements at 1.5 T revealed forces similar to peak forces exerted by the beating

NIH Rad & IS MRI Contrast Information and Questionnaire

Your doctor requested an MRI scan that is performed with the administration of "MRI contrast" by vein. MRI contrast is used to "enhance" the MRI pictures which can help to see the effects of certain diseases and aid in making diagnoses. Although MRI contrast agents are extremely safe, as with any medication, there is a potential for side effects or adverse reactions.

During the injection, it is not uncommon to have a metallic taste in your mouth of to feel warm or cold at the site where the injection is performed. These are expected, and not considered adverse reactions.

Minor adverse reactions, such as nausea and vomiting as well as allergic reactions, such as itching or hives are possible during the injection.

Serious reactions rarely occur, however it is possible. A serious reaction can include shortness of breath, asthmatic attacks, convulsions, shock, or even death. Life threatening reactions are exceedingly rare. We estimate life threatening reactions will occur about 7 times per one million injections.

The need for blood work prior to the administration of IV contrast media depends on many factors such as age, a history of diabetes, and a history of kidney or liver failure or transplant. Your technologies will review these potential risk factors prior to starting your exam.

You may refuse the contrast injection at any time, However please be aware that this may limit our ability to answer the clinical questions being asked by your doctor. If you have any questions, please ask to speak to the Radiology Nurse, Technologist, or Radiologist. They will be happy to answer your questions.

Please check: Yes No Unsure	**Please check:** Yes No
O O O I have you had MRI contrast before?	O O Diabetic
O O O Have you had a bad reaction to MRI contrast?	O O Dialysis
O O O Have you had MRI contrast in the last 2 days?	O O Kidney tumors
	O O Kidney or Liver disease
	O O Abnormal Kidney function

Signature: _____

Patient/Parent/Guardiant:
(Circle one)

TIME-OUT: Tech 1 _____ Tech 2 _____ DATE: _____

Fig. 9.1 Sample patient safety questionnaire

Fig. 9.1 (continued)

NIH Rad & IS MRI Safety Questionnaire

If you are a woman

Y	N	
O	O	Breast feeding
O	O	IUD, or pessary
O	O	Tissue Expanders (breast)
O	O	Pregnant (possibly pregnant)

Eye

Y	N	
O	O	Eye Implants
O	O	History of or currently a welder
O	O	Prior injury to the eye involving metal

Other

Y	N	
O	O	Bullet or shrapnel injury
O	O	Tattoos or tattooed eye-liner
O	O	Metal fragments in your body
O	O	Dental braces, spacers, bridges, or dentures

Implanted Medical Devices

No data in implant registry

Y	N	
O	O	Internal electrodes
O	O	Mechanical device
O	O	Prosthetic heart valve
O	O	Aneurysm clips or coils
O	O	Artificial limbs or joints
O	O	Radiation seeds or implants
O	O	Ear Implants (e.g. cochlear)
O	O	Prosthesis (breast or penile)
O	O	Pins, screws, or other fixation hardware
O	O	Stent, filter, or coil within the last 3 mos.

MRI Conditional devices*

Y	N	
O	O	Programmable shunt
O	O	Deep brain stimulator
O	O	Vagal nerve stimulator
O	O	Pacemaker or pacer-wires
O	O	Baclofen / medication pump

* must be assessed before and/or after MRI procedure

Devices which must be removed prior to MRI:

Y	N		Y	N	
O	O	Insulin Pump	O	O	Body piercing/ jewelry metal clothing
O	O	Hearing Aides(must be removed)	O	O	Skin medication (transdermal) patch

Please explain any "yes"answers in detail:

PATIENT:

Signature: _____ Date: _____

TECHNOLOGIST: *I have reviewed this document and verbally interviewed the patient prior to performing the MRI*

Signature: _____ Date: _____

heart itself [7], leading to initial recommendations to exclude patients with this device series from MRI procedures. However, later studies revealed lower peak forces exerted even on this prosthetic series, and cardiac MRI is considered safe in these patients [12]. Mechanical valves do not appear to be prone to induced lead currents [9].

Although there are no reports of patient injury in the MRI environment caused by the presence of a heart valve, there are theoretical concerns about MRI at 1.5 T and higher field strengths. One such theoretical concern is the tendency of a metallic object to develop an opposing magnetic field to that through which it moves (the Lenz effect). Such a secondary magnetic field may result in a resistive pressure to opening and closing of a disk prosthesis within the valve [13]. Bjork-Shiley convex/concave heart valves (Shiley, Irvine, CA) are associated with an increased risk of mechanical failure because of outlet strut fracture. These valves are associated with large susceptibility artifacts under MRI, and such artifacts may increase in size in fractured valves [14].

Edwards et al. evaluated multiple heart valve prostheses for MRI-related forces in static fields up to 4.7 T. Most were found to be safe based on current criteria. However, valves made of Elgiloy, a Ni-Co-Cr base paramagnetic engineering material [15], such as the Carpentier-Edwards Physio Ring were found to be prone to rotational forces at such high field strengths [16].

Transcatheter-placed heart valves are sutureless and therefore could be more susceptible to magnetically induced valve dehiscence during MRI. Percutaneous aortic valves in particular have the theoretical potential for coronary occlusion with dislodgement. Limited initial reports have shown cardiac MRI to be safe in patients with pulmonary and aortic transcatheter-placed valves [17], though further studies are warranted and specific guidelines should be followed, most

frequently found at the company's website. If MRI is deemed necessary, a waiting period of 6-week post-implant to allow firm fixation by tissue ingrowth is preferred, similar to recommendations for sutureless septal occluder devices.

Coronary Stents

In vitro studies have shown minimal heating of coronary stents in the MRI environment [18]. Stent dislodgement, even micro-dislodgement, is of theoretical concern because of the potential for dissection, embolism, and thrombosis. However, most stents are made of materials with little or no ferromagnetism, such as stainless steel, nitinol, or titanium. In vitro and in vivo studies of stent movement have shown minimal movement caused by MRI [19, 20]. Despite manufacturer recommendations to wait 8 weeks after stent placement prior to imaging, no adverse effects have been noted because of MRI even in the acute post-stent period [21, 22].

A study of acute MRI after deployment of drug-eluting coronary stents (Taxus, Boston Scientific, Natick, MA; Cypher, Cordis, Johnson & Johnson, New Brunswick, NJ) revealed no acute thrombosis and 9-month adverse events comparable to that expected without MRI [23]. In vitro testing of another drug-eluting stent (Endeavor, cobalt alloy, Medtronic Vascular, Santa Rosa, CA) has also been performed, revealing minor magnetic field interactions, heating (+0.5 °C), and artifacts [24]. Electric resonating "active" coronary stents designed to act as electric resonating circuits, thus functioning as inductively coupled transmit coils to allow high-resolution imaging of in-stent restenosis, have been tested in vitro and in animal models [25]. However, thus far, no studies have examined the safety profile of these stents in clinical human cardiac MRI.

New stents are continuously developed, and each patient should be individually evaluated whether cardiac MRI can be performed safely. MRI should never be performed if there is a suspicion that a stent is not positioned properly.

Non-coronary Stents

MRI of non-ferromagnetic nickel titanium aortic stents has been safely performed in patients with minimal artifact [26]. Ex vivo studies have revealed no deflection forces and minimal heating, limited to 1.1 °C. Despite the recommendation by some authorities to delay MRI for 6 weeks after implant in the case of ferromagnetic large vessel stents [27], safe imaging has been reported in the acute post-implant period [28]. Similar to coronary stents, each patient should be individually evaluated, since, to date, not all stents have undergone MRI testing and new stents are continuously developed.

Coils

In vitro tests of non-ferromagnetic platinum microcoils have revealed no coil migration and minimal susceptibility artifacts [29]. Three-dimensional time-of-flight MRI has been performed for follow-up of patients with Guglielmi detachable coils within a week post-deployment for treatment of intracranial aneurysms [30]. Substitution of digital subtraction angiography by MRI in this patient population was safe, produced minimal artifact, and helped identify thromboembolic events associated with balloon-assisted deployment [31, 32]. Chronic studies have revealed that time-of-flight MRI is not only safe but also may indeed be more sensitive at identifying residual flow in coiled aneurysms than traditional plain radiographs and digital subtraction angiography [33, 34]. In a case series of diffusion and perfusion MRI in patients with ruptured and unruptured intracranial aneurysms treated by intravascular coiling, no MRI-related complications were reported, and stents and platinum coils added negligible effects on the quality of images [35]. Multiple coils have been evaluated at 3-Tesla, and though magnetic field interactions are stronger than at 1.5 Tesla, similar to other implants, fixation by tissue ingrowth is sufficient to prevent dislocation [36]. Therefore, postponing MRI until at least 6 weeks after implantation is prudent. If there is a clinical indication for MRI in the acute setting, the diagnostic benefits of MRI probably outweigh the risks of MRI.

Filters

Initial testing of Greenfield filters for deflection at 1.5 T found large variations in the amount of deflection experienced by each device [37]. However, in vivo studies showed no evidence of migration [38]. Although the stainless steel filters such as Tulip and Bird's Nest filters cause extensive signal voids, the susceptibility artifacts associated with most filters appear to be minimal [39]. Imaging of the tantalum or titanium alloy filters is associated with such minimal artifact that even intraluminal tilting of the device, post-filter turbulence, and thrombi trapped within the filters can be visualized [40, 41]. A study comparing the sensitivity of MRI vs. ultrasound to assess inferior vena cava patency in the setting of Simon nitinol filters concluded that MRI is the superior modality [42]. It is recommended to wait at least 6 weeks after filter placement before MRI to allow firm tissue fixation. If clinically necessary, earlier MRI can be considered on an individual base as long as there is no suspicion of a non-properly positioned filter. Placement of vena cava filters guided by MRI has been attempted; however, it is limited by only passive visualization of the implanted device [43]. Techniques to improve real-time visualization of the vessel and interventional instruments are under development [44].

Septal Defect Closure Devices

An in vitro study to evaluate the safety of 12 different occluders used to treat patients with patent ductus arteriosus, atrial septal defects, and ventricular septal defects in a 1.5-T system was performed by Shellock and Morisoli. Occluders made of 304 stainless steels were ferromagnetic and displayed deflection forces of 248–299 dynes, whereas those made of MP35n were non-ferromagnetic. Artifacts were variable depending on the type and amount of metal used to construct the implant. The authors recommended a waiting period of 6 weeks post-implant to allow tissue growth and a stronger implant-tissue interface prior to MRI [45].

Real-time MRI guidance with the use of intravascular antenna guidewires has been used to image atrial septal defects and deploy Amplatzer Septal Occluders in swine [46]. CardioSEAL Septal Repair and STARFlex Septal Repair Implants have been tested for MRI compatibility at 3 T. Only minor translational attraction or torque was noted, leading the authors to conclude that MRI even at 3 T could be performed immediately post-implantation. Temperature rises were limited to 0.5 °C, and artifacts were minimal [47]. However, if there is any doubt about the integrity of the fixation parts of a ferromagnetic septal closure device, no MRI should be performed to prevent dislocation.

Vascular Access Ports and Catheters

Shellock and Shellock tested a variety of vascular access catheters made of titanium, polysulfone, barium sulfate, or silicone, such as the commonly used Vital-Port and Hickman catheters, for MRI safety. Vascular access ports have been assessed at 3 T, and no significant magnetic interaction was noted. Interestingly, even nonmetallic vascular access ports are seen on MRI because they contain silicone, and the signal should not be interpreted as an abnormality [48, 49].

Guidewires, Angiography, and Electrophysiology Catheters

Guidewires are typically made from stainless steel or nitinol (nickel/titanium alloy) and are prone to heating and lead currents in the MRI environment, even leading to iatrogenic skin burns in one case report [50]. However, the use of guidewires with RF decoupling to reduce heating may lead to successful MRI-guided wire and catheter placement [51]. Angiography and electrophysiology catheters with any form of internal or external conductive wire may be prone to heating or induced lead currents and are contraindicated in the MRI environment. Patients with cardiovascular catheters with internal or external conductive wires therefore should not undergo MRI, unless specific testing of the hardware has demonstrated otherwise. However, multifunctional electrophysiology catheters that also act as long loop receivers, allowing for catheter visualization, intracardiac electrogram recording, and ablation during MRI, have been developed and are currently under testing [52–54].

Swan-Ganz and Thermodilution Catheters

Swan-Ganz and thermodilution catheters contain long wires made of paramagnetic or magnetic materials, and the tips are not fixed. Therefore, they may be prone to movement, heating, and induction of current and are not safe in the MRI environment [27].

Implantable Monitors

The SJM Confirm (St. Jude Medical, Sylmar, CA) and Reveal LINQ (Medtronic, Minneapolis, MN) are insertable cardiac monitoring systems that can be activated by preset heart rate limits or a patient trigger. These devices are considered MRI conditional. Specific MRI scanning for these devices can be found at their respective manufacturer's website.

Temporary Pacemakers

To our knowledge, there are no studies assessing the safety of temporary pacemakers in the MRI environment. Unlike permanent devices, temporary pacemakers typically have unfixed leads and are more prone to movement. Furthermore, the leads are longer and may be more prone to induction of lead currents. Finally, the electronic platform of external temporary pacemakers is less sophisticated and has less filtering compared to modern implantable pacemakers. Therefore, such devices are likely more susceptible to electromagnetic interference.

Permanent Pacemakers and Implantable Cardioverter Defibrillators

Because of underlying structural heart disease and accompanying conduction system disease or risk of ventricular arrhythmia, a significant proportion of patients referred for cardiac MRI have permanent pacemakers and implantable defibrillators [55–57]. It has been estimated that a patient with a pacemaker or implanted defibrillator has a 50–75% likelihood of having a clinically indicated MRI over the lifetime of their device [58]. The potential for movement of the

device [59], programming changes, asynchronous pacing, activation of tachyarrhythmia therapies, inhibition of demand pacing [60], and induced lead currents leading to heating and cardiac stimulation [61] has led to concerns from device manufacturers [62–64] and MRI authorities [65, 66] regarding the performance of MRI procedures in cardiac implantable device recipients. For these reasons, a pacemaker historically has been considered a contraindication for MRI.

However, several case series have reported the safety of MRI in the setting of pacemakers [67–71]. A small case series has also reported neurological MRI in the setting of selected implantable cardioverter defibrillator systems (ICDs) [72]. Overall, safety has been reported, but acute changes in battery voltage, lead thresholds, and programming can be seen. More recent pacemakers have decreased ferromagnetic components and more streamlined electronic wiring and are less prone to interactions with the MRI magnetic field. The first pacemaker labeled as "MR conditional" became available in 2011 (Revo MRI SureScan by Medtronic). According to the 2013 ESC guidelines on cardiac pacing and cardiac resynchronization therapy, patients with these pacemakers can undergo MRI following strict guidelines and manufacturer's instructions [73]. The US Food and Drug Administration (FDA) has currently approved two major groups of MRI conditional devices for safe human MRI scan (SureScan group of devices by Medtronic and ProMRI group by Biotronik).

At our institution, we have developed a protocol regarding the management of "MRI conditional" pacemakers that are *FDA approved*. This protocol is listed below:

A. Scheduling of the exam:
   1. MRI should be performed six or more weeks post device implantation.
   2. MRI exam should only be performed on anatomical areas approved by the device manufacturer guidelines.
   3. Obtain cardiology consult:
      (a) Identify the exact make and model of the device and leads implanted.
      (b) Confirm device six or more weeks post implantation.
      (c) Contact vendor as necessary to verify the patients' pacing system.
      (d) If required, perform and evaluate screening x-ray to confirm appropriate device and device position.
   4. Contact radiology MRI chief technologist/MRI physician leads.
      (a) Confirm the device MRI safety with the manufacturer manual.
      (b) Confirm anatomic coverage.
      (c) Discuss scheduling considerations and staff availability.
      (d) Assist with scheduling options on 1.5 T scanner.
   5. Schedule MRI examination. Order must include the following information:
      (a) Body part to be examined.
      (b) Precise device type/model number.
      (c) Statement that cardiology consult has been obtained.

B. Performance of the MRI scan:
   1. Interface with manufacturer representative to program the device to MRI safe program mode before the scan.
   2. A certified health care provider will be present during the entire scan (e.g., online training for SureScan devices: http://www.medtronic.com/mrisurescan-us/radiologytutorial.html).
   3. MRI is performed during normal business hours, so that the code team is expected to be available (i.e., availability in MRI expected to be less than 2 min.)
   4. MRI technologist:
      (a) Confirm device type.
      (b) Perform standard MRI safety screening.
      (c) Insure that manufacturer-specific conditions are met (correct slew rate and SAR).
      (d) Perform the exam on 1.5 T scanners.
      (e) Continuous monitoring of the patient during the exam is mandatory; verbal contact, ECG monitoring, and pulse oximetry.
      (f) Discontinue scan/remove patient from scan room in the case of patient distress, loss of verbal contact, ECG monitoring, or pulse oximetry.
      (g) Radiology or other physician staff needs to be physically present in the department.

C. On completion of scan, consult with cardiology if reprogramming of the device following completion of the scan is necessary.

Steps detailed above are related to FDA-approved devices only and not all the conditional devices. *MRI scanning of devices that are not FDA approved or under conditions that are not FDA approved is not covered by this policy and is not to be electively performed.*

Non-FDA-Approved Devices For specialized centers with the staff expertise in electrophysiology, a number of centers have developed approaches to performing MRI scans in patients with non-FDA-approved pacemakers and ICDs. An outline at our institution with programming steps to reduce the risk of inappropriate pacemaker inhibition or activation or inappropriate activation of tachyarrhythmia functions is shown in Fig. 9.2 [74]. Note that extensive device experience is required to safely evaluate non-FDA-approved devices, and on-site programming capability is required.

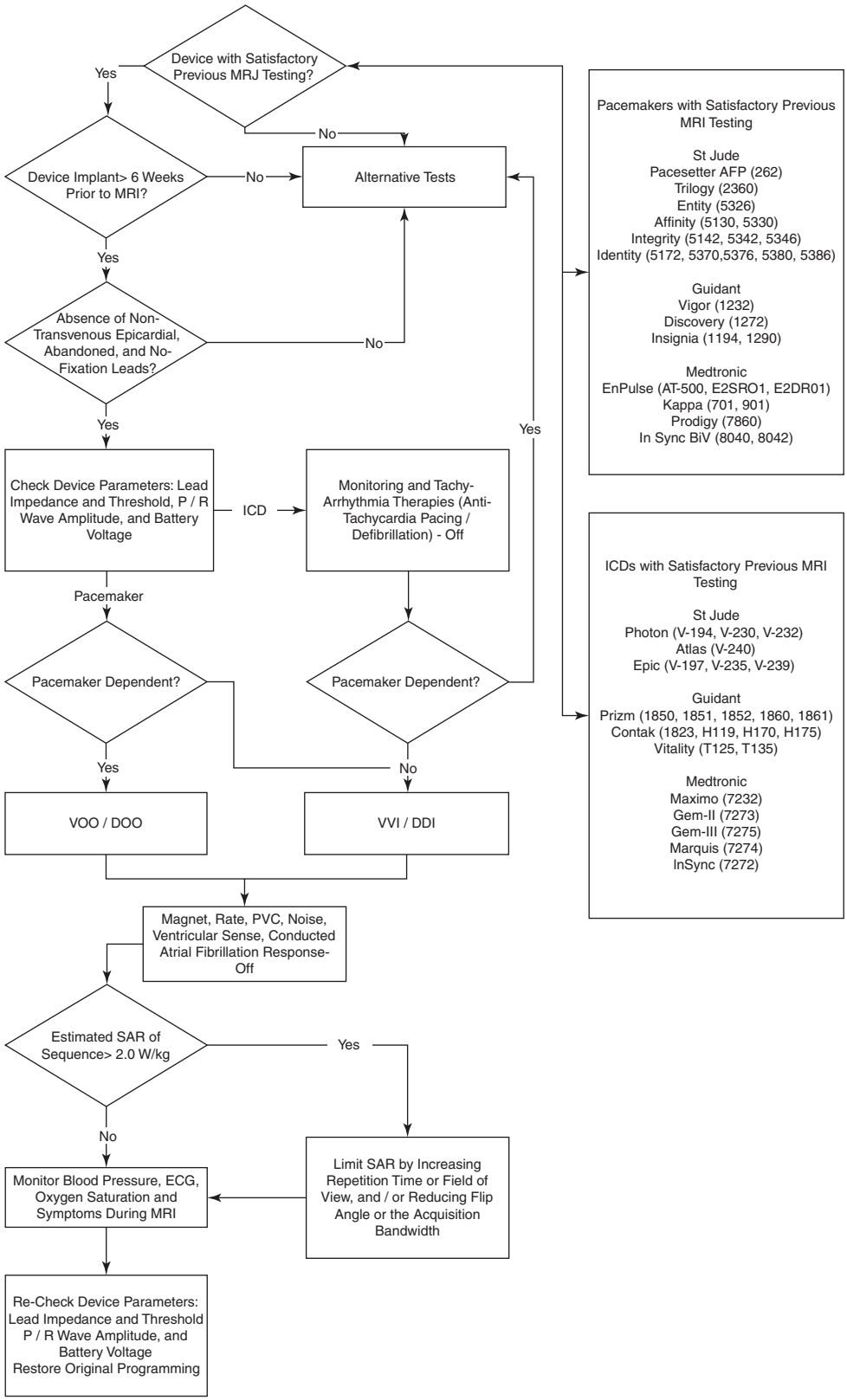

Fig. 9.2 Safety protocol for MRI of patients with non-FDA-approved permanent pacemakers and implantable defibrillators [74]. Reprinted from Nazarian et al. [[74]], http://circ.ahajournals.org/content/114/12/1277 with permission from Wolters Kluwer Health

Devices should be programmed to minimize inappropriate activation or inhibition of brady-/tachyarrhythmia therapies, and MRI sequences should be used with a specific absorption rate (SAR) of maximum 2.0 W/kg. It is important to note, however, that because of poor correlation of heating at different specific absorption rates across different scanners even within those of the same manufacturer, the specific absorption rates from the authors' results should not be directly applied to other MRI systems [75].

In general, ICDs tend to be more problematic than conventional pacemakers as they contain more ferromagnetic components and electrodes placed inside the myocardium. Strict adherence to manufacturer guidelines therefore remains essential when scanning these patients, as potential problems are still reported [76, 77].

Neurostimulation Systems

In vitro studies of a chronic deep brain stimulation system (Soletra model 7426, Medtronic) at 1.5 T have revealed temperature rises as high as 25 °C depending on the type of RF coil used, positioning of the electrodes, and the specific absorption rate of sequences [66, 78]. Such excessive heating was thought to be avoidable by using send/receive head RF coils and limiting the SAR of sequences to 2.4 W/kg using a 1.5-T/64-mHz Vision MR imaging system (Siemens Medical Systems, Iselin, NJ) [79]. Another in vitro study using a 1.5-T Sonata MRI system (Siemens Medical Systems) to scan bilateral neurostimulation systems (Soletra 7246, 7495, and 3389, Medtronic) revealed temperature rises limited to 2.1 °C [80]. Criteria to permit MRI up to 3 T are further defined by recent studies, including MRI-guided neurostimulator placement to increase placement accuracy and reduced intervention time [81–83].

Note should be made that a study has revealed poor correlation of heating at different SAR across different scanners even within those of the same manufacturer, and therefore the results of the previous studies *should not be applied* to other MRI systems [75]. Importantly, several reports of injury during MRI of patients with neurostimulation systems exist in the literature, and experts advise judicious use of MRI, only when clinically warranted, following the specific guidelines of the manufacturer, using send/receive head RF coils, and limiting the SAR to 0.4 W/kg [78, 84–86]. Note that limiting SAR in combination with send/receive RF coils is not currently approved for all MRI scanners in conjunction with deep brain stimulators.

Intra-aortic Balloon Pumps

An animal study assessed the recovery of left ventricular function after myocardial infarction with and without balloon counterpulsation via MRI. During this study, the intra-aortic balloon pump was paused during the scan. Although MRI safety was not the primary outcome assessed; no untoward side effects of MRI in this setting were reported [86]. More studies are needed to assess the safety of MRI in the setting of intra-aortic balloon counterpulsation prior to human studies with MRI.

Ventricular Assist Devices

Ventricular assist devices have high metal content, complicated circuitry, and in some cases magnetic field dependence for appropriate function. There is no literature regarding MRI in patients with implanted assist devices. Because of the issues listed and high potential for catastrophic device failure, MRI is an absolute contraindication in patients with current ventricular assist devices.

Orthopedic Implants

Most orthopedic implants have been reported to be non-ferromagnetic or weakly ferromagnetic and therefore are safe for undergoing MRI at 1.5 T [87]. The Perfix interference screw (Instrument Macar, Okemos, MI) used for anterior cruciate ligament reconstruction is the only hardware found to be highly ferromagnetic. However, the strength of the surrounding tissue provides sufficient retentive force to provide for safe imaging of patients with these implants. Some non-ferromagnetic hardware, especially cervical and external fixation systems, show significant heating due to their shape and the formation of conductive loops, especially at 3 T [88].

Shellock tested a variety of orthopedic implants at 3 T and found low torque measurements for most devices except for the bone fusion stimulator. However, this device is also likely safe for imaging given its typical position in the patient with respect to the static magnetic field of MRI and retentive strength of the subcutaneous and granulation tissue [10].

Image Artifacts

The presence of ferromagnetic materials can cause variations in the surrounding magnetic field, resulting in image distortion, signal voids or bright areas, and poor fat suppression, especially at 3 T [89]. Susceptibility artifacts appear to be most pronounced on inversion recovery and steady-state free precession sequences.

In our experience, artifacts on inversion recovery prepared delayed cardiac MRI show high signal intensity and can mimic areas of delayed enhancement, which would otherwise indicate myocardial scar. Correlation of suspect areas on different pulse sequences can help avoid misidentification

of artifact. Using imaging planes perpendicular to the plane of the device generator, shortening of the echo time, and using spin echo and fast spin-echo sequences appear to reduce the qualitative extent of artifact.

Risks Associated with the Use of Gadolinium-Based Contrast Agents

Pharmacokinetics of Gadolinium-Based Contrast Agents: Relation with Kidney Function

GBCAs are administrated intravenously with rapid equilibration in the extracellular fluid space which consists of the intravascular and interstitial compartments. Six out of nine currently clinically approved GBCAs (gadopentetate dimeglumine [Magnevist], gadodiamide [Omniscan], gadoversetamide [OptiMARK], gadoterate dimeglumine [Dotarem], gadobutrol [Gadovist], and gadoteridol [Prohance]) only distribute in the extracellular fluid space. These agents are almost exclusively eliminated by the kidneys with a half-life time in the blood of 1.5 h in patients with normal kidney function [90–94].

Gadobenate dimeglumine [Multihance] and gadoxetate disodium [Eovist in the USA, Primovist in Europe] are specifically used for imaging of the hepatobiliary system. They are taken up by hepatocytes and partially cleared by the hepatobiliary system (2–4% for gadobenate dimeglumine and 50% for gadoxetate disodium), with renal excretion for the remainder [95]. Gadofosveset trisodium [Ablavar in the USA, not approved in Europe] is a blood pool agent used for MRI angiography. Gadofosveset reversibly binds serum albumin which limits its distribution mainly to the intravascular space. Like other GBCAs it is mainly renally excreted [96].

Given the central role of renal excretion, the clearance rate of GBCAs is strongly correlated with kidney function. Chronic kidney disease (CKD) is divided into five stages based on the glomerular filtration rate (GFR), and GBCA half-life increases exponentially with more severe stages of CKD [97]:

Stage		GFR (mL/min/1.73m^2)
Stage 1	*Normal* kidney function but urine or other abnormalities point to kidney disease	≥90
Stage 2	*Mildly* reduced kidney function, urine, or other abnormalities point to kidney disease	60–89
Stage 3	*Moderately* reduced kidney function	30–59
Stage 4	*Severely* reduced kidney function	15–29
Stage 5	*Very severe* or *end-stage* kidney failure/dialysis	<15 (or dialysis)

Delayed elimination of GBCAs in patients with renal insufficiency has important consequences. One possible side effect is the dissociation of the GBCA molecule in a free gadolinium ion (Gd^{3+}) and ligand. Free gadolinium had poor solubility, precipitates in the interstitial tissue, and is extremely toxic. Another side effect is the slow diffusion of the contrast agent into different deep compartments. Several reports have shown enhancement of the cerebrospinal fluid space on MRI 1–2 days after GBCA administration in patients with renal failure [98, 99]. Possible health risks associated with free gadolinium diffusion include nephrogenic systemic fibrosis (NSF) and recent observations of gadolinium deposition in the brain which are discussed below.

To prevent these adverse health effects, renal function should be assessed in all patients before GBCA administration. The creatinine clearance rate is the golden standard to assess kidney function before MRI and shows good correlation with the blood half-life of GBCAs. However, its assessment requires blood sampling and is time-consuming. An alternative approach is the use of the "Choyke questionnaire," originally developed in 1998 to prevent iodinated contrast agent-induced nephropathy [100, 101]. A completely negative response to this six-question patient survey (history of (1) preexisting renal disease, (2) proteinuria, (3) prior kidney surgery, (4) hypertension, (5) gout, or (6) diabetes) can identify patients with normal creatinine levels with a sensitivity of 94%.

Immediate Adverse Reactions

The first GBCA was approved for clinical use in 1988 (gadopentetate dimeglumine, Magnevist, Bayer Healthcare Pharmaceuticals, Wayne, NJ), and >200 million doses have been administered worldwide since then. GBCAs are well tolerated by the vast majority of patients, and the frequency of immediate adverse reactions in GBCAs is lower than in iodinated contrast agents [102, 103]. Contrary to iodinated contrast agents, the risk of reaction is not related to the osmolality of GBCAs as the low doses used make the osmolar load very small. The frequency of all acute adverse effects after clinical GBCA injection (0.1–0.2 mmol/kg) ranges from 0.07% to 2.4%. Most of these adverse effects are mild and non-allergic, including nausea, dizziness, headache, and local paresthesia. Allergic reactions are extremely rare with an estimated frequency of 0.004–0.079%. Urticaria and rash are the most common allergic reactions, while severe, life-threatening anaphylactic reactions are exceedingly rare (0.001–0.01%).

Risk factors for allergic reactions to GBCAs are female sex, asthma, and various allergies, including previous allergic reaction to iodinated contrast agents. The recurrence rate of hypersensitivity reactions in patients with previous reaction to GBCAs is estimated at 30%, and appropriate premedication should be considered in patients with a previous

allergic reaction [104]. The treatment of immediate adverse reactions to GBBAs is similar to that for adverse reactions to iodinated contrast agents. Guidelines for treatment of adverse reactions to iodinated and gadolinium-based contrast agents can be found on the websites of the American College of Radiology and the European Society of Urogenital Radiology (www.ACR.com and www.ESUR.org).

Late Adverse Reactions

Nephrogenic Systemic Fibrosis

Nephrogenic systemic fibrosis (NSF) is a potentially fatal disorder first identified in 1997 and reported in 2000 [105]. NSF is characterized by progressive tissue fibrosis, predominately involving the skin but also affecting internal organs such as the heart, lungs, liver, and muscles. In 2006, an association between gadodiamide (Omniscan, GE Healthcare, Piscataway, NJ) and NSF was proposed [106].

Free gadolinium ions (Gd^{3+}) have been shown to stimulate the expression of profibrotic cytokines and growth factors in vitro and in vivo [107]. Therefore, the dissociation of free gadolinium ions from the chelate GBCA molecule is generally accepted to be the primary etiology of NSF. The stability of GBCAs is dependent on their molecular structure with two major determining factors: linear versus macrocyclic and ionic versus nonionic structure. Macrocyclic agents are more stable than linear ones, while ionic agents are more stable than nonionic ones. Thus, ionic macrocyclic GBCAs are least likely to release free gadolinium which may induce NSF, followed by nonionic macrocyclic, ionic linear, and nonionic linear GBCAs, respectively. In an in vitro stability study in human serum, nonionic linear GBCAs showed 20% dissociation, while ionic linear GBCAs demonstrated only 1.1–1.9% gadolinium release. All three macrocyclic GBCAs showed no detectable free gadolinium dissociation [108]. Consequently, the least stable GBCA (gadodiamide) is associated with the most cases of NSF in the current literature. Reduced kidney function is another important risk factor for NSF, as the slower renal excretion of GBCAs in these patients allows more time for gadolinium dissociation [109, 110].

The American College of Radiology 2013 Manual on Contrast Media classifies GBCAs in three groups based on the association with NSF [111]:

- Group 1 agents (gadodiamide, gadopentetate dimeglumine, and gadoversetamide) are the least stable and are associated with the majority of NSF cases.
- Group 2 agents (gadobenate dimeglumine, gadobutrol, gadoterate meglumine, and gadoteridol) are associated with few, if any, unconfounded cases of NSF. (Gadoterate meglumine is a relatively newer contrast agent; it is a macrocyclic agent and will likely also be classified as a Group 2 agent.)
- Group 3 agents (gadofosveset trisodium and gadoxetate disodium) only recently appeared on the market with only limited data for these agents, though to date, no, if any, cases of NSF have been associated with these agents.

GBCAs can be used at label doses, only if the added diagnostic information is essential and not obtainable with non-contrast-enhanced MRI. The use of group 1 agents in patients with GFR $\leq$ 40 mL/min/1.73m^2 is not recommended by the American College of Radiology. The US Food and Drug Administration (FDA) has indicated these group 1 agents are contraindicated for GFR $\leq$ 30 mL/min/1.73m^2. Both the American College of Radiology and the European Society for Urogenital Radiology have published guidelines for the use of GBCAs in patients at risk for NSF [111, 112]. Cautious use of GBCAs in patients with reduced kidney function and a shift to more stable agents have resulted in no confirmed cases of NSF since 2009.

Multiple treatment modalities have been attempted in NSF patients with limited benefit, including physical therapy, ultraviolet A phototherapy, imatinib mesylate, sirolimus, and extracorporeal photopheresis. None of these therapies have been as effective as spontaneous restoration of kidney function or renal transplantation in NSF symptom reduction [113–117]. For patients who are eligible, early transplantation should be considered to halt or reverse the progression of NSF.

Gadofosveset has a specific label indication in the United States for MR angiography for evaluation of aortoiliac occlusive disease in adults with known or suspected peripheral vascular disease. MRI of the heart is considered off-label use of gadolinium contrast agents. The use of these agents is supported by a large number of literature studies, often at doses that exceed that used of other parts of the body [118].

Gadolinium Deposition in the Brain

The first reports of increased signal intensity in the dentate nucleus and globus pallidus on unenhanced T1 brain images in patients who received multiple doses of linear GBCAs were published in 2014 [119]. Autopsy studies provided pathologic confirmation that the T1 shortening is the result of gadolinium deposition with a dose-response relationship with higher gadolinium deposition in patients who received more doses of linear GBCAs [120, 121]. Interestingly, there was no association with renal function nor administration of macrocyclic GBCAs. Similar to NSF, it is presumed that dissociation of gadolinium from the chelate molecule leads to gadolinium deposition in the brain.

To date, the available information does not identify any adverse health effects of brain gadolinium deposition (http://www.fda.gov/downloads/Drugs/DrugSafety/UCM455390.pdf). However, there is sufficient evidence to critically

review GBCA administration policy. In our institution, a set of recommendations has been adopted: (1) strictly follow FDA label indications and dosing schemes for GBCA administration; (2) only use GBCAs when clinically indicated or when specified in a research protocol; (3) consider using a macrocyclic GBCA rather than a linear agent; and (4) for patients with document adverse reactions to macrocyclic agents, linear agents can be used [122]. The choice of GBCA should be individualized at each institution, based on specific indications and experience. Further research is warranted to evaluate the hazardous effects, if any, of brain gadolinium deposition.

Cardiac MRI and Pregnancy

Present data have not conclusively documented any adverse effects of MRI on the developing human fetus. Nevertheless, it is recommended to screen all females of reproductive age for pregnancy before MRI. According to the 2013 ACR guidance document on MR safe practices, MRI can be performed during pregnancy if the diagnostic information cannot be obtained by other nonionizing methods (e.g., ultrasonography), the diagnosis will affect the patient care or fetus *during* the pregnancy, and the referring physician believes that it is not feasible to wait until the patient is no longer pregnant [123]. The ACR does not give special consideration to the first trimester of pregnancy, though many institutions still discourage MRI during the first trimester as some animal studies have shown deleterious effects during this phase of pregnancy [65, 124].

GBCAs should not routinely be administered to pregnant patients. To date, there is no evidence of teratogenesis or mutagenesis after fetal exposure to GBCAs during pregnancy [125, 126]. However, at least some of the GBCAs readily pass through the placental barrier. After fetal renal clearance, these agents may remain in the amniotic fluid, potentially allowing for release of toxic-free gadolinium ions. Even though a recent study suggests that the fetal concentration of GBCAs may be lower than previously thought, the risk of GBCA administration remains unknown, and GBCAs should only be administered if their usage is absolutely necessary and the potential benefits outweigh the risks to the fetus [127]. The dose of the GBCA should be as low as possible with a preference for a stable (macrocyclic) agent.

Premedication is indicated in a pregnant patient with a previous allergic reaction to GBCAs. Most schemes consist of an H1 antihistamine (diphenhydramine) and a steroid (prednisone or methylprednisolone). Diphenhydramine is classified in FDA category B (animal reproduction studies have failed to demonstrate a risk to the fetus, and there are no adequate and well-controlled studies in pregnant women), while prednisone and methylprednisolone are considered FDA category C (animal reproduction studies have shown an adverse effect on the fetus, and there are no adequate and well-controlled studies in humans, but potential benefits may warrant the use of the drug in pregnant women despite potential risks). Steroids may lead to fetal adrenal suppression, and methylprednisolone slightly increases risk for cleft lip in the fetus if used before 10 weeks of gestation [128].

Excretion of GBCA in breast milk is minimal, and available data suggest that interruption of breastfeeding is not necessary after maternal GBCA administration [111, 129]. However, if the patient is concerned, breastfeeding may be interrupted for 12–24 h to allow for excretion of the contrast agent.

Summary The diagnostic benefits of cardiovascular MRI are of critical importance in the management of an ever-increasing number of patients with cardiovascular disease. Patients with higher morbidity are referred for MRI, raising specific safety concerns. Although techniques for safe imaging in the setting of certain devices have been developed, the potential for catastrophic complications still exists and dictates a high degree of vigilance for safe imaging. The reader is encouraged to consult websites that provide more specific information regarding individual devices and safe administration of GBCAs (e.g., www.mrisafety.com and www.ACR.org). The final decision to perform cardiac MRI should be made on an individual basis considering the potential benefit of MRI relative to the associated risks.

References

1. Prasad SK, Pennell DJ. Safety of cardiovascular magnetic resonance in patients with cardiovascular implants and devices. Heart. 2004;90(11):1241–4.
2. Manner I, Alanen A, Komu M, Savunen T, Kantonen I, Ekfors T. MR imaging in the presence of small circular metallic implants: assessment of thermal injuries. Acta Radiol. 1996;37(4):551–4.
3. Okamura Y, Yamada Y, Mochizuki Y, et al. [Evaluation of coronary artery bypass grafts with magnetic resonance imaging]. [Zasshi][Journal] Nihon Kyobu Geka Gakkai. 1997;45(6):801–805.
4. Hartnell GG, Spence L, Hughes LA, Cohen MC, Saouaf R, Buff B. Safety of MR imaging in patients who have retained metallic materials after cardiac surgery. AJR Am J Roentgenol. 1997;168(5):1157–9.
5. Murphy KJ, Cohan RH, Ellis JH. MR imaging in patients with epicardial pacemaker wires. AJR Am J Roentgenol. 1999;172(3):727–8.
6. Roguin A, Zviman MM, Meininger GR, et al. Modern pacemaker and implantable cardioverter/defibrillator systems can be magnetic resonance imaging safe in vitro and in vivo assessment of safety and function at 1.5 T. Circulation. 2004;110(5):475–82.
7. Soulen RL, Budinger TF, Higgins CB. Magnetic resonance imaging of prosthetic heart valves. Radiology. 1985;154(3):705–7.
8. Edwards M, Taylor KM, Shellock FG. Prosthetic heart valves: evaluation of magnetic field interactions, heating, and artifacts at 1.5 T. J Magn Reson Imaging. 2000;12(2):363–9.
9. Shellock FG. Prosthetic heart valves and annuloplasty rings: assessment of magnetic field interactions, heating, and artifacts at 1.5 Tesla. J Cardiovasc Magn Reson. 2001;3(4):317–24.

10. Shellock FG. Biomedical implants and devices: assessment of magnetic field interactions with a 3.0-Tesla MR system. J Magn Reson Imaging. 2002;16(6):721–32.
11. Edwards M-B, Draper ERC, Hand JW, Taylor KM, Young IR. Mechanical testing of human cardiac tissue: some implications for MRI safety. J Cardiovasc Magn Reson. 2005;7(5):835–40.
12. Shellock FG. Magnetic resonance safety update 2002: implants and devices. J Magn Reson Imaging. 2002;16(5):485–96.
13. Condon B, Hadley DM. Potential MR hazard to patients with metallic heart valves: the Lenz effect. J Magn Reson Imaging. 2000;12(1):171–6.
14. van Gorp MJ, van der Graaf Y, de Mol BAJM, et al. Björk-Shiley convexoconcave valves: susceptibility artifacts at brain MR imaging and mechanical valve fractures 1. Radiology. 2004;230(3):709–14.
15. Ho JC, Shellock FG. Magnetic properties of Ni–Co–Cr-base Elgiloy. J Mater Sci Mater Med. 1999;10(9):555–60.
16. Edwards M, Ordidge RJ, Hand JW, Taylor KM, Young IR. Assessment of magnetic field (4.7 T) induced forces on prosthetic heart valves and annuloplasty rings. J Magn Reson Imaging. 2005;22(2):311–7.
17. Sherif MA, Abdel-Wahab M, Beurich H-W, et al. Haemodynamic evaluation of aortic regurgitation after transcatheter aortic valve implantation using cardiovascular magnetic resonance. EuroIntervention J Eur Collab with Work Gr Interv Cardiol Eur Soc Cardiol. 2011;7(1):57–63.
18. Strohm O, Kivelitz D, Gross W, et al. Safety of implantable coronary stents during H-magnetic resonance imaging at 1.0 and 1.5 T. J Cardiovasc Magn Reson. 1999;1(3):239–45.
19. Scott NA, Pettigrew RI. Absence of movement of coronary scents after placement in a magnetic resonance imaging field. Am J Cardiol. 1994;73(12):900–1.
20. Hug J, Nagel E, Bornstedt A, Schnackenburg B, Oswald H, Fleck E. Coronary arterial stents: safety and artifacts during MR imaging 1. Radiology. 2000;216(3):781–7.
21. Gerber TC, Fasseas P, Lennon RJ, et al. Clinical safety of magnetic resonance imaging early after coronary artery stent placement. J Am Coll Cardiol. 2003;42(7):1295–8.
22. Kaya MG, Okyay K, Yazici H, et al. Long-term clinical effects of magnetic resonance imaging in patients with coronary artery stent implantation. Coron Artery Dis. 2009;20(2):138–42.
23. Porto I, Selvanayagam J, Ashar V, Neubauer S, Banning AP. Safety of magnetic resonance imaging one to three days after bare metal and drug-eluting stent implantation. Am J Cardiol. 2005;96(3):366–8.
24. Shellock FG, Forder JR. Drug eluting coronary stent: in vitro evaluation of magnet resonance safety at 3 tesla. J Cardiovasc Magn Reson. 2005;7(2):415–9.
25. Busch M, Vollmann W, Bertsch T, et al. On the heating of inductively coupled resonators (stents) during MRI examinations. Magn Reson Med. 2005;54(4):775–82.
26. Engellau L, Olsrud J, Brockstedt S, et al. MR evaluation ex vivo and in vivo of a covered stent-graft for abdominal aortic aneurysms: ferromagnetism, heating, artifacts, and velocity mapping. J Magn Reson Imaging. 2000;12(1):112–21.
27. Ahmed S, Shellock FG. Magnetic resonance imaging safety: implications for cardiovascular patients. J Cardiovasc Magn Reson. 2001;3(3):171–82.
28. Stables RH, Mohiaddin R, Panting J, Pennell DJ, Pepper J, Sigwart U. Exclusion of an aneurysmal segment of the thoracic aorta with covered stents. Circulation. 2000;101(15):1888–9.
29. Marshall MW, Teitelbaum GP, Kim HS, Deveikis J. Ferromagnetism and magnetic resonance artifacts of platinum embolization microcoils. Cardiovasc Intervent Radiol. 1991;14(3):163–6.
30. Okahara M, Kiyosue H, Hori Y, Yamashita M, Nagatomi H, Mori H. Three-dimensional time-of-flight MR angiography for evaluation of intracranial aneurysms after endosaccular packing with Guglielmi detachable coils: comparison with 3D digital subtraction angiography. Eur Radiol. 2004;14(7):1162–8.
31. Soeda A, Sakai N, Sakai H, et al. Thromboembolic events associated with Guglielmi detachable coil embolization of asymptomatic cerebral aneurysms: evaluation of 66 consecutive cases with use of diffusion-weighted MR imaging. Am J Neuroradiol. 2003;24(1):127–32.
32. Albayram S, Selcuk H, Kara B, et al. Thromboembolic events associated with balloon-assisted coil embolization: evaluation with diffusion-weighted MR imaging. Am J Neuroradiol. 2004;25(10):1768–77.
33. Cottier JP, Bleuzen-Couthon A, Gallas S, et al. Follow-up of intracranial aneurysms treated with detachable coils: comparison of plain radiographs, 3D time-of-flight MRA and digital subtraction angiography. Neuroradiology. 2003;45(11):818–24.
34. Yamada N, Hayashi K, Murao K, Higashi M, Iihara K. Time-of-flight MR angiography targeted to coiled intracranial aneurysms is more sensitive to residual flow than is digital subtraction angiography. Am J Neuroradiol. 2004;25(7):1154–7.
35. Cronqvist M, Wirestam R, Ramgren B, et al. Diffusion and perfusion MRI in patients with ruptured and unruptured intracranial aneurysms treated by endovascular coiling: complications, procedural results, MR findings and clinical outcome. Neuroradiology. 2005;47(11):855–73.
36. Karacozoff AM, Shellock FG, Wakhloo AK. A next-generation, flow-diverting implant used to treat brain aneurysms: in vitro evaluation of magnetic field interactions, heating and artifacts at 3-T. Magn Reson Imaging. 2013;31(1):145–9.
37. Williamson MR, McCowan TC, Walker CW, Ferris EJ. Effect of a 1.5 tesla magnetic field on greenfield filters in vitro and in dogs. Angiology. 1988;39(12):1022–4.
38. Liebman CE, Messersmith RN, Levin DN, Lu C-T. MR imaging of inferior vena caval filters: safety and artifacts. Am J Roentgenol. 1988;150(5):1174–6.
39. Honda M, Obuchi M, Sugimoto H. Artifacts of vena cava filters ex vivo on MR angiography. Magn Reson Med Sci. 2003;2(2):71–7.
40. Teitelbaum GP, Ortega HV, Vinitski S, et al. Low-artifact intravascular devices: MR imaging evaluation. Radiology. 1988;168(3):713–9.
41. Grassi CJ, Matsumoto AH, Teitelbaum GP. Vena caval occlusion after Simon nitinol filter placement: identification with MR imaging in patients with malignancy. J Vasc Interv Radiol. 1992;3(3):535–9.
42. Kim D, Edelman RR, Margolin CJ, et al. The Simon nitinol filter: evaluation by MR and ultrasound. Angiology. 1992;43(7):541–8.
43. Frahm C, Gehl H, Lorch H, et al. MR-guided placement of a temporary vena cava filter: technique and feasibility. J Magn Reson Imaging. 1998;8(1):105–9.
44. Bücker A, Neuerburg JM, Adam GB, et al. Real-time MR guidance for inferior vena cava filter placement in an animal model. J Vasc Interv Radiol. 2001;12(6):753–6.
45. Shellock FG, Morisoli SM. Ex vivo evaluation of ferromagnetism and artifacts of cardiac occluders exposed to a 1.5-T MR system. J Magn Reson Imaging. 1994;4(2):213–5.
46. Rickers C, Jerosch-Herold M, Hu X, et al. Magnetic resonance image-guided transcatheter closure of atrial septal defects. Circulation. 2003;107(1):132–8.
47. Shellock FG, Valencerina S. Septal repair implants: evaluation of magnetic resonance imaging safety at 3 T. Magn Reson Imaging. 2005;23(10):1021–5.
48. Shellock FG, Shellock VJ. Vascular access ports and catheters: ex vivo testing of ferromagnetism, heating, and artifacts associated with MR imaging. Magn Reson Imaging. 1996;14(4):443–7.

49. Titterington B, Shellock FG. Evaluation of MRI issues for an access port with a radiofrequency identification (RFID) tag. Magn Reson Imaging. 2013;31(8):1439–44.
50. Masaki F, Shuhei Y, Riko K, Yohjiro M. Iatrogenic second-degree burn caused by a catheter encased tubular braid of stainless steel during MRI. Burns. 2007;33(8):1077–9.
51. Razavi R, Hill DLG, Keevil SF, et al. Cardiac catheterisation guided by MRI in children and adults with congenital heart disease. Lancet. 2003;362(9399):1877–82.
52. Susil RC, Yeung CJ, Halperin HR, Lardo AC, Atalar E. Multifunctional interventional devices for MRI: a combined electrophysiology/MRI catheter. Magn Reson Med. 2002;47(3):594–600.
53. Krämer NA, Krüger S, Schmitz S, et al. Preclinical evaluation of a novel fiber compound MR guidewire in vivo. Investig Radiol. 2009;44(7):390–7.
54. Saikus CE, Lederman RJ. Interventional cardiovascular magnetic resonance imaging: a new opportunity for image-guided interventions. JACC Cardiovasc Imaging. 2009;2(11):1321–31.
55. Brown DW, Croft JB, Giles WH, Anda RF, Mensah GA. Epidemiology of pacemaker procedures among Medicare enrollees in 1990, 1995, and 2000. Am J Cardiol. 2005;95(3):409–11.
56. Moss AJ, Zareba W, Hall WJ, et al. Prophylactic implantation of a defibrillator in patients with myocardial infarction and reduced ejection fraction. N Engl J Med. 2002;346(12):877–83.
57. Bardy GH, Lee KL, Mark DB, et al. Amiodarone or an implantable cardioverter–defibrillator for congestive heart failure. N Engl J Med. 2005;352(3):225–37.
58. Kalin R, Stanton MS. Current clinical issues for MRI scanning of pacemaker and defibrillator patients. Pacing Clin Electrophysiol. 2005;28(4):326–8.
59. Shellock FG, Tkach JA, Ruggieri PM, Masaryk TJ. Cardiac pacemakers, Icds, and loop recorder: evaluation of translational attraction using conventional ("long-bore") and "short-bore" 1.5- and 3.0-tesla Mr systems: SAFETY. J Cardiovasc Magn Reson. 2003;5(2):387–97.
60. Erlebacher JA, Cahill PT, Pannizzo F, Knowles RJR. Effect of magnetic resonance imaging on DDD pacemakers. Am J Cardiol. 1986;57(6):437–40.
61. Hayes DL, Holmes DR, Gray JE. Effect of 1.5 tesla nuclear magnetic resonance imaging scanner on implanted permanent pacemakers. J Am Coll Cardiol. 1987;10(4):782–6.
62. Smith JM. Industry viewpoint: Guidant: pacemakers, ICDs, and MRI. Pacing Clin Electrophysiol. 2005;28(4):264.
63. Stanton MS. Industry viewpoint: medtronic: pacemakers, ICDs, and MRI. Pacing Clin Electrophysiol. 2005;28(4):265.
64. Levine PA. Industry viewpoint: St. Jude medical: pacemakers, ICDs and MRI. Pacing Clin Electrophysiol. 2005;28(4):266–7.
65. Shellock FG, Crues JV. MR procedures: biologic effects, safety, and patient care 1. Radiology. 2004;232(3):635–52.
66. Faris OP, Shein MJ. Government viewpoint: US food & drug administration: pacemakers, ICDs and MRI. Pacing Clin Electrophysiol. 2005;28(4):268–9.
67. Gimbel J, Johnson D, Levine PA, Wilkoff BL. Safe performance of magnetic resonance imaging on five patients with permanent cardiac pacemakers. Pacing Clin Electrophysiol. 1996;19(6):913–9.
68. Sommer T, Vahlhaus C, Lauck G, et al. MR imaging and cardiac pacemakers: in vitro evaluation and in vivo studies in 51 patients at 0.5 T 1. Radiology. 2000;215(3):869–79.
69. Vahlhaus C, Sommer T, Lewalter T, et al. Interference with cardiac pacemakers by magnetic resonance imaging: are there irreversible changes at 0.5 Tesla? Pacing Clin Electrophysiol. 2001;24(4):489–95.
70. Martin ET, Coman JA, Shellock FG, Pulling CC, Fair R, Jenkins K. Magnetic resonance imaging and cardiac pacemaker safety at 1.5-Tesla. J Am Coll Cardiol. 2004;43(7):1315–24.
71. Del Ojo J, Moya F, Villalba J, et al. Is magnetic resonance imaging safe in cardiac pacemaker recipients? Pacing Clin Electrophysiol. 2005;28(4):274–8.
72. Gimbel J, Kanal E, Schwartz KM, Wilkoff BL. Outcome of magnetic resonance imaging (MRI) in selected patients with implantable cardioverter defibrillators (ICDs). Pacing Clin Electrophysiol. 2005;28(4):270–3.
73. Brignole M, Auricchio A, Baron-Esquivias G, et al. ESC guidelines on cardiac pacing and cardiac resynchronization therapy. Eur Heart J. 2013;2013:eht150.
74. Nazarian S, Roguin A, Zviman MM, et al. Clinical utility and safety of a protocol for noncardiac and cardiac magnetic resonance imaging of patients with permanent pacemakers and implantable-cardioverter defibrillators at 1.5 tesla. Circulation. 2006;114(12):1277–84.
75. Baker KB, Tkach JA, Nyenhuis JA, et al. Evaluation of specific absorption rate as a dosimeter of MRI-related implant heating. J Magn Reson Imaging. 2004;20(2):315–20.
76. Gimbel J. Magnetic resonance imaging of implantable cardiac rhythm devices at 3.0 tesla. Pacing Clin Electrophysiol. 2008;31(7):795–801.
77. Mollerus M, Albin G, Lipinski M, Lucca J. Ectopy in patients with permanent pacemakers and implantable cardioverter-defibrillators undergoing an MRI scan. Pacing Clin Electrophysiol. 2009;32(6):772–8.
78. Rezai AR, Phillips M, Baker KB, et al. Neurostimulation system used for deep brain stimulation (DBS): MR safety issues and implications of failing to follow safety recommendations. Investig Radiol. 2004;39(5):300–3.
79. Finelli DA, Rezai AR, Ruggieri PM, et al. MR imaging-related heating of deep brain stimulation electrodes: in vitro study. Am J Neuroradiol. 2002;23(10):1795–802.
80. Bhidayasiri R, Bronstein JM, Sinha S, et al. Bilateral neurostimulation systems used for deep brain stimulation: in vitro study of MRI-related heating at 1.5 T and implications for clinical imaging of the brain. Magn Reson Imaging. 2005;23(4):549–55.
81. Baker KB, Nyenhuis JA, Hrdlicka G, Rezai AR, Tkach JA, Shellock FG. Neurostimulation systems: assessment of magnetic field interactions associated with 1.5-and 3-Tesla MR systems. J Magn Reson Imaging. 2005;21(1):72–7.
82. Fraix V, Chabardes S, Krainik A, et al. Effects of magnetic resonance imaging in patients with implanted deep brain stimulation systems: clinical article. J Neurosurg. 2010;113(6):1242–5.
83. Foltynie T, Zrinzo L, Martinez-Torres I, et al. MRI-guided STN DBS in Parkinson's disease without microelectrode recording: efficacy and safety. J Neurol Neurosurg Psychiatry. 2011;82(4):358–63.
84. Henderson JM, Tkach J, Phillips M, Baker K, Shellock FG, Rezai AR. Permanent neurological deficit related to magnetic resonance imaging in a patient with implanted deep brain stimulation electrodes for Parkinson's disease: case report. Neurosurgery. 2005;57(5):E1063.
85. Rezai AR, Baker KB, Tkach JA, et al. Is magnetic resonance imaging safe for patients with neurostimulation systems used for deep brain stimulation? Neurosurgery. 2005;57(5):1056–62.
86. Azevedo CF, Amado LC, Kraitchman DL, et al. The effect of intra-aortic balloon counterpulsation on left ventricular functional recovery early after acute myocardial infarction: a randomized experimental magnetic resonance imaging study. Eur Heart J. 2005;26(12):1235–41.
87. Kumar R, Lerski RA, Gandy S, Clift BA, Abboud RJ. Safety of orthopedic implants in magnetic resonance imaging: an experimental verification. J Orthop Res. 2006;24(9):1799–802.
88. Liu Y, Chen J, Shellock FG, Kainz W. Computational and experimental studies of an orthopedic implant: MRI-related heating at 1.5-T/64-MHz and 3-T/128-MHz. J Magn Reson Imaging. 2013;37(2):491–7.
89. Bernstein MA, Huston J, Ward HA. Imaging artifacts at 3.0 T. J Magn Reson Imaging. 2006;24(4):735–46.
90. Weinmann HJ, Laniado M, Mützel W. Pharmacokinetics of GdDTPA/dimeglumine after intravenous injection into healthy volunteers. Physiol Chem Phys Med NMR. 1983;16(2):167–72.

91. Van Wagoner M, Worah D. Gadodiamide injection: first human experience with the nonionic magnetic resonance imaging enhancement agent. Investig Radiol. 1993;28:S44–8.
92. McLachlan SJ, Eaton S, De Simone DN. Pharmacokinetic behavior of gadoteridol injection. Investig Radiol. 1992;27:S16.
93. Tombach B, Bremer C, Reimer P, et al. Pharmacokinetics of 1M gadobutrol in patients with chronic renal failure. Investig Radiol. 2000;35(1):35.
94. Baker JF, Kratz LC, Stevens GR, Wible JH Jr. Pharmacokinetics and safety of the MRI contrast agent gadoversetamide injection (OptiMARK) in healthy pediatric subjects. Investig Radiol. 2004;39(6):334–9.
95. Pascolo L, Cupelli F, Anelli PL, et al. Molecular mechanisms for the hepatic uptake of magnetic resonance imaging contrast agents. Biochem Biophys Res Commun. 1999;257(3):746–52.
96. McMurry TJ, Parmelee DJ, Sajiki H, et al. The effect of a phosphodiester linking group on albumin binding, blood half-life, and relaxivity of intravascular diethylenetriaminepentaacetato aquo gadolinium (III) MRI contrast agents. J Med Chem. 2002;45(16):3465–74.
97. Levey AS, Eckardt K-U, Tsukamoto Y, et al. Definition and classification of chronic kidney disease: a position statement from kidney disease: improving global outcomes (KDIGO). Kidney Int. 2005;67(6):2089–100.
98. Rai AT, Hogg JP. Persistence of gadolinium in CSF: a diagnostic pitfall in patients with end-stage renal disease. Am J Neuroradiol. 2001;22(7):1357–61.
99. Morris JM, Miller GM. Increased signal in the subarachnoid space on fluid-attenuated inversion recovery imaging associated with the clearance dynamics of gadolinium chelate: a potential diagnostic pitfall. Am J Neuroradiol. 2007;28(10):1964–7.
100. Choyke PL, Cady J, DePollar SL, Austin H. Determination of serum creatinine prior to iodinated contrast media: is it necessary in all patients? Tech Urol. 1998;4(2):65–9.
101. Sena BF, Stern JP, Pandharipande PV, et al. Screening patients to assess renal function before administering gadolinium chelates: assessment of the Choyke questionnaire. Am J Roentgenol. 2010;195(2):424–8.
102. Murphy KPJ, Szopinski KT, Cohan RH, Mermillod B, Ellis JH. Occurrence of adverse reactions to gadolinium-based contrast material and management of patients at increased risk: a survey of the American Society of Neuroradiology Fellowship Directors. Acad Radiol. 1999;6(11):656–64.
103. Prince MR, Zhang H, Zou Z, Staron RB, Brill PW. Incidence of immediate gadolinium contrast media reactions. Am J Roentgenol. 2011;196(2):W138–43.
104. Jung J-W, Kang H-R, Kim M-H, et al. Immediate hypersensitivity reaction to gadolinium-based MR contrast media. Radiology. 2012;264(2):414–22.
105. Cowper SE, Robin HS, Steinberg SM, Su LD, Gupta S, LeBoit PE. Scleromyxoedema-like cutaneous diseases in renal-dialysis patients. Lancet. 2000;356(9234):1000–1.
106. Grobner T. Gadolinium–a specific trigger for the development of nephrogenic fibrosing dermopathy and nephrogenic systemic fibrosis? Nephrol Dial Transplant. 2006;21(4):1104–8.
107. Morcos SK. Experimental studies investigating the pathophysiology of nephrogenic systemic fibrosis; what did we learn so far? Eur Radiol. 2011;21(3):496–500.
108. Frenzel T, Lengsfeld P, Schirmer H, Hütter J, Weinmann H-J. Stability of gadolinium-based magnetic resonance imaging contrast agents in human serum at 37 C. Investig Radiol. 2008;43(12):817–28.
109. Martin DR, Krishnamoorthy SK, Kalb B, et al. Decreased incidence of NSF in patients on dialysis after changing gadolinium contrast-enhanced MRI protocols. J Magn Reson Imaging. 2010;31(2):440–6.
110. Kuo PH. Gadolinium-containing MRI contrast agents: important variations on a theme for NSF. J Am Coll Radiol. 2008;5(1):29–35.
111. American College of Radiology (ACR) Website. ACR manual on contrast media, version 10.1. http://www.acr.org/~/media/ACR/Documents/PDF/QualitySafety/Resources/ContrastManual/2015_Contrast_Media.pdf. Accessed 16 Mar 2016.
112. Thomsen HS, Morcos SK, Almén T, et al. Nephrogenic systemic fibrosis and gadolinium-based contrast media: updated ESUR contrast medium safety committee guidelines. Eur Radiol. 2013;23(2):307–18.
113. Tran KT, Prather HB, Cockerell CJ, Jacobe H. UV-A1 therapy for nephrogenic systemic fibrosis. Arch Dermatol. 2009;145(10):1170–4.
114. Elmholdt TR, Buus NH, Ramsing M, Olesen AB. Antifibrotic effect after low-dose imatinib mesylate treatment in patients with nephrogenic systemic fibrosis: an open-label non-randomized, uncontrolled clinical trial. J Eur Acad Dermatology Venereol. 2013;27(6):779–84.
115. Ross C, De Rosa N, Marshman G, Astill D. Nephrogenic systemic fibrosis in a gadolinium-naïve patient: successful treatment with oral sirolimus. Australas J Dermatol. 2015;56(3):e59–62.
116. Mathur K, Morris S, Deighan C, Green R, Douglas KW. Extracorporeal photopheresis improves nephrogenic fibrosing dermopathy/nephrogenic systemic fibrosis: three case reports and review of literature. J Clin Apher. 2008;23(4):144–50.
117. Panesar M, Banerjee S, Barone GW. Clinical improvement of nephrogenic systemic fibrosis after kidney transplantation. Clin Transpl. 2008;22(6):803–8.
118. Nacif MS, Arai AE, Lima JA, Bluemke DA. Gadolinium-enhanced cardiovascular magnetic resonance: administered dose in relationship to United States Food and Drug Administration (FDA) guidelines. J Cardiovasc Magn Reson. 2012;14:18.
119. Kanda T, Ishii K, Kawaguchi H, Kitajima K, Takenaka D. High signal intensity in the dentate nucleus and globus pallidus on unenhanced T1-weighted MR images: relationship with increasing cumulative dose of a gadolinium-based contrast material. Radiology. 2013;270(3):834–41.
120. Kanda T, Fukusato T, Matsuda M, et al. Gadolinium-based contrast agent accumulates in the brain even in subjects without severe renal dysfunction: evaluation of autopsy brain specimens with inductively coupled plasma mass spectroscopy. Radiology. 2015;276(1):228–32.
121. McDonald RJ, McDonald JS, Kallmes DF, et al. Intracranial gadolinium deposition after contrast-enhanced MR imaging. Radiology. 2015;275(3):772–82.
122. Malayeri AA, Brooks KM, Bryant LH, et al. National Institutes of Health perspective on reports of gadolinium deposition in the brain. J Am Coll Radiol. 2016;13:237.
123. Kanal E, Barkovich AJ, Bell C, et al. ACR guidance document on MR safe practices: 2013. J Magn Reson Imaging. 2013;37(3):501–30.
124. Saito K, Suzuki H, Suzuki K. Teratogenic effects of static magnetic field on mouse fetuses. Reprod Toxicol. 2006;22(1):118–24.
125. Marcos HB, Semelka RC, Worawattanakul S. Normal placenta: gadolinium-enhanced dynamic MR imaging. Radiology. 1997;205(2):493–6.
126. Shoenut JP, Semelka RC, Silverman R, Yaffe CS, Micflikier AB. MRI in the diagnosis of Crohn's disease in two pregnant women. J Clin Gastroenterol. 1993;17(3):244–7.
127. Oh KY, Roberts VHJ, Schabel MC, Grove KL, Woods M, Frias AE. Gadolinium chelate contrast material in pregnancy: fetal biodistribution in the nonhuman primate. Radiology. 2015;276(1):110–8.
128. Wang PI, Chong ST, Kielar AZ, et al. Imaging of pregnant and lactating patients: part 1, evidence-based review and recommendations. Am J Roentgenol. 2012;198(4):778–84.
129. Kubik-Huch RA, Gottstein-Aalame NM, Frenzel T, et al. Gadopentetate Dimeglumine excretion into human breast milk during lactation 1. Radiology. 2000;216(2):555–8.

Acute Myocardial Infarction and Postinfarction Remodeling

10

Christopher M. Kramer and Michael Salerno

Introduction

Cardiac magnetic resonance (CMR) is ideally suited to evaluate the consequences of myocardial ischemia and infarction (MI) because of its excellent spatial resolution and ability to characterize tissue. With the advent of surface coils and segmented k-space cine imaging in the early 1990s enabling imaging in a breath-hold, CMR became practical in patients with acute coronary syndromes (ACS) including MI. Initial studies in acute MI involved imaging of myocardial function, infarct artery patency, and first-pass myocardial perfusion imaging [1]. It was noted that in some infarcts, areas of microvascular obstruction could be visualized which denoted worse outcome for those patients [2]. At the turn of the millennium, the development of an inversion recovery gradient echo pulse sequence [3] allowed excellent nulling of normal myocardial signal, and thus late gadolinium enhancement became a gold standard method of imaging and sizing of infarction and assessing viability [4]. After 2005 or so, T2-weighted (W) imaging of myocardial edema came to the fore as a means to assess the area at risk [5]. T2*-W imaging was later noted to optimally delineate intramyocardial hemorrhage [6]. More lately, T1- and T2-mapping techniques have begun to replace qualitative imaging of infarct size and area at risk [7]. Many of these findings can aid in the prediction of subsequent LV dilation and dysfunction, termed LV remodeling. CMR can identify post-MI complications including myocardial rupture, ventricular septal defects, papillary muscle rupture, and pericarditis. Putting all of these techniques together has advanced the field and has allowed CMR to develop into a comprehensive imaging method for assessing the myocardium in the patient with acute MI.

C. M. Kramer (✉)
Departments of Radiology and Medicine, University of Virginia Health System, Charlottesville, VA, USA
e-mail: ckramer@virginia.edu

M. Salerno
Departments of Medicine, Radiology, and Biomedical Engineering, University of Virginia Health System, Charlottesville, VA, USA

Guideline Indication for CMR in Acute MI

A recent consensus statement examined the role of CMR in a number of cardiac conditions including acute MI [8]. This document reviewed the use of LGE, the identification of MO, and the identification of border zones around the acute infarct. The ACC/AHA 2005 Guideline Update for heart failure identified the use of LGE to identify myocardial scar and assess viability [9]. The Appropriateness Criteria for CMR identified the appropriate use of CMR for assessing patients post-MI including scar and MO and to assess the likelihood of recovery of function with revascularization [10]. Multimodality Appropriate Use Criteria are presently in development to identify the appropriate use of imaging modalities including CMR in acute coronary syndromes and after acute MI. As the use of CMR continues to expand, it is quite likely future guidelines will identify additional appropriate uses of this versatile technology.

CMR Techniques Used in Acute MI

Cine Imaging: LV Structure and Function

In the wake of an acute myocardial infarction (AMI), accurate assessment of the left ventricle (LV) is of paramount importance as functional impairment and/or chamber dilation predicts increased mortality. In a study of 866 post-infarct patients, a resting LV ejection fraction (EF) <40% predicted higher 1-year mortality than did an LVEF >40% [11]. Although LVEF is a powerful predictor of post-infarct survival, end-systolic volume (ESV) is superior as a prognostic parameter. This was demonstrated by White et al. who enrolled 605 patients following AMI and followed them for an average of 78 months. Ultimately, ESV was the best predictor of survival, and neither LVEF nor end-diastolic volume (EDV) added prognostic value [12].

R. Y. Kwong et al. (eds.), *Cardiovascular Magnetic Resonance Imaging*, Contemporary Cardiology,
https://doi.org/10.1007/978-1-4939-8841-9_10

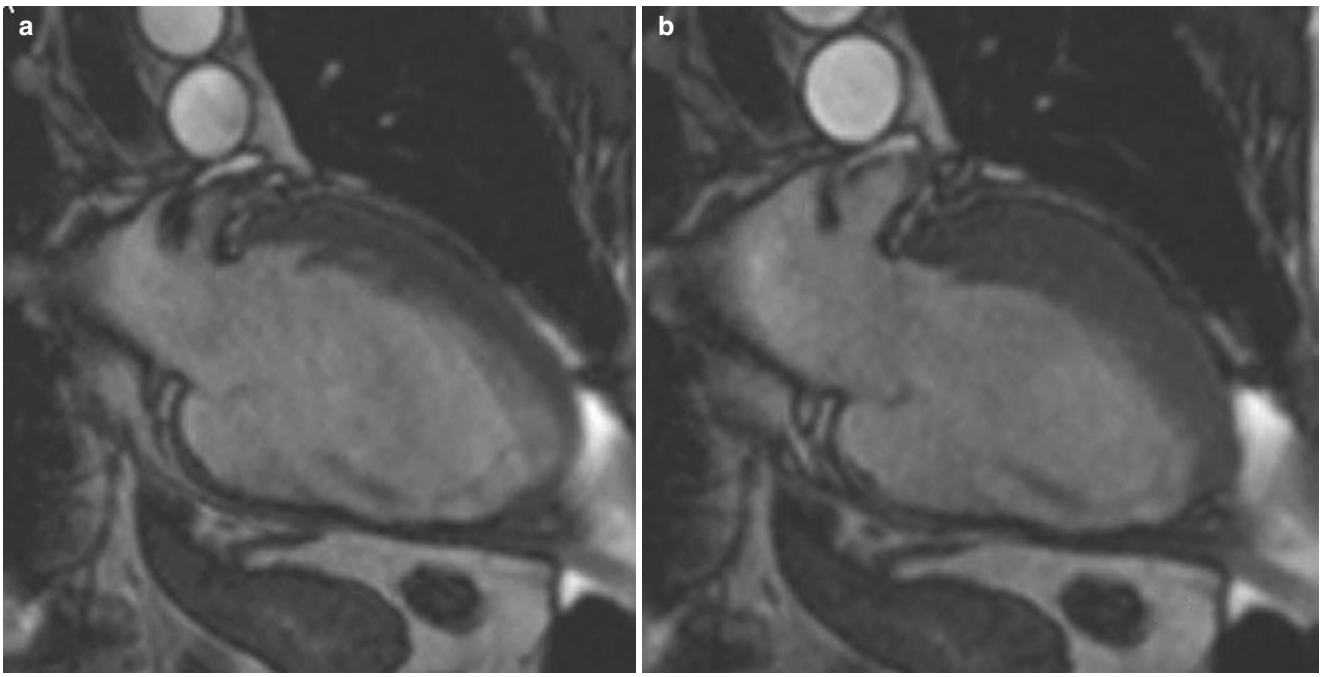

Fig. 10.1 (**a**) End-diastolic 2-chamber long-axis SSFP image in a patient with a chronic inferior wall MI with wall thinning. (**b**) End-systolic image from the same series demonstrating normal thickening of the anterior wall and akinesis of the inferior wall

Steady-state free precession cine CMR covering the LV short axis from apex to base allows generation of a complete three-dimensional data set with high temporal and spatial resolution (Fig. 10.1). Measurements made with this data set do not require geometric assumptions and are therefore less prone to error than 2D methods such as 2D echocardiography, particularly in ventricles deformed by MI. Furthermore, the large field of view and excellent contrast generated between the myocardium and blood pool facilitates accurate assessment of chamber dimensions and both regional and global function [13]. Interstudy and interscan reproducibility is high, allowing for reduced sample sizes in clinical trials examining interventions in post-MI patients [14, 15].

Techniques such as myocardial tissue tagging [16] or cine displacement-encoded stimulated echo imaging [17] allow more detailed analysis of regional myocardial motion and deformation than cine imaging. Such techniques have demonstrated dysfunction adjacent to [18] and remote from [19] the infarct zone early post-MI that gradually improves over time [18, 20]. Studies have used tagging to demonstrate persistent diastolic dysfunction in regions that have recovered systolic function after reperfused MI [21].

Late Gadolinium Enhancement

Histopathologic studies of AMI have consistently revealed the complex, heterogeneous, and *dynamic* character of infarct zones [22]. This heterogeneity is a consequence of many factors including the presence and opening of collaterals during and after injury, magnitude of the ischemic insult, and impact of therapeutic interventions [23]. Furthermore, it has been demonstrated that infarcts evolve over time, generally passing through an early, necrotic phase followed by both a fibrotic and remodeling phase that is dominated by the laying down of new collagen and infarct involution [24, 25]. In fact, infarct scar remains biologically active long after ischemic injury, populated by cells involved in collagen turnover and scar tissue contraction, and may therefore never truly reach a "stable" configuration [22].

Late gadolinium enhancement (LGE) refers to regions of scar, necrosis, and/or inflammation discriminated from normal tissue by prolonged retention of gadolinium-based contrast agents (Fig. 10.2). Since the mid-1980s, investigators have appreciated T1 shortening (increased enhancement) in regions of infarction following gadolinium administration [26–28]. However, these early imaging techniques were limited by long acquisition times, artifacts, and insufficient contrast between normal and abnormal regions. With faster imaging sequences using k-space segmentation, LGE can be performed in a single breath-hold with collection of data during the diastolic phase of the cardiac cycle when there is less cardiac motion. Implementation of an inversion recovery pulse sequence with inversion time set to null normal myocardium increases the signal difference between normal and infarcted segments by 500–1000% [3].

Using this approach, Kim et al. demonstrated that the spatial extent of LGE seen on CMR closely mirrored the

Fig. 10.2 4-chamber long-axis phase-sensitive inversion recovery image obtained 15 min after gadolinium administration in a patient with a prior anterior MI. Note the 75% transmural LGE in the apical septum and apex

distribution of myocyte necrosis in the early period following infarction and that of collagenous scar seen at 8 weeks ($R = 0.97$, $P < 0.001$) [4], while in regions of the heart subjected to *reversible* injury, the retention of contrast did *not* occur [29]. LGE accurately delineates infarction as defined by histology at various time points following injury [30]. When compared to other noninvasive techniques, LGE is more reliable in detecting infarct scar. In a study of 91 patients with suspected or known CAD, Wagner et al. performed both LGE and SPECT imaging to evaluate the location, extent, and size of infarction [31]. Although SPECT correctly identified all patients with transmural or near-transmural scar seen on LGE, SPECT failed to correctly identify nearly half of those with subendocardial infarction. SPECT is less sensitive to smaller, non-Q wave, primarily inferior infarcts [32]. Klein et al. compared LGE to PET in 31 patients with ischemic heart failure [33]. Infarct mass correlated well between the two modalities ($r = 0.81$, $p < 0.0001$), but LGE more frequently identified scar than PET, again reflecting the superior spatial resolution of CMR.

Transmural extent of infarct scar, as determined by LGE, is a powerful predictor of functional recovery following acute MI. Choi et al. performed LGE-CMR on 24 patients within 7 days of successful revascularization post-MI [34]. Scans were repeated at 8–12 weeks to assess functional recovery. There was an inverse relationship between transmural extent of infarction and segmental recovery of function ($p = 0.001$). Moreover, the best predictor of improved wall thickening and global function was the extent of dysfunctional myocardium that was either without LGE or had <25% transmural LGE.

Investigators have exploited the enhanced sensitivity of CMR to study small infarctions after both percutaneous intervention [35, 36] and coronary artery bypass surgery [37]. Ricciardi et al. utilized LGE to demonstrate the etiology of CK-MB release following successful elective percutaneous coronary intervention (PCI) [36]. Fourteen patients without evidence of prior MI were imaged following elective PCI. Nine experienced elevation of cardiac enzymes following the procedure while five did not. In all patients with an enzyme leak (median CK-MB was 21 ng/mL), a discrete area of LGE was seen in the target vessel zone indicating periprocedural MI. This LGE persisted in all but one of the patients at follow-up scan 3–12 months later, while LGE was not detected in any control patient.

It should be noted that infarct size is dynamic. Measurement of infarct size histologically or with LGE demonstrates a peak in infarct size within the first few days after MI, followed by a gradual decline until 4–6 weeks after the event, after which infarct size is generally stable [38]. Infarct size in a representative canine MI study was 41% of LV size at 4 days but only 11% of LV size at 28 days. Histological examination revealed a 25% increase in water content within the acute infarct at 4 days, with dense scarring and decreased water content after 28 days [23]. In humans, infarct size has been shown to decrease by 25–30% over the first 8–12 weeks post-MI as evidenced by the decline in size of late gadolinium enhancement [39–42]. Early on after MI, the increase in infarct size is likely due to an increase in interstitial edema and necrotic cellular debris, whereas chronic infarcts are characterized by dense scarring with an increase in collagen deposition and loss of cellular structure and edema. In both acute and chronic infarcts, there is an increase in extracellular space, which causes an increased volume of distribution for gadolinium and thus increased signal intensity.

Recent evidence suggests LGE may be a valuable tool for predicting major adverse cardiac events (MACE). In a study by Kwong et al., 195 patients were evaluated for LGE as part of an assessment for CAD [43]. After 16 months of follow-up, LGE was found to be the strongest predictor of MACE (hazard ratio (HR) 8.3) and cardiac mortality (HR 10.9), even after adjustment for other clinical variable. This was true even for those patients with smaller regions of LGE (lowest tertile), as they had a sevenfold increase in MACE. Another study of 857 patients followed for 4.4 years showed that the scar index as defined by LGE predicted a composite endpoint of all-cause mortality or cardiac transplantation (HR 1.26) [44]. Those with LGE showed worse outcome over time, similarly to those with reduced LV function. A study of 349 patients with ischemic cardiomyopathy

followed for 2.6 years demonstrated that quantified scar burden above the median predicted events (51 deaths and 5 transplants) with a relative risk of 1.75 [45].

Microvascular Obstruction

In the acute phase of infarction, typically at the subendocardial core, there is often microvascular obstruction (MO). MO may result from microembolization and platelet activation as well as capillary bed compression due to edema, although the exact mechanisms are unclear [46]. These events may be exacerbated by reperfusion itself. These areas are generally devoid of blood flow and have also been described as "no-reflow zones" with the extent of no-reflow related to total infarct size [47]. The region surrounding areas of no-reflow is often comprised of myocytes subjected to significant, but varying, degrees of ischemic injury. Many undergo necrosis with loss of membrane integrity and depletion of cellular energy stores [48]. In this acute phase, tissue edema, hemorrhage, and inflammation can increase infarct volume by as much as 25% [23].

The time course of MO is an important factor in understanding of the acuity of MI. Several studies have shown that the extent of MO usually peaks from 2 h to 2 days after reperfusion occurs [49–51], after which it tends to be stable in size until at least day 9 [52]. Thereafter areas of MO involute and regress and are rarely seen on follow-up CMR beyond 1–2 months after MI. Because of the timing of MO, techniques performed at the time of intervention are likely to underestimate the final extent of MO. CMR thus offers a potential advantage in that it can measure MO up to 7–10 days after infarction with good spatial resolution and without dependence on acoustic windows.

MO can be assessed by CMR using two separate techniques. Early MO is visualized early after first-pass perfusion. Typical protocols using this method define MO as hypoenhancement within the first 2–5 min after contrast injection either on first-pass perfusion imaging or on inversion recovery T1-W imaging. The second technique is LGE images 10–20 min after contrast injection and appears as an area or areas of hypoenhancement encompassed within the core of LGE, often extending from the subendocardium. This latter method is termed persistent or late MO (Fig. 10.3). The prevalence of early and late MO based on a systematic review was 65% and 54%, respectively [53]. Some of the variability between studies is due to differences in study populations, imaging methods, and timing of imaging.

There is still no consensus on whether early or late MO should be the preferred technique for evaluating MO. The spatial extent of early MO correlates well with histology and myocardial contrast echo [52]. A study of 17 patients on day 4 post-MI demonstrated that regions with early MO were nonviable as no recovery of function was noted at 7 weeks post-MI in these territories [54]. Early MO has been shown to be predictive of LV function and remodeling at 1-year follow-up and was a better marker of 1-year infarct size than late MO [55]. However, both early and late MO are also associated with more shrinkage of infarct size at long-term follow-up compared to those patients without MO [42].

Fig. 10.3 Short-axis phase-sensitive inversion recovery image obtained 15 min after gadolinium administration in a patient with a recent anteroseptal MI. Within the 100% transmural LGE in the anteroseptum, an area of MO is clearly seen

Wu et al. found that early MO predicts infarct transmurality, LV function, and remodeling after 16 months and was also a powerful independent prognostic indicator of hard cardiac events even after controlling for infarct size [2]. In a study of 60 MI patients undergoing CMR at 5 days and 4 months, both early and late MO correlated with poor ST-segment resolution; however, neither method correlated well with angiographic parameters of TIMI flow grade or angiographic blush grade [56]. Late MO does, however, correlate with invasive coronary flow velocity measures of microvascular obstruction [57]. However, a meta-analysis suggested that early MO only shows a trend toward prediction of cardiac mortality, recurrent MI, and heart failure hospitalization [53].

Late MO predicts follow-up LV function and remodeling better than early MO and lends additional prognostic information beyond that of infarct size or transmurality. In a study by Nijveldt et al., 63 acute MI patients who received PCI and optimal medical management were assessed for early, mid-, and late MO 4–7 days after MI and followed up with CMR at 4 months. They found that late MO was a better predictor of follow-up LV ejection fraction, LV end-diastolic volume, and LV end-systolic volume than early MO [58]. In a study of 110 MI patients, Hombach et al. found that late MO independently portended an increase in cardiac events at 8-month follow-up

and gave additional prognostic information over and above infarct size alone [59]. This was corroborated in a study by Bruder et al. of 67 STEMI patients followed for 14 months which showed that late MO was a better predictor of adverse cardiac events than infarct size or baseline ejection fraction. The meta-analysis mentioned above has demonstrated that late MO has a strong relationship with both LV remodeling and major cardiac adverse events including cardiac death, recurrent MI, and heart failure hospitalization [53]. A study by Cochet et al. that directly compared the 2 methods in 187 patients showed that late MO had a hazard ratio over 3x that of early MO for prediction of MACE [60].

Recent larger clinical studies underscore the prognostic importance of MO. A multicenter study of 738 STEMI patients demonstrated that independent predictors of MACE included MO and TIMI risk score [61]. Both MO and infarct size improved prognostication over and above clinical risk and LVEF with an increase in the C-statistic from 0.76 to 0.80, $p < 0.04$.

A pooled analysis of 1025 patients with STEMI followed for 2 years showed that MO was an independent predictor of MACE with a HR of 3.74, whereas infarct size was not [62].

T2-Weighted Imaging

An understanding of the time course of edema after cardiac injury is a major key to the accurate interpretation of T2-W imaging (Fig. 10.4). Abdel-Aty et al. noted in a canine model of myocardial infarction that the onset of edema on CMR first became apparent 28 ± 4 min after experimental coronary artery occlusion and well before the appearance of LGE or troponin elevation, signifying that CMR can visualize edema before the onset of irreversible myocardial injury [63]. Microsphere analysis in a canine model of reperfused acute MI suggested that T2-W imaging performed 2 days post-MI can be used to delineate the area at risk (AAR) [64].

The persistence of increased T2 signal post-MI has been variable across studies. A study of ten patients with transmural ST-elevation MI found that myocardial T2 signal persisted a median of 6 months after the event, with three of the ten cases persisting out to 1 year, although even in these cases, the extent and intensity of the T2 signal diminished over time [65]. Larger studies have shown that increased myocardial T2 signal after an ischemic event gradually dissipates over 1–3 months [5]. In the first 2–4 weeks after MI, the edematous area at risk of patients or experimental animals, as determined by T2-W CMR or histology, is nearly always transmural [66, 67]; however, multiple studies have noted that T2 signal resolves early on in the epicardium, whereas persistent T2 signal, if present, is often limited to the endocardial surface and may represent changes in myocardial structure from the infarct itself [5, 65].

When used in conjunction with late gadolinium-enhanced CMR, T2-W imaging confers the ability to differentiate acute from chronic infarcts. This was demonstrated in a study by Abdel-Aty et al. [5] who used LGE and T2-W CMR to evaluate 58 patients with either acute or chronic infarction.

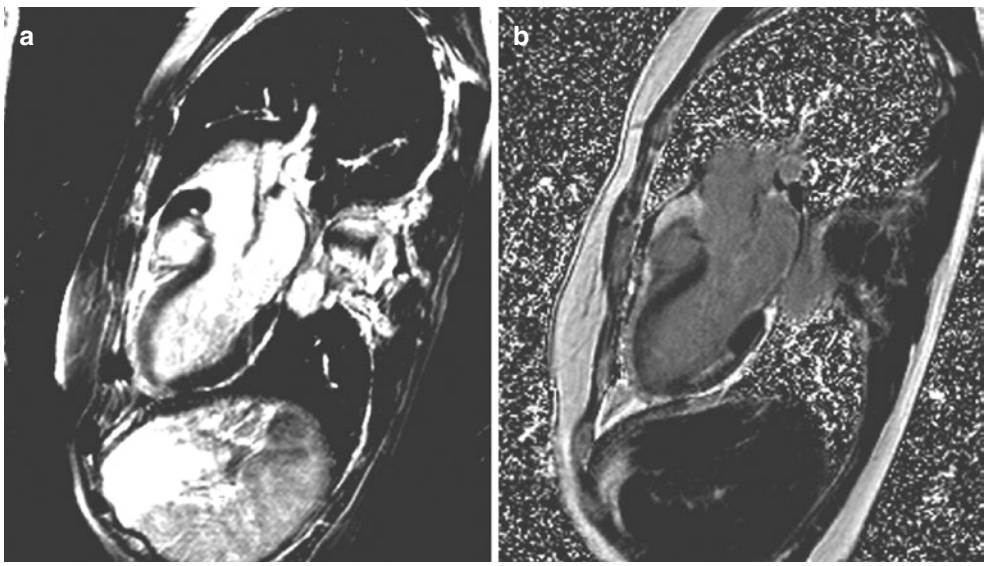

Fig. 10.4 (**a**) 3-chamber long-axis hybrid turbo spin echo-SSFP bright-blood T2-W image demonstrating anteroapical high signal intensity consistent with edema in a patient with chest pain, elevated troponins, and transiently occluded LAD from a coronary artery dissection. (**b**) 3-chamber long-axis phase-sensitive inversion recovery image obtained 15 min after gadolinium administration in the same patient demonstrating absent LGE in the anteroapex but evidence of a prior 50% transmural inferior MI. The patient subsequently demonstrated complete recovery of function in the anteroapex

Blinded observers were able to differentiate acute from chronic infarction with specificity between 92% and 100% and sensitivity between 91% and 94%, depending on the observer.

There are several potential limitations of traditional T2-W imaging [68]. These limitations cause some investigators to urge against using T2-W imaging as a surrogate for area at risk [69]. Firstly, the T2-W signal intensity is dependent on proximity to the phased array coil. This leads to a propensity to overestimate edema in myocardium close to the chest wall due to its brighter signal and to underappreciate the T2-W signal from more distant structures. Another potential shortcoming with currently employed dark blood T2-W sequences is that slow-flowing blood appears bright, making it difficult at times to discern between a true increase in subendocardial T2 signal and blood pool artifact. Bright-blood approaches have been used, and some studies suggest improved accuracy for identifying the culprit coronary artery as well as AAR [70]. Finally, T2-W imaging tends to be sensitive to motion. Experimental protocols have used T2 mapping to overcome these limitations [68] and have been applied successfully in animal models [71].

The ability for T2-W imaging to determine the area at risk (AAR) and LGE to identify necrotic regions enables the calculation of the difference as the area of salvaged myocardium after reperfusion. Validation studies have been performed in canine models to demonstrate the ability of T2 mapping to delineate the AAR as defined by microspheres [72]. This concept has now been applied to clinical studies of acute MI. A study of 50 consecutive patients demonstrated a strong relationship of the MR assessment of AAR using a T2-prepared SSFP sequence and angiographic measures of myocardial salvage [73]. Eitel et al. studied 208 patients with acute STEMI who underwent primary PCI and used CMR with T2-W imaging and LGE to calculate myocardial salvage [74]. They showed that patients with myocardial salvage index below the median had a higher MACE rate (22.1%) over 6-month follow-up than those with an index ≥ the median (2.9%). In fact, myocardial salvage index was the strongest predictor of MACE, outperforming MO and infarct size. When follow-up of these same patients was continued over 18 months, mortality was shown to be significantly reduced in the group with salvage less than the median (2 vs. 12 deaths, $p < 0.001$) [75].

Native T1 and Post-Contrast T1 Mapping

T1 in the myocardium can be measured by mapping with a modified Look-Locker inversion (MOLLI) recovery sequence. So-called native T1 can be measured before contrast infusion (Fig. 10.5), and then post-contrast T1 measures can be used to calculate extracellular volume fraction in the myocardium. The first application of T1 mapping in 24 patients with MI demonstrated that native T1 maps detected areas of regional wall motion abnormalities with high accuracy [76]. The agreement between T1 maps and LGE was higher in chronic than acute MI. This finding was validated in a canine model that showed that T1 maps overestimated infarct size in acute MI but not in chronic MI [7]. T1 mapping has been demonstrated to be equivalent to T2-W imaging for detecting myocardial injury in patients with ST-elevation MI and superior to T2-W imaging for non-ST-elevation MI [77]. In the latter study, the higher the native T1 values, the lower the likelihood of functional recovery at 6 months post-MI. A study of post-contrast T1 times in

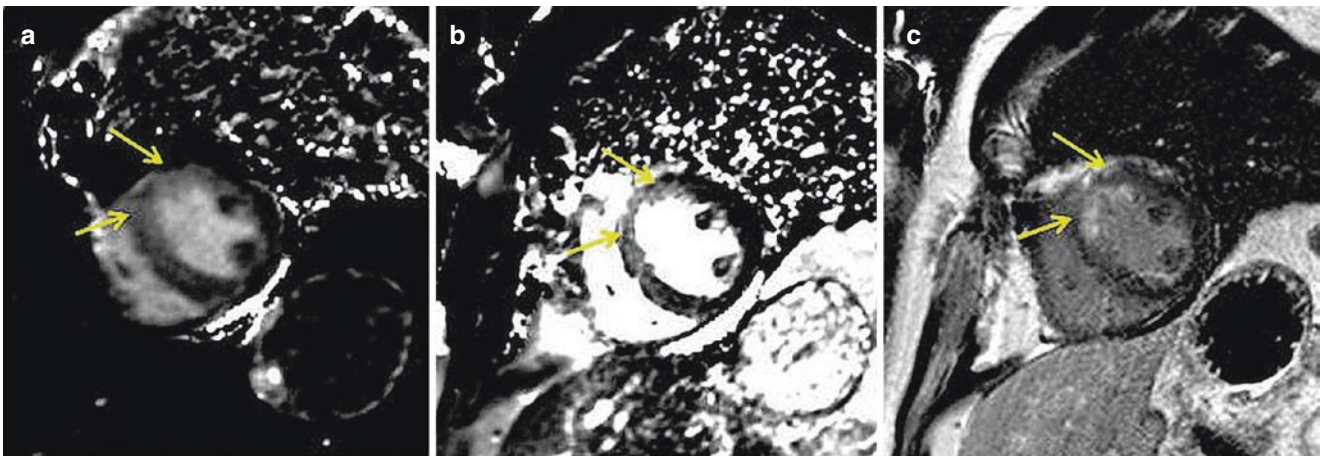

Fig. 10.5 (**a**) Short-axis native (pre-contrast) T1 map from a MOLLI acquisition in a patient after reperfused anterior MI. Note the transmural high T1 signal in the anteroseptum. (**b**) Corresponding short-axis T2-prep-based T2 map in the same patient showing transmural high T2 signal in the same region. Both the T1 and T2 maps demonstrate the area at risk. (**c**) LGE image in the same patient demonstrates 50% transmural enhancement, significantly smaller than the area at risk demonstrated on the T1 and T2 maps

patients with acute MI showed lower post-contrast T1 times in remote noninfarcted regions associated with reductions in wall thickening compared to controls, suggesting a contribution to LV remodeling in those regions [78].

T2*-W Imaging and Intramyocardial Hemorrhage

Intramyocardial hemorrhage (IMH) often follows MO development in the core of an infarct with a tendency to expand for several hours post-reperfusion (Fig. 10.6). It is caused by vascular endothelial damage and accumulation of red blood cells in the myocardial extracellular space [48]. It is unclear whether IMH is the cause or result of severe ischemia-reperfusion injury [79]. A high correlation between infarct size (IS) and IMH has been identified on histopathologic studies [48]. In most studies IMH is identified only in the presence of MO. The correlation (r^2) of IMH has been reported to be 0.55 with early MO and between 0.8 and 0.95 for late MO [80–82].

IMH can confound the assessment of myocardial edema and AAR as it causes a change in the T2 signal. Hemorrhage can have variable effects on the MR signal depending upon the acuity of the event, but within the first week following MI, the paramagnetic effect of iron in deoxyhemoglobin usually predominates. This causes a decrease in both T2 and T2*, resulting in signal loss and potential underestimation of the AAR. A CMR study of 70 STEMI patients demonstrated that significant T2-W signal dropout within the infarct core was sufficient to impair threshold-based assessment of the area at risk in 11% [83]. Thus, boundary detection methods for quantitative assessment of edema are probably more accurate than thresholding methods in this setting.

Most studies have used T2-W short-tau inversion recovery (STIR) or T2*-W gradient echo pulse sequences [6] to assess for IMH. T2*-W imaging is felt to be more sensitive for detection of IMH but has lower signal to noise than T2-W images and is more sensitive to off-resonance artifacts. T2* values are lowest acutely in the IMH core but gradually normalize to that of the rest of the infarct at 4 weeks, due to extensive collagen deposition and absence of iron [84]. A recent study in 14 STEMI patients and in 20 canines with acute reperfused myocardial infarction suggests that T2* is more suitable than T2 imaging in the identification of IMH [85]. The T2* dropped on average 54% in hemorrhagic infarctions and was 6% higher in nonhemorrhagic infarctions as compared to remote myocardium. By comparison, T2 was increased by 17% in hemorrhagic infarcts and by 38% in nonhemorrhagic infarcts.

A meta-analysis including 9 studies and 1106 patients demonstrated that IMH is associated with increased infarct size, larger LV end-diastolic and end-systolic volumes, and reduced EF compared to those without IMH [53]. IMH was seen predominantly in anterior infarcts [86] and in infarcts involving >80% of LV thickness [87]. One study of 48 patients found an independent correlation of IMH with LV remodeling and a significant improvement of diagnostic area under the curve (from 0.699 to 0.826) by adding IMH to a multivariate model including LVEF and infarct size [88]. Three studies, using T2 STIR including a total of 991 patients with a follow-up of 6 months to 3 years, examined the impact of IMH on adverse cardiovascular outcomes [80, 89, 90]. The pooled univariate hazard ratio for IMH for predicting MACE was 3.88. One study that compared the graded impact of no MO, MO only, and MO with IMH on LV remodeling or MACE detected a strong incremental association [89]. Thus there is likely a spectrum between MO and MO with IMH, with the presence of IMH suggesting greater cellular damage resulting in greater adverse remodeling and poorer outcomes.

Assessment of the Infarct Border Zone

A number of studies have used different methodologies to identify the border zone of acute MI that is thought to be associated with higher risk of ventricular tachyarrhythmias and mortality. One study investigated patients with ischemic cardiomyopathies referred for implantable cardiac defibrillators

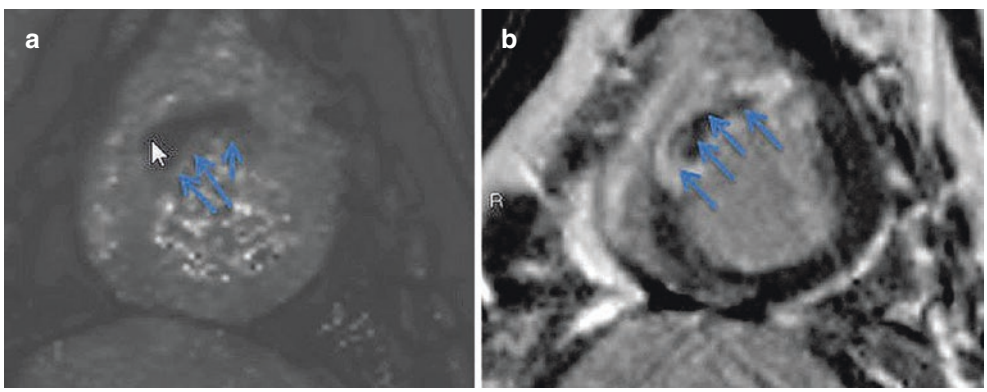

Fig. 10.6 (**a**) Short-axis T2*-weighted image from a porcine model of reperfused MI demonstrating intramyocardial hemorrhage in the anteroseptum. (**b**) Short-axis phase-sensitive inversion recovery LGE image in the same animal demonstrating transmural LGE with a midwall region of intramyocardial hemorrhage

(ICD) in order to determine if heterogeneity in peri-infarct regions can be established using contrast-enhanced CMR with the idea that adjacent areas of necrosis and viable myocardium could be fertile ground for reentrant arrhythmias [91]. The infarct core was defined as myocardium with signal intensity greater than 50% maximum. Tissue heterogeneity in the infarct periphery or "gray zone" was defined as having signal intensity greater than that of remote myocardium but less than 50% of the maximum. The region of intermediate late gadolinium enhancement, characterized as the "gray zone" at the periphery of myocardial scar, was related to inducibility of monomorphic ventricular tachycardia [91].

Yan et al. tested the hypothesis that the degree of gray zone measured by contrast-enhanced CMR would be an independent predictor of mortality post-MI [92]. In this study, the total infarct size was measured semiquantitatively and divided into the core region (>3 SD above normal remote myocardium) and the gray zone or peri-infarct regions (with signal intensity between 2 and 3 SD above normal myocardium). The peri-infarct zone was then normalized as a percentage of total infarct size. After adjusting for age and LVEF, the normalized peri-infarct zone was independently associated with all-cause and CV mortality (adjusted HR, 1.42 and 1.49, respectively).

Another study evaluated patients with ischemic cardiomyopathy referred for ICD by contrast-enhanced CMR to establish a relationship between extent of peri-infarct gray zone and spontaneous ventricular arrhythmia [93]. Roes et al. found the presence of peri-infarct tissue heterogeneity on contrast-enhanced MRI in patients with prior MI to be a stronger predictor of spontaneous ventricular arrhythmia and ICD therapy when compared to total infarct size and LV function. Thus, gray zone may ultimately be useful in choosing post-MI patients for ICD therapy.

There are several limitations of the "gray zone" approach. One is that there is significant concern in regard to difficulty measuring the gray zone in that it suffers from inadequate spatial resolution of LGE imaging and thus partial volume effects at the border of normal and infarcted myocardium [94]. In addition, there is as of yet no standardization between laboratories of methodologies used to measure the area of "gray zone." In fact, of the three manuscripts discussed above, each used a completely independent method to make this measurement. The assessment of "gray zone" will require standardization before it can move forward and be clinically useful.

Detection of Infarct Complications

Due to its high spatial resolution and ability to differentiate tissue types, CMR can readily detect ventricular wall pathology such as ventricular septal defects (Fig. 10.7), or free wall aneurysms, and can differentiate aneurysm from pseudoaneurysm (Fig. 10.8) [95], with its accompanying treatment implications. Right ventricular infarction is also very well visualized by LGE-CMR [96].

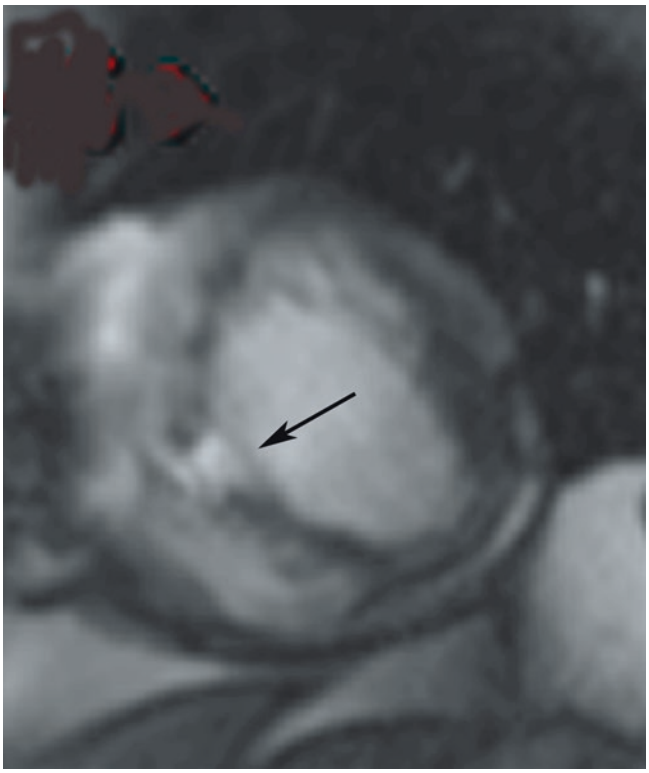

Fig. 10.7 Short-axis SSFP image at end diastole in a patient after non-reperfused anteroseptal MI demonstrating an apical VSD (black arrow)

Visualization of LGE within the papillary muscles is indicative of infarction and has been reported in post-MI CMR studies to occur in 26–53% of patients [59, 97]. In a study of 60 patients with old MI, bilateral papillary muscle infarction was seen by LGE in 17% of cases and was associated with a higher incidence of severe mitral regurgitation and LV remodeling than in those with unilateral or no papillary muscle infarction [97]. Mitral leaflet LGE has been seen more commonly in post-MI patients [98].

Inflammatory pericarditis is visualized by LGE of the pericardium with high sensitivity and specificity after MI [99] and has been reported to occur in as many as 40% of STEMI patients [59]. High T2-W signal can be visualized in inflammatory pericarditis [100], although this has not been studied specifically in post-MI patients.

The presence of intraventricular thrombi has been reported in 7–29% of patients with decreased ejection fraction, depending on the population studied [101, 102], and is associated with a higher risk of thromboembolic events, including stroke [101, 103]. The most prominent risk factors for the development of LV thrombus include anterior infarction (Fig. 10.9), infarct size, LV aneurysm, and decreased ejection fraction (≤40%) [102, 104]. Contrast-enhanced (LGE) CMR

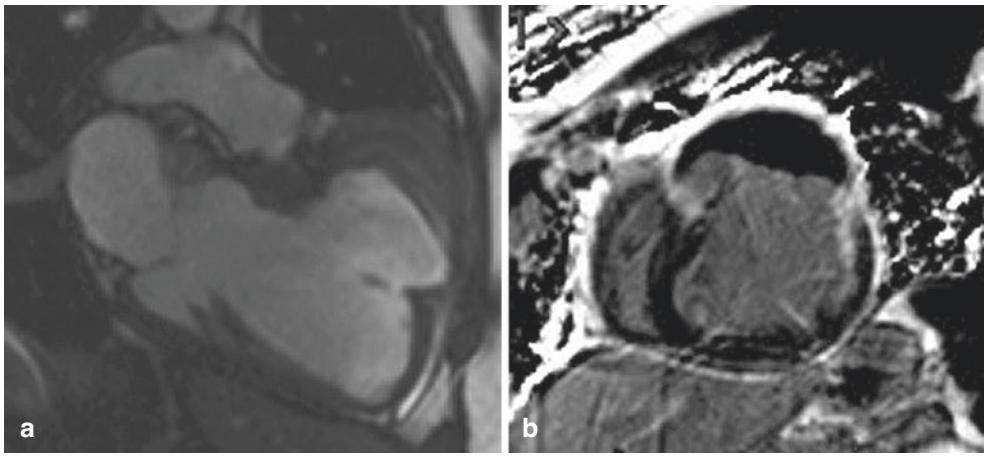

Fig. 10.8 (**a**) A 2-chamber long-axis SSFP cine image at end diastole in a patient 5 years after anterior MI demonstrating a chronic anterior pseudoaneurysm. (**b**) Short-axis phase-sensitive inversion recovery LGE image from the same patient demonstrating enhancement of the fibrous outer layer of the pseudoaneurysm which is lined with thrombus which appears black

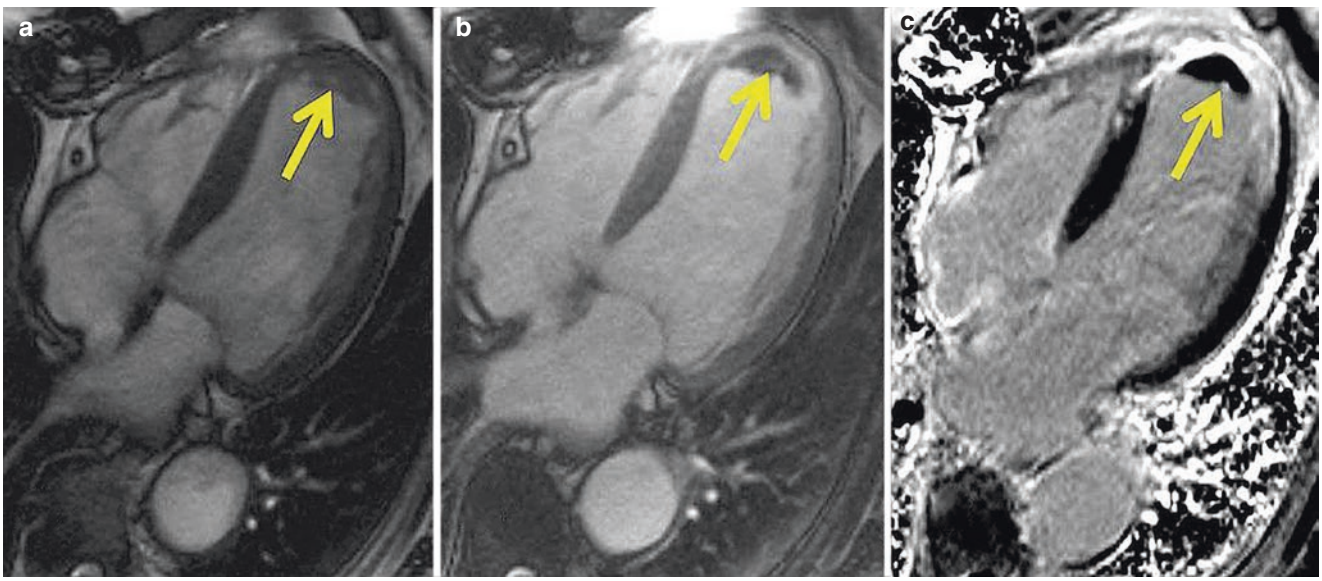

Fig. 10.9 (**a**) 4-chamber long-axis cine steady-state free precession (SSFP) image in a patient after late reperfusion of an anterior MI. Prior to contrast, it is difficult to discern whether there is thrombus in the apex. (**b**) Post-contrast 4-chamber SSFP image provides greater contrast between the slightly enhancing myocardium and nonenhancing thrombus at the apex. (**c**) LGE imaging clearly demonstrates the black thrombus at the apex adjacent to the transmural apical infarct

has been shown to more accurately diagnose thrombi within the LV than transthoracic echocardiography or transesophageal echocardiography. In a multimodality imaging study of 361 patients with ischemic cardiomyopathy undergoing cardiac surgery, the presence of LV thrombus by LGE-CMR, TTE, and TEE was compared to pathology and was found to have sensitivities and specificities of 88% and 99% for LGE, 23% and 96% for TTE, and 40% and 96% for TEE, respectively [101]. While contrast echocardiography nearly doubles the sensitivity of non-contrast echo, mural and small apical LV thrombi are still frequently missed [102]. Recently, the use of prolonged inversion times (600 ms) during LGE imaging has been shown to increase the sensitivity of LGE for detecting thrombus [102]. Post-contrast SSFP cine imaging can be quite useful as well in this regard (Fig. 10.9).

Post-MI LV Remodeling

After MI, the LV undergoes a series of adaptive and maladaptive changes [105], proportional to the size and transmurality of the infarct, which extend well beyond the infarcted segment. Remodeling in the early post-MI period is characterized by infarct expansion and thinning, with subsequent cavity dilation in the infarcted area due to weakening of the infarct from myocyte slippage and loss [106, 107]. Over time, the necrotic, infarcted myocardium is replaced by fibrous scar, while adjacent viable segments undergo eccentric hypertrophy [19] and fibrous deposition [108] causing global increases in ventricular volumes and worsened mechanical function (Fig. 10.10) [20]. Although these changes attempt to restore stroke volume and cardiac

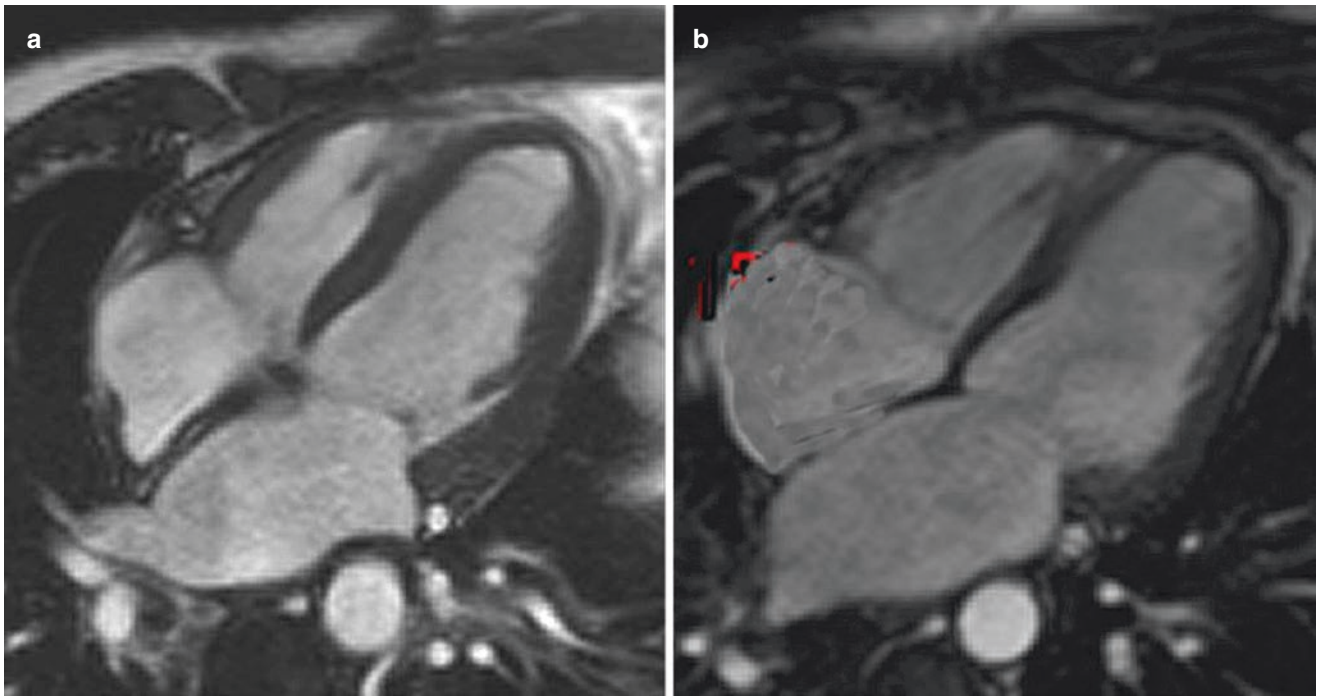

Fig. 10.10 (**a**) 4-chamber long-axis SSFP cine image in a patient 3 days after anterior MI. (**b**) 4-chamber long-axis SSFP cine image in the same patient 6 months later. Note the interval dilation of the LV consistent with adverse remodeling as well as dilation of the RV and both atria

output, they are associated with worsened mortality [12, 109]. Therapies which successfully attenuate post-MI remodeling have been shown to improve outcomes.

Because of its marked prognostic significance after MI, there is substantial interest in finding accurate predictors of remodeling which can be assessed at the time of MI. Baseline measurements of left ventricular function and volumes are a tempting target, and baseline ejection fraction and LV volumes have been shown to be modestly predictive of remodeling on follow-up [110]. However, due to the remodeling process and the frequent presence of stunned, but viable, myocardium in the peri-infarct area [111], measurements of systolic performance immediately post-MI are inherently unreliable. Clinical parameters, such as the ST-segment resolution and the time from symptom onset to reperfusion, have also been shown to be associated with poor LV function at follow-up [112] but are also relatively poor and indirect markers of follow-up function. Multiple studies have demonstrated that several CMR-based parameters are much better predictors of long-term LV remodeling. In a study of 73 STEMI patients in whom CMR was performed within 1 week and again 3 months after MI, infarct size, as measured by LGE, was shown to be a better determinant of follow-up EF than was the baseline EF [113]. Larose et al. confirmed this finding in a study of 103 STEMI patients, demonstrating that infarct size was the most powerful predictor of 6-month LV dysfunction, with an area under the receiver-operator characteristic curve of 0.92 for infarct size, compared to 0.84, 0.79, and 0.71 for baseline ejection fraction, peak enzyme elevation, and time from symptom onset to revascularization, respectively [110].

Microvascular obstruction (MO) as a marker for subsequent remodeling was first demonstrated angiographically [114], and CMR-based assessment of MO has since been shown to be a powerful predictor of poor LV function, as discussed earlier in this chapter. MO and IMH directly relate to poor functional recovery and adverse LV remodeling [115]. Myocardial salvage index is a relatively recent measure for predicting post-MI prognosis, but initial studies are very promising. In a study of 137 reperfused acute STEMI patients, MSI was shown to be more predictive of adverse LV remodeling at 4 months than infarct size, MO, or traditional measures of prognosis [116]. Therapies that limit reperfusion injury and thus limit MO and IMH and maximize myocardial salvage will prevent subsequent adverse remodeling.

References

1. Kramer CM, Rogers WJ, Geskin G, Power TP, Theobald TM, Hu YL, et al. Usefulness of magnetic resonance imaging early after acute myocardial infarction. Am J Cardiol. 1997;80(6):690–5.
2. Wu KC, Zerhouni EA, Judd RM, Lugo-Olivieri CH, Barouch LA, Schulman SP, et al. Prognostic significance of microvascular obstruction by magnetic resonance imaging in patients with acute myocardial infarction. Circulation. 1998;97(8):765–72.

3. Simonetti OP, Kim RJ, Fieno DS, et al. An improved MR imaging technique for the visualization of myocardial infarction. Radiology. 2001;218:215–23.
4. Kim RJ, Fieno DS, Parrish TB, Harris K, Chen E-L, Simonetti O, et al. Relationship of MRI delayed contrast enhancement to irreversible injury, infarct age and contractile function. Circulation. 1999;100:1992–2002.
5. Abdel-Aty H, Zagrosek A, Schulz-Menger J, Taylor AJ, Messroghli D, Kumar A, et al. Delayed enhancement and T2-weighted cardiovascular magnetic resonance imaging differentiate acute from chronic myocardial infarction. Circulation. 2004;109(20):2411–6.
6. Kumar A, Green JD, Sykes JM, Ephrat P, Carson JJL, Mitchell AJ, et al. Detection and quantification of myocardial reperfusion hemorrhage using T2*-weighted CMR. JACC Cardiovasc Imaging. 2011;4(12):1274–83.
7. Kali A, Cokic I, Tang RLQ, Yang HJ, Sharif B, Marbán E, et al. Determination of location, size, and transmurality of chronic myocardial infarction without exogenous contrast media by using cardiac magnetic resonance imaging at 3 T. Circ Cardiovasc Imaging. 2014;7(3):471–81.
8. Hundley WG, Bluemke DA, Finn JP, Flamm SD, Fogel MA, Friedrich MG, et al. ACCF/ACR/AHA/NASCI/SCMR 2010 expert consensus document on cardiovascular magnetic resonance: a report of the American College of Cardiology Foundation task force on expert consensus documents. J Am Coll Cardiol. 2010;55(23):2614–62.
9. Hunt SA, Abraham WT, Chin MH, Feldman AM, Francis GS, Ganiats TG, et al. 2009 focused update incorporated into the ACC/AHA 2005 guidelines for the diagnosis and management of heart failure in adults: a report of the American College of Cardiology Foundation/American Heart Association Task Force on practice guidelines developed in collaboration with the International Society for Heart and Lung Transplantation. J Am Coll Cardiol. 2009;53(15):e1–e90.
10. Hendel RC, Patel MR, Kramer CM, Poon M, Hendel RC, Carr JC, et al. ACCF/ACR/SCCT/SCMR/ASNC/NASCI/SCAI/SIR 2006 appropriateness criteria for cardiac computed tomography and cardiac magnetic resonance imaging: a report of the American College of Cardiology Foundation Quality Strategic Directions Committee Appropriateness Criteria Working Group, American College of Radiology, Society of Cardiovascular Computed Tomography, Society for Cardiovascular Magnetic Resonance, American Society of Nuclear Cardiology, North American Society for Cardiac Imaging, Society for Cardiovascular Angiography and Interventions, and Society of Interventional Radiology. J Am Coll Cardiol. 2006;48(7):1475–97.
11. The Multicenter Postinfarction Research Group. Risk stratification and survival after myocardial infarction. N Engl J Med. 1983;309(6):331–6.
12. White HD, Norris RM, Brown MA, Brandt PW, Whitlock RM, Wild CJ. Left ventricular end-systolic volume as the major determinant of survival after recovery from myocardial infarction. Circulation. 1987;76(1):44–51.
13. Isbell DC, Kramer CM. Cardiovascular magnetic resonance: structure, function, perfusion, and viability. J Nucl Cardiol. 2005;12:324–36
14. Grothues F, Smith GC, Moon JCC, Bellenger NG, Collins P, Klein HU, et al. Comparison of interstudy reproducibility of cardiovascular magnetic resonance with two-dimensional echocardiography in normal subjects and in patients with heart failure or left ventricular hypertrophy. Am J Cardiol. 2002 Jul 1;90:29–34.
15. Bellenger NG, Davies LC, Francis JM, Coats AJS, Pennell DJ. Reduction in sample size for studies of remodeling in heart failure by the use of cardiovascular magnetic resonance. J Cardiovasc Magn Reson. 2000;2(4):271–8.
16. Zerhouni EA, Parish DM, Rogers WJ, Yang A, Shapiro EP. Human heart: tagging with MR imaging: a new method for noninvasive assessment of myocardial motion. Radiology. 1988;169:59–63.
17. Kim D, Gilson WD, Kramer CM, Epstein FH. Myocardial tissue tracking with two-dimensional cine displacement-encoded MR imaging: development and initial evaluation. Radiology. 2004;230(3):862–71.
18. Kramer CM, Lima JAC, Reichek N, Ferrari VA, Llaneras MR, Palmon LC, et al. Regional differences in function within noninfarcted myocardium during left-ventricular remodeling. Circulation. 1993;88(3):1279–88.
19. Kramer CM, Rogers WJ, Theobald TM, Power TP, Petruolo S, Reichek N. Remote noninfarcted region dysfunction soon after first anterior myocardial infarction. A magnetic resonance tagging study. Circulation. 1996;94(4):660–6.
20. Kramer CM, Rogers WJ, Theobald TM, Power TP, Geskin G, Reichek N. Dissociation between changes in intramyocardial function and left ventricular volumes in the eight weeks after first anterior myocardial infarction. J Am Coll Cardiol. 1997;30(7):1625–32.
21. Azevedo CF, Amado LC, Kraitchman DL, Gerber BL, Osman NF, Rochitte CE, et al. Persistent diastolic dysfunction despite complete systolic functional recovery after reperfused acute myocardial infarction demonstrated by tagged magnetic resonance imaging. Eur Heart J. 2004;25(16):1419–27.
22. Sun Y, Kiani MF, Postlethwaite AE, Weber KT. Infarct scar as living tissue. Basic Res Cardiol. 2002;97(5):343–7.
23. Reimer KA, Jennings RB. Changing anatomic reference base of evolving myocardial-infarction – underestimation of myocardial collateral blood-flow and over-estimation of experimental anatomic infarct size due to tissue edema. Hemorrhage Acute-Inflamm Circ. 1979;60(4):866–76.
24. Fishbein MC, Maclean D, Maroko PR. The histopathologic evolution of myocardial infarction. Chest. 1978;73(6):843–9.
25. Jugdutt BI, Amy RW. Healing after myocardial infarction in the dog: changes in infarct hydroxyproline and topography. J Am Coll Cardiol. 1986;7(1):91–102.
26. Rehr RB, Peshock RM, Malloy CR, Keller AM, Parkey RW, Buja LM, et al. Improved in vivo magnetic resonance imaging of acute myocardial infarction after intravenous paramagnetic contrast agent administration. Am J Cardiol. 1986;57(10):864–8.
27. Peshock RM, Malloy CR, Buja LM, Nunnally RL, Parkey RW, Willerson JT. Magnetic resonance imaging of acute myocardial infarction: gadolinium diethylenetriamine pentaacetic acid as a marker of reperfusion. Circulation. 1986;74(6):1434–40.
28. de Roos A, Doornbos J, van der Wall EE, Van Voorthuisen AE. MR imaging of acute myocardial infarction: value of Gd-DTPA. AJR Am J Roentgenol. 1988;150(3):531–4.
29. Rehwald WG, Fieno DS, Chen EL, Kim RJ, Judd RM. Myocardial magnetic resonance imaging contrast agent concentrations after reversible and irreversible ischemic injury. Circulation. 2002;105(2):224–9.
30. Fieno DS, Kim RJ, Chen EL, Lomasney JW, Klocke FJ, Judd RM. Contrast-enhanced magnetic resonance imaging of myocardium at risk – distinction between reversible and irreversible injury throughout infarct healing. J Am Coll Cardiol. 2000;36(6):1985–91.
31. Wagner A, Mahrholdt H, Holly TA, Elliott MD, Regenfus M, Parker M, Klocke FJ, et al. Contrast-enhanced MRI and routine single photon emission computed tomography (SPECT) perfusion imaging for detection of subendocardial myocardial infarcts: an imaging study. Lancet. 2003;361:374–9.
32. Ibrahim T, Bulow HP, Hackl T, Hornke M, Nekolla SG, Breuer M, et al. Diagnostic value of contrast-enhanced magnetic resonance imaging and single-photon emission computed tomography for detection of myocardial necrosis early after acute myocardial infarction. J Am Coll Cardiol. 2007;49(2):208–16.
33. Klein C, Nekolla SG, Bengel FM, Momose M, Sammer A, Haas F, et al. Assessment of myocardial viability with contrast-enhanced magnetic resonance imaging: comparison with positron emission tomography. Circulation. 2002;105:162–7.

34. Choi KM, Kim RJ, Gubernikoff G, Vargas JD, Parker M, Judd RM. Transmural extent of acute myocardial infarction predicts long-term improvement in contractile function. Circulation. 2001;104(10):1101–7.
35. Choi JW, Gibson CM, Murphy SA, Davidson CJ, Kim RJ, Ricciardi MJ. Myonecrosis following stent placement: association between impaired TIMI myocardial perfusion grade and MRI visualization of microinfarction. Catheter Cardiovasc Interv. 2004;61(4):472–6.
36. Ricciardi MJ, Wu E, Davidson CJ, Choi KM, Klocke FJ, Bonow RO, et al. Visualization of discrete microinfarction after percutaneous coronary intervention associated with mild creatine kinase-MB elevation. Circulation. 2001;103(23):2780–3.
37. Steuer J, Bjerner T, Duvernoy O, Jideus L, Johansson L, Ahlstrom H, et al. Visualisation and quantification of peri-operative myocardial infarction after coronary artery bypass surgery with contrast-enhanced magnetic resonance imaging. Eur Heart J. 2004;25(15):1293–9.
38. Kim HW, Farzaneh-Far A, Kim RJ. Cardiovascular magnetic resonance in patients with myocardial infarction. J Am Coll Cardiol. 2009;55(1):1–16.
39. Choi CJ, Haji-Momenian S, DiMaria JM, Epstein FH, Rogers WJ, Kramer CM. Infarct involution and improved function during healing of acute myocardial infarction: the role of microvascular obstruction. J Cardiovasc Magn Reson. 2004;6:915–23.
40. Ingkanisorn WP, Rhoads KL, Aletras AH, Kellman P, Arai AE. Gadolinium delayed enhancement cardiovascular magnetic resonance correlates with clinical measures of myocardial infarction. J Am Coll Cardiol. 2004;43:2253–9.
41. Nijveldt R, Beek AM, Hofman MBM, Umans VAWM, Algra PR, Spreeuwenberg MD, et al. Late gadolinium-enhanced cardiovascular magnetic resonance evaluation of infarct size and microvascular obstruction in optimally treated patients after acute myocardial infarction. J Cardiovasc Magn Reson. 2007;9(5):765–70.
42. Weir RAP, Murphy CA, Petrie CJ, Martin TN, Balmain S, Clements S, et al. Microvascular obstruction remains a portent of adverse remodeling in optimally treated patients with left ventricular systolic dysfunction after acute myocardial infarction. Circ Cardiovasc Imaging. 2010;3(4):360–7.
43. Kwong RY, Chan AK, Brown KA, Chan CW, Reynolds HG, Tsang S, et al. Impact of unrecognized myocardial scar detected by cardiac magnetic resonance imaging on event-free survival in patients presenting with signs or symptoms of coronary artery disease. Circulation. 2006;113(23):2733–43.
44. Cheong BYC, Muthupillai R, Wilson JM, Sung A, Huber S, Amin S, et al. Prognostic significance of delayed-enhancement magnetic resonance imaging survival of 857 patients with and without left ventricular dysfunction. Circulation. 2009;120(21):2069–76.
45. Kwon DH, Halley CM, Carrigan TP, Zysek V, Popovic ZB, Setser R, et al. Extent of left ventricular scar predicts outcomes in ischemic cardiomyopathy patients with significantly reduced systolic function: a delayed hyperenhancement cardiac magnetic resonance study. JACC Cardiovasc Imaging. 2009;2(1):34–44.
46. Reffelmann T, Kloner RA. Microvascular alterations after temporary coronary artery occlusion: the no-reflow phenomenon. J Cardiovasc Pharmacol Ther. 2004;9(3):163–72.
47. Kramer CM. The prognostic significance of microvascular obstruction after myocardial infarction as defined by cardiovascular magnetic resonance. Eur Heart J. 2005;26(6):532–3.
48. Kloner RA, Ganote CE, Jennings RB. The “no-reflow” phenomenon after temporary coronary occlusion in the dog. J Clin Invest. 1974;54(6):1496–508.
49. Reffelmann T, Kloner RA. Microvascular reperfusion injury: rapid expansion of anatomic no reflow during reperfusion in the rabbit. Am J Physiol-Heart Circ Physiol. 2002;283(3):H1099–107.
50. Ambrosio G, Weisman HF, Mannisi JA, Becker LC. Progressive impairment of regional myocardial perfusion after initial restoration of postischemic blood-flow. Circulation. 1989;80(6):1846–61.
51. Rochitte CE, Lima JAC, Bluemke DA, Reeder SB, McVeigh ER, Furuta T, et al. Magnitude and time course of microvascular obstruction and tissue injury after acute myocardial infarction. Circulation. 1998;98(10):1006–14.
52. Wu KC, Kim RJ, Bluemke DA, Rochitte CE, Zerhouni EA, Becker LC, et al. Quantification and time course of microvascular obstruction by contrast-enhanced echocardiography and magnetic resonance imaging following acute myocardial infarction and reperfusion. J Am Coll Cardiol. 1998;32(6):1756–64.
53. Hamirani YS, Wong A, Kramer CM, Salerno M. The effect of microvascular obstruction and intramyocardial hemorrhage by CMR on left ventricular remodeling and outcomes post-MI: a systematic review and meta-analysis. JACC Cardiovasc Imaging. 2014;7(9):940–52.
54. Rogers WJ, Kramer CM, Geskin G, Hu YL, Theobald TM, Vido DA, et al. Early contrast-enhanced MRI predicts late functional recovery after reperfused myocardial infarction. Circulation. 1999;99(6):744–50.
55. Orn S, Manhenke C, Greve OJ, Larsen AI, Bonarjee VVS, Edvardsen T, et al. Microvascular obstruction is a major determinant of infarct healing and subsequent left ventricular remodelling following primary percutaneous coronary intervention. Eur Heart J. 2009;30(16):1978–85.
56. Nijveldt R, Beek AM, Hirsch A, Hofman MBM, Umans VAWM, Algra PR, et al. ‘No-reflow’ after acute myocardial infarction: direct visualisation of microvascular obstruction by gadolinium-enhanced CMR. Netherlands Heart J. 2008;16(5):179–81.
57. Hirsch A, Nijveldt R, Haeck JDE, Beek AM, Koch KT, Henriques JPS, et al. Relation between the assessment of microvascular injury by cardiovascular magnetic resonance and coronary Doppler flow velocity measurements in patients with acute anterior wall myocardial infarction. J Am Coll Cardiol. 2008;51(23):2230–8.
58. Nijveldt R, Hofman MBM, Hirsch A, Beek AM, Umans VAWM, Algra PR, et al. Assessment of microvascular obstruction and prediction of short-term remodeling after acute myocardial infarction: cardiac MR imaging study. Radiology. 2009;250(2):363–70.
59. Hombach V, Grebe O, Merkle N, Waldenmaier S, Hoher M, Kochs M, et al. Sequelae of acute myocardial infarction regarding cardiac structure and function and their prognostic significance as assessed by magnetic resonance imaging. Eur Heart J. 2005;26(6):549–57.
60. Cochet A, Lorgis L, Lalande A, Zeller M, Beer JC, Walker P, et al. Major prognostic impact of persistent microvascular obstruction as assessed by contrast-enhanced cardiac magnetic resonance in reperfused acute myocardial infarction. Eur Radiol. 2009;19(9):2117–26.
61. Eitel I, de Waha S, Wöhrle J, Fuernau G, Lurz P, Pauschinger M, et al. Comprehensive prognosis assessment by CMR imaging after ST-segment elevation myocardial infarction. J Am Coll Cardiol. 2014;64(12):1217–26.
62. van Kranenburg M, Magro M, Thiele H, de Waha S, Eitel I, Cochet A, et al. Prognostic value of microvascular obstruction and infarct size, as measured-áby CMR in STEMI patients. JACC: Cardiovascu Imaging. 2014;7(9):930–9.
63. Abdel-Aty H, Cocker M, Meek C, Tyberg JV, Friedrich MG. Edema as a very early marker for acute myocardial ischemia a cardiovascular magnetic resonance study. J Am Coll Cardiol. 2009;53(14):1194–201.
64. Aletras AH, Tilak GS, Natanzon A, Hsu LY, Gonzalez FM, Hoyt RF Jr, et al. Retrospective determination of the area at risk for reperfused acute myocardial infarction with T2-weighted cardiac magnetic resonance imaging: histopathological and displacement

encoding with stimulated echoes (DENSE) functional validations. Circulation. 2006;113(15):1865–70.
65. Nilsson JC, Nielsen G, Groenning BA, Fritz-Hansen T, Sondergaard L, Jensen GB, et al. Sustained postinfarction myocardial oedema in humans visualised by magnetic resonance imaging. Heart. 2001;85(6):639–42.
66. Karolle BL, Carlson RE, Aisen AM, Buda AJ. Transmural distribution of myocardial edema by NMR relaxometry following myocardial-ischemia and reperfusion. Am Heart J. 1991;122(3):655–64.
67. Friedrich MG, Abdel-Aty H, Taylor A, Schulz-Menger J, Messroghli D, Dietz R. The salvaged area at risk in reperfused acute myocardial infarction as visualized by cardiovascular magnetic resonance. J Am Coll Cardiol. 2008;51(16):1581–7.
68. Giri S, Chung YC, Merchant A, Mihai G, Rajagopalan S, Raman SV, et al. T2 quantification for improved detection of myocardial edema. J Cardiovasc Magn Reson. 2009;30:11.
69. Croisille P, Kim HW, Kim RJ. Controversies in cardiovascular MR imaging: T2-weighted imaging should not be used to delineate the area at risk in ischemic myocardial injury. Radiology. 2012;265(1):12–22.
70. Payne AR, Casey M, McClure J, McGeoch R, Murphy A, Woodward R, et al. Bright-blood T2-weighted MRI has higher diagnostic accuracy than dark-blood short tau inversion recovery MRI for detection of acute myocardial infarction and for assessment of the ischemic area at risk and myocardial salvage. Circ Cardiovasc Imaging. 2011;4(3):210–9.
71. Hammer-Hansen S. Distinction of salvaged and infarcted myocardium within the ischaemic area-at-risk with T2 mapping. Eur Heart J Cardiovasc Imaging. 2014;15(9):1048–53.
72. Ugander M, Bagi PS, Oki AJ, Chen B, Hsu LY, Aletras AH, et al. Myocardial edema as detected by pre-contrast T1 and T2 CMR delineates area at risk associated with acute myocardial infarction. JACC Cardiovasc Imaging. 2012;5(6):596–603.
73. Berry C, Kellman P, Mancini C, Chen MY, Bandettini WP, Lowrey T, et al. Magnetic resonance imaging delineates the ischemic area at risk and myocardial salvage in patients with acute myocardial infarction. Circ Cardiovasc Imaging. 2010;3(5):527–35.
74. Eitel I, Desch S, Fuernau G, Hildebrand L, Gutberlet M, Schuler G, et al. Prognostic significance and determinants of myocardial salvage assessed by cardiovascular magnetic resonance in acute reperfused myocardial infarction. J Am Coll Cardiol. 2010;52:2470–9.
75. Eitel I, Desch S, de Waha S, Fuernau G, Gutberlet M, Schuler G, et al. Long-term prognostic value of myocardial salvage assessed by cardiovascular magnetic resonance in acute reperfused myocardial infarction. Heart. 2011;97(24):2038–45.
76. Messroghli DR, Walters K, Plein S, Sparrow P, Friedrich MG, Ridgway JP, et al. Myocardial T1 mapping: application to patients with acute and chronic myocardial infarction. Magn Reson Med. 2007;58(1):34–40.
77. Dall'Armellina E, Piechnik S, Ferreira V, Si QL, Robson M, Francis J, et al. Cardiovascular magnetic resonance by non contrast T1-mapping allows assessment of severity of injury in acute myocardial infarction. J Cardiovasc Magn Reson. 2012;14(1):15.
78. Chan W, Duffy SJ, White DA, Gao XM, Du XJ, Ellims AH, et al. Acute left ventricular remodeling following myocardial infarction: coupling of regional healing with remote extracellular matrix expansion. JACC Cardiovasc Imaging. 2012;5(9):884–93.
79. Yellon DM, Hausenloy DJ. Myocardial reperfusion injury. N Engl J Med. 2007;357(11):1121–35.
80. Husser O, Monmeneu JV, Sanchis J, Nunez J, Lopez-Lereu MP, Bonanad C, et al. Cardiovascular magnetic resonance-derived intramyocardial hemorrhage after STEMI: influence on long-term prognosis, adverse left ventricular remodeling and relationship with microvascular obstruction. Int J Cardiol. 2013;167(5):2047–54.
81. Jensen C, Eberle H, Nassenstein K, Schlosser T, Farazandeh M, Naber C, et al. Impact of hyperglycemia at admission in patients with acute ST-segment elevation myocardial infarction as assessed by contrast-enhanced MRI. Clin Res Cardiol. 2011;100(8):649–59.
82. O'Regan DP, Ahmed R, Karunanithy N, Neuwirth C, Tan Y, Durighel G, et al. Reperfusion hemorrhage following acute myocardial infarction: assessment with T2*mapping and effect on measuring the area at risk. Radiology. 2009;250(3):916–22.
83. Francone M, Bucciarelli-Ducci C, Carbone I, Canali E, Scardala R, Calabrese FA, et al. Impact of primary coronary angioplasty delay on myocardial salvage, infarct size, and microvascular damage in patients with ST-segment elevation myocardial infarction insight from cardiovascular magnetic resonance. J Am Coll Cardiol. 2009;54(23):2145–53.
84. Robbers LFHJ, Eerenberg ES, Teunissen PFA, Jansen MF, Hollander MR, Horrevoets AJG, et al. Magnetic resonance imaging-defined areas of microvascular obstruction after acute myocardial infarction represent microvascular destruction and haemorrhage. Eur Heart J. 2013;34(30):2346–53.
85. Kali A, Tang RLQ, Kumar A, Min JK, Dharmakumar R. Detection of acute reperfusion myocardial hemorrhage with cardiac MR imaging: T2 versus T2*. Radiology. 2013;269(2):387–95.
86. Ochiai K, Shimada T, Murakami Y, Ishibashi Y, Sano K, Kitamura J, Inoue S, et al. Hemorrhagic myocardial infarction after coronary reperfusion detected in vivo by magnetic resonance imaging in humans: prevalence and clinical implication. J Cardiovasc Magn Reson. 1999;1:247–56.
87. O'Regan DP, Ariff B, Neuwirth C, Tan Y, Durighel G, Cook SA. Assessment of severe reperfusion injury with T2* cardiac MRI in patients with acute myocardial infarction. Heart. 2010;96(23):1885–91.
88. Mather AN, Fairbairn TA, Ball SG, Greenwood JP, Plein S. Reperfusion haemorrhage as determined by cardiovascular MRI is a predictor of adverse left ventricular remodelling and markers of late arrhythmic risk. Heart. 2011;97(6):453–9.
89. Eitel I, Kubusch K, Strohm O, Desch S, Mikami Y, de Waha S, et al. Prognostic value and determinants of a hypointense infarct core in T2-weighted cardiac magnetic resonance in acute reperfused ST-ElevationGÇôMyocardial infarction. Circ Cardiovasc Imaging. 2011;4(4):354–62.
90. Amabile N, Jacquier A, Shuhab A, Gaudart J, Bartoli JM, Paganelli F, et al. Incidence, predictors, and prognostic value of intramyocardial hemorrhage lesions in ST elevation myocardial infarction. Cathet Cardiovasc Intervent. 2012;79(7):1101–8.
91. Schmidt A, Azevedo CF, Cheng A, Gupta SN, Bluemke DA, Foo TK, et al. Infarct tissue heterogeneity by magnetic resonance imaging identifies enhanced cardiac arrhythmia susceptibility in patients with left ventricular dysfunction. Circulation. 2007;115(15):2006–14.
92. Yan AT, Shayne AJ, Brown KA, Gupta SN, Chan CW, Luu TM, et al. Characterization of the peri-infarct zone by contrast-enhanced cardiac magnetic resonance imaging is a powerful predictor of post-myocardial infarction mortality. Circulation. 2006;114(1):32–9.
93. Roes SD, Borleffs CJ, van der Geest RJ, Westenberg JJ, Marsan NA, Kaandorp TA, et al. Infarct tissue heterogeneity assessed with contrast-enhanced MRI predicts spontaneous ventricular arrhythmia in patients with ischemic cardiomyopathy and implantable cardioverter-defibrillator. Circ Cardiovasc Imaging. 2009;2:183–90.
94. Schelbert EB, Hsu LY, Anderson SA, Mohanty BD, Karim SM, Kellman P, et al. Late gadolinium-enhancement cardiac magnetic resonance identifies postinfarction myocardial fibrosis and the

border zone at the near cellular level in ex vivo rat heart. Circ Cardiovasc Imaging. 2010;3(6):743–52.
95. Shambrook JS, Chowdhury R, Brown IW, Peebles CR, Harden SP. Cross-sectional imaging appearances of cardiac aneurysms. Clin Radiol. 2010;65(5):349–57.
96. Kumar A, Abdel-Aty H, Kriedemann I, Schulz-Menger J, Gross CM, Dietz R, et al. Contrast-enhanced cardiovascular magnetic resonance imaging of right ventricular infarction. J Am Coll Cardiol. 2006;48(10):1969–76.
97. Okayama S, Uemura S, Soeda T, Onoue K, Somekawa S, Ishigami KI, et al. Clinical significance of papillary muscle late enhancement detected via cardiac magnetic resonance imaging in patients with single old myocardial infarction. Int J Cardiol. 2011;146:73–9.
98. Bogabathina H, Doyle M, Williams R, Yamrozik J, Vido D, Biederman RWW. Is there an alternative explanation to post-myocardial infarction emergence of mitral regurgitation? A CMR-LGE observational study. J Heart Valve Dis. 2013;22:669–74.
99. Taylor AM, Dymarkowski S, Verbeken EK, Bogaert J. Detection of pericardial inflammation with late-enhancement cardiac magnetic resonance imaging: initial results. Eur Radiol. 2006;16(3):569–74.
100. Bogaert J, Francone M. Cardiovascular magnetic resonance in pericardial diseases. J Cardiovasc Magn Reson. 2009;4:11.
101. Srichai MB, Junor C, Rodriguez LL, Stillman AE, Grimm RA, Lieber ML, et al. Clinical, imaging, and pathological characteristics of left ventricular thrombus: a comparison of contrast-enhanced magnetic resonance imaging, transthoracic echocardiography, and transesophageal echocardiography with surgical or pathological validation. Am Heart J. 2006;152(1):75–84.
102. Weinsaft JW, Kim HW, Shah DJ, Klem I, Crowley AL, Brosnan R, et al. Detection of left ventricular thrombus by delayed-enhancement cardiovascular magnetic resonance – prevalence and markers in patients with systolic dysfunction. J Am Coll Cardiol. 2008;52(2):148–57.
103. Greaves SC, Zhi G, Lee RT, Solomon SD, MacFadyen J, Rapaport E, et al. Incidence and natural history of left ventricular thrombus following anterior wall acute myocardial infarction. Am J Cardiol. 1997;80(4):442–8.
104. Chiarella F, Santoro E, Domenicucci S, Maggioni A, Vecchio C. Predischarge two-dimensional echocardiographic evaluation of left ventricular thrombosis after acute myocardial infarction in the GISSI-3 study. Am J Cardiol. 1998;81(7):822–7.
105. Pfeffer MA, Braunwald E. Ventricular remodeling after myocardial-infarction – experimental-observations and clinical implications. Circulation. 1990;81(4):1161–72.
106. Hutchins GM, Bulkley BH. Infarct expansion versus extension – 2 different complications of acute myocardial-infarction. Am J Cardiol. 1978;41(7):1127–32.
107. Weisman HF, Bush DE, Mannisi JA, Weisfeldt ML, Healy B. Cellular mechanisms of myocardial infarct expansion. Circulation. 1988;78(1):186–201.
108. Weber KT, Sun Y, Katwa LC. Wound healing following myocardial infarction. Clin Cardiol. 1996;19(6):447–55.
109. Moss AJ. Risk stratification and survival after myocardial-infarction. N Engl J Med. 1983;309(6):331–6.
110. Larose E, Rodes-Cabau J, Pibarot P, Rinfret S, Proulx G, Nguyen CM, et al. Predicting late myocardial recovery and outcomes in the early hours of ST-segment elevation myocardial infarction traditional measures compared with microvascular obstruction, salvaged myocardium, and necrosis characteristics by cardiovascular magnetic resonance. J Am Coll Cardiol. 2010;55(22):2459–69.
111. Geskin G, Kramer CM, Rogers WJ, Theobald TM, Pakstis D, Hu Y-L, et al. Quantitative assessment of myocardial viability after infarction by dobutamine magnetic resonance tagging. Circulation. 1998;98:217–23.
112. Klug G, Trieb T, Schocke M, Nocker M, Skalla E, Mayr A, et al. Quantification of regional functional improvement of infarcted myocardium after primary PTCA by contrast-enhanced magnetic resonance imaging. J Magn Reson Imaging. 2009;29(2):298–304.
113. Rubenstein JC, Ortiz JT, Wu E, Kadish A, Passman R, Bonow RO, et al. Imaging and diagnostic testing – the use of periinfarct contrast-enhanced cardiac magnetic resonance imaging for the prediction of late postmyocardial infarction ventricular dysfunction. Am Heart J. 2008;156(3):498–505.
114. Morishima I, Sone T, Okumura K, Tsuboi H, Kondo J, Mukawa H, et al. Angiographic no-reflow phenomenon as a predictor of adverse long-term outcome in patients treated with percutaneous transluminal coronary angioplasty for first acute myocardial infarction. J Am Coll Cardiol. 2000;36(4):1202–9.
115. Symons R, Masci PG, Goetschalckx K, Doulaptsis K, Janssens S, Bogaert J. Effect of infarct severity on regional and global left ventricular remodeling in patients with successfully reperfused ST segment elevation myocardial infarction. Radiology. 2014;10:132746.
116. Masci PG, Ganame J, Strata E, Desmet W, Aquaro GD, Dymarkowski S, et al. Myocardial salvage by CMR correlates with LV remodeling and early ST-segment resolution in acute myocardial infarction. JACC Cardiovasc Imaging. 2010;3(1):45–51.

Exercise and Dobutamine Stress CMR

11

Karolina M. Zareba and Subha V. Raman

Introduction

Cardiovascular magnetic resonance (CMR) has developed into a superior technique for noninvasive detection of obstructive coronary artery disease. The comprehensive nature of CMR with its ability to evaluate ventricular function, wall motion, perfusion, and viability makes it an excellent diagnostic and prognostic tool for patients with known or suspected coronary artery disease. The last two decades has seen rapid growth of stress CMR beginning with the first clinical experience with dobutamine CMR (DCMR) reported in 1992 [1], to the most recent emergence of in-room treadmill exercise CMR [2]. The addition of first-pass perfusion imaging to wall motion analysis has further enhanced the interpretation of these studies. In the current era of faster and higher-resolution sequences, stress CMR has the potential to become the mainstay modality of ischemic evaluation. This chapter will review the indications, technique, and interpretation of DCMR, as well as introduce treadmill exercise stress CMR.

Imaging Techniques

The challenge of dobutamine and exercise stress imaging is the ability to obtain diagnostic images at fast heart rates while limiting extensive breath-holding. Over the last two decades, several techniques have been used with their respective advantages and disadvantages [3]. The most commonly used sequence for cine imaging is segmented *k*-space acquisition with steady-state free precession (SSFP) readout [4]. However, segmented k-space acquisition is subject to artifact from cardiac arrhythmias or inability to breath-hold. Since its development, real-time imaging has been very useful in those situations. Post-exercise and during dobutamine infusion, breath-holding becomes difficult, and ECG triggering may be unreliable at fast heart rates. Real-time imaging is thus becoming the sequence of choice for stress CMR. A small study comparing real-time imaging to segmented SSFP found that real-time imaging allowed for accurate detection of wall motion abnormalities under stress [5].

New sequences with shorter scan times and improved image quality are emerging in the field of stress CMR. Accelerated 4D k-t BLAST (broad-use linear acquisition speedup technique) wall motion imaging was compared to conventional cine SSFP in patients with suspected or known coronary artery disease [6]. Jahnke and colleagues demonstrated that accelerated cine imaging at rest and at dobutamine stress was rapid and feasible with excellent agreement and reliable detection of hemodynamically significant stenoses.

Myocardial tagging and strain-encoded imaging have also been studied in the field of DCMR. Kuijpers and colleagues evaluated patients with chest pain and found that myocardial tagging detected more new wall motion abnormalities as compared to DCMR without tagging [7]. Another study by Paetsch and colleagues demonstrated that with myocardial tagging, a quantitative analysis of systolic and diastolic function was feasible during DCMR [8]. The authors noted that the diastolic parameter of time to peak untwist assessed during low-dose dobutamine stress reliably identified patients with significant coronary artery disease. The diagnostic accuracy of strain-encoded CMR was evaluated by Korosoglou and colleagues in patients with suspected coronary artery disease [9]. Strain-encoded CMR yielded significantly higher sensitivity than cine for significant stenoses at peak dobutamine stress. Interestingly, at intermediate levels of stress, strain-encoded imaging was able to detect inducible ischemia prior to the development of inducible wall motion abnormalities. Over the next decade, these new techniques will allow for faster, safer, and more accurate noninvasive diagnosis of coronary artery disease.

K. M. Zareba · S. V. Raman (✉)
The Ohio State University Wexner Medical Center, Department of Internal Medicine/Cardiovascular Medicine, Columbus, OH, USA
e-mail: karolina.zareba@osumc.edu; raman.1@osu.edu

R. Y. Kwong et al. (eds.), *Cardiovascular Magnetic Resonance Imaging*, Contemporary Cardiology,
https://doi.org/10.1007/978-1-4939-8841-9_11

Stress Agents

One of the earliest manifestations of stress-induced ischemia is the development of wall motion abnormalities, thus making dobutamine a prime agent for stress testing [10]. Dobutamine is a synthetic catecholamine with strong beta1 receptor and mild alpha1- and beta2-receptor agonist activity. At low doses (<10 μg/kg/min), it has marked inotropic effects, while at higher doses (20–40 μg/kg/min), the chronotropic effect is present along with increased myocardial oxygen demand and myocardial work [11, 12]. In the presence of hemodynamically significant coronary artery stenosis, the increase in oxygen demand cannot be met by an adequate increase in blood flow, thus creating a supply demand mismatch [13]. Subsequently, ischemia develops, and regional wall motion abnormalities appear which can be detected by CMR. Dobutamine's short onset of action and half-life (approximately 2 min) due to its rapid metabolism make it suitable for stress testing [14]. The major contraindications for the use of dobutamine are severe systemic hypertension (>220/120), unstable angina, severe aortic stenosis, complex cardiac arrhythmias, hypertrophic obstructive cardiomyopathy, myocarditis, endocarditis, pericarditis, and uncontrolled congestive heart failure [15].

The greatest diagnostic accuracy for identifying flow-limiting coronary artery disease is achieved when heart rate during stress exceeds 85% of the maximum age-predicted heart rate [16]. Dobutamine alone may result in a suboptimal chronotropic response, thus necessitating the additional use of atropine. Atropine is a competitive antagonist of muscarinic cholinergic receptors and increases heart rate by inhibiting vagal tone. The major contraindications to its use are narrow-angle glaucoma, myasthenia gravis, obstructive uropathy, and obstructive gastrointestinal disorders [15]. While not the most common approach to stress CMR, the combined dobutamine/atropine protocol is a well-established stress CMR approach.

Indications and Applications of DCMR

Stress CMR is able to overcome many of the challenges associated with other stress imaging modalities. Despite the widespread use of dobutamine stress echo, approximately 15–20% of patients have poor acoustic windows, even with contrast administration, which are inadequate to visualize all myocardial segments [17]. The accuracy of the test not only depends on the patient characteristics but also on the experience of the sonographer as well as the interpreting physician. Nuclear stress imaging techniques have their own limitations with attenuation artifacts, limited spatial resolution, as well as radiation exposure. CMR can visualize the myocardium in multiple planes with high-quality images not hindered by acoustic windows and with standardized protocols, thus minimizing reliance on the technique of a technologist. Stress CMR is thus becoming a method of choice for comprehensive ventricular, valvular, and ischemic evaluation. A specific advantage of DCMR is the more physiologic stress response to dobutamine as compared to vasodilator infusion. The ability to have additional perfusion data at peak stress along with wall motion data improves the accuracy of the test as well [18].

The American College of Cardiology Foundation along with key specialty and subspecialty societies developed appropriateness criteria for CMR in 2006 [19]. The risks and benefits of each imaging test were evaluated for numerous indications and clinical scenarios and subsequently scores based on a scale of 1–9. A score of 7–9 implied that a test was acceptable and a reasonable approach, and a score of 4–6 indicated an uncertain clinical scenario, while a score of 1–3 implied that the test was not acceptable and not a reasonable approach. These appropriateness criteria were further endorsed and expanded in 2013 (http://dx.doi.org/10.1016/j.cardfail.2013.12.002).

DCMR has multiple upper- and midrange clinical indications based on the appropriateness criteria including evaluation of chest pain syndromes, acute chest pain, risk assessment in light of prior test result, as well as preoperative evaluation for non-cardiac surgery. Detailed indications are listed in Table 11.1. Given further advances in CMR protocols and sequences, as well as greater emphasis on noninvasive testing, subsequent guidelines have incorporated more indications for DCMR.

Dobutamine Stress CMR Protocol

The DCMR protocol parallels the standard high-dose dobutamine/atropine regimen used in stress echocardiography. After careful patient selection and exclusion of any contraindications to stress agents, contrast, or CMR scanning, patients are asked to refrain from food and drink for approximately 4 h prior to the test, as well as hold any beta blockers or nitrates for 24 h prior to stress testing [15]. A baseline ECG is performed outside of the magnet room and IV access is obtained. The patient's blood pressure, pulse oximetry, heart rate, and rhythm are monitored throughout the exam. Since the magnetic field alters the appearance of ST segments and T waves, the ECG is only used to monitor the patient's rhythm. As wall motion abnormalities precede ECG changes in the ischemic cascade, the interpreting physician must review the images in real time to assess for global and regional myocardial contractility during the infusion [20].

After acquisition of localization scans, baseline cine imaging is performed in six planes (HLA, VLA, 3CH, basal SAX, mid SAX, apical SAX) [15]. Dobutamine is infused

Table 11.1 Appropriate indications for dobutamine stress CMR

Evaluation of chest pain syndrome	Appropriateness criteria (median score)
Low pretest probability of CAD ECG interpretable *and* able to exercise	I (2)
Intermediate pretest probability of CAD ECG interpretable *and* able to exercise	U (4)
Intermediate pretest probability of CAD ECG uninterpretable OR unable to exercise	A (7)
High pretest probability of CAD	U (5)
Acute chest pain	
Intermediate pretest probability of CAD No ECG changes *and* serial cardiac enzymes are negative	U (6)
High pretest probability of CAD ST segment elevation and/or positive cardiac enzymes	I(1)
Risk assessment with prior test result	
Normal prior stress test (exercise, echo, nuclear, MRI) High CHD risk (Framingham) Within 1 year of prior stress test	I (2)
Equivocal stress test (exercise, stress SPECT, stress echo) Intermediate CHD risk (Framingham)	U (6)
Coronary angiography (catheterization or CT) Stenosis of unclear significance	A (7)
Preoperative evaluation for non-cardiac surgery	
Low-risk surgery with intermediate perioperative risk	I (2)
Intermediate- or high-risk surgery with intermediate perioperative risk	U (6)

Reprinted from Hendel et al. [19], © 2006, with permission from Elsevier

intravenously at a typical starting dose of 10 μg/kg/min (5 μg/kg/min if viability is being assessed). The dobutamine dose is increased every 3 min in 10 μg/kg/min increments (with the addition of atropine up to 1 mg IV if needed) up to a maximum dose of 40 μg/kg/min or until one of the following endpoints is achieved [20]:

- Target heart rate [(220 – Age) × 0.85]
- Blood pressure decrease > 20 mmHg systolic below baseline systolic blood pressure or decrease > 40 mmHg from a previous level
- Blood pressure increase > 240/120 mmHg
- Intractable symptoms
- New or worsening wall motion abnormalities in at least 2 adjacent left ventricular segments (out of 16)
- Complex cardiac arrhythmias
- Patient request

Cine imaging is repeated in the same six planes at each stage as well as after a period of 10–15 min of recovery to confirm return to baseline function if ejection fraction declines or wall motion abnormalities appear. In addition, perfusion imaging may be obtained at peak dobutamine stress and after recovery. Following rest perfusion, further assessment with late gadolinium enhancement imaging is performed.

Safety and Monitoring

During any stress examination, careful monitoring is necessary and includes direct contact between the patient and examiner. Communication during DCMR is a coordinated effort between a nurse who remains in the scanner room with the patient and can directly assess symptoms and the supervising physician who typically is at the scanner console with the technologist reviewing images as they are reconstructed. In addition, special safety measures have to be undertaken in the CMR environment with essential equipment such as infusion pumps and monitors that are suitable for use in the MR environment. A suitably equipped crash cart with appropriate medications needs to be readily available outside the scanner room. Regular practice of safe and rapid patient evacuation from the scanner room along with initiation of resuscitation should be performed.

The safety and feasibility of high-dose dobutamine/atropine CMR were evaluated in 1000 consecutive cases over a 5-year period by Wahl and colleagues [21]. There were 895 diagnostic tests and 105 nondiagnostic tests which were related to poor ECG triggering, insufficient image quality, maximum stress infusion, or limiting side effects. The total number of side effects noted during DCMR was 64 (6.4%), as noted in Table 11.2, with only 1 case of sustained ventricular tachycardia. Observations of prior studies have also noted that major events were associated with continued administration of pharmacologic stress in the setting of con-

Table 11.2 Adverse effects of dobutamine stress CMR in a cohort of 1000 studies

Adverse effect	N
Ventricular tachycardia	5
Atrial fibrillation	16
Severe increase in blood pressure (>240/120 mmHg)	5
Drop of >40 mmHg in systolic blood pressure	5
Nausea	31

Reprinted from Wahl et al. [21], by permission of Oxford University Press

current ischemia and many side effects occurred in patients with known coronary artery disease and poor baseline left ventricular function [22]. The safety profile of stress CMR is thus similar to dobutamine stress echo, and close monitoring needs to be available.

Interpretation

The interpretation of wall motion abnormalities along with perfusion data, if available, is performed during dobutamine/atropine infusion in order to identify myocardial ischemia promptly [4]. Wall motion assessment is usually done visually, while perfusion assessment may be qualitative or quantitative.

After evaluation of baseline function, multiple cine loops can be displayed side by side and compared to baseline for the development of regional wall motion abnormalities (Fig. 11.1). The ventricle is analyzed by segment according to the 17-segment model [23]. Each segment is scored as 1 = normal, 2 = hypokinetic, 3 = akinetic, and 4 = dyskinetic, and the sum of points is divided by the number of segments analyzed, thus yielding a wall motion score. A lack of increase or reduction in wall motion or systolic wall thickening is regarded as abnormal. The final interpretation ideally involves reviewing wall motion abnormalities in the context of late gadolinium enhancement (LGE) imaging to define infarcted and ischemic segments. In the absence of LGE data, such as in the case of the patient who cannot receive gadolinium contrast, DCMR can still be performed with regional wall motion and ischemia assessed as done with dobutamine stress echocardiography. Careful review of wall motion in response to low, intermediate, and high dobutamine doses can help distinguish fixed wall motion abnormalities due to nonviable myocardium (with no contractile reserve at lower doses) from stunned and akinetic but viable myocardium that shows some contractile response to lower doses.

Diagnostic Performance

Over two decades ago, several studies demonstrated the feasibility and diagnostic accuracy of DCMR. The first clinical use of DCMR was reported by Pennell and colleagues in 25 patients with exertional chest pain undergoing concurrent thallium-201 single-photon emission computed tomography (SPECT) and coronary angiography [1]. DCMR sensitivity for identifying ischemia was 91% and agreement with SPECT was 90%. Another study by Baer and colleagues in patients with high-grade coronary artery stenoses (>70%

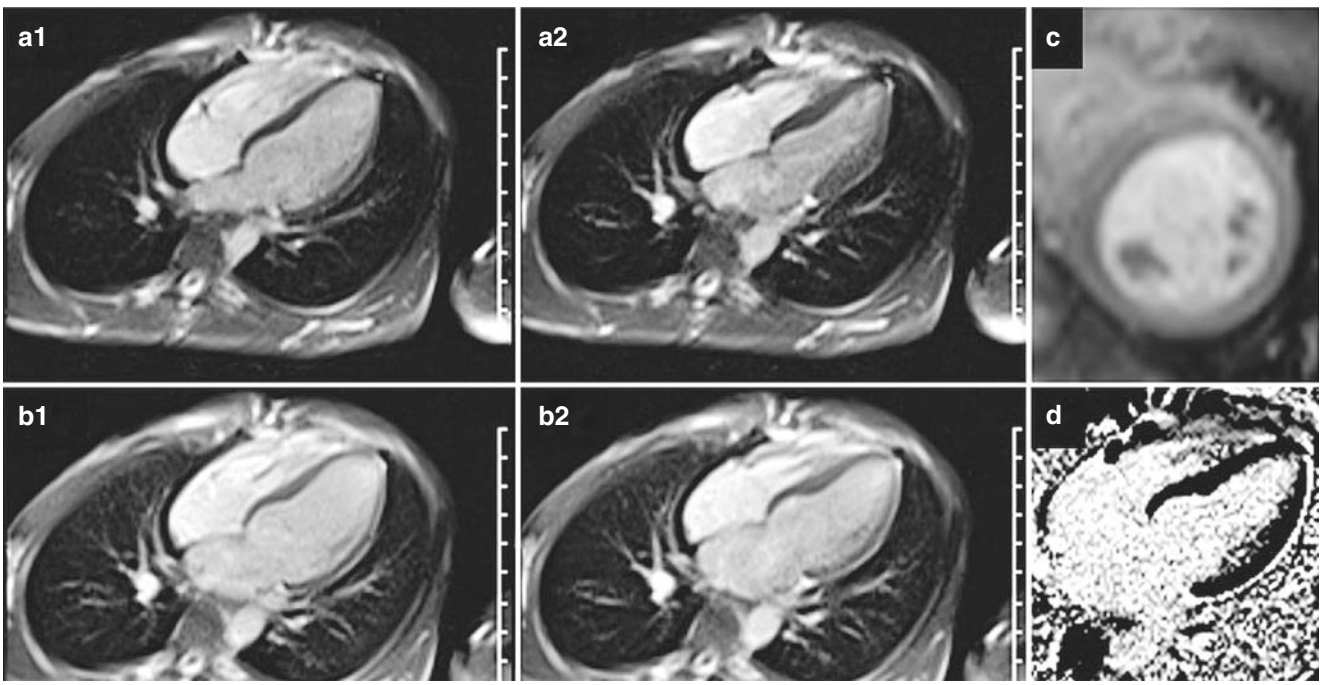

Fig. 11.1 A 25-year-old male with severe discoid lupus and chest pain was referred for dobutamine stress CMR. Resting systolic function was normal, as seen on comparison with end-diastolic (**a-1**) and end-systolic (**a-2**) frames from the baseline horizontal long-axis cine scan. Severe, global LV systolic dysfunction developed with dobutamine infusion (end-diastolic and end-systolic frames in the same plane are shown in **b-1** and **b-2**, respectively) paralleled by diffuse subendocardial perfusion defect at peak stress (**c**). Late gadolinium enhancement imaging (**d**) showed no infarct scar. Cardiac catheterization showed angiographically normal coronary arteries, supporting a diagnosis of severely impaired myocardial perfusion reserve

diameter) found that single-vessel disease was identified with 73% sensitivity and multivessel disease with 100% sensitivity [24]. Two studies by Van Rugge and colleagues evaluated the diagnostic accuracy of DCMR with visual and quantitative wall motion assessment in patients referred for coronary angiography [25, 26]. The overall sensitivity and specificity with visual assessment were 81% and 100%, respectively, while quantitative wall motion assessment had a sensitivity of 91%, specificity of 80%, and accuracy of 90%. These studies, although small in sample size, showed that DCMR was an accurate method for detecting and localizing myocardial ischemia.

Subsequent studies compared DCMR to dobutamine stress echo (DSE) thus solidifying its clinical utility further. Nagel and colleagues evaluated patients with suspected coronary artery disease by means of DCMR and DSE prior to coronary angiography [27]. DCMR had superior sensitivity (86% vs. 74%), specificity (86% vs. 70%), and diagnostic accuracy (86% vs. 70%) as compared to DSE. A more recent large study demonstrated similar results with DCMR-induced wall motion abnormalities being associated with a higher risk of subsequent cardiac events as compared to DSE [28]. Hundley and colleagues evaluated a specific population of patients with nondiagnostic DSE and found that sensitivity and specificity were both 83% in detecting significant coronary artery disease by DCMR [29]. Interpretation of DSE can be difficult in patients with resting wall motion abnormalities; thus, Wahl and colleagues evaluated the clinical utility of DCMR in patients who underwent revascularization and had pre-existing wall motion abnormalities [30]. Overall sensitivity and specificity for detection of significant CAD were 89% and 84%, respectively, thus establishing that DCMR is highly accurate in follow-up of patients after coronary revascularization. A more recent study evaluated DCMR in patients with left bundle branch block and suspected coronary artery disease as stress echo and SPECT both have limitations in this patient population [31]. Mordi and colleagues concluded that a comprehensive exam including DCMR, perfusion, and late gadolinium enhancement significantly boosted specificity and sensitivity in patients with left bundle branch block over DSE, potentially saving them from invasive angiography.

Direct comparison of DCMR wall motion analysis and adenosine stress CMR wall motion and perfusion analysis was performed by Paetsch and colleagues [32]. During the same study, patients underwent initial adenosine stress testing with perfusion and subsequent dobutamine stress testing. The investigators noted that dobutamine was more accurate, sensitive, and specific than perfusion assessment alone in identifying inducible ischemia.

DCMR demonstrates a high overall sensitivity and specificity for diagnosis of ischemia in patients with suspected or known coronary artery disease. A recent meta-analysis confirmed the overall sensitivity and specificity to be 83% and 86%, respectively [33]. In addition, DCMR is highly reproducible and has good interobserver variability [34, 35].

Prognostic Value of Stress CMR

The long-term predictive value of DCMR has been established in several studies over the last decade. Hundley and colleagues were the first to report prognostic data of DCMR in patients referred for detection of inducible ischemia [36]. Patients were followed for an average of 20 months for the occurrence of myocardial infarction, coronary artery revascularization, unstable angina, congestive heart failure requiring hospitalization, cardiac death, or death attributable to any cause. The presence of inducible ischemia and a left ventricular ejection fraction <40% was associated with future myocardial infarction or cardiac death independent of atherosclerosis risk factors. Furthermore, inducible ischemia involving the left ventricular apex was associated with future myocardial infarction and cardiac death, while ischemia in the basal and middle segments was not [37].

The utility of DCMR for assessment of preoperative cardiac risk was studied in patients with poor endocardial border definition by DSE [38]. Rerkpattanapipat and colleagues evaluated patients prior to non-cardiac surgery and assessed them for perioperative congestive heart failure, myocardial infarction, and death. Inducible ischemia on DCMR was independently associated with major cardiac events during or after surgery.

In patients with suspected myocardial ischemia, DCMR is able to assess risk levels for coronary events with high accuracy. Kuijpers and colleagues showed that DCMR has a high positive and negative predictive value of 95% and 93%, respectively [39]. In patients without evidence of ischemia, the cardiovascular event-free survival rate was 96.2%. Another study by Jahnke and colleagues compared DCMR with adenosine stress CMR and showed similar prognostic accuracy for both tests [40]. In patients with normal adenosine stress perfusion or DCMR, the 3-year event-free survival rate was 99.2%.

DCMR in Women

Cardiovascular disease is the leading cause of mortality for women in the United States [41]. A recent update from the American Heart Association reported that a greater proportion of women die of sudden cardiac death than men and women have more heart failure and strokes after their first myocardial infarction. Approximately one third more women than men die in the hospital with an acute myocardial infarction, as well as within 1 and 5 years after their infarction

[41]. The evaluation of coronary artery disease in women presents difficult and unique challenges for clinicians due to their greater symptom burden, lower functional capacity, worse clinical outcome, greater microvascular disease, and lower prevalence of obstructive coronary disease than men [42]. The discrepancy in outcomes between women and men highlights the importance of noninvasive testing in early identification of women at risk of coronary disease. CMR is a well-suited modality for women given the lack of ionizing radiation and excellent soft tissue characterization without attenuation artifact or the need for adequate imaging windows.

Recent studies have shown superior diagnostic accuracy of stress CMR in women. Gebker and colleagues evaluated 745 patients (204 women) undergoing dobutamine/atropine stress CMR and subsequent coronary angiography and showed no gender-based differences in the detection of hemodynamically significant obstructive coronary artery disease, with a sensitivity of 85% and specificity of 86% in women [43]. In the aforementioned study by Nagel and colleagues, sensitivity and specificity were greatly increased with the use of DCMR as compared to DSE in their subanalysis of women [27].

Raman and colleagues prospectively enrolled women with abnormal stress nuclear testing results thought to require further evaluation with coronary angiography [44]. All women who underwent successful DCMR demonstrated no evidence of ischemia despite abnormal stress nuclear results. The majority of women also underwent coronary angiography, and none were found to have significant obstructive disease. The prognostic value of DCMR was evaluated in 266 women over an average follow-up period of 6.2 years by Wallace and colleagues [45]. Inducible left ventricular wall motion abnormalities on DCMR were able to independently predict cardiac death and myocardial infarction in women. DCMR thus appears to be a useful and accurate method in predicting significant obstructive disease in women.

Stress Perfusion

First-pass myocardial perfusion has been extensively utilized with adenosine stress CMR techniques to detect significant coronary artery disease, as well as more recently to detect microvascular disease. However, the additional data obtained from myocardial perfusion is highly complementary to wall motion analysis during DCMR. The principle of first-pass perfusion imaging is based on tracking an intravenous bolus of contrast dynamically as it courses through the cardiac chambers and into the myocardium. Signal enhancement should be uniform throughout the myocardium in a normal patient without ischemia. The presence of hypointense regions in the myocardium indicates hypoperfusion from a hemodynamically significant coronary lesion. Analysis of perfusion is usually done visually; however, multiple semi-quantitative and quantitative methods exist.

During DCMR stress perfusion imaging is obtained at peak dobutamine stress as well as in recovery to evaluate for rest perfusion. Images are interpreted in light of late gadolinium enhancement findings [4]. Normal stress and rest perfusion without enhancement suggests no infarction or ischemia. Ischemia is diagnosed when there are abnormal stress perfusion, normal rest perfusion, and no late gadolinium enhancement. Abnormal stress and rest perfusion without enhancement is suggestive of either artifact or hibernating myocardium.

Two studies have examined the additional value of first-pass myocardial perfusion during peak dobutamine dose of DCMR. Gebker and colleagues performed DCMR with perfusion in 455 patients scheduled for coronary angiography and noted that the addition of perfusion imaging improved sensitivity for the diagnosis of coronary artery disease [46]. Lubbers and colleagues found that first-pass myocardial perfusion reduced the number of false-positive wall motion abnormalities noted on DCMR and thus improved the detection of ischemia [18].

Exercise CMR

Physiologic stress testing has significant advantages as it offers additional data regarding functional capacity and hemodynamic response to exercise. Advancements in CMR imaging techniques allow for rapid image acquisition, thus allowing its applicability to exercise stress testing. Roest and colleagues were the first to study the feasibility of exercise CMR in healthy volunteers using a CMR-compatible bicycle ergometer [47]. Stroke volume and ejection fraction increased in both ventricles from rest to exercise, while biventricular end-systolic volume decreased and end-diastolic volume remained unchanged. This initial study validated that exercise CMR can assess physiologic changes in the left and right ventricles.

The first study to examine the use of treadmill exercise in combination with CMR in patients with exertional chest pain was conducted by Rerkpattanapipat and colleagues [48]. Patients exercised on a treadmill positioned just outside the MR scanner room and were scanned within 1 min to evaluate for wall motion abnormalities. The sensitivity and specificity for detecting significant coronary artery disease (>70% stenosis on coronary angiography) were 79% and 85%, respectively. Imaging immediately after exercise ces-

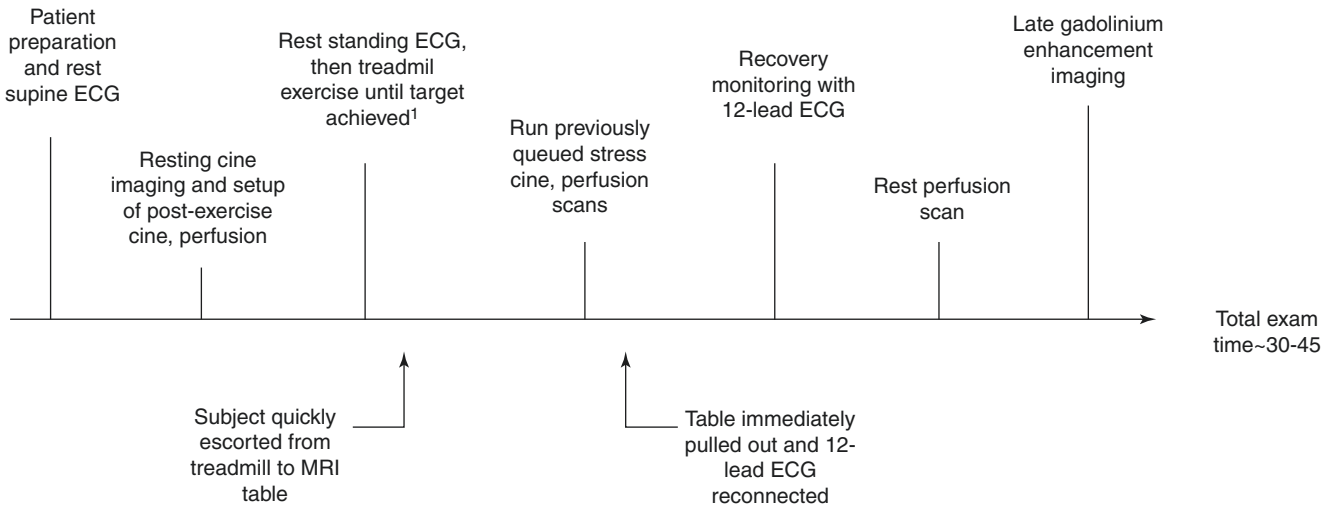

[1]Stress may be terminated by symptoms, target heart rate, patient request, significant arrhythmia, supervising staff or physician discretion

Fig. 11.2 The timing of treadmill stress CMR acquisition events is shown

sation is crucial to true peak stress wall motion assessment. Jekic and colleagues developed an MRI-compatible treadmill which led to the first feasibility study of exercise stress testing inside the MRI room [2]. Twenty healthy volunteers exercised under the Bruce protocol and subsequently were escorted quickly to the CMR table (Fig. 11.2). Real-time cine of seven slices without breath-holding or ECG gating was completed within 45 s of exercise, followed by stress perfusion imaging with an average time to peak enhancement of 57 s from cessation of exercise. Cardiac output and myocardial perfusion reserve index correlated with published values at peak stress. In addition, image quality was sufficient for visual assessment of wall motion in all ventricular segments, thus demonstrating the feasibility of in-room treadmill exercise CMR.

Raman and colleagues compared the utility of the newly developed in-room treadmill exercise CMR with SPECT imaging in patients with suspected ischemic heart disease [49]. In this special combined protocol, 43 patients underwent a rest technetium-99 SPECT and resting cine CMR and then proceeded to exercise on a modified CMR safe treadmill with ECG monitoring. At peak stress, technetium-99 was injected, and the patient returned to the CMR scanner for post-exercise cine and perfusion imaging and lastly was sent to complete the SPECT stress portion. Agreement between SPECT and CMR was moderate (kappa = 0.58), while the accuracy in eight patients who underwent coronary angiography was 7/8 for CMR and 5/8 for SPECT (Fig. 11.3).

A recent study by the same group compared exercise treadmill CMR to exercise echo performed 1 week apart in healthy volunteers in order to evaluate adequacy of endocardial visualization and confidence of study interpretation [50]. Average time to acquisition of stress images was shorter with exercise CMR, and the number of adequately visualized myocardial segments was significantly higher with CMR at rest and stress compared to exercise echo. A higher confidence in the interpretation was also achieved with CMR than it was with echo. This study further demonstrated that treadmill exercise CMR is feasible and is able to provide data superior to stress echo imaging.

Future Directions

Dobutamine and exercise stress CMR are two feasible and highly accurate modalities which are becoming mainstay in the assessment of coronary artery disease. Ongoing technical advances continue to improve the diagnostic utility of stress CMR. DCMR with perfusion at 3.0 T is becoming feasible with a high procedural success showing additional diagnostic value compared to DCMR alone regarding the extent of stress-induced ischemia [51]. The combined spoiled gradient-echo and tagged gradient-echo DCMR protocol at 3.0 T has shown increased sensitivity [52]. DCMR and late gadolinium enhancement imaging at 1.0 T high-field open non-cylindrical system was found to be an accurate and sedation-saving method in obese or claustro-

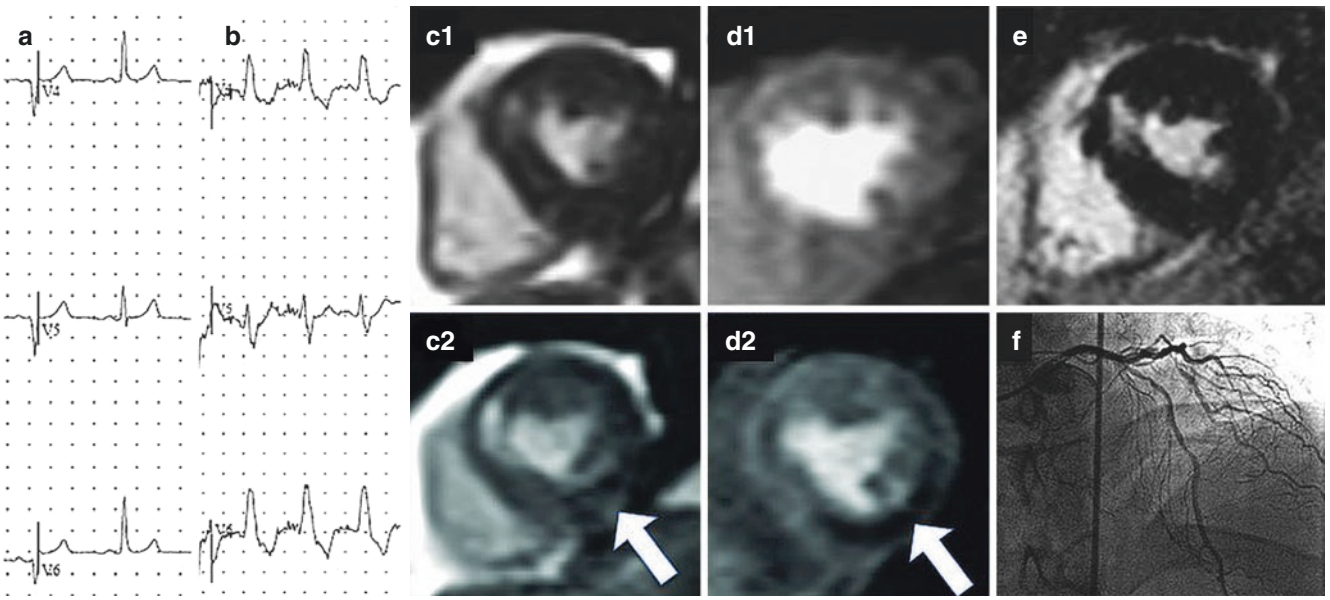

Fig. 11.3 A 60-year-old male with known coronary artery disease and atypical chest pain underwent treadmill stress cardiac MRI. Baseline 12-lead electrocardiography showed no abnormalities (**a**), but left bundle branch block developed with exercise (**b**). Rest vs. post-exercise end-systolic cine frames (**c-1** and **c-2**, respectively) and rest vs. post-exercise perfusion images (**d-1** and **d-2**, respectively) show the development of an inferolateral wall motion abnormality accompanied by stress-induced perfusion defect. The region of inducible ischemia showed no infarct scar on late gadolinium enhancement imaging (**e**), though old infarct scar in the anteroseptum is seen. Invasive angiography (**f**) showed high-grade stenosis of the left anterior descending coronary artery that supplied an occluded right coronary artery, prompting coronary revascularization

phobic patients [53]. With increased availability of stress CMR centers, pharmacologic and physiologic stress testing combined with high-resolution imaging of cardiac structure and function offers improved diagnosis and risk stratification of patients with known or suspected cardiovascular disease.

References

1. Pennell DJ, Underwood SR, Manzara CC, Swanton RH, Walker JM, et al. Magnetic resonance imaging during dobutamine stress in coronary artery disease. Am J Cardiol. 1992;70:34–40.
2. Jekic M, Foster EL, Ballinger MR, Raman SV, Simonetti OP. Cardiac function and myocardial perfusion immediately following maximal treadmill exercise inside the mri room. J Cardiovasc Magn Reson. 2008;10:3.
3. Charoenpanichkit C, Hundley WG. The 20 year evolution of dobutamine stress cardiovascular magnetic resonance. J Cardiovasc Magn Reson. 2010;12:59.
4. Raman SV. Color atlas and synopsis of cardiovascular mr and ct. New York: McGraw-Hill; 2014.
5. Schalla S, Klein C, Paetsch I, Lehmkuhl H, Bornstedt A, Schnackenburg B, et al. Real-time mr image acquisition during high-dose dobutamine hydrochloride stress for detecting left ventricular wall-motion abnormalities in patients with coronary arterial disease. Radiology. 2002;224:845–51.
6. Jahnke C, Paetsch I, Gebker R, Bornstedt A, Fleck E, Nagel E. Accelerated 4d dobutamine stress mr imaging with k-t blast: feasibility and diagnostic performance. Radiology. 2006;241:718–28.
7. Kuijpers D, Ho KY, van Dijkman PR, Vliegenthart R, Oudkerk M. Dobutamine cardiovascular magnetic resonance for the detection of myocardial ischemia with the use of myocardial tagging. Circulation. 2003;107:1592–7.
8. Paetsch I, Foll D, Kaluza A, Luechinger R, Stuber M, Bornstedt A, et al. Magnetic resonance stress tagging in ischemic heart disease. Am J Physiol Heart Circ Physiol. 2005;288:H2708–14.
9. Korosoglou G, Lehrke S, Wochele A, Hoerig B, Lossnitzer D, Steen H, et al. Strain-encoded cmr for the detection of inducible ischemia during intermediate stress. JACC Cardiovasc Imaging. 2010;3:361–71.
10. Braunwald E. Control of myocardial oxygen consumption: physiologic and clinical considerations. Am J Cardiol. 1971;27:416–32.
11. Iskandrian AS, Verani MS, Heo J. Pharmacologic stress testing: mechanism of action, hemodynamic responses, and results in detection of coronary artery disease. J Nucl Cardiol. 1994;1:94–111.
12. Pennell DJ, Underwood SR. The cardiovascular effects of dobutamine assessed by magnetic resonance imaging. Postgrad Med J. 1991;67(Suppl 1):S1–8; discussion S8-9
13. Warltier DC, Zyvoloski M, Gross GJ, Hardman HF, Brooks HL. Redistribution of myocardial blood flow distal to a dynamic coronary arterial stenosis by sympathomimetic amines: comparison of dopamine, dobutamine and isoproterenol. Am J Cardiol. 1981;48:269–79.
14. Ruffolo RR Jr. The pharmacology of dobutamine. Am J Med Sci. 1987;294:244–8.
15. Kramer CM, Barkhausen J, Flamm SD, Kim RJ, Nagel E, Society for Cardiovascular Magnetic Resonance Board of Trustees Task Force on Standardized P. Standardized cardiovascular magnetic resonance (cmr) protocols 2013 update. J Cardiovasc Magn Reson. 2013;15:91.

16. McNeill AJ, Fioretti PM, el-Said SM, Salustri A, Forster T, Roelandt JR. Enhanced sensitivity for detection of coronary artery disease by addition of atropine to dobutamine stress echocardiography. Am J Cardiol. 1992;70:41–6.
17. Geleijnse ML, Fioretti PM, Roelandt JR. Methodology, feasibility, safety and diagnostic accuracy of dobutamine stress echocardiography. J Am Coll Cardiol. 1997;30:595–606.
18. Lubbers DD, Janssen CH, Kuijpers D, van Dijkman PR, Overbosch J, et al. The additional value of first pass myocardial perfusion imaging during peak dose of dobutamine stress cardiac mri for the detection of myocardial ischemia. Int J Cardiovasc Imaging. 2008;24:69–76.
19. Hendel RC, Patel MR, Kramer CM, Poon M, Hendel RC, Carr JC, et al. American College of Cardiology Foundation Quality Strategic Directions Committee Appropriateness Criteria Working G, American College of R, Society of Cardiovascular Computed T, Society for Cardiovascular Magnetic R, American Society of Nuclear C, North American Society for Cardiac I, Society for Cardiovascular A, Interventions, Society of Interventional R. Accf/acr/scct/scmr/asnc/nasci/scai/sir 2006 appropriateness criteria for cardiac computed tomography and cardiac magnetic resonance imaging: A report of the american college of cardiology foundation quality strategic directions committee appropriateness criteria working group, American College of radiology, society of cardiovascular computed tomography, society for cardiovascular magnetic resonance, american society of nuclear cardiology, North American society for cardiac imaging, society for cardiovascular angiography and interventions, and society of interventional radiology. J Am Coll Cardiol. 2006;48:1475–97.
20. Nagel E, Lorenz C, Baer F, Hundley WG, Wilke N, Neubauer S, et al. Stress cardiovascular magnetic resonance: consensus panel report. J Cardiovasc Magn Reson. 2001;3:267–81.
21. Wahl A, Paetsch I, Gollesch A, Roethemeyer S, Foell D, Gebker R, et al. Safety and feasibility of high-dose dobutamine-atropine stress cardiovascular magnetic resonance for diagnosis of myocardial ischaemia: experience in 1000 consecutive cases. Eur Heart J. 2004;25(14):1230–6.
22. Pedone C, Bax JJ, van Domburg RT, Rizzello V, Biagini E, Schinkel AF, et al. Long-term prognostic value of ejection fraction changes during dobutamine-atropine stress echocardiography. Coron Artery Dis. 2005;16:309–13.
23. Cerqueira MD, Weissman NJ, Dilsizian V, Jacobs AK, Kaul S, Laskey WK, et al. Standardized myocardial segmentation and nomenclature for tomographic imaging of the heart: a statement for healthcare professionals from the cardiac imaging committee of the council on clinical cardiology of the American Heart Association. Circulation. 2002;105:539–42.
24. Baer FM, Theissen P, Smolarz K, Voth E, Sechtem U, et al. Dobutamine versus dipyridamole magnetic resonance tomography: safety and sensitivity in the detection of coronary stenoses. Z Kardiol. 1993;82:494–503.
25. van Rugge FP, van der Wall EE, de Roos A, Bruschke AV. Dobutamine stress magnetic resonance imaging for detection of coronary artery disease. J Am Coll Cardiol. 1993;22:431–9.
26. van Rugge FP, van der Wall EE, Spanjersberg SJ, de Roos A, Matheijssen NA, Zwinderman AH, et al. Magnetic resonance imaging during dobutamine stress for detection and localization of coronary artery disease. Quantitative wall motion analysis using a modification of the centerline method. Circulation. 1994;90:127–38.
27. Nagel E, Lehmkuhl HB, Bocksch W, Klein C, Vogel U, Frantz E, et al. Noninvasive diagnosis of ischemia-induced wall motion abnormalities with the use of high-dose dobutamine stress mri: comparison with dobutamine stress echocardiography. Circulation. 1999;99:763–70.
28. Bikiri E, Mereles D, Voss A, Greiner S, Hess A, Buss SJ, et al. Dobutamine stress cardiac magnetic resonance versus echocardiography for the assessment of outcome in patients with suspected or known coronary artery disease. Are the two imaging modalities comparable? Int J Cardiol. 2014;171:153–60.
29. Hundley WG, Hamilton CA, Thomas MS, Herrington DM, Salido TB, Kitzman DW, et al. Utility of fast cine magnetic resonance imaging and display for the detection of myocardial ischemia in patients not well suited for second harmonic stress echocardiography. Circulation. 1999;100:1697–702.
30. Wahl A, Paetsch I, Roethemeyer S, Klein C, Fleck E, Nagel E. High-dose dobutamine-atropine stress cardiovascular mr imaging after coronary revascularization in patients with wall motion abnormalities at rest. Radiology. 2004;233:210–6.
31. Mordi I, Stanton T, Carrick D, McClure J, Oldroyd K, et al. Comprehensive dobutamine stress cmr versus echocardiography in lbbb and suspected coronary artery disease. JACC Cardiovasc Imaging. 2014;7:490–8.
32. Paetsch I, Jahnke C, Wahl A, Gebker R, Neuss M, et al. Comparison of dobutamine stress magnetic resonance, adenosine stress magnetic resonance, and adenosine stress magnetic resonance perfusion. Circulation. 2004;110:835–42.
33. Nandalur KR, Dwamena BA, Choudhri AF, Nandalur MR, Carlos RC. Diagnostic performance of stress cardiac magnetic resonance imaging in the detection of coronary artery disease: a meta-analysis. J Am Coll Cardiol. 2007;50:1343–53.
34. Paetsch I, Jahnke C, Ferrari VA, Rademakers FE, Pellikka PA, Hundley WG, et al. Determination of interobserver variability for identifying inducible left ventricular wall motion abnormalities during dobutamine stress magnetic resonance imaging. Eur Heart J. 2006;27:1459–64.
35. Syed MA, Paterson DI, Ingkanisorn WP, Rhoads KL, Hill J, et al. Reproducibility and inter-observer variability of dobutamine stress cmr in patients with severe coronary disease: implications for clinical research. J Cardiovasc Magn Reson. 2005;7:763–8.
36. Hundley WG, Morgan TM, Neagle CM, Hamilton CA, Rerkpattanapipat P, Link KM. Magnetic resonance imaging determination of cardiac prognosis. Circulation. 2002;106:2328–33.
37. Hundley WG, Rerkpattanapipat P, Little WC, Link KM, Morgan TM. Relation of cardiac prognosis to segment location with apical left ventricular ischemia. Am J Cardiol. 2003;92:1206–8.
38. Rerkpattanapipat P, Morgan TM, Neagle CM, Link KM, Hamilton CA, Hundley WG. Assessment of preoperative cardiac risk with magnetic resonance imaging. Am J Cardiol. 2002;90:416–9.
39. Kuijpers D, van Dijkman PR, Janssen CH, Vliegenthart R, Zijlstra F, Oudkerk M. Dobutamine stress mri. Part ii. Risk stratification with dobutamine cardiovascular magnetic resonance in patients suspected of myocardial ischemia. Eur Radiol. 2004;14:2046–52.
40. Jahnke C, Nagel E, Gebker R, Kokocinski T, Kelle S, Manka R, et al. Prognostic value of cardiac magnetic resonance stress tests: adenosine stress perfusion and dobutamine stress wall motion imaging. Circulation. 2007;115:1769–76.
41. Go AS, Mozaffarian D, Roger VL, Benjamin EJ, Berry JD, Borden WB, et al. American Heart Association Statistics C, Stroke Statistics S. Heart disease and stroke statistics – 2013 update: a report from the American Heart Association. Circulation 2013;127:e6–e245.
42. Shaw LJ, Bairey Merz CN, Pepine CJ, Reis SE, Bittner V, Kelsey SF, et al. Investigators W. Insights from the nhlbi-sponsored women's ischemia syndrome evaluation (wise) study: part i: gender differences in traditional and novel risk factors, symptom evaluation, and gender-optimized diagnostic strategies. J Am Coll Cardiol 2006;47:S4–S20.
43. Gebker R, Jahnke C, Hucko T, Manka R, Mirelis JG, Hamdan A, et al. Dobutamine stress magnetic resonance imaging for the detection of coronary artery disease in women. Heart. 2010;96:616–20.

44. Raman SV, Donnally MR, McCarthy B. Dobutamine stress cardiac magnetic resonance imaging to detect myocardial ischemia in women. Prev Cardiol. 2008;11:135–40.
45. Wallace EL, Morgan TM, Walsh TF, Dall'Armellina E, Ntim W, et al. Dobutamine cardiac magnetic resonance results predict cardiac prognosis in women with known or suspected ischemic heart disease. JACC Cardiovasc Imaging. 2009;2:299–307.
46. Gebker R, Jahnke C, Manka R, Hamdan A, Schnackenburg B, et al. Additional value of myocardial perfusion imaging during dobutamine stress magnetic resonance for the assessment of coronary artery disease. Circ Cardiovasc Imaging. 2008;1:122–30.
47. Roest AA, Kunz P, Lamb HJ, Helbing WA, van der Wall EE, de Roos A. Biventricular response to supine physical exercise in young adults assessed with ultrafast magnetic resonance imaging. Am J Cardiol. 2001;87:601–5.
48. Rerkpattanapipat P, Gandhi SK, Darty SN, Williams RT, Davis AD, Mazur W, et al. Feasibility to detect severe coronary artery stenoses with upright treadmill exercise magnetic resonance imaging. Am J Cardiol. 2003;92:603–6.
49. Raman SV, Dickerson JA, Jekic M, Foster EL, Pennell ML, et al. Real-time cine and myocardial perfusion with treadmill exercise stress cardiovascular magnetic resonance in patients referred for stress spect. J Cardiovasc Magn Reson. 2010;12:41.
50. Thavendiranathan P, Dickerson JA, Scandling D, Balasubramanian V, Pennell ML, Hinton A, et al. Comparison of treadmill exercise stress cardiac mri to stress echocardiography in healthy volunteers for adequacy of left ventricular endocardial wall visualization: a pilot study. J Magn Reson Imaging. 2014;39:1146–52.
51. Gebker R, Berger A, Schneeweis C, Hucko T, Schnackenburg B, Klein C, et al. High-dose dobutamine stress magnetic resonance perfusion imaging at 3.0 tesla. Abstracts of the 16th Annual SCMR Scientific Sessions. 2013.
52. Thomas D, Meyer C, Strach K, Naehle CP, Mazraeh J, Gampert T, et al. Dobutamine stress tagging and gradient-echo imaging for detection of coronary heart disease at 3 t. Br J Radiol. 2011;84:44–50.
53. Petry PG, Lossnitzer D, Haberkorn SM, aus dem Siepen F, Seitz SA, et al. Feasibility of high dose dobutamine stress and scar imaging in high field open mri in patients with suspected coronary artery disease. Abstracts of the 16th Annual SCMR Scientific Sessions. 2013.

12 Myocardial Perfusion and Late Gadolinium Enhancement Imaging in Cardiovascular Magnetic Resonance to Assess Coronary Artery Disease

Andrew E. Arai and Li-Yueh Hsu

Introduction

Cardiovascular magnetic resonance (CMR) is a well-established imaging modality in assessing patients with coronary artery disease. In a relatively short examination, CMR can provide in high image quality, information about myocardial anatomy, function, perfusion, and viability. These are all critical elements in the diagnosis and management of coronary artery disease. These parameters can be acquired with high image quality by CMR. Cine CMR is an excellent method for assessing left ventricular anatomy and function. A gadolinium-enhanced CMR first-pass study can assess rest and stress perfusion. Late gadolinium enhancement (LGE) imaging is currently the most validated modality in assessing for the presence and size of chronic myocardial infarction. In patients presenting with acute symptoms, imaging of myocardial edema by incorporating T1-weighted or T2-weighted imaging can estimate the acuteness of the myocardial infarction. This chapter describes imaging of myocardial perfusion and chronic infarction in a unified context based on the concept that unique physiological information can be extracted from different time periods after gadolinium contrast injection.

Characteristics of Gadolinium Contrast as Perfusion and Fibrosis Agents in Cardiovascular Magnetic Resonance

Myocardial enhancement represents the amount the myocardium brightens on the perfusion images. While it would be easy to discuss perfusion if the myocardium enhanced proportionately with myocardial perfusion, the physics of T1-weighted imaging and the physiology of the commonly used gadolinium contrast agents are complex. Thus, the reader will be encouraged to learn about factors that alter the relationship between signal intensity and gadolinium contrast agent concentration.

Theoretically, there are two types of contrast agents that make ideal perfusion tracers. One form of ideal perfusion tracer is characterized as intravascular, meaning it is restricted to the intravascular space. Large particles like radioactive-labeled red blood cells are intravascular agents. Since these agents are physically restricted to the intravascular space, they are inherently perfusion agents but are also indicators of the intramyocardial vascular volume. Gadofosveset is the only gadolinium-based contrast agent with approval from the US Food and Drug Administration that is described as an intravascular contrast agent. After intravenous injection, gadofosveset rapidly combines with albumen which is a large enough protein to keep significant amounts of the agent in the blood pool. This characteristic is good for magnetic resonance angiography [1, 2]. However, a significant fraction of gadofosveset leaks into the interstitial space of myocardium, making it less than ideal for myocardial perfusion imaging [3].

Alternatively, a contrast agent that is completely extracted on the first passage through the heart is also ideal for perfusion. The classic example of complete extraction is the 15 micron plastic microsphere used in physiology experiments. Microspheres of this size exhibit about 99% extraction during the first passage through the myocardium as they are about 3 times the diameter of red blood cells and are too large and inflexible to pass through myocardial capillaries. Thus, the distribution of microspheres is almost completely dependent on perfusion, and their distribution is 99% representative of first-pass delivery of the microspheres to the myocardium. Currently, no completely extracted contrast agents are approved for use in humans.

Unfortunately, most commonly used gadolinium-based contrast agents are called extracellular contrast agents [4]. These contrast agents are injected intravenously but rapidly

A. E. Arai (✉) · L.-Y. Hsu
National Institutes of Health, National Heart, Lung and Blood Institute, Bethesda, MD, USA
e-mail: araia@nih.gov; lyhsu@nih.gov

R. Y. Kwong et al. (eds.), *Cardiovascular Magnetic Resonance Imaging*, Contemporary Cardiology,
https://doi.org/10.1007/978-1-4939-8841-9_12

traverse capillaries and enter the interstitial space. Thus, they are neither intravascular nor completely extracted. This intermediate characteristic is not ideal from the perspective of simple perfusion analysis. This type of perfusion tracer may benefit from analytic models that address both perfusion and interstitial loading. The following contrast agents are considered extracellular agents: gadopentetate dimeglumine, gadodiamide, gadoterate meglumine, gadoteridol, gadobutrol, gadobenate dimeglumine, and gadoversetamide.

While the extracellular contrast agents may be less than ideal for simple perfusion analysis, the extracellular contrast agents are well suited to imaging myocardial infarction [5, 6], nonischemic myocardial fibrosis [7], and diffuse increases in the extracellular volume fraction [8]. The volume of distribution or partition coefficient for gadolinium in infarcted myocardium is much higher than in normal myocardium. In simple terms, there is more gadolinium contrast agent per gram of infarcted myocardium relative to normal myocardium (Fig. 12.1). This relative difference in the amount of gadolinium is true for both acute and chronic myocardial infarction. Thus, on most CMR images of myocardial infarction, the fibrotic scar is bright or "hyperenhanced" relative to normal myocardium. In the best validated methodology, the acquisition parameters are individually adjusted to make normal myocardium appear dark [9]. The time from about 10–30 min after contrast administration is extremely useful for imaging myocardial infarction and other forms of myocardial fibrosis.

Three Time Periods of Myocardial Enhancement After Injection of Contrast

If extracellular contrast agents are less than ideal for simple perfusion imaging but good for fibrosis imaging, one might ask how these agents can be used for both purposes. Conceptually, myocardial enhancement after a bolus injection of gadolinium contrast agents is determined by both perfusion and accumulation of gadolinium in the myocardial interstitial space and such enhancement is influenced by different time periods after the injection. Simplistically, there are three different time periods during and after contrast enhancement: first-pass perfusion, early gadolinium enhancement, and late gadolinium enhancement (Fig. 12.2).

The first pass of contrast through the myocardium is most dependent on perfusion. In a patient with normal cardiac out-

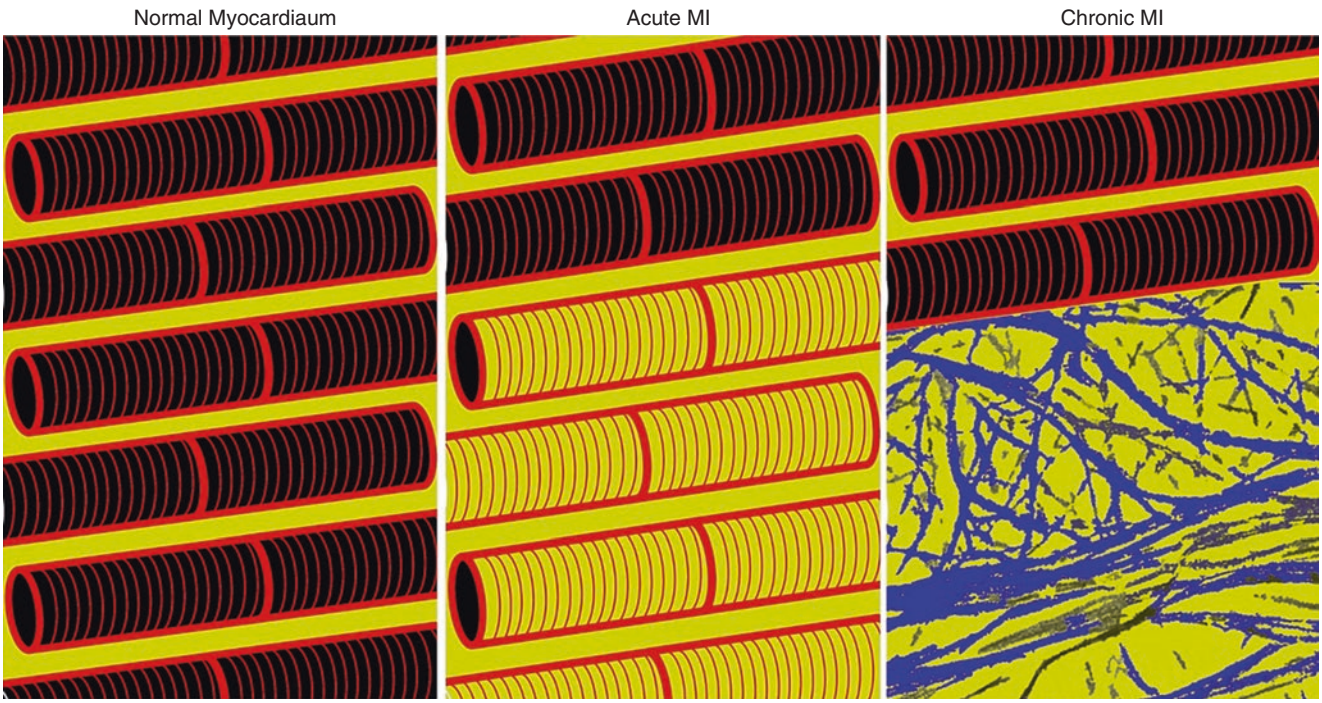

Fig. 12.1 Gadolinium enhancement of normal myocardium, acute myocardium infarction, and chronic myocardial infarction. Even though viable myocardium appears dark on late gadolinium-enhanced images, there is actually a significant amount of gadolinium in the myocardium. In normal myocardium, the gadolinium is restricted to the interstitial space and the intravascular space, which combined are termed the extracellular space. The gadolinium contrast agents are excluded from the intracellular space by intact cell membranes. In acute myocardial infarction (MI), ruptured cell membranes allow gadolinium into what used to the intracellular space. Thus, acutely infarcted myocardium enhances to a greater degree than normal myocardium. The cells and interstitial space in the acute MI diagram are increased by 10% to represent myocardial edema. In the case of chronic MI, the collage replacement scar enhances more than the normal myocardium since there are relatively few cells in this type of fibrosis and a greater extracellular volume where gadolinium can accumulate. In this diagram, red represents cardiomyocytes, blue represents collagen scar and fibroblasts, and yellow represents where extracellular contrast agents accumulate

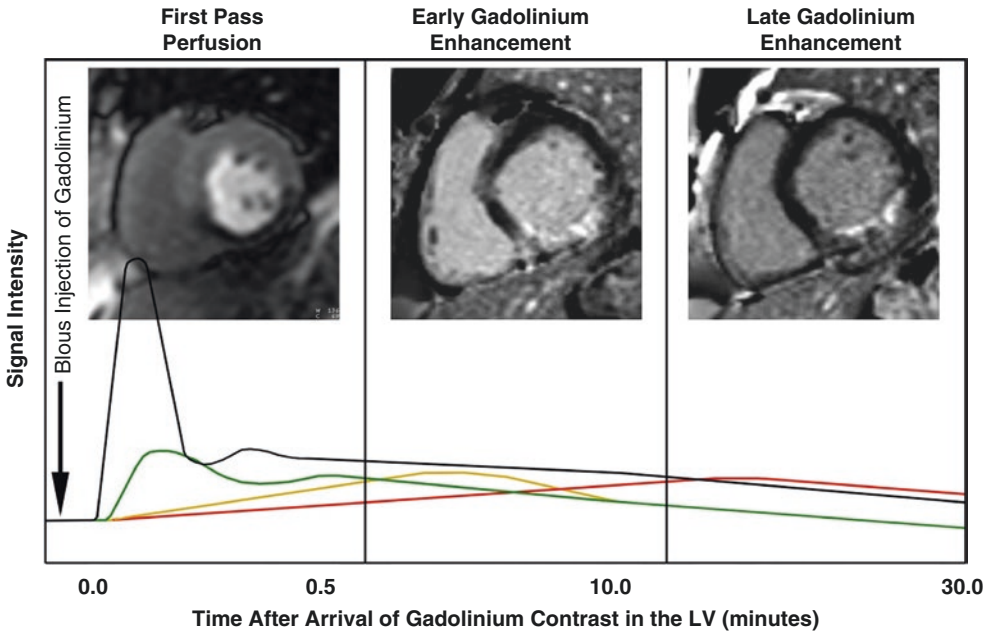

Fig. 12.2 Three physiologically relevant time periods after injection of gadolinium contrast agents. Images acquired during the first approximately 15–30 s after arrival of contrast in the left ventricle are most dependent on perfusion. Late gadolinium-enhanced images are generally acquired 10–30 min after contrast and detect myocardial infarction and other forms of myocardial scar. Between 1 and about 10 min after injection of contrast, early gadolinium enhancement images exhibit a mixture of characteristics including perfusion (late perfusion?), edema, and vascularity. In this example, the perfusion images were from one patient, while the other images are from a different patient. The signal intensity as a function of time is plotted at the bottom of the figure for the left ventricular cavity (black line), normal myocardium (green line), ischemic myocardium (orange line), and infarcted myocardium (red line)

put, first-pass perfusion lasts about 20–40 s. Early gadolinium enhancement (EGE) roughly occurs between about a minute after contrast arrival in the myocardium to about 10 min after contrast administration. EGE represents a combination of perfusion, hypervascularity, and partial loading of gadolinium into the interstitial space. EGE is a time period that is not fully understood; there are relatively fewer studies of EGE compared with first-pass perfusion or late gadolinium enhancement studies.

Eventually, the late gadolinium enhancement (LGE) within the myocardium approaches a pseudo-steady state relative to gadolinium concentration in the blood. The term pseudo-steady state refers to the gradual and continuous renal clearance of gadolinium contrast agents from the blood. Simultaneously, there is a nearly balanced exchange of contrast concentration between the blood and the interstitial space. At that stage, the gadolinium concentrations generally represent the extracellular volume fraction which represents vascular space and the interstitial space. LGE primarily represents loading of gadolinium into the extracellular space but can still be influenced by severe perfusion abnormalities. Most importantly, LGE images are a powerful method for imaging myocardial infarction and other forms of myocardial fibrosis. In situations with extremely low perfusion, parts of the myocardium can appear darker than surrounding strongly enhanced myocardium. The most common situation where low perfusion modulates enhancement is called microvascular obstruction (MVO). In the setting of recent and reperfused acute myocardial infarction, despite bright enhancement of most of the myocardial infarction, there may be dark areas within the infarct which result from such low perfusion that contrast could not penetrate that area by the time LGE imaging was performed.

Finally, the three time periods are not completely distinct due to overlap in the physiological processes, but they are still useful clinically as different information can be determined from these three time periods after contrast administration. To extract the information encoded in different time periods after contrast injection, the field has developed distinct methodologies optimized for either perfusion imaging of myocardial ischemia or LGE imaging of myocardial infarction. These methods are variations on T1-weighted images. The various methods will be described in the individual sections that follow.

Principles of Imaging Contrast-Enhanced First-Pass Perfusion

First-pass perfusion imaging and LGE imaging are both T1-weighted methods which share many similarities in basic MRI physics. Although CMR can image myocardial perfu-

sion with many methods, first-pass perfusion studies using gadolinium contrast have the highest signal-to-noise ratio and the most extensive published experience for different clinical applications.

The fundamental principle of first-pass perfusion imaging is relatively simple. A series of T1-weighted images are acquired as an intravenous bolus of contrast traverses the cardiac chambers and perfuses through the myocardium. While the image acquisition techniques continue to evolve, the most common protocols acquire at least three short axis slices of the left ventricle every heartbeat or every other heartbeat. This provides perfusion information in 16 of the 17 sectors summarized by the AHA 17-segment model [10]. Newer approaches have shown promise with three-dimensional acquisition methods that offer more complete cardiac coverage [11–13].

Typically, a saturation prepared T1-weighted image acquisition sequence [14] is used to acquire the first-pass perfusion images. Since normal myocardium has a relatively long native or pre-contrast myocardial T1, myocardium appears dark on T1-weighted perfusion images prior to the arrival of contrast (Fig. 12.3). Blood has an even longer native T1 than myocardium, so it appears dark on perfusion images prior to the arrival of contrast in the cardiac chambers. Fat around the heart is brighter due to the inherently shorter T1 unless one adds a fat suppression pulse to reduce its signal intensity.

Because gadolinium-based contrast agents primarily reduce T1 of the blood or tissue, the cardiac chambers and myocardium will become brighter on the perfusion images when contrast arrives. The change in signal intensity is related to but not linearly proportional to the amount of contrast in the blood or myocardium. An intravenous injection of contrast arrives in the right ventricle first, so this cardiac chamber enhances while the left side of the heart remains dark (Fig. 12.3). After the bolus of contrast traverses the lungs, the left ventricular cavity starts to enhance. Notice that the LV myocardium remains dark at that time. The LV myocardium begins to brighten one or two heartbeats after the LV cavity due to the time it takes contrast to enter the aorta and course down the coronaries into the myocardium. While most of the myocardium enhances to a relatively uniform gray signal intensity, the perfusion defect remains darker because contrast arrives more slowly (Fig. 12.3, red arrows).

Diagnosis of Coronary Artery Disease with Stress Perfusion

Clinical Interpretation of Stress Perfusion Studies

The majority of clinical CMR first-pass perfusion scans are interpreted qualitatively. Three patients' scans are summarized in Fig. 12.4 to illustrate the relative contributions of cine CMR, perfusion, and LGE imaging. To start with the most simplistic level of describing the images, the cine CMR can be interpreted in a way that is analogous to 2-D echocardiography with respect to wall motion abnormalities and global left ventricular function. On properly acquired LGE images, the viable myocardium appears close to black, while areas of myocardial infarction appear bright, typically as

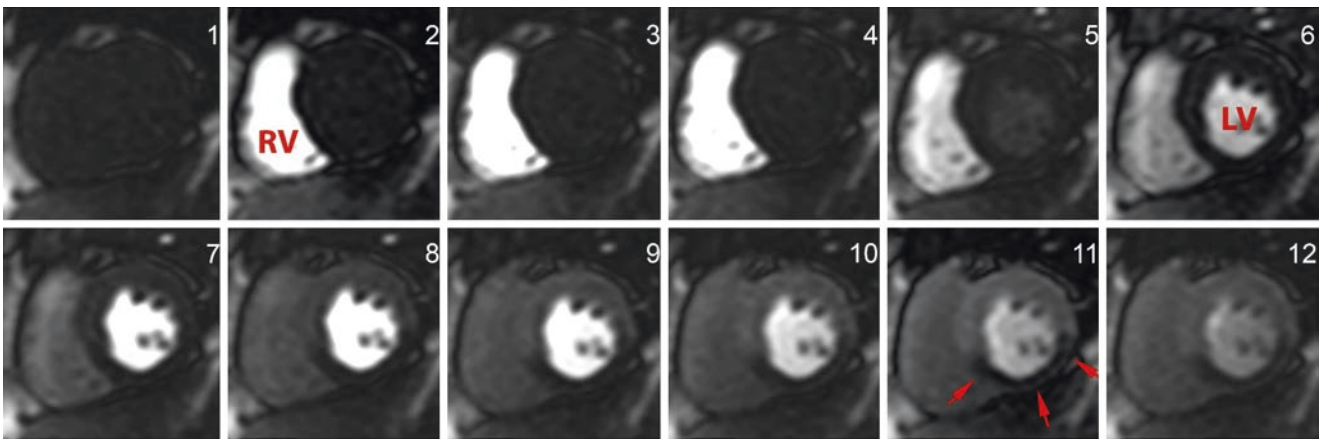

Fig. 12.3 Dipyridamole stress first-pass perfusion study in a patient with severe right coronary artery disease and no myocardial infarction. Prior to contrast arrival in the heart, the myocardium and blood appears dark (first frame). When contrast arrives in the right ventricular (RV) cavity, the blood becomes very bright. After contrast traverses the pulmonary circulation, the left ventricular (LV) cavity starts to enhance. Over the course of the subsequent approximately 12 heartbeats, the well-perfused myocardium enhances to an intermediate gray. Red arrows point to a dark perfusion defect in the inferior wall of the left ventricular myocardium. The perfusion defect appears dark as contrast arrives more slowly into this part of the myocardium, and thus there is less contrast than the other coronary territories. This patient had severe right coronary stenosis but no myocardial infarction. This figure includes 12 of the 60 images acquired including every other image after LV cavity enhancement. The numbers on each image represent time order (not sequential images)

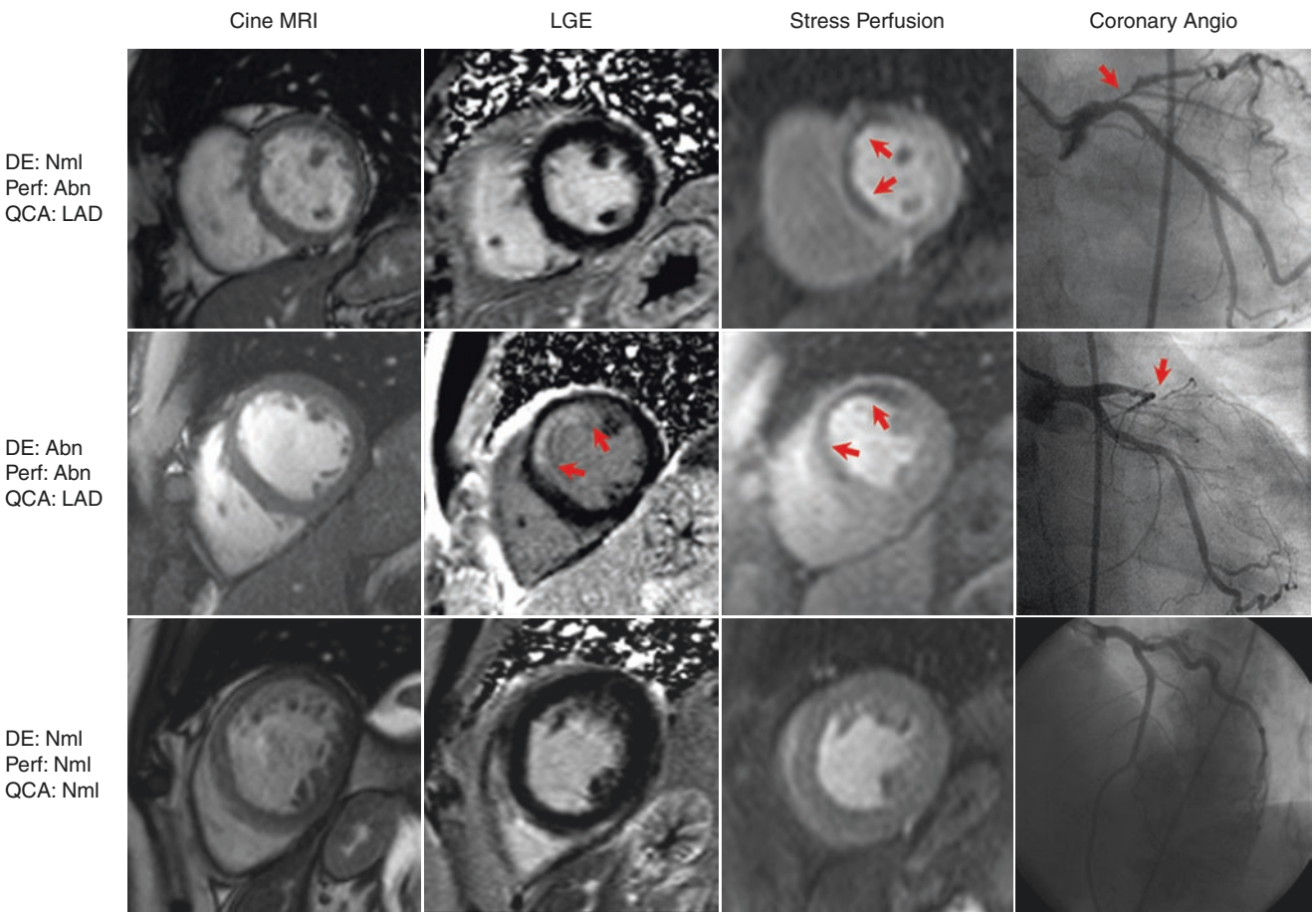

Fig. 12.4 Three different examples of CMR stress perfusion scans in patients. The top row summarizes a patient with a severe stenosis in the left anterior descending coronary artery (LAD) as seen on the invasive coronary angiogram (arrow). There is abnormal stress perfusion (double arrows). The LGE image is uniformly dark consistent with no myocardial infarction. Thus, this first patient has a stress-induced perfusion defect in the absence of myocardial infarction. The second row summarizes a patient with an occluded LAD. This caused a subendocardial myocardial infarction as seen on the LGE images. The arrows point to the circumferential extent of the myocardial infarction. The stress perfusion images show a defect in the anteroseptum, the anterior wall, and the anterolateral wall which is more extensive than the myocardial infarction. Thus, this case represents inducible perfusion defects around the infarct. The bottom row summarizes a normal stress perfusion with normal LGE images. (Adapted and reprinted with permission from Mordini et al. [15], with permission from Elsevier)

bright as or brighter than the blood. Myocardial infarctions typically start at the endocardial border of the myocardium and involve a variable percent of the wall thickness within that coronary distribution. The CMR terminology is to describe the "transmural" extent of infarction across the left ventricular wall. On first-pass perfusion images acquired around the time of peak myocardial enhancement, well-perfused myocardium appears gray, while perfusion defects are darker. Perfusion defects are also typically most severe near the endocardial border with the blood pool and sometimes are severe enough to involve the whole thickness of the left ventricular wall. Myocardial infarctions and perfusion defects due to coronary artery disease tend to follow typical coronary artery distributions except in patients that have had bypass surgery or have a coronary artery anomaly.

The first patient in Fig. 12.4 has normal left ventricular function on cine CMR, no myocardial infarction on the LGE images, but has a perfusion defect on the stress perfusion images. This corresponds to a severe stenosis in the left anterior descending (LAD) coronary artery on invasive coronary angiography. The red arrows point to the darker color stress perfusion defect on the midventricular short axis image. The perfusion defect involves the anteroseptum and the anterior wall at this level which is consistent with the stenosis in the LAD stenosis. Importantly, the myocardium looks uniformly black consistent with viable myocardium. This patient does not have a myocardial infarction. The ability to register all three CMR imaging methods is an important characteristic for helping conclude this is a case of inducible ischemia without myocardial infarction.

The second patient in Fig. 12.4 has both a subendocardial myocardial infarction and a stress-induced perfusion defect in the LAD distribution. These abnormalities correspond to an occluded LAD on invasive coronary angiography with the

distal LAD filling via collaterals. One could not know the extent of the myocardial infarction from the occluded coronary artery on the coronary angiogram. There are a few characteristics of these CMR images that provide important insight into the pathophysiological status of the patient. First, the LGE as shown by the red arrows is limited to the inner layers of the anteroseptum and the anterior wall but spares some of the epicardial layers. This is not a transmural MI despite a completely occluded LAD. Clearly this MI is within the LAD distribution. The stress perfusion defect has a greater circumferential extent than the myocardial infarction. When the perfusion defect has a greater circumferential extent than the infarction, there must be an inducible defect beyond the border of the infarct. If the perfusion defect has the same circumferential extent as the infarct, then it can be harder to determine whether there is inducible ischemia on a single frame assessment of myocardial perfusion. However, the fact that the transmural extent of LGE only extends about halfway from the endocardium to epicardium is an indicator that the remainder of the wall is viable. Viable myocardium downstream from a severe stenosis could also explain residual inducible ischemia.

The final images are from a patient with a mild, nonischemic dilated cardiomyopathy (Fig. 12.4). The LV cavity is mildly dilated on the cine CMR. The LGE image is uniformly black consistent with viable myocardium and no myocardial infarction. The stress perfusion defect is uniformly gray suggesting no perfusion defects. The coronary angiography confirms the patient does not have epicardial coronary artery stenoses. While this case does illustrate a true negative stress perfusion study, one must always consider the possibility of an inadequate vasodilator response due to caffeine or other agents that might block the coronary vasodilatory response. The simple rest and stress perfusion images can look very similar, so one needs to consider ancillary analyses which will be discussed in the quantitative analysis section of this chapter.

Results from Clinical Trials

Since about 2007, there has been a gradual shift in the diagnosis and management of stable coronary artery disease. The Clinical Outcomes Utilizing Revascularization and Aggressive Drug Evaluation (COURAGE) trial found that percutaneous intervention (PCI) did not significantly improve patient outcomes relative to optimal medical therapy [16]. Adding PCI to optimal medical therapy seemed to reduce ischemia patients from the COURAGE study better than optimal medical therapy alone [17]. Thus, COURAGE led investigators to promote the concept that the amount of ischemic myocardium was important in the management of stable coronary artery disease. The FAME studies showed that patient outcomes improved when fractional flow reserve was used to determine whether an angiographic stenosis should undergo PCI [18–20]. Since fractional flow reserve is essentially a stenosis-specific quantitative vasodilator stress test during invasive coronary angiography, the challenge is for noninvasive tests to provide similar levels of information regarding the presence or absence of physiologically significant coronary stenoses.

While stress perfusion CMR has been validated against many standards, there has been a new wave of validation literature that used fractional flow reserve as the reference standard to determine the significance of coronary artery stenosis (Table 12.1) [21]. Overall, stress CMR perfusion had a sensitivity of 0.89, specificity of 0.89, positive predictive value of 0.87, negative predictive value of 0.87, and overall area under the curve (AUC) of 0.94 on a per patient basis for detecting physiologically significant coronary artery disease defined by invasive fractional flow reserve. Those statistics summarize 10 studies and a total of 798 patients.

In the same meta-analysis, stress perfusion positron emission tomography (PET) studies had similar diagnostic accuracy statistics as CMR. For PET, the sensitivity was 0.83, specificity was 0.89, and accuracy was 0.93 from 224

Table 12.1 Per patient diagnostic accuracy of stress perfusion CMR for coronary artery disease from recent studies that used invasively measured fractional flow reserve as the reference standard

Study	Year	# of patients	CAD (%)	Sensitivity	Specificity	PPV	NPV	Accuracy
Watkins [22]	2009	101	77	0.95	0.84	0.97	0.91	0.94
Bernhardt [23]	2012	34	62	0.90	0.87	1.00	1.00	0.94
Jogiya [12]	2012	53	64	0.91	0.85	0.94	0.89	0.91
Manka [13]	2012	120	58	0.90	0.86	0.87	0.82	0.87
Walcher [24]	2012	36	47	0.88	0.89	0.88	0.89	0.89
Bettencourt [25]	2013	103	44	0.89	0.91	0.85	0.88	0.88
Chiribiri [26]	2013	67	46	0.90	0.91	0.82	0.83	0.87
Groothuis [27]	2013	88	30	0.85	0.93	0.67	0.82	0.83
Pereira [28]	2013	80	46	0.81	0.85	0.91	0.93	0.88
Ebersberger [29]	2013	116	34	0.85	0.92	0.77	0.87	0.86
Total		798		0.89	0.89	0.87	0.87	0.88

Adapted from Takx et al. [21]

patients derived from 3 different publications [21]. On the other hand, single photon emission tomography (SPECT) myocardial perfusion imaging and stress echocardiography are performed at a lower level. SPECT had a sensitivity of 0.61, a specificity of 0.84, and an AUC of 0.83 as combined from 8 different studies that included a total of 533 patients. In 4 studies with 177 patients, stress echocardiography had a sensitivity of 0.69, specificity of 0.84, and AUC of 0.83. Thus, in clinical trials where invasive fractional flow reserve was used as the reference standard for defining physiologically significant coronary artery disease, stress perfusion CMR performs extremely well and compares quite favorable relative to more commonly used tests like SPECT and echocardiography.

Several clinical trials that did not use fractional flow reserve as a reference standard to define coronary artery disease warrant special mention. The CE-MARC study [30] aimed to determine the diagnostic accuracy of a multiparametric CMR protocol with X-ray coronary angiography as the reference standard in patients with suspected coronary heart disease. CE-MARC also specifically compared CMR with SPECT [31]. CE-MARC recruited 752 patients, and 39% had significant coronary artery disease. The sensitivity of CMR was 0.87, and positive predictive value of CMR was 0.77 and statistically better than 99mTc tetrofosmin which had a sensitivity of 0.67 and a positive predictive value of 0.71 ($p < 0.0001$ level for both comparisons). The specificity of CMR and SPECT was similar and not significantly different with 0.83 vs 0.83, respectively.

The MR-IMPACT [32] and MR-IMPACT II [33] studies are a little more difficult to interpret but are also important large multicenter clinical trials. MR-IMPACT was both a dose finding study as well as a diagnostic accuracy study using diameter stenosis of ≥50% by quantitative coronary angiography to define significant coronary artery disease. Between 45 and 50 patients were included in five different doses of gadodiamide (0.01, 0.025, 0.05, 0.075, and 0.10 mmol/kg). When the CMR analysis was restricted to the 42 participants with interpretable CMR studies done with the highest dose of contrast, the AUC was 0.86. By comparison, in those same 42 subjects, the AUC of SPECT was 0.75 ($p = 0.12$ vs CMR). The AUC for all interpretable SPECT scans ($n = 212$) was 0.67 vs CMR ($p = 0.013$). The lower doses of gadodiamide had similar AUC to SPECT. The small sample size of each dosing group is an important limitation of the results and could explain the nonsignificant difference in AUC in analysis restricted to the highest gadodiamide group. Overall, the diagnostic performance of SPECT was lower than experts expected, and methodological or quality assurance questions have been raised even though restricting analysis to patients that had gated SPECT ($n = 95$) did not change the results. The use of AUC was controversial for the US Food and Drug Administration. Regulatory agencies prefer binary results on a per patient basis and based on the interpretation of the individual studies, not a retrospective determination of an optimal cut point from receiver operating curve analysis. Despite possible criticisms, the field should recognize MR-IMPACT as an important multicenter perfusion trial that indicted that CMR perfusion imaging had better overall diagnostic accuracy than SPECT.

The MR-IMPACT II study results have been published in two different major papers [33, 34]. In brief, MR-IMPACT II was a multicenter ($n = 33$ US and European centers) study that enrolled 533 patients but only 515 received the CMR contrast agent (gadodiamide 0.075 mmol/kg). Adenosine stress CMR was again compared with SPECT for diagnostic accuracy of detecting patients with a reference standard of ≥50% diameter stenosis by quantitative coronary angiography in a non-inferiority design for both sensitivity and specificity. With regard to the primary endpoints, stress perfusion CMR had superior sensitivity than SPECT (0.67 vs 0.59, respectively, $p = 0.024$) but lower specificity than SPECT (0.61 vs 0.71, respectively, $p = 0.038$) [33]. In secondary analyses, stress perfusion CMR was superior to SPECT in a wide range of analyses [34]. With respect to AUC, CMR was superior to both SPECT overall (0.75 vs 0.65, respectively, $p = 0.0004$) and gated SPECT (0.75 vs 0.69, respectively, $p = 0.018$). CMR was also statistically better than SPECT in men, in women, in patients with multivessel disease, and in patients that did not have myocardial infarction. Thus, CMR outperformed SPECT in all metrics except the binary determination of specificity, one of the two primary endpoints.

Analysis of Contrast-Enhanced First-Pass Perfusion Imaging

Two of the clinical cases presented in Fig. 12.4 represent abnormalities that are obvious since they result from truly severe coronary stenoses. The normal perfusion images are relatively artifact-free and thus also easy to interpret. However, there are times when perfusion defects can be subtle. A deeper understanding of CMR physics and some consideration of first-pass perfusion physiology helps explain why signal intensity on CMR perfusion images is not linearly proportional to perfusion.

Figure 12.5 illustrates the expected signal intensity as a function of time after the 90° saturation pulse used to provide T1 weighting on the subsequent perfusion image. The most important characteristic of the recovery of signal intensity after a 90° saturation pulse is the exponential relationship describing signal intensity as a function of when the imaging is performed after the saturation pulse. More precisely, magnetization along the z-axis:

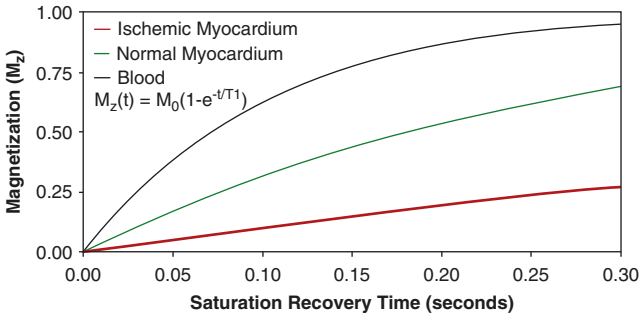

Fig. 12.5 Physics of saturation recovery as used for first-pass perfusion imaging

$$M_z(t) = M_0\left(1 - e^{-t/T1}\right)$$

$M_z(t)$ represents net magnetization at a given time (t) after the saturation pulse. One can think of $M_z(t)$ as the amount of signal one can get from an optimal imaging sequence at a point in time. A perfect 90° saturation pulse theoretically leaves no residual magnetization along the z-axis. Thus, if one were able to image immediately after the saturation pulse, there would be no signal. M_0 represents the maximum possible magnetization a long time after the saturation pulse (when the protons have had enough time to realign with the main magnetic field). The exponential term ($1–e^{-t/T1}$) determines how quickly the magnetization realigns with the main magnetic field. T1 is the spin-lattice relaxation time and is an exponential time constant that describes how quickly the protons realign with the main magnetic field. Here, the time "t" is sometimes described as T_{sat} (saturation recovery time) or TI (inversion time even though there might have been a saturation pulse rather than an inversion pulse) in different literatures. In summary, signal intensity on CMR perfusion images does not increase linearly with gadolinium concentration in the tissue. Instead, the signal intensity is modulated by an exponential relationship determined by the T1 of the blood or myocardium and imaging parameters.

Since the myocardium is composed of about 8–10% blood volume, the macroscopic concentration of gadolinium is roughly 10 times higher in the left ventricular cavity than the myocardium. While this description is an oversimplification since CMR signal intensities can be modulated by phenomena at microscopic levels, it does help one understand that the signal intensity in the blood cavity is typically not nearly as bright as one would expect for the much higher concentration of gadolinium in blood compared with myocardium. Depending on the dose of contrast used and the imaging parameters used, it is possible for the blood signal intensity to be 85% lower than expected [35]. In the myocardium, the effects are less severe but again are dependent on contrast concentrations and image acquisition parameters. For myocardial concentrations of gadopentetate dimeglumine around 1 mmol/kg, one can encounter 6.6–17.7% lower signal intensity than expected based solely on the T_{sat} selected for the image acquisition [36]. The implication of this concept is that the brightness on a perfusion image is not directly related to perfusion or even gadolinium concentration and that the brightest areas on the image may markedly underestimate gadolinium concentration, particularly in the blood pool.

Since the concentration of gadolinium in the blood and the myocardium is also modulated by transit times through the cardiac chambers and the pulmonary vasculature as well as cardiac function, there are physiological variables that further alter the relationships between signal intensity and perfusion that make relying on simple assessments of signal intensity imprecise. A final take home message from this section is that while the signal intensity is the easiest things to see on perfusion images, there are subtleties that make it possible to miss mild and possibly moderate perfusion defects if one only simply relies on signal intensities to interpret the images. This concept will be illustrated in practical terms in the next section of this chapter.

Semiquantitative and Fully Quantitative Analysis of Perfusion

While most clinical stress perfusion cases are interpreted qualitatively by physicians looking at a series of images in an animated sequence and/or as individual raw images, there are potential advantages to quantitative measurements generated from the images that relate to perfusion. Quantitative and semiquantitative analyses can be performed using many methods, but almost all are dependent on the measurement of signal intensities from different parts of the image as a function of time during the first pass of contrast through the heart. Figure 12.6 summarizes measurements of the signal intensity in the normal or remote myocardium versus an ischemic territory. In this example with a severe coronary stenosis in the right coronary artery, the normal and ischemic curves separate during the first few beats of myocardial enhancement and remain separated throughout the perfusion scan. Quantification is not needed to detect such severe abnormalities.

However, perfusion defects are more difficult to appreciate with less severe coronary stenoses. In controlled experiments, moderate perfusion defects can exhibit subtle differences in signal intensity compared with the severity of blood flow abnormalities [37]. The top row of Fig. 12.7 summarizes an experiment with no coronary stenosis. The myocardium has uniform signal intensity on the MRI and the SPECT scan. A circumferential summary of time signal intensity or relative microsphere perfusion to measure relative regional flow (RRF) shows similar variability by sectors around the heart. The MRI signal intensity versus time (time

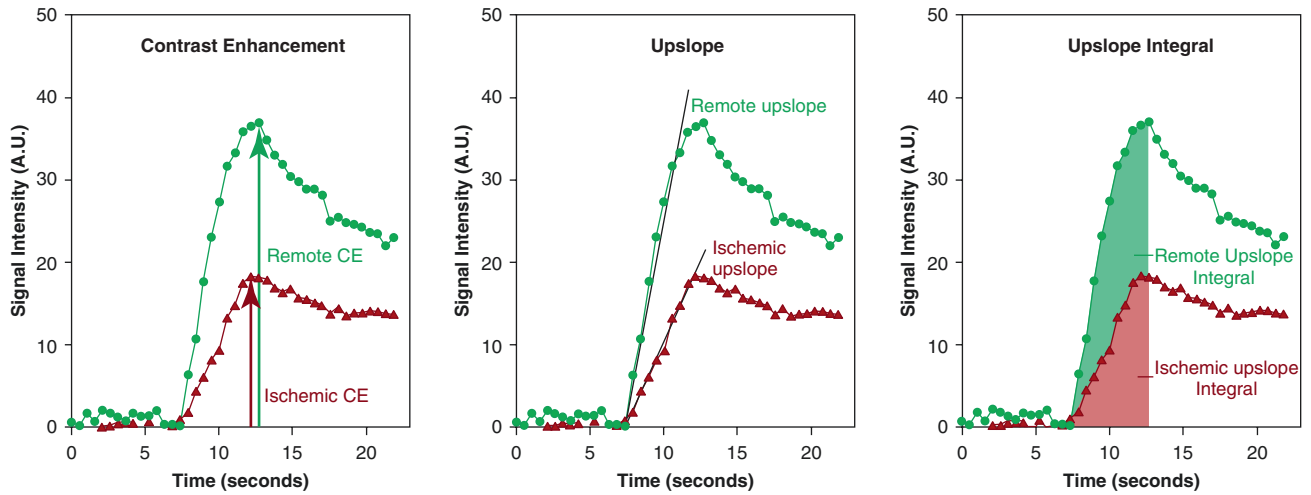

Fig. 12.6 Methods for semiquantitative analysis of perfusion. The plots represent signal intensity as a function of time in a region of the myocardium downstream from a severe right coronary artery stenosis ("ischemic") and in the anterior wall ("remote"). These measurements were from the perfusion scan illustrated in Fig. 12.3. There are three commonly used semiquantitative indices of perfusion that can be measured from these time intensity curves. Contrast enhancement is simply how much the signal intensity increased from baseline. A related measurement, contrast enhancement ratio is contrast enhancement divided by baseline signal intensity. Upslope is the initial rate of enhancement in the myocardium. This parameter is frequently corrected for the rate of enhancement in the blood. Finally, the upslope integral represents the area under the time intensity curve from the onset of myocardial enhancement to the peak of enhancement in the normal region. All time intensity curves were corrected for surface coil intensity variation and baseline subtracted

intensity curves) indicates that all parts of the heart enhance at a similar time and rate, have similar peak signal intensity, and exhibit washout of contrast with a uniform time course.

The middle row of Fig. 12.7 summarizes an experiment with a moderate coronary stenosis. The SPECT scan looks normal. Even circumferential measurements of tracer uptake miss the moderate perfusion defect. The MRI scan detects the regional abnormality in myocardial perfusion with circumferential measurements of myocardial upslope integral as relative regional flow. These measurements agree well with the microsphere determinations of blood flow. It is also evident in the plot of signal intensity versus time that some sectors of the heart enhance at a slower rate and develop a lower peak enhancement than the remote normal sectors. The rate of washout is also slower from those same sectors (less steep down slope after the peak). Despite the dissimilar time signal intensity measurements from the CMR scans, the overall perfusion defect as appears in the MRI image is subtle.

A severe perfusion defect is quite evident on both the MRI and SPECT images as shown in the bottom row of Fig. 12.7. The corresponding CMR time intensity curves and the summaries of relative regional flow are correspondingly more severe than for a moderate stenosis and markedly more abnormal than the normal study.

The difficulty of detecting moderate coronary stenoses in CMR or SPECT may be explainable based on the nonlinear relationship between image intensities from contrast concentrations or trace activities versus perfusion. By analogy, myocardial activity does not increase as much as myocardial perfusion for all clinical SPECT tracers, primarily in the vasodilated range. In Fig. 12.8, tracer uptake in the myocardium is plotted versus myocardial blood flow. With the exception of the PET agent 15O-labeled H2O, the other SPECT and PET tracers underestimate vasodilated blood flow. 201Th is the best SPECT tracer from the perspective of amount of increase in myocardial tracer uptake versus increase in blood flow. 99mSestamibi exhibits a very flat relationship between tracer uptake and myocardial blood flow over the range from 2 to 5 ml•min-1•g-1 of tissue. The consequence of the nonlinearity is that the relative decrease in tracer activity can be much smaller than the decrease in blood flow. This makes perfusion defects in the image more and more subtle in the vasodilated range. For example, a 20% decrease in myocardial blood flow can result in only a 5–6% decrease in 201Thallium uptake and even smaller changes with 99msestamibi when one achieves maximal vasodilation.

The current generation extracellular CMR contrast agents show similar nonlinearity for many of the semiquantitative indices measurable from the perfusion images [35]. For example, contrast enhancement ratio and myocardial upslope have nonlinearity problems comparable in severity to 99msestamibi. The myocardial upslope integral performs reasonably well. However, fully quantitative analysis converting CMR signal into estimates of myocardial perfusion in units of ml•min-1•g-1 of tissue shows excellent linearity across the entire range of perfusion encountered clinically [36].

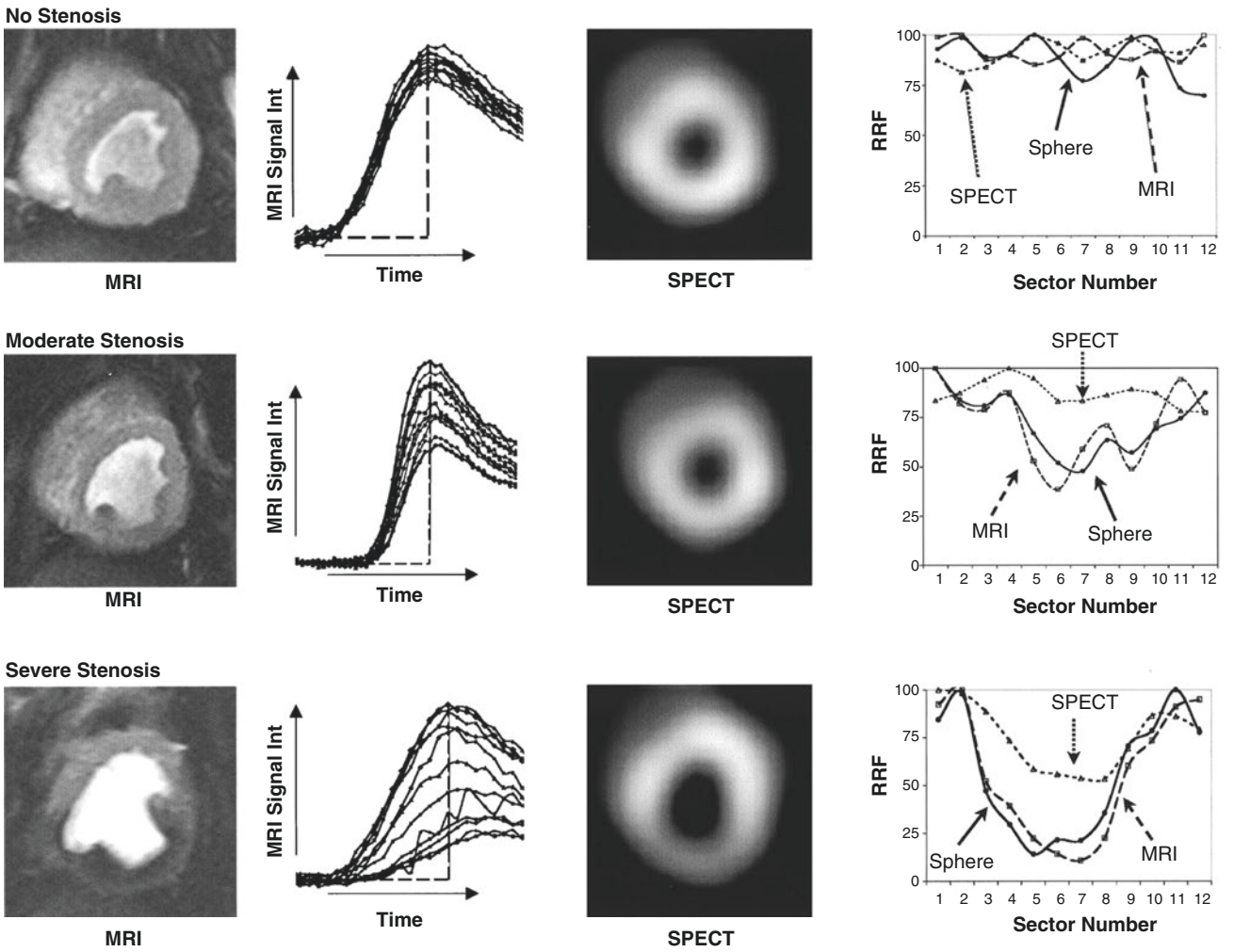

Fig. 12.7 Canine model of moderate and severe coronary stenoses comparing SPECT and CMR perfusion imaging with microspheres. See text for explanation [38]. (Reprinted with permission from Lee et al. [38], http://circ.ahajournals.org/content/110/1/58, with permission from Wolters Kluwer Health, Inc. (RFF relative regional flow, a measure of relative perfusion allowing comparison of the various techniques))

Fully quantitative perfusion analysis has been validated against invasive fractional flow reserve in patients [37, 41]. Comparisons between fully quantitative perfusion analysis by PET and CMR showed fair agreement but good agreement when used to calculate myocardial perfusion reserve [42]. Fully quantitative CMR perfusion analysis is also reproducible [43].

While there are relatively few clinical trials that have fully quantitative CMR perfusion and shown a benefit over other methodologies, Patel et al. found that quantitative CMR perfusion could determine the extent of coronary artery disease better than clinical interpretation [44]. The importance of this concept was raised earlier in this chapter as analyses of the COURAGE trial have focused attention on the extent of perfusion defects as a prognostically important parameter [17]. Mordini et al. compared the diagnostic accuracy of qualitative interpretation, semiquantitative perfusion analysis, and fully quantitative perfusion analysis [15]. That was the first study to show higher diagnostic accuracy of fully quantitative analysis compared with standard clinical interpretation of semiquantitative analysis. While much more work needs to be done, fully quantitative perfusion analysis shows significant promise and may offer an objective assessment of the severity of stress perfusion defects that allows reliable noninvasive determination of the physiological significance of coronary artery stenoses.

Myocardial Viability

Myocardial viability has been assessed by different imaging modalities. Comparison of results across different modalities is challenging given the pathophysiological mechanisms underlying different modality specific defini-

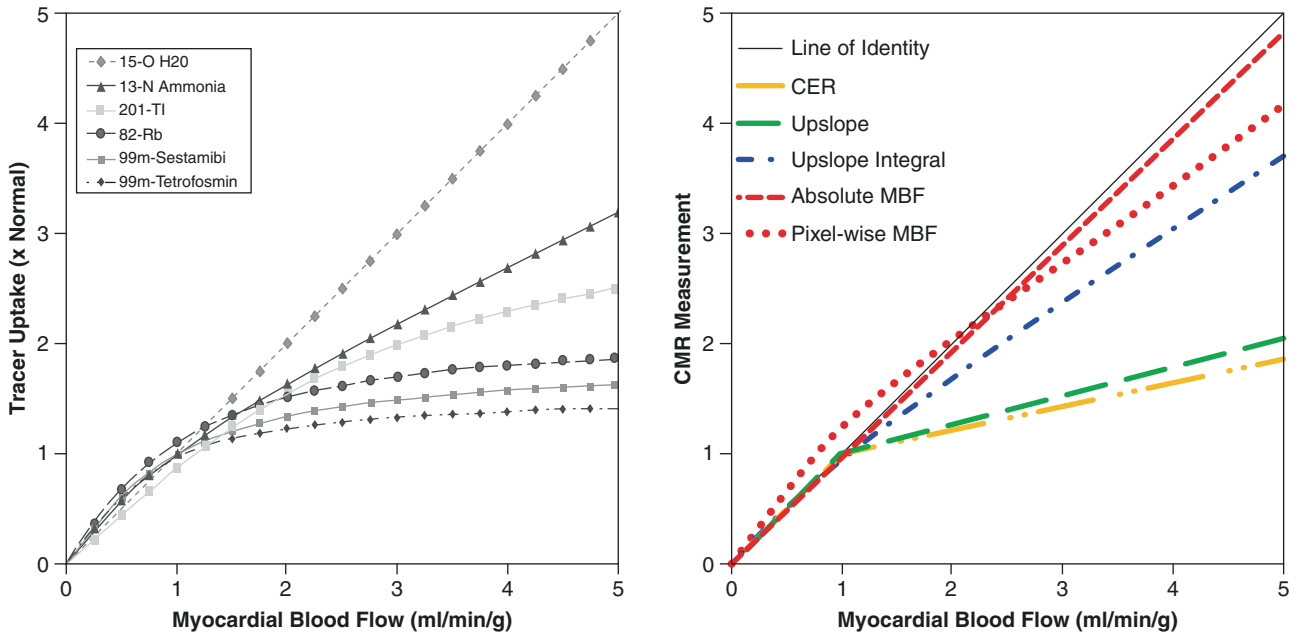

Fig. 12.8 Nonlinear relationship between MBF versus uptake of **various nuclear tracers and** versus CMR **semiquantitative indices of perfusion** [35, 39, 40]. (Left panel used with permission from Salerno and Beller [39], http://circimaging.ahajournals.org/content/2/5/412, with permission from Wolters Kluwer Health. Data for right panel used and adapted from [35, 40])

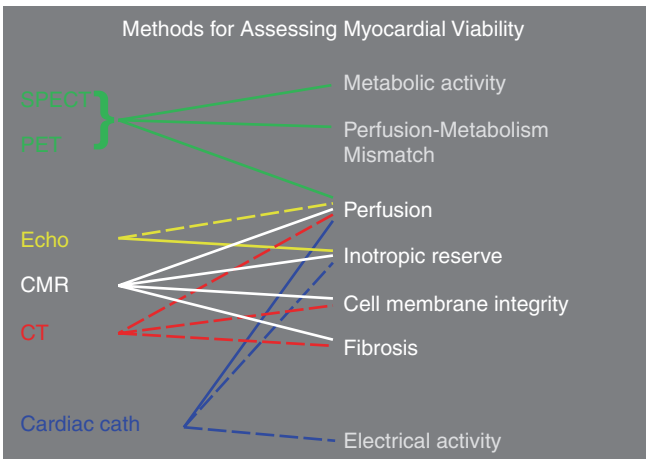

Fig. 12.9 Different modalities assess viability based on a variety of metabolic and pathophysiological mechanisms. These differences affect direct comparisons of the various viability imaging methods. Solid lines are intended to indicate the primary approaches used within a specific modality. Dashed lines are either theoretically possible or published methods that are not clinically used on a routine basis

tions for viability. As summarized in Fig. 12.9, SPECT and PET assess viability based on perfusion, metabolic activity, and perfusion-metabolism mismatch. While echocardiography can quantify myocardial perfusion, the primary echocardiographic method for assessing viability utilizes inotropic reserve. Inotropic reserve is often considered the most specific index of viability and thus also used to as an endpoint to verify viability predictions. The recovery of regional and global left ventricular function has also been used in the literature as a surrogate marker for predicting clinical improvement after coronary revascularization. The first report of contractile reserve was from observations during invasive left ventriculography [45]. Currently, TIMI frame counts or myocardial blush is used to assess adequacy of reperfusion during coronary interventions. Intracoronary electrograms are also local indices of viability that currently can only be made during cardiac catheterization.

Wall Thickness and Contractile Reserve by CMR

In line with echocardiographic data, severely thinned myocardium is unlikely to recover function. Baer et al. showed that a diastolic wall thickness of 5.5 mm could be used to discriminate regions of myocardium with preserved metabolic function and those without, as assessed by FDG PET [46]. In a subsequent paper, the group demonstrated that there was almost never recovery of function if diastolic wall thickness was <5.5 mm; however, the converse was not always true. Recovery of function did not universally occur in regions with wall thickness > 5.5 mm. Thus, assessment of the diastolic wall thickness, while sensitive, is poorly specific in the detection of recovery of function. Contractile reserve of 2 mm wall thickening during low-dose dobutamine improved the specificity in Baer's study to 92% while maintaining a sensitivity of 86% to predict functional recovery post revascularization [47].

Dobutamine stress CMR and stress echocardiography consistently have high specificity for predicting recovery of function after revascularization. On a less subjective level, tissue tagging and analysis of strain offer the potential of a more quantitative approach, although whether this will translate to greater clinical benefit is yet to be proven.

Late Gadolinium Enhancement (LGE)

The use of contrast-enhanced T1-weighted imaging to define the infarcted and irreversibly damaged myocardium has been one of the most significant steps forward in CMR in the past two decades [5]. The mechanisms of gadolinium enhancement were discussed earlier in this chapter (see Fig. 12.2). While some animal studies have shown that the size and transmural depth of infarction may be slightly overestimated (9–12%) in the immediate postinfarction period, these are stable indicators of scar extent beyond 1 week.

Principles of Imaging LGE

An inversion recovery sequence is employed to maximize the contrast between normal and enhanced myocardium, using either FLASH or SSFP readout [9]. This method will be described in this chapter as "conventional magnitude inversion recovery" (MAGIR) LGE.

Figure 12.10 summarizes the physics of inversion recovery LGE imaging using MAGIR but also for the phase-sensitive inversion recovery (PSIR) LGE method [48]. The y-axis plots magnetization (M_z) which is the vector representing the net strength of the protons aligned parallel and antiparallel to the main magnetic field. The x-axis plots the inversion time (TI), an image acquisition parameter that summarizes the time from the inversion pulse and the middle of the acquisition of raw image data. The inversion pulse inverts the protons, essentially resulting in a net negative M_z (pointing antiparallel to the main magnetic field). T1 recovery is the time constant describing how quickly the protons realign parallel to the main magnetic field. If one was to image prior to any inversion pulse, M_z would equal 1.00, and an image readout would produce a certain image intensity. If one could image very quickly and immediately after an inversion pulse (TI approaching 0 s), the PSIR LGE detects M_z as a negative value (−1.00) which represents the net alignment of protons is antiparallel to the main magnetic field (M_z = −1.00). For all other inversion times, M_z and therefore image signal intensity are somewhere between −1.00 and 1.00. The infarcted myocardium has higher gadolinium concentration, shorter T1, and faster recovery of protons compared with the normal myocardium.

If one correctly selects a TI that will null normal myocardium (TI_{null}), then M_z will be zero, and normal myocardium will be dark on the LGE image. Since infarcted myocardium has more gadolinium than normal myocardium and therefore shorter T1, infarcted myocardium will have a signal intensity that is brighter than the nulled normal myocardium (and a M_z greater than zero). The concept that an infarct will be bright against a nearly black background of normal myocardium produces excellent contrast for visualizing the MI.

For inversion times longer than the TI_{null} that nulls normal myocardium, both Mag IR and PSIR plots of M_z recover toward M_z = 1.00 (i.e., have net positive signal intensity). Both Mag IR and PSIR have the same M_z and signal intensity for TI at or longer than the TI that nulls normal myocardium. When TI is less than TI_{null}, the Mag IR curve is more complicated. Since magnitude reconstruction is analogous to taking the absolute value of the vector, Mag IR only has positive signal intensity or M_z. This property means there is a TI where normal myocardium and infarcted myocardium have equal signal intensity (green dotted line and solid red line intersect in Fig. 12.10). There is also a TI where the infarcted myocardium appears nulled or has nearly black signal inten-

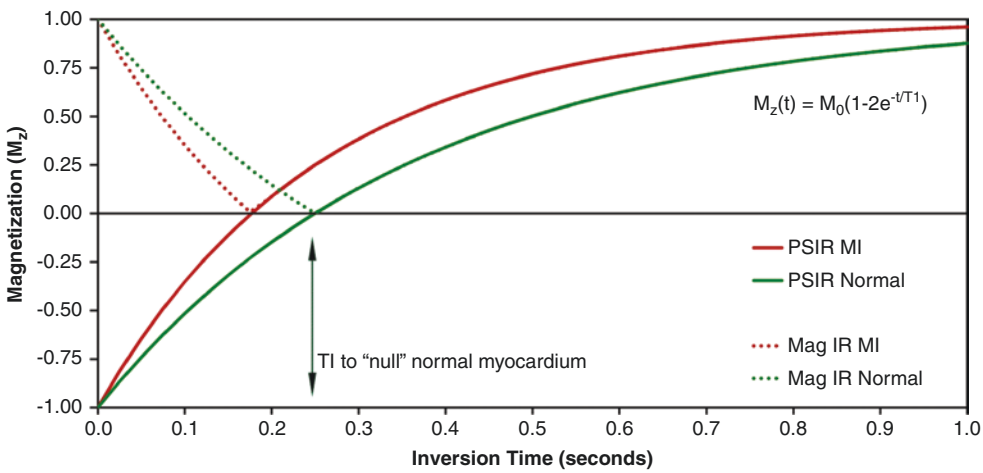

Fig. 12.10 Physics of inversion recovery as used for late gadolinium-enhanced imaging of myocardial infarction

sity ($M_z = 0$), while normal myocardium is dark. In addition, many advances have been made toward reducing the influence of correct selection of TI time such as using the phase-sensitive inversion recovery (PSIR) technique, which minimizes the effect of small TI differences on contrast [48]. The PSIR reconstruction produces a brighter infarct than normal myocardium at all inversion times since it properly handles negative values.

There are important practical consequences to the physics described for Mag IR and PSIR reconstructions for LGE imaging. For Mag IR, it is critical that the technologist select the correct TI to null normal myocardium (within about 25 ms of the correct value). Selecting a TI that is too short can result in incorrect relative signal intensity of MI and normal myocardium (Fig. 12.10).

For PSIR, the selection of TI is not as critical, but it is still important to get close to the correct TI to maximize contrast between normal and infarcted myocardium. It also is necessary for the physician reading the study to adjust the window and level on the diagnostic image display to null normal myocardium and make it appears nearly black.

The inversion recovery preparation pulse allows for differentiation of normal or infarcted myocardium but is dependent on correctly setting of the TI (inversion time) to null (blacken) normal myocardium and interactive modification of this setting as necessary during the acquisition of sequential slices to achieve optimal contrast between the normal and infarcted myocardium. Using this technique infarcted areas appear bright, can be localized according to standardized descriptors of LV anatomy, and quantified both in terms of the circumferential and longitudinal extent of myocardium affected as well as transmurality, the transmural extent of infarction being the crucially important factor in determining the potential for recovery of infarcted myocardium. Despite the need for optimization of TI on a per patient basis, conventional MAGIR LGE imaging has been shown to be a highly reproducible technique.

LGE Sequence Developments and Improvements

There have been several improvements in imaging LGE beyond conventional Mag IR and PSIR methods. 3D IR techniques, with or without respiratory navigator, have become routine methods to reduce image acquisition time and to reduce respiratory artifacts [49].

Several groups have spearheaded black blood LGE methods to improve the contrast between blood and subendocardial myocardial infarctions. Kellman et al. introduced an inversion recovery (IR) T2 preparation that was combined with single-shot steady-state free precession imaging to provide dark blood LGE images in a sequence that includes motion correction to allow free-breathing acquisitions [50]. Another dark blood LGE method [51] uses a flow-independent technique that uses a low power magnetization transfer preparation to reduce radio frequency energy requirements associated with the similar flow-independent dark blood "FIDDLE" technique. The main benefit of this type of advanced LGE methodology is detecting subendocardial myocardial infarctions that are difficult to discern from blood [52] on the conventional bright blood LGE methods previously described.

The T1 mapping techniques have improved enough that one can create "synthetic inversion recovery" MAGIR or PSIR images from a post-contrast modified MOLLI acquisition. This method eliminates a user selected inversion time but can reconstruct images as they would look if acquired at any arbitrary inversion time (Fig. 12.11) [53].

Validation of LGE in Animals

Basic scientists recognized that the subendocardial myocardium was more vulnerable to infarction than the midmyocardium or epicardium (Fig. 12.12) [54]. This means that infarcted myocardium starts in the subendocardium and gradually extends in a more transmural extent with more severe ischemia and particularly longer duration of ischemia. Finally, the ischemic area at risk or myocardium at risk is typically a transmural perfusion defect during a total acute coronary occlusion. Thus, the myocardial infarction is a subset of the area at risk. Myocardial salvage can be determined by subtracting the infarcted myocardium from the area at risk.

The first descriptions of LGE enhancement were published in the mid-1980s [55–58]. High quality of validation studies using inversion recovery LGE methods [5, 6] led to a renewed appreciation of the power of extracellular gadolinium-based contrast agents for delineating regions of myocardial infarction. Improvements in the image acquisition methods used to obtain LGE images [9] enhanced the feasibility of using this method for diagnostic purposes.

Kim et al. validated LGE infarct size against histopathology in a landmark study published in 1999 [5]. The quality of their ex vivo CMR images displayed next to histopathological specimens provided convincing evidence that LGE with gadolinium-based contrast corresponded to myocardial infarction down to a millimeter-by-millimeter basis. There were close correlations between infarct size by CMR and histopathology on day 1, day 3, and week 8 post-infarct (Fig. 12.13). Furthermore, stunned myocardium induced by brief coronary occlusion of a non-infarct-related coronary artery did not exhibit LGE. This work was extended by the same group in 24 canine infarcts studied 4 h, 1 day, 3 days, 10 days, 4 weeks, and 8 weeks after infarction [59]. Elegant

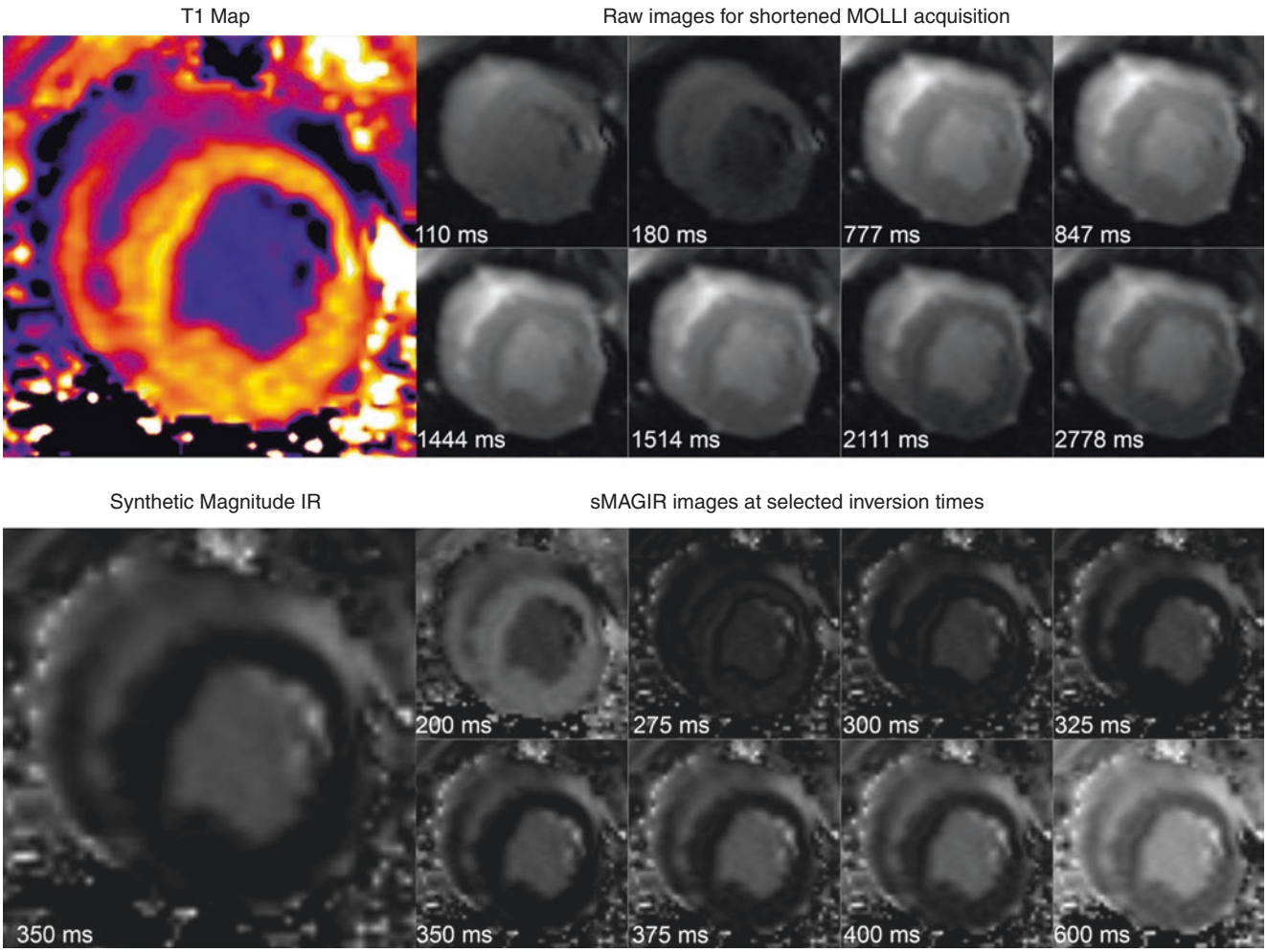

Fig. 12.11 Synthetic magnitude inversion recovery images of myocardial infarction generated from a single shortened MOLLI acquisition [53]. The first five raw images were acquired after a first inversion pulse. After a 3-s delay, a second inversion pulse was used to provide T1 weighting for the last three raw images. All images were acquired in diastole. The post-contrast T1 map was acquired about 15 min after administration of gadolinium DTPA and was generated from the raw images. Note that none of the raw images look like a conventional LGE image dark myocardium and bright infarct since none of the images were at an inversion time to null normal myocardium. However, if one has a good estimate of T1 at each pixel of the image, one should be able to generate the expected appearance of a synthetic magnitude inversion recovery (sMAGIR) image at any possible inversion time. The selected sMAGIR images shown have TI 200 ms, 275 ms, 300 ms, 325 ms, 350 ms, 375 ms, 400 ms, and 600 ms

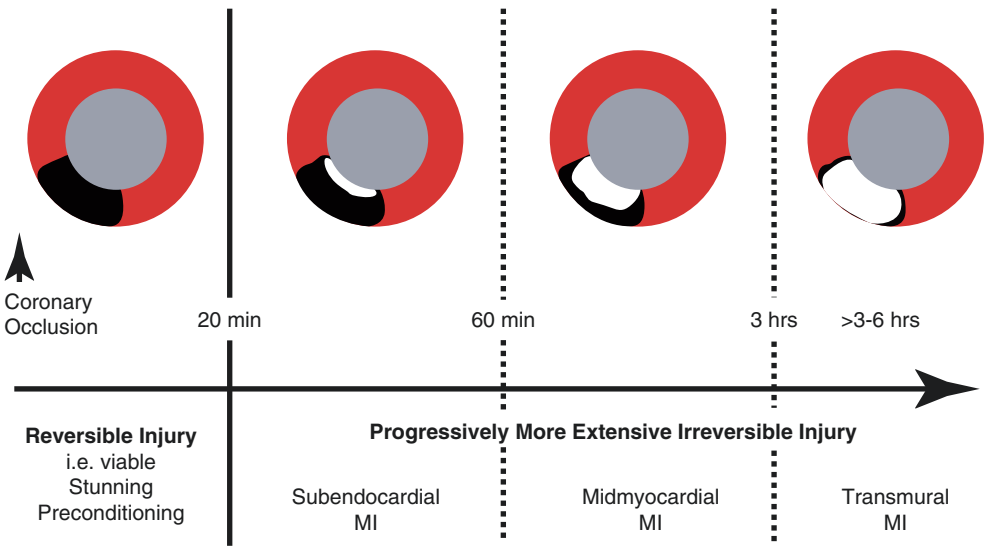

Fig. 12.12 The duration of ischemia is a major determinant of infarct size and the transmural extent of infarction [54]. (Adapted from Kloner et al. [54])

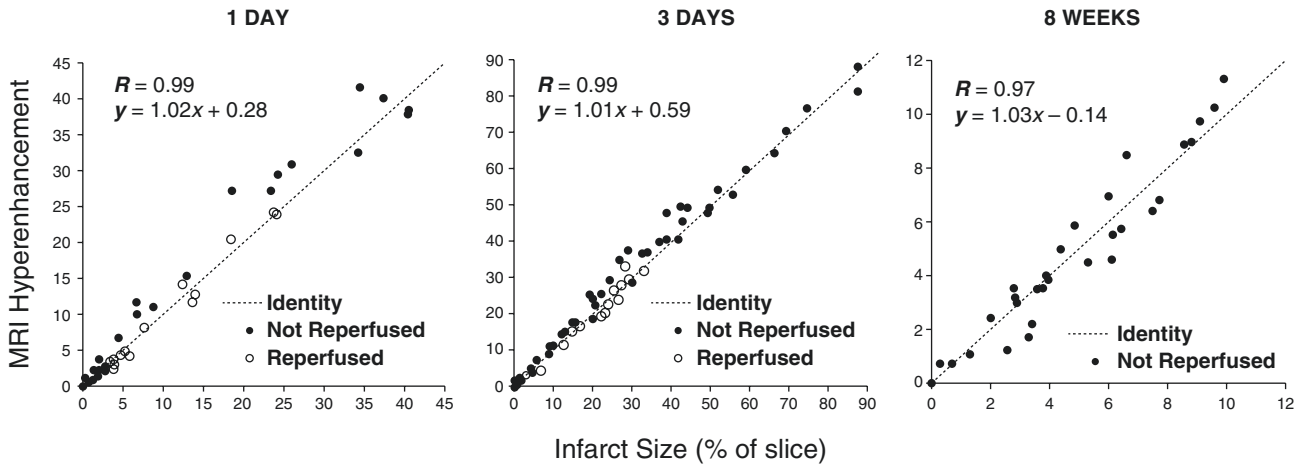

Fig. 12.13 Correlation between hyperenhancement on CMR **(LGE) and size of the myocardial infarction from TTC-stained myocardium 1 day** (n **= 2), 3 days** (n **= 2), and 8 weeks** (n **= 2) after acute myocardial infarction** [5]. (Reprinted from Kim et al. [5], http://circ.ahajournals.org/content/100/19/1992, with permission from Wolters Kluwer Health)

experiments using electron probe X-ray microanalysis documented that gadolinium closely paralleled the distribution of abnormally elevated sodium and low potassium when comparing infarcted and remote myocardium [60]. An example of CMR LGE correlation with histopathologic confirmation of infarct size is shown in Fig. 12.14.

Ex vivo, high-resolution, spectrally sensitive radionuclide imaging allowed comparison of the myocardial distribution of two nuclear viability agents (99Tc sestamibi and 18F-FDG [18F-fluorodeoxyglucose]) with 111In-DTPA (diethyltriaminepentaacetic acid) in pathological specimens of myocardial infarction [62]. This study supported the conclusion that gadolinium-DTPA distributes in the extracellular space, and this space represents a large percentage of fibrotic myocardium relative to normal myocardium.

Pharmacology experiments using slow continuous infusions of gadolinium have determined that the gadolinium contrast agents distribute into the myocardium proportionately to the partition coefficient of gadolinium [63, 64] and thus the extracellular volume fraction. The slow infusion minimizes the influence of perfusion on gadolinium concentration within the myocardium. Although theoretically superior to bolus injections of gadolinium, these hour-long continuous infusions are not practical in patients.

Validation of LGE in Patients

LGE was the first clinically relevant imaging method that could routinely resolve the transmural extent of myocardial infarction. Subendocardial LGE is sensitive and highly specific for the detection of myocardial infarction. In addition, the detection of myocardial LGE is associated with a significantly increased risk of subsequent death and adverse cardiac events, adding incremental prognostic information to assessment of left ventricular function. Finally, the extent of LGE is emerging as a potent tool to determine response to novel medical and interventional therapies.

The seminal study in this field by Kim et al. assessed the effect of revascularization on regional recovery of function according to transmural extent of infarction by CMR in patients with ischemic LV dysfunction [6]. The likelihood of functional recovery (per segment) was inversely related to the transmural extent of infarction. Of akinetic and dyskinetic segments with 0–25% transmural extent of infarction, 82% showed recovery of function; of similar segments with 26–50% transmural extent, 45% showed recovery of function; of segments with 51–75% transmural extent, 7% recovered; and none of the segments with >75% transmural extent of infarction demonstrated recovery of function with similar patterns were observed for all dysfunctional segments. Selvanayagam et al. corroborated these results to remarkable detail [65] (Fig. 12.15).

The validations of LGE imaging of myocardial infarction were extensive during the first decade after these methods became available. LGE had 91% sensitivity for MI and 100% specificity based on presence and location of the scar [67]. LGE was much more sensitive to subendocardial MI than SPECT in a canine model and in humans [68]. While PET viability methods generally correlated with CMR LGE of MI [69, 70], CMR seemed more sensitive to subendocardial MI than PET [70]. LGE estimates of the size of myocardial infarction were quite reproducible [71].

Despite the outstanding work validating LGE as a measure of myocardial viability, at least two studies have suggested that dobutamine viability assessments may be slightly better predictors of functional recovery after revascularization. In a head-to-head comparison, Wellenhofer et al. found

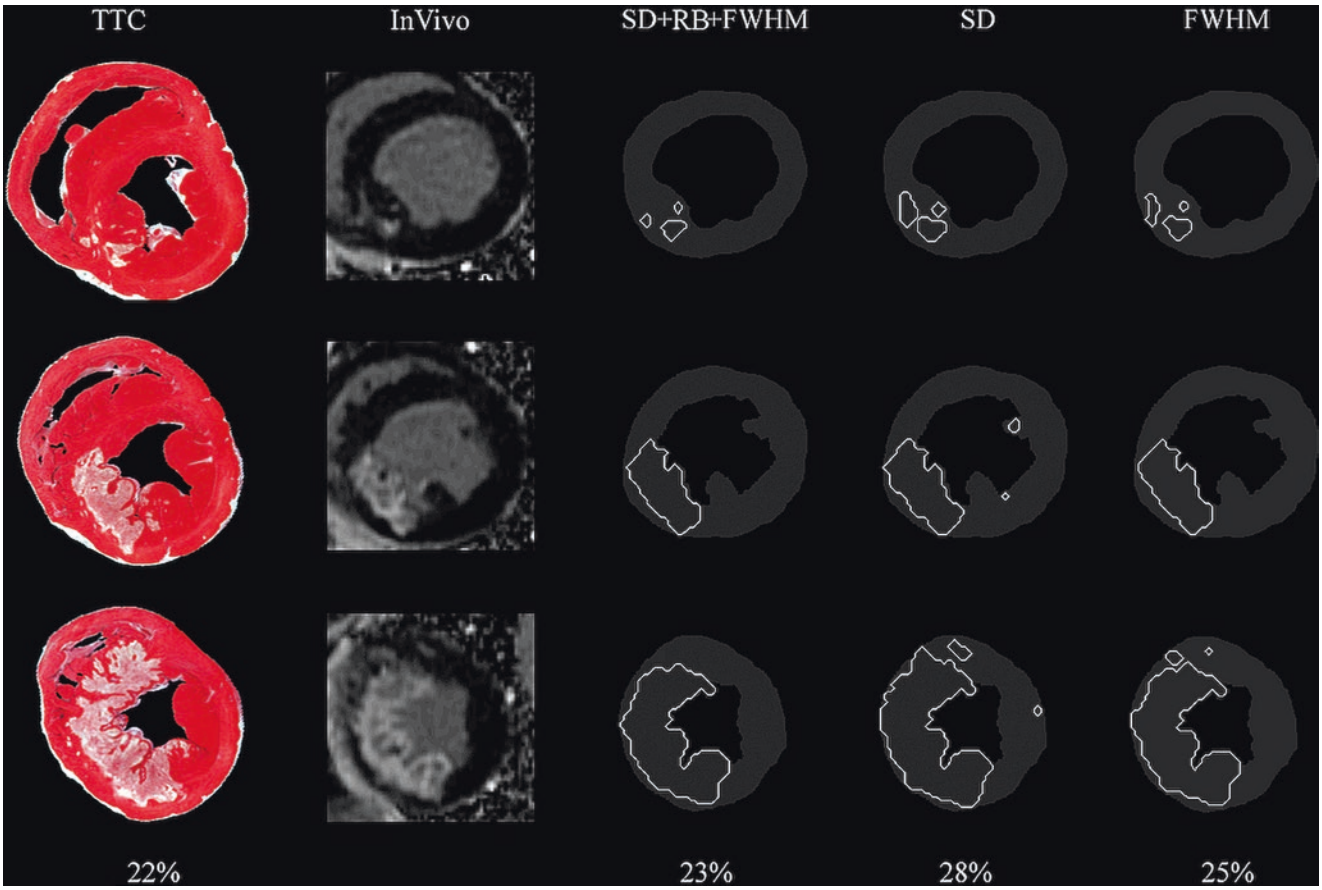

Fig. 12.14 In vivo late gadolinium enhancement images of infarct size compared with histopathology and three quantitative analysis methods. On the triphenoltetrazolium (TTC)-stained myocardium, viable tissue appears dark, and areas of myocardial infarction are white. The commonly used two standard deviation (SD) threshold overestimates infarct size. The full-width half-maximum (FWHM) method is more accurate but still overestimates infarct size. A more sophisticated computer program that involves stepwise incorporation of SD, regional-based feature analysis (RB), and FWHM provided the most precise approach in measuring infarct size [61]. (Adapted and reprinted from Hsu et al. [61])

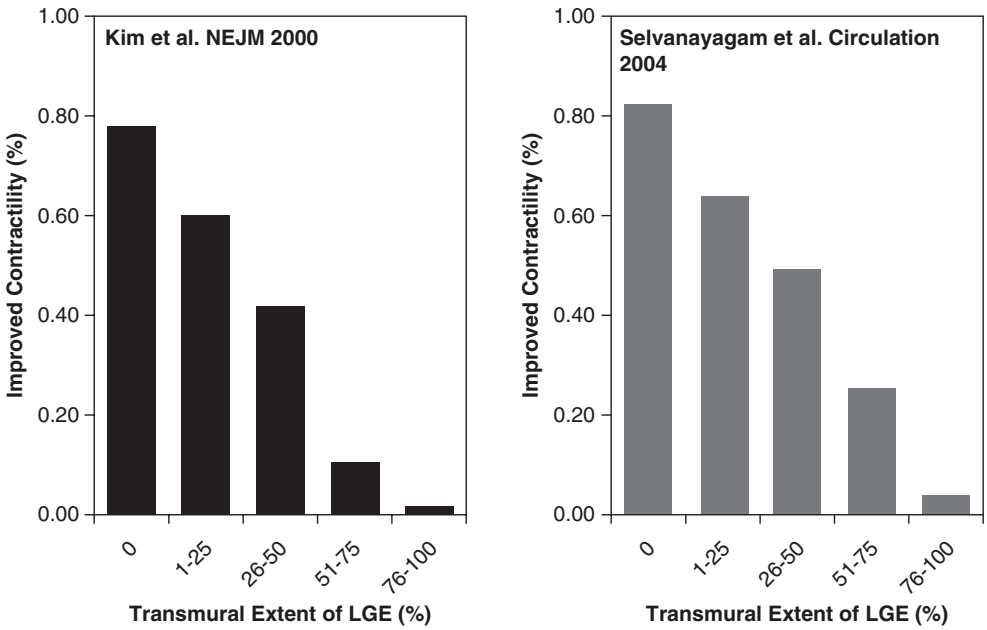

Fig. 12.15 Two studies showed nearly identical results in predicting the recovery of function after coronary revascularization as predicted by the preoperative transmural extent of myocardial infarction on LGE imaging. (Redrawn with similar axes and format from Kim et al. [6], Selvanayagam et al. [65] and Knuesel et al. [66])

that dobutamine stress CMR predicted recovery of function better than the transmural extent of infarction by LGE [72]. Similarly, dobutamine stress echocardiography predicted recovery of function better than the transmural extent of infarction. While mean Tl uptake and change in wall motion score decreased with increasing transmural extent of infarction, almost half of segments with 25–75% transmural extent of scar had contractile reserve [73]. Thus, when the LGE shows either a transmural MI or minimal to no scar, the prediction of functional recovery after revascularization is good. For segments with intermediate transmural extent of infarction, a test of contractile reserve should be considered.

A wide range of studies have reported that LGE consistent with MI has prognostic value in a wide range of clinical and research settings. Steele et al. had one of the first studies showing that LGE had prognostic significance in patients that presented to the hospital with symptoms of coronary artery disease [74]. Coelho-Filho et al. also found that unrecognized myocardial infarction had prognostic significance in patients with diabetes [75]. Cheong et al. reported that LGE had prognostic significance in patients with or without left ventricular dysfunction [76]. Several studies have looked at the additive or comparative prognostic importance of LGE in patients undergoing stress CMR [77–79]. The extent of viable myocardium in ischemic cardiomyopathy has also been shown to be predictive of ventricular arrhythmias [80]. CMR assessment of myocardial scar may prove useful in selection of patients who will benefit for resynchronization therapy [81].

Acknowledgments This research was supported in part by the Intramural Research Program of the National Institutes of Health (NIH) and National Heart, Lung, and Blood Institute (NHLBI).

References

1. Anzidei M, Napoli A, Marincola BC, et al. Gadofosveset-enhanced MR angiography of carotid arteries: does steady-state imaging improve accuracy of first-pass imaging? Comparison with selective digital subtraction angiography. Radiology. 2009;251:457–66.
2. Perreault P, Edelman MA, Baum RA, et al. MR angiography with gadofosveset trisodium for peripheral vascular disease: phase II trial. Radiology. 2003;229:811–20.
3. Bane O, Lee DC, Benefield BC, et al. Leakage and water exchange characterization of gadofosveset in the myocardium. Magn Reson Imaging. 2014;32:224–35.
4. Aime S, Caravan P. Biodistribution of gadolinium-based contrast agents, including gadolinium deposition. J Magn Reson Imaging. 2009;30:1259–67.
5. Kim RJ, Fieno DS, Parrish TB, et al. Relationship of MRI delayed contrast enhancement to irreversible injury, infarct age, and contractile function. Circulation. 1999;100:1992–2002.
6. Kim RJ, Wu E, Rafael A, et al. The use of contrast-enhanced magnetic resonance imaging to identify reversible myocardial dysfunction. N Engl J Med. 2000;343:1445–53.
7. Mahrholdt H, Wagner A, Judd RM, Sechtem U, Kim RJ. Delayed enhancement cardiovascular magnetic resonance assessment of non-ischaemic cardiomyopathies. Eur Heart J. 2005;26:1461–74.
8. Ugander M, Oki AJ, Hsu LY, et al. Extracellular volume imaging by magnetic resonance imaging provides insights into overt and subclinical myocardial pathology. Eur Heart J. 2012;33:1268–78.
9. Simonetti OP, Kim RJ, Fieno DS, et al. An improved MR imaging technique for the visualization of myocardial infarction. Radiology. 2001;218:215–23.
10. Cerqueira MD, Weissman NJ, Dilsizian V, et al. Standardized myocardial segmentation and nomenclature for tomographic imaging of the heart. A statement for healthcare professionals from the Cardiac Imaging Committee of the Council on Clinical Cardiology of the American Heart Association. Circulation. 2002;105:539–42.
11. Kellman P, Derbyshire JA, Agyeman KO, McVeigh ER, Arai AE. Extended coverage first-pass perfusion imaging using slice-interleaved TSENSE. Magn Reson Med. 2004;51:200–4.
12. Jogiya R, Kozerke S, Morton G, et al. Validation of dynamic 3-dimensional whole heart magnetic resonance myocardial perfusion imaging against fractional flow reserve for the detection of significant coronary artery disease. J Am Coll Cardiol. 2012;60:756–65.
13. Manka R, Paetsch I, Kozerke S, et al. Whole-heart dynamic three-dimensional magnetic resonance perfusion imaging for the detection of coronary artery disease defined by fractional flow reserve: determination of volumetric myocardial ischaemic burden and coronary lesion location. Eur Heart J. 2012;33:2016–24.
14. Kellman P, Arai AE. Imaging sequences for first pass perfusion –a review. J Cardiovasc Magn Reson. 2007;9:525–37.
15. Mordini FE, Haddad T, Hsu LY, et al. Diagnostic accuracy of stress perfusion CMR in comparison with quantitative coronary angiography: fully quantitative, semiquantitative, and qualitative assessment. JACC Cardiovasc Imaging. 2014;7:14–22.
16. Boden WE, O'Rourke RA, Teo KK, et al. Optimal medical therapy with or without PCI for stable coronary disease. N Engl J Med. 2007;356:1503–16.
17. Shaw LJ, Berman DS, Maron DJ, et al. Optimal medical therapy with or without percutaneous coronary intervention to reduce ischemic burden: results from the Clinical Outcomes Utilizing Revascularization and Aggressive Drug Evaluation (COURAGE) trial nuclear substudy. Circulation. 2008;117:1283–91.
18. De Bruyne B, Pijls NH, Kalesan B, et al. Fractional flow reserve-guided PCI versus medical therapy in stable coronary disease. N Engl J Med. 2012;367:991–1001.
19. De Bruyne B, Fearon WF, Pijls NH, et al. Fractional flow reserve-guided PCI for stable coronary artery disease. N Engl J Med. 2014;371:1208–17.
20. Tonino PA, De Bruyne B, Pijls NH, et al. Fractional flow reserve versus angiography for guiding percutaneous coronary intervention. N Engl J Med. 2009;360:213–24.
21. Takx RA, Blomberg BA, El Aidi H, et al. Diagnostic accuracy of stress myocardial perfusion imaging compared to invasive coronary angiography with fractional flow reserve meta-analysis. Circ Cardiovasc Imaging. 2015;8:e002666.
22. Watkins S, McGeoch R, Lyne J, et al. Validation of magnetic resonance myocardial perfusion imaging with fractional flow reserve for the detection of significant coronary heart disease. Circulation. 2009;120:2207–13.
23. Bernhardt P, Walcher T, Rottbauer W, Wohrle J. Quantification of myocardial perfusion reserve at 1.5 and 3.0 Tesla: a comparison to fractional flow reserve. Int J Cardiovasc Imaging. 2012;28:2049–56.
24. Walcher T, Manzke R, Hombach V, Rottbauer W, Wohrle J, Bernhardt P. Myocardial perfusion reserve assessed by T2-prepared steady-state free precession blood oxygen level-dependent magnetic resonance imaging in comparison to fractional flow reserve. Circ Cardiovasc Imaging. 2012;5:580–6.

25. Bettencourt N, Chiribiri A, Schuster A, et al. Cardiac magnetic resonance myocardial perfusion imaging for detection of functionally significant obstructive coronary artery disease: a prospective study. Int J Cardiol. 2013;168:765–73.
26. Chiribiri A, Hautvast GL, Lockie T, et al. Assessment of coronary artery stenosis severity and location: quantitative analysis of transmural perfusion gradients by high-resolution MRI versus FFR. JACC Cardiovasc Imaging. 2013;6:600–9.
27. Groothuis JG, Beek AM, Brinckman SL, et al. Combined non-invasive functional and anatomical diagnostic work-up in clinical practice: the magnetic resonance and computed tomography in suspected coronary artery disease (MARCC) study. Eur Heart J. 2013;34:1990–8.
28. Pereira E, Bettencourt N, Ferreira N, et al. Incremental value of adenosine stress cardiac magnetic resonance in coronary artery disease detection. Int J Cardiol. 2013;168:4160–7.
29. Ebersberger U, Makowski MR, Schoepf UJ, et al. Magnetic resonance myocardial perfusion imaging at 3.0 Tesla for the identification of myocardial ischaemia: comparison with coronary catheter angiography and fractional flow reserve measurements. Eur Heart J Cardiovasc Imaging. 2013;14:1174–80.
30. Greenwood JP, Maredia N, Radjenovic A, et al. Clinical evaluation of magnetic resonance imaging in coronary heart disease: the CE-MARC study. Trials. 2009;10:62.
31. Greenwood JP, Maredia N, Younger JF, et al. Cardiovascular magnetic resonance and single-photon emission computed tomography for diagnosis of coronary heart disease (CE-MARC): a prospective trial. Lancet. 2012;379:453–60.
32. Schwitter J, Wacker CM, van Rossum AC, et al. MR-IMPACT: comparison of perfusion-cardiac magnetic resonance with single-photon emission computed tomography for the detection of coronary artery disease in a multicentre, multivendor, randomized trial. Eur Heart J. 2008;29:480–9.
33. Schwitter J, Wacker CM, Wilke N, et al. MR-IMPACT II: Magnetic Resonance Imaging for Myocardial Perfusion Assessment in Coronary artery disease Trial: perfusion-cardiac magnetic resonance vs. single-photon emission computed tomography for the detection of coronary artery disease: a comparative multicentre, multivendor trial. Eur Heart J. 2013;34:775–81.
34. Schwitter J, Wacker CM, Wilke N, et al. Superior diagnostic performance of perfusion-cardiovascular magnetic resonance versus SPECT to detect coronary artery disease: the secondary endpoints of the multicenter multivendor MR-IMPACT II (Magnetic Resonance Imaging for Myocardial Perfusion Assessment in Coronary Artery Disease Trial). J Cardiovasc Magn Reson. 2012;14:61.
35. Christian TF, Rettmann DW, Aletras AH, et al. Absolute myocardial perfusion in canines measured by using dual-bolus first-pass MR imaging. Radiology. 2004;232:677–84.
36. Hsu LY, Kellman P, Arai AE. Nonlinear myocardial signal intensity correction improves quantification of contrast-enhanced first-pass MR perfusion in humans. J Magn Reson Imaging. 2008;27:793–801.
37. Lockie T, Ishida M, Perera D, et al. High-resolution magnetic resonance myocardial perfusion imaging at 3.0-Tesla to detect hemodynamically significant coronary stenoses as determined by fractional flow reserve. J Am Coll Cardiol. 2011;57:70–5.
38. Lee DC, Simonetti OP, Harris KR, et al. Magnetic resonance versus radionuclide pharmacological stress perfusion imaging for flow-limiting stenoses of varying severity. Circulation. 2004;110:58–65.
39. Salerno M, Beller GA. Noninvasive assessment of myocardial perfusion. Circ Cardiovasc Imaging. 2009;2:412–24.
40. Hsu LY, Groves DW, Aletras AH, Kellman P, Arai AE. A quantitative pixel-wise measurement of myocardial blood flow by contrast-enhanced first-pass CMR perfusion imaging: microsphere validation in dogs and feasibility study in humans. JACC Cardiovasc Imaging. 2012;5:154–66.
41. Kuhl HP, Katoh M, Buhr C, et al. Comparison of magnetic resonance perfusion imaging versus invasive fractional flow reserve for assessment of the hemodynamic significance of epicardial coronary artery stenosis. Am J Cardiol. 2007;99:1090–5.
42. Morton G, Chiribiri A, Ishida M, et al. Quantification of absolute myocardial perfusion in patients with coronary artery disease: comparison between cardiovascular magnetic resonance and positron emission tomography. J Am Coll Cardiol. 2012;60:1546–55.
43. Morton G, Jogiya R, Plein S, Schuster A, Chiribiri A, Nagel E. Quantitative cardiovascular magnetic resonance perfusion imaging: inter-study reproducibility. Eur Heart J Cardiovasc Imaging. 2012;13:954–60.
44. Patel AR, Antkowiak PF, Nandalur KR, et al. Assessment of advanced coronary artery disease: advantages of quantitative cardiac magnetic resonance perfusion analysis. J Am Coll Cardiol. 2010;56:561–9.
45. Popio KA, Gorlin R, Bechtel D, Levine JA. Postextrasystolic potentiation as a predictor of potential myocardial viability: preoperative analyses compared with studies after coronary bypass surgery. Am J Cardiol. 1977;39:944–53.
46. Baer FM, Voth E, Schneider CA, Theissen P, Schicha H, Sechtem U. Comparison of low-dose dobutamine-gradient-echo magnetic resonance imaging and positron emission tomography with [18F] fluorodeoxyglucose in patients with chronic coronary artery disease. A functional and morphological approach to the detection of residual myocardial viability. Circulation. 1995;91:1006–15.
47. Baer FM, Theissen P, Schneider CA, et al. Dobutamine magnetic resonance imaging predicts contractile recovery of chronically dysfunctional myocardium after successful revascularization. J Am Coll Cardiol. 1998;31:1040–8.
48. Kellman P, Arai AE, McVeigh ER, Aletras AH. Phase-sensitive inversion recovery for detecting myocardial infarction using gadolinium-delayed hyperenhancement. Magn Reson Med. 2002;47:372–83.
49. Peukert D, Laule M, Taupitz M, Kaufels N, Hamm B, Dewey M. 3D and 2D delayed-enhancement magnetic resonance imaging for detection of myocardial infarction: preclinical and clinical results. Acad Radiol. 2007;14:788–94.
50. Kellman P, Xue H, Olivieri LJ, et al. Dark blood late enhancement imaging. J Cardiovasc Magn Reson. 2016;18:77.
51. Muscogiuri G, Rehwald WG, Schoepf UJ, et al. T(Rho) and magnetization transfer and INvErsion recovery (TRAMINER)-prepared imaging: a novel contrast-enhanced flow-independent dark-blood technique for the evaluation of myocardial late gadolinium enhancement in patients with myocardial infarction. J Magn Reson Imaging. 2016;45:1429–37.
52. Bandettini WP, Kellman P, Mancini C, et al. MultiContrast Delayed Enhancement (MCODE) improves detection of subendocardial myocardial infarction by late gadolinium enhancement cardiovascular magnetic resonance: a clinical validation study. J Cardiovasc Magn Reson. 2012;14:83.
53. Xue H, Shah S, Greiser A, et al. Motion correction for myocardial T1 mapping using image registration with synthetic image estimation. Magn Reson Med. 2012;67:1644–55.
54. Kloner RA, Jennings RB. Consequences of brief ischemia: stunning, preconditioning, and their clinical implications: part 1. Circulation. 2001;104:2981–9.
55. Wesbey GE, Higgins CB, McNamara MT, et al. Effect of gadolinium-DTPA on the magnetic relaxation times of normal and infarcted myocardium. Radiology. 1984;153:165–9.
56. McNamara MT, Tscholakoff D, Revel D, et al. Differentiation of reversible and irreversible myocardial injury by MR imaging with and without gadolinium-DTPA. Radiology. 1986;158:765–9.
57. Peshock RM, Malloy CR, Buja LM, Nunnally RL, Parkey RW, Willerson JT. Magnetic resonance imaging of acute myocardial infarction: gadolinium diethylenetriamine pentaacetic acid as a marker of reperfusion. Circulation. 1986;74:1434–40.

58. Rehr RB, Peshock RM, Malloy CR, et al. Improved in vivo magnetic resonance imaging of acute myocardial infarction after intravenous paramagnetic contrast agent administration. Am J Cardiol. 1986;57:864–8.
59. Fieno DS, Kim RJ, Chen EL, Lomasney JW, Klocke FJ, Judd RM. Contrast-enhanced magnetic resonance imaging of myocardium at risk: distinction between reversible and irreversible injury throughout infarct healing. J Am Coll Cardiol. 2000;36:1985–91.
60. Rehwald WG, Fieno DS, Chen EL, Kim RJ, Judd RM. Myocardial magnetic resonance imaging contrast agent concentrations after reversible and irreversible ischemic injury. Circulation. 2002;105:224–9.
61. Hsu LY, Natanzon A, Kellman P, Hirsch GA, Aletras AH, Arai AE. Quantitative myocardial infarction on delayed enhancement MRI. Part I: animal validation of an automated feature analysis and combined thresholding infarct sizing algorithm. J Magn Reson Imaging. 2006;23:298–308.
62. Maskali F, Poussier S, Marie PY, et al. High-resolution simultaneous imaging of SPECT, PET, and MRI tracers on histologic sections of myocardial infarction. J Nucl Cardiol. 2005;12:229–30.
63. Thornhill RE, Prato FS, Wisenberg G, Moran GR, Sykes J. Determining the extent to which delayed-enhancement images reflect the partition-coefficient of Gd-DTPA in canine studies of reperfused and unreperfused myocardial infarction. Magn Reson Med. 2004;52:1069–79.
64. Moran GR, Thornhill RE, Sykes J, Prato FS. Myocardial viability imaging using Gd-DTPA: physiological modeling of infarcted myocardium, and impact on injection strategy and imaging time. Magn Reson Med. 2002;48:791–800.
65. Selvanayagam JB, Kardos A, Francis JM, et al. Value of delayed-enhancement cardiovascular magnetic resonance imaging in predicting myocardial viability after surgical revascularization. Circulation. 2004;110:1535–41.
66. Knuesel PR, Nanz D, Wyss C, et al. Characterization of dysfunctional myocardium by positron emission tomography and magnetic resonance: relation to functional outcome after revascularization. Circulation. 2003;108:1095–100.
67. Wu E, Judd RM, Vargas JD, Klocke FJ, Bonow RO, Kim RJ. Visualisation of presence, location, and transmural extent of healed Q-wave and non-Q-wave myocardial infarction. Lancet. 2001;357:21–8.
68. Wagner A, Mahrholdt H, Holly TA, et al. Contrast-enhanced MRI and routine single photon emission computed tomography (SPECT) perfusion imaging for detection of subendocardial myocardial infarcts: an imaging study. Lancet. 2003;361:374–9.
69. Kuhl HP, Beek AM, van der Weerdt AP, et al. Myocardial viability in chronic ischemic heart disease: comparison of contrast-enhanced magnetic resonance imaging with (18)F-fluorodeoxyglucose positron emission tomography. J Am Coll Cardiol. 2003;41:1341–8.
70. Klein C, Nekolla SG, Bengel FM, et al. Assessment of myocardial viability with contrast-enhanced magnetic resonance imaging: comparison with positron emission tomography. Circulation. 2002;105:162–7.
71. Mahrholdt H, Wagner A, Holly TA, et al. Reproducibility of chronic infarct size measurement by contrast-enhanced magnetic resonance imaging. Circulation. 2002;106:2322–7.
72. Wellnhofer E, Olariu A, Klein C, et al. Magnetic resonance low-dose dobutamine test is superior to SCAR quantification for the prediction of functional recovery. Circulation. 2004;109:2172–4.
73. Nelson C, McCrohon J, Khafagi F, Rose S, Leano R, Marwick TH. Impact of scar thickness on the assessment of viability using dobutamine echocardiography and thallium single-photon emission computed tomography: a comparison with contrast-enhanced magnetic resonance imaging. J Am Coll Cardiol. 2004;43:1248–56.
74. Steel K, Broderick R, Gandla V, et al. Complementary prognostic values of stress myocardial perfusion and late gadolinium enhancement imaging by cardiac magnetic resonance in patients with known or suspected coronary artery disease. Circulation. 2009;120:1390–400.
75. Coelho-Filho OR, Seabra LF, Mongeon FP, et al. Stress myocardial perfusion imaging by CMR provides strong prognostic value to cardiac events regardless of patient's sex. JACC Cardiovasc Imaging. 2011;4:850–61.
76. Cheong BY, Muthupillai R, Wilson JM, et al. Prognostic significance of delayed-enhancement magnetic resonance imaging: survival of 857 patients with and without left ventricular dysfunction. Circulation. 2009;120:2069–76.
77. Bertaso AG, Richardson JD, Wong DT, et al. Prognostic value of adenosine stress perfusion cardiac MRI with late gadolinium enhancement in an intermediate cardiovascular risk population. Int J Cardiol. 2013;167:2055–60.
78. Bingham SE, Hachamovitch R. Incremental prognostic significance of combined cardiac magnetic resonance imaging, adenosine stress perfusion, delayed enhancement, and left ventricular function over preimaging information for the prediction of adverse events. Circulation. 2011;123:1509–18.
79. Bodi V, Sanchis J, Lopez-Lereu MP, et al. Prognostic value of dipyridamole stress cardiovascular magnetic resonance imaging in patients with known or suspected coronary artery disease. J Am Coll Cardiol. 2007;50:1174–9.
80. Bello D, Fieno DS, Kim RJ, et al. Infarct morphology identifies patients with substrate for sustained ventricular tachycardia. J Am Coll Cardiol. 2005;45:1104–8.
81. Bleeker GB, Kaandorp TA, Lamb HJ, et al. Effect of posterolateral scar tissue on clinical and echocardiographic improvement after cardiac resynchronization therapy. Circulation. 2006;113:969–76.

Coronary Magnetic Resonance Angiography: Techniques and Clinical Results

13

Masaki Ishida and Hajime Sakuma

Introduction

Coronary artery disease is one of the leading causes of morbidity and mortality in many industrialized countries [1]. Catheter X-ray coronary angiography has been used as the gold standard for identifying significant luminal narrowing of the coronary arteries. However, X-ray coronary angiography entails small but definable risks [2], and a considerable number of patients undergoing elective X-ray coronary angiography are found to have no significant coronary artery disease [3]. Consequently there is a strong need for a noninvasive test that can reliably delineate narrowing of the coronary arteries.

During the past two decades, considerable progress has been made in the field of noninvasive imaging of the coronary arteries by using magnetic resonance (MR) angiography and computed tomography (CT). Contrast-enhanced multi-slice spiral CT has rapidly emerged as a noninvasive method that can provide visualization of the coronary arteries and detection of the luminal narrowing. Introduction of 64 slice CT scanners significantly improved the quality of coronary CT images in terms of both spatial and temporal resolution [4, 5]. Recent multicenter studies reported that significant coronary arterial stenosis was detected by using a 64-slice CT scanner with a sensitivity of 85–95% and a specificity of 83–90% compared with catheter X-ray coronary angiography [6, 7]. However, multi-slice CT has several disadvantages of requiring rapid injection of iodinated contrast medium and exposing patients to ionizing radiation. Due to recent technical advancements, estimated effective radiation dose of multi-slice CT coronary angiography has been dramatically reduced from 15 to 20 mSv to less than 5 mSv [4, 5, 8]. However, the radiation dose of the latest coronary CT angiography is not negligible in children and young adult patients, in addition to patients who require serial assessment of their coronary arteries. From a patient's point of view, coronary MR angiography is more preferable to coronary CT angiography for the detection of coronary artery disease, because it does not expose the patient to radiation or necessitates rapid injection of iodinated contrast material. In addition, the coronary arterial lumen can be readily visualized by coronary MR angiography in patients with heavy calcification of the atherosclerotic coronary plaques, an additional limitation of CT angiography.

Despite these potential advantages of coronary MR angiography, noninvasive MR imaging of the coronary artery is technically demanding due to the small size and tortuous course of the coronary artery and the complex motion caused by cardiac contraction and respiration. Sufficient contrast between the coronary arterial lumen and the surrounding tissue is crucial for visualization of the coronary artery. In addition, high spatial resolution and volume coverage of the coronary artery tree are required, and time available within the cardiac cycle for MR image data acquisition is limited to overcome complex motion of the coronary artery caused by cardiac contraction and respiration. In this chapter, the techniques currently used for coronary MR angiography are briefly reviewed. Then the current roles of coronary MR angiography for the evaluation of the coronary artery disease and other abnormalities such as anomalous coronary arteries and Kawasaki disease are explained. Moreover, new methods to improve visualization of the coronary artery will be updated in relation to future perspective.

Techniques of Coronary MR Angiography

Two-Dimensional and Three-Dimensional Acquisitions

Assessment of coronary artery disease with coronary MR angiography was initiated in the early 1990s by using breath-hold two-dimensional (2D)-segmented k-space gradi-

M. Ishida · H. Sakuma (✉)
Mie University Hospital, Department of Radiology, Tsu, Japan
e-mail: mishida@clin.medic.mie-u.ac.jp; sakuma@clin.medic.mie-u.ac.jp

R. Y. Kwong et al. (eds.), *Cardiovascular Magnetic Resonance Imaging*, Contemporary Cardiology,
https://doi.org/10.1007/978-1-4939-8841-9_13

ent-echo techniques [9–11]. Breath-hold 2D approach was relatively easy to implement and had some success in the visualization of the proximal coronary arteries. However, breath-hold 2D coronary MR angiography has several limitations, including slice misregistration due to inconsistent diaphragm positions between breath-held acquisitions, patient fatigue from multiple repeated breath-holdings, suboptimal signal-to-noise ratio due to 2D acquisition of thin slice, and high operator dependency to successfully image tortuous coronary arteries with 2D imaging slices. In order to overcome these limitations of breath-hold 2D methods, three-dimensional (3D) gradient-echo coronary MR angiography sequences were developed either by employing a breath-hold method or respiratory-gated method. The advantages of 3D coronary MR angiography are improved signal-to-noise ratio, volumetric coverage of the coronary arteries, and no misregistration between slices within each 3D volume acquisition. These features of 3D coronary MR angiography permit 3D post-processing of the coronary artery tree. In the past decade, volume coverage, acquisition speed, and arterial contrast of 3D coronary MR angiography were substantially improved with the use of steady-state free precession sequences and parallel imaging techniques, allowing for the acquisition of high-quality 3D MR angiograms encompassing the entire coronary arteries within a reasonably short imaging time.

The most fundamental weakness of 3D coronary MR angiography as compared with recent multi-slice CT scanners is slow acquisition speed of 3D volume data. For example, imaging of 3D data with 300 × 300 × 100 mm volume coverage and 0.6 × 0.6 × 0.6 mm acquisition resolution necessitates more than 20,000 phase encoding steps when parallel imaging factor of 2 and half scan are employed, which corresponds to approximately 1 min of non-ECG-gated imaging time with a repetition time of 3 ms. In contrast, acquisition of the same 3D volume can be completed in less than several hundred milliseconds by using area detector CT or dual-source CT. Due to slow speed constraints of MR, acquisition of 3D coronary MR angiography remains highly challenging. Several competing requirements, including optimal suppression of respiratory motion, high temporal resolution within the cardiac cycle, high spatial resolution, large 3D volume coverage, and good arterial contrast-to-noise, need to be simultaneously satisfied.

Suppression of Respiratory Motion

Breath-Hold 3D Coronary MR Angiography

In order to overcome limitations of 2D coronary MR angiography such as slice misregistration between breath-hold scans and suboptimal signal-to-noise ratio, 3D breath-hold coronary MR angiography sequences were developed [12–15]. Wielopolski et al. [11] proposed a breath-hold 3D coronary MR angiography with volume-targeted imaging (VCATS: volume coronary angiography with targeted volumes). Each coronary arterial segment was imaged with 24-mm-thick double-oblique 3D volume by using a single end-expiratory breath-hold. The entire major coronary arteries were covered in fewer than 13 breath holds. The diagnostic accuracy of the VCATS approach was evaluated in 38 patients by van Geuns et al. [15]. They found that 69% segments were assessable with this approach, and the sensitivity and specificity of 3D breath-hold MR coronary angiography for the detection of >50% luminal stenoses were 92% and 68%. Breath-hold 3D coronary MR angiography has advantages in terms of time efficiency compared with free-breathing 3D coronary MA angiography [16]. Another benefit of breath-hold 3D coronary MR angiography is that this method can utilize first-pass contrast enhancement of the coronary arterial blood following an intravenous injection of extracellular MR contrast medium such as Gd-DTPA [17–20]. Regenfus et al. obtained breath-hold 3D coronary MR angiography in 50 patients with suspected coronary artery disease, by injecting extracellular MR contrast medium at a flow rate of 1 ml/s immediately prior to breath-hold 3D acquisitions [20]. The sensitivity and specificity were 94% and 57% for detecting patients having significant coronary artery disease with contrast-enhanced breath-hold 3D coronary MR angiography.

Breath-hold 3D coronary MR angiography has several limitations. Short imaging time of breath-hold 3D acquisition is achieved at the expense of spatial resolution and 3D volume coverage. In addition, many patients with heart disease or pulmonary disease cannot hold their breath for a long time. Another important limitation of breath-hold MR acquisition is that breath-holding does not eliminate motion of the diaphragm. A continued drift of the diaphragm position was observed during breath-holding which can cause significant blurring on breath-hold 3D coronary MR angiography [21].

Free-Breathing 3D Coronary MR Angiography

Free-breathing, respiratory-gated 3D coronary MR angiography is currently the most commonly used MR approach for the assessment of coronary arteries in patients with heart disease. Respiratory bellows belt were initially used to obtain free-breathing coronary MR angiography [21, 22]. Oshinski et al. reported that free-breathing 2D coronary MR angiography with respiratory belt provides improved resolution, aligned sections of coronary arteries, and improves patient tolerance [22]. However, respiratory motion artifacts and blurring were inevitable with respiratory bellows belt because it cannot detect drift of the diaphragm position. Free-breathing coronary MR angiography has been substantially improved with respiratory navigators which measure the position of the right lung-diaphragm interface by using

MR signal. The initial implementations of free-breathing 3D coronary MR angiography were based on retrospective navigator gating [23–26]. With retrospective navigator echo sequences, image data were over sampled by acquiring each phase encoding step data several times regardless of the respiratory motion. During reconstruction, only image data acquired within a respiratory gating window were used for generating coronary MR angiography. Retrospective navigator gating has been replaced by a prospective real-time navigator gating method [27–30]. Current free-breathing 3D coronary MR angiography sequences utilize radiofrequency excitation pulse to excite a column of tissue perpendicular to the right lung-diaphragm interface (Fig. 13.1). In each cardiac cycle, both navigator echo data for respiratory gating and image data were acquired. If position of the lung-diaphragm interface is within a predefined acceptance window (typically ±2.5 mm) at the end-expiratory level, image data are accepted and stored for image reconstruction. Otherwise, image data are rejected and acquisition is repeated in the next cardiac cycle. Coronary MRA data acquisition is continued until all necessary data in k-space are collected. In addition to respiratory gating, navigator echo data is used for adaptive real-time motion correction of 3D imaging volume [27–31]. If the lung-diaphragm interface is within an acceptance window, the superior-to-inferior position of 3D acquisition volume is corrected on a real-time basis by utilizing the positional offset information of the lung-diaphragm interface measured by navigator echo.

There are several advantages in free-breathing 3D coronary MR angiography with prospective navigator gating. Since there is no constraint of imaging time caused by breath-holding, 3D coronary MR images can be acquired with improved spatial resolution, larger 3D volume overage of the coronary artery tree, and improved signal-to-noise. The major disadvantage of free-breathing 3D coronary MR angiography is a long scan time, which typically ranged from several minutes to 15 min. Another limitation is that acquisition of free-breathing 3D coronary MR angiography often fails in patients with irregular breathing pattern and those showing a drift of diaphragm position over time. To overcome this problem, several approaches have been proposed. First, the use of 32-channel cardiac coils and a higher parallel imaging factor has been proposed. In a study by Nagata et al., the mean imaging time of whole-heart coronary MRA at 1.5 T significantly reduced from 12.3 ± 4.2 min with five-channel coils to 6.3 ± 2.2 min by using 32-channel coils [32]. The reduction of imaging time leads to an improved study success rate (100%) without noticeable worsening of image quality [32]. Second, the abdominal belt helps to shorten the imaging time of whole-heart coronary MRA because it reduces the amplitude of diaphragmatic position and improves scan efficiency (Fig. 13.2). A recent

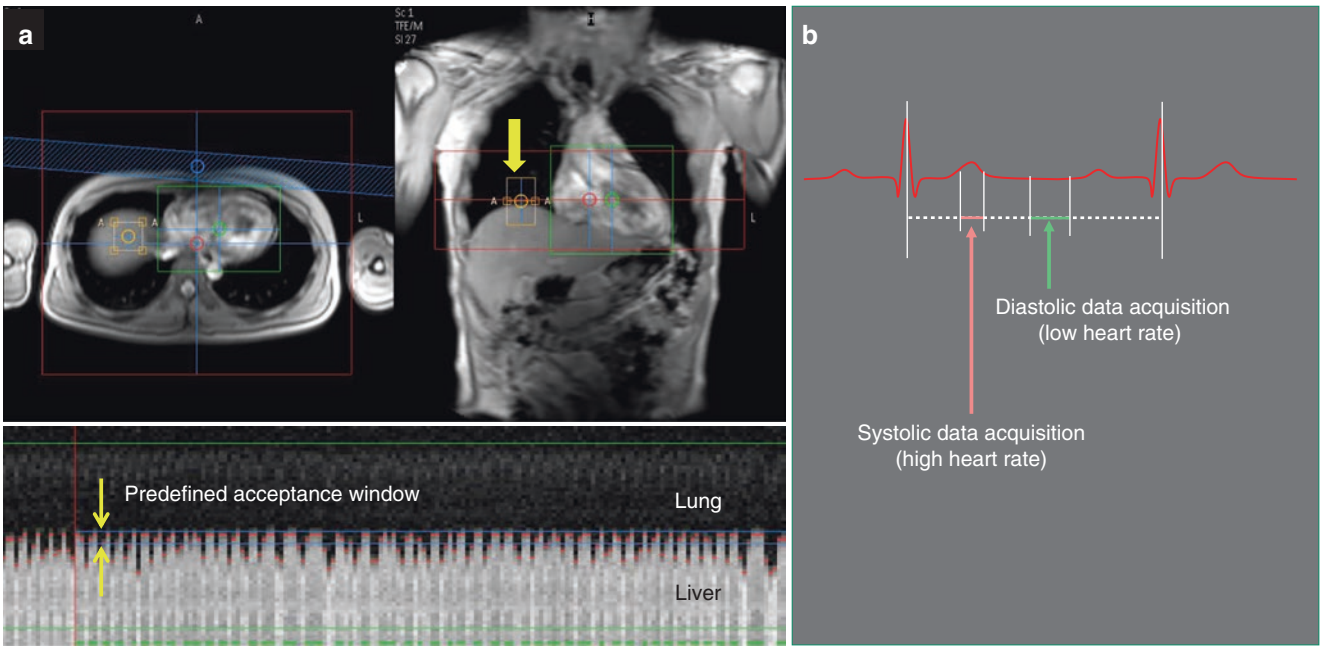

Fig. 13.1 Respiratory-gated acquisition with a prospective real-time navigator echo method. (**a**), A selective 2D radiofrequency excitation pulse to excite a column of tissue perpendicular to the right lung-diaphragm interface. If position of the lung-diaphragm interface is within a previously defined acceptance window at the end-expiratory level, image data are accepted and stored for image reconstruction. (**b**), Coronary MR angiography can be acquired either in end-systole or during diastole. In patients with a high heart rate, narrow acquisition window is critically important for reducing motion blurring of the coronary MRA. Even in patients with low heart rate, narrow acquisition window of 30–50 ms is helpful to obtain sharp coronary MR angiograms

Fig. 13.2 The 20-cm wide abdominal belt was wrapped tightly around the patient's abdomen during end-expiration to suppress diaphragmatic motion

study by Ishida et al. showed that the application of the abdominal belt significantly improved scan efficiency and image quality of navigator-gated whole-heart coronary MRA both in the UK and Japanese patient population [33].

Suppression of Cardiac Motion

X-ray coronary angiography can provide high-resolution images of the coronary artery real time without using cardiac gating or respiratory gating, because acquisition time per image frame is short enough (<20 ms) to eliminate motion blurring of the coronary artery. In contrast, electrocardiographic (ECG) gating is required in coronary MR angiography because MR imaging time is too long to freeze the motion of the coronary artery by cardiac contraction and diastolic relaxation. In most initial studies of coronary MR angiography, image data were acquired during mid-diastolic phase by using a fixed delayed time after ECG R-wave trigger. However, the optimal delay time and width of acquisition window in the cardiac cycle to minimize coronary arterial motion is different from patient to patient. Therefore, both trigger delay time and acquisition window in the cardiac cycle should be optimized in each patient. Stuber et al. proposed the following equation to calculate the delay after R-wave trigger to start data acquisition: $Td = [(tRR - 350) \times 0.3] + 350$, where tRR refers to the time between two consecutive ECG R-waves [34]. This equation is based on a principle in cardiac physiology that the systolic duration in the cardiac cycle remains relatively constant and the diastolic duration is reduced as the heart rate increases. The approach using this equation allows for an automated calculation of the acquisition delayed time in the cardiac cycle. However, the rest period of the coronary artery in the cardiac cycle is substantially different in each patient depending not only on patients' heart rate but also other hemodynamic factors, which may cause inconsistent image quality of coronary MR angiography with the standardized ECG trigger delay calculated form heart rate [35]. The use of subject-specific data acquisition window in the cardiac cycle is recommended to improve quality of coronary MR angiography and is especially critical for the visualization of the right coronary artery [36], since the right coronary artery moves more than twice as much as the left coronary arteries. There are several approaches to determine a subject-specific acquisition window in the cardiac cycle. Wang et al. proposed an ECG-triggered M-mode navigator echo technique to monitor cardiac motion and identify the period of minimal cardiac motion in the cardiac cycle [35]. Recently, high temporal resolution cine MR images acquisition is more commonly performed in order to determine the subject-specific data acquisition window in the cardiac cycle [37]. A trigger delay time and an interval of minimal motion of the coronary artery are visually determined on cine MR images for the subsequent coronary MR angiography acquisition, typically by referring the RCA.

Free-breathing acquisition with the navigator echo technique allows for the use of narrow acquisition windows in the cardiac cycle that can effectively reduce motion blurring of the coronary artery. However, as the acquisition window is shortened, the overall scan time is prolonged. Higher parallel imaging factor achieved by 32-channel cardiac coils can reduce overall data acquisition time of coronary MRA, which can be utilized not only to reduce total study time but also to narrow the acquisition window in the cardiac cycle without extending the scan time. In a study reported by Nagata et al., the mean acquisition window in the cardiac cycle by using 32-channel cardiac coils and parallel imaging factor of 4 (84 ± 57 ms for diastolic acquisition and 48 ± 18 ms for systolic acquisition) was approximately half of that in a previous study using 5-channel cardiac coils (152 ± 67 ms for diastolic acquisition and 98 ± 26 ms for systolic acquisition), while the success rate, image quality, and overall scan time were substantially improved [32, 38]. In patients with a high heart rate, narrow acquisition window in the cardiac cycle (<50 ms) is critically important for reducing motion blurring of the coronary artery on whole-heart coronary MRA. It should be noted that even in patients with low heart rate, narrow acquisition window of 30–50 ms is helpful to obtain sharp coronary MR angiograms.

Contrast of the Coronary Artery

Pulse Sequence and Magnetic Field Strength

On 2D gradient-echo coronary MR angiography, high luminal blood signal is primarily generated by the in-flow effect of unsaturated blood spins flowing into thin 2D imaging slice. Although an introduction of 3D gradient-echo coronary MR

angiography eliminates many of the drawbacks of 2D coronary MR angiography, 3D gradient-echo approach has one significant downside, that is, reduced in-flow effect. Blood spins in thick 3D volume is progressively saturated by repeated radiofrequency excitations, and the arterial blood signal intensity on 3D gradient-echo coronary MR angiography is substantially attenuated when 3D imaging volume is large. Therefore, relatively thin 3D volume (2–3 cm total thickness) targeting one of the major coronary arteries is preferable to 3D gradient-echo coronary MR angiography [29, 30].

3D coronary MR angiography sequences with steady-state free precession acquisition (true FISP, fast imaging in steady-state precession; balanced TFE, balanced turbo field echo; FIESTA, fast imaging employing steady-state acquisition) permit acquisition of MRA images with high blood contrast without administration of MR contrast media. Because steady-state free precession sequence is sensitive to magnetic field inhomogeneities, short repetition time, and volume shimming capability to achieve homogeneous magnetic field in the imaging volume are important to obtain good coronary MR angiograms. With steady-state free precession sequences, the blood signal intensity on 3D coronary MR angiography is considerably higher than that of 3D gradient-echo sequence [39, 40]. As a result, 3D coronary MR angiography with steady-state free precession acquisition is not dependent on in-flow effect and excellent 3D coronary MR angiograms with high blood signal can be obtained by using thick 3D volume coverage. Image quality of 3D steady-state coronary MR angiography is further improved with an optimization of k-space sampling strategy. Reduced motion artifacts and superior vessel sharpness were observed with the 3D steady-state coronary MR angiographic sequence with radial k-space sampling when compared with those by cartesian 3D steady-state coronary MR angiography and 3D gradient-echo coronary MR angiography [41].

Whole-heart coronary MR angiography using a free-breathing 3D steady-state free precession has been introduced as a method that can provide visualization of all three major coronary arteries with a single 3D acquisition [42] (Figs. 13.3 and 13.4). Steady-state free precession sequences permit acquisition of thick 3D axial volume that encompasses the entire heart without losing arterial contrast. By using this whole-heart approach, one can visualize all three major coronary arteries with a reduced total examination time in comparison with targeted double-oblique 3D gradient-echo MR angiography. In addition, planning of whole-heart coronary MR angiography is quite simple, which eliminates time-consuming 3-point planning that was required for the targeted double-oblique approach. Although 3D coronary MR angiography using targeted double-oblique acquisitions demonstrated relatively good accuracy for identifying stenoses in the proximal and middle coronary arterial segments, coverage of the distal segments was often limited. For example, the proportion of assessable segments was 68% for the middle left circumflex artery with targeted double-oblique 3D coronary MR angiography [30]. With the whole-heart approach, long segments of all major coronary arteries can be imaged. The proportion of distal segments exhibiting good or excellent image quality was over 90% for all major coronary arteries in our study using the whole-heart approach [32, 38, 43].

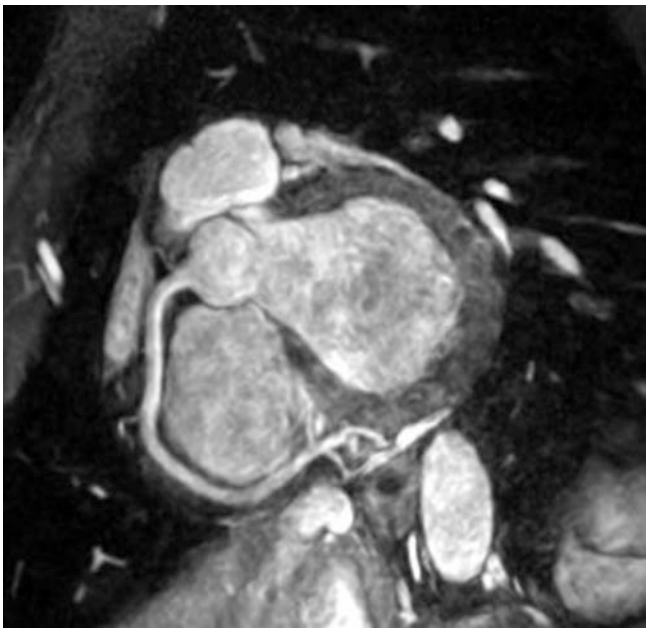

Fig. 13.3 Free-breathing 3D coronary MR angiography of the right coronary artery acquired with a steady-state free precession sequence (balanced TFE) with fat saturation and T2 preparation and a double-oblique targeted volume approach. Respiratory gating was performed with a prospective real-time navigator echo technique. Three-point planning was used to define double-oblique 3D slices parallel to the right coronary artery. No stenosis in the coronary artery is demonstrated in this case

Steady-state free precession (SSFP) sequences are generally preferred to gradient-echo sequences at 1.5 T because the high T2/T1 ratio of the blood acts as an intrinsic contrast medium for SSFP coronary and helps to increase the blood signal on non-contrast-enhanced coronary MRA [39, 40] (Figs. 13.5 and 13.6). Higher magnetic field strength at 3 T is increasingly used for cardiac MRI, because high-field MR imaging can provide improved SNR [44, 45]. The difficulties of 3 T cardiac MRI include increased off-resonance effect caused by magnetic field inhomogeneity and high specific adsorption rate (SAR). As the result, coronary MRA using SSFP acquisition is particularly challenging at higher field strength, because SSFP sequence is susceptible to inhomogeneity of magnetic field and requires higher flip angles to obtain enough contrast between the blood and the myocardium. Consequently, at 3 T, gradient-echo sequences are generally preferred to SSFP for coronary MRA acquisition [46] (Fig. 13.7).

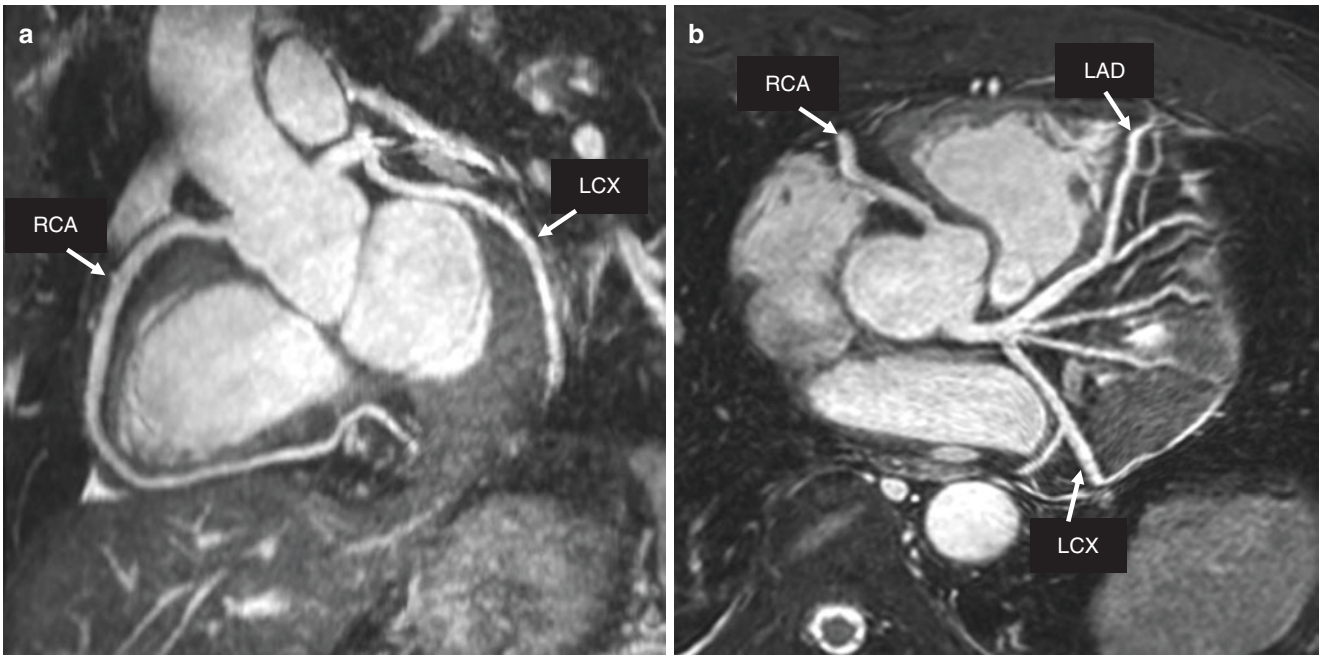

Fig. 13.4 Free-breathing, navigator echo-gated whole-heart coronary MR angiography acquired with a steady-state free precession sequence (balanced TFE) with fat saturation and T2 preparation in a subject with normal coronary artery. (**a**), Left anterior oblique whole-heart coronary MR angiogram reformatted with curved multi-planar reformatting clearly depicts the right coronary artery (RCA) and left circumflex (LCX) arteries. (**b**), Oblique axial whole-heart coronary MR angiogram reformatted with curved multi-planar reformatting visualizes the left main coronary artery, left anterior descending (LAD) artery, proximal RCA and LCX arteries [43]. (Reprinted with permission from Sakuma et al. [43], Copyright 2005, with permission from Radiological Society of North America)

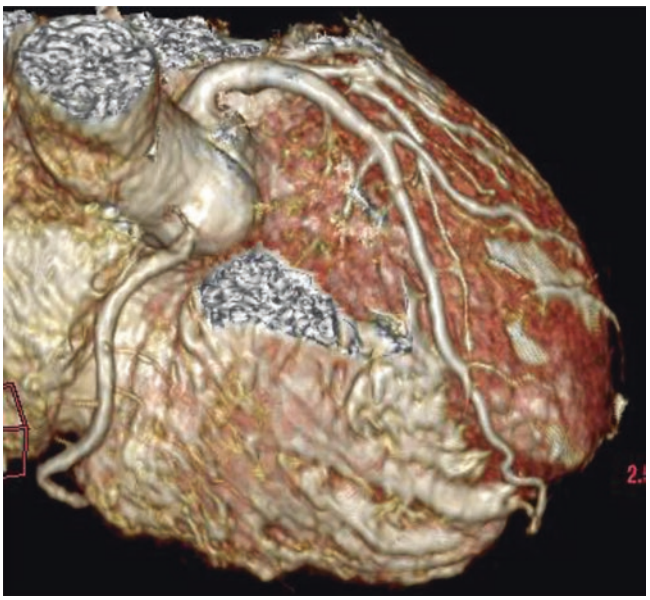

Fig. 13.5 Whole-heart coronary MR angiography acquired with a free-breathing steady-state free precession sequence in a subject with normal coronary artery. Volume rendering image of whole-heart coronary MR angiography is useful for three-dimensional anatomical recognition of the right coronary artery, left anterior descending artery, and its branches

Recently an interesting findings were reported by Soleomanifard et al., demonstrating that the 3D bSSFP acquisition, using advances in 3.0 T MR scanner equipped with recently available technologies such as multi-transmit, 32-channe cardiac coil, and localized B0 and B1+ shimming, provides high-quality noninvasive imaging of the proximal to distal segments of the major coronary arteries employing a single breath-hold volume-targeted coronary MRA [47].

Preparation Pulses for Ensuring Sufficient Image Contrast

The contrast between luminal blood and surrounding tissue needs to be maximized for the better delineation of the coronary artery on MR angiography. With "bright blood" coronary MR angiography, the pulse sequences are designed to enhance the signal from coronary arterial blood and to suppress the signal from the surrounding structures such as pericardial fat and myocardium [10]. In contrast to 3D time-of-flight MRA of the cerebral arteries, in-flow effect of the arterial blood is less prominent on coronary MRA. Therefore, suppression of the signal from the surrounding structures such as pericardial fat and myocardium is important to obtain sufficient arterial contrast on coronary MRA [10, 48]. Suppression of fat signal can be achieved by

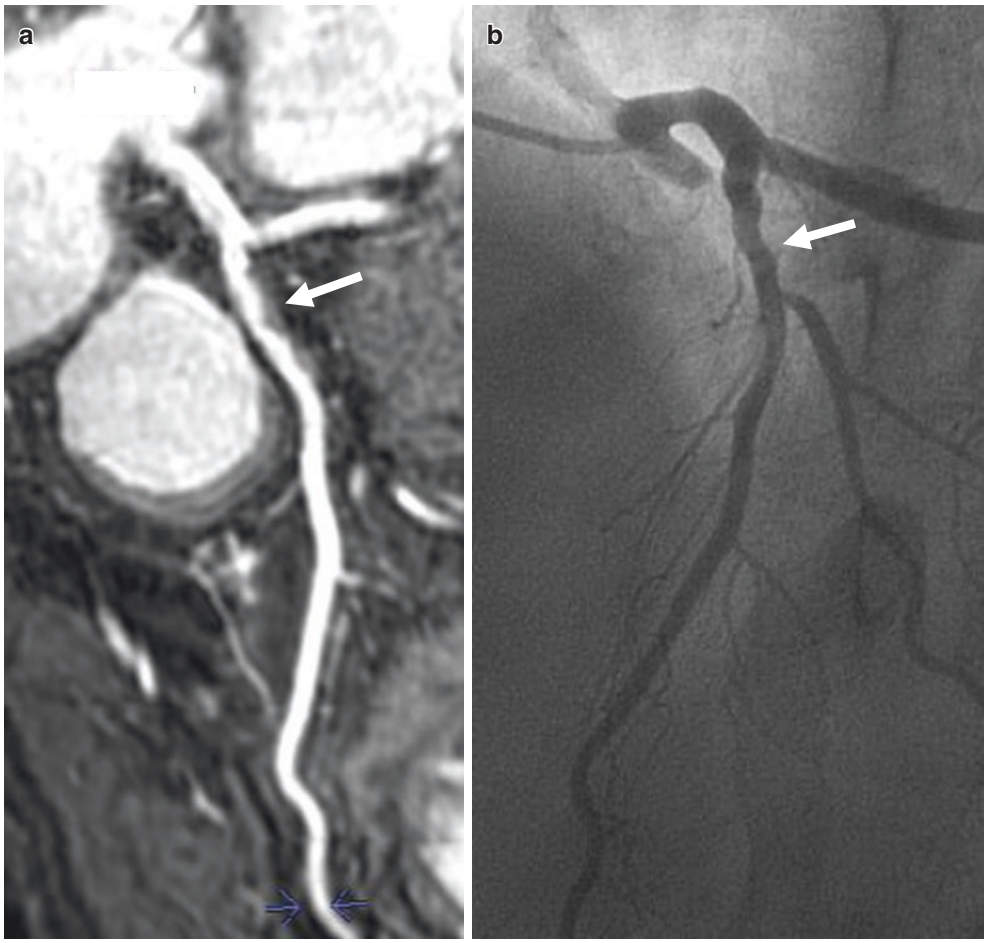

Fig. 13.6 Whole-heart coronary MR angiography acquired with a free-breathing, steady-state free precession sequence in a patient with suspected coronary artery disease. (**a**) Curved multi-planar reformatted image of whole-heart coronary MR angiography clearly reveals proximal and distal segments of the left anterior descending artery. Although no significant luminal narrowing is observed, MR image reveals the presence of atherosclerotic plaque in the coronary arterial wall (arrow). (**b**) X-ray coronary angiography in the same subject

applying a fat saturation pulse that selectively saturates the longitudinal magnetization of fat spins prior to image acquisition. Another alternative approach to suppress fat signal is use of a spectral selective radiofrequency pulse that selectively excites water spins. Currently fat saturation pulses are more widely used because short repetition time, which is critical to obtain good coronary MR angiographic images with steady-state free precession sequences, is more easily achieved. Recently, highly resolved, dual-echo Dixon CMRA approaches have been developed to enhance CMRA image quality by improved fat suppression and to provide additionally fat-only information [49]. In their study, it has been shown that Dual-echo Dixon can help to improve whole-heart CMRA image quality significantly. The additional whole-heart fat information delivered by this approach also has a potential to evaluate the diagnostic and the predictive value of intramyocardial and extramyocardial fatty deposits.

Suppression of myocardial signal is important for the visualization of distal coronary arteries and branch arteries. A T2-weighted magnetization preparation pulse is used to suppress myocardial signal [28]. Another advantage of T2 preparation pulse is a suppression of venous blood signal in the epicardial veins. T2 relaxation time of deoxygenated venous blood is substantially shorter than that of oxygenated arterial blood, resulting in the reduction of venous blood signal with T2 preparation pulse.

This T2 preparation prepulse is commonly applied without spatial selection to minimize flow sensitivity, but the nonselective implementation results in a reduced magnetization of the in-flowing blood and a related penalty in signal-to-noise ratio. Soleimanifard et al. have proposed the use of spatially selective T2 preparation prepulse where the user could freely adjust angulation and position of the T2Prep slab to avoid covering the ventricular blood pool and saturating the in-flowing spins [47]. They demonstrated that the spatially selective T2Prep increased in vivo human coronary artery signal-to-noise ratio (42.3 6 2.9 vs. 31.4 6 2.2, n 5 22, $P < 0.0001$) and contrast-to-noise ratio (18.6 6 1.5 vs. 13.9 6 1.2, P 5 0.009) as compared to those of the nonselective T2Prep [47].

Contrast Medium

Administration of T1 shortening MR contrast medium is useful to improve blood contrast on 3D gradient-echo coronary MR angiography. In the presence of T1 shortening MR

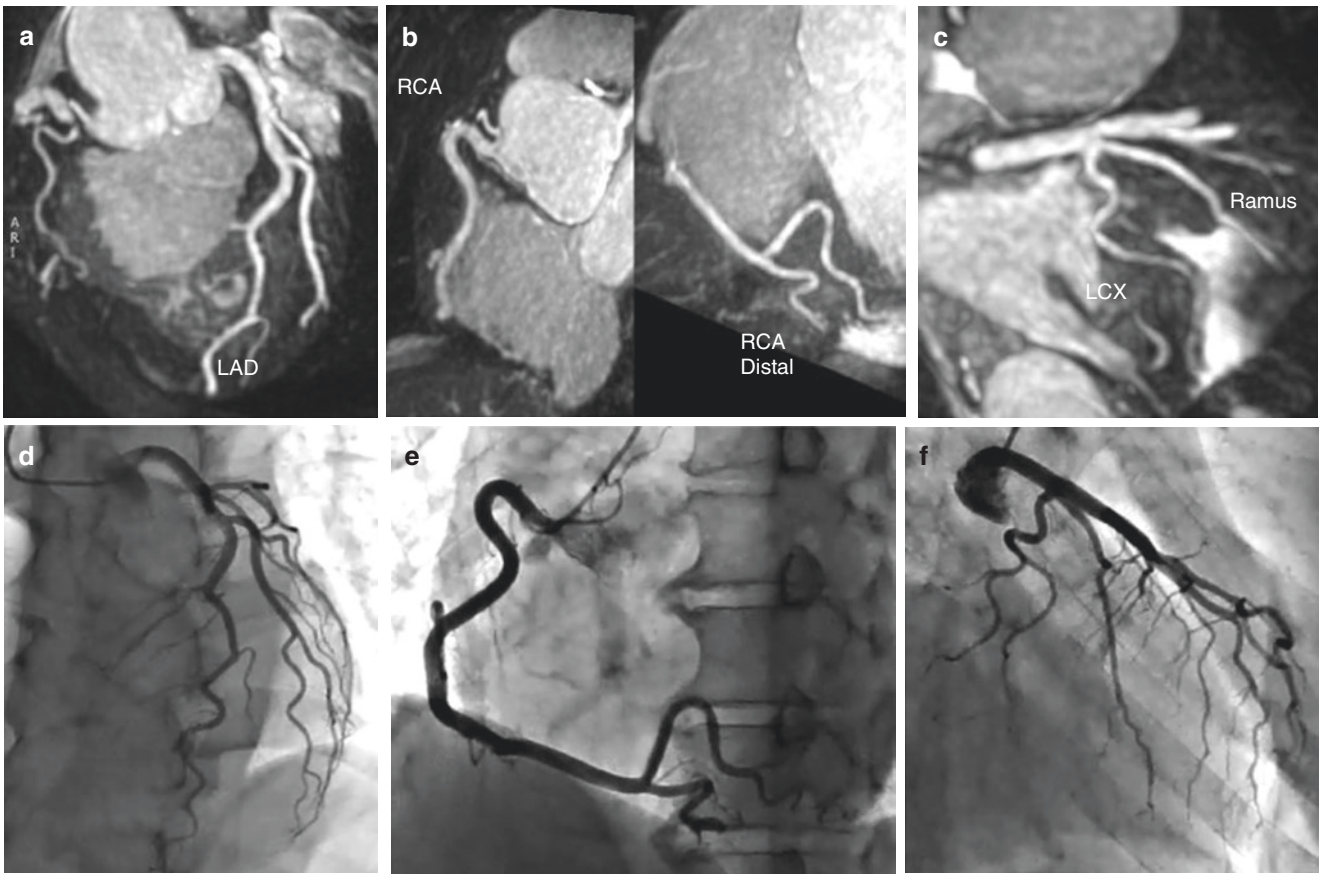

Fig. 13.7 Thin-slab maximum-intensity projection images of whole-heart coronary MR angiography acquired with a gradient-echo sequence in a subject with normal coronary artery at 3.0 tesla MR imager for the left anterior descending artery (LAD) (**a**), right coronary artery (RCA) (**b**), and circumflex artery (LCx) (**c**). MRA data was acquired after late gadolinium contrast-enhance MRI (0.15 mmol/kg) using T1-weighted gradient-echo sequence with T2 preparation and SPIR. Corresponding X-ray coronary angiogram was demonstrated (**d–f**)

contrast medium, magnetization of blood spins rapidly recovers after radiofrequency pulse, preventing saturation of the blood signal. With sufficient blood concentration of MR contrast medium, the blood signal intensity is primarily determined by T1 relaxation time of the blood instead of inflow effect, and one can utilize high radiofrequency flip angle to maximize the blood signal. In addition, contrast enhancement allows for acquiring 3D gradient-echo coronary MR angiograms with large 3D volume coverage. There are three different types of contrast medium currently available, as follows: (1) extracellular contrast medium [20], (2) intravascular contrast medium [50], and (3) slightly albumin-binding contrast medium [51]. Conventional extracellular contrast medium exhibits nonspecific distribution in the extracellular space and rapidly extravasates from intravascular space to the interstitial space after intravenous administration. Sufficient T1 shortening of the blood is only maintained during the first pass following venous administration [17, 18]. In contrast, intravascular MR contrast media remain in the blood pool longer than the extravascular contrast media. These intravascular contrast media, either iron particles [52, 53] or gadolinium molecules with [54, 55] and without albumin-binding [56], are distributed in the blood pool and exhibited greater T1 shortening effects in comparison with conventional extracellular contrast media. Slightly albumin-binding contrast medium exhibits relatively prolonged retention time in the blood and high relaxivities [57] while maintaining late enhancement abilities [58]. Several investigators have demonstrated that administration of intravascular or slightly albumin-binding agent is highly useful in improving arterial contrast on 3D gradient-echo coronary MR angiography [51–56]. When sufficient shortening of T1 relaxation time of the blood is achieved by administration of intravascular agent or high-dose slightly albumin-binding agent, gradient-echo MRA with inversion-recovery prepulse exhibits high blood contrast as well as good fat saturation. Recently, Raman et al. performed an intraindividual comparison of intravascular contrast agent, gadofosveset (0.03 mmol/kg), and extracellular agent, Gd-BOPTA (0.1 mmol/kg), for free-breathing 3D coronary MRA at 3.0 T using a relatively slow injection scheme with 20 mL saline flush at a flow rate of 0.66 mL/s [59]. They conclude that the

use of an intravascular contrast agent performed as well as, or slightly better than, a primarily extravascular extracellular contrast agent for coronary MRA at 3 T [59].

Recent Improvements in Acquisition Speed and Resolution

Imaging Acceleration with Parallel Imaging Techniques

Imaging speed is very important not only for breath-hold 3D coronary MR angiography but also for free-breathing 3D coronary MR angiography, as reduced scan time leads to improved study success rate and higher patient throughput. Parallel imaging techniques in image space such as SENSE (sensitivity encoding) or in k-space such as generalized autocalibrating partially parallel acquisition (GRAPPA) and simultaneous acquisition of spatial harmonics (SMASH) enable substantial scan time reduction in cardiac MR imaging [60–62] and are now widely used to reduce scan time of clinical 3D coronary MR angiography. The major drawback of using fast imaging techniques such as parallel imaging and half scan is loss of signal-to-noise ratio. Therefore, it is important to have an appropriate balance between speed and image quality when determining imaging parameters of coronary MR angiography. Multichannel coils and high-field MR system are two approaches that can provide substantial improvement in the signal-to-noise ratio of coronary MR angiography. In a study by Reeder et al., 32-channel cardiac coils demonstrated significantly improved signal-to-noise ratio and geometry factor, which permits to use parallel imaging acceleration factor of up to 4 [63], while the acceleration rates using 5–16 element cardiac-coil arrays is up to twofold.

High-Field Coronary MR Angiography for Improved Resolution and SNR

There has been an increasing interest in high-field coronary MR angiography, because signal-to-noise ratio increases approximately linearly with field strength, and substantial improvement in signal-to-noise ratio is expected with a magnetic field strength of 3.0 T [45, 46]. This gain in signal-to-noise ratio enables the acquisition of images with higher spatial resolution or reduced imaging time, both of which are especially important in coronary MR angiography. In 2002, Stuber et al. demonstrated the feasibility of human coronary MR angiography using a 3.0 T MR imager [44]. There are several important impediments to high-field cardiac imaging, which include high radiofrequency power deposition quadratically increased with field strength, susceptibility-related local magnetic field variations, increased sensitivity to motion artifacts, impaired ECG R-wave triggering due to augmented magnetohydrodynamic effects. However, 3.0 T MR imager has become a platform of choice for high-resolution coronary MR angiography because whole-heart coronary MR angiography at 3.0 T has shown significantly improved image quality and diagnostic accuracy as compared with those at 1.5 T with a use of gadolinium contrast administration and gradient-echo sequence [36, 59]. Recently, excellent volume-targeted coronary MR angiograms with submillimeter spatial resolution ($0.35 \times 0.35 \times 1.5$ mm^3) were demonstrated at 3.0 T, allowing for improved detection of stenosis [64]. However, such high-resolution targeted acquisitions require a 9-min scan time per vessel assuming 100% navigator gating efficiency. Thus, further imaging acceleration technique will be desirable.

Clinical Applications of Coronary MR Angiography

Anomalous Coronary Arteries

Anomalous origin of the coronary artery is relatively uncommon but important cause of chest pain and sudden cardiac death. The incidence of anomalous coronary arteries in subjects without known congenital heart disease was reported to be 0.3–0.9% [65, 66]. Among various types of anomalous coronary arteries, the coronary arteries that pass between the aorta and pulmonary artery have a potential to impair myocardial perfusion and can cause sudden death. The diagnostic method of choice for detecting coronary artery anomalies has been catheter X-ray coronary angiography. However, X-ray coronary angiography provides only a 2D view of a vessel's complex 3D path and is associated with several limitations including invasiveness and radiation exposure. Coronary MR angiography has been shown to have high sensitivity and specificity for detecting anomalous coronary arteries and for delineating proximal courses of the vessels [67–69] (Fig. 13.8). A recent study demonstrated that anomalous coronary arteries can be accurately assessed by contrast-enhanced multi-slice CT as well [70]. However, coronary MR angiography seems to be more preferable to CT, because many patients with suspected anomalous coronary arteries are in younger age and MR angiography can provide equivalent diagnostic information for the detection of anomalous coronary arteries and for the identification of their proximal courses without exposing the patients to radiation.

Kawasaki Disease

Kawasaki disease is an acute febrile illness with mucosal inflammation, skin rash, and cervical lymphadenopathy in young children [71] and produces coronary artery aneurysms in up to 25% of untreated cases. Size of coronary artery aneurysm often changes over time and is correlated with the risk of

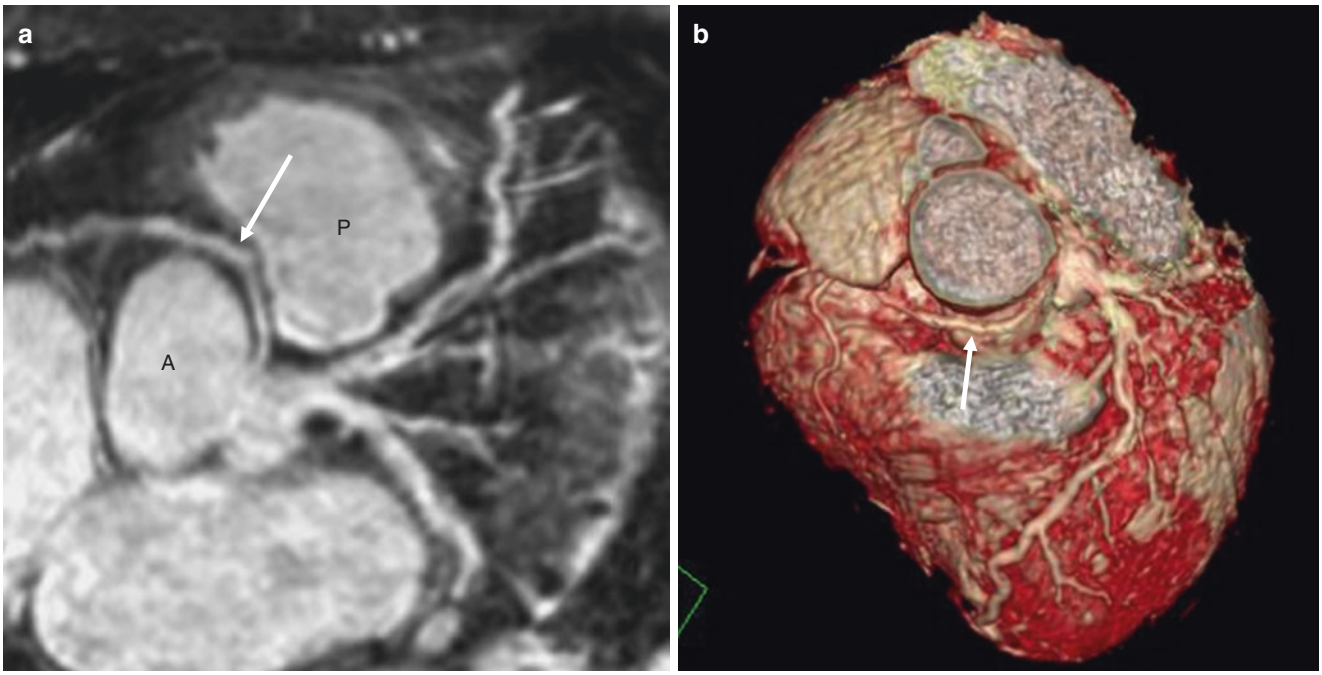

Fig. 13.8 Whole-heart coronary MR angiography in a patient with anomalous right coronary artery. Curved multi-planar reformatted MR angiographic image (**a**) and volume rendering image (**b**) demonstrate that the anomalous right coronary artery arises from the left sinus of Valsalva. The proximal course of the right coronary artery with anomalous origin (arrow) is located between the aortic root (A) and right ventricular outflow tract to proximal pulmonary artery (P)

coronary thrombosis and development of coronary artery stenoses. Thus, serial assessment of aneurismal size is important in risk stratification and therapeutic management. Serial evaluation with X-ray angiography in children carries risks associated with invasive catheterization and exposure to ionizing radiation. Transthoracic echocardiography is widely used and is often sufficient for the assessment of coronary artery aneurysm in young children. As children grow, however, visualization and characterization of the coronary artery become more difficult. Coronary MR angiography provides noninvasive detection and size measurement of coronary artery aneurysms in patients with Kawasaki disease and can be used as an alternative imaging method when image quality of transthoracic echocardiography is insufficient [72] (Fig. 13.9). Another recent study demonstrated that MR coronary angiography and X-ray coronary angiography shows excellent agreement in the diagnosis of coronary artery aneurysm, and the maximal diameter and length of the aneurysm by MR angiography and X-ray coronary angiography were similar [73].

Coronary Artery Disease

Diagnostic Accuracy of Visual Assessment of Coronary MRA

Detection of coronary arterial stenoses with coronary MR angiography is challenging, because sufficient spatial resolution is required to correctly identify luminal narrowing of the coronary artery. Table 13.1 summarizes the sensitivity and specificity of coronary MR angiography for the detection of coronary arterial stenoses in representative previous studies [10, 15, 20, 26, 30, 32, 74–80]. The sensitivity (50–96%) and specificity (42–97%) of coronary MR angiography for predicting coronary artery stenoses on X-ray coronary angiography were considerably variable in these studies. Because coronary MR angiography sequences have undergone considerable technical improvements over the past 20 years, the diagnostic accuracy of coronary MR angiography has significantly improved over time.

The first multicenter study was reported by Kim and colleagues by using free-breathing, navigator-gated 3D gradient-echo coronary MR angiography [30]. In this study, 109 patients with suspected coronary artery disease were evaluated, and 84% (636/759) of the proximal and middle coronary artery segments were interpretable on MR angiography. The sensitivity and specificity of coronary MR angiography for identifying a patient as having significant coronary artery disease were 93% and 42%. In the subgroup of patients with the left main coronary artery disease or three-vessel disease, coronary MR angiography demonstrated the sensitivity of 100% and the specificity of 85%, indicating the value of free-breathing 3D coronary MRA for excluding severe coronary artery disease.

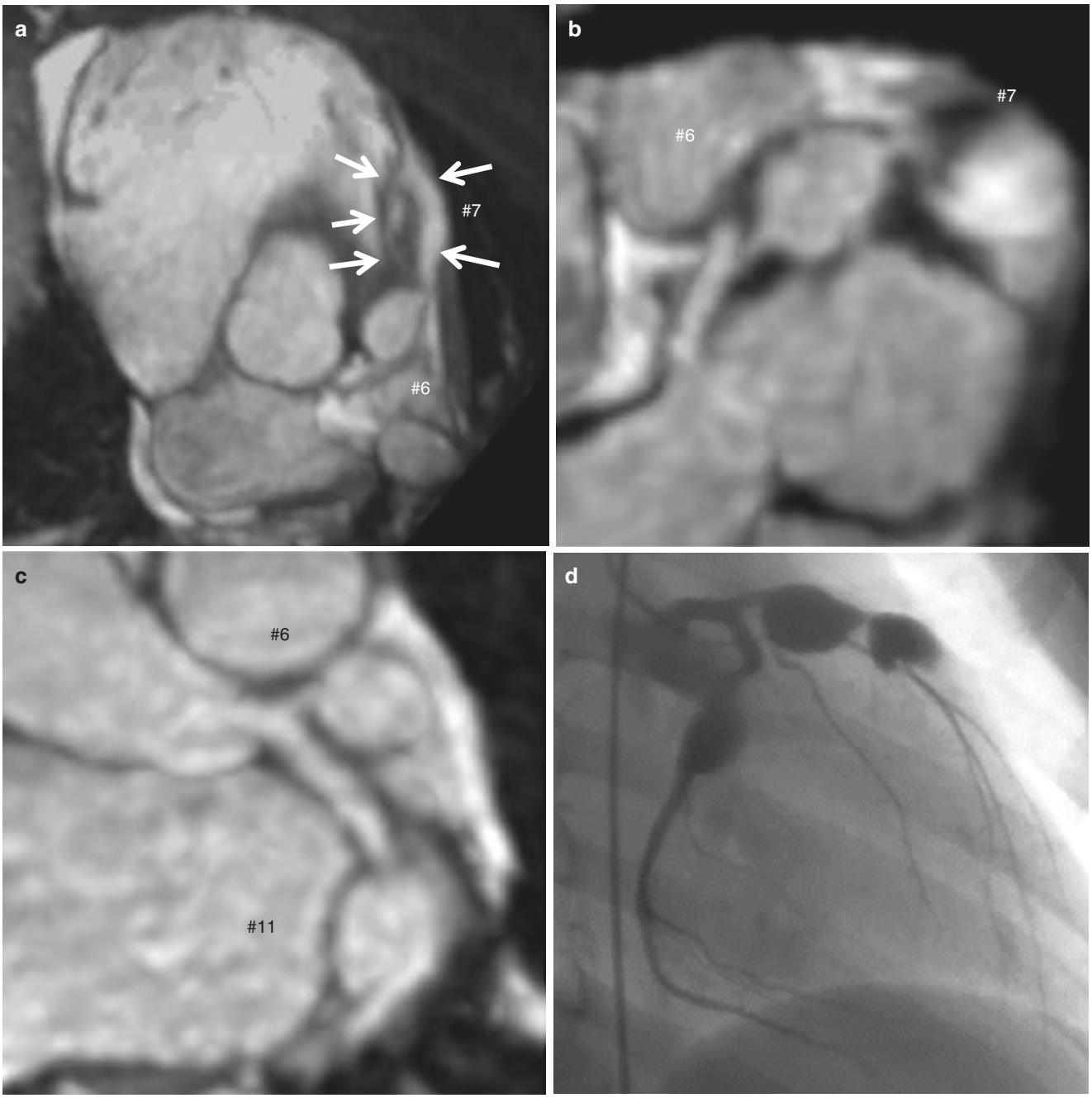

Fig. 13.9 Whole-heart coronary MR angiogram in an 8-year-old boy with Kawasaki disease. (**a**–**c**), Thin-slab maximum-intensity projection images of coronary MRA demonstrates multiple aneurysms in LAD and LCx. It should be noted that partial luminal thrombus is visualized demonstrated in the aneurysm located on LAD #7, which is confirmed on invasive X-ray angiography (**d**)

An introduction of steady-state free precession sequences has considerably improved contrast of 3D coronary MR angiography, because steady-state sequences can provide inherently high blood signal intensity without using MR contrast medium. Jahnke et al. compared the diagnostic performances of breath-hold 3D coronary MR angiography and free-breathing coronary MR angiography by using the steady-state free precession sequence, double-oblique targeted volume acquisition [81]. They found that more coronary artery segments were assessable with free-breathing coronary MR angiography (79%) than breath-hold coronary MR angiography (45%). In addition, free-breathing coronary MRA angiography was superior to breath-hold coronary MR angiography both in terms of image quality and diagnostic accuracy, with overall sensitivity and specificity of 72% and 92% by free-breathing approach and 63% and 82% by breath-hold approach.

Table 13.1 Detection of significant coronary arterial stenoses with coronary MR angiography in representative previous studies [10, 15, 20, 26, 30, 32, 74–80]

Investigator	Reference	Method	Sensitivity (%)	Specificity (%)
Manning WJ	NEJM 1993;328:828 [10]	2D breath-hold	90	92
Duerinckx AJ	Radiology 1994;193:731 [74]	↑	63	82
Van Geuns RJ	Radiology 2000;217:270 [15]	3D breath-hold	68	97
Regenfus M	JACC 2000;36:44 [20]	↑	94	57
Woodard PK	AJR 1998;170:883 [26]	3D navigator, retrospective	73	N/A
Sandstede JJ	AJR 1999;172:135 [75]	↑	81	89
Sardanelli F	Radiology 2000;214:808 [76]	↑	82	89
Kim WY	NEJM 2001;345:1863 [30]	3D navigator, prospective	93	42
Bogaert J	Radiology 2003;226:770 [77]	↑	50	90
Kefer J	JACC 2005;46:92 [78]	↑	75	77
Kato S	JACC 2010;56:983 [79]	↑	88	72
Nagata M	Radiology 2011;259:384 [32]	↑	87	86
Yang Q	Circ Cardiovasc Imaging 2012;5:573 [80]	↑	96	87

Free-breathing coronary MR angiography with axial 3D slices covering the whole-heart has become feasible by utilizing a navigator-gated 3D steady-state free precession sequence. Whole-heart coronary MR angiography can provide visualization of the entire coronary artery trees in a single 3D acquisition [38, 42, 43, 82]. An initial study in our group demonstrated that acquisition of whole-heart coronary MR angiography was successful in 34 (87.2%) of 39 patients, with the averaged acquisition duration of 13.8 ± 3.8 min [43]. In addition, long segments of all major coronary arteries including the distal segments can be imaged. The sensitivity and specificity of 1.5 T whole-heart coronary MR angiography in 20 patients for detecting patients having at least one coronary arterial stenosis were 83.3% and 75.0% in this initial study.

For the further improvement of detection of coronary artery disease, whole-heart coronary MR angiography was acquired in 131 patients by using an optimized acquisition window [38]. In contrast to our previous study, a patient-specific acquisition window was set either during systole or during diastole, depending on the phase of minimal motion of the right coronary artery on cine MR images. Coronary MR angiograms were acquired during diastole in 83 patients (delay after R-wave trigger, 627 ms ± 64) and during systole in 48 patients (delay after R-wave trigger, 259 ms ± 39). The study success rate of whole-heart coronary MR angiography (86%) was not improved by using an optimized patient-specific acquisition window either during systole or diastole. However, the sensitivity, specificity, positive predictive value and negative predictive value of whole-heart coronary MR angiography for detecting patients having significant stenosis were 82%, 90%, 88%, 86% [38], being higher than the results in our previous study using subject-specific acquisition windows exclusively in the diastolic phase.

A more recent multicenter study showed that non-contrast-enhanced whole-heart coronary MRA at 1.5 T with five-channel cardiac coils and a parallel imaging factor of 2 can detect significant CAD with high sensitivity (88%) and moderate specificity (72%). In particular, a negative predictive value of 88% indicates that whole-heart coronary MRA can effectively be used to rule out CAD [79]. Of note, the negative predictive value reported by this multicenter study is similar to the negative predictive value of the CORE-64 CTA multicenter study [6].

An introduction of 32-channel cardiac coils and a higher parallel imaging factor has considerably reduced the lengthy scan time as well as acquisition window and improved success rate of free-breathing whole-heart 3D coronary MR angiography. In a study by Nagata et al. that employed 32-channel cardiac coils, parallel imaging factor of 4, and abdominal belt technique, the sensitivity, specificity, positive predictive value, and negative predictive value of whole-heart coronary MRA at 1.5 T were 87%, 86%, 89%, and 83%, respectively, which was comparable to the diagnostic accuracy obtained by whole-heart coronary MRA using 5-channel coils but achieved those results in almost a half imaging time of whole-heart coronary MRA using 5-channel coils [32, 38] (Fig. 13.10).

Contrast-enhanced whole-heart coronary MRA at 3 T is a promising approach for a more accurate assessment of CAD. In a recent single-center study by Yang et al., 3 T MRA data were acquired with a gradient-echo sequence with inversion-recovery preparation during a slow infusion of double dose slightly albumin-binding contrast medium (gadopentetate dimeglumine; Multihance, Braco Imaging S.p.A, Milan, Italy) in consecutive 69 patient with suspected CAD. The sensitivity and specificity of 3 T whole-heart coronary MRA was 94% and 82%, respectively, for the detection of patients with >50% stenoses in the coronary arteries [80]. The same group recently conducted another single-center study by acquiring 3 T MRA data with 32-channel cardiac coils during a slow infusion of double

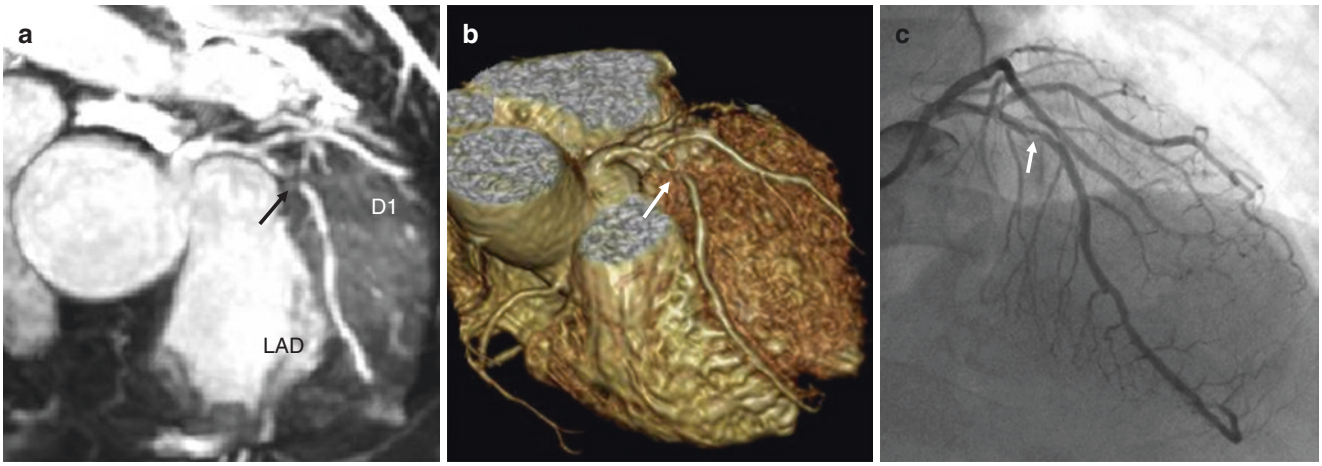

Fig. 13.10 A 50-year-old male patient with chest pain on effort. Significant stenosis in the proximal left anterior descending (LAD) thin SLAB maximum-intensity projection image (black arrow) (**a**), the volume-rendered image (white arrow) (**b**). The X-ray angiogram shows significant coronary artery stenosis in the proximal LAD (white arrow) (**c**) [32]. (Reprinted with permission from Nagata et al. [32], Copyright 2011, with permission from Radiological Society of North America)

dose same slightly albumin-binding contrast medium. Diagnostic quality MRA images were acquired in 101 of 110 (92%) patients with average imaging time of 7.0 ± 1.8 min [51]. The sensitivity, specificity, positive predictive value, and negative predictive value of 3 T contrast-enhanced whole-heart coronary MRA were 95.9%, 86.5%, 87.0%, and 95.7%, respectively, on a patient-based analysis, indicating that the diagnostic performance of 3 T contrast-enhanced whole-heart coronary MRA approaches to the diagnostic performance of 64-slice MDCT [6, 51]. Thus, whole-heart coronary MR angiography can be used as an alternative to coronary CT in ruling out significant coronary artery disease in patients with suspected coronary artery disease.

Diagnostic Accuracy of Quantitative Assessment of Whole-Heart Coronary MRA

Because of relatively limited spatial resolution of coronary MRA, accurate detection of the border of the coronary artery lumen and subsequent quantification of % stenosis is challenging. However, in contrast to coronary CTA, the signal intensity of the coronary arteries on MRA is little influenced by calcification of the coronary artery wall. By utilizing the insusceptibility to calcification, Yonezawa et al. [83] recently developed a method for quantitative analysis of stenosis on coronary MRA on the basis of the signal intensity profile along the vessel. The signal intensity profile along the vessel on 1.5 T whole-heart coronary MRA permits quantitative assessment of the severity of luminal narrowing in the coronary artery, with a sensitivity of 90% and a specificity of 80% in detecting >50% stenosis on X-ray coronary angiography. In addition, excellent agreement was observed between % stenoses determined by coronary MRA and X-ray coronary angiography, with a correlation coefficient of 0.84 ($P < 0.001$).

Additive Value of Whole-Heart Coronary MRA in a Comprehensive CMR Protocol

First-pass myocardial perfusion MRI with pharmacological stress allows for accurate assessment of myocardial ischemia caused by flow-limiting coronary artery disease (CAD) [84]. Since stress perfusion MRI can detect functional alteration of myocardial perfusion and coronary MRA can reveal morphological narrowing caused by atherosclerotic CAD, combined use of stress perfusion MRI and coronary MRA may be of important value in improving the diagnostic performance of CMR in detecting obstructive CAD. In a previous study by Klein et al. published in 2008 [85], however, the combination of coronary MRA and stress perfusion MRI failed to improve the diagnostic performance of stress perfusion MRI alone for the detection of stenosis >50% on invasive coronary angiography. In another study by Bettencourt et al. addition of whole-heart coronary MRA did not significantly improve the diagnostic accuracy of stress-rest myocardial perfusion and LGE MRI study for the detection of functionally significant coronary artery disease determined by invasive fractional flow reserve [86]. The sub-analysis of the recent multicenter prospective trial, CE-MARC study, also has concluded that the inclusion of coronary MRA provided no additional benefit when compared to the combination of stress perfusion, cine, and LGE CMR [87]. In CE-MARC study, however, the overall CMR result was judged positive if any CMR component was positive. This algorithm trends toward the overestimation of the grade of

coronary artery disease. Heer et al. applied a more differentiated algorithm, restricting coronary MRA integration to low confidence results of stress perfusion CMR and showed that combination of stress perfusion CMR and whole-heart coronary MRA in one comprehensive examination increases in specificity (from 79.3% to 88.9%) without worsening sensitivity (from 86.7% to 95.7%) [88].

Prognostic Performance of Whole-Heart Coronary MRA

An increasing number of studies demonstrated the prognostic value of coronary CTA for predicting the future cardiovascular events. However, the prognostic value of coronary MRA has not been investigated. A recent study by Yoon et al. evaluated the prognosis of 207 patients with suspected CAD who underwent 1.5 T whole-heart coronary MRA. They found that the presence of >50% stenosis on coronary MRA is strongly associated with the future cardiac death and major adverse cardiac events, indicating the value of whole-heart coronary MRA in predicting the future risk for cardiac events in patients with suspected CAD [89]. For example, the event-free survival for all cardiac events was 6.3% in patients with stenosis and 0.3% in those without stenosis ($P < 0.001$), indicating that the absence of significant stenosis on whole-heart coronary MRA is associated with a very low risk of cardiac events (Fig. 13.11).

Coronary MR Angiography vs. Coronary CT Angiography

Newer 64-slice CT imagers have a shorter rotation time and offer shorter scan time, higher spatial resolution (0.4 mm), and higher temporal resolution (165 ms) compared with previous generation CT scanners [5]. A recent study directly compared the diagnostic performances of 64-slice CT and volume-targeted coronary thin-slab FIESTA MR angiography [90]. High-resolution 3D FIESTA coronary MR angiography and coronary CT angiography demonstrated a similar accuracy in detecting proximal coronary stenosis. Compared to coronary angiography, sensitivity, specificity, and positive predictive value and negative predictive value for detecting >50% proximal coronary stenosis were 83.0%, 86.9%, 58.8%, and 96.5% for coronary MRA and 85.1%, 87.2%, 60.0%, and 95.6% for coronary CTA, respectively. For the 24 calcified stenoses, MRA correctly predicted the presence or absence of stenosis in 16 segments that were overestimated on CTA.

Despite the excellent diagnostic accuracy, coronary CT angiography has several non-negligible limitations. While estimated radiation dose during CT coronary has been substantially reduced over the past 10 years, radiation exposure to the patients is not negligible particularly in children and young adults. In addition, the diagnostic performance of

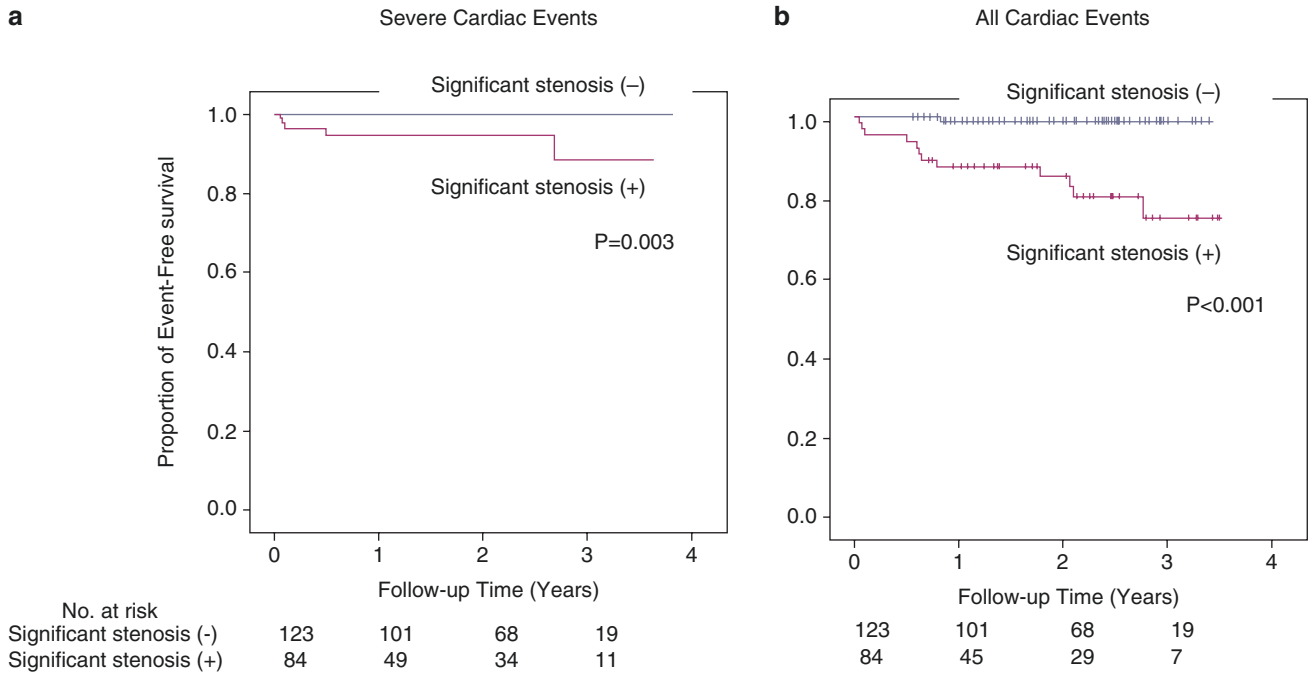

Fig. 13.11 Kaplan-Meier event-free survival curves for (**a**) severe cardiac events and (**b**) all cardiac events. The frequency of severe cardiac events as well as all cardiac events were significantly higher in patients with significant stenosis on whole-heart coronary MR angiography in comparison with patients without significant stenosis. The absence of significant stenosis on whole-heart coronary MR angiography can identify a population with a very low risk for severe cardiac events (0%) and al cardiac events (0.3%) during a median follow-up period [89]. (Reprinted from Yoon et al. [89], Copyright 2012, with permission from Elsevier)

coronary AT angiography is substantially impaired in patients with heavy coronary calcification. Coronary MR angiography and multi-slice coronary CT angiography are complement one another rather than to compete with one another, and coronary MR angiography seems to be useful in the following circumstances:

1. Coronary artery anomalies
2. Coronary artery aneurysm in patients with Kawasaki disease
3. Coronary arterial stenoses in patients with renal failure
4. Coronary arterial stenoses in patients with heavy calcification

Coronary MR angiography can successfully delineate anomalous coronary arteries and coronary artery aneurysms in Kawasaki disease without exposing the patients to radiation. Non-contrast-enhanced coronary MR angiography is well suited for assessing coronary artery disease in patients with renal failure. Coronary MR angiography is also useful in the visualization of coronary arterial lumen in patients with heavy coronary calcification (Fig. 13.12). Coronary MR angiography may have a role in screening coronary artery disease in asymptomatic subjects and those with relatively low likelihood of coronary artery disease, since coronary images can be obtained without exposing the subjects to ionizing radiation or administrating contrast medium. However, further study is required to determine the effectiveness of coronary MR angiography in screening coronary artery disease in the subjects with low prevalence of the disease, because false-positive cases may undergo unnecessary coronary CT angiography or invasive coronary angiography.

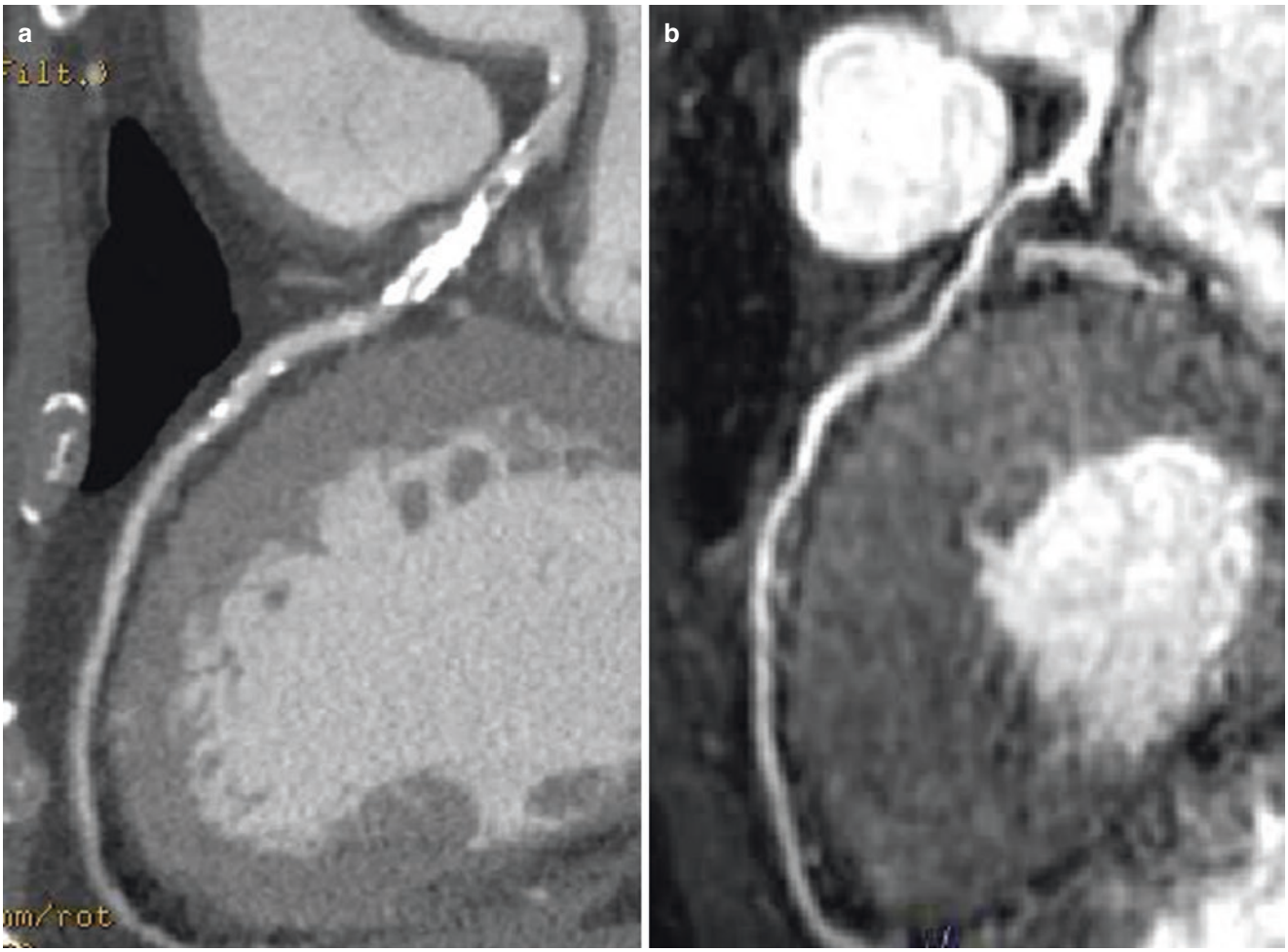

Fig. 13.12 Coronary CT angiography (64-slice VCT) and whole-heart coronary MR angiography in a 71-year-old man with anterior chest pain on effort. (**a**), Curved multi-planar reformatted image of 64-slice contrast-enhanced CT angiography demonstrates severely calcified plaque in the proximal left anterior descending artery. Luminal narrowing of the coronary artery cannot be assessed in this segment due to heavy coronary calcification. (**b**), Curved multi-planar reformatted image of non-contrast-enhanced whole-heart coronary MR angiography can clearly identify luminal narrowing in the proximal left anterior descending artery

Coronary Artery Wall Imaging

Non-contrast-Enhanced Approach

Several clinical studies demonstrated the ability of coronary artery wall imaging to assess coronary artery wall thickness and outward positive remodeling with relative lumen preservation using non-contrast CMR in patients with subclinical coronary artery disease [91, 92] and in patients with type 1 diabetes mellitus and in a multiethnic population cohort [93]. Additionally, Jansen et al. have demonstrated that non-contrast-enhanced T1-weighed (TIW) MRI allows direct thrombus visualization in patients with acute myocardial infarction [94]. Kawasaki et al. have previously shown that the presence of coronary high-intensity plaques (HIPs) detected by non-contrast T1W MRI is associated with positive coronary artery remodeling, low density on coronary CTA, and ultrasound attenuation [95]. Recently, Noguchi evaluated the relationship between HIPs and subsequent coronary events, demonstrating that HIPs identified by non-contrast-enhanced T1W MRI are significantly associated with coronary events and may be a promising predictive factor in patients [96]. In their study, the plaque-to-myocardium signal intensity ratio (PMR) was determined in each coronary plaque. Multivariate analysis showed that the presence of plaques with PMRs 1.4 is the significant independent predictor of coronary events (hazard ratio: 3.96; 95% confidence interval: 1.92–8.17; $p < 0.001$) compared with the presence of CAD (hazard ratio: 3.56; 95% confidence interval: 1.76–7.20; $p < 0.001$) and other traditional risk factors (Fig. 13.13). More recently, the same group

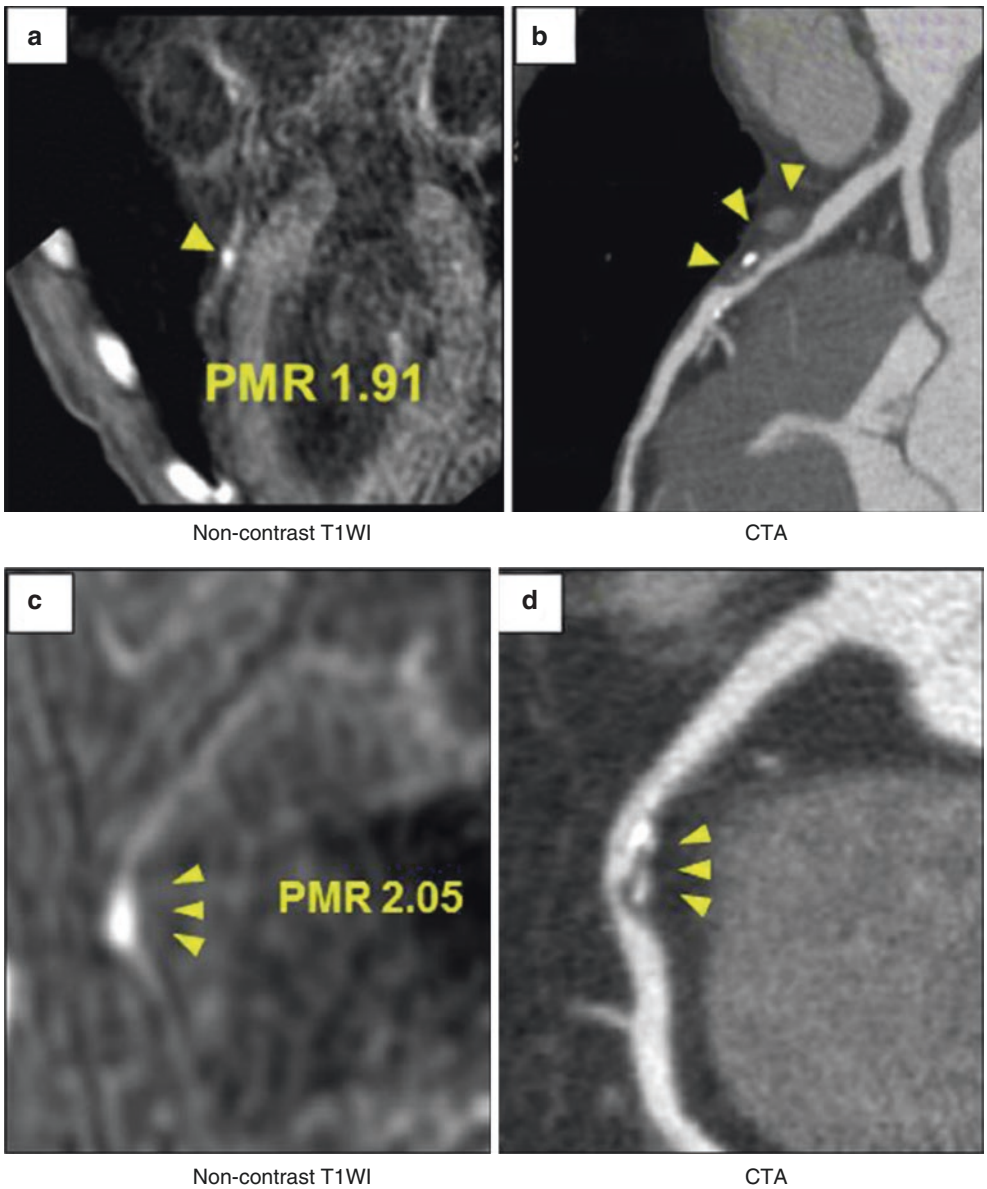

Fig. 13.13 Representative images of high-intensity plaques (HIP) on CMR. Representative non-contrast T1-weighted images of high-intensity plaques (HIPs) (yellow arrowheads) in the proximal left anterior descending coronary artery (**a**) and the right coronary artery (**c**), in which plaque-to-myocardium signal intensity ratios (PMRs) were 1.91 and 2.05, respectively. These high-intensity signals each correspond to the left and right coronary plaques on computed tomographic angiography (CTA) (yellow arrowheads on curved multi-planar reformation images, **b** and **d**) [96]. (Reprinted with permission from Noguchi et al. [96], © 2014, with permission from Elsevier)

investigated if intensive statin therapy can reduce the PMR of high-intensity plaques [97]. Non-contrast-enhanced T1W MRI was performed at baseline and after 12 months in 48 patients with coronary artery disease who underwent intensive statin treatment. In 48 control subjects with coronary artery disease who were not treated with statin, the PMR significantly increased (from 1.22 to 1.49, a 19.2% increase; $p < 0.001$). In contrast, 12 months of statin therapy significantly reduced the PMR (1.38–1.11, an 18.9% reduction; $p < 0.001$).

Contrast-Enhanced Approach

Coronary arterial wall contrast-enhanced CMR with MR contrast agent represents an alternative approach for the characterization of the atherosclerotic coronary arterial wall. Clinically approved MR contrast agents with extracellular distribution showed nonspecific uptake in coronary plaques both in patients with chronic angina [98] and in patients with acute coronary syndromes [99]. In patients with stable angina, gadolinium contrast enhancement in the coronary arterial wall is associated with calcified or mixed plaques on MSCT, while patients with ACS exhibited transit contrast uptake. These studies demonstrated that contrast agent uptake in the coronary artery wall could be associated with both atherosclerotic plaque composition and inflammation.

Several novel target-specific contrast agents have been developed and tested in animal models. Currently, two targeted contrast agents are approved for human use: (1) an albumin-binding contrast agent (gadofosveset trisodium; Lantheus Medical Imaging, North Billerica, MA) and (2) iron oxide-based contrast agent (ferumoxytol; Advanced Magnetics Inc., Cambridge, MA). Albumin-binding contrast agent has been developed for MR angiography of the large and coronary vessels. The accumulation of albumin-binding contrast agent in the coronary arterial wall is associated with increased endothelial permeability and/or increased neovascularization [100, 101]. Furthermore, iron oxide-based contrast agent (USPIO) also has been shown to be useful for the imaging of inflammatory cell infiltration after myocardial infarction [102, 103], and enhancement by USPIO is associated with increased endothelial permeability of the vessel wall.

Future Perspectives

Despite the recent advance of hardware and software of clinical MR system, several limitations still remain for coronary MRA such as long scan times, limited spatial resolution, and SNR compared to coronary CTA. To overcome these limitations, direct respiratory motion estimation techniques of the heart and compressed sensing techniques have been intensively investigated in the recent several years in addition to the abovementioned variety of the techniques. Although those recent technical advancements have not yet been applied to routine clinical practices, these new technologies may substantially expand the use of MR coronary imaging in patients with coronary artery disease in the future.

Sophisticated Respiratory Motion Compensation Technique

Free-breathing coronary MRA with conventional one-dimensional respiratory navigator uses a simplified model for respiratory motion correction, typically with a fixed correction factor of 0.6, which accounts for respiratory-induced superior-inferior (SI) translational motion of the heart only [34]. This simple linear model cannot fully compensate the bulk respiratory-induced heart motion. Therefore, respiratory gating with 1D navigator echoes considerably reduce motion artifact only when narrow respiratory gating windows are employed. However, it leads to prolonged scan time since only a fraction of the acquired data is accepted for reconstruction. Recently, several approaches have been proposed to overcome some of these problems such as (1) self-gating technique [104–107], (2) image-based navigation techniques [108–110], and "respiratory binning" techniques with 3D affine motion correction [111–114] (Fig. 13.14).

Self-Gating Technique

With self-gating, information about the respiratory displacement of the heart is directly extracted from the very same data used for imaging. Furthermore, the placement of the navigator is no longer necessary and no delay between motion detection and data acquisition has to be account for. Scan efficiency increases to 100% as all data segments are used for the final image reconstruction [104, 105]. In this approach, typically a 1D projection image of the heart is acquired in superior-inferior (SI) direction. One of these SI projections is taken as reference. Then, the relative displacement between the position of the heart in each acquired projection and the references is determined and corrected. One study reported that the use of end-expiration as a respiratory reference position is the most promising in terms of image quality on self-navigation coronary MRA in healthy adult subjects [106]. However, in case of more irregular respiration and respiratory drift as often occurring in patients, this may no longer be correct, and alternative strategies may be needed. Ginami et al. developed an iterative self-navigator technique that no longer depends on the choice of a specific respiratory reference position [107].

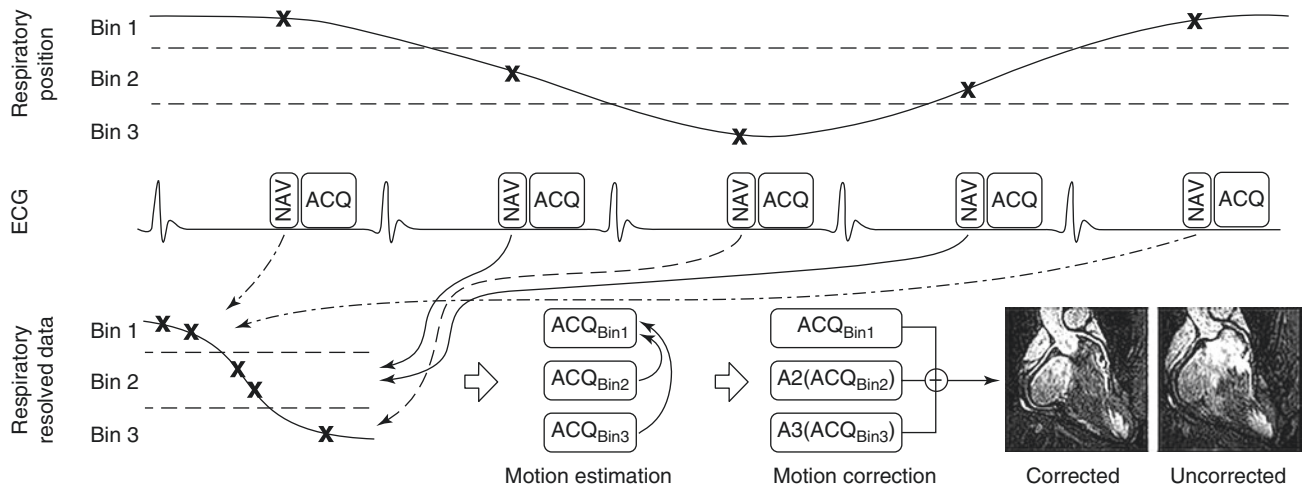

Fig. 13.14 Schematic of a general respiratory binning, motion estimation, and correction procedure. The respiratory position is measured using a navigator (NAV) for each k-space acquisition (ACQ) and allocated to a respiratory bin. Respiratory resolved data from each bin can be reconstructed separately (ACQ_{Bin1-3}) although undersampled. For non-Cartesian k-space sampling the undersampled data from each bin can be used to estimate motion between bins. However, additional fully sampled navigator data is necessary for Cartesian k-space sampling. The respiratory motion is typically estimated by registering ACQ_{Bin2} and ACQ_{Bin3} to the end-expiratory ACQ_{Bin1} to generate the transformations A_2 and A_3. The motion corrected CMRA data can be obtained by applying these transformations to the CMRA data in the corresponding bins and summing the results. Note, in this example 3 respiratory bins are used; however, in practice 4–6 bins are typically employed. (Image courtesy of Dr. Markus Henningsson, Kings College London, UK)

Image-Based Navigation Techniques

Image-based navigation techniques commonly use 2D or 3D image navigators [108–110]. Most of these image-based approaches correct respiratory motion in a beat-to-beat fashion. Henningsson et al. developed a 2D navigator to allow for prospective correction of translational motion of the heart in two directions [108, 109]. In this method the startup pulse of SSFP have been used to spatially encode a low-resolution image immediately before the acquisition of k-space data. The respiratory-induced heart motion is estimated along the SI and RL directions using the low-resolution 2D images and is used to correct the high-resolution data. This implementation of 2D navigator allows for increased scan efficiency without comprising image quality and more flexibility to separately determine the imaging and navigator parameters. More recently, Moghari et al. proposed 3D heart locator technique for whole-heart coronary MR angiography, which is a 3D version of image-based navigation techniques [110].

"Respiratory Binning" Techniques with 3D Affine Motion Correction

To account for more complex and 3D motion, "respiratory binning" techniques with 3D affine motion correction have been recently proposed [111–114]. With this approach the respiratory signal is divided into several states of the breathing cycle or "bins" and afterward corrected to a reference position using the motion estimated from low-resolution images [111]. These methods achieve 100% scan efficiency and therefore reduce the acquisition time. Several investigators have recently applied 3D affine motion correction scheme to self-gating and image-based navigations [112–114]. Pang J et al. have developed an improved respiratory motion correction scheme with 3D self-navigation and image-based affine motion correction [112], reducing the imaging time to 7.1 ± 0.5 min from 13.9 ± 2.6 min with conventional navigator gating. Aitken et al. combined "beat-to-beat" translational motion correction using 2D navigator with "bin-to-bin" affine motion correction for 3D whole-heart coronary MR angiography [113]. Those above-mentioned studies employed radial k-space trajectories. SENSE has been proven effective for non-Cartesian trajectories and is usually accomplished by inverting the encoding matrix using iterative methods such as conjugated-gradients (iterative SENSE) [114]. As the self-navigation utilizes non-Cartesian trajectories, k-space central region for the self-navigation is oversampled and can be used to reconstruct alias-free low-resolution images for the estimation of sensitivity map without the need for extra scan. Consequently, Pang et al. combined 3D self-navigation scheme with self-calibrating iterative SENSE reconstruction, demonstrating that this combined method significantly improves the image quality compared with self-navigation with an image-based 3D-affine motion correction only [111]. However, the radial k-space trajectories have intrinsically lower SNR compared to Cartesian trajectories. Henningsson et al. recently proposed the 3D affine motion correction for Cartesian whole-heart coronary MR

angiography using a 3D image-based navigator to allow for data acquisition throughout the whole respiratory cycle and demonstrated that this technique can be used to acquire Cartesian whole-heart 3D coronary artery images with 100% scan efficiency with similar image quality as compared with the state-of-the-art-gated and corrected method with approximately 50% scan efficiency [115].

Compressed Sensing and Iterative K-Space Reconstruction

Compressed sensing (CS) is a new image reconstruction method for accelerated acquisitions with incoherently undersampled k-space data, which can be achieved by random undersampling in the ky–kz plane for 3D Cartesian acquisitions by exploiting the sparsity of the image in a transform domain [116]. Recently, a CS-based reconstruction strategy for high-resolution CMR, called low-dimensional-structure self-learning and thresholding (LOST), has been developed, providing reconstructions with reduced blurring compared to conventional CS techniques [117]. This CS technique was successfully utilized in non-contrast- and contrast-enhanced whole-heart coronary MRI [118]. Then, Akcakaya et al. employed this CS technique for highly accelerated submillimeter whole-heart coronary MRA and performed a head-to-head comparison of such CS techniques utilizing prospective random k-space undersampling versus parallel imaging with prospective uniform undersampling [119]. They demonstrated that the image quality and SNR of the CS images were significantly higher than those of coronary MA images accelerated by parallel imaging [119].

CS can be also utilized for the respiratory motion compensation by estimating the motion-corrupted k-space data without reacquiring k-space data [120], because the quasiperiodic nature of the respiratory pattern yields a randomly undersampled k-space in CMR. Moghari et al. proposed a joint prospective-retrospective navigator echo motion compensation algorithm. In this technique, the inner k-space region is acquired using a prospective navigator, while, for the outer k-space, a navigator is only used to reject the motion-corrupted data without reacquiring them. Subsequently, those unfilled k-space lines are retrospectively estimated using compressed sensing reconstruction [120]. This approach yields a scan time reduction in coronary MRI, maintaining subjective and objective image quality of coronary MRA [121].

Forman et al. employed a different approach, which combined weighted iterative reconstruction technique with self-navigated free-breathing coronary MRA for retrospective reduction of respiratory motion artifact. They found that total imaging time was reduced with sufficient suppression of respiratory motion artifacts [121].

Four-Dimensional Whole-Heart MR Imaging

While prospective acquisition is commonly used for coronary MRA, a retrospective navigator gating is also possible and useful for improved gating efficiency or completion of scan in a fixed amount of time. Cardiac cine MR imaging commonly employs retrospective ECG gating to address cardiac motion. When data acquisition is performed continuously in a free running mode with retrospective ECG gating in combination with retrospective respiratory self-gating, 4D whole-heart imaging can be achieved. Coppo et al. have developed a free running 4D whole-heart self-navigated coronary MR imaging using golden angle k-space filling, enabling the assessment of both coronary anatomy and ventricular function simultaneously, with retrospective and flexible acquisition window selection for the best visualization of each coronary segment [122]. Furthermore, as cardiac phase information also can be obtained by cardiac self-gating, compensation of both cardiac and respiratory motion also enables 4D coronary MR imaging. Pang et al. have developed a free-breathing and free running 4D coronary MRA technique with simultaneously cardiac and respiratory self-gating, golden angle 3D radial k-space sampling, and feasibility of isotropic whole-heart MR imaging has been demonstrated [123].

References

1. Writing Group Memebers. Heart disease and stroke statistics—2015 update a report from the American Heart Association. Circulation. 2015;131:e29–e322.
2. Scanlon PJ, Faxon DP, Audet AM, et al. ACC/AHA guidelines for coronary angiography. A report of the American College of Cardiology/American Heart Association Task Force on practice guidelines (Committee on Coronary Angiography). Developed in collaboration with the Society for Cardiac Angiography and Interventions. J Am Coll Cardiol. 1999;33:1756–824.
3. Budoff MJ, Georgiou D, Brody A, et al. Ultrafast computed tomography as a diagnostic modality in the detection of coronary artery disease: a multicenter study. Circulation. 1996;93:898–904.
4. Raff GL, Gallagher MJ, O'Neill WW, Goldstein JA. Diagnostic accuracy of noninvasive coronary angiography using 64-slice spiral computed tomography. J Am Coll Cardiol. 2005;46:552–7.
5. Mollet NR, Cademartiri F, van Mieghem CA, Runza G, McFadden EP, Baks T, et al. High-resolution spiral computed tomography coronary angiography in patients referred for diagnostic conventional coronary angiography. Circulation. 2005;112:2318–23.
6. Miller JM, Rochitte CE, Dewey M, Arbab-Zadeh A, Niinuma H, Gottlieb I, et al. Diagnostic performance of coronary angiography by 64-row ct. N Engl J Med. 2008;359:2324–36.
7. Budoff MJ, Dowe D, Jollis JG, Gitter M, Sutherland J, Halamert E, et al. Diagnostic performance of 64-multidetector row coronary computed tomographic angiography for evaluation of coronary artery stenosis in individuals without known coronary artery disease: results from the prospective multicenter ACCURACY (Assessment by Coronary Computed Tomographic Angiography of Individuals Undergoing Invasive Coronary Angiography) trial. J Am Coll Cardiol. 2008;52:1724–32.

8. Chinnaiyan KM, Boura JA, DePetris A, Gentry R, Abidov A, Share DA, et al. Progressive radiation dose reduction from coronary computed tomography angiography in a statewide collaborative quality improvement program: results from the Advanced Cardiovascular Imaging Consortium. Circ Cardiovasc Imaging. 2013;6:646–54.
9. Edelman RR, Manning WJ, Pearlman J, Li W. Human coronary arteries: projection angiograms reconstructed from breath-hold two-dimensional MR images. Radiology. 1993;187:719–22.
10. Manning WJ, Li W, Edelman RR. A preliminary report comparing magnetic resonance coronary angiography with conventional angiography. N Eng J Med. 1993;328:828–32.
11. Sakuma H, Caputo GR, Steffens JC, O'Sullivan M, Bourne MW, Shimakawa A, et al. Breath-hold MR cine angiography of coronary arteries in healthy volunteers: value of multiangle oblique imaging planes. Am J Roentgenol. 1994;163:533–7.
12. Wielopolski PA, Manning WJ, Edelman RR. Single breath-hold volumetric imaging of the heart using magnetization-prepared 3-dimensional segmented echo planar imaging. J Magn Reson Imaging. 1995;5:403–9.
13. Bornert P, Jensen D. Coronary artery imaging at 0.5 T using segmented 3D echo planar imaging. Magn Reson Med. 1995;34:779–85.
14. Wielopolski PA, van Geuns RJ, de Feyter PJ, Oudkerk M. Breath-hold coronary MR angiography with volume-targeted imaging. Radiology. 1998;209:209–129.
15. van Geuns RJ, Wielopolski PA, de Bruin HG, Rensing BJ, Hulshoff M, van Ooijen PM, et al. MR coronary angiography with breath-hold targeted volumes: preliminary clinical results. Radiology. 2000;217:270–27.
16. Foo TK, Ho VB, Saranathan M, Cheng LQ, Sakuma H, Kraitchman DL, et al. Feasibility of integrating high-spatial-resolution 3D breath-hold coronary MR angiography with myocardial perfusion and viability examinations. Radiology. 2005;235:1025–30.
17. Goldfarb JW, Edelman RR. Coronary arteries: breath-hold, adolinium-enhanced, three-dimensional MR angiography. Radiology. 1998;206:830–4.
18. Kessler W, Laub G, Achenbach S, Ropers D, Moshage W, Daniel WG. Coronary arteries: MR angiography with fast contrast-enhanced three-dimensional breath-hold imaging–initial experience. Radiology. 1999;210:566–72.
19. Li D, Carr JC, Shea SM, Zheng J, Deshpande VS, et al. Coronary arteries: magnetization-prepared contrast-enhanced three-dimensional volume-targeted breath-hold MR angiography. Radiology. 2001;219:270–7.
20. Regenfus M, Ropers D, Achenbach S, Kessler W, Laub G, et al. Noninvasive detection of coronary artery stenosis using contrast-enhanced three-dimensional breath-hold magnetic resonance coronary angiography. J Am Coll Cardiol. 2000;36:44–50.
21. Holland AE, Goldfarb JW, Edelman RR. Diaphragmatic and cardiac motion during suspended breathing: preliminary experience and implications for breath-hold MR imaging. Radiology. 1998;209:483–9.
22. Oshinski JN, Hofland L, Mukundan S Jr, Dixon WT, Parks WJ, Pettigrew RI. Two-dimensional coronary MR angiography without breath holding. Radiology. 1996;201:737–43.
23. McConnell MV, Khasgiwala VC, Savord BJ, Chen MH, Chuang ML, et al. Comparison of respiratory suppression methods and navigator locations for MR coronary angiography. Am J Roentgenol. 1997;168:1369–75.
24. Li D, Kaushikkar S, Haacke EM, et al. Coronary arteries: three-dimensional MR imaging with retrospective respiratory gating. Radiology. 1996;201:857–63.
25. Post JC, van Rossum AC, Hofman MB, Valk J, Visser CA. Three-dimensional respiratory-gated MR angiography of coronary arteries: comparison with conventional coronary angiography. Am J Roentgenol. 1996;166:1399–404.
26. Woodard PK, Li D, Haacke EM, Dhawale PJ, Kaushikkar S, Barzilai B, et al. Detection of coronary stenoses on source and projection images using three-dimensional MR angiography with retrospective respiratory gating: preliminary experience. Am J Roentgenol. 1998;170:883–8.
27. Stuber M, Botnar RM, Danias PG, Kissinger KV, Manning WJ. Submillimeter three-dimensional coronary MR angiography with real-time navigator correction: comparison of navigator locations. Radiology. 1999;212:579–87.
28. Botnar RM, Stuber M, Danias PG, Kissinger KV, Manning WJ. Improved coronary artery definition with T2-weighted, free-breathing, three-dimensional coronary MRA. Circulation. 1999;99:3139–48.
29. Stuber M, Botnar RM, Danias PG, Sodickson DK, Kissinger KV, Van Cauteren M, et al. Double-oblique free-breathing high resolution three-dimensional coronary magnetic resonance angiography. J Am Coll Cardiol. 1999;34:524–31.
30. Kim WY, Danias PG, Stuber M, Flamm SD, Plein S, Nagel E, et al. Coronary magnetic resonance angiography for the detection of coronary stenoses. N Eng J Med. 2001;345:1863–9.
31. Nagel E, Bornstedt A, Schnackenburg B, Hug J, Oswald H, Fleck E. Optimization of realtime adaptive navigator correction for 3D magnetic resonance coronary angiography. Magn Reson Med. 1999;42:408–11.
32. Nagata M, Kato S, Kitagawa K, et al. Diagnostic accuracy of 1.5-T unenhanced whole-heart coronary MR angiography performed with 32-channel cardiac coils: initial single-center experience. Radiology. 2011;259:384–92.
33. Ishida M, Schuster A, Takase S, et al. Impact of an abdominal belt on breathing patterns and scan efficiency in whole-heart coronary magnetic resonance angiography: comparison between the UK and Japan. J Cardiovasc Magn Reson. 2011;13:71–81.
34. Stuber M, Botnar RM, Danias PG, Kissinger KV, Manning WJ. Submillimeter 3D coronary MRA using real-time navigator correction: comparison of navigator locations. Radiology. 1999;212:579–87.
35. Wang Y, Vidan E, Bergman GW. Cardiac motion of coronary arteries: variability in the rest period and implications for coronary MR angiography. Radiology. 1999;213:751–8.
36. Kim WY, Stuber M, Kissinger KV, Andersen NT, Manning WJ, Botnar RM. Impact of bulk cardiac motion on right coronary MR angiography and vessel wall imaging. J Magn Reson Imaging. 2001;14:383–90.
37. Plein S, Jones TR, Ridgway JP, Sivananthan MU. Three-dimensional coronary MR angiography performed with subject-specific cardiac acquisition windows and motion-adapted respiratory gating. Am J Roentgenol. 2003;180:505–12.
38. Sakuma H, Ichikawa Y, Chino S, Hirano T, Makino K, Takeda K. Detection of coronary artery stenosis with whole-heart coronary magnetic resonance angiography. J Am Coll Cardiol. 2006;48:1946–50.
39. Carr JC, Simonetti O, Bundy J, Li D, Pereles S, Finn JP. Cine MR angiography of the heart with segmented true fast imaging with steady-state precession. Radiology. 2001;219:828–34.
40. McCarthy RM, Shea SM, Deshpande VS, Green JD, Pereles FS, Carr JC, et al. Coronary MR angiography: true FISP imaging improved by prolonging breath holds with preoxygenation in healthy volunteers. Radiology. 2003;227:283–8.
41. Spuentrup E, Katoh M, Buecker A, Manning WJ, Schaeffter T, Nguyen TH, et al. Free-breathing 3D steady-state free precession coronary MR angiography with radial k-space sampling: comparison with cartesian k-space sampling and cartesian gradient-echo coronary MR angiography – pilot study. Radiology. 2004;231:581–6.
42. Weber OM, Martin AJ, Higgins CB. Whole-heart steady-state free precession coronary artery magnetic resonance angiography. Magn Reson Med. 2003;50:1223–8.

43. Sakuma H, Ichikawa Y, Suzawa N, Hirano T, Makino K, Koyama N, et al. Assessment of coronary arteries with total study time of less than 30 minutes by using whole-heart coronary MR angiography. Radiology. 2005;237:316–21.
44. Stuber M, Botnar RM, Fischer SE, et al. Preliminary report on in vivo coronary MRA at 3 Tesla in humans. Magn Reson Med. 2002;48:425–9.
45. Sommer T, Hackenbroch M, Hofer U, Schmiedel A, Willinek WA, Flacke S, et al. Coronary MR angiography at 3.0 T versus that at 1.5 T: initial results in patients suspected of having coronary artery disease. Radiology. 2005;234:718–25.
46. Kaul MG, Stork A, Bansmann PM, et al. Evaluation of balanced steady-state free precession (TrueFISP) and K-space segmented gradient echo sequences for 3D coronary MR angiography with navigator gating at 3 Tesla. Rofo. 2004;176:1560–5.
47. Soleimanifard S, Schär M, Hays AG, Prince JL, Weiss RG, Stuber M. Spatially selective implementation of the adiabatic T2Prep sequence for magnetic resonance angiography of the coronary arteries. Magn Reson Med. 2013;70:97–105.
48. Li D, Paschal CB, Haacke EM, Adler LP. Coronary arteries: three-dimensional MR imaging with fat saturation and magnetization transfer contrast. Radiology. 1993;187:401–6.
49. Börnert P, Koken P, Nehrke K, Eggers H, Ostendorf P. Water/fat-resolved whole-heart Dixon coronary MRA: an initial comparison. Magn Reson Med. 2014;71:156–63.
50. Tang L, Merkle N, Schär M, et al. Volume-targeted and whole-heart coronary magnetic resonance angiography using an intravascular contrast agent. J Magn Reson Imaging. 2009;30:1191–6.
51. Yang Q, Li K, Liu X, et al. Contrast-enhanced whole-heart coronary magnetic resonance angiography at 3.0-T: a comparative study with X-ray angiography in a single center. J Am Coll Cardiol. 2009;54:69–76.
52. Reimer P, Bremer C, Allkemper T, Engelhardt M, Mahler M, et al. Myocardial perfusion and MR angiography of chest with SH U 555 C: results of placebo-controlled clinical phase i study. Radiology. 2004;231:474–81.
53. Klein C, Schalla S, Schnackenburg B, Bornstedt A, Hoffmann V, et al. Improvement of image quality of non-invasive coronary artery imaging with magnetic resonance by the use of the intravascular contrast agent Clariscan (NC100150 injection) in patients with coronary artery disease. J Magn Reson Imaging. 2003;17:656–62.
54. Stuber M, Botnar RM, Danias PG, McConnell MV, Kissinger KV, Yucel EK, Manning WJ. Contrast agent-enhanced, free-breathing, three-dimensional coronary magnetic resonance angiography. J Magn Reson Imaging. 1999;10:790–9.
55. Paetsch I, Huber ME, Bornstedt A, Schnackenburg B, Boesiger P, Stuber M, et al. Improved three-dimensional free-breathing coronary magnetic resonance angiography using gadocoletic acid (B-22956) for intravascular contrast enhancement. J Magn Reson Imaging. 2004;20:288–93.
56. Herborn CU, Barkhausen J, Paetsch I, Hunold P, Mahler M, et al. Coronary arteries: contrast-enhanced MR imaging with SH L 643A – experience in 12 volunteers. Radiology. 2003;229:217–23.
57. Laurent S, Elst LV, Muller RN. Comparative study of the physicochemical properties of six clinical low molecular weight gadolinium contrast agents. Contrast Media Mol Imaging. 2006;1:128–37.
58. Krombach GA, Hahnen C, Lodemann KP, et al. Gd-BOPTA for assessment of myocardial viability on MRI: changes of T1 value and their impact on delayed enhancement. Eur Radiol. 2009;19:2136–46.
59. Raman FS, Nacif MS, Cater G, Gai N, Jones J, Li D, et al. 3.0-T whole-heart coronary magnetic resonance angiography: comparison of gadobenate dimeglumine and gadofosveset trisodium. Int J Cardiovasc Imaging. 2013;29:1085–94.
60. Pruessmann KP, Weiger M, Scheidegger MB, Boesiger P. SENSE: sensitivity encoding for fast MRI. Magn Reson Med. 1999;42:952–62.
61. Griswold MA, Jakob PM, Heidemann RM, Nittka M, Jellus V, Wang J, et al. Generalized autocalibrating partially parallel acquisitions (GRAPPA). Magn Reson Med. 2002;47:1202–10.
62. Sodickson DK, Manning WJ. Simultaneous acquisition of spatial harmonics (SMASH): fast imaging with radiofrequency coil arrays. Magn Reson Med. 1997;38:591–603.
63. Reeder SB, Wintersperger BJ, Dietrich O, Lanz T, Greiser A, Reiser MF, et al. Practical approaches to the evaluation of signal-to-noise ratio performance with parallel imaging: application with cardiac imaging and a 32-channel cardiac coil. Magn Reson Med. 2005;54:748–54.
64. Gharib AM, Abd-Elmoniem KZ, Ho VB, Födi E, Herzka DA, Ohayon J, et al. The feasibility of 350 μm spatial resolution coronary magnetic resonance angiography at 3 T in humans. Invest Radiol. 2012;47:339–45.
65. Donaldson RM, Raphael MJ, Yacoub MH, Ross DN. Hemodynamically significant anomalies of the coronary arteries: surgical aspects. Thorac Cardiovasc Surg. 1982;30:7–13.
66. Click RL, Holmes DR Jr, Vlietstra RE, Kosinski AS, Kronmal RA. Anomalous coronary arteries: location, degree of atherosclerosis and effect on survival: a report from the Coronary Artery Surgery Study. J Am Coll Cardiol. 1989;13:531–7.
67. McConnell MV, Ganz P, Selwyn AP, Edelman RR, Manning WJ. Identification of anomalous coronary arteries and their anatomic course by magnetic resonance coronary angiography. Circulation. 1995;92:3158–62.
68. Taylor AM, Thorne SA, Rubens MB, Jhooti P, Keegan J, Gatehouse PD, et al. Coronary artery imaging in grown up congenital heart disease: complementary role of magnetic resonance and x-ray coronary angiography. Circulation. 2000;101:1670–8.
69. Bunce NH, Lorenz CH, Keegan J, Lesser J, Reyes EM, et al. Coronary artery anomalies: assessment with free-breathing three-dimensional coronary MR angiography. Radiology. 2003;227:201–8.
70. Datta J, White CS, Gilkeson RC, Meyer CA, Kansal S, Jani ML, et al. Anomalous coronary arteries in adults: depiction at multidetector row CT angiography. Radiology. 2005;235:812–8.
71. Kato H, Sugimura T, Akagi T, Sato N, Hashino K, Maeno Y, et al. Long-term consequences of Kawasaki disease. A 10- to 21-year follow-up study of 594 patients. Circulation. 1996;94:1379–85.
72. Greil GF, Stuber M, Botnar RM, Kissinger KV, Geva T, Newburger JW, et al. Coronary magnetic resonance angiography in adolescents and young adults with Kawasaki disease. Circulation. 2002;105:908–11.
73. Mavrogeni S, Papadopoulos G, Douskou M, Kaklis S, Seimenis I, Baras P, et al. Magnetic resonance angiography is equivalent to X-ray coronary angiography for the evaluation of coronary arteries in Kawasaki disease. J Am Coll Cardiol. 2004;43:649–52.
74. Duerinckx AJ, Urman MK. Two-dimensional coronary MR angiography: analysis of initial clinical results. Radiology. 1994;193:731–8.
75. Sandstede JJ, Pabst T, Beer M, Geis N, Kenn W, et al. Three-dimensional MR coronary angiography using the navigator technique compared with conventional coronary angiography. Am J Roentgenol. 1999;172:135–9.
76. Sardanelli F, Molinari G, Zandrino F, Balbi M. Three-dimensional, navigator-echo MR coronary angiography in detecting stenoses of the major epicardial vessels, with conventional coronary angiography as the standard of reference. Radiology. 2000;214:808–14.
77. Bogaert J, Kuzo R, Dymarkowski S, Beckers R, Piessens J, Rademakers FE. Coronary artery imaging with real-time navigator three-dimensional turbo-field-echo MR coronary angiography: initial experience. Radiology. 2003;226:707–16.

78. Kefer J, Coche E, Legros G, Pasquet A, Grandin C, Van Beers BE, et al. Head-to-head comparison of three-dimensional navigator-gated magnetic resonance imaging and 16-slice computed tomography to detect coronary artery stenosis in patients. J Am Coll Cardiol. 2005;46:92–100.
79. Kato S, Kitagawa K, Ishida N, Ishida M, Nagata M, Ichikawa Y, et al. Assessment of coronary artery disease using magnetic resonance coronary angiography: A national multicenter trial. J Am Coll Cardiol. 2010;56:983–91.
80. Yang Q, Li K, Liu X, Du X, Bi X, Huang F, et al. 3.0 T whole-heart coronary magnetic resonance angiography performed with 32-channel cardiac coils: a single-center experience. Circ Cardiovasc Imaging. 2012;5:573–9.
81. Jahnke C, Paetsch I, Schnackenburg B, Bornstedt A, Gebker R, et al. Coronary MR angiography with steady-state free precession: individually adapted breath-hold technique versus free-breathing technique. Radiology. 2004;232:669–76.
82. Jahnke C, Paetsch I, Nehrke K, Schnackenburg B, Gebker R, et al. Rapid and complete coronary arterial tree visualization with magnetic resonance imaging: feasibility and diagnostic performance. Eur Heart J. 2005;26:2313–9.
83. Yonezawa M, Nagata M, Kitagawa K, Kato S, Yoon Y, Nakajima H, et al. Quantitative analysis of 1.5-T whole-heart coronary MR angiograms obtained with 32-channel cardiac coils: a comparison with conventional quantitative coronary angiography. Radiology. 2014;271:356–64.
84. Jaarsma C, Leiner T, Bekkers SC, Crijns HJ, Wildberger JE, Nagel E, et al. Diagnostic performance of noninvasive myocardial perfusion imaging using single-photon emission computed tomography, cardiac magnetic resonance, and positron emission tomography imaging for the detection of obstructive coronary artery disease: a meta-analysis. J Am Coll Cardiol. 2012;59:1719–28.
85. Klein C, Gebker R, Kokocinski T, et al. Combined magnetic resonance coronary artery imaging, myocardial perfusion and late gadolinium enhancement in patients with suspected coronary artery disease. J Cardiovasc Magn Res. 2008;10:45–54.
86. Bettencourt N, Ferreira N, Chiribiri A, Schuster A, Sampaio F, Santos L, et al. Additive value of magnetic resonance coronary angiography in a comprehensive cardiac magnetic resonance stress-rest protocol for detection of functionally significant coronary artery disease: a pilot study. Circ Cardiovasc Imaging. 2013;6:730–8.
87. Ripley DP, Motwani M, Brown JM, Nixon J, Everett CC, Bijsterveld P, et al. Individual component analysis of the multiparametric cardiovascular magnetic resonance protocol in the CE-MARC trial. J Cardiovasc Magn Reson. 2015;17:59.
88. Heer T, Reiter S, Höfling B, Pilz G. Diagnostic performance of non-contrast-enhanced whole-heart magnetic resonance coronary angiography in combination with adenosine stress perfusion cardiac magnetic resonance imaging. Am Heart J. 2013;166:999–1009.
89. Yoon YE, Kitagawa K, Kato S, et al. Prognostic value of coronary magnetic resonance angiography for prediction of cardiac events in patients with suspected coronary artery disease. J Am Coll Cardiol. 2012;60(22):2316–22.
90. Cheng L, Ma L, Schoenhagen P, Ye H, Lou X, Gao Y, et al. Comparison of three-dimensional volume-targeted thin-slab FIESTA magnetic resonance angiography and 64-multidetector computed tomographic angiography for the identification of proximal coronary stenosis. Int J Cardiol. 2013;167:2969–76.
91. Makowski MR, Henningsson M, Spuentrup E, Kim WY, Maintz D, et al. Characterization of coronary atherosclerosis by magnetic resonance imaging. Circulation. 2013;128:1244–55.
92. Kim WY, Stuber M, Bornert P, Kissinger KV, Manning WJ, Botnar RM. Three-dimensional black-blood cardiac magnetic resonance coronary vessel wall imaging detects positive arterial remodeling in patients with nonsignificant coronary artery disease. Circulation. 2002;106:296–9.
93. Kim WY, Astrup AS, Stuber M, Tarnow L, Falk E, Botnar RM, et al. Subclinical coronary and aortic atherosclerosis detected by magnetic resonance imaging in type 1 diabetes with and without diabetic nephropathy. Circulation. 2007;115:228–35.
94. Jansen CH, Perera D, Makowski MR, Wiethoff AJ, Phinikaridou A, Razavi RM, et al. Detection of intracoronary thrombus by magnetic resonance imaging in patients with acute myocardial infarction. Circulation. 2011;124:416–24.
95. Kawasaki T, Koga S, Koga N, Noguchi T, Tanaka H, Koga H, et al. Characterization of hyperintense plaque with noncontrast T(1)-weighted cardiac magnetic resonance coronary plaque imaging: comparison with multislice computed tomography and intravascular ultrasound. JACC Cardiovasc Imaging. 2009;2:720–8.
96. Noguchi T, Kawasaki T, Tanaka A, Yasuda S, Goto Y, Ishihara M, et al. High-intensity signals in coronary plaques on noncontrast T1-weighted magnetic resonance imaging as a novel determinant of coronary events. J Am Coll Cardiol. 2014;63(10):989–99.
97. Noguchi T, Tanaka A, Kawasaki T, Goto Y, Morita Y, Asaumi Y, et al. Effect of intensive statin therapy on coronary high-intensity plaques detected by noncontrast T1-weighted imaging: The AQUAMARINE Pilot Study. J Am Coll Cardiol. 2015;66:245–56.
98. Yeon SB, Sabir A, Clouse M, Martinezclark PO, Peters DC, Hauser TH, et al. Delayed-enhancement cardiovascular magnetic resonance coronary artery wall imaging: Comparison with multislice computed tomography and quantitative coronary angiography. J Am Coll Cardiol. 2007;50:441–7.
99. Ibrahim T, Makowski MR, Jankauskas A, Maintz D, Karch M, Schachoff S, et al. Serial contrast-enhanced cardiac magnetic resonance imaging demonstrates regression of hyperenhancement within the coronary artery wall in patients after acute myocardial infarction. JACC Cardiovasc Imaging. 2009;2:580–8.
100. Lobbes MB, Miserus RJ, Heeneman S, Passos VL, Mutsaers PH, Debernardi N, et al. Atherosclerosis: contrast-enhanced mr im- aging of vessel wall in rabbit model–comparison of gadofosveset and gadopentetate dimeglumine. Radiology. 2009;250:682–91.
101. Phinikaridou A, Andia ME, Protti A, Indermuehle A, Shah A, Smith A, et al. Noninvasive magnetic resonance imaging evaluation of endothelial permeability in murine atherosclerosis using an albumin-binding contrast agent. Circulation. 2012;126:707–19.
102. Kooi ME, Cappendijk VC, Cleutjens KB, Kessels AG, Kitslaar PJ, Borgers M, et al. Accumulation of ultrasmall superparamagnetic particles of iron oxide in human atherosclerotic plaques can be detected by in vivo magnetic resonance imaging. Circulation. 2003;107:2453–8.
103. Tang TY, Howarth SP, Miller SR, Graves MJ, Patterson AJ, U-King-Im JM, et al. The atheroma (atorvastatin therapy: effects on reduction of macrophage activity) study. Evaluation using ultrasmall superparamagnetic iron oxide-enhanced magnetic resonance imaging in carotid disease. J Am Coll Cardiol. 2009;53:2039–50.
104. Piccini D, Monney P, Sierro C, Coppo S, Bonanno G, van Heeswijk RB, et al. Respiratory self-navigated postcontrast whole-heart coronary MR angiography: initial experience in patients. Radiology. 2014;270:378–86.
105. Stehning C, Börnert P, Nehrke K, Eggers H, Stuber M. Free-breathing whole-heart coronary MRA with 3D radial SSFP and self-navigated image reconstruction. Magn Reson Med. 2005;54:476–80.
106. Piccini D, Bonanno G, Ginami G, Littmann A, Zenge MO, Stuber M. Is there an optimal respiratory reference position for self-navigated whole-heart coronary MR angiography? J Magn Reson Imaging. 2015 July 14. [Epub ahead of print].

107. Ginami G, Bonanno G, Schwitter J, Stuber M, Piccini D. An iterative approach to respiratory self-navigated whole-heart coronary MRA significantly improves image quality in a preliminary patient study. Magn Reson Med. 2015 May 8. [Epub ahead of print].
108. Henningsson M, Koken P, Stehning C, Razavi R, Prieto C, Botnar RM. Whole-heart coronary MR angiography with 2D self-navigated image reconstruction. Magn Reson Med. 2012;67:437–45.
109. Henningsson M, Smink J, Razavi R, Botnar RM. Prospective respiratory motion correction for coronary MR angiography using a 2D image navigator. Magn Reson Med. 2012;69:486–94.
110. Moghari MH, Roujol S, Henningsson M, Kissinger KV, Annese D, Nezafat R, et al. Three-dimensional heart locator for whole-heart coronary magnetic resonance angiography. Magn Reson Med. 2014;71:2118–26.
111. Prieto C, Doneva M, Usman M, Henningsson M, Greil G, et al. Highly efficient respiratory motion compensated free-breathing coronary MRA using golden-step Cartesian acquisition. J Magn Reson Imaging. 2015;41:738–46.
112. Pang J, Bhat H, Sharif B, Fan Z, Thomson LE, LaBounty T, et al. Whole-heart coronary MRA with 100% respiratory gating efficiency: self-navigated three-dimensional retrospective image-based motion correction (TRIM). Magn Reson Med. 2014;71:67–74.
113. Aitken AP, Henningsson M, Botnar RM, Schaeffter T, Prieto C. 100% Efficient three-dimensional coronary MR angiography with two-dimensional beat-to-beat translational and bin-to-bin affine motion correction. Magn Reson Med. 2015;74:756–64.
114. Lustig M, Donoho DL, Pauly JM. Sparse MRI: the application of compressed sensing for rapid MR imaging. Magn Reson Med. 2007;58(6):1182–95.
115. Henningsson M, Prieto C, Chiribiri A, Vaillant G, Razavi R, Botnar RM. Whole-heart coronary MRA with 3D affine motion correction using 3D image-based navigation. Magn Reson Med. 2014;71:173–81.
116. Akçakaya M, Rayatzadeh H, Basha TA, et al. Accelerated late gadolinium enhancement cardiac MR imaging with isotropic spatial resolution using compressed sensing: initial experience. Radiology. 2012;264:691–9.
117. Akcakaya M, Basha TA, Goddu B, Goepfert LA, Kissinger KV, Tarokh V, et al. Low-dimensional-structure self-learning and thresholding: regularization beyond compressed sensing for MRI Reconstruction. Magn Reson Med. 2011;66:756–67.
118. Akcakaya M, Basha TA, Chan RH, Rayatzadeh H, Kissinger KV, Goddu B, et al. Accelerated contrast-enhanced whole-heart coronary MRI using low-dimensional-structure self-learning and thresholding. Magn Reson Med. 2012;67:1434–43.
119. Akçakaya M, Basha TA, Chan RH, et al. Accelerated isotropic sub-millimeter whole-heart coronary MRI: compressed sensing versus parallel imaging. Magn Reson Med. 2014;71:815–22.
120. Moghari MH, Akçakaya M, O'Connor A, Basha TA, Casanova M, Stanton D, et al. Compressed-sensing motion compensation (CosMo): a joint prospective-retrospective respiratory navigator for coronary MRI. Magn Reson Med. 2011;66:1674–81.
121. Forman C, Piccini D, Grimm R, Hutter J, Hornegger J, Zenge MO. Reduction of respiratory motion artifacts for free-breathing whole-heart coronary MRA by weighted iterative reconstruction. Magn Reson Med. 2015;73(5):1885–95.
122. Coppo S, Piccini D, Bonanno G, Chaptinel J, Vincenti G, Feliciano H, et al. Free-running 4D whole-heart self-navigated golden angle MRI: initial results. Magn Reson Med. 2014 Nov 5. [Epub ahead of print].
123. Pang J, Sharif B, Fan Z, Bi X, Arsanjani R, et al. ECG and navigator-free four-dimensional whole-heart coronary MRA for simultaneous visualization of cardiac anatomy and function. Magn Reson Med. 2014;72:1208–17.

Atherosclerotic Plaque Imaging

14

Begoña Lavin-Plaza, Alkystis Phinikaridou, Marcelo E. Andia, Sara Lacerda, Markus Henningsson, Marcus R. Makowski, and René M. Botnar

Introduction

Cardiovascular disease (CVD) remains the leading cause of death worldwide despite improvements in prevention (e.g., blood pressure control, cholesterol lowering, and smoking cessation) and advances in diagnosis and treatment. Clinical risk scoring systems do not allow satisfactory identification of individuals with subclinical disease and at high risk for coronary events [1, 2]. Coronary artery disease (CAD) and myocardial infarction account for more than 50% of CVD deaths and are the result of atherosclerosis and plaque rupture with subsequent thrombosis. A major challenge of CAD diagnosis is that the majority of patients who die suddenly of CVD have no previous symptoms according to the 2013 AHA statistics [3]. The clinical challenge is that the majority of these plaques do not lead to coronary narrowing and/or ischemia but are characterized by inflammation, increased plaque burden, outward remodeling, spotty calcification, neovascularization, and intraplaque hemorrhage.

Current imaging tests such as X-ray angiography and computed tomography (CT) have failed to identify patients that are at risk of coronary plaque rupture and subsequent heart attack or stroke [4–6]. Catheter-based imaging techniques such as intravascular ultrasound (IVUS), optical coherence tomography (OCT), and near-infrared spectroscopy (NIRS) allow some limited plaque characterization but are invasive and thus not useful as a screening test [7–9]. Therefore, new noninvasive approaches to detect potentially unstable plaque are urgently needed.

Recent studies with positron emission tomography (PET)/CT and the radiopharmaceuticals ^{18}F-FDG (*inflammation*) [10] and ^{18}F-NaF (*spotty calcification*) [11] have demonstrated the feasibility of coronary plaque imaging with promising results but are beyond the scope of this chapter, and the reader is referred to recent publications [10, 11].

Molecular magnetic resonance imaging (mMRI) using target-specific imaging agents is an noninvasive alternative imaging modality that can provide more accurate information about plaque composition and biology including endothelial dysfunction, inflammation, and vascular remodeling and hemorrhage. Molecular MRI thus may improve the prediction of future coronary events, allow earlier and more aggressive medical treatment, monitor the effectiveness of medical and/or interventional treatment in patients, and may provide novel data on the pathogenesis of atherosclerosis in vivo. Subclinical atherosclerosis may precede the development of clinical disease by many decades, thereby offering the opportunity to use image-guided diagnosis and to target primary prevention therapies to those at highest risk [12].

Studies investigating subclinical and clinical coronary atherosclerosis have included noncontrast-enhanced (NCE) and contrast-enhanced (CE) coronary vessel wall cardiovascular magnetic resonance (CMR). NCE-CMR can identify and quantify early atherosclerotic changes and vascular remodeling [13–17]. Additionally, it can be applied for the detection of intraplaque hemorrhage [18–21], a known marker of plaque instability. Selective visualization of residual coronary thrombus following plaque rupture has been also demonstrated with NCE-CMR [22] and was confirmed by optical coherence tomography (OCT) [23]. Furthermore,

B. Lavin-Plaza (✉) · A. Phinikaridou · S. Lacerda · M. Henningsson
Division of Imaging Sciences and Biomedical Engineering, King's College London, St Thomas' Hospital, London, UK
e-mail: begona.lavin_plaza@kcl.ac.uk; alkystis.1.phinikaridou@kcl.ac.uk; sara.lacerda@kcl.ac.uk; markus.henningsson@kcl.ac.uk

M. E. Andia
Radiology Department, School of Medicine, Pontificia Universidad Catolica de Chile, Santiago, Chile
e-mail: mandia@med.puc.cl

M. R. Makowski
Department of Radiology, Institut für Radiologie, Berlin, Germany
e-mail: marcus.makowski@charite.de

R. M. Botnar
Division of Imaging Sciences and Biomedical Engineering, King's College London, St Thomas' Hospital, London, UK

The British Heart Foundation Centre of Excellence, Cardiovascular Division, King's College London, London, UK

R. Y. Kwong et al. (eds.), *Cardiovascular Magnetic Resonance Imaging*, Contemporary Cardiology,
https://doi.org/10.1007/978-1-4939-8841-9_14

time-resolved bright-blood NCE-CMR in concert with an endothelium-dependent stressor allows assessment of coronary endothelial function, which represents an important predictor for cardiovascular events [18, 24–27]. To gain additional information, CE-CMR can be utilized. Retention of nontargeted contrast agents is associated with the severity of atherosclerosis and the degree of coronary inflammation [28, 29]. The potential of targeted CE-CMR for biological characterization of coronary thrombus and plaque has also been demonstrated in small and large animal models and in humans [30–34].

Pathophysiology of Atherosclerosis

Atherosclerosis is an inflammatory disease that affects medium and large size arteries and usually remains asymptomatic until late-stage disease when plaques enlarge and reduce arterial blood supply or suddenly rupture, thereby causing thrombotic occlusion and ultimately ischemic events [12, 35] (Fig. 14.1) [36]. It is widely accepted that vascular inflammation is the result of endothelial damage and the subsequent accumulation of low density lipoproteins (LDL) that initiate a complex signalling cascade leading to the recruitment of monocytes and macrophages and the deposition of extracellular matrix (ECM) proteins in the inner layer of the vessel wall [12, 37]. Recent studies have also reported a role of the adventitia [38–40]. Atherosclerosis usually occurs at predilection sites with disturbed laminar flow, such as branch points or at sites with oscillating shear stress [41]. The initial phase is characterized by endothelial dysfunction with structural and molecular alterations, including increasing width of the tight junctions [42, 43] and the activation of cell adhesion molecules, such as intercellular and vascular cell adhesion molecule-1 (ICAM-1 and VCAM-1) and E- and P-selectins [12]. Overexpression of ICAM-1 and VCAM-1 molecules is

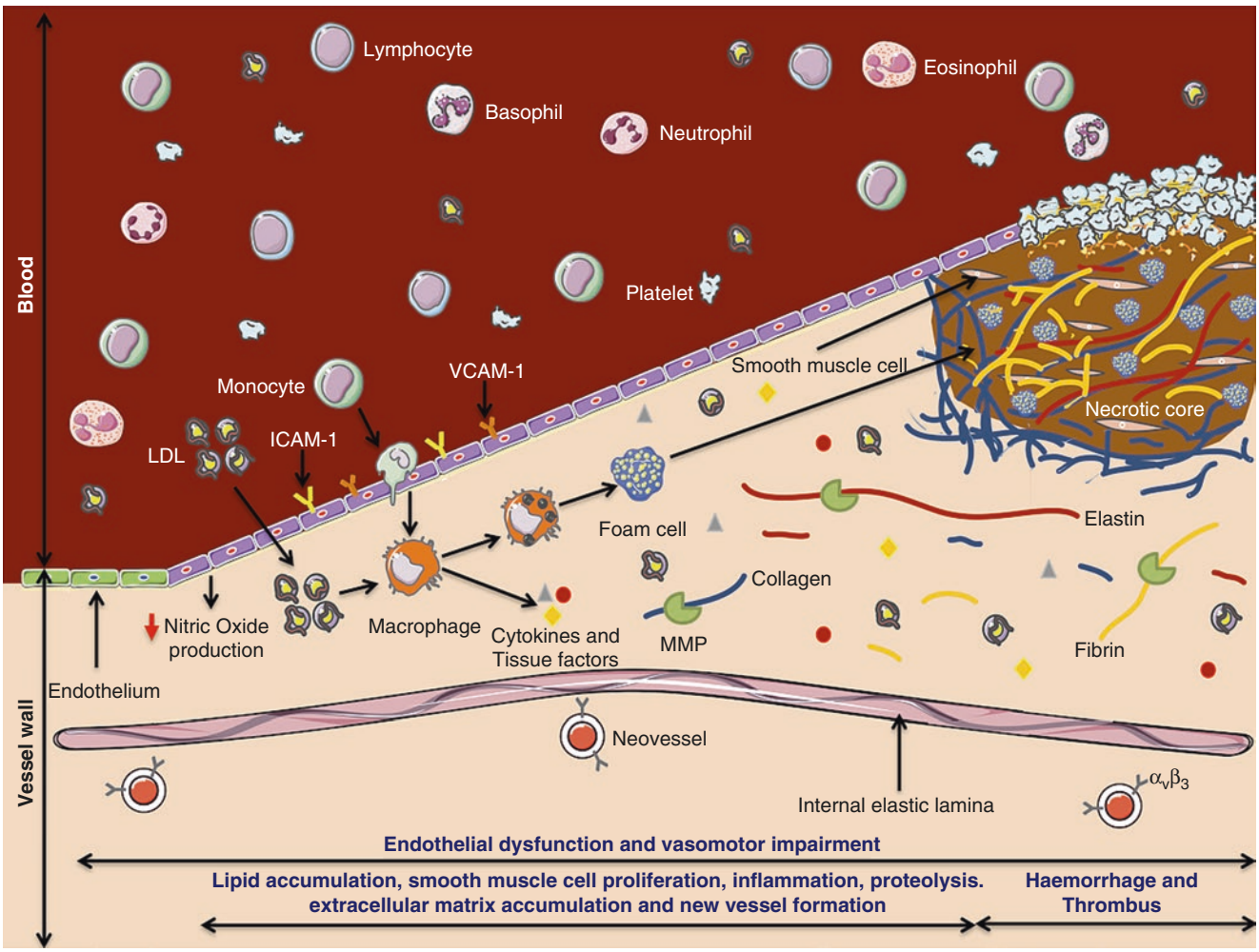

Fig. 14.1 Pathogenesis of atherosclerotic plaque development. Endothelial dysfunction initiates inflammatory processes and leads to the migration of immune cells and LDL into the vessel wall where monocytes differentiate into macrophages which transform themselves with increasing intake of lipids and cholesterol into foam cells. Subsequently, atherosclerotic plaques develop which are characterized by activation of platelets and smooth muscle cells, followed by deposition of extracellular connective matrix components and endothelial proliferation and necrotic core formation. (Adapted and reprinted from Springer, © 2014, online, Fig. 1, Lavin et al. [36], © 2014, with kind permission from Springer Nature)

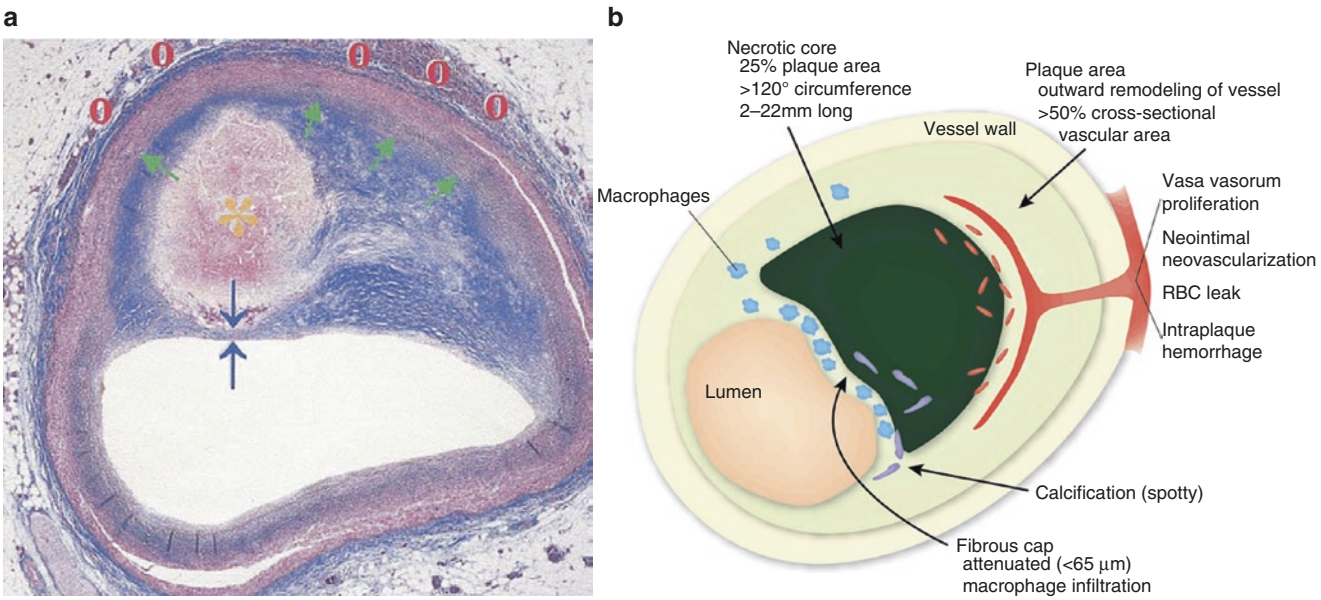

Fig. 14.2 Morphological and biological features of vulnerable plaque. (**a**) Cross section of a rupture-prone coronary artery plaque with a (1) large lipid-rich necrotic core (orange asterisk), (2) thin fibrous cap (blue arrows), (3) expansive remodeling (green arrow), and (4) vasa vasorum and neovascularization (red circles) [47]. (Adapted and reprinted from Falk [47], © 2006, with permission from Elsevier). (**b**) Schematic of a vulnerable plaque highlighting the features associated with plaque instability. (Adapted and reprinted by permission from Narula and Strauss [48], © 2007)

directly related with an increase in monocyte infiltration in the vessel wall where they differentiate into tissue-resident macrophages [44]. Recruitment of immune cells into the artery wall plays a central role in all stages of atherosclerosis. Macrophages uptake oxidized LDL using the scavenger receptors, and as a result of continued intracellular LDL accumulation in macrophages (cytosolic droplets), they transform into foam cells [12, 37]. Subsequent steps include secretion of inflammatory cytokines, activation of platelets, smooth muscle cell proliferation, accumulation of apoptotic cells, and deposition of ECM proteins such as collagen and elastin that collectively contribute to the formation of complex plaque including a necrotic lipid core due to foam cell apoptosis at advanced stages [45]. Alteration and degradation of the ECM by the release of matrix metalloproteinases (MMPs) from macrophages can lead to the progression and destabilization of the plaque [46]. Clinically, the aim is to divide atherosclerotic lesions into low risk (stable plaques) and high risk (vulnerable plaques). Postmortem studies have demonstrated that vulnerable plaques are characterized by a large plaque volume and large necrotic core, low amount of fibrous tissue, accumulation of macrophages, and a thin fibrous cap (Fig. 14.2).

At advanced disease stages, the enlargement of the plaque results in intraplaque hypoxia that triggers additional inflammatory cell infiltration and promotes local neovascularization. Stable plaques are characterized by a thick fibrous cap, high amounts of fibrous tissues, and a small number of macrophages [49, 50].

Cardiovascular Imaging

Cardiac MRI has become a clinically accepted imaging modality for assessment of left ventricular morphology and function, myocardial perfusion, viability, and tissue characterization including the measurement of diffuse myocardial fibrosis [51–55]. Due to ongoing technical advances in MR acquisition and reconstruction and contrast agent development, coronary MRI and vessel wall imaging are an emerging noninvasive imaging technique for comprehensive coronary assessment. Compared to other clinical imaging modalities such as single-photon emission computed tomography (SPECT) and position emission tomography computed tomography (PET/CT), MRI provides high spatial and temporal resolution allowing for a comprehensive cardiac evaluation including morphology, function, perfusion, and myocardial tissue characterization [51–55]. The development of novel plaque-specific MR contrast agents also allows imaging of biological processes in the vessel wall without exposure of the patient to harmful ionizing radiation or iodinated contrast agents.

MRI is based on the nuclear magnetic properties of atoms (mainly hydrogen) and involves the interplay of three components to generate tomographic images: the main magnetic field of the scanner (static magnetic field) which generates a net magnetization along the scanner axis, the gradient fields which are used for spatial localization, and the oscillating magnetic field of the radio-frequency (RF) pulses. RF pulses

are used to change the orientation of the magnetization, inducing excitation of the water protons. Following the RF pulse excitation, protons return to their equilibrium stage, and specific receiver coils detect the energy emitted during this relaxation. The most important proton properties used by MRI are the proton density and two characteristic relaxation times called spin-lattice relaxation time and spin-spin relaxation time, denoted as T_1 and T_2, respectively. Signal intensity primarily depends on the local values of R_1 ($1/T_1$) and R_2 ($1/T_2$) relaxation rate of water protons [56]. Considering the relatively low sensitivity of MRI, the use of specific contrast agents aids the detection of differences between pathological and normal surrounding tissues. For that, local concentrations of a contrast agent are needed to alter the relaxation rate of water protons sufficiently for detectable signal effects. An important consideration to take into account during vessel wall imaging is the distribution of the contrast agent in non-targeted regions and the adjacent blood pool. In some cases, to distinguish between the luminal area and the vessel wall contrast uptake, it might be necessary to wait for the contrast agent to clear sufficiently from the blood.

Imaging Sequences

Vessel wall MRI can be achieved without contrast agents by exploiting the ability of MRI to suppress signal from adjacent tissues which mainly include luminal blood and epicardial fat. Fat suppression is commonly performed using spectrally selective inversion magnetization preparation pulses, where the image acquisition is timed to coincide with the nulling point of the fat signal. Alternatively, signal from fat can be minimized using water-selective RF pulses for imaging [57] or using the DIXON water-fat separation technique [58, 59]. To suppress blood signal (so-called black-blood MRI), traditionally, flow-dependent techniques have been employed such as double inversion recovery (DIR) [60, 61]. However, DIR is typically limited to two-dimensional cross-sectional imaging of the vessel wall or requires local inversion pulses for three-dimensional coronary vessel wall imaging [62] (Fig. 14.3). More recently, motion-sensitized driven equilibrium (MSDE) [63], delay altering with nutation for tailored excitation (DANTE) [64], and variable flip-angle turbo spin echo with flow-sensitive dephasing have been proposed to allow for flow-dependent three-dimensional coverage [65]. Such volumetric coverage is desirable due to the long and tortuous geometry of the coronary arteries and simplifies MRI scan planning compared to DIR. A schematic overview of a ECG-triggered black-blood imaging sequence is provided in Fig. 14.4. Blood signal suppression can also be achieved using flow-independent techniques which typically rely on the difference in T1 or T2 between vessel wall, thrombus, and blood [19, 21, 27, 66, 67] or a combination of T2 and T1 [65, 68] (Fig. 14.5).

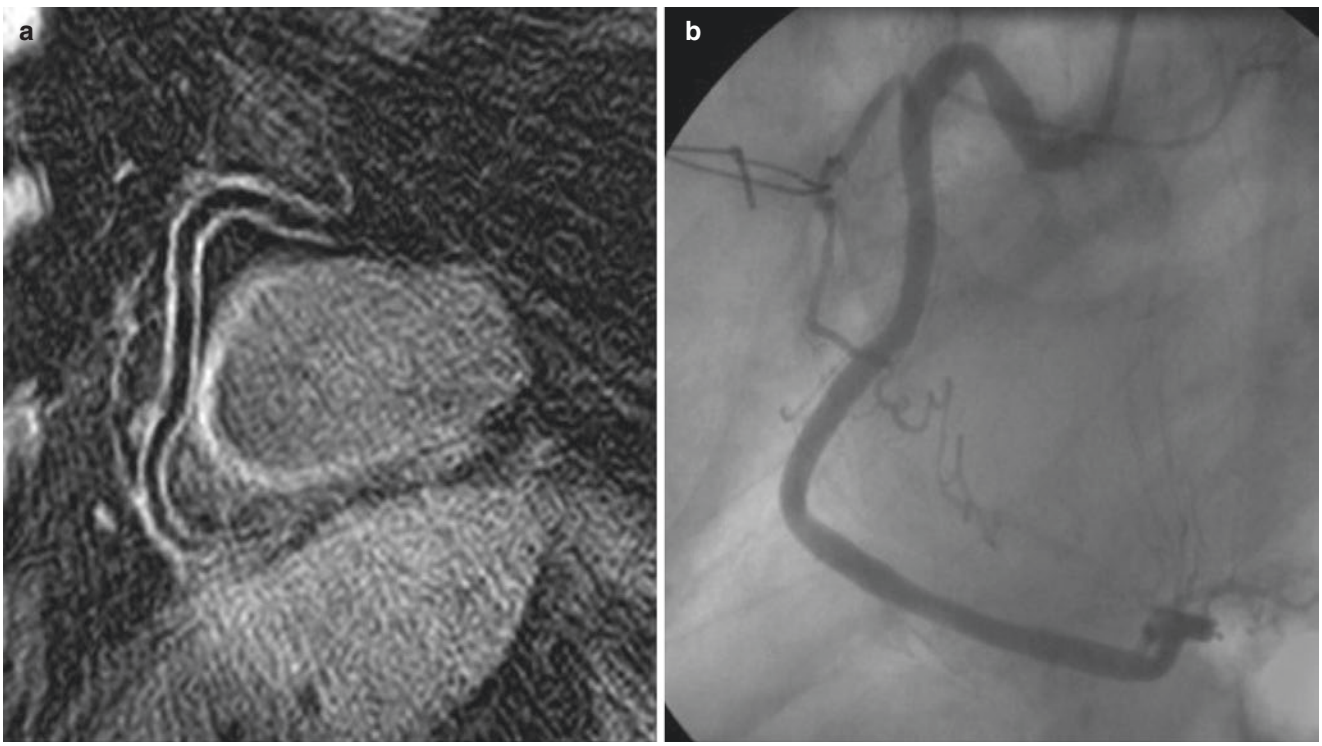

Fig. 14.3 Local inversion black-blood coronary wall imaging for the quantification coronary arterial remodeling and plaque burden. (**a**) 3D black-blood vessel wall image of the right coronary artery wall (RCA) in a patient with nonsignificant coronary artery disease on X-ray coronary angiography. (**b**) Vessel wall images demonstrate some minor wall thickening in the proximal and mid RCA segment

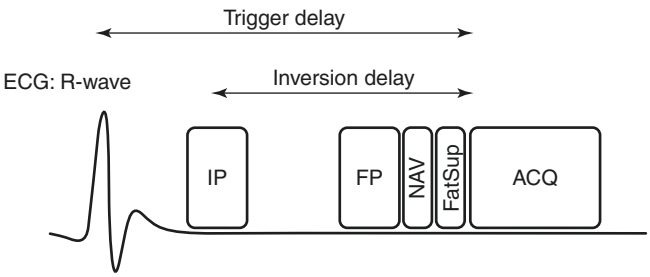

Fig. 14.4 Generic black-blood vessel wall MRI pulse sequence. Cardiac motion is compensated for by synchronizing the image acquisition (ACQ) with an electrocardiogram (ECG) and using a trigger delay from the R-wave to time ACQ to mid-diastole. Respiratory motion compensation can be performed using respiratory navigation (NAV) which typically precedes ACQ. Fat suppression is performed prior to ACQ using a fat-selective RF pulse to null the fat signal. Black-blood contrast can be achieved either with inversion preparation (IP) where an inversion delay is used to null signal from the blood or alternatively using flow preparation (FP) where signal from flowing blood is destroyed using dephasing gradients or a combination of small RF pulses and gradients. (Adapted and reprinted from Springer, © 2014, online, Fig. 2, Lavin et al. [36], © 2014, with kind permission from Springer Nature)

Flow independence overcomes the problem of inadequate blood suppression in the case of slow laminar flow and facilitates volumetric whole-heart coverage (Fig. 14.6).

Vessel wall MRI can also be performed using contrast agents, either with T1-shortening gadolinium-based agents or T2/T2* shortening iron-based agents. Contrast agent quantification is then typically done using T1 and T2/T2* mapping sequences of which several implementations exist. The most commonly used T1 mapping sequences are the Look Locker (Fig. 14.7), the modified Look Locker inversion recovery (MOLLI) [69], and the saturation recovery single-shot acquisition (SASHA) [70] sequence and combinations of it [71]. T2 and T2* mapping is typically done with a multi-echo spin-echo and gradient-echo (Fig. 14.8) technique, respectively. Recent implementations also include the use of T2 prep pulses with varying echo times for cardiac T2 mapping [72–74].

An important requirement for coronary vessel wall visualization is high spatial resolution. Although improved spatial resolution can be achieved with the use of dedicated

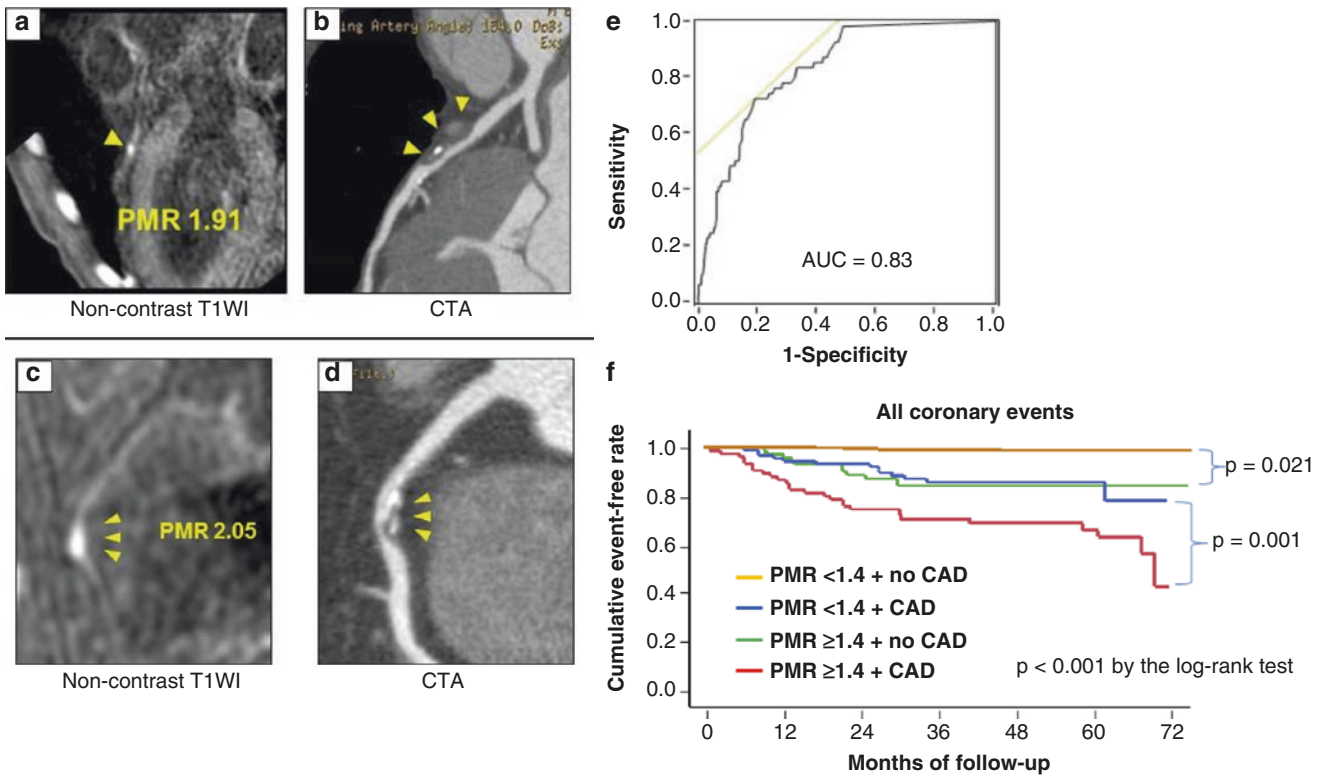

Fig. 14.5 Representative images of HIPs with PMRs ≥1.4. Representative noncontrast T1-weighted images of high-intensity plaques (HIPs) (yellow arrowheads) in the proximal left anterior descending coronary artery (**a**) and the right coronary artery (**c**), in which plaque-to-myocardium signal intensity ratios (PMRs) were 1.91 and 2.05, respectively. These high-intensity signals each correspond to the left and right coronary plaques on computed tomographic angiography (CTA) (yellow arrowheads on curved multiplanar reformation images), (**b**) and (**d**). T1WI = T1-weighted imaging. (**e**) ROC Curve Analysis for Developing Coronary Events and Flowchart of Study Patients on the Basis of PMR. From receiver-operating characteristic (ROC) curve analysis, a plaque-to-myocardium signal intensity ratio (PMR) of 1.4 was identified as the best cutoff value for predicting cardiac events, with 69.5% sensitivity and 82.3% specificity. The calculated area under the curve (AUC) was 0.83. (**f**) Kaplan-Meier curves comparing the probability of all coronary events. Coronary event–free survival was worst in the group with plaque-to-myocardium. Signal intensity ratios (PMRs) ≥ 1.4 and coronary artery disease (CAD) (red line) and best in the group with PMRs < 1.4 but no CAD group (orange line). The rate in the group with PMRs ≥ 1.4 and no CAD (green line) was intermediate but comparable with that in the group with PMRs <1.4 and CAD (blue line) (Adapted and reprinted from, Noguchi et al. [19], © 2014, with permission from Elsevier)

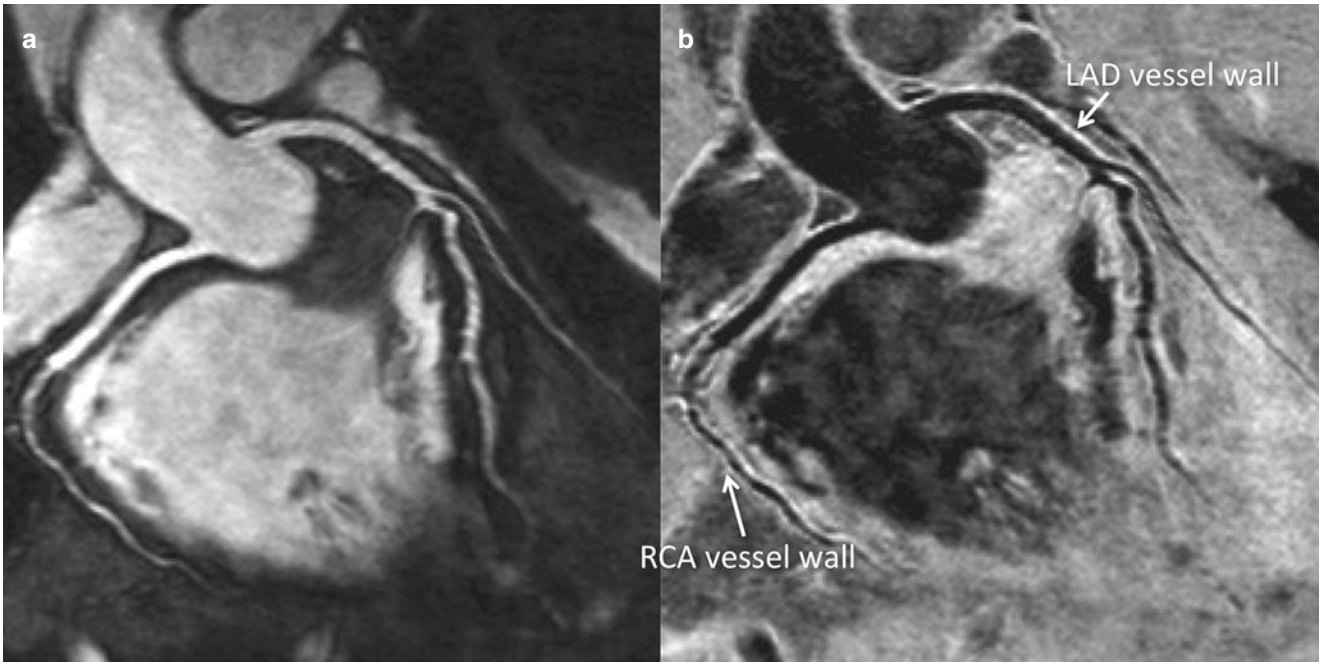

Fig. 14.6 Flow-independent 3D whole heart coronary vessel wall imaging using an interleaved T2 prep imaging sequence. (**a**) 3D bright-blood SSFP coronary artery image in a healthy volunteer without history of coronary artery disease demonstrating normal left and right coronary arteries. (**b**) Corresponding whole heart vessel wall image clearly delineates the coronary vessel wall both in the proximal and distal segments due to the flow-insensitive nature of the iT2 prep imaging sequence. (Adapted from, Andia et al. [67], © 2012, with permission of John Wiley and Sons)

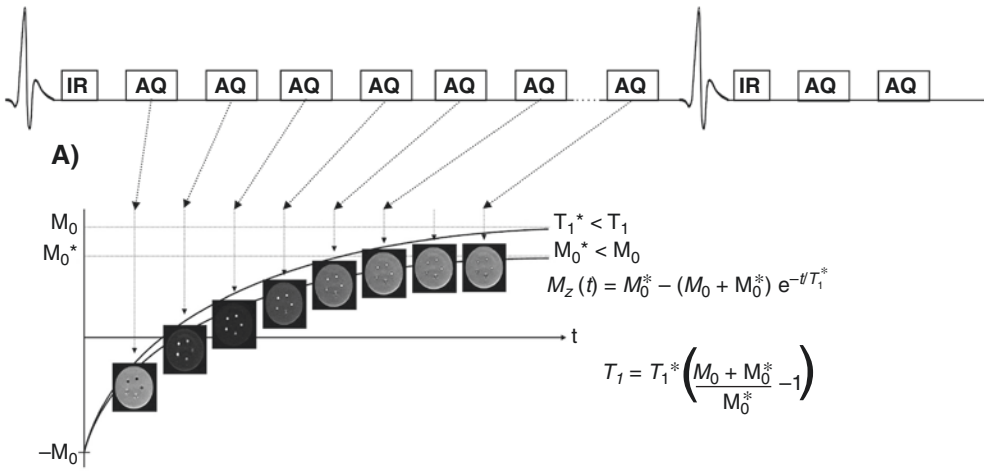

Fig. 14.7 Schematic of inversion recovery Look Locker (LL) T_1 mapping sequence. The inversion pulse precedes the imaging sequence (AQ), which allows pixel-wise sampling of the recovery of the Mz magnetization of, e.g., tissues, fluids, or blood. A least square fit of the measured Mz values to the Bloch equation allows pixel-wise estimation of T_1 and estimation of the local contrast agent concentration [Gd^{3+}]. A T_1 correction is usually performed as the repetitive use of RF pulses alters the recovery of the M_z magnetization leading to a lower value for the steady-state magnetization, $M_0^* < M_0$, and thus to a shorter value for the relaxation time $T_1^* < T_1$

multichannel cardiac receiver coils, coronary vessel wall imaging is challenging due to the slow acquisition speed of MRI relative to the physiological motion. This includes both cardiac and respiratory motions, which are both one order of magnitude larger than the achievable spatial resolution. However, to mitigate the effects of motion, which include image blurring and ghosting, cardiac and respiratory motion compensation methods have been introduced. Cardiac motion can be effectively minimized by synchronizing the MRI scanner with an electrocardiogram (ECG) and limit the data acquisition to the most quiescent cardiac phase. Although the timing and duration of the cardiac rest period is

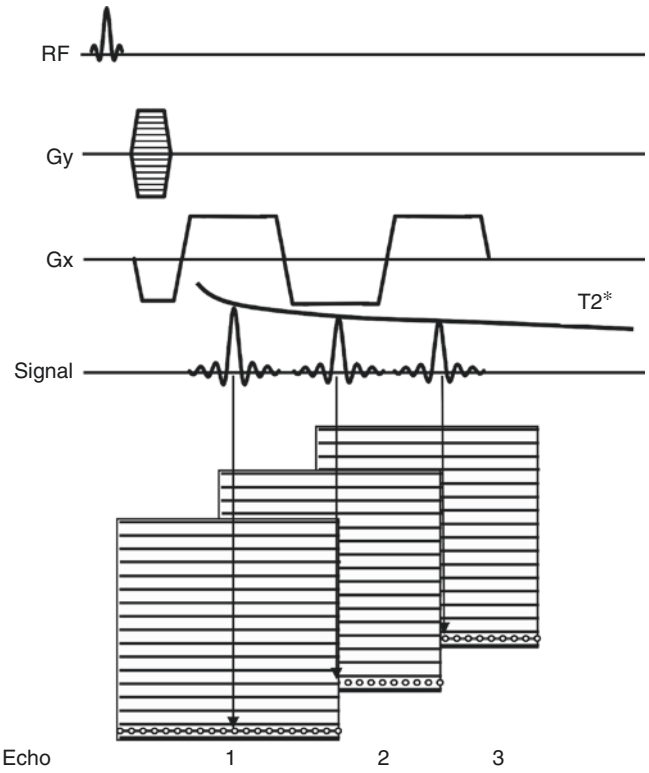

Fig. 14.8 Schematic of T_2* mapping sequence using Cartesian k-space sampling. Acquisition of multiple echoes allows sampling the T_2* decay envelope and thus to estimate the T_2^* relaxation time of tissues and blood

subject and heart rate dependent, time-resolved MRI cine scans can be used to identify the most suitable acquisition window. For respiratory motion compensation, a so-called respiratory navigator can be used. Conventional respiratory navigator techniques involve measuring the displacement of the lung-liver interface in feet-head direction and only accept data acquired within a narrow "gating window," typically defined around end-expiration. Furthermore the measured navigator position can be used to update the MR image in real time based on a motion model which is often assumed to be a linear relationship of 0.6. A drawback of this approach is that the scan time is prolonged because a large portion of the data falls outside the gating window and has to be remeasured (typically only 20–50% is inside the window), as well as the indirect motion measurement requiring a motion model. Recently, technical advances have allowed for direct measurement of respiratory induced motion using self-gating or image navigators, which directly measure the respiratory motion of the heart which and thus obviate the need for a gating window and reduce scan time [57]. Currently, several flavors exist which include beat-to-beat [75, 76] or bin-to-bin [77, 78] motion correction or a combination of it [79, 80]. These techniques now allow correcting for respiratory motion in two or three dimensions and to apply more sophisticated motion correction algorithms including affine and nonrigid transformations and also integrating motion correction directly into image reconstruction [77]. Latest developments do not require neither ECG synchronization nor respiratory gating and acquire data continuously throughout the cardiac cycle [81, 82]. Data are typically acquired with the golden angle approach and a 3D radial trajectory with repetitive acquisition of the center k-space line in foot-head (FH) direction. The self-gating signal allows estimation of both the ECG and the respiratory signal using principal component analysis and thus to retrospectively sort the cardiac phases and to perform respiratory binning. These 4D datasets allow selecting the cardiac phase with best vessel lumen and wall visualization.

T1 Contrast Agents

The most commonly used contrast agents are based on gadolinium (Gd) complexes that lead to positive contrast detected as a local increase in MRI signal intensity or brightness [83]. Gd(III) is a metallic element with seven symmetrical, unpaired electrons characterized by a strong paramagnetic susceptibility, which produces a slow electron spin relaxation rate that significantly affects the surrounding water protons. Therefore, it has the effect of shortening T_1 relaxation time in tissues where it accumulates, enhancing the signal in post-contrast T_1-weighted images. Following Gd(III) administration, they rapidly distribute into the extracellular fluid space. Subsequently, they are then gradually excreted via the kidneys with a 60–90 min half-life for most small molecular weight agents (~1000 Da) in patients with normal renal function and completely eliminated after 24 h [83]. Due to its toxicity, Gd(III) must be chelated for in vivo application. Several chelating approaches have been published with cyclic chelates (DOTA) demonstrating better metabolic stability than linear chelates (DTPA) [84]. Another important aspect is the optimization of the relaxivity properties of these Gd(III) complexes to improve signal enhancement and therefore the sensitivity of these imaging agents. For protein- or cell-specific imaging, targeting moieties have been attached to Gd(III) chelates to allow the evaluation of molecular or cellular changes associated with different disease stages. The relaxivity of gadolinium chelates is dependent on several parameters such as molecular motion and water exchange [83] (Fig. 14.9).

A good example of the impact of these two parameters on relaxivity is the Gd-DTPA analog gadofosveset trisodium, Ablavar (Lantheus Medical Imaging, North Billerica, USA), which binds to human serum albumin and increases its relaxivity by five-fold compared to the unbound fraction [86]. This effect is known as receptor-induced magnetization enhancement (RIME) [87] and has been exploited for other protein-binding imaging agents including the elastin-binding contrast agent (ESMA) [88] or a fibrin-binding contrast agent,

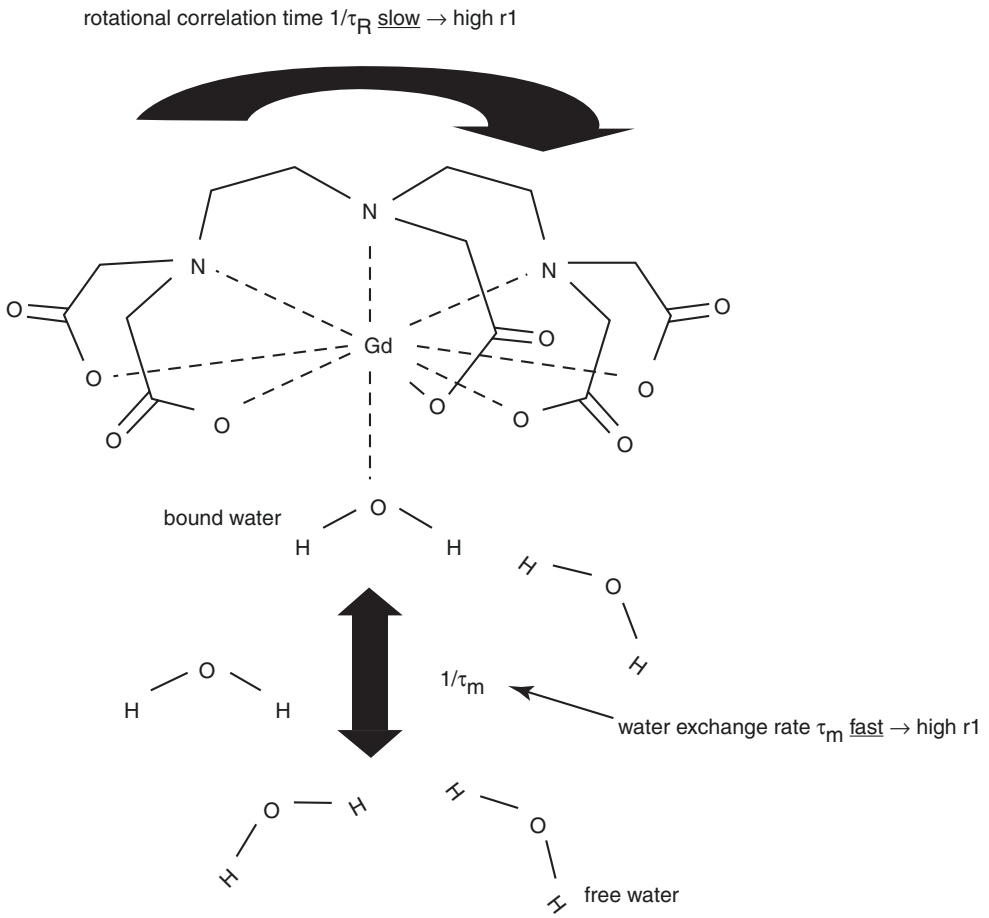

Fig. 14.9 Schematic of water exchange between bound and free water of a gadolinium chelate. The proton bound to gadolinium exchanges its magnetic properties with the free water leading to a shortening of T_1 in the vicinity of the contrast agent. Fast water exchange leads to a more efficient energy transfer between gadolinium and free water, thereby creating a higher relaxivity r_1. The amount of T_1 shortening is given by the relaxivity (r_1) of the contrast agent, which depends on the number of bound protons, the water exchange rate ($1/\tau_m$), and the T_1 relaxation time of bound water (T_{1m}). T_{1m} itself depends on several factors including the distance to the gadolinium atom and the rotational correlation time ($1/\tau_r$). Upon binding to a large protein or cell, $1/\tau_r$ significantly decreases thereby increasing r_1 and thus increasing the T_1-shortening effect of the contrast agent. Construction of macromolecular agents (e.g., dendrimers) is another means of slowing down the rotational motion of Gd compounds. (Adapted from Caravan [85])

EP-2104R [89]. Other approaches to improve r_1 relaxivity is the use of lipid-perfluorocarbon emulsions that allow increasing the number of Gd(III) atoms per probe. A good example of these lipid-perfluorocarbon emulsions is a fibrin-specific contrast agent where multiple Gd(III) atoms were targeted with biotin that can bind to avidin derivatized with an antibody to recognize fibrin (present in the clot) [90]. Another approach is the use of a lipid tail to increase the number of Gd(III) per molecule. A contrast agent that detects angiogenesis by αvβ3-targeting is an example of this design [91].

T2 and T2* Contrast Agents

Although Gd(III)-based contrast agents usually increase $1/T_1$ and $1/T_2$ (R_1 and R_2, respectively) in similar amounts [85, 92, 93], it is well established that iron particle-based contrast agents have a much stronger effect on increasing R2 [94]. The paramagnetic properties of iron particles usually disturb the surrounding magnetic field causing a negative contrast effect detected as a decrease of signal intensity or darkness. This effect can be accurately detected with T2- and T2*-weighted imaging sequences. Moreover, it has also been demonstrated that iron-based particles can provide higher sensitivity in target detection compared to gadolinium-based contrast agents [95]. Depending on the size range of these particles, they can be divided into micron-sized iron oxide particles (MPIO) ≈ 10 μm in diameter, monocrystalline iron oxide particles (MION) ≈ 3 nm in diameter, ultrasmall superparamagnetic iron oxide particles (USPIO) ≈ 15–30 nm, and superparamagnetic iron oxide particles (SPIO) ≈ 60–180 nm. SPIOs have an iron oxide core that is stabilized with a monomer or polymer coating. SPIOs are characterized by good suspensibility, uniform

particle size distribution, highly reactive surface, and the possibility of coating modifications to attach specific ligands for biomedical applications. The size and surface properties (in particular charge) have a decisive influence on the elimination, cell response, and toxicity. The maximum effect of SPIO in tissue is usually detected 24–48 h after administration [96]. The non-specific uptake of SPIOs by the mononuclear phagocyte system after intravenous administration is well established. This process allows the use of SPIOs in both to image organs, in particular the liver, spleen, lymph nodes, and bone marrow [97]. One of the major drawbacks of iron-containing particles due to the non-specific uptake by mononuclear phagocytes is the short blood half-life that limits their application in MRI. In order to increase the blood half-life of these particles, several approaches have been implemented, of which modifying the probe coating and decreasing their hydrodynamic diameter (e.g., USPIO) are the most frequent. USPIOs are iron oxide nanoparticles composed of Fe_2O_3 and Fe_3O_4 stabilized by different coating agents. USPIOs are predominantly used for molecular imaging of atherosclerosis [98], myocardial infarction [99], and cancer [100]. Various studies have demonstrated the possibility to identify carotid plaque inflammation noninvasively using USPIOs in both animals and human [101–104]. The use of USPIO particles has allowed the direct visualization of macrophage infiltration in carotid atheroma in vivo [105, 106]. Additionally, USPIOs have a high r_1, which produces an increase in signal intensity using T1-weighted sequences. At low USPIO concentrations, a T_1-enhancing effect can be observed, whereas at higher doses, the susceptibility phenomenon balances the T_1 effect (nonlinearity in the signal-concentration relationship). Thus, according to the sequence and the local concentration of USPIO, T_1-, T_2-, and T_2*-enhancing effects can be observed independently. In this regard, USPIOs can also be used for T1-weighted imaging to acquire angiograms of the coronary arteries, carotid arteries, and aorta.

Contrast Agents

Endothelial Dysfunction

During the first stages of atherosclerosis, the endothelium develops several functional alterations due to cardiovascular risk factors such as smoking, diabetes, hypercholesterolemia, and obesity, a condition known as endothelial dysfunction [42]. Under these circumstances, endothelial cells are characterized by a reduction in the net production of nitric oxide (NO), leading to impaired vasodilation and an increase in endothelial permeability that allows the influx of LDL and inflammatory cells into the vessel wall [12]. Additionally, endothelial cells increase the expression of surface-specific adhesion molecules such as VCAM-1, ICAM-1, and E- and P-selectins that contribute to the adhesion and infiltration of immune cells into the vessel wall [12]. Several studies have observed a correlation between endothelial dysfunction and plaque burden, representing an interesting imaging target [24]. Gadofosveset is a clinically approved contrast agent with a long blood half-life time due to binding to human serum albumin and thus ideally suited for MR angiography [85, 86]. Recent studies by our group have demonstrated the ability of gadofosveset to detect changes in endothelial permeability in the brachiocephalic artery of atherosclerotic ApoE$^{-/-}$ mice [107] (Fig. 14.10) and for monitoring effectiveness of interventions in retarding plaque progression [108].

Gadofosveset enhancement has been also correlated with leaky neovessels in atherosclerotic rabbits [110], stent-induced coronary injury in swine [111], and patients with carotid artery disease [109]. Endothelial adhesion molecules are highly expressed in the early stages of atherosclerosis, and therefore different approaches have been developed to specifically image those molecules. In vivo imaging of atherosclerotic plaque has been successfully performed in ApoE$^{-/-}$ mice using VCAM-1-specific nanoparticles [112, 113].

Hypoxia: Angiogenesis and Apoptosis

During the progression of atherosclerosis, the size and composition of the vessel wall changes and local hypoxic areas can contribute to the generation of new vessels, a process known as angiogenesis [114]. This process plays a central role in plaque enlargement and disease progression, and the density of neovessels has been linked with vulnerable or unstable plaques [115]. Gadofosveset has been successfully used to image neovessel-rich areas in different animal models and patients [109, 116, 117]. In contrast to healthy tissues, endothelial cells of immature neovessels are activated and express the surface marker $\alpha_v\beta_3$ in significant amounts [118, 119]. It has been demonstrated that $\alpha_v\beta_3$-targeted paramagnetic nanoparticles allow the noninvasive assessment of $\alpha_v\beta_3$-integrin expression in the aortic wall of hyperlipidemic rabbits during the first stages of atherosclerosis [91]. Alternative approaches include the use of dynamic contrast-enhanced T1-weighted MR imaging using clinically approved contrast agents such as gadopentetate dimeglumine [120].

Hypoxic conditions can also lead to the apoptosis of immune cells which has been described as another marker of plaque instability [121]. During apoptosis, cells express specific surface markers like annexin 5 or caspases [122]. An annexin A5-functionalized micellar contrast agent has been successfully used to image apoptosis in atherosclerotic ApoE$^{-/-}$ mice [123]. Moreover, a novel caspase-3/7-

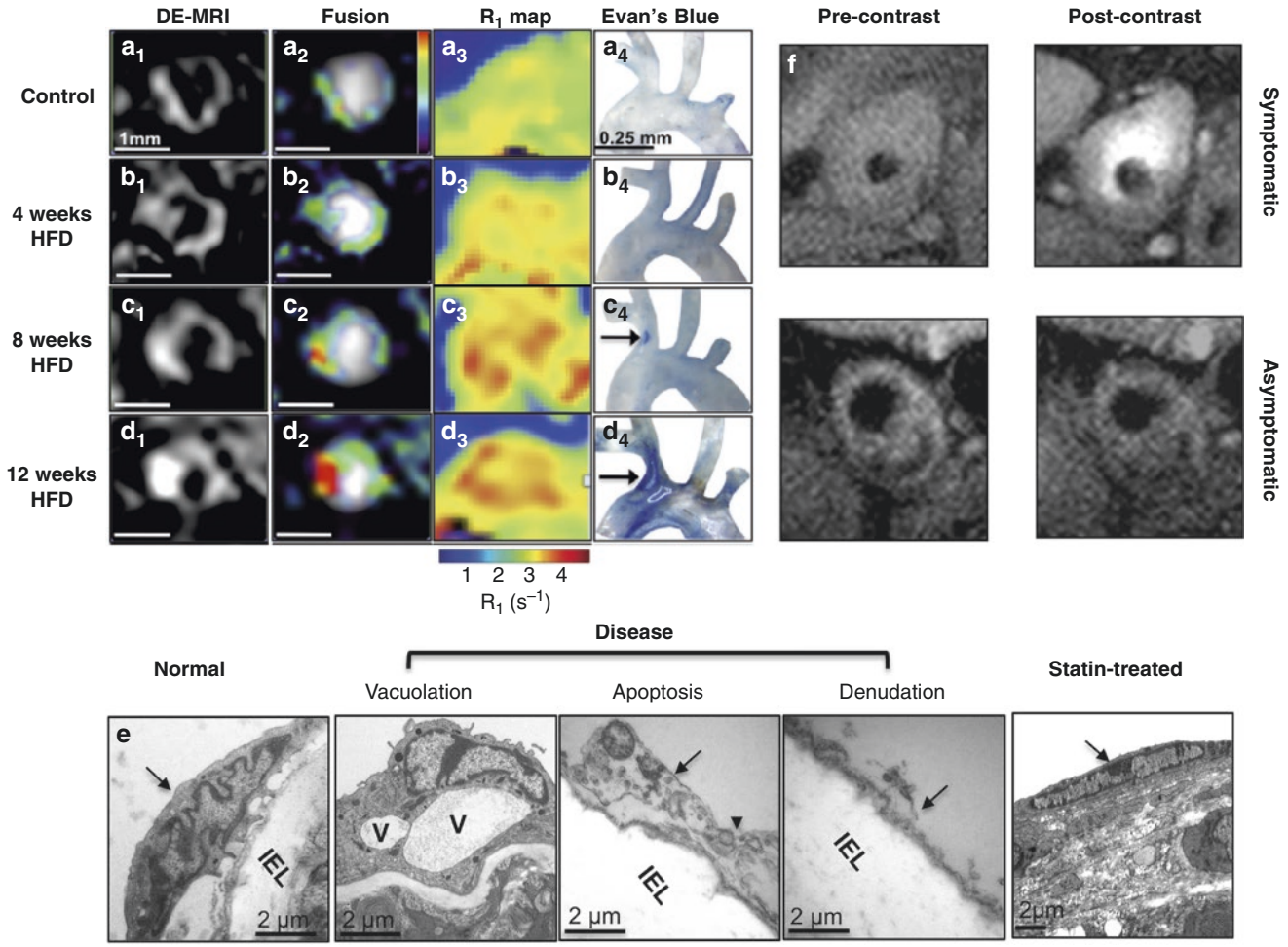

Fig. 14.10 Uptake of an albumin-binding MR contrast agent correlates with endothelial permeability and plaque progression. Late gadolinium enhancement (LGE) MRI and T_1 mapping of endothelial permeability throughout the course of plaque development in high-fat diet (HFD)-fed apoE$^{-/-}$ mice using an albumin-binding contrast agent, gadofosveset, (**a_1–d_1**) and (**a_3–d_3**). Evan's blue dye staining of the artic arch and brachiocephalic artery shows good agreement (**a_4–d_4**). TEM of endothelial cell (EC) morphology (**e**) showed gradual disease development starting with vacuolation and almost complete EC denudation after 12 weeks of HFD and normalization in mice treated with statins Fig. 14.10a–e. (Adapted and reprinted from, Phinikaridou et al. [107], © 2012, with permission from Wolters Kluwer Health). Clinical data (**f**) demonstrate increased gadofosveset uptake in patients with symptomatic carotid artery disease, which correlated with increased neovessel density and macrophage count Fig. 14.10f. (Adapted and reprinted from, Lobbes et al. [109], © 2010, with permission from Wolters Kluwer Health)

activatable Gd-based probe (C-SNAM) has been successfully used to image apoptosis in experimental mouse tumor models [124].

Macrophages

During the progression of atherosclerosis, there is a constant influx of immune cells into the vessel wall. The most prominent immune cells that invade these lesions are monocytes that differentiate into plaque resident macrophages where they uptake large amounts of cholesterol to generate so-called foam cells filled with numerous cholesterol ester droplets [12]. Macrophages can alter their phenotype and function in response to the local microenvironment also known as macrophage polarization [125]. In this regard, there is evidence suggesting that different stages of atherosclerosis are associated with distinct macrophage subtypes, M1, classically activated or pro-inflammatory macrophages, and M2, alternatively activated or resolving macrophages [125]. Although different strategies have been developed to target monocytes, none of them has had the ability to distinguish between macrophage subtypes. Thus, the development of an M1- or M2-specific probe remains an interesting challenge. The phagocytic properties of macrophages have been used for the passive targeting using different types of iron particles in both animal models [103, 126–131] and humans [97, 104, 132–135] (Fig. 14.11).

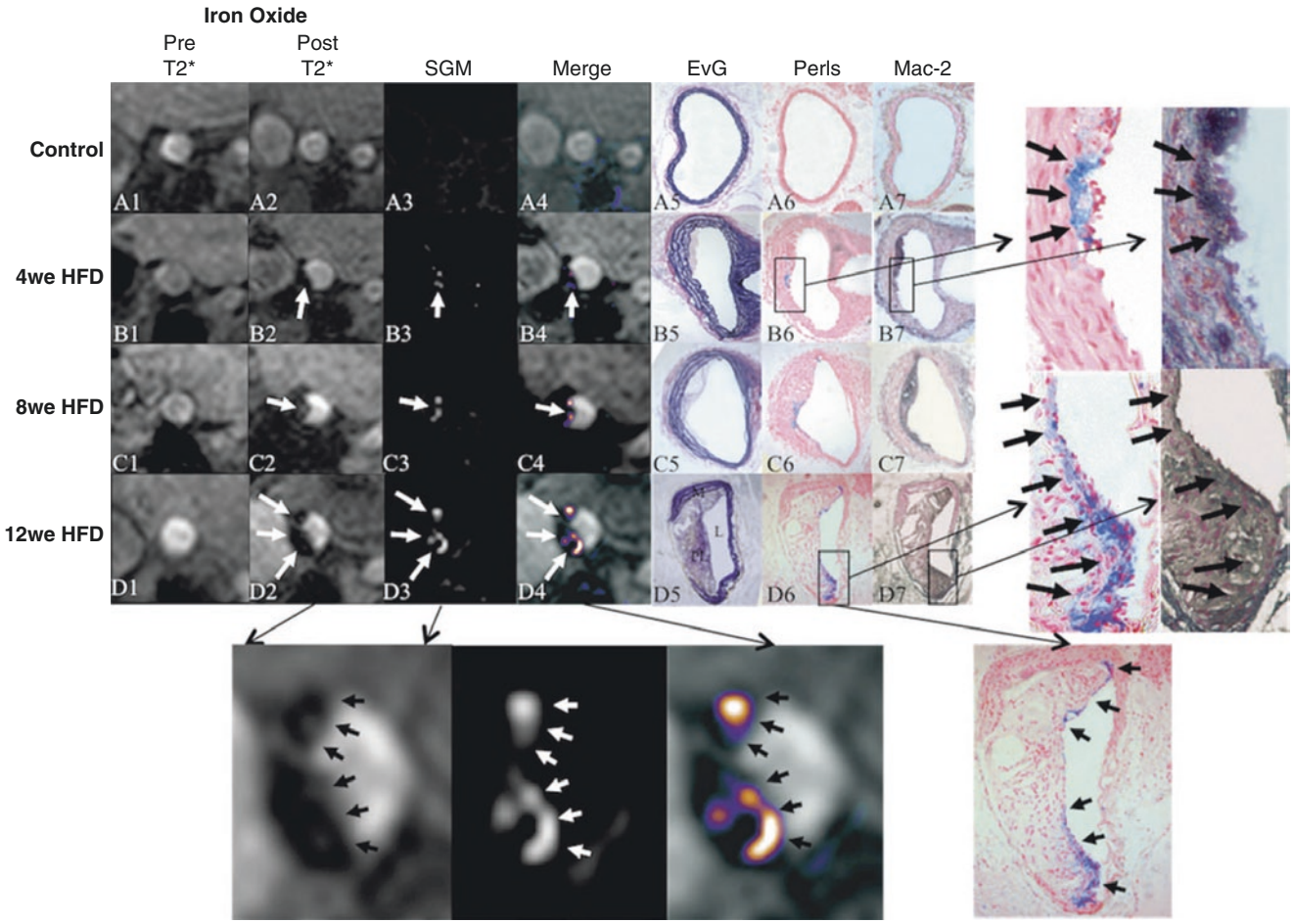

Fig. 14.11 In vivo imaging of macrophages in the brachiocephalic artery of apoE/mice on HFD. Bright-blood imaging was performed such that a 2D slice was obtained perpendicular through the brachiocephalic artery ($\mathbf{a}_{1-2}$, $\mathbf{b}_{1-2}$, $\mathbf{c}_{1-2}$, and $\mathbf{d}_{1-2}$). SGM-positive contrast images were derived and merged with the bright-blood images ($\mathbf{a}_{3-4}$, $\mathbf{b}_{3-4}$, $\mathbf{c}_{3-4}$, and $\mathbf{d}_{3-4}$). Representative images after the injection of the iron oxide agent from control as well as mice on the HFD for 4, 8, and 12 weeks and corresponding elastica van Gieson stain, Perls stain, and immunohistochemical analysis for Mac-2 (macrophage marker). Contiguous histological sections were taken in a similar orientation as the in vivo MRI of the brachiocephalic artery. Perls staining was used to demonstrate colocalization of iron-positive areas ($\mathbf{a}_6$, $\mathbf{b}_6$, $\mathbf{c}_6$, and $\mathbf{d}_6$) with Mac-2-positive ($\mathbf{a}_7$, $\mathbf{b}_7$, $\mathbf{c}_7$, and $\mathbf{d}_7$) (M indicates media, Pl plaque, and L lumen). HFD high-fat diet. (Adapted and reprinted from, Makowski et al. [131], © 2011, with permission from Wolters Kluwer Health)

An alternative to non-specific nanoparticles are receptor-specific probes. The scavenger receptors are macrophage-specific surface proteins that are significantly overexpressed on activated macrophages and foam cells, but not expressed on other cells [102]. With the use of gadolinium, immunomicelles targeted to the macrophage scavenger receptor CD206-activated macrophages have been successfully imaged in atherosclerotic plaque of ApoE$^{-/-}$ mice [102]. An alternative approach for macrophage imaging has been developed using gadolinium-loaded LDL-based nanoparticles and modified HDL nanoparticles. Fluorine-containing nanoparticles are avidly taken up by macrophages and therefore can be used to quantify the recruitment of inflammatory cells into atherosclerotic lesions. Since fluorine is absent in the human body, the measurement of fluorine uptake offers a unique possibility to directly detect and quantify the temporal and spatial evolution of the inflammatory response. In vivo imaging of cardiac and cerebral ischemia has been successfully performed in mice using this approach [136].

Lipids

Uptake of lipids into the vessel wall is one of the processes present throughout the development of atherosclerosis [12, 125]. There is a strong relationship between high serum lipid levels, especially of low-density lipoproteins (LDL), and coronary risk [137]. Since oxidized LDL is one of the drivers of vessel wall inflammation, it represents an interesting imaging target. Gadofluorine M is a gadolinium-based contrast agent that has been successfully used to image increased

neovascularization in advanced lipid-rich atherosclerotic lesions in rabbits [138]. Moreover, the incorporation of an apoE-derived lipopeptide (P2fA2) into the lipid layer of HDL nanoparticles (rHDL-P2A2) has been developed as a platform for molecular MRI of macrophages in atherosclerotic plaques in vivo [139].

Extracellular Plaque Components and Proteolytic Enzymes

Another approach to noninvasively image atherosclerosis is targeting extracellular plaque components. The extracellular matrix is a protein- and carbohydrate-based lattice. In atherosclerotic vessels, smooth muscle cells and macrophages increase the synthesis and secretion of ECM components such as collagen and elastin, and this turnover is related with vascular wall remodeling [140]. To detect the alteration of the ECM under pathological conditions, a small molecular weight elastin-specific gadolinium-based contrast agent (ESMA) has been developed. The ability of ESMA to detect plaque burden and ECM remodeling has been demonstrated at different stages of atherosclerosis in a murine model and in a porcine model of coronary injury [32, 141] (Figs. 14.12 and 14.13).

In addition to quantifying the plaque burden using the ESMA, a study using a rabbit model of experimentally induced thrombosis allowed in vivo classification of vascular remodeling in negative, intermediate, and positive for the detection of "high-risk/vulnerable" plaque [142] (Fig. 14.14).

Similarly, to prospective clinical studies in humans with coronary artery disease [49, 143, 144], the rabbit study showed that positive remodeling measured after administration of ESMA was associated with plaque instability.

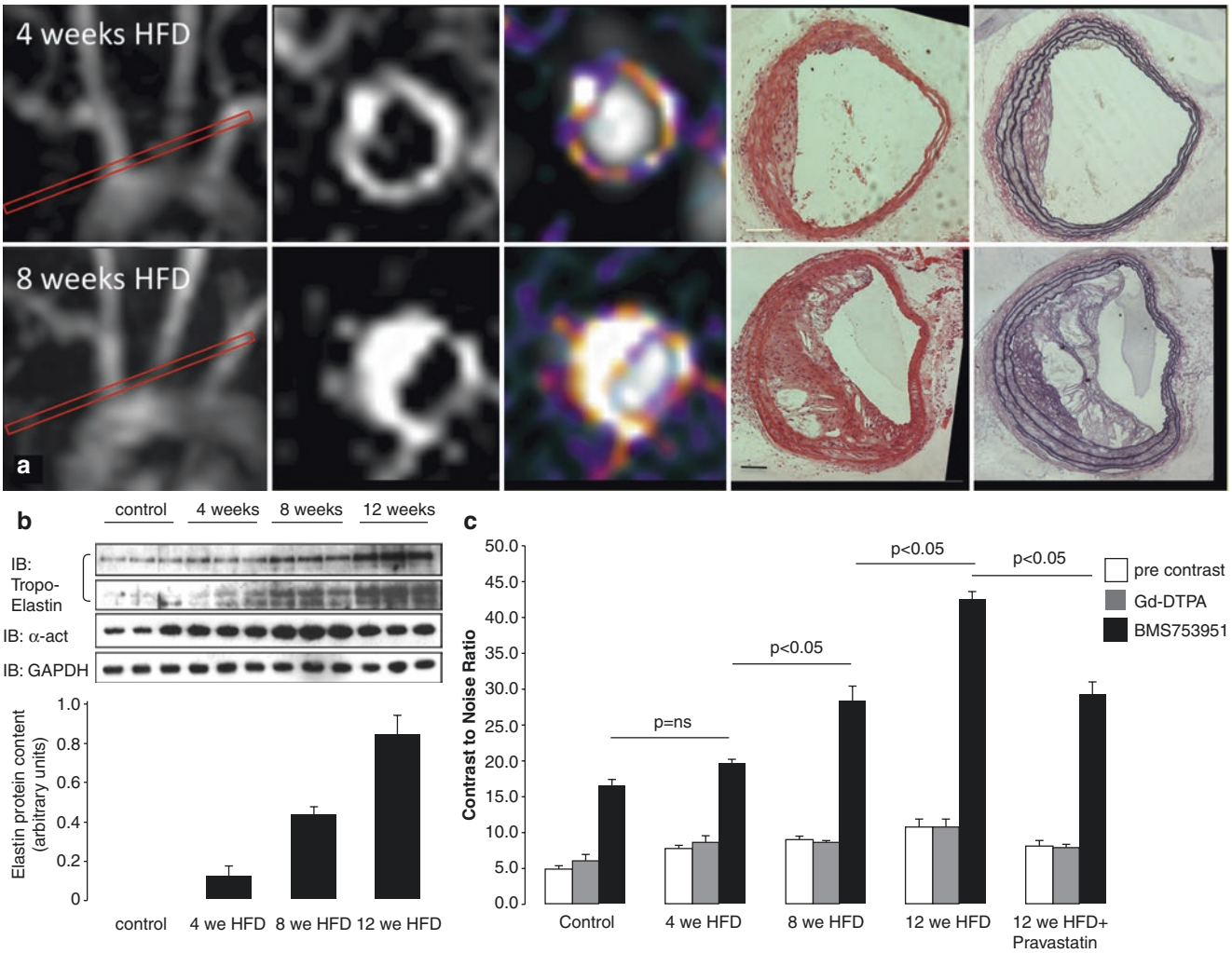

Fig. 14.12 MRI of extracellular matrix remodeling in an apoE$^{-/-}$ mouse model of accelerated atherosclerosis at 4 and 8 weeks after commencement of HFD using an elastin-specific MR contrast agent (**a**), ESMA (Lantheus Medical Systems, North Billerica, MA, USA). (**b**) Tropoelastin content as measured by Western blotting increased with the duration of the HFD, which was paralleled by an increased contrast-to-noise values after ESMA injection (**c**) (Adapted from Makowski [88])

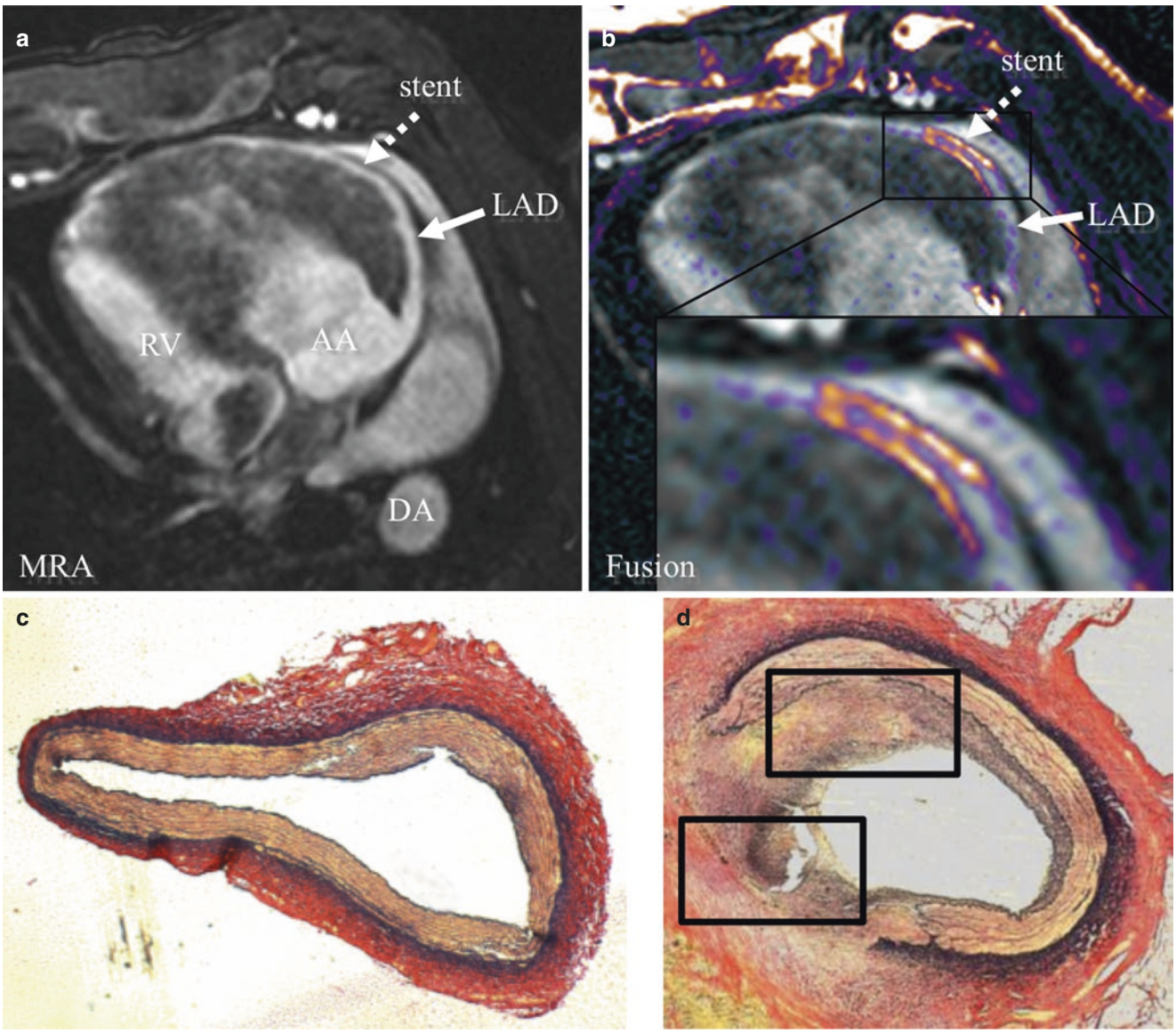

Fig. 14.13 Elastin imaging of coronary remodeling. Comparison of coronary MRA (**a**), delayed-enhancement MRI (**b**), and positron-emission CT-like fusion of a and b (**c**) of stented and control coronary vessel segments and corresponding histology (**d**) and (**e**). Strong enhancement can be observed at the stent location (dotted white arrow), whereas little to no enhancement is visible in the normal noninjured left anterior descending artery segment (**b**) and (**c**). Elastica van Gieson stain of noninjured coronary vessel segment (**d**) shows intact internal elastic lamina (IEL) and circular arranged elastin fibers (black) in the media. Elastica van Gieson of stented vessel segment (**e**) demonstrates disruption of IEL and neointima formation with diffuse elastin deposition (black dots). (Adapted and reprinted from, von Bary et al. [32], © 2011, with permission from Wolters Kluwer Health)

An alternative to directly imaging the ECM is to target proteolytic enzymes that are implicated in the degradation of ECM components such as collagen and elastin [140, 145]. These enzymes are mainly secreted by macrophages and are known as matrix metalloproteinases or MMPs. MMPs have been linked to plaque instability [145]. Noninvasive imaging of MMPs has been successfully performed using a gadolinium chelate targeted to a MMP inhibitor (P947) in murine and rabbit experimental models [146, 147]. Moreover, the enzyme myeloperoxidase (MPO) has been used as an emerging biomarker of plaque instability and future acute events [148]. It has also been demonstrated the feasibility of a specific gadolinium-based probe that targets MPO-Gd to image atherosclerosis in hyperlipidemic rabbits [149]. In addition, MPO-Gd enhancement colocalizes with plaque areas rich in infiltrated macrophages [149].

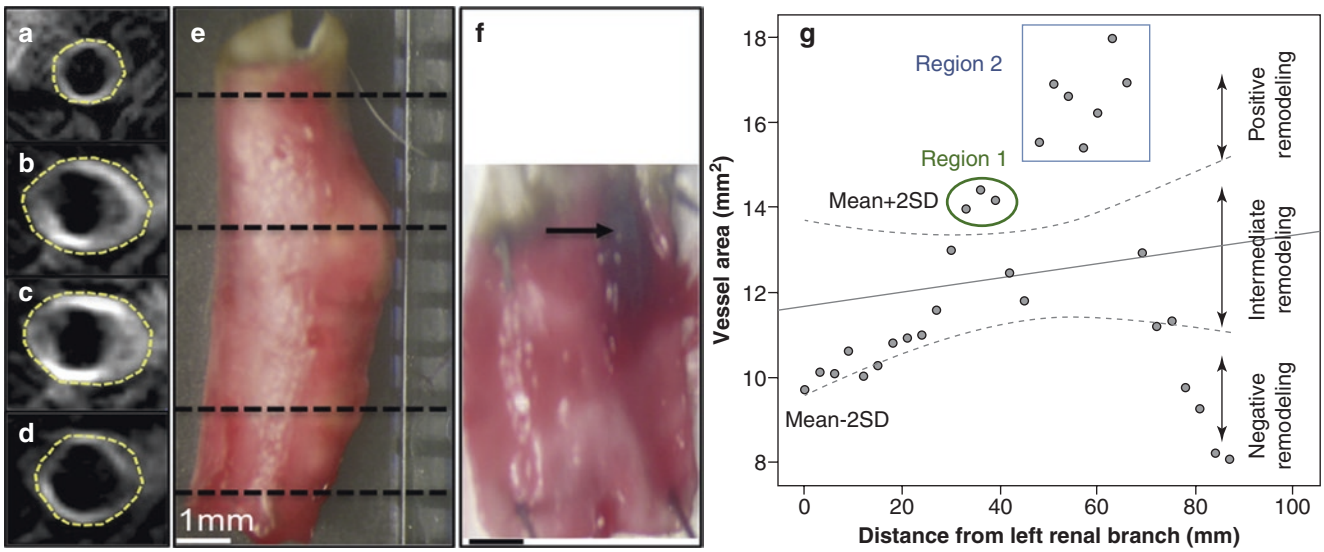

Fig. 14.14 Positive vascular remodeling in disrupted plaques. (**a**–**d**) DE MR images obtained after administration of elastin-specific contrast agent show positive remodeling, as defined by enlargement of vessel area (yellow contours). (**e**) Corresponding *en face* photograph verifies presence of positive vascular remodeling. (**f**) *En face* photograph of longitudinally open vessel shows thrombus (arrow) attached to vessel wall at proximal end of positive remodeling. (**g**) Scatterplot shows change in vessel area measured on consecutive slices along aorta, starting from left renal branch (0 mm) to iliac bifurcation (86 mm). Two regions of the vessel wall underwent positive remodeling, with vessel areas falling above the mean + 2 SD margin. Both plaques disrupted after triggering. Four of seven sections covering the vulnerable region 2 are illustrated in (**a**–**d**). (Adapted and reprinted from Phinikaridou et al. [142], © 2014, with permission from RSNA)

Fibrin and Thrombus Formation

Fibrin plays a central role in thrombus formation, but it has been also identified in atherosclerotic lesions of the aorta and coronary arteries [150]. Fibrin I and II are present in several types of atherosclerotic plaque, with fibrin II predominating in later stages and usually colocalizes with macrophages [150]. Although fibrin may enter the intima after mural thrombi originating from plaque rupture or erosion, fragile newly formed vessels may also provide a site of entry [151]. Different fibrin-specific contrast agents have been evaluated in different vascular beds. Gadolinium-based nanoparticles and small peptides (EP-2104R) targeted to fibrin have been successfully used to image atherosclerosis in both animal models and humans [30, 31, 33, 34, 89]. The ability of EP-2104R to detect coronary thrombosis has been first demonstrated in a swine model of intrastent thrombus and has been subsequently successfully translated in a small clinical feasibility study of aortic and carotid thrombosis [19] (Fig. 14.15).

Conclusion

Molecular MR imaging is a promising approach to evaluate biological processes involved in coronary artery disease. This methodology has been successfully validated to image cellular and structural changes in the vessel wall during atherosclerosis progression in animal models and humans. Coronary vessel wall NCE-MR and CE-MR in patients after myocardial infarction have shown potential for the noninvasive characterization of coronary artery plaque (e.g., endothelial dysfunction, hemorrhage, and fibrosis) without the use of ionizing radiation. For additional characterization of atherosclerotic lesions, target-specific imaging probes have been developed, which allowed successful imaging of extracellular matrix remodeling and coronary thrombosis. In the future, visualization of both early and late biological changes of coronary lesions may allow a more accurate assessment of disease burden and monitoring of the effectiveness of interventions.

Acknowledgments The authors acknowledge financial support from (1) the British Heart Foundation (RG/12/1/29262), (2) the Centre of Excellence in Medical Engineering funded by the Wellcome Trust and EPSRC (WT 088641/Z/09/Z), (3) the British Heart Foundation Centre of Excellence, and (4) the Department of Health via the National Institute for Health Research (NIHR) comprehensive Biomedical Research Centre award to Guy's and St Thomas' NHS Foundation Trust in partnership with King's College London and King's College Hospital NHS Foundation Trust. The views expressed are those of the authors and not necessarily those of the NHS, the NIHR, or the Department of Health.

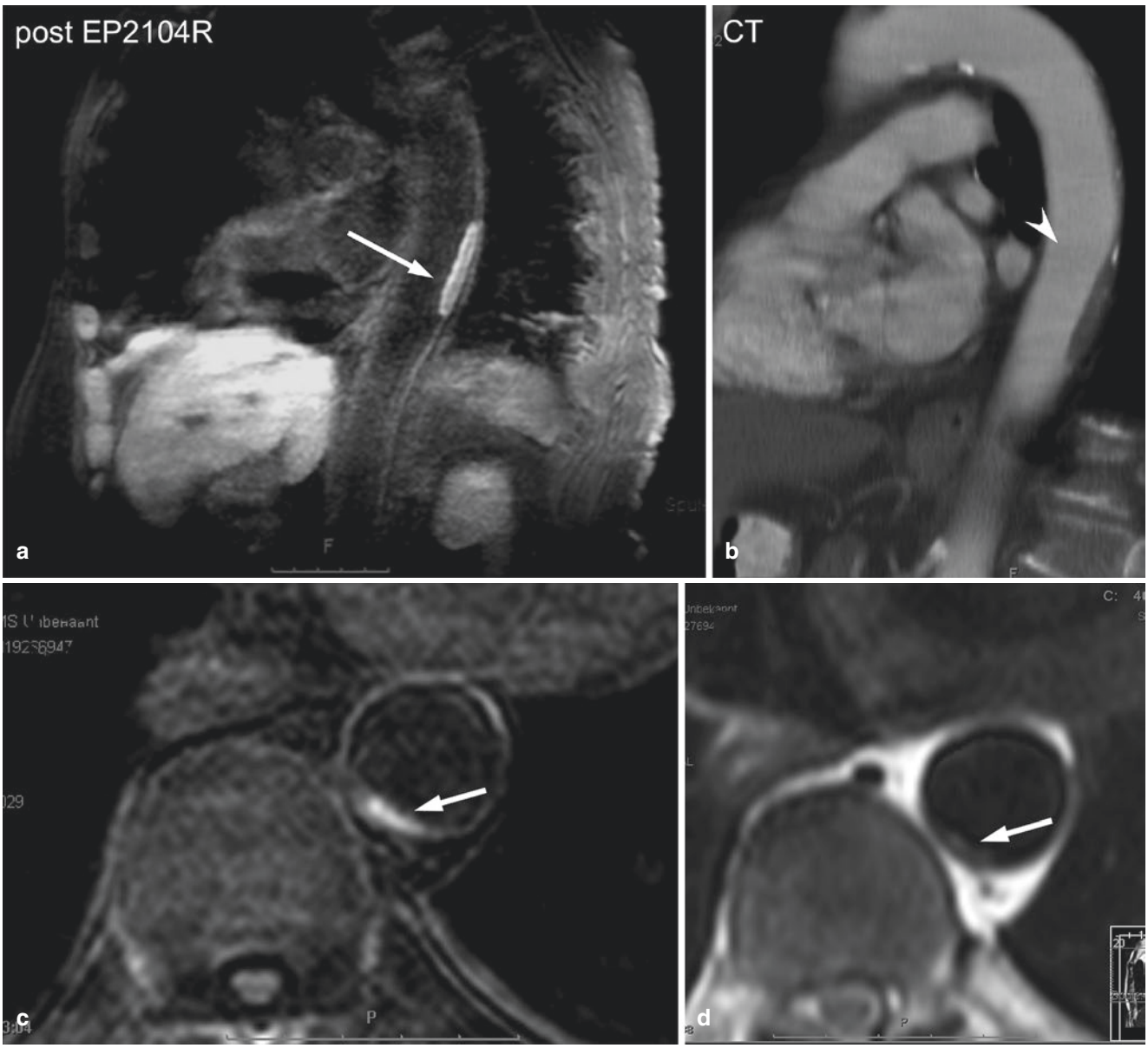

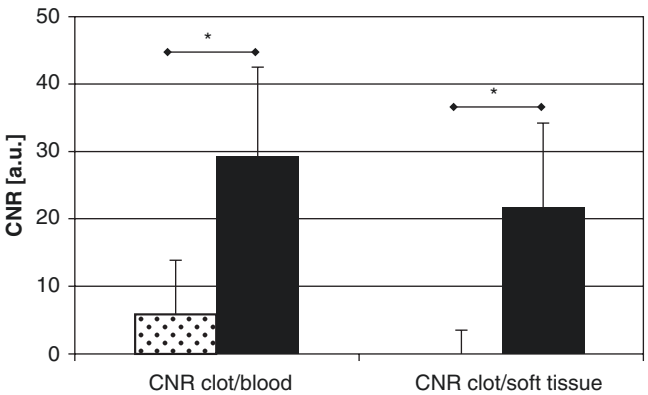

Fig. 14.15 Phase II clinical trial validating clinical feasibility of fibrin-specific MR contrast agent. Human thrombus imaging using EP-2104R, a fibrin-binding contrast agent, in a patient with aortic thrombus. A mural aortic thrombus is well delineated on in-plane post-EP-2104R black-blood MR images (**a**) while differentiation between thrombus and vessel wall is poor on multi slice CT images (**b**). Excellent aortic thrombus visualization on cross-sectional delayed enhancement images post-EP-2104R (**c**) while differentiation between thrombus and vessel wall is poor on pre-contrast black-blood turbo spin echo (**d**) MR images. (Adapted and reprinted from Springer, © 2008, Spuentrup et al. [34], Figs. 3, 5, 7, with kind permission from Springer Nature)

References

1. Rodgers A, Ezzati M, Vander Hoorn S, Lopez AD, Lin R-B, Murray CJL, Group Comparative Risk Assessment C. Distribution of major health risks: findings from the global burden of disease study. PLoS Med 2004;1:e27.
2. Ridker PM, Paynter NP, Rifai N, Gaziano JM, Cook NR. C-reactive protein and parental history improve global cardiovascular risk prediction: the Reynolds risk score for men. Circulation. 2008;118:2243–51.
3. Go AS, Mozaffarian D, Roger VL, Benjamin EJ, Berry JD, Borden WB, et al. Executive summary: heart disease and stroke statistics – 2013 update: a report from the american heart association. Circulation. 2013;127:143–52.
4. Ambrose JA, Tannenbaum MA, Alexopoulos D, Hjemdahl-Monsen CE, Leavy J, Weiss M, et al. Angiographic progression of coronary artery disease and the development of myocardial infarction. J Am Coll Cardiol. 1988;12:56–62.
5. Varnava AM, Mills PG, Davies MJ. Relationship between coronary artery remodeling and plaque vulnerability. Circulation. 2002;105:939–43.
6. Glagov S, Weisenberg E, Zarins CK, Stankunavicius R, Kolettis GJ. Compensatory enlargement of human atherosclerotic coronary arteries. N Engl J Med. 1987;316:1371–5.
7. Ali ZA, Roleder T, Narula J, Mohanty BD, Baber U, Kovacic JC, et al. Increased thin-cap neoatheroma and periprocedural myocardial infarction in drug-eluting stent restenosis: multimodality intravascular imaging of drug-eluting and bare-metal stents. Circ Cardiovasc Interv. 2013;6:507–17.
8. Madder RD, Wohns DH, Muller JE. Detection by intracoronary near-infrared spectroscopy of lipid core plaque at culprit sites in survivors of cardiac arrest. J Invasive Cardiol. 2014;26:78–9.
9. de Boer SP, Brugaletta S, Garcia-Garcia HM, Simsek C, Heo JH, Lenzen MJ, et al. Determinants of high cardiovascular risk in relation to plaque-composition of a non-culprit coronary segment visualized by near-infrared spectroscopy in patients undergoing percutaneous coronary intervention. Eur Heart J. 2014;35:282–9.
10. Wykrzykowska J, Lehman S, Williams G, Parker JA, Palmer MR, Varkey S, et al. Imaging of inflamed and vulnerable plaque in coronary arteries with 18f-fdg pet/ct in patients with suppression of myocardial uptake using a low-carbohydrate, high-fat preparation. J Nucl Med. 2009;50:563–8.
11. Joshi NV, Vesey AT, Williams MC, Shah AS, Calvert PA, Craighead FH, et al. 18f-fluoride positron emission tomography for identification of ruptured and high-risk coronary atherosclerotic plaques: a prospective clinical trial. Lancet. 2014;383:705–13.
12. Libby P, Ridker PM, Hansson GK. Progress and challenges in translating the biology of atherosclerosis. Nature. 2011;473:317–25.
13. Miao C, Chen S, Macedo R, Lai S, Liu K, Li D, Wasserman BA, et al. Positive remodeling of the coronary arteries detected by magnetic resonance imaging in an asymptomatic population: mesa (multi-ethnic study of atherosclerosis). J Am Coll Cardiol. 2009;53:1708–15.
14. Gerretsen SC, Kooi ME, Kessels AG, Schalla S, Katoh M, van der Geest RJ, et al. Visualization of coronary wall atherosclerosis in asymptomatic subjects and patients with coronary artery disease using magnetic resonance imaging. PLoS One. 2010;5:e12998.
15. Botnar RM, Bucker A, Kim WY, Viohl I, Gunther RW, Spuentrup E. Initial experiences with in vivo intravascular coronary vessel wall imaging. J Magn Reson Imaging. 2003;17:615–9.
16. Schar M, Kim WY, Stuber M, Boesiger P, Manning WJ, Botnar RM. The impact of spatial resolution and respiratory motion on MR imaging of atherosclerotic plaque. J Magn Reson Imaging. 2003;17:538–44.
17. Kim WY, Astrup AS, Stuber M, Tarnow L, Falk E, Botnar RM, et al. Subclinical coronary and aortic atherosclerosis detected by magnetic resonance imaging in type 1 diabetes with and without diabetic nephropathy. Circulation. 2007;115:228–35.
18. Maintz D, Ozgun M, Hoffmeier A, Fischbach R, Kim WY, Stuber M, et al. Selective coronary artery plaque visualization and differentiation by contrast-enhanced inversion prepared MRI. Eur Heart J. 2006;27:1732–6.
19. Noguchi T, Kawasaki T, Tanaka A, Yasuda S, Goto Y, Ishihara M, et al. High-intensity signals in coronary plaques on noncontrast t1-weighted magnetic resonance imaging as a novel determinant of coronary events. J Am Coll Cardiol. 2014;63(10):989–99.
20. Noguchi T, Yamada N, Higashi M, Goto Y, Naito H. High-intensity signals in carotid plaques on t1-weighted magnetic resonance imaging predict coronary events in patients with coronary artery disease. J Am Coll Cardiol. 2011;58:416–22.
21. Tanaka A, Kawasaki T, Noguchi T, Koga S, Hiramatsu Y, Fukuyama T, Koga N. Hyperintense plaque with noncontrast t1-weighted magnetic resonance coronary plaque imaging leading to acute coronary syndrome. Circulation. 2009;120:2400–1.
22. Jansen CH, Perera D, Makowski MR, Wiethoff AJ, Phinikaridou A, Razavi RM, et al. Detection of intracoronary thrombus by magnetic resonance imaging in patients with acute myocardial infarction. Circulation. 2011;124:416–24.
23. Ehara S, Hasegawa T, Nakata S, Matsumoto K, Nishimura S, Iguchi T, et al. Hyperintense plaque identified by magnetic resonance imaging relates to intracoronary thrombus as detected by optical coherence tomography in patients with angina pectoris. Eur Heart J Cardiovasc Imaging. 2012;13:394–9.
24. Hays AG, Hirsch GA, Kelle S, Gerstenblith G, Weiss RG, Stuber M. Noninvasive visualization of coronary artery endothelial function in healthy subjects and in patients with coronary artery disease. J Am Coll Cardiol. 2010;56:1657–65.
25. Hays AG, Kelle S, Hirsch GA, Soleimanifard S, Yu J, Agarwal HK, et al. Regional coronary endothelial function is closely related to local early coronary atherosclerosis in patients with mild coronary artery disease: pilot study. Circ Cardiovasc Imaging. 2012;5:341–8.
26. Hays AG, Stuber M, Hirsch GA, Yu J, Schar M, Weiss RG, Gerstenblith G, Kelle S. Non-invasive detection of coronary endothelial response to sequential handgrip exercise in coronary artery disease patients and healthy adults. PLoS One. 2013;8:e58047.
27. Kawasaki T, Koga S, Koga N, Noguchi T, Tanaka H, Koga H, et al. Characterization of hyperintense plaque with noncontrast t1-weighted cardiac magnetic resonance coronary plaque imagingcomparison with multislice computed tomography and intravascular ultrasound. JACC Cardiovasc Imaging. 2009;2:720–8.
28. Yeon SB, Sabir A, Clouse M, Martinezclark PO, Peters DC, Hauser TH, et al. Delayed-enhancement cardiovascular magnetic resonance coronary artery wall imaging: comparison with multislice computed tomography and quantitative coronary angiography. J Am Coll Cardiol. 2007;50:441–7.
29. Ibrahim T, Makowski MR, Jankauskas A, Maintz D, Karch M, Schachoff S, et al. Serial contrast-enhanced cardiac magnetic resonance imaging demonstrates regression of hyperenhancement within the coronary artery wall in patients after acute myocardial infarction. JACC Cardiovasc Imaging. 2009;2:580–8.
30. Botnar RM, Buecker A, Wiethoff AJ, Parsons EC Jr, Katoh M, Katsimaglis G, Weisskoff RM, et al. In vivo magnetic resonance imaging of coronary thrombosis using a fibrin-binding molecular magnetic resonance contrast agent. Circulation. 2004;110:1463–6.
31. Botnar RM, Perez AS, Witte S, Wiethoff AJ, Laredo J, Hamilton J, et al. In vivo molecular imaging of acute and subacute thrombosis using a fibrin-binding magnetic resonance imaging contrast agent. Circulation. 2004;109:2023–9.

32. von Bary C, Makowski M, Preissel A, Keithahn A, Warley A, Spuentrup E, et al. MRI of coronary wall remodeling in a swine model of coronary injury using an elastin-binding contrast agent. Circ Cardiovasc Imaging. 2011;4(2):147–55.
33. Vymazal J, Spuentrup E, Cardenas-Molina G, Wiethoff AJ, Hartmann MG, Caravan P, Parsons EC Jr. Thrombus imaging with fibrin-specific gadolinium-based MR contrast agent ep-2104r: results of a phase ii clinical study of feasibility. Investig Radiol. 2009;44:697–704.
34. Spuentrup E, Botnar RM, Wiethoff A, Ibrahim T, Sebastin K, Katho M, et al. MR imaging of thrombi using ep-2104r, a fibrin specific contrast agent: initial results in patients. Eur Radiol. 2008;18(9):1995–2005. (1911)
35. Sato Y, Hatakeyama K, Marutsuka K, Asada Y. Incidence of asymptomatic coronary thrombosis and plaque disruption: comparison of non-cardiac and cardiac deaths among autopsy cases. Thromb Res. 2009;124:19–23.
36. Lavin B, Phinikaridou A, Henningsson M, Botnar RM. Current development of molecular coronary plaque imaging using magnetic resonance imaging towards clinical application. Curr Cardiovasc Imaging Rep. 2014;7(12):9309.
37. Choudhury RP, Fuster V, Fayad ZA. Molecular, cellular and functional imaging of atherothrombosis. Nat Rev Drug Discov. 2004;3:913–25.
38. Wilcox JN, Scott NA. Potential role of the adventitia in arteritis and atherosclerosis. Int J Cardiol. 1996;54(Suppl):S21–35.
39. Shi Y, O'Brien JE, Fard A, Mannion JD, Wang D, Zalewski A. Adventitial myofibroblasts contribute to neointimal formation in injured porcine coronary arteries. Circulation. 1996;94:1655–64.
40. Zhao L, Funk CD. Lipoxygenase pathways in atherogenesis. Trends Cardiovasc Med. 2004;14:191–5.
41. Chiu JJ, Chien S. Effects of disturbed flow on vascular endothelium: pathophysiological basis and clinical perspectives. Physiol Rev. 2011;91:327–87.
42. Cines DB, Pollak ES, Buck CA, Loscalzo J, Zimmerman GA, McEver RP, et al. Endothelial cells in physiology and in the pathophysiology of vascular disorders. Blood. 1998;91:3527–61.
43. Brodsky SV, Goligorsky MS. Endothelium under stress: local and systemic messages. Semin Nephrol. 2012;32:192–8.
44. Galkina E, Ley K. Vascular adhesion molecules in atherosclerosis. Arterioscler Thromb Vasc Biol. 2007;27:2292–301.
45. Weber C, Noels H. Atherosclerosis: current pathogenesis and therapeutic options. Nat Med. 2011;17:1410–22.
46. Silvestre-Roig C, de Winther MP, Weber C, Daemen MJ, Lutgens E, Soehnlein O. Atherosclerotic plaque destabilization: mechanisms, models, and therapeutic strategies. Circ Res. 2014;114:214–26.
47. Falk E. Pathogenesis of atherosclerosis. J Am Coll Cardiol. 2006;47(8):C7–12.
48. Narula J, Strauss HW. The popcorn plaques. Nat Med. 2007;13(5):532–4.
49. Stone GW, Maehara A, Lansky AJ, de Bruyne B, Cristea E, Mintz GS, et al. Prospect Investigators. A prospective natural-history study of coronary atherosclerosis. N Engl J Med. 2011;364:226–35.
50. Narula J, Garg P, Achenbach S, Motoyama S, Virmani R, Strauss HW. Arithmetic of vulnerable plaques for noninvasive imaging. Nat Clin Pract Cardiovasc Med. 2008;5(Suppl 2):S2–10.
51. Dabir D, Child N, Kalra A, Rogers T, Gebker R, Jabbour A, et al. Reference values for healthy human myocardium using a t1 mapping methodology: results from the international t1 multicenter cardiovascular magnetic resonance study. J Cardiovasc Magn Reson. 2014;16:69.
52. Kawel N, Nacif M, Zavodni A, Jones J, Liu S, Sibley CT, Bluemke DA. T1 mapping of the myocardium: intra-individual assessment of the effect of field strength, cardiac cycle and variation by myocardial region. J Cardiovasc Magn Reson. 2012;14:27.
53. Robson MD, Piechnik SK, Tunnicliffe EM, Neubauer S. T measurements in the human myocardium: the effects of magnetization transfer on the sasha and molli sequences. Magn Reson Med. 2013;70(3):664–70.
54. Salerno M, Janardhanan R, Jiji RS, Brooks J, Adenaw N, Mehta B, et al. Comparison of methods for determining the partition coefficient of gadolinium in the myocardium using t1 mapping. J Magn Reson Imaging. 2013;38:217–24.
55. Ichikawa Y, Sakuma H, Suzawa N, Kitagawa K, Makino K, Hirano T, Takeda K. Late gadolinium-enhanced magnetic resonance imaging in acute and chronic myocardial infarction. Improved prediction of regional myocardial contraction in the chronic state by measuring thickness of nonenhanced myocardium. J Am Coll Cardiol. 2005;45:901–9.
56. Nitz WR, Reimer P. Contrast mechanisms in MR imaging. Eur Radiol. 1999;9:1032–46.
57. Keegan J, Gatehouse PD, Yang GZ, Firmin DN. Non-model-based correction of respiratory motion using beat-to-beat 3d spiral fat-selective imaging. J Magn Reson Imaging. 2007;26:624–9.
58. Dixon WT. Simple proton spectroscopic imaging. Radiology. 1984;153:189–94.
59. Glover GH, Schneider E. Three-point Dixon technique for true water/fat decomposition with b0 inhomogeneity correction. Magn Reson Med. 1991;18:371–83.
60. Fayad ZA, Fuster V, Fallon JT, Jayasundera T, Worthley SG, Helft G, et al. Noninvasive in vivo human coronary artery lumen and wall imaging using black-blood magnetic resonance imaging. Circulation. 2000;102:506–10.
61. Botnar RM, Stuber M, Kissinger KV, Kim WY, Spuentrup E, Manning WJ. Noninvasive coronary vessel wall and plaque imaging with magnetic resonance imaging. Circulation. 2000;102:2582–7.
62. Botnar RM, Kim WY, Bornert P, Stuber M, Spuentrup E, Manning WJ. 3d coronary vessel wall imaging utilizing a local inversion technique with spiral image acquisition. Magn Reson Med. 2001;46:848–54.
63. Wang J, Yarnykh VL, Hatsukami T, Chu B, Balu N, Yuan C. Improved suppression of plaque-mimicking artifacts in black-blood carotid atherosclerosis imaging using a multislice motion-sensitized driven-equilibrium (msde) turbo spin-echo (tse) sequence. Magn Reson Med. 2007;58:973–81.
64. Li L, Miller KL, Jezzard P. Dante-prepared pulse trains: a novel approach to motion-sensitized and motion-suppressed quantitative magnetic resonance imaging. Magn Reson Med. 2012;68:1423–38.
65. Fan Z, Zhang Z, Chung YC, Weale P, Zuehlsdorff S, Carr J, Li D. Carotid arterial wall MRI at 3t using 3d variable-flip-angle turbo spin-echo (tse) with flow-sensitive dephasing (fsd). J Magn Reson Imaging. 2010;31:645–54.
66. Oei ML, Ozgun M, Seifarth H, Bunck A, Fischbach R, Orwat S, et al. T1-weighted MRI for the detection of coronary artery plaque haemorrhage. Eur Radiol. 2010;20:2817–23.
67. Andia ME, Henningsson M, Hussain T, Phinikaridou A, Protti A, Greil G, Botnar RM. Flow-independent 3d whole-heart vessel wall imaging using an interleaved t2-preparation acquisition. Magn Reson Med. 2013;69(1):150–7.
68. Xie J, Bi X, Fan Z, Bhat H, Shah S, Zuehlsdorff S, Li D. 3d flow-independent peripheral vessel wall imaging using t(2)-prepared phase-sensitive inversion-recovery steady-state free precession. J Magn Reson Imaging. 2010;32:399–408.
69. Messroghli DR, Radjenovic A, Kozerke S, Higgins DM, Sivananthan MU, Ridgway JP. Modified look-locker inversion recovery (molli) for high-resolution t1 mapping of the heart. Magn Reson Med. 2004;52:141–6.

70. Chow K, Flewitt JA, Green JD, Pagano JJ, Friedrich MG, Thompson RB. Saturation recovery single-shot acquisition (sasha) for myocardial t(1) mapping. Magn Reson Med. 2014;71:2082–95.
71. Roujol S, Weingartner S, Foppa M, Chow K, Kawaji K, Ngo LH, et al. Accuracy, precision, and reproducibility of four t1 mapping sequences: a head-to-head comparison of molli, shmolli, sasha, and sapphire. Radiology. 2014;272:683–9.
72. van Heeswijk RB, Piccini D, Feliciano H, Hullin R, Schwitter J, Stuber M. Self-navigated isotropic three-dimensional cardiac t mapping. Magn Reson Med. 2015;73(4):1549–54.
73. van Heeswijk RB, Feliciano H, Bongard C, Bonanno G, Coppo S, Lauriers N, et al. Free-breathing 3 t magnetic resonance t2-mapping of the heart. JACC Cardiovasc Imaging. 2012;5:1231–9.
74. Ding H, Fernandez-de-Manuel L, Schar M, Schuleri KH, Halperin H, He L, et al. Three-dimensional whole-heart t mapping at 3t. Magn Reson Med. 2015;74(3):803–16.
75. Henningsson M, Koken P, Stehning C, Razavi R, Prieto C, Botnar RM. Whole-heart coronary MR angiography with 2d self-navigated image reconstruction. Magn Reson Med. 2012;67:437–45.
76. Stehning C, Bornert P, Nehrke K, Eggers H, Stuber M. Free-breathing whole-heart coronary MRA with 3d radial ssfp and self-navigated image reconstruction. Magn Reson Med. 2005;54:476–80.
77. Prieto C, Doneva M, Usman M, Henningsson M, Greil G, Schaeffter T, Botnar RM. Highly efficient respiratory motion compensated free-breathing coronary MRA using golden-step cartesian acquisition. J Magn Reson Imaging. 2015;41:738–46.
78. Pang J, Bhat H, Sharif B, Fan Z, Thomson LE, LaBounty T, et al. Whole-heart coronary MRA with 100% respiratory gating efficiency: self-navigated three-dimensional retrospective image-based motion correction (trim). Magn Reson Med. 2014;71:67–74.
79. Henningsson M, Prieto C, Chiribiri A, Vaillant G, Razavi R, Botnar RM. Whole-heart coronary MRA with 3d affine motion correction using 3d image-based navigation. Magn Reson Med. 2014;71:173–81.
80. Aitken AP, Henningsson M, Botnar RM, Schaeffter T, Prieto C. 100% efficient three-dimensional coronary MR angiography with two-dimensional beat-to-beat translational and bin-to-bin affine motion correction. Magn Reson Med. 2015;74:756–64.
81. Pang J, Sharif B, Fan Z, Bi X, Arsanjani R, Berman DS, Li D. Ecg and navigator-free four-dimensional whole-heart coronary MRA for simultaneous visualization of cardiac anatomy and function. Magn Reson Med. 2014;72:1208–17.
82. Coppo S, Piccini D, Bonanno G, Chaptinel J, Vincenti G, Feliciano H, et al. Free-running 4d whole-heart self-navigated golden angle MRI: initial results. Magn Reson Med. 2015;74(5):1306–16.
83. Caravan P. Strategies for increasing the sensitivity of gadolinium based MRI contrast agents. Chem Soc Rev. 2006;35:512.
84. Calcagno C, Ramachandran S, Izquierdo-Garcia D, Mani V, Millon A, Rosenbaum D, Tawakol A, et al. The complementary roles of dynamic contrast-enhanced MRI and 18f-fluorodeoxyglucose pet/ct for imaging of carotid atherosclerosis. Eur J Nucl Med Mol Imaging. 2013;40:1884–93.
85. Caravan P, Ellison JJ, McMurry TJ, Lauffer RB. Gadolinium(iii) chelates as MRI contrast agents: structure, dynamics, and applications. Chem Rev. 1999;99:2293–352.
86. Caravan P, Cloutier NJ, Greenfield MT, McDermid SA, Dunham SU, Bulte JW, et al. The interaction of ms-325 with human serum albumin and its effect on proton relaxation rates. J Am Chem Soc. 2002;124:3152–62.
87. Nivorozhkin AL, Kolodziej AF, Caravan P, Greenfield MT, Lauffer RB, McMurry TJ. Enzyme-activated gd(3+) magnetic resonance imaging contrast agents with a prominent receptor-induced magnetization enhancement. Angew Chem Int Ed Engl. 2001;40:2903–6.
88. Makowski MR, Wiethoff AJ, Blume U, Cuello F, Warley A, Jansen CH, et al. Assessment of atherosclerotic plaque burden with an elastin-specific magnetic resonance contrast agent. Nat Med. 2011;17:383–8.
89. Andia ME, Saha P, Jenkins J, Modarai B, Wiethoff AJ, Phinikaridou A, Grover SP, et al. Fibrin-targeted magnetic resonance imaging allows in vivo quantification of thrombus fibrin content and identifies thrombi amenable for thrombolysis. Arterioscler Thromb Vasc Biol. 2014;34:1193–8.
90. Flacke S, Fischer S, Scott MJ, Fuhrhop RJ, Allen JS, McLean M, et al. Novel MRI contrast agent for molecular imaging of fibrin: implications for detecting vulnerable plaques. Circulation. 2001;104:1280–5.
91. Winter PM, Morawski AM, Caruthers SD, Fuhrhop RW, Zhang H, Williams TA, et al. Molecular imaging of angiogenesis in early-stage atherosclerosis with alpha(v)beta3-integrin-targeted nanoparticles. Circulation. 2003;108:2270–4.
92. Weinmann HJ, Brasch RC, Press WR, Wesbey GE. Characteristics of gadolinium-dtpa complex: a potential nmr contrast agent. AJR Am J Roentgenol. 1984;142:619–24.
93. Laniado M, Weinmann HJ, Schorner W, Felix R, Speck U. First use of gddtpa/dimeglumine in man. Physiol Chem Phys Med NMR. 1984;16:157–65.
94. Weissleder R, Elizondo G, Wittenberg J, Rabito CA, Bengele HH, Josephson L. Ultrasmall superparamagnetic iron oxide: characterization of a new class of contrast agents for MR imaging. Radiology. 1990;175:489–93.
95. Farrar CT, Dai G, Novikov M, Rosenzweig A, Weissleder R, Rosen BR, Sosnovik DE. Impact of field strength and iron oxide nanoparticle concentration on the linearity and diagnostic accuracy of off-resonance imaging. NMR Biomed. 2008;21:453–63.
96. Wang YX, Xuan S, Port M, Idee JM. Recent advances in superparamagnetic iron oxide nanoparticles for cellular imaging and targeted therapy research. Curr Pharm Des. 2013;19:6575–93.
97. Tang TY, Muller KH, Graves MJ, Li ZY, Walsh SR, Young V, et al. Iron oxide particles for atheroma imaging. Arterioscler Thromb Vasc Biol. 2009;29:1001–8.
98. Segers FM, den Adel B, Bot I, van der Graaf LM, van der Veer EP, Gonzalez W, et al. Scavenger receptor-ai-targeted iron oxide nanoparticles for in vivo MRI detection of atherosclerotic lesions. Arterioscler Thromb Vasc Biol. 2013;33:1812–9.
99. Yilmaz A, Rosch S, Klingel K, Kandolf R, Helluy X, Hiller KH, et al. Magnetic resonance imaging (MRI) of inflamed myocardium using iron oxide nanoparticles in patients with acute myocardial infarction – preliminary results. Int J Cardiol. 2013;163:175–82.
100. Islam T, Harisinghani MG. Overview of nanoparticle use in cancer imaging. Cancer Biomark. 2009;5:61–7.
101. Briley-Saebo KC, Shaw PX, Mulder WJ, Choi SH, Vucic E, Aguinaldo JG, et al. Targeted molecular probes for imaging atherosclerotic lesions with magnetic resonance using antibodies that recognize oxidation-specific epitopes. Circulation. 2008;117:3206–15.
102. Amirbekian V, Lipinski MJ, Briley-Saebo KC, Amirbekian S, Aguinaldo JG, Weinreb DB, et al. Detecting and assessing macrophages in vivo to evaluate atherosclerosis noninvasively using molecular MRI. Proc Natl Acad Sci U S A. 2007;104:961–6.
103. Ruehm SG, Corot C, Vogt P, Kolb S, Debatin JF. Magnetic resonance imaging of atherosclerotic plaque with ultrasmall superparamagnetic particles of iron oxide in hyperlipidemic rabbits. Circulation. 2001;103:415–22.
104. Kooi ME, Cappendijk VC, Cleutjens KBJM, Kessels AGH, Kitslaar PJEHM, Borgers M, et al. Accumulation of ultrasmall superparamagnetic particles of iron oxide in human atherosclerotic plaques can be detected by in vivo magnetic resonance imaging. Circulation. 2003;107:2453–8.

105. Tang TY, Howarth SP, Miller SR, Graves MJ, U-King-Im JM, Li ZY, et al. Correlation of carotid atheromatous plaque inflammation using uspio-enhanced MR imaging with degree of luminal stenosis. Stroke. 2008;39:2144–7.
106. Tang TY, Howarth SP, Miller SR, Graves MJ, U-King-Im JM, Li ZY, et al. Comparison of the inflammatory burden of truly asymptomatic carotid atheroma with atherosclerotic plaques in patients with asymptomatic carotid stenosis undergoing coronary artery bypass grafting: an ultrasmall superparamagnetic iron oxide enhanced magnetic resonance study. Eur J Vasc Endovasc Surg. 2008;35:392–8.
107. Phinikaridou A, Andia ME, Protti A, Indermuehle A, Shah A, Smith A, Warley A, Botnar RM. Noninvasive magnetic resonance imaging evaluation of endothelial permeability in murine atherosclerosis using an albumin-binding contrast agent. Circulation. 2012;126(6):707–19.
108. Phinikaridou A, Andia ME, Passacquale G, Ferro A, Botnar RM. Noninvasive MRI monitoring of the effect of interventions on endothelial permeability in murine atherosclerosis using an albumin-binding contrast agent. J Am Heart Assoc. 2013;2:e000402.
109. Lobbes MB, Heeneman S, Passos VL, Welten R, Kwee RM, van der Geest RJ, et al. Gadofosveset-enhanced magnetic resonance imaging of human carotid atherosclerotic plaques: a proof-of-concept study. Investig Radiol. 2010;45(5):275–81.
110. Lobbes MB, Miserus RJ, Heeneman S, Passos VL, Mutsaers PH, Debernardi N, et al. Atherosclerosis: contrast-enhanced MR imaging of vessel wall in rabbit model – comparison of gadofosveset and gadopentetate dimeglumine. Radiology. 2009;250:682–91.
111. Pedersen SF, Thrysoe SA, Paaske WP, Thim T, Falk E, Ringgaard S, Kim WY. CMR assessment of endothelial damage and angiogenesis in porcine coronary arteries using gadofosveset. J Cardiovasc Magn Reson. 2011;13:10.
112. McAteer MA, Schneider JE, Ali ZA, Warrick N, Bursill CA, von zur Muhlen C, et al. Magnetic resonance imaging of endothelial adhesion molecules in mouse atherosclerosis using dual-targeted microparticles of iron oxide. Arterioscler Thromb Vasc Biol. 2008;28:77–83.
113. Nahrendorf M, Jaffer FA, Kelly KA, Sosnovik DE, Aikawa E, Libby P, Weissleder R. Noninvasive vascular cell adhesion molecule-1 imaging identifies inflammatory activation of cells in atherosclerosis. Circulation. 2006;114:1504–11.
114. Sluimer JC, Kolodgie FD, Bijnens AP, Maxfield K, Pacheco E, Kutys B, et al. Thin-walled microvessels in human coronary atherosclerotic plaques show incomplete endothelial junctions relevance of compromised structural integrity for intraplaque microvascular leakage. J Am Coll Cardiol. 2009;53:1517–27.
115. Kolodgie FD, Narula J, Yuan C, Burke AP, Finn AV, Virmani R. Elimination of neoangiogenesis for plaque stabilization: is there a role for local drug therapy? J Am Coll Cardiol. 2007;49:2093–101.
116. Russell DA, Abbott CR, Gough MJ. Vascular endothelial growth factor is associated with histological instability of carotid plaques. Br J Surg. 2008;95:576–81.
117. Virmani R, Kolodgie FD, Burke AP, Finn AV, Gold HK, Tulenko TN, Wrenn SP, Narula J. Atherosclerotic plaque progression and vulnerability to rupture: angiogenesis as a source of intraplaque hemorrhage. Arterioscler Thromb Vasc Biol. 2005;25:2054–61.
118. Manduteanu I, Simionescu M. Inflammation in atherosclerosis: a cause or a result of vascular disorders? J Cell Mol Med. 2012;16:1978–90.
119. Purushothaman KR, Sanz J, Zias E, Fuster V, Moreno PR. Atherosclerosis neovascularization and imaging. Curr Mol Med. 2006;6:549–56.
120. Kerwin WS, O'Brien KD, Ferguson MS, Polissar N, Hatsukami TS, Yuan C. Inflammation in carotid atherosclerotic plaque: a dynamic contrast-enhanced MR imaging study. Radiology. 2006;241:459–68.
121. Jaffer FA, Nahrendorf M, Sosnovik D, Kelly KA, Aikawa E, Weissleder R. Cellular imaging of inflammation in atherosclerosis using magnetofluorescent nanomaterials. Mol Imaging. 2006;5:85–92.
122. Tait JF. Imaging of apoptosis. J Nucl Med. 2008;49:1573–6.
123. van Tilborg GA, Vucic E, Strijkers GJ, Cormode DP, Mani V, Skajaa T, et al. Annexin a5-functionalized bimodal nanoparticles for MRI and fluorescence imaging of atherosclerotic plaques. Bioconjug Chem. 2010;21:1794–803.
124. Ye D, Shuhendler AJ, Cui L, Tong L, Tee SS, Tikhomirov G, et al. Bioorthogonal cyclization-mediated in situ self-assembly of small-molecule probes for imaging caspase activity in vivo. Nat Chem. 2014;6:519–26.
125. Pello OM, Silvestre C, De Pizzol M, Andres V. A glimpse on the phenomenon of macrophage polarization during atherosclerosis. Immunobiology. 2011;216:1172–6.
126. Durand E, Raynaud JS, Bruneval P, Brigger I, Al Haj Zen A, et al. Magnetic resonance imaging of ruptured plaques in the rabbit with ultrasmall superparamagnetic particles of iron oxide. J Vasc Res. 2007;44:119–28.
127. Morishige K, Kacher DF, Libby P, Josephson L, Ganz P, Weissleder R, Aikawa M. High-resolution magnetic resonance imaging enhanced with superparamagnetic nanoparticles measures macrophage burden in atherosclerosis. Circulation. 2010;122:1707–15.
128. Schmitz SA, Coupland SE, Gust R, Winterhalter S, Wagner S, Kresse M, et al. Superparamagnetic iron oxide-enhanced MRI of atherosclerotic plaques in watanabe hereditable hyperlipidemic rabbits. Investig Radiol. 2000;35:460–71.
129. Sigovan M, Boussel L, Sulaiman A, Sappey-Marinier D, Alsaid H, Desbleds-Mansard C, et al. Rapid-clearance iron nanoparticles for inflammation imaging of atherosclerotic plaque: initial experience in animal model. Radiology. 2009;252:401–9.
130. Smith BR, Heverhagen J, Knopp M, Schmalbrock P, Shapiro J, Shiomi M, et al. Localization to atherosclerotic plaque and biodistribution of biochemically derivatized superparamagnetic iron oxide nanoparticles (spions) contrast particles for magnetic resonance imaging (MRI). Biomed Microdevices. 2007;9:719–27.
131. Makowski MR, Varma G, Wiethoff AJ, Smith A, Mattock K, Jansen CH, et al. Noninvasive assessment of atherosclerotic plaque progression in apoe-/- mice using susceptibility gradient mapping. Circ Cardiovasc Imaging. 2011;4(3):295–303.
132. Tang TY, Patterson AJ, Miller SR, Graves MJ, Howarth SPS, U-King-Im JM, et al. Temporal dependence of in vivo uspio-enhanced MRI signal changes in human carotid atheromatous plaques. Neuroradiology. 2009;51:457–65.
133. Tang TY, Howarth SP, Miller SR, Graves MJ, U-King-Im JM, Trivedi RA, et al. Comparison of the inflammatory burden of truly asymptomatic carotid atheroma with atherosclerotic plaques contralateral to symptomatic carotid stenosis: an ultra small superparamagnetic iron oxide enhanced magnetic resonance study. J Neurol Neurosurg Psychiatry. 2007;78:1337–43.
134. Tang TY, Howarth SP, Li ZY, Miller SR, Graves MJ, U-King-Im JM, et al. Correlation of carotid atheromatous plaque inflammation with biomechanical stress: utility of uspio enhanced MR imaging and finite element analysis. Atherosclerosis. 2008;196:879–87.
135. Trivedi RA, Mallawarachi C, U-King-Im J-M, Graves MJ, Horsley J, Goddard MJ, et al. Identifying inflamed carotid plaques using in vivo uspio-enhanced MR imaging to label plaque macrophages. Arterioscler Thromb Vasc Biol. 2006;26:1601–6.
136. Flogel U, Ding Z, Hardung H, Jander S, Reichmann G, Jacoby C, Schubert R, Schrader J. In vivo monitoring of inflammation after cardiac and cerebral ischemia by fluorine magnetic resonance imaging. Circulation. 2008;118:140–8.

137. Burnett JR. Lipids, lipoproteins, atherosclerosis and cardiovascular disease. Clin Biochem Rev. 2004;25:2.
138. Sirol M, Itskovich VV, Mani V, Aguinaldo JG, Fallon JT, Misselwitz B, et al. Lipid-rich atherosclerotic plaques detected by gadofluorine-enhanced in vivo magnetic resonance imaging. Circulation. 2004;109:2890–6.
139. Chen W, Vucic E, Leupold E, Mulder WJ, Cormode DP, Briley-Saebo KC, et al. Incorporation of an apoe-derived lipopeptide in high-density lipoprotein MRI contrast agents for enhanced imaging of macrophages in atherosclerosis. Contrast Media Mol Imaging. 2008;3:233–42.
140. Katsuda S, Kaji T. Atherosclerosis and extracellular matrix. J Atheroscler Thromb. 2003;10:267–74.
141. Makowski MR, Preissel A, von Bary C, Warley A, Schachoff S, Keithan A, et al. Three-dimensional imaging of the aortic vessel wall using an elastin-specific magnetic resonance contrast agent. Investig Radiol. 2012;47:438–44.
142. Phinikaridou A, Andia ME, Indermuehle A, Onthank DC, Cesati RR, Smith A, et al. Vascular remodeling and plaque vulnerability in a rabbit model of atherosclerosis: comparison of delayed-enhancement MR imaging with an elastin-specific contrast agent and unenhanced black-blood MR imaging. Radiology. 2014;271:390–9.
143. Motoyama S, Kondo T, Sarai M, Sugiura A, Harigaya H, Sato T, et al. Multislice computed tomographic characteristics of coronary lesions in acute coronary syndromes. J Am Coll Cardiol. 2007;50:319–26.
144. Motoyama S, Sarai M, Harigaya H, Anno H, Inoue K, Hara T, et al. Computed tomographic angiography characteristics of atherosclerotic plaques subsequently resulting in acute coronary syndrome. J Am Coll Cardiol. 2009;54:49–57.
145. Gough PJ, Gomez IG, Wille PT, Raines EW. Macrophage expression of active mmp-9 induces acute plaque disruption in apoe-deficient mice. J Clin Invest. 2006;116:59–69.
146. Lancelot E, Amirbekian V, Brigger I, Raynaud JS, Ballet S, David C, et al. Evaluation of matrix metalloproteinases in atherosclerosis using a novel noninvasive imaging approach. Arterioscler Thromb Vasc Biol. 2008;28:425–32.
147. Hyafil F, Vucic E, Cornily JC, Sharma R, Amirbekian V, Blackwell F, et al. Monitoring of arterial wall remodelling in atherosclerotic rabbits with a magnetic resonance imaging contrast agent binding to matrix metalloproteinases. Eur Heart J. 2011;32:1561–71.
148. Nicholls SJ, Hazen SL. Myeloperoxidase and cardiovascular disease. Arterioscler Thromb Vasc Biol. 2005;25:1102–11.
149. Ronald JA, Chen JW, Chen Y, Hamilton AM, Rodriguez E, Reynolds F, et al. Enzyme-sensitive magnetic resonance imaging targeting myeloperoxidase identifies active inflammation in experimental rabbit atherosclerotic plaques. Circulation. 2009;120:592–9.
150. Tavora F, Cresswell N, Li L, Ripple M, Burke A. Immunolocalisation of fibrin in coronary atherosclerosis: implications for necrotic core development. Pathology. 2010;42:15–22.
151. Falk E, Shah PK, Fuster V. Coronary plaque disruption. Circulation. 1995;92:657–71.

Assessment of Cardiomyopathies and Cardiac Transplantation

15

Róisín B. Morgan and Raymond Y. Kwong

Introduction

In recent years, the use of cardiac magnetic resonance imaging (MRI) has become an integral part of the assessment of cardiomyopathy patients. Indeed, with the recent advances in cardiac MRI techniques and imaging sequences, the improved scanner capabilities, and reduced scanning time, this tool is now an integral part of the assessment of conditions, such as suspected myocarditis, myocardial infarction (MI), acute and chronic ischemic cardiomyopathy, as well as a wealth of other inherited and non-inherited cardiomyopathies.

This chapter will outline the techniques used in cardiac MRI scanning for the assessment of such conditions with case examples to highlight the clinical use of this imaging technique in current-day cardiology practice. Recent MR imaging advances and future tools will also be discussed, as we explore the significant addition that a cardiac MRI makes to the clinical care of cardiac patients with cardiomyopathy.

Cardiomyopathies

The term cardiomyopathy applies to disease specifically affecting the heart muscle. With its unique tissue-characterizing capabilities, CMR plays an important role in detecting the presence of cardiomyopathy and determining its likely underlying pathology.

Cardiomyopathies can be divided into genetic and nongenetic forms. The classic genetic cardiomyopathies consist of the following: dilated cardiomyopathy (DCM); hypertrophic cardiomyopathy (HCM); arrhythmogenic cardiomyopathy (AC), also called arrhythmogenic right ventricular cardiomyopathy (ARVC); and restrictive cardiomyopathy (RCM), each of which may be the cause of a heart failure syndrome. The most common nongenetic cardiomyopathy, i.e., acquired, is ischemic cardiomyopathy, usually a consequence of atherosclerotic cardiovascular disease.

In practice, there is considerable overlap between the inherited phenotypes [1]; e.g., HCM, left ventricular noncompaction cardiomyopathy (LVNC), or AC may progress into a dilated ventricle with systolic dysfunction and hence the appearance of DCM. The use of cardiac MRI, and other imaging techniques such as echocardiography, offers refinement of this structurally based classification with the addition of functional information to complement the morphological phenotype, thus providing insight into contractility, diastolic function, strain, synchrony, and fibrosis.

Imaging Techniques Used in the Assessment of Cardiomyopathy

Echocardiography

The use of echocardiography (echo) in the assessment of right and left ventricular parameters, such as morphology, function, volumes, and wall motion and the use of echo contrast to gain better endocardial definition make echo an essential initial tool in the assessment of suspected cardiomyopathy. Echo has proven to be widely accessible, reproducible, efficient, and economical, as well as having the advantage of avoiding the use of ionizing radiation during image acquisition. Indeed, the use of echocardiography has been included in practice guidelines for the diagnosis and management of conditions such as HCM [2]. In such patients, two-dimensional echocardiography has demonstrated the heterogeneity of the hypertrophic phenotype, particularly with regard to distribution of LV hypertrophy and mechanisms of outflow obstruction [3–5]. However, there remain certain patients in whom the diagnosis of HCM is suspected, but the echo is inconclusive, mostly because of

R. B. Morgan · R. Y. Kwong (✉)
Non-invasive Cardiovascular Imaging, Cardiovascular Division, Department of Medicine, Brigham and Women's Hospital, Harvard Medical School, Boston, MA, USA
e-mail: rykwong@bwh.harvard.edu

R. Y. Kwong et al. (eds.), *Cardiovascular Magnetic Resonance Imaging*, Contemporary Cardiology,
https://doi.org/10.1007/978-1-4939-8841-9_15

suboptimal imaging from poor acoustic windows or when hypertrophy is localized to regions of the LV myocardium not well visualized by echo [6]. In multiple studies, patients with suspected HCM were identified with increased LV wall thickness (predominantly in the anterolateral wall) by CMR but not by echo [7, 8]. In addition, hypertrophy confined to the apex (i.e., apical HCM) may be difficult to visualize with echo but is evident with CMR [9, 10].

Echocardiography is also useful in the assessment of other forms of cardiomyopathy, such as DCM, and is often the first-line investigation ordered by the clinician. Indeed in the current ACCF/AHA guidelines for the diagnosis and management of heart failure, an initial echo is supported by level of evidence class IC [11]. It is also a useful tool in follow-up of patients and assessment of response to therapy [11].

The measurement of diastolic function and echo-derived strain data is of immense importance in patients with particular types of restrictive cardiomyopathy, where left ventricular systolic function often remains normal until advanced stage of disease is reached, such is the case in cardiac amyloidosis [12].

Overall, echo is a robust tool, used frequently in the diagnosis and follow-up of patients with cardiomyopathy; however, it does suffer the limitations of poor image quality in obese patients or those with inadequate echo windows, and the use of myocardial perfusion techniques are not readily available using this modality, as they are with CMR.

Cardiac MRI

In certain patients, in whom echo image quality is suboptimal, or in whom a diagnosis of cardiomyopathy is still suspected despite a normal echo, cardiac MRI is a very useful tool. Indeed the current ACCF/AHA guidelines for diagnosis and treatment of heart failure state that MRI is reasonable to evaluate ejection fraction (EF) and volumes and to detect myocardial infiltration and scar [11]. In addition, myocardial perfusion, viability, and fibrosis from MRI can help identify the etiology of the underlying suspected cardiomyopathy and assess prognosis in these patients.

An important application of cardiac MRI, and the rationale behind the inclusion of this imaging modality in the current guidelines, is the characterization of tissues using special pulse sequences. The most widely used tools are T1- and T2-weighted imaging, fat suppression, and gadolinium enhancement in both the early (less than 5 min) and late phases (>10–15 min) [13]. T1-weighted images provide anatomic assessment of the myocardium and great vessels. They characterize lesions with short T1 relaxation times, and they are useful in the assessment of contrast enhancement. They can be obtained using spin echo or spoiled gradient echo sequences. The following are bright with this sequence: lipid, hemorrhagic products, proteinaceous fluid, melanin, gadolinium, and certain other metals. T1-weighted spin echo or fast spin echo sequences are ECG-gated during cardiac MRI acquisition.

T2-weighted images are valuable for the detection and characterization of pathology with long T2 times [13]. They are generally performed with spin echo or fast spin echo sequences. T2-star (T2*)-weighted imaging is particularly useful in the detection of iron overload in suspected cardiac involvement in cases of hemochromatosis. Fat suppression is a useful tool to help distinguish whether lesions that are high in signal intensity on T1-weighted images contain fat [14]. On T2-weighted fast spin echo images, fat has high signal intensity. Contrast-enhanced T1-weighted imaging is also helpful when trying to characterize myocardial and pericardial pathology. Contrast enhancement is assessed with black blood ECG-gated T1-weighted spin echo sequences. As an alternative, fat-suppressed T1-weighted spoiled gradient echo imaging can be used [14]. Late gadolinium enhancement (LGE) imaging is particularly useful in the characterization of myocardial infarction, sarcoidosis, HCM, acute myocarditis, and ARVC. Approximately 10–30 min after intravenous injection of gadolinium chelates, delayed washout of contrast material from abnormal myocardium generates a hyperintense signal named LGE. This form of imaging is described in further detail in the cardiomyopathy subsections below.

Cardiac MRI is also an excellent tool for the accurate and reproducible assessment of right and left ventricular volumes, utilizing the short-axis multi-slice acquisition, which is an important part of standardized clinical cardiac MRI protocols and shows good correlation with in vivo standards and radionuclide angiography [15, 16]. In addition, the high spatial resolution of cardiac MRI is extremely valuable in the assessment of cardiac morphology in cases such as ARVC or LVNC.

Cardiac Computed Tomography (CT)

Cardiac computed tomography can also provide accurate assessment of cardiac structure and function, including the epicardial coronary arteries. As it is not a commonly used initial tool in the assessment of patients with cardiomyopathy, reports of cardiac CT in patients with suspected cardiomyopathy and HF are limited. Furthermore, during cardiac CT in patients with elevated heart rates or arrhythmia, image quality can be suboptimal. Thus, as it stands, routine use of cardiac CT in the assessment of patients with cardiomyopathy and heart failure is not routinely recommended [11].

Stress Nuclear Imaging (Single Photon Emission Computed Tomography (SPECT) or Positron Emission Tomography (PET))

In certain patients with a newly diagnosed cardiomyopathy, in whom underlying coronary ischemia is suspected, and invasive coronary angiography is contraindicated, myocardial perfusion imaging using SPECT or PET may be considered [11]. In patients with known ischemic cardiomyopathy, these tools may be useful in determining the degree of underlying ischemia in unrevascularized territories or in the assessment of scar and viability (see Chap. 12).

Types of Cardiomyopathy (with Clinical Examples)

Ischemic Cardiomyopathy

The CMR assessment of patients with suspected or known ischemic cardiomyopathy has two important components: presence and severity of myocardial ischemia and extent of myocardial fibrosis/scar. A standard CMR for these patients involves imaging sequences to evaluate LV and RV function and standard morphology as assessed by four-chamber, three-chamber, and two-chamber views in addition to short-axis slices through both ventricles. For the perfusion sequences, first-pass contrast-enhanced stress perfusion is typically carried out before rest perfusion, with the use of intravenous vasodilators such as regadenoson to achieve maximal hyperemia. Intravenous gadolinium-based agents are used, at a dose of 0.1 mmol/kg weight, which have been shown to produce excellent results in perfusion and late gadolinium-enhanced images [17–19]. Myocardial perfusion imaging is based on measuring the delivery of contrast agent to the myocardium during the first pass following a bolus injection [20]. The signal intensity is enhanced by the contrast agent, which shortens the T1 relaxation time and results in a brighter signal using a T1-weighted imaging sequence. Myocardial regions with reduced blood flow will appear hypointense and may be detected given adequate image quality. Regions with prior MI may appear hypointense despite normal blood flow, following revascularization, due to the low flow into scar tissue [20]. Therefore, the interpretation of perfusion images usually also incorporates viability assessment by delayed enhancement imaging as described in the chapter on viability.

Experience with CMR LGE imaging for the evaluation of subacute or chronic infarct is extensive [17, 21–23]. The transmural extent of LGE predicts response to coronary revascularization: infarcts that span less than 50% of the segmental wall thickness have the greatest likelihood of recovery of function following successful revascularization [13]. In contrast, those infarcts that span >50% of the myocardium have been shown to be less likely to improve functionally post successful revascularization [22]. The location and extent of LGE have also been shown to be useful in identifying those individuals who will respond to cardiac resynchronization therapy (CRT) [24].

Case 1

A 77-year-old male patient with a history of myelodysplastic syndrome (MDS), on chemotherapy, coronary artery disease (CAD) status post remote inferior MI and coronary artery bypass graft (CABG) surgery, and resultant ischemic cardiomyopathy (ICM) with a known depressed left ventricular systolic function of 15%. He also had a history of atrial fibrillation/atrial flutter on oral anticoagulation and was admitted to hospital with increasing dyspnea and palpitations and found to be experiencing runs of monomorphic ventricular tachycardia on a monitor. He underwent a resting viability protocol MRI to evaluate the burden of scar prior to a planned electrophysiology study (EPS) (Fig. 15.1).

Following the CMR the patient underwent an electrophysiology study (EPS) and catheter ablation for VT and placement of an implantable cardioverter defibrillator (ICD).

Myocarditis

Acute cases of myocarditis most commonly occur in the setting of systemic viral disease [25]. During the initial days of viral myocarditis, there is direct cardiomyocyte injury, accompanied by edema, necrosis, and regional or even global contractile dysfunction [26]. The virus typically clears from the tissue within 5 days; however, reactive inflammation may last for several weeks. In uncomplicated cases, there is full tissue and functional recovery within 3–4 weeks, whereas in more severe disease, necrosis results in myocardial scarring. Prolonged autoimmune response or virus persistence may lead to chronic inflammation and is considered a frequent cause of dilated cardiomyopathy [27].

In recent years, CMR has become an important diagnostic tool in patients with suspected myocarditis due to its ability to noninvasively assess underlying myocardial inflammation. In fact, CMR is now the reference diagnostic tool to diagnose myocarditis, as recommended by the Lake Louise consensus criteria [28]. In cases of myocarditis, T2-weighted imaging identifies edema (see Fig. 15.2a, b), which has been described as a marker of inflammation in acute or active disease, and the pattern of LGE is typically patchy or subepicardial, thus differentiating it from ischemic cardiomyopathy, which tends to be present in a more focal pattern. The presence of edema in the absence of necrosis or scar represents reversible injury, and thus its presence or absence can predict functional recovery [29, 30].

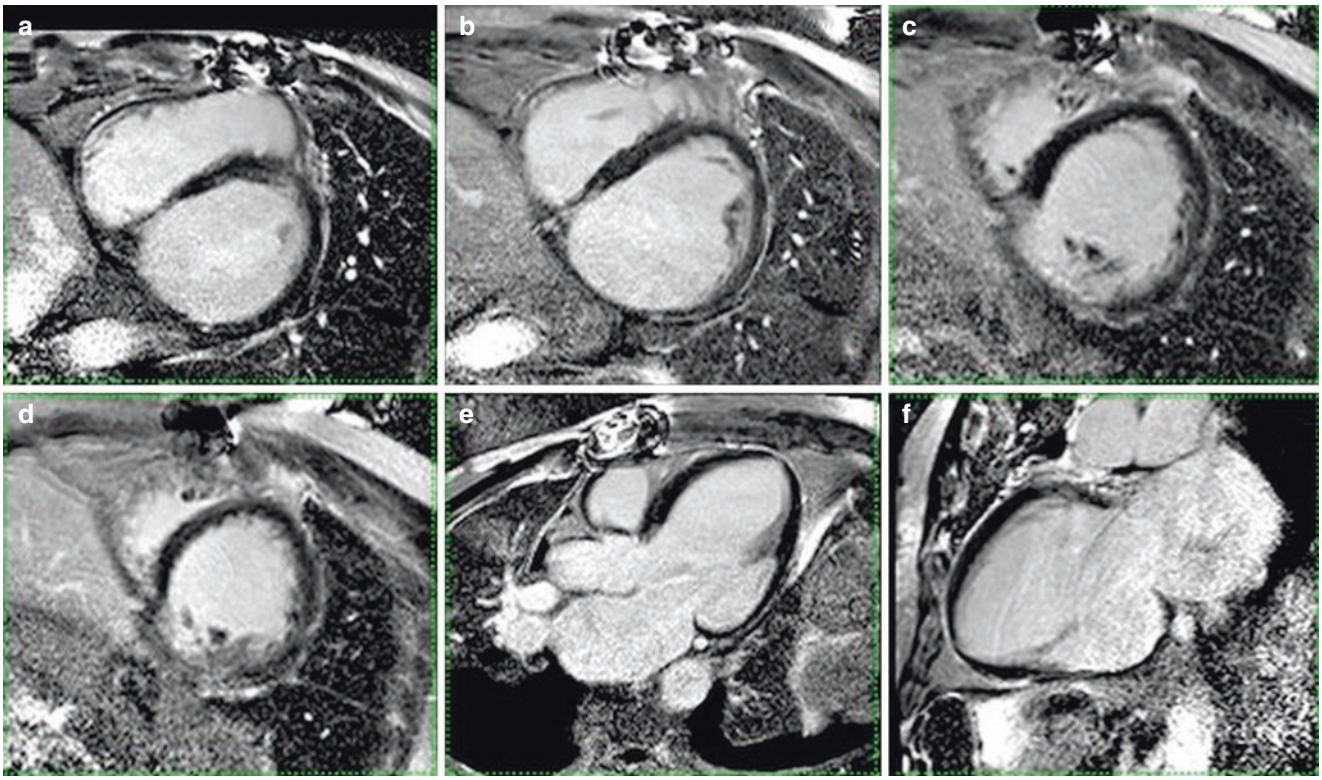

Fig. 15.1 Ischemic cardiomyopathy. Delayed enhancement imaging of basal (**a**, **b**), mid (**c**), and apical (**d**) short-axis slices, three-chamber (**e**) and two-chamber (**f**) LGE images

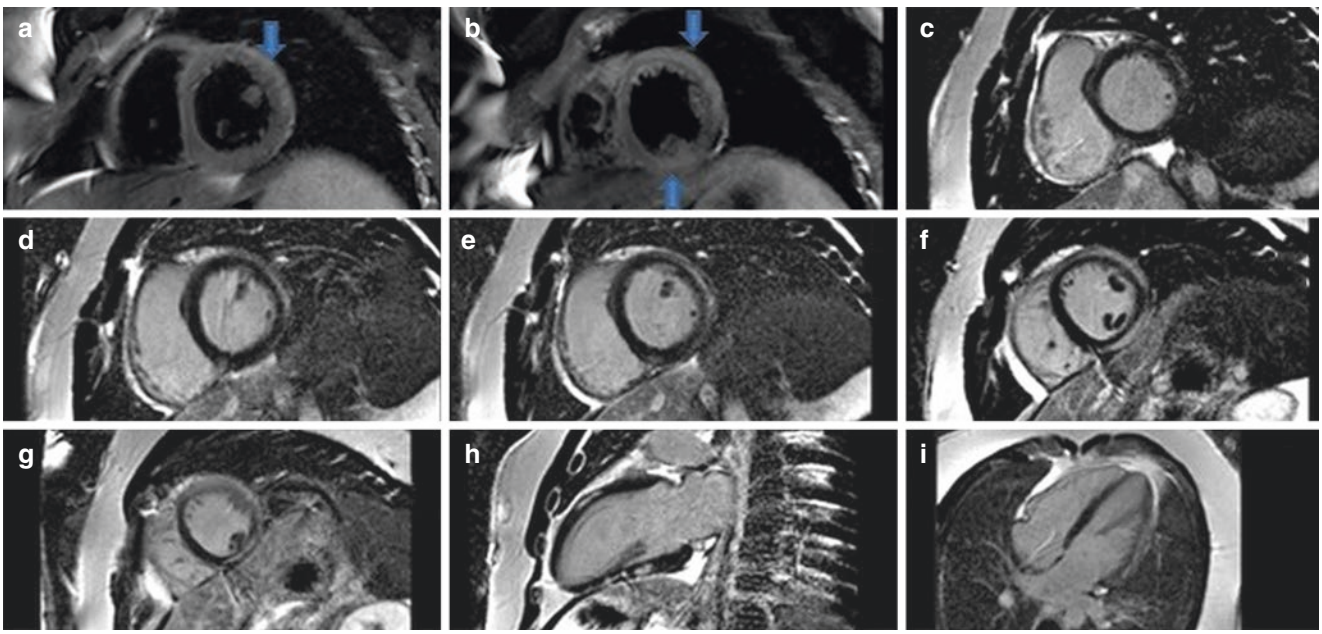

Fig. 15.2 Myocarditis. T2 hyperintensity is seen within the basal and mid anterior, anterolateral, and inferolateral walls, as well as the mid inferior wall (**a** and **b** blue arrows indicate edema), sparing the subendocardium, suggestive of myocardial edema. On the post-contrast images (**c**–i), there is subepicardial LGE of corresponding segments of the myocardium suggestive of inflammation/scar. In addition, there was a resting perfusion defect of the basal and mid anterolateral and inferolateral segments sparing the subendocardial layer suggestive of microvascular obstruction/myocardial necrosis

A number of technical aspects are pivotal for CMR edema imaging: triple inversion-recovery spin echo protocols carried out with fat and flow suppression (short inversion time inversion recovery and spectral presaturation with inversion recovery) are used because of their specific sensitivity to water [31]. The use of the body coil (or an efficient correction algorithm for surface coils) is necessary for homogeneous signal distribution. In addition, adequate flow suppression, acquisition timing during diastolic diastasis, sufficiently thick slices (12 mm), and acquisition of data during regular heart rates are required for image acquisition [28]. Short-axis views are recommended to reduce artifacts associated with slow transplanar blood flow.

The ability of CMR to accurately assess right and left ventricular volumes and systolic function makes it an ideal diagnostic tool in cases of myocarditis. Cine imaging is typically performed using an SSFP gradient echo sequence with 20–30 phases per heartbeat. Ever-improving state-of-the-art scanners using parallel imaging can acquire several slices within a single breath hold [26]. Pericardial involvement may also be assessed accurately, allowing detection of the volume and hemodynamic relevance. Overall, the combined imaging sequences in CMR have a reported sensitivity of 76% and specificity of 96% [32] for the diagnosis of myocarditis.

Case 2

A 19-year-old male with a history of infectious mononucleosis in the recent past presenting with substernal chest pain and an elevated troponin (troponin T 2.01ng/ml). The patient denied a history of cocaine use and had no family history of premature coronary artery disease. ECG revealed 1 mm diffuse ST segment elevation throughout all leads. Echocardiography revealed mildly reduced LV systolic function, with no regional wall motion abnormalities. A cardiac MRI was ordered to evaluate for possible underlying myopericarditis.

Dilated Cardiomyopathy

Dilated cardiomyopathy (DCM) is the most common form of nonischemic cardiomyopathy (NICM) and is characterized by dilation of the left ventricle (LV), systolic dysfunction, and resultant progressive heart failure. It is also associated with a high risk of fatal arrhythmias and a high mortality rate [33]. Although the majority of cases are idiopathic, DCM may include several unclear etiologies, including chronic myocarditis, tachycardia-induced cardiomyopathy, undiagnosed sarcoidosis, and end-stage HCM [34–36].

In cine CMR sequences, all cardiac chambers are typically enlarged, and a reduced LVEF is evident. Most often LV wall thickness is normal or reduced but is relatively homogenous. In delayed enhancement images, DCM has been shown to demonstrate either a lack of LGE or the presence of mid-wall enhancement, and a small number of cases show patchy or diffuse-striated LGE [37]. The proposed mechanisms of myocardial fibrosis in DCM are complex and include inflammation, genetic predisposition, microvascular ischemia, and neurohumoral changes [38].There are a number of different thresholds used to detect LGE, which may also affect the variation in the prevalence of LGE in DCM. Newer tissue mapping strategies, both T1 and T2, are quantitative techniques that offer the promise of standardizing CMR measurements of myocardial tissue properties, no longer leaving the interpretation to the eye of the beholder [39]. T1 mapping can be performed with or without contrast; the pulse sequence for T1 mapping has been recently improved with shorter breath-hold duration. Recent data comparing hypertrophic cardiomyopathy (HCM) and nonischemic dilated cardiomyopathy (DCM) patients with control subjects studied T1 values prior to and sequentially at 10-min intervals after contrast infusion to calculate extracellular volume (ECV) fraction [40]. In this study native T1 was significantly longer in cardiomyopathy patients (HCM 1,254 ± 43 ms and DCM 1,239 ± 57 ms) than in controls (1,070 ± 55 ms); the accuracy was high with an area under the receiver operating curve (ROC) of 0.99. Indeed, native T1 performed better than post-contrast T1 and ECV measurements.

The pathophysiologic basis of the elevated T1 values in conditions such as DCM is not well understood. The link between post-contrast T1 shortening and fibrosis is fairly well-established in fibrotic diseases [41]. It has been hypothesized that the increase in native T1 may be due to increased extracellular volume due to expansion of the interstitial space from fibrosis in HCM patients or fibrillar deposits in cardiac amyloidosis. The underlying mechanism in DCM is less well understood. While ECV and native T1 mapping appear likely to affect clinical decision-making, they lack multicenter application and face significant challenges [42]. At present, ECV and native T1 mapping techniques appear sufficiently robust for many diseases; however, additional research is required before these techniques can be used routinely in clinical MRI practice.

Case 3

A 63-year-old man with history of systemic hypertension, mild aortic stenosis, and obesity. Transthoracic echo revealed severely impaired LV systolic function with an EF of 20% and diffuse LV hypokinesis (Fig. 15.3).

Genetic Cardiomyopathies

Hypertrophic Cardiomyopathy

Hypertrophic cardiomyopathy (HCM) is the one of the most common genetic cardiac disorders, with a reported prevalence of 1:500 in the general population [43]. In up to

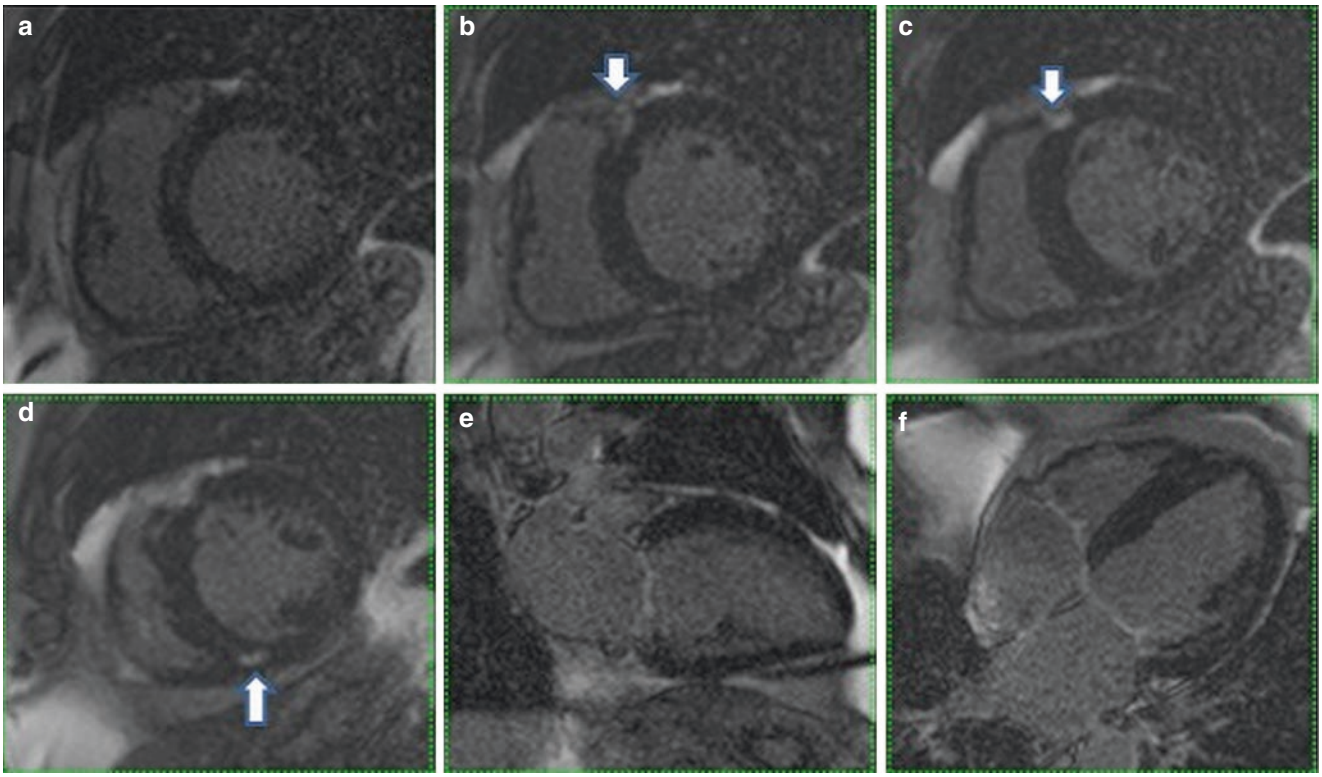

Fig. 15.3 *Dilated cardiomyopathy*. LGE images from base, mid, and apical short-axis slices (**a**–**d**), two-chamber (**e**) and four-chamber (**f**) images reveal focal subepicardial and mid-wall LGE in the basal and mid anteroseptum and inferoseptum, at the RV insertion points (arrows). In addition, there is patchy, mostly mid-wall, LGE involving the basal and mid inferolateral walls

60% of cases, the mode of inheritance is autosomal dominant, and over 600 mutations have been identified in sarcomeric genes to date [44]. It is thought that these mutations cause an increase in myocyte stress and impaired myocyte function which eventually leads to left ventricular hypertrophy (LVH) and fibrosis. CMR is an ideal diagnostic tool for the assessment of suspected or known HCM. Long- and short-axis stacks of SSFP images allow measurements of overall wall thickness and function assessment, and short-axis tagging sequences are used for myocardial strain analysis. Resting first-pass perfusion and LGE images assess for underlying perfusion defects from associated microvascular ischemia and the presence of scar in hypertrophied segments, respectively. Increased LV wall thickness is most commonly seen at the junction of the basal anteroseptum with the contiguous anterior free wall [45], and indeed hypertrophy involving both of these segments is present in up to 70% of HCM patients.

Myocardial tagging was initially designed to analyze myocardial contraction during systole [46]. Noninvasive markers, known as tags, are created within the myocardial tissue by a process involving locally induced perturbations of the magnetization, with selective radiofrequency saturation of multiple, thin tag planes. This occurs in a plane perpendicular to the imaging plane prior to image acquisition [47, 48]. These perturbations then produce regions of reduced signal intensity that appear as dark lines in the acquired images [48]. Tags are typically ECG-gated and generated in line with the QRS complex of the ECG. The generated tags then follow a myocardial motion during the cardiac cycle, thus reflecting the underlying myocardial deformation [47]. Currently, CMR tagging remains the reference standard for assessment of regional function [49]. Spoiled gradient echo imaging is the most commonly used sequence for tag generation at the widely available 1.5T magnets. However recent studies [50, 51] have proposed implementing SSFP to achieve better contrast and longer tag persistence. Using high-field-strength magnets such as 3T for tagging acquisition may also reduce the problem of tag fading. Indeed, despite the potential increase in susceptibility effects during cardiac imaging, applying myocardial tagging at higher-field, such as 3T, strength appears to provide a better contrast-to-noise ratio (CNR) as well as improve tag persistence. This can be explained by a higher baseline signal-to-noise ratio (SNR) seen with 3T systems and prolongation of myocardial T1, which both improve the contrast between the tissue and the tag lines at end-diastole [52]. Providing persistent tags allows quantification of cardiac strain evolution during late diastole, which can be used to assess diastolic myocardial dysfunction. Also, using the multi-planar capabilities of

CMR, tag lines can be applied in the short- or long-axis cardiac planes to facilitate sophisticated three-dimensional (3D) strain analysis.

First-pass perfusion CMR reveals an abnormal rest perfusion in a significant proportion of patients with HCM. These abnormalities are typically associated with the presence and distribution of myocardial scar and the degree of hypertrophy. Patients with rest perfusion abnormalities have been shown to have an increased incidence of NSVT on Holter monitoring, independent of the presence of myocardial fibrosis [53].

Approximately half of HCM patients demonstrate LGE, with a diverse pattern and location, although most commonly involving hypertrophied segments of the LV wall [54]. After IV injection of gadolinium, areas of hyper-enhancement within the myocardium can be identified and the amount quantified as a percentage of the total LV mass. Observations from imaging and histologic studies suggest that LGE in HCM patients may stem from a pathophysiologic cascade during which repetitive episodes of microvascular ischemia result from structurally abnormal intramural coronary arteries. This, in turn, leads to myocyte cell death and repair in the form of replacement fibrosis. An alternative hypothesis suggests that the causative sarcomeric gene mutations may directly cause increased myocardial connective tissue deposition. Moon et al. showed a direct correlation between the percentage of LGE and the amount of histologic collagen in an explanted HCM heart [55]. LGE most often involves the interventricular septum, at the thickest regions detected on SSFP imaging, in particular the anteroseptal mid to basal segments and the right ventricular insertion points [56].

Numerous techniques have been used to assess LGE in HCM, including semiautomated algorithms that identify high-signal-intensity LGE pixels in the LV wall after applying a grayscale threshold a number of SDs above the mean signal intensity within a remote region containing normal "nulled" myocardium (i.e., 2, 4, 5, or 6 SD) [57]. An alternative method is the full-width at half maximum (FWHM) method (pixels with a signal intensity >50% of the maximum intensity of the brightest region of hyper-enhancement) [34]. These quantification algorithms were initially validated in patients with coronary artery disease in whom lower signal intensity thresholds (i.e., 2 SD) correlate well with the spatial extent of infarct tissue [58]. This is related to the fact that post-MI scar is composed of focal, high signal intensity, homogeneous hyper-enhancement surrounded by otherwise structurally normal myocardium. However, the optimal approach to quantifying LGE in HCM is still not well defined. Some reasons why this is the case have been put forward including the following: as opposed to ischemic cardiomyopathy, HCM is characterized by diffuse histopathological abnormalities involving the entire LV myocardium, including replacement fibrosis or expanded extracellular matrix due to interstitial fibrosis and/or myocyte disarray [54]. This results in a gradient of gadolinium deposition in the myocardium with focal areas of dense concentration producing high signal intensity hyper-enhancement and diffuse regions of concentration resulting in lower signal intensity [58, 59]. Secondly, the limited spatial resolution of in vivo imaging can result in partial volume effects and, along with inappropriate nulling and background noise, can generate areas of increased signal intensity that appear visually as LGE but do not represent abnormal substrate [34, 58]. Thirdly, elucidating precisely the histological basis of LGE in HCM patients with normal LV function has not been possible due to the lack of a spontaneous HCM animal model [54].

Myocardial ECV measurement is a novel addition to the assessment of HCM patients by CMR. Ho et al. [60] demonstrated how myocardial ECV is increased in HCM sarcomere mutation carriers even in the absence of LVH. T1mapping is an important technique with the unique ability to track changes in the myocardium. It does this by (1) native T1, a non-contrast method which reflects myocardial disease involving the myocyte and interstitium, or (2) the extracellular volume (ECV) fraction – a direct Gd-based measurement of the size of the extracellular space, which has been shown to reflect interstitial disease [60]. Going forward, quantifying ECV may help characterize the development of myocardial fibrosis in HCM at an early stage.

End-stage HCM is characterized by LV systolic dysfunction and enlargement of the LV cavity [61]. Differentiation between end-stage HCM and DCM can be difficult because the clinical condition in end-stage HCM often resembles that seen in DCM. This is especially encountered if the hypertrophy was undiagnosed or underestimated during the natural course of the disease. Cine CMR images clearly show that LV wall thickness in end-stage HCM is normal or relatively larger than that observed in DCM and is inhomogeneous among LV segments [37]. LGE in end-stage HCM distributes more diffusely into all the LV segments, whereas that in DCM is localized mainly in the interventricular septum [36, 38, 55]. The correct interpretation of both cine CMR and LGE CMR can help in the differentiation of end-stage HCM from DCM as well as other secondary cardiomyopathies that exhibit LV dysfunction with hypertrophy (e.g., cardiac amyloidosis and Anderson-Fabry disease).

Case 4

A 38-year-old male with symptomatic nonobstructive hypertrophic cardiomyopathy diagnosed by echocardiogram at age 21 years. He was referred for CMR to assess for septal thickness, with a view to possible myomectomy, given symptoms of reduced effort tolerance and dyspnea (Figs. 15.4 and 15.5).

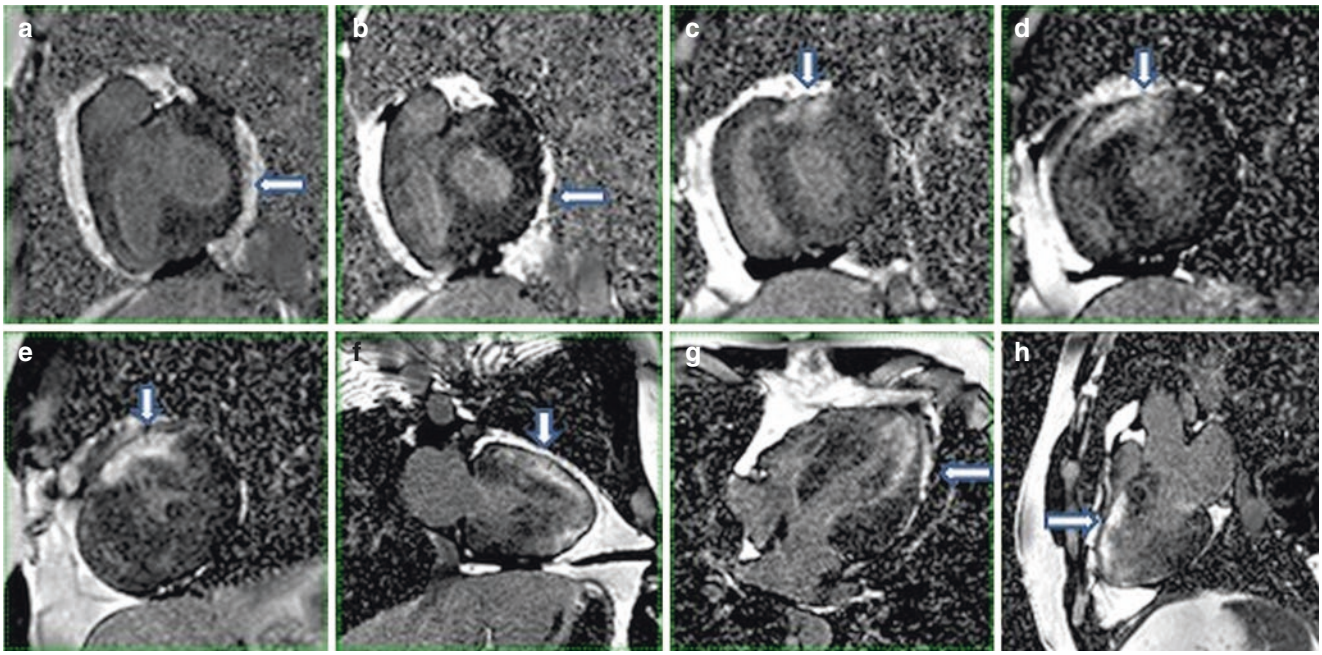

Fig. 15.4 *Hypertrophic cardiomyopathy*. Short-axis basal (**a, b**), mid (**c, d**), and apical (**e**) slices, two-chamber (**f**), three-chamber (**g**), and four-chamber (**h**) views of LGE images show a large amount of patchy LGE involving the basal anterior and anteroseptal walls (**a, b, f, h** arrows), mid anterior and anteroseptal walls (**c, d**, arrows) and apical anterior and lateral walls (e.g., arrows). Perfusion images (additional supplementary material) reveal a stress-induced perfusion defect involving the basal anterior and anteroseptal walls, mid anterior and anteroseptal walls, and apical anterior and inferior walls, corresponding with the thickest segments

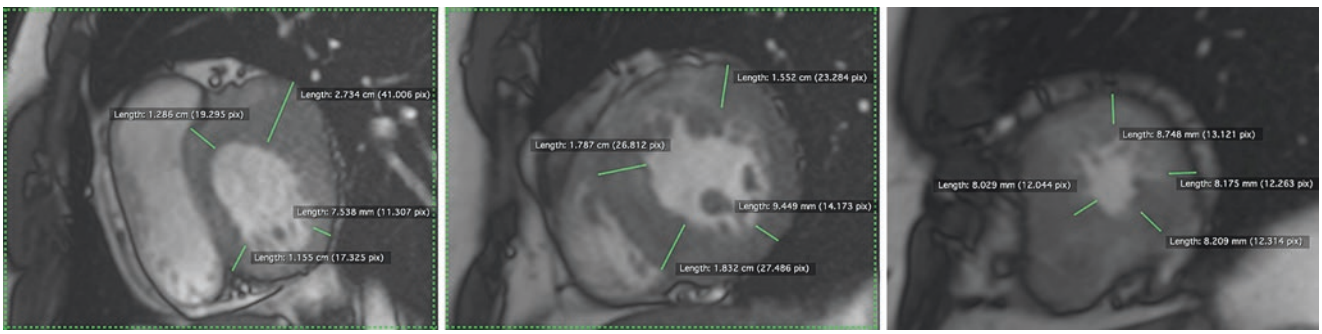

Fig. 15.5 *HCM. Wall measurements performed in short axis*. Short-axis SSFP images reveal the following wall thickness measurements at end diastole: basal anterior, 27 mm; basal anteroseptum, 12.8 mm; basal inferoseptum, 13.5 mm; basal inferolateral, 7.5 mm; mid anterior, 15 mm; mid anteroseptum, 18 mm; mid inferoseptum, 18 mm; mid inferolateral, 9.5 mm; apical anterior, 9 mm; apical septum, 8 mm; apical inferior, 8 mm; apical lateral, 8 mm

Arrhythmogenic Right Ventricular Cardiomyopathy (ARVC)

ARVC is a genetic myocardial disorder characterized by a progressive fibrofatty degeneration preferentially affecting the right ventricular (RV) myocardium [62]. ARVC patients can experience potentially fatal ventricular arrhythmias, EKG, and structural abnormalities as well as evidence of biventricular regional and global dysfunction on imaging studies [63]. With its excellent spatial resolution, CMR plays an important role in the detection of structural and functional abnormalities in this condition. Both T1- and T2-weighted sequences allow the differentiation of fatty from myocardial tissue, cine sequences allow for the accurate and reproducible quantification of RV systolic function, and both RV and LV LGE imaging have a very high sensitivity for the detection of myocardial scar tissue, although this is a relatively uncommon finding. In a recent study of 156 patients who met diagnostic criteria for ARCV [64], only 12 patients (8%) in total demonstrated LGE. Of these 12, 5 patients (3%) had left ventricular LGE, and 5 patients (3%) had right ventricular LGE. Two patients (1.3%) had biventricular LGE [65].

In 2010 the ARVC task force criteria (TFC), originally written in 1994, were revised in order to improve the diagnostic accuracy in this condition [64]. The original criteria

were flawed by significant inter-observer variability. The revised criteria, however, define specific cutoff values for end-diastolic volume and EF. Despite this modification, the currently used 2010 criteria are still based on subjective image interpretation and are limited as a result [66]. Per these criteria, ventricular dilation or dysfunction should be accompanied by the visual identification of regional wall motion abnormalities to meet minor or major disease-defining criteria (Table 15.1).

In practice, it remains a difficult diagnosis to make, even with the additional tools that CMR offers. In fact the clinical picture of an ARVC patient often mimics RVOT tachycardia, myocarditis, or even cardiac sarcoidosis. By the revised criteria, which also include echo parameters, repolarization abnormalities on ECG and arrhythmias, family history, and RV wall tissue characteristics, definite diagnosis is met by the following: two major or one major and two minor criteria or four minor from different categories; borderline diagnosis is made by one major and one minor or three minor criteria from different categories; and possible diagnosis is made by one major or two minor criteria from different categories [64].

Given the limitations of the 2010 Task Force Revised Criteria, potential tools such as MRI strain analysis in suspected ARVC cases have been studied [63]. A strain method using feature tracking (FT) could serve as a quantifiable measure to confirm global and regional ventricular dysfunction in ARVC patients. This would thus allow the detection of early forms of ARVC, when global volumetric parameters are still normal. One study found that RV global longitudinal strain rates in ARVC and borderline ARVC were significantly reduced in comparison with healthy volunteers (P = 0.05) [63]. In addition to longitudinal strain in ARVC patients, RV global circumferential strain and strain rates at the basal level were significantly reduced compared with healthy volunteers [63]. Thus CMR-based strain analysis could be an objective and useful measure for the quantification of wall motion abnormalities in ARVC subjects.

Table 15.1 Task force criteria for diagnosis of ARVC

Original task force criteria	Revised (MRI criteria)
Major	
Severe dilation and reduction of RV ejection fraction with no (or only mild) LV impairment Localized RV aneurysms (akinetic or dyskinetic areas with diastolic bulging) Severe segmental dilation of the RV	Regional RV akinesia or dyskinesia or dyssynchronous RV contraction and one of the following: Ratio of RV end-diastolic volume to BSA ≥110 ml/m^2 (male) or ≥100 ml/m^2 (female) or RV ejection fraction ≤40%
Minor	
Mild global RV dilation and/or ejection fraction reduction with normal LV Mild segmental dilation of the RV Regional RV hypokinesia	Regional RV akinesia or dyskinesia or dyssynchronous RV contraction and one of the following: Ratio of RV end-diastolic volume to BSA ≥100 to <110 ml/m^2 (male) or ≥90 to <100 ml/m^2 (female) or RV ejection fraction >40% to ≤45%

Original and Revised MRI Criteria portion reprinted from Marcus et al. [64]. https://doi.org/10.1161/CIRCULATIONAHA.108.840827, © 2010, with permission from Wolters Kluwer Health

Case 5

A 43-year-old-male with palpitations and a family history of ARVC found to be a carrier of the TMEM43 mutation. Cardiac MRI revealed mildly reduced RV systolic function, with a calculated RVEF of 39% and normal indexed RV and LV volumes. There was dyssynchronous motion of the basal RV free wall, with aneurysmal bulging of the mid-free wall. In addition there was LGE of the RV myocardium in the region of dyssynchrony. Thus the patient fulfilled two major criteria for the diagnosis of ARVC, and primary preventive ICD was advised (Fig. 15.6).

Left Ventricular Noncompaction (LVNC)

First described in 1926 [67], and originally called spongy myocardium [68], left ventricular noncompaction (LVNC) is a congenital cardiomyopathy in which the myocardial trabecular layer fails to recede during cardiac embryogenesis. As a result, the left ventricle is filled with complex trabeculations that project into the chamber, interposed by deep intertrabecular recesses [69]. The clinical impact can vary significantly, from an asymptomatic incidental presentation to the development of progressive heart failure, thromboembolic disease, and sudden cardiac death [70]. The changes associated with LVNC are most pronounced in the apex and lateral walls of the heart and occur in the absence of any coexisting congenital lesion [71–73]. The currently accepted criteria for the diagnosis of LVNC are based on the ratio of noncompacted (NC) to compacted (C) myocardium. To measure the NC/C ratio, it is recommended to take three long-axis views in diastole and choose the myocardial segment with the most prominent myocardial trabeculations [74–76]. Imaging features typically include LV systolic dysfunction with reduced LVEF <40% and wall motion abnormalities involving the regions of noncompaction (Fig. 15.7).

A substantial proportion of LVNC has a defined genetic basis with reported mutations in three genes: β-myosin heavy chain (*MYH7*), α-cardiac actin (*ACTC*), and cardiac troponin T (*TNNT2*). There is a familial link with MYH7 and ACTC, but sporadic mutations of MYH7 as well as TNNT2 have also been identified [77]. The true prevalence and incidence of adult LVNC among the general population is unknown. Unlike in pediatric populations, it occurs more sporadically with less familial occurrences, 12–18% [78]. Clinical presentations of LVNC include heart failure, symptomatic

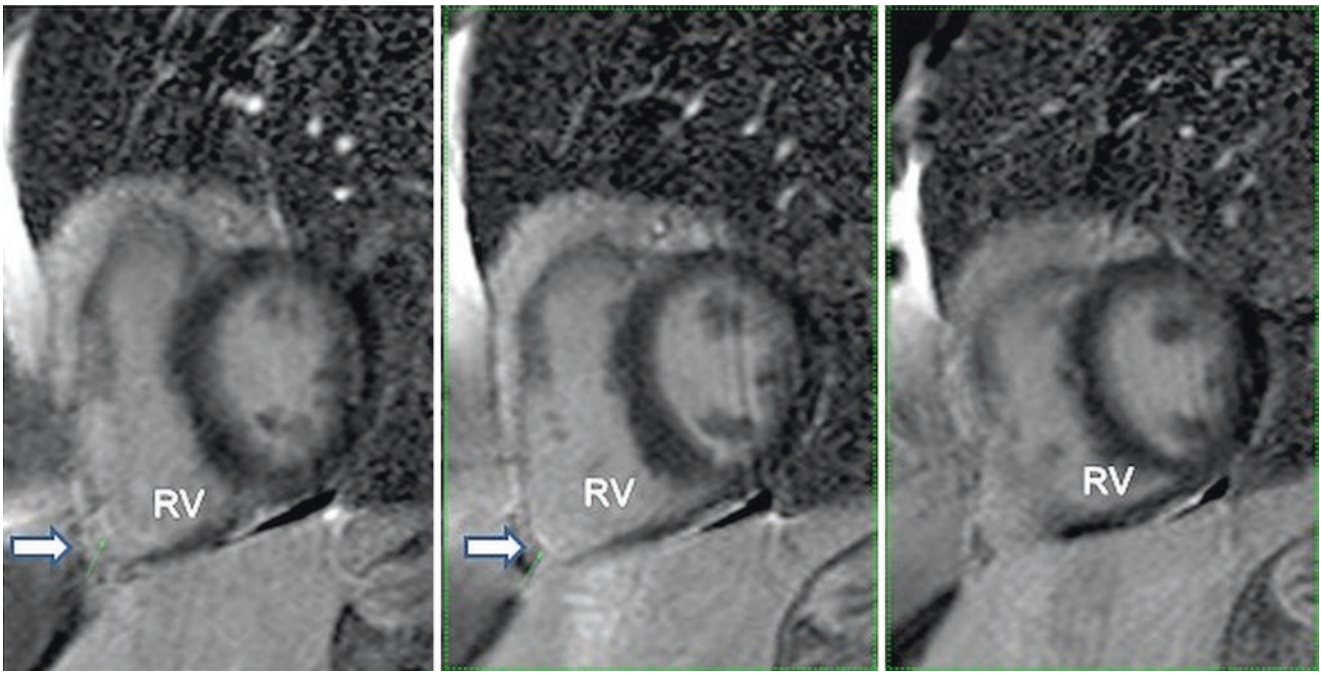

Fig. 15.6 *ARVC* LGE of the basal RV free wall (arrows) and no LGE of the left ventricular myocardium. In combination with the abnormal wall motion on axial SSFP images, this patient had two major criteria for diagnosis of ARVC

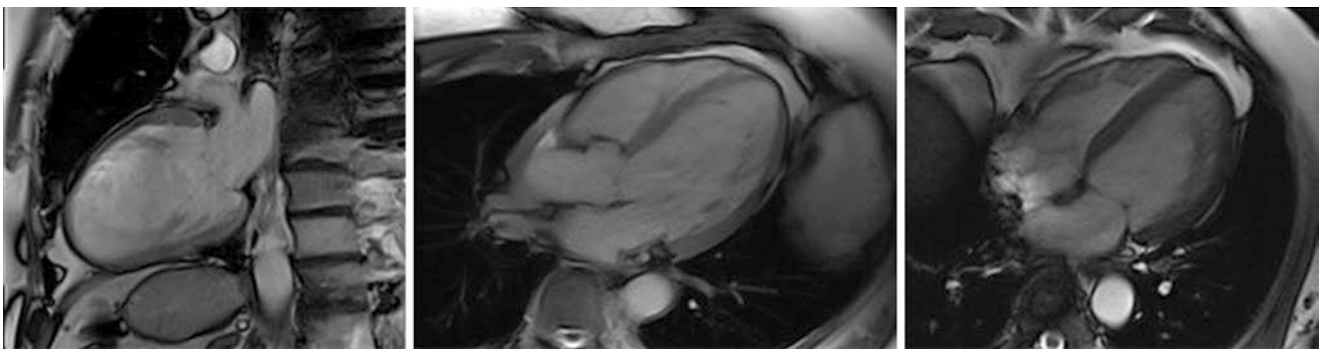

Fig. 15.7 *LV noncompaction.* Two-chamber-, three-chamber-, and four-chamber-long axis are used to measure a noncompacted to compacted ratio of 2.6 (average of 2.55 from two-chamber, 1.96 from three-chamber, and 3.5 from four-chamber)

or silent arrhythmias, and propensity for thromboembolism, occurring in up to 25% of cases. The increased risk for thromboembolism is believed to be multifactorial and is due to the combination of impaired LV function, perhaps simultaneous occurrence of atrial fibrillation, and the presence of abnormal myocardial trabeculae [78]. The clinical course of LVNC is variable; however, reported adverse outcomes are high with mortality from case series ranging from 35% to 47% over a 42–72-month follow-up period from diagnosis [79, 80].

Case 6

A 72-year-old male with new LBBB, nonobstructive coronary disease, and reduced LF systolic function on echo, referred for cardiac MRI for further characterization (Fig. 15.7)

Infiltrative Cardiomyopathies

Infiltrative cardiomyopathy can result from a wide spectrum of both inherited and acquired conditions with varying systemic manifestations. These conditions usually carry poor progrnosis with only a few exceptions (i.e., glycogen storage disease), in which case early diagnosis can result in potentially curative treatment. The extent of cardiac abnormalities is variable and is usually based on the degree of infiltration which results in increased ventricular wall thickness, chamber dilation, and disruption of the conduction system. Such changes often lead to the development of clinical syndromes encompassing heart failure, atrioventricular (AV) block, and ventricular arrhythmia. Due to the rare nature of these conditions, a high degree of clinical suspicion is important for

diagnosis. Basic investigations such as electrocardiography and echocardiography are helpful, but advanced techniques including CMR are increasingly preferred. Treatment of the condition depends on the etiology and extent of the disease and most often involves medical therapy, device therapy, and, in some cases, organ transplantation. Cardiac amyloid is the archetype of the infiltrative cardiomyopathies and is discussed in detail below.

Cardiac Amyloidosis

The amyloidosis includes a number of conditions which may affect the heart. Systemic amyloid light-chain (AL) amyloidosis is a multi-organ, infiltrative disorder which is due to an underlying plasma cell dyscrasia and is typically characterized by tissue and organ amyloid deposition with resultant interstitial expansion. Cardiac involvement is present in approximately 50% of patients at presentation and is the principal driver of prognosis [81].

Hereditary transthyretin-derived (ATTR) amyloid is an autosomal dominant condition that classically manifests in the 6th decade of life and is caused by 1 of 80 known mutations in the sequence encoding the protein transthyretin (TTR). Senile systemic and secondary amyloidosis are other types of amyloidosis, seen in clinical practice. The "gold standard" test for diagnosis of cardiac amyloidosis is myocardial biopsy [82], but this is invasive and can produce false-negative results. In practice, therefore, the diagnosis of cardiac amyloidosis is usually made by echo, supported by a diagnostic noncardiac biopsy [83]. In recent years, CMR has also become an important tool in the assessment of amyloid patients. Typical CMR features include increased LV wall thickness, restriction of diastolic filling, and disproportionate atrial enlargement. The amyloid protocol in our institution includes four-chamber and short-axis cine SSFP images to assess LV size and function, resting first-pass perfusion, and delayed enhancement imaging, including an early TI scout.

LV hyper-enhancement in cardiac amyloidosis is usually diffuse [84]. Although the subendocardium may be involved, as is the pattern seen in ischemic heart disease, the distribution more often is global and does not match any specific coronary artery perfusion territory [84]. From a technical perspective, this diffuse involvement may make the setting of the parameters, i.e., the inversion time (TI) for delayed enhancement imaging difficult. This is because it may be unclear which myocardial areas are normal, making the nulling of the normal myocardium more difficult. In this situation, a helpful approach may be to acquire multiple images of the same view using different inversion times (e.g., TI SCOUT, Siemens Medical Systems, Erlangen, Germany)

Not infrequently, myocardial amyloidosis results in suboptimal LGE images [85]. Not uncommonly, myocardial amyloidosis patients also have large pleural and pericardial effusions, which can cause artifacts on the delayed enhancement sequence. Rarely, differentiation between infarct and myocardial amyloidosis using DE-CMR in a typical coronary arterial territory may also be difficult.

Multiple patterns of post gadolinium nulling in cardiac amyloidosis have been described [84]. In normal patients, the blood pool null time precedes the myocardial nulling which is equal to that of splenic nulling (Type 1 pattern) [86]. Studies of amyloid patients have revealed the following patterns: some patients are observed to have a myocardial null time preceding or coincident with blood pool (Type 2 pattern) (Fig 15.8); some have a myocardial null time non-coincident with splenic nulling (Type 3 pattern); and some patients have a myocardial null time non-coincident with both blood pool and splenic nulling (type 4 pattern) [86]. Type 1 nulling has been associated with a lower risk of myocardial amyloidosis and Types 2–4 have been associated with a higher risk ($p < 0.05$) [86].

In early work on LGE imaging in amyloid patients, Macera et al. describe how amyloid patients followed a pattern of LGE, with a dominant subendocardial distribution matching the transmural distribution of amyloid protein [84]. The enhancement pattern in their study was subendocardial, diffuse, and global, which was different from that seen in myocardial infarction and other cardiomyopathies as well as in conditions such as HCM and hypertension.

Case 7

A 75-year-old man with chronic atrial fibrillation, left ventricular hypertrophy, and impaired diastolic function on echocardiogram presenting with symptoms and signs of heart failure. Cardiac MRI, serum SPEP, PYP, and free light chains were assessed for further evaluation. Serum SPEP revealed elevated free kappa light chain and free kappa lambda rat. NT-proBNP was significantly elevated. Cardiac MRI images are shown in Fig. 15.9 below. PYP imaging was abnormal with increased LV uptake of tracer consistent with TTR amyloidosis.

There is extensive literature available on the use of CMR in the diagnosis of amyloidosis [87, 88] describing how LGE can follow a diffuse or focal pattern and how focal areas of LV contrast enhancement are located mainly in the mid and basal segments of the anterior, lateral, and septal myocardium. Pre-contrast, native myocardial T1 mapping has recently been shown to correlate with cardiac disease burden and may be used to detect early disease in amyloid patients [89]. T1 mapping pre- and post-contrast can be utilized to derive the partition coefficient and, with the hematocrit, the myocardial ECV [41, 90] which is a direct measurement of expansion of the myocardial interstitium and therefore a potential surrogate marker of amyloid burden. Recent T1 mapping data [81] confirmed earlier results that ECV increases with established disease and may be a marker of early cardiac involvement in cardiac amyloidosis [91].

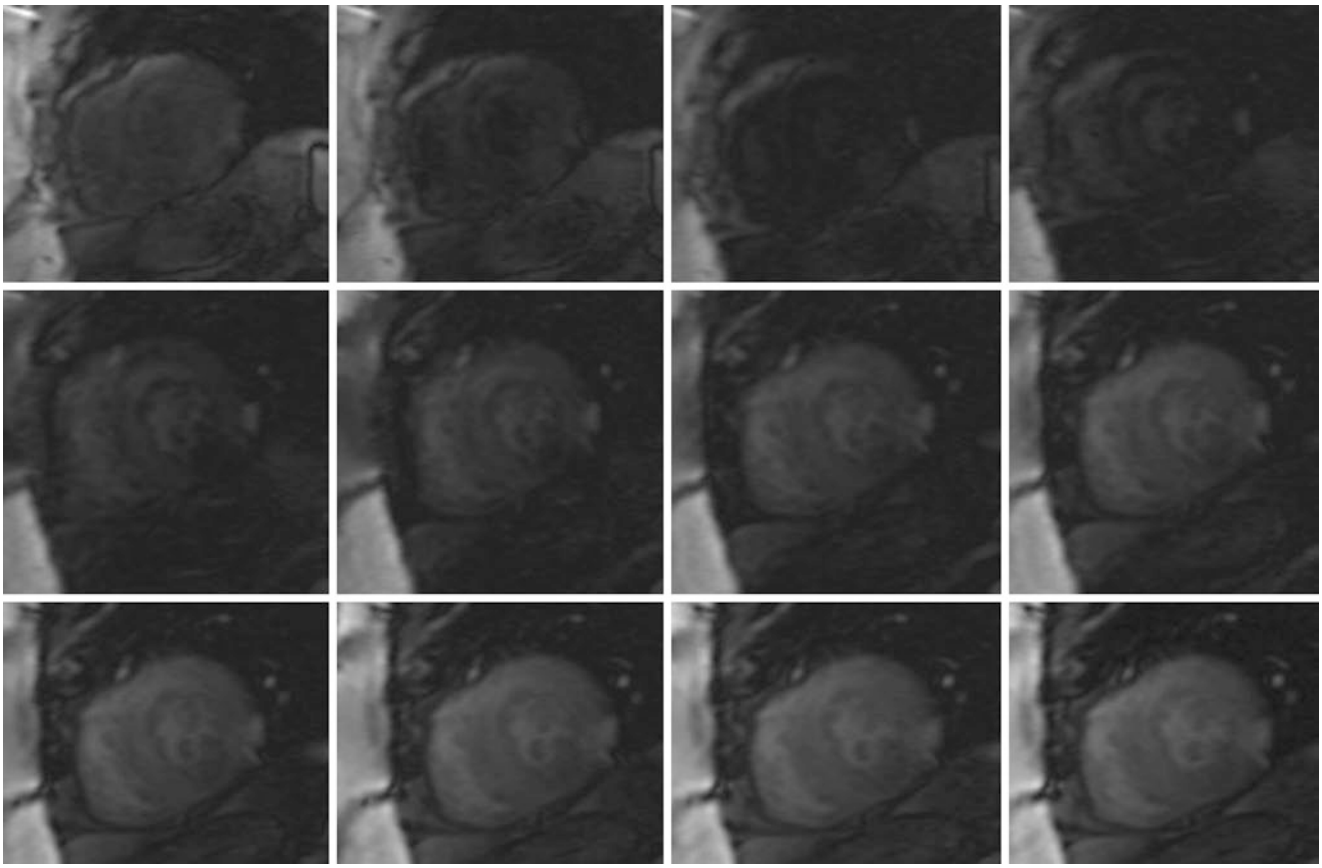

Fig. 15.8 TI scout classical for cardiac amyloidosis with blood pool seen to null before the LV myocardium. The TI time is seen to increase in each frame from top left to bottom right panel

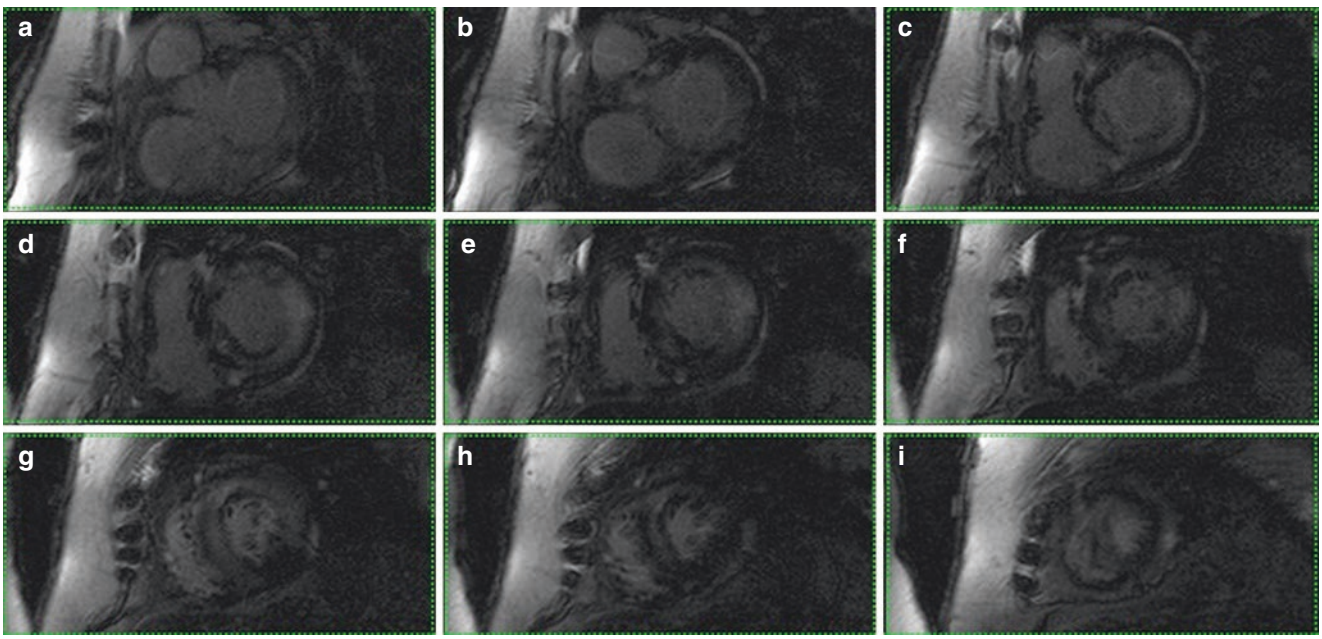

Fig. 15.9 *Cardiac amyloidosis*. LGE images of the basal (**a–d**), mid (**e–g**), and apical (**h, i**) LV and RV reveal extensive concentric early and late gadolinium enhancement in a subendocardial pattern with relative sparing of the epicardium, in a pattern classical for cardiac amyloidosis

While MRI is an excellent tool for the detection of fibrosis in cardiac amyloid, distinction between different forms is not possible with currently available techniques. That said, it is still a very important tool in evaluation of suspected cases and together with other complementary imaging modalities such as technetium pyrophosphate (PYP) scanning is a commonly used tool in clinical practice.

Cardiac Sarcoidosis

Sarcoidosis is a chronic multisystem disorder of unclear etiology. It is characterized by the accumulation of T-lymphocytes and mononuclear phagocytes into noncaseating granuloma [92–94]. The most commonly affected organ systems include the lungs, lymph nodes, skin, eyes, and the central nervous system. Common cardiac modes of presentation can be divided into arrhythmic, cardiomyopathic, and pericardial [94, 95]. Less commonly reported manifestations include direct granulomatous involvement of individual heart valves [96], coronary artery granulomatous disease causing myocardial ischemia [97], constrictive pericarditis [98], and intracardiac masses [96]. It has been described how the presence of cardiomyopathy with LVEF <50% and clinical heart failure carries a particularly poor prognosis [99]. The annual incidence of sarcoidosis in the USA is 10.9 per 100,000 in Caucasians and 35.5 per 100,000 in African Americans [100]. Women aged 20–40 carry the highest incidence of systemic sarcoidosis, although myocardial sarcoidosis seems to carry no gender predilection. Up to one third of all patients with sarcoidosis have pathologic cardiac involvement [95]. Despite this, only approximately 3–5% of all sarcoid patients will have clinically evident cardiac involvement [101]. It is thus likely that many cases of cardiac sarcoidosis go clinically unrecognized. Cardiac involvement from sarcoidosis accounts for up to 25% of all deaths from sarcoidosis in the USA and up to 85% of deaths in Japanese patients with sarcoidosis [102]. A recent paper from Europe has suggested that the incidence of isolated cardiac sarcoidosis could be as high as 65% [103]. Thus the detection of possible cases of this condition becomes ever more important.

With its high spatial resolution and excellent performance characteristics, cardiac MRI is emerging as the gold standard for the diagnosis of cardiac involvement in sarcoidosis. Early enhancement of sarcoid granulomas in T2-weighted images suggests the presence of inflammation and edema, whereas delayed enhancement indicates fibrotic changes and scarring [104, 105]. CMR can also demonstrate both active inflammation and areas of myocardial scar [106, 107], to establish a response to treatment help to determine prognosis. LGE is often found in the mid myocardium and epicardium, often in the basal and lateral segments of the LV and the papillary muscles [106], as well as at the RV insertion points, at the basal anterolateral and inferolateral walls. This is in contrast to the endocardial pattern seen in ischemic cardiomyopathy, which typically follows a coronary artery distribution. In cases where tissue diagnosis is sought, areas of inflammation on T2-weighted imaging or LGE images can be targeted for endomyocardial biopsy. It is likely that a future iteration of diagnostic criteria for cardiac sarcoidosis may rely heavily on CMR findings [95].

Case 8

A 57-year-old female with a diagnosis of neurological sarcoidosis (based on lumbar puncture) and thoracic lymph node biopsy-proven systemic sarcoidosis, referred for CMR to evaluate for suspected cardiac involvement due to recurrent syncope. Transthoracic echocardiography was normal apart from grade I diastolic dysfunction (Figs. 15.10 and 15.11)**.**

Fabry Disease

Anderson-Fabry disease (AFD) is an X-linked lysosomal storage disease caused by a deficient activity of the enzyme a-galactosidase A [108]. An inborn error in metabolism, it can result in the accumulation of glycosphingolipid in multiple organs, including the heart. The cardiac manifestations of AFD include conduction defects, supraventricular and ventricular arrhythmias, and HF symptoms with associated progressive LV dysfunction. AFD patients can present in a similar fashion to HCM patients, with concentric LVH on echocardiography and heart failure symptoms. Contrast-enhanced CMR can be useful to differentiate between such cases by allowing myocardial tissue characterization, which may influence diagnosis. CMR findings can include concentric LVH, biatrial enlargement, and LGE confined to the mid myocardium, typically of the inferolateral wall.

Recent work investigating the use of T1 mapping in distinguishing the different causes of LVH, including hypertension, severe aortic stenosis, HCM, AL amyloid, and AFD [109], studied 227 subjects with these conditions, including healthy volunteers. Compared with healthy volunteers, septal T1 was found to be lower in AFD and higher in other diseases ($P < 0.0001$). In patients with LVH ($n = 105$), T1 effectively discriminated between AFD and other diseases with no overlap [109]. In AFD, T1 correlated inversely with wall thickness ($r = -0.51$; $P = 0.0004$) and was abnormal in 40% of subjects who did not have evidence of LV hypertrophy. Thus non-contrast T1 mapping, a method not currently in routine clinical use, shows its potential as a unique and powerful measurement in the imaging assessment of LVH and AFD.

Iron Overload

Myocardial iron overload can occur as a result of conditions such as hereditary hemochromatosis or frequent blood transfusions in thalassemia patients. Iron deposition within the myocardium and other organs results in fibrosis which can be detected by MRI. Even cases of mild myocardial fibrosis may present with conduction disturbances or systolic or

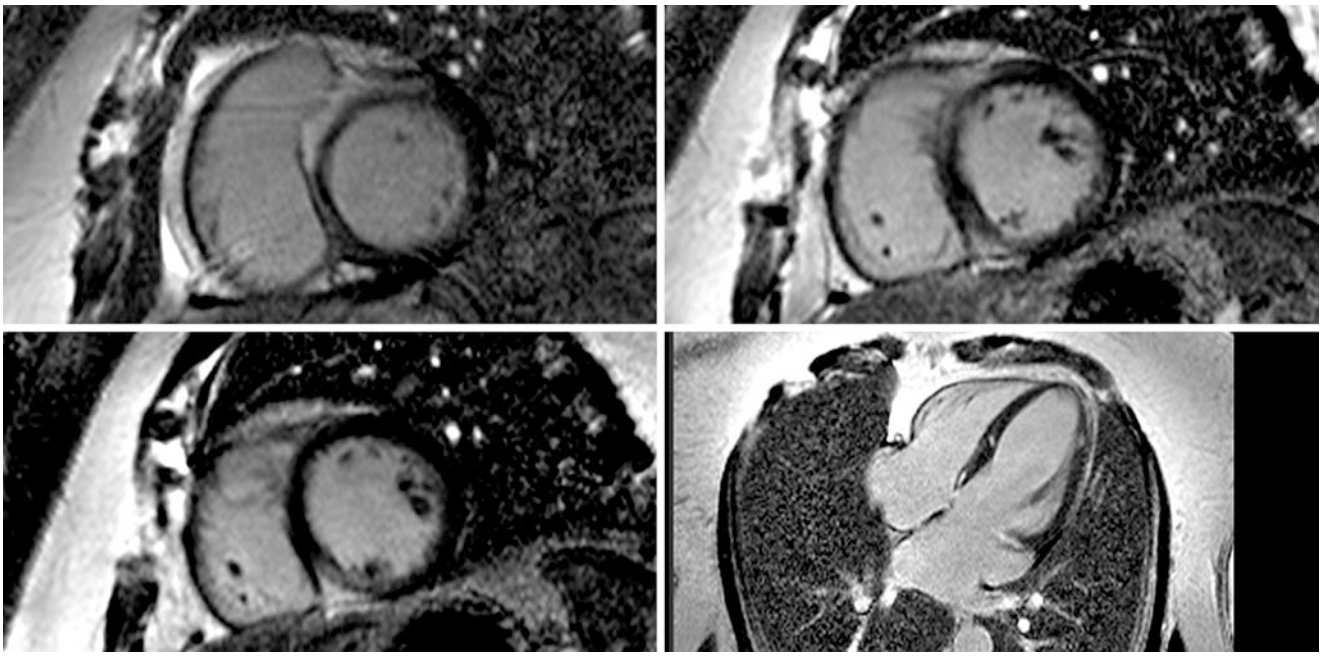

Fig. 15.10 *Cardiac sarcoidosis*. LGE images of the basal, mid, and apical LV and RV reveal multiple foci of epicardial LGE involving the basal and mid anteroseptum and inferoseptum at the RV insertion points, in a pattern classical for cardiac sarcoidosis

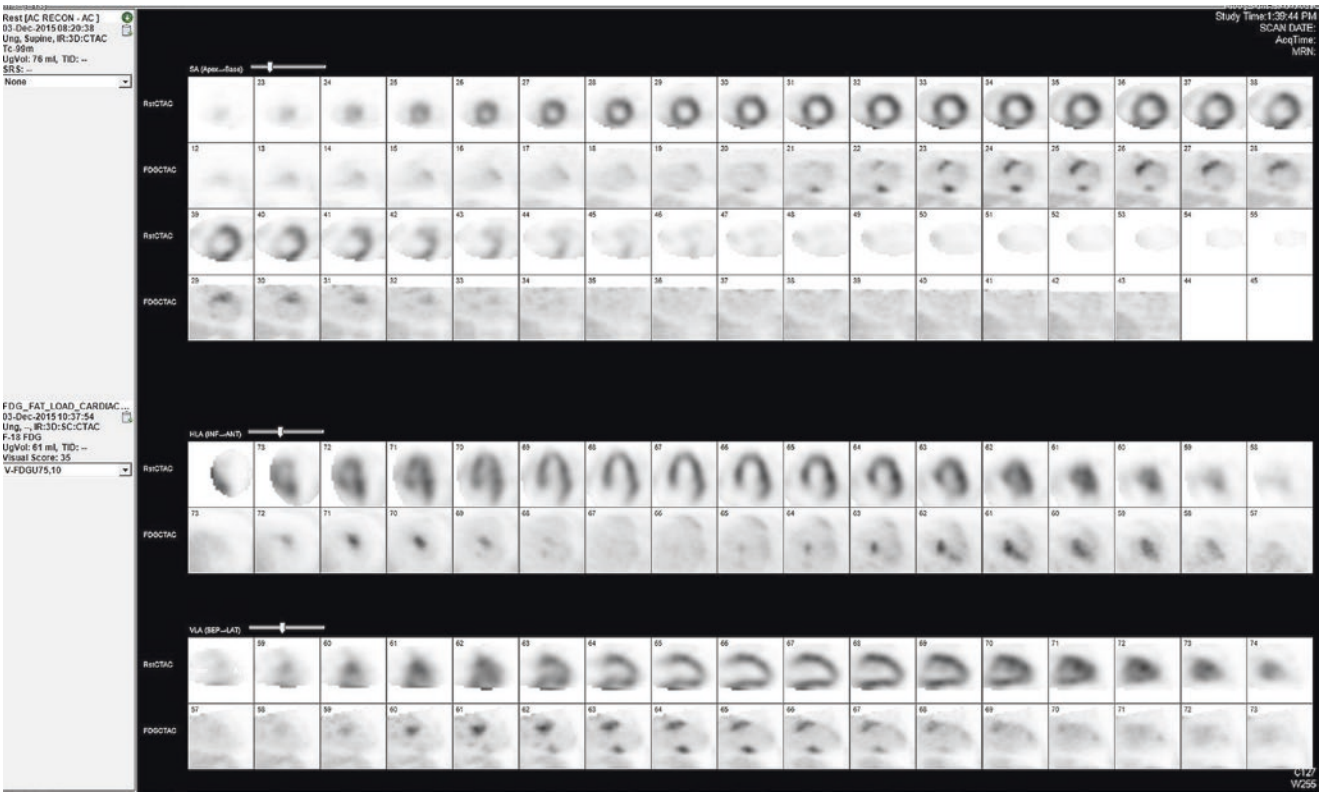

Fig. 15.11 Rest perfusion (top row) and FDG (bottom row) PET images reveal short-axis slices from apex (left) to base (right) and consistent with a small perfusion defect of mild intensity involving the mid and basal anteroseptal wall, with an associated matching focus of intense FDG uptake (perfusion-FDG mismatch). There is also a small perfusion defect of mild intensity in the mid inferoseptal wall, also associated with focal FDG uptake. The vertical (bottom images) and horizontal (middle images) long-axis images confirm these findings

diastolic dysfunction [110]. Quantification of iron content by CMR utilizes the magnetic interaction on a molecular level of iron and hydrogen protons which generates a detectable signal. This method can follow the effectiveness of chelation therapy and ultimately determine prognosis.

By using gradient-echo images collected from stepwise prolonged echo times (TEs), the signal intensity of the myocardium weakens accordingly due to T2* effects. By plotting a region of interest over the myocardium, such a rate of signal decay can be quantified by an exponential decay curve [111]. At a field strength of 1.5 T, the reported normal value for T2* is 36–68 ms. Myocardial iron overload is present when T2* is <20 ms [112], and heart failure usually only occurs when myocardial T2* is <10 ms [113]. Myocardial iron assessment is possible also at 3T [114]; however, in cases where iron overload is known or suspected, we prefer to scan at 1.5T as this is a more validated method.

Peripartum Cardiomyopathy

Peripartum cardiomyopathy is a condition marked by the development of maternal systolic heart failure late in pregnancy or early in the postpartum period [115]. The incidence is approximately 1 in 1,000 to 1 in 4,000 in the USA. Known risk factors for the development of this condition include the presence of preeclampsia, twin gestation, and advanced maternal age [116]. Among patients affected by this condition, heart failure can resolve but often does not: mortality rates of 5–10% are common, and 4% of cardiac transplantations in the USA among women are performed for the treatment of peripartum cardiomyopathy [116]. Peripartum cardiomyopathy shares some clinical features with idiopathic dilated cardiomyopathy, including decreased systolic function, enlarged cardiac dimensions, and nonspecific histologic findings on biopsy. Cardiac MRI is usually avoided during pregnancy as the risks of magnetic radiation and gadolinium-based compounds during pregnancy are unknown. CMR is a very useful tool in the postpartum period, however, and can also be useful in the follow-up of these patients to assess the evolution of LV systolic function and response to therapies. Typical findings are similar to those of DCM, and with the genetic overlap between these two conditions, it is thought that pregnancy may serve as a trigger for the development of symptoms in patients destined to develop DCM due to their genetic makeup.

Case 9

A 31-year-old lady with a history of hypertension who developed signs and symptoms of heart failure at 36-weeks' gestation during her first pregnancy. Echocardiography revealed severely reduced LV systolic function, with an EF of 15–20%. She improved clinically postdelivery, and a cardiac MRI was requested to evaluate for possible underlying cardiomyopathy (Fig. 15.12).

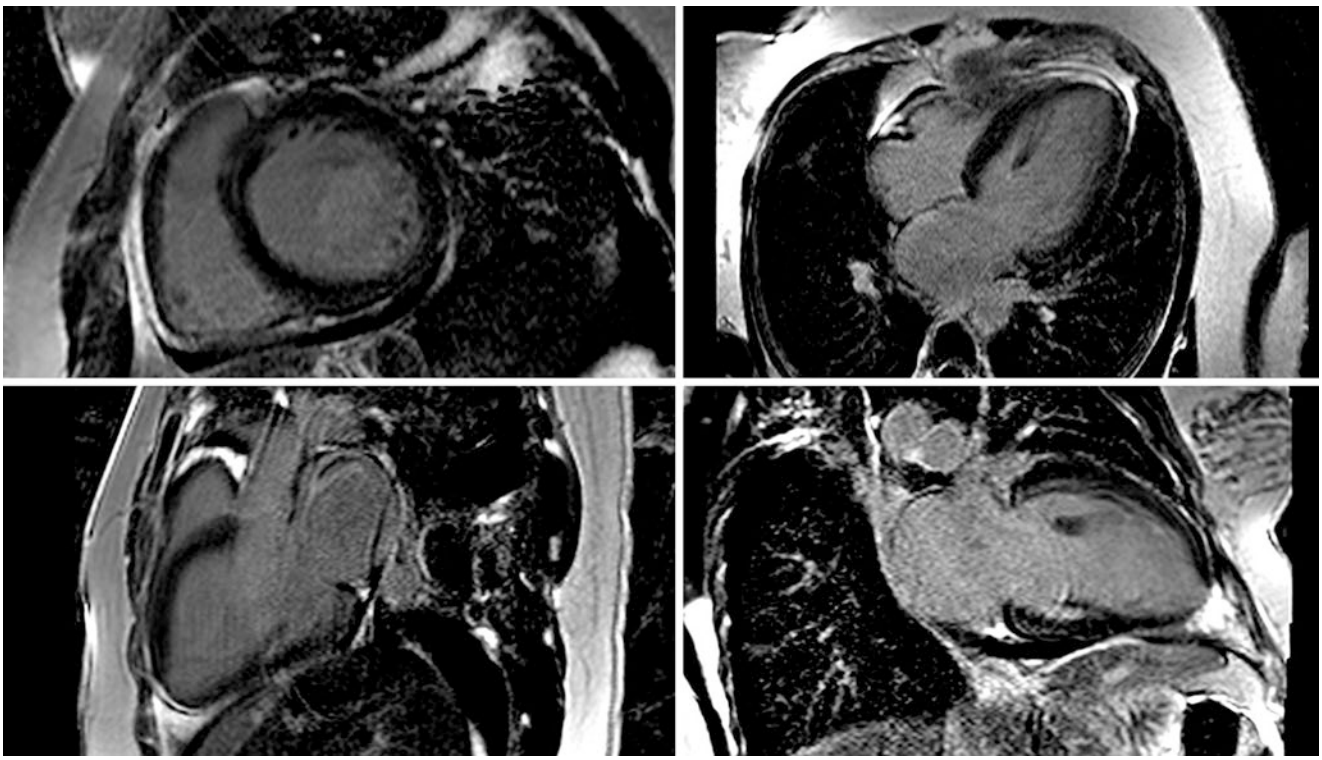

Fig. 15.12 Peripartum cardiomyopathy. LGE images of the basal short-axis RV and LV, four-chamber, three-chamber, and two-chamber views reveal no evidence of LGE. In addition there was no evidence of myocardial edema by T2-weighted imaging. LV systolic function was severely reduced with severe global hypokinesis (LVEF 25%—see additional cine images online). There was no evidence of iron overload on T2* measurement

Subsequent history obtained from the patient revealed that her estranged father had a history of dilated cardiomyopathy. She is being further evaluated with genetic testing as a result.

Takotsubo Cardiomyopathy (Stress Cardiomyopathy)

Takotsubo cardiomyopathy is characterized by a classical clinical presentation with sudden-onset chest pain, EKG changes, elevated cardiac enzymes, and LV apical hypokinesis in the setting of nonobstructed epicardial coronary arteries. Cases classically occur in the setting of acute emotional upset or stress, and the condition is more commonly encountered in women. The underlying cause remains unknown, but theories such as sudden transient increases in catecholamine levels versus aborted MI have been proposed [110]. Typically, CMR reveals a hypokinetic or akinetic apex with sparing of the basal myocardial segments which typically show normal contractility. Also typical is the absence of left ventricular LGE despite significant ventricular dysfunction. Follow-up evaluation characteristically shows resolution of wall motion abnormalities and LV ejection fraction [117, 118].

Case 10

An 88-year-old female with acute-onset chest pain and LV dysfunction by echocardiography. CMR revealed all four apical segments, and the true apex was severely hypokinetic, with hyperdynamic motion of the basal segments. Resting first-pass perfusion was normal, and there was no LGE to suggest prior infarction, inflammation, or fibrosis. There was no myocardial edema by T2-weighted imaging. The patient had classical appearance on left ventriculogram at cardiac cath of Takotsubo cardiomyopathy. CMR findings were in keeping with the clinical- and cath-based diagnosis.

Diagnostic and Prognostic Performance of Cardiac MRI

Ischemia

In recent years, numerous trials have studied the performance of stress perfusion CMR with other diagnostic imaging modalities such as dobutamine echo and myocardial SPECT imaging. The MR-IMPACT II trial [119], including 533 patients in 33 centers, compared the diagnostic performance of CMR vs. SPECT for the detection of perfusion deficits in CAD (defined as ≥75% area reduction in coronary vessels in conventional X-ray coronary angiography CXA). Patients were characterized by the presence of CAD by CXA (reference standard), perfusion CMR, and SPECT. Overall the results showed the primary endpoint of non-inferiority of CMR vs. SPECT for the detection of CAD was met for sensitivity, but not for specificity. This large multicenter perfusion trial demonstrates a higher sensitivity of perfusion CMR to detect perfusion deficits in CAD than SPECT. However, this level of sensitivity was associated with a specificity for CMR lower than that for SPECT, sensitivity and specificity for CMR of 75% (69–80%) and 59% (52–65%), respectively, as compared to a sensitivity and specificity of 59% and 72%, respectively, for SPECT. The relatively low specificity of perfusion CMR may be related to the fact that perfusion was compared with the macroscopic coronary artery anatomy, which does not assess, for example, collateral flow on the microvascular level. The MR-IMPACT II results are in agreement with the large CE-MARC single-center CMR study [120]. In this trial, a sensitivity of 80% on the receiver-operator characteristic (ROC) curve corresponds to a specificity of ~70% for perfusion CMR [120].

CMR perfusion sequences offer several theoretical and practical advantages over both stress echo and nuclear perfusion [121]. They provide substantially better temporal (≤45 ms) and spatial resolution (1.5 mm × 1.5 mm in-plane resolution) to nuclear imaging and avoid the limitations associated with suboptimal echo windows during stress echo. In addition, CMR involves no ionizing radiation unlike SPECT imaging. Early work that demonstrated the feasibility of dobutamine stress CMR and encouraging results for diagnostic accuracy has been confirmed [122]. In subsequent years, multiple studies were published using regional wall motion abnormalities on stress CMR to detect flow-limiting coronary disease, reporting sensitivities of 78–91% and specificities of 75–100%. There have been significant advances in cine CMR image acquisition techniques that have added to the strength of the technique, with fast gradient echo sequences being largely superseded by cine SSFP at the more common 1.5T environment, thus allowing for superior myocardial to blood pool contrast. In relation to the type of stress, exercise has been employed as a stressor [123], but the logistics of achieving a sufficiently high level of exercise to provoke ischemia are limited by the confines of the magnet. Therefore, current pharmacological stress is almost universally employed in clinical practice, although studies are ongoing to establish feasibility and accuracy of exercise stress CMR. Cine imaging during vasodilator stress is associated with lower sensitivity [124] and higher specificity for detecting underlying obstructive coronary disease compared to inotropic drugs. This can be explained by the fact that flow heterogeneity does not lead directly to ischemic wall motion abnormalities unless there is a severe perfusion abnormality, where real ischemia is generated. Pharmacologic stress data comparing adenosine and dobutamine reveals sensitivities and specificities for detection of coronary disease by cine CMR imaging of 40% and 96% for adenosine and 89% and 80% for dobutamine [125]. The clinical utility of dobu-

tamine cine CMR has been examined in detail. In a study comparing ischemia-induced wall motion abnormalities between dobutamine cine CMR and dobutamine stress echocardiography (DSE) in consecutive patients with suspected CAD prior to cardiac catheterization, dobutamine cine CMR possessed better sensitivity (89% vs. 74%) and specificity (86% vs. 70%) than DSE for detecting >50% coronary artery stenosis [126]. In a similar study, Hundley et al. performed dobutamine cine CMR on 163 patients with poor echo windows and demonstrated 83% sensitivity and specificity in detecting >50% coronary stenosis on quantitative coronary angiography [127]. In addition, dobutamine cine CMR was associated with a negative predictive value of 97% for cardiac events over the subsequent 8-month period [128].

Low-dose dobutamine CMR may be used as a predictor of functional recovery following revascularization [129] and has proven particularly useful in those patients with intermediate transmurality of myocardial necrosis. However, the alternative LGE technique has been shown to be a better predictor of functional recovery compared to low-dose dobutamine stress. Data from Gutberlet et al. [130] demonstrated how, in 20 patients examined before and 6 months after successful revascularization, the LGE method showed the best results for predicting functional recovery compared to alternative methods such as low-dose dobutamine stress, wall thickness, and also SPECT imaging. Other recent work from Bodi et al. [131] reveals how a comprehensive CMR assessment is useful for stratifying risk soon after STEMI and how the extent of systolic dysfunction and transmural necrosis provides independent prognostic information.

DCM

The presence and extent of LGE as a marker of fibrosis in DCM have been linked to increased risk of ventricular arrhythmias and sudden cardiac death, independent of other markers of risk such as reduced left ventricular systolic function [132, 133]. Additional data from Wu et al. who studied patients with DCM referred for implantation of an ICD reported an eightfold increased risk of heart failure, ventricular arrhythmias, and cardiac death in patients with evidence of LGE on delayed enhancement imaging [134].

ARVC

In ARVC patients, the presence of myocardial late gadolinium enhancement as part of a dedicated protocol appears as the most discriminating factor with a high diagnostic sensitivity and specificity [135]. Although the prognostic value of CMR in ARVC is still under investigation, LGE appears to have the ability to predict inducibility of sustained ventricular tachycardia and occurrence of RV dysfunction [136]. However, lack of specificity of the pattern of LGE combined with recent revision of taskforce imaging criteria (requiring the combination of wall motion abnormality with global RV dilation or dysfunction) may not have improved the sensitivity of cardiac MRI in detection of ARVC despite keeping high specificity [137, 138].

HCM

Echocardiography has in the past failed to demonstrate LV hypertrophy in HCM patients and indeed has been seen to underestimate hypertrophy, particularly in the anterolateral wall, when compared to CMR [7]. Due to occasional difficulty visualizing the apex clearly by echocardiography, it is also possible to miss the diagnosis of apical-variant HCM by this technique, as seen in cases subsequently identified by CMR [9]. LGE imaging in HCM patients is a significant advantage of CMR over echo. The extent of LGE in HCM patients appears to be related to the occurrence of ventricular arrhythmias both at rest and during exercise, as well as increased risk of sudden cardiac death [139, 140]. Taken together with other adverse risk factors (such as hypotensive blood pressure response to exercise, gene mutations, family history of SCD, and septal thickness exceeding 30 mm), LGE can be useful in determining prognosis in HCM patients but is not currently useful as an independent risk factor for adverse prognosis [141]. Bruder et al. [142] showed that in HCM patients, the presence of LGE was associated with an odds ratio of 5.47 for all-cause mortality and 8.01 for cardiac mortality. This odds ratio was greater than that associated with the presence of two clinical risk factors for SCD and held up as a strong predictor of the primary endpoints in multivariate analysis.

CMR-detected myocardial fibrosis in HCM is associated with increased incidence of atrial fibrillation (AF) and heart failure, heralding advanced LV remodeling and systolic dysfunction [138, 141]. Interestingly, while HCM patients without LGE have been observed to have an excellent prognosis, LGE involving ≥5% of LV mass, septal thickness ≥30 mm, and AF are independent predictors of death and ICD discharges [138].

Sarcoidosis

CMR has been shown to be more sensitive for disease detection in cardiac sarcoidosis than thallium SPECT and gallium SPECT [105]. Studies have demonstrated that 18 F-2-fluoro-2-deoxyglucose positron emission tomography (FDG-PET) is as sensitive as CMR for detection of earlier stages of sarcoidosis [143]. Studies using the widely described Japanese

Ministry of Health, Labour, and Welfare criteria as a gold standard have shown CMR to have a diagnostic sensitivity of 100% [144]. LGE appears to be twice as sensitive as current consensus criteria for detection of cardiac sarcoidosis, and in one study the presence of LGE portended a ninefold higher rate of adverse events including cardiac death [145]. Patients with LGE have a higher rate of diastolic dysfunction, reduced RVEF, and evidence of non-sustained ventricular tachycardia [146]. Myocardial LGE may also be used as a guide for localization during endomyocardial biopsy and in addition is helpful in monitoring the efficacy of steroid therapy [147]. However, LGE pattern is nonspecific in cardiac sarcoidosis, and the predictive value of a negative CMR remains unknown.

Use of CMR in Posttransplant Evaluation

Despite significant advances in antirejection therapy in recent years, acute cellular allograft rejection remains a leading cause of early mortality among cardiac transplant patients. The diagnostic gold standard technique for detection is repeated endomyocardial biopsy, a procedure largely limited by insensitivity. Posttransplant CMR can assist the detection of rejection, through measurement of myocardial T2 relaxation time. This technique typically has sensitivities and specificities approaching 90%, except during the early perioperative period which is characterized by normal postoperative edema [148]. A complete normalization of T2 relaxation times has been described following treatment of rejection [149]. It has also been suggested that the high sensitivity of such CMR techniques might help to predict rejection in some biopsy-negative patients [149].

Although many transplant centers use echocardiography to detect cardiac allograft systolic dysfunction in the setting of cardiac rejection, CMR enables imaging throughout the cardiac cycle and provides excellent spatial resolution to accurately measure diastolic and systolic volumes and hence left and right ventricular ejection fraction [150].

Beyond the first year, transplant coronary artery disease (TCAD) is the second most common cause of death after malignancy. Patterns and prevalence of LGE have been studied in cardiac transplant patients undergoing routine coronary angiography [151]. While 50% of patients had a nonischemic pattern of LGE, 30% of event-free patients with nonobstructive coronary disease at catheterization had a typical infarction pattern associated with worse LV function and higher BNP values. The presence of LGE might therefore help earlier diagnosis of TCAD allowing intensification of therapy in selected patients. Data on prognostic implications are awaited.

The use of T1 mapping in posttransplant patients shows promise for detection of increased myocardial ECV in patients with no detectable LGE to date. T1 mapping may be performed before (pre-contrast or native T1, reflecting composite water signal from extracellular space and myocytes) but also after contrast media injection (allowing determination of extracellular volume fraction). T1 mapping seems to have the potential to detect early rejection of transplanted hearts, which may avoid the need for more invasive endomyocardial biopsy, especially in the case of primary graft dysfunction [152].

In general, CMR studies in posttransplant patients have been limited by small sample size with few confirmatory validations. In addition, gadolinium use in patients with acute or chronic severe renal insufficiency (estimated glomerular filtration rate <30 ml/min), which a significant number of these patients have, carries a significant risk for development of nephrogenic systemic fibrosis. Because of these drawbacks and the lack of widespread availability, the role of CMR in evaluation of ACR is still evolving.

The Use of Novel Techniques Such as T1/T2 Mapping

The two most important causes of native T1 augmentation are edema due to (1) increase in tissue water (indicative of recent infarction or inflammation) and (2) increase in interstitial space related to fibrosis (infarction scar, cardiomyopathy) or to cardiac amyloidosis.

Normal native longitudinal relaxation (T1) values at 1.5T measured with MOLLI have been reported to lie between 900 and 1100 ms [153], but these values depend on several physiological and technical parameters. In particular, with increasing magnet strength from 1.5 to 3.0 Tesla field, the augmentation of T1 values has been reported to lie between 14% and 28% [153].

As mentioned above, the T1 is increased in edema resulting from myocardial injury or inflammation, cellular edema, and myocyte necrosis. In addition, T1 is increased in cases of extracellular space expansion, induced by amyloidosis fibril infiltration or by fibrosis, either focal or diffuse. Thus, T1 increase is ubiquitous, and therefore the use of other complementary imaging sequences such as T2-STIR and LGE sequences is required when interpreting these images, as well as bearing in mind the clinical context. On the other hand, the main causes of T1 reduction include fatty infiltration (lipomatous metaplasia), intracellular sphingolipids overload (Anderson-Fabry), and iron overload diseases.

Elevation of T1 values, several SDs above normal, in edematous myocardial tissue allows for the identification of acute MI with sensitivity and specificity >90% [154, 155].

The degree of LGE in such cases appears less extensive than the increased T1 area but is more specific to myocardial necrosis. The difference between the area at risk (indicated

by T1 increase) and necrosis (LGE, with a smaller size) corresponds to the salvaged myocardium. T1 mapping seems to be a more robust technique with increased reproducibility compared to T2-weighted imaging. Indeed increased T1 values have proven prognostic significance [153]. The surface area of abnormal myocardium may be visually estimated and manually drawn; however, this method is prone to subjective over- or underestimation. In practice more "objective" criteria, which are not operator-dependent, should be used, such as pixel count lying over a cutoff value (e.g., >3 SD of the mean normal values) [154]. The timing of T1 sequences is important, e.g., T1 area smaller than LGE area may be seen if imaging is performed too late after the acute event. T1 area smaller than LGE may also be seen in the case of poor slice co-localization (misregistration) or subendocardial infarction. A focal area of increased T1 and T2 may be seen in conditions such as myocarditis and Takotsubo syndrome, as well as recent infarction. In cases of acute myocarditis, this abnormal area is co-localized with regions of LGE [156, 157] because of associated cellular destruction. In contrast, no associated LGE is seen in cases of Takotsubo [156]. Interestingly, diffuse increase in myocardial T1 values, although of lower magnitude, is also observed in acute myocardial conditions as compared with healthy myocardium. In cases of acute myocarditis, the inflammatory process may be diffuse rather than discrete. In this setting, using ShMOLLI at 1.5 T, T1 mapping with a cutoff value of 990 ms offers optimal sensitivity (90%) and specificity (88%) as compared with T2-STIR and LGE imaging native T1 mapping of the heart [153]. It has also been described how the T1 threshold approach is able to diagnose extra cases with small focal islands of myocardial injury, not detected by T2-STIR and LGE imaging [158]. Myocardial inflammation related to several other diseases may also provide focal or diffuse increase in T1 values. Systemic disorders that can affect the heart, such as sarcoïdosis, lupus erythematosus, and systemic sclerosis, are known to induce tissue edema in the acute stage with elevated T2 (and T1) values [159]. In these cases, T1 quantification may be useful to identify cardiac involvement, thus assisting the clinicians determination of organ involvement and prognosis.

Limitations of CMR in Cardiomyopathy Assessment

Certain metallic implants and intracardiac devices (pacemaker, ICD) remain the only absolute contraindication to cardiac MRI, but this will hopefully be overcome in the near future by new-generation CMR-compatible pacing that leads currently in clinical trials. Severe claustrophobia, clinical instability, and the first trimester of pregnancy are among the relative contraindications. Even though gadolinium contrast agents are relatively safe, their use is restricted in chronic renal failure (GFR < 30 ml/min) due to the small but tangible risk of nephrogenic systemic fibrosis (NSF) which is enhanced by concomitant heart failure [160]. On the basis of current available data, in patients with severe renal failure, the first step is to determine whether a non-gadolinium sequence is available and could provide adequate data. If the clinical benefits of LGE-CMR outweigh the risk of NSF, and if no other imaging method can be used to answer the clinical question, following a joint discussion between the referring physician and the patient, stable agents such as gadobenate dimeglumine should be used as the lowest possible dose, avoiding repeat scans within a short time period [161]. Among the few limitations for the use of CMR, the most restrictive issue probably still remains the limited distribution and availability of CMR scanners. With improvements in sequence timing and technological advances in coming years, it is hoped that clinical CMR scans will take at most 30–40 min to complete, and thus widespread use of CMR will become more feasible.

References

1. Cahill TJ, Ashrafian H, Watkins H. Genetic cardiomyopathies causing heart failure. Circ Res. 2013;113(6):660–75.
2. Gersh BJ, Maron BJ, Bonow RO, Dearani JA, Fifer MA, Link MS, et al. 2011 ACCF/AHA guideline for the diagnosis and treatment of hypertrophic cardiomyopathy: executive summary: a report of the American College of Cardiology Foundation/American Heart Association Task Force on Practice Guidelines. J Am Coll Cardiol. 2011;58(25):2703–38.
3. Fananapazir L, Epstein ND, Curiel RV, Panza JA, Tripodi D, McAreavey D. Long-term results of dual-chamber (DDD) pacing in obstructive hypertrophic cardiomyopathy. Evidence for progressive symptomatic and hemodynamic improvement and reduction of left ventricular hypertrophy. Circulation. 1994;90(6):2731–42.
4. Erwin JP 3rd, Nishimura RA, Lloyd MA, Tajik AJ. Dual chamber pacing for patients with hypertrophic obstructive cardiomyopathy: a clinical perspective in 2000. Mayo Clin Proc. 2000;75(2):173–80.
5. Spirito P, Bellone P, Harris KM, Bernabo P, Bruzzi P, Maron BJ. Magnitude of left ventricular hypertrophy and risk of sudden death in hypertrophic cardiomyopathy. N Engl J Med. 2000;342(24):1778–85.
6. Maron MS, Maron BJ, Harrigan C, Buros J, Gibson CM, Olivotto I, et al. Hypertrophic cardiomyopathy phenotype revisited after 50 years with cardiovascular magnetic resonance. J Am Coll Cardiol. 2009;54(3):220–8.
7. Rickers C, Wilke NM, Jerosch-Herold M, Casey SA, Panse P, Panse N, et al. Utility of cardiac magnetic resonance imaging in the diagnosis of hypertrophic cardiomyopathy. Circulation. 2005;112(6):855–61.
8. Maron MS, Lesser JR, Maron BJ. Management implications of massive left ventricular hypertrophy in hypertrophic cardiomyopathy significantly underestimated by echocardiography but identified by cardiovascular magnetic resonance. Am J Cardiol. 2010;105(12):1842–3.
9. Moon JC, Fisher NG, McKenna WJ, Pennell DJ. Detection of apical hypertrophic cardiomyopathy by cardiovascular magnetic

resonance in patients with non-diagnostic echocardiography. Heart. 2004;90(6):645–9.
10. Maron MS, Finley JJ, Bos JM, Hauser TH, Manning WJ, Haas TS, et al. Prevalence, clinical significance, and natural history of left ventricular apical aneurysms in hypertrophic cardiomyopathy. Circulation. 2008;118(15):1541–9.
11. Yancy CW, Jessup M, Bozkurt B, Butler J, Casey DE Jr, Drazner MH, et al. 2013 ACCF/AHA guideline for the management of heart failure: executive summary: a report of the American College of Cardiology Foundation/American Heart Association Task Force on practice guidelines. Circulation. 2013;128(16):1810–52.
12. Banypersad SM, Moon JC, Whelan C, Hawkins PN, Wechalekar AD. Updates in cardiac amyloidosis: a review. J Am Heart Assoc. 2012;1(2):e000364.
13. Morgan RB, Kwong R. Role of cardiac MRI in the assessment of cardiomyopathy. Curr Treat Options Cardiovasc Med. 2015;17(11):53.
14. Kim TK, Lee HJ, Jang HJ, Kim AY, Han JK, Choi BI. T2-weighted breath-hold MRI of the liver at 1.0 T: comparison of turbo spin-echo and HASTE sequences with and without fat suppression. J Magn Reson Imaging. 1998;8(6):1213–8.
15. Shors SM, Fung CW, Francois CJ, Finn JP, Fieno DS. Accurate quantification of right ventricular mass at MR imaging by using cine true fast imaging with steady-state precession: study in dogs. Radiology. 2004;230(2):383–8.
16. Lelieveldt BP, van der Geest RJ, Lamb HJ, Kayser HW, Reiber JH. Automated observer-independent acquisition of cardiac short-axis MR images: a pilot study. Radiology. 2001;221(2):537–42.
17. Kim RJ, Wu E, Rafael A, Chen EL, Parker MA, Simonetti O, et al. The use of contrast-enhanced magnetic resonance imaging to identify reversible myocardial dysfunction. N Engl J Med. 2000;343(20):1445–53.
18. de Mello RA, Nacif MS, dos Santos AA, Cury RC, Rochitte CE, Marchiori E. Diagnostic performance of combined cardiac MRI for detection of coronary artery disease. Eur J Radiol. 2012;81(8):1782–9.
19. Kim RJ, Fieno DS, Parrish TB, Harris K, Chen EL, Simonetti O, et al. Relationship of MRI delayed contrast enhancement to irreversible injury, infarct age, and contractile function. Circulation. 1999;100(19):1992–2002.
20. Kellman P, Arai AE. Imaging sequences for first pass perfusion – a review. J Cardiovasc Magn Reson. 2007;9(3):525–37.
21. Kim RJ, Judd RM, Chen EL, Fieno DS, Parrish TB, Lima JA. Relationship of elevated 23Na magnetic resonance image intensity to infarct size after acute reperfused myocardial infarction. Circulation. 1999;100(2):185–92.
22. Pegg TJ, Selvanayagam JB, Jennifer J, Francis JM, Karamitsos TD, Dall'Armellina E, et al. Prediction of global left ventricular functional recovery in patients with heart failure undergoing surgical revascularisation, based on late gadolinium enhancement cardiovascular magnetic resonance. J Cardiovasc Magn Reson. 2010;12:56.
23. Bourantas CV, Nikitin NP, Loh HP, Lukaschuk EI, Sherwi N, de Silva R, et al. Prevalence of scarred and dysfunctional myocardium in patients with heart failure of ischaemic origin: a cardiovascular magnetic resonance study. J Cardiovasc Magn Reson. 2011;13:53.
24. Chalil S, Foley PW, Muyhaldeen SA, Patel KC, Yousef ZR, Smith RE, et al. Late gadolinium enhancement-cardiovascular magnetic resonance as a predictor of response to cardiac resynchronization therapy in patients with ischaemic cardiomyopathy. Europace. 2007;9(11):1031–7.
25. Cooper LT Jr. Myocarditis. N Engl J Med. 2009;360(15):1526–38.
26. Friedrich MG, Marcotte F. Cardiac magnetic resonance assessment of myocarditis. Circ Cardiovasc Imaging. 2013;6(5):833–9.
27. Kindermann I, Barth C, Mahfoud F, Ukena C, Lenski M, Yilmaz A, et al. Update on myocarditis. J Am Coll Cardiol. 2012;59(9):779–92.
28. Friedrich MG, Sechtem U, Schulz-Menger J, Holmvang G, Alakija P, Cooper LT, et al. Cardiovascular magnetic resonance in myocarditis: a JACC White Paper. J Am Coll Cardiol. 2009;53(17):1475–87.
29. Eitel I, von Knobelsdorff-Brenkenhoff F, Bernhardt P, Carbone I, Muellerleile K, Aldrovandi A, et al. Clinical characteristics and cardiovascular magnetic resonance findings in stress (takotsubo) cardiomyopathy. JAMA. 2011;306(3):277–86.
30. Dall'Armellina E, Piechnik SK, Ferreira VM, Si QL, Robson MD, Francis JM, et al. Cardiovascular magnetic resonance by non contrast T1-mapping allows assessment of severity of injury in acute myocardial infarction. J Cardiovascr Magn Reson. 2012;14:15.
31. h-Ici DO, Ridgway JP, Kuehne T, Berger F, Plein S, Sivananthan M, et al. Cardiovascular magnetic resonance of myocardial edema using a short inversion time inversion recovery (STIR) black-blood technique: diagnostic accuracy of visual and semi-quantitative assessment. J Cardiovasc Magn Reson. 2012;14:22.
32. Abdel-Aty H, Boye P, Zagrosek A, Wassmuth R, Kumar A, Messroghli D, et al. Diagnostic performance of cardiovascular magnetic resonance in patients with suspected acute myocarditis: comparison of different approaches. J Am Coll Cardiol. 2005;45(11):1815–22.
33. Maron BJ, Towbin JA, Thiene G, Antzelevitch C, Corrado D, Arnett D, et al. Contemporary definitions and classification of the cardiomyopathies: an American Heart Association Scientific Statement from the Council on Clinical Cardiology, Heart Failure and Transplantation Committee; Quality of Care and Outcomes Research and Functional Genomics and Translational Biology Interdisciplinary Working Groups; and Council on Epidemiology and Prevention. Circulation. 2006;113(14):1807–16.
34. Flett AS, Hasleton J, Cook C, Hausenloy D, Quarta G, Ariti C, et al. Evaluation of techniques for the quantification of myocardial scar of differing etiology using cardiac magnetic resonance. JACC Cardiovasc Imaging. 2011;4(2):150–6.
35. Bohl S, Wassmuth R, Abdel-Aty H, Rudolph A, Messroghli D, Dietz R, et al. Delayed enhancement cardiac magnetic resonance imaging reveals typical patterns of myocardial injury in patients with various forms of non-ischemic heart disease. Int J Cardiovasc Imaging. 2008;24(6):597–607.
36. Satoh H, Sano M, Suwa K, Saitoh T, Nobuhara M, Saotome M, et al. Distribution of late gadolinium enhancement in various types of cardiomyopathies: Significance in differential diagnosis, clinical features and prognosis. World J Cardiol. 2014;6(7):585–601.
37. Machii M, Satoh H, Shiraki K, Saotome M, Urushida T, Katoh H, et al. Distribution of late gadolinium enhancement in end-stage hypertrophic cardiomyopathy and dilated cardiomyopathy: differential diagnosis and prediction of cardiac outcome. Magn Reson Imaging. 2014;32(2):118–24.
38. Matoh F, Satoh H, Shiraki K, Saitoh T, Urushida T, Katoh H, et al. Usefulness of delayed enhancement magnetic resonance imaging to differentiate dilated phase of hypertrophic cardiomyopathy and dilated cardiomyopathy. J Cardiac Fail. 2007;13(5):372–9.
39. Kramer CM, Narula J. Viability is in the eye of the beholder. JACC Cardiovasc Imaging. 2012;5(5):574–5.
40. Puntmann VO, Voigt T, Chen Z, Mayr M, Karim R, Rhode K, et al. Native T1 mapping in differentiation of normal myocardium from diffuse disease in hypertrophic and dilated cardiomyopathy. JACC Cardiovasc Imaging. 2013;6(4):475–84.
41. Flett AS, Hayward MP, Ashworth MT, Hansen MS, Taylor AM, Elliott PM, et al. Equilibrium contrast cardiovascular magnetic resonance for the measurement of diffuse myocardial fibrosis: preliminary validation in humans. Circulation. 2010;122(2):138–44.

42. Moon JC, Messroghli DR, Kellman P, Piechnik SK, Robson MD, Ugander M, et al. Myocardial T1 mapping and extracellular volume quantification: a Society for Cardiovascular Magnetic Resonance (SCMR) and CMR Working Group of the European Society of Cardiology consensus statement. J Cardiovasc Magn Reson. 2013;15:92.
43. Maron BJ, Maron MS. Hypertrophic cardiomyopathy. Lancet. 2013;381(9862):242–55.
44. Bos JM, Towbin JA, Ackerman MJ. Diagnostic, prognostic, and therapeutic implications of genetic testing for hypertrophic cardiomyopathy. J Am Coll Cardiol. 2009;54(3):201–11.
45. Basso C, Thiene G, Mackey-Bojack S, Frigo AC, Corrado D, Maron BJ. Myocardial bridging, a frequent component of the hypertrophic cardiomyopathy phenotype, lacks systematic association with sudden cardiac death. Eur Heart J. 2009;30(13):1627–34.
46. Zerhouni EA, Parish DM, Rogers WJ, Yang A, Shapiro EP. Human heart: tagging with MR imaging – a method for noninvasive assessment of myocardial motion. Radiology. 1988;169(1):59–63.
47. Shehata ML, Cheng S, Osman NF, Bluemke DA, Lima JA. Myocardial tissue tagging with cardiovascular magnetic resonance. J Cardiovasc Magn Reson. 2009;11:55.
48. Pai VM, Axel L. Advances in MRI tagging techniques for determining regional myocardial strain. Curr Cardiol Rep. 2006;8(1):53–8.
49. Edvardsen T, Gerber BL, Garot J, Bluemke DA, Lima JA, Smiseth OA. Quantitative assessment of intrinsic regional myocardial deformation by Doppler strain rate echocardiography in humans: validation against three-dimensional tagged magnetic resonance imaging. Circulation. 2002;106(1):50–6.
50. Zwanenburg JJ, Kuijer JP, Marcus JT, Heethaar RM. Steady-state free precession with myocardial tagging: CSPAMM in a single breathhold. Magn Reson Med. 2003;49(4):722–30.
51. Herzka DA, Guttman MA, McVeigh ER. Myocardial tagging with SSFP. Magn Reson Med. 2003;49(2):329–40.
52. Kramer U, Deshpande V, Fenchel M, Klumpp B, Laub G, Finn JP, et al. [Cardiac MR tagging: optimization of sequence parameters and comparison at 1.5 T and 3.0 T in a volunteer study]. RoFo: Fortschritte auf dem Gebiete der Rontgenstrahlen und der Nuklearmedizin. 2006;178(5):515–24. Epub 2006/04/06. Kardiales MR-Tagging: Parameteroptimierung und Sequenzvergleich bei 1.5 T und 3.0 T an einem Probandenkollektiv.
53. Chiribiri A, Leuzzi S, Conte MR, Bongioanni S, Bratis K, Olivotti L, et al. Rest perfusion abnormalities in hypertrophic cardiomyopathy: correlation with myocardial fibrosis and risk factors for sudden cardiac death. Clin Radiol. 2015;70(5):495–501.
54. Maron MS. Clinical utility of cardiovascular magnetic resonance in hypertrophic cardiomyopathy. J Cardiovasc Magn Reson. 2012;14:13.
55. Moon JC, Reed E, Sheppard MN, Elkington AG, Ho SY, Burke M, et al. The histologic basis of late gadolinium enhancement cardiovascular magnetic resonance in hypertrophic cardiomyopathy. J Am Coll Cardiol. 2004;43(12):2260–4.
56. Moon JC, McKenna WJ, McCrohon JA, Elliott PM, Smith GC, Pennell DJ. Toward clinical risk assessment in hypertrophic cardiomyopathy with gadolinium cardiovascular magnetic resonance. J Am Coll Cardiol. 2003;41(9):1561–7.
57. Maron MS. Contrast-enhanced CMR in HCM: what lies behind the bright light of LGE and why it now matters. JACC Cardiovasc Imaging. 2013;6(5):597–9.
58. Kwong RY, Farzaneh-Far A. Measuring myocardial scar by CMR. JACC Cardiovasc Imaging. 2011;4(2):157–60.
59. Harrigan CJ, Peters DC, Gibson CM, Maron BJ, Manning WJ, Maron MS, et al. Hypertrophic cardiomyopathy: quantification of late gadolinium enhancement with contrast-enhanced cardiovascular MR imaging. Radiology. 2011;258(1):128–33.
60. Ho CY, Abbasi SA, Neilan TG, Shah RV, Chen Y, Heydari B, et al. T1 measurements identify extracellular volume expansion in hypertrophic cardiomyopathy sarcomere mutation carriers with and without left ventricular hypertrophy. Circ Cardiovasc Imaging. 2013;6(3):415–22.
61. Harris KM, Spirito P, Maron MS, Zenovich AG, Formisano F, Lesser JR, et al. Prevalence, clinical profile, and significance of left ventricular remodeling in the end-stage phase of hypertrophic cardiomyopathy. Circulation. 2006;114(3):216–25.
62. Azaouagh A, Churzidse S, Konorza T, Erbel R. Arrhythmogenic right ventricular cardiomyopathy/dysplasia: a review and update. Clin Res Cardiol. 2011;100(5):383–94.
63. Heermann P, Hedderich DM, Paul M, Schulke C, Kroeger JR, Baessler B, et al. Biventricular myocardial strain analysis in patients with arrhythmogenic right ventricular cardiomyopathy (ARVC) using cardiovascular magnetic resonance feature tracking. J Cardiovasc Magn Reson. 2014;16:75.
64. Marcus FI, McKenna WJ, Sherrill D, Basso C, Bauce B, Bluemke DA, et al. Diagnosis of arrhythmogenic right ventricular cardiomyopathy/dysplasia: proposed modification of the task force criteria. Circulation. 2010;121(13):1533–41.
65. Frans van Hoorn JP, Spears D, Nguyen ET, Wald RM, Ley S, Torres FS, et al. Low diagnostic yield of Late Gadolinium Enhancement (LGE) in screening patients with suspected Arrhythmogenic Right Ventricular Cardiomyopathy (ARVC) by Cardiovascular Magnetic Resonance (CMR). J Cardiovasc Magn Reson. 2012;14(Suppl 1):141.
66. Bluemke DA. ARVC: imaging diagnosis is still in the eye of the beholder. JACC Cardiovasc Imaging. 2011;4(3):288–91.
67. Grant RT. An unusual anomaly of the coronary vessels in the malformed heart of a child. Heart. 1926;13:273–83.
68. Freedom RM, Yoo SJ, Perrin D, Taylor G, Petersen S, Anderson RH. The morphological spectrum of ventricular noncompaction. Cardiol Young. 2005;15(4):345–64.
69. Zhang W, Chen H, Qu X, Chang CP, Shou W. Molecular mechanism of ventricular trabeculation/compaction and the pathogenesis of the left ventricular noncompaction cardiomyopathy (LVNC). Am J Med Genet C Semin Med Genet. 2013;163C(3):144–56.
70. Bax JJ, Atsma DE, Lamb HJ, Rebergen SA, Bootsma M, Voogd PJ, et al. Noninvasive and invasive evaluation of noncompaction cardiomyopathy. J Cardiovasc Magn Reson. 2002;4(3):353–7.
71. Weiford BC, Subbarao VD, Mulhern KM. Noncompaction of the ventricular myocardium. Circulation. 2004;109(24):2965–71.
72. Roberts WC, Karia SJ, Ko JM, Grayburn PA, George BA, Hall SA, et al. Examination of isolated ventricular noncompaction (hypertrabeculation) as a distinct entity in adults. Am J Cardiol. 2011;108(5):747–52.
73. Murphy RT, Thaman R, Blanes JG, Ward D, Sevdalis E, Papra E, et al. Natural history and familial characteristics of isolated left ventricular non-compaction. Eur Heart J. 2005;26(2):187–92.
74. Petersen SE, Selvanayagam JB, Wiesmann F, Robson MD, Francis JM, Anderson RH, et al. Left ventricular non-compaction: insights from cardiovascular magnetic resonance imaging. J Am Coll Cardiol. 2005;46(1):101–5.
75. Daimon Y, Watanabe S, Takeda S, Hijikata Y, Komuro I. Two-layered appearance of noncompaction of the ventricular myocardium on magnetic resonance imaging. Circ J. 2002;66(6):619–21.
76. Alsaileek AA, Syed I, Seward JB, Julsrud P. Myocardial fibrosis of left ventricle: magnetic resonance imaging in noncompaction. J Magn Reson Imaging. 2008;27(3):621–4.
77. Klaassen S, Probst S, Oechslin E, Gerull B, Krings G, Schuler P, et al. Mutations in sarcomere protein genes in left ventricular noncompaction. Circulation. 2008;117(22):2893–901.
78. Shemisa K, Li J, Tam M, Barcena J. Left ventricular noncompaction cardiomyopathy. Cardiovasc Diag Ther. 2013;3(3):170–5.

79. Oechslin EN, Attenhofer Jost CH, Rojas JR, Kaufmann PA, Jenni R. Long-term follow-up of 34 adults with isolated left ventricular noncompaction: a distinct cardiomyopathy with poor prognosis. J Am Coll Cardiol. 2000;36(2):493–500.
80. Ritter M, Oechslin E, Sutsch G, Attenhofer C, Schneider J, Jenni R. Isolated noncompaction of the myocardium in adults. Mayo Clin Proc. 1997;72(1):26–31.
81. Banypersad SM, Fontana M, Maestrini V, Sado DM, Captur G, Petrie A, et al. T1 mapping and survival in systemic light-chain amyloidosis. Eur Heart J. 2015;36(4):244–51.
82. Duston MA, Skinner M, Shirahama T, Cohen AS. Diagnosis of amyloidosis by abdominal fat aspiration. Analysis of four years' experience. Am J Med. 1987;82(3):412–4.
83. Falk RH, Skinner M. The systemic amyloidoses: an overview. Adv Intern Med. 2000;45:107–37.
84. Maceira AM, Joshi J, Prasad SK, Moon JC, Perugini E, Harding I, et al. Cardiovascular magnetic resonance in cardiac amyloidosis. Circulation. 2005;111(2):186–93.
85. vanden Driesen RI, Slaughter RE, Strugnell WE. MR findings in cardiac amyloidosis. Am J Roentgenol. 2006;186(6):1682–5.
86. Pandey T, Jambhekar K, Shaikh R, Lensing S, Viswamitra S. Utility of the inversion scout sequence (TI scout) in diagnosing myocardial amyloid infiltration. Int J Cardiovasc Imaging. 2013;29(1):103–12.
87. Xia R, Gao F, Sun J, Xia C, Hu Z, Guo Y. Cardiac magnetic resonance imaging of systemic amyloidosis patients with normal left ventricular ejection fraction: an initial study. Pak J Med Sci. 2013;29(6):1300–5.
88. Syed IS, Glockner JF, Feng D, Araoz PA, Martinez MW, Edwards WD, et al. Role of cardiac magnetic resonance imaging in the detection of cardiac amyloidosis. JACC Cardiovasc Imaging. 2010;3(2):155–64.
89. Karamitsos TD, Piechnik SK, Banypersad SM, Fontana M, Ntusi NB, Ferreira VM, et al. Noncontrast T1 mapping for the diagnosis of cardiac amyloidosis. JACC Cardiovasc Imaging. 2013;6(4):488–97.
90. Brooks J, Kramer CM, Salerno M. Markedly increased volume of distribution of gadolinium in cardiac amyloidosis demonstrated by T1 mapping. J Magn Reson Imaging. 2013;38(6):1591–5.
91. Banypersad SM, Sado DM, Flett AS, Gibbs SD, Pinney JH, Maestrini V, et al. Quantification of myocardial extracellular volume fraction in systemic AL amyloidosis: an equilibrium contrast cardiovascular magnetic resonance study. Circ Cardiovasc Imaging. 2013;6(1):34–9.
92. Newman LS, Rose CS, Maier LA. Sarcoidosis. N Engl J Med. 1997;336(17):1224–34.
93. Johns CJ, Scott PP, Schonfeld SA. Sarcoidosis. Annu Rev Med. 1989;40:353–71.
94. Sekhri V, Sanal S, Delorenzo LJ, Aronow WS, Maguire GP. Cardiac sarcoidosis: a comprehensive review. Arch Med Sci. 2011;7(4):546–54.
95. Houston BA, Mukherjee M. Cardiac sarcoidosis: clinical manifestations, imaging characteristics, and therapeutic approach. Clin Med Insights Cardiol. 2014;8(Suppl 1):31–7.
96. Lewin RF, Mor R, Spitzer S, Arditti A, Hellman C, Agmon J. Echocardiographic evaluation of patients with systemic sarcoidosis. Am Heart J. 1985;110(1 Pt 1):116–22.
97. Lam CS, Tolep KA, Metke MP, Glockner J, Cooper LT Jr. Coronary sarcoidosis presenting as acute coronary syndrome. Clin Cardiol. 2009;32(6):E68–71.
98. Garrett J, O'Neill H, Blake S. Constrictive pericarditis associated with sarcoidosis. Am Heart J. 1984;107(2):394.
99. Mantini N, Williams B Jr, Stewart J, Rubinsztain L, Kacharava A. Cardiac sarcoid: a clinician's review on how to approach the patient with cardiac sarcoid. Clin Cardiol. 2012;35(7):410–5.
100. Rybicki BA, Major M, Popovich J Jr, Maliarik MJ, Iannuzzi MC. Racial differences in sarcoidosis incidence: a 5-year study in a health maintenance organization. Am J Epidemiol. 1997;145(3):234–41.
101. Silverman KJ, Hutchins GM, Bulkley BH. Cardiac sarcoid: a clinicopathologic study of 84 unselected patients with systemic sarcoidosis. Circulation. 1978;58(6):1204–11.
102. Doughan AR, Williams BR. Cardiac sarcoidosis. Heart. 2006;92(2):282–8.
103. Kandolin R, Lehtonen J, Airaksinen J, Vihinen T, Miettinen H, Ylitalo K, et al. Cardiac sarcoidosis: epidemiology, characteristics, and outcome over 25 years in a nationwide study. Circulation. 2015;131(7):624–32.
104. Greulich S, Deluigi CC, Gloekler S, Wahl A, Zurn C, Kramer U, et al. CMR imaging predicts death and other adverse events in suspected cardiac sarcoidosis. JACC Cardiovasc Imaging. 2013;6(4):501–11.
105. Smedema JP, Snoep G, van Kroonenburgh MP, van Geuns RJ, Dassen WR, Gorgels AP, et al. Evaluation of the accuracy of gadolinium-enhanced cardiovascular magnetic resonance in the diagnosis of cardiac sarcoidosis. J Am Coll Cardiol. 2005;45(10):1683–90.
106. Kim JS, Judson MA, Donnino R, Gold M, Cooper LT Jr, Prystowsky EN, et al. Cardiac sarcoidosis. Am Heart J. 2009;157(1):9–21.
107. Vignaux O. Cardiac sarcoidosis: spectrum of MRI features. Am J Roentgenol. 2005;184(1):249–54.
108. Nagueh SF. Fabry disease. Heart. 2003;89(8):819–20.
109. Sado DM, White SK, Piechnik SK, Banypersad SM, Treibel T, Captur G, et al. Identification and assessment of Anderson-Fabry disease by cardiovascular magnetic resonance noncontrast myocardial T1 mapping. Circ Cardiovasc Imaging. 2013;6(3):392–8.
110. Steel KE, Kwong RY. Application of cardiac magnetic resonance imaging in cardiomyopathy. Curr Heart Fail Rep. 2008;5(3):128–35.
111. Westwood M, Anderson LJ, Firmin DN, Gatehouse PD, Charrier CC, Wonke B, et al. A single breath-hold multiecho T2* cardiovascular magnetic resonance technique for diagnosis of myocardial iron overload. J Magn Reson Imaging. 2003;18(1):33–9.
112. He T, Gatehouse PD, Kirk P, Mohiaddin RH, Pennell DJ, Firmin DN. Myocardial T*2 measurement in iron-overloaded thalassemia: an ex vivo study to investigate optimal methods of quantification. Magn Reson Med. 2008;60(2):350–6.
113. Kirk P, Roughton M, Porter JB, Walker JM, Tanner MA, Patel J, et al. Cardiac T2* magnetic resonance for prediction of cardiac complications in thalassemia major. Circulation. 2009;120(20):1961–8.
114. Guo H, Au WY, Cheung JS, Kim D, Jensen JH, Khong PL, et al. Myocardial T2 quantitation in patients with iron overload at 3 Tesla. J Magn Reson Imaging. 2009;30(2):394–400.
115. Elkayam U. Clinical characteristics of peripartum cardiomyopathy in the United States: diagnosis, prognosis, and management. J Am Coll Cardiol. 2011;58(7):659–70.
116. Ware JS, Li J, Mazaika E, Yasso CM, DeSouza T, Cappola TP, et al. Shared genetic predisposition in Peripartum and dilated cardiomyopathies. N Engl J Med. 2016;374(3):233–41.
117. Mitchell JH, Hadden TB, Wilson JM, Achari A, Muthupillai R, Flamm SD. Clinical features and usefulness of cardiac magnetic resonance imaging in assessing myocardial viability and prognosis in Takotsubo cardiomyopathy (transient left ventricular apical ballooning syndrome). Am J Cardiol. 2007;100(2):296–301.
118. Scholte AJ, Bax JJ, Stokkel MP, Plokker T, Kaandorp TA, Lamb HJ, et al. Multimodality imaging to diagnose takotsubo cardiomyopathy. J Nuclear Cardiol. 2006;13(1):123–6.
119. Schwitter J, Wacker CM, Wilke N, Al-Saadi N, Sauer E, Huettle K, et al. MR-IMPACT II: Magnetic Resonance Imaging for Myocardial Perfusion Assessment in Coronary artery disease Trial: perfusion-cardiac magnetic resonance vs. single-photon emission computed tomography for the detection of coronary

artery disease: a comparative multicentre, multivendor trial. Eur Heart J. 2013;34(10):775–81.
120. Greenwood JP, Maredia N, Younger JF, Brown JM, Nixon J, Everett CC, et al. Cardiovascular magnetic resonance and single-photon emission computed tomography for diagnosis of coronary heart disease (CE-MARC): a prospective trial. Lancet. 2012;379(9814):453–60.
121. Daly C, Kwong RY. Cardiac MRI for myocardial ischemia. Methodist Debakey Cardiovasc J. 2013;9(3):123–31.
122. Pennell DJ, Underwood SR, Manzara CC, Swanton RH, Walker JM, Ell PJ, et al. Magnetic resonance imaging during dobutamine stress in coronary artery disease. Am J Cardiol. 1992;70(1):34–40.
123. Rerkpattanapipat P, Gandhi SK, Darty SN, Williams RT, Davis AD, Mazur W, et al. Feasibility to detect severe coronary artery stenoses with upright treadmill exercise magnetic resonance imaging. Am J Cardiol. 2003;92(5):603–6.
124. Pennell DJ, Underwood SR, Ell PJ, Swanton RH, Walker JM, Longmore DB. Dipyridamole magnetic resonance imaging: a comparison with thallium-201 emission tomography. Br Heart J. 1990;64(6):362–9.
125. Paetsch I, Jahnke C, Wahl A, Gebker R, Neuss M, Fleck E, et al. Comparison of dobutamine stress magnetic resonance, adenosine stress magnetic resonance, and adenosine stress magnetic resonance perfusion. Circulation. 2004;110(7):835–42.
126. Nagel E, Lehmkuhl HB, Bocksch W, Klein C, Vogel U, Frantz E, et al. Noninvasive diagnosis of ischemia-induced wall motion abnormalities with the use of high-dose dobutamine stress MRI: comparison with dobutamine stress echocardiography. Circulation. 1999;99(6):763–70.
127. Hundley WG, Hamilton CA, Thomas MS, Herrington DM, Salido TB, Kitzman DW, et al. Utility of fast cine magnetic resonance imaging and display for the detection of myocardial ischemia in patients not well suited for second harmonic stress echocardiography. Circulation. 1999;100(16):1697–702.
128. Hundley WG, Morgan TM, Neagle CM, Hamilton CA, Rerkpattanapipat P, Link KM. Magnetic resonance imaging determination of cardiac prognosis. Circulation. 2002;106(18):2328–33.
129. Wellnhofer E, Olariu A, Klein C, Grafe M, Wahl A, Fleck E, et al. Magnetic resonance low-dose dobutamine test is superior to SCAR quantification for the prediction of functional recovery. Circulation. 2004;109(18):2172–4.
130. Gutberlet M, Frohlich M, Mehl S, Amthauer H, Hausmann H, Meyer R, et al. Myocardial viability assessment in patients with highly impaired left ventricular function: comparison of delayed enhancement, dobutamine stress MRI, end-diastolic wall thickness, and TI201-SPECT with functional recovery after revascularization. Eur Radiol. 2005;15(5):872–80.
131. Bodi V, Sanchis J, Nunez J, Mainar L, Lopez-Lereu MP, Monmeneu JV, et al. Prognostic value of a comprehensive cardiac magnetic resonance assessment soon after a first ST-segment elevation myocardial infarction. JACC Cardiovasc Imaging. 2009;2(7):835–42.
132. Assomull RG, Prasad SK, Lyne J, Smith G, Burman ED, Khan M, et al. Cardiovascular magnetic resonance, fibrosis, and prognosis in dilated cardiomyopathy. J Am Coll Cardiol. 2006;48(10):1977–85.
133. Lehrke S, Lossnitzer D, Schob M, Steen H, Merten C, Kemmling H, et al. Use of cardiovascular magnetic resonance for risk stratification in chronic heart failure: prognostic value of late gadolinium enhancement in patients with non-ischaemic dilated cardiomyopathy. Heart. 2011;97(9):727–32.
134. Wu KC, Weiss RG, Thiemann DR, Kitagawa K, Schmidt A, Dalal D, et al. Late gadolinium enhancement by cardiovascular magnetic resonance heralds an adverse prognosis in nonischemic cardiomyopathy. J Am Coll Cardiol. 2008;51(25):2414–21.
135. Sen-Chowdhry S, Prasad SK, Syrris P, Wage R, Ward D, Merrifield R, et al. Cardiovascular magnetic resonance in arrhythmogenic right ventricular cardiomyopathy revisited: comparison with task force criteria and genotype. J Am Coll Cardiol. 2006;48(10):2132–40.
136. Tandri H, Saranathan M, Rodriguez ER, Martinez C, Bomma C, Nasir K, et al. Noninvasive detection of myocardial fibrosis in arrhythmogenic right ventricular cardiomyopathy using delayed-enhancement magnetic resonance imaging. J Am Coll Cardiol. 2005;45(1):98–103.
137. Vermes E, Strohm O, Otmani A, Childs H, Duff H, Friedrich MG. Impact of the revision of arrhythmogenic right ventricular cardiomyopathy/dysplasia task force criteria on its prevalence by CMR criteria. JACC Cardiovasc Imaging. 2011;4(3):282–7.
138. Parsai C, O'Hanlon R, Prasad SK, Mohiaddin RH. Diagnostic and prognostic value of cardiovascular magnetic resonance in non-ischaemic cardiomyopathies. J Cardiovasc Magn Reson. 2012;14:54.
139. Leonardi S, Raineri C, De Ferrari GM, Ghio S, Scelsi L, Pasotti M, et al. Usefulness of cardiac magnetic resonance in assessing the risk of ventricular arrhythmias and sudden death in patients with hypertrophic cardiomyopathy. Eur Heart J. 2009;30(16):2003–10.
140. van Rijsingen IA, Bekkers SC, Schalla S, Hermans-van Ast JF, Snoep G, Alzand BS, et al. Exercise related ventricular arrhythmias are related to cardiac fibrosis in hypertrophic cardiomyopathy mutation carriers. Neth Heart J. 2011;19(4):168–74.
141. Maron MS, Appelbaum E, Harrigan CJ, Buros J, Gibson CM, Hanna C, et al. Clinical profile and significance of delayed enhancement in hypertrophic cardiomyopathy. Circ Heart Fail. 2008;1(3):184–91.
142. Bruder O, Wagner A, Jensen CJ, Schneider S, Ong P, Kispert EM, et al. Myocardial scar visualized by cardiovascular magnetic resonance imaging predicts major adverse events in patients with hypertrophic cardiomyopathy. J Am Coll Cardiol. 2010;56(11):875–87.
143. Sharma S. Cardiac imaging in myocardial sarcoidosis and other cardiomyopathies. Curr Opin Pulm Med. 2009;15(5):507–12.
144. Manins V, Habersberger J, Pfluger H, Taylor AJ. Cardiac magnetic resonance imaging in the evaluation of cardiac sarcoidosis: an Australian single-centre experience. Int Med J. 2009;39(2):77–82.
145. Patel MR, Cawley PJ, Heitner JF, Klem I, Parker MA, Jaroudi WA, et al. Detection of myocardial damage in patients with sarcoidosis. Circulation. 2009;120(20):1969–77.
146. Patel AR, Klein MR, Chandra S, Spencer KT, Decara JM, Lang RM, et al. Myocardial damage in patients with sarcoidosis and preserved left ventricular systolic function: an observational study. Eur J Heart Fail. 2011;13(11):1231–7.
147. Shimada T, Shimada K, Sakane T, Ochiai K, Tsukihashi H, Fukui M, et al. Diagnosis of cardiac sarcoidosis and evaluation of the effects of steroid therapy by gadolinium-DTPA-enhanced magnetic resonance imaging. Am J Med. 2001;110(7):520–7.
148. Wisenberg G, Pflugfelder PW, Kostuk WJ, McKenzie FN, Prato FS. Diagnostic applicability of magnetic resonance imaging in assessing human cardiac allograft rejection. Am J Cardiol. 1987;60(1):130–6.
149. Marie PY, Angioi M, Carteaux JP, Escanye JM, Mattei S, Tzvetanov K, et al. Detection and prediction of acute heart transplant rejection with the myocardial T2 determination provided by a black-blood magnetic resonance imaging sequence. J Am Coll Cardiol. 2001;37(3):825–31.
150. Estep JD, Shah DJ, Nagueh SF, Mahmarian JJ, Torre-Amione G, Zoghbi WA. The role of multimodality cardiac imaging in the transplanted heart. JACC Cardiovasc Imaging. 2009;2(9):1126–40.
151. Steen H, Merten C, Refle S, Klingenberg R, Dengler T, Giannitsis E, et al. Prevalence of different gadolinium enhancement patterns in patients after heart transplantation. J Am Coll Cardiol. 2008;52(14):1160–7.

152. Miller CA, Sarma J, Naish JH, Yonan N, Williams SG, Shaw SM, et al. Multiparametric cardiovascular magnetic resonance assessment of cardiac allograft vasculopathy. J Am Coll Cardiol. 2014;63(8):799–808.
153. Germain P, El Ghannudi S, Jeung MY, Ohlmann P, Epailly E, Roy C, et al. Native T1 mapping of the heart – a pictorial review. Clin Med Insights Cardiol. 2014;8(Suppl 4):1–11.
154. Messroghli DR, Walters K, Plein S, Sparrow P, Friedrich MG, Ridgway JP, et al. Myocardial T1 mapping: application to patients with acute and chronic myocardial infarction. Magn Reson Med. 2007;58(1):34–40.
155. h-Ici DO, Jeuthe S, Al-Wakeel N, Berger F, Kuehne T, Kozerke S, et al. T1 mapping in ischaemic heart disease. Eur Heart J Cardiovasc Imaging. 2014;15(6):597–602.
156. Ferreira VM, Piechnik SK, Dall'Armellina E, Karamitsos TD, Francis JM, Choudhury RP, et al. Non-contrast T1-mapping detects acute myocardial edema with high diagnostic accuracy: a comparison to T2-weighted cardiovascular magnetic resonance. J Cardiovasc Magn Reson. 2012;14:42.
157. Ferreira VM, Piechnik SK, Dall'Armellina E, Karamitsos TD, Francis JM, Ntusi N, et al. Native T1-mapping detects the location, extent and patterns of acute myocarditis without the need for gadolinium contrast agents. J Cardiovasc Magn Reson. 2014;16:36.
158. Ferreira VM, Piechnik SK, Dall'Armellina E, Karamitsos TD, Francis JM, Ntusi N, et al. T(1) mapping for the diagnosis of acute myocarditis using CMR: comparison to T2-weighted and late gadolinium enhanced imaging. JACC Cardiovasc Imaging. 2013;6(10):1048–58.
159. Mirakhur A, Anca N, Mikami Y, Merchant N. T2-weighted imaging of the heart – a pictorial review. Eur J Radiol. 2013;82(10):1755–62.
160. Hillege HL, Nitsch D, Pfeffer MA, Swedberg K, McMurray JJ, Yusuf S, et al. Renal function as a predictor of outcome in a broad spectrum of patients with heart failure. Circulation. 2006;113(5):671–8.
161. Cheong BY, Muthupillai R. Nephrogenic systemic fibrosis: a concise review for cardiologists. Texas Heart Inst J/from the Texas Heart Institute of St Luke's Episcopal Hospital, Texas Children's Hospital. 2010;37(5):508–15.

CMR Assessment of Cardiac Masses

16

Ayaz Aghayev and Michael L. Steigner

Introduction

Cardiac and paracardiac masses can be classified as benign, malignant, and nontumoral mass lesions (Fig. 16.1) [1]. Benign or malignant primary cardiac masses are rare with an incidence of 0.01–0.28% in autopsy and echocardiography series; however, secondary involvement of the heart and pericardium from extracardiac tumors is 20–40 times more than primary cardiac masses [2–4]. In autopsy series, metastatic cardiac involvement has been shown in 10–12% of patients with malignancy [5, 6]. About 75% of all primary cardiac tumors are benign histologically, the most common in adults being myxomas (51%), lipomas (15–20%), papillary fibroelastomas (20%), hemangiomas (5%), fibromas (3%), and rhabdomyomas (1%) [7–9]. Less common benign primary cardiac tumors include paragangliomas, teratomas, neurofibromas, lymphangiomas, and cystic tumor of the atrioventricular node [10]. The remaining 25% of primary cardiac tumors are malignant, 95% of these tumors being sarcomas and 5% lymphomas [11]. Sarcomas represent the second most common primary cardiac tumor after myxomas, and because of the mesenchymal origin of these masses, they may display a wide variety of morphological features. Angiosarcoma (28%) is the most common, followed by undifferentiated sarcoma (12%), rhabdomyosarcoma (11%), fibrosarcoma (8%), osteosarcoma (7%), malignant fibrous histiocytoma (6%), leiomyosarcoma (5%), and others [11].

A. Aghayev (✉) · M. L. Steigner
Brigham and Women's Hospital, Harvard Medical School, Department of Radiology, Boston, MA, USA
e-mail: aaghayev@bwh.harvard.edu; msteigner@bwh.harvard.edu

Clinical Presentation

Most of the cardiac tumors are asymptomatic until they become large enough to cause symptoms [12]. Based on location, size, mobility, and invasiveness, these tumors can produce wide range of symptoms and are known to be great masqueraders of cardiac and systemic diseases [13]. In general, clinical manifestations of cardiac tumors can be classified into four categories: cardiac, systemic, embolic, and metastatic disease [7].

Cardiac Manifestations

The cardiac manifestations of cardiac tumors can result from disrupted electrophysiologic conduction, intracardiac obstruction that can alter hemodynamics, mechanical interference of valvular function, interruption of coronary flow, and pericardial tamponade or constriction [13, 14]. Intramural tumors within the cardiac conduction pathways can cause a wide variety of arrhythmias [15]. Cardiac tumors with a large intracavitary component tend to create more symptoms with hemodynamic alteration due to outflow obstruction or interference of valve function. Usually cardiac symptoms depend on the location and type of tumors.

Systemic Manifestations

Cardiac tumors can cause constitutional symptoms such as fever, chills, fatigue, malaise, and weight loss, which can mimic connective tissue diseases and/or vasculitides [16]. Interestingly not only malignant but also benign lesions are capable of producing these systemic symptoms by releasing various secretory products. It has been shown that cytokine interleukin-6 (IL-6) is responsible for such symptoms in patients with cardiac myxomas [17].

R. Y. Kwong et al. (eds.), *Cardiovascular Magnetic Resonance Imaging*, Contemporary Cardiology,
https://doi.org/10.1007/978-1-4939-8841-9_16

CARDIAC MASSES		MORPHOLOGY/APPEARANCE	LOCATIONS	IMAGING SEQUENCES					
				CINE (SFFP, GRE)	TISSUE CHARACTERIZATION			POST-CONTRAST	
					T_2 DIR	T_2 DIR	T_2 DIR fs	FPP	LGE
BENIGN	Myxoma	Polypoid mass with smooth or villous surface, thin stalk	Left atrium> right atrium; Interatrial septum	Mobile; ↓ to blood pool; ↑ to myocardium	~	↑	–	+, –	Homogeneous
	Lipoma	Encapsulated mass with smooth surface	Any chamber; Subepicardial> intramyocardial	May be mobile, ↑	↑	↑	+	–	Homogeneous
	Papillary Fibroelastoma	Papillary frondlike mass, thin stalk	Cardiac valves	Mobile, ↓, peritumoral turbulent flow	~	~	–	–	Homogeneous
	Hemangioma	Smooth polypoid or infiltrative mass	Any chamber; Lateral left ventricle wall	Mobile if polypoid; ↑	~	↑	–	+++	Heterogeneous
	Fibroma	Well circumscribed mass	Ventricular septum > left ventricle free wall	Non mobile; ↓	~/↑	↓	–	–	Markedly homogeneous
	Rhabdomyoma	Well circumscribed pseudocapsulated mass	Ventricular wall; larger tumors protruding into the lumen	Non mobile; thickened ventricular wall	~	↑	–	+, –	Homogeneous
	Paraganglioma	Encapsulated mass; may appear infiltrative	left atrium> right atrium> AV sulcus; intramural	Non mobile; ↑	~	↑	–	+++	Markedly homogeneous
	Cystic tumor of atrioventricular node	Multi–cystic nodules filled with fluid	Region of atrioventricular node	Non mobile; ↑	↑	↑	–	+, –	Homogeneous
	Lymphangioma	Multiloculated well circumscribed mass	Epicardial surface	Non mobile; ↑	↓	↑	–	–	–
MALIGNANT	Angiosarcoma	1. Focal mass 2. Diffuse mass along atrium	1. RA Interatrial septum 2. RA free wall	1. Mobile; ↑ 2. Non mobile; ↑; "cauliflower" appearance	⇑	⇑	–	Avid peripheral enhancement; "sunray" appearance	Heterogeneous enhancement
	Undifferentiated sarcoma	Infiltrative mass	Left atrium	Non mobile	~	~	–	+	Heterogeneous enhancement
	Osteosarcoma	Infiltrative mass or well circumscribed pseudocapsulated	Left atrium; away from the fossa ovalis	Non mobile, ~	⇑	⇑	–	+	Heterogeneous enhancement
	Fibrosarcoma	Infiltrative mass; may infiltrate pericardium	Left atrium	Non mobile, ↑	~	↑	–	+	Heterogeneous enhancement
	Liposarcoma	Lobulated mass with broad base	Atrium> ventricle	Non mobile, ↑	–	–	+	–	Heterogeneous enhancement
	Lymphoma	~; well circumscribed mass spared coronary arteries	Right atrium> right ventricle	Non mobile, ↑	~	↑	–	+++	Homogeneous enhancement
	Metastases	~	Intramyocardial	~; ↑	~	~/↑	~	+	Homogeneous enhancement
NON–NEOPLASTIC	Thrombus	~; intraluminal mass	Left atrium > left ventricle	~, ~	↓	~/↓	–	–	–
	LHIS	Well circumscribed mass	Interatrial septum	Non mobile, ↑	↑	↑	+	–	–
	Pericardial cyst	Well circumscribed mass	Pericardial mass	Non mobile; ↑	↓	↑	–	–	–

Fig. 16.1 Classification of cardiac masses and cardiac magnetic resonance (MR) imaging findings. SSFP steady-state free precession, GRE gradient-recalled echo, DIR double inversion recovery, FPP first-pass perfusion, LGE late gadolinium enhancement, ↑ hyperintense, ↓ hypointense, ⇑ heterogeneous hyperintense, ~ variable or isointense, +++ avid enhancement, + present, – absent

Embolic Manifestations

Cardiac tumors can cause systemic or pulmonary embolism secondary to the embolization of tumor fragments or thrombus that are formed on the surface of the tumor [7, 18]. Although the brain is the most common site of involvement, cardiac tumors can embolize to almost any organ, which can result in ischemia, infarction, or aneurysm formation [19, 20]. Paradoxically, smaller cardiac tumors in patients with minimal hemodynamic alterations tend to have more embolic events than patients with larger and symptomatic cardiac tumors [18]. Cardiac myxomas are the most common type of benign primary cardiac tumor associated with embolic manifestation followed by papillary fibroelastomas and hemangiomas [21–23]. Embolic events can be seen with malignant primary cardiac tumors as well, due to their friable texture, although systemic and pulmonary metastases should be excluded since they may have similar symptoms.

Phenomena Secondary to Metastatic Disease

Malignant cardiac tumors are usually present with metastatic disease at a late advanced stage of their course; although, rarely symptoms due to metastases can occur as an initial manifestation [24]. The most common locations for cardiac tumor metastases are the lung, brain, and bone; however, virtually all malignant cardiac tumors can metastasize to any organ or tissue in the body [25].

Role of Imaging in Cardiac Masses

For initial evaluation of patients with clinical suspicion for cardiac masses, transthoracic echocardiography remains the first-line noninvasive imaging modality [26, 27]. Although it is readily available and inexpensive with somewhat useful information regarding tissue characteristics, there are certain disadvantages including restricted field of view, operator

dependence, and limited evaluation of extracardiac involvement [14]. Cardiac computed tomography (CT) is commonly used as a second-line noninvasive imaging modality. There is an added risk of ionizing radiation and nephrotoxicity due to contrast material limit, which may limit usage [28]. Also, cardiac CT has lower temporal and soft tissue contrast resolution [29]. Thus, cardiac magnetic resonance (MR) imaging is typically the next step when cardiac tumor is seen on echocardiography; moreover, conjugate use of these two modalities is recommended for diagnosis and monitoring [30–32]. Cardiac MR has various advantages over other modalities including superior spatial and temporal resolution, multi-planar imaging, tumor tissue characterization, and assessment of tumor blood flow and enhancement with gadolinium-based contrast agents [26, 33]. In addition to these features, it can assess cardiac function and extracardiac involvement. MR imaging features are found to have high diagnostic accuracy to distinguish malignant from benign cardiac masses [34].

MR Imaging Protocol for Cardiac Masses

For cardiac mass MR imaging, it is important that the imager be available to supervise the technologist during the scan since obtaining nonstandard planes is inevitable and also additional sequences may be applied for complete characterization of the mass. It is also helpful in reducing scan time by omitting sequences that are not appropriate for the particular mass. Although cardiac MR can be tailored based on prior imaging and location of the tumor, most institutions use standard sequences including high-resolution cine images, myocardial tagging, tissue characterization images, and post-gadolinium-enhanced images (Fig. 16.2).

Dynamic assessment of the mass can be done with high-resolution cine images, usually *steady-state free precession (SSFP)* or *gradient-recalled echo (GRE)* sequences in multiple planes. These sequences are helpful to localize the mass, assess morphology, assess mobility, and evaluate its effects on cardiac function and valvular structures [35]. At least two standard planes, such as short-axis and four-chamber planes, must be obtained, and in some cases nonstandard imaging planes may be obtained based on anatomy and extent of the tumors [36]. In addition, for small and mobile masses, high spatial resolution cine stack images through the mass may be obtained by reducing section thickness (4–6 mm) and gap size. One should keep in mind that tissue contrast in SSFP sequences is dependent on the $\sqrt{(T2/T1)}$ ratios of the tissue; therefore, masses with similar $\sqrt{(T2/T1)}$ ratios to blood may be poorly visualized with this sequence.

For the large masses or in the case of close proximity to the pericardium, *myocardial tissue tagging* should be performed for assessment of subtle regions of contractile dysfunction due to tissue infiltration [37]. Tagging is also very helpful when evaluating involvement of adjacent structures such as the pericardium.

The next step in MR imaging is tissue characterization, which includes *double inversion recovery (DIR) fast spin-echo T1-* and *T2-weighted* images with and without fat suppression and pre- and post-contrast-enhanced images. *DIR T1- and T2-weighted* sequences are also known as black-blood sequences and give high-resolution images to infer the tissue composition of the mass [34]. Fat suppression prepulses are necessary to characterize fatty component of the tumor, edema, and regions of coagulative necrosis [35, 38]. Post-contrast sequences for further tissue characterization include *first-pass perfusion*, *early gadolinium enhancement (EGE)*, and *late gadolinium enhancement (LGE)* sequences. *First-pass perfusion* images can be obtained in multiple planes through the largest area of the mass with 0.05–0.1 mmol/kg of gadolinium-based contrast agent [35]. *EGE* are acquired immediately following *first-pass perfusion. LGE* are usually acquired 7–10 min after the contrast injection. *LGE* with *phase-sensitive inversion recovery (PSIR)* sequences through the mass are helpful to characterize tissue composition. Due to the cellular breakdown as a result of tumor invasion, gadolinium chelates become intracellular and therefore persist in acutely disrupted myocardium [34, 35].

Benign Cardiac Tumors

Myxoma

Clinical Features

Cardiac myxomas are the most common type of primary cardiac tumor and account for 30–50% of all benign primary cardiac tumors [16, 39]. They usually present in adults between 30 and 50 years of age, with a female predominance (3:1) [8, 40]. Clinical presentation can vary based on location, size, and mobility of tumor, although majority of symptomatic patients with cardiac myxomas present with one of the clinical manifestations of cardiac, embolic, or systemic symptoms. The majority of the tumors are located in the left atrium (80%). Less common locations include the right atrium (15–20%), ventricles (0.6–1.7%), and biatrial (1.3%) [40] (Fig. 16.3). Dyspnea, dizziness, cough, pulmonary edema, cardiac arrhythmia, and heart failure are the most common symptoms of cardiac manifestations. Approximately 70% of patients with left atrial myxoma have heart failure and

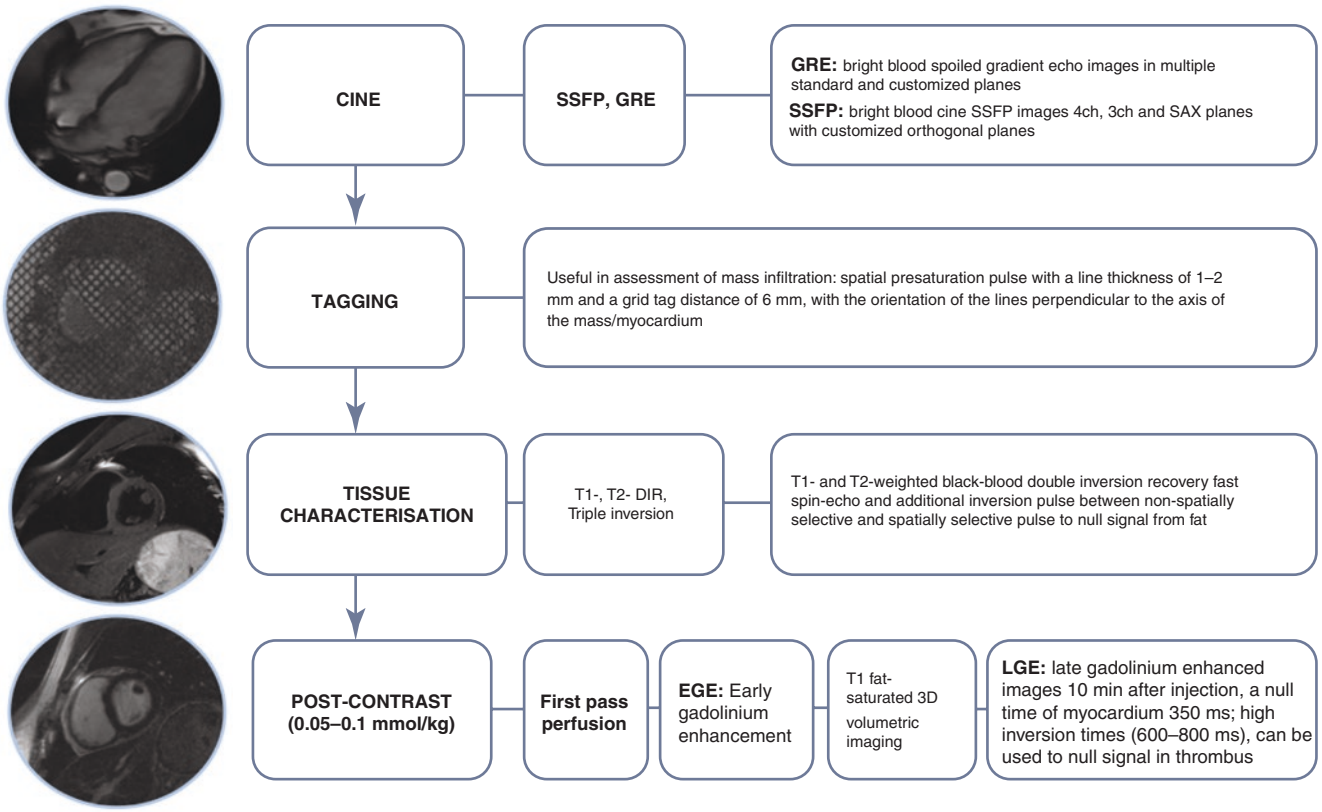

Fig. 16.2 Cardiac MR imaging protocol for cardiac masses. SSFP steady-state free precession, GRE gradient-recalled echo, LGE late gadolinium enhancement, DIR double inversion recovery, T1 T1-weighted images, T2 T2-weighted images

syncope. Patients with right atrial myxomas can present with right-sided heart failure [41]. These symptoms are usually positional as a result of outflow obstruction, mitral valve regurgitation, and tricuspid obstruction [41]. Nearly 20% of patients with cardiac myxomas have cardiac arrhythmias, including atrial fibrillation and flutter [42]. Cardiac myxomas are known to be the most common primary cardiac tumor to produce emboli and can embolize virtually in any organ or tissue although brain is the most common location [21]. Half of the patients with cerebral emboli have concomitant peripheral extremity embolization [16]. Nonspecific systemic symptoms such as fever, weight loss, fatigue, and arthralgia secondary to cardiac myxomas are common and believed to be related to IL-6 release by the tumor cells [17].

Although majority of cardiac myxomas are sporadic (93%), they also can be part of heritable syndrome, which is known as "Carney syndrome"[43]. The Carney syndrome is an autosomal dominant, inherited disease that includes cardiac myxoma, hyperpigmented skin lesions, pituitary adenoma, breast fibroadenoma, and melanotic schwannoma. Cardiac myxomas in patients with Carney syndrome develop in early ages (20 years) with male predominance. Tumors associated with this syndrome account for 7% of all myxomas, tend to be multicentric, and may recur after resection [44].

Pathological Findings

Myxomas are solitary tumors, usually polypoid or pedunculated, and vary in size from 1 to 15 cm in diameter with a smooth and lobular or villous and friable surface [16, 45]. They originate from subendocardial layer of multipotent mesenchymal cells and histologically consist of scattered tumor cells ("spindle cells") within a mucopolysaccharide stroma [39, 45, 46]. Surface of the tumor can be covered with thrombus, and internally they can contain cysts, calcification, and hemorrhagic components [47]. There is no histopathological difference between sporadic and familial type of myxomas [48].

MR Imaging Findings

Myxomas usually appear as a highly mobile mass with attachment to the endocardial surface on cine images, and they can prolapse through the mitral value and cause obstruction; thus, these images are helpful to visualize the hemodynamic effects of a mobile mass (Fig. 16.4). Myxomas are usually hypointense relative to the blood pool and hyperintense to myocardium on SSFP sequences [26]. Based on their myxomatous component, they usually appear isointense on T1-weighted and hyperintense on T2-weighted images [49]. However, the presence of calcification or hemorrhage may

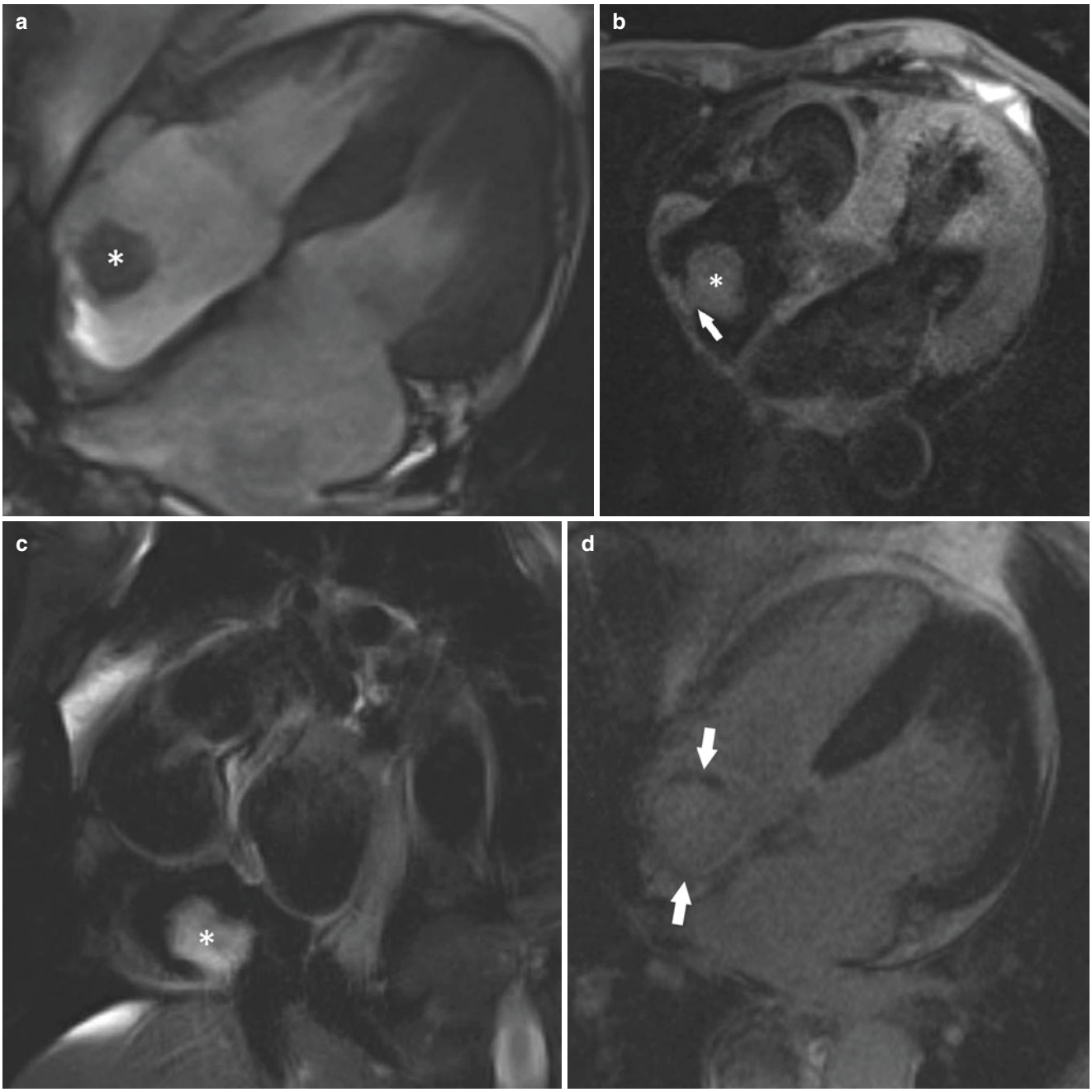

Fig. 16.3 (**a**) Cine steady-state free precession (SSFP) image, four-chamber view in an 81-year-old female with a right atrial lesion at echocardiography, shows well-defined pedunculated myxoma (*asterisk*). The mass (*asterisk*) is isointense on (**b**) fat-suppressed T1-weighted double inversion recovery (DIR) image, four-chamber view with a peduncle (*arrow*), and hyperintense on (**c**) fat-suppressed T2-weighted DIR image, short-axis slice. (**d**) Late gadolinium enhancement (LGE) image, four-chamber view, showed enhancement of the mass (arrows)

result in a heterogeneous appearance on T1- and T2-weighted images [50]. Hemorrhage can have a variable appearance depending on the chronicity [51]. First-pass perfusion of myxomas is usually mild or not apparent; however, based on histopathologic features, most of them (90%) demonstrate heterogeneous enhancement [15, 36].

Treatment

Treatment for cardiac myxoma is surgical resection, which has excellent long-term prognosis [52]. Tumor recurrence is reported between 3% and 13 %, and the rate is high in hereditary form and thus likely related to multifocal disease rather than incomplete surgical resection [9, 53].

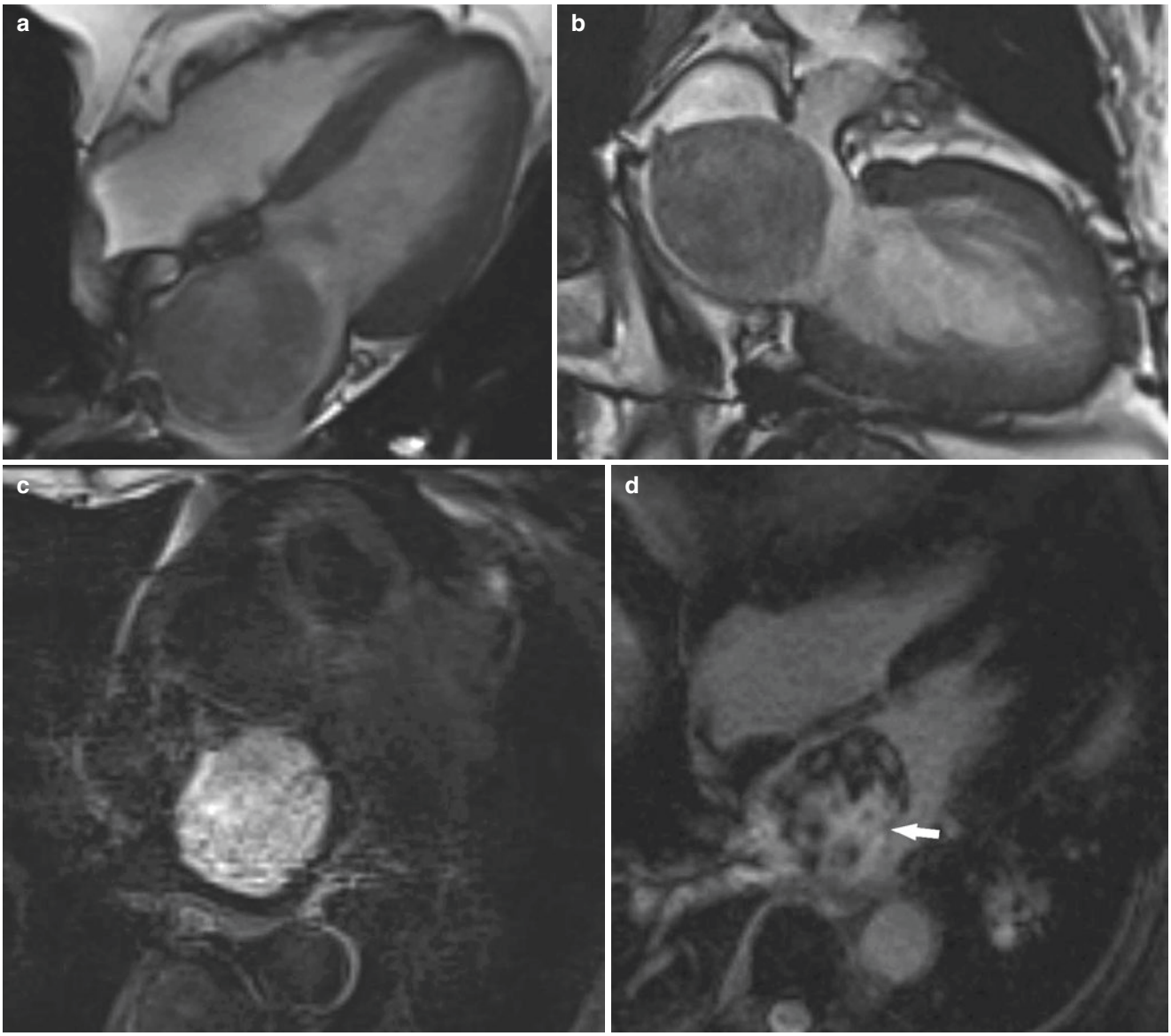

Fig. 16.4 A 78-year-old female incidentally found to have a large left atrial myxoma. Cine steady-state free precession (SSFP) images (**a**) four-chamber and (**b**) two-chamber views demonstrate a 5 × 3 cm mass with slightly hyperintense signal relative to the myocardium. (**c**) Fat-suppressed T2-weighted double inversion recovery (DIR) image, four-chamber view, revealed a large hyperintense mass in the left atrium, which has heterogeneous enhancement on (**d**) late gadolinium enhancement (LGE) image (arrow)

Lipoma

Clinical Features

Cardiac lipomas are the second most common primary tumors of the heart (10%) and can occur sporadically at all ages with equal frequency in both sexes [8, 54]. Most of the patients with cardiac lipomas are asymptomatic; although, based on size and location, they can produce symptoms. Majority of lipomas are located in the subepicardial region; however, they can occur less commonly in other sites such as intramyocardial or intracavitary [55, 56]. Subepicardial lipomas are usually asymptomatic; however, large lipomas can cause compression on ventricles or may cause shortness of breath due to lung compression without interfering with heart function [57–59]. It has been reported that intracavitary lipomas can interfere with the function of the heart resulting in heart failure [60]. Intramyocardial lipomas can cause arrhythmias including atrial fibrillation, ventricular tachycardia, and atrioventricular block [61, 62].

Pathological Findings

Cardiac lipomas are encapsulated, homogeneous tumors with a broad pedicle consisting of adipocytes usually arising from the epicardium [10]. They can also grow within

the myocardium, endocardium, and interatrial septum with extension into the cardiac chambers [57, 63].

MR Imaging Findings

MR imaging is diagnostic for lipoma and demonstrates encapsulated, smooth lesion with homogeneous high signal intensity on T1-weighted and slightly less high signal intensity on T2-weighted images [55, 64]. Important sequence for cardiac lipomas is DIR T1-weighted sequence with additional fat-saturation prepulses, which will suppress the tumor [33]. They usually demonstrate high signal intensity on cine SSFP sequences [50]. Lipomas may have a few thin septations; however, there should be no soft tissue component and contrast enhancement, which are the features for the sarcomatous transformation [55].

Treatment

Surgical excision is the choice of treatment; although, it may not possible for the large tumors that encase or displace coronary arteries or infiltrate the myocardium [65]. They tend to grow slowly over years of follow-up and can reach enormous sizes that result in heart compression and death [55, 66].

Papillary Fibroelastoma

Clinical Features

Papillary fibroelastoma, which is also known as "endocardial papilloma," is the third most common primary cardiac tumor with an incidence of 0.02% [67]. Prevalence of the tumor in general population is unknown since it is asymptomatic in most cases. The mean age at presentation is 60 without any gender predilection [10, 68]. However, it has been reported that patients with papillary fibroelastoma usually present with embolic manifestations, such as transient ischemic attack, stroke, myocardial infarction, and pulmonary embolism [67]. In contrast to other cardiac tumors, embolic materials are found to be thrombus or fibrin. Tumor fragments are rarely found in the vessel of interest [69]. The association with hypertrophic cardiomyopathy, prior cardiac surgery, and mediastinal irradiation has been described [70]. Usually, right-sided fibroelastomas are asymptomatic [71].

Pathological Findings

Papillary fibroelastomas are small (<1.5 cm) benign endocardial tumors that predominantly affect the cardiac valves (90%) with the aortic valve being most common (44%), followed by mitral (35%), tricuspid (15%), and pulmonary valves (8%). They are usually solitary and found away from the valvular free edges, in contrast to Lambl's excrescences, which are small filiform structures [72, 73]. However, fibroelastomas can rarely be multiple and grow on atrial or ventricular endocardial surfaces [47, 68, 74]. They are papillary frond-like masses attached to the endocardium by a short pedicle composed of a fine meshwork of collagen and elastic fibers lined by the endothelium and can exhibit a typical "sea anemone" appearance [75].

MR Imaging Findings

Papillary fibroelastoma detection with cardiac MR imaging can be challenging because of the small size of the tumors and high mobility. They usually appear as a homogeneous mass with intermediate signal intensity on T1 and high signal intensity on T2-weighted images without signal dropout on fat-saturation prepulses [76, 77]. Based on their fibroelastic composition of the tumor, LGE images show homogeneous enhancement [78]. On cine images, fibroelastomas demonstrate peritumoral turbulent flow [50]. Since papillary fibroelastomas are usually away from the valvular free edges, valvular incompetence is not a feature of the tumor and can help to distinguish them from the infective endocarditis vegetations [79] (Fig. 16.5). Tumors located in the atrial or ventricular surfaces may sometimes be confused with myxomas although the pattern of LGE could help to differentiate these two entities (Fig. 16.6).

Treatment

Recommended treatment is surgical excision with possible leaflet repair or valve replacement although it should be preserved for symptomatic patients or in those with larger (>1 cm), highly mobile, and left-sided tumors [74, 80].

Hemangioma

Clinical Features

Cardiac hemangiomas are considered to be rare benign vascular lesions and account for 5–10% of primary cardiac neoplasms [8, 22]. They can occur in patients of all ages with mean age at the time of diagnosis of 43 years [50]. Clinically, most of the patients are asymptomatic; however, depending on the nature and location of the tumor, they can present with various symptoms, including palpitations, arrhythmias, pseudoangina, and cerebral embolism [22, 81, 82].

Pathological Findings

Cardiac hemangiomas can vary in size from less than 1 cm up to 8 cm [7]. They can occur in any cardiac chamber; however, most are seen in the ventricles, particularly in the lateral wall of the left ventricle, the anterior wall of the right ventricle, and the interventricular septum [10]. Histologically, they contain endothelial-lined thin-walled spaces, capillary-like vessels, or malformed vasculature; thus, they can be classified as cavernous, capillary, or arteriovenous hemangiomas, based on the size of the vascular channels [83].

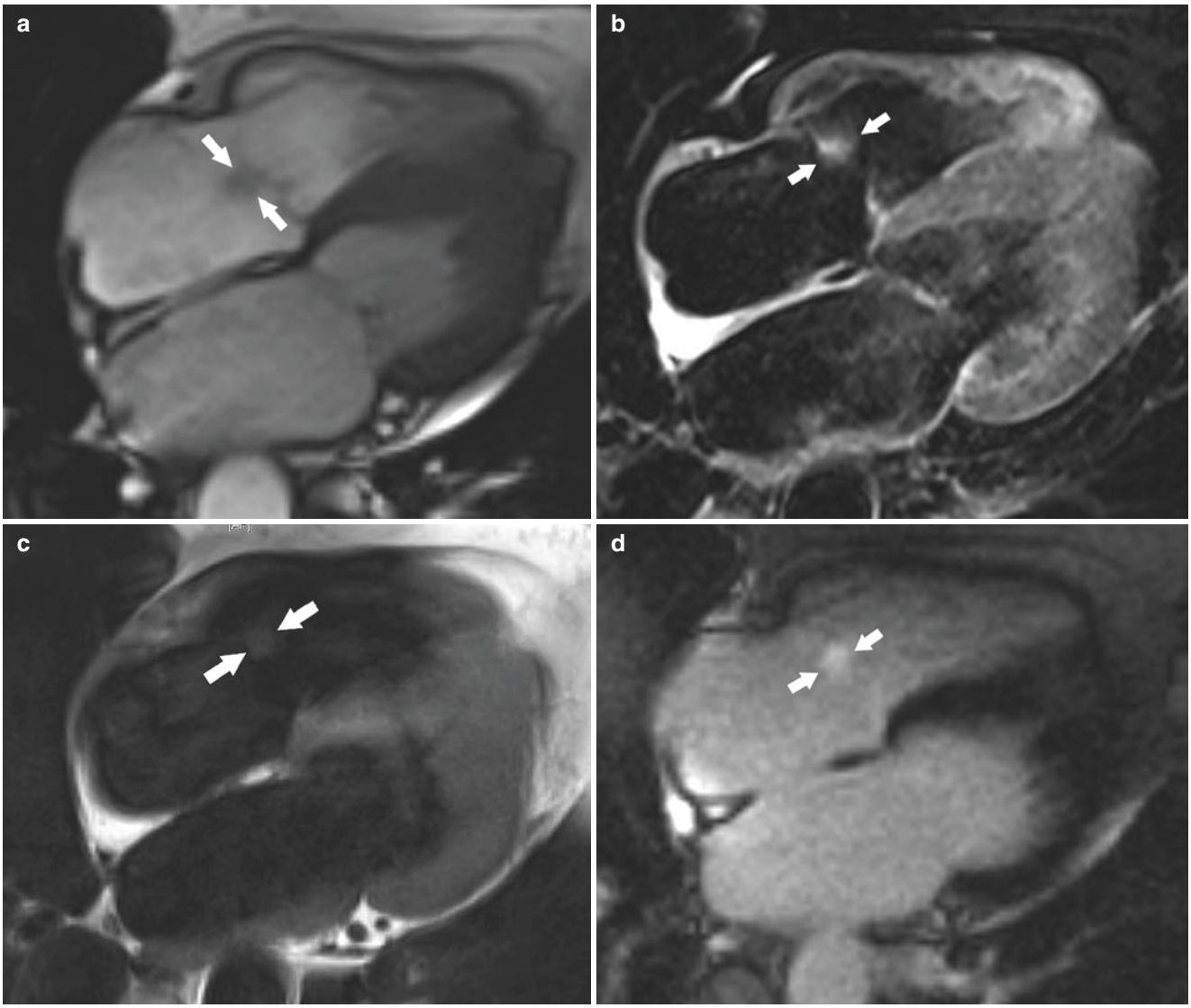

Fig. 16.5 (**a**) Cine steady-state free precession (SSFP) image, four-chamber view, shows small papillary fibroelastoma (arrows) at the mitral valve, which appears hyperintense on (**b**) fat-suppressed T2-weighted double inversion recovery (DIR) image, four-chamber view (arrows). The mass (arrows) is isointense on (**c**) T1-weighted DIR image four-chamber view and homogeneously enhanced on (**d**) LGE image, four-chamber view (arrows)

MR Imaging Findings

Hemangiomas appear heterogeneously isointense on T1-weighted and hyperintense on T2-weighted images without any signal dropout on fat-suppressed images [84] (Fig. 16.7). On cine images, cardiac hemangiomas show a well-defined, mobile hyperintense mass within the cardiac chambers [50]. First-pass perfusion images demonstrate avid enhancement due to the vascular nature of the tumor although some may show heterogeneous enhancement because of the calcification and fibrous septa [84].

Treatment

Symptomatic patients can benefit from the surgery, and the postoperative prognosis is excellent [85]. It has been shown that cardiac hemangiomas may regress spontaneously; therefore, conservative management should be considered in asymptomatic patients to avoid high-risk surgical resections [86].

Fibroma

Clinical Features

Cardiac fibromas primarily affect children; however, they are less frequently encountered in adulthood and account for approximately 3% of benign primary cardiac tumors [4, 87]. They have roughly equal sex predilection, and most of the tumors appear to be sporadic [10]. However, cardiac fibro-

mas can develop as a part of Gorlin-Goltz syndrome, which is an autosomal dominant condition characterized by skeletal anomalies, odontogenic keratocysts, basal cell carcinoma, and tendency toward the other cancers [88]. Clinically, cardiac fibromas present with heart failure due to mass effect or syncope as a result of outflow obstruction and arrhythmias [89]. Cardiac fibromas are associated with sudden death due to arrhythmia [90, 91].

Pathological Findings

Cardiac fibromas are usually solitary, well-circumscribed solid intramural tumors, consisting of fibroblasts and

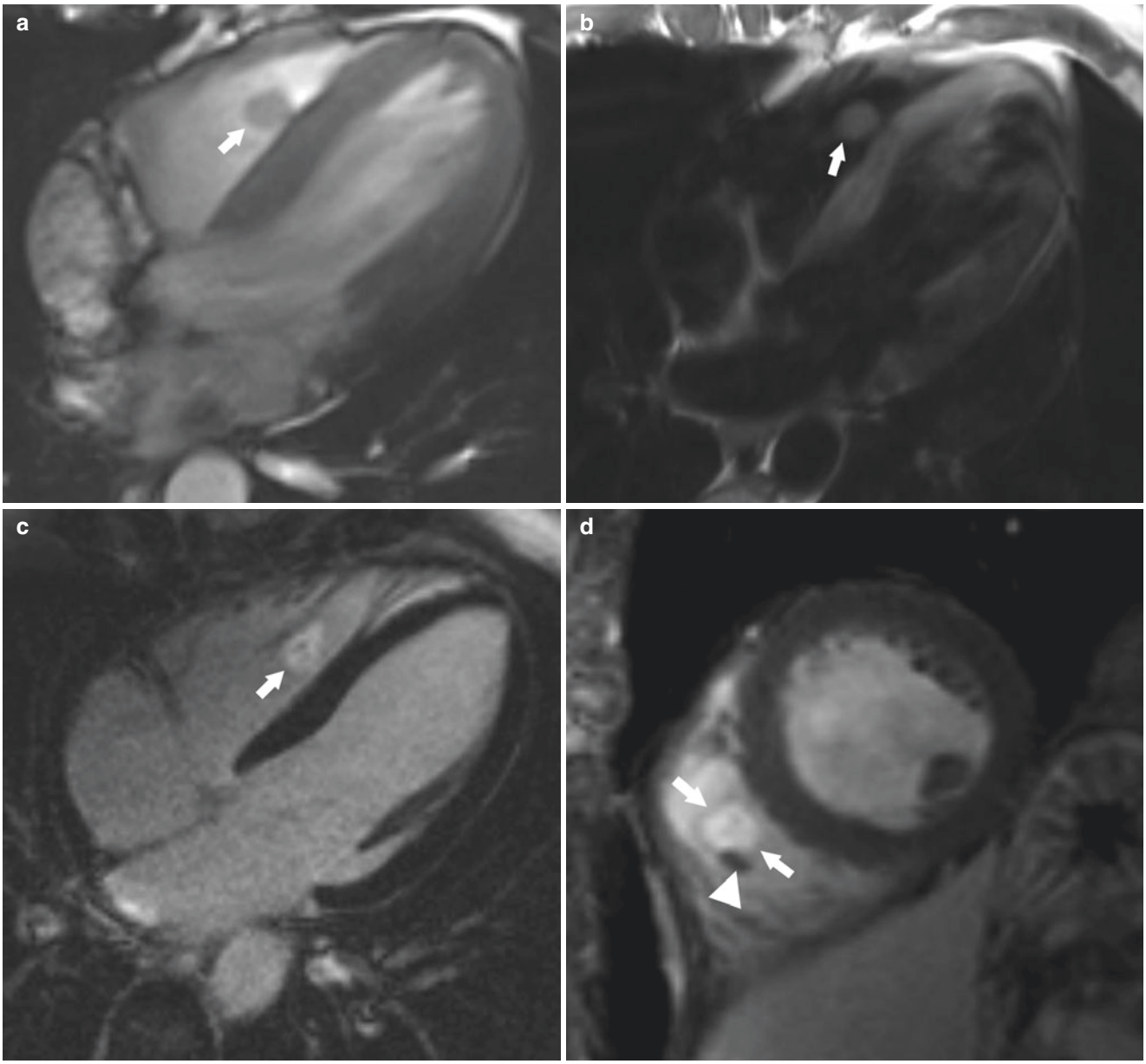

Fig. 16.6 An asymptomatic 36-year-old male presented with a heart murmur. Echocardiography revealed a right ventricular and bicuspid aortic valve papillary fibroelastoma: (**a**) cine steady-state free precession (SSFP) image, four-chamber view, demonstrates slightly hyperintense well-defined mass (*arrows*) in the right ventricle, while (**b**) T1-weighted double inversion recovery (DIR) image, four-chamber view, demonstrates an isointense mass (*asterisk*) to the myocardium. Late gadolinium enhancement image with (**c**) regular inversion time (TI), four-chamber view, and (**d**) long-TI time (600 ms), short-axis view shows homogeneous enhancement of the mass attached to the moderator band (*arrowhead*) of the right ventricle. A companion case of an 82-year-old female with an atrial fibrillation presented with an incidental right ventricular myxoma on echocardiography. (**e**) Cine gradient-recalled echo (GRE) image, four-chamber view, shows a pedunculated mass (*asterisk*) in the right ventricle, and (**f**) T1-weighted DIR, four-chamber view, demonstrates isointense mass (*asterisk*). LGE, four-chamber view (**g**) with regular inversion time (TI) image shows heterogeneous enhancement of the mass (arrows) as opposed to the previous case of myxoma (**h**) long-TI time (600 ms) which demonstrates more gadolinium retention within the mass (arrows)

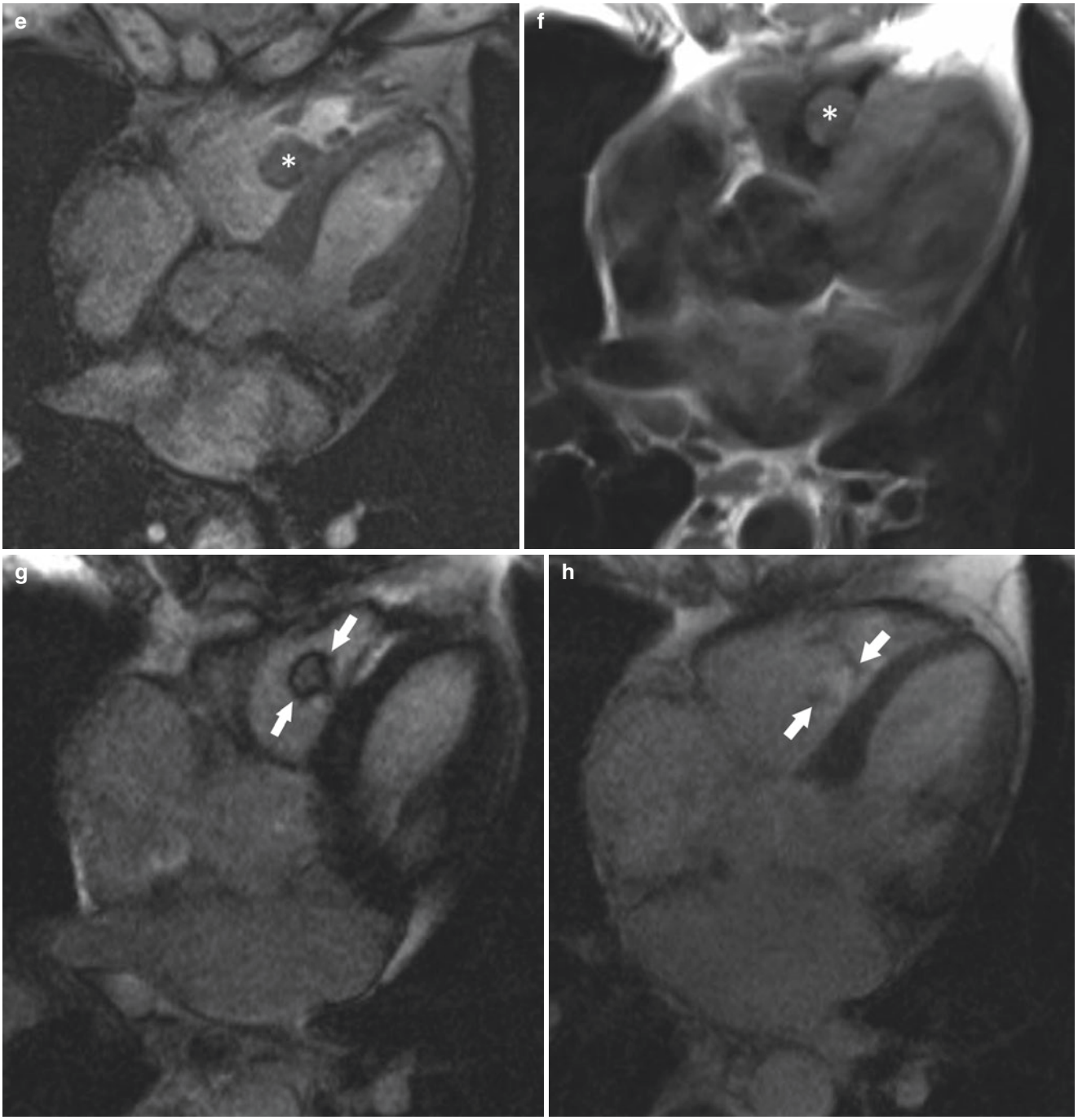

Fig. 16.6 (continued)

collagen and frequently contain foci of calcifications [92]. It is uncommon to see hemorrhage, necrosis, or cystic changes within the tumors [92]. They are usually large with an average diameter of 5 cm, and tumors up to 10 cm have been reported [93]. Common locations for cardiac fibromas are ventricular septum or left ventricular free wall although less commonly they occur in the right ventricle or atria [10].

MR Imaging Findings

Since cardiac fibromas consist of fibroblasts dispersed within collagen with low water content, MR images will demonstrate characteristics of fibrous tissue, in such a manner that T1-weighted images will demonstrate isointense to hyperintense signal intensity relative to myocardium and hypointense on T2-weighted images [34, 94] (Fig. 16.8). They usually appear as a discrete intramural mass or focal thickening of the

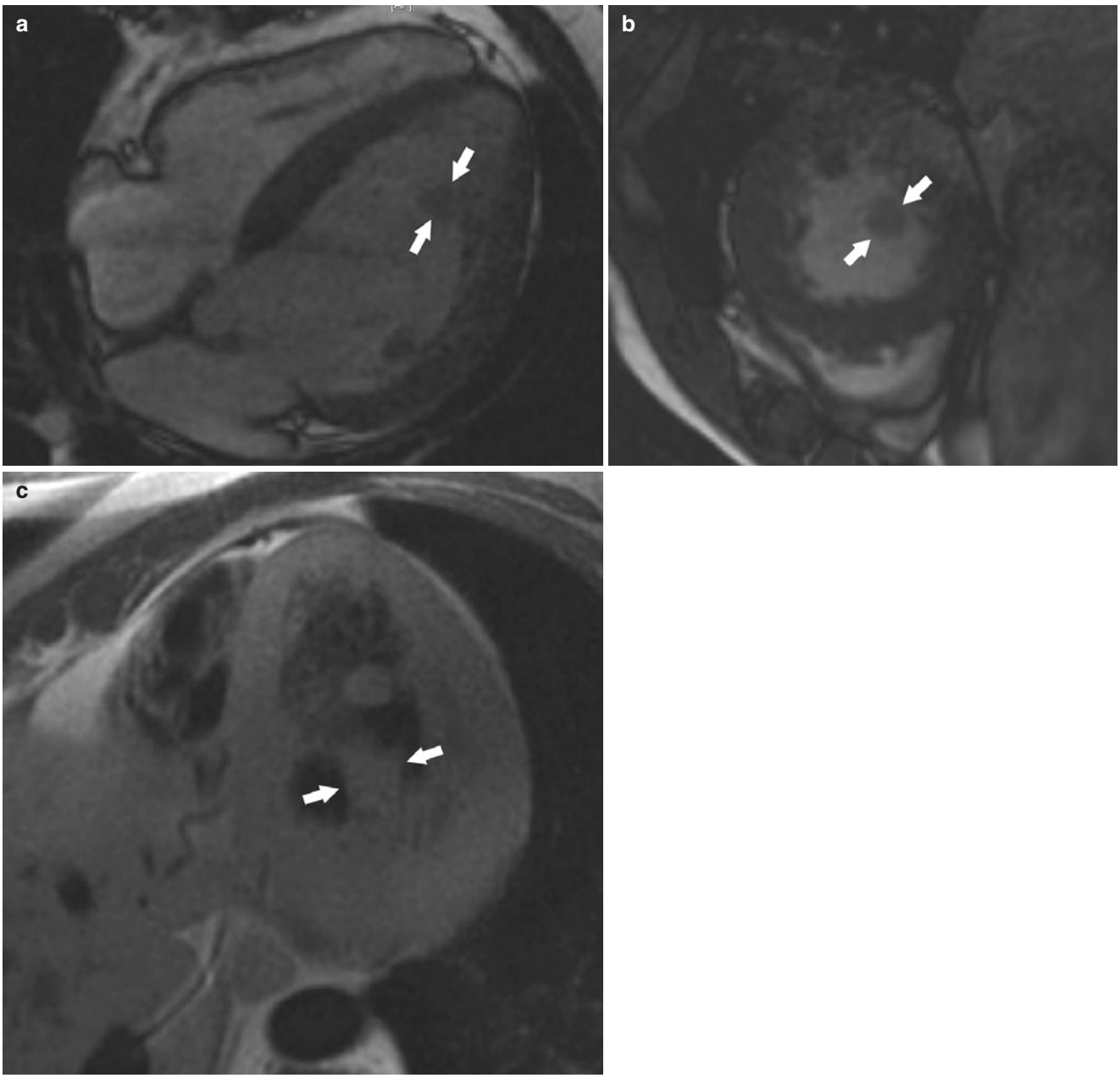

Fig. 16.7 Left ventricular hemangioma in a 43-year-old male with a history of familial cardiomyopathy; (**a, b**) cine steady-state free precession images with four-chamber and short-axis views demonstrate a 1.5 cm mass (arrows) in the left ventricle adjacent to the inferiolateral wall, which is slightly hyperintense relative to the myocardium and isointense on (**c**) T1-weighted double inversion recovery (DIR) image, four-chamber view. First-pass perfusion and late gadolinium enhancement images show enhancement of the mass (not shown)

myocardium, which results in distortion of ventricular anatomy. Based on amount of calcification, it can appear heterogeneous in all sequences. On cine images, cardiac fibromas will demonstrate hypointense signal intensity relative to the myocardium. First-pass perfusion images will show avascular lesion because of the low vascularity of the tumor; however, fibromas will retain gadolinium within the interstitial space and thus will markedly enhance on LGE images [29, 36, 95].

Treatment

For symptomatic patients, surgery could be treatment of choice with high success rate; however, asymptomatic patients can be treated conservatively since occasionally they can regress [92]. Infants and adult patients with large cardiac fibromas usually benefit less from surgery; however, palliative partial surgery or heart transplant should be considered for these patients [10].

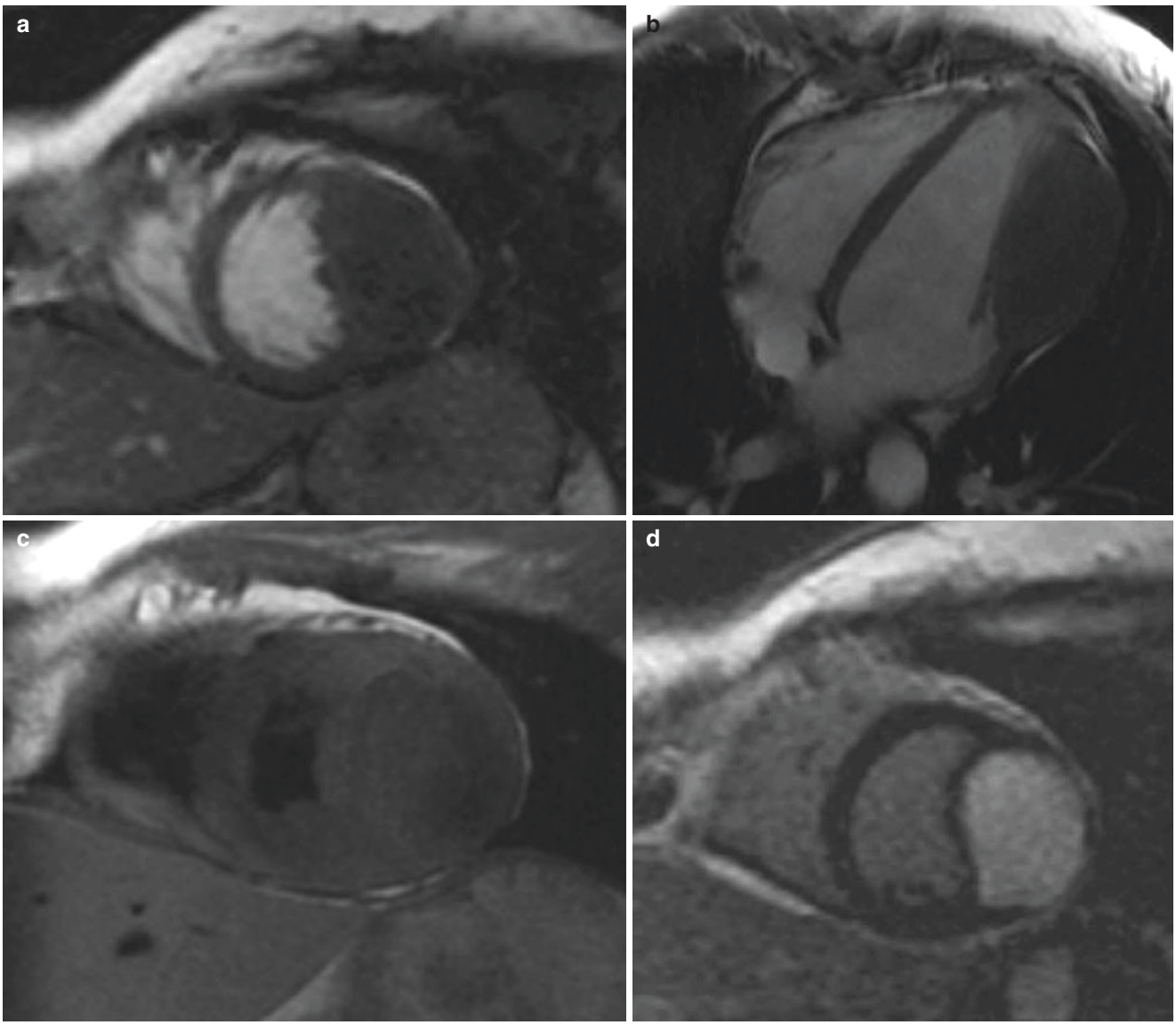

Fig. 16.8 A 33-year-old female found to have a left ventricular mass on echocardiography and was referred for further evaluation with cardiac MR imaging. (**a, b**) Cine steady-state free precession images, four-chamber view and short-axis slice, demonstrate a mass occupying the lateral wall of the left ventricle and appearing isointense to the myocardium. (**c**) T1-weighted double inversion recovery (DIR) image shows an isointense mass relative to the myocardium. On (**d**) late gadolinium enhancement (LGE) image, short-axis slice demonstrates avid enhancement of the mass due to the retention of gadolinium within the interstitial space. Histopathology of the mass was consistent with cardiac fibroma

Rhabdomyoma

Clinical Features

Cardiac rhabdomyomas are the most common primary cardiac tumor (up to 90%) in children, and 50% of cases are associated with tuberous sclerosis complex [96]. Although less than 25% of adults with tuberous sclerosis have cardiac tumors, it has been associated with the fact that they can spontaneously regress [97]. During prenatal or infancy, rhabdomyomas can protrude into the ventricular chambers, which may cause symptoms; however, most of the cases regress before the age of 4 without intervention. Adult patients with sporadic cardiac rhabdomyomas are extremely rare and usually asymptomatic; however, they may present with arrhythmias, murmurs, and heart failure. Arrhythmia has been described as the most common symptom in adult-type rhabdomyomas [98, 99].

Pathological Findings

Cardiac rhabdomyomas are well-circumscribed tumors with multifocal 1–3 cm intramural nodules mostly in the ventricles [10, 100]. Histologically rhabdomyomas have pathog-

nomonic cell configuration called "spider cells," which are stretched septa from the cell membrane to a centrally placed nucleus giving the spiderlike appearance [10]. Adult-type cardiac rhabdomyomas are characteristic with high degree of cellularity without typical spider cells and histologically resemble the extracardiac rhabdomyomas found in head and neck region of adults [98].

MR Imaging Findings

Cardiac rhabdomyoma appears smooth, broad base intramural homogeneous mass isointense to adjacent myocardium on T1-weighted and hyperintense on T2-weighted images [29, 101]. Cine MR imaging demonstrates focal thickened myocardium with abnormal contractility, which can also be evaluated with additional myocardial tissue tagging sequences [37]. First-pass perfusion or LGE images show minimal or no enhancement with gadolinium-based contrast agents [29, 102]. In pediatric patients, cardiac MR imaging can be done for surgical planning [95].

Treatment

No intervention required for cardiac rhabdomyoma, since most of the patients are asymptomatic and usually regresses by age 4 [103]. However, for symptomatic patients, surgical excision is recommended [104, 105]. Prognosis of the disease is excellent, and there has been no report regarding recurrence of the tumor.

Paraganglioma

Clinical Features

Cardiac paragangliomas are extremely rare (<1% of all benign cardiac tumors) neuroendocrine tumors arising from the intrinsic cardiac paraganglial cells [106]. Mean age of presentation is 40 years (range between 18 and 85 years), and almost all tumors are found to be sporadic [107]. There is only one reported case of cardiac paraganglioma associated with Carney's triad (not to be confused with Carney's syndrome), which is a rare syndrome defined by coexistence of three tumors including extra-adrenal paraganglioma, gastrointestinal stromal tumors (GIST), and pulmonary chondroma [108]. As expected, patients with cardiac paragangliomas present with symptoms related to catecholamine excess, such as hypertension, headache, palpitation, and flushing [107]. Biochemical abnormalities will manifest in symptomatic patients including increased level of urinary norepinephrine, vanillylmandelic acid, total plasma metanephrine, plasma norepinephrine, and epinephrine [109]. Approximately 20% of cardiac paraganglioma cases were found to have paragangliomas in other locations, such as the carotid body, adrenal gland, and bladder [110].

Pathological Findings

Cardiac paragangliomas are large soft, fleshy masses that range between 3 and 8 cm and composed of nests of paraganglial cells ("zellballen" cells) [111]. They are usually poorly circumscribed; however, paragangliomas can be encapsulated or infiltrative in nature [110, 112, 113]. Large cardiac paragangliomas may undergo central necrosis (50% of all paragangliomas) although it is extremely rare to have calcification within the tumor; thus, only one reported case demonstrated calcification [110]. Typically tumors are located on the epicardial surfaces of the roof or posterior wall of the left atrium although rare locations for cardiac paragangliomas have been reported such as interatrial septum or along the coronary arteries [107, 114–116].

MR Imaging Findings

Similar to extracardiac paragangliomas, they are usually isointense on T1-weighted and hyperintense on T2-weighted images [117]. There is a reported case, which demonstrates hypointense signal intensity on T2-weighted images [109]. Because of the high vascularity of the tumors, first-pass perfusion and LGE images show marked enhancement after contrast injections; however, heterogeneous enhancement also can be seen due to central necrosis [118] (Fig. 16.9).

Treatment

Surgical excision of cardiac paraganglioma usually results in complete cure and relief of symptoms [119]. There are potential surgical risks including perioperative hemorrhage due to high vascularity and hypertensive crisis; thus, for selective cases, preoperative embolization should be considered [120]. Moreover, cardiac bypass or cardiac autotransplantation may be required for large and complex cases [119].

Cystic Tumor of the Atrioventricular Nodal Region

Clinical Features

Cystic tumor of the atrioventricular nodal region (CTAN) is a rare tumor located in the region of atrioventricular node [121]. Tumors occur at all ages ranging from newborn to 86 years (mean age, 38 years), with predilection in females [122]. Patients can present with ventricular tachycardia, fibrillation, or various degree of heart blockage, including complete heart block [123]. Size of the tumors can be up to 30 cm without a relationship between size of the tumor and occurrence of arrhythmia, and they have been described as "smallest tumor, which causes sudden death" [124, 125]. CTAN also has been reported in association with X-linked recessive disease Emery-Dreifuss muscular dystrophy [126].

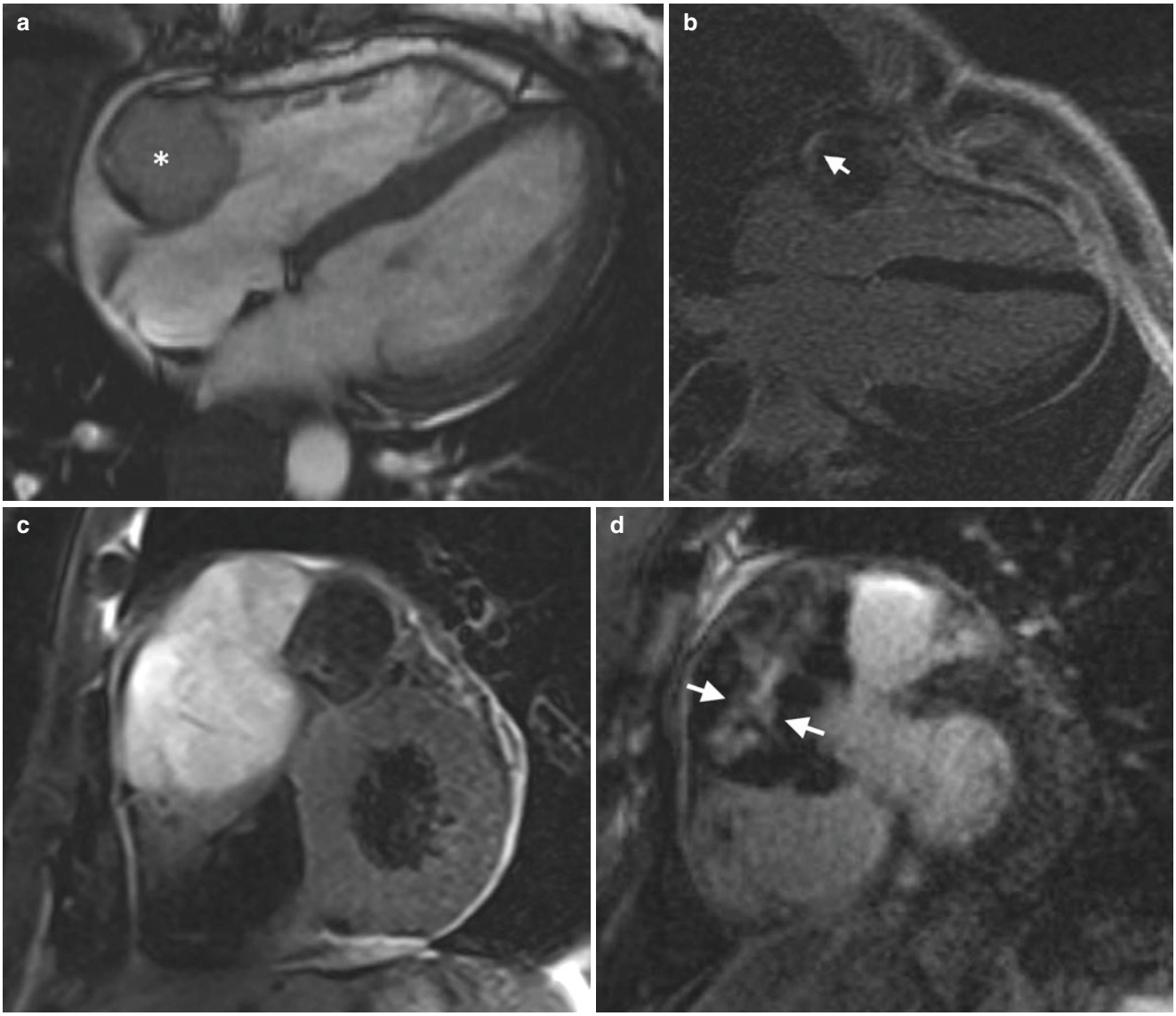

Fig. 16.9 A 37-year-old female presented with headache, nausea, and vomiting. (**a**) Cine steady-state free precession (SSFP) image with four-chamber view demonstrates hyperintense mass (asterisk) at the right atrioventricular groove. (**b**) Late gadolinium enhancement (LGE) image, four-chamber view, displays minimal peripheral enhancement (arrow) within the mass. The mass was removed, and histopathology of the tumor confirmed the diagnosis of paraganglioma. A companion case of 62-year-old female presented with palpitation and dyspnea. Chest CT revealed a mass (not shown) in the mediastinum, which was abutting the cardiac structures and was referred for cardiac MRI exam. (**c**) A T2-weighted double inversion recovery (DIR) image revealed a large, hyperintense mass encasing the left ventricular outflow tract and demonstrated heterogeneous enhancement on (**d**) LGE image, short-axis slice (arrows)

Pathological Findings

Tumors appear as multicystic nodules filled with fluid arising from the atrioventricular node although gross findings of small tumors are subtle [127]. Histologically these cysts usually form two layers including inner cuboidal and deeper transitional cells [10].

MR Imaging Findings

MR images demonstrate well-defined mass with increased intensity on T1- and T2-weighted images, which reflects keratin composition [128]. However, tissue characteristics including post-contrast images, particularly LGE, can mimic cardiac myxomas; thus, clinical correlation and location of the tumor should be taken into consideration [129].

Treatment

Treatment choices for CTAN are still controversial; however, given the complications that can happen due to the tumor, surgical resection should be considered. Few cases with even small tumors showed satisfactory results [130]. Patients with

complete or partial surgical resection may require subsequent pacemaker implant [131].

Lymphangioma

Clinical Features

Primary lymphangioma originating from the heart is extremely rare, and most of them occur during childhood [10, 132]. These are benign lesions; however, patients can present with arrhythmia, tamponade, heart failure, and myocardial ischemia [133]. These tumors are commonly located on the epicardial surface; however, ventricular lymphangiomas have also been reported [50, 133].

Pathological Findings

Cardiac lymphangiomas contain lymph; however, they are isolated from the lymphatic system and are histologically composed of endothelial-lined, thin-walled spaces [10].

MR Imaging Findings

Lymphangiomas appear to be low-intermediate signal intensity on T1-weighted and hyperintense on T2-weighted images [132, 134]. Given that they are a multiloculated lymphatic structure, there will be no enhancement on post-contrast images [50, 135].

Treatment

Lymphangiomas may present with serious symptoms; therefore, complete excision of tumors is recommended [133]. Although sometimes based on the location or size of the tumor, surgical treatment may not be the best option [133].

Malignant Cardiac Tumors

Angiosarcoma

Clinical Features

Cardiac angiosarcomas are rare tumors with frequency of less than 1% (0.0001–0.030%); however, they are the most common primary cardiac malignant tumor and account for 37% of all sarcoma cases [2, 136]. These tumors usually occur in adults with a median age of 39; however, reportedly they can appear in any age group between 2 and 80 years with slight male predilection [25, 136]. Cardiac angiosarcomas are almost always sporadic; however, there is single familial type of cardiac angiosarcoma that has been reported [137]. Patients present with phenomena secondary to metastatic disease, and more than 65% of cases already demonstrate metastasis at initial presentation [24, 138]. Chest pain, dyspnea, arrhythmia, fever, and heart failure are also common nonspecific symptoms that can be seen in patients with cardiac angiosarcoma [139]. More severe symptoms, such as a tamponade, have been reported due to hemorrhagic pericardial effusion [140].

Pathological Findings

Cardiac angiosarcomas are typically located in the right atrium near the atrioventricular groove, in contradistinction to other sarcomas, which usually prefer the left atrium [141]. Morphologically, two types of angiosarcoma have been described. The first type is "focal mass" protruding into the atrium, and second type is a "diffuse mass" extending along the pericardium [142]. Although most of the tumors are bulky and multi-lobular, they can present as right atrial wall thickening or a well-defined mass in the interatrial septum, which could mimic myxoma [10, 143–145]. Due to the location and invasive nature, they can infiltrate right coronary artery (RCA) and cause pseudoaneurysm of the right atrium [146, 147]. Histologically, cardiac angiosarcomas are tumors of mesenchymal origin and exhibit ill-defined anastomotic vascular spaces covered with endothelial cells. On the contrary to the benign vascular tumors, the endothelial cells are anaplastic and form irregular anastomosing sinusoid structures [138].

MR Imaging Findings

MR images usually demonstrate large, heterogeneous mass arising from the right atrial wall, which is also involving the pericardium. Signal intensity of T1- and T2-weighted images depends on amount of necrosis and hemorrhage of the tumors. Usually cardiac angiosarcomas are heterogeneous with predominant hyperintensity on T2-weighted images [148, 149] (Fig. 16.10). On cine images, tumors also appear to be heterogeneously hyperintense, and they tend to have a "cauliflower" appearance [150, 151]. Because of the nature of the tumor, first-pass perfusion will show diffuse and avid enhancement peripherally; however, less perfusion is present centrally due to the necrosis [149, 151]. Diffuse oblong cardiac angiosarcomas with pericardial infiltration show linear contrast enhancement with hypointense, necrotic core giving rise to "sunray" appearance [152, 153].

Treatment

Cardiac angiosarcomas are aggressive, and most of the patients present in the later stages of disease. Thus, they are associated with poor prognosis and survival of 9–10 months [154]. Unfortunately, there is no single effective treatment available for cardiac angiosarcoma patients; however, combination of treatments including surgery, irradiation, chemotherapy, and immunotherapy has been advocated [24, 154, 155].

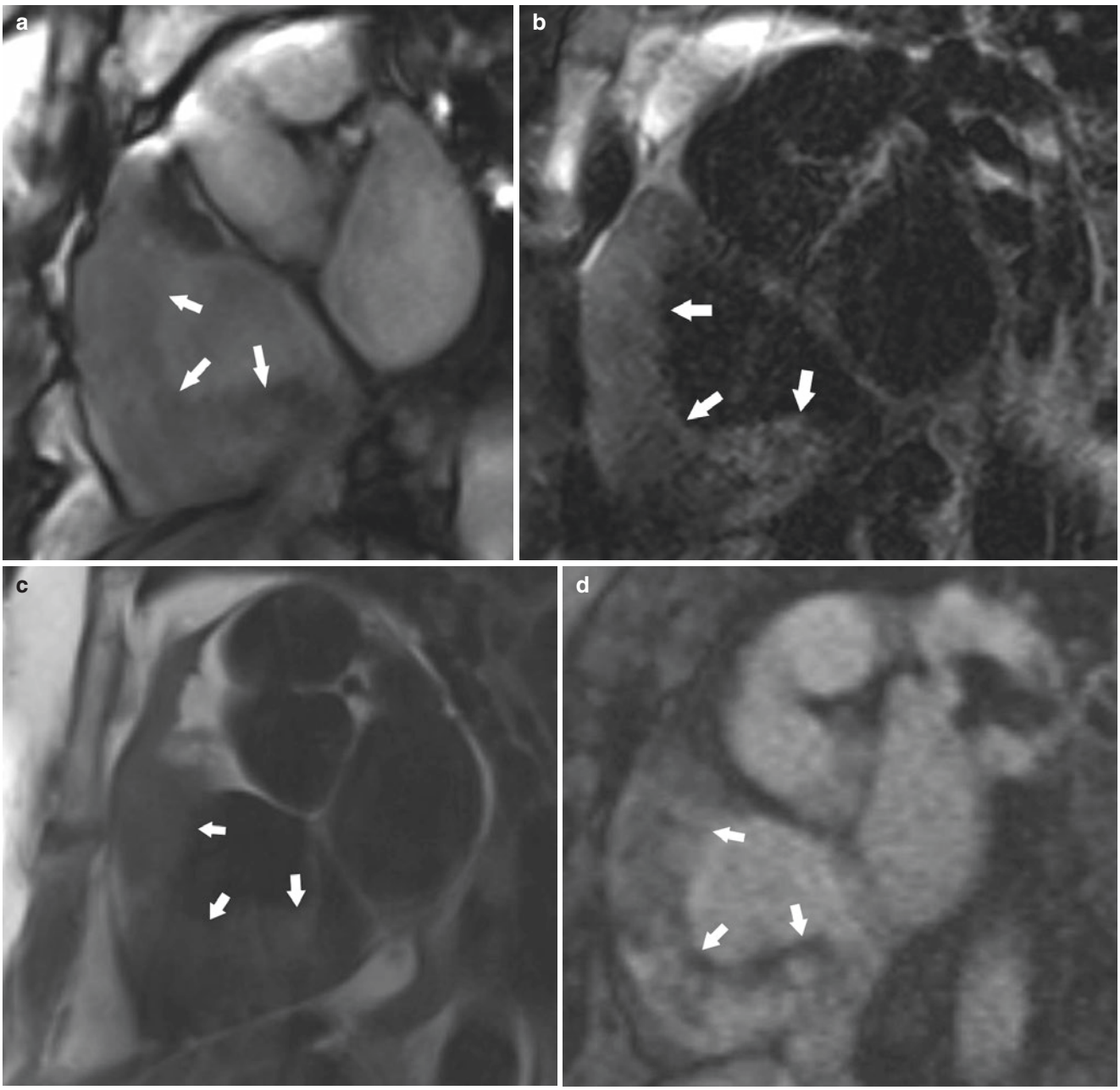

Fig. 16.10 A 70-year-old female presented with shortness of breath and echocardiography revealed a right atrial wall mass (not shown). (**a**) Steady-state free precession (SSFP) image, short-axis slice, shows an infiltrative, cardiac angiosarcoma (arrows) along the right atrial wall, which is hyperintense on (**b**) T2-weighted double inversion recovery (DIR) image, short-axis view (arrows), and isointense on (**c**) T1-weighted DIR image, short-axis view (arrows). (**d**) First-pass perfusion (FFP) image short-axis view demonstrates avid enhancement throughout the infiltrative mass (arrows)

Undifferentiated Sarcoma

Clinical Features

Undifferentiated sarcomas or undifferentiated pleomorphic sarcomas are very rare tumors and the most common second cardiac sarcomas after angiosarcomas with frequency of 0–24% [156]. They are malignant neoplasms without specific histologic features and typically occur in the fourth or fifth decade. They present with constitutional symptoms, including chest pain, dyspnea, and weight loss [36, 156]. They are usually found in the left atrium with an infiltrative pattern; however, biatrial involvement and extension into the cardiac valves have been reported [46, 157, 158].

Pathological Findings

Undifferentiated sarcomas may appear as a discrete or irregular mass with necrosis and hemorrhagic components. Diagnosis of these tumors depends on the histopathology and immunohistochemistry, since imaging patterns can mimic other sarcomas [159]. Histologically, tumors can be characterized by a proliferation of nondescript spindle cells without specific line of differentiation and are positive for vimentin on immunohistochemistry [160].

MR Imaging Findings

Unfortunately, there is not much described regarding MR features in the literature; however, polypoid mass within the left atrium with invasive features should be considered in the differential diagnosis [142]. Also, in terms of the signal intensity of undifferentiated cardiac tumors appear to be isointense on T1 and slight hyperintense on T2-weighted images [50] (Fig. 16.11). Sometimes these tumors mimic angiosarcoma especially when a hemorrhagic mass is replacing pericardium [142].

Treatment

Undifferentiated sarcomas have very poor prognosis with rapid proliferation and metastases [161]. Surgical excision of the tumor should be initial treatment, followed up with chemoradiotherapy although effectiveness of these therapies remains controversial [162]. When surgical resection is not possible due to extensive invasion, autotransplantation is an option for complete resection and repair [162, 163].

Rhabdomyosarcoma

Clinical Features

Cardiac rhabdomyosarcomas are rare tumors with an incidence less than 0.07% and account for 20% of all sarcomas [8]. They are most common type of sarcomas in pediatric population, but average age of presentation is the second decade of life with male predilection [164, 165]. Clinical presentation could be with arrhythmia, heart failure, and/or constitutional symptoms. It has been reported that patients with cardiac rhabdomyosarcoma may present with hypereosinophilia [166].

Pathological Findings

Cardiac rhabdomyosarcomas arise from the myocardium, striated muscle, and there is no chamber predilection although mostly originate from the ventricles [10, 142]. Large tumors contain areas of central necrosis invading pericardium and involving cardiac valves more than other sarcomas [142]. In contrary to angiosarcomas, rhabdomyosarcomas tend to invade the pericardium in nodular appearance rather than sheet-like spread, and also a portion of tumor should always involve the myocardium [142, 167, 168]. Histologically, two types of cardiac rhabdomyosarcomas are known: embryonal neoplasm, which is mostly seen in pediatric population, and pleomorphic type, a rare type mostly seen in adults [10].

MR Imaging Findings

MR images demonstrate multiple, large infiltrative masses or focally hypertrophied myocardium isointense to muscle on T1-weighted images [169–171]. They can appear heterogeneously with high signal intensity on T2-weighted images, due to central necrosis in all sequences [36, 142]. Generally, rhabdomyosarcomas demonstrate diffuse homogeneous enhancement of the tumor [142].

Treatment

Cardiac rhabdomyosarcomas are very aggressive with survival less than a year and have tendency to produce local or distant metastases [170]. Surgical resection is the choice of treatment. Although due to infiltrative nature, it can be difficult to perform and also have poor response to chemoradiotherapy [172].

Osteosarcoma

Clinical Features

Cardiac osteosarcomas are rare cardiac masses which account for 3–9% of all sarcomas [10]. The age of presentation varies between 14 and 77 years, and median age is in the fourth decade with a female predilection [173]. Patients usually present with congestive heart failure because of the location of the tumor [174]. Osteosarcomas are almost always located in the left atrium and have a broad base of attachment at a location away from the fossa ovalis with invasive features [36]. There have been case reports published of cardiac osteosarcomas in the right atrium or ventricle [175, 176]. Because of the left-sided location, small lesions can be confused with myxomas, especially when images do not reveal calcifications [177, 178]. Because of this feature, it has been suggested cardiac osteosarcoma should be considered in all atypical left atrial myxomas [174].

Pathological Findings

Cardiac osteosarcomas are osteoid tumors that contain malignant bone-producing cells and spindle-cells, and depending on cell types, they can be subgrouped as osteoblastic, chondroblastic, or fibroblastic type [36]. They are well-circumscribed and pseudoencapsulated or irregularly lobulated infiltrative tumors with “gritty” or “stone hard”

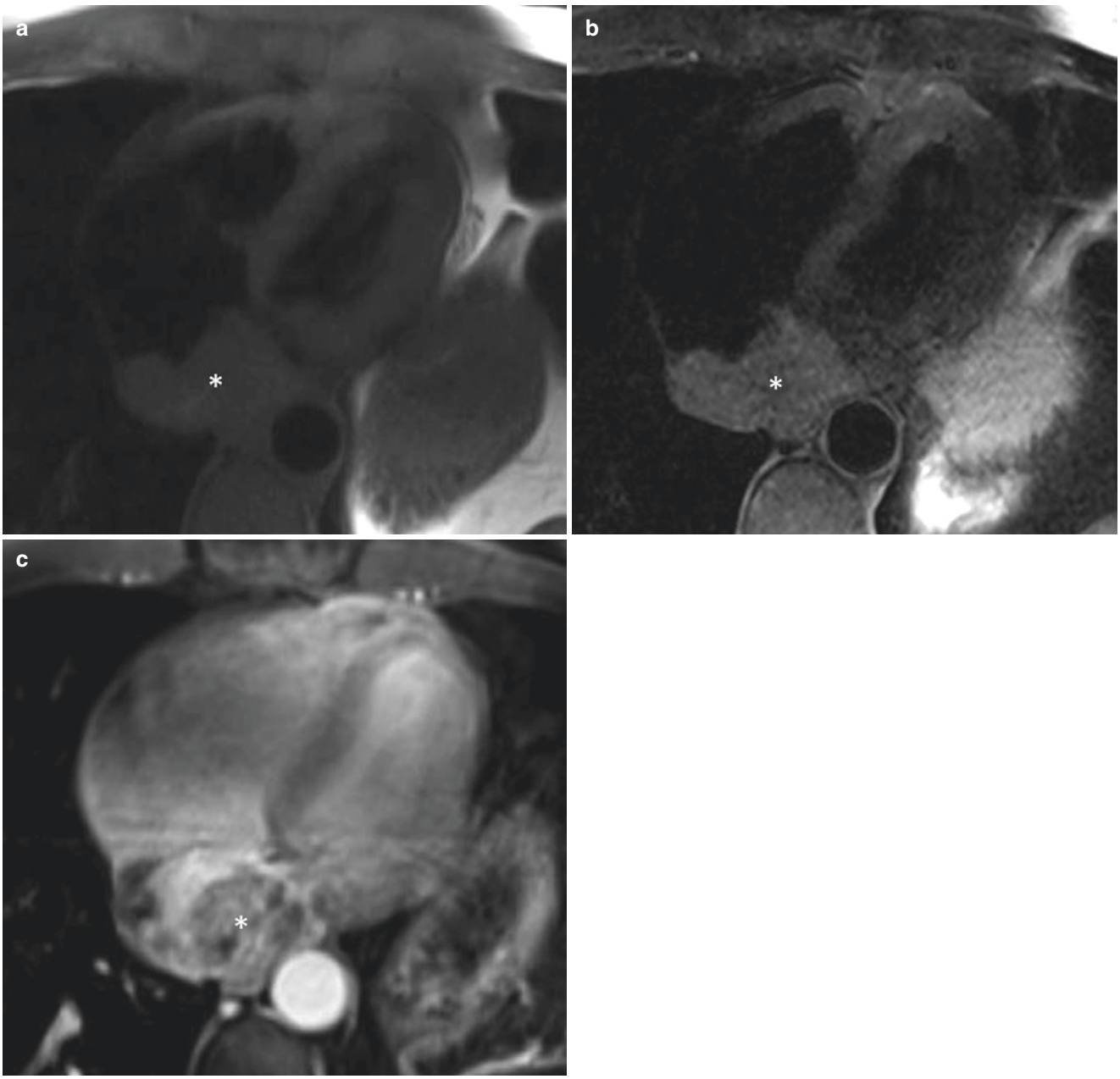

Fig. 16.11 A 43-year-old male with remote history of Hodgkin's disease and mantle radiation treatment presented with hoarseness in his voice due to vocal cord paralysis. Chest CT was performed (not shown) and revealed enlarged mediastinal metastatic lymph nodes, which account for the vocal cord paralysis. Also, CT of the chest demonstrated left atrial mass, and patient was referred for cardiac MRI exam. (**a**) T1-weighted double inversion recovery (DIR) image, four-chamber view, demonstrates isointense infiltrative mass (asterisk) arising from the left atrial wall, abutting the descending thoracic aorta. (**b**) T2-weighted DIR image, four-chamber view, shows hyperintense signal intensity (asterisk), and (**c**) T1-weighted 3D gradient-recalled echo (GRE) sequence, axial post-contrast image displays heterogeneous enhancement (asterisk). Histopathology of the mass demonstrated undifferentiated pleomorphic sarcoma

appearance of calcifications upon gross sectioning [142, 179, 180]. Osteosarcomas commonly contain large amount of calcifications; however, in their early stages, they can contain minimal calcifications and can be mistaken for benign, dystrophic calcifications [29, 174]. Tumors usually contain scattered areas of necrosis and hemorrhage [174].

MR Imaging Findings

MR images usually demonstrate a mass with invasive features and heterogeneous signal intensity both on T1- and T2-weighted images [36, 181, 182]. High signal intensity areas on T2-weighted images will demonstrate enhancement on post-contrast images suggesting hypercellular components

of the tumor [182]. This heterogeneity attributes to the histologic composition as described above.

Treatment

Although cardiac osteosarcomas are very aggressive with high frequency of recurrence and metastases, surgical resection should be done to avoid tricuspid obstruction and restore biventricular diastolic function [183].

Leiomyosarcoma

Clinical Features

Cardiac leiomyosarcomas are malignant tumors representing 1% of all cardiac tumors and 8–9% of all cardiac sarcomas. They differentiate from smooth muscle lining the subendocardium. Most of the tumors arise from the muscles of the pulmonary arteries and extend into the heart [29, 142]. Patients with cardiac leiomyosarcoma typically present in the fourth decade of life [10]. Because of the predilection for the left atrium and pulmonary vein invasion, clinically patients present with dyspnea and cardiac failure from mitral obstruction [184].

Pathological Findings

Leiomyosarcomas appear to be multiple (30% of cases), sessile masses with nuclear atypia, high mitotic activity, and myxoid stroma on histologic evaluation [36, 185].

MR Imaging Findings

Tissue characterization on MR sequences is nonspecific, including intermediate signal intensity on T1-weighted and increased signal intensity on T2-weighted images [186]. Leiomyosarcomas appear to be avid enhancing lesions on post-contrast images [187]. However, they also contain hypoperfused areas on perfusion studies, correlating to necrotic areas [188].

Treatment

Surgical treatment is indicated in cardiac leiomyosarcomas because of the highly aggressive and locally invasive nature. If complete surgical excision of the tumors is not possible at the time of diagnosis, extensive resection with reconstruction followed by chemotherapy can be performed [189]. However, surgical resection alone is still preferred for palliation and prolonged survival [190]. The mean survival rate of patients with leiomyosarcoma is 6 months after the diagnosis [189].

Fibrosarcoma

Clinical Features

Fibrosarcomas are another rare cardiac tumors and represent about 5% of cardiac sarcomas [10]. Similar to most other sarcomas, they tend to occur in the left atrium and usually manifests as congestive heart failure [10, 142].

Pathological Findings

Cardiac fibrosarcomas are malignant composed of cells with morphologic features of fibroblasts [10]. On gross examination, cardiac fibrosarcomas have soft, lobulated, gelatinous appearance [191, 192]. They are broad-based tumors and may infiltrate the pericardium by direct invasion or by deposition of tumor nodules [142].

MR Imaging Findings

Because of the low number of cases, limited MR imaging descriptions of fibrosarcoma exist in the literature [142]. Usually these tumors are heterogeneous or isointense on T1-weighted images and hyperintense on T2-weighted and SSFP images [193, 194]. Post-contrast images reveal mild contrast enhancement [194].

Treatment

Generally cardiac fibrosarcomas have very poor prognosis, although Putnam et al. have shown that combination of surgery and chemotherapy may improve survival [195].

Liposarcoma

Clinical Features

Cardiac liposarcomas are extremely rare malignant mesenchymal neoplasms that contain lipoblasts [10]. Patients usually manifest with dyspnea and arrhythmia; however, presentation with pericardial tamponade also has been reported [10, 196]. These tumors usually occur in adults and arise from the atrium with an endoluminal growth pattern simulating cardiac myxomas [197]. Case reports in the English literature have shown liposarcomas in both ventricles and with involvement of cardiac valves [198, 199].

Pathological Findings

Liposarcomas are typically multi-lobulated yellowish masses on gross examination, and histologically four subtypes have been described: well-differentiated, undifferentiated, pleomorphic, and myxoid liposarcomas [10, 200].

MR Imaging Findings

MR imaging findings of cardiac liposarcomas are nonspecific and depend on histologic subtypes. For example, tissue characteristics of myxoid type may mimic cardiac myxomas; however, all types tend to have broad-based attachments in contradiction to benign lesions [201, 202]. Since they rarely contain significant amounts of macroscopic fat, it is difficult to diagnose liposarcoma confidently. Due to the necrosis and hemorrhage, signal intensities appear to be heterogeneous in all sequences [203].

Treatment

Patients with cardiac liposarcoma present in advanced stages, and thus complete surgical excision is almost impossible. In these cases, resection is usually performed only for palliation, and like other cardiac sarcomas, liposarcomas possess very poor prognosis [183, 201]. There is no established single medical or radiotherapeutic treatment available for cardiac liposarcomas [201].

Synovial Sarcoma

Clinical Features

Synovial sarcomas represent only a small proportion of cardiac sarcomas with male predilection, and mean age of presentation is 37.1 years [204]. Clinically most of the patients present with a shortness of breath and cardiac manifestations [205]. They can arise anywhere from the heart or pericardium, predominantly from the right atrium [206].

Pathological Findings

On gross examination, cardiac synovial sarcomas are usually polypoid, solid masses with a well-circumscribed external surface [207, 208]. They tend to appear as a bulky mass with a broad base and do not diffusely infiltrate the surrounding structures [209]. Histologically, they are biphasic, characterized by epithelial and spindle cell components or just spindle cell components [207].

MR Imaging Findings

Nonspecific imaging findings include a lobulated mass mostly on the right side of the heart with isointense signal intensity to the myocardium on T1-weighted images and mild hyperintense appearance on T2-weighted and cine images [210, 211]. Tumors demonstrate an enhancement on post-contrast images [210].

Treatment

Similar to other sarcomas, surgical resection is the choice of treatment, although broad-based tumor with infiltrative pattern can make impossible complete resection; thus, cardiac transplantation can be the option [212, 213].

Cardiac Lymphoma

Clinical Features

Primary cardiac lymphomas are rare malignant neoplasms and account for 1.3–2% of all primary cardiac tumors [8]. They are almost always aggressive B-cell lymphomas [214]. Primary cardiac lymphomas have a slight male predominance and usually present at sixth decade with a range of 13–90 years [215, 216]. Most common symptoms during presentation are chest pain, heart failure, pericardial effusion, palpitation, and arrhythmia [215, 217]. Patients may also present with cardiac tamponade, pulmonary embolism, superior vena cava syndrome, or sudden death, although these are less common [216, 218]. The prevalence of primary cardiac lymphoma is higher in immunocompromised patients; however, they can arise in immunocompetent individuals as well [214]. Also, lymphoma can occur in patients with HIV or posttransplantation lymphoproliferative disease (PTLD), which is caused by chronic immunosuppression and Epstein-Barr virus [219, 220].

Pathological Findings

Seventy percent of primary cardiac lymphomas arise from the right side of the heart, particularly right atrium, and appear as a single lesion in most of the cases [215, 216]. However, they can arise from any chambers of the heart, including pericardium [214]. At gross examination, tumors appear firm nodular lesion without necrotic component in contradistinction to the primary sarcomas [10]. Because of the contiguous pericardial invasion, massive pericardial effusion can be seen.

MR Imaging Findings

Cardiac MRI has the highest sensitivity for detection cardiac lymphomas [215]. MR usually demonstrates isointense or hypointense large polypoid or infiltrative lesion on T1-weighted and hyperintense on T2-weighted images [142] (Fig. 16.12). Typically large tumors encase the vasculature, particularly coronary arteries; however, lumen of the vessels is preserved. First-pass images show diffuse homogeneous enhancement of the tumor, and heterogeneous enhancement is seen on LGE images.

Treatment

Early diagnosis and treatment with chemotherapy result in a longer survival and remission of the disease, although for palliation surgical debulking may be effective [221]. Monoclonal antibody targets (e.g., rituximab) in combination with conventional chemotherapy improve survival of the patients [222]. Despite all available treatments, prognosis of the primary cardiac lymphomas still remains worse, and 60% of patients die within 2 months after diagnosis [216].

Cardiac Metastasis

Clinical Features and Pathophysiology

Cardiac metastases are secondary cardiac tumors reported to be 20–40 times more than primary cardiac tumors [4, 8]. Ten to twelve percent of patients with known malignant tumor demonstrated cardiac metastases in autopsy studies [5, 6]. The most common source of cardiac metastases is lung

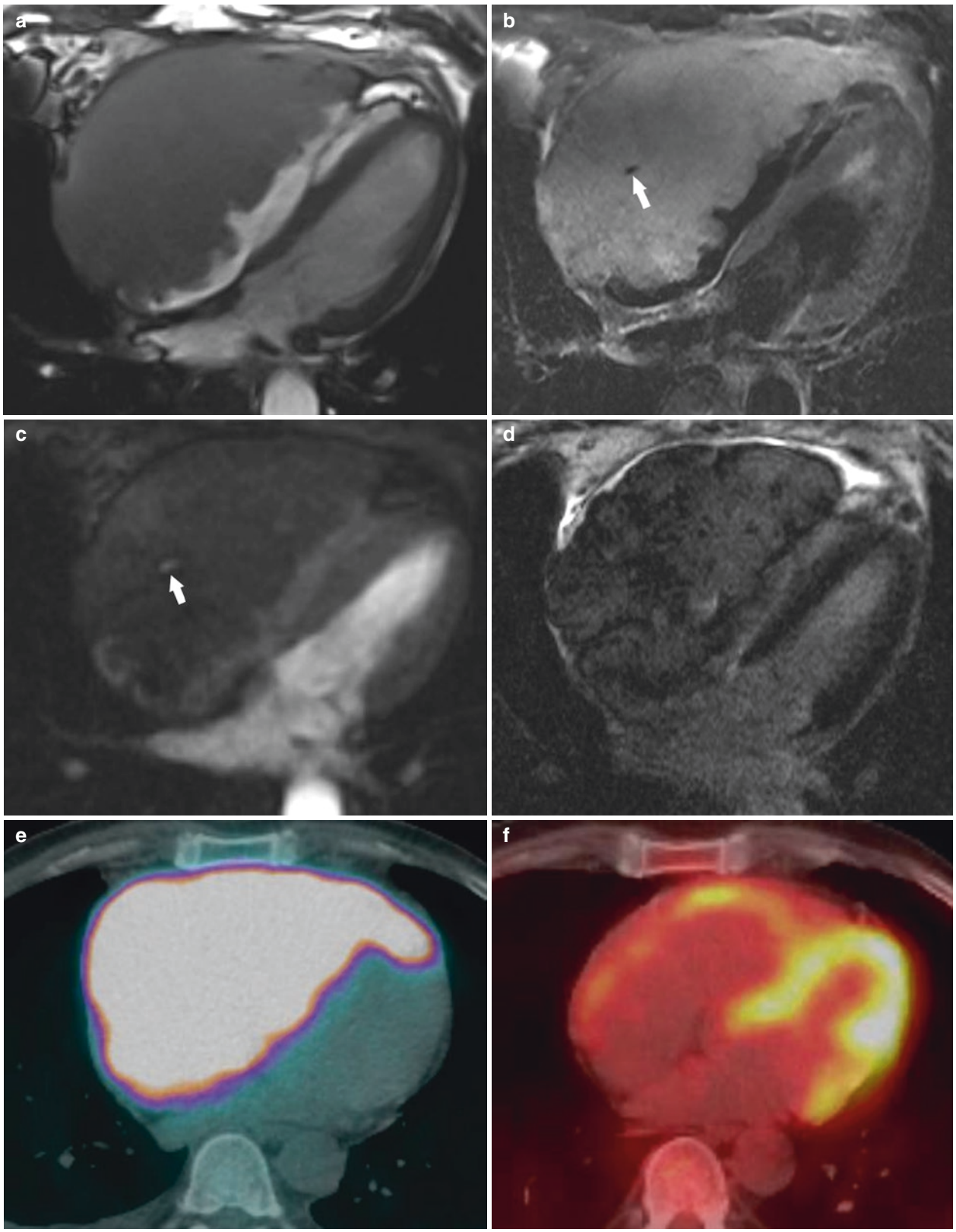

Fig. 16.12 A 55-year-old male presented with chest pain and shortness of breath. Echocardiography revealed a large mass arising from the right ventricular free wall. (**a**) Steady-state free precession (SSFP) image, four-chamber view, demonstrates a large, isointense mass along the right ventricular and atrial wall. The mass is hyperintense on (**b**) fat-suppressed T2-weighted double inversion recovery (DIR) image, four-chamber view, and right coronary artery (RCA) appears to be patent, which can be seen as a flow void (arrow). Early cycle of (**c**) first-pass perfusion (FPP) image, four-chamber view, demonstrates the patent RCA (arrow) as well, and there is heterogeneous enhancement on (**d**) late gadolinium enhancement (LGE). Histopathology of the mass revealed a large B-cell lymphoma with high-grade features. Pretreatment (**e**) PET/CT image demonstrates intensely fludeoxyglucose (FDG)-avid mass, which is completely resolved on posttreatment (**f**) images

carcinoma because of its prevalence and proximity to the heart, followed by breast cancer, lymphoma, and cancer of the esophagus [6]. Melanoma has the highest frequency of metastases to the heart, and more than half of all patients who have metastatic melanoma have cardiac involvement [223].

Malignant tumors can involve the heart through the four pathways: (1) lymphatic spread, (2) hematogenous spread, (3) direct extension, and (4) transvenous spread [224]. Lymphatic spread is the most common pathway through the tracheal and bronchomediastinal lymphatic channels in the mediastinum and results in epicardial implants and pleural effusion [225]. Hematogenous spreads to the myocardium occur through the coronary arteries, and usually metastases in other organs, particularly in the lungs, are present at the time of cardiac metastasis [226]. Most common tumors that are spreading into the heart via hematogenous pathway are melanomas and sarcomas [10] (Fig. 16.13). The third pathway, direct extension of malignant tumors into the heart, is typically seen by lung, breast, esophageal, thymic, and other mediastinal malignancies [227] (Fig. 16.14). Transvenous spread into the heart, particularly to the right atrium, occurs as an extension of malignant tumor through the superior or inferior vena cava [228]. Typically, lung, renal, adrenal, and liver cancers can metastasize with this pathway, although renal cancers are the most common malignancy.

Ninety percent of patients with metastatic involvement of the heart are clinically silent and may be discovered during autopsy [13]. However, new symptoms such as chest pain, dyspnea, or arrhythmia in patients with known malignancy are suggestive findings of cardiac metasta-

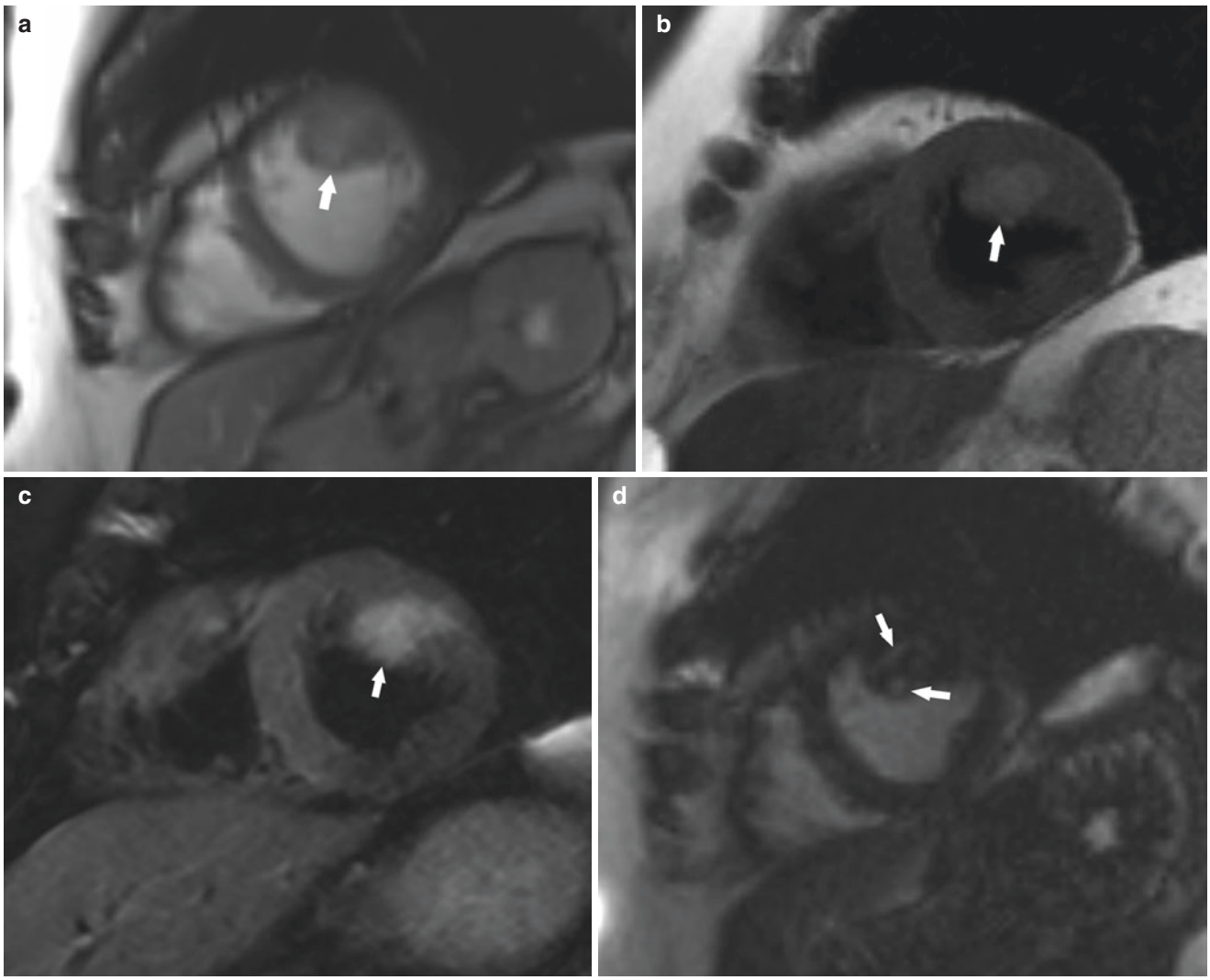

Fig. 16.13 A 70-year-old female with a cutaneous melanoma presented with arrhythmia. (**a**) Steady-state free precession (SSFP) image, short-axis slice, demonstrates hyperintense mass (arrow) in the left ventricular wall extending into the lumen. The mass (arrows) appears to be hyperintense on (**b**) T1- and (**c**) T2-weighted double inversion recovery (DIR) images, short-axis slices. On late gadolinium enhancement (LGE) image, short-axis slice displays heterogeneous enhancement (arrows) (**d**)

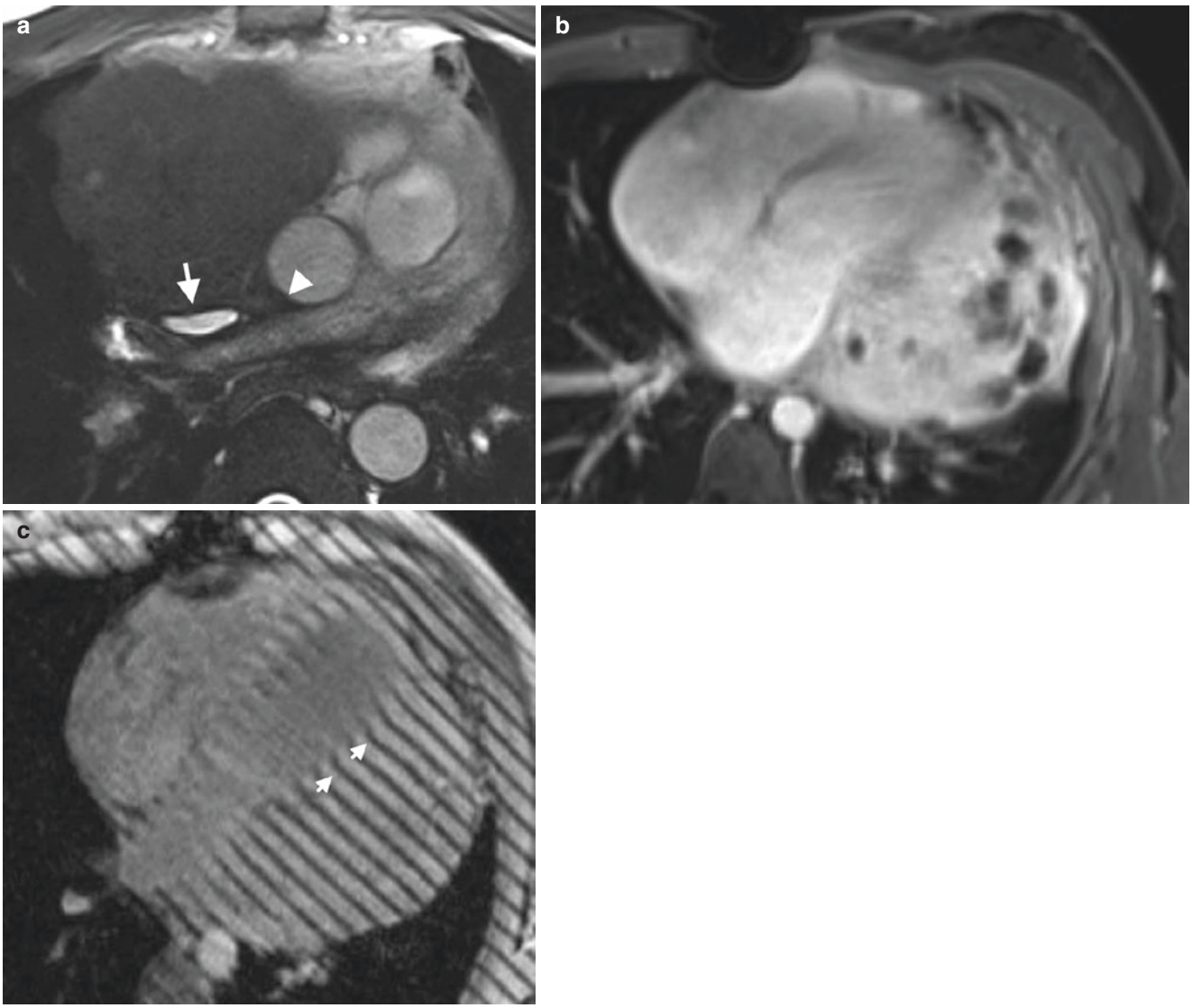

Fig. 16.14 A 50-year-old male presented with right arm and right chest pain. Chest CT revealed a large mediastinal mass, and biopsy revealed squamous carcinoma arising from the thymus. The patient was referred for evaluation of the extension of the mass to the adjacent structures. (**a**) Steady-state free precession (SSFP) image, axial slice, revealed a large hyperintense mass in the anterior mediastinum, displacing superior vena cava (SVC) (arrow), ascending aorta posteriorly, and extending into the aorticopulmonary recess (arrowhead). (**b**) SSFP image, right ventricular outflow tract view, demonstrates a large hyperintense mass in the anterior mediastinum, which is invading into the roof of the right atrium (arrow) and anterior wall of the SVC (arrowhead). On (**c**) late gadolinium enhancement (LGE) image, axial slice demonstrates heterogeneously enhancing mass

ses [224]. Chest pain, especially pleuritic type in patients with known primary malignancy, is the sign of pericardial involvement and usually present with pericardial effusion [229]. Pericardial effusion can be hemorrhagic and progress into cardiac tamponade [230]. Dyspnea or symptoms related to congestive heart failure can be seen in patients with extensive myocardial involvement or obstruction of the cardiac lymphatic drainage system. The most common symptom of myocardial involvement by malignant tumor is arrhythmia [231].

MR Imaging Findings

MR imaging tissue characteristics and enhancement patterns of cardiac metastases are variable depending on the type of tumor. Most of the tumors are isointense to hypointense on T1- and hyperintense on T2-weighted images, except malignant melanoma appears to be hyperintense in both sequences [232] (Fig. 16.12). As expected, almost all cardiac metastases are enhancing on post-contrast images [233]. Tagging sequences are helpful to determine ventricular wall infiltration or adhe-

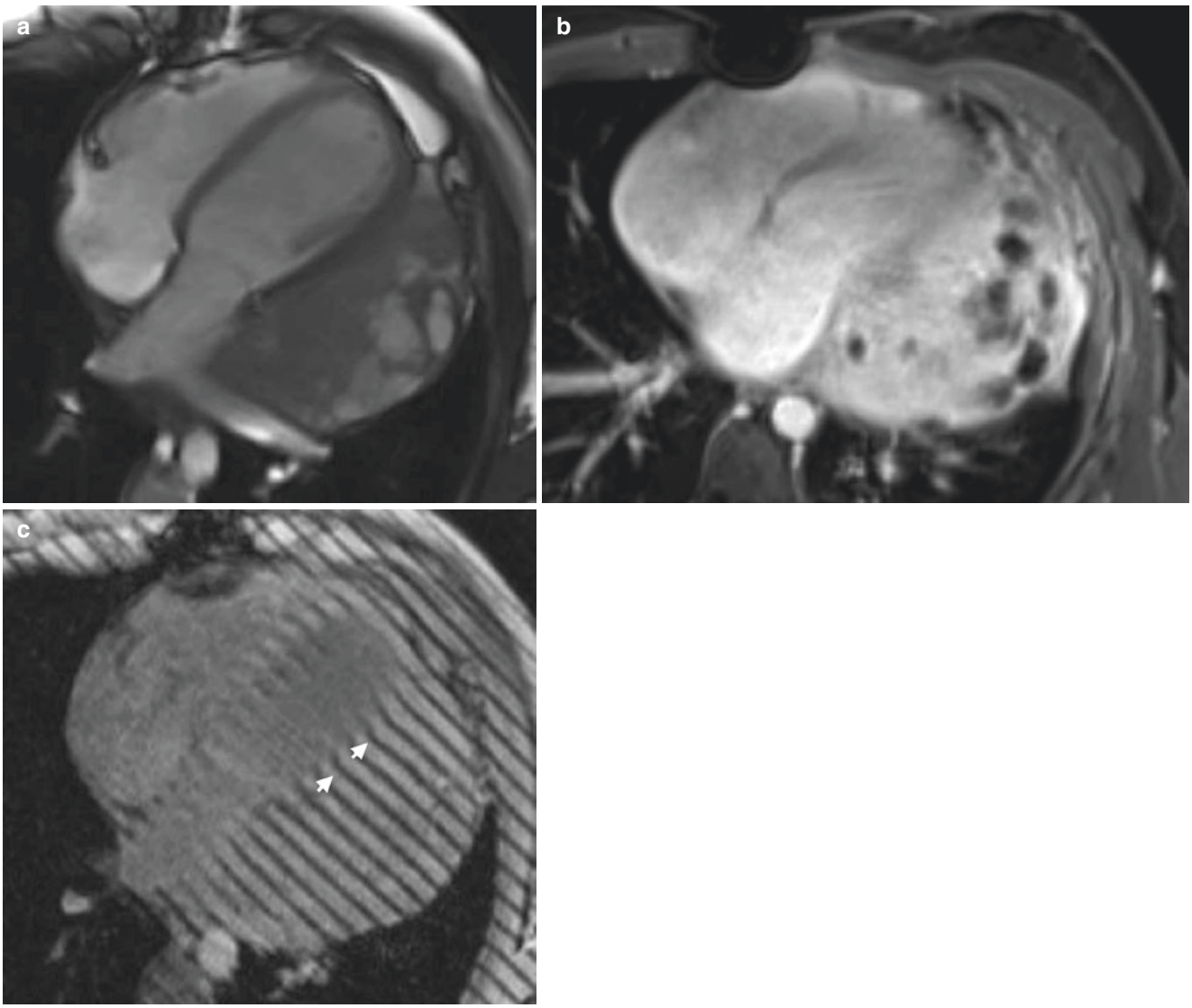

Fig. 16.15 A 21-year-old male, status post-chemoradiation treatment for a choroid plexus carcinoma at age 4, presented with shortness of breath and was referred for cardiac MRI evaluation. (**a**) Steady-state free precession image, four-chamber view, demonstrates a large, hyperintense mass with cystic components, along the left ventricle free wall. The mass enhances avidly on (**b**) T1-weighted 3D gradient-recalled echo (GRE) sequence, axial post-contrast image. There is tethering of the mid anterolateral, lateral, and inferiolateral walls of the left ventricle on (**c**) pulsed tagging sequence, four-chamber view, suggestive of adhesion or infiltration of the left ventricle. Histopathology of the mass was mesothelioma

sion (Fig. 16.15). MR imaging plays an important role in showing extent of tumor within the chamber for surgical treatments either for complete resection or palliative debulking.

Treatment

Based on the type of the primary malignant tumor, cardiac metastases can be treated with radical surgery combined with chemoradiation. For recurring malignant pericardial effusions, surgical "pericardial window" creation and administration of chemical toxins, such as radioactive gold, fluorouracil, and tetracycline for pericardial sclerosis, are the choices [234]. Temporary and permanent pacemakers can be implanted if the patients experience arrhythmia.

Nontumoral Masses

Thrombus

Clinical Features

Thrombus is the most common intracardiac mass and accountable for thromboembolic events; therefore, identification and monitoring impact the patient care [235]. Cardiac

thrombus most commonly occurs in the left atria, particularly in the left atrial appendage in patients with atrial fibrillation; however, in the setting of diminished left ventricular ejection fraction or apical aneurysm, left ventricular thrombi may occur [236]. Left ventricular thrombus prevalence is higher among patients with ischemic cardiomyopathy, as compared with those with nonischemic cardiomyopathy [236].

MR Imaging Findings

Most of the cardiac thrombi appear to be small, homogeneous, and immobile masses within the chambers [236, 237]. Signal characteristics and enhancement patterns of thrombus vary based on the age of the thrombus. An acute thrombus usually demonstrates high signal intensity on both T1- and T2-weighted images, whereas subacute thrombus will show high signal intensity on T1-weighted and low on T2-weighted images due to methemoglobin [237, 238]. Over a certain period of time, when thrombus changes in macromolecular composition and replaces with fibrous tissue, it demonstrates low signal intensity in both T1- and T2-weighted images [239] (Fig. 16.16). Contrast-enhanced images, either first-pass perfusion or LGE images, demonstrate no evidence of enhancement because of the avascular nature of the thrombi [236, 240]. Although, rarely chronic organized thrombi may represent mild enhancement peripherally due to the fibrotic content [237, 241] (Fig. 16.17). During LGE sequences, "long inversion time" (long-TI) images can be obtained with TI time of 600 ms, which will null avascular tissue such as thrombus, whereas typical inversion time for LGE is approximately around 300 ms. This long-TI images can easily differentiate thrombus from a neoplastic mass [236] (Fig. 16.18).

Lipomatous Hypertrophy of Interatrial Septum

Clinical Features

Lipomatous hypertrophy of interatrial septum (LHIS) is a rare finding with accumulation of adipose tissue in the interatrial septum [63]. The incidence of LHIS was reported 1–2.2% in autopsy series; however, with imaging, particularly in the echocardiography studies, incidence reaches to 8% [242–244]. The exact etiology is unknown; however, several predisposing factors have been associated with LHIS, including advanced age, female gender, obesity, and long-term parenteral nutrition [242, 245, 246]. It is also can be found more frequently in patients with metabolic disorders, such as cerebrotendinous xanthomatosis and mediastino-abdominal lipomatosis [247, 248]. Typically, LHIS is asymptomatic; however, degree of hypertrophy correlated with arrhythmias and also massive lipomatous hypertrophy can cause obstruction of the superior vena cava [225, 249, 250].

Pathological Findings

LHIS is composed of non-encapsulated accumulation of mature and fetal adipose tissue and atypical cardiac myocytes within the interatrial septum [244]. Typically, it involves the anterior and superior portion of the interatrial septum and spares the fossa ovalis [251].

MR Imaging Findings

LHIS usually appears to be a dumbbell-shaped thickened atrial septum on axial images, and tumor can be up to 10 cm in largest dimension [63] (Fig. 16.19). All sequences demonstrate similar imaging findings to lipoma and subcutaneous fat, which is bright on T1-weighted and has slightly less high signal intensity on T2-weighted images with signal drop-out on fat-saturated sequences [36]. LHIS does not show enhancement after contrast administration [252].

Treatment

In the rare cases of superior vena cava obstruction or clinically significant arrhythmias, patients undergo partial surgical resection and septal reconstruction [249, 253].

Pericardial Cyst

Clinical Features

Pericardial cysts are benign congenital masses that occur anywhere in the mediastinum and along the margin of the pericardium and account for 7% of all mediastinal tumors [254]. Majority of the pericardial cysts are located in the right cardiophrenic space. Clinically almost all patients are asymptomatic and discovered incidentally on chest radiography or echocardiography.

Pathological Findings

Pericardial cysts are unilocular cystic structures and contain water-based fluid without internal septa. Calcification within the wall of the cyst and hemorrhage can occur. They do not have any connection with pericardium, in contradistinction to pericardial diverticulum.

MR Imaging Findings

Due to cystic structures, pericardial cysts appear to be hypointense on T1-weighted images and hyperintense on T2-weighted images, although cysts with proteinaceous content may appear hyperintense on T1-weighted images [36]. They are hyperintense on SSFP images and do not enhance on post-contrast images (Fig. 16.20).

Treatment

Usually, because of the asymptomatic course, no treatment is needed for pericardial cysts. Treatment may be desired to alleviate symptoms; however, the pericardial cyst may recur.

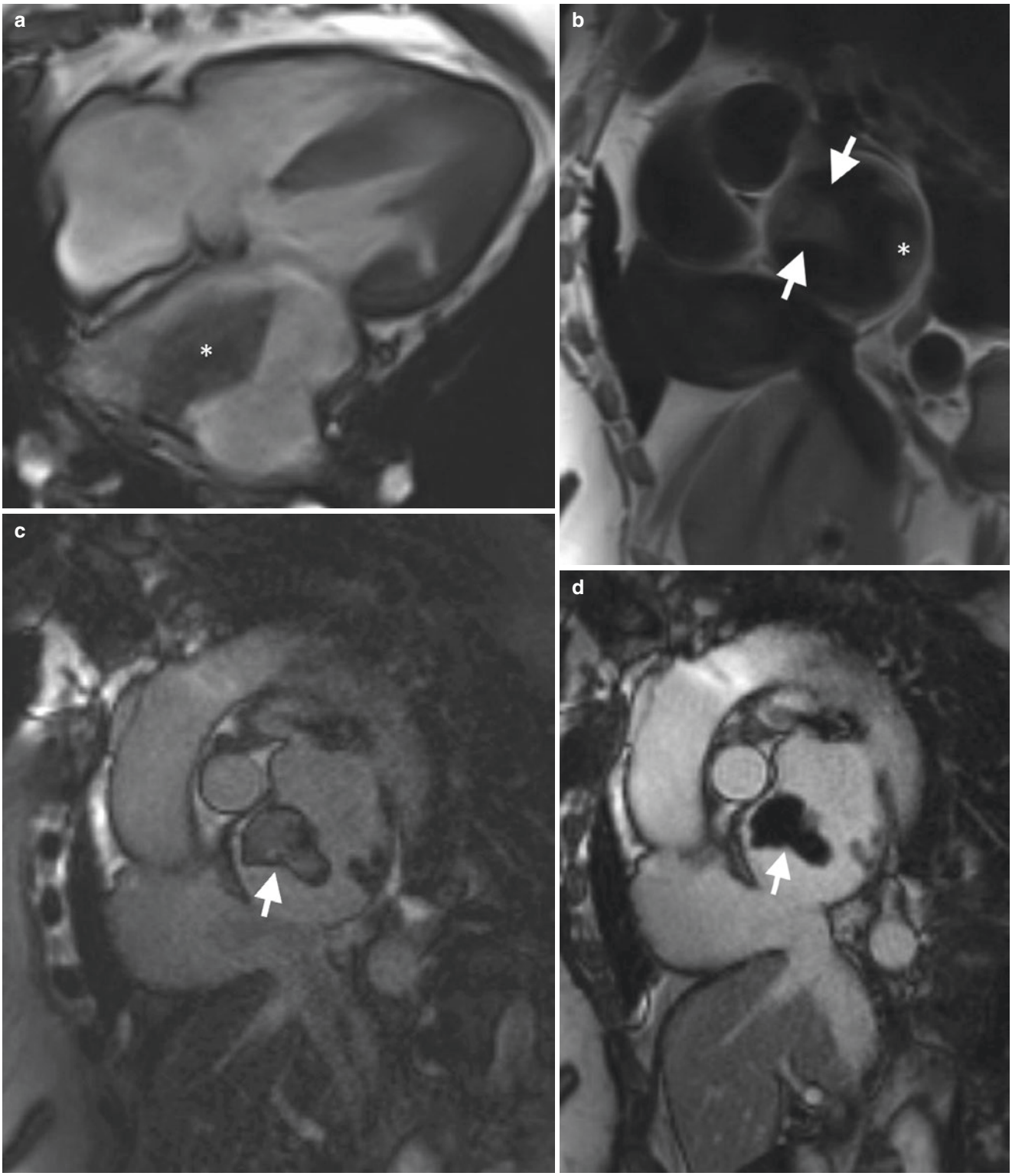

Fig. 16.16 A 66-year-old female with factor V Leiden mutation and antiphospholipid syndrome was found to have a mass on echocardiography and thus referred for cardiac MR evaluation. (**a**) Steady-state free precession image, four-chamber view, demonstrates an isointense mass in the left atrium posterior wall. (**b**) T1-weighted double inversion recovery (DIR) image, short-axis view, demonstrates an isointense mass attached to the left atrial wall *(arrows)*. There is another small mass in the posterior wall of the atrium *(asterisk)*. On (**c**) late gadolinium enhancement (LGE) image, short-axis view, the mass appears to be heterogeneously hyperintense, while on (**d**) LGE, long inversion time (TI) image (600 ms), short-axis view, the mass was nulled completely suggesting lack of enhancement

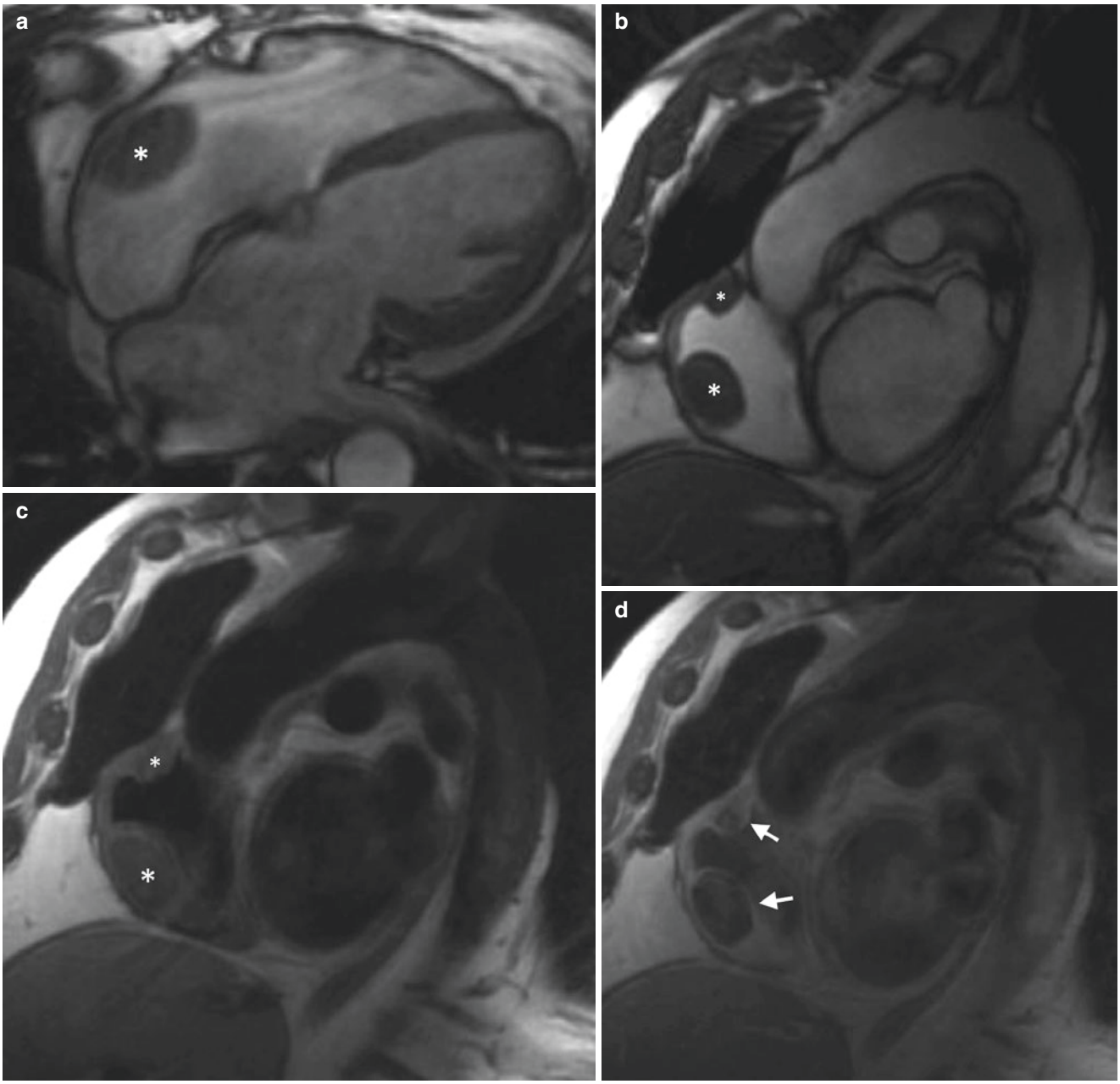

Fig. 16.17 61-year-old male status post-heart transplantation found to have masses on echocardiography. Steady-state free precession (SSFP) image, (**a**) four-chamber view, demonstrates a well-circumscribed, isointense mass in the right atrium (asterisk), and on (**b**) short-axis slice, two isointense masses can be seen (*asterisks*). On (**c**) T1-weighted double inversion recovery (DIR) image, short-axis slice shows two iso- to hypointense masses in the right atrium (*asterisks*), which are slightly enhancing peripherally on (**d**) post-contrast T1-weighted DIR image, short-axis slice (*arrows*)

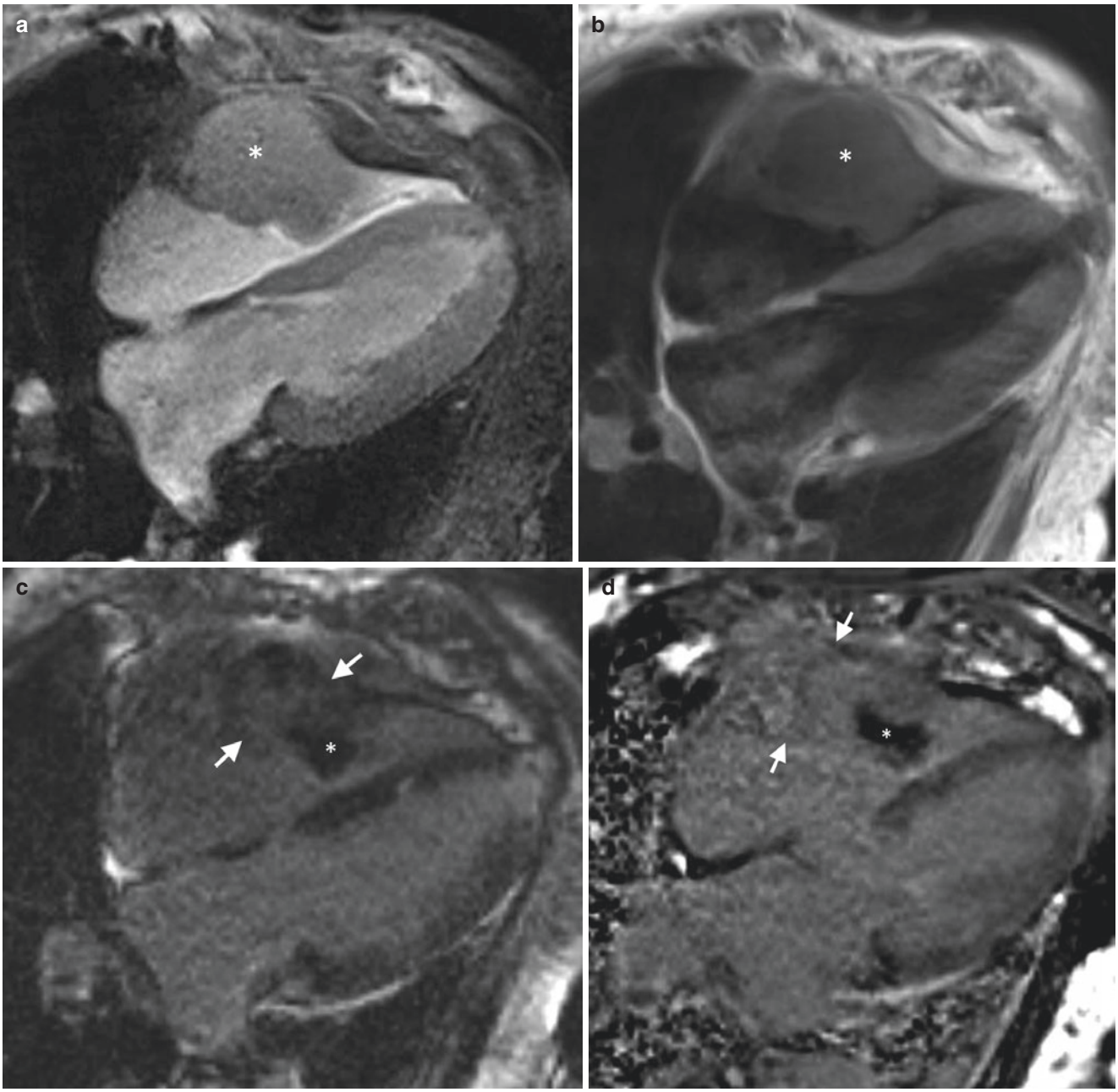

Fig. 16.18 An 81-year-old male with a renal dysfunction and bladder cancer. Further staging work-up revealed a metastatic mass in the right atrium. (**a**) Gradient-recalled echo (GRE) sequence four-chamber view image demonstrates homogeneous, isointense mass (*asterisk*) in the right atrial wall extending into the lumen. The mass appears to be iso- to hypointense on (**b**) T1-weighted double inversion recovery (DIR) sequence, four-chamber view (*asterisk*). On (**c**) late gadolinium enhancement (LGE), long inversion time (TI) image (600 ms), four-chamber view displays heterogeneously enhancing mass (arrows) without enhancing component (*asterisk*), which was confirmed with (**d**) LGE-phase-sensitive inversion recovery (PSIR) sequence four-chamber image

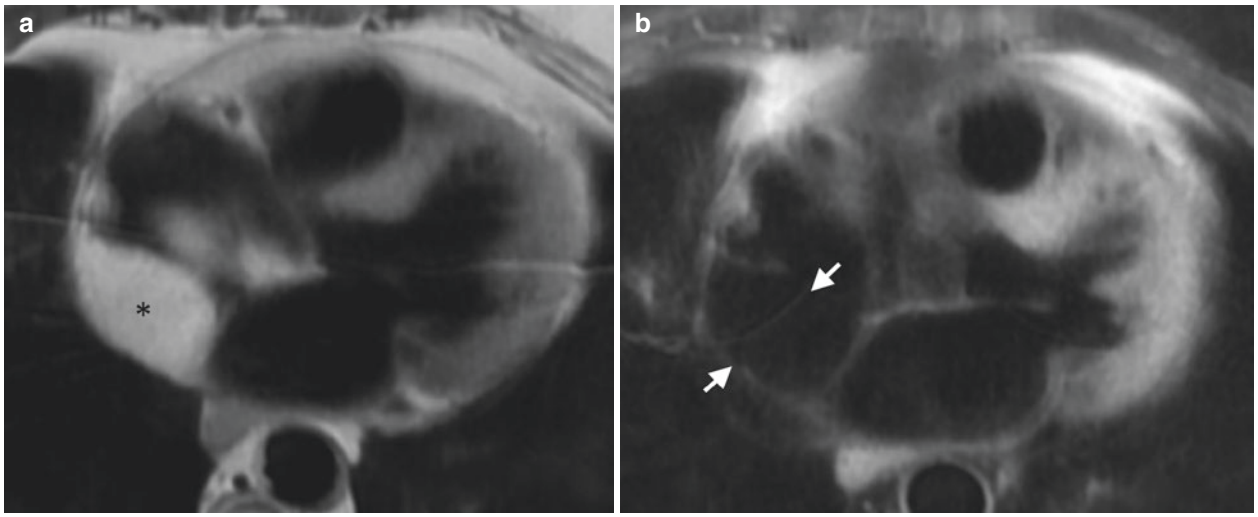

Fig. 16.19 A 61-year-old-male presented with pre-syncope, and CT revealed a mass in the right atrium. On (**a**) T1 double inversion recovery (DIR) image, four-chamber view demonstrates large, hyperintense mass in the right atrium (asterisk), which is partially obstructing the superior vena cava (not shown). On (**b**) fat-suppressed T1-weighted DIR images, four-chamber view image displays suppressed signal intensity of the mass (arrows), and subsequent surgery revealed a large, lipomatous hypertrophy of the interatrial septum

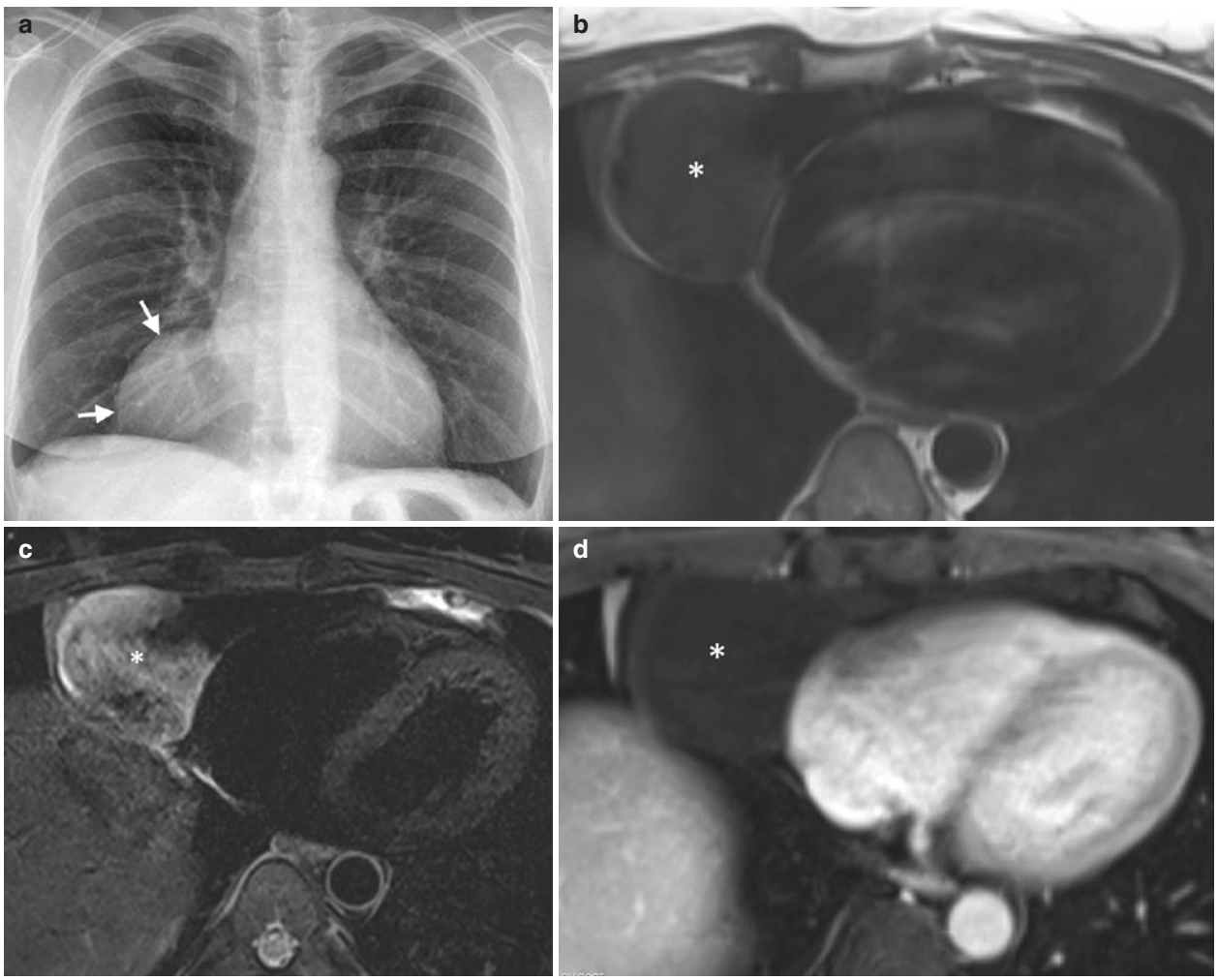

Fig. 16.20 Asymptomatic 32-year-old male found to have paracardiac opacity on (**a**) chest x-ray (arrows). On (**b**) T1-weighted double inversion recovery (DIR) image, four-chamber view demonstrates a large, hypointense right-sided paracardiac mass (asterisk), which appears to be hyperintense on (**c**) T2-weighted DIR image, four-chamber view (asterisk). T1-weighted 3D gradient-recalled echo (GRE) sequence, axial post-contrast image displays non-enhancing paracardiac mass (asterisk) (**d**)

References

1. Travis WD, World Health Organization, International Agency for Research on Cancer, International Association for the Study of Lung Cancer, International Academy of Pathology. Pathology and genetics of tumours of the lung, pleura, thymus and heart. Lyon/Oxford: IARC Press/Oxford University Press (distributor); 2004. 344 pgs.
2. Reynen K. Frequency of primary tumors of the heart. Am J Cardiol. 1996;77(1):107.
3. Sutsch G, Jenni R, von Segesser L, Schneider J. Heart tumors: incidence, distribution, diagnosis. Exemplified by 20,305 echocardiographies. Schweizerische Medizinische Wochenschrift. 1991;121(17):621–9.
4. Lam KY, Dickens P, Chan AC. Tumors of the heart. A 20-year experience with a review of 12,485 consecutive autopsies. Arch Pathol Lab Med. 1993;117(10):1027–31.
5. Abraham KP, Reddy V, Gattuso P. Neoplasms metastatic to the heart: review of 3314 consecutive autopsies. Am J Cardiovasc Pathol. 1990;3(3):195–8.
6. Klatt EC, Heitz DR. Cardiac metastases. Cancer. 1990;65(6):1456–9.
7. McManus B. Primary tumors of the heart. In: Bonow RO, Mann DL, Zipes DP, et al., editors. Braunwald's heart disease. 9th ed. Philadelphia: Elsevier Saunders; 2012. p. 1638–50.
8. McAllister HA Jr. Primary tumors and cysts of the heart and pericardium. Curr Probl Cardiol. 1979;4(2):1–51.
9. Elbardissi AW, Dearani JA, Daly RC, Mullany CJ, Orszulak TA, Puga FJ, et al. Survival after resection of primary cardiac tumors: a 48-year experience. Circulation. 2008;118(14 Suppl):S7–15.
10. Burke A, Virmani R. Tumors of the heart and great vessels: atlas of tumor pathology. 3rd ed. Washington, DC: Armed Forces Institute of Pathology; 1996.
11. Roberts WC. Primary and secondary neoplasms of the heart. Am J Cardiol. 1997;80(5):671–82.
12. Burazor I, Aviel-Ronen S, Imazio M, Markel G, Grossman Y, Yosepovich A, et al. Primary malignancies of the heart and pericardium. Clin Cardiol. 2014;37(9):582–8.
13. Butany J, Nair V, Naseemuddin A, Nair GM, Catton C, Yau T. Cardiac tumours: diagnosis and management. Lancet Oncol. 2005;6(4):219–28.
14. Bruce CJ. Cardiac tumours: diagnosis and management. Heart. 2011;97(2):151–60.
15. Grebenc ML, Rosado-de-Christenson ML, Green CE, Burke AP, Galvin JR. Cardiac myxoma: imaging features in 83 patients. Radiographics. 2002;22(3):673–89.
16. Pinede L, Duhaut P, Loire R. Clinical presentation of left atrial cardiac myxoma. A series of 112 consecutive cases. Medicine. 2001;80(3):159–72.
17. Mendoza CE, Rosado MF, Bernal L. The role of interleukin-6 in cases of cardiac myxoma. Clinical features, immunologic abnormalities, and a possible role in recurrence. Tex Heart Inst J. 2001;28(1):3–7.
18. Elbardissi AW, Dearani JA, Daly RC, Mullany CJ, Orszulak TA, Puga FJ, et al. Embolic potential of cardiac tumors and outcome after resection: a case-control study. Stroke. 2009;40(1):156–62.
19. Ekinci EI, Donnan GA. Neurological manifestations of cardiac myxoma: a review of the literature and report of cases. Intern Med J. 2004;34(5):243–9.
20. Sabolek M, Bachus-Banaschak K, Bachus R, Arnold G, Storch A. Multiple cerebral aneurysms as delayed complication of left cardiac myxoma: a case report and review. Acta Neurol Scand. 2005;111(6):345–50.
21. Acebo E, Val-Bernal JF, Gomez-Roman JJ, Revuelta JM. Clinicopathologic study and DNA analysis of 37 cardiac myxomas: a 28-year experience. Chest. 2003;123(5):1379–85.
22. Kocak H, Ozyazicioglu A, Gundogdu C, Sevimli S. Cardiac hemangioma complicated with cerebral and coronary embolization. Heart Vessel. 2005;20(6):296–7.
23. Fox E, Brunson C, Campbell W, Aru G. Cardiac papillary fibroelastoma presents as an acute embolic stroke in a 35-year-old African American male. Am J Med Sci. 2006;331(2):91–4.
24. Pomper GJ, Gianani R, Johnston RJ, Rizeq MN. Cardiac angiosarcoma: an unusual presentation with cutaneous metastases. Arch Pathol Lab Med. 1998;122(3):273–6.
25. Sinatra R, Brancaccio G, di Gioia CRT, De Santis M, Sbraga F, Gallo P. Integrated approach for cardiac angiosarcoma. Int J Cardiol. 2003;88(2–3):301–4.
26. Motwani M, Kidambi A, Herzog BA, Uddin A, Greenwood JP, Plein S. MR imaging of cardiac tumors and masses: a review of methods and clinical applications. Radiology. 2013;268(1):26–43.
27. Meng Q, Lai H, Lima J, Tong W, Qian Y, Lai S. Echocardiographic and pathologic characteristics of primary cardiac tumors: a study of 149 cases. Int J Cardiol. 2002;84(1):69–75.
28. Hendel RC, Patel MR, Kramer CM, Poon M, Hendel RC, Carr JC, et al. ACCF/ACR/SCCT/SCMR/ASNC/NASCI/SCAI/SIR 2006 appropriateness criteria for cardiac computed tomography and cardiac magnetic resonance imaging: a report of the American College of Cardiology Foundation Quality Strategic Directions Committee Appropriateness Criteria Working Group, American College of Radiology, Society of Cardiovascular Computed Tomography, Society for Cardiovascular Magnetic Resonance, American Society of Nuclear Cardiology, North American Society for Cardiac Imaging, Society for Cardiovascular Angiography and Interventions, and Society of Interventional Radiology. J Am Coll Cardiol. 2006;48(7):1475–97.
29. O'Donnell DH, Abbara S, Chaithiraphan V, Yared K, Killeen RP, Cury RC, et al. Cardiac tumors: optimal cardiac MR sequences and spectrum of imaging appearances. AJR Am J Roentgenol. 2009;193(2):377–87.
30. Altbach MI, Squire SW, Kudithipudi V, Castellano L, Sorrell VL. Cardiac MRI is complementary to echocardiography in the assessment of cardiac masses. Echocardiography. 2007;24(3):286–300.
31. Hundley WG, Bluemke DA, Finn JP, Flamm SD, Fogel MA, Friedrich MG, et al. ACCF/ACR/AHA/NASCI/SCMR 2010 expert consensus document on cardiovascular magnetic resonance: a report of the American College of Cardiology Foundation Task Force on Expert Consensus Documents. Circulation. 2010;121(22):2462–508.
32. Pennell D, Sechtem U, Higgins C, Manning W, Pohost G, Rademakers F, et al. Clinical indications for cardiovascular magnetic resonance (CMR): Consensus Panel report. J Cardiovasc Magn Reson. 2004;6(4):727–65.
33. Fussen S, De Boeck BW, Zellweger MJ, Bremerich J, Goetschalckx K, Zuber M, et al. Cardiovascular magnetic resonance imaging for diagnosis and clinical management of suspected cardiac masses and tumours. Eur Heart J. 2011;32(12):1551–60.
34. Hoffmann U, Globits S, Schima W, Loewe C, Puig S, Oberhuber G, et al. Usefulness of magnetic resonance imaging of cardiac and paracardiac masses. Am J Cardiol. 2003;92(7):890–5.
35. Kramer CM, Barkhausen J, Flamm SD, Kim RJ, Nagel E, Society for Cardiovascular Magnetic Resonance Board of Trustees Task Force on Standardized P. Standardized cardiovascular magnetic resonance (CMR) protocols 2013 update. J Cardiovasc Magn Reson. 2013;15:91.
36. Sparrow PJ, Kurian JB, Jones TR, Sivananthan MU. MR imaging of cardiac tumors. Radiographics. 2005;25(5):1255–76.
37. Bouton S, Yang A, McCrindle BW, Kidd L, McVeigh ER, Zerhouni EA. Differentiation of tumor from viable myocardium using cardiac tagging with MR imaging. J Comput Assist Tomogr. 1991;15(4):676–8.

38. Simonetti OP, Finn JP, White RD, Laub G, Henry DA. "Black blood" T2-weighted inversion-recovery MR imaging of the heart. Radiology. 1996;199(1):49–57.
39. Reynen K. Cardiac myxomas. N Engl J Med. 1995;333 (24):1610–7.
40. Kuon E, Kreplin M, Weiss W, Dahm JB. The challenge presented by right atrial myxoma. Herz. 2004;29(7):702–9.
41. Bjessmo S, Ivert T. Cardiac myxoma: 40 years' experience in 63 patients. Ann Thorac Surg. 1997;63(3):697–700.
42. Premaratne S, Hasaniya NW, Arakaki HY, Mugiishi MM, Mamiya RT, McNamara JJ. Atrial myxomas: experiences with 35 patients in Hawaii. Am J Surg. 1995;169(6):600–3.
43. Carney JA, Gordon H, Carpenter PC, Shenoy BV, Go VL. The complex of myxomas, spotty pigmentation, and endocrine overactivity. Medicine. 1985;64(4):270–83.
44. Farah MG. Familial cardiac myxoma. A study of relatives of patients with myxoma. Chest. 1994;105(1):65–8.
45. Pucci A, Gagliardotto P, Zanini C, Pansini S, di Summa M, Mollo F. Histopathologic and clinical characterization of cardiac myxoma: review of 53 cases from a single institution. Am Heart J. 2000;140(1):134–8.
46. Orlandi A, Ferlosio A, Dell'Anna V, Quitadamo R, Pellegrino A, Spagnoli LG. Undifferentiated sarcoma of the heart: a rare clinicopathologic presentation. J Thorac Cardiovasc Surg. 2002;124(1):192–3.
47. Tazelaar HD, Locke TJ, McGregor CG. Pathology of surgically excised primary cardiac tumors. Mayo Clin Proc. 1992;67(10):957–65.
48. McCarthy PM, Piehler JM, Schaff HV, Pluth JR, Orszulak TA, Vidaillet HJ Jr, et al. The significance of multiple, recurrent, and "complex" cardiac myxomas. J Thorac Cardiovasc Surg. 1986;91(3):389–96.
49. Kaminaga T, Takeshita T, Kimura I. Role of magnetic resonance imaging for evaluation of tumors in the cardiac region. Eur Radiol. 2003;13(Suppl 6):L1–L10.
50. Syed IS, Feng D, Harris SR, Martinez MW, Misselt AJ, Breen JF, et al. MR imaging of cardiac masses. Magn Reson Imaging Clin N Am. 2008;16(2):137–64, vii.
51. Masui T, Takahashi M, Miura K, Naito M, Tawarahara K. Cardiac myxoma: identification of intratumoral hemorrhage and calcification on MR images. AJR Am J Roentgenol. 1995;164(4):850–2.
52. Larsson S, Lepore V, Kennergren C. Atrial myxomas: results of 25 years' experience and review of the literature. Surgery. 1989;105(6):695–8.
53. Castells E, Ferran V, Octavio de Toledo MC, Calbet JM, Benito M, Fontanillas C, et al. Cardiac myxomas: surgical treatment, long-term results and recurrence. J Cardiovasc Surg. 1993;34(1):49–53.
54. Salanitri JC, Pereles FS. Cardiac lipoma and lipomatous hypertrophy of the interatrial septum: cardiac magnetic resonance imaging findings. J Comput Assist Tomogr. 2004;28(6):852–6.
55. Hananouchi GI, Goff WB 2nd. Cardiac lipoma: six-year follow-up with MRI characteristics, and a review of the literature. Magn Reson Imaging. 1990;8(6):825–8.
56. Kamiya H, Ohno M, Iwata H, Ohsugi S, Sawada K, Koike A, et al. Cardiac lipoma in the interventricular septum: evaluation by computed tomography and magnetic resonance imaging. Am Heart J. 1990;119(5):1215–7.
57. King SJ, Smallhorn JF, Burrows PE. Epicardial lipoma: imaging findings. AJR Am J Roentgenol. 1993;160(2):261–2.
58. Mullen JC, Schipper SA, Sett SS, Trusler GA. Right atrial lipoma. Ann Thorac Surg. 1995;59(5):1239–41.
59. Doshi S, Halim M, Singh H, Patel R. Massive intrapericardial lipoma, a rare cause of breathlessness. Investigations and management. Int J Cardiol. 1998;66(2):211–5.
60. Akram K, Hill C, Neelagaru N, Parker M. A left ventricular lipoma presenting as heart failure in a septuagenarian: a first case report. Int J Cardiol. 2007;114(3):386–7.
61. Grande AM, Minzioni G, Pederzolli C, Rinaldi M, Pederzolli N, Arbustini E, et al. Cardiac lipomas. Description of 3 cases. J Cardiovasc Surg. 1998;39(6):813–5.
62. Vanderheyden M, De Sutter J, Wellens F, Andries E. Left atrial lipoma: case report and review of the literature. Acta Cardiol. 1998;53(1):31–2.
63. Burke AP, Litovsky S, Virmani R. Lipomatous hypertrophy of the atrial septum presenting as a right atrial mass. Am J Surg Pathol. 1996;20(6):678–85.
64. Araoz PA, Mulvagh SL, Tazelaar HD, Julsrud PR, Breen JF. CT and MR imaging of benign primary cardiac neoplasms with echocardiographic correlation. Radiographics. 2000; 20(5):1303–19.
65. Sankar NM, Thiruchelvam T, Thirunavukkaarasu K, Pang K, Hanna WM. Symptomatic lipoma in the right atrial free wall. A case report. Tex Heart Inst J. 1998;25(2):152–4.
66. Ashar K, van Hoeven KH. Fatal lipoma of the heart. Am J Cardiovasc Pathol. 1992;4(1):85–90.
67. Howard RA, Aldea GS, Shapira OM, Kasznica JM, Davidoff R. Papillary fibroelastoma: increasing recognition of a surgical disease. Ann Thorac Surg. 1999;68(5):1881–5.
68. Gowda RM, Khan IA, Nair CK, Mehta NJ, Vasavada BC, Sacchi TJ. Cardiac papillary fibroelastoma: a comprehensive analysis of 725 cases. Am Heart J. 2003;146(3):404–10.
69. Roberts WC. Papillary fibroelastomas of the heart. Am J Cardiol. 1997;80(7):973–5.
70. Kumar G, Macdonald RJ, Sorajja P, Edwards WD, Ommen SR, Klarich KW. Papillary fibroelastomas in 19 patients with hypertrophic cardiomyopathy undergoing septal myectomy. J Am Soc Echocardiogr. 2010;23(6):595–8.
71. Scalia D, Basso C, Rizzoli G, Lupia M, Budano S, Thiene G, et al. Should right-sided fibroelastomas be operated upon? J Heart Valve Dis. 1997;6(6):647–50.
72. Aggarwal A, Leavitt BJ. Images in clinical medicine. Giant Lambl's excrescences. N Engl J Med. 2003;349(25):e24.
73. Matsumoto N, Sato Y, Kusama J, Matsuo S, Kinukawa N, Kunimasa T, et al. Multiple papillary fibroelastomas of the aortic valve: case report. Int J Cardiol. 2007;122(1):e1–3.
74. Edwards FH, Hale D, Cohen A, Thompson L, Pezzella AT, Virmani R. Primary cardiac valve tumors. Ann Thorac Surg. 1991;52(5):1127–31.
75. Sun JP, Asher CR, Yang XS, Cheng GG, Scalia GM, Massed AG, et al. Clinical and echocardiographic characteristics of papillary fibroelastomas : a retrospective and prospective study in 162 patients. Circulation. 2001;103(22):2687–93.
76. Wintersperger BJ, Becker CR, Gulbins H, Knez A, Bruening R, Heuck A, et al. Tumors of the cardiac valves: imaging findings in magnetic resonance imaging, electron beam computed tomography, and echocardiography. Eur Radiol. 2000;10(3):443–9.
77. Kondruweit M, Schmid M, Strecker T. Papillary fibroelastoma of the mitral valve: appearance in 64-slice spiral computed tomography, magnetic resonance imaging, and echocardiography. Eur Heart J. 2008;29(6):831.
78. Kelle S, Chiribiri A, Meyer R, Fleck E, Nagel E. Images in cardiovascular medicine. Papillary fibroelastoma of the tricuspid valve seen on magnetic resonance imaging. Circulation. 2008;117(11):e190–1.
79. Klarich KW, Enriquez-Sarano M, Gura GM, Edwards WD, Tajik AJ, Seward JB. Papillary fibroelastoma: echocardiographic characteristics for diagnosis and pathologic correlation. J Am Coll Cardiol. 1997;30(3):784–90.
80. Shahian DM, Labib SB, Chang G. Cardiac papillary fibroelastoma. Ann Thorac Surg. 1995;59(2):538–41.
81. Eftychiou C, Antoniades L. Cardiac hemangioma in the left ventricle and brief review of the literature. J Cardiovasc Med. 2009;10(7):565–7.

82. Kipfer B, Englberger L, Stauffer E, Carrel T. Rare presentation of cardiac hemangiomas. Ann Thorac Surg. 2000;70(3):977–9.
83. Zanati SG, Hueb JC, Cogni AL, de Morais MG, de Almeida Prado Franceschi LE, et al. Cardiac hemangioma of the right atrium. Eur J Echocardiogr. 2008;9(1):52–3.
84. Oshima H, Hara M, Kono T, Shibamoto Y, Mishima A, Akita S. Cardiac hemangioma of the left atrial appendage: CT and MR findings. J Thorac Imaging. 2003;18(3):204–6.
85. Kojima S, Sumiyoshi M, Suwa S, Tamura H, Sasaki A, Kojima T, et al. Cardiac hemangioma: a report of two cases and review of the literature. Heart Vessels. 2003;18(3):153–6.
86. Palmer TE, Tresch DD, Bonchek LI. Spontaneous resolution of a large, cavernous hemangioma of the heart. Am J Cardiol. 1986;58(1):184–5.
87. Beroukhim RS, Prakash A, Buechel ER, Cava JR, Dorfman AL, Festa P, et al. Characterization of cardiac tumors in children by cardiovascular magnetic resonance imaging: a multicenter experience. J Am Coll Cardiol. 2011;58(10):1044–54.
88. Herman TE, Siegel MJ, McAlister WH. Cardiac tumor in Gorlin syndrome. Nevoid basal cell carcinoma syndrome. Pediatr Radiol. 1991;21(3):234–5.
89. Walpot J, Shivalkar B, Bogers JP, Salgado R, Rodrigus I, Van Marck E, et al. A patient with cardiac fibroma and a subvalvular aortic stenosis caused by a subvalvular membrane. J Am Soc Echocardiogr. 2007;20(7):906 e1-4.
90. Cina SJ, Smialek JE, Burke AP, Virmani R, Hutchins GM. Primary cardiac tumors causing sudden death: a review of the literature. Am J Forensic Med Pathol. 1996;17(4):271–81.
91. Patel J, Patel S, Sheppard MN. Benign cardiac tumours associated with sudden death. Europace. 2014;16(6):855–60.
92. Burke AP, Rosado-de-Christenson M, Templeton PA, Virmani R. Cardiac fibroma: clinicopathologic correlates and surgical treatment. J Thorac Cardiovasc Surg. 1994;108(5):862–70.
93. Goel S, Chen O, Brichkov I, Lipton J, Seemanthini L, Shani J. Asymptomatic giant cardiac fibroma presenting as mitral valve prolapse in an adult patient. Int J Cardiovasc Imaging. 2015;31(2):315–7.
94. Luna A, Ribes R, Caro P, Vida J, Erasmus JJ. Evaluation of cardiac tumors with magnetic resonance imaging. Eur Radiol. 2005;15(7):1446–55.
95. Kiaffas MG, Powell AJ, Geva T. Magnetic resonance imaging evaluation of cardiac tumor characteristics in infants and children. Am J Cardiol. 2002;89(10):1229–33.
96. Beghetti M, Gow RM, Haney I, Mawson J, Williams WG, Freedom RM. Pediatric primary benign cardiac tumors: a 15-year review. Am Heart J. 1997;134(6):1107–14.
97. Grebenc ML, Rosado de Christenson ML, Burke AP, Green CE, Galvin JR. Primary cardiac and pericardial neoplasms: radiologic-pathologic correlation. Radiographics. 2000;20(4):1073–103; Quiz 110-1, 112.
98. Burke AP, Gatto-Weis C, Griego JE, Ellington KS, Virmani R. Adult cellular rhabdomyoma of the heart: a report of 3 cases. Hum Pathol. 2002;33(11):1092–7.
99. Krasuski RA, Hesselson AB, Landolfo KP, Ellington KJ, Bashore TM. Cardiac rhabdomyoma in an adult patient presenting with ventricular arrhythmia. Chest. 2000;118(4):1217–21.
100. Chen X, Hoda SA, Edgar MA. Cardiac rhabdomyoma. Arch Pathol Lab Med. 2002;126(12):1559.
101. Berkenblit R, Spindola-Franco H, Frater RW, Fish BB, Glickstein JS. MRI in the evaluation and management of a newborn infant with cardiac rhabdomyoma. Ann Thorac Surg. 1997;63(5):1475–7.
102. Fieno DS, Saouaf R, Thomson LE, Abidov A, Friedman JD, Berman DS. Cardiovascular magnetic resonance of primary tumors of the heart: A review. J Cardiovasc Magn Reson. 2006;8(6):839–53.
103. Bosi G, Lintermans JP, Pellegrino PA, Svaluto-Moreolo G, Vliers A. The natural history of cardiac rhabdomyoma with and without tuberous sclerosis. Acta Paediatr. 1996;85(8):928–31.
104. Burke A, Virmani R. Pediatric heart tumors. Cardiovasc Pathol. 2008;17(4):193–8.
105. Nir A, Tajik AJ, Freeman WK, Seward JB, Offord KP, Edwards WD, et al. Tuberous sclerosis and cardiac rhabdomyoma. Am J Cardiol. 1995;76(5):419–21.
106. Lin JC, Palafox BA, Jackson HA, Cohen AJ, Gazzaniga AB. Cardiac pheochromocytoma: resection after diagnosis by 111-indium octreotide scan. Ann Thorac Surg. 1999;67(2):555–8.
107. Jeevanandam V, Oz MC, Shapiro B, Barr ML, Marboe C, Rose EA. Surgical management of cardiac pheochromocytoma. Resection versus transplantation. Ann Surg. 1995;221(4):415–9.
108. Schirpenbach C, Hoppert T, Aleksic I, Neumann HP, Hahner S, Fassnacht M, et al. A 47-year-old patient with paroxysmal arterial hypertension and gastric tumors. Internist. 2012;53(9):1119–24.
109. Heufelder AE, Hofbauer LC. Greetings from below the aortic arch! The paradigm of cardiac paraganglioma. J Clin Endocrinol Metab. 1996;81(3):891–5.
110. Hamilton BH, Francis IR, Gross BH, Korobkin M, Shapiro B, Shulkin BL, et al. Intrapericardial paragangliomas (pheochromocytomas): imaging features. AJR Am J Roentgenol. 1997;168(1):109–13.
111. Rana O, Gonda P, Addis B, Greaves K. Image in cardiovascular medicine. Intrapericardial paraganglioma presenting as chest pain. Circulation. 2009;119(12):e373–5.
112. Cane ME, Berrizbeitia LD, Yang SS, Mahapatro D, McGrath LB. Paraganglioma of the interatrial septum. Ann Thorac Surg. 1996;61(6):1845–7.
113. Goldstein DJ, Oz MC, Rose EA, Fisher P, Michler RE. Experience with heart transplantation for cardiac tumors. J Heart Lung Transplant. 1995;14(2):382–6.
114. Orenstein HH, Green GE, Kancherla PL. Aortocoronary paraganglioma. Anatomic relationship of left coronary artery to paraganglia of aorta. New York State J Med. 1984;84(1):33–6.
115. Lee HH, Brenner WI, Vardhan I, Hyatt J, Terlecki M. Cardiac pheochromocytoma originating in the interatrial septum. Chest. 1990;97(3):760–2.
116. Stowers SA, Gilmore P, Stirling M, Morantz JM, Miller AB, Meyer LJ, et al. Cardiac pheochromocytoma involving the left main coronary artery presenting with exertional angina. Am Heart J. 1987;114(2):423–7.
117. Buckley O, Madan R, Kwong R, Rybicki FJ, Hunsaker A. Cardiac masses, part 2: key imaging features for diagnosis and surgical planning. AJR Am J Roentgenol. 2011;197(5):W842–51.
118. Tomasian A, Lai C, Ruehm S, Krishnam MS. Cardiovascular magnetic resonance and PET-CT of left atrial paraganglioma. J Cardiovasc Magn Reson. 2010;12:1.
119. Yendamuri S, Elfar M, Walkes JC, Reardon MJ. Aortic paraganglioma requiring resection and replacement of the aortic root. Interact Cardiovasc Thorac Surg. 2007;6(6):830–1.
120. Rakovich G, Ferraro P, Therasse E, Duranceau A. Preoperative embolization in the management of a mediastinal paraganglioma. Ann Thorac Surg. 2001;72(2):601–3.
121. Burke AP, Anderson PG, Virmani R, James TN, Herrera GA, Ceballos R. Tumor of the atrioventricular nodal region. A clinical and immunohistochemical study. Arch Pathol Lab Med. 1990;114(10):1057–62.
122. Sharma G, Linden MD, Schultz DS, Inamdar KV. Cystic tumor of the atrioventricular node: an unexpected finding in an explanted heart. Cardiovasc Pathol. 2010;19(3):e75–8.
123. Monma N, Satodate R, Tashiro A, Segawa I. Origin of so-called mesothelioma of the atrioventricular node. An immunohistochemical study. Arch Pathol Lab Med. 1991;115(10):1026–9.
124. Wolf PL, Bing R. The smallest tumor which causes sudden death. JAMA. 1965;194(6):674–5.
125. Guo J, Zuo S, Lin C, Ji Y. Surgical treatment of a giant cystic tumor of the atrioventricular nodal region. Interact Cardiovasc Thorac Surg. 2009;8(5):592–3.

126. Strom EH, Skjorten F, Stokke ES. Polycystic tumor of the atrioventricular nodal region in a man with Emery-Dreifuss muscular dystrophy. Pathol Res Pract. 1993;189(8):960–4; Discussion 5–7.
127. Law KB, Feng T, Nair V, Cusimano RJ, Butany J. Cystic tumor of the atrioventricular node: rare antemortem diagnosis. Cardiovasc Pathol. 2012;21(2):120–7.
128. Randhawa K, Ganeshan A, Hoey ET. Magnetic resonance imaging of cardiac tumors: part 1, sequences, protocols, and benign tumors. Curr Probl Diagn Radiol. 2011;40(4):158–68.
129. Tran TT, Starnes V, Wang X, Getzen J, Ross BD. Cardiovascular magnetics resonance diagnosis of cystic tumor of the atrioventricular node. J Cardiovasc Magn Reson. 2009;11:13.
130. Balasundaram S, Halees SA, Duran C. Mesothelioma of the atrioventricular node: first successful follow-up after excision. Eur Heart J. 1992;13(5):718–9.
131. Saito S, Kobayashi J, Tagusari O, Bando K, Niwaya K, Nakajima H, et al. Successful excision of a cystic tumor of the atrioventricular nodal region. Circ J. 2005;69(10):1293–4.
132. Kaji T, Takamatsu H, Noguchi H, Tahara H, Matsuda H, Nomura Y, et al. Cardiac lymphangioma: case report and review of the literature. J Pediatr Surg. 2002;37(10):1–3.
133. Huang Z. Lymphangioma of the left ventricle. J Cardiac Surg. 2013;28(1):24–6.
134. Jougon J, Laborde MN, Parrens M, MacBride T. Cystic lymphangioma of the heart mimicking a mediastinal tumor. Eur J Cardiothorac Surg. 2002;22(3):476–8.
135. Pennec PY, Blanc JJ. Cardiac lymphangioma: a benign cardiac tumour. Eur Heart J. 2006;27(24):2913.
136. Look Hong NJ, Pandalai PK, Hornick JL, Shekar PS, Harmon DC, Chen YL, et al. Cardiac angiosarcoma management and outcomes: 20-year single-institution experience. Ann Surg Oncol. 2012;19(8):2707–15.
137. Casha AR, Davidson LA, Roberts P, Nair RU. Familial angiosarcoma of the heart. J Thorac Cardiovasc Surg. 2002;124(2):392–4.
138. Best AK, Dobson RL, Ahmad AR. Best cases from the AFIP: cardiac angiosarcoma. Radiographics. 2003;23 Spec No:S141–5.
139. Afzal MN, Alguacil-Garcia A. Primary cardiac angiosarcoma: clinical and pathological diagnostic problems. Can J Cardiol. 1997;13(3):293–6.
140. van Beek EJ, Stolpen AH, Khanna G, Thompson BH. CT and MRI of pericardial and cardiac neoplastic disease. Cancer Imaging. 2007;7:19–26.
141. Herrmann MA, Shankerman RA, Edwards WD, Shub C, Schaff HV. Primary cardiac angiosarcoma: a clinicopathologic study of six cases. J Thorac Cardiovasc Surg. 1992;103(4):655–64.
142. Araoz PA, Eklund HE, Welch TJ, Breen JF. CT and MR imaging of primary cardiac malignancies. Radiographics. 1999;19(6):1421–34.
143. Khanji M, Lee E, Ionescu A. Blushing primary cardiac angiosarcoma. Heart. 2014;100(3):266.
144. Puppala S, Hoey ET, Mankad K, Wood AM. Primary cardiac angiosarcoma arising from the interatrial septum: magnetic resonance imaging appearances. Br J Radiol. 2010;83(995):e230–4.
145. Rodrigues AG, Tardif JC, Petitclerc R, Mercier LA, Paquet E, Leung TK, et al. Angiosarcomas of the interatrial septum mimicking atrial myxomas. J Am Soc Echocardiogr. 1996;9(2):209–12.
146. Chaturvedi A, Vummidi D, Shuman WP, Dubinsky TJ, Maki JH. Cardiac angiosarcoma: an unusual cause of coronary artery pseudoaneurysm. J Thorac Imaging. 2012;27(1):W8–9.
147. Berry MF, Williams M, Welsby I, Lin S. Cardiac angiosarcoma presenting with right coronary artery pseudoaneurysm. J Cardiothorac Vasc Anesth. 2010;24(4):633–5.
148. Kakizaki S, Takagi H, Hosaka Y. Cardiac angiosarcoma responding to multidisciplinary treatment. Int J Cardiol. 1997;62(3):273–5.
149. Valeviciene N, Mataciunas M, Tamosiunas A, Petrulioniene Z, Briediene R. Primary heart angiosarcoma detected by magnetic resonance imaging. Acta Radiol. 2006;47(7):675–9.
150. Kim EE, Wallace S, Abello R, Coan JD, Ewer MS, Salem PA, et al. Malignant cardiac fibrous histiocytomas and angiosarcomas: MR features. J Comput Assist Tomogr. 1989;13(4):627–32.
151. Deetjen AG, Conradi G, Mollmann S, Hamm CW, Dill T. Cardiac angiosarcoma diagnosed and characterized by cardiac magnetic resonance imaging. Cardiol Rev. 2006;14(2):101–3.
152. Yahata S, Endo T, Honma H, Ino T, Hayakawa H, Ogawa M, et al. Sunray appearance on enhanced magnetic resonance image of cardiac angiosarcoma with pericardial obliteration. Am Heart J. 1994;127(2):468–71.
153. Akkaya Z, Gursoy A, Erden A. The disastrous "sun ray" sign in cardiac magnetic resonance: an indicator of angiosarcoma. Cardiol Young. 2014;24(5):929–31.
154. Kurian KC, Weisshaar D, Parekh H, Berry GJ, Reitz B. Primary cardiac angiosarcoma: case report and review of the literature. Cardiovasc Pathol. 2006;15(2):110–2.
155. Brandt RR, Arnold R, Bohle RM, Dill T, Hamm CW. Cardiac angiosarcoma: case report and review of the literature. Zeitschrift fur Kardiologie. 2005;94(12):824–8.
156. Burke AP, Cowan D, Virmani R. Primary sarcomas of the heart. Cancer. 1992;69(2):387–95.
157. Donsbeck AV, Ranchere D, Coindre JM, Le Gall F, Cordier JF, Loire R. Primary cardiac sarcomas: an immunohistochemical and grading study with long-term follow-up of 24 cases. Histopathology. 1999;34(4):295–304.
158. Itoh K, Matsumura T, Egawa Y, Watanabe M, Ohshio T, Ohta A, et al. Primary mitral valve sarcoma in infancy. Pediatr Cardiol. 1998;19(2):174–7.
159. Bi W, Qu R, Ren W. A primary pericardial undifferentiated sarcoma invading the right atrium and superior vena cava. Echocardiography. 2012;29(8):E182–5.
160. Turhan N, Ozguler Z, Cagli K, Cagli K, Golbasi Z. Primary cardiac undifferentiated sarcoma: role of intraoperative imprint cytology and frozen section of two cases. Cardiovasc Pathol. 2011;20(4):232–7.
161. Furukawa N, Gummert J, Borgermann J. Complete resection of undifferentiated cardiac sarcoma and reconstruction of the atria and the superior vena cava: case report. J Cardiothorac Surg. 2012;7:96.
162. Bakaeen FG, Jaroszewski DE, Rice DC, Walsh GL, Vaporciyan AA, Swisher SS, et al. Outcomes after surgical resection of cardiac sarcoma in the multimodality treatment era. J Thorac Cardiovasc Surg. 2009;137(6):1454–60.
163. Doty DB, Doty JR, Reid BB, Anderson JL. Left atrial sarcoma: resection and repair by cardiac autotransplant and in situ pericardial patch. Ann Thorac Surg. 2006;82(4):1514–7.
164. Hui KS, Green LK, Schmidt WA. Primary cardiac rhabdomyosarcoma: definition of a rare entity. Am J Cardiovasc Path. 1988;2(1):19–29.
165. Castorino F, Masiello P, Quattrocchi E, Di Benedetto G. Primary cardiac rhabdomyosarcoma of the left atrium: an unusual presentation. Tex Heart Inst J. 2000;27(2):206–8.
166. Lo Re V 3rd, Fox KR, Ferrari VA, Scott CH, Kossev PM, Kostman JR. Hypereosinophilia associated with cardiac rhabdomyosarcoma. Am J Hematol. 2003;74(1):64–7.
167. Raaf HN, Raaf JH. Sarcomas related to the heart and vasculature. Semin Surg Oncol. 1994;10(5):374–82.
168. Geyer SJ. Rhabdomyosarcoma of the heart with cerebral metastases. West J Med. 1987;147(5):596–7.
169. Schvartzman PR, White RD. Imaging of cardiac and paracardiac masses. J Thorac Imaging. 2000;15(4):265–73.
170. Villacampa VM, Villarreal M, Ros LH, Alvarez R, Cozar M, Fuertes MI. Cardiac rhabdomyosarcoma: diagnosis by MR imaging. Eur Radiol. 1999;9(4):634–7.
171. Vujin B, Benc D, Srdic S, Bikicki M, Vuckovic D, Dodic S. Rhabdomyosarcoma of the heart. Herz. 2006;31(8):798–800.

172. Dirican A, Kucukzeybek Y, Erten C, Somali I, Can A, Bayoglu IV, et al. Cardiac rhabdomyosarcoma of the left atrium. Contemp Oncol. 2014;18(1):73–5.
173. Ye Z, Shi H, Peng T, Han A. Clinical and pathological features of high grade primary cardiac osteosarcoma. Interact Cardiovasc Thorac Surg. 2011;12(1):94–5.
174. Burke AP, Virmani R. Osteosarcomas of the heart. Am J Surg Pathol. 1991;15(3):289–95.
175. Dohi T, Ohmura H, Daida H, Amano A. Primary right atrial cardiac osteosarcoma with congestive heart failure. Eur J Cardiothorac Surg. 2009;35(3):544–6.
176. Sogabe O, Ohya T. Right ventricular failure due to primary right ventricle osteosarcoma. Gen Thorac Cardiovasc Surg. 2007;55(1):19–22.
177. Hashimoto W, Hashizume K, Ariyoshi T, Taniguchi S, Miura T, Kinoshita N, et al. Primary cardiac osteosarcoma with imaging that revealed no calcification. Gen Thorac Cardiovasc Surg. 2011;59(3):184–6.
178. Bradford WT, Arora H, Sheridan BC, Sileshi B, Kumar PA. A left atrial mass in a middle-aged woman: just another myxoma? J Cardiothorac Vasc Anesth. 2013;27(4):816–8.
179. Takeuchi I, Kawaguchi T, Kimura Y, Kojima J, Shimamura H, Shimizu N, et al. Primary cardiac osteosarcoma in a young man with severe congestive heart failure. Intern Med. 2007;46(10):649–52.
180. Gomez-Rubin MC, Rios JC, Dobarro D, Sanchez-Recalde A, Bret-Zurita M, Filgueiras D, et al. A recidivant primary cardiac osteosarcoma: the role of bone scans. Cardiovasc Pathol. 2010;19(1):55–8.
181. Yamagishi M, Yamada N, Kuribayashi S. Images in cardiology: magnetic resonance imaging of cardiac osteosarcoma. Heart. 2001;85(3):311.
182. Ahn S, Choi JA, Chung JH, Choi H, Chun EJ, Choi SI, et al. MR imaging findings of a primary cardiac osteosarcoma and its bone metastasis with histopathologic correlation. Korean J Radiol. 2011;12(1):135–9.
183. Neragi-Miandoab S, Kim J, Vlahakes GJ. Malignant tumours of the heart: a review of tumour type, diagnosis and therapy. Clin Oncol. 2007;19(10):748–56.
184. Clarke NR, Mohiaddin RH, Westaby S, Banning AP. Multifocal cardiac leiomyosarcoma. Diagnosis and surveillance by transoesophageal echocardiography and contrast enhanced cardiovascular magnetic resonance. Postgrad Med J. 2002;78(922):492–3.
185. Willaert W. Leiomyosarcoma of the right ventricle extending into the pulmonary trunk. Heart. 2001;86(1):e2.
186. Lo FL, Chou YH, Tiu CM, Lan GY, Hwang JH, Chern MS, et al. Primary cardiac leiomyosarcoma: imaging with 2-D echocardiography, electron beam CT and 1.5-Tesla MR. Eur J Radiol. 1998;27(1):72–6.
187. Durand E, Vanel D, Mousseaux E, Meingan P, Fornes P, Bittoun J. A recurrent left atrium leiomyosarcoma. Eur Radiol. 1998;8(1):97–9.
188. Jellis C, Doyle J, Sutherland T, Gutman J, Macisaac A. Cardiac epithelioid leiomyosarcoma and the role of cardiac imaging in the differentiation of intracardiac masses. Clin Cardiol. 2010;33(6):E6–9.
189. Antunes MJ, Vanderdonck KM, Andrade CM, Rebelo LS. Primary cardiac leiomyosarcomas. Ann Thorac Surg. 1991;51(6):999–1001.
190. Panday VR, Cramer MJ, Elbers HR, de la Riviere AB, Ernst SM, Plokker HW. Primary leiomyosarcoma of the heart presenting as obstruction to the pulmonary trunk. Am Heart J. 1997;133(4):465–6.
191. Knobel B, Rosman P, Kishon Y, Husar M. Intracardiac primary fibrosarcoma. Case report and literature review. Thorac Cardiovasc Surg. 1992;40(4):227–30.
192. Kim DG, Lee SY, Chung SK, Park SK, Chun YK, Chi JG. Brain metastasis from myxofibrosarcoma of the heart. Acta Neurochir. 1997;139(1):88–9.
193. Coskun H, Bozkurt AK, Ozbay G, Demirkesen C, Kaynak K, Vural FS. Primary fibrosarcoma of the heart. Aus N Z J Surg. 1995;65(1):66–8.
194. Hoffstetter P, Djavidani B, Feuerbach S, Hofstadter F, Seitz J. Myxoid fibrosarcoma of a pulmonary vein with extension into the left atrium. AJR Am J Roentgenol. 2006;186(2):365–7.
195. Putnam JB Jr, Sweeney MS, Colon R, Lanza LA, Frazier OH, Cooley DA. Primary cardiac sarcomas. Ann Thorac Surg. 1991;51(6):906–10.
196. Can C, Arpaci F, Celasun B, Gunhan O, Finci R. Primary pericardial liposarcoma presenting with cardiac tamponade and multiple organ metastases. Chest. 1993;103(1):328.
197. Nzayinambaho K, Noel H, Brohet C, Cosyns J, Reding R, Sonnet J, et al. Primary cardiac liposarcoma simulating a left atrial myxoma. Thorac Cardiovasc Surg. 1985;33(3):193–5.
198. Paraf F, Bruneval P, Balaton A, Deloche A, Mikol J, Maitre F, et al. Primary liposarcoma of the heart. Am J Cardiovasc Path. 1990;3(2):175–80.
199. Murtra M, Mestres CA, Igual A, Cubells J, Espinosa M, Benasco C, et al. Primary liposarcoma of the right ventricle and pulmonary artery: surgical excision and replacement of the pulmonic valve by a Bjork-Shiley tilting disc valve. Thorac Cardiovasc Surg. 1983;31(3):172–4.
200. Pino PG, Zampi G, Pergolini A, Pero G, Polizzi V, Sbaraglia F, et al. Metastatic liposarcoma of the heart. Case series and brief literature review. Herz. 2013;38(8):938–42.
201. Wu TP, Zhou F, DeAnda A Jr, Melamed J, Lim RP, Balsam LB. Surgical management of cardiac liposarcomas. J Card Surg. 2012;27(2):192–5.
202. Hoey ET, Mankad K, Puppala S, Gopalan D, Sivananthan MU. MRI and CT appearances of cardiac tumours in adults. Clin Radiol. 2009;64(12):1214–30.
203. Schrem SS, Colvin SB, Weinreb JC, Glassman E, Kronzon I. Metastatic cardiac liposarcoma: diagnosis by transesophageal echocardiography and magnetic resonance imaging. J Am Soc Echocardiogr. 1990;3(2):149–53.
204. Wang JG, Li NN. Primary cardiac synovial sarcoma. Ann Thorac Surg. 2013;95(6):2202–9.
205. Bittira B, Tsang J, Huynh T, Morin JF, Huttner I. Primary right atrial synovial sarcoma manifesting as transient ischemic attacks. Ann Thorac Surg. 2000;69(6):1949–51.
206. Kim CH, Dancer JY, Coffey D, Zhai QJ, Reardon M, Ayala AG, et al. Clinicopathologic study of 24 patients with primary cardiac sarcomas: a 10-year single institution experience. Hum Pathol. 2008;39(6):933–8.
207. Hannachi Sassi S, Zargouni N, Saadi Dakhlia M, Mrad K, Cammoun M, Ben Romdhane K. Primary synovial sarcoma of the heart. A clinicopathologic study of one case and review of the literature. Pathologica. 2004;96(1):29–34.
208. Lv X, Guo X, Chen X, He Z, Shen J, Jin T, et al. Primary cardiac synovial sarcoma. J Cardiac Surg. 2010;25(3):288–90.
209. Provenzano SC, Con R, Jones OD, Grant PW. Synovial sarcoma of the heart. Heart Lung Circ. 2006;15(4):278–9.
210. Wolf M, Van den Brande J, Rodrigus I, Paelinck BP. Giant primary right ventricular synovial sarcoma. Eur Heart J. 2014;35(37):2509.
211. Sakai M, Takami H, Joyama S, Tomita Y, Yamamoto T, Araki N, et al. Cardiac synovial sarcoma swinging through the aortic valve. Ann Thorac Surg. 2011;92(3):1129.
212. Kumar N, Agarwal S, Ahuja A, Das P, Airon B, Ray R. Spectrum of cardiac tumors excluding myxoma: Experience of a tertiary center with review of the literature. Pathol Res Pract. 2011;207(12):769–74.
213. Siebenmann R, Jenni R, Makek M, Oelz O, Turina M. Primary synovial sarcoma of the heart treated by heart transplantation. J Thorac Cardiovasc Surg. 1990;99(3):567–8.
214. Ceresoli GL, Ferreri AJ, Bucci E, Ripa C, Ponzoni M, Villa E. Primary cardiac lymphoma in immunocompetent

patients: diagnostic and therapeutic management. Cancer. 1997;80(8):1497–506.
215. Anghel G, Zoli V, Petti N, Remotti D, Feccia M, Pino P, et al. Primary cardiac lymphoma: report of two cases occurring in immunocompetent subjects. Leuk Lymphoma. 2004;45(4):781–8.
216. Chalabreysse L, Berger F, Loire R, Devouassoux G, Cordier JF, Thivolet-Bejui F. Primary cardiac lymphoma in immunocompetent patients: a report of three cases and review of the literature. Virchows Arch. 2002;441(5):456–61.
217. Rockwell L, Hetzel P, Freeman JK, Fereshetian A. Cardiac involvement in malignancies. Case 3. Primary cardiac lymphoma. J Clin Oncol. 2004;22(13):2744–5.
218. Engelen MA, Juergens KU, Breithardt G, Eckardt L. Interatrial conduction delay and atrioventricular block due to primary cardiac lymphoma. J Cardiovasc Electrophysiol. 2005;16(8):926.
219. Nelson KH, Chatzizisis YS, Steigner ML, Mitchell RN, Blankstein R, Givertz MM. Cardiac allograft involvement by post-transplantation lymphoproliferative disorder. J Am Coll Cardiol. 2013;62(10):937.
220. Nart D, Nalbantgil S, Yagdi T, Yilmaz F, Hekimgil M, Yuce G, et al. Primary cardiac lymphoma in a heart transplant recipient. Transplant Proc. 2005;37(2):1362–4.
221. Chim CS, Chan AC, Kwong YL, Liang R. Primary cardiac lymphoma. Am J Hematol. 1997;54(1):79–83.
222. Dawson MA, Mariani J, Taylor A, Koulouris G, Avery S. The successful treatment of primary cardiac lymphoma with a dose-dense schedule of rituximab plus CHOP. Ann Oncol. 2006;17(1):176–7.
223. Tas F, Mudun A, Kirma C. Cardiac involvement in melanoma: a case report and review of the literature. J Cancer Res Ther. 2010;6(3):359–61.
224. Bussani R, De-Giorgio F, Abbate A, Silvestri F. Cardiac metastases. J Clin Pathol. 2007;60(1):27–34.
225. Hancock EW. Neoplastic pericardial disease. Cardiol Clin. 1990;8(4):673–82.
226. Weiss L. An analysis of the incidence of myocardial metastasis from solid cancers. Br Heart J. 1992;68(5):501–4.
227. Petersen CD, Robinson WA, Kurnick JE. Involvement of the heart and pericardium in the malignant lymphomas. Am J Med Sci. 1976;272(2):161–5.
228. Schoen FJ, Berger BM, Guerina NG. Cardiac effects of noncardiac neoplasms. Cardiol Clin. 1984;2(4):657–70.
229. Thurber DL, Edwards JE, Achor RWP. Secondary malignant tumors of the pericardium. Circulation. 1962;26(2):228–41.
230. El Allaf D, et al. Cardiac tamponade as the first manifestation of cardiothoracic malignancy: a study of 10 cases. Eur Heart J. 1986;7:247–53.
231. Sheldon R, Isaac D. Metastatic melanoma to the heart presenting with ventricular tachycardia. Chest. 1991;99(5):1296–8.
232. Mousseaux E, Meunier P, Azancott S, Dubayle P, Gaux JC. Cardiac metastatic melanoma investigated by magnetic resonance imaging. Magn Reson Imaging. 1998;16(1):91–5.
233. Vogel-Claussen J, Rochitte CE, Wu KC, Kamel IR, Foo TK, Lima JA, et al. Delayed enhancement MR imaging: utility in myocardial assessment. Radiographics. 2006;26(3):795–810.
234. Shepherd FA. Malignant pericardial effusion. Curr Opin Oncol. 1997;9(2):170–4.
235. Sacco RL, Adams R, Albers G, Alberts MJ, Benavente O, Furie K, et al. Guidelines for prevention of stroke in patients with ischemic stroke or transient ischemic attack: a statement for healthcare professionals from the American Heart Association/American Stroke Association Council on Stroke: co-sponsored by the Council on Cardiovascular Radiology and Intervention: the American Academy of Neurology affirms the value of this guideline. Stroke. 2006;37(2):577–617.
236. Weinsaft JW, Kim HW, Shah DJ, Klem I, Crowley AL, Brosnan R, et al. Detection of left ventricular thrombus by delayed-enhancement cardiovascular magnetic resonance prevalence and markers in patients with systolic dysfunction. J Am Coll Cardiol. 2008;52(2):148–57.
237. Pazos-Lopez P, Pozo E, Siqueira ME, Garcia-Lunar I, Cham M, Jacobi A, et al. Value of CMR for the differential diagnosis of cardiac masses. JACC Cardiovasc Imaging. 2014;7(9):896–905.
238. Paydarfar D, Krieger D, Dib N, Blair RH, Pastore JO, Stetz JJ Jr, et al. In vivo magnetic resonance imaging and surgical histopathology of intracardiac masses: distinct features of subacute thrombi. Cardiology. 2001;95(1):40–7.
239. Corti R, Osende JI, Fayad ZA, Fallon JT, Fuster V, Mizsei G, et al. In vivo noninvasive detection and age definition of arterial thrombus by MRI. J Am Coll Cardiol. 2002;39(8):1366–73.
240. Barkhausen J, Hunold P, Eggebrecht H, Schuler WO, Sabin GV, Erbel R, et al. Detection and characterization of intracardiac thrombi on MR imaging. AJR Am J Roentgenol. 2002;179(6):1539–44.
241. Mollet NR. Visualization of Ventricular Thrombi With Contrast-Enhanced Magnetic Resonance Imaging in Patients With Ischemic Heart Disease. Circulation. 2002;106(23):2873–6.
242. Gay JD, Guileyardo JM, Townsend-Parchman JK, Ross K. Clinical and morphologic features of lipomatous hypertrophy ("massive fatty deposits") of the interatrial septum. Am J Forensic Med Pathol. 1996;17(1):43–8.
243. Pochis WT, Saeian K, Sagar KB. Usefulness of transesophageal echocardiography in diagnosing lipomatous hypertrophy of the atrial septum with comparison to transthoracic echocardiography. Am J Cardiol. 1992;70(3):396–8.
244. Heyer CM, Kagel T, Lemburg SP, Bauer TT, Nicolas V. Lipomatous hypertrophy of the interatrial septum: a prospective study of incidence, imaging findings, and clinical symptoms. Chest. 2003;124(6):2068–73.
245. Shirani J, Roberts WC. Clinical, electrocardiographic and morphologic features of massive fatty deposits ("lipomatous hypertrophy") in the atrial septum. J Am Coll Cardiol. 1993;22(1):226–38.
246. Beau P, Michel P, Coisne D, Morichau-Beauchant M. Lipomatous hypertrophy of the cardiac interatrial septum: an unusual complication in long-term home parenteral nutrition in adult patients. J Parenter Enter Nutr. 1991;15(6):659–62.
247. Dotti MT, Mondillo S, Plewnia K, Agricola E, Federico A. Cerebrotendinous xanthomatosis: evidence of lipomatous hypertrophy of the atrial septum. J Neurol. 1998;245(11):723–6.
248. Enzi G, Busetto L, Ceschin E, Coin A, Digito M, Pigozzo S. Multiple symmetric lipomatosis: clinical aspects and outcome in a long-term longitudinal study. Int J Obesity Rel Metabol Dis. 2002;26(2):253–61.
249. Cheezum MK, Jezior MR, Carbonaro S, Villines TC. Lipomatous hypertrophy presenting as superior vena cava syndrome. J Cardiovasc Comput Tomogr. 2014;8(3):250–1.
250. Hutter AM Jr, Page DL. Atrial arrhythmias and lipomatous hypertrophy of the cardiac interatrial septum. Am Heart J. 1971;82(1):16–21.
251. Nadra I, Dawson D, Schmitz SA, Punjabi PP, Nihoyannopoulos P. Lipomatous hypertrophy of the interatrial septum: a commonly misdiagnosed mass often leading to unnecessary cardiac surgery. Heart. 2004;90(12):e66.
252. Bajaj RR, Deva D, Kirpalani A, Yan RT, Chow CM, Lo V, et al. Cardiac magnetic resonance imaging for non-invasive diagnosis of lipomatous hypertrophy of inter-atrial septum. Indian Heart J. 2014;66(2):244–6.
253. Christiansen S, Stypmann J, Baba HA, Hammel D, Scheld HH. Surgical management of extensive lipomatous hypertrophy of the right atrium. Cardiovasc Surg. 2000;8(1):88–90.
254. Patel J, Park C, Michaels J, Rosen S, Kort S. Pericardial cyst: case reports and a literature review. Echocardiography. 2004;21(3):269–72.

Advanced Imaging of Pericardial Diseases

17

Ana Paula de Faria, Thiago Quinaglia A. C. Silva, Rodrigo Modolo, and Otávio Rizzi Coelho-Filho

Introduction

Normal Pericardium

Anatomically, the pericardium is constituted of two distinct layers surrounding the heart: (1) a visceral, which is a serous membrane with a single layer of cells adjacent to the myocardium, and (2) a parietal fibrous layer, which involves a larger portion of the heart containing elastin fibers and collagen. A serous fluid, of about 15–30 ml, is found within a virtual space between these two layers. The normal visceral pericardium may be undetectable by most imaging modalities. However, the presence of pericardial fat – which can be found either on the surface of the fibrous pericardium, within the pericardial space, or on the epicardial surface between the heart and visceral layer – along with the pericardial fluid may enable visualization of the pericardial layers due to the differences in signal intensities of these cardiac structures through magnetic resonance (MR) [1]. Pathological studies demonstrate that the normal parietal pericardium thickness ranges from 0.5 mm to 1 mm, most prominently developed adjacent to the right ventricular free wall and to the inferior and apical aspects of the left ventricle [2, 3].

A physiological restriction effect on diastolic cardiac pressure and volume is the main mechanical property of the pericardium. And, although these tissues restrict cardiac dilation in the acute conditions of volume loading, it does not appear to restrict cardiac function in the chronic pathologic states, allowing accommodation of marked elevations of cardiac volume. Thus, pericardial tissue growth is apparently present in response to chronic stretch [4]. Other important pericardial functions comprise friction reduction between the heart and surrounding structures and also a physical barrier precluding propagation of a mediastinal infection to the heart [5].

Normal Pericardium by CMR

Normal pericardium may be evaluated by CMR imaging – best measured by black blood spin-echo or cine gradient-echo images [6, 7] – as a thin parietal pericardium, a dark line surrounding the heart, measuring <4 mm in thickness. The best conditions to view the normal parietal pericardium are by means of axial images, when pericardium is surrounded by bright fat on T1-weighted spin-echo images, or, also, in the presence of pericardial effusion, using steady-state free precession (SSFP) sequence. On the other hand, the visceral pericardium is a very thin-layered tissue adjacent to the myocardium, which can only be appreciated by cardiac magnetic resonance (CMR) in pathologic states due to the increasing of its thickness (Fig. 17.1).

Epidemiology

Pericarditis is the most common disorder in clinical practice involving the pericardium. The incidence of acute pericarditis has been reported in about 0.1–0.2% of hospitalized patients and in 5% of patients admitted to the emergency department for nonischemic chest pain [8]. The populations at greater risk

Electronic supplementary material The online version of this chapter (https://doi.org/10.1007/978-1-4939-8841-9_17) contains supplementary material, which is available to authorized users.

A. P. de Faria
State University of Campinas, Faculty of Medical Science, University Hospital, Department of Pharmacology, Campinas, Brazil

T. Q. A. C. Silva · O. R. Coelho-Filho (✉)
State University of Campinas, Faculty of Medical Science, University Hospital, Department of Medicine, Campinas, Brazil

R. Modolo
State University of Campinas, Faculty of Medical Science, University Hospital, Department of Internal Medicine, Campinas, Brazil

R. Y. Kwong et al. (eds.), *Cardiovascular Magnetic Resonance Imaging*, Contemporary Cardiology,
https://doi.org/10.1007/978-1-4939-8841-9_17

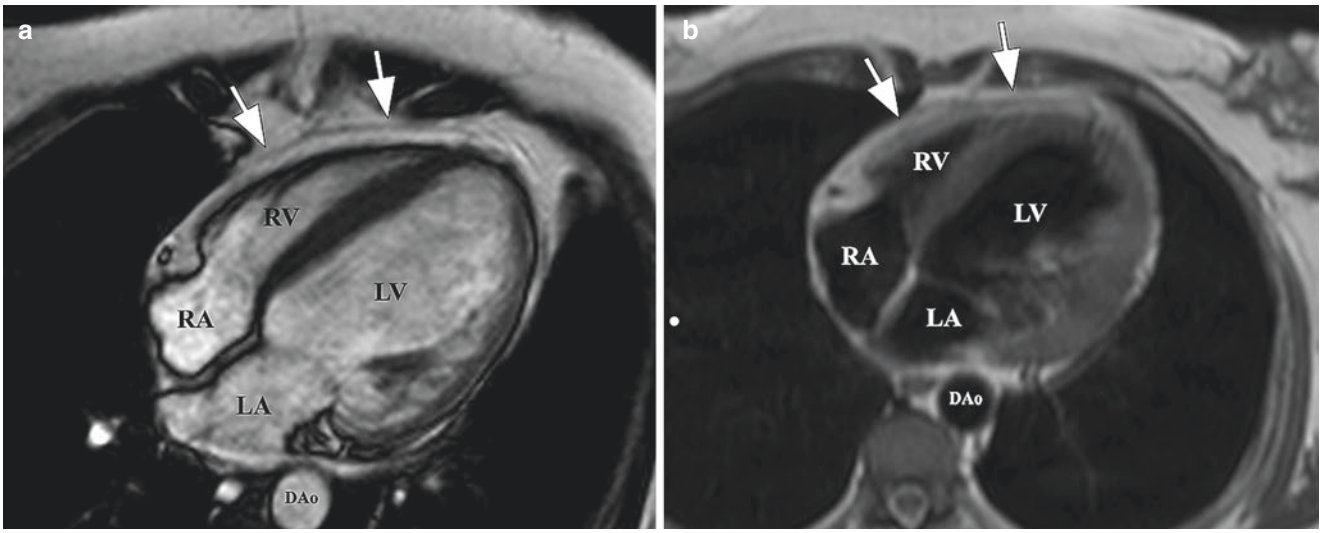

Fig. 17.1 Normal Pericardium. The parietal pericardium appears as a thin, dark line surrounding the heart, measuring <3–4 mm in thickness. Four-chamber SSFP in diastole (**a**) and axial spin-echo T1-weighted (**b**) images showing a normal appearing pericardium (white arrows) (LV left ventricle, RV right ventricle, LA left atrium, RA right atrium, DAo descending aorta)

for pericarditis are men in ages between 16 and 65 years of age, with the highest risk occurring among young adults [9]. Mortality during hospitalization for acute pericarditis is low, reaching 1.1%, and increases with age and associated comorbidities [9]. These episodes of acute pericarditis usually last for 2 weeks at most. Few epidemiologic studies are currently available concerning persistent pericarditis (also termed incessant and chronic pericarditis), which occurs when the disease process remains present for more than 4–6 weeks despite anti-inflammatory therapy initiation and adjustment.

Constrictive pericarditis may follow virtually any acute pericardial process. However, the bacterial etiology is most commonly related to progression to constrictive pericarditis (20–30%) [10]. Viral and immune-mediated as well as neoplastic diseases are less associated with further constriction after the acute phase. Although rare in developed countries, tuberculosis still frequently occurs in developing countries [11]. In developed countries, the most commonly reported causes are idiopathic or viral (42–49%), post-cardiac surgery (11–37%), postradiation therapy (9–31%), and connective tissue disorder (3–7%).

Assessment of Pericardial Diseases by CMR

Several specific conditions may be described as etiological factors of pericardial diseases (PD), although the great majority of settings are considered as idiopathic – which denotes no specific cause found through investigating by several diagnostic tests. Also, misinterpretation of normal structures may result in false-positive diagnoses. The superior aspects of the parietal pericardium, reflected at the level of the great vessels to form the visceral layer, can be mistaken by abnormal conditions. The transverse sinus may simulate aortic dissection or mediastinal lymphadenopathy, whereas the oblique sinus may simulate an esophageal lesion or a bronchogenic cyst.

PD have primarily been evaluated by echocardiography due to its widespread availability, easy portability, and limited costs. CMR may be indicated when echocardiographic measurements are difficult to interpret or conflicting with clinical findings. CMR imaging, also a noninvasive method, has drawn attention in this setting due to its particular accuracy in defining pericardial anatomy, as well as its high sensitivity for the diagnosis of pericardial conditions [12]. In fact, it has been supported as the preferred imaging methodology in assessment of PD by the 2015 European Society of Cardiology (ESC) Guidelines for the diagnosis and management of PD [13, 14].

CMR Imaging Techniques

General Considerations

CMR imaging utilizes a variety of dedicated sequences to provide morphological imaging and tissue characterization along with functional information so as to assess ventricular filling patterns and ventricular interdependence, as well as intracardiac flows. It may also provide information about myocardial inflammation and its pattern allowing specific diagnoses to be made [15]. The advantage of CMR imaging has increased over the years compared with the standard techniques for PD assessment. The main advantages of CMR are described as (1) the integration of anatomic and functional assessment within a single examination, (2) tis-

sue characterization, and (3) determination of the presence/degree of inflammation and activity of disease. In addition, CMR is able to accurately assess the rest of the heart, in particular the myocardium [16]. The recommended CMR protocol for PD encompasses the following sequences: (i) cine imaging (including real-time free-breathing sequences), (ii) black blood imaging of the heart and pericardium, (iii) tagging, (iv) phase-contrast sequences, and (v) late gadolinium enhancement (LGE) imaging in order to determine the presence or absence of gadolinium enhancement within the pericardium [15]. As represented in Table 17.1, SSFP-type cine technique can assess cardiac chamber sizes and function and discriminate structural changes of the ventricles from those of pericardial constrictive physiology. T1-weighted fast spin-echo technique can assess the pericardial thickness and must be compared with the imaging data of the cine SSFP technique acquired in similar or identical scan planes. In addition, T2-weighted fast spin-echo techniques may also characterize fluid-rich structures such as effusion when moderate- to large-sized pericardial effusion is present, enabling the distinction between transudate versus exudate. Myocardial cine tagging can delineate adhesion of the pericardial layers in constrictive pericarditis (CP). The late enhancement imaging delimits any regional myocardial fibrosis or pericardial inflammation. Finally, other evidence of constriction can be assessed by phase-contrast imaging of vena cava blood flow.

CMR Assessment in Specific Pericardial Conditions

Pericardial Effusion

Pericardial effusion may be caused by similar conditions to those of pericarditis. Accumulation of more than 100 ml if occurs rapidly may lead to hemodynamic compromise (Fig. 17.2). This occurs in four functional phases: (1) undetectable slow fluid production, (2) effusion without cardiac compression, (3) effusion with cardiac compression, and finally (4) cardiac tamponade. A compensatory response comprises sympathetic hyperactivity at the expense of parasympathetic activity resulting in tachycardia and increased contractility. Dyspnea, pericardial pain or friction rub, and reduced cardiac output and blood pressure levels might be observed. Paradoxical pulse may also occur [17]. Echocardiogram is considered the noninvasive first-line method to detect pericardial effusion, but in selected cases CMR contributes to decision-making and etiologic determination [18]. The urgency to treatment of pericardial effusion depends on the presence of cardiac tamponade [19]. Pericardial effusion after cardiac surgery rarely promotes tamponade because of its short duration; on the other hand, acquired infections through bacteria, fungi or HIV, as well as, neoplasm-related pericardial effusion are reported as highly associated with cardiac tamponade.

Pericardial Effusion by CMR

Echocardiography has also been generally used in the diagnosis of pericardial effusion because of its high sensitivity and specificity for detecting pericardial effusion, its potential for identifying hemodynamic effects, and portability, enabling prompt use in unstable patients. More recently, three-dimensional echocardiography has been evolving to detect loculated and more complex effusions. CMR is of specific importance in stable subjects because of its tomographic imaging field and greater sensitivity to small amounts of pericardial effusion. Like echocardiography, CMR can also demonstrate features of instability, such as diastolic collapse of right-sided chambers preceding cardiac tamponade (Fig. 17.3).

Also, cine SSFP CMR enables quantification of pericardial effusion volumes with greater accuracy than echocar-

Table 17.1 Protocol for the evaluation of PD by CMR imaging modality

Clinical investigation	Sequences	Contrast	Orientation	Slice thickness
Function, pericardial effusion	Steady-state free precession (SSFP) cine	–	Multiple short axis *and* multiple long axis	8 mm or 10 mm (no gap)
Pericardial thickness and edema	T1- and T2-weighted black blood fast spin echo	–	Multiple long axis	10–15 mm
Pericardial adherence	Myocardial cine tagging	–	Multiple short axis *and* multiple long axis	8–10 mm
Pericardial mass	Contrast enhanced myocardial perfusion if pericardial mass present	0.1–0.15 mmol/kg of gadolinium (recommended injection rate 4–5 ml/sec, followed by 15–25 ml of normal saline)	Multiple short axis *or* multiple long axis	10 mm
Pericardial late gadolinium enhancement	T1-weighted, inversion recovery prepared gradient echo with fat-sat prepulse, if available	10–15 min. After a cumulative dose of 0.1–0.15 mmol/kg of gadolinium	Multiple short axis *and* multiple long axis	8–10 mm
Pericardial constriction	Phase contrast	–	Multiple short axis *or* multiple long axis	8–10 mm

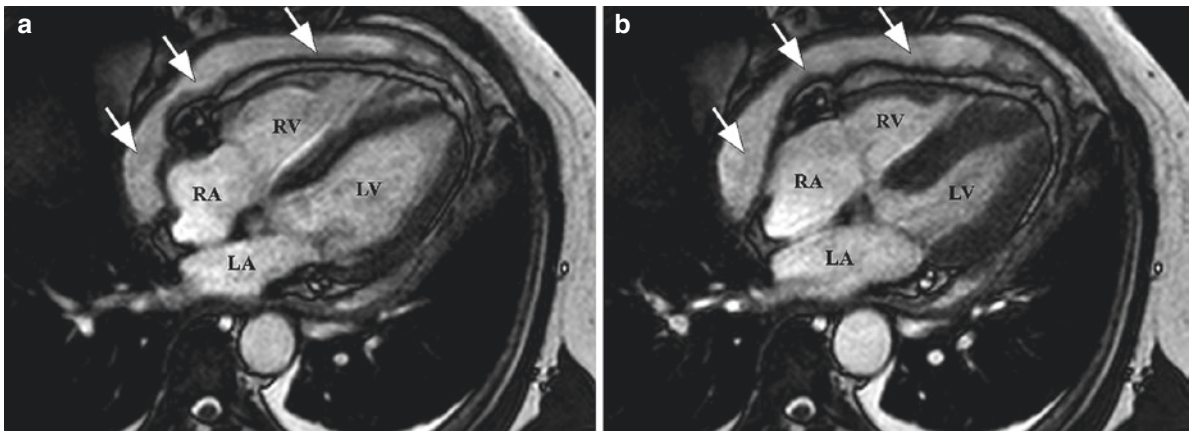

Fig. 17.2 Pericardial effusion. Four-chamber cine SSFP in diastole (**a**) and systole (**b**), demonstrating large loculated pericardial effusion (arrows) (LV left ventricle, RV right ventricle, LA left atrium, RA right atrium)

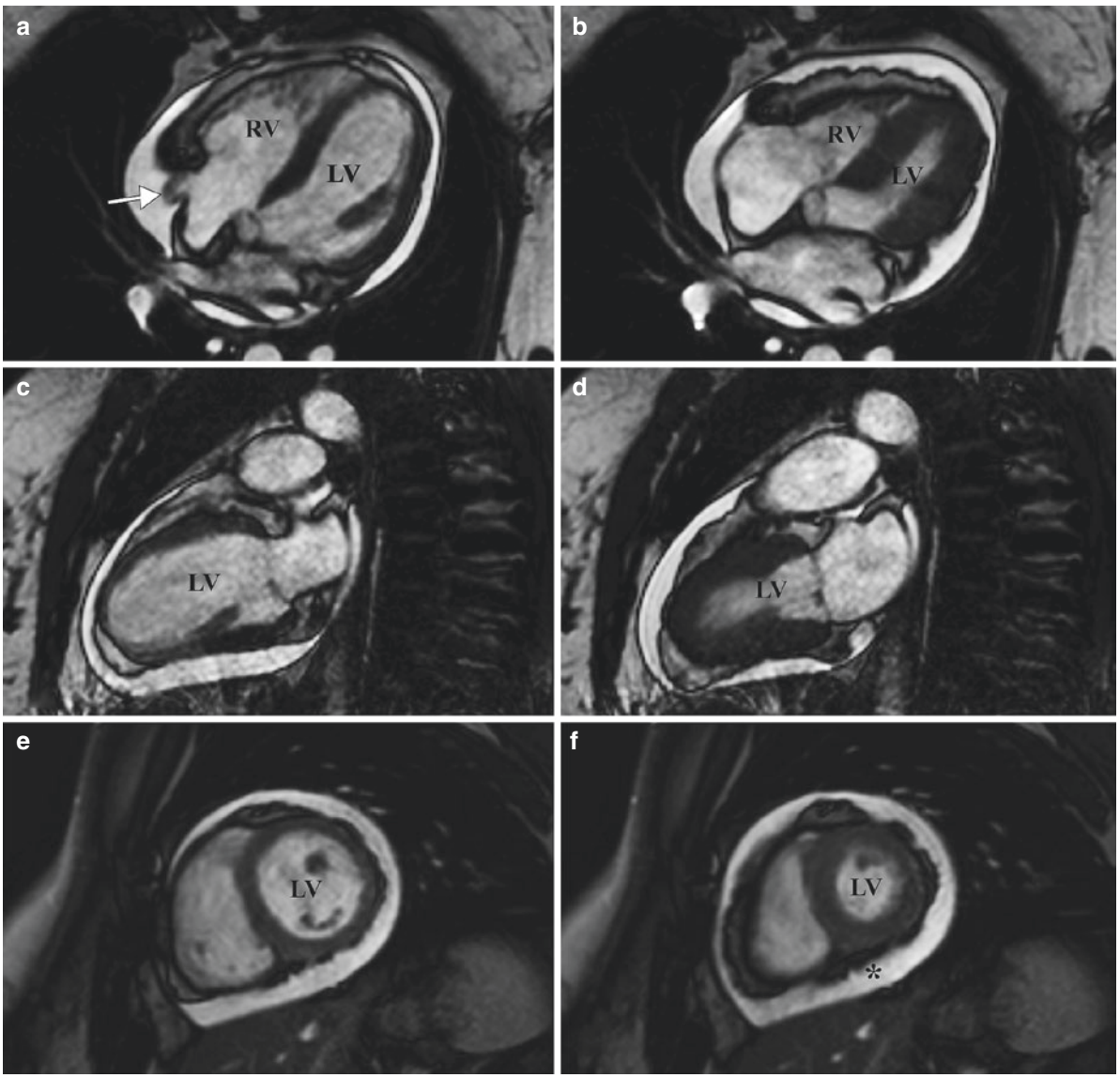

Fig. 17.3 Pericardial effusion with early diastolic inversion of the right atrium. Cine SSFP images in four-chamber (**a**, **b**), two-chamber (**c**, **d**) and short axis (**e, f**) views during diastole and systole, respectively; showing large pericardial effusion with early diastolic inversion of the right atrium (**a**, arrow) (LV left ventricle, RV right ventricle)

diography. It should also be considered – class of recommendation IIa and level of evidence C – when there is suspicion of loculated pericardial effusion due to a wider field of view, especially in the anterior and superior locations; when there is pericardial thickening and associated tumor or masses; as well as when there are chest abnormalities [15].

In large pericardial effusions, low-voltage QRS and electrical alternans in the ECG may be present, and special attention should be given to the gating process in order to avoid artifacts. In cine gradient-echo CMR imaging, fluid mobility and changes in pericardial sac local dimensions during the cardiac cycle allow differentiation of pericardial effusion, more "deformable," from epicardial fat, which is somewhat inelastic [20].

Another advantage of CMR compared with other modalities consists of its ability to differentiate fluid characteristics – transudative from exudative pericardial fluid, as well as hemorrhagic using various sequences. Fluids with few cells and low protein content (e.g., transudative effusions) have long T1-weigthed imaging and hence low signal intensity on T1-weighted spin-echo imaging, whereas fluids filled with cellular and protein content (e.g., exudative or hemorrhagic effusions) have short T1 and a medium or high signal intensity on T1-weighted spin echo. Chylous effusions also show short T1 imaging because of the increased protein content, therefore, appearing as a bright intense signal on T1-weighted spin echo. Pericardial effusion is evaluated through the intensity degree of the signal compared to that of the myocardium (hyper-, iso-, hypointense) and the homogeneity of the signal at CMR [21].

T2-weighted spin-echo imaging may help differentiate the period of time since a hemorrhagic pericardial effusion started based on the formation of methemoglobin within the fluid. High intensity signals indicate acute bleeding, while heterogeneous signal intensity associated with patchy areas of high signal intensity on T1W and T2W points toward an older established effusion, about 1–4 weeks. Aged and organized hematomas appear with a dark peripheral rim and low intensity internal foci due to calcification, fibrosis, or hemosiderin deposition.

Acute Pericarditis

Acute pericarditis (AP) is a condition where the clinical presentation – chest pain, pericardial friction, and typical electrocardiographic (ECG) changes – results from pericardium inflammation usually lasting for a maximum period of 2 weeks. The chest pain is usually retrosternal, is ventilatory related, and worsens while in supine position. A pathognomonic finding in physical examination consists of a pericardial friction rub in cardiac auscultation. In addition, a diffuse ST-segment elevation in ECG may be present, with electrical alternans if pericardial effusion is associated. Thoracic radiography may reveal an increased cardiac silhouette along with nonspecific inflammatory findings in biochemical tests. Its incidence is difficult to assess due to a high number of underdiagnosed cases, but seasonal prevalence of viral infections—considered the major cause associated to idiopathic AP—may affect it. Bacteria, neoplasia, connective tissue diseases (Fig. 17.4), radiation, myocardial infarction (Fig. 17.5), and trauma are also attributable causes of AP [14, 22]. The number of new cases of this condition has significantly declined after the introduction of thrombolytic agents, as well as mechanical revascularization – percutaneous coronary intervention. The clinical features of acute and constrictive pericarditis are shown in Table 17.2.

Acute Pericarditis by CMR

The diagnosis of AP, as briefly showed in Table 17.2, is mainly based on (i) ECG tracing, (ii) echocardiography, (iii) chest X-ray, and (iv) assessment of inflammatory and myocardial injury markers, all of which received the same class I recommendation and level of evidence C, according to 2015 ESC Guidelines [14]. Although not routinely recommended, in acute pericarditis with small or absent effusions, CMR may aid in the evaluation of suspected concomitant myocarditis – even in the absence of wall motion abnormalities on echocardiography – and differentiate from ischemic disease. Characteristics of myocarditis appear as high signal in mid- or epicardial areas on T2-weighted images (myocardial edema), T1-weigthed early (capillary hyperemia), and late (fibrosis) gadolinium enhancement images with possible adjacent wall motion abnormalities on cine CMR [23]. Pericardial effusion is a common finding in patients presenting with myocarditis, occurring in 32–57% of individuals with confirmed diagnosis [24–26]. In the Lake Louise consensus criteria for diagnosis of myocarditis (which includes (1) regional or global myocardial SI increase in T2-weighted images, (2) increased global myocardial early gadolinium enhancement ratio between myocardium and skeletal muscle in gadolinium-enhanced T1-weighted images, and (3) focal lesion with nonischemic regional distribution in IR-prepared gadolinium-enhanced T1-weighted images), presence of pericardial effusion provides additional and supportive evidence for active inflammation [20]. This reinforces the importance its assessment in patients with suspected myocarditis. Moreover novel CMR techniques based on non-contrast T1 mapping may also aid in myocarditis diagnosis without the need of gadolinium contrast administrations [27].

In the setting of acute pericarditis with moderate-to-large effusion, CMR can be indicated whenever echocardiography is equivocal due to improper imaging quality or when adjacent associated lesions are suspected (traumatic or neoplastic diseases). CMR enables assessment of the extension and staging of associated conditions, as well as the evaluation of possible contained post-MI free wall rupture. Finally, in

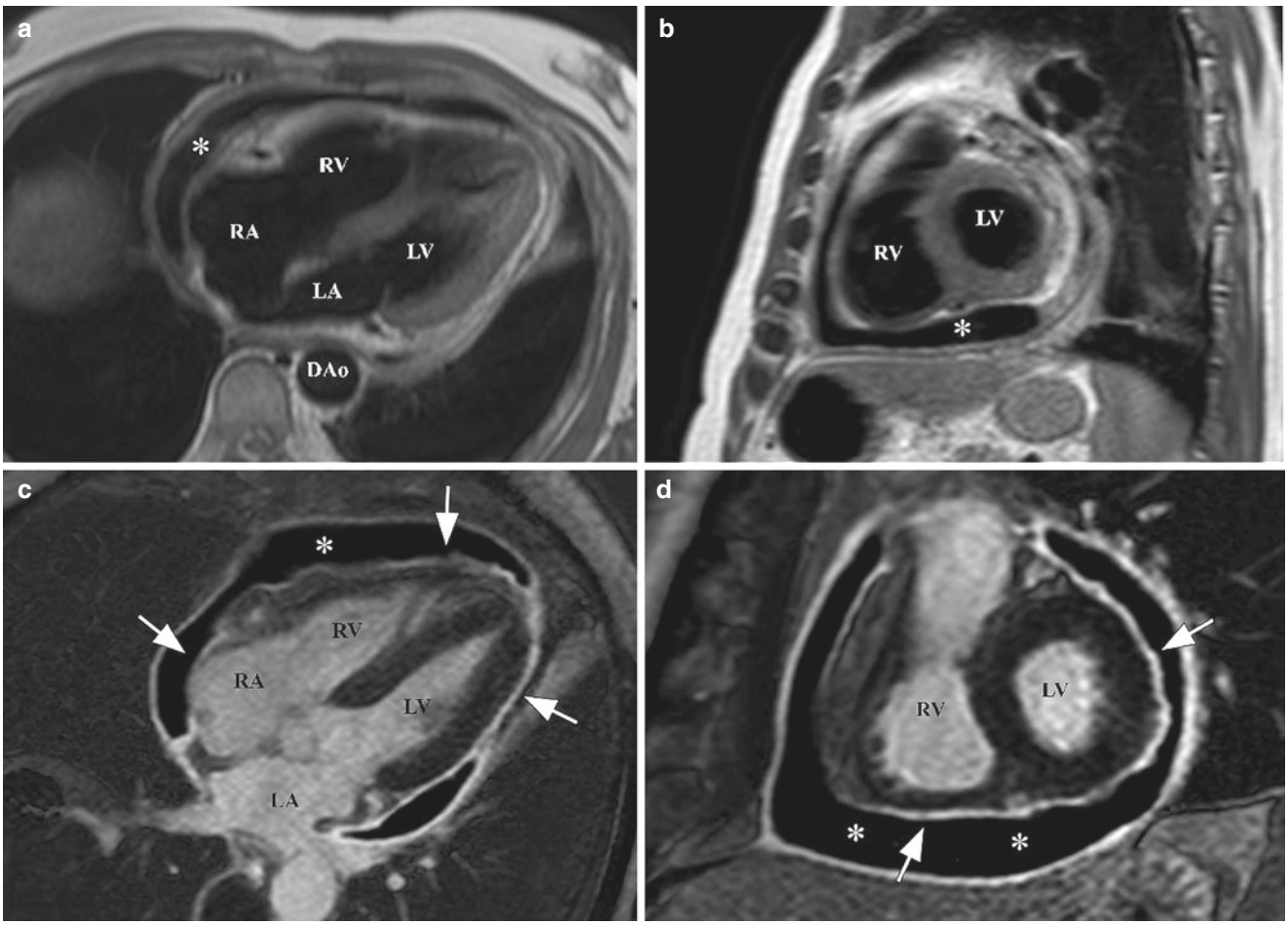

Fig. 17.4 Acute pericarditis T1-weighted spin-echo images (**a**, **b**) in axial and short axis views of a 37-year-old women with rheumatoid arthritis presenting with acute chest pain, demonstrating moderate-sized pericardial effusion (asterisks). Matching LGE images (**c**, **d**) showing diffuse severe pericardial gadolinium enhancement consistent with acute pericarditis (LV left ventricle, RV right ventricle, LA left atrium, RA right atrium, DAo descending aorta)

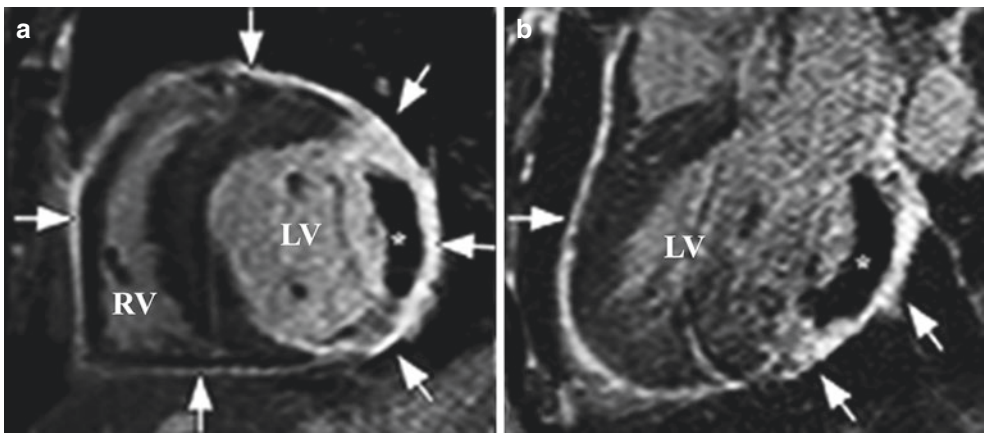

Fig. 17.5 Acute pericarditis associated with transmural lateral myocardial infarction. Late gadolinium imaging, in short axis (**a**) and long axis (**b**) views, demonstrating a large transmural infarct with microvascular obstruction (white asterisks) associate with severe acute pericarditis with diffuse gadolinium enhancement within the pericardium (white arrows) (LV left ventricle, RV right ventricle)

Table 17.2 The clinical features of acute and constrictive pericarditis

	Acute pericarditis [11, 18, 19, 20]	Constrictive pericarditis [14, 19]
Medical history	Acute and pleuritic chest pain (major complaint); radiates to one or both trapezius ridges; relief on bending forward; worse at bedtime; dyspnea; fever; cough. Review prior medical history. Commonly confused conditions: pneumonia with pleurisy; pulmonary embolism; costochondritis; gastroesophageal reflux; aortic dissection; pneumothorax	Clinical signals and symptoms of heart failure; lower limb edema; passive liver congestion; abdominal complaints; dyspnea on exertion and orthopnea; atrial fibrillation and tricuspid regurgitation; severe fatigue, muscle weakness and weight loss due to low cardiac output
Clinical Examination	Pericardial friction rub; sinus tachycardia; mild fever; anxiety. Attention to pleural effusion and coexisting myocarditis	Prominent jugular venous distension; Kussmaul sign; muffled heart; paradoxal pulse (~30%); hepatomegaly (with or without ascites)
Diagnostic tests	ECG: concave diffuse ST-segment elevation; PR-segment depression Blood cell count: leucocytosis	ECG: atrial fibrillation; nonspecific T-wave changes; low voltage
	Biochemical tests: creatine phosphokinase-MB and troponin I [19] Chest X-ray: generally normal; small pleural effusion; pulmonary infiltrates; enlarged lymph nodes (neoplasia) Echocardiogram: normal or bright pericardium; assess silent pericardial effusion; and associated severe myocarditis Cardiac magnetic resonance: gadolinium-DTPA retention by pericardium with fibrosis and/or inflammation	Chest X-ray: large cardiac silhouette (if coexisting pericardial effusion); pericardial calcification; pulmonary vascular congestion Echocardiogram: pericardial thickening eventually associated with acoustic shadows; immobility; abrupt displacement of the interventricular septum and systemic venous congestion; premature pulmonary valve opening Cardiac catheterization and angiography: hemodynamic difference between CP and restrictive cardiomyopathy; suspected coronary heart disease; cardiac compression Computed tomography: pericardial calcification (even minimal) Cardiac magnetic resonance: gadolinium-DTPA retention by pericardium with inflammation; detectable pericardial thickening >4 mm; atrial enlargement; dilated inferior vena cava; pericardial adherence; tubular right ventricle; septal inversion with inspiration; septal bounce or "shiver"
Treatment	Nonsteroidal anti-inflammatory drugs (NSAID); colchicine [20] or prednisone if NSAID fails	Pericardiotomy; diuretics and sodium restriction may aid relief symptoms (high-risk patients for surgery); corticosteroids for transient constriction; medical therapy for specific etiologies (e.g., tuberculous pericarditis)

recurrent pericarditis, CMR may provide clues on the persistent presence and severity of inflammation. High signals in pericardial layers, assessed by late gadolinium-enhanced imaging following administration of gadolinium-DTPA, suggest acute inflammation [28, 29] (Figs. 17.4 and 17.5).

Constrictive Pericarditis

Constrictive pericarditis (CP) is characterized by a fibrous thickening of the pericardium that usually arises in a chronic phase of the inflammatory process. Chronic inflammation may lead to pericardium calcification and adherence of both layers jeopardizing cardiac compliance and proper diastolic filling. Increase of intracardiac, systemic venous and pulmonary pressure, as well as heart failure-related clinical manifestations, is also observed. The most common etiological factors associated to CP are radiation therapy, post-cardiac surgery-related inflammation, neoplastic diseases, infectious diseases (mostly tuberculosis), and autoimmune connective tissue diseases, and some cases are considered idiopathic [14, 19]. The clinical examination and diagnostic tests and treatment of CP are presented in Table 17.2. Although CP-related clinical presentation is quite common, constriction may regress to normal physiology and normal pericardial thickness in up to 20% of the cases [30].

The assessment of CP is based on a multimodality evaluation [15, 31, 32]. The diagnosis and therapy of CP may be determined and complemented by different imaging methods, chest X-ray and echocardiography (first recommended assessments), CT and CMR (indicated as second-level imaging techniques), and, ultimately, cardiac catheterization (indicated when those previous noninvasive diagnostic methods do not provide a definite diagnosis of constriction) [14].

Constrictive Pericarditis Versus Restrictive Cardiomyopathy

The differentiation between CP and restrictive cardiomyopathy (RC) remains a complex but important clinical challenge. Since RC may have a similar clinical setting than CP, it is of utmost importance to distinguish them because treatment is considerably different. Although the distinction between constriction and restriction must firstly be guided by the patient's history (e.g., surgery or infection, as opposed to myocardial hypertrophy or infiltration), sometimes this approach is more challenging. Cardiac amyloidosis – main suspected cause of RC – is rarely a diagnostic concern because it follows clear signs and symptoms. On the other hand, other forms of RC, such as post-radiotherapy RC, sarcoidosis, hemochromatosis, endomyocardial fibroelastosis, and primary RC, may complicate differential diagnosis with CP. Hence, imaging techniques may provide features of both conditions and contribute with distinction. Also, myocardial enhancement patterns, on late gadolinium-DTPA, provide indications of specific myocardial infiltrative or storage diseases. In addition, T2-weighted images may also be useful to investigate iron deposition in the heart using the myocardial T2* ("T2 star") time of the heart (in msec). Myocardial T2* is defined as the exponential rate of signal decay acquired during progressive lengthening of the echo time (TE). The myocardial T2* is inversely related to the amount of iron deposition in the heart [33, 34], therefore shorter T2* times are associated with worsening LV dysfunction and heart failure [35, 36].

In RC, echocardiographic assessment may demonstrate hypertrophic ventricles and impaired ventricular relaxation, while CP presents commonly with pericardial thickening, diastolic septal bounce, and preserved ventricular relaxation [37]. Chest radiography aids by showing calcifications in CP (~1/3 of cases), but not in RC. At echocardiography, CP presents with (1) septal bounce or ventricular septal shift in diastole associated with either septal e′ > 8.0 cm/s or hepatic vein expiratory diastolic reversal ratio of >0.78 (sensitivity 87%, specificity 91% [38]), (2) pericardial thickness and calcifications, (3) respiratory variation of the mitral peak E velocity of >25% (84% sensitivity and 91% specificity [37]) and variation in the pulmonary venous peak D flow velocity of >20% (79% sensitivity and 91% specificity [37]), and (4) color M-mode flow propagation velocity (Vp) > 45 cm/s. Differently in the RC, echocardiography contributes to show (1) small left ventricles with large atria and possible increased wall thickness, (2) E/A ratio > 2 and short deceleration time, (3) no respiratory variations of mitral inflow and color M-mode flow propagation velocity (Vp) < 45 cm/s, and (4) tissue Doppler: peak septal e' < 8.0 cm/s [38, 39]. Pericardial adhesions, in constrictive pericarditis, may also be detected by echocardiography strain and evaluation of LV mechanical twisting. Adhesions may cause tethering and, thus, loss of circumferential strain and LV twist mechanics, while sparing subendocardial strain assessed by speckle-tracking echocardiography [40, 41].

Conventional cardiac catheterization presents a predictive accuracy of 75% to diagnose CP. The method shows in CP (1) dip and plateau' or "square root" sign, equal right ventricular diastolic, and left ventricular diastolic pressures and (2) the novel ventricular interdependence index (assessed by the systolic area index – defined as the ratio of the RV area (mmHg × s) to the LV area (mmHg × s) in inspiration versus expiration) > 1.1 (sensitivity of 97% and a predictive accuracy of 100% for the identification of patients with surgically documented CP); contrarily, the findings in RC are (1) marked right ventricular systolic hypertension (> 50 mmHg) and (2) left ventricular end-diastolic pressure exceeding right ventricular end-diastolic pressure at rest or during exercise by 5 mmHg or more [32]. The invasive nature of the procedure and the exposure to ionizing radiation and potentially damaging iodinated contrast are among the potentially significant disadvantages of this imaging method. CT has been indicated as more sensitive for the detection of increased pericardial thickness compared with the abovementioned image methods [30]. Indeed, CT imaging can define, even minimal, pericardial calcification in CP, unlike in RC where no calcifications are found. CMR is helpful in defining a CP or RC diagnosis (class I indication) [42, 43]. The use of breath-hold cine CMR may distinguish both conditions by showing early diastolic septal flattening or inversion, which is a common finding in the majority of CP patients, but it is absent in RC subjects [44].

Constrictive Pericarditis by CMR

CMR imaging further clarifies the diagnosis in patients with equivocal or indeterminate findings at echocardiography and evidences pericardial thickening [18]. Indeed, echocardiography is not highly accurate in the depiction of pericardial thickening [45]. CMR has been proposed as having superior tissue contrast and spatial resolution compared with echocardiography [46], showing a dilated right atrium, an elongated right ventricle, and ventricular interdependence by real-time cine technique [44]. Thus, CMR allows assessing the presence, severity and distribution of pericardial involvement, and characterize effusion [31] (Fig. 17.6).

Compared with CT—although this has the advantage of proving a better spatial resolution and detecting pericardial calcification accurately [14]—CMR does not require iodinated nephrotoxic contrast agents, ionizing radiation, or additional image processing [47]. In addition, CT imaging presents lower temporal resolution than CMR, which subsequently may not help to detect subtle changes, such as a septal bounce [48], and it cannot assess, unlike CRM, the hemodynamic relevance of a constriction when it is indeed present. Thus advantages of CMR over CT are (i) it pro-

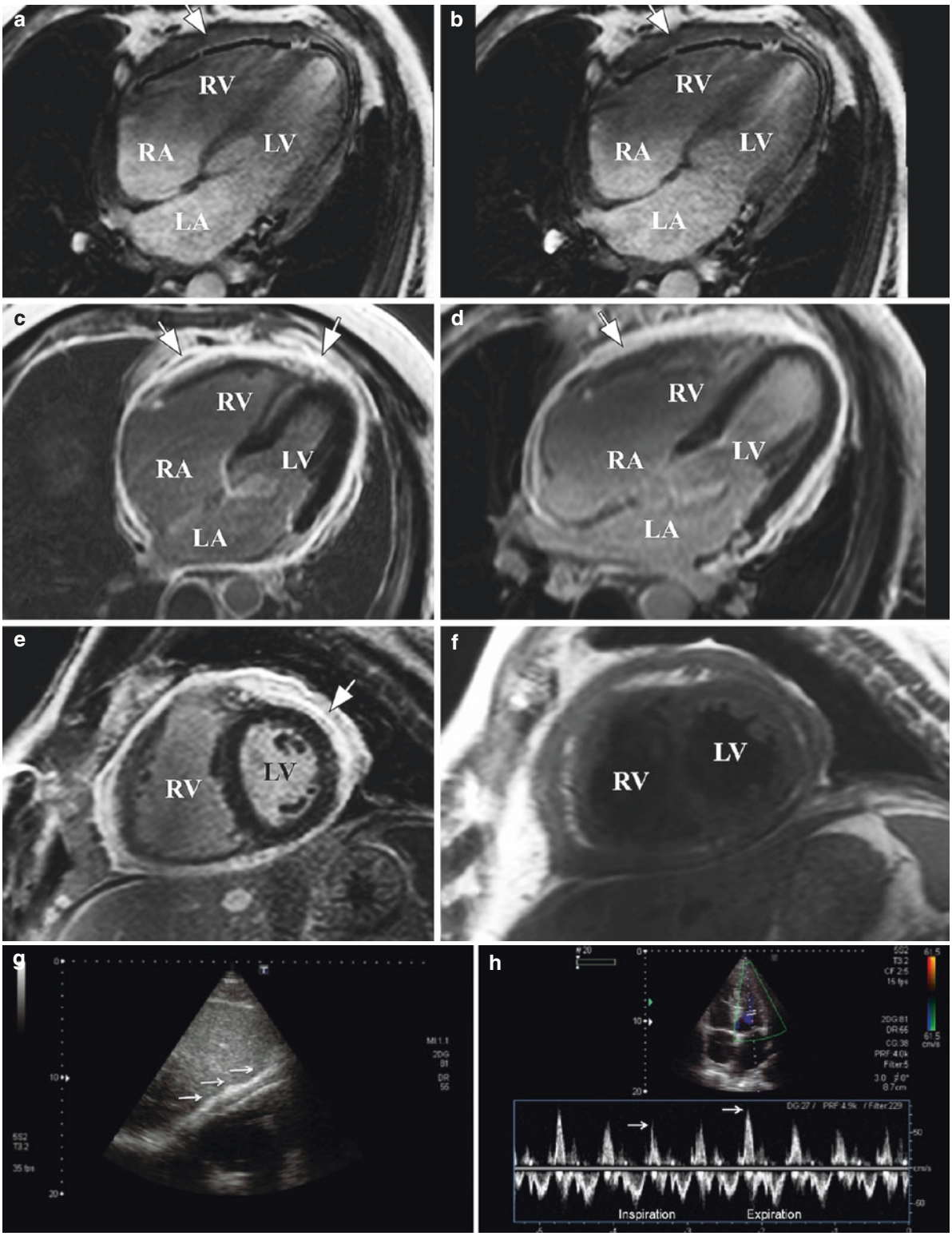

Fig. 17.6 Constrictive pericarditis. Four-chamber cine SSFP during diastole (**a**) and systole (**b**) demonstrating diffuse pericardial thickening (arrows), associated with severe bi-atrial enlargement in a 56 year-old male presenting with classical signs of constrictive pericarditis. Supplemental four-chamber (Video 17.1) and short axis real-time videos (Video 17.2) showing abnormal septal motion, confirming the presence of constrictive physiology. Long and short axis LGE images (**c**, **d** and **e**) demonstrating severe diffuse pericardial enhancement. Matching short axis T1 weighted also showing pericardial thickening (**f**). Thickened pericardium of the same patient assessed by subcostal echocardiography view (**g**) (arrows). As in cardiac tamponade, intrapleural respiratory variation is not fully transmitted to intracardiac chambers creating marked respiratory changes in inflow patterns. The image demonstrates E wave velocity change of >25% (arrows) (**h**) suggesting ventricular interdependence (which may be associated with septal bounce), in this case, caused by thickened pericardium (LV left ventricle, RV right ventricle, LA left atrium, RA right atrium)

vides information with regard to the hemodynamic consequences of the non-compliant pericardium on cardiac filling [49, 50]; (ii) it has the potential of showing fibrotic fusion of pericardial layers [51]; and (iii) although sharing the advantages of CT in patients with congenital pericardial condition and pericardial malignancy, CMR allows better tissue characterization and assessment of functional consequences [52].

CMR is useful in the diagnosis of atypical presentations of constrictive pericardial syndromes [29, 53], such as transient CP and effusive CP [54]. This last is considered difficult to be diagnosed by echocardiography at the time of presentation when associated with a cardiac tamponade [29, 55, 56]. Gadolinium-enhanced images have the ability to detect inflammation and predict reversibility of constrictive physiology [56]. CMR allows assessment of both anatomic (pericardial thickness) and physiologic (interventricular septum motion) features of constriction. This has been demonstrated in patients with surgically proven constriction (sensitivity of 100% and specificity of 90%) [57]. CMR also helps differentiate CP from RC by assessing myocardial involvement and its pattern, as well as the other intrathoracic structures [15]. Pericardial thickening is usually >4 mm in patients with those condition. Since studies have highlighted that up to 18% of patients with histologically proven CP have a normal pericardial thickness (<2 mm), the real-time CMR modality may be of interest on describing increased ventricular coupling in those patients in whom the morphologic pericardial abnormalities are minimal or absent [13, 30]. The SSFP cine imaging has been supported as the reference sequence to assess and quantify cardiac volumes, myocardial mass, and ventricular function. When acquired in real time, this sequence can be used to assess ventricular coupling by assessing the changes in ventricular septal shape and motion over the respiratory cycle [49, 58]. Pathologic ventricular coupling refers to an exaggerated and sudden left-sided interventricular septal shift at the beginning of inspiration. This is a pathognomonic abnormal motion of the septum and allows differentiation between CP and RC (Fig. 17.6). Coronal and axial spin-echo CMR imaging demonstrated a sensitivity of 88%, specificity of 100%, and diagnostic accuracy of 93% for CP diagnosis [59]. T1-weighted sequence is often the first of the imaging sequences used in evaluating CP because of its ability in delineating cardiac structures and mediastinal and pulmonic structures [47]. Sequential gradient-echo cine T1- and T2-weighted imaging sequences in matching slice locations contribute to precise delineation with further definition on pericardial structure and its associated hemodynamic effects on the cardiac chambers. For instance, the assessment with T2/T1 ratios provides tissue differentiation between those with a high ratio – appearing bright and indicating blood, fluid, and fat – and tissues with low T2/T1 ratios, appearing dark and indicating muscle and myocardium [60, 61].

Either T1- and T2-weighted spin-echo CMR or cine imaging presents a low signal for thickened fibrotic and/or calcified pericardium. In addition, no enhancement after gadolinium was found in chronic stage fibrosing forms of CP [29]. Pericardial enhancement is suggestive of residual inflammation, and certain patterns of late enhancement may also help in determining the etiology of the CP, such as with tuberculous pericarditis [62] (Fig. 17.6). Additionally, a study has demonstrated an associated improvement in systemic inflammatory markers, such as C-reactive protein, and late gadolinium-DTPA enhancement, which suggests a future role for CMR in predicting pericardial inflammation reversibility [56].

CMR myocardial tagging sequence can be used to evaluate adherence and immobility of the pericardial–myocardial interface [51]. In this modality, tag lines are seen as dark saturation bands 4–5 mm thick and spaced at intervals of approximately 1 cm over the entire image. Normal patients present those bands break (lose continuity) at both parietal and visceral pericardium during the cardiac cycle, indicating a normal sliding motion between the pericardial layers. On the other hand, in patients with CP and adhesions between the layers, the bands bend but remain unbroken, indicating abnormal tethering of the pericardium [63]. Thus, CMR might not only demonstrate fibrotic adhesion of pericardial layers but reveal the extension of the disease and to assess myocardial implication in CP [13].

Impaired diastolic ventricular filling in CP is a result of increased rigidity and poor distensibility due to pericardial fibrosis and calcification [64]. The diagnosis of CP may also rely on qualitative hemodynamic assessments of the right atrium and ventricle in relation to distension of the great cardiac veins [61]. CMR can quantify the abrupt restriction of ventricular filling by assessing ventricular volume over time. CMR phase-encoding velocimetry can accurately assess forward flow and the rate of blood return from the (superior) vena cava during ventricular systole, contributing to CP diagnosis [61].

On the other hand, the major disadvantages of CMR include (1) contraindications in patients with a metallic device, (2) claustrophobia, (3) relatively long scan time, (4) gadolinium-associated nephrogenic sclerosing fibrosis in patients with severe renal failure, (5) the high costs, and (6) availability. Finally, the overestimation of pericardial thickness on CMR imaging may be explained by motion of pericardial layers during image acquisition, lack of sufficient spatial resolution and chemical shift artifacts at the fat–fluid interface on cine imaging [13].

Recent publications have been focusing on the role of CMR in determining which patients with CP may potentially

benefit of anti-inflammatory treatment – due to residual pericardial enhancement characterizing the reversible forms of constriction – in contrast to others in which pericardiectomy is the best indication, in the absence of pericardial enhancement on late gadolinium-DTPA imaging [65]. In addition, the use of CMR is helpful for excluding patients with extensive myocardial fibrosis and/or atrophy, which significantly reduces the mortality rate for pericardiotomy [66]. Therefore, by reporting the inflammatory process, CMR imaging may potentially provide important prognostic information with respect to the need for further pericardiectomy. CMR has been recommended as an exam to guide indication for CP therapy (class IIb and level of evidence C) [14]. Additionally, CMR is recommended as a reasonable tool assessment for the follow-up of patients [15].

Future Directions

Advanced cardiovascular imaging with CMR will probably increase its role in the evaluation of pericardial inflammation reported by delayed gadolinium enhancement imaging. Thus, the use of CMR imaging in the diagnosis and/or follow-up of CP may indicate the treatment strategy in some patients, suggesting an approach to reduce inflammation instead of surgery. In addition, serial CMR could be useful guiding anti-inflammatory treatment duration, particularly regarding early CP that may be transient and reversible. Future studies are necessary to determine whether this indication for CMR is worthwhile and cost-effective, also to establish standard protocols of evaluation [67]. Novel techniques, such as diffusion-weighted and dynamic contrast-enhanced magnetic resonance imaging have opened perspectives for improvements of tissue characterization [68].

Conclusions

PD is consequence of numerous causes and still contributes to significant cardiovascular morbidity and mortality. Recent advances in CMR technology have provided significant improvements in pericardium assessment from a static morphologic assessment toward a dynamic morphological and functional approach. In the acute setting, CMR provides clues of etiological factors, as well as inflammatory presence and extension. Whereas, in the chronic scenario, CMR provides accurate diagnosis and helps distinguishing CP from RC enabling appropriate treatment and follow-up to patients. It is worth to mention that the strategy on multimodality imaging techniques has been strongly encouraged for the management of PD in concert with clinical findings to provide a confident diagnosis and improve clinical management of patients [14].

References

1. Kumar V, Abbas A, Fausto N. Pathologic basis of disease. 7th ed., ed. Robbins SL, Cotran RS. Philadelphia: Elsevier Saunders; 2005. p. 1525.
2. Jöbsis PD, Ashikaga H, Wen H, Rothstein EC, Horvath KA, McVeigh ER, Balaban RS. The visceral pericardium: macromolecular structure and contribution to passive mechanical properties of the left ventricle. Am J Physiol Heart Circ Physiol. 2007;293(6):H3379–87.
3. Johnson D. The pericardium. In: Standring S, Ellis H, Healy JC, et al., editors. Gray's anatomy. London: Elsevier Churchill Livingstone; 2005. p. 995–6.
4. LeWinter MM, Myhre EESP, Slinker BK. Influence of pericardium and ventricular interaction on diastolic function. In: Gaasch WH, LeWinter MM, editors. Heart failure and left ventricular diastolic function. Philadelphia: Lea & Febiger; 1993. p. 103–17.
5. Lee MC, Fung YC, Shabetai R, LeWinter MM. Biaxial mechanical properties of human pericardium and canine comparisons. Am J Phys. 1987;253(1 Pt 2):H75–82.
6. Sechtem U, Tscholakoff D, Higgins CB. MRI of the normal pericardium. AJR Am J Roentgenol. 1986;147(2):239–44.
7. Stark DD, Higgins CB, Lanzer P, Lipton MJ, Schiller N, Crooks LE, et al. Magnetic resonance imaging of the pericardium: normal and pathologic findings. Radiology. 1984;150(2):469–74.
8. Maisch B, Seferović PM, Ristić AD, Erbel R, Rienmüller R, Adler Y, et al. Task force on the Diagnosis and Management of Pricardial Diseases of the European Society of Cardiology. [Guidelines on the diagnosis and management of pericardial diseases. Executive summary]. Rev Esp Cardiol. 2004;57(11):1090–114.
9. Kyto V, Sipila J, Rautava P. Clinical profile and influences on outcomes in patients hospitalized for acute pericarditis. Circulation. 2014;130(18):1601–6.
10. Imazio M, Brucato A, Maestroni S, Cumetti D, Belli R, Trinchero R, Adler Y. Risk of constrictive pericarditis after acute pericarditis. Circulation. 2011;124(11):1270–5.
11. Mutyaba AK, Balkaran S, Cloete R, du Plessis N, Badri M, Brink J, Mayosi BM. Constrictive pericarditis requiring pericardiectomy at Groote Schuur Hospital, Cape Town, South Africa: causes and perioperative outcomes in the HIV era (1990–2012). J Thorac Cardiovasc Surg. 2014;148(6):3058–65. e1
12. Wang ZJ, Reddy GP, Gotway MB, Yeh BM, Hetts SW, Higgins CB. CT and MR imaging of pericardial disease. Radiographics. 2003;23 Spec No:S167–80.
13. Bogaert J, Francone M. Cardiovascular magnetic resonance in pericardial diseases. J Cardiovasc Magn Reson. 2009;11:14.
14. Adler Y, Charron P, Imazio M, Badano L, Barón-Esquivias G, Bogaert J; European Society of Cardiology (ESC), et al. 2015 ESC Guidelines for the diagnosis and management of pericardial diseases: the Task Force for the Diagnosis and Management of Pericardial Diseases of the European Society of Cardiology (ESC)Endorsed by: The European Association for Cardio-Thoracic Surgery (EACTS). Eur Heart J. 2015;36(42):2921–64.
15. Cosyns B, Plein S, Nihoyanopoulos P, Smiseth O, Achenbach S, Andrade MJ; European Association of Cardiovascular Imaging (EACVI); European Society of Cardiology Working Group (ESC WG) on Myocardial and Pericardial diseases, et al. European Association of Cardiovascular Imaging (EACVI) position paper: multimodality imaging in pericardial disease. Eur Heart J Cardiovasc Imaging. 2015;16(1):12–31.
16. Bogaert J, Taylor AM. Pericardial disease. In: Clinical cardiac MRI. Berlin/Heidelberg: Springer; 2012. p. 383–409.
17. LeWinter MM. Pericardial diseases. In: Libby P, et al., editors. Braunwald's heart disease. Philadelphia: Sauders Elsevier; 2008. p. 1829–53.

18. Oyama N, Oyama N, Komuro K, Nambu T, Manning WJ, Miyasaka K. Computed tomography and magnetic resonance imaging of the pericardium: anatomy and pathology. Magn Reson Med Sci. 2004;3(3):145–52.
19. Hoit BD. Management of effusive and constrictive pericardial heart disease. Circulation. 2002;105(25):2939–42.
20. Friedrich MG, Sechtem U, Schulz-Menger J, Holmvang G, Alakija P, Cooper LT; International Consensus Group on Cardiovascular Magnetic Resonance in Myocarditis,et al. Cardiovascular magnetic resonance in myocarditis: a JACC White Paper. J Am Coll Cardiol. 2009;53(17):1475–87.
21. Kwong RY. Pericardium: pericardial disease. American College of Cardiology (ACC) Cardiac MRI – Self Assessment Program (CMRSAP); 2004.
22. Lange RA, Hillis LD. Clinical practice. Acute pericarditis. N Engl J Med. 2004;351(21):2195–202.
23. Mahrholdt H, Wagner A, Deluigi CC, Kispert E, Hager S, Meinhardt G, et al. Presentation, patterns of myocardial damage, and clinical course of viral myocarditis. Circulation. 2006;114(15):1581–90.
24. Karjalainen J, Heikkila J. "Acute pericarditis": myocardial enzyme release as evidence for myocarditis. Am Heart J. 1986;111(3):546–52.
25. Ammann P, Naegeli B, Schuiki E, Straumann E, Frielingsdorf J, Rickli H, Bertel O. Long-term outcome of acute myocarditis is independent of cardiac enzyme release. Int J Cardiol. 2003;89(2–3):217–22.
26. Carniel E, Sinagra G, Bussani R, Di Lenarda A, Pinamonti B, et al. Fatal myocarditis: morphologic and clinical features. Ital Heart J. 2004;5(9):702–6.
27. Ferreira VM, Piechnik SK, Dall'Armellina E, Karamitsos TD, Francis JM, Ntusi N, et al. Native T1-mapping detects the location, extent and patterns of acute myocarditis without the need for gadolinium contrast agents. J Cardiovasc Magn Reson. 2014;16:36.
28. Kovanlikaya A, Burke LP, Nelson MD, Wood J. Characterizing chronic pericarditis using steady-state free-precession cine MR imaging. AJR Am J Roentgenol. 2002;179(2):475–6.
29. Taylor AM, Dymarkowski S, Verbeken EK, Bogaert J. Detection of pericardial inflammation with late-enhancement cardiac magnetic resonance imaging: initial results. Eur Radiol. 2006;16(3):569–74.
30. Talreja DR, Edwards WD, Danielson GK, Schaff HV, Tajik AJ, et al. Constrictive pericarditis in 26 patients with histologically normal pericardial thickness. Circulation. 2003;108(15):1852–7.
31. Klein AL, Abbara S, Agler DA, Appleton CP, Asher CR, Hoit B, et al. American Society of Echocardiography clinical recommendations for multimodality cardiovascular imaging of patients with pericardial disease: endorsed by the Society for Cardiovascular Magnetic Resonance and Society of Cardiovascular Computed Tomography. J Am Soc Echocardiogr. 2013;26(9):965–1012. e15
32. Talreja DR, Nishimura RA, Oh JK, Holmes DR. Constrictive pericarditis in the modern era: novel criteria for diagnosis in the cardiac catheterization laboratory. J Am Coll Cardiol. 2008;51(3):315–9.
33. Clinical cardiac MRI. 1st ed., ed. Bogaert J, Dymarkowski S, Taylor AM. Berlin/Heidelberg/New York: Springer; 2005.
34. McDermott S, O'Neill AC, Ridge CA, Dodd JD. Investigation of cardiomyopathy using cardiac magnetic resonance imaging part 1: common phenotypes. World J Cardiol. 2012;4(4):103–11.
35. Westwood M, Anderson LJ, Firmin DN, Gatehouse PD, Charrier CC, Wonke B, Pennell DJ. A single breath-hold multiecho T2* cardiovascular magnetic resonance technique for diagnosis of myocardial iron overload. J Magn Reson Imaging. 2003;18(1):33–9.
36. Tanner MA, Galanello R, Dessi C, Westwood MA, Smith GC, Nair SV, et al. Myocardial iron loading in patients with thalassemia major on deferoxamine chelation. J Cardiovasc Magn Reson. 2006;8(3):543–7.
37. Rajagopalan N, Garcia MJ, Rodriguez L, Murray RD, Appersonhansen C, Stugaard M, et al. Comparison of new Doppler echocardiographic methods to differentiate constrictive pericardial heart disease and restrictive cardiomyopathy. Am J Cardiol. 2001;87(1):86–94.
38. Welch TD, Ling LH, Espinosa RE, Anavekar NS, Wiste HJ, Lahr BD, et al. Echocardiographic diagnosis of constrictive pericarditis: Mayo Clinic criteria. Circ Cardiovasc Imaging. 2014;7(3):526–34.
39. Imazio M, Brucato A, Mayosi BM, Derosa FG, Lestuzzi C, Macor A, et al. Medical therapy of pericardial diseases: part II: noninfectious pericarditis, pericardial effusion and constrictive pericarditis. J Cardiovasc Med (Hagerstown). 2010;11(11):785–94.
40. Alharthi MS, Jiamsripong P, Calleja A, Sengupta PP, McMahon EM, Khandheria B, et al. Selective echocardiographic analysis of epicardial and endocardial left ventricular rotational mechanics in an animal model of pericardial adhesions. Eur J Echocardiogr. 2009;10(3):357–62.
41. Sengupta PP, Narula J. Reclassifying heart failure: predominantly subendocardial, subepicardial, and transmural. Heart Fail Clin. 2008;4(3):379–82.
42. Pohost GM, Hung L, Doyle M. Clinical use of cardiovascular magnetic resonance. Circulation. 2003;108(6):647–53.
43. Skouri HN, Dec GW, Friedrich MG, Cooper LT. Noninvasive imaging in myocarditis. J Am Coll Cardiol. 2006;48(10):2085–93.
44. Giorgi B, Mollet NR, Dymarkowski S, Rademakers FE, Bogaert J. Clinically suspected constrictive pericarditis: MR imaging assessment of ventricular septal motion and configuration in patients and healthy subjects. Radiology. 2003;228(2):417–24.
45. Engel PJ. Echocardiographic findings in pericardial disease. In: Fowler NO, editor. The pericardium in health and disease. Armonk: Futura; 1985. p. 99–151.
46. Manning WJ, Pennell DJ. Cardiovascular magnetic resonance. London: Churchill Livingstone; 2002.
47. Ariyarajah V, Jassal DS, Kirkpatrick I, Kwong RY. The utility of cardiovascular magnetic resonance in constrictive pericardial disease. Cardiol Rev. 2009;17(2):77–82.
48. Groves R, Chan D, Zagurovskaya M, Teague SD. MR imaging evaluation of pericardial constriction. Magn Reson Imaging Clin N Am. 2015;23(1):81–7.
49. Bogaert J, Francone M. Pericardial disease: value of CT and MR imaging. Radiology. 2013;267(2):340–56.
50. Francone M, Dymarkowski S, Kalantzi M, Rademakers FE, Bogaert J. Assessment of ventricular coupling with real-time cine MRI and its value to differentiate constrictive pericarditis from restrictive cardiomyopathy. Eur Radiol. 2006;16(4):944–51.
51. Kojima S, Yamada N, Goto Y. Diagnosis of constrictive pericarditis by tagged cine magnetic resonance imaging. N Engl J Med. 1999;341(5):373–4.
52. Psychidis-Papakyritsis P, de Roos A, Kroft LJ. Functional MRI of congenital absence of the pericardium. AJR Am J Roentgenol. 2007;189(6):W312–4.
53. Klein C, Graf K, Fleck E, Nagel E. Images in cardiovascular medicine. Acute fibrinous pericarditis assessed with magnetic resonance imaging. Circulation. 2003;107(13):e82.
54. Aquaro GD, Barison A, Cagnolo A, Todiere G, Lombardi M, Emdin M. Role of tissue characterization by cardiac magnetic resonance in the diagnosis of constrictive pericarditis. Int J Cardiovasc Imaging. 2015;31(5):1021–31.
55. Verhaert D, Gabriel RS, Johnston D, Lytle BW, Desai MY, Klein AL. The role of multimodality imaging in the management of pericardial disease. Circ Cardiovasc Imaging. 2010;3(3):333–43.
56. Feng D, Glockner J, Kim K, Martinez M, Syed IS, Araoz P, et al. Cardiac magnetic resonance imaging pericardial late gadolinium enhancement and elevated inflammatory markers can predict the reversibility of constrictive pericarditis after antiinflammatory medical therapy: a pilot study. Circulation. 2011;124(17):1830–7.
57. Bolen MA, Rajiah P, Kusunose K, Collier P, Klein A, Popović ZB, Flamm SD. Cardiac MR imaging in constrictive pericarditis: mul-

tiparametric assessment in patients with surgically proven constriction. Int J Cardiovasc Imaging. 2015;31(4):859–66.
58. Frank H, Globits S. Magnetic resonance imaging evaluation of myocardial and pericardial disease. J Magn Reson Imaging. 1999;10(5):617–26.
59. Masui T, Finck S, Higgins CB. Constrictive pericarditis and restrictive cardiomyopathy: evaluation with MR imaging. Radiology. 1992;182(2):369–73.
60. Axel L. Blood flow effects in magnetic resonance imaging. AJR Am J Roentgenol. 1984;143(6):1157–66.
61. Gatehouse PD, Keegan J, Crowe LA, Masood S, Mohiaddin RH, Kreitner KF, Firmin DN. Applications of phase-contrast flow and velocity imaging in cardiovascular MRI. Eur Radiol. 2005;15(10):2172–84.
62. Hayashi H, Kawamata H, Machida M, Kumazaki T. Tuberculous pericarditis: MRI features with contrast enhancement. Br J Radiol. 1998;71(846):680–2.
63. Rajiah P. Cardiac MRI: part 2, pericardial diseases. AJR Am J Roentgenol. 2011;197(4):W621–34.
64. Spodick DH. Pericardial diseases. In: Braunwald E, Zipes DP, Libby P, editors. Heart disease: a textbook of cardiovascular medicine. Philadelphia: WB Saunders Co; 2001. p. 1823–70.
65. Syed FF, Schaff HV, Oh JK. Constrictive pericarditis—a curable diastolic heart failure. Nat Rev Cardiol. 2014;11(9):530–44.
66. Reinmüller R, Gürgan M, Erdmann E, Kemkes BM, Kreutzer E, Weinhold C. CT and MR evaluation of pericardial constriction: a new diagnostic and therapeutic concept. J Thorac Imaging. 1993;8(2):108–21.
67. McRee CW, Mergo P, Parikh P, Pollak A, Shapiro BP. Modern advances in cardiovascular imaging: cardiac computed tomography and cardiovascular MRI in pericardial disease. Futur Cardiol. 2014;10(6):769–79.
68. Coolen J, De Keyzer F, Nafteux P, De Wever W, Dooms C, Vansteenkiste J, et al. Malignant pleural disease: diagnosis by using diffusion-weighted and dynamic contrast-enhanced MR imaging—initial experience. Radiology. 2012;263(3):884–92.

Valvular Heart Disease Assessment by CMR

18

Patrycja Z. Galazka and Raymond Y. Kwong

General Overview

Cardiovascular magnetic resonance (CMR) has unique capabilities which can greatly benefit the assessment of the patient with cardiac valve disease [1]. In the last 20 years, CMR has emerged as an alternative to noninvasive modality without ionizing radiation that is applicable in patients with valvular heart disease. Echocardiography remains the standard tool for the initial assessment of valvular pathology; however, it may be inconclusive in some patients at which time CMR might accurately answer the clinical question. CMR provides images of valve anatomy and allows qualitative and quantitative evaluation of stenosis and regurgitation. CMR can also confidently discern the consequences of particular valvular lesions, including the effects of ventricular volume or pressure overload and alternations in systolic function [2]. Furthermore, CMR is able to evaluate great vessel anatomy and the presence of the myocardial scar which can be of prognostic significance. Therefore, CMR's versatility in assessment of valvular heart disease can significantly guide the clinician and advance patient's care.

Valvular Anatomy

Although 2D echocardiography remains the primary imaging modality for visualization of valvular anatomy, the CMR also has potential to visualize all parts of the valve (leaflets, chordae tendineae, and papillary muscles) throughout the entire cardiac cycle [2]. An important advantage of CMR is its ability to provide unlimited imaging planes tailored to individual anatomy [2, 3]. The most frequently used CMR pulse sequence to assess valve anatomy is steady-state free-precession (SSFP) sequence which is the workhorse of the CMR imaging. This sequence has excellent blood to myocardium contrast and a high intrinsic signal to noise ratio and has largely replaced gradient echo as the preferred pulse sequence for cine imaging of valve anatomy, although gradient-echo sequences also can be used to assess for valvular pathology when there is significant off resonance artifact.

The typical CMR study for evaluation of a valvular lesion involves performing a complete set of sequential short-axis (every 10 mm from base to apex) and long-axis (two-, three-, four-chamber views) cine images using the SSFP sequence depending on the valve of interest [4] (Fig. 18.1). To produce SSFP cine image throughout the systole and diastole, image acquisition is gated to ECG and occurs over several cardiac cycles and is obtained in a single breath-hold (over 6–12 s). The typical spatial resolution is 1.5–2.0 per pixel with 6 mm slice thickness, and using the ultrafast pulse sequence, temporal resolution of 25–35 ms (frame rates of 30–40 cm/s) can be achieved within 5–6 second breath-hold [4]. Spoiled gradient-echo sequences remain useful on occasions for visualizing the extent of flow disturbance in selected cases [1].

In addition to valvular anatomy such as evaluation of congenital abnormalities (bicuspid aortic valve, parachute mitral valve, aberrant papillary muscles, and chordal attachments), CMR can provide visualization of a cardiac valvular masses such as vegetations, thrombi, or tumors [2]. Non-cine pulse sequences, T1 weighted and T2 weighted based on gradient recalled echo or turbo spin-echo techniques with or without fat suppression, and segment recovery gradient may aid in tissue characterization of the masses as well as can be beneficial in assessment of extra-cardiac anatomy and thoracic vasculature [2, 5].

P. Z. Galazka
Non-invasive Cardiovascular Imaging, Cardiovascular Division, Department of Medicine and Department of Radiology, Brigham and Women's Hospital, Harvard Medical School, Boston, MA, USA

R. Y. Kwong (✉)
Non-invasive Cardiovascular Imaging, Cardiovascular Division, Department of Medicine, Brigham and Women's Hospital, Harvard Medical School, Boston, MA, USA
e-mail: rykwong@bwh.harvard.edu

R. Y. Kwong et al. (eds.), *Cardiovascular Magnetic Resonance Imaging*, Contemporary Cardiology,
https://doi.org/10.1007/978-1-4939-8841-9_18

Flow and Velocity Quantification

The unique advantage of CMR is its direct ability to quantify flow using through-plane phase-contrast velocity mapping. In contrast to echocardiography or invasive catheterization techniques, flow quantification with CMR does not rely on geometric and mathematical assumptions [6]. For phase contrast, two opposing gradient pulses known as velocity encoding are added to the imaging sequence of pulses. In pixels containing static tissue, the effects of the two pulses cancel, but if the tissue moves in the time between the pulses, they leave a phase shift in that pixel accurately proportional to the velocity along the gradient's direction [7]. This net-phase shift can be displayed as a phase map with differences in signal intensity representing different velocities. Pixels depicting flow in the phase-encoding direction appear bright and opposite to phase-encoding direction appear dark. Objects with a phase-shift zero appear gray or speckled [2] (Fig. 18.2).

These images can be further enhanced with color-coding of the anterograde (red) and retrograde (blue) dynamic flow (Fig. 18.3).

Velocity mapping requires that the appropriate maximum encoding velocity (VENC) is programmed into the pulse sequence [2]. The VENC refers to the velocity that is encoded as the phase shift of 180 degrees and thus represents the maximum velocity that is displayed unambiguously on the velocity maps [5]. If the velocity phase shift exceeds 180 degrees range, it cannot be distinguished from one within + 180 degree range, which is displayed instead known as velocity aliasing (wrap-around) [7]. The closer the programmed maximum velocity is to the maximum velocity present, the greater the sensitivity and accuracy of this technique to detect lower velocities within the region of interest [2]. As a compromise between high sensitivity and avoiding aliasing artifacts, it is recommended that the predicted peak velocity should cover approximately two-thirds of the interval set by the VENC [8]. Typical VENC's for normal aortic

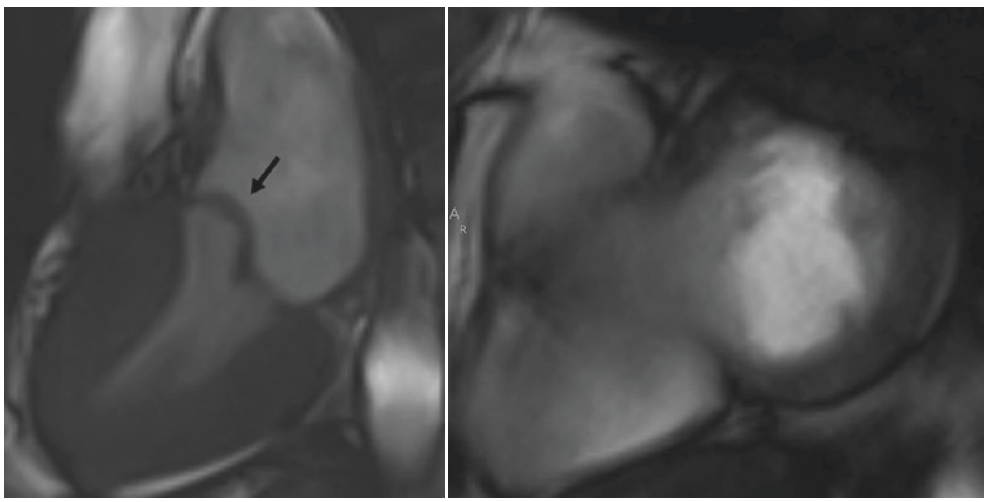

Fig. 18.1 SSFP cine image of two-chamber image allows for excellent visualization of anterior mitral valve prolapse (arrow) (left) and an axial SSFP short-axis image of the mitral valve in diastole (right)

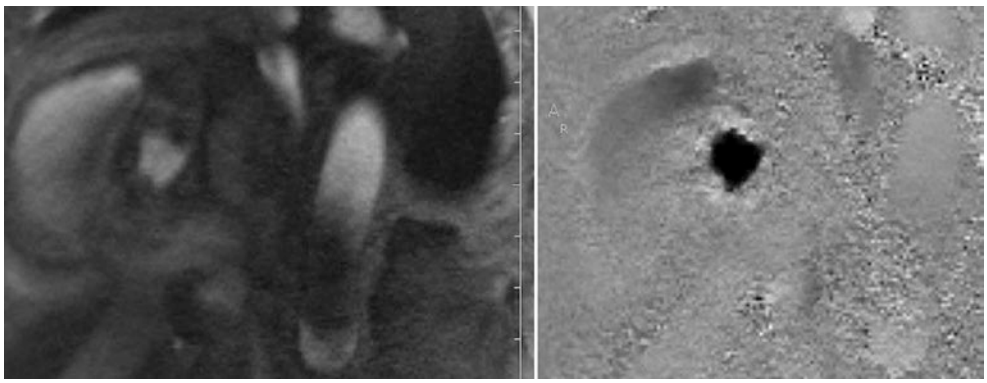

Fig. 18.2 Example of ECG-gated cine phase-contrast mangintude (right) and phase (left) images during systole at the normal functioning pulmonic valve level

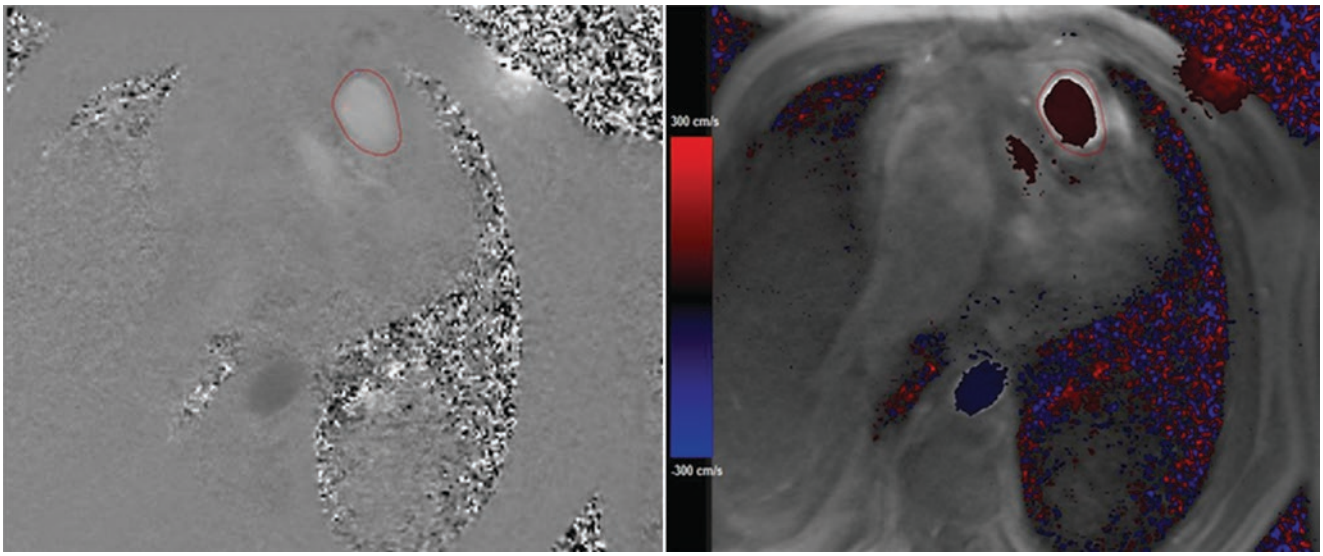

Fig. 18.3 Example of phase-contrast image at the level of pulmonary artery (left) and color-coded image (right) showing forward flow in the pulmonary artery and antegrade flow in the descending thoracic aorta

flow are in the region of 150 cm/sec increasing to 400 cm/sec or more for aortic stenosis [9]. The velocity mapping produces two sets of images: magnitude image and phase-velocity maps. The magnitude image is used for anatomic orientation of the imaging slice and to identify the boundaries of the vessel imaged [2]. The phase map encodes the velocities within each pixel. The uncontrolled phase errors must be removed to detect only the velocity-phase shift, so two scans typically "reference" and "velocity encoded" usually are acquired together. Subtracting the reference phase image from the velocity-encoded phase image makes the phase-contrast velocity map [7] (Fig. 18.4).

For "through-plane" velocity mapping, used for flow quantification, the operator should prescribe the image plane perpendicular to the direction of blood flow. Velocities can also be measured "in-plane" phase-contrast sequences, which measure velocities within the plane of the slice [6]. Ideally the in-plane sequences allow a long-axis visualization of the transvalvular jet and should be acquired before through-plane velocity mapping as they can demonstrate the origin and direction of the jet. This can be useful when planning subsequent perpendicular or through-plane slice [6]. The in-plane velocities are generally less accurate for measuring peak velocities especially in a stenotic valve due to partial volume effects, relatively low temporal resolution as compared to echocardiography, signal loss due to turbulence, and phase-shift errors [6]. The through-plane velocity mapping is a method of choice for assessing high-velocity jets. We in general obtain a stack of 3–5 parallel slices to ensure the data acquisition closest to the stenotic orifice, where maximum jet can be accurately assessed (Fig. 18.5).

Assessment of Ventricular Volumes, Function and Mass

Precise measurement of both left and right ventricular volumes, function and mass is very important for determining the impact of valve lesion on the ventricle [1]. It has been shown that both ventricular dilatation and reduced systolic function are poor prognostic indicators [10]. CMR is the most accurate and reproducible technique for assessing both right and left ventricular volumes and mass and is considered the gold standard [11–13]. The accuracy of CMR calculated volumes has been validated through both in vitro and in vivo methods [14]. Right ventricular volumes are especially difficult to assess with other modalities due to crescentic shape of the RV; therefore, CMR can be especially useful [1]. The technique that has won widespread acceptance is the short-axis multi-slice (multiple 2D or 3D) cine acquisition, where both ventricles are sampled from the atrioventricular ring to the apex, with subsequent planimetry of the endocardial and epicardial borders of the ventricles to derive the required volume and mass parameters [15]. During a breath-hold, a stack of 6–8 mm slices in SSFP sequence is obtained that covers the length of both ventricles. The ventricular volume is obtained from careful tracing endocardial borders in end-systolic and end-diastolic views which provide end-systolic and end-diastolic volumes from which stroke volume, cardiac output, and ejection fraction can be calculated [5]. Myocardial volume is the area occupied between the endocardial and epicardial border multiplied by the interslice distance. Similar to echocardiography, left ventricular mass is the product of this vol-

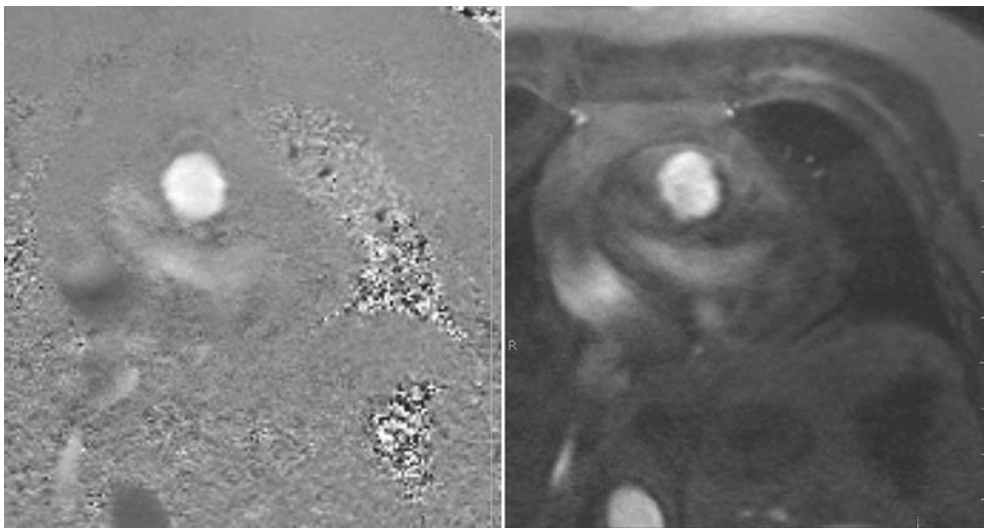

Fig. 18.4 Example of ECG-gated cine phase-contrast mangintude (right) and phase (left) images during systole at the normal functioning pulmonic valve level

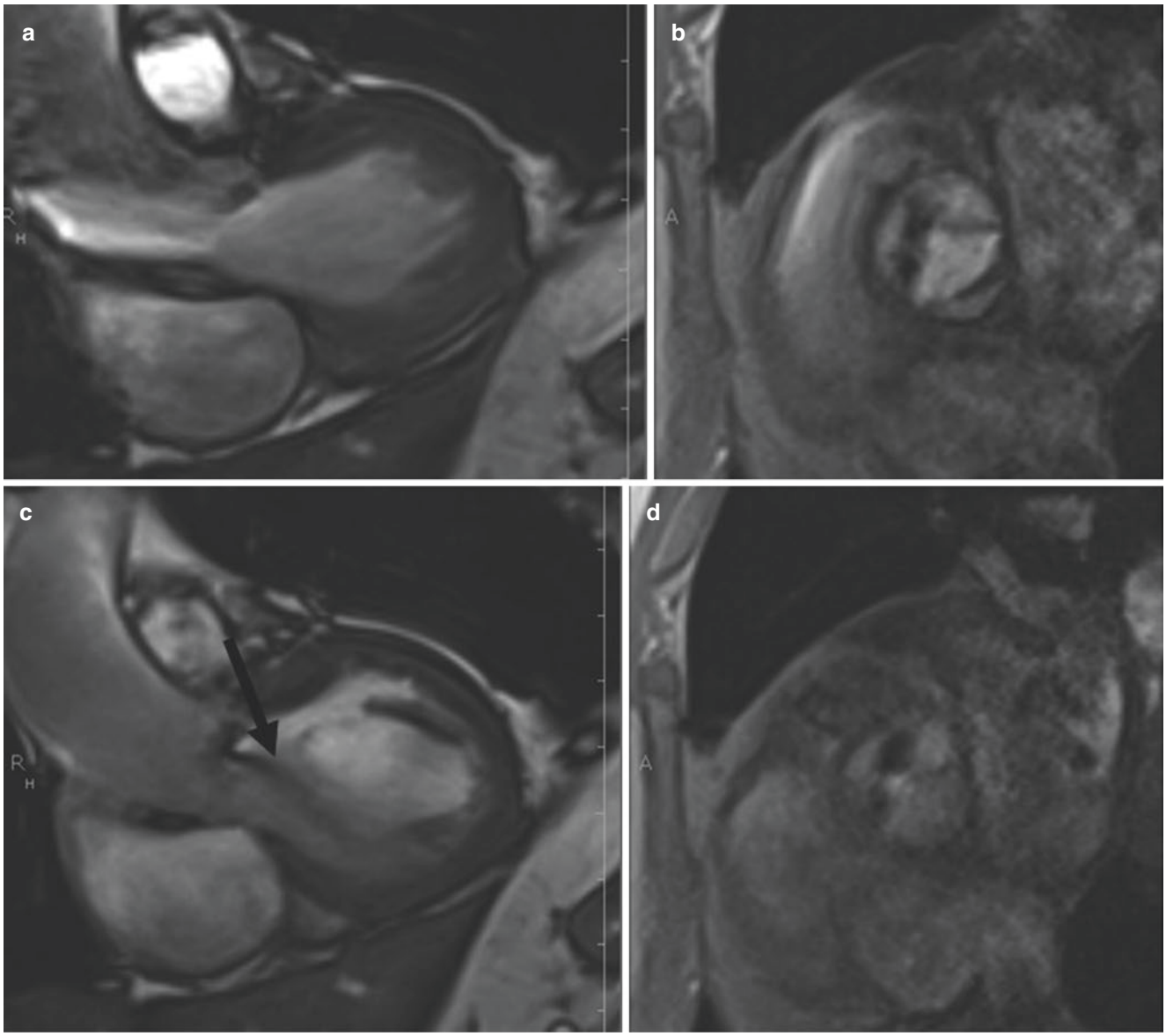

Fig. 18.5 SSFP cine left ventricular outflow oblique view image (**a**) in systole. This view allows to obtain a short-axis view at the aortic valve level which shows a bicuspid aortic valve in systole with right and left cusp fusion (**b**). From the short-axis view, through-plane velocity mapping can be planned out. Same views obtained in diastole showing aortic regurgitation (arrow) as a signal void in LVOT (**c**) and short-axis view at the aortic valve level which shows a bicuspid aortic valve in diastole (**d**)

ume and the density of the myocardium [16]. Papillary muscles and endocardial trabeculae should be excluded from the LV volume and included in the LV mass. LV mass is usually taken from the end-diastolic images [15].

Assessment of Aortic Stenosis

Aortic stenosis can be characterized by congenital or acquired impedance of blood flow from the left ventricle into the aorta and may be of subvalvular, supra-valvular, or most commonly of valvular etiology. Current guidelines by the American Heart Association/American College of Cardiology (AHA/ACC) recommend aortic valve surgery in virtually all symptomatic patients with severe aortic stenosis (Class I) and support surgical intervention for asymptomatic patients who demonstrated left ventricular systolic dysfunction or exertional hypotension (Class IIa) [10]. A CMR assessment of aortic stenosis can be enhanced with CMR through accurate assessment of the anatomy of the valve and the aortic root, precise quantification of the LV mass and function, and measurements of the velocity of the stenotic jet in instances when it is difficult to do with echo [1]. Similar to echocardiography, cardiac MRI allows for the assessment of aortic stenosis severity by use of two different approaches. One of them is direct planimetry by obtaining of the maximal anatomical orifice area using cine CMR imaging of the valve tips in systole [17, 18]. The excellent visualization of anatomy provided by SSFP cine short-axis image plane allows superb evaluation of severity of aortic stenosis with direct planimetry of the aortic valve orifice [19]. Second technique calculates functional orifice area by the continuity equation and the velocity time integrals obtained at the valve tips and through left ventricular outflow tract with phase-contrast imaging [20]. In contrast to echocardiography, the cross-sectional area of the left ventricular outflow tract (LVOT) can be directly measured without making geometric assumption. The continuity equation states that the flow at the LVOT level must equal the flow at the level of the aortic valve. Such measurement in CMR has been shown to have a high rate of intra- and inter-observer reproducibility [18, 21].

$$\text{Aortic Valve Area} = \frac{\text{LVOT velocity}}{\text{Aortic Valve velocity}} * \text{LVOT area}$$

After localization of the heart using three plane and oblique images, a three-chamber view and an oblique coronal breath-hold SSFP view cine should be prescribed where left ventricular outflow can be visualized well [22]. These are also optimal planes for identifying the signal void corresponding to the abnormal flow jet [23]. From these images, short-axis SSFP image is prescribed by placing the imaging plane through the aortic valve tips in systole. Free-breathing, SSFP image slices should be thin (4–5 mm), and multiple slices parallel to the aortic valve opening should be acquired as they may aid in identifying the true valve orifice [1]. There is an excellent agreement between the planimetry of the aortic valve area using SSFP cine images and transesophageal echocardiography [17, 18, 20].

For the continuity equation, LVOT area, LVOT VTI, and AV VTI need to be assessed. One of the advantages of the CMR over echocardiography in continuity equation is ability to directly measure LVOT. Free-breathing, cine-gradient echo-segmented pulse sequences for through-plane phase-contrast imaging and velocity encoding should be acquired in the short-axis plane positioned just beyond the aortic leaflet tips and in the LVOT approximately 2 cm below the aortic annulus. The optimal short-axis slice position for measurement of peak transvalvular velocities is at the vena contracta just at or beyond the anatomic valve orifice in systole. In straight pipes with planar circular orifice plates, the vena contracta occurs about one orifice diameter downstream from the orifice [24]. The velocity encoding should be set in the through-plane direction at the maximal encoding velocity depending on severity of aortic stenosis (at least 4 m/sec in cases of severe aortic stenosis) for the transvalvular phase-contrast image and at least at 2.0 m/sec in the LVOT to avoid aliasing [22]. Due to small width of very high-velocity jets and partial volume effects, lower temporal resolution as compared to echocardiography, and artifacts from turbulent jets, the peak aortic velocity obtained by velocity mapping may be underestimated as compared to continuous wave Doppler obtained by echo [1]. Pressure gradient and valvular area measurements obtained with these imaging techniques have been shown to correlate accurately with data from cardiac catheterization and Doppler echocardiography [21].

Other advantages of CMR include ability to assess and differentiate between supra-valvular and subvalvular stenosis with accurate assessment of site of velocity acceleration with in-plane velocity mapping [1]. CMR can also accurately assess the diameter of the ascending aorta which is especially important in case of bicuspid aortic valves. Additionally, very accurate left ventricular mass assessment provides information regarding effect of aortic stenosis on the left ventricle [1]. Lastly, the presence of LGE which usually occurs patchy and mid-wall in the basal lateral wall indicating focal fibrosis or unrecognized infarct is an independent predictor of mortality in patients with AS undergoing AVR [25].

Assessment of Aortic Regurgitation

Per AHA/ACC 2014 Valvular guidelines, CMR is indicated in patients with moderate or severe aortic regurgitation (stages B, C, and D) and suboptimal echocardiographic images for the assessment of LV systolic function, systolic and diastolic volumes, and measurement of AR severity [10].

The severity of the aortic insufficiency can be semiquantitatively assessed by manually tracing the area and measuring the greatest length of the depicted signal void in left ventricle on cine imaging [26]. The signal void of the aortic regurgitant flow in diastole is best demonstrated by multi-planar imaging in the coronal plane centered on the LVOT and in the long axis of the left ventricle [27] (Fig. 18.6).

While this assessment of jet area ($r = 0.91$) and jet length ($r = 0.85$) is comparable to that of transesophageal echocardiography and provides a crude assessment of the severity of the regurgitant lesion, it cannot be overemphasized that the appearance of the signal void varies depending on the valvular abnormality, volume and pressure in the receiving cavity, and imaging parameters particularly the degree of dephasing allowed by the predefined TE [7, 28, 29]. The advantage of CMR in evaluation of aortic regurgitation is direct quantitative assessment of the degree of regurgitation and its consequences on LV volume and function which is especially important when serial measurements are required as per AHA/ACC guidelines; aortic valve replacement is supported in asymptomatic patients with severe left ventricular dilatation (>75 mm end-diastolic and >55 mm end-systolic echocardiographic diameters or LVEF < 50%) [3, 30]. Myerson et al. showed that patients with aortic regurgitant fraction >33% quantified by CMR was associated with symptoms and progression to surgery [30].

CMR can accurately quantify the amount of regurgitation using through-plane phase-contrast velocity mapping from which derived values such as regurgitant fraction or regurgitant volume can be obtained. Flow can be measured by prescribing the imaging slice just above and below the aortic valve, quantifying both forward and regurgitant flow per cardiac cycle [31]. For forward flow, it is important to position the imaging plane just above the aortic valve as otherwise the velocity can be underestimated if it is placed in the ascending aorta [1]. Free-breathing, SSFP image slices should be thin (4–5 mm), and multiple slices above and below the aortic valve opening should be obtained. A magnitude image with the manually traced cross-sectional area of the valvular annulus is transferred to the corresponding phase image for each time frame. This enables measurement of the average velocity and provides the flow volume per heartbeat [32, 33].

$$\text{Regurgitant Fraction} = \frac{\text{Regurgitant Volume}}{\text{Forward Volume}}$$

It is also possible to calculate aortic regurgitation with ventricular volumes when a single-valve lesion such as aortic valve regurgitation is present. The regurgitant volume can be calculated from the difference of right ventricular and left ventricular stroke volumes using the modified Simpson method, in which the volumes of the ventricles are measured on a stack of parallel short-axis views [34].

$$\text{SV(LV)} \quad \text{SV(RV)} = \text{Aortic Valve Regurgitant Volume}$$

The measurement of regurgitant flow with phase contrast correlates well with the semiquantative angiographic or echocardiographic grades of severity [31, 35]. The accuracy of aortic regurgitation quantification using CMR through-plane velocity mapping is also excellent when compared to in vitro studies [1].

Additionally, CMR also enables visualization of the aortic arch and may help determine the etiology of aortic regurgitation. For example, uniform dilatation of the aortic annulus and proximal ascending aorta is a finding that is compatible with aortoannular ectasia. Therefore, CMR allows for comprehensive assessment of the valve and its function as well as the aorta. Lastly, a new emerging technique of 4D flow CMR which refers to phase-contrast CMR with flow encoding in all three spatial directions that is resolved relative to all three dimensions of space and to the dimension of time along the cardiac cycle (3D + time = 4D) has been promising in estimating aortic regurgitation volume and fraction [27] (Fig. 18.7).

Assessment of Mitral Stenosis

Echocardiography, especially transesophageal echocardiography, remains the first-line technique for assessment of mitral stenosis, but cardiac MRI can be useful in selected cases of mitral stenosis as in patients with poor acoustic windows [1, 6]. Restriction in mitral valve opening during diastole results in mitral stenosis and produces a diastolic pressure gradient between the left atrium and left ventricle. As an alternative to echocardiography, CMR provides good visualization of the restricted leaflets and in particular an excellent visualization of the left ventricular outflow track [6]. Direct planimetry of the stenotic orifice can be performed in similar way as in the aortic stenosis. The imaging plane should be placed at the mitral valve tips in diastole [6]. Djavidani et al. showed that planimetry of the mitral valve by magnetic resonance imaging has good correlation with echocardiography although slightly overestimates MVA when compared to the PHT method by echocardiography and to invasive hemodynamics [36]. Diastolic flow and velocity also can also be measured in this image plane with velocity-encoding cine magnetic resonance imaging which also shows good correlation with Doppler transthoracic echocardiography [37]. Velocity-encoded CMR can quantify MVA using the PHT method in a similar manner to that used in transthoracic echocardiography which is also comparable to a transthoracic echocardiography [38]. Atrial fibrillation in severe mitral stenosis can reduce the accuracy of flow measurements [6]. CMR also can be helpful in identifying LAA or LA thrombus especially in patients being considered for percutaneous mitral balloon commissurotomy [39].

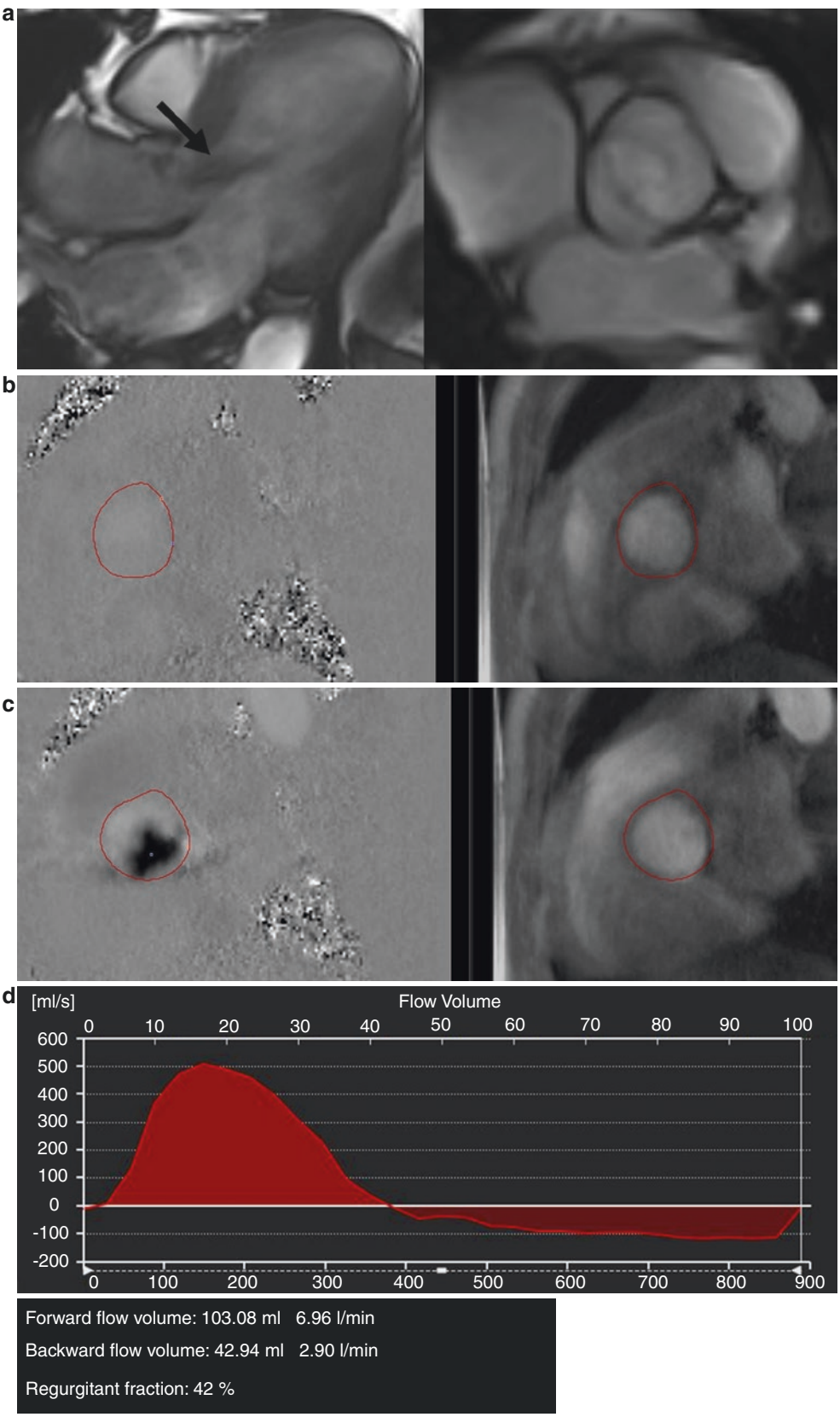

Fig. 18.6 A 50-year-old male with history of bicuspid aortic valve. (**a**) SSFP cine three-chamber view showing eccentrically directed aortic regurgitation jet (arrow) (left) SSFP short axis at aortic valve level shows right and left coronary cusp fusion in a bicuspid valve (right). (**b**) Phase and magnitude images below the aortic valve shows forward aortic flow in black. (**c**) Phase and magnitude images obtained below the aortic valve shows regurgitant aortic flow in black. (**d**) Corresponding plots of velocity vs time-volume curve showing antegrade and retrograde flow with resultant regurgitation fraction of 42%

Fig. 18.7 MRA of dilated ascending thoracic aorta in a patient with bicuspid aortic valve

Mitral Regurgitation

Mitral regurgitation is caused by insufficiency of an abnormal mitral valvular apparatus that results in backward flow of blood from the left ventricle into the left atrium and produces an increase in total stroke volume. The AHA/ACC 2014 valvular guidelines recommend valve replacement in patients with severe mitral regurgitation with symptoms of congestive heart failure or left ventricular systolic dysfunction (LVEF 60%) and recommend the use of CMR to assess LV and RV size and function, as well as severity of MR, in situations where TTE is technically limited [10]. The main advantages of CMR over echocardiography are in quantitative assessment of both the regurgitation fraction as well as ventricular function and volume [1, 40]. In ischemic mitral regurgitation, CMR can also assess regional myocardial function and viability. Therefore, accurate assessment of severity of regurgitation, knowing the dysfunction responsible for it, the etiology of the condition, and LV size and function is very important.

An understanding anatomy of the mitral valve is very important for accurate imaging. CMR can assess mitral leaflets morphology and determine the etiology of the mitral regurgitation which has a very good agreement with transesophageal echocardiography. Multi-slice contiguous cines (5 mm slices) can be used for full evaluation of the mitral valve morphology and identification of prolapse and regurgitation of scallops which has correlated well with transesophageal echocardiography in patients prior to mitral repair [40]

Following standard two-, three-, and four-chamber long-axis views, a balanced SSFP end expiratory breath-hold cines, with ECG gating, and a short-axis stack (starting at the mitral annulus and continuing through the LV apex using 8 mm slice thickness) allow for accurate assessment of mitral anatomy [40]. From a basal short-axis image where mitral valve is well seen, a contiguous stack of oblique slices can be aligned orthogonal to the central line of the coaptation, oriented approximately parallel to the three-chamber LVOT long-axis plane. The stack of cines starts the superior (anterolateral) commissure adjacent to A1-P1 and progress toward the inferior (posteromedial) commissure adjacent to A3-P3 using a slice thickness of 5mm and inter-slice gap [40]. Additional orthogonal imaging slices are acquired through the commissures at each end of the mitral valve (A1-P1 and A3-P3) to better visualize theses scallops. From the mitral stack and commissural images, each scallop of the mitral leaflet is well visualized, and the pathology can be delineated (Fig. 18.8).

Quantification of mitral regurgitation is usually performed with phase-contrast velocity mapping. First, aortic velocity mapping is performed in the ascending aorta above the sino-tubular junction which is then subtracted from the left ventricular stroke volume in order to calculate mitral regurgitation volume which when divided by left ventricular stroke volume gives the regurgitant fraction [40].

$$\text{Mitral Regurgitant Volume}\left(\text{ml / beat}\right) = \text{LVSV} - \text{AoSV}$$

$$\text{Regurgitant Fraction} = \frac{\left(\text{MRV}\right)\times 100\%}{\text{LVSV}}$$

For quality control, the aortic forward volume should be within 5% of the pulmonary artery forward flow in the absence of intracardiac shunt [40]. And just as in the case of aortic regurgitation and the absence of other regurgitant lesions, MRV can also be calculated by subtracting RV stroke volume from LV stroke volume if there are no other regurgitant lesions.

$$\text{MRV} = \text{LVSV} - \text{RVSV}$$

The quantification of the mitral regurgitation correlates well with echocardiographic and angiographic assessment and has good reproducibility [41, 42]. The AHA/ACC 2014 valvular guidelines grade severe MR by echocardiography as regurgitant volume >60 ml and regurgitant fraction >50%. Myerson et al. followed 109 patients with CMR who had echocardiographic moderate to severe mitral regurgitation and showed that regurgitant volume >55 ml and regurgitant fraction >40% were associated with development of symptoms and need for surgery and showed better discriminatory ability than reference standard CMR-derived ventricular vol-

umes [43]. CMR should be considered in those patients when mitral regurgitation severity as assessed by echocardiography is influencing an important clinical decision, such as the decision to undergo surgery [44].

Pulmonary Stenosis

CMR is particularly valuable in assessment of pulmonary valve especially in congenital heart disease such as tetralogy of Fallot as it might be difficult to visualize the RVOT and the pulmonic valve with echocardiography due to its location immediately behind the sternum. Therefore, CMR should be considered as a gold standard for evaluation of the pulmonic valve and RV outflow track [1]. Balanced SSFP imaging of an oblique sagittal plane of RV outflow tract should be obtained which comprehensively includes the proximal pulmonary trunk and foreshortened view of right ventricle [1].

In order to visualize all three pulmonary leaflets, a double-oblique coronal plane is obtained along the pulmonary artery perpendicular to the valve. Then the plane through the now visible pulmonary cusps results in true short valvular axis [45].

A qualitative assessment of severity of pulmonary stenosis can be made from cine imaging by visualizing the valve motion and the stenotic jet [1]. As in the case of evaluation of mitral valve stenosis, direct planimetry of the valve orifice obtained in systole from the cine images at the valve tips is the preferred method for evaluating the severity [1]. Quantitative assessment

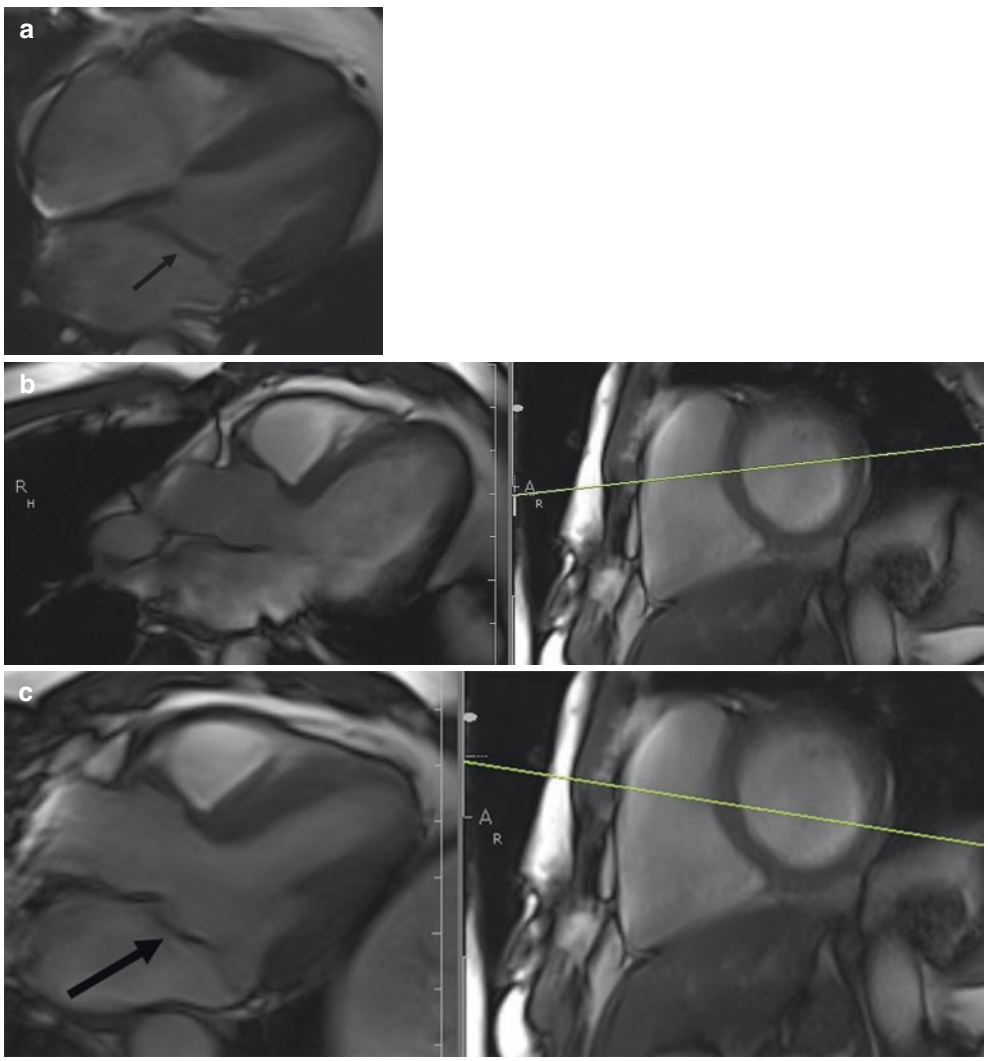

Fig. 18.8 A 50-year-old female with history of mitral regurgitation. (**a**) SSFP cine four-chamber view of anteriorly directed mitral regurgitation jet (arrow) seen in systole. (**b**) A1/P1 scallop assessment planned from the short-axis view at the mitral valve level. (**c**) A2/P2 scallop assessment planned from the short-axis view at the mitral valve level showing anteriorly directed mitral regurgitation jet (arrow) originating from prolapsed P2 scallop. (**d**)A3/P3 scallop assessment from the short-axis view at the mitral valve level. (**e**) Magnitude (right) and phase (left) images at the mitral valve level in diastole. (**f**) Magnitude (right) and phase (left) images at the mitral valve level in systole showing mitral regurgitation in dark

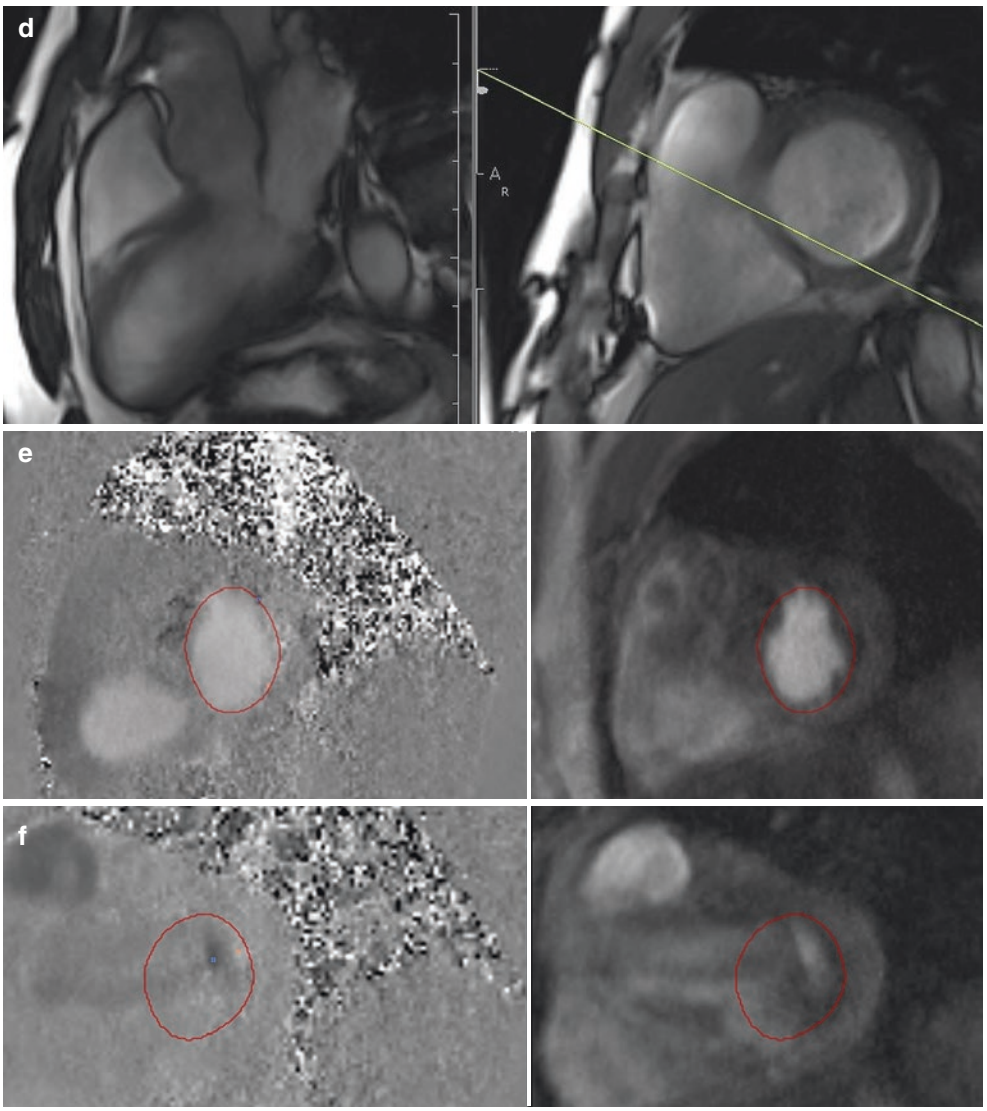

Fig. 18.8 (continued)

of pulmonic velocity can be made by measuring peak velocity with through-plane phase-velocity mapping imaging in similar way to aortic stenosis [1]. Long-axis cine view through the RVOT also enables to assess for supra-valvular or subvalvular pulmonic stenosis. CMR also allows for accurate right ventricular mass and function assessment and determination of hemodynamic effect of pulmonic stenosis [6].

Pulmonary Regurgitation

Evaluation of pulmonary regurgitation is especially important in patients with Tetralogy of Fallot whose statuses are post-repair and where accurate estimation of regurgitation severity and right ventricular volume/function are extremely important [1].

Pulmonary regurgitation can be visualized in the steady-state free-precession cine imaging as a signal void in the RVOT. It should be noted, though, that the degree of turbulence might be lower due to lower pressures and the wide jet of PR with mostly laminar flow on the right side which can make visualization of regurgitation might more difficult [6] (Fig. 18.9).

Hence, the in-plane phase-contrast velocity mapping is usually preferred for visualization of the regurgitant jet [6]. Quantification of regurgitant flow with through-plane velocity mapping is performed on an image slice placed just above the pulmonary valve [1]. On the in-plane velocity mapping,

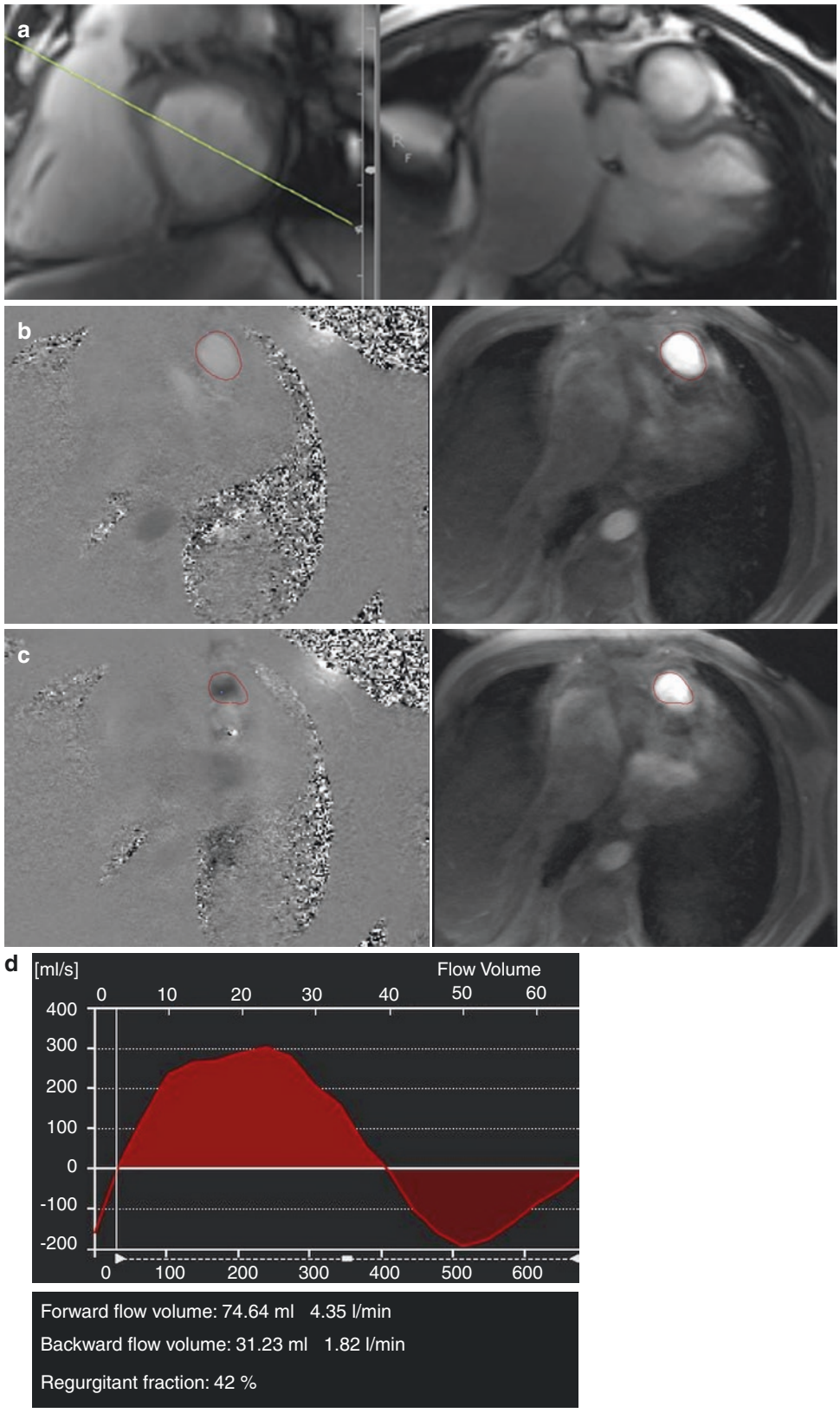

Fig. 18.9 A 52-year-old male with history of pulmonic stenosis status post-valvulotomy in childhood and now presenting with dyspnea on exertion. (**a**) Sagittal SSFP cine image through the right ventricular outflow tract and pulmonary artery (left) and short-axis SSFP slice below the pulmonic valve (right) for the phase-contrast positioning. (**b**) Magnitude and phase-contrast images below the pulmonic valve in systole. (**c**) Magnitude and phase-contrast images below the pulmonic valve in diastole showing pulmonic regurgitation in black which calculated to be moderate to severe. (**d**) Corresponding plots of velocity vs time-volume curve showing antegrade and retrograde flow with resultant regurgitation fraction of 42%=severe pulmonary regurgitation

the wide regurgitant jet is clearly seen in as black. Robenberg et al. showed that CMR velocity mapping is an accurate method for the noninvasive, volumetric quantification of pulmonary regurgitation after surgical correction of tetralogy of Fallot [46]. Mercer-Rosa et al. showed that when comparing echocardiography with CMR in patients with repaired TOF, where regurgitant fraction >40% is considered severe, echocardiography continues to have a limited ability to quantify PR and RV function as compared with CMR [47]. Furthermore, Li et al. showed that when evaluated in adults with repaired tetralogy of Fallot, direct quantification of the pulmonary regurgitation with CMR agrees well with echocardiographic parameters [48]. CMR also can be helpful in determining timing for pulmonary valve replacement as it accurately assesses RV volume and function [49].

Tricuspid Stenosis

Tricuspid stenosis is very rare and is not commonly assessed by CMR. If needed, cine SSFP images can be obtained which easily can visualize the anatomy and function of the leaflets. The tricuspid valve area can be assessed by placing image slice through the valve tips in diastole, in similar way in assessment of mitral stenosis. The forward velocity can also be measured through the valve with phase-velocity imaging as well although it might be less useful [1].

Tricuspid Regurgitation

CMR is particularly useful in assessment of leaflet morphology such as in Ebstein's anomaly [50]. For example, four-chamber SSFP cine image can identify the displacement of the valve or abnormal movement of the leaflets. Due to thin nature of the tricuspid leaflets and limited spatial resolution of CMR, it might be difficult to assess for adherence of the tricuspid leaflets to the myocardium [1]. Qualitatively, the tricuspid regurgitation can be evaluated by in-plane phase imaging in the four-chamber view or in the two-chamber view focusing on the right atrium and the right ventricle. The velocity encoding setting should be around ~150 cm/sec. (Fig. 18.10).

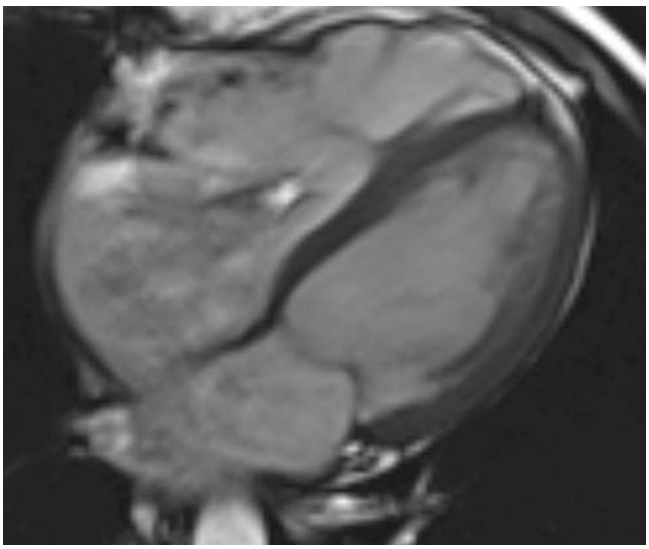

Fig. 18.10 SSFP cine four-chamber image showing severe tricuspid regurgitation with apical displacement of tricuspid septal leaflet in a patient with Ebstein's anomaly. The RA and RV are moderately dilated

Special Considerations

Prosthetic Valves

Cardiac magnetic resonance (CMR) could be an alternative noninvasive imaging modality that can be utilized to assess prosthetic valve function by direct planimetry of the anatomic orifice area (AOA) and for assessment of peak through-plane velocity by use of phase- contrast (PC) techniques. Maragiannis et al. showed that estimation of effective orifice area with phase contrast is a feasible, accurate, and reproducible parameter that may be calculated to assess both normal and abnormal bioprosthetic aortic valve functions [51]. Mechanical heart valves often produce complex flow patterns that make precise assessment via Doppler echocardiography challenging. In this respect, CMR can be quite helpful in addition to defining structure, position, and flow across the orifice and associated changes in the valvular apparatus and chambers. However, these valves can induce susceptibility artifacts and often necessitate phase-contrast imaging in particular, to be acquired outside the magnetic field distortion [52]. The SSFP cine sequence is very sensitive to artifacts from ferromagnetic objects which can both arise from both mechanical and bioprosthetic valves. Currently all mechanical valves are considered safe for imaging in a 1.5 Tesla environment because heating and torque due to the magnetic field is considerably small [52, 53], unless if clinical valvular dehiscence is suspected, then CMR imaging may pose additional risk to the patient with an already impaired heart artificial valve.

CMR can also be an alternative method for assessment of new percutaneous valves. Hamilton Craig et al. showed that CMR performs very well in the quantitation of MR after MitraClip insertion, with excellent reproducibility compared to echocardiographic methods [54]. Secchi et al. evaluated patient status post-tetralogy of Fallot repair and showed that CMR demonstrated restored pulmonary conduit function, reduced RV volumes, and increased RV and LV function but did not predict valve fracture/restenosis [50]. Hartlage et al.

showed that CMR more accurately classifies severity of paravalvular aortic regurgitation, providing superior prognostic value compared with echocardiography, as patients with greater than mild paravalvular regurgitation by CMR, defined as regurgitant fraction >20%, had a higher incidence of adverse events [55].

Pre- and Postsurgical Assessment

In pre- and postsurgical assessment, CMR not only provides comprehensive information on valvular and ventricular function, but it may also assist in prognosis of the patient. CMR can also aid in determining the type of surgical procedure and the impact that the procedure holds on cardiac hemodynamics during recovery. Barone-Rochette et al. showed that the presence of LGE indicating focal fibrosis or unrecognized infarct by CMR is an independent predictor of mortality in patients with AS undergoing AVR and could provide additional information in the preoperative evaluation of risk in these patients [25]. CMR is also very useful in presurgical planning and for postsurgical evaluation in congenital patients. Fogel et al. demonstrated that single-ventricle patients not requiring an intervention can undergo successful Fontan completion with CMR and echo alone with similar short-term outcomes to patient who underwent catheterization, which was used as a control, preventing an invasive test and exposure to radiation [56]. Geva et al. evaluated patients with post-tetralogy of Fallot repair and showed that severe RV dilatation and either LV or RV dysfunction assessed by CMR predicted major adverse clinical events in this population [57].

In patients who had received a mechanical valve compared to those with nonmechanical ones, CMR was able to demonstrate a greater decrease in the absolute value of systolic strain [58]. Effects on left ventricular mass among patients with severe aortic stenosis who had undergone stentless versus stented porcine valve replacement can also be compared with some precision with CMR [59]. The extent of left atrial and left ventricular reverse remodeling and impact on absolute left ventricular strain can also been demonstrated by CMR [60]. Tissue-tagging is another useful tool in CMR for comparing the type of prosthetic valve used in aortic valve replacement and its impact on incompletely recovered systolic strain in chronic aortic regurgitation [43, 46] Moreover, CMR is able to assess surgical approaches to valve sparing with regard to preservation of the native sinuses of Valsalva where it has demonstrated that such aortic vortical blood flow is absent in postoperative patients with Marfan syndrome [61]. The determination of regurgitant fraction, ventricular dimensions and functions, and graft diameters allows standardized imaging protocols with a high reproducibility, which may lead to this technique being favored for the follow-up of patients after surgery involving the heart valves or the great vessels.

Limitations

Arrhythmias can greatly affect the image quality and can also disrupt accurate ventricular volume acquisition as well as valvular flow assessment [62]. Difficulty with breath-holding may also negatively impact the image. Visual assessment from cine images alone should not be done as turbulent flow can produce signal void which can mimic regurgitation. In some instances, slice orientation may not be placed directly perpendicular to the flow in which case VENC may underestimate velocities. Velocities may be also underestimated due to partial volume averaging. Therefore, careful planning needs to be done for each valvular assessment.

Summary

Cardiovascular magnetic resonance allows for a comprehensive evaluation of simple and complex valvular heart disease. The main advantage of CMR for assessment of valvular heart disease is its true and reproducible measurements of ventricular volumes and function which can guide a clinician regarding appropriate timing of surgery. CMR can also provide quantitative measure of valvular stenosis and regurgitation which is comparable to echocardiography. Currently, studies evaluating clinical outcomes by CMR are being investigated, some of which already have shown that aortic regurgitation fraction of >33%, pulmonary regurgitation fraction of >40%, and mitral regurgitation fraction >50% predict symptom development and the need for valve replacement [1, 30, 62]. Therefore, CMR is an attractive alternative or complimentary modality for through assessment of valvular pathology.

References

1. Myerson SG. Heart valve disease: investigation by cardiovascular magnetic resonance. J Cardiovasc Magn Reson. 2012;14:7.
2. Cawley PJ, Maki JH, Otto CM. Cardiovascular magnetic resonance imaging for valvular heart disease: technique and validation. Circulation. 2009;119(3):468–78.
3. Han Y, Peters DC, Salton CJ, Bzymek D, Nezafat R, Goddu B, et al. Cardiovascular magnetic resonance characterization of mitral valve prolapse. JACC Cardiovasc Imaging. 2008;1(3):294–303.
4. Lopez-Mattei JC, Shah DJ. The role of cardiac magnetic resonance in valvular heart disease. Methodist Debakey Cardiovasc J. 2013;9(3):142–8.
5. Sommer G, Bremerich J, Lund G. Magnetic resonance imaging in valvular heart disease: clinical application and current role for patient management. J Magn Reson Imaging. 2012;35(6):1241–52.

6. Karamitsos TD, Myerson SG. The role of cardiovascular magnetic resonance in the evaluation of valve disease. Prog Cardiovasc Dis. 2011;54(3):276–86.
7. Gatehouse PD, Keegan J, Crowe LA, Masood S, Mohiaddin RH, Kreitner KF, et al. Applications of phase-contrast flow and velocity imaging in cardiovascular MRI. Eur Radiol. 2005;15(10):2172–84.
8. Kilner PJ, Firmin DN, Rees RS, Martinez J, Pennell DJ, Mohiaddin RH, et al. Valve and great vessel stenosis: assessment with MR jet velocity mapping. Radiology. 1991;178(1):229–35.
9. O'Brien KR, Gabriel RS, Greiser A, Cowan BR, Young AA, Kerr AJ. Aortic valve stenotic area calculation from phase contrast cardiovascular magnetic resonance: the importance of short echo time. J Cardiovasc Magn Reson. 2009;11:49.
10. Nishimura RA, Otto CM, Bonow RO, Carabello BA, Erwin JP 3rd, Guyton RA, et al. 2014 AHA/ACC guideline for the management of patients with valvular heart disease: a report of the American College of Cardiology/American Heart Association Task Force on Practice Guidelines. J Thorac Cardiovasc Surg. 2014;148(1):e1–e132.
11. Bellenger NG, Burgess MI, Ray SG, Lahiri A, Coats AJ, Cleland JG, et al. Comparison of left ventricular ejection fraction and volumes in heart failure by echocardiography, radionuclide ventriculography and cardiovascular magnetic resonance; are they interchangeable? Eur Heart J. 2000;21(16):1387–96.
12. Myerson SG, Bellenger NG, Pennell DJ. Assessment of left ventricular mass by cardiovascular magnetic resonance. Hypertension. 2002;39(3):750–5.
13. Koch JA, Poll LW, Godehardt E, Korbmacher B, Modder U. Right and left ventricular volume measurements in an animal heart model in vitro: first experiences with cardiac MRI at 1.0 T. Eur Radiol. 2000;10(3):455–8.
14. Walsh TF, Hundley WG. Assessment of ventricular function with cardiovascular magnetic resonance. Magn Reson Imaging Clin N Am. 2007;15(4):487–504. v
15. Pennell DJ. Ventricular volume and mass by CMR. J Cardiovasc Magn Reson. 2002;4(4):507–13.
16. Armstrong AC, Gidding S, Gjesdal O, Wu C, Bluemke DA, Lima JA. LV mass assessed by echocardiography and CMR, cardiovascular outcomes, and medical practice. JACC Cardiovasc Imaging. 2012;5(8):837–48.
17. John AS, Dill T, Brandt RR, Rau M, Ricken W, Bachmann G, et al. Magnetic resonance to assess the aortic valve area in aortic stenosis: how does it compare to current diagnostic standards? J Am Coll Cardiol. 2003;42(3):519–26.
18. Kupfahl C, Honold M, Meinhardt G, Vogelsberg H, Wagner A, Mahrholdt H, et al. Evaluation of aortic stenosis by cardiovascular magnetic resonance imaging: comparison with established routine clinical techniques. Heart. 2004;90(8):893–901.
19. Kramer CM, Barkhausen J, Flamm SD, Kim RJ, Nagel E. Standardized cardiovascular magnetic resonance imaging (CMR) protocols, society for cardiovascular magnetic resonance: board of trustees task force on standardized protocols. J Cardiovasc Magn Reson. 2008;10:35. https://doi.org/10.1186/1532-429X-10-35.
20. Caruthers SD, Lin SJ, Brown P, Watkins MP, Williams TA, Lehr KA, et al. Practical value of cardiac magnetic resonance imaging for clinical quantification of aortic valve stenosis: comparison with echocardiography. Circulation. 2003;108(18):2236–43.
21. Sondergaard L, Hildebrandt P, Lindvig K, Thomsen C, Stahlberg F, Kassis E, et al. Valve area and cardiac output in aortic stenosis: quantification by magnetic resonance velocity mapping. Am Heart J. 1993;126(5):1156–64.
22. Pouleur AC, le Polain de Waroux JB, Pasquet A, Vancraeynest D, Vanoverschelde JL, Gerber BL. Planimetric and continuity equation assessment of aortic valve area: head to head comparison between cardiac magnetic resonance and echocardiography. J Magn Reson Imaging. 2007;26(6):1436–43.
23. Mohiaddin RH, Kilner PJ. Valvular heart disease. In: Manning WJ, Pennell DJ, editors. Cardiovascular magnetic resonance. Philadelphia: Churchill Livingstone; 2002. p. 387–404.
24. O'Brien KR, Gabriel RS, Greiser A, Cowan BR, Young AA, Kerr AJ. Aortic valve stenotic area calculation from phase contrast cardiovascular magnetic resonance: the importance of short echo time. J Cardiovasc Magn Reson. 2009;11:49.
25. Barone-Rochette G, Pierard S, De Meester de Ravenstein C, Seldrum S, Melchior J, Maes F, et al. Prognostic significance of LGE by CMR in aortic stenosis patients undergoing valve replacement. J Am Coll Cardiol. 2014;64(2):144–54.
26. Wagner S, Auffermann W, Buser P, Lim TH, Kircher B, Pflugfelder P, Higgins CB. Diagnostic accuracy and estimation of the severity of valvular regurgitation from the signal void on cine magnetic resonance images. Am Heart J. 1989;118:760–7.
27. Dyverfeldt P, Bissell M, Barker AJ, Bolger AF, Carlhall CJ, Ebbers T, et al. 4D flow cardiovascular magnetic resonance consensus statement. J Cardiovasc Magn Reson. 2015;17(1):72.
28. Keegan J, Gatehouse PD, John AS, Mohiaddin RH, Firmin DN. Breath-hold signal-loss sequence for the qualitative assessment of flow disturbances in cardiovascular MR. J Magn Reson Imaging. 2003;18(4):496–501.
29. Nishimura T, Yamada N, Itoh A, Miyatake K. Cine MR imaging in mitral regurgitation: comparison with color Doppler flow imaging. AJR Am J Roentgenol. 1989;153:721–4.
30. Myerson SG, d'Arcy J, Mohiaddin R, Greenwood JP, Karamitsos TD, Francis JM, et al. Aortic regurgitation quantification using cardiovascular magnetic resonance: association with clinical outcome. Circulation. 2012;126(12):1452–60.
31. Sondergaard L, Lindvig K, Hildebrandt P, Thomsen C, Stahlberg F, Joen T, et al. Quantification of aortic regurgitation by magnetic resonance velocity mapping. Am Heart J. 1993;125(4):1081–90.
32. Suzuki JI, Caputo GR, Kondo C, Higgins CB. Cine MR imaging of valvular heart disease: display and imaging parameters affect the size of the signal void caused by valvular regurgitation. AJR Am J Roentgenol. 1990;155:723–7.
33. Sechtem U, Pflugfelder PW, Cassidy MM, White RD, Cheitlin MD, et al. Mitral or aortic regurgitation: quantification of regurgitant volumes with cine MR imaging. Radiology. 1988;167(2):425–30.
34. Baldy C, Douek P, Croisille P, Magnin IE, Revel D, Amiel M. Automated myocardial edge detection from breath-hold cine-MR images: evaluation of left ventricular volumes and mass. Magn Reson Imaging. 1994;12(4):589–98.
35. Chatzimavroudis GP, Oshinski JN, Franch RH, Pettigrew RI, Walker PG, Yoganathan AP. Quantification of the aortic regurgitant volume with magnetic resonance phase velocity mapping: a clinical investigation of the importance of imaging slice location. J Heart Valve Dis. 1998;7(1):94–101.
36. Djavidani B, Debl K, Lenhart M, Seitz J, Paetzel C, Schmid FX, et al. Planimetry of mitral valve stenosis by magnetic resonance imaging. J Am Coll Cardiol. 2005;45(12):2048–53.
37. Heidenreich PA, Steffens J, Fujita N, O'Sullivan M, Caputo GR, Foster E, et al. Evaluation of mitral stenosis with velocity-encoded cine-magnetic resonance imaging. Am J Cardiol. 1995;75(5):365–9.
38. Lin SJ, Brown PA, Watkins MP, Williams TA, Lehr KA, Liu W, et al. Quantification of stenotic mitral valve area with magnetic resonance imaging and comparison with Doppler ultrasound. J Am Coll Cardiol. 2004;44(1):133–7.
39. Ohyama H, Hosomi N, Takahashi T, Mizushige K, Osaka K, Kohno M, et al. Comparison of magnetic resonance imaging and transesophageal echocardiography in detection of thrombus in the left atrial appendage. Stroke. 2003;34(10):2436–9.

40. Chan KM, Wage R, Symmonds K, Rahman-Haley S, Mohiaddin RH, Firmin DN, et al. Towards comprehensive assessment of mitral regurgitation using cardiovascular magnetic resonance. J Cardiovasc Magn Reson. 2008;10:61.
41. Stork A, Franzen O, Ruschewski H, Detter C, Mullerleile K, Bansmann PM, et al. Assessment of functional anatomy of the mitral valve in patients with mitral regurgitation with cine magnetic resonance imaging: comparison with transesophageal echocardiography and surgical results. Eur Radiol. 2007;17(12):3189–98.
42. Gelfand EV, Hughes S, Hauser TH, Yeon SB, Goepfert L, Kissinger KV, et al. Severity of mitral and aortic regurgitation as assessed by cardiovascular magnetic resonance: optimizing correlation with Doppler echocardiography. J Cardiovasc Magn Reson. 2006;8(3):503–7.
43. Benjamin J. Pomerantz, Marc D. Krock, Jason R. Wollmuth, Brian P. Cupps, Nicholas T. Kouchoukos, Victor G. Davila-Roman, Michael K. Pasque. Aortic Valve Replacement for Aortic Insufficiency: Valve Type as a Determinant of Systolic Strain Recovery. J Cardiac Surg. 2005;20(6):524–9.
44. Uretsky S, Gillam L, Lang R, Chaudhry FA, Argulian E, Supariwala A, et al. Discordance between echocardiography and MRI in the assessment of mitral regurgitation severity: a prospective multicenter trial. J Am Coll Cardiol. 2015;65(11):1078–88.
45. Morello A, Gelfand EV. Cardiovascular magnetic resonance imaging for valvular heart disease. Curr Heart Fail Rep. 2009;6(3):160–6.
46. Rebergen SA, Chin JG, Ottenkamp J, van der Wall EE, de Roos A. Pulmonary regurgitation in the late postoperative follow-up of tetralogy of Fallot. Volumetric quantitation by nuclear magnetic resonance velocity mapping. Circulation. 1993;88(5 Pt 1):2257–66.
47. Mercer-Rosa L, Yang W, Kutty S, Rychik J, Fogel M, Goldmuntz E. Quantifying pulmonary regurgitation and right ventricular function in surgically repaired tetralogy of Fallot: a comparative analysis of echocardiography and magnetic resonance imaging. Circ Cardiovasc Imaging. 2012;5(5):637–43.
48. Li W, Davlouros PA, Kilner PJ, Pennell DJ, Gibson D, Henein MY, et al. Doppler-echocardiographic assessment of pulmonary regurgitation in adults with repaired tetralogy of Fallot: comparison with cardiovascular magnetic resonance imaging. Am Heart J. 2004;147(1):165–72.
49. Geva T. Indications and timing of pulmonary valve replacement after tetralogy of fallot repair. Semin Thorac Cardiovasc Surg Pediatr Card Surg Annu. 2006:11–22.
50. Secchi F, Resta EC, Cannao PM, Tresoldi S, Butera G, Carminati M, et al. Four-year cardiac magnetic resonance (CMR) follow-up of patients treated with percutaneous pulmonary valve stent implantation. Eur Radiol. 2015;25(12):3606–13.
51. Maragiannis D, Jackson MS, Flores-Arredondo JH, Autry K, Schutt RC, Alvarez PA, et al. Functional assessment of bioprosthetic aortic valves by CMR. JACC Cardiovasc Imaging. 2016 Jul;9(7):785–93.
52. Edwards MB, Taylor KM, Shellock FG. Prosthetic heart valves: evaluation of magnetic field interactions, heating, and artifacts at 1.5 T. J Magn Reson Imaging. 2000;12(2):363–9.
53. Edwards MB, Draper ER, Hand JW, Taylor KM, Young IR. Mechanical testing of human cardiac tissue: some implications for MRI safety. J Cardiovasc Magn Reson. 2005;7(5):835–40.
54. Hamilton-Craig C, Strugnell W, Gaikwad N, Ischenko M, Speranza V, Chan J, et al. Quantitation of mitral regurgitation after percutaneous MitraClip repair: comparison of Doppler echocardiography and cardiac magnetic resonance imaging. Ann Cardiothorac Surg. 2015;4(4):341–51.
55. Hartlage GR, Babaliaros VC, Thourani VH, Hayek S, Chrysohoou C, Ghasemzadeh N, et al. The role of cardiovascular magnetic resonance in stratifying paravalvular leak severity after transcatheter aortic valve replacement: an observational outcome study. J Cardiovasc Magn Reson. 2014;16:93.
56. Fogel MA, Pawlowski TW, Whitehead KK, Harris MA, Keller MS, Glatz AC, et al. Cardiac magnetic resonance and the need for routine cardiac catheterization in single ventricle patients prior to Fontan: a comparison of 3 groups: pre-Fontan CMR versus cath evaluation. J Am Coll Cardiol. 2012;60(12):1094–102.
57. Geva T. Repaired tetralogy of Fallot: the roles of cardiovascular magnetic resonance in evaluating pathophysiology and for pulmonary valve replacement decision support. J Cardiovasc Magn Reson. 2011;13:9.
58. Pomerantz BJ, Krock MD, Wollmuth JR, Cupps BP, Kouchoukos NT, et al. Aortic valve replacement for aortic insufficiency: valve type as a determinant of systolic strain recovery. J Card Surg. 2005;20(6):524–9.
59. Perez de Arenaza D, Lees B, Flather M, Nugara F, Husebye T, Jasinski M, et al. ASSERT (Aortic Stentless versus Stented valve assessed by Echocardiography Randomized Trial) investigators. Randomized comparison of stentless versus stented valves for aortic stenosis: effects on left ventricular mass. Circulation. 2005;112(17):2696–702.
60. Westenberg JJ, van der Geest RJ, Lamb HJ, Versteegh MI, Braun J, Doornbos J, et al. MRI to evaluate left atrial and ventricular reverse remodeling after restrictive mitral annuloplasty in dilated cardiomyopathy. Circulation. 2005;112(9 Suppl):I 437–442.
61. Kvitting JP, Ebbers T, Wigstrom L, Engvall J, Olin CL, Bolger AF. Flow patterns in the aortic root and the aorta studied with time-resolved, 3-dimensional, phase-contrast magnetic resonance imaging: implications for aortic valve-sparing surgery. J Thorac Cardiovasc Surg. 2004;127(6):1602–7.
62. Myerson SG, Francis JM, Neubauer S. Direct and indirect quantification of mitral regurgitation with cardiovascular magnetic resonance, and the effect of heart rate variability. MAGMA. 2010;23(4):243–9.

Magnetic Resonance Imaging Evaluation of Complex Congenital Heart Disease

19

Ashwin Prakash and Tal Geva

Introduction

Congenital heart disease (CHD) occurs in ~8 of every 1,000 live births, half of whom require surgical or other forms of treatment. Complex CHD has no precise acceptable definition. For the purposes of this chapter, we define complex CHD to include conotruncal anomalies and single ventricle heart disease. Conotruncal anomalies refer to a group of congenital heart defects involving the outflow tracts of the heart and the great vessels. Single ventricle heart disease refers to a heterogeneous group of anomalies in which one of the two ventricular sinuses is absent (anatomic single ventricle) or to hearts with complex anatomy in which biventricular physiology cannot be attained (functional single ventricle).

Cardiovascular magnetic resonance imaging (CMR) plays an important role in the evaluation of patients with complex CHD. It overcomes many of the limitations of echocardiography (e.g., restricted acoustic windows), computed tomography (e.g., exposure to ionizing radiation, limited functional information), and cardiac catheterization (e.g., exposure to ionizing radiation, morbidity, high cost) [1]. This chapter discusses the clinical aspects of conotruncal anomalies and single ventricle heart disease and their evaluation by CMR.

Tetralogy of Fallot (TOF)

TOF is the most common type of cyanotic CHD with an incidence of 356 per million live births [2]. Although TOF involves several anatomic components, the anomaly is thought to result from a single developmental anomaly – underdevelopment of the subpulmonary infundibulum (conus) [3, 4]. The anatomy is characterized by infundibular and valvar pulmonary stenosis associated with anterior, superior, and leftward deviation of the infundibular (conal) septum, hypoplasia of the pulmonary valve annulus, and thickened leaflets (Fig. 19.1a). The degree of right ventricular outflow tract (RVOT) obstruction varies from mild to complete obstruction (i.e., TOF with pulmonary atresia). The size of the mediastinal pulmonary arteries varies considerably. Although in some patients they can be dilated (e.g., TOF with absent pulmonary valve syndrome), more commonly their diameter ranges from normal to hypoplastic. In some patients, the pulmonary arteries are discontinuous or absent. In patients with pulmonary atresia or diminutive or absent branch pulmonary arteries, pulmonary blood flow may come from a patent ductus arteriosus, from collateral vessels arising from the aorta or its branches, or from both sources (Fig. 19.1b). The VSD in TOF is usually located between the malaligned conal septum superiorly and the muscular septum inferiorly (termed *conoventricular septal defect*) [6]. The VSD is usually large, but it can rarely be restrictive [7]. The aortic valve is rotated clockwise (as viewed from the apex) and is positioned above the ventricular septal crest, committing to both the LV and to the RV. In 5–6% of patients with TOF, a major coronary artery crosses the RVOT [8]. Most commonly, the left anterior descending coronary artery originates from the right coronary artery and traverses the infundibular free wall before reaching the anterior interventricular groove. Preoperative identification of a major coronary artery crossing the RVOT is important to avoid inadvertent damage to the coronary artery during surgery.

The etiology of TOF is unknown, but recent data suggests that genetic abnormalities may play an important role, especially chromosome 22q11 deletion and other genetic defects [9–17]. Additional cardiovascular and non-cardiac anomalies can be associated with TOF [18]. Although the

A. Prakash · T. Geva (✉)
Department of Cardiology, Boston Children's Hospital, Boston, MA, USA

Department of Pediatrics, Harvard Medical School, Boston, MA, USA
e-mail: ashwin.prakash@cardio.chboston.org; tal.geva@cardio.chboston.org

R. Y. Kwong et al. (eds.), *Cardiovascular Magnetic Resonance Imaging*, Contemporary Cardiology,
https://doi.org/10.1007/978-1-4939-8841-9_19

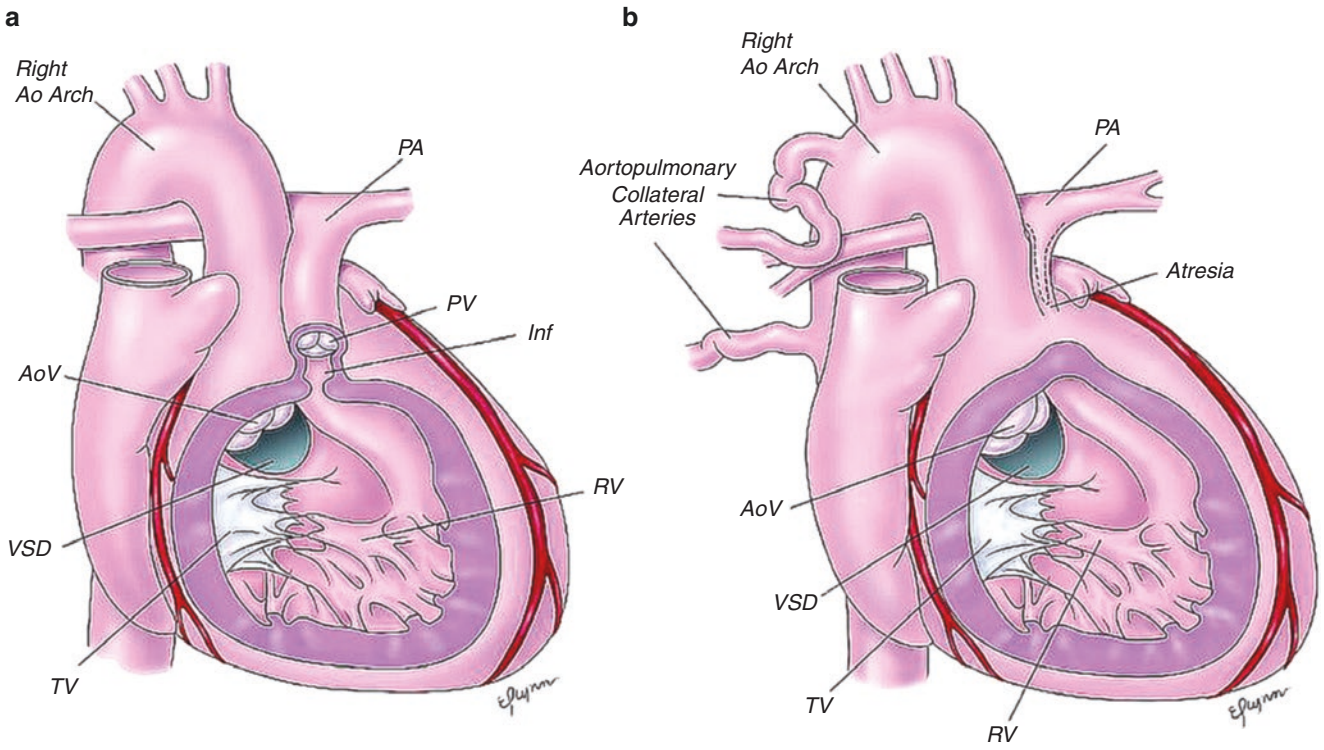

Fig. 19.1 Types of tetralogy of Fallot (TOF). (**a**) *TOF with pulmonary stenosis*: Diagram showing anterior-leftward deviation of the infundibular septum (IS) relative to the muscular ventricular septum, narrowed subpulmonary infundibulum (Inf), pulmonary valve (PV) stenosis, right ventricular (RV) hypertrophy, aortic override, and right aortic arch. The ventricular septal defect (VSD) is enclosed anteriorly and posteriorly between the limbs of the septal band (SB) and superiorly by infundibular septum and the junction of the anterior limb of the septal band and RV free wall. This anterior malalignment type of conoventricular septal defect is typical of TOF. (**b**) *TOF with pulmonary atresia*: The subpulmonary infundibulum is obliterated by marked anterior-leftward malalignment of the conal septum. The pulmonary arteries are hypoplastic and aortopulmonary collateral vessels are shown. The anterior malalignment type of conoventricular septal defect is the same as in TOF with pulmonary stenosis. (Reproduced with permission from Lai et al. [5])

clinical presentation and course of patients with TOF vary, most develop cyanosis during the first year of life. Some patients with mild or no RVOT obstruction are not cyanotic at birth ("pink TOF") and may exhibit signs and symptoms of pulmonary overcirculation similar to patients with a large VSD. As these patients grow, the subpulmonary infundibulum becomes progressively obstructive and cyanosis ensues [19].

Surgical repair of TOF is usually performed during the first year of life, often during the first 6 months [20]. A typical repair includes patch closure of the VSD and relief of the RVOT obstruction using a combination of resection of obstructive muscle bundles and an overlay patch. When the pulmonary valve annulus is moderately or severely hypoplastic, the RVOT patch extends across the pulmonary valve into the main pulmonary artery, resulting in pulmonary regurgitation. In patients with TOF and pulmonary atresia, or when a major coronary artery crosses the RVOT, a conduit—either a homograft or a prosthetic tube—is placed between the RVOT and the pulmonary arteries. The results of surgical repair of TOF have improved dramatically since the introduction of open-heart surgery. Early mortality is currently less than 2%, and the 20-year survival nears 90% [21–23]. The majority of these patients, however, have residual hemodynamic abnormalities, primarily due to RV volume load from chronic pulmonary regurgitation (Table 19.1) [24–30]. Because of these late morbidities, these patients require lifelong surveillance.

Table 19.1 Long-term morbidity after TOF repair

Problem	Potential intervention
Chronic PR, RV dilation and dysfunction	Pulmonary valve replacement
RV outflow obstruction	Catheter or surgical intervention
Branch PA stenosis	Catheter dilation or stenting
Tricuspid regurgitation	Surgical valvuloplasty
LV dysfunction and failure	Medical management
Aortic dilation	Aortic replacement/reduction (if extreme)
Arrhythmias	Medication/pacemaker/catheter ablation

LV left ventricle, *PA* pulmonary artery, *PR* pulmonary regurgitation, *RV* right ventricle

Imaging Considerations

Preoperative Imaging

In the modern era, TOF repair is usually performed during infancy, and echocardiography generally provides all the necessary diagnostic information for surgical repair, and additional imaging with CMR is not necessary in most patients [8, 31]. Additional imaging of the pulmonary arterial supply is necessary in patients with pulmonary atresia and major aortopulmonary collaterals (MAPCAs). Because these patients can have a complicated pulmonary vascular anatomy with varying and often dual source of blood flow to various lung segments, this evaluation is usually performed using selective angiography during cardiac catheterization. Several studies have shown that spin echo and 2D gradient echo cine MRI techniques provide excellent imaging of the central pulmonary arteries and MAPCAs. MRA has also been shown to be highly accurate in delineating the aortopulmonary collaterals in these patients and may be used to provide a "roadmap" for the cardiac catheterization [32].

Post-operative Surveillance

The major long-term morbidity after TOF repair is related to chronic RV volume overload caused by pulmonary regurgitation (Fig. 19.2). Although RV dilation can be tolerated for a long period of time, excessive dilation may result in irreversible myocardial damage [33]. This can be prevented by timely pulmonary valve replacement (PVR). Traditionally, this is performed surgically using a

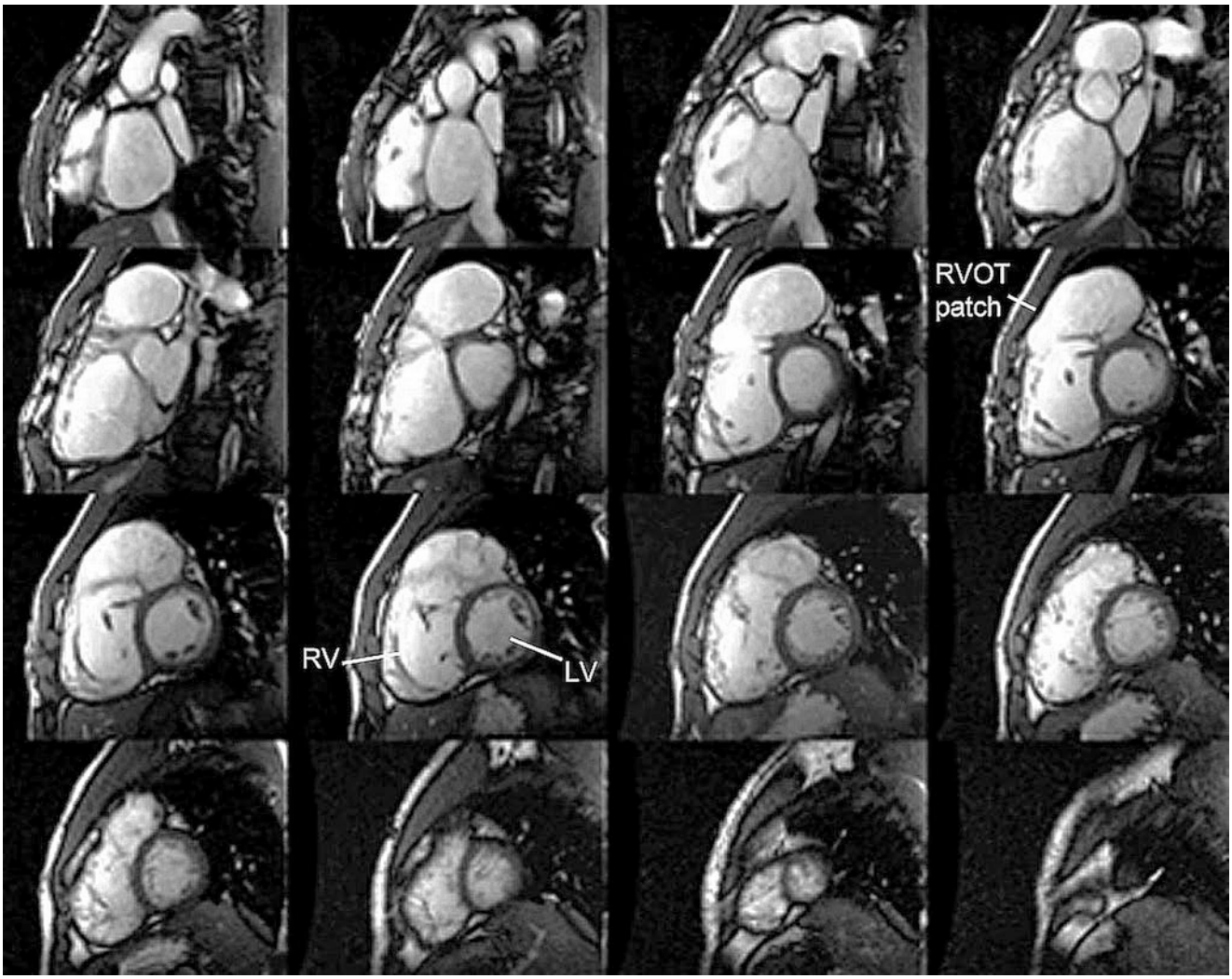

Fig. 19.2 Cine steady-state free precession (SSFP) images in the short-axis plane from a patient with tetralogy of Fallot (TOF). The right ventricle (RV) is markedly dilated due to chronic pulmonary regurgitation. The right ventricular outflow tract is aneurysmal related to prior transannular patch

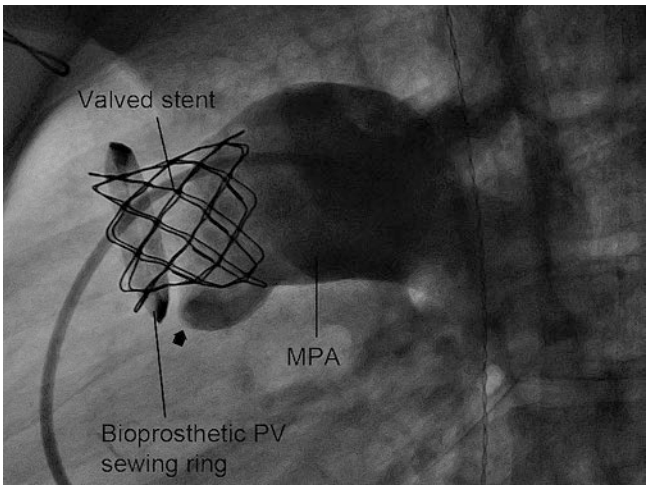

Fig. 19.3 Lateral x-ray angiography image showing an injection in the main pulmonary artery (MPA) in a TOF patient with a previous surgically placed bioprosthetic pulmonary valve. After deterioration of the bioprosthetic valve, a new transcatheter pulmonary valve (valved stent) was placed within the prior sewing ring. The arrowhead denotes the coaptation plane of the transcatheter valve with no significant residual pulmonary regurgitation

bioprosthetic valve, but more recently, transcatheter placement of a stent-covered jugular venous valve has become possible in patients who have a RV-to-PA conduit in place (Fig. 19.3) [34, 35]. Appropriate timing of PVR requires careful serial surveillance of RV size and function. Echocardiography can provide a qualitative estimate of RV size but is unreliable in quantifying the degree of RV dilation and dysfunction, especially in adults. The accuracy and reliability of CMR in serial assessment of RV and LV size and function have been previously demonstrated [36], and CMR parameters of RV size and function have been shown to be associated with adverse clinical events [37]. The use of CMR in the serial follow-up of TOF patients is now considered standard of care [38, 39]. Although the indications for pulmonary valve replacement continue to be refined, guidelines utilizing CMR parameters to help with this decision now exist [33].

The goals of the CMR examination relate to the common long-term morbidities after TOF repair, and a recommended imaging protocol along with key reporting elements is shown in Table 19.2. The standard protocol is recommended for initial evaluation, and some elements can be eliminated in follow-up scans. Accurate and reproducible reporting of ventricular volumes and ejection fraction are critical. In patients being considered for transcatheter pulmonary valve replacement, assessment of the anatomy of the RVOT and proximity to major coronary artery branches is essential for assessing the feasibility of the procedure.

Table 19.2 Imaging protocol after TOF repair

Imaging sequence	Key reporting elements
Standard	
Cine SSFP in ventricular long and short-axis planes	LV and RV size and function
Cine SSFP in long axis of RVOT	Pulmonary stenosis
Cine SSFP in long axis of LVOT[a]	Aortic root diameter
Cine SSFP in axial plane for PA branches[a]	Branch PA stenosis
Contrast MRA[a]	Branch PA stenosis/dilation, aortic dimensions aortopulmonary collaterals
Flow measurements: MPA, ascending aorta, AV valves	Pulmonary regurgitation fractions. When >mild, aortic and tricuspid regurgitation fractions
Late gadolinium enhancement: ventricular long- and short-axis planes[a]	Areas of fibrosis
Case specific	
Cine SSFP of aortic root in short axis	Aortic root diameter
Turbo or fast spin echo in axial plane	Branch PA stenosis
Flow measurements in branch PAs	Differential PA flow
Coronary artery imaging	Proximity of coronary artery to RVOT (prior to planned percutaneous valve replacement)

[a]May be eliminated during follow-up examinations; *AV* atrioventricular, *LV* left ventricle, *LVOT* left ventricular outflow tract, *MPA* main pulmonary artery, *MRA* magnetic resonance angiography, *PA* pulmonary artery, *RV* right ventricle, *RVOT* right ventricular outflow tract, *SSFP* steady-state free precession

Transposition of the Great Arteries (TGA)

TGA is defined as discordant connections between the ventricles and the great arteries; the aorta arises from the RV, and the pulmonary artery arises from the LV. There are several anatomical types of TGA, depending on the viscero-atrial situs (solitus or inversus) and the type of ventricular loop (D or L) [40].

D-Loop TGA

The most common type of TGA is in viscero-atrial situs solitus (S), ventricular D-loop (D), and dextro malposition of the aortic valve relative to the pulmonary valve (D) (Fig. 19.4). This anatomical arrangement can be summarized as {S,D,D} TGA or D-loop TGA. The incidence of D-loop TGA is estimated at 303 per million live births [2]. The principal physiological abnormality in D-loop TGA is that systemic venous blood returns to the aorta and

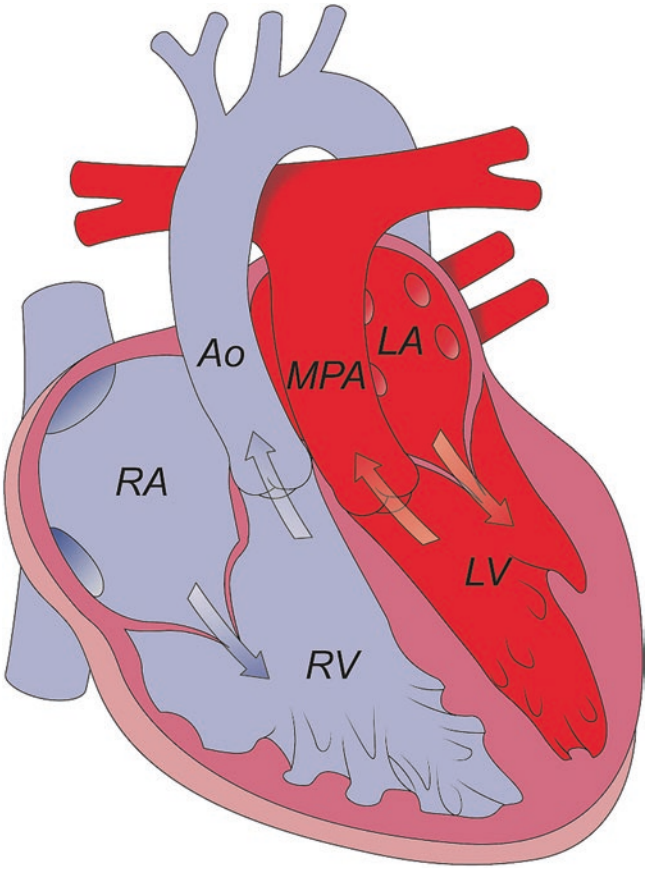

Fig. 19.4 Diagram of D-loop transposition of the great arteries with atrioventricular concordance and ventriculoarterial discordance. Ao aorta, LA left atrium, LV left ventricle, MPA main pulmonary artery, RA right atrium, RV right ventricle. (Reproduced with permission from Lai et al. [5])

oxygenated pulmonary venous blood returns to the lungs, resulting in profound hypoxemia. Consequently, survival is dependent on communication(s) that allow mixing of blood between the systemic and pulmonary circulations through the ductus arteriosus, ASD, and/or VSD. Associated anomalies include VSD in ~45% of patients, coarctation or interrupted aortic arch in ~12%, pulmonary stenosis in ~5%, and RV hypoplasia in ~4% [41].

Surgical management of D-loop TGA in the 1960s and 1970s consisted of an atrial switch procedure – the Senning and Mustard operations. In both procedures, the systemic and pulmonary venous blood returns are redirected within the atria so that the pulmonary venous blood reaches the tricuspid valve, RV, and aorta, whereas the systemic venous blood reaches the mitral valve, LV, and pulmonary arteries. The main technical difference between these procedures is the use of pericardium (Mustard) versus native atrial tissue (Senning) to create the atrial baffle [42]. Although the atrial switch operation restores the normal series arrangement of the systemic and pulmonary circulations, it leaves the RV as the systemic ventricle. Although early survival rates are excellent, these patients are at risk for several long-term problems, outlined in Table 19.3 [43–45]. Because of these morbidities, these patients require lifelong surveillance.

Table 19.3 Long-term morbidity after Mustard/Senning operation

Problem	Potential intervention
RV dysfunction/failure	Medical treatment, transplant if end stage
Tricuspid regurgitation	Surgical valvuloplasty
Systemic venous pathway stenosis	Stent placement or surgical revision
Pulmonary venous pathway stenosis	Surgical revision or stenting
Baffle leak	Catheter device or surgical closure
Atrial tachyarrhythmia	Antiarrhythmics, catheter ablation
Sinus node dysfunction	Pacemaker if severe
Subpulmonary stenosis	Rarely requires intervention

RV right ventricle

Beginning in the late 1970s and rapidly gaining popularity in the 1980s, the arterial switch operation (ASO) largely replaced the atrial switch procedures [46, 47]. The advantages of the ASO over the atrial switch procedures include reestablishment of the LV as the systemic ventricle and avoidance of extensive suture lines in the atria [48]. Recent data on late outcome of the ASO continues to show excellent overall survival and low morbidity [49]. However, there is a small but significant risk for several long-term complications outlined in the section on After Arterial Switch Operation [50–52].

Imaging Considerations

CMR is seldom requested for preoperative assessment of infants with D-loop TGA because echocardiography usually provides all necessary diagnostic information [41]. In postoperative TGA, CMR assumes an increasing role due to its ability to noninvasively evaluate most clinically relevant issues [53–61].

After Mustard or Senning Operation

Because most of these patients are now adults and have poor echocardiographic windows, evaluation by echocardiography is often incomplete. Echocardiography is particularly limited in quantifying RV size and function and in evaluating for baffle narrowing or leakage. CMR is useful in these patients because of its ability to quantify RV size and function, quantify tricuspid regurgitation, and assess for baffle leakage (Fig. 19.5) or obstruction. Because a significant proportion of these patients have a pacemaker (strong relative contraindication to CMR), gated cine CT scans can be used to obtain this information at critical decision points.

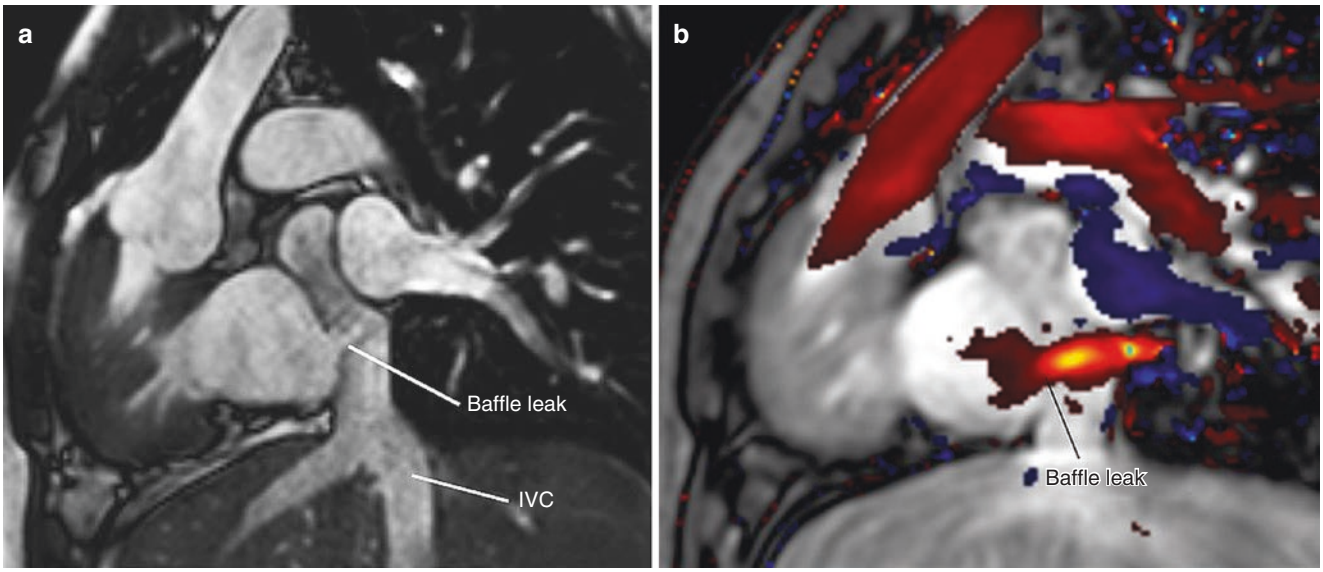

Fig. 19.5 Baffle leak after Mustard operation. (**a**) Still frame from an oblique sagittal steady-state free precession cine image showing the inferior vena cava (IVC) pathway with a baffle leak evidenced by a dephasing flow jet from the pulmonary venous pathway into the IVC pathway. (**b**) Corresponding still frame from a phase contrast image with in-plane flow encoding demonstrating flow through the baffle leak

Table 19.4 Imaging protocol after Mustard or Senning operation

Imaging sequence	Key reporting elements
Standard	
Cine SSFP in axial and coronal planes	Patency of venous baffles, baffle leaks
Cine SSFP in ventricular long- and short-axis planes	LV and RV size and function
Cine SSFP in long axis of RVOT	Aortic regurgitation
Cine SSFP on long axis of LVOT[a]	Subvalvar pulmonary stenosis
Cine SSFP in oblique planes for SVC/IVC pathways	Patency of pathways, baffle leaks
Contrast MRA[a]	Branch PA stenosis/dilation, aortic dimensions aortopulmonary collaterals
Flow measurements: MPA, ascending aorta, tricuspid and mitral valves	Qp/Qs, tricuspid regurgitation fraction
Late gadolinium enhancement: ventricular long- and short-axis planes[a]	Areas of fibrosis
Case specific	
Whole heart 3D SSFP imaging of whole heart	Venous pathways, if not seen on cine SSFP
Flow measurements in branch PAs	Differential PA flow

[a]May be eliminated during follow-up examinations; *LV* left ventricle, *LVOT* left ventricular outflow tract, *MPA* main pulmonary artery, *MRA* magnetic resonance angiography, *PA* pulmonary artery, *RV* right ventricle, *RVOT* right ventricular outflow tract, *SSFP* steady-state free precession

The goals of CMR imaging are related to the common long-term morbidities associated with an atrial switch operation (Table 19.3), and a recommended imaging protocol with key reporting elements is shown in Table 19.4. In patients with RV dysfunction, post-gadolinium delayed myocardial enhancement can be used to detect myocardial fibrosis [62]. The response of the systemic RV to pharmacological stress (dobutamine) or to exercise can be tested by CMR, but the clinical utility of this information awaits further study [59, 61].

After Arterial Switch Operation

During early childhood, imaging by echocardiography is often sufficient but as patients approach adolescence, poor echocardiographic windows limit the usefulness of this modality, and CMR can be useful in the assessment of several long-term problems (Table 19.5). A recommended imaging protocol with key reporting elements is shown in Table 19.6. The branch pulmonary arteries can be compressed by the dilated neo-aorta leading to stenosis. Assessment of the coronary artery anastomosis is important, especially prior to clearance for competitive sports. To optimize imaging of the coronary arteries, the use of a β-blocker should be considered in patients with rapid heart rate, and a blood pool contrast agent such as gadofosveset may improve the quality of 3D SSFP coronary angiography (Fig. 19.6) [63, 64]. CMR stress imaging can be useful if reversible ischemia is suspected [65].

L-Looped TGA (Physiologically "Corrected" Transposition of the Great Arteries)

The second most common type of TGA is in viscero-atrial situs solitus (S), L-ventricular loop (L), and levo-malposition of the aortic valve relative to the pulmonary valve (L). This

Table 19.5 Long-term morbidity after an arterial switch operation

Problem	Potential intervention
Neo-aortic root dilation	Root replacement, if extreme
Neo-aortic valve regurgitation	Valve repair/replacement, if severe
Branch pulmonary artery stenosis or compression	Transcatheter stenting or surgical repair
Coronary artery stenosis or occlusion	Transcatheter or surgical treatment if symptomatic or with documented reversible ischemia

Table 19.6 Imaging protocol after an arterial switch operation

Imaging sequence	Key reporting elements
Standard	
Cine SSFP in ventricular long- and short-axis planes	LV and RV size and function, regional wall motion abnormalities
Cine SSFP in long axis of RVOT	Main PA stenosis at anastomosis site
Cine SSFP on long axis of LVOT	Neo-aortic root diameter, neo-aortic regurgitation
Cine SSFP in axial plane for PA branches	Branch PA stenosis/ compression
Cine SSFP of neo-aortic root in short axis	Neo-aortic root diameter
Contrast MRA	Branch PA stenosis aortic dimensions
Coronary artery imaging using ECG and respiratory navigator-gated 3D SSFP sequence[a]	Coronary artery pattern, stenosis, torsion or occlusion
Flow measurements: main and branch PAs, ascending aorta	Neo-aortic or pulmonary regurgitation fractions, differential pulmonary artery flow
Late gadolinium enhancement: ventricular long- and short-axis planes[a]	Myocardial scar
Case specific	
Turbo or fast spin echo in axial plane	Branch PA stenosis
Flow measurements in the AV valves	Mitral or tricuspid regurgitation fraction
Stress CMR imaging	Presence of reversible ischemia

[a]May be eliminated during follow-up examinations; *AV* atrioventricular, *LV* left ventricle, *LVOT* left ventricular outflow tract, *MPA* main pulmonary artery, *MRA* magnetic resonance angiography, *PA* pulmonary artery, *RV* right ventricle, *RVOT* right ventricular outflow tract, *SSFP* steady-state free precession

anatomical arrangement can be summarized as {S,L,L} TGA or L-loop TGA [66–69]. It is also known as "physiologically corrected" TGA because the systemic venous return reaches the pulmonary circulation through the right-sided LV and the pulmonary venous return reaches the aorta through the left-sided RV. Although some patients remain asymptomatic through adulthood and are diagnosed incidentally, a large proportion suffer morbidities related to failure of the systemic RV, and associated anomalies include tricuspid valve abnormalities (e.g., Ebstein anomaly), RV hypoplasia, VSD,

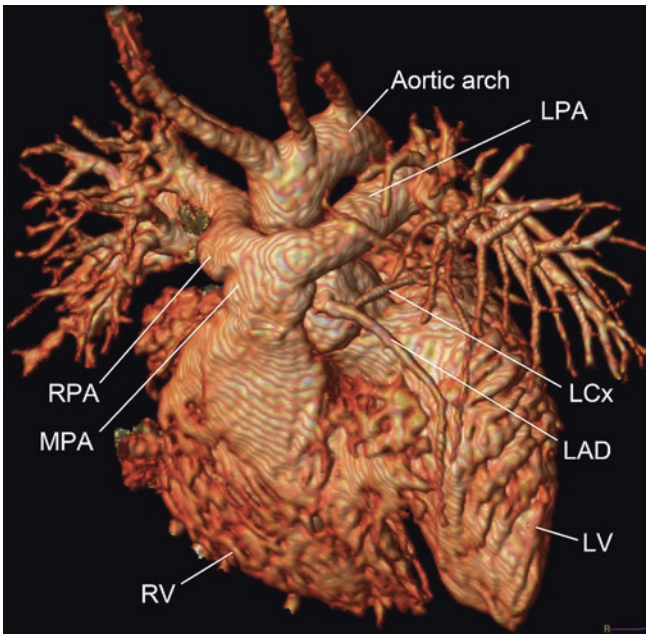

Fig. 19.6 Anterior view of volume-rendered ECG and respiratory navigator-gated magnetic resonance angiogram after intravenous injection of the blood pool contrast agent gadofosveset in a patient who underwent an arterial switch operation for D-loop transposition of the great arteries. The pulmonary artery bifurcation is positioned anterior to the aorta, as is typical after a Lecompte maneuver. Mild narrowing of the right pulmonary artery (RPA) due to a fold is noted, while the left pulmonary artery (LPA) is unobstructed. The left main coronary artery is seen arising from the anterior surface of the aortic root, dividing into the left anterior descending (LAD) and left circumflex (LCx) coronary arteries. (*LV* left ventricle, *MPA* main pulmonary artery, *RV* right ventricle)

subvalvar and valvar pulmonary stenosis, as well as conduction abnormalities, including complete heart block [66–69]. Anatomic correction using a "double-switch operation" can restore the LV as the systemic ventricle, but the indications and selection criteria for this complex procedure await refinement [70]. Because the major long-term morbidity in patients with physiologically corrected TGA is related to dysfunction of the RV and the tricuspid valve, accurate and reproducible assessment of RV size and function by CMR is essential in follow-up. The goals of the examination include quantification of RV and LV size and function and tricuspid regurgitation fraction. An imaging protocol similar to that described for tetralogy of Fallot (Table 19.2) can be used.

Double-Outlet Right Ventricle (DORV)

DORV is defined as a specific type of ventriculoarterial alignment in which both great vessels arise from the RV or from the infundibulum. The incidence of DORV is estimated at 127 per million live births [2]. It is important to recognize the wide spectrum of anatomic and physiologic

variations that share this type of ventriculoarterial alignment. In fact, the clinical course and management of patients with DORV are dictated in large part by the size and location of the ventricular septal defect in relation to the semilunar valves, the anatomy of the infundibulum and the semilunar valves, the position of the infundibular septum, the size of the LV and RV sinuses, and the anatomy of the AV valves. The LV can be normal sized, hypoplastic, or absent. The RV is usually good sized but in rare circumstances can be hypoplastic or even absent (double-outlet infundibulum). Both semilunar valves can be patent, but stenosis or atresia is relatively common. The presence of a straddling mitral or tricuspid valve is particularly important with regard to surgical planning. Examples of some of the common anatomic-physiologic variations encountered in patients with DORV include:

- DORV with VSD physiology: subaortic VSD and no pulmonary stenosis
- DORV with tetralogy of Fallot physiology: subaortic VSD and pulmonary stenosis
- DORV with transposition of the great arteries physiology: subpulmonary VSD, with or without systemic (aortic) outflow obstruction (Taussig-Bing-type DORV)
- DORV with single ventricle physiology: mitral atresia, unbalanced AV canal, or severe hypoplasia of one of the ventricular sinuses (often in association with heterotaxy syndrome)

The ultimate goal of surgical management of DORV is to align the LV with the systemic outflow and the RV with the pulmonary outflow. In DORV with a subaortic VSD, the LV can be aligned with the aorta by placing a patch on the right ventricular aspect of the defect, leaving the aortic valve on the left ventricular side. Resection of RVOT obstruction, with or without an outflow patch, may be necessary in patients with subvalvar or valvar pulmonary stenosis, analogous to TOF repair. In DORV with a subpulmonary VSD (Taussig-Bing variety), the VSD is closed with a patch that directs the blood from the LV to the pulmonary valve accompanied by an arterial switch procedure. Concomitant repair of an aortic arch anomaly (e.g., hypoplasia, interruption, or coarctation) is often required as well. More complex forms of DORV with heterotaxy syndrome, severe hypoplasia or absence of one of the ventricular sinuses, major straddling of an AV valve, or mitral atresia are palliated as a single ventricle with an eventual Fontan procedure.

Late complications in patients with repaired DORV are relatively common and vary with their underlying anatomy, physiology, and surgical repair. Subaortic stenosis can develop after the LV is baffled to the aorta [71]. The complications after repair of DORV with pulmonary outflow tract obstruction are similar to those seen after TOF repair, including chronic pulmonary regurgitation, dilation and dysfunction of the RV, and arrhythmia. Aortic arch obstruction can be found in patients after coarctation or interrupted aortic arch repair. Those who undergo an arterial switch operation may have the same problems described above for this procedure.

Pre-operative MRI

Because echocardiography is usually sufficient for diagnosis and surgical planning in most newborns or infants with DORV, CMR is seldom requested for preoperative evaluation in this age group. Exceptions include patients with complex anomalies of the aortic arch, pulmonary arteries, aortopulmonary collaterals, and systemic or pulmonary venous anomalies that are not completely delineated by echocardiography. In addition, in DORV patients with associated complex disease such as heterotaxy syndrome and unbalanced atrioventricular canal, CMR can be useful in assessing suitability for complex biventricular repair [72]. Several investigators have demonstrated the use of CMR for the assessment of the relationship between the great vessels and the VSD as well as the position of the great vessels in relation to the conal septum [73–77].

The imaging strategy is tailored to address the specific clinical question(s). In general, gadolinium-enhanced 3D MRA is particularly helpful for evaluation of great vessel anatomy (Fig. 19.7). Intracardiac anatomy is assessed by cine SSFP MRI and fast (turbo) spin echo with double inversion recovery ECG, and respiratory navigator-gated 3D SSF imaging is particularly useful [78]. Image quality can be enhanced by the use of a blood pool contrast agent such as gadofosveset [63].

Post-operative MRI

The role of CMR after DORV repair increases as patients grow, and their acoustic windows become progressively more limited. The examination strategy is tailored based on the underlying anatomy, the operation(s) performed, and the specific clinical and other diagnostic findings. Although no single generic imaging protocol covers all possible scenarios after DORV repair, certain patterns are recognized. Patients with a "TOF-like" DORV repair have similar long-term sequelae as those after TOF repair, and the CMR examination protocol is comparable (Table 19.2). Similarly, in those with Taussig-Bing-type DORV, the postoperative issues are similar to those encountered after the arterial switch operation for TGA (Table 19.6).

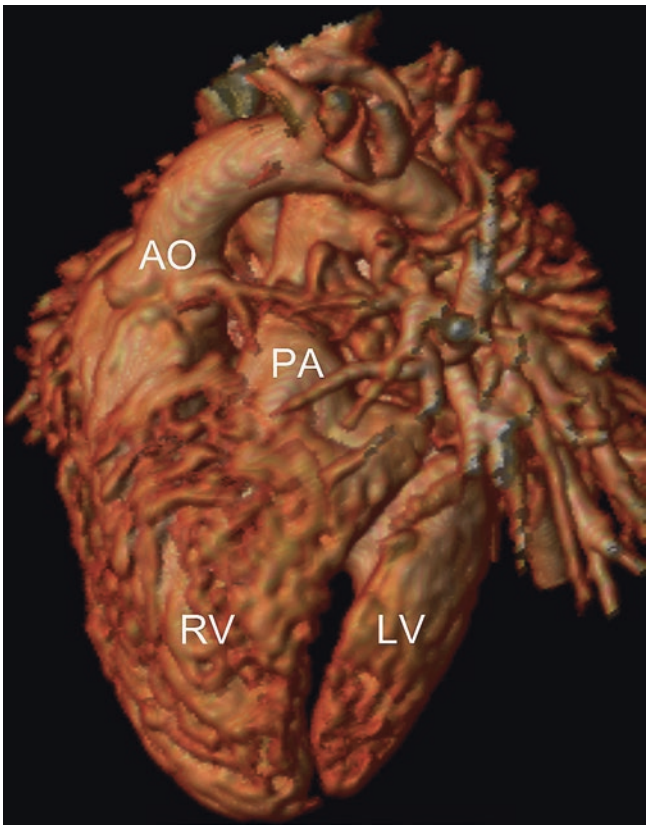

Fig. 19.7 Lateral view of volume-rendered 3D gadolinium-MRA in a patient with double-outlet right ventricle. Both the aorta (AO) and main pulmonary artery (PA) arise from the right ventricle (RV). The left ventricle (LV) is mildly hypoplastic

Truncus Arteriosus

Truncus arteriosus is an uncommon conotruncal anomaly with a reported incidence of 94 per million live births [2]. It is defined by the presence of a single artery arising from the heart with a single semilunar valve, giving rise to the coronary arteries, aorta, and at least one branch pulmonary artery. Van Praagh and Van Praagh [79] modified the original classification of Collett and Edwards (Fig. 19.8) [80]:

- Type I: The branch pulmonary arteries arise from a short main pulmonary artery.
- Type II: The branch pulmonary arteries arise directly from the arterial trunk through separate orifices.
- Type III: Only one branch pulmonary artery arises from the ascending segment of the trunk. Collateral vessels usually supply the contralateral lung.
- Type IV: Truncus arteriosus with aortic arch hypoplasia, coarctation, or interruption (usually type B distal to the left common carotid artery). In this anatomic variation, there is usually a well-formed main pulmonary artery and a small ascending aorta.

In the majority of cases, there is a subtruncal VSD over which the truncal valve sits, similar to TOF. Rarely, the ventricular septum is intact. The conal septum is usually absent, and the truncal valve is in direct fibrous continuity with the mitral valve. In rare circumstances, the truncal valve may be supported by a complete infundibulum and relate exclusively

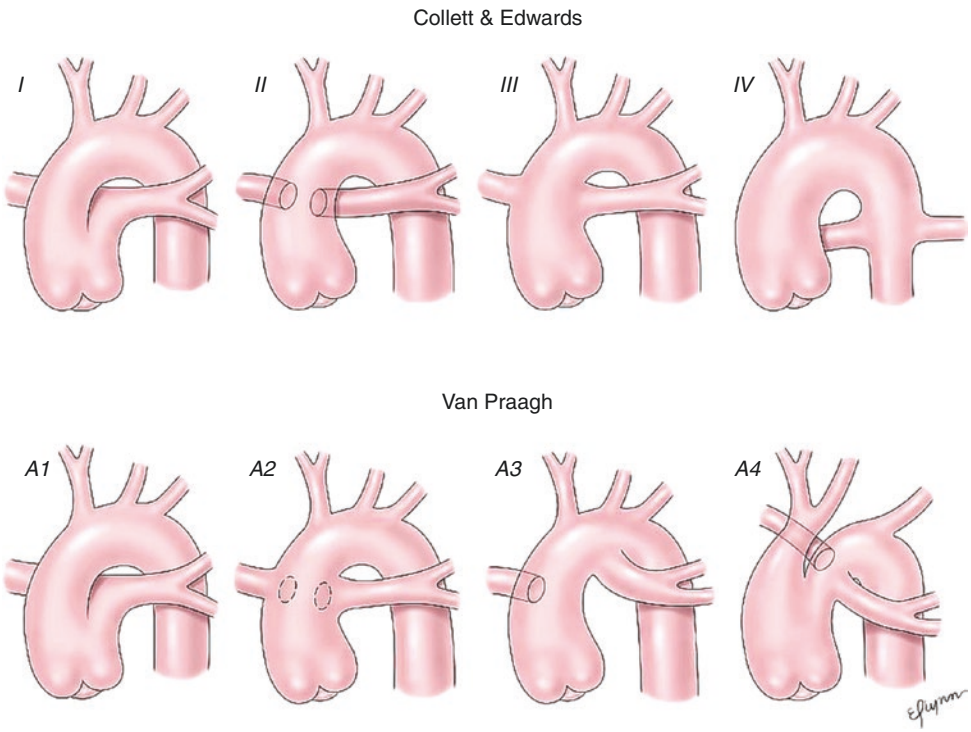

Fig. 19.8 Types of truncus arteriosus. *Top panel*: Collett and Edwards. *Bottom panel*: Van Praagh. Note that Van Praagh type A4 is not represented in Collett and Edwards (Reproduced with permission from Lai et al. [5])

to the RV. The truncal valve is most commonly tricommissural, followed by bicommissural morphology, and least common is a quadricommissural valve. The valve can be thickened and redundant with stenosis, regurgitation, or both.

Associated cardiovascular and non-cardiac anomalies are frequent. Examples of associated cardiovascular anomalies include multiple VSDs, partial and complete atrioventricular canal defects, mitral atresia, mitral stenosis, aortic atresia, hypoplastic left ventricle, double-inlet left ventricle, tricuspid atresia, straddling tricuspid valve, Ebstein malformation, heterotaxy syndrome, aberrant origin of the right or left subclavian artery, coarctation of the aorta, secundum atrial septal defect, partially and completely anomalous pulmonary venous connections, left superior vena cava to coronary sinus, retro-aortic innominate vein, and left pulmonary artery sling [81]. Various non-cardiac anomalies have been described in patients with truncus arteriosus. DiGeorge syndrome, velocardiofacial syndrome, and chromosome 22q11 deletion are frequently associated. A large series found the 22q11 deletion in 34.5% of patients with truncus arteriosus [82].

Most patients with truncus arteriosus are diagnosed early in life, and echocardiography is sufficient for diagnosis and surgical planning in almost all. Surgical repair usually follows the diagnosis. Typically, the VSD is closed with a patch so that the truncal valve is aligned with the LV (becoming the neo-aortic valve), and the pulmonary arteries are detached from the arterial trunk and connected to the RV with a valved homograft. Surgical repair of the truncal valve for stenosis or regurgitation is uncommon during the initial repair. Surgical mortality is low and has improved with the overall advances in surgical management of infants. The use of a nongrowing homograft in infancy makes additional operations inevitable as patients grow. Important residual lesions after truncus arteriosus repair include progressive stenosis and regurgitation of the RV-to-pulmonary artery homograft, branch pulmonary artery stenosis, and regurgitation or stenosis of the neo-aortic (truncal) valve. Aortic arch obstruction can complicate the course of patients with coarctation or interrupted aortic arch repair.

Pre-operative MRI

CMR is rarely requested for preoperative evaluation in an infant with truncus arteriosus because echocardiography is

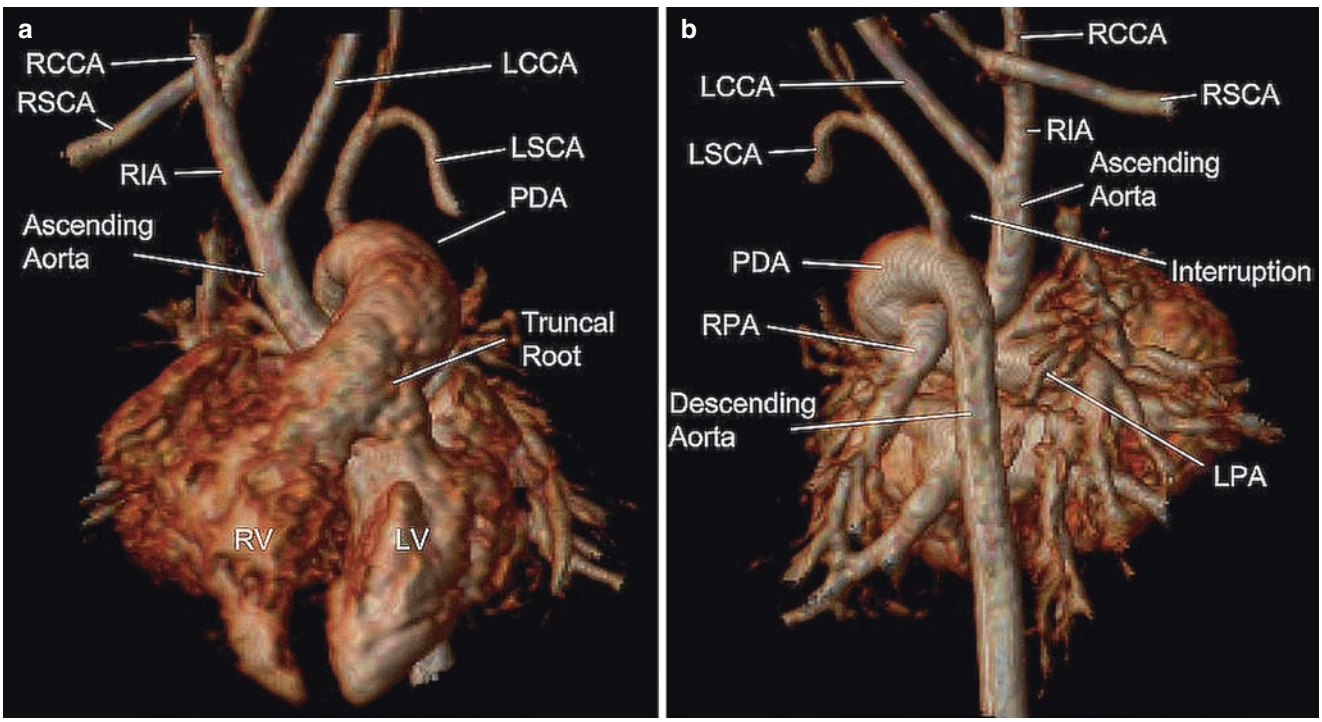

Fig. 19.9 Volume-rendered 3D magnetic resonance angiogram from a newborn infant with Van Praagh type A4 truncus arteriosus (with interrupted aortic arch). (**a**) *Anterior view*: A single large arterial root (truncal root) overrides the ventricular septum, arising from both left (LV) and right (RV) ventricles and gives rise to a small ascending aorta. The right innominate artery (RIA) and left common carotid artery (LCCA) arise from the ascending aorta which does not continue into the transverse aortic arch, which is interrupted. (**b**) *Posterior view*: The aortic arch is interrupted between the origins of the LCCA and the left subclavian artery (LSCA) (Type B interrupted arch). The left (LPA) and right (RPA) pulmonary arteries arise from the posterior aspect of the truncal root. A large patent ductus arteriosus (PDA) arises from the superior aspect of the pulmonary arteries, supplying the descending aorta. RCCA, right common carotid artery; RSCA, right subclavian artery

almost always adequate [83]. Exceptions include complex aortic arch (Fig. 19.9) or pulmonary venous anomalies that require further delineation and the occasional older patient with an unrepaired truncus arteriosus.

Post-operative MRI

The role of CMR in patients with repaired truncus arteriosus increases with their age. The anatomic and functional issues in these patients are similar to those encountered in patients with repaired TOF, especially in those with TOF and pulmonary atresia. Neo-aortic valve dysfunction and aortic arch obstruction are additional issues that may require investigation. Therefore, imaging can be performed with modifications of the protocol described above for TOF (Table 19.2) and individualized for the patient's anatomic and hemodynamic issues.

Interrupted Aortic Arch (IAA)

Interruption of the aortic arch (IAA) is an uncommon congenital cardiovascular malformation characterized by anatomic discontinuity between segments of the aortic arch. The prevalence of IAA is 19 per million live births or 1.3% of infants with congenital heart disease in the New England Regional Infant Cardiac Program [84]. This condition should be distinguished from aortic arch atresia where there is anatomic continuity between the arch segments through a fibrous strand, but the aortic lumen is completely obstructed. Because of their identical hemodynamic consequences, both conditions will be discussed together.

The classification proposed by Celoria and Patton in 1959 is widely used to date (Fig. 19.10) [85]. Type A denotes interruption distal to the left subclavian artery, type B between the left common carotid and the left subclavian arteries, and type C between the common carotid arteries. Type B is the most common anatomic variation accounting for approximately 62% of IAA cases, type A for 37%, and type C for 1%. Aberrant origin of the right subclavian artery from the proximal descending aorta is found in roughly 50% of patients with type B IAA but only in a minority of those with type A interruption. Other rare variations include interruption of a right aortic arch [86] and interruption of a cervical arch [87].

Survival of patients with IAA depends on a patent ductus arteriosus. Intravenous administration of prostaglandin E begins immediately once the diagnosis is suspected and is followed by surgical repair. In most institutions, the preferred surgical approach is direct anastomosis of the interrupted (or atretic) aortic segments. When the distance between the interrupted aortic arch segments is large, homograft augmentation may be added to the arch reconstruction. The use of a tubular conduit to bridge between the arch segments is usually reserved for unusually long-segment interruptions or for reoperations. In patients with an associated VSD, the defect is closed at the time of the arch repair. In type B IAA with posterior malalignment of the conal septum and markedly hypoplastic left ventricular outflow tract, the VSD can be baffled to the pulmonary valve, the main pulmonary artery is transected and anastomosed to the ascending aorta, and a conduit (usually a valved homograft) is placed between the RV and the pulmonary arteries.

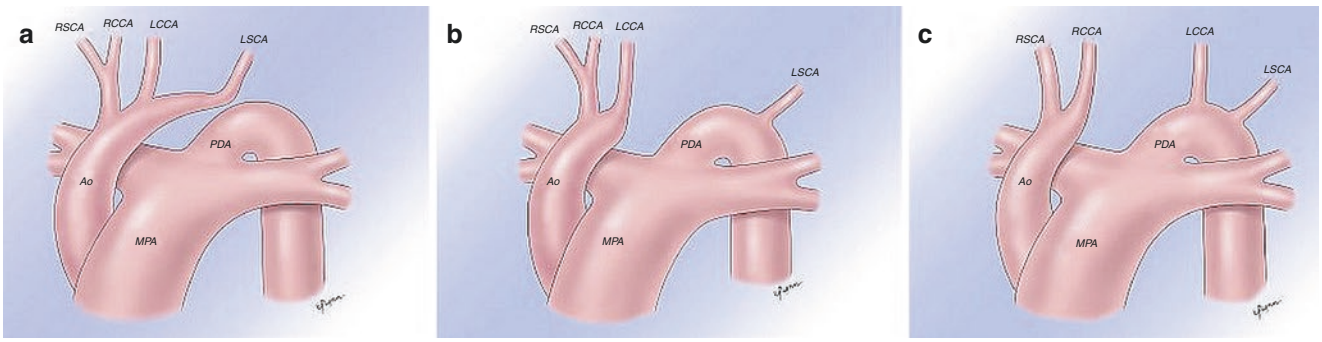

Fig. 19.10 Types of interrupted aortic arch. (**a**) *Type A*: The interruption is distal to the left subclavian artery (LSCA), and the descending aorta (DAo) is supplied via the patent ductus arteriosus (PDA). The ascending aorta (AAo) gives rise to all the brachiocephalic arteries. (**b**) *Type B*: The interruption is situated between the left common carotid artery (LCCA) and LSCA. The DAo and LSCA are supplied via the ductus arteriosus (arrow). The right subclavian artery (RSCA) and both common carotid arteries are supplied from the AAo. *Type B with aberrant right subclavian artery*: As usual with type B, the interruption is between the LCCA and the LSCA. However, the RSCA arises from the proximal DAo and is supplied by the PDA. It courses posterior to the trachea and esophagus. The AAo gives rise to only both common carotid arteries. (**c**) *Type C*: The interruption is between the right (RCCA) and left (LCCA) common carotid arteries. The DAo, LCCA, and the LSCA are supplied by the PDA. The AAo supplies only the RSCA and the RCCA

MRI Evaluation

Echocardiography is usually adequate for preoperative diagnosis of interrupted aortic arch and associated anomalies [88]. CMR is used in selected patients in whom the anatomy is not clearly defined by echocardiography [89, 90]. CMR assumes a larger role in patients with repaired IAA as they grow, and their acoustic windows become restricted.

Pre-operative MRI

The goal of the CMR examination is to delineate the anatomy of the aortic arch and the branching pattern of the brachiocephalic arteries and associated anomalies (Fig. 19.9). It is important to fully evaluate the vascular anatomy to exclude any associated anomalies (e.g., systemic and pulmonary venous anomalies). Gadolinium-enhanced 3D MR angiography is the most robust and time-efficient technique to achieve these goals [90]. Black-blood imaging and ECG and respiratory navigator-gated 3D SSFP can also be useful. Evaluation of intracardiac anatomy is usually not necessary since the information should be available from echocardiography.

Post-operative MRI

The goal of the CMR examination after IAA surgery is to evaluate residual or recurrent anatomic and hemodynamic problems. Often the focus is on imaging of the aortic arch and the repair site for evaluation of obstruction or aneurysm formation. However, other abnormalities such as left ventricular outflow tract obstruction, aortic valve stenosis or regurgitation, residual VSD, left ventricular size and function, and other anomalies should be examined as well. Analysis of the flow pattern in the abdominal descending aorta can be useful in assessing the hemodynamic severity of residual arch obstruction [91]. These objectives can be achieved with an imaging protocol similar to the one used for coarctation of aorta.

Single Ventricle

The normal human heart is composed of three chambers at the ventricular level (between the atrioventricular [AV] valves and the semilunar valves): the LV sinus, the RV sinus, and the infundibulum. From an anatomic standpoint, single ventricle is defined as a circumstance in which one of the two ventricular sinuses is absent. The infundibulum is always present and has been described by various terms such as infundibular outlet chamber, rudimentary or hypoplastic right ventricle, and rudimentary chamber. As defined above, single ventricle accounts for approximately 1% of CHD with a median incidence of 85 per million live births [2]. There are other congenital cardiac anomalies in which the anatomy precludes establishment of biventricular physiology. These conditions, which are often treated with one of the modification of the Fontan operation, are often grouped under the term "functional single ventricle" or "functional univentricular hearts." Examples include tricuspid atresia, mitral atresia, unbalanced common AV canal defect, pulmonary atresia with intact ventricular septum and diminutive RV and tricuspid valve, and others.

From an anatomical perspective, there are two types of single ventricle:

1. Single LV: Several anatomic types of single LV are recognized. Common to all is the absence of the right ventricular sinus and the presence of a left ventricle and an infundibulum. The following anatomic features characterize hearts with a single LV:
   (a) The different anatomic types of single LV vary according to the type of ventricular loop present and the types of AV and ventriculoarterial alignments.
   (b) There is communication between the LV and the infundibulum, termed the bulboventricular foramen.
   (c) When two AV valves enter the LV (double-inlet LV), their different papillary muscle architectures reflect their identity. The tricuspid valve is typically closer to the septum (septophilic); it may have chordal attachments on the septum or to the VSD margin, or both, and sometimes into the infundibulum. By contrast, the mitral valve attaches to the free wall papillary muscles (septophobic). If the two AV valves share the LV cavity, usually one, and rarely both, is abnormal. If only the mitral valve enters the LV (i.e., tricuspid atresia), it is typically structurally normal. Other types of AV alignments in single LV include common inlet, when a common AV valve is present, and mitral atresia with a large LV.
   (d) The types of ventriculoarterial connections include (1) normally related great arteries (Holmes heart), in which the aorta arises from the LV and the pulmonary artery from the infundibulum; (2) transposition of the great arteries, in which the pulmonary artery arises from the LV and the aorta from the infundibulum; and (3) double-outlet infundibulum, in which

both the aorta and pulmonary artery arise from the infundibulum. Pulmonary stenosis or atresia, aortic stenosis or atresia, and aortic arch anomalies (most commonly coarctation) may be associated with single LV.

2. Single RV: In hearts with a single RV, the ventricular mass consists of the right ventricular sinus and the infundibulum, both forming a common chamber. The septal band is present, indicating the location of a ventricular septum, but there is no macroscopically recognizable LV sinus on the other side of the septum. Several anatomic types of single RV are recognized:
   (a) Double-inlet RV: Both AV valves open into the RV. The tricuspid valve attaches in the inlet (sinus) portion of the RV, and the mitral valve attaches in the outflow or infundibulum. Both valves exhibit attachments to the septal band.
   (b) Common-inlet single RV: A single AV valve connects both atria with the RV. The morphology is often that of a tricuspid valve, but the presence of an ostium primum defect and the alignment of both atria with the single RV indicate that this is a common AV valve mimicking a tricuspid valve. This type of single RV usually occurs in association with visceral heterotaxy and asplenia. Associated malformations include anomalies of the systemic and pulmonary venous connections, absence or marked deficiency of the atrial septum, absence of the coronary sinus, and pulmonary outflow tract stenosis or atresia. In both types of single RV, both great arteries originate from the infundibulum, and the resulting ventriculoarterial alignment is that of double-outlet RV.

Single ventricle physiology is characterized by complete mixing of the systemic and pulmonary venous return flows. The proportion of the ventricular output distributed to the pulmonary or systemic vascular bed is determined by the relative resistance to flow in the two circuits. The clinical presentation and course in patients with single ventricle depends on the hemodynamic profile:

1. Diminished pulmonary blood flow: patients are cyanotic with arterial oxygen saturation typically <75%; no signs and symptoms of congestive heart failure.
2. Increased pulmonary blood flow: patients may be asymptomatic in the newborn and early neonatal periods; arterial oxygen saturation typically >85%, and cyanosis may not be evident; signs and symptoms of congestive heart failure develop during the first few weeks of life as pulmonary vascular resistance decreases and pulmonary blood flow increases.
3. Balanced circulation: patients exhibit mild or moderate cyanosis with arterial oxygen saturation of 75–85%; no signs and symptoms of congestive heart failure.
4. Closing duct: patients with a duct-dependent pulmonary circulation and a closing duct present with profound cyanosis and acidemia. Patients with a duct-dependent systemic circulation present with a clinical picture of shock, hypoperfusion, poor peripheral pulses, oliguria or anuria, and acidemia.
5. Atypical clinical picture due to the progressive nature of certain anatomic and hemodynamic factors (e.g., progressive narrowing of a bulboventricular foramen leading to severe subaortic stenosis).

The goals of current surgical therapy in patients with single ventricle are to separate the systemic and pulmonary circulations and to eliminate volume overload on the ventricle. These goals are often achieved with staged palliative procedures, leading to one of the modifications of the Fontan operation (Fig. 19.11). The principal aim of the procedure is to divert the systemic venous return from the inferior and superior vena cava to the pulmonary arteries, which separates the poorly oxygenated systemic venous return from the oxygenated pulmonary venous return. Since it was first described in 1971 [92], the Fontan operation has undergone multiple modifications, including direct anastomosis of the right atrial appendage to the MPA (called atrio-pulmonary anastomosis) [93], RA-to-RV conduit, lateral tunnel between the IVC and the undersurface of the ipsilateral branch pulmonary artery [94], fenestration of the lateral tunnel baffle [95], and an extracardiac conduit between the IVC and the ipsilateral branch pulmonary artery [96]. With refinement of the criteria for patient selection, management strategies, and surgical techniques, the short- and medium-term results of the Fontan operation have gradually improved [97]. Nevertheless, this growing patient population continues to be at risk for mortality and morbidities listed in Table 19.7 [97–106]. Prompt detection of these complications is, therefore, an important element of managing these patients.

MRI Evaluation

MRI is particularly well suited for the detailed investigation of the divergent and often complex anatomy of single ventricle heart disease. While echocardiography is typically adequate for initial diagnosis in the infant with a single ventricle, MRI is assuming an increasingly

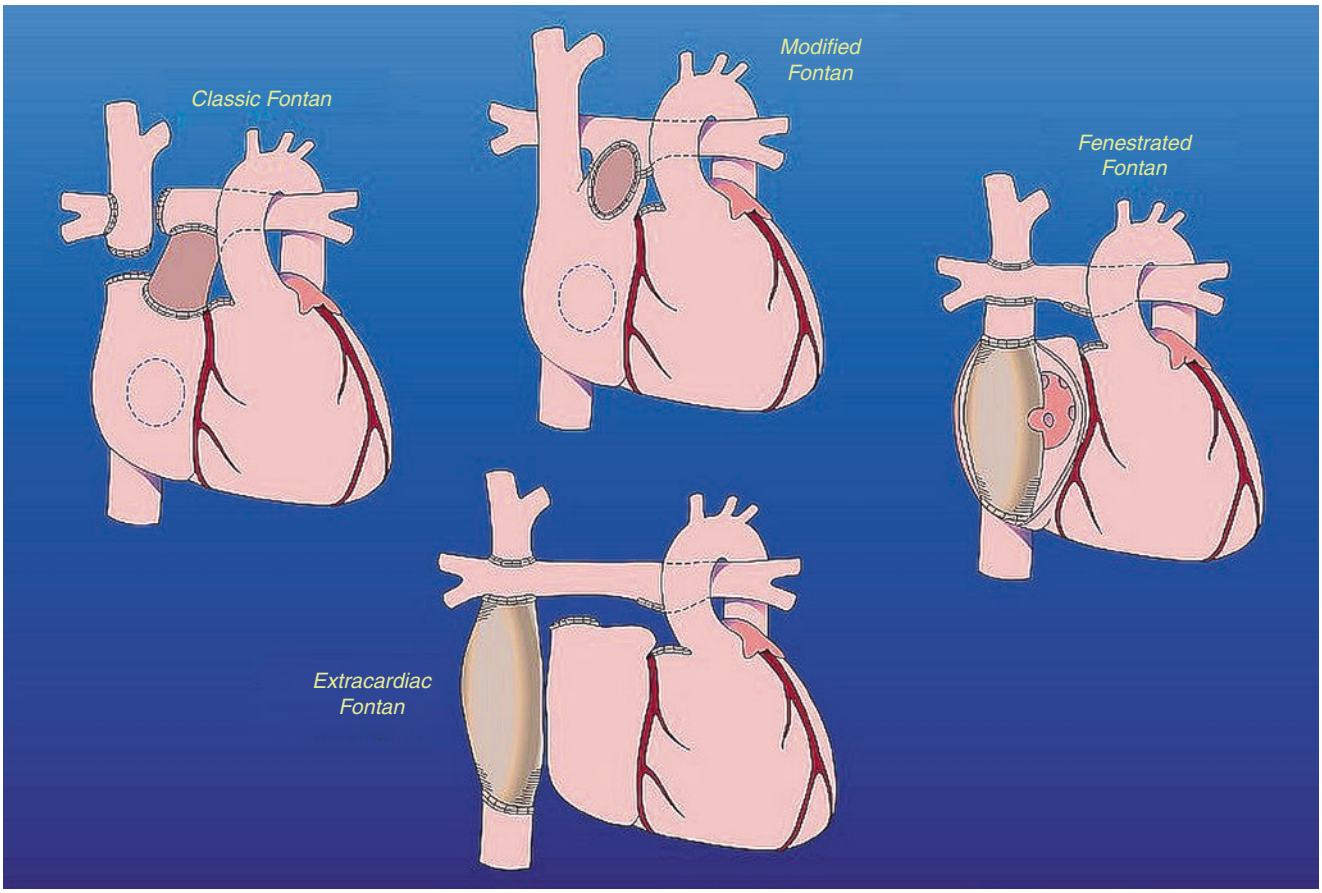

Fig. 19.11 Types of Fontan operation. All types result in total diversion of systemic venous return directly into the pulmonary arterial circulation (total cavopulmonary anastomosis). *Classic Fontan*: The right superior vena cava is connected to the distal right pulmonary artery, which is disconnected from the left pulmonary artery. The right atrial appendage is connected to the left pulmonary artery via an aortic homograft. The main pulmonary artery is disconnected from the heart, and the atrial septal defect is closed. *Modified Fontan*: In a modification of the classic technique, the right pulmonary artery and the superior vena cava are left intact. Instead, the right atrial appendage is anastomosed directly to the underside of the pulmonary artery bifurcation. The atrial septal defect is closed. *Fenestrated (lateral tunnel) Fontan*: In this more current modification, a tunnel is created along the lateral aspect of the right atrium to connect the inferior vena cava to the underside of the right pulmonary artery. The right superior vena cava is also anastomosed to the right pulmonary artery. A small fenestration is punched into the lateral tunnel to allow partial decompression of the Fontan pathway into the pulmonary venous atrium. The atrial septal defect is left open. *Extracardiac Fontan*: The pathway from the inferior vena cava to the underside of the right pulmonary artery is created outside the right atrium using a Gore-Tex tube graft. The right superior vena cava is anastomosed to the right pulmonary artery, and the atrial septal defect is left open

important role in the evaluation of patients before and after later stages of palliation. In addition to anatomic assessment, several novel MRI techniques for studying the complex physiology of these patients have recently been developed [107–111].

MRI Evaluation During Staged Palliation of Single Ventricle

Staged palliation of single ventricle disease often includes the superior cavopulmonary anastomosis (bidirectional Glenn operation), typically performed at 4–6 months of age, and the Fontan operation, typically performed at 2–4 years of age. Traditionally, these procedures are preceded by diagnostic cardiac catheterization for anatomic and physiologic information. MRI may offer an alternative for cardiac catheterization in selected cases [112, 113]. The goals of CMR prior to the pre-bidirectional Glenn or Fontan operations include (1) quantitative assessment of ventricular mass, volumes, and function; (2) imaging the anatomy of the pulmonary veins, pulmonary arteries, and aortic arch; (3) imaging the anatomy of any prior surgical intervention (e.g., aortic arch reconstruction); (4) evaluating for the presence of

Table 19.7 Long-term morbidity in single ventricle patients

Problem	Potential intervention
Ventricular dysfunction	Medical management/transplantation
Atrioventricular valve regurgitation	Surgical repair if ≥moderate
Aortic regurgitation	Surgical repair if ≥moderate
Thrombosis in Fontan pathway or branch PAs	Anticoagulation, surgical/transcatheter treatment if severe
Branch PA stenosis	Transcatheter and/or surgical treatment
Pulmonary vein stenosis	Transcatheter and/or surgical treatment
Aorta-pulmonary or systemic-pulmonary venous collaterals	Transcatheter coiling of collaterals
Restriction of atrial septal defect	Transcatheter or surgical enlargement
Hepatic congestion/fibrosis	Medical management/transplantation
Arrhythmias	Medical management/pacemaker/defibrillator
Congestive heart failure, protein-losing enteropathy, plastic bronchitis ("failed Fontan circulation")	Medical management/Fontan revision/cardiac transplantation

Table 19.8 Imaging protocol for functionally single ventricle

Imaging sequence	Key reporting elements
Standard	
Cine SSFP in axial plane through the thorax	Systemic and pulmonary veins, branch PAs, ASD fenestration/baffle leak/thrombus in Fontan baffle
Cine SSFP in ventricular long- and short-axis planes	Ventricular size and function, AV valve regurgitation
Cine SSFP in long axis of outflow tract(s)	Aortic/pulmonary regurgitation/stenosis
Cine SSFP in long axis of the aortic arch	Arch obstruction
Contrast MRA	Branch PAs, pulmonary and systemic veins, patency of shunts, aortopulmonary or veno-venous collateral vessels
Flow measurements: ascending aorta, branch pulmonary arteries, SVC, IVC, pulmonary veins, descending aorta, AV valves	Aortic regurgitation, differential lung flow, AV valve regurgitation, aortopulmonary collateral flow
Late gadolinium enhancement: ventricular long- and short-axis planes[a]	Ventricular scar
Case specific	
Turbo or fast spin echo in axial plane	Branch PA stenosis, pulmonary vein anatomy, in patients with ferromagnetic artifact
Cine SSFP in coronal plane	To further clarify anatomy
ECG and respiratory navigator-gated 3D SSFP sequence.	Intracardiac spatial relationships
Gadolinium enhancement imaging with long-inversion time	To confirm the presence of thrombus suspected on cine imaging

[a]May be eliminated during follow-up examinations; *ASD* atrial septal defect, *AV* atrioventricular, *IVC* inferior vena cava, *MRA* magnetic resonance angiography, *PA* pulmonary artery, *RVOT* right ventricular outflow tract, *SSFP* steady-state free precession, *SVC* superior vena cava

aortopulmonary or veno-venous collateral vessels; (5) quantification of AV or semilunar valve regurgitation; and (6) quantification of aortopulmonary collateral burden. These objectives can be achieved by the imaging protocol shown in Table 19.8.

Post-Fontan MRI

The clinical utility of CMR in patients with the Fontan circulation increases as these patients grow, and their acoustic windows become more restricted, limiting evaluation by echocardiography. The goals of the MRI examination in patients with the Fontan circulation include assessment for the long-term problems listed in Table 19.7, and this can be accomplished by using the imaging protocol shown in Table 19.8 and Fig. 19.12. Fast (turbo) spin echo with double inversion recovery sequence may be used to minimize artifacts from metallic implants, which are common in this patient population [114]. In recent years, several investigators have reported novel applications to study the physiology of Fontan patients including assessment of flow dynamics, aortopulmonary collateral flow, hepatic stiffness, and late gadolinium enhancement [106, 115–118].

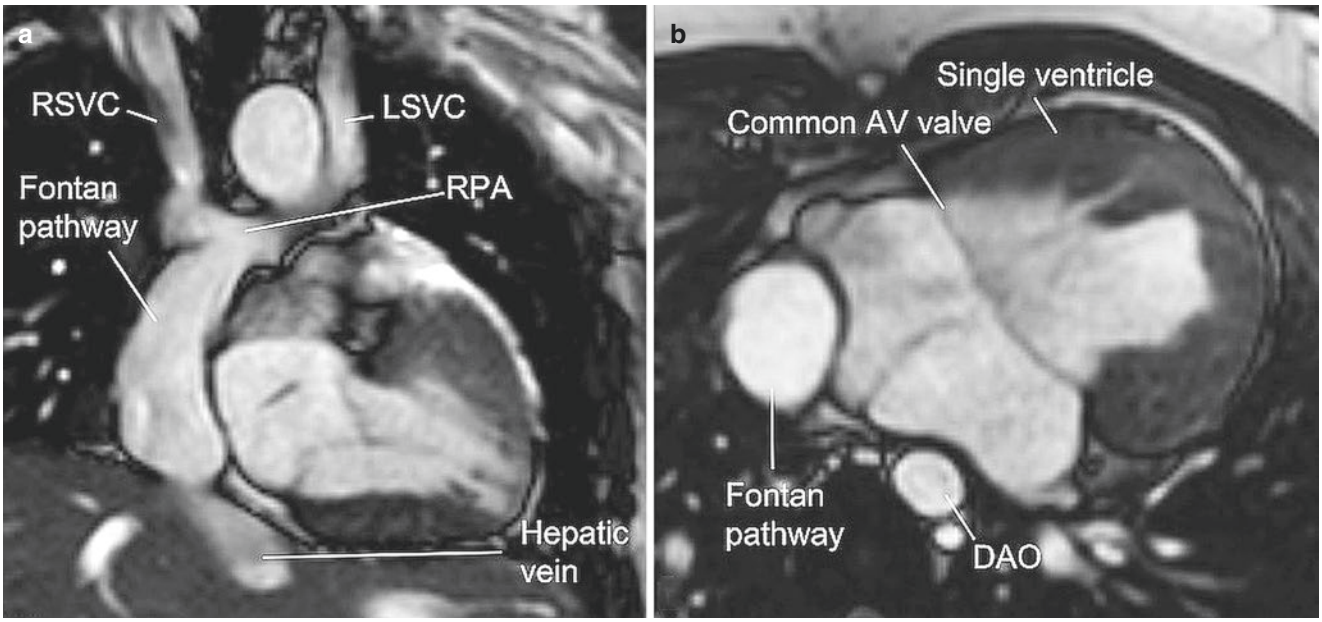

Fig. 19.12 Still frames from cine steady-state free precession imaging in a patient who has undergone a lateral tunnel Fontan operation. (**a**) *Coronal view*: The lateral tunnel is seen along the rightward aspect of the atrium connecting the inferior vena cava (not shown) to the right pulmonary artery (RPA) superiorly. The right superior vena cava (RSVC) is also connected to the RPA. The patient also has a left superior vena cava (LSVC) not communicating with the RSVC. The LSVC has been connected to the left pulmonary artery (anastomosis not shown). (**b**) *Axial view* shows the lateral tunnel Fontan pathway along the rightward aspect of the right-sided atrium. The atria are aligned via a common atrioventricular (AV) valve to a single ventricle of right ventricular morphology. DAO, descending aorta

References

1. Prakash A, Powell AJ, Geva T. Multimodality noninvasive imaging for assessment of congenital heart disease. Circ Cardiovasc Imaging. 2010;3:112–25.
2. Hoffman JI, Kaplan S. The incidence of congenital heart disease. J Am Coll Cardiol. 2002;39:1890–900.
3. Van Praagh R, Van Praagh S, Nebesar RA, Muster AJ, Sinha SN, Paul MH. Tetralogy of Fallot: underdevelopment of the pulmonary infundibulum and its sequelae. Am J Cardiol. 1970;26:25–33.
4. Van Praagh R. Etienne-Louis. Arthur Fallot and his tetralogy: a new translation of Fallot's summary and a modern reassessment of this anomaly. Eur J Cardiothorac Surg. 1989;3:381–6.
5. Lai WW, Mettens LL, Cohen MS, Geva T, editors. Echocardiography in pediatric and congenital heart disease: from fetus to adult. Chichester: Blackwell Publishing Ltd; 2009.
6. Van Praagh R, Geva T, Kreutzer J. Ventricular septal defects: how shall we describe, name and classify them? J Am Coll Cardiol. 1989;14:1298–9.
7. Flanagan MF, Foran RB, Van Praagh R, Jonas R, Sanders SP. Tetralogy of Fallot with obstruction of the ventricular septal defect: spectrum of echocardiographic findings. J Am Coll Cardiol. 1988;11:386–95.
8. Need LR, Powell AJ, del Nido P, Geva T. Coronary echocardiography in tetralogy of Fallot: diagnostic accuracy, resource utilization and surgical implications over 13 years. J Am Coll Cardiol. 2000;36:1371–7.
9. Lu JH, Chung MY, Betau H, Chien HP, Lu JK. Molecular characterization of tetralogy of Fallot within Digeorge critical region of the chromosome 22. Pediatr Cardiol. 2001;22:279–84.
10. Marino B, Digilio MC, Toscano A, et al. Anatomic patterns of conotruncal defects associated with deletion 22q11. Genet Med. 2001;3:45–8.
11. Momma K, Takao A, Matsuoka R, et al. Tetralogy of Fallot associated with chromosome 22q11.2 deletion in adolescents and young adults. Genet Med. 2001;3:56–60.
12. Boudjemline Y, Fermont L, Le Bidois J, Lyonnet S, Sidi D, Bonnet D. Prevalence of 22q11 deletion in fetuses with conotruncal cardiac defects: a 6-year prospective study. J Pediatr. 2001;138:520–4.
13. Goldmuntz E, Geiger E, Benson DW. NKX2.5 mutations in patients with tetralogy of Fallot. Circulation. 2001;104:2565–8.
14. Hokanson JS, Pierpont E, Hirsch B, Moller JH. 22q11.2 microdeletions in adults with familial tetralogy of Fallot. Genet Med. 2001;3:61–4.
15. McElhinney DB, Krantz ID, Bason L, et al. Analysis of cardiovascular phenotype and genotype-phenotype correlation in individuals with a JAG1 mutation and/or Alagille syndrome. Circulation. 2002;106:2567–74.
16. Masuda K, Nomura Y, Yoshinaga M, et al. Inverted duplication/deletion of the short arm of chromosome 8 in two patients with tetralogy of Fallot. Pediatr Int. 2002;44:534–6.
17. Grunert M, Dorn C, Schueler M, et al. Rare and private variations in neural crest, apoptosis and sarcomere genes define the polygenic background of isolated tetralogy of Fallot. Hum Mol Genet. 2014;23:3115–28.
18. Marino B, Digilio MC, Grazioli S, et al. Associated cardiac anomalies in isolated and syndromic patients with tetralogy of Fallot. Am J Cardiol. 1996;77:505–8.
19. Geva T, Ayres NA, Pac FA, Pignatelli R. Quantitative morphometric analysis of progressive infundibular obstruction in tetral-

ogy of Fallot. A prospective longitudinal echocardiographic study. Circulation. 1995;92:886–92.
20. Kaulitz R, Jux C, Bertram H, Paul T, Ziemer G, Hausdorf G. Primary repair of tetralogy of Fallot in infancy—the effect on growth of the pulmonary arteries and the risk for late reinterventions. Cardiol Young. 2001;11:391–8.
21. Bacha EA, Scheule AM, Zurakowski D, et al. Long-term results after early primary repair of tetralogy of Fallot. J Thorac Cardiovasc Surg. 2001;122:154–61.
22. Murphy JG, Gersh BJ, Mair DD, et al. Long-term outcome in patients undergoing surgical repair of tetralogy of Fallot. N Engl J Med. 1993;329:593–9.
23. Nollert G, Fischlein T, Bouterwek S, Bohmer C, Klinner W, Reichart B. Long-term survival in patients with repair of tetralogy of Fallot: 36-year follow-up of 490 survivors of the first year after surgical repair. J Am Coll Cardiol. 1997;30:1374–83.
24. Saul JP, Alexander ME. Preventing sudden death after repair of tetralogy of Fallot: complex therapy for complex patients. J Cardiovasc Electrophysiol. 1999;10:1271–87.
25. Kugler JD. Predicting sudden death in patients who have undergone tetralogy of Fallot repair: is it really as simple as measuring ECG intervals? J Cardiovasc Electrophysiol. 1998;9:103–6.
26. Bricker JT. Sudden death and tetralogy of Fallot. Risks, markers, and causes. Circulation. 1995;92:158–9.
27. Gatzoulis MA, Till JA, Somerville J, Redington AN. Mechanoelectrical interaction in tetralogy of Fallot. QRS prolongation relates to right ventricular size and predicts malignant ventricular arrhythmias and sudden death. Circulation. 1995;92:231–7.
28. Berul CI, Hill SL, Geggel RL, et al. Electrocardiographic markers of late sudden death risk in postoperative tetralogy of Fallot children. J Cardiovasc Electrophysiol. 1997;8:1349–56.
29. Hokanson JS, Moller JH. Significance of early transient complete heart block as a predictor of sudden death late after operative correction of tetralogy of Fallot. Am J Cardiol. 2001;87:1271–7.
30. Hamada H, Terai M, Jibiki T, Nakamura T, Gatzoulis MA, Niwa K. Influence of early repair of tetralogy of Fallot without an outflow patch on late arrhythmias and sudden death: a 27-year follow-up study following a uniform surgical approach. Cardiol Young. 2002;12:345–51.
31. Mackie AS, Gauvreau K, Perry SB, del Nido PJ, Geva T. Echocardiographic predictors of aortopulmonary collaterals in infants with tetralogy of Fallot and pulmonary atresia. J Am Coll Cardiol. 2003;41:852–7.
32. Geva T, Greil GF, Marshall AC, Landzberg M, Powell AJ. Gadolinium-enhanced 3-dimensional magnetic resonance angiography of pulmonary blood supply in patients with complex pulmonary stenosis or atresia: comparison with x-ray angiography. Circulation. 2002;106:473–8.
33. Geva T. Repaired tetralogy of Fallot: the roles of cardiovascular magnetic resonance in evaluating pathophysiology and for pulmonary valve replacement decision support. J Cardiovasc Magn Reson. 2011;13:9.
34. Bonhoeffer P, Boudjemline Y, Saliba Z, et al. Percutaneous replacement of pulmonary valve in a right-ventricle to pulmonary-artery prosthetic conduit with valve dysfunction. Lancet. 2000;356:1403–5.
35. McElhinney DB, Hellenbrand WE, Zahn EM, et al. Short- and medium-term outcomes after transcatheter pulmonary valve placement in the expanded multicenter US melody valve trial. Circulation. 2010;122:507–16.
36. Blalock SE, Banka P, Geva T, Powell AJ, Zhou J, Prakash A. Interstudy variability in cardiac magnetic resonance imaging measurements of ventricular volume, mass, and ejection fraction in repaired tetralogy of Fallot: a prospective observational study. J Magn Reson Imaging. 2013;38:829–35.
37. Valente AM, Gauvreau K, Assenza GE, et al. Contemporary predictors of death and sustained ventricular tachycardia in patients with repaired tetralogy of Fallot enrolled in the INDICATOR cohort. Heart. 2014;100:247–53.
38. Kilner PJ, Geva T, Kaemmerer H, Trindade PT, Schwitter J, Webb GD. Recommendations for cardiovascular magnetic resonance in adults with congenital heart disease from the respective working groups of the European Society of Cardiology. Eur Heart J. 2010;31:794–805.
39. Valente AM, Cook S, Festa P, et al. Multimodality imaging guidelines for patients with repaired tetralogy of Fallot: a report from the American Society of Echocardiography: developed in collaboration with the Society for Cardiovascular Magnetic Resonance and the Society for Pediatric Radiology. J Am Soc Echocardiogr. 2014;27:111–41.
40. Van Praagh R. The importance of segmental situs in the diagnosis of congenital heart disease. Semin Roentgenol. 1985;20:254–71.
41. Blume ED, Altmann K, Mayer JE, Colan SD, Gauvreau K, Geva T. Evolution of risk factors influencing early mortality of the arterial switch operation. J Am Coll Cardiol. 1999;33:1702–9.
42. Levinsky L, Srinivasan V, Alvarez-Diaz F, Subramanian S. Reconstruction of the new atrial septum in the Senning operation. New technique. J Thorac Cardiovasc Surg. 1981;81:131–4.
43. Myridakis DJ, Ehlers KH, Engle MA. Late follow-up after venous switch operation (Mustard procedure) for simple and complex transposition of the great arteries. Am J Cardiol. 1994;74:1030–6.
44. Redington AN, Rigby ML, Oldershaw P, Gibson DG, Shinebourne EA. Right ventricular function 10 years after the Mustard operation for transposition of the great arteries: analysis of size, shape, and wall motion. Br Heart J. 1989;62:455–61.
45. Deanfield J, Camm J, Macartney F, et al. Arrhythmia and late mortality after Mustard and Senning operation for transposition of the great arteries. An eight-year prospective study. J Thorac Cardiovasc Surg. 1988;96:569–76.
46. Van Praagh R, Jung WK. The arterial switch operation in transposition of the great arteries: anatomic indications and contraindications. Thorac Cardiovasc Surg. 1991;39(Suppl 2):138–50.
47. Wernovsky G, Jonas RA, Colan SD, et al. Results of the arterial switch operation in patients with transposition of the great arteries and abnormalities of the mitral valve or left ventricular outflow tract. J Am Coll Cardiol. 1990;16:1446–54.
48. Ruys TP, van der Bosch AE, Cuypers JA, et al. Long-term outcome and quality of life after arterial switch operation: a prospective study with a historical comparison. Congenit Heart Dis. 2013;8:203–10.
49. Khairy P, Clair M, Fernandes SM, et al. Cardiovascular outcomes after the arterial switch operation for D-transposition of the great arteries. Circulation. 2013;127:331–9.
50. Angeli E, Formigari R, Pace Napoleone C, et al. Long-term coronary artery outcome after arterial switch operation for transposition of the great arteries. Eur J Cardiothorac Surg. 2010;38:714–20.
51. Co-Vu JG, Ginde S, Bartz PJ, Frommelt PC, Tweddell JS, Earing MG. Long-term outcomes of the neoaorta after arterial switch operation for transposition of the great arteries. Ann Thorac Surg. 2013;95:1654–9.
52. Koolbergen DR, Manshanden JS, Yazdanbakhsh AP, et al. Reoperation for neoaortic root pathology after the arterial switch operation. Eur J Cardiothorac Surg. 2014;46:474–9; discussion 479.
53. Chung KJ, Simpson IA, Glass RF, Sahn DJ, Hesselink JR. Cine magnetic resonance imaging after surgical repair in patients with transposition of the great arteries. Circulation. 1988;77:104–9.
54. Lorenz CH, Walker ES, Graham TP Jr, Powers TA. Right ventricular performance and mass by use of cine MRI late after atrial repair of transposition of the great arteries. Circulation. 1995;92:II233–9.

55. Hardy CE, Helton GJ, Kondo C, Higgins SS, Young NJ, Higgins CB. Usefulness of magnetic resonance imaging for evaluating great-vessel anatomy after arterial switch operation for D-transposition of the great arteries. Am Heart J. 1994;128:326–32.
56. Beek FJ, Beekman RP, Dillon EH, et al. MRI of the pulmonary artery after arterial switch operation for transposition of the great arteries. Pediatr Radiol. 1993;23:335–40.
57. Theissen P, Kaemmerer H, Sechtem U, et al. Magnetic resonance imaging of cardiac function and morphology in patients with transposition of the great arteries following mustard procedure. Thorac Cardiovasc Surg. 1991;39(Suppl 3):221–4.
58. Rees S, Somerville J, Warnes C, et al. Comparison of magnetic resonance imaging with echocardiography and radionuclide angiography in assessing cardiac function and anatomy following Mustard's operation for transposition of the great arteries. Am J Cardiol. 1988;61:1316–22.
59. Tulevski II, Lee PL, Groenink M, et al. Dobutamine-induced increase of right ventricular contractility without increased stroke volume in adolescent patients with transposition of the great arteries: evaluation with magnetic resonance imaging. Int J Card Imaging. 2000;16:471–8.
60. Tulevski II, van der Wall EE, Groenink M, et al. Usefulness of magnetic resonance imaging dobutamine stress in asymptomatic and minimally symptomatic patients with decreased cardiac reserve from congenital heart disease (complete and corrected transposition of the great arteries and subpulmonic obstruction). Am J Cardiol. 2002;89:1077–81.
61. Roest AA, Lamb HJ, van der Wall EE, et al. Cardiovascular response to physical exercise in adult patients after atrial correction for transposition of the great arteries assessed with magnetic resonance imaging. Heart. 2004;90:678–84.
62. Babu-Narayan SV, Goktekin O, Moon JC, et al. Late gadolinium enhancement cardiovascular magnetic resonance of the systemic right ventricle in adults with previous atrial redirection surgery for transposition of the great arteries. Circulation. 2005;111:2091–8.
63. Makowski MR, Wiethoff AJ, Uribe S, et al. Congenital heart disease: cardiovascular MR imaging by using an intravascular blood pool contrast agent. Radiology. 2011;260:680–8.
64. Raman FS, Nacif MS, Cater G, et al. 3.0-T whole-heart coronary magnetic resonance angiography: comparison of gadobenate dimeglumine and gadofosveset trisodium. Int J Cardiovasc Imaging. 2013;29:1085–94.
65. Strigl S, Beroukhim R, Valente AM, et al. Feasibility of dobutamine stress cardiovascular magnetic resonance imaging in children. J Magn Reson Imaging. 2009;29:313–9.
66. Van Praagh R, Papagiannis J, Grunenfelder J, Bartram U, Martanovic P. Pathologic anatomy of corrected transposition of the great arteries: medical and surgical implications. Am Heart J. 1998;135:772–85.
67. Beauchesne LM, Warnes CA, Connolly HM, Ammash NM, Tajik AJ, Danielson GK. Outcome of the unoperated adult who presents with congenitally corrected transposition of the great arteries. J Am Coll Cardiol. 2002;40:285–90.
68. Colli AM, de Leval M, Somerville J. Anatomically corrected malposition of the great arteries: diagnostic difficulties and surgical repair of associated lesions. Am J Cardiol. 1985;55:1367–72.
69. Van Praagh R. What is congenitally corrected transposition? N Engl J Med. 1970;282:1097–8.
70. Murtuza B, Barron DJ, Stumper O, et al. Anatomic repair for congenitally corrected transposition of the great arteries: a single-institution 19-year experience. J Thorac Cardiovasc Surg. 2011;142:1348–57. e1
71. Belli E, Serraf A, Lacour-Gayet F, et al. Surgical treatment of subaortic stenosis after biventricular repair of double-outlet right ventricle. J Thorac Cardiovasc Surg. 1996;112:1570–8; discussion 1578–80.
72. Banka P, Schaetzle B, Komarlu R, Emani S, Geva T, Powell AJ. Cardiovascular magnetic resonance parameters associated with early transplant-free survival in children with small left hearts following conversion from a univentricular to biventricular circulation. J Cardiovasc Magn Reson. 2014;16:73.
73. Yoo SJ, Kim YM, Choe YH. Magnetic resonance imaging of complex congenital heart disease. Int J Card Imaging. 1999;15:151–60.
74. Beekmana RP, Roest AA, Helbing WA, et al. Spin echo MRI in the evaluation of hearts with a double outlet right ventricle: usefulness and limitations. Magn Reson Imaging. 2000;18:245–53.
75. Beekman RP, Beek FJ, Meijboom EJ, Wenink AC. MRI appearance of a double inlet and double outlet right ventricle with supero-inferior ventricular relationship. Magn Reson Imaging. 1996;14:1107–12.
76. Igarashi H, Kuramatsu T, Shiraishi H, Yanagisawa M. Criss-cross heart evaluated by colour Doppler echocardiography and magnetic resonance imaging. Eur J Pediatr. 1990;149:523–5.
77. Niezen RA, Beekman RP, Helbing WA, van der Wall EE, de Roos A. Double outlet right ventricle assessed with magnetic resonance imaging. Int J Card Imaging. 1999;15:323–9.
78. Sorensen TS, Korperich H, Greil GF, et al. Operator-independent isotropic three-dimensional magnetic resonance imaging for morphology in congenital heart disease: a validation study. Circulation. 2004;110:163–9.
79. Van Praagh R, Van Praagh S. The anatomy of common aorticopulmonary trunk (truncus arteriosus communis) and its embryologic implications. A study of 57 necropsy cases. Am J Cardiol. 1965;16:406–25.
80. Collett RW, Edwards JE. Persistent truncus arteriosus: a classification according to anatomic types. Surg Clin North Am. 1949;29:1245–70.
81. Litovsky SH, Ostfeld I, Bjornstad PG, Van Praagh R, Geva T. Truncus arteriosus with anomalous pulmonary venous connection. Am J Cardiol. 1999;83:801–4. A10
82. Goldmuntz E, Clark BJ, Mitchell LE, et al. Frequency of 22q11 deletions in patients with conotruncal defects. J Am Coll Cardiol. 1998;32:492–8.
83. Tworetzky W, McElhinney DB, Brook MM, Reddy VM, Hanley FL, Silverman NH. Echocardiographic diagnosis alone for the complete repair of major congenital heart defects. J Am Coll Cardiol. 1999;33:228–33.
84. Fyler DC, Buckley LP, Hellenbrand WE, Cohn HE. Report of the New England regional infant cardiac program. Pediatrics. 1980;65:377–461.
85. Celoria GC, Patton RB. Congenital absence of the aortic arch. Am Heart J. 1959;58:407–13.
86. Geva T, Gajarski RJ. Echocardiographic diagnosis of type B interruption of a right aortic arch. Am Heart J. 1995;129:1042–5.
87. Kutsche LM, Van Mierop LH. Cervical origin of the right subclavian artery in aortic arch interruption: pathogenesis and significance. Am J Cardiol. 1984;53:892–5.
88. Kaulitz R, Jonas RA, van der Velde ME. Echocardiographic assessment of interrupted aortic arch. Cardiol Young. 1999;9:562–71.
89. Varghese A, Gatzoulis M, Mohiaddin RH. Images in cardiovascular medicine: magnetic resonance angiography of a congenitally interrupted aortic arch. Circulation. 2002;106:E9–10.
90. Tsai-Goodman B, Geva T, Odegard KC, Sena LM, Powell AJ. Clinical role, accuracy, and technical aspects of cardiovascular magnetic resonance imaging in infants. Am J Cardiol. 2004;94:69–74.
91. Nielsen J, Powell AJ, Gauvreau K, Marcus E, Geva T. Magnetic resonance imaging predictors of the hemodynamic severity of aortic coarctation. J Am Coll Cardiol. 2004;43:24A.
92. Fontan F, Baudet E. Surgical repair of tricuspid atresia. Thorax. 1971;26:240–8.

93. Kreutzer GO, Vargas FJ, Schlichter AJ, et al. Atriopulmonary anastomosis. J Thorac Cardiovasc Surg. 1982;83:427–36.
94. Jonas RA, Castaneda AR. Modified Fontan procedure: atrial baffle and systemic venous to pulmonary artery anastomotic techniques. J Card Surg. 1988;3:91–6.
95. Bridges ND, Mayer JE Jr, Lock JE, et al. Effect of baffle fenestration on outcome of the modified Fontan operation. Circulation. 1992;86:1762–9.
96. Tireli E. Extracardiac Fontan operation without cardiopulmonary bypass: how to perform the anastomosis between inferior vena cava and conduit. Cardiovasc Surg. 2003;11:225–7.
97. Gentles TL, Mayer JE Jr, Gauvreau K, et al. Fontan operation in five hundred consecutive patients: factors influencing early and late outcome. J Thorac Cardiovasc Surg. 1997;114:376–91.
98. Wilson WR, Greer GE, Tobias JD. Cerebral venous thrombosis after the Fontan procedure. J Thorac Cardiovasc Surg. 1998;116:661–3.
99. Day RW, Boyer RS, Tait VF, Ruttenberg HD. Factors associated with stroke following the Fontan procedure. Pediatr Cardiol. 1995;16:270–5.
100. Jacobs ML. Complications associated with heterotaxy syndrome in Fontan patients. Semin Thorac Cardiovasc Surg Pediatr Card Surg Annu. 2002;5:25–35.
101. Lam J, Neirotti R, Becker AE, Planche C. Thrombosis after the Fontan procedure: transesophageal echocardiography may replace angiocardiography. J Thorac Cardiovasc Surg. 1994;108:194–5.
102. Deal BJ, Mavroudis C, Backer CL. Beyond Fontan conversion: surgical therapy of arrhythmias including patients with associated complex congenital heart disease. Ann Thorac Surg. 2003;76:542–53; discussion 553–4.
103. Kreutzer J, Keane JF, Lock JE, et al. Conversion of modified Fontan procedure to lateral atrial tunnel cavopulmonary anastomosis. J Thorac Cardiovasc Surg. 1996;111:1169–76.
104. Atz AM, Zak V, Mahony L, et al. Survival data and predictors of functional outcome an average of 15 years after the Fontan procedure: the pediatric heart network Fontan cohort. Congenit Heart Dis. 2014;10(1):E30–42.
105. d'Udekem Y, Iyengar AJ, Galati JC, et al. Redefining expectations of long-term survival after the Fontan procedure: twenty-five years of follow-up from the entire population of Australia and New Zealand. Circulation. 2014;130:S32–8.
106. Kutty SS, Peng Q, Danford DA, et al. Increased hepatic stiffness as consequence of high hepatic afterload in the Fontan circulation: a vascular Doppler and elastography study. Hepatology. 2014;59:251–60.
107. Prakash A, Rathod RH, Powell AJ, McElhinney DB, Banka P, Geva T. Relation of systemic-to-pulmonary artery collateral flow in single ventricle physiology to palliative stage and clinical status. Am J Cardiol. 2012;109:1038–45.
108. Prakash A, Travison TG, Fogel MA, et al. Relation of size of secondary ventricles to exercise performance in children after Fontan operation. Am J Cardiol. 2010;106:1652–6.
109. Khiabani RH, Whitehead KK, Han D, et al. Exercise capacity in single-ventricle patients after Fontan correlates with haemodynamic energy loss in TCPC. Heart. 2015;101(2):139–43. Epub 2014 Sep 2.
110. Latus H, Gummel K, Diederichs T, et al. Aortopulmonary collateral flow is related to pulmonary artery size and affects ventricular dimensions in patients after the fontan procedure. PLoS One. 2013;8:e81684.
111. Rathod RH, Prakash A, Kim YY, et al. Cardiac magnetic resonance parameters predict transplantation-free survival in patients with Fontan circulation. Circ Cardiovasc Imaging. 2014;7:502–9.
112. Brown DW, Gauvreau K, Powell AJ, et al. Cardiac magnetic resonance versus routine cardiac catheterization before bidirectional Glenn anastomosis: long-term follow-up of a prospective randomized trial. J Thorac Cardiovasc Surg. 2013;146:1172–8.
113. Prakash A, Khan MA, Hardy R, Torres AJ, Chen JM, Gersony WM. A new diagnostic algorithm for assessment of patients with single ventricle before a Fontan operation. J Thorac Cardiovasc Surg. 2009;138:917–23.
114. Garg R, Powell AJ, Sena L, Marshall AC, Geva T. Effects of metallic implants on magnetic resonance imaging evaluation of Fontan palliation. Am J Cardiol. 2005;95:688–91.
115. Restrepo M, Tang E, Haggerty CM, et al. Energetic implications of vessel growth and flow changes over time in Fontan patients. Ann Thorac Surg. 2015;99(1):163–70. Epub 2014 Nov 20.
116. Dori Y, Glatz AC, Hanna BD, et al. Acute effects of embolizing systemic-to-pulmonary arterial collaterals on blood flow in patients with superior cavopulmonary connections: a pilot study. Circ Cardiovasc Interv. 2013;6:101–6.
117. Grosse-Wortmann L, Hamilton R, Yoo SJ. Massive systemic-to-pulmonary collateral arteries in the setting of a cavopulmonary shunt and pulmonary venous stenosis. Cardiol Young. 2007;17:548–50.
118. Rathod RH, Prakash A, Powell AJ, Geva T. Myocardial fibrosis identified by cardiac magnetic resonance delayed enhancement is associated with ventricular dysfunction and nonsustained ventricular tachycardia after Fontan operation. J Am Coll Cardiol. 2009;53:A356.

Congenital Heart Disease: Indications, Patient Preparation, and Simple Lesions

20

Rahul H. Rathod and Andrew J. Powell

Introduction

Technical advances over the past two decades have greatly expanded the diagnostic role of cardiac magnetic resonance (CMR) in pediatric and adult patients with congenital heart disease. In addition to high-resolution anatomic information, CMR provides physiological information about the cardiovascular system such as ventricular function and blood flow. Along with these improved capabilities, the speed and efficiency of imaging have also increased thereby allowing a comprehensive examination to be obtained within a timeframe acceptable to both patient and operator. The first part of this chapter reviews the indications, patient preparation and monitoring, and sedation strategies for CMR in patients with congenital heart disease. The second part details the CMR evaluation of several "simple" congenital heart lesions: atrial septal defects (ASD) and other interatrial communications, ventricular septal defects (VSD), patent ductus arteriosus (PDA), partially anomalous pulmonary venous connections (PAPVC), coarctation of the aorta, and vascular rings. More "complex" lesions are discussed in Chap. 19. Despite being classified as "simple", many of the conditions in this chapter have important anatomic subtypes and variable physiology. Thus, summaries of the anatomic considerations and clinical management decisions are provided for each lesion.

Indications for CMR Evaluation of Congenital Heart Disease

CMR is rarely the initial or sole diagnostic imaging modality in patients with congenital heart disease (CHD). Rather, it compliments echocardiography, provides a noninvasive alternative to x-ray angiography, and avoids the ionizing radiation exposure of x-ray angiography and computed tomography. Minimizing diagnostic testing which employs ionizing radiation is especially important in the pediatric age population as younger patients have a greater lifetime risk for cancer with such exposure than adults [1–4].

Expert consensus recommendations and guidelines for the use of CMR in children and adults with CHD have been published [5–8]. Table 20.1 summarizes the primary indications for CMR in 2396 consecutive patients evaluated at Boston Children's Hospital from 2012 to 2013 illustrating the wide range of cardiovascular anomalies evaluated. More generally, the clinical indications for a CMR examination often involve one or more of the following situations:

1. When transthoracic echocardiography is incapable of providing the required diagnostic information
2. When clinical assessment and other diagnostic tests are inconsistent
3. As an alternative to diagnostic cardiac catheterization with its associated risks and higher cost
4. To obtain diagnostic information for which CMR offers unique advantages (e.g., blood flow measurements and myocardial fibrosis)

The indications for CMR in infants and toddlers are somewhat different than in older patients. In part, this is because young children typically have excellent acoustic windows and echocardiography can provide the necessary diagnostic information in most patients. In addition, CMR examinations in this age group usually require the use of sedation or anesthesia, which raises the threshold for ordering the procedure.

Electronic Supplementary Material The online version of this chapter (https://doi.org/10.1007/978-1-4939-8841-9_20) contains supplementary material, which is available to authorized users.

R. H. Rathod · A. J. Powell (✉)
Department of Cardiology, Boston Children's Hospital, Boston, MA, USA

Department of Pediatrics, Harvard Medical School, Boston, MA, USA
e-mail: rahul.rathod@cardio.chboston.org; andrew.powell@cardio.chboston.org

R. Y. Kwong et al. (eds.), *Cardiovascular Magnetic Resonance Imaging*, Contemporary Cardiology,
https://doi.org/10.1007/978-1-4939-8841-9_20

Table 20.1 Primary diagnoses in patients who underwent CMR at Boston Children's Hospital (2012–2013)

Referral diagnosis	N = 2396
Tetralogy of Fallot	429 (18%)
Aortic valve stenosis and/or regurgitation	261 (11%)
Transposition of the great arteries (TGA)	205 (9%)
D-Loop TGA, S/P arterial switch or Rastelli operation	103
D-Loop TGA, S/P atrial switch operation	52
Congenitally corrected TGA, repaired, and unrepaired	50
Measurement of myocardial and/or hepatic iron	195 (8%)
Single ventricle heart disease	194 (8%)
Coarctation and aortic arch anomalies	186 (7%)
Cardiomyopathies (HCM, ARVD, DCM)	115 (5%)
Septal defects	101 (4%)
Atrial septal defects or sinus venous defects	73
Ventricular septal defects	28
Connective tissue disease	93 (4%)
Assessment of ventricular function, myocardial viability, or myocarditis	78 (3%)
Pulmonary valve stenosis or regurgitation	77 (3%)
Pulmonary atresia with intact ventricular septum	69 (3%)
Tricuspid valve stenosis or regurgitation (including Ebstein's anomaly)	66 (3%)
Pulmonary vein anomalies	50 (2%)
Endocardial cushion defects	49 (2%)
Coronary anomalies	49 (2%)
Truncus arteriosus	44 (2%)
Cardiac tumor or thrombus	20 (1%)
Mitral valve stenosis or regurgitation	19 (1%)
Vascular ring	17 (1%)
Pulmonary hypertension	14 (1%)
Others	65 (2%)

A review of 87 consecutive CMR examinations in patients less than 1 year of age at Boston Children's Hospital from 2012 to 2013 found that the most common indications were assessment for biventricular repair in patients with complex cardiac anatomy or a borderline small ventricle (56%), evaluation of patients with a functionally single ventricle (24%), and the delineation of thoracic vessels (e.g., aortic coarctation, anomalously draining pulmonary veins, and vascular rings) (20%). Technical advancements in respiratory motion compensation [9] and faster imaging are likely to reduce the need for sedation or anesthesia, resulting in the expansion of the use of CMR in younger patients.

Patient Preparation, Sedation, and Monitoring

Patients undergoing CMR examinations must remain still in the scanner for up to 60 minutes to minimize motion artifact during image acquisition and allow planning of successive imaging sequences. Accordingly, the need for performing the examination under sedation or anesthesia and an assessment of the risk-benefit ratio for proceeding under these circumstances should be determined well before the examination date. Multiple factors are taken into account when deciding whether a patient should have an examination with sedation, including the length of the anticipated examination protocol, the child's developmental age and maturity, the child's experience with prior procedures, and the parents' opinion of their child's capability to cooperate with the examination. True claustrophobia in the pediatric age group is rare. In general, most children 7 years of age and older can cooperate sufficiently for a good-quality CMR study. Use of a magnetic resonance-compatible video system so that the child can view a movie during the examination may improve patient compliance and reduce the need for sedation [10]. Parents should be provided with a detailed description of the examination and asked to discuss it with their child in an age-appropriate manner in advance to increase the likelihood of a successful study. After proper screening, parents can be allowed into the scanner room to help their child complete the examination.

Strategies for sedation and anesthesia in CMR vary and often depend on institutional preference and personnel resources. Although it is possible to wait for young children to fall into a natural sleep, [11] this approach may be time-consuming and complicated by early awakening. Sedation can be employed with a variety of medications (e.g., pentobarbital, propofol, fentanyl, midazolam, chloral hydrate, dexmedetomidine) and is a reasonable approach [12–17]. Its principal drawbacks are an unprotected airway and reliance on spontaneous respiratory effort with the associated risks of aspiration, airway obstruction, and hypoventilation. In addition, because images are often acquired over several seconds, respiratory motion will degrade image quality. This motion artifact can be reduced by synchronizing image data acquisition to the respiratory cycle tracked by either a bellows device around the abdomen or by navigator echoes that concurrently image the position of the diaphragm or heart. An alternative strategy to reduce respiratory motion artifact is to acquire multiple images at the same location and average them, thereby minimizing variations from respiration. The principal limitations of both of these strategies are prolonged scan times and incomplete elimination of respiratory motion that can lead to reduced image quality.

Because of these safety and image quality concerns, we and others frequently prefer to perform CMR examinations under general anesthesia in children who cannot undergo an awake examination. This approach, described in detail elsewhere, [18, 19] is safe, consistently achieves adequate sedation, protects the airway, and offers control of ventilation. Respiratory motion artifact can be completely eliminated by suspending ventilation

in conjunction with neuromuscular blockade. Breath-hold periods of 30–60 seconds are typically well-tolerated and allow multiple locations to be scanned efficiently.

When utilizing either sedation or anesthesia, it is important that both the nurses and physicians have sufficient experience with these procedures in children with cardiovascular disorders. Continuous monitoring of the electrocardiogram, pulse oximetry, end-tidal carbon dioxide, anesthetic gases, temperature, and blood pressure with a magnetic resonance-compatible physiologic monitoring system is required. Magnetic resonance-compatible anesthesia machines are available which can be located in the scanner room and connected to the patient's endotracheal tube by an extended breathing circuit. To maximize patient safety and examination quality, it is recommended that different healthcare providers be responsible for supervising the imaging and sedation/anesthesia aspects of the study and that both communicate closely with each other.

Prior to bringing the patient into the scanner room, the physician and technologists should review the patient's history, safety screening form, and the most recent chest radiograph to identify implanted devices which may be hazardous in the CMR environment or produce image artifact. Detailed safety information regarding specific devices should be obtained by consulting the manufacturer or a comprehensive database (e.g., www.mrisafety.com). In general, sternal wires, prosthetic heart valves, and most stents, occluders, and vascular coils in place for greater than 6 weeks have been deemed safe. In situations where implantation time is less than 6 weeks, or the safety data are inconclusive, the referring and performing physicians must evaluate the risks and benefits of the examination for the individual patient. Previously, pacemakers and defibrillators were considered to be absolute contraindications to undergoing CMR examinations [20, 21]; however, more recent reports have challenged this position and demonstrated that, with appropriate provisions, selected patients with conventional pacemakers can safely have CMR examinations [22–25]. Moreover, in the last few years, pacemakers designed and approved to be safe in the CMR environment under specified conditions have become available [26, 27].

Following safety screening, physiologic monitoring devices and hearing protection (for both awake and anesthetized patients) are put in place. A high-quality electrocardiogram signal is essential for optimum image quality in cardiac-gated sequences. The signal should be checked both when the patient is outside and then inside the scanner bore. In patients with dextrocardia, electrocardiogram leads are best placed on the right chest. Because young children dissipate body heat faster than adults, the scanner room temperature should be adjusted and pre-warmed blankets applied to minimize heat loss.

The imaging coil should be chosen to maximize the signal-to-noise ratio over the entire body region to be examined. Because congenital heart disease often involves abnormalities of the thoracic vasculature, the coil will usually need to be large enough to cover the entire thorax rather than just the heart. Adult head or knee coils may be appropriate for infants weighing less than 10 kg. Adequate coil coverage and placement should be confirmed early in the examination by reviewing the localizing images.

Principles of CMR Evaluation of Congenital Heart Disease

Pre-examination planning is crucial given the wide array of imaging sequences available and the often complex nature of the clinical, anatomic, and functional issues in patients with congenital heart disease. The importance of a careful review of the patient's medical history, including details of all cardiovascular surgical procedures, interventional catheterizations, findings of previous diagnostic tests, and current clinical status, cannot be overemphasized. As with echocardiography and cardiac catheterization, CMR examination of congenital heart disease is a dynamic diagnostic procedure that is optimally performed with continuous review and interpretation of the data by the supervising physician. Unexpected findings or suboptimal image quality often requires adjustment of the examination protocol, imaging planes, techniques, and sequence parameters. Reliance on standardized protocols and post-examination review alone in these patients may result in incomplete or even erroneous interpretation.

One of the strengths of CMR is its ability to accurately and precisely measure ventricular and vascular structures. Care must be taken, however, when determining whether these measurements fall in the normal range as adjustment for the variation in body size remains challenging. Simple indexing to body surface area (BSA) is inadequate for most parameters, particularly in children and unusually large or small adults [28]. Several authors have shown that linear dimensions (e.g., ascending aorta diameter) are best adjusted to the square root of BSA, area measurements to BSA, and volumetric measurements to BSA raised to the 1.3–1.4 power [29–31]. Thus, one cannot simply apply normative ranges for ventricular volume indexed to BSA that was derived in adults to children. CMR-based normative data from children are available, though they are often limited by a smaller than ideal sample size, particularly in the youngest age range [32–38]. Furthermore, it is essential to apply the same measurement technique (e.g., whether to include papillary muscles or trabeculations in the blood pool) as was used to derive the normative data.

Simple Congenital Heart Lesions

Atrial Septal Defects and Other Interatrial Communications

Anatomy

Anatomically, five different defects can lead to an interatrial shunt (Fig. 20.1). (1) A patent foramen ovale is bordered on the left by septum primum and by the superior limbic band of the fossa ovalis (septum secundum) on the right. It is an important and nearly universally present communication during fetal life. Following the transition to a postnatal circulation, septum primum opposes the superior limbic band of the fossa ovalis, and the foramen ovale narrows. A patent foramen ovale is seen in almost all newborns and decreases in frequency with age [39]. (2) A secundum ASD is the most common cause of an atrial level shunt after patent foramen ovale. Usually the defect is due to deficiency of septum primum (the valve of the fossa ovalis), but rarely, it results from a deficiency of septum secundum (the muscular limb of the fossa ovalis). The defect may be single or multiple with several fenestrations of septum primum. (3) A primum ASD is a variant of incomplete common atrioventricular canal and is the third most common interatrial communication. This defect involves the septum of the atrioventricular canal and is almost always associated with a cleft anterior mitral valve leaflet. Any associated defect within the fossa ovale (secundum ASD) is regarded as a separate abnormality. (4) A sinus venosus septal defect results from deficiency of the sinus venosus septum which separates the pulmonary veins from the systemic veins and the sinus venosus component of the right atrium (Fig. 20.2). Most commonly, a sinus venosus defect is between the right upper pulmonary vein and the cardiac end of the superior vena cava. Rarely, the defect involves the right lower and/or middle pulmonary veins and the inferior aspect of the right atrium at its junction with the inferior vena cava. From an anatomic standpoint, a sinus venosus defect is not an ASD because it does not allow direct communication between the left and right atria. Instead, the interatrial flow travels between the left atrium, one or more of the pulmonary veins, the sinus venosus septal defect, the superior (or inferior) vena cava, and the right atrium. The defect usually allows pulmonary vein flow to drain to the right atrium through the defect as well. Patients with sinus venosus defects commonly have additional accessory right upper pulmonary veins which connect to the superior vena cava or azygous vein. (5) A coronary sinus septal defect is a rare type of interatrial communication in which the septum between the coronary sinus and the left atrium is either par-

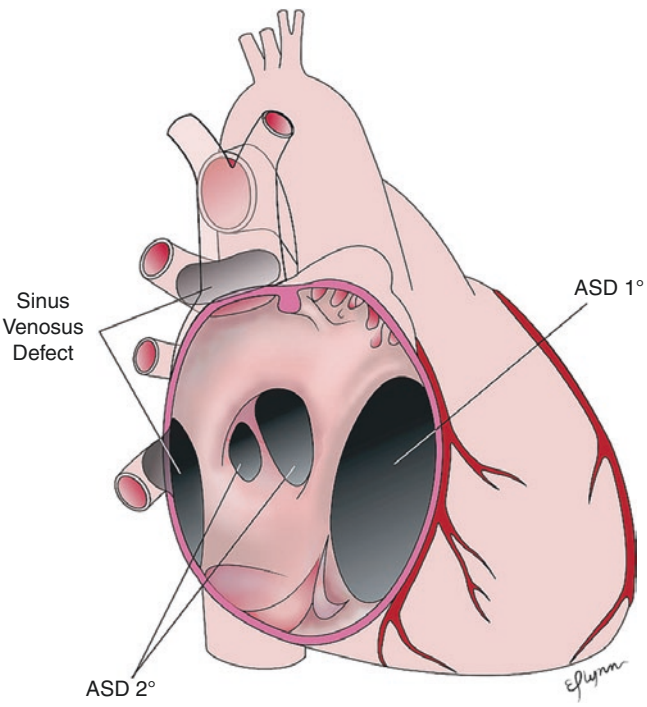

Fig. 20.1 Anatomic types of atrial communications (see text for details). ASD 1^0 denotes primum atrial septal defect; ASD 2^0 denotes secundum atrial septal defect

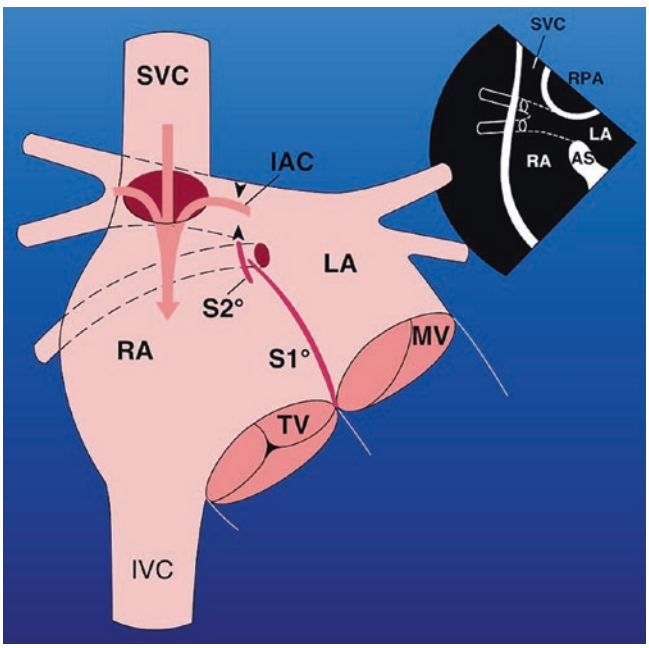

Fig. 20.2 Diagrammatic representation of a sinus venosus septal defect. Absence of the common wall between the right superior vena cava (SVC) and the right upper pulmonary vein allows drainage of blood from the right upper pulmonary vein into the SVC and right atrium (RA). The interatrial communication (IAC) is not a defect; rather it is the anatomic orifice of the right upper pulmonary vein (arrowheads) which allows blood to flow from the left atrium (LA) into the RA. The inset shows the normal course of the right upper pulmonary vein posterior to the SVC. AS, atrial septum; IVC, inferior vena cava; MV, mitral valve; RPA, right pulmonary artery; S1°, septum primum; S2°, septum secundum; TV, tricuspid valve

tially or completely unroofed, allowing the right and left atria to communicate through the defect and the coronary sinus orifice. Sometimes there is also a persistent left superior vena cava draining to the coronary sinus. If the coronary sinus is completely unroofed, the left superior vena cava will drain to the left atrium. The coexistence of a coronary sinus septal defect and persistent left superior vena cava is termed Raghib syndrome and may result in cyanosis [40].

Clinical Course and Management

Regardless of the specific anatomic type, the amount of shunting through an interatrial communication is determined by the defect size and relative compliance of the right and left ventricles. Over the first few months of life, right ventricular compliance typically rises leading to an increasing left-to-right shunt. During adulthood, left ventricular compliance normally decreases further augmenting the left-to-right flow. Shunt flow through the right heart and lungs leads to dilation of the right atrium, right ventricle, pulmonary arteries, and pulmonary veins. Most young children tolerate this increased pulmonary blood flow well and are asymptomatic; a few develop dyspnea or growth failure. Defects in this age group are typically detected after auscultation of a heart murmur or incidentally when an echocardiogram is obtained for other indications. Up to 10% of patients with a significant left-to-right shunt may develop pulmonary vascular disease by adulthood leading to pulmonary hypertension. Adults with unrepaired atrial level defects are also at risk for exercise intolerance, atrial arrhythmias, and paradoxical emboli.

In general, current practice is to refer patients for atrial septal defect closure if the patient is symptomatic or the defect results in a significant left-to-right shunt. Evidence for the later includes a defect diameter >5 mm, right ventricular dilation, flattening of the ventricular septum in diastole (caused by elevated right ventricular diastolic pressure from the volume load), and a pulmonary-to-systemic flow ratio >1.5–2.0. One must also be aware that secundum ASDs may become smaller or close spontaneously in the first few years of life; thereafter, defects tend to become larger with time [41]. Primum ASDs, sinus venosus septal defects, and coronary sinus septal defects almost never become smaller with time. Although a patent foramen ovale typically produces only a small shunt, closure may be indicated when there is a history consistent with a paradoxical embolus [42, 43].

All of these defect types can be closed surgically with a very low mortality and morbidity in centers with expertise. The timing of surgery depends on multiple factors including the size of the defect, associated cardiac abnormalities, symptoms, and local experience, but there is rarely a reason to delay surgical closure beyond 3 years of age. Over the past two decades, transcatheter treatment for secundum ASDs and patent foramen ovales by occluding them with various devices has become available at specialized centers. Although device closure is generally favored over surgical closure for a patent foramen ovale [44], there is yet no consensus on the specific circumstances under which device closure is superior for secundum ASDs.

With regard to surgical technique, secundum ASDs are either closed primarily or with a patch. For primum ASDs, the defect is closed with a patch, and, in some cases, the associated mitral valve cleft is partially sutured. Sinus venosus septal defects can often be closed by placing a patch to reconstruct the missing portion of the sinus venosus septum thereby eliminating interatrial and right pulmonary vein to right atrial flow ("single-patch repair"). A second patch may be placed anteriorly on the superior vena cava to enlarge it ("two-patch repair"). In some cases, especially when a right upper pulmonary vein drains relatively high to the superior vena cava, the superior vena cava is transected superior to the anomalous veins and the distal caval end anastomosed to the right atrial appendage (Warden procedure) [50]. The sinus venosus septal defect is then closed in such a way that the proximal superior vena cava and anomalous veins drain to the left atrium. Short-term outcomes for all three techniques are excellent, but caval or pulmonary venous obstruction may develop over time [45]. For a coronary sinus septal defect, the os of the coronary sinus is usually patched closed. If a left superior vena cava is present, it is redirected to the right atrial side either through ligation when an adequate left innominate vein is present or via a baffle to the right atrium.

Much less commonly, interatrial flow through the various types of defects is bidirectional or right to left. This typically occurs when right ventricular compliance is low as the result of right ventricular outflow tract obstruction or pulmonary hypertension (i.e., increased pulmonary vascular resistance). Right-to-left shunt flow causes cyanosis and its sequelae including exercise intolerance, paradoxical emboli, and polycythemia. Closure of defects in this clinical setting is often contraindicated as it would exacerbate pulmonary hypertension and right heart failure.

CMR Evaluation

Transthoracic echocardiography is the primary imaging technique for the evaluation of ASDs and is usually sufficient for clinical decision-making in the pediatric age range. However, CMR can often be helpful in patients, usually adolescents and adults, with a known or suspected ASD and inconclusive clinical or transthoracic echocardiographic findings. For example, CMR provides a [51] noninvasive alternative to transesophageal echocardiography and to diagnostic catheterization in patients with evidence of right ventricular volume overload in whom transthoracic echocardiography cannot demonstrate the source of the left-to-right shunt. The option for transcatheter occlusion of ASDs has also increased the need for accurate anatomic

information to determine whether a patient is an appropriate candidate for this intervention versus surgery.

In the pre-intervention situation, the specific goals of the CMR examination include delineation of the location, size, rims, and number of ASDs; evaluation of pulmonary venous return; determination of suitability for transcatheter closure; estimation of right ventricular pressure; and assessment of the hemodynamic burden by quantifying the pulmonary-to-systemic flow (Qp/Qs) ratio and right ventricular size and systolic function. In patients who have undergone transcatheter device closure of an ASD, additional goals include excluding device malposition, interference with the atrioventricular valves and venous blood flow, thrombus formation, and a residual shunt. Patients who have undergone a repair of a sinus venosus defect are at risk for superior vena cava and right pulmonary vein obstruction. Mitral regurgitation from a residual cleft is often present after primum ASD repair and should be assessed quantitatively with velocity-encoded cine (VEC) CMR.

The anatomic issues should be addressed by acquiring high-resolution images of the atrial septum and adjacent structures including the vena cava, the pulmonary veins, and the atrioventricular valves. Our preference is to image in at least two planes by acquiring a contiguous stack of locations in the axial or four-chamber plane and a stack in an oblique sagittal plane (Fig. 20.3, Video 20.1a, b). The most useful commonly available techniques for this task are fast (turbo) spin-echo and segmented k-space cine steady-state free precession pulse sequences, both performed with breath-holding and ECG-gating. Unless image quality is optimal, thin structures such as septum primum may not be clearly demonstrated, leading to an overestimation of the defect's size or to a false-positive diagnosis. Moreover, it may be difficult to appreciate the precise anatomy of a secundum ASD with multiple fenestrations. For these reasons, it is also useful to image the atrial septum using VEC CMR both in the plane of the septum to yield an en face view as well as in orthogonal planes planned from the en face view [51]. A non-ECG-gated gadolinium-enhanced three-dimensional magnetic resonance angiogram (3D MRA) sequence is not ideally suited for evaluation of ASDs because of blurring of intracardiac structures from heart motion. However, this technique is helpful in the anatomic evaluation of the pulmonary veins, especially in patients with sinus venosus septal defects which invariably involve the pulmonary veins (Fig. 20.4, Video 20.2a, b).

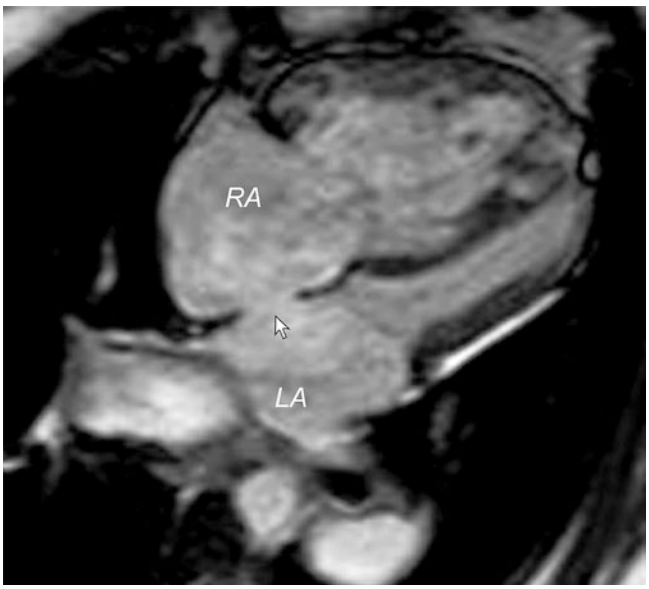

Fig. 20.3 ECG-triggered steady-state free precession cine CMR in the four-chamber plane showing a secundum atrial septal defect (arrow). Note the dilated right atrium (RA) and right ventricle. LA, left atrium

In patients with known or suspected ASDs, left and right ventricular size and systolic function should be quantified by acquiring a stack of cine steady-state free precession images in a ventricular short-axis plane. This image series also allows one to make a qualitative estimate of right ventricular systolic pressure based on the configuration of the ventricular septum. The septal geometry is concave toward the right ventricle when the right ventricle-to-left ventricle pressure ratio is low and assumes a flat configuration, or even a concave shape toward the left ventricle, as the right ventricle-to-left ventricle pressure ratio increases. Interpretation of the septal configuration may be confounded by factors such as dyssynchronous contraction of the right ventricle, intraventricular conduction delay (e.g., right or left bundle branch block, preexcitation), and a high left ventricular pressure.

Measurement of the Qp/Qs ratio is clinically useful in patients with ASDs. Multiple studies have shown that VEC CMR calculation of the Qp/Qs ratio by measuring flow in the main pulmonary artery (Qp) and ascending aorta (Qs) agrees closely with catheterization-based oximetry measurements of Qp/Qs [46–49]. In the absence of significant valve regurgitation or an additional shunt, Qp/Qs can also be derived from the right (Qp) and left (Qs) ventricular stroke volumes calculated from the short-axis cine stack of the ventricles. In clinical practice, it is recommended to measure the Qp/Qs ratio by both of these methods and check the data for consistency.

Several studies have assessed the role of CMR in evaluating ASDs. Early reports utilized conventional spin-echo imaging to compare the apparent defect size with measurements made at surgery and yielded generally good agreement [50–52]. A later study, however, showed that conventional spin-echo imaging in planes perpendicular to the ASD overestimated the defect due to "signal dropout" in the thin portion of the septum [53]. Alternatively, ASD size and shape can be delineated by performing VEC CMR carefully positioned in the plane of the ASD to visualize the defect en face [53, 54]. Several studies which compared the

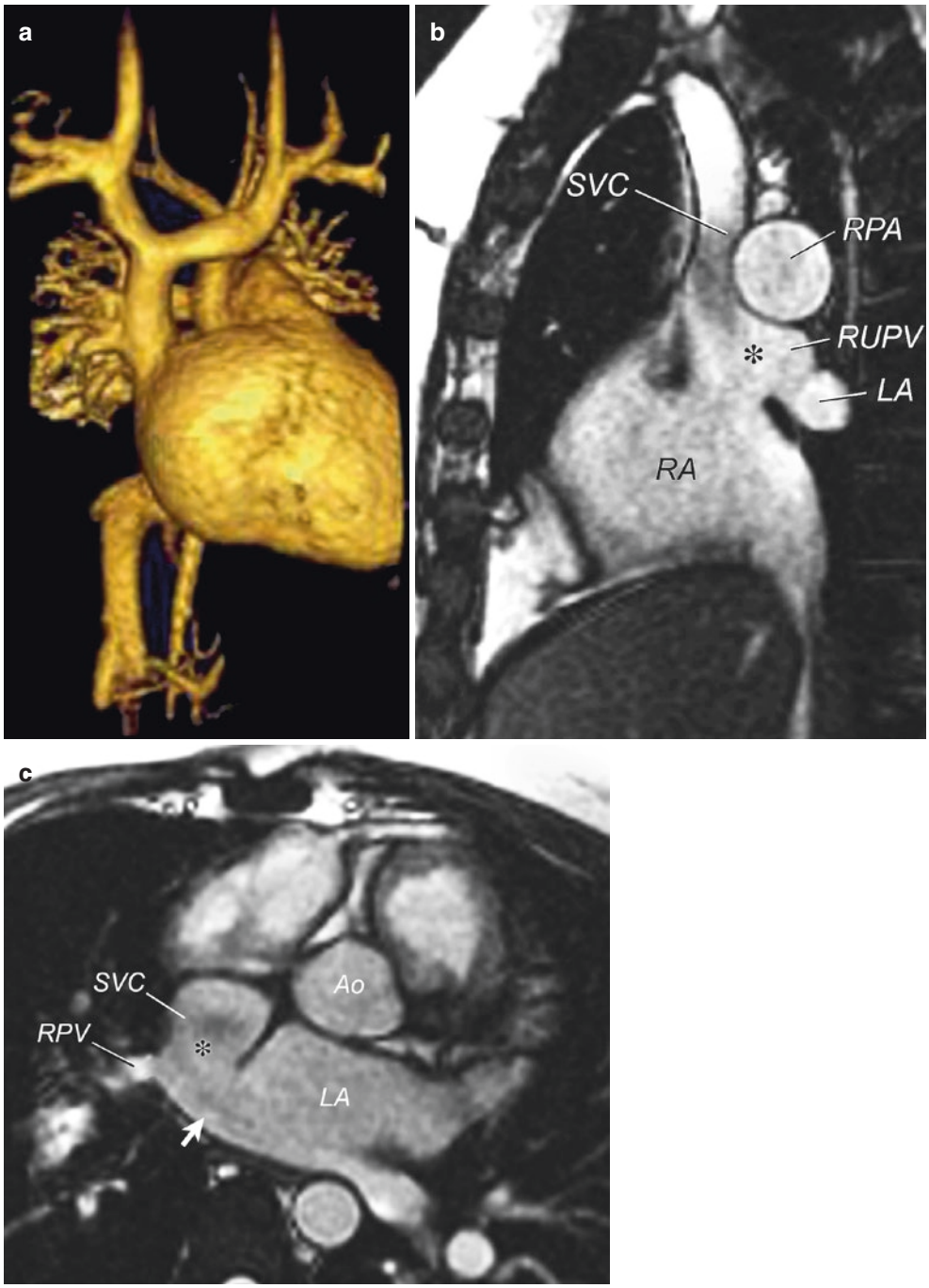

Fig. 20.4 Sinus venosus defect. (**a**) Three-dimensional reconstruction of gadolinium-enhanced 3D MRA showing several pulmonary veins from the right upper lobe draining into the superior vena cava. (**b**) ECG-triggered steady-state free precession cine MR in the sagittal plane showing the defect (*) between the right upper pulmonary vein (RUPV) and the superior vena cava (SVC). (**c**) ECG-triggered steady-state free precession cine CMR in the axial plane showing the defect between the RUPV and the SVC (*). The arrow points to the left atrial orifice of the RUPV. Left-to-right shunt results from drainage of the RUPV to the SVC and from left atrial blood entering the right atrium (RA) through the orifice of the RUPV (arrow) and the unroofed wall between the RUPV and the SVC (*). Ao, ascending aorta; LA, left atrium

assessment of ASDs by CMR versus transesophageal echocardiography showed that CMR is an acceptable noninvasive alternative [55–58]. In these studies, CMR was able to accurately estimate ASD size, shape, proximity to adjacent structures, and associated findings (e.g., anomalous pulmonary venous return). Transesophageal echocardiography is probably superior for measurement of defect rims, but measurements by CMR were usually within 5 mm [56]. When imaging is inconclusive by transthoracic echocardiography, CMR can be a noninvasive alternative to transesophageal echocardiography for determining which patients are candidates for percutaneous device closure rather than surgery [58, 60, 63, 64].

Ventricular Septal Defects

Anatomy

A VSD is a communication between the right and left ventricles through an opening in the ventricular septum. It is one

of the most common forms of congenital heart disease and is found frequently in association with complex heart disease. This section will focus on VSDs in the absence of complex congenital heart disease.

Several VSD anatomic classification systems are in use. Figure 20.5 shows one such system modified from Van Praagh et al., which includes the following: (1) defects at the junction between the conal septum and the muscular septum, which may be confined to the membranous portion (referred to as membranous or perimembranous defects) or associated with malalignment of the conal septum (conoventricular defects), (2) defects in the muscular septum (called muscular or trabecular defects), (3) defects in the inlet septum (known as atrioventricular canal-type or inlet defects), and (4) defects in the outlet septum (variably called outlet, doubly committed subarterial, subpulmonary, conal septal, or supracristal defects) [59].

Clinical Course and Management

The natural history of a VSD is related to the size and location of the defect. Defects in the membranous or muscular septum often become smaller over time and may spontaneously close. In contrast, malalignment conoventricular defects, outlet septum defects, and atrioventricular canal-type defects are usually large and remain so. Consequently, such patients often undergo surgical closure in infancy. Venturi effects associated with VSDs in the membranous or outlet septum may cause aortic valve leaflets (usually the right coronary cusp) to prolapse through the defect. Although the leaflet prolapse typically reduces the effective orifice size of the defect, this may also lead to aortic insufficiency. VSDs, particularly those associated with turbulent flow jets, also predispose patients to the development of endocarditis.

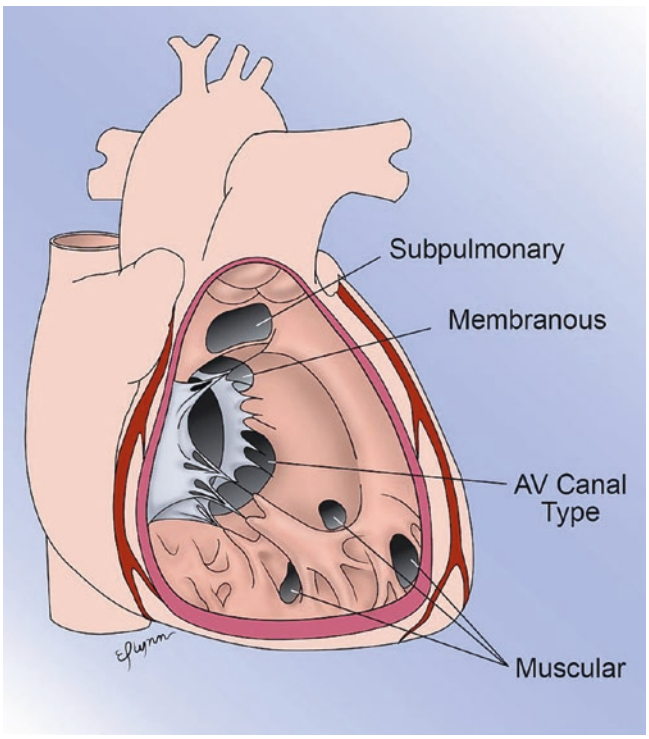

Fig. 20.5 Anatomic types of ventricular septal defects (see text for details)

Symptoms are predominantly determined by the size of the shunt through the VSD, which, in turn, is related to the defect size and the relative resistances of the pulmonary vascular and the systemic vascular beds. In most situations, pulmonary resistance is lower than systemic resistance, and there is a left-to-right shunt. The resulting increased blood flow to the lungs and left heart may lead to dilation of the pulmonary arteries, pulmonary veins, left atrium, and left ventricle. Because most of the shunt flow passes through the VSD into the right ventricle in systole, right ventricular dilation is usually not present. If the shunt is small and the patient is asymptomatic, an intervention to close the defect is not warranted. When the shunt is large, symptoms from pulmonary overcirculation (e.g., tachypnea, diaphoresis, poor feeding, and slow weight gain) may develop in the first few months of life. If the defect is unlikely to become small over time or if these symptoms cannot be managed medically, surgical closure in infancy is recommended. Untreated, patients with VSDs and large left-to-right shunts may develop irreversible pulmonary hypertension from elevated pulmonary vascular resistance. In such cases, the flow through the defect will become increasingly right to left resulting in cyanosis (Eisenmenger syndrome). Occasionally, one may encounter older patients with VSDs of intermediate size who are minimally symptomatic and have normal pulmonary artery pressure yet have a large enough shunt to result in left ventricular dilation. VSD closure is probably warranted under these circumstances given its low risk and the potential beneficial impact on ventricular function in long term.

A surgical approach is by far the most common technique used to close VSDs and carries a low mortality risk even when performed in the first few months of life [60]. Typically, the surgeon works through the tricuspid valve and applies a patch to cover the defect. Experience with transcatheter delivery of occlusion devices is growing, and this approach may be appropriate in selected circumstances [61, 62].

CMR Evaluation

Transthoracic echocardiography is the primary diagnostic imaging modality in patients with suspected or known VSDs and is usually adequate. Occasionally in larger patients, acoustic windows may be insufficient, and CMR is indicated to define the defect size and location as well as identify associated conditions such as aortic valve prolapse. CMR may also be of use when the hemodynamic burden of a defect is uncertain by providing reliable quantitative data on the Qp/Qs ratio and ventricular dimensions and function.

VSD location and size can be demonstrated by cine gradient-echo or spin-echo sequences [63–65]. Very small defects may be difficult to resolve; however, the associated turbulent flow can be made conspicuous on gradient-echo sequences provided the echo time is long enough to allow for sufficient spin dephasing (Fig. 20.6, Video 20.3). It is useful to assess the ventricular septum using stacks of images oriented in at least two planes. The four-chamber plane provides base-to-apex localization, whereas the short-axis plane shows the location in the anterior-to-posterior axis (Fig. 20.7, Video 20.4). Additional imaging in other planes can be used as needed to demonstrate defect position relative to key adjacent structures (e.g., atrioventricular or semilunar valves). Bremerich et al. have reported that CMR is an important, noninvasive test in the diagnosis and management of defects in the outlet septum as echocardiography was felt to inadequately image this region of the ventricular septum [66]. Yoo et al. demonstrated how CMR can provide an "en face" view of a VSD, which is particularly advantageous in complex anatomy, such as double-inlet ventricle with transposed great arteries in which systemic blood flow is dependent on passage through the defect [67, 68]. ECG and navigator-gated isotropic three-dimensional steady-state free precession sequences can be useful in assessing intracardiac anatomy in patients with congenital heart disease. The resulting high-resolution block of anatomic data can be reformatted in multiple planes to characterize VSDs and other abnormalities [69].

Measurement of ventricular dimensions and function is also a key element of the CMR evaluation in a patient with a VSD. This can be done from the ventricular short-axis cine CMR image stack mentioned above. Typically, larger left-to-right shunts will result in left ventricular dilation but not right ventricular dilation. Ventricular systolic function is usually normal. As described in the section on ASDs above, ventricular septal configuration can be used to estimate right ventricular pressure. Finally, quantification of the VSD shunt should be performed by calculating the Qp/Qs ratio. This can be accomplished by measuring the net blood flow in the main pulmonary artery (Qp) and the ascending aorta (Qs) using VEC CMR [47, 49, 70]. Alternatively, in the absence of significant valve regurgitation or other shunts, the ventricular volumetric data can be used. The Qp/Qs ratio is equal to right ventricular stroke volume divided by left ventricular stroke volume. In practice, both approaches are recommended, and the two results should be compared for consistency.

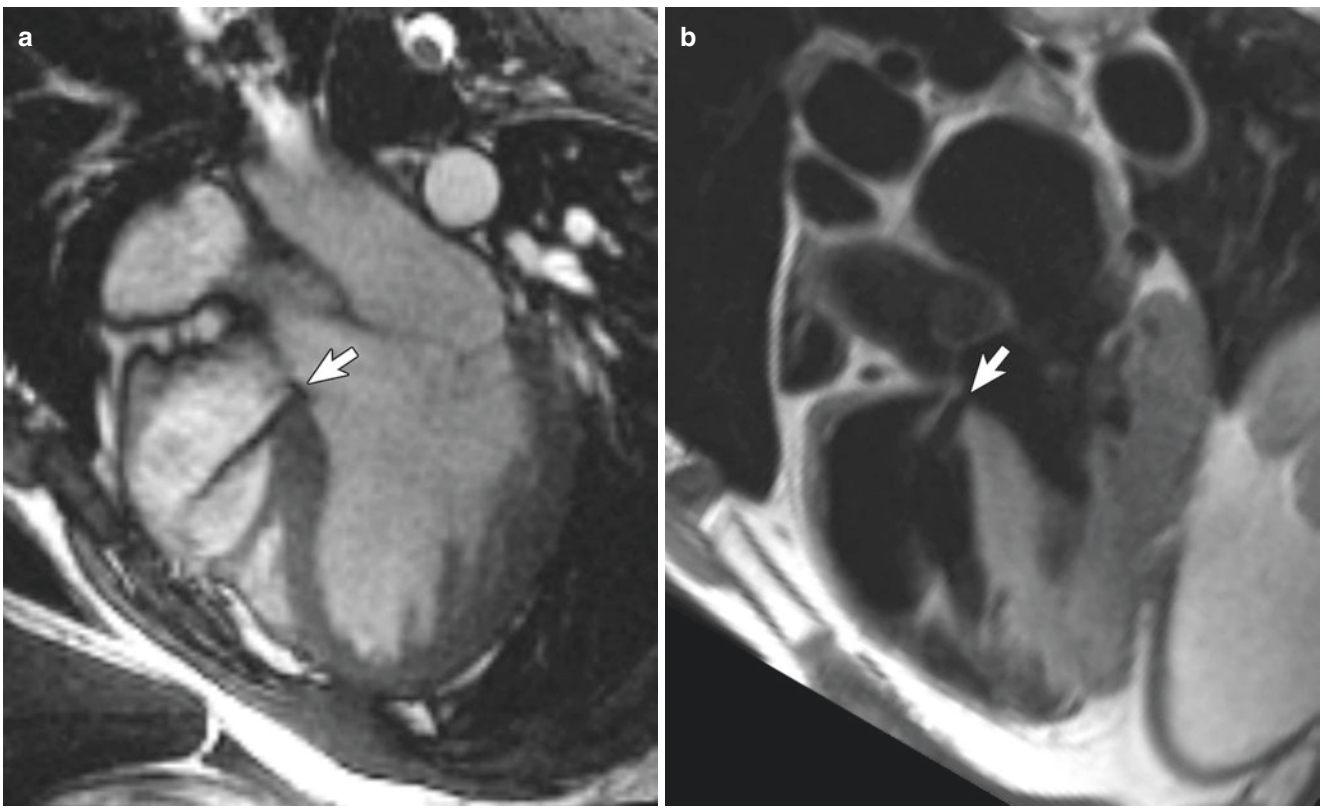

Fig. 20.6 Membranous ventricular septal defect (arrow). (**a**) ECG-triggered steady-state free precession cine CMR in a four-chamber plane showing the defect and associated flow jet into the right ventricle. (**b**) ECG-gated fast spin-echo image in a four-chamber plane

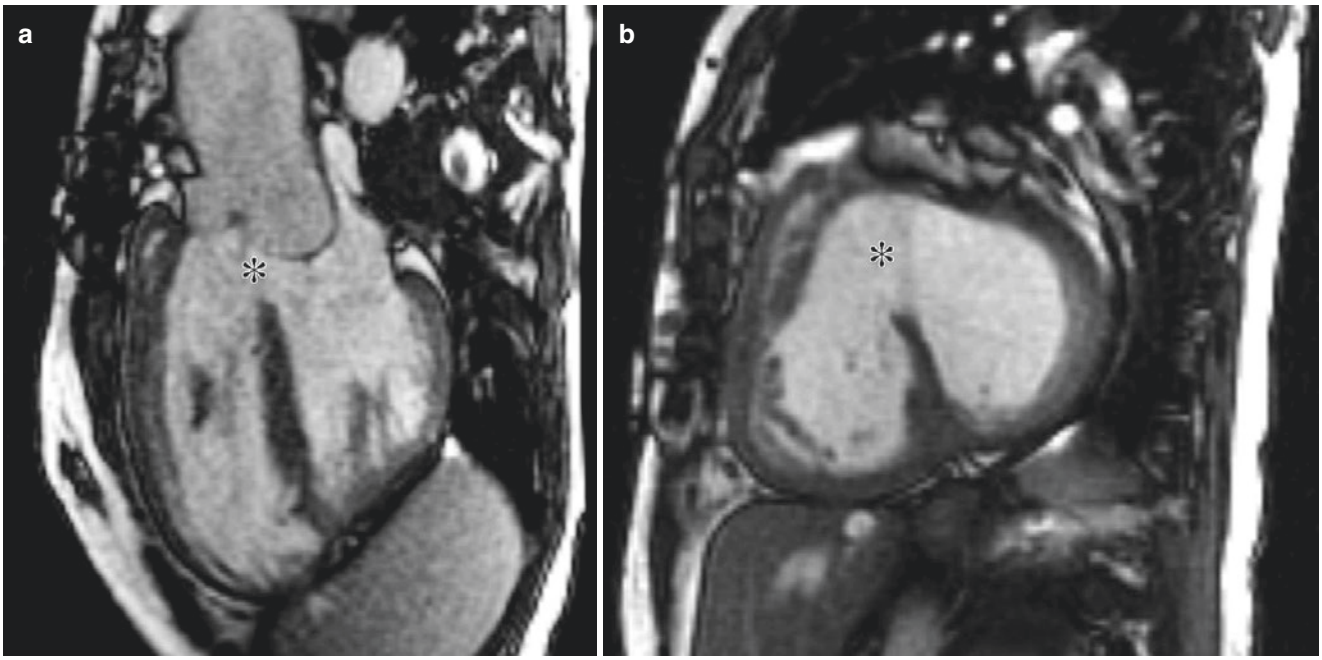

Fig. 20.7 Malalignment conoventricular septal defect (*) imaged with ECG-triggered steady-state free precession cine CMR in ventricular long-axis (**a**) and short-axis (**b**)

Patent Ductus Arteriosus

Anatomy, Clinical Course, and Management

The ductus arteriosus is a vascular channel that usually connects the aortic isthmus with the origin of either the left or the right pulmonary artery. During fetal life, the ductus arteriosus allows the majority of the right ventricular output to bypass the lungs by carrying blood flow to the descending aorta. Normally, the ductus arteriosus closes shortly after birth. It may persist in patients with congenital heart disease allowing communication between the systemic and pulmonary circulations. A persistent PDA is common in premature infants and is associated with increased morbidity. In full-term infants and children, the clinical course and sequelae of an isolated PDA are usually related to the ductus size and the direction of flow. In the absence of elevated pulmonary vascular resistance, isolated PDAs have left-to-right flow leading to increased pulmonary flow and a volume load to the left heart. Larger PDAs cause a significant left-to-right shunt and, if untreated, lead to pulmonary overcirculation, respiratory distress, growth failure, and, eventually, pulmonary vascular disease. Smaller ducts place the patient at some minor risk for infective endarteritis. The benefit of closing clinically silent PDAs in the older children or adults is debated [71]. This can be accomplished either surgically or in the catheterization laboratory using occluding devices.

CMR Evaluation

CMR is seldom requested primarily for assessment of an isolated PDA as this usually presents in childhood and is a straightforward echocardiographic diagnosis. In several types of complex congenital heart disease, evaluation of the ductus arteriosus is an important element of the examination. For example, in patients with tetralogy of Fallot and pulmonary atresia, the ductus arteriosus may persist and be a significant source of pulmonary blood supply. A gadolinium-enhanced 3D MRA is a particularly helpful imaging technique in these patients because it allows accurate delineation of all sources of pulmonary blood supply, including a PDA, aortopulmonary collaterals, and the central pulmonary arteries (Fig. 20.8, Video 20.5) [72]. Cine CMR is also useful in detecting PDAs, particularly those which are small with turbulent flow. As with VSD jets, a longer echo time will allow more time for spin dephasing and make the turbulent flow more conspicuous. When a PDA is detected, VEC CMR is useful to evaluate the direction of flow across the ductus and quantify the Qp/Qs ratio. Note that with a PDA and no other shunting lesions, systemic flow (Qs) is equal to the main pulmonary artery flow and pulmonary flow (Qp) is equal to ascending aorta flow. In patients with a PDA, it is also helpful to measure ventricular volumes and function and assess right ventricular pressure by evaluating ventricular septal position in systole.

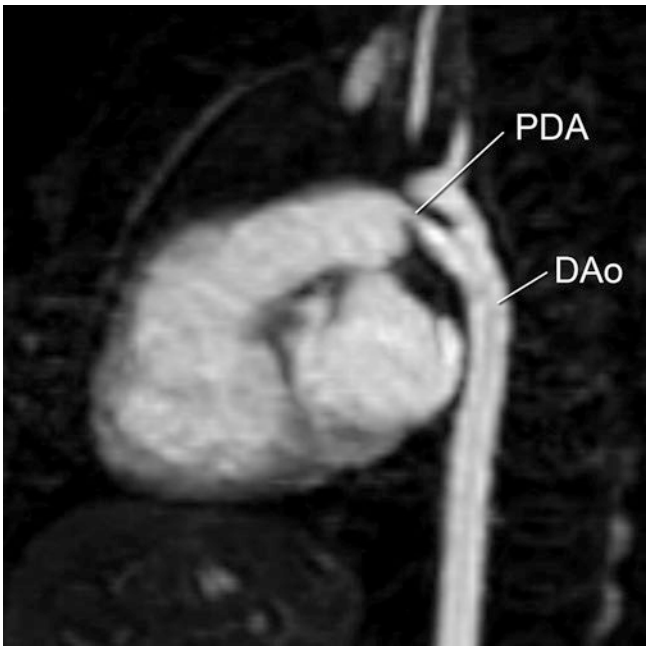

Fig. 20.8 Gadolinium-enhanced 3D MRA (oblique sagittal subvolume maximal intensity projection) in an infant illustrating a patent ductus arteriosus (PDA). DAo, descending aorta

Partially Anomalous Pulmonary Venous Connection

Anatomy

In PAPVC, one or more but not all of the pulmonary veins connect to a systemic vein. PAPVC may be seen in isolation or as a component in complex congenital heart lesions, particularly heterotaxy syndrome with polysplenia. There is wide variability in the number of abnormal veins, the site of their termination, and the caliber of the associated connecting vessels. A detailed description of the variety of lesions captured by this diagnosis may be found elsewhere [73]. Common PAPVC types include anomalous connection to the left innominate vein, to the right superior vena cava, to the azygous vein, or to the inferior vena cava. Anomalous connection of some or all of the right pulmonary veins to the inferior vena cava is termed scimitar syndrome. The name is derived from the curvilinear shadow in the right lung on chest radiography caused by the anomalous vein as it descends toward the right hemidiaphragm which resembles a scimitar or Turkish sword. Other abnormalities commonly seen in scimitar syndrome include hypoplasia of the right lung and pulmonary artery, secondary dextrocardia, and anomalous systemic arterial supply usually from the descending aorta to the right lung [74].

Clinical Course and Management

PAPVC results in a left-to-right shunt – blood draining from the lungs returns to the lungs via the systemic veins and right heart without passing through the systemic arterial circulation. This physiology leads to increased pulmonary blood flow and resembles that of an ASD. The magnitude of the shunt is determined by the number of involved veins, the site of their connections, the pulmonary vascular resistance, and the presence of associated defects. Dilation is commonly seen in the systemic veins downstream of the anomalous pulmonary vein insertion site, the right atrium and ventricle, and the pulmonary arteries. Young patients are usually asymptomatic, while dyspnea on exertion becomes increasingly common in the third and fourth decades of life. Development of pulmonary hypertension is very rare. Patients may come to attention after auscultation of a pulmonary flow murmur or when diagnostic imaging is performed for another indication. Evidence of right ventricular volume overload with no apparent intracardiac shunt should prompt a search for PAPVC. The presentation of scimitar syndrome varies widely depending on the severity of the associated abnormalities. Infants may be critically ill with respiratory compromise, whereas adults may have minimal symptoms. Pulmonary hypertension may develop from a combination of stenosis of the pulmonary veins, arterial blood supply from the descending aorta, pulmonary hypoplasia, and parenchymal pulmonary abnormalities.

For the most part, anomalous veins can be surgically corrected, but the likelihood of success and probable benefits must be weighed carefully. A single small anomalous pulmonary vein is associated with a modest left-to-right shunt and does not require intervention [75]. In those with much or all of the left pulmonary veins returning to the left innominate vein, the connecting vertical vein is usually large and long enough to detach from the innominate vein and anastomose to the left atrium. For veins connecting to the superior vena cava, a baffle within the superior vena cava and across the atrial septum can be constructed to channel the pulmonary venous return to the left atrium. Alternatively, the superior vena cava can be transected superior to the anomalous veins and the caval end anastomosed to the right atrial appendage. A baffle across the atrial septum is then created to direct the pulmonary venous flow in the cardiac end of the superior vena cava to the left atrium. Pulmonary veins entering the inferior vena cava can either be baffled through the right atrium to the left atrium or directly anastomosed to the left atrium. The most common postoperative complications seen in patients with PAPVC correction are obstruction and residual leaks in the surgically created pathways.

CMR Evaluation

The acoustic properties of lung tissue may make it difficult by echocardiography to trace possible anomalous veins back into the lungs to confirm that they are pulmonary rather than systemic veins. If a clinical concern for PAPVC cannot be resolved by echocardiography with confidence, CMR is the next most appropriate diagnostic imaging test.

The goals of CMR evaluation of PAPVC include precise delineation of the anatomy and quantification of the imposed hemodynamic burden. Gadolinium-enhanced 3D MRA is an effective and efficient technique to define the thoracic vasculature anatomy including the pulmonary veins, pulmonary arteries, and aortopulmonary collateral vessels (Figs. 20.9 and 20.10, Videos 20.6 and 20.7). The image data set can be reformatted in any plane to illustrate spatial relationships and has sufficient resolution to detect vessels <1 mm. For added diagnostic confidence, additional imaging of the vascular anatomy can be obtained using cine CMR or fast spin-echo with blood signal nulling sequences.

Several studies assessing the accuracy and utility of gadolinium-enhanced 3D MRA for PAPVC have shown similar results [76–78]. There was high level of agreement between findings on MR angiography compared with surgical inspection and x-ray angiography. MR angiography was uniformly more accurate than transthoracic and transesophageal echocardiography. CMR studies often diagnosed previously unknown PAPVC or added new clinically important information regarding PAPVC anatomy.

Fig. 20.10 Gadolinium-enhanced 3D MRA (oblique coronal subvolume maximal intensity projection) in an adult with scimitar syndrome

Fig. 20.9 Gadolinium-enhanced 3D MRA (oblique coronal subvolume maximal intensity projection) illustrating partially anomalous pulmonary venous connection of the left upper pulmonary vein (arrow) to the left innominate vein

Patients with PAPVC should also have their ventricular dimensions and function measured by CMR. Particular attention should be devoted to quantifying right ventricular end-diastolic volume, as this should be proportional to the size of the left-to-right shunt. The shunt should also be measured directly by obtaining VEC CMR flow measurements in the main pulmonary artery (Qp) and the ascending aorta (Qs). In some cases, it may also be possible to measure the flow in the anomalously draining vein itself. In the absence of significant valvular insufficiency, the ventricular stoke volume differential should be equal to the shunt size and thus serves as a useful check. It is worth noting that in patients with PAPVC, Qp/Qs ratio measurements by oximetry in the catheterization laboratory are inherently inaccurate because of the difficulty in obtaining a reliable, representative mixed systemic venous saturation. Because blood flow is measured directly, these concerns do not apply to CMR measurements. In cases where there is a hypoplastic pulmonary artery or pulmonary venous pathway obstruction, it is also useful to calculate differential pulmonary blood flow using VEC CMR measurements in the branch pulmonary arteries.

Coarctation of the Aorta

Anatomy

Coarctation of the aorta is a discrete narrowing most commonly located just distal to the left subclavian artery, at the site of insertion of the ductus arteriosus. It is thought to arise either from an abnormal flow pattern through the arch during development or from extension of ductal tissue into the aortic wall. Hypoplasia and elongation of the distal transverse arch is a frequent association. Coarctation may be present alone or in combination with other heart lesions including bicuspid aortic valve (the most frequent associated intracardiac defect), aortic stenosis (valvular or subvalvular), mitral valve abnormalities, ASD, VSD, persistent PDA, and conotruncal anomalies [79, 80].

Clinical Course and Management

Infants tend to present with symptoms of heart failure and systemic hypoperfusion as the ductus arteriosus closes; if untreated, they may progress to shock or death. Older children and adults typically have isolated coarctation and are usually relatively asymptomatic. A heart murmur, systemic hypertension, or rib notching on a chest x-ray from collateral vessels often leads to the diagnosis. Even in asymptomatic patients, relief of the aortic obstruction is indicated for hemodynamically significant lesions because of the high rate of late complications including congestive heart failure, systemic hypertension, premature coronary artery disease, ruptured aortic or cerebral aneurysms, stroke, aortic dissection, infective endarteritis, and premature death [81].

Therapeutic options for coarctation include surgical repair and percutaneous balloon angioplasty and stent placement. Currently, resection of the coarctation with an end-to-end anastomosis and augmentation of the transverse arch if needed is the most widely practiced surgical repair and has the lowest incidence of recurrent obstruction. Other approaches have included subclavian flap aortoplasty, patch augmentation, and conduit interposition. These latter techniques have fallen out of favor as postoperative complications, such as aneurysm formation at the site of the prosthetic patch and recurrent arch obstruction, have become increasingly recognized [82, 83]. Coarctation in infants is treated surgically in the majority of centers because of the lower risk of residual obstruction, recurrence, and technique-related complications compared with percutaneous interventions [84]. For isolated coarctation, the surgical mortality approaches zero [85]. In the event of recurrent coarctation following surgical repair, balloon angioplasty with or without stent placement is often the first line of therapy. Coarctation in older children or adults is increasingly being treated primarily by percutaneous interventions [86, 87]. Regardless of the initial treatment, subsequent surveillance is warranted [6]. A recent long-term follow-up study [93] of 247 patients after repaired coarctation found restenosis in 31%, and discrete aneurysm formation in 9%, usually after a patch repair [88].

CMR Evaluation

Transthoracic echocardiography is usually the only diagnostic imaging needed for evaluation of young children with suspected coarctation or following intervention for coarctation. With increasing age, acoustic windows typically deteriorate leading to an incomplete anatomic assessment by echocardiography. In these circumstances, CMR is able to provide high-quality anatomic imaging of the aortic arch in its entirety, an assessment of the hemodynamic severity of the obstruction, and evaluation of left ventricular mass and function. In a retrospective study of 84 adult patients following intervention for coarctation of the aorta, Therrien et al. showed that the combination of clinical assessment and CMR on every patient was more "cost-effective" for detecting complications than combinations that relied on echocardiography or chest radiography as imaging modalities [89]. Other studies have shown the utility of CMR in infants and children with coarctation and other anomalies of the aortic arch [90–92]. Computed tomography can also provide excellent anatomic imaging of the aorta but has the disadvantage of ionizing radiation exposure making it a less attractive modality for serial follow-up.

A comprehensive CMR evaluation of patients with suspected coarctation or following intervention for coarctation includes assessment of aortic anatomy; cine CMR sequences to measure ventricular size, function, and mass; and VEC CMR sequences to evaluate the severity of obstruction. With regard to aortic anatomy, attention should be given to the transverse aortic arch and isthmus, brachiocephalic vessels, collateral vessels that may bypass obstruction, and possible aneurysms or dissections at the repair sites. Regions of vessel narrowing should ideally be measured in cross section as elliptical segments are common. If a coarctation is present, its diameter, length, and distance to neighboring vessels should be reported as this may influence decisions regarding percutaneous intervention. Given the association of a bicuspid aortic valve with coarctation, the aortic valve morphology should be noted as well as the dimensions of the aortic root and ascending aorta.

Gadolinium-enhanced 3D MRA is an efficient technique to assess aortic anatomy (Fig. 20.11, Video 20.8a, b). Using subvolume maximal intensity projections and reformatting, most of the relevant anatomic issues can be addressed and measurements performed [13, 93–95]. Cine CMR of the aortic arch in long-axis is useful to identify the sites of obstruction because the associated high-velocity turbulent jets produce systolic signal voids. Cine CMR is also helpful for assessment of the aortic valve morphology and aortic root

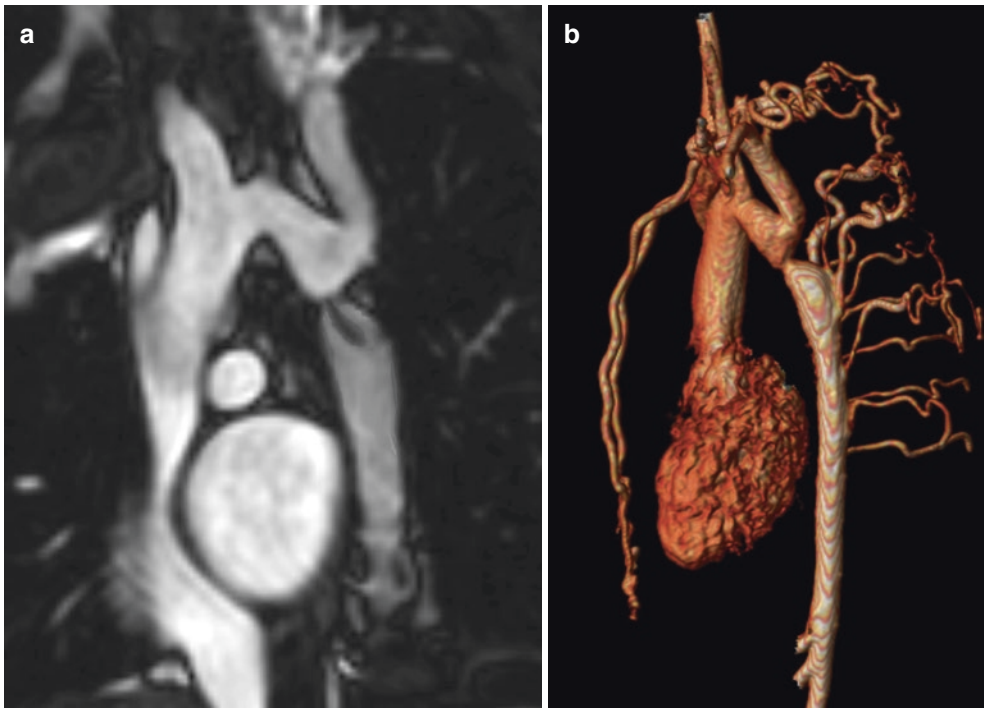

Fig. 20.11 Aortic coarctation. (**a**) Cine CMR (oblique sagittal plane) showing elongation and hypoplasia of the distal transverse arch and severe discrete narrowing at the isthmus. Note the flow jet at the isthmus. (**b**) Volume-rendered gadolinium-enhanced 3D MRA in the same patient revealing several tortuous collateral vessels and dilated internal mammary arteries

dimensions. Finally, turbo spin-echo sequences with nulling of the blood signal can be used to produce high-resolution, high-contrast images of the aorta. They are particularly valuable following endovascular stent placement because there is less metallic susceptibility artifact than with gradient-echo sequences. For anatomic definition of the coarctation site, multiple investigators have demonstrated good correlation between these various CMR imaging techniques and x-ray angiography [101].

CMR evaluation of coarctation should also include calculation of left ventricular dimensions, systolic function, mass, and mass-to-volume ratio. This data is clinically relevant because hypertension is often present and may lead to ventricular hypertrophy and dysfunction. Upper body hypertension may be caused by aortic arch obstruction, but systemic hypertension is also prevalent following coarctation repair even without residual coarctation, particularly in patients who had surgery later in life. It is good practice to measure upper and lower extremity cuff blood pressures at the time of the CMR examination to help identify patients with hypertension and estimate the pressure gradient across any aortic obstruction. Note that there may be little upper-to-lower extremity blood pressure differential even with important aortic obstruction when there is a significant collateral circulation bypassing the obstruction.

VEC CMR measurements have been used to gain insight into the functional significance of an obstruction. One approach has been to assess the flow pattern in the descending aorta distal to the coarctation and preferably at the level of the diaphragm [96]. Characteristics suggestive of a hemodynamically significant coarctation include decreased peak flow, decreased time-averaged flow, delayed onset of descending aorta flow compared with the onset of flow in the ascending aorta, decreased acceleration rate, increased collateral flow in the descending aorta, and prolonged deceleration with increased antegrade diastolic flow [97–99, 101]. A model to predict the probability of a hemodynamically significant coarctation pressure gradient (defined as ≥20 mm Hg measured during cardiac catheterization) was developed at our institution [100]. A combination of the smallest cross-sectional area of the aorta (measured from the gadolinium-enhanced 3D MRA) and the heart rate-adjusted mean deceleration of flow in the descending aorta (measured by VEC CMR distal to the coarctation) predicted a gradient ≥20 mm Hg with 95% sensitivity and 82% specificity, 90% positive and negative predictive values, and an area under the receiver-operator characteristics curve of 0.94. Subsequently, a multicenter study confirmed the utility of these two parameters and simplified the prediction formula [101].

Another approach to assessing coarctation severity is to measure the peak coarctation jet velocity and estimate a pressure gradient using the modified Bernoulli equation. Mohiaddin et al. compared the peak coarctation jet velocity measured by VEC CMR with that obtained by continuous wave Doppler and found a high correlation ($r = 0.95$) as well as close agreement (mean difference = 0.12 ± 0.23 m/s) [98]. Nevertheless, they note that such measurements are technically difficult in a long, tortuous coarctation segment

and that such pressure estimates may not be indicative of anatomic severity because of collateral flow. In support of the latter notion, they found a poor inverse correlation between peak coarctation jet velocity and coarctation diameter ($r = -0.48$). Consequently, they performed additional VEC CMR flow measurements in the ascending and descending aorta distal to the coarctation. Compared to controls, coarctation patients had a significantly lower descending-to-ascending aorta flow ratio as well as a smaller, more blunted descending aortic flow profile. Similarly, Steffens et al. found that although there was close correlation between gradients obtained by VEC CMR and Doppler echocardiography ($r = 0.95$), both methods showed poorer correlation with cuff blood pressure gradients ($r = 0.63$ for Doppler echocardiography and $r = 0.54$ for PVC CMR) [99]. In an effort to improve accuracy, Oshinski et al. proposed that the Bernoulli equation be adapted to take into account hemodynamic variables associated with stenosis severity [102]. More recently, three-dimensional VEC CMR (4D flow) has been used to measure pressure differences across any vascular structure [103, 104]. Riesenkampff et al. used 4D flow techniques to noninvasively estimate the pressure drop across 5 locations in the aortic arch in 13 patients with coarctation and compared these results with directly measured values in the catheterization laboratory [104]. They found good agreement with the correlation coefficients ranging between 0.86 and 0.97 ($p < 0.001$).

Finally, VEC CMR has been used to quantify collateral flow entering the descending aorta distal to the obstruction via retrograde flow from the intercostal arteries or vessels arising off the aortic arch and arch branches in coarctation patients [99, 105–107]. Increased collateral flow suggests more severe obstruction. Moreover, higher collateral flow would be expected to decrease the likelihood of spinal cord ischemic injury during surgical correction, which involves interruption of aortic flow. If little collateral flow is suspected, the surgeon may elect to perform left heart bypass to the descending aorta during the repair. Steffens, et al. quantified collateral flow entering the descending aorta via retrograde flow from the intercostal arteries by performing flow measurements slightly distal to the coarctation site and at the level of the diaphragm [99]. Total flow from proximal to distal descending aorta decreased by 7 ± 6% in normal volunteers compared to an increase of 83 ± 50% in patients with moderate to severe coarctation ($p < 0.01$). The amount of flow increase in the distal aorta correlated directly with the severity of anatomic narrowing ($r = 0.94$) and the extremity cuff blood pressure gradient ($r = 0.84$). Nevertheless, the added clinical benefit of this approach is unclear since the extent of collateral flow necessitating left heart bypass to prevent spinal cord ischemic injury during surgical correction has not been defined.

Vascular Rings

Anatomy

A vascular ring is a congenital anomaly of the aortic arch which results in complete encirclement of the trachea and esophagus. The encircling structures may be patent vessels or fibrous remnants such as the ductal ligament or an atretic segment of the aorta [108]. Vascular rings can occur as an isolated anomaly but are also associated with chromosome 22q11 deletions, conotruncal cardiac defects, and other noncardiac anomalies [109]. There are several different anatomic combinations that can form a vascular ring. As this is not intended to be a comprehensive discussion of every type of vascular ring, we will highlight two of the more common types: (1) double aortic arch and (2) right aortic arch with an aberrant left subclavian artery.

In a double aortic arch, both the embryonic right and left arches persist, arising from the ascending aorta, passing on both sides of the trachea and esophagus, and joining posteriorly to form the descending aorta (Fig. 20.12, Video 20.9). Both the trachea and esophagus are therefore completely encircled by aortic structures. The carotid and subclavian arteries will typically arise separately in a symmetric fashion with the carotid and subclavian arteries arising from the ipsilateral arch. In approximately 75% of cases, the right arch is the dominant and larger arch and is typically higher as well [111]. Occasionally, a segment of the arch between the carotid and subclavian arteries or between the subclavian artery and the descending aorta may be hypoplastic or ligamentous (not patent). Note that even a ligamentous segment can contribute to the ring; however, it is usually not visible by any imaging modality; so its presence must be inferred by the tenting of the adjoining segments toward each other, the identification of a dimple or diverticulum at its attachment sites, or tracheal narrowing.

Another common form of vascular ring is a right aortic arch with an aberrant origin of the left subclavian artery. In this case, the left subclavian artery arises as the last branch from the aortic arch and courses posterior to the esophagus to reach the left arm. A vascular ring is present if there is a persistent left-sided ductal ligament from the base of the left subclavian artery that courses to the left of the trachea and connects to the proximal left pulmonary artery (Fig. 20.13, Video 20.10). As mentioned above, ligamentous structures cannot be visualized, but the clue to its presence is the bulbous dilatation at the base of the left subclavian artery, termed the diverticulum of Kommerell. Thus, the ring is comprised of the right arch, the diverticulum, and the left-sided ductal ligament. In cases in which the ductal ligament is only right-sided – from the descending aorta to the right pulmonary artery – there is no encirclement and no diverticulum at the base of the left subclavian artery.

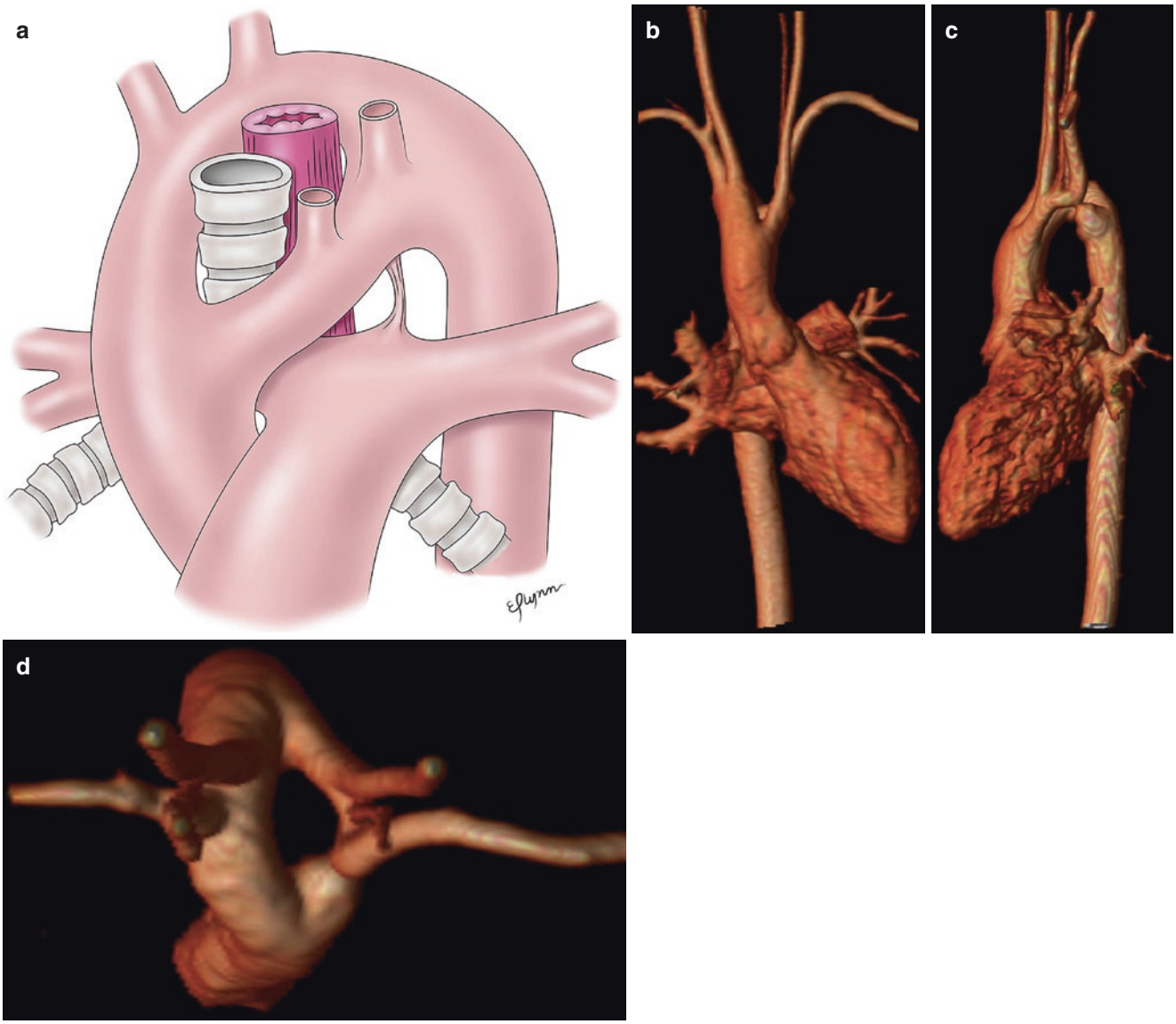

Fig. 20.12 Vascular ring comprised of a double aortic arch. (**a**) Diagram. Volume-rendered gadolinium-enhanced 3D MRA shown from anterior (**b**), left (**c**), and superior (**d**) perspectives. In this patient the left common carotid artery arises from the transverse arch, and there is a coarctation distal to the left subclavian artery takeoff (Reprinted with permission from Powell [110])

Clinical Course and Management

The degree of trachea and esophagus compression from a vascular ring is variable and accounts for the variety of clinical manifestations. Patients with more significant compression will often present in infancy with respiratory symptoms of stridor, dyspnea, and/or a barking cough [112–115]. It is not uncommon for the diagnosis to be delayed as clinicians focus on other respiratory etiologies including asthma and bronchomalacia. Symptoms related to esophageal compression are less frequent and include vomiting, choking, and chronic feeding difficulties. Occasionally, older children and adults will describe dysphagia or difficulty eating solids compared to liquids, suggesting the diagnosis of a vascular ring.

In vascular ring patients with minimal symptoms and minimal tracheal compression, no intervention is required. In those with respiratory- or airway-related symptoms, surgical division of the ring is performed. Tomographic imaging by CMR or computed tomography is very helpful for determining the surgical approach – left versus right thoracotomy – and open versus thoracoscopic approach. In a double aortic arch, usually the smaller arch and any ductal ligament on that side are divided. In a right aortic arch with an aberrant origin of the left subclavian artery, the ductal ligament is

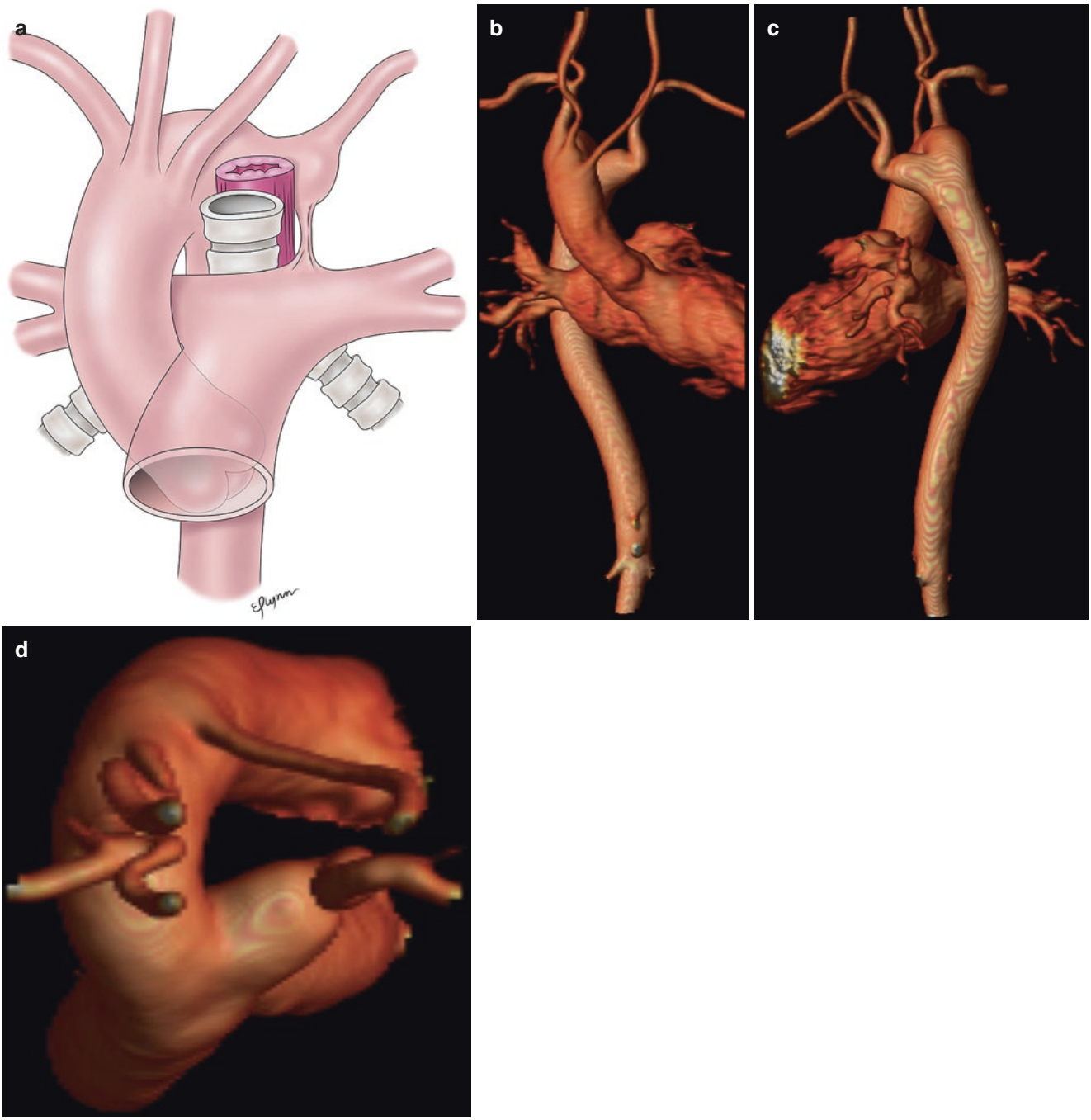

Fig. 20.13 Vascular ring comprised of a right aortic arch with an aberrant left subclavian artery. (**a**) Diagram. Volume-rendered gadolinium-enhanced 3D MRA shown from anterior (**b**), posterior (**c**), and superior (**d**) perspectives (Reprinted with permission from Powell [110])

divided, and, in some circumstances, the diverticulum of Kommerell is plicated, and the left subclavian artery is repositioned.

CMR Evaluation

The CMR examination should demonstrate the aortic arch and its branches as well as the trachea and proximal bronchi. The esophagus at the level of the arch may be collapsed and not easily identified. Stacks of high-resolution turbo spin-echo images with blood suppression show the aortic vessels and airway nicely. Axial images should be oriented orthogonal to the tracheal long-axis and sagittal and coronal images oriented parallel to the trachea. This information can be augmented by high-resolution 3D angiography, either with a gadolinium-based contrast agent or using an ECG and respiratory navigator-gated SSFP sequence. Three-dimensional

volume rendering of the data facilitates the understanding of spatial relationships and the detection of vessel traction, dimples, and diverticula, which may be indirect evidence of ligamentous structures that are not visible on the images.

Summary

CMR is a valuable tool for the diagnosis and management of children and adults with congenital heart disease. Although transthoracic echocardiography remains the primary imaging modality for this group, deterioration of acoustic windows as patients grow or undergo surgery often limits its utility. In such circumstances, CMR provides a noninvasive alternative to transesophageal echocardiography and cardiac catheterization. Moreover, the superior ability of CMR to depict anatomy in three dimensions, evaluate ventricular size and function, and measure vessel-specific blood flow makes it the preferred imaging modality in a variety of clinical circumstances involving simple congenital heart lesions. In order to ensure a high-quality, complete CMR evaluation in these situations, the supervising physician should have a thorough understanding of the relevant anatomic and physiologic issues as well as CMR techniques. One must also be mindful that CMR strategies for evaluating congenital heart disease will continue to evolve as experience grows and new imaging techniques are developed.

References

1. Walsh MA, Noga M, Rutledge J. Cumulative radiation exposure in pediatric patients with congenital heart disease. Pediatr Cardiol. 2015;36(2):289–94. Epub 2014
2. Ait-Ali L, Andreassi MG, Foffa I, Spadoni I, Vano E, Picano E. Cumulative patient effective dose and acute radiation-induced chromosomal DNA damage in children with congenital heart disease. Heart. 2010;96:269–74.
3. Song S, Liu C, Zhang M. Radiation dose and mortality risk to children undergoing therapeutic interventional cardiology. Acta Radiol. 2015;56(7):867–72. Epub 2014
4. Glatz AC, Purrington KS, Klinger A, King AR, Hellinger J, Zhu X, et al. Cumulative exposure to medical radiation for children requiring surgery for congenital heart disease. J Pediatr. 2014;164:789–94. e710
5. Fratz S, Chung T, Greil GF, Samyn MM, Taylor AM, Valsangiacomo Buechel ER, et al. Guidelines and protocols for cardiovascular magnetic resonance in children and adults with congenital heart disease: SCMR expert consensus group on congenital heart disease. J Cardiovasc Magn Reson. 2013;15:51.
6. Kilner PJ, Geva T, Kaemmerer H, Trindade PT, Schwitter J, Webb GD. Recommendations for cardiovascular magnetic resonance in adults with congenital heart disease from the respective working groups of the european society of cardiology. Eur Heart J. 2010;31:794–805.
7. American College of Cardiology Foundation Task Force on Expert Consensus D, Hundley WG, Bluemke DA, Finn JP, Flamm SD, Fogel MA, Friedrich MG, et al. ACCF/ACR/AHA/NASCI/SCMR 2010 expert consensus document on cardiovascular magnetic resonance: A report of the american college of cardiology foundation task force on expert consensus documents. Circulation. 2010;121:2462–508.
8. Pennell DJ, Sechtem UP, Higgins CB, Manning WJ, Pohost GM, Rademakers FE, et al. Society for cardiovascular magnetic resonance; working group on cardiovascular magnetic resonance of the European Society of Cardiology. Clinical indications for cardiovascular magnetic resonance (CMR): consensus panel report. J Cardiovasc Magn Reson. 2004;6:727–65.
9. Moghari MH, Komarlu R, Annese D, Geva T, Powell AJ. Free-breathing steady-state free precession cine cardiac magnetic resonance with respiratory navigator gating. Magn Reson Med Magn Reson Med. 2015;73(4):1555–61.
10. Harned RK 2nd, Strain JD. MRI-compatible audio/visual system: impact on pediatric sedation. Pediatr Radiol. 2001;31:247–50.
11. Windram J, Grosse-Wortmann L, Shariat M, Greer ML, Crawford MW, Yoo SJ. Cardiovascular MRI without sedation or general anesthesia using a feed-and-sleep technique in neonates and infants. Pediatr Radiol. 2012;42:183–7.
12. Gutierrez FR. Magnetic resonance imaging of congenital heart disease. Top Magn Reson Imaging. 1995;7:246–57.
13. Masui T, Katayama M, Kobayashi S, Ito T, Seguchi M, Koide M, et al. Gadolinium-enhanced MR angiography in the evaluation of congenital cardiovascular disease pre- and postoperative states in infants and children. J Magn Reson Imaging. 2000;12:1034–42.
14. Schlesinger AE, Hernandez RJ. Magnetic resonance imaging in congenital heart disease in children. Tex Heart Inst J. 1996;23:128–43.
15. Fogel MA, Donofrio MT, Ramaciotti C, Hubbard AM, Weinberg PM. Magnetic resonance and echocardiographic imaging of pulmonary artery size throughout stages of Fontan reconstruction. Circulation. 1994;90:2927–36.
16. Beekman RP, Hoorntje TM, Beek FJ, Kuijten RH. Sedation for children undergoing magnetic resonance imaging: efficacy and safety of rectal thiopental. Eur J Pediatr. 1996;155:820–2.
17. Didier D, Ratib O, Beghetti M, Oberhaensli I, Friedli B. Morphologic and functional evaluation of congenital heart disease by magnetic resonance imaging. J Magn Reson Imaging. 1999;10:639–55.
18. Tsai-Goodman B, Geva T, Odegard KC, Sena LM, Powell AJ. Clinical role, accuracy, and technical aspects of cardiovascular magnetic resonance imaging in infants. Am J Cardiol. 2004;94:69–74.
19. Odegard KC, DiNardo JA, Tsai-Goodman B, Powell AJ, Geva T, Laussen PC. Anaesthesia considerations for cardiac MRI in infants and small children. Paediatr Anaesth. 2004;14:471–6.
20. Ahmed S, Shellock FG. Magnetic resonance imaging safety: implications for cardiovascular patients. J Cardiovasc Magn Reson. 2001;3:171–82.
21. Shellock FG, O'Neil M, Ivans V, Kelly D, O'Connor M, et al. Cardiac pacemakers and implantable cardioverter defibrillators are unaffected by operation of an extremity MR imaging system. AJR Am J Roentgenol. 1999;172:165–70.
22. Loewy J, Loewy A, Kendall EJ. Reconsideration of pacemakers and MR imaging. Radiographics. 2004;24:1257–67. discussion 1267–1258
23. Martin ET, Coman JA, Shellock FG, Pulling CC, Fair R, Jenkins K. Magnetic resonance imaging and cardiac pacemaker safety at 1.5-tesla. J Am Coll Cardiol. 2004;43:1315–24.
24. Naehle CP, Kreuz J, Strach K, Schwab JO, Pingel S, Luechinger R, et al. Safety, feasibility, and diagnostic value of cardiac magnetic resonance imaging in patients with cardiac pacemakers and implantable cardioverters/defibrillators at 1.5 t. Am Heart J. 2011;161:1096–105.

25. Roguin A, Zviman MM, Meininger GR, Rodrigues ER, Dickfeld TM, Bluemke DA, et al. Modern pacemaker and implantable cardioverter/defibrillator systems can be magnetic resonance imaging safe: in vitro and in vivo assessment of safety and function at 1.5 t. Circulation. 2004;110:475–82.
26. Shinbane JS, Colletti PM, Shellock FG. Magnetic resonance imaging in patients with cardiac pacemakers: era of "MR conditional" designs. J Cardiovasc Magn Reson. 2011;13:63.
27. Wollmann CG, Thudt K, Kaiser B, Salomonowitz E, Mayr H, Globits S. Safe performance of magnetic resonance of the heart in patients with magnetic resonance conditional pacemaker systems: the safety issue of the estimate study. J Cardiovasc Magn Reson. 2014;16:30.
28. Dewey FE, Rosenthal D, Murphy DJ Jr, Froelicher VF, Ashley EA. Does size matter? Clinical applications of scaling cardiac size and function for body size. Circulation. 2008;117:2279–87.
29. Sluysmans T, Colan SD. Theoretical and empirical derivation of cardiovascular allometric relationships in children. J Appl Physiol. 2005;99:445–57.
30. Gutgesell HP, Rembold CM. Growth of the human heart relative to body surface area. Am J Cardiol. 1990;65:662–8.
31. Cantinotti M, Scalese M, Molinaro S, Murzi B, Passino C. Limitations of current echocardiographic nomograms for left ventricular, valvular, and arterial dimensions in children: a critical review. J Am Soc Echocardiogr. 2012;25:142–52.
32. Alfakih K, Plein S, Thiele H, Jones T, Ridgway JP, Sivananthan MU. Normal human left and right ventricular dimensions for MRI as assessed by turbo gradient echo and steady-state free precession imaging sequences. J Magn Reson Imaging. 2003;17:323–9.
33. Buechel EV, Kaiser T, Jackson C, Schmitz A, Kellenberger CJ. Normal right- and left ventricular volumes and myocardial mass in children measured by steady state free precession cardiovascular magnetic resonance. J Cardiovasc Magn Reson. 2009;11:19.
34. Hudsmith LE, Petersen SE, Francis JM, Robson MD, Neubauer S. Normal human left and right ventricular and left atrial dimensions using steady state free precession magnetic resonance imaging. J Cardiovasc Magn Reson. 2005;7:775–82.
35. Robbers-Visser D, Boersma E, Helbing WA. Normal biventricular function, volumes, and mass in children aged 8 to 17 years. J Magn Reson Imaging. 2009;29:552–9.
36. Sarikouch S, Peters B, Gutberlet M, Leismann B, Kelter-Kloepping A, Koerperich H, et al. Sex-specific pediatric percentiles for ventricular size and mass as reference values for cardiac MRI: assessment by steady-state free-precession and phase-contrast MRI flow. Circ Cardiovasc Imaging. 2010;3:65–76.
37. Kaiser T, Kellenberger CJ, Albisetti M, Bergstrasser E, Valsangiacomo Buechel ER. Normal values for aortic diameters in children and adolescents – assessment in vivo by contrast-enhanced CMR-angiography. J Cardiovasc Magn Reson. 2008;10:56.
38. Voges I, Jerosch-Herold M, Hedderich J, Pardun E, Hart C, Gabbert DD, et al. Normal values of aortic dimensions, distensibility, and pulse wave velocity in children and young adults: a cross-sectional study. J Cardiovasc Magn Reson. 2012;14:77.
39. Hagen PT, Scholz DG, Edwards WD. Incidence and size of patent foramen ovale during the first 10 decades of life: an autopsy study of 965 normal hearts. Mayo Clin Proc. 1984;59:17–20.
40. Raghib G, Ruttenberg HD, Anderson RC, Amplatz K, Adams P Jr, Edwards JE. Termination of left superior vena cava in left atrium, atrial septal defect, and absence of coronary sinus; a developmental complex. Circulation. 1965;31:906–18.
41. Radzik D, Davignon A, van Doesburg N, Fournier A, Marchand T, Ducharme G. Predictive factors for spontaneous closure of atrial septal defects diagnosed in the first 3 months of life. J Am Coll Cardiol. 1993;22:851–3.
42. Furlan AJ, Reisman M, Massaro J, Mauri L, Adams H, Albers GW, et al. Closure or medical therapy for cryptogenic stroke with patent foramen ovale. N Engl J Med. 2012;366:991–9.
43. Udell JA, Opotowsky AR, Khairy P, Silversides CK, Gladstone DJ, et al. Patent foramen ovale closure vs medical therapy for stroke prevention: meta-analysis of randomized trials and review of heterogeneity in meta-analyses. Can J Cardiol. 2014;30(10):1216–24.
44. Homma S, Sacco RL. Patent foramen ovale and stroke. Circulation. 2005;112:1063–72.
45. Said SM, Burkhart HM, Schaff HV, Cetta F Jr, Phillips SD, Barnes RD, et al. Single-patch, 2-patch, and caval division techniques for repair of partial anomalous pulmonary venous connections: does it matter? J Thorac Cardiovasc Surg. 2012;143:896–903.
46. Powell AJ, Tsai-Goodman B, Prakash A, Greil GF, Geva T. Comparison between phase-velocity cine magnetic resonance imaging and invasive oximetry for quantification of atrial shunts. Am J Cardiol. 2003;91:1523–5. A1529
47. Beerbaum P, Korperich H, Barth P, Esdorn H, Gieseke J, Meyer H. Noninvasive quantification of left-to-right shunt in pediatric patients: phase-contrast cine magnetic resonance imaging compared with invasive oximetry. Circulation. 2001;103:2476–82.
48. Hundley WG, Li HF, Lange RA, Pfeifer DP, Meshack BM, Willard JE, et al. Assessment of left-to-right intracardiac shunting by velocity-encoded, phase-difference magnetic resonance imaging. A comparison with oximetric and indicator dilution techniques. Circulation. 1995;91:2955–60.
49. Arheden H, Holmqvist C, Thilen U, Hanseus K, Bjorkhem G, Pahlm O, et al. Left-to-right cardiac shunts: comparison of measurements obtained with MR velocity mapping and with radionuclide angiography. Radiology. 1999;211:453–8.
50. Diethelm L, Dery R, Lipton MJ, Higgins CB. Atrial-level shunts: sensitivity and specificity of MR in diagnosis. Radiology. 1987;162:181–6.
51. Dinsmore RE, Wismer GL, Guyer D, Thompson R, Liu P, Stratemeier E, et al. Magnetic resonance imaging of the interatrial septum and atrial septal defects. AJR Am J Roentgenol. 1985;145:697–703.
52. Sakakibara M, Kobayashi S, Imai H, Watanabe S, Masuda Y, Inagaki Y. Diagnosis of atrial septal defect using magnetic resonance imaging. J Cardiol. 1987;17:817–29.
53. Holmvang G, Palacios IF, Vlahakes GJ, Dinsmore RE, Miller SW, Liberthson RR, et al. Imaging and sizing of atrial septal defects by magnetic resonance. Circulation. 1995;92:3473–80.
54. Thomson LE, Crowley AL, Heitner JF, Cawley PJ, Weinsaft JW, Kim HW, et al. Direct en face imaging of secundum atrial septal defects by velocity-encoded cardiovascular magnetic resonance in patients evaluated for possible transcatheter closure. Circ Cardiovasc Imaging. 2008;1:31–40.
55. Beerbaum P, Korperich H, Esdorn H, Blanz U, Barth P, Hartmann J, et al. Atrial septal defects in pediatric patients: noninvasive sizing with cardiovascular MR imaging. Radiology. 2003;228:361–9.
56. Piaw CS, Kiam OT, Rapaee A, Khoon LC, Bang LH, Ling CW, et al. Use of non-invasive phase contrast magnetic resonance imaging for estimation of atrial septal defect size and morphology: a comparison with transesophageal echo. Cardiovasc Intervent Radiol. 2006;29:230–4.
57. Teo KS, Disney PJ, Dundon BK, Worthley MI, Brown MA, et al. Assessment of atrial septal defects in adults comparing cardiovascular magnetic resonance with transoesophageal echocardiography. J Cardiovasc Magn Reson. 2010;12:44.
58. Durongpisitkul K, Tang NL, Soongswang J, Laohaprasitiporn D, Nanal A. Predictors of successful transcatheter closure of atrial septal defect by cardiac magnetic resonance imaging. Pediatr Cardiol. 2004;25:124–30.

59. Van Praagh R, Geva T, Kreutzer J. Ventricular septal defects: how shall we describe, name and classify them? J Am Coll Cardiol. 1989;14:1298–9.
60. Bol-Raap G, Weerheim J, Kappetein AP, Witsenburg M, Bogers AJ. Follow-up after surgical closure of congenital ventricular septal defect. Eur J Cardiothorac Surg. 2003;24:511–5.
61. Kumar K, Lock JE, Geva T. Apical muscular ventricular septal defects between the left ventricle and the right ventricular infundibulum. Diagnostic and interventional considerations. Circulation. 1997;95:1207–13.
62. Knauth AL, Lock JE, Perry SB, McElhinney DB, Gauvreau K, Landzberg MJ, et al. Transcatheter device closure of congenital and postoperative residual ventricular septal defects. Circulation. 2004;110:501–7.
63. Didier D, Higgins CB, Fisher MR, Osaki L, Silverman NH, Cheitlin MD. Congenital heart disease: gated MR imaging in 72 patients. Radiology. 1986;158:227–35.
64. Lowell DG, Turner DA, Smith SM, Bucheleres GH, Santucci BA, et al. The detection of atrial and ventricular septal defects with electrocardiographically synchronized magnetic resonance imaging. Circulation. 1986;73:89–94.
65. Baker EJ, Ayton V, Smith MA, Parsons JM, Ladusans EJ, Anderson RH, et al. Magnetic resonance imaging at a high field strength of ventricular septal defects in infants. Br Heart J. 1989;62:305–10.
66. Bremerich J, Reddy GP, Higgins CB. MRI of supracristal ventricular septal defects. J Comput Assist Tomogr. 1999;23:13–5.
67. Yoo SJ, Lim TH, Park IS, Hong CY, Song MG, Kim SH. Defects of the interventricular septum of the heart: En face MR imaging in the oblique coronal plane. AJR Am J Roentgenol. 1991;157:943–6.
68. Yoo SJ, Kim YM, Choe YH. Magnetic resonance imaging of complex congenital heart disease. Int J Card Imaging. 1999;15:151–60.
69. Sorensen TS, Korperich H, Greil GF, Eichhorn J, Barth P, Meyer H, et al. Operator-independent isotropic three-dimensional magnetic resonance imaging for morphology in congenital heart disease: a validation study. Circulation. 2004;110:163–9.
70. Mohiaddin RH, Underwood R, Romeira L, Anagnostopoulos C, Karwatowski SP, et al. Comparison between cine magnetic resonance velocity mapping and first-pass radionuclide angiocardiography for quantitating intracardiac shunts. Am J Cardiol. 1995;75:529–32.
71. Fortescue EB, Lock JE, Galvin T, McElhinney DB. To close or not to close: the very small patent ductus arteriosus. Congenit Heart Dis. 2010;5:354–65.
72. Geva T, Greil GF, Marshall AC, Landzberg M, Powell AJ. Gadolinium-enhanced 3-dimensional magnetic resonance angiography of pulmonary blood supply in patients with complex pulmonary stenosis or atresia: comparison with x-ray angiography. Circulation. 2002;106:473–8.
73. Geva T, Van Praagh S. Anomalies of the pulmonary veins. In: Allen HD, Gutgessel HP, Clark EB, Driscoll DJ, editors. Moss & Adams' heart disease in infants, children, and adolescents. Philadelphia: Lippincott Williams & Wilkins; 2001. p. 736–72.
74. Neill CA, Ferencz C, Sabiston DC, Sheldon H. The familial occurrence of hypoplastic right lung with systemic arterial supply and venous drainage "scimitar syndrome". Bull Johns Hopkins Hosp. 1960;107:1–21.
75. Dyme JL, Prakash A, Printz BF, Kaur A, Parness IA, Nielsen JC. Physiology of isolated anomalous pulmonary venous connection of a single pulmonary vein as determined by cardiac magnetic resonance imaging. Am J Cardiol. 2006;98:107–10.
76. Greil GF, Powell AJ, Gildein HP, Geva T. Gadolinium-enhanced three-dimensional magnetic resonance angiography of pulmonary and systemic venous anomalies. J Am Coll Cardiol. 2002;39:335–41.
77. Prasad SK, Soukias N, Hornung T, Khan M, Pennell DJ, et al. Role of magnetic resonance angiography in the diagnosis of major aortopulmonary collateral arteries and partial anomalous pulmonary venous drainage. Circulation. 2004;109:207–14.
78. Ferrari VA, Scott CH, Holland GA, Axel L, Sutton MS. Ultrafast three-dimensional contrast-enhanced magnetic resonance angiography and imaging in the diagnosis of partial anomalous pulmonary venous drainage. J Am Coll Cardiol. 2001;37:1120–8.
79. Roos-Hesselink JW, Scholzel BE, Heijdra RJ, Spitaels SE, Meijboom FJ, Boersma E, et al. Aortic valve and aortic arch pathology after coarctation repair. Heart. 2003;89:1074–7.
80. Konen E, Merchant N, Provost Y, McLaughlin PR, Crossin J, Paul NS. Coarctation of the aorta before and after correction: the role of cardiovascular MRI. AJR Am J Roentgenol. 2004;182:1333–9.
81. Campbell M. Natural history of coarctation of the aorta. Br Heart J. 1970;32:633–40.
82. Bogaert J, Gewillig M, Rademakers F, Bosmans H, Verschakelen J, et al. Transverse arch hypoplasia predisposes to aneurysm formation at the repair site after patch angioplasty for coarctation of the aorta. J Am Coll Cardiol. 1995;26:521–7.
83. Parks WJ, Ngo TD, Plauth WH Jr, Bank ER, Sheppard SK, et al. Incidence of aneurysm formation after dacron patch aortoplasty repair for coarctation of the aorta: long-term results and assessment utilizing magnetic resonance angiography with three-dimensional surface rendering. J Am Coll Cardiol. 1995;26:266–71.
84. Rao PS, Jureidini SB, Balfour IC, Singh GK, Chen SC. Severe aortic coarctation in infants less than 3 months: successful palliation by balloon angioplasty. J Invasive Cardiol. 2003;15:202–8.
85. Corno AF, Botta U, Hurni M, Payot M, Sekarski N, et al. Surgery for aortic coarctation: a 30 years experience. Eur J Cardiothorac Surg. 2001;20:1202–6.
86. Walhout RJ, Lekkerkerker JC, Ernst SM, Hutter PA, Plokker TH, Meijboom EJ. Angioplasty for coarctation in different aged patients. Am Heart J. 2002;144:180–6.
87. Fawzy ME, Awad M, Hassan W, Al Kadhi Y, Shoukri M, Fadley F. Long-term outcome (up to 15 years) of balloon angioplasty of discrete native coarctation of the aorta in adolescents and adults. J Am Coll Cardiol. 2004;43:1062–7.
88. Chen SS, Dimopoulos K, Alonso-Gonzalez R, Liodakis E, Teijeira-Fernandez E, Alvarez-Barredo M, et al. Prevalence and prognostic implication of restenosis or dilatation at the aortic coarctation repair site assessed by cardiovascular MRI in adult patients late after coarctation repair. Int J Cardiol. 2014;173:209–15.
89. Therrien J, Thorne SA, Wright A, Kilner PJ, Somerville J. Repaired coarctation: a "cost-effective" approach to identify complications in adults. J Am Coll Cardiol. 2000;35:997–1002.
90. Simpson IA, Chung KJ, Glass RF, Sahn DJ, Sherman FS, Hesselink J. Cine magnetic resonance imaging for evaluation of anatomy and flow relations in infants and children with coarctation of the aorta. Circulation. 1988;78:142–8.
91. Mendelsohn AM, Banerjee A, Donnelly LF, Schwartz DC. Is echocardiography or magnetic resonance imaging superior for precoarctation angioplasty evaluation? Catheter Cardiovasc Diagn. 1997;42:26–30.
92. Rupprecht T, Nitz W, Wagner M, Kreissler P, Rascher W, Hofbeck M. Determination of the pressure gradient in children with coarctation of the aorta by low-field magnetic resonance imaging. Pediatr Cardiol. 2002;23:127–31.
93. Prince MR, Narasimham DL, Jacoby WT, Williams DM, Cho KJ, et al. Three-dimensional gadolinium-enhanced MR angiography of the thoracic aorta. AJR Am J Roentgenol. 1996;166:1387–97.
94. Krinsky GA, Rofsky NM, DeCorato DR, Weinreb JC, Earls JP, Flyer MA, et al. Thoracic aorta: comparison of gadolinium-enhanced three-dimensional MR angiography with conventional MR imaging. Radiology. 1997;202:183–93.
95. Bogaert J, Kuzo R, Dymarkowski S, Janssen L, Celis I, et al. Follow-up of patients with previous treatment for coarctation of the thoracic aorta: comparison between contrast-enhanced

MR angiography and fast spin-echo MR imaging. Eur Radiol. 2000;10:1847–54.
96. Muzzarelli S, Ordovas KG, Hope MD, Meadows JJ, Higgins CB, Meadows AK. Diagnostic value of the flow profile in the distal descending aorta by phase-contrast magnetic resonance for predicting severe coarctation of the aorta. J Magn Reson Imaging. 2011;33:1440–6.
97. Muhler EG, Neuerburg JM, Ruben A, Grabitz RG, Gunther RW, et al. Evaluation of aortic coarctation after surgical repair: role of magnetic resonance imaging and doppler ultrasound. Br Heart J. 1993;70:285–90.
98. Mohiaddin RH, Kilner PJ, Rees S, Longmore DB. Magnetic resonance volume flow and jet velocity mapping in aortic coarctation. J Am Coll Cardiol. 1993;22:1515–21.
99. Steffens JC, Bourne MW, Sakuma H, O'Sullivan M, Higgins CB. Quantification of collateral blood flow in coarctation of the aorta by velocity encoded cine magnetic resonance imaging. Circulation. 1994;90:937–43.
100. Nielsen JC, Powell AJ, Gauvreau K, Marcus EN, Prakash A, Geva T. Magnetic resonance imaging predictors of coarctation severity. Circulation. 2005;111:622–8.
101. Muzzarelli S, Meadows AK, Ordovas KG, Hope MD, Higgins CB, Nielsen JC, et al. Prediction of hemodynamic severity of coarctation by magnetic resonance imaging. Am J Cardiol. 2011;108:1335–40.
102. Oshinski JN, Parks WJ, Markou CP, Bergman HL, Larson BE, Ku DN, et al. Improved measurement of pressure gradients in aortic coarctation by magnetic resonance imaging. J Am Coll Cardiol. 1996;28:1818–26.
103. Rengier F, Delles M, Eichhorn J, Azad YJ, von Tengg-Kobligk H, Ley-Zaporozhan J, et al. Noninvasive pressure difference mapping derived from 4D flow MRI in patients with unrepaired and repaired aortic coarctation. Cardiovasc Diagn Ther. 2014;4:97–103.
104. Riesenkampff E, Fernandes JF, Meier S, Goubergrits L, Kropf S, Schubert S, et al. Pressure fields by flow-sensitive, 4D, velocity-encoded CMR in patients with aortic coarctation. JACC Cardiovasc Imaging. 2014;7:920–6.
105. Holmqvist C, Stahlberg F, Hanseus K, Hochbergs P, Sandstrom S, et al. Collateral flow in coarctation of the aorta with magnetic resonance velocity mapping: correlation to morphological imaging of collateral vessels. J Magn Reson Imaging. 2002;15:39–46.
106. Araoz PA, Reddy GP, Tarnoff H, Roge CL, Higgins CB. MR findings of collateral circulation are more accurate measures of hemodynamic significance than arm-leg blood pressure gradient after repair of coarctation of the aorta. J Magn Reson Imaging. 2003;17:177–83.
107. Julsrud PR, Breen JF, Felmlee JP, Warnes CA, Connolly HM, Schaff HV. Coarctation of the aorta: collateral flow assessment with phase-contrast MR angiography. AJR Am J Roentgenol. 1997;169:1735–42.
108. Weinberg PM. Aortic arch anomalies. In: Allen HD, Gutgesell HP, Clark EB, Driscoll DJ, editors. Moss & Adams' heart disease in infants, children, and adolescents. Philadelphia: Lippincott Williams & Wilkins; 2001. p. 707–35.
109. McElhinney DB, Clark BJ III, Weinberg PM, Kenton ML, McDonald-McGinn D, Driscoll DA, et al. Association of chromosome 22q11 deletion with isolated anomalies of aortic arch laterality and branching. J Am Coll Cardiol. 2001;37:2114–9.
110. Powell AJ. Vascular rings and slings (chapter 30). In: Lai WW, Mertens LL, Cohen MS, Geva T, editors. Echocardiography in pediatric and congenital heart disease. Oxford: Wiley-Blackwell; 2009. p. 523–36.
111. Moes CAF. Vascular rings and related conditions. In: Freedom RM, Mawson JB, Yoo SJ, Benson LN, editors. Congenital heart disease: textbook of angiocardiography. Armonk: Futura Publishing Company; 1997. p. 947–83.
112. van Son JA, Julsrud PR, Hagler DJ, Sim EK, Pairolero PC, Puga FJ, et al. Surgical treatment of vascular rings: the mayo clinic experience. Mayo Clin Proc. 1993;68:1056–63.
113. Bonnard A, Auber F, Fourcade L, Marchac V, Emond S, Revillon Y. Vascular ring abnormalities: a retrospective study of 62 cases. J Pediatr Surg. 2003;38:539–43.
114. Woods RK, Sharp RJ, Holcomb GW III, Snyder CL, Lofland GK, et al. Vascular anomalies and tracheoesophageal compression: a single institution's 25-year experience. Ann Thorac Surg. 2001;72:434–8.
115. Backer CL, Ilbawi MN, Idriss FS, DeLeon SY. Vascular anomalies causing tracheoesophageal compression. Review of experience in children. J Thorac Cardiovasc Surg. 1989;97:725–31.

MRA of the Aorta and Peripheral Arteries

21

Servet Tatli and E. Kent Yucel

Introduction

Magnetic resonance angiography (MRA) can be used as the primary imaging tool for the evaluation of the aorta and its branches for numerous indications [1–13]. MRA has many obvious advantages over conventional X-ray angiography, the primary one being its lack of invasiveness. Compared with X-ray angiography and computed tomographic angiography, it uses no ionizing radiation and in many situations can be performed without contrast. Compared with color Doppler ultrasound, it is not as operator-dependent and is not limited by bone or bowel gas [3]. Optimization of the imaging plane to the targeted anatomy maximized efficiency. MRA sequences can also be used to evaluate the vessel wall, which has important advantages in the detection, characterization, and understanding of many aortic diseases, such as intramural hematoma (IMH) and atherosclerotic plaque [9]. In addition, physiologic properties of blood flow can be accurately calculated by phase-contrast (PC) MRA in the same imaging session.

Principle MRA Techniques

Currently, there are several MRA techniques in daily practice. MRA techniques are divided into two major categories according to the mechanism of depiction of the blood vessel.

Electronic Supplementary Material The online version of this chapter (https://doi.org/10.1007/978-1-4939-8841-9_21) contains supplementary material, which is available to authorized users.

S. Tatli (✉)
Department of Radiology, Lehigh Valley Health Network, Allentown, PA, USA
e-mail: servet.tatli@lvhn.org

E. K. Yucel
Tufts Medical Center, Department of Radiology, Boston, MA, USA
e-mail: kyucel@tuftsmedicalcenter.org

Flow-dependent MRA techniques rely on the direction of blood flow to demonstrate a vessel, such as time-of-flight (TOF) MRA, phase-contrast (PC) MRA, and systolic-diastolic subtraction MRA. Flow-independent MRA techniques include contrast-enhanced (CE) MRA, which employs the T_1-shortening effect of circulating gadolinium-containing contrast material [13], and balanced gradient echo imaging, in which all water-containing structures, including blood vessels, are bright based on the relatively long T_2 of water [14].

Time-of-Flight (TOF) MRA

As the oldest MRA technique, TOF MRA today is limited to use mainly for the circle of Willis in the brain and the carotid arteries in the neck. TOF MRA relies on flow-related enhancement of the spins by blood flowing through the slices. Background tissue signal is suppressed by saturation by radio-frequency pulses applied to the imaged section. Vessels appear much brighter compared to background tissue because of the continuous inflow of the fresh unsaturated blood (Fig. 21.1a). Two-dimensional (2D) or three-dimensional (3D) flow-compensated gradient echo sequences are used to acquire multiple, thin, sequential slices, which can be either viewed individually or processed using the maximum intensity projection (MIP) technique to obtain a 3D projectional image (Fig. 21.1b, c). The technique extracts the brightest pixel along multiple viewing directions, projecting 3D imaging intensity onto multiple 2D displays which can then be rotated for full 3D visualization [15]. Selective arterial imaging can be achieved by using an appropriately placed presaturation pulse to eliminate venous signal. TOF has important limitations, explaining the predominance of CE MRA. These limitations include (1) turbulent flow producing low of signal may simulate disease; (2) vessels not perpendicular to the plane of acquisition may show saturation effects, which causes low signal and simulates disease; (3) triphasic

R. Y. Kwong et al. (eds.), *Cardiovascular Magnetic Resonance Imaging*, Contemporary Cardiology,
https://doi.org/10.1007/978-1-4939-8841-9_21

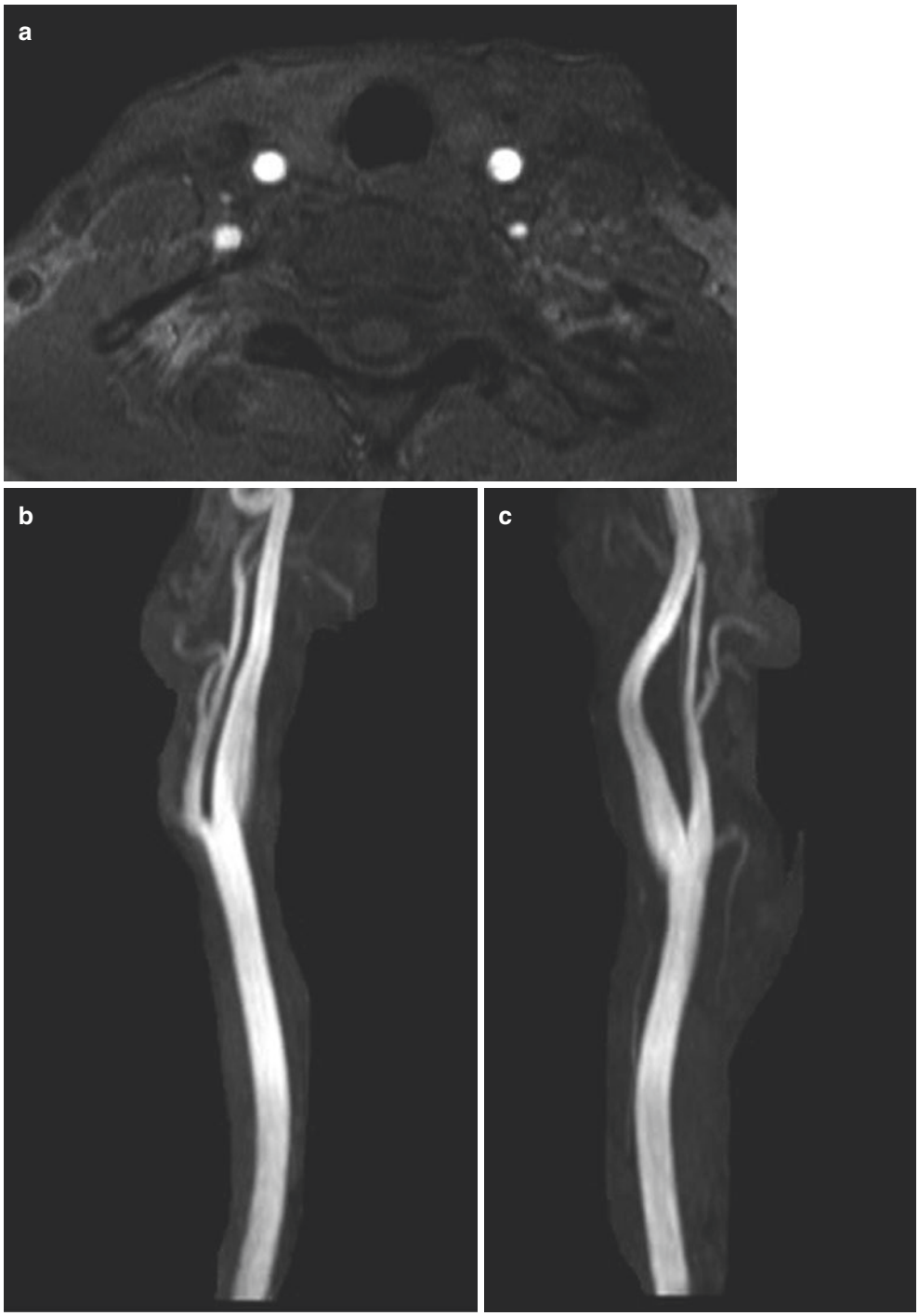

Fig. 21.1 Axial source (**a**), coronal MIP of right carotid bifurcation (**b**), coronal MIP of left carotid bifurcation (**c**) of 3D time-of-flight (TOF) carotid MRA

pulsatile flow produces ghosting artifacts; and (4) retrograde flow in collateral and reconstituted vessels may be saturated along with veins, artifactually increasing the apparent length of occlusions [16, 17].

Phase-Contrast (PC) MRA

PC is an MRI technique that permits the evaluation of physiologic properties of blood flow [18, 19]. A spin within flowing blood moving along a magnetic field gradient acquires a phase shift in its rotation proportional to the velocity of the blood, which can be detected through bipolar, phase-encoding gradients. Flow sensitive and reference acquisitions are performed which are automatically subtracted and processed into two image sets: magnitude and phase images (Fig. 21.2). The magnitude images resemble a normal bright blood image and are used for anatomical orientation. In the phase images, the pixel value is proportional to blood velocity, and flow direction is encoded by black or

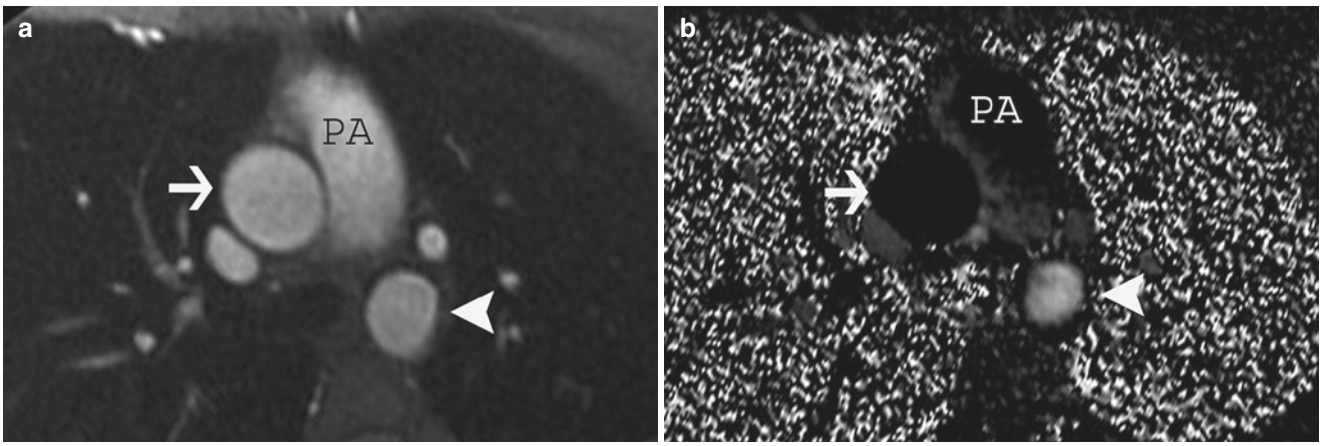

Fig. 21.2 Axial magnitude (**a**) and phase image (**b**) of PC MRA from the level of the main pulmonary artery (PA). The ascending thoracic aorta (arrow) appears black, and the descending thoracic aorta (arrowhead) white since the flow-encoded gradient is chosen as superior to inferior. Using special software, the velocity and volume of the blood flow can be calculated

white tones on a neutral background. They can also be displayed as absolute values (all white on a black background), in which case the slices can be processed using MIP technique to produce angiograms just like TOF slices. However, this is rarely done in current clinical practice due to the long time required to produce these scans as well as their susceptibility to a variety of flow artifacts. In current practice, PC is used to evaluate flow and velocity in the aorta and pulmonary artery for a variety of purposes [20–23], including assessing the degree of valvular regurgitation or stenosis, aorta to pulmonary flow ratios in congenital heart disease, and severity of aortic coarctation.

Black-Blood MRI

It is also possible to obtain fast spin-echo MRI images in which blood is black prior to CE MRA as an overview of gross anatomy and as road map for subsequent MRA prescriptions [23]. While not actually MR angiography as not able to be processed into 3D projections images, such black-blood images are valuable in vascular MRI for evaluation of the vessel wall, adjacent soft tissue, and surrounding organs. Flowing blood appears dark in signal intensity in these images because of a double-inversion recovery (DIR) preparation pulse [24–26] (Fig. 21.3). This technique uses two 180° inversion pulses; one is non-slice selective, inverting the magnetization in the entire imaging volume, and the second is slice selective, restoring the magnetization in the slice. A delay (time to inversion) timed to suppress the T_1 of blood is allowed before obtaining the fast spin-echo imaging sequence, which allows the inverted, suppressed blood that experienced only the initial 180° pulse to flow into the imaging slice. The technique obtains sequential sections with cardiac gating. Breath-holding is also possible.

Fig. 21.3 Axial DIR MRA image obtained with cardiac gating and breath-holding shows excellent suppression of the intraluminal signal in the ascending (arrow) and descending (arrowhead) thoracic aorta

Repetition time (TR) equals 1 R-R interval for T_1- or proton-density weighting, depending on heart rate, or 2–3 R-R for T_2 weighting. To maximize through-plane blood flow and the black-blood effect, the imaging plane should be chosen as perpendicular to the vessel of interest; usually the axial plane works well.

Steady-State Free Precession (SSFP)

This technique, which goes by various vendor-specific acronyms (trueFISP, Siemens; balanced TFE, Philips; FIESTA, GE), is a T_2-weighted, gradient echo technique that is widely used in cine imaging of the heart due to its ability to produce flow-independent high signal from blood [27, 28] (Fig. 21.4). Cine imaging is especially useful for visualizing the aortic root and ascending aorta [29]. SSFP can also be implemented

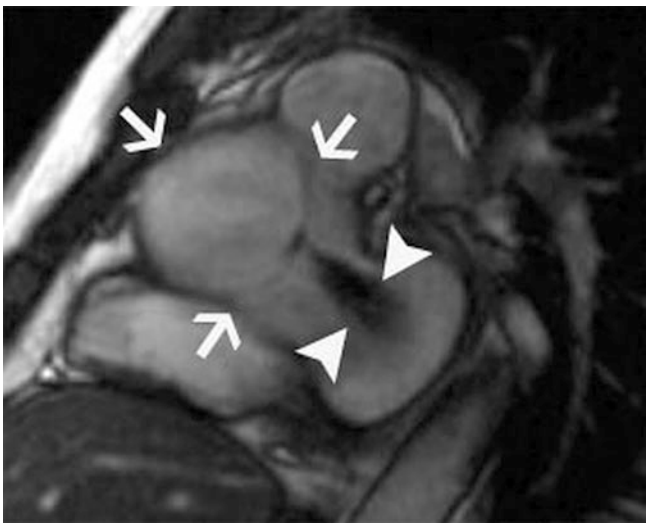

Fig. 21.4 Oblique sagittal image from cine, steady-state free precession (SSFP) acquisition obtained with a cardiac gating and breath-holding at the level of the aortic root (arrows) shows retrograde flow during diastole (arrowheads)

in non-cine mode for blood vessel imaging, either without or with [30] cardiac gating.

Contrast-Enhanced (CE) MRA

Basic Principles of CE MRA

CE MRA is a crucial technique for MRA. It is fast, robust, and accurate without the limitations of the flow-based techniques described earlier. CE MRA has become possible on a routine basis with the widespread adoption of faster MRI scanners, allowing high-resolution acquisitions with a single breath-hold (less than 20–25 s), which permits imaging of the arterial first pass of a rapidly injected bolus of paramagnetic contrast material. All of the gadolinium-based paramagnetic agents are in general use for MRA although only gadobenate and gadofosveset have specific MRA indications. Iron compounds have also been investigated for MRA applications [31] although no agents are currently approved in the USA for MRA. All these agents provide reliably bright signal in blood on T_1-weighted imaging regardless of the flow pattern, direction, or velocity (Fig. 21.5a–c). When the general MRI agents are used for MRA, signal intensity of arterial blood and therefore image quality depend on a high intra-arterial contrast material concentration; therefore, synchronization of image acquisition and peak intra-arterial contrast material concentration are crucial. The following comments address the use of these general-purpose agents for MRA. Comments on blood pool contrast will come in a later section.

k-Space Filling

In MRI, image contrast depends primarily on the central *k*-space data, whereas the peripheral lines of *k*-space contain data primarily for spatial resolution [32]. For this reason, acquisition of the central portion of *k*-space should be matched to peak arterial transit of the contrast bolus to obtain selective arterial enhancement—details are discussed in a separate section below.

The type of *k*-space filling (sequential, centric, elliptical centric) can be selected by the MRI operator, depending on the vessel of interest. Centric and elliptical centric acquisition help to minimize venous contamination, especially in the carotids, aortic arch, and lower stations of a peripheral runoff, by acquiring the central lines of *k*-space at the start of the acquisition rather than the standard location in the middle. Scanning these central lines too early, while contrast concentration is rising, results in suboptimal images with low signal and ringing artifacts, whereas scanning too late produces venous and soft tissue enhancement [33–35] (Fig. 21.6).

Imaging Parameters

CE MRA technique uses a 3D T_1-weighted gradient echo sequence with very short TR and TE. Flip angles depend on TR and are chosen to optimize signal to noise (SNR) and maximize background suppression. Use of a rectangular field of view (FOV) is generally advisable to minimize imaging time and to maximize resolution. Imaging plane is chosen to be along the long axis of the vessel of interest (sagittal oblique for thoracic aorta; coronal for arch vessels, abdominal aorta, and renal arteries; and sagittal for mesenteric arteries).

Contrast Dose, Rate, and Timing

Doses in the range of 0.1–0.3 mmol/kg at injection rates of 1–3 cc/sec of conventional gadolinium contrast are generally used. This is followed by a saline flush to ensure that the contrast material is delivered in the central venous system and does not pool with the tubing or peripheral veins. There are two basic methods to determine the optimal delay between the start of intravenous contrast material and the start of image acquisition: (1) a 2–3 cc timing bolus injected at the same rate and with the same saline bolus as the main injection and (2) fluoroscopic triggering where the technologist observes the contrast as it moves through the vascular system using real-time MRI and starts the scan when the contrast is in the appropriate location [33, 36–38].

Breath-Holding

Image acquisition should be obtained with breath-holding, which significantly improves image quality, especially in

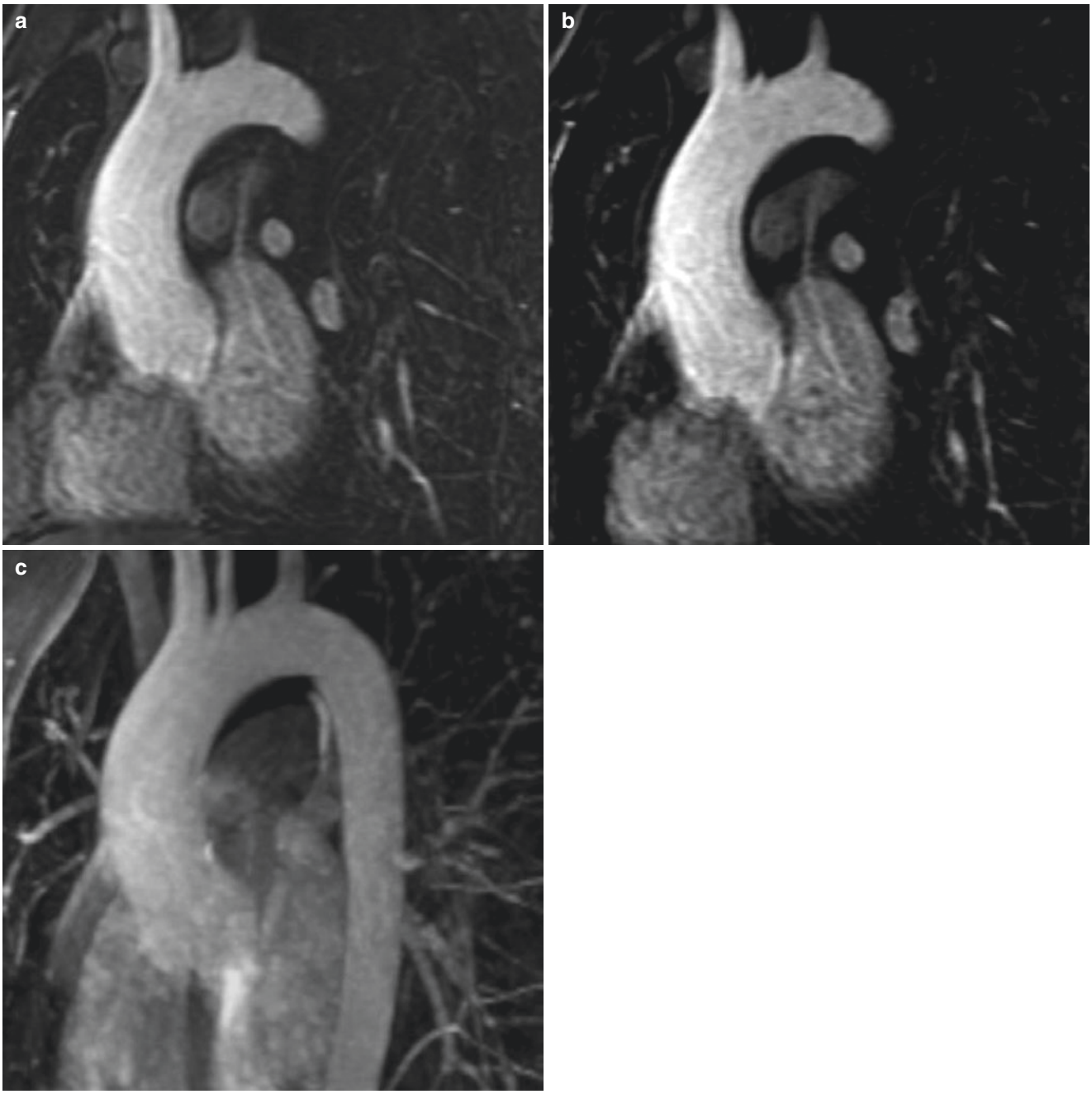

Fig. 21.5 Sagittal oblique source (**a**), masked (**b**), MIP (**c**) image from a CE MRA of the thoracic aorta. Note better background suppression on the masked image compared to source image resulting in good quality of MIP reconstruction

thoracic aortic imaging. Breath-holding capacity can be improved by supplemental oxygen and hyperventilation [39]. In patients with limited breath-holding capacity, normal shallow breathing often results in adequate diagnostic images. Both mask and actual CE MRA acquisitions should be obtained with breath-holding at the same phase of inspiration/expiration for better matching of images.

Image Optimization

Phased array coils significantly increase signal-to-noise ratio compared to body coil and should be preferred whenever possible. Obtaining mask image slices prior to contrast and subtracting it from the CE MRA slices optimize background suppression (Fig. 21.5a). A second, venous phase can be obtained routinely and can be helpful in recovering

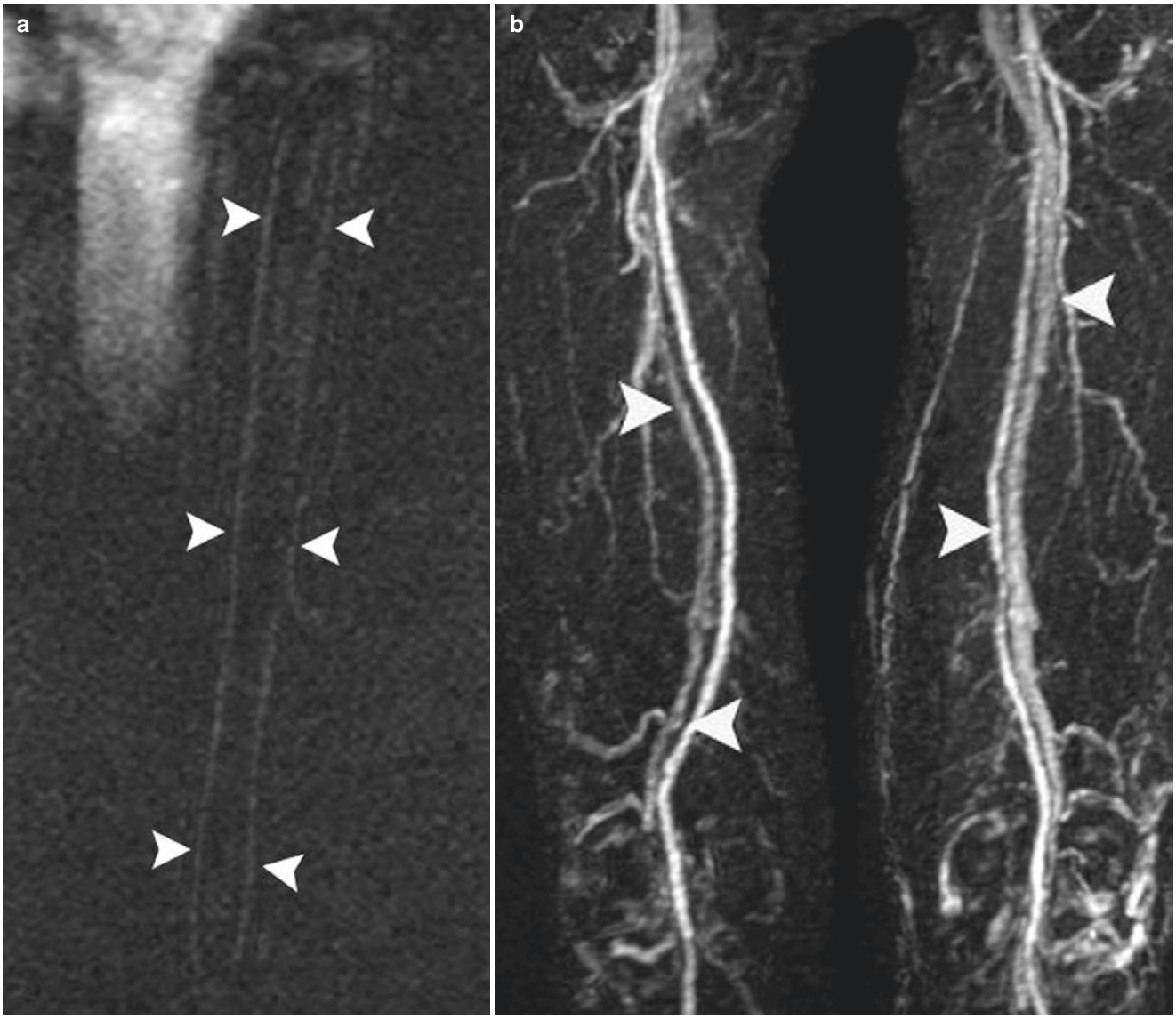

Fig. 21.6 Coronal image from a CE MRA of the abdominal aorta (**a**) shows very low intraluminal signal with ringing artifacts (arrowhead) because of filling the central lines of k-space before the contrast arrival. Coronal MIP reformation of CE MRA (**b**) from thigh station of another patient shows not only arterial enhancement but also enhancement of veins (arrowheads), which is superimposing on the arteries and limiting use of 3D reformat

diagnostic information in case of mistiming or to evaluate late-enhancing vascular structures.

Postprocessing

The subtracted slices processed to obtain final 3D MRA images for clinical evaluation. This step can either be performed on the scanner or on separate workstation. The obtained projection images can be interpreted individually or placed in a cine loop for demonstration purposes (see Video 21.1). As with non-contrast MRA, MIP processing is most commonly used as this produces 2D images that can be rotated to permit full 3D evaluation and is most comparable to conventional digital subtraction angiography (DSA) [40, 41] (Fig. 21.5c). Blood vs. background contrast is high enough on CE MRA for volume rendering (VR) to be used an alternative postprocessing method (Fig. 21.7). This technique retains all the pixel intensity information from the individual slices and can generate a 3D display of the vasculature using thresholding and sub-voluming techniques from user-selected points of view outside the vessel [40, 41].

Another technique that is essential to interpretation of CE MRA images is multiplanar reformatting. Scanning is performed in the plane that is most time-effective, not necessarily the plane that is most useful for diagnosis. Therefore, the ability to create transverse, sagittal, coronal plane, and oblique reformats is very helpful for diagnosis. It is essential

for accurate measurement of stenosis. Cross-sectional reformats through the vessel are very important for defining intraluminal pathology, such as thrombus, intimal flaps, or atheromas [40] (Fig. 21.8).

Time-Resolved CE MRA

Time-resolved CE MRA techniques have been developed using a variety of MR undersampling and view-sharing techniques (TRICKS, GE; TWIST, Siemens; 4D TRAK, Philips) [42–49]. These techniques eliminate the need for contrast timing and demonstrate temporal information about relative rates of enhancement of various structures (Fig. 21.9). By eliminating the need for contrast timing, these acquisitions become essentially just like X-ray digital subtraction angiography (DSA). However, since each time point generates a full 3D set of images, clear guidelines for how to manage and display images are important. Generally, a cine MIP display in one plane—often anteroposterior – followed by a rotating MIP of the best time point works well.

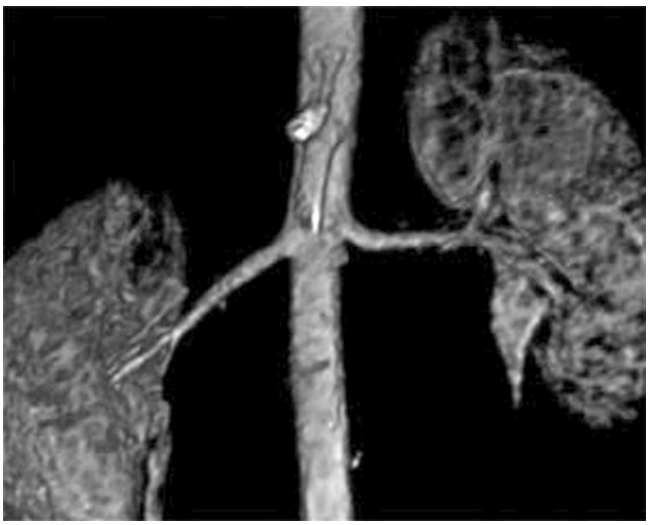

Fig. 21.7 Coronal CE MRA reconstructed with volume rendering (VR) technique, allowing comprehensive evaluation of outer surface of the vessel lumen but providing no information within the lumen

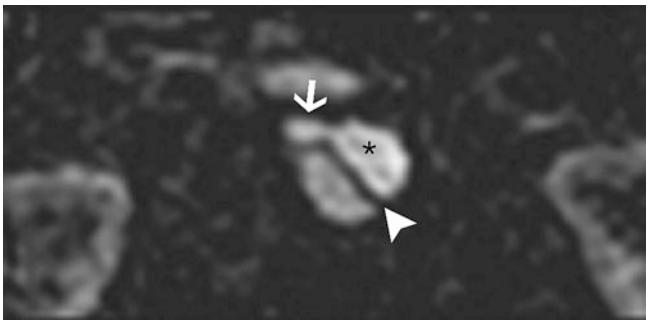

Fig. 21.8 Axial reformation of CE MRA of a patient with aortic dissection clearly shows intimal flap (arrowhead). Note the right renal artery (arrow) is arising from the true lumen (asterisk)

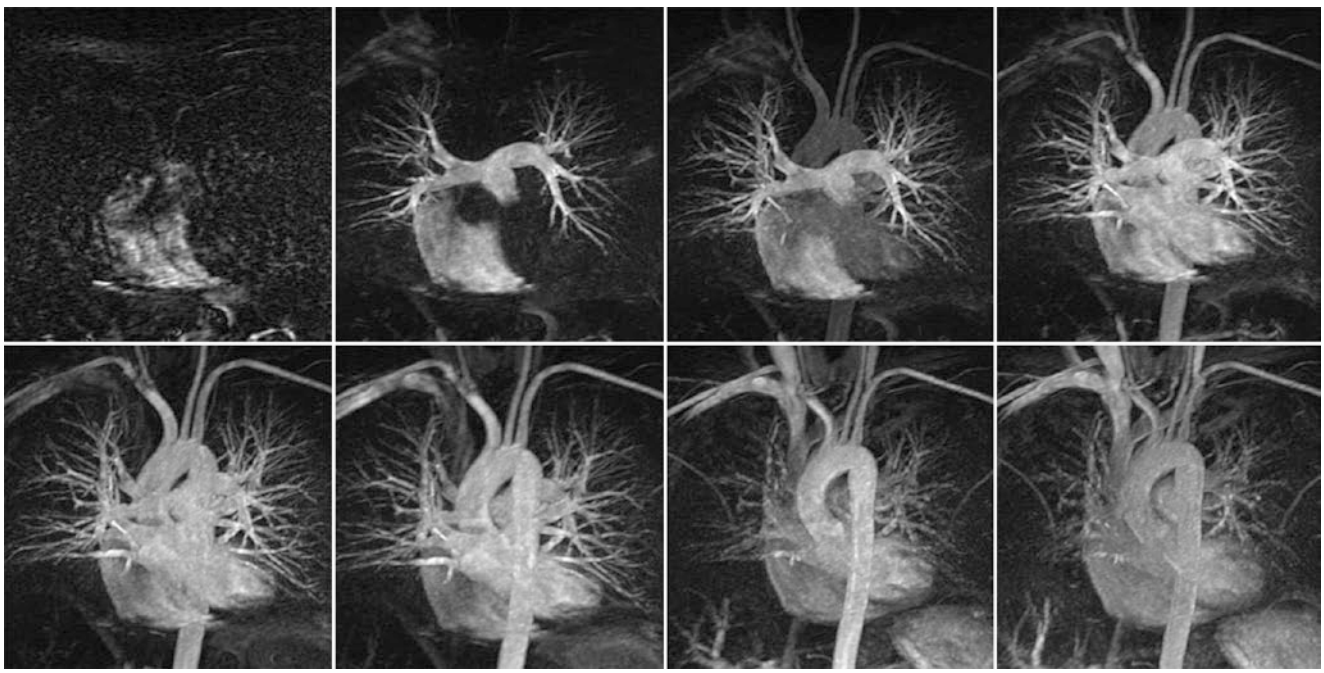

Fig. 21.9. Series of coronal images from CE MRA of chest obtained with TRICKS show relative enhancement order of the cardiovascular structures as contrast bolus reach these structures. Note enhancement of the right atrium (the first image on the upper row), the pulmonary artery (the second image on the upper row), the left ventricle and aorta (the third image on the upper row), and then superior vena cava and branches (the images on the lower row)

CE MRA of Peripheral Arteries

To evaluate the arterial system of the lower extremity for peripheral vascular disease, demonstration of a long segment of the vascular tree is needed, which requires at least three stations (aortoiliac, thigh, and calf) because of limited superior-inferior field of view of the magnet. Moving-table technology allows table translation so the contrast bolus can be "chased" from proximal to distal so all three or more stations can be imaged following a single contrast injection [50, 51], hence the alternative name, bolus-chase CE MRA. This approach provides routinely high-quality images down to the knee; nondiagnostic calf images are a problem because imaging is often not be fast enough to get to the calf before venous contamination occurs in many patients. This problem is more frequent in patients with limb-threatening pedal ischemia, in whom the demonstration of the status of the tibial vessels is especially important for proper surgical planning. A hybrid MRA approach has been developed to deal with this problem. With this approach, two contrast injections are performed. First is a stationary, time-resolved MRA of the calf followed by a multistation bolus-chase MRA [52–54] (Fig. 21.10). Mask imaging performed just before the bolus-chase exam prevents contrast material from the earlier injection to be subtracted. A 15–20 min delay is also useful between examinations to allow time for gadolinium contrast to distribute outside of the vascular space [51] (see Video 21.2).

CE MRA with Blood Pool Contrast

Contrast agents have recently become available which, unlike conventional gadolinium contrast, have long residence times in the blood, allowing for prolonged imaging of the vascular tree. There is one agent which has been approved by the Food and Drug Administration for aortoiliac MRA, gadofosveset (Ablavar®), at a dose of 0.03 mmol/kg (0.12 ml/kg). This agent binds reversibly to serum albumin which tends causes it to be retained in the blood pool as well as boosting the relaxivity of the gadolinium. It is renally excreted with a half-life of 16 hr. Blood pool MRA has been performed up to 1 h after administration [55]. It can also be imaged dynamically during arterial transit just like conventional agents. There is another agent which, while not approved for MRA, has been studied successfully as a blood pool MRA agent, ferumoxytol (Feraheme®) [31]. This agent has been approved for iron replacement therapy in patients with chronic kidney disease. The iron is not excreted, but rather the agent is taken up by the reticuloendothelial system and added to body iron stores with a half-life of 15 hr. Therefore, use is contraindicated in patients with iron overload. Another concern is the relatively high rate of adverse reactions (hypotension in 1.9% and serious hypersensitivity reactions in 0.2%). However, despite this, it has elicited interest for use in MRA in patients with severe chronic kidney disease (eGFR <30 ml/min/1.73m^2) and acute kidney injury who are at risk for developing nephrogenic systemic fibrosis (NSF) with gadolinium agents.

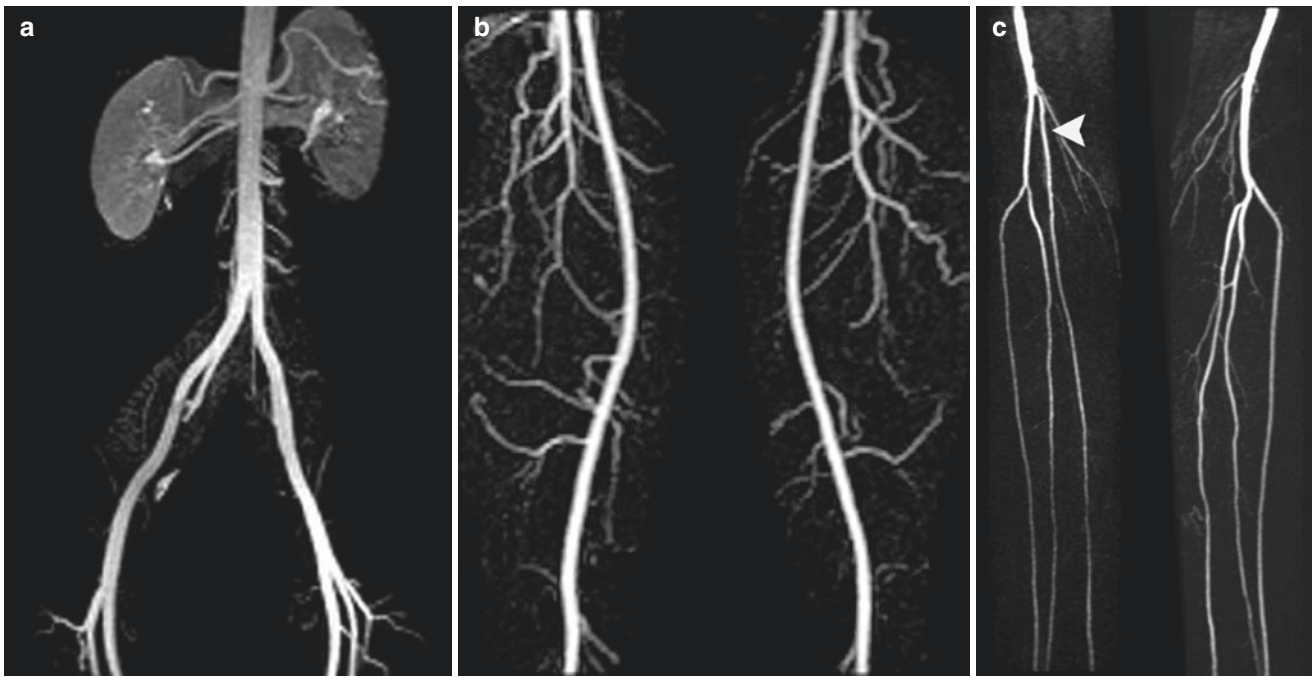

Fig. 21.10 Coronal MIP reformations of pelvis (**a**), thigh (**b**), and calf (**c**) stations of CE MRA of the lower extremity obtained with hybrid technique using a separate injection for the calf but single injection for the pelvis and thigh stations. Only arterial structures enhance, and there is excellent background suppression. Note anomalous high origin of the right posterior tibial artery (arrowhead on image **c**)

Fig. 21.11 Coronal MIP reformation of gadofosveset MRA obtained during venous phase demonstrates superior mesenteric vein thrombosis (arrow) with numerous collateral vessels

While blood pool contrast agents can be imaged in the arterial phase just like conventional agents, the true promise of these agents is to image them in the blood pool phase. In this phase, scan times are not limited to the few seconds of the arterial transit phase, which permits higher-resolution imaging for several minutes [55]. However, clinical use is limited by the fact that MIP processing is no longer useful as the smaller arteries are obscured by overlying venous structures. Until more advanced image processing tools become routinely available for arteriovenous separation on these images, clinical interpretation is limited to review of axial reformations (Fig. 21.11). Another promising, albeit unapproved, indication is for venous imaging due to the prolonged, dramatic venous enhancement that is seen with these agents [56].

Clinical Applications

Aorta

Imaging Protocol

The typical imaging protocol of the aorta includes a combination of CE MRA with axial, T_1-weighted, black-blood images to visualize both the lumen and the wall of the aorta. CE MRA images should be reviewed in coronal and sagittal MIPs as well as axial reformations. Post-contrast 2D or 3D gradient echo T_1-weighted images with fat suppression can also be obtained following the arterial phase images, especially with blood pool agents, and are helpful for some pathological conditions of the aorta, such as infectious or inflammatory diseases aortic ulcerations, and intimal flaps, as well as for evaluation of surrounding soft tissue and organs.

Congenital Aortic Disease

MRA is a valuable tool in the pre- and postoperative evaluation of congenital aortic disease. In aortic coarctation, CE MRA can demonstrate the luminal narrowing associated with primary or postoperative coarctation (Fig. 21.12). The flow through the aorta can be measured using PC to evaluate the hemodynamic significance of the coarctation [57]. The flow measurement is performed at two levels: just distal to the coarctation and at the level of the diaphragm. In the case

Fig. 21.12 Oblique sagittal MIP reformation of CE MRA of thoracic aorta of 27-year-old woman with a history of repaired aortic coarctation and now complaining of weakness and claudication in her lower extremities. The image shows focal narrowing in the descending thoracic aorta (arrowhead) just distal to the left subclavian artery (arrow) consistent with aortic coarctation. Note a large internal mammary artery (curved arrow) indicating hemodynamic significance of coarctation

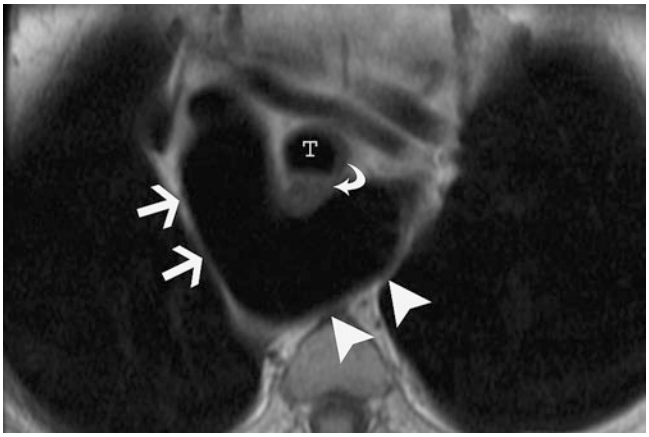

Fig. 21.13 Axial T1-weighted DIR image at the level of aortic arch shows a right-sided aortic arch (arrows) on this 76-year-old man. There is also a large vessel (arrowheads) arising from the arch and crossing the midline posterior to the esophagus (curved arrow) and trachea (T) consistent with aneurysmal dilatation of the origin of the aberrant left subclavian artery, which is also called as "diverticulum of Kommerell." The patient had no complaint related to these anomalies

of hemodynamically significant coarctation, the distal flow exceeds the proximal flow (proximal to distal flow ratio greater than 1.0) because of reversed flow through the intercostal arteries.

Aortic arch anomalies may cause compression on the esophagus or the trachea and may be silent until adulthood. Arch anomalies are well evaluated with CE MRA combined with black-blood imaging. The most common anomaly is an aberrant right subclavian from a normal left arch, but an aberrant left subclavian artery is the most common arch anatomy when there is a right arch. When the origin of an aberrant subclavian artery from either a right or left arch dilates, it is called a diverticulum of Kommerell [58] (Fig. 21.13).

Aortic Aneurysm

An aneurysm of an artery is defined as an increase in the outer diameter to at least 50% greater than normal. Aneurysms can be fusiform, involving the full circumference of the aorta, or saccular, involving only a portion of the wall with or without a neck. Atherosclerotic aneurysms, associated with aging, are typically fusiform. False aneurysms, in which part of the wall is disrupted, for example, mycotic aneurysms, are typically saccular. For abdominal aortic aneurysms (AAA), the most common type, a standard diameter measurement of 2.5–3.0 cm is conventionally used as the definition [59, 60]. When AAA reach a diameter of 5.0–5.5 cm, risk of rupture is sufficient to consider treatment either with surgery or endoluminal stent placement. While computed tomographic angiography (CTA) remains generally favored for evaluation of AAA due to its higher resolution and ability to demonstrate calcification, a combination of CE MRA can also evaluate aneurysm extent, branch patency, and relationship to the aneurysm [61, 62] (Fig. 21.14). Fusiform aneurysmal dilatation can also affect the ascending aorta and aortic root (aortoannular ectasia), which is associated with cystic medial necrosis, which in turn is associated with Marfan syndrome [63] (Fig. 21.15). Aortic stenosis can also cause secondary aneurysmal dilatation of the proximal ascending aorta, although the sinotubular junction typically remains uninvolved. Saccular aneurysms are unusual compared with fusiform aneurysms and can be secondary to atherosclerosis, traumatic injury, or infection. Mycotic aneurysms result from weakening of the vessel wall by bacterial infection, causing saccular aneurysms, most commonly involving the abdominal aorta (Fig. 21.16). Because CE MRA demonstrates only the lumen and contains little information about the morphology of the aortic wall and adjacent soft tissue, it should be complemented by axial, black-blood, T_1-weighted and post-contrast, fat-suppressed, T_1-weighted images [25]. The true diameter of an aneurysm should be measured on these T_1-weighted images because CE MRA is a luminogram and fails to

Fig. 21.14 Coronal MIP reformation of CE MRA shows diffuse fusiform aneurysmal dilatation of the abdominal aorta (arrowheads) involving supra- as well as infrarenal segments of the aorta. The contour irregularities are due to severe atherosclerosis. Note also a focal high-grade stenosis (arrow) at the origin of the right renal artery

Fig. 21.15 Oblique sagittal MIP reconstruction of CE MRA of a 33-year-old man with a history Marfan syndrome shows aneurysmal dilatation of the proximal ascending aorta including the aortic root and sinotubular junction (arrowheads), which is classic for this syndrome

demonstrate mural thrombus, which must be included in the measurement (Fig. 21.17). Routine measurement of the short-axis diameter if the aorta has an oval contour on axial images prevents overestimation of the diameter of tortuous segments.

Aortic Dissection

Aortic dissection occurs when blood enters the medial of the aortic wall because of an intimal tear, resulting in two lumens: the normal anatomical or true lumen and a false lumen, which is an artificial lumen between the intimal flap and the remaining layers of the aortic wall. Initial interruption of the intima frequently starts at two sites: the proximal ascending aorta and the proximal descending aorta just distal to the origin of the left subclavian artery.

Aortic dissections are divided into two groups according to the segment involved: Stanford type A when the ascending aorta is involved and Stanford type B if the descending aorta is dissected with sparing of the ascending aorta (Fig. 21.18). The abdominal aorta may or may not be involved. Stanford type A dissection is a surgical emergency with high mortality and may be complicated by contained rupture into the pericardium, which may cause cardiac tamponade; involvement of coronary arteries, causing acute myocardial ischemia; disruption of the aortic valve, resulting in acute aortic regurgitation and heart failure; or extension to the arch branches, compromising brain perfusion [64–68].

Stanford type B dissections are treated medically unless there is evidence of significant aortic expansion or end-organ ischemia. Paraplegia caused by spinal cord ischemia because of disruption of the artery of Adamkiewicz is a frequent complication of surgery of the descending thoracic aorta and is observed in up to 30% of individuals after such surgery [67]. Recently endovascular stent-grafting techniques have been used in type B patients requiring intervention with reduced mortality and morbidity [69].

CTA is the first-line modality for emergency imaging of patients with suspected aortic dissection. It is fast, well tolerated by patients, and widely available. It is highly accurate, especially when cardiac gating is used for aortic root visualization. MRA has similar accuracy to CTA [68], but its use is limited in the emergency setting and reserved only for patients with allergy to iodine and renal failure. In renal failure, MRA is limited to non-contrast techniques due to the risk of NSF, but axial black-blood and cine-balanced gradient echo images are very effective for diagnosing and classifying dissection, although overall coverage is limited by scan time. However, MRA is the preferred imaging tool for follow-up of chronic dissections and post-surgery due to its lack of ionizing radiation. The extent of dissection, true and false lumen size, false lumen patency, and branch vessel involvement are important imaging features and can be adequately evaluated by MRA.

In the diagnosis of aortic dissection, the demonstration of an intimal flap is the key finding (Fig. 21.19). Black-blood and cine-balanced gradient echo images may actually demonstrate the flap most crisply due to pulsatile movement of the flap with the cardiac cycle. Nevertheless, CE MRA or post-contrast T_1-weighted images are also effective at demonstrating the flap. These contrast techniques are also most sensitive at detecting slow flow in the false lumen. The false lumen can be distinguished from the true lumen by following the true lumen to the aortic root and LV cavity. The false lumen also typically has greater cross-sectional area and slower flow.

The amount of thrombus in the false lumen is an indirect indicator of the degree of communication between the true and false lumens. In cases of limited communication, low blood pressure and flow in the false lumen may lead to partial or complete thrombosis. In cases with high pressures in the false lumen, this lumen may enlarge and compromise

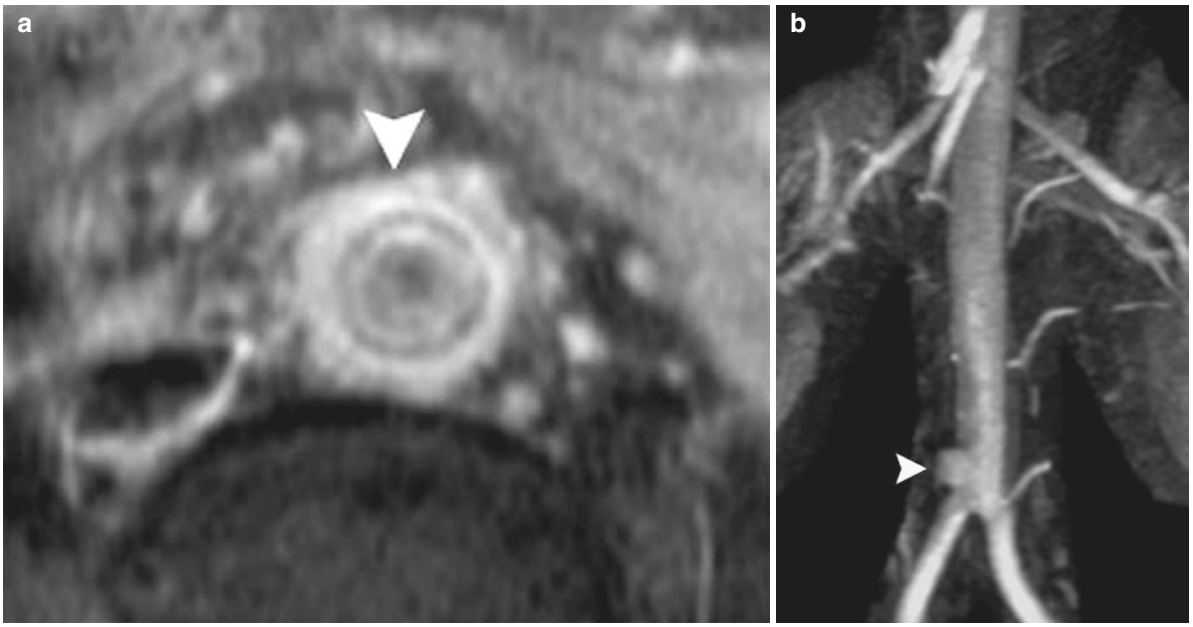

Fig. 21.16 56-year-old immunosuppressed woman with disseminated fungal infection in the setting of lung transplantation. Axial, fat-suppressed, post-contrast T1-weighted image (**a**) shows marked, circumferential wall thickening of the abdominal aorta (arrowhead), which also shows significant enhancement consistent with infectious aortitis. Coronal MIP reformation of CE MRA (**b**) obtained 3 months later shows interval development of a saccular aneurysm (so-called mycotic aneurysm) at the same level

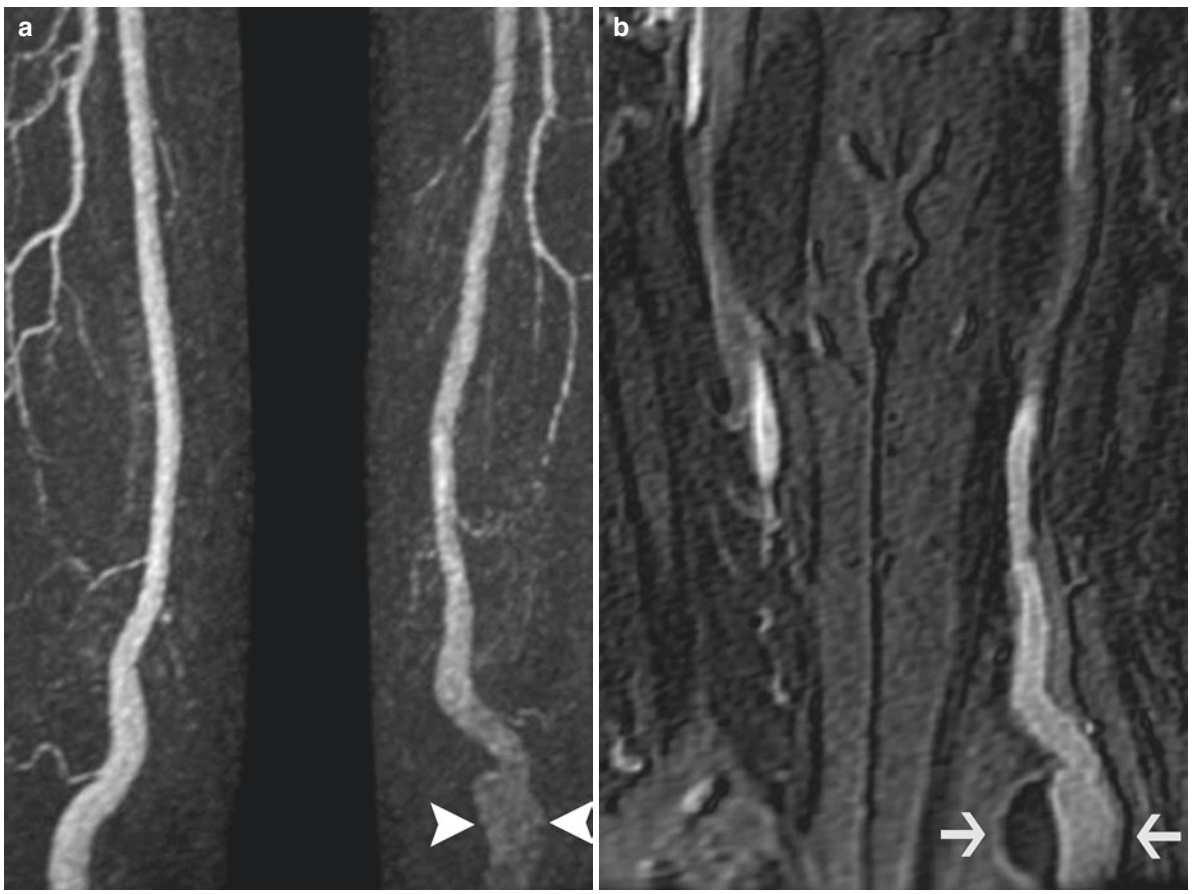

Fig. 21.17 Coronal MIP reformation (**a**) and source image (**b**) from a CE MRA of the thigh shows an aneurysm of the left popliteal artery (arrowheads). Note the maximal diameter of the aneurysm (arrows) is significantly underestimated if the measurement is performed on MIP reformation

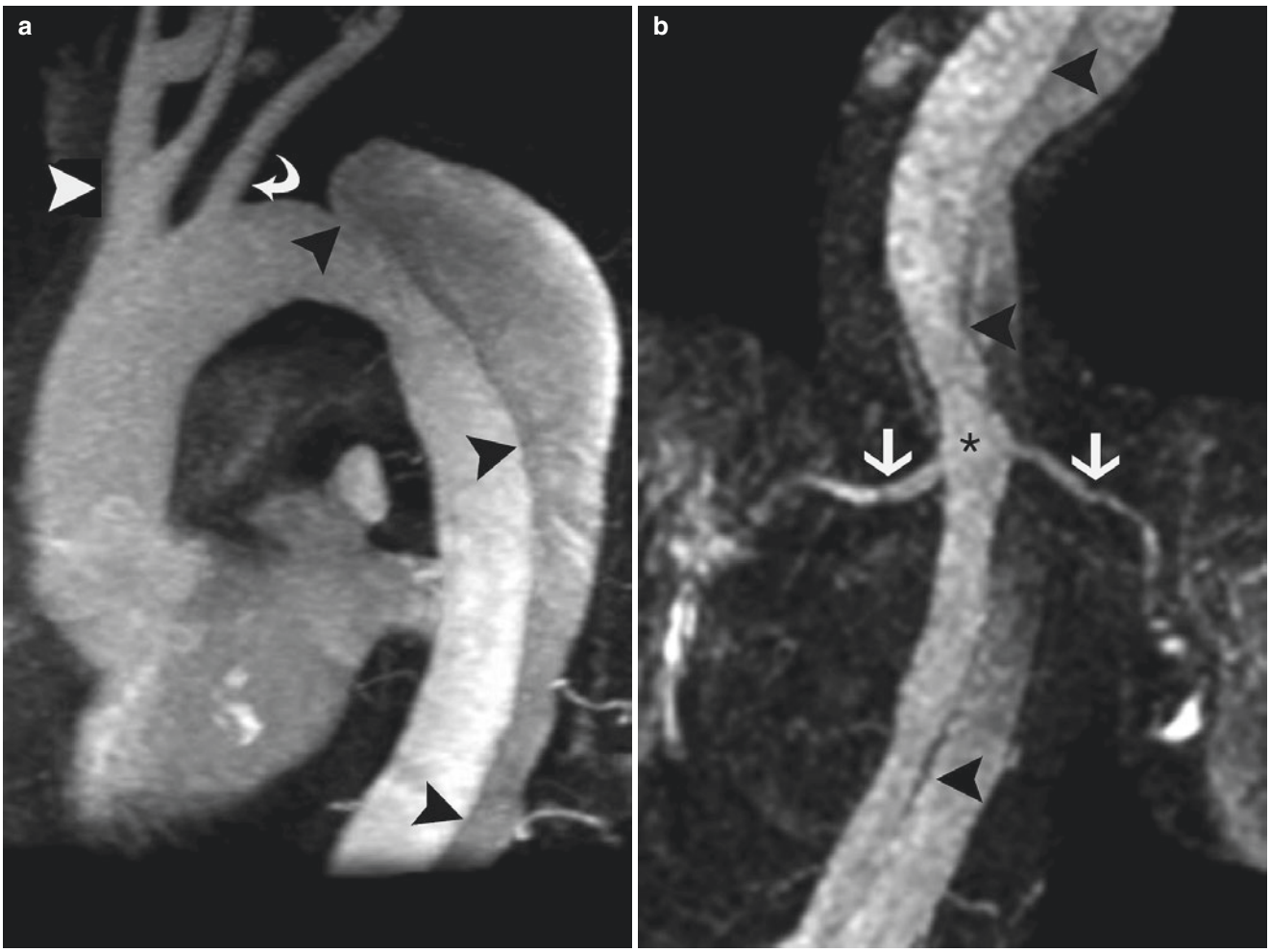

Fig. 21.18 MIP reformation of CE MRA for thoracic (**a**) and abdominal (**b**) aorta on a patient with type B dissection. There is an intimal flap (arrowheads) starting just distal to the origin of the left subclavian artery (curved arrow) and extending distally to the abdominal aorta. Both renal arteries (arrows) are arising from the true lumen (asterisk). Note a common origin of right brachiocephalic and left common carotid arteries (black arrowhead), so-called "bovine-type" arch

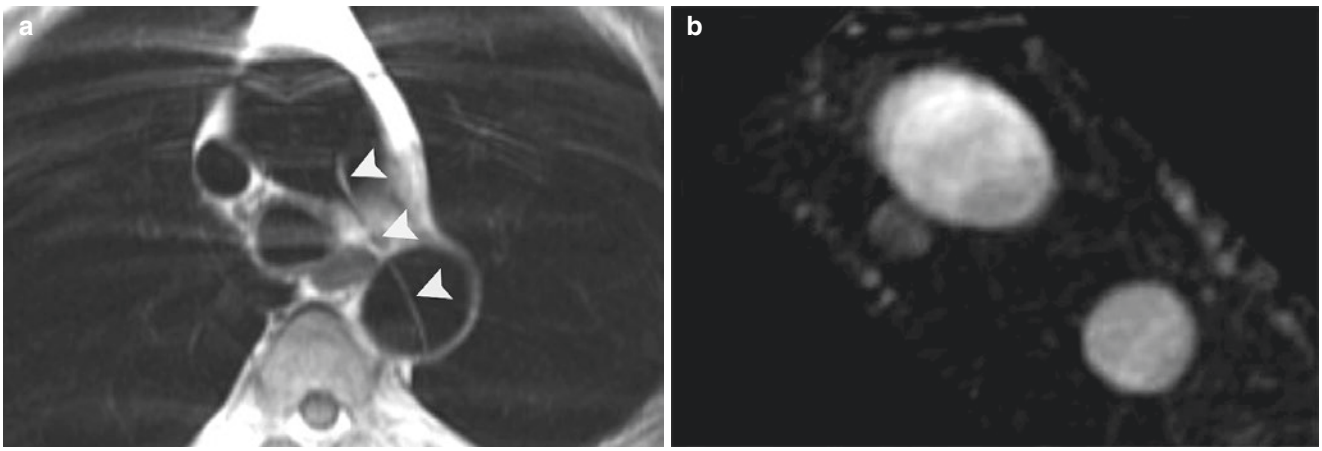

Fig. 21.19 Axial T1-weighted DIR (**a**) and axial reformation of CE MRA (**b**) at the level of aortic arch on this study performed to rule out an aortic dissection for a patient presenting with a chest pain. On T1-weighted image (**a**), there is linear signal intensity (arrowheads) within the lumen of the descending aorta, which could be misinterpreted as an intimal flap. Note the linear signal intensity is extending beyond the contour of the aorta suggestive of an artifact, which likely arose from the aortic arch due to pulsation. No intimal flap is seen on the post-contrast image (**b**)

branch vessel flow by two mechanisms: by compressing the true lumen proximal to their takeoff and by the flap mechanically compromising the vessels. A patent false lumen may also enlarge over time and become aneurysmal, leading to risk of rupture (Fig. 21.20). Cine-balanced gradient echo imaging is useful in type A dissections to evaluate aortic valve involvement or sometimes to identify entry and reentry sites.

Intramural Hematoma

Intramural hematoma (IMH) is characterized by aortic wall hematoma without flow on both sides of an intimal flap [70] and can be considered an atypical form of classical aortic dissection. It was more difficult to diagnose in the angiographic era, but in the cross-sectional imaging era, it has been increasingly diagnosed, accounting for 12–22% of patients with acute aortic syndromes in published series [65,

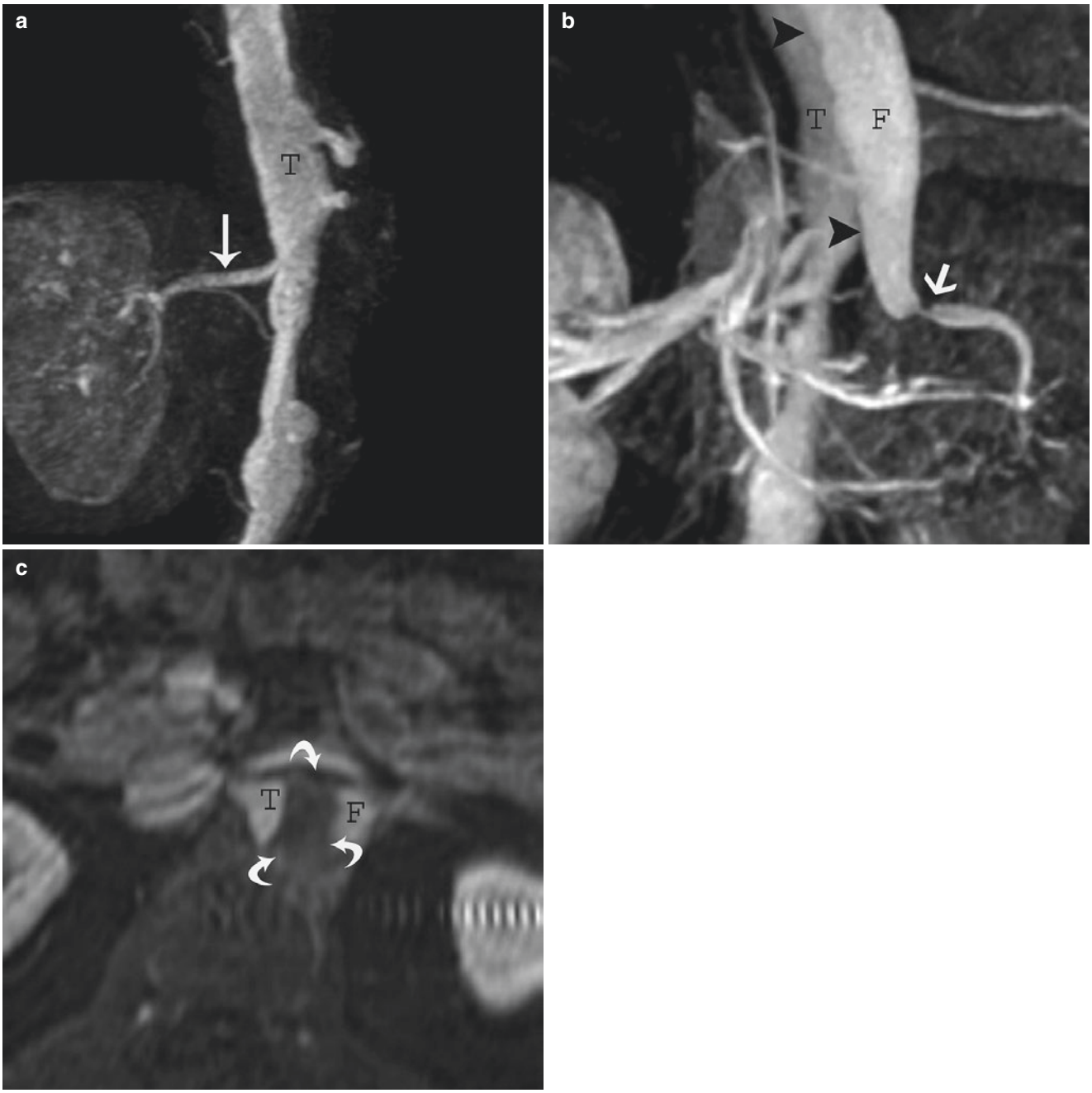

Fig. 21.20 Coronal first phase (**a**), second phase (**b**) MIP and axial reformation (**c**) of CE MRA show enhancement of the true lumen (T) on the first phase from which right renal artery (long arrow) is arising. The false lumen (F) is filled only on the second phase due to slow flow and gives rise to left renal artery, which shows a focal narrowing at the origin (arrow). Note extensive thrombus (curved arrows) in the false lumen (**c**) likely due to lack of a reentry tear, preventing unrestricted blood flow through the false lumen

71, 72]. Arterial hypertension has been the most frequent predisposing factor [72]. Spontaneous rupture of the vasa vasorum of the aortic wall or penetrating aortic ulcer (PAU) has been suggested as an initiating factor [73, 74].

IMH exhibits a regional distribution along the aorta, to classical dissection, typically involving the ascending and/or proximal descending thoracic aorta [8]. Patients who present with intramural hematoma can progress to a classic dissection, or patients may manifest variation between intramural hematoma and classic areas of dissection along the course of the aorta. As a possible precursor to classical dissection [72], the symptoms, prognostic impact of the location, and the treatment have been considered similar to those of classic aortic dissection; however, there have been published studies reporting favorable responses to medical treatment with complete absorption of type A IMH without surgical intervention [70, 75–78].

On MRA, IMH is diagnosed as thickening of the aortic wall, which is generally crescent-shaped but can be nearly circumferential. The signal intensity of IMH is variable, depending on the age of the blood, but acute blood is generally bright on T_1-weighted images (Fig. 21.21). Fat-saturated images may be helpful for demonstration of this signal intensity difference and separation of the wall of the aorta from the mediastinal fat. When the signal intensity of the IMH is not high, it may be difficult to differentiate IMH from mural thrombus of atherosclerosis, but its smooth nature and spiraling course are important features.

Penetrating Aortic Ulcer (PAU)

A PAU occurs when an ulcerated atherosclerotic plaque penetrates through the intima into the media of the aortic wall, causing an outpouching of the lumen beyond its expected contour. It is usually seen in elderly individuals with hypertension and severe atherosclerotic disease [79] and typically involves the descending thoracic aorta. PAU can be associated with a variable amount of intramural hematoma within the aortic wall in the acute stage, or IMH may develop a focal outpouching resembling PAU [79–82]. PAU located in the ascending aorta is usually treated surgically, whereas more distal PAU without clinical signs of instability is managed medically with follow-up imaging [83]. Unstable descending aorta PAU is considered for more aggressive treatment such as stent-graft placement, which is becoming a popular method to treat this entity given that the disease tends to occur in elderly patients with a high surgical risk because of other comorbidities [81].

On MRA, a PAU is seen as a focal outpouching extending beyond the expected contour of the lumen (Fig. 21.22). Axial reformations of the CE MRA are especially useful for demonstrating the focal outpouching, which is connected to the lumen of the aorta and fills with contrast material. The appearance of PAU can be indistinguishable from saccular aneurysms and/or focal dissection. When such an appearance is seen in asymptomatic patients, follow-up is usually advised as many remain stable over time [84].

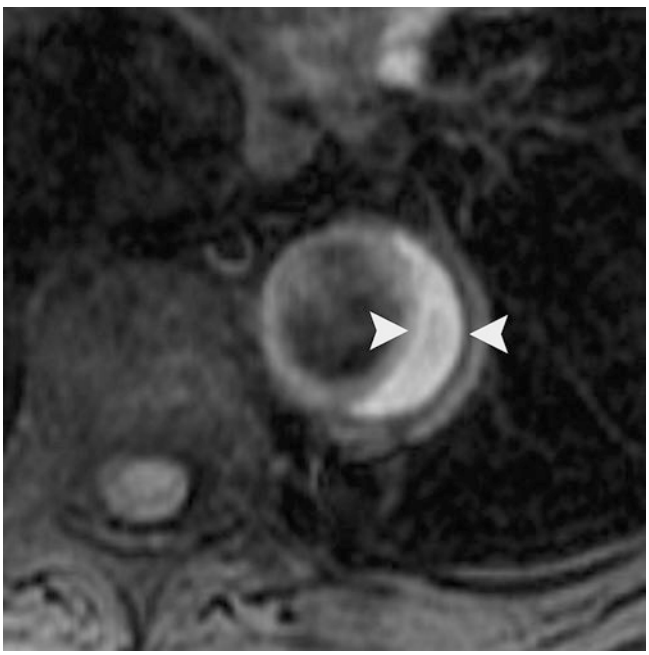

Fig. 21.21 Axial fat-suppressed DIR, T1-weighted image shows crescent shape high signal intensity (arrowheads) in the wall of the descending aorta suggestive of intramural hematoma

Fig. 21.22 Coronal MIP reformation of CE MRA shows a focal outpouching (arrowhead) that extends beyond the expected contour of the lumen likely represents a penetrating atherosclerotic ulcer

Infectious and Inflammatory Disease of the Aorta

Takayasu's arteritis is inflammation of the aorta and major branches (most often the thoracic aorta), resulting in stenosis and occlusions, hence its moniker, pulseless disease [85]. It can also manifest as aneurysms. The disease most frequently affects young Asian women and is characterized initially by systemic signs and symptoms. The significant imaging feature of this early phase is aortic wall thickening. The occlusive complications of the late phase usually take years to develop. Axial, black-blood, T_1-weighted images are highly sensitive for demonstrating the wall thickening of the early phase [8, 85, 86]. Fat-suppressed, T_1-weighted, post-contrast images are used to reveal the enhancement of the thickened wall, which is suggestive of active inflammation [87]. MIP reformations for the CE MRA are helpful in determining the degree and extent of occlusive disease of the aorta and arch branches during the late phase [8] (Fig. 21.23).

Giant cell arteritis is the most common form of vasculitis seen in the elderly, most commonly in women, which has very similar considerations for vascular involvement and therefore imaging as Takayasu's arteritis [87, 88].

Aorta After Surgical or Endovascular Repair

As discussed, many aortic diseases are treated by intervention, either endovascular or surgical. In surgery, the diseased aortic segment is replaced by a synthetic graft; the native aorta can be wrapped around the graft [89]. For ascending repair, a segment of graft can be left free within the native descending thoracic aorta to facilitate future descending repair ("elephant trunk" graft) [90]. After surgery, follow-up imaging is routinely recommended to confirm graft stability and evaluate for possible complications, such as graft dehiscence and pseudoaneurysm, or to ensure the stability of the remaining unrepaired segments of the aorta.

On MRA, the graft and/or the anastomosis may be recognized as a segment showing an abrupt caliber change relative to the native aorta, which also may show atherosclerotic change (Fig. 21.24). A metallic prosthetic aortic valve is seen as a signal void area in the expected location of the aortic valve because of magnetic susceptibility artifact. Stable fluid or soft tissue intensity material surrounding or adjacent to the aortic graft in a patient without evidence of infection likely represents old hematoma and/or scarring and may remain long after surgery.

Stent grafts are increasingly being used for treating aortic diseases. While they are generally safe to image (following manufacturer guidelines), the metal in their frames may obscure the surrounding vascular structures to a greater or lesser extent depending on their exact structure and composition, possibly compromising the ability to assess for endoleak. For this reason, CT is generally preferred for imaging these devices.

Fig. 21.23 55-year-old female with a known history of Takayasu disease. Coronal MIP reformation of CE MRA shows total occlusion of the proximal segment of the left subclavian artery (arrowhead), which is patent distally likely due to a retrograde flow through the left vertebral artery (arrow) (so-called subclavian steal syndrome)

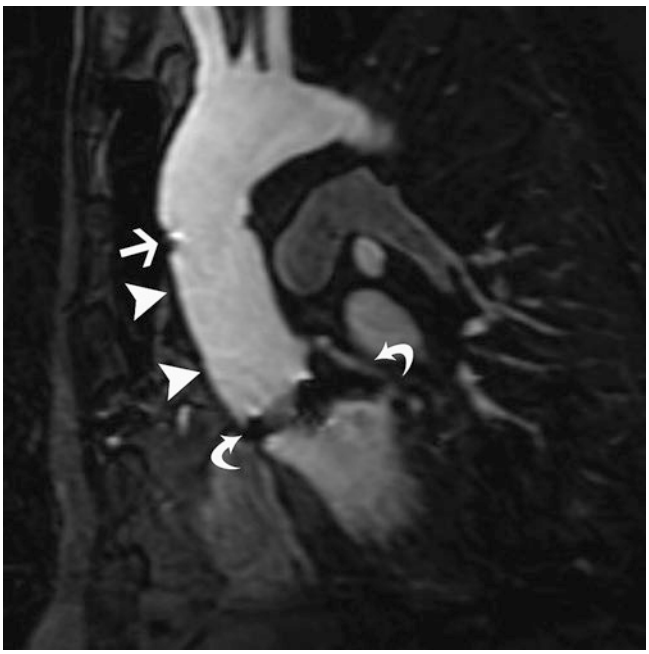

Fig. 21.24 Oblique sagittal CE MRA image of a patient with a history of ascending aorta repair with a Dacron graft (arrowheads). Note the distal anastomosis (arrow) and metallic susceptibility artifact from the prosthetic aortic valve (curved arrows)

Renal Arteries

Imaging Protocol

CE MRA has been the principal MRA technique for evaluation of the renal arteries. Patients should be imaged in the supine position on a torso phased array coil to maximize SNR, and a coronal FOV placed starting from the celiac axis to the common iliac arteries inferiorly because accessory renal arteries may rarely arise this low. It is important to make sure the imaged volume extends a couple centimeters anterior to the aorta as the right renal artery in particular often has a quite anterior arc. Posteriorly, the majority of the renal parenchyma is generally covered by scanning through the posterior aspect of the aorta. Excluding the most posterior portion of the kidneys helps decrease acquisition time. Coronal MIP and thin axial reformations should be obtained. Axial or coronal single-shot T_2-weighted and post-contrast fat-suppressed T_1-weighted gradient echo scans are helpful in evaluating the full renal parenchyma, adrenals, and adjacent abdominal organs. 3D PC images, while suboptimal for imaging purposes due to turbulence-related signal voids, have been used as an adjunct to CE MRA anatomic imaging as an indirect assessment of the hemodynamic significance of lesions [91]. Since the recognition of gadolinium-based contrast agents as a risk factor for NSF, there has been renewed interest in non-contrast techniques for renal artery evaluation. One approach which has achieved good results is the use of 3D balanced gradient echo with navigator-gated imaging to allow free breathing [92] (Fig. 21.25).

Clinical Applications

Although atherosclerotic renal artery stenosis is a well-known cause of high blood pressure, accounting for approximately 5% of patients with hypertension, interventional treatment of the renal arteries by angioplasty and stenting has been controversial. The recent CORAL trial [93] which concluded that medical therapy was as efficacious as renal artery stenting has markedly diminished interest in identifying renal artery stenosis and consequently in renal MRA. Nevertheless, CE MRA has a proven track record of high accuracy in identifying atherosclerotic renal artery stenosis [94–97]. On MRA, atherosclerotic lesions typically involve the origin and proximal segment of the renal arteries, often with post-stenotic dilatation (Fig. 21.26). As always when evaluating for stenosis, review of thin axial reformation in addition to coronal MIP image is important.

Fibromuscular dysplasia (FMD) is a much less frequent cause of renovascular hypertension, which, however, exhibits a clear response to angioplasty. It occurs mainly in young women and may affect both renal arteries. Unlike atherosclerotic lesions, it typically affects the mid to distal artery and can even occur in intrarenal branches. On imaging, medial fibroplasia, the most common form of FMD, is seen as alternating foci of short segmental narrowings and aneurysmal dilatations, the so-called string of beads appearance (Fig. 21.27). The efficacy of MRA for FMD has never been fully documented, and some FMD, especially distal or

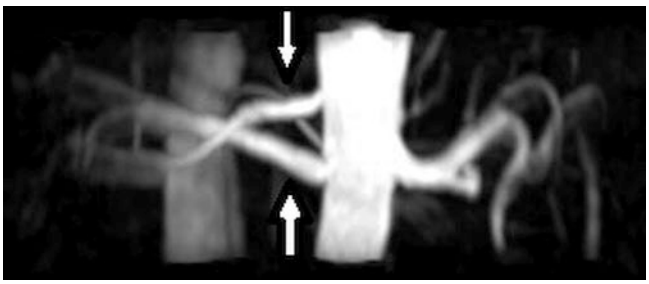

Fig. 21.25 Coronal anteroposterior MIP reformation of 3D balanced gradient echo renal MRA obtained with navigator gating and free breathing shows two renal arteries on the right (arrows)

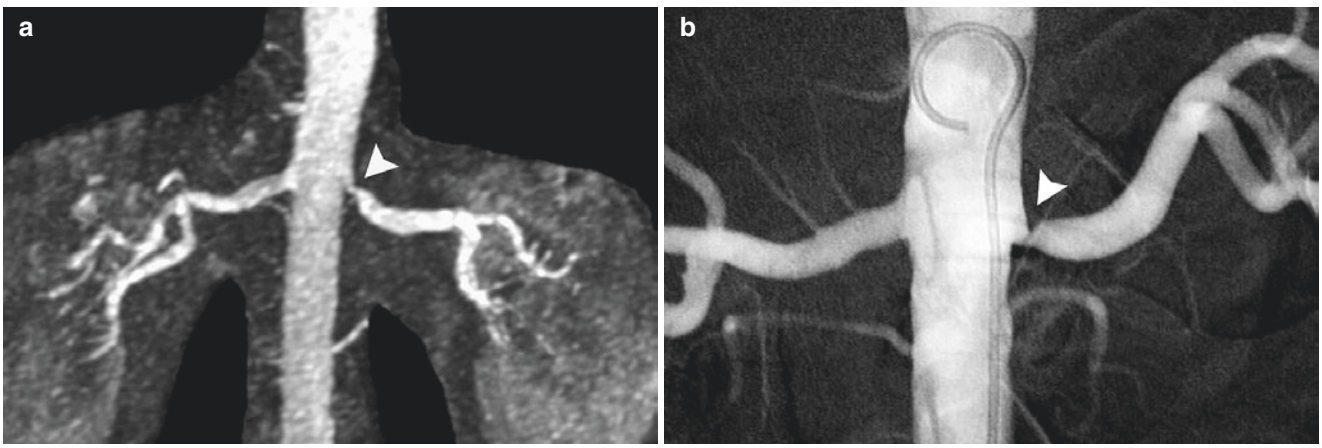

Fig. 21.26 Coronal MIP reformation of CE MRA (**a**) and digital subtraction contrast angiography (**b**) shows focal stenosis (arrowhead) at the origin of the left renal artery. Note the overestimation of the degree of stenosis on the MIP image

branch vessel, may be below the spatial resolution of MRA. Any patient who is clinically suspected of having FMD and in whom MRA is negative should be further evaluated with conventional angiography.

CE MRA is a safe, noninvasive method to evaluate the artery of a transplant kidney, provided patient does not have severe renal failure [98] (Fig. 21.28). CE MRA can also be used for comprehensive evaluation of potential renal donors prior to harvesting, including number, length, and location of renal arteries, as well as any anatomical variants of renal veins [99] (Fig. 21.29). In this indication, a delayed coronal T_1-weighted 3D gradient echo sequence can be added to the imaging protocol to demonstrate the collecting system. For better delineating the collecting system, a small amount of diuretic can be administered intravenously to increase the amount of gadolinium excretion and distend the collecting system.

Fig. 21.27 Coronal MIP of CE MRA (**a**) of a 47-year-old woman, presenting with high blood pressure, show a beading appearance (arrowhead) in the mid-segment of the right renal artery, which could be due to fibromuscular dysplasia. Confirmation of the disease with conventional angiography is necessary since artifacts sometimes may mimic this appearance

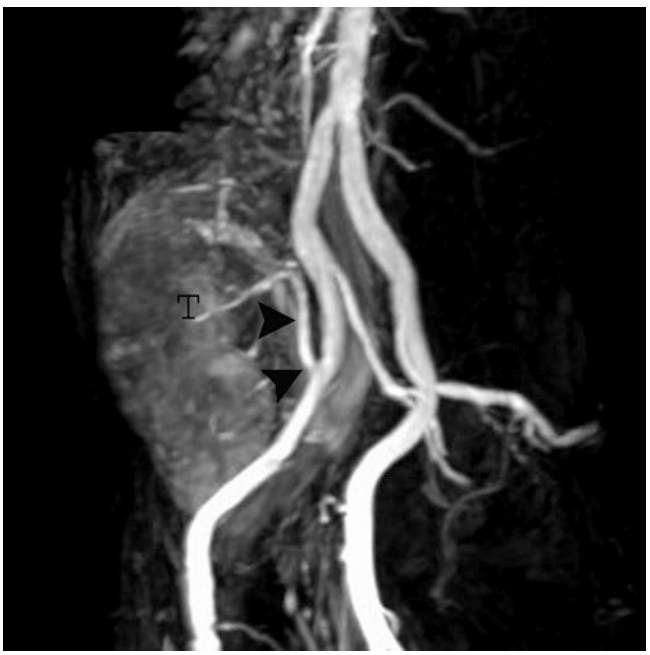

Fig. 21.28 Oblique coronal MIP of CE MRA shows patent artery (arrowheads) of a transplanted kidney (T) originating from the right external iliac artery

Aneurysms of the renal artery are most often due to atherosclerosis, but a substantial number can be attributed to other causes, such as FMD, neurofibromatosis, and polyarteritis nodosa [100]. Although CE MRA can demonstrate main renal artery aneurysms well, smaller intrarenal aneurysms such as those seen in polyarteritis nodosa are beyond the resolution of CE MRA. Arteriovenous malformations, or more commonly biopsy-related arteriovenous fistulas, can also involve the kidneys and be depicted by CE MRA (Fig. 21.30).

Mesenteric Arteries

CE MRA is again the technique of choice for mesenteric MRA. The sagittal imaging plane is optimal that it encompasses all three main mesenteric arteries in the smallest space and can be supplemented by coronal and axial reformations as needed. Flow measurements with PC MRA of the superior mesenteric artery (SMA) and vein have been used as a complementary approach to assess the physiological significance of SMA lesions [101, 102].

Mesenteric ischemia occurs when the blood supply to the intestine is insufficient. The majority of mesenteric ischemia is secondary to atherosclerotic disease and seen in elderly individuals. Because of a rich splanchnic collateral network,

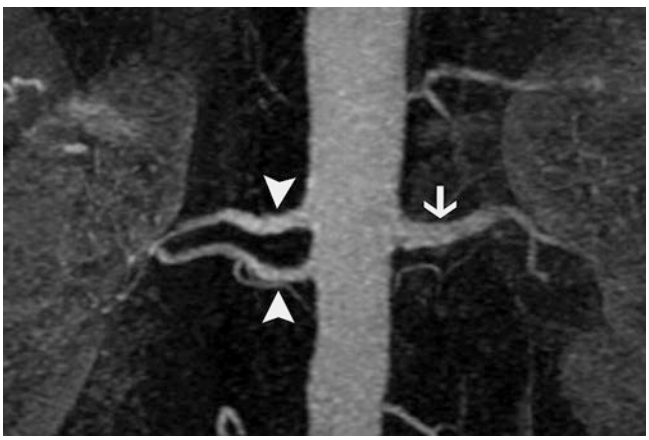

Fig. 21.29 Oblique coronal MIP of CE MRA of a health renal donor shows two renal arteries on the right side (arrowheads), which is important for surgeon to know prior to surgery. Note a single left renal artery (arrow)

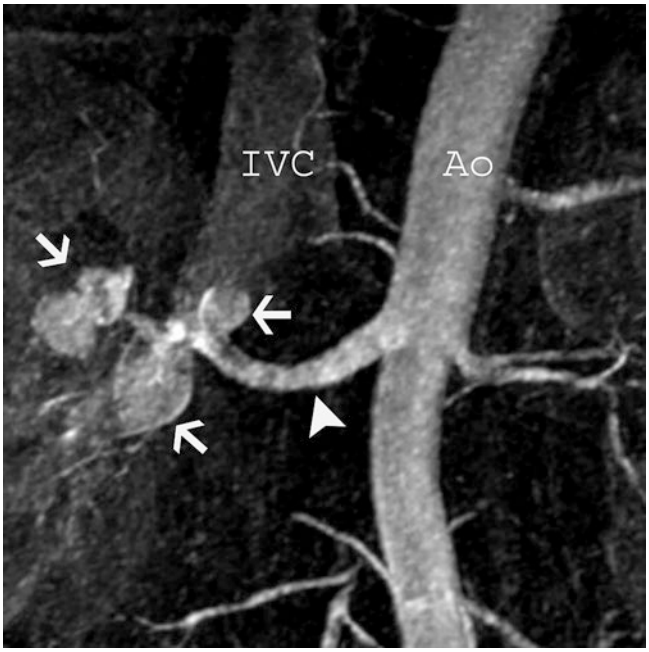

Fig. 21.30 Coronal MIP reformation of CE MRA of a 47-year-old woman presenting with hematuria shows a large right renal artery (arrowhead) and multiple contrasts filled vascular structures in the renal hilum (arrows) and early filling of the renal vein and inferior vena cava (IVC) consistent with renal arteriovenous malformation

mesenteric arterial disease may be clinically silent until at least two of three mesenteric arteries are severely narrowed or occluded. Atherosclerotic disease typically involves the proximal segments of the mesenteric arteries, which CE MRA has the capability to display with excellent diagnostic accuracy (Fig. 21.31). The distal mesenteric branches, however, may not be demonstrated well on CE MRA.

The celiac artery can sometimes be compressed by the adjacent median arcuate ligament, which joins both diaphragmatic crura. On MRA, this extrinsic compression has a characteristic appearance: the celiac axis is deviated inferiorly rather than taking its normal perpendicular course relative to the aorta (Fig. 21.32). The degree of compression is accentuated in expiration. In rare cases, spontaneous dissection of the SMA may be seen. An embolic event can be identified by CE MRA if the embolus lodges in the proximal segment of the artery (Fig. 21.33). Aneurysms can also be identified arising from the celiac and SMA, typically on MRA obtained for other purposes.

Arteries of the Lower Extremity

Imaging Protocol

Although CE MRA with moving-table and bolus-chasing technique after a single injection of contrast material may be sufficient, the hybrid technique with dual injections as described earlier under MRA techniques is more reliable, especially in patients with limb-threatening ischemia. Time-resolved MRI should be used for the calf and hindfoot, if available. With the recognition of the risk of NSF associated with the use of gadolinium-based compounds for MRA, there has been a resurgence of interest in non-contrast techniques for MRA, especially of the lower extremities due to the high incidence of peripheral arterial disease (PAD) in diabetics, who often have associated renal insufficiency. A technique that hearkens back to the earliest days of MRA [103], but has become clinically useful with advances in fast spin-echo technology, is the use of systolic-diastolic imaging. In this approach, bright-blood fast spin-echo images are obtained in systole and diastole. In diastole, both arteries and veins are bright. In systole, the pulsatile flow in arteries tends to make them dark. By accentuating this effect and subtracting the systolic and diastolic images, it is possible to obtain

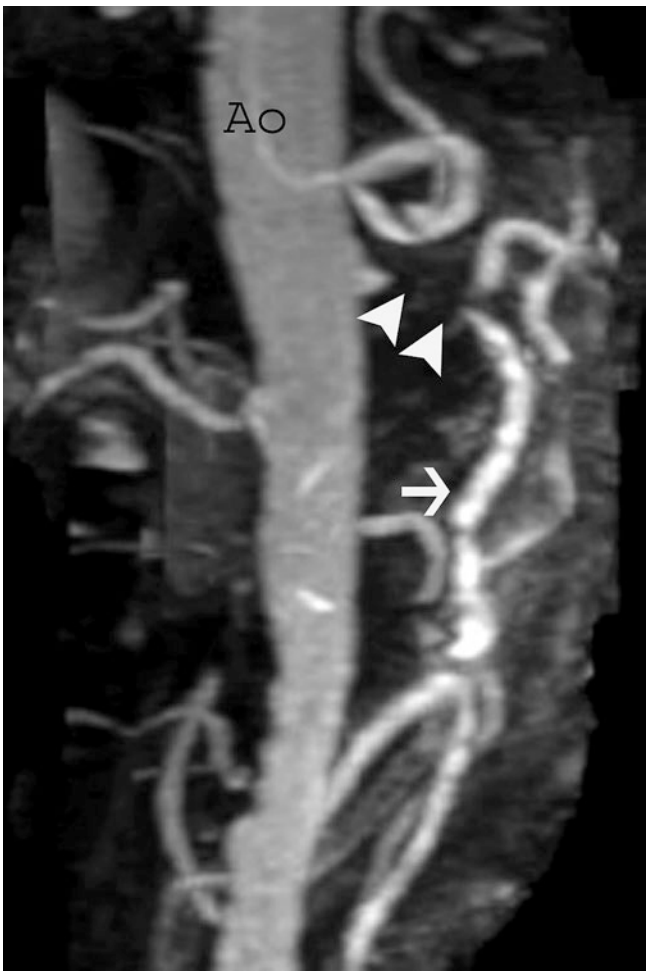

Fig. 21.31 Oblique sagittal MIP of CE MRA of a patient with a history of significant peripheral vascular disease and multiple episodes of mesenteric ischemia show occlusion of the proximal segment of the superior mesenteric artery (SMA) (arrowheads) with diffuse distal aneurysmatic dilatation (arrow). Note the visualized segment of the SMA shows significant contour irregularities due to atherosclerosis

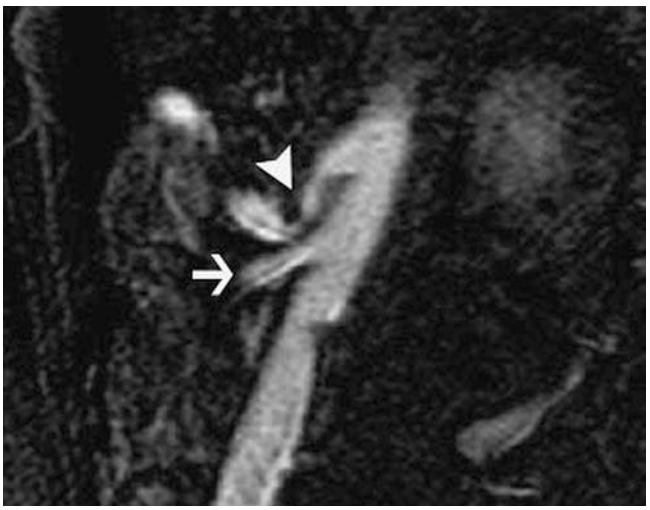

Fig. 21.32 Sagittal CE MRA of a 50-year-old woman presenting with postprandial epigastric pain and epigastric bruit on clinical exam show inferiorly displaced proximal segment of the celiac artery with a suggestion of superior external compression (arrowhead). This appearance is typical for median arcuate ligament compression in appropriate clinical setting. Note patent superior mesenteric artery (arrow)

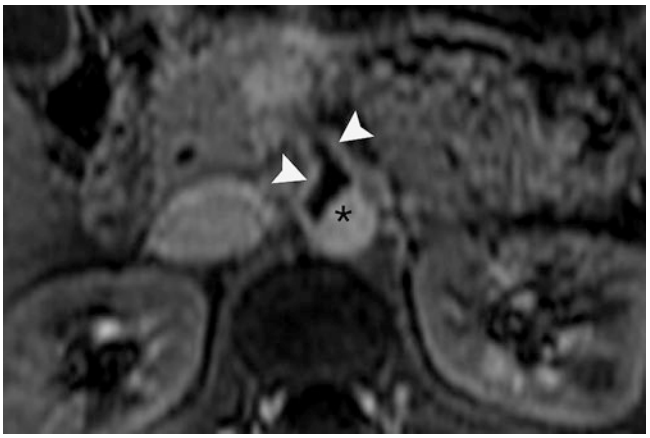

Fig. 21.33 Axial, T1-weighted post-contrast image of a 36-year-old otherwise healthy woman, presenting with abdominal pain and diarrhea. The image at the level of SMA shows hypointense filling defects in the SMA (arrowhead) and the right renal artery (not shown here) consistent with thrombus. Note patent abdominal aorta (asterisk)

an arteriogram with excellent background suppression (Fig. 21.34) [104]. While this technique clearly can provide high-quality MRA images in pulsatile vessels, its applicability in patients with severe PAD in whom the reconstituted vessels tend to have markedly damped pulsatility remains to be seen. Another interesting technique that is in development is the quiescent interval steady-state (QISS) MRA technique which uses a combination of time-of-flight (in plane

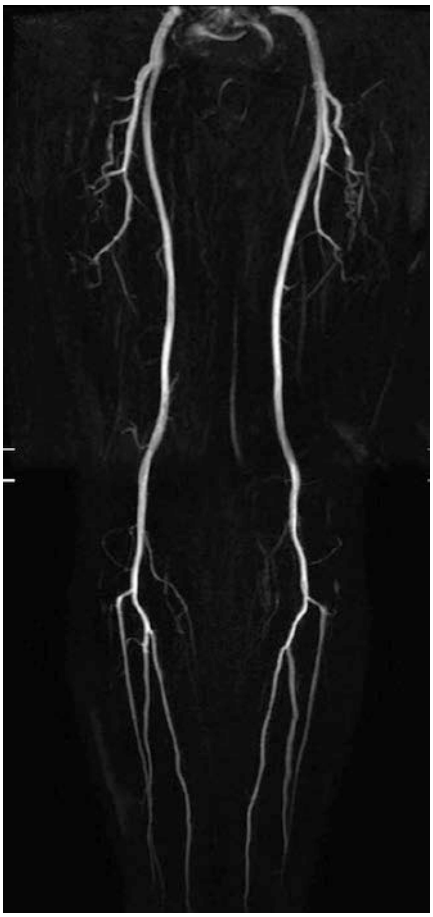

Fig. 21.34 Coronal MIP reformation of electrocardiography-triggered three-dimensional half-Fourier fast spin-echo MRA of the peripheral arteries of lower extremity

saturation with through-plane replacement by unsaturated spins, venous spatial presaturation) and balanced gradient echo imaging [105]. Advantages of this technique include the potential for higher sensitivity to slow, nonpulsatile flow in reconstituted tibial vessels. While promising, this technique is not yet widely available.

Atherosclerotic Disease of Peripheral Arteries

PAD is a common problem, especially in developed countries, affecting 8–12 million Americans [106]. Patients may present with claudication, a chronically threatened limb, or an acute limb-threatening event. The results of limb-threatening disease include nonhealing wounds, gangrene, and even amputation. Although abnormal leg blood pressure measurements may indicate the presence of disease, planning of surgical or endovascular treatment required precise anatomical mapping. CE MRA is an ideal noninvasive

technique for this purpose in patients without severe renal insufficiency and has replaced conventional angiography in many centers. It can demonstrate the location, severity, and extent of the disease with reliable identification of reconstituted vessels. Many investigators have demonstrated the superiority of CE MRA over conventional DSA for the identification of patent arterial segments in infrapopliteal runoff vessels (arteries of the calf and foot) suitable for bypass grafting, especially in patients with limb-threatening ischemia [107–110].

Branching sites and mechanical stress points such as aortic and iliac bifurcations, the origin and distal (segment through the adductor canal) of the superior femoral artery, and popliteal bifurcations are frequent sites of atherosclerotic disease. The distribution of vascular disease can be specific to underlying systemic diseases, such as isolated aortoiliac disease in middle-aged smokers (Fig. 21.35) and distal peripheral arterial disease in patients with adult-onset diabetes and end-stage renal disease (Fig. 21.36).

In addition to occlusive disease, atherosclerosis may result in aneurysms. The popliteal artery is the most common site of lower extremity aneurysms and can be complicated by occlusion of the artery because of thrombosis or ischemic symptoms caused by peripheral embolism. Atherosclerosis is not the only cause for arterial stenosis or occlusion, and asymmetric isolated disease, especially in younger patients, should raise the possibility of other causes, such as embolism, vasculitis, or external compression (Fig. 21.37). Popliteal entrapment syndrome is seen in young athletes because of compression of the popliteal artery by the

Fig. 21.35 Coronal MIP reformation of CE MRA of the pelvis and thigh of a 48-year-old woman presenting with severe buttock and thigh claudication shows occlusion of the distal abdominal aorta and both iliac arteries (arrows). The patient had hypertension as well as tobacco use as risk factors

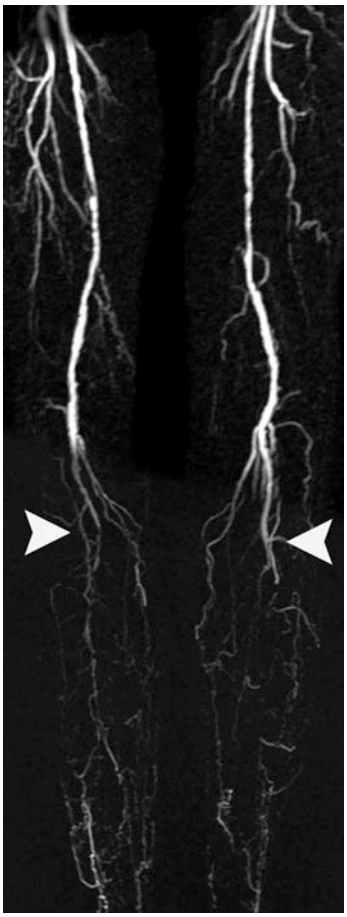

Fig. 21.36 Coronal MIP reformation of CE MRA of the thigh and calf of a 65-year-old woman with diabetes and renal failure presenting with progressive bilateral claudication. The image shows occlusion of both popliteal arteries (arrowheads) at the trifurcation with no significant distal reconstitution

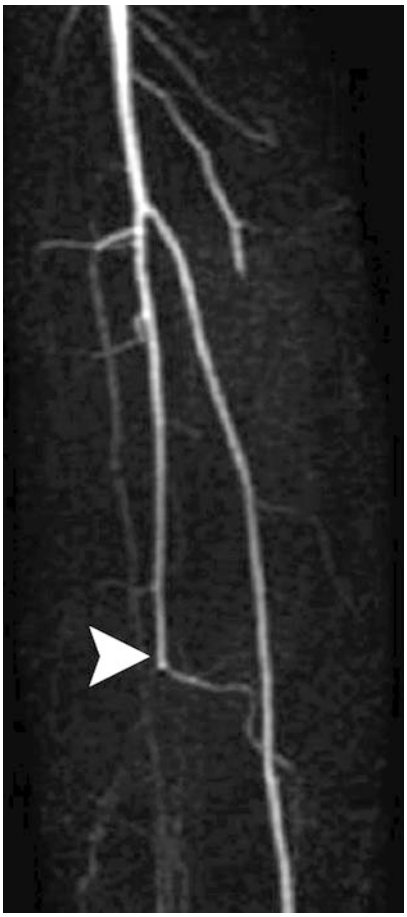

Fig. 21.37 Coronal MIP of calf CE MRA of 33-year-old woman, presenting with right lower extremity claudication following a C-section for preeclampsia, shows abrupt occlusion of the right peroneal artery (arrowhead) likely due to an embolic event

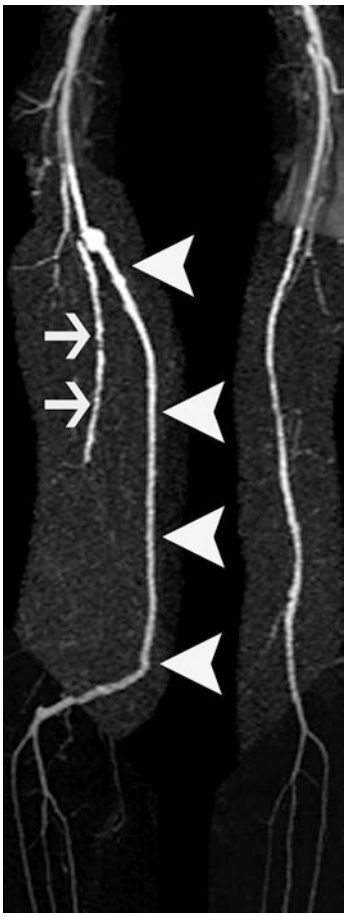

Fig. 21.38 Coronal MIP reformation of CE MRA of the thigh and calf of a patient with prior history of right femoropopliteal bypass grafting shows widely patent graft (arrowheads) with no evidence of disease. Note occluded native right superficial femoral artery (arrows)

gastrocnemius muscle tendon [111, 112]. CE MRA can also be utilized for evaluating bypass graft [113]. It is important for a reader to know the details of prior vascular surgery or percutaneous intervention as well as the classical appearance and artifacts produced by grafts, stents, clips, or other postoperative changes for accurate interpretation (Fig. 21.38).

References

1. Koelemay MJ, Lijmer JG, Stoker J, Legemate DA, Bossuyt PM. Magnetic resonance angiography for the evaluation of lower extremity arterial disease: a meta-analysis. JAMA. 2001;285(10):1338–45.
2. Yucel EK, Anderson CM, Edelman RR, Grist TM, Baum RA, Manning WJ, et al. AHA scientific statement. Magnetic resonance angiography : update on applications for extracranial arteries. Circulation. 1999;100(22):2284–301.
3. Grist TM. MRA of the abdominal aorta and lower extremities. J Magn Reson Imaging. 2000;11(1):32–43.
4. Ho VB, Corse WR, Hood MN, Rowedder AM. MRA of the thoracic vessels. Semin Ultrasound CT MR. 2003;24(4):192–216.
5. Green D, Parker D. CTA and MRA: visualization without catheterization. Semin Ultrasound CT MR. 2003;24(4):185–91.
6. Czum JM, Corse WR, Ho VB. MR angiography of the thoracic aorta. Magn Reson Imaging Clin N Am. 2005;13(1):41–64. V
7. Mcguigan EA, Sears ST, Corse WR, Ho VB. MR angiography of the abdominal aorta. Magn Reson Imaging Clin N Am. 2005;13(1):65–89. V–Vi
8. Tatli S, Lipton MJ, Davison BD, Skorstad RB, Yucel EK. From the RSNA refresher courses: MR imaging of aortic and peripheral vascular disease. Radiographics. 2003;23 Spec No: S59–78.
9. Tatli S, Yucel EK, Lipton MJ. CT and MR imaging of the thoracic aorta: current techniques and clinical applications. Radiol Clin N Am. 2004;42(3):565–85. Vi
10. Carroll TJ, Grist TM. Technical developments in MR angiography. Radiol Clin N Am. 2002;40(4):921–51.
11. Carr JC, Finn JP. MR imaging of the thoracic aorta. Magn Reson Imaging Clin N Am. 2003;11(1):135–48.
12. Rajagopalan S, Prince M. Magnetic resonance angiographic techniques for the diagnosis of arterial disease. Cardiol Clin. 2002;20(4):501–12. V
13. Neimatallah MA, Ho VB, Dong Q, Williams D, Patel S, et al. Gadolinium-enhanced 3d magnetic resonance angiography of the thoracic vessels. J Magn Reson Imaging. 1999;10(5):758–70.

14. Davis CP, Hany TF, Wildermuth S, Schmidt M, Debatin JF. Postprocessing techniques for gadolinium-enhanced three-dimensional MR angiography. Radiographics. 1997;17(5):1061–77.
15. Fuchs F, Laub G, Othomo K. Truefisp–technical considerations and cardiovascular applications. Eur J Radiol. 2003;46(1):28–32.
16. Kaufman JA, Mccarter D, Geller SC, Waltman AC. Two-dimensional time-of-flight MR angiography of the lower extremities: artifacts and pitfalls. AJR Am J Roentgenol. 1998;171(1):129–35.
17. Anderson CM, Saloner D, Tsuruda JS, Shapeero LG, Lee RE. Artifacts in maximum-intensity-projection display of MR angiograms. AJR Am J Roentgenol. 1990;154(3):623–9.
18. Walker MF, Souza SP, Dumoulin CL. Quantitative flow measurement in phase contrast MR angiography. J Comput Assist Tomogr. 1988;12(2):304–13.
19. Dumoulin CL. Phase contrast MR angiography techniques. Magn Reson Imaging Clin N Am. 1995;3(3):99–411.
20. Evans AJ, Iwai F, Grist TA, Sostman HD, Hedlund LW, et al. Magnetic resonance imaging of blood flow with a phase subtraction technique. In vitro and in vivo validation. Investig Radiol. 1993;28(2):109–15.
21. Kondo C, Caputo GR, Semelka R, Foster E, Shimakawa A, Higgins CB. Right and left ventricular stroke volume measurements with velocity-encoded cine MR imaging: in vitro and in vivo validation. AJR Am J Roentgenol. 1991;157(1):9–16.
22. Lotz J, Meier C, Leppert A, Galanski M. Cardiovascular flow measurement with phase-contrast MR imaging: basic facts and implementation. Radiographics. 2002;22(3):651–71.
23. Lee VS, Spritzer CE, Carroll BA, Pool LG, Bernstein MA, et al. Flow quantification using fast cine phase-contrast MR imaging, conventional cine phase-contrast MR imaging, and Doppler sonography: in vitro and in vivo validation. AJR Am J Roentgenol. 1997;169(4):1125–31.
24. RR E, Chien D, Kim D. Fast selective black blood MR imaging. Radiology. 1991;181(3):655–60.
25. Stehling MK, Holzknecht NG, Laub G, Böhm D, Von Smekal A, Reiser M. Single-shot T1- and T2-weighted magnetic resonance imaging of the heart with black blood: preliminary experience. MAGMA. 1996;4(3–4):231–40.
26. Jara H, Barish MA. Black-blood MR angiography. Techniques, and clinical applications. Magn Reson Imaging Clin N Am. 1999;7(2):303–17.
27. Carr JC, Simonetti O, Bundy J, Li D, Pereles S, Finn JP. Cine MR angiography of the heart with segmented true fast imaging with steady-state precession. Radiology. 2001;219(3):828–34.
28. Barkhausen J, Ruehm SG, Goyen M, Buck T, Laub G, Debatin JF. MR evaluation of ventricular function: true fast imaging with steady-state precession versus fast low-angle shot cine MR imaging: feasibility study. Radiology. 2001;219(1):264–9.
29. Pereles FS, Mccarthy RM, Baskaran V, Carr JC, Kapoor V, et al. Thoracic aortic dissection and aneurysm: evaluation with nonenhanced true Fisp MR angiography in less than 4 minutes. Radiology. 2002;223(1):270–4.
30. Krishnam MS, Tomasian A, Malik S, Desphande V, Laub G, Ruehm SG. Image quality and diagnostic accuracy of unenhanced SSFP MR angiography compared with conventional contrast-enhanced MR angiography for the assessment of thoracic aortic diseases. Eur Radiol. 2010;20(6):1311–20.
31. Stabi KL, Bendz LM. Ferumoxytol use as an intravenous contrast agent for magnetic resonance angiography. Ann Pharmacother. 2011;45(12):1571–5.
32. Mezrich R. A perspective on K-space. Radiology. 1995;195(2):297–315.
33. Earls JP, Rofskky NM, Decorato DR, Krinsky GA, Weinreb JC. Breath-hold single-dose gadolinium-enhanced three-dimensional MR aortography: usefulness of a timing examination and MR power injector. Radiology. 1996;201(3):705–10.
34. Maki JH, Wilson GJ, Eubank WB, Hoogeveen RM. Utilizing sense to achieve lower station sub-millimeter isotropic resolution and minimal venous enhancement in peripheral MR angiography. J Magn Reson Imaging. 2002;15(4):484–91.
35. Svensson J, Petersson JS, Ståhlberg F, Larsson EM, Leander P. Olsson Le. Image artifacts due to a time-varying contrast medium concentration in 3d contrast-enhanced MRA. J Magn Reson Imaging. 1999;10(6):919–28.
36. Hany TF, Mckinnon GC, Leung DA, Pfammatter T, Debatin JF. Optimization of contrast timing for breath-hold three-dimensional MR angiography. J Magn Reson Imaging. 1997;7(3):551–6.
37. Foo TK, Saranathan M, Prince MR, Chenevert TL. Automated detection of bolus arrival and initiation of data acquisition in fast, three-dimensional. Gadolinium-Enhanced MR Angiography Radiology. 1997;203(1):275–80.
38. Wilman AH, Riederer SJ, King BF, Debbins JP, Rossman PJ, Ehman RL. Fluoroscopically triggered contrast-enhanced three-dimensional MR angiography with elliptical centric view order: application to the renal arteries. Radiology. 1997;205(1):137–46.
39. Marks B, Mitchell DG, Simelaro JP. Breath-holding in healthy and pulmonary-compromised populations: effects of hyperventilation and oxygen inspiration. J Magn Reson Imaging. 1997;7(3):595–7.
40. Laub G. Displays for MR angiography. Magn Reson Med. 1990;14(2):222–9.
41. Cline HE, Dumoulin CL, Lorensen WE, Souza SP, Adams WJ. Volume rendering and connectivity algorithms for MR angiography. Magn Reson Med. 1991;18(2):384–94.
42. Kvitting JP, Ebbers T, Wigström L, Engvall J, Olin C, Bolger AF. Flow patterns in the aortic root and the aorta studied with time-resolved, 3-dimensional, phase-contrast magnetic resonance imaging: implications for aortic valve-sparing surgery. J Thorac Cardiovasc Surg. 2004;127(6):1602–7.
43. Zhang HL, Khilnani NM, Prince MR, Winchester PA, Golia P, et al. Diagnostic accuracy of time-resolved 2d projection MR angiography for symptomatic Infrapopliteal arterial occlusive disease. AJR Am J Roentgenol. 2005;184(3):938–47.
44. Du J, Carroll TJ, Brodsky E, Lu A, Grist TM, et al. Contrast-enhanced peripheral magnetic resonance angiography using time-resolved vastly Undersampled isotropic projection reconstruction. J Magn Reson Imaging. 2004;20(5):894–900.
45. Wieben O, Grist TM, Hany TF, Thornton FJ, Glaser JK, et al. Time-resolved 3d MR angiography of the abdomen with a real-time system. Magn Reson Med. 2004;52(4):921–6.
46. Johnson KR, Patel SJ, Whigham A, Hakim A, Pettigrew RI, Oshinski JN. Three-dimensional, time-resolved motion of the coronary arteries. J Cardiovasc Magn Reson. 2004;6(3):663–73.
47. Swan JS, Carroll TJ, Kennell TW, Heisey DM, Korosec FR, et al. Time-resolved three-dimensional contrast-enhanced MR angiography of the peripheral vessels. Radiology. 2002;225(1):43–52.
48. Korosec FR, Frayne R, Grist TM, Mistretta CA. Time-resolved contrast-enhanced 3d MR angiography. Magn Reson Med. 1996;36(3):345–51.
49. Barger AV, Block WF, Toropov Y, Grist TM, Mistretta CA. Time-resolved contrast-enhanced imaging with isotropic resolution and broad coverage using an undersampled 3d projection trajectory. Magn Reson Med. 2002;48(2):297–305.
50. Ho KY, Leiner T, De Haan MW, Kessels AG, Kitslaar PJ, Van Engelshoven JM. Peripheral vascular tree stenoses: evaluation with moving-bed infusion-tracking MR angiography. Radiology. 1998;206(3):683–92.
51. Meaney JF, Ridgway JP, Chakraverty S, Robertson I, Kessel D, et al. Stepping-table gadolinium-enhanced digital subtraction MR

angiography of the aorta and lower extremity arteries: preliminary experience. Radiology. 1999;211(1):59–67.
52. Janka R, Fellner FA, Fellner C, Lang W, Requardt M, et al. A hybrid technique for the automatic floating table MRA of peripheral arteries using a dedicated phased-Array coil combination. ROFO. 2000;172(5):477–81.
53. Von Kalle T, Gerlach A, Hatopp A, Klinger S, Prodehl P, Arlart IP. Contrast-enhanced Mr angiography (Cemra) in peripheral arterial occlusive disease (Paod): conventional moving table technique versus hybrid technique. ROFO. 2004;176(1):62–9.
54. Schmitt R, Coblenz G, Cherevatyy O, Brunner H, Fröhner S, et al. Comprehensive MR angiography of the lower limbs: a hybrid dual-bolus approach including the pedal arteries. Eur Radiol. 2005;15(12):2513–24.
55. Rapp JH, Wolff SD, Quinn SF, Soto JA, Meranze SG, et al. Aortoiliac occlusive disease in patients with known or suspected peripheral vascular disease: safety and efficacy of gadofosveset-enhanced MR angiography–multicenter comparative phase iii study. Radiology. 2005;236(1):71–8.
56. Huang SY, Kim CY, Miller MJ, Gupta RT, Lessne ML, et al. Abdominopelvic and lower extremity deep venous thrombosis: evaluation with contrast-enhanced MR venography with a blood-pool agent. AJR Am J Roentgenol. 2013;201(1):208–14.
57. Julsrud PR, Breen JF, Felmlee JP, Warnes CA, Connolly HM, Schaff HV. Coarctation of the aorta: collateral flow assessment with phase-contrast MR angiography. AJR Am J Roentgenol. 1997;169(6):1735–42.
58. Vandyke CW, White RD. Congenital abnormalities of the thoracic aorta presenting in the adult. J Thorac Imaging. 1994;9(4):230–45.
59. Khosa F, Krinsky G, Macari M, Yucel EK, Berland LL. Managing incidental findings on abdominal and pelvic CT and MRI, part 2: white paper of the ACR incidental findings committee II on vascular findings. J Am Coll Radiol. 2013;10(10):789–94.
60. Brown PM, Sobolev B, Zelt DT. Selective management of abdominal aortic aneurysms smaller than 5.0 cm in a prospective sizing program with gender-specific analysis. J Vasc Surg. 2003;38(4):762–5.
61. Nasim A, Thompson MM, Sayers RD, Boyle JR, Hartshorne T, et al. Role of magnetic resonance angiography for assessment of abdominal aortic aneurysm before endoluminal repair. Br J Surg. 1998;85(5):641–4.
62. Prince MR, Narasimham DL, Stanley JC, Wakefield TW, Messina LM, et al. Gadolinium-enhanced magnetic resonance angiography of abdominal aortic aneurysms. J Vasc Surg. 1995;21(4):656–69.
63. Nollen GJ, Van Schijndel KE, Timmermans J, Groenink M, Barentsz JO, et al. Magnetic resonance imaging of the main pulmonary artery: reliable assessment of dimensions in Marfan patients on a simple axial spin Echo image. Int J Cardiovasc Imaging. 2003;19(2):141–7. discussion 149–50
64. Mészáros I, Mórocz J, Szlávi J, Schmidt J, Tornóci L, Nagy L, Szép L. Epidemiology and clinicopathology of aortic dissection. Chest. 2000;117(5):1271–8.
65. Hagan PG, Nienaber CA, Isselbacher EM, Bruckman D, Karavite DJ, et al. The international registry of acute aortic dissection (IRAD): new insights into an old disease. JAMA. 2000;283(7):897–903.
66. Nienaber CA, Von Kodolitsch Y, Nicolas V, Siglow V, Piepho A, et al. The diagnosis of thoracic aortic dissection by noninvasive imaging procedures. N Engl J Med. 1993;328(1):1–9.
67. Nienaber CA, Eagle KA. Aortic dissection: new frontiers in diagnosis and management: part I: from etiology to diagnostic strategies. Circulation. 2003;108(5):628–35.
68. Nienaber CA, Eagle KA. Aortic dissection: new frontiers in diagnosis and management: part II: therapeutic management and follow-up. Circulation. 2003;108(6):772–8.
69. Nienaber CA, Rousseau H, Eggebrecht H, Kische S, Fattori R, et al. Instead trial. Randomized comparison of strategies for type B aortic dissection: the investigation of stent grafts in aortic dissection (instead) trial. Circulation. 2009;120(25):2519–28.
70. Kaji S, Akasaka T, Horibata Y, Nishigami K, Shono H, et al. Long-term prognosis of patients with type a aortic intramural hematoma. Circulation. 2002;106(12 Suppl 1):I248–52.
71. Evangelista A, Dominguez R, Sebastia C, Salas A, Permanyer-Miralda G, et al. Long-term follow-up of aortic intramural hematoma: predictors of outcome. Circulation. 2003;108(5):583–9.
72. Nienaber CA, Von Kodolitsch Y, Petersen B, Loose R, Helmchen U, Haverich A, Spielmann RP. Intramural hemorrhage of the thoracic aorta. Diagnostic and Therapeutic Implications Circulation. 1995;92(6):1465–72.
73. Stanson AW, Kazmier FJ, Hollier LH, Edwards WD, Pairolero PC, et al. Penetrating atherosclerotic ulcers of the thoracic aorta: natural history and clinicopathologic correlations. Ann Vasc Surg. 1986;1(1):15–23.
74. Gore I. Pathogenesis of dissecting aneurysm of the aorta. AMA Arch Pathol. 1952;53(2):42–53.
75. Sawhney NS, Demaria AN, Blanchard DG. Aortic intramural hematoma: an increasingly recognized and potentially fatal entity. Chest. 2001;120(4):1340–6.
76. Shimizu H, Yoshino H, Udagawa H, Watanuki A, Yano K, et al. Prognosis of aortic intramural hemorrhage compared with classic aortic dissection. Am J Cardiol. 2000;85(6):792–5. A10
77. Song JK, Kim HS, Kang DH, Lim TH, Song MG, et al. Different clinical features of aortic intramural hematoma versus dissection involving the ascending aorta. J Am Coll Cardiol. 2001;37(6):1604–10.
78. Song JK, Kim HS, Song JM, Kang DJ, Ha JW, et al. Outcomes of medically treated patients with aortic intramural hematoma. Am J Med. 2002;113(3):181–7.
79. Harris JA, Bis KG, Glover JL, Bendick PJ, Shetty A, Brown OW. Penetrating atherosclerotic ulcers of the aorta. J Vasc Surg. 1994;19(1):90–8. discussion 98–9
80. Wann S, Jaff M, Dorros G, Sampson C. Intramural hematoma of the aorta caused by a penetrating atheromatous ulcer. Clin Cardiol. 1996;19(5):438–9.
81. Ganaha F, Miller DC, Sugimoto K, Do YS, Minamiguchi H, et al. Prognosis of aortic intramural hematoma with and without penetrating atherosclerotic ulcer: a clinical and radiological analysis. Circulation. 2002;106(3):342–8.
82. Rubinowitz AN, Krinsky GA, Lee VS. Intramural hematoma of the ascending aorta secondary to descending thoracic aortic penetrating ulcer: findings in two patients. J Comput Assist Tomogr. 2002;26(4):613–6.
83. Quint LE, Williams DM, Francis IR, Monaghan HM, Sonnad SS, et al. Ulcerlike lesions of the aorta: imaging features and natural history. Radiology. 2001;218(3):719–23.
84. Von Kodolitsch Y, Nienaber CA. Ulcer of the thoracic aorta: diagnosis, therapy and prognosis. Z Kardiol. 1998;87(12):917–27.
85. Choe YH, Kim DK, Koh EM, Do YS, Lee WR. Takayasu arteritis: diagnosis with Mr imaging and MR angiography in acute and chronic active stages. J Magn Reson Imaging. 1999;10(5):751–7.
86. Yamada I, Nakagawa T, Himeno Y, Kobayashi Y, Numano F, Shibuya H. Takayasu arteritis: diagnosis with breath-hold contrast-enhanced three-dimensional MR angiography. J Magn Reson Imaging. 2000;11(5):481–7.
87. Maksimowicz-Mckinnon K, Clark TM, Hoffman GS. Takayasu arteritis and giant cell arteritis: a spectrum within the same disease? Medicine (Baltimore). 2009;88(4):221–6.
88. Hunder G. Vasculitis: Diagnosis and Therapy. Am J Med. 1996;100(2a):37s–45s.

89. Riley P, Rooney S, Bonser R, Guest P. Imaging the post-operative thoracic aorta: normal anatomy and pitfalls. Br J Radiol. 2001;74(888):1150–8.
90. Schepens MA. Aortic arch replacement: the conventional 'elephant trunk' technique. Multimed Man Cardiothorac Surg. 2007;2007(102). Mmcts 2006 002006.
91. De Cobelli F, Mellone R, Salvioni M, Vanzulli A, Sironi S, Manunta P. Renal artery stenosis: value of screening with three-dimensional phase-contrast MR angiography with a phased-Array multicoil. Radiology. 1996;201(3):697–703.
92. Maki JH, Wilson GJ, Eubank WB, Glickerman DJ, Pipavath S, Hoogeveen RM. Steady-state free precession MRA of the renal arteries: breath-hold and navigator-gated techniques vs. CE-MRA J Magn Reson Imaging. 2007;26(4):966–73.
93. Cooper CJ, Murphy TP, Cutlip DE, Jamerson K, Henrich W, et al. Coral investigators. Stenting and medical therapy for atherosclerotic renal-artery stenosis. N Engl J Med. 2014;370(1):13–22.
94. Hany TF, Debatin JF, Leung DA, Pfammatter T. Evaluation of the aortoiliac and renal arteries: comparison of breath-hold, contrast-enhanced, three-dimensional MR angiography with conventional catheter angiography. Radiology. 1997;204(2):357–62.
95. Holland GA, Dougherty L, Carpenter JP, et al. Breath-hold ultrafast three-dimensional gadolinium-enhanced MR angiography of the aorta and the renal and other visceral abdominal arteries. AJR Am J Roentgenol. 1996;166(4):971–81.
96. Snidow JJ, Johnson MS, Harris VJ, Margosian PM, Aisen AM, Lalka SG, et al. Three-dimensional gadolinium-enhanced MR angiography for aortoiliac inflow assessment plus renal artery screening in a single breath hold. Radiology. 1996;198(3):725–32.
97. Steffens JC, Link J, Grässner J, Mueller-Huelsbeck S, Brinkmann G, Reuter M, Heller M. Contrast-enhanced, K-space-centered, breath-hold MR angiography of the renal arteries and the abdominal aorta. J Magn Reson Imaging. 1997;7(4):617–22.
98. Ferreiros J, Mendez R, Jorquera M, Gallego J, Lezana A, Prats D, Pedrosa CS. Using gadolinium-enhanced three-dimensional MR angiography to assess arterial inflow stenosis after kidney transplantation. AJR Am J Roentgenol. 1999;172(3):751–7.
99. Jha RC, Korangy SJ, Ascher SM, Takahama J, Kuo PC, Johnson LB. MR angiography and preoperative evaluation for laparoscopic donor nephrectomy. AJR Am J Roentgenol. 2002;178(6):1489–95.
100. Schoenberg SO, Prince MR, Knopp MV, Allenberg JR. Renal MR Angiography. Magn Reson Imaging Clin N Am. 1998;6(2):351–70.
101. Li KC, Whitney WS, Mcdonnell CH, Fredrickson JO, Pelc NJ, Dalman RL, Jeffrey RB Jr. Chronic mesenteric ischemia: evaluation with phase-contrast cine MR imaging. Radiology. 1994;190(1):175–9.
102. Wasser MN, Geelkerken RH, Kouwenhoven M, Van Bockel JH, Hermans J, Schultze Kool LJ, De Roos A. Systolically gated 3d phase contrast MRA of mesenteric arteries in suspected mesenteric ischemia. J Comput Assist Tomogr. 1996;20(2):262–8.
103. Wedeen VJ, Meuli RA, Edelman RR, Geller SC, Frank LR, Brady TJ, Rosen BR. Projective imaging of pulsatile flow with magnetic resonance. Science. 1985;230(4728):946–8.
104. Miyazaki M, Takai H, Sugiura S, Wada H, Kuwahara R, Urata J. Peripheral MR angiography: separation of arteries from veins with flow-spoiled gradient pulses in electrocardiography-triggered three-dimensional half-Fourier fast spin-echo imaging. Radiology. 2003;227(3):890–6.
105. Hodnett PA, Koktzoglou I, Davarpanah AH, Scanlon TG, Collins JD, Sheehan JJ, et al. Evaluation of peripheral arterial disease with nonenhanced quiescent-interval single-shot MR angiography. Radiology. 2011;260(1):282–93.
106. Hirsch AT, Criqui MH, Treat-Jacobson D, Regensteiner JG, Creager MA, Olin JW, et al. Peripheral arterial disease detection, awareness, and treatment in primary care. JAMA. 2001;286(11):1317–24.
107. Kreitner KF, Kalden P, Neufang A, Düber C, Krummenauer F, Küstner E, et al. Diabetes and peripheral arterial occlusive disease: prospective comparison of contrast-enhanced three-dimensional MR angiography with conventional digital subtraction angiography. AJR Am J Roentgenol. 2000;174(1):171–9.
108. Loewe C, Schoder M, Rand T, Hoffmann U, Sailer J, Kos T, et al. Peripheral vascular occlusive disease: evaluation with contrast-enhanced moving-bed MR angiography versus digital subtraction angiography in 106 patients. AJR Am J Roentgenol. 2002;179(4):1013–21.
109. Dorweiler B, Neufang A, Kf K, Schmiedt W, Oelert H. Magnetic resonance angiography unmasks reliable target vessels for pedal bypass grafting in patients with diabetes mellitus. J Vasc Surg. 2002;35(4):766–72.
110. Morasch MD, Collins J, Pereles FS, Carr JC, Eskandari MK, Pearce WH, Finn JP. Lower extremity stepping-table magnetic resonance angiography with multilevel contrast timing and segmented contrast infusion. J Vasc Surg. 2003;37(1):62–71.
111. Atilla S, Ilgit ET, Akpek S, Yücel C, Tali ET, Işik S. MR imaging and MR angiography in popliteal artery entrapment syndrome. Eur Radiol. 1998;8(6):1025–9.
112. Turnipseed WD. Functional popliteal artery entrapment syndrome: a poorly understood and often missed diagnosis that is frequently mistreated. J Vasc Surg. 2009;49(5):1189–95.
113. Loewe C, Cejna M, Schoder M, Loewe-Grgurin M, Wolf F, Lammer J, Thurnher SS. Contrast material-enhanced, moving-table MR angiography versus digital subtraction angiography for surveillance of peripheral arterial bypass grafts. J Vasc Interv Radiol. 2003;14(9 Pt 1):1129–37.

CMR Guidance of RFA to Atrial Arrhythmias

22

Leenhapong Navaravong and Nassir Marrouche

Introduction

Atrial fibrillation (AF) is the most common arrhythmia worldwide. The prevalence is about 1% in people younger than 60 years of age but significantly increases to approximately 9% in people older than 80 years old [1]. Clinical presentation of atrial fibrillation ranges from asymptomatic to serious events such as congestive heart failure and thromboembolic events.

The American College of Cardiology/American Heart Association/Heart Rhythm Society guideline for management of AF emphasizes on clinical risk stratifications utilizing clinical parameters, such as CHADS2-VASC, and management strategies [2]. However, routine clinical management does not incorporate important aspects of disease, including pathological changes of the left atrium (LA), nor prediction of clinical outcomes.

Currently, radiofrequency catheter ablation (RFA) is the standard of care for AF patients who failed antiarrhythmic drugs [3]. The aggressive management with RFA has increased in popularity among physicians. The ablation strategies include circumferential lesions around pulmonary veins with or without additional left atrial ablation. Although catheter ablation is an effective therapeutic option for AF, the success of the procedure has been demonstrated only in a moderate percentage of AF patients. Thus, the dilemma lies in defining the appropriate ablation candidate that would benefit most from an ablation procedure.

L. Navaravong
Bangkok Heart Hospital, Bangkok, Thailand

UnityPoint Clinic – Cardiology, Iowa Methodist Medical Center, Des Moines, IA, USA
e-mail: leenhapong.navaravong@unitypoint.org

N. Marrouche (✉)
University of Utah School of Medicine, Comprehensive Arrhythmia Research and Management Center, Salt Lake City, UT, USA
e-mail: nassir.marrouche@carma.utah.edu

LGE imaging of the LA by CMR is superior to computed tomography (CT) or echocardiography because it can assess the structural remodeling/fibrosis [4]. This allows us to identify left atrial disease, predict the thromboembolic risks and success of RFA, and evaluate of complications of RFA.

Imaging Techniques

MRI and MRA Acquisition

Prior to RFA, it is now standard of care for obtaining cardiac imaging to evaluate the LA and pulmonary vein (PV) structures. The extension of atrial myocytes into the pulmonary vein ostium can trigger atrial fibrillation. Electrical isolation of PV by circumferential radiofrequency ablation around the PV ostia is the standard technique of RFA in AF. Information about size and diameter of PV ostia prior to ablation will help the electrophysiologist in selecting the right size of circular catheter during ablation.

These structures can be identified using standard anatomic and functional cardiac magnetic resonance imaging (CMR). These methods help identify left atrial, PV, and thoracic structures. Contrast-enhanced MRI can provide more detail of LA and PV. At our institution, we perform cine steady-state free precession for cardiac structure and function.

We use ECG-gated, respiratory-navigated three-dimensional gradient echo sequences with fast contrast injection (half dose, 1.0 ml/sec) followed by slow infusion (half dose, 0.1 ml/sec) magnetic resonance angiography (MRA) for characterization of LA and PV anatomy. Saturation pulses are applied with every heartbeat, and fat saturation is applied immediately before data acquisition during LA diastole. Additional scan parameters were axial imaging volume, FOV = 400 × 400 × 110, voxel size = 1.25 × 1.25 × 2.5 mm, TR/TE = 2.8/1.3 ms, flip angle of 15 degrees, TI = 150 ms, and phase-encoding direction: left to right. Typical scan time ranges from 3 to 5 min.

R. Y. Kwong et al. (eds.), *Cardiovascular Magnetic Resonance Imaging*, Contemporary Cardiology,
https://doi.org/10.1007/978-1-4939-8841-9_22

Pulmonary Vein Anatomy and Its Variation

Typically, there are four PVs that enter into the LA: right superior, right inferior, left superior, and left inferior veins (Fig. 22.1). Each vein enters the left atrium on its respective side, with superior veins projecting supero-anterior and inferior veins projecting infero-posterior. Normal variants of PV anatomy have been reported in 38% of patients who underwent RFA for AF [5]. The two most common variants are the presence of a single left common pulmonary vein or an additional right middle pulmonary vein. The diameter of all four PVs did not differ significantly, but the PV diameter appeared larger in AF patients versus those in sinus rhythm. The ostia of PV are typically oval with longer supero-inferior diameter compared to antero-posterior diameter.

The measurement of PV size is very important in the diagnosis of PV stenosis, which is one of the known complications of RFA of AF. Identification of the true PV orifice is difficult as there is no obvious anatomical landmark. The simple and widely accepted method in measuring PV size is using the sagittal plane [6]. The maximal diameter, perimeter, and cross-sectional area are measured in the sagittal plane at the location in which the pulmonary veins separate from the LA and from each other. Interestingly, one study demonstrated that larger total PV cross-sectional area (summation of all four PV cross-sectional area) predicts AF recurrent after RFA independent of the type of AF or LA size, but PV diameter does not [7, 8].

Detection of Left Atrial Appendage Thrombus and Spontaneous Echocardiographic Contrast

Currently, transesophageal echocardiography (TEE) is considered the gold standard for detection of left atrial appendage (LAA) thrombus and spontaneous echo contrast (SEC). Early studies utilizing inversion recovery dark blood imaging showed the feasibility of CMR for detecting LAA thrombus [9]. However, limited spatial resolution and artifacts caused by slow flow (which can mimic thrombus) reduce clinical utility. Other MRI protocols, such as 2D perfusion and contrast-enhanced 3D FLASH (fast low-angle shot) sequence imaging, do encounter the similar drawback of limited spatial resolution [9–11].

Imaging protocols with high spatial resolution and 3D coverage, such as those currently used in coronary magnetic resonance angiography using both navigator and electrocardiographic gating, might be of great potential in assessing the LAA. Recently, Rathi and colleagues have demonstrated promising results with 100% concordance between TEE and CMR in detecting LAA thrombus in 97 patients who underwent AF ablation [12]. Although using CMR in detection of LAA thrombus or SEC is not currently a gold standard, these findings are promising.

LGE Image Acquisition

At our institution, all studies were obtained on a 1.5 Tesla (T) Avanto clinical scanner or 3 T Trio scanner (Siemens Medical

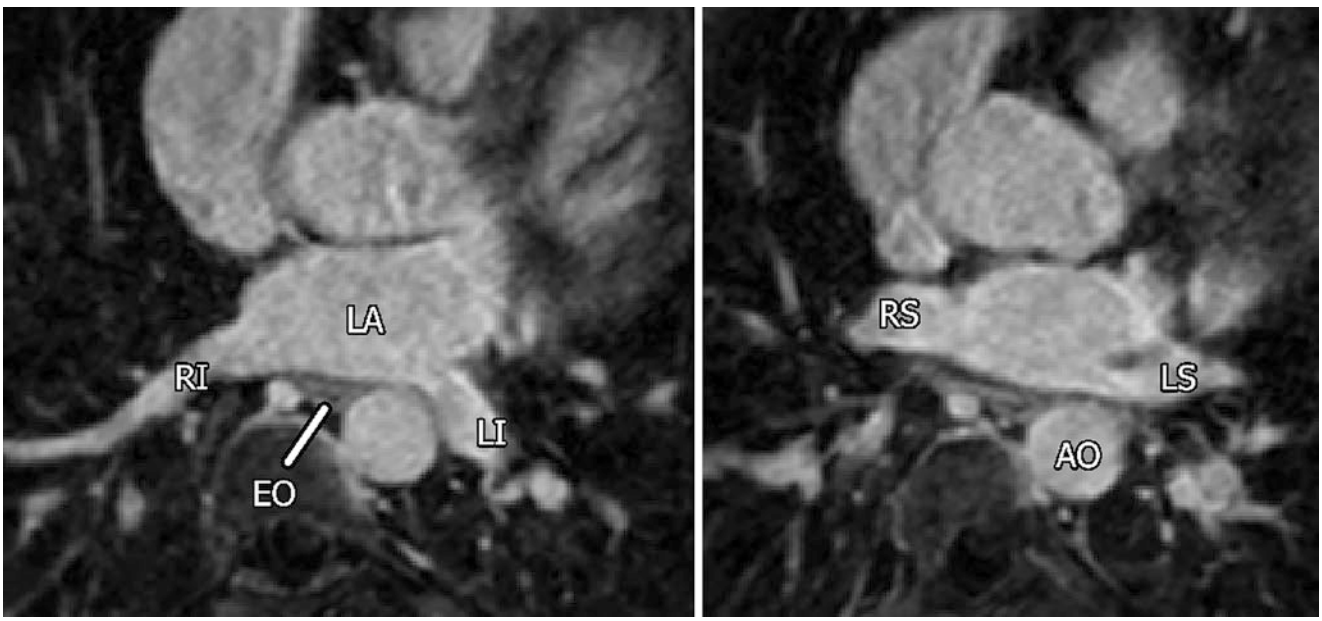

Fig. 22.1 Anatomy of left atrium, pulmonary veins, and adjacent structures. Images show left atrium (LA); four pulmonary veins; left superior (LS), left inferior (LI), right superior (RS), right inferior (RI) pulmonary veins; esophagus (EO); and descending aorta (AO)

Solutions, Erlangen, Germany) using a total imaging matrix phased-array receiver coil. At approximately 10 min after contrast agent injection (0.1 mmol/kg, Multihance [Bracco Diagnostic Inc., Monroe Township, NJ, USA]), the scans are performed using a three-dimensional (3D) inversion recovery and respiration navigated, ECG-gated, gradient echo pulse sequence.

Typical acquisition parameters were free breathing using navigator gating and a transverse imaging volume with voxel size = 1.25 × 1.25 × 2.5 mm (reconstructed to 0.625 × 0.625 × 1.25 mm). Flip angles of 20° and 13° are used for the 1.5 T and 3 T scanners, respectively. The inversion time is identified using a scout scan and typically ranges between 270 and 310 ms for a 1.5 T scan and 280–330 ms for a 3 T scan. The repetition time and the echo time determine the signal's strength. The echo time is optimized to ensure that fat and water are out of phase and to reduce the signal intensity of partial volume fat-tissue voxels, thus optimizing delineation of the LA wall boundary. Typical repetition time to echo time ratios are 5.24:2.3 (1.5-T) and 3.3:1.4 (3-T). Generalized autocalibrating partially parallel acquisition (GRAPPA) was set with R = 2 and 46 reference lines. ECG gating was used to acquire a small subset of phase-encoding views during the diastolic phase of the LA cardiac cycle. The time interval between the R-peak of the ECG and the start of data acquisition were defined using the cine images of the LA. Fat saturation was used to suppress fat signal. The TE of the scan (2.3 ms) was chosen such that fat and water are out of phase and the signal intensity of partial volume fat-tissue voxels was reduced allowing improved delineation of the LA wall boundary.

The TI value for the LGE scan was identified using a scout scan. Typical scan time for the LGE study was 5–10 min depending on subject respiratory and heart rate.

Minimizing Artifacts in LGE Images

Sources of imaging artifacts include motion artifacts, rapid and irregular heart rates, acquisition errors, and device artifacts. To minimize motion artifacts, the respiratory navigator was attached on the right hemidiaphragm and data acquired at end expiration. LA motion artifacts were minimized by capturing images during LA diastole for 120 ms and setting the image acquisition to the time period with minimal LA motion (based on cine imaging as earlier). With this protocol, we are able to obtain acceptable LGE images for heart rates up to 100 bpm, regardless of the presence of sinus rhythm or AF. The implantable cardiac device artifacts are another factor that impaired the LGE quality. Recently, the novel wideband sequence replaced the nonselective adiabatic inversion pulse of approximately 1 kHz with a wideband hyperbolic secant inversion pulse of 3.8 kHz bandwidth. This allows myocardium to become properly inverted and eliminates the hyperintensity artifacts from the device [13]. However, this application was evaluated in the ventricular myocardium. Whether this can be applied to the thinner LA wall is uncertain.

Pre-Ablation Fibrosis Quantification

LA wall volumes were manually segmented by expert observers from the LGE images, using the Corview image processing software (MARREK Inc., Salt Lake City, UT, USA). First, the endocardial border of the LA and proximal part of PV were defined, by manually tracing the LA-PV blood pool in each slice of the LGE MRI volume. Next, the endocardial segmentation was morphologically dilated and then manually adjusted to fit the boundary of the epicardial LA surface, and then the endocardial segmentation was subtracted from the epicardial segmentation to define a wall segmentation. Finally, the segmentation of the LA wall was manually edited to exclude the mitral valve and PVs. The final 3D images have both LA and PV antra.

To delineate regions of fibrosis in LGE images, we defined enhancement through an intensity threshold that was determined by expert inspection. To assist this process, initial visualization using a volume-rendering tool in Corview allows the operator to visualize the distribution of enhancement in 3D. A custom transfer function allowed the operator to define gradations of enhancements while suppressing blood and normal tissue with a transfer function.

The threshold was defined for each patient at two standard deviations above the mean enhancement. Quantification of atrial tissue fibrosis was reported as a percentage of the LA wall volume. The process is summarized in Fig. 22.2.

With the threshold-based algorithm to quantify LA fibrosis, there is some degree of subjectivity to this approach. Despite these sources of imaging variability, a low degree of inter-observer variability has been shown in our recent study [14]. The correlation coefficient of inter-observer agreement, among three observers, ranged from 0.79 to 0.97. The high degree of agreement reflects the high scan quality and experience of the observers.

Correlation Between LGE of Left Atrium and Histological Findings

To evaluate this relationship, tissue biopsy of left atrium was obtained from ten patients with LGE, who underwent open heart surgery (nine with history of atrial fibrillation and one without history of atrial fibrillation) [14]. All tissue

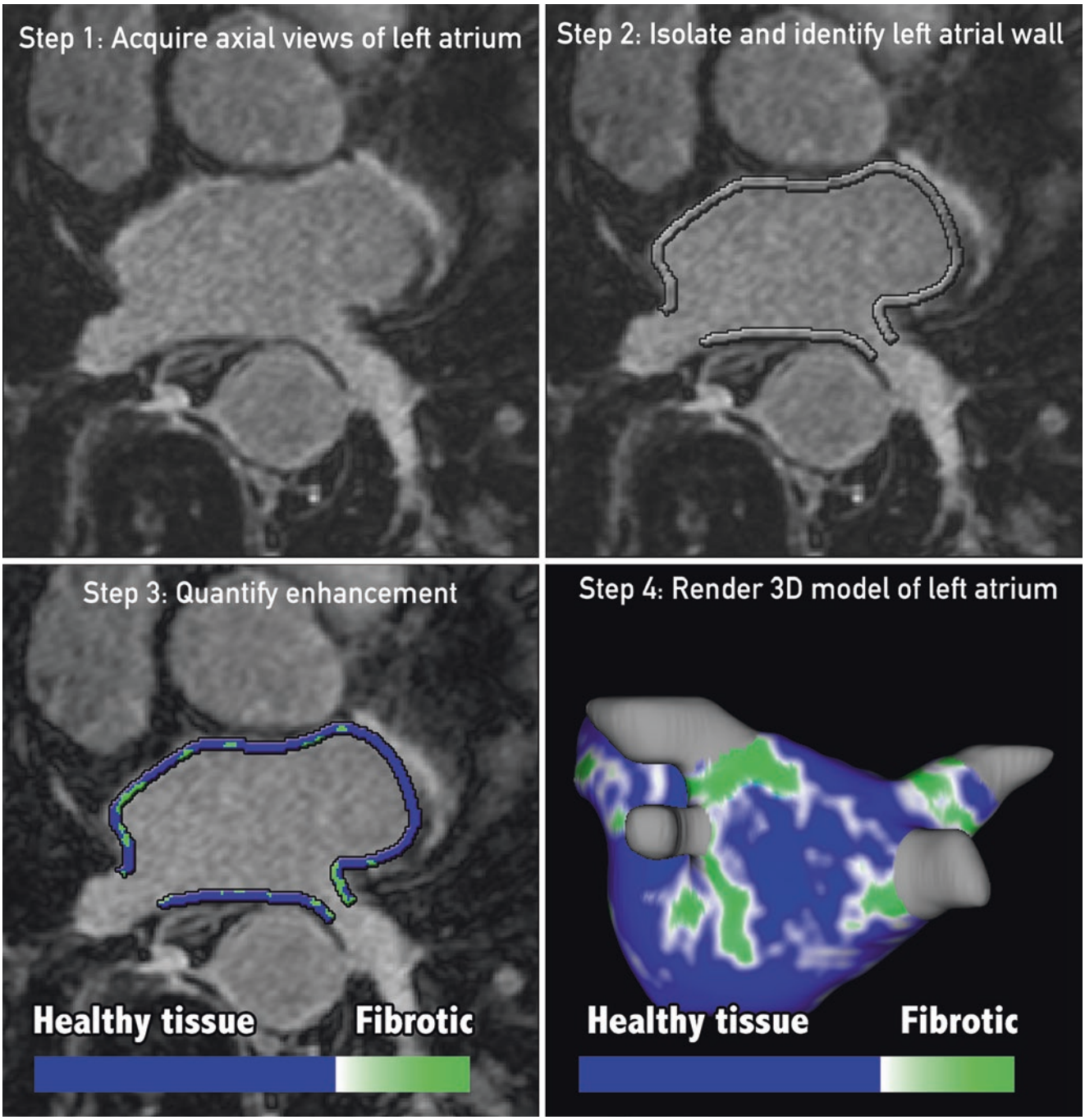

Fig. 22.2 After LGE images were acquired, each LA segment was manually contoured to identify endocardial and epicardial wall. The area of abnormal enhancement in LA wall segment was identified based on the relative abnormal intensity. Each segment was then combined to make 3D model of LA, and fibrosis was projected on the surface

specimens from area of abnormal enhancement demonstrated significant amount of interstitial fibrosis on Masson trichrome stain. Similarly, tissue specimen from non-enhanced area showed no or minimal fibrosis (Fig. 22.3). This study has confirmed the relationship between LA wall enhancement and histological findings.

Safety and Contraindication

End-stage renal disease, abandoned pacemaker/defibrillator leads, and severe claustrophobia represent standard contraindications for MRI. Prior to MRI, operators should determine whether the implantable devices are "MR safe," "MR

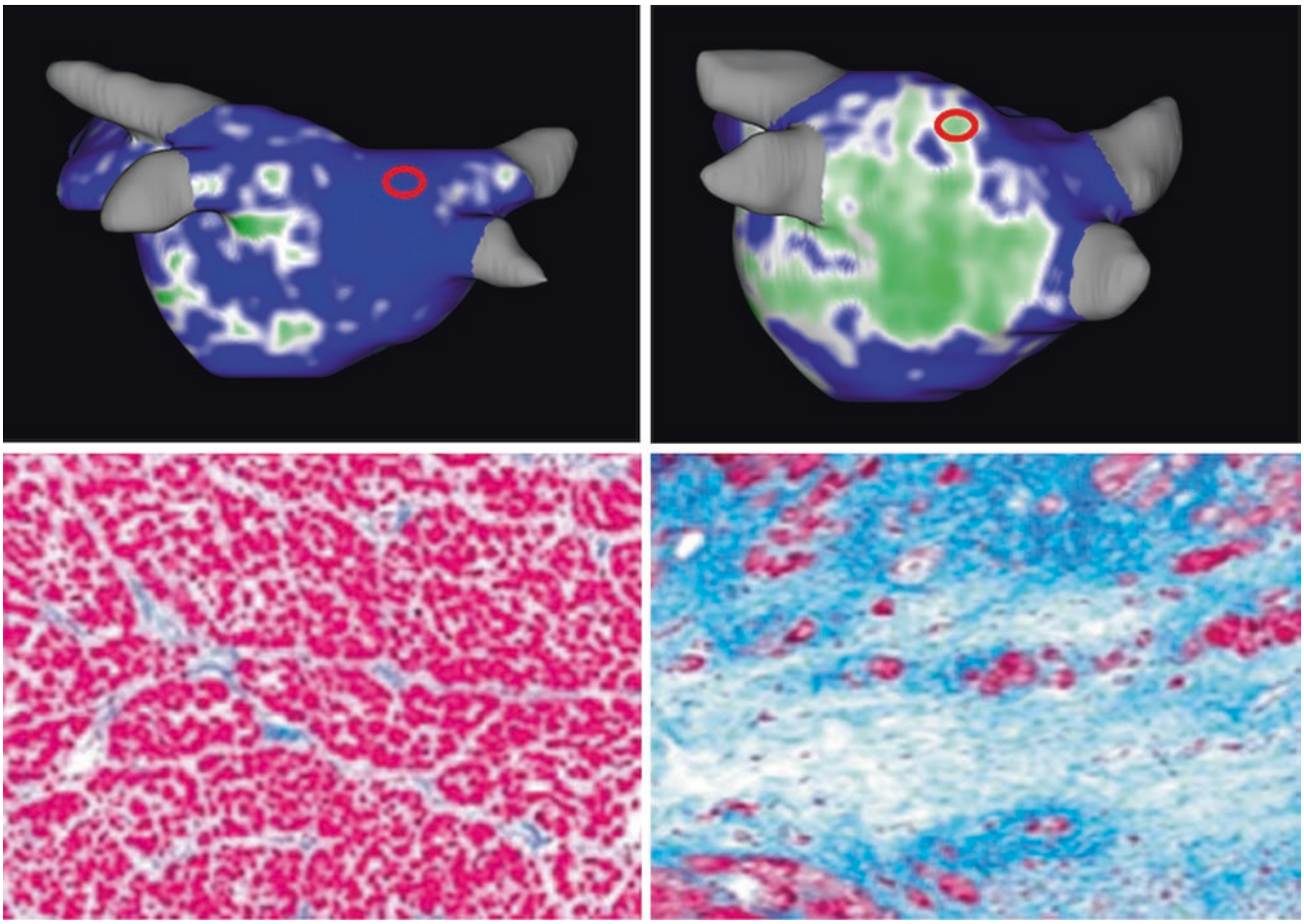

Fig. 22.3 Correlations between abnormal enhancement on LGE and tissue histology. The left panel demonstrates the area of non-enhancement on LGE, which has no fibrosis on histological examination. The right panel shows the area with significantly abnormal enhancement and its corresponding fibrosis on histology

conditional," or "not MR safe." While the MRI can be performed in certain pacemakers or implantable cardioverter-defibrillators (ICDs), each case should be reviewed for risk/benefit [15]. In setting of impaired renal function, one of the most serious adverse events is "nephrogenic systemic fibrosis." Generally, gadolinium infusion is contraindicated in patient with GFR < 30 ml/min/m2.

Benefit of LGE MRI in Atrial Fibrillation

Atrial Fibrosis and Atrial Fibrillation

Structural changes and interstitial fibrosis of the LA wall is well described in patients with AF in histological studies [16–20]. Tissue examination of the left atrium (LA) has also confirmed the presence of fibrosis in regions of low-voltage tissue [21]. Our group evaluated atrial fibrosis using LGE MRI in non-AF participants and compared the fibrosis burden to AF patients. We found that AF patients have a significantly higher LA fibrosis compared to non-AF participants ($16.6 \pm 11.2\%$ versus $3.1 \pm 1.9\%$; $P < 0.0001$). Whether fibrotic transformation of atrial myocardium is a cause or consequence of AF in patients with cardiovascular disease remains unclear.

Atrial Fibrosis by LGE MRI and Clinical Presentation

AF is classified as paroxysmal (episodes of arrhythmia are self-terminating within 7 days), persistent (AF episode lasts longer than 7 days or that needs pharmacologic or electrical cardioversion to terminate), long-standing persistent (persistent AF with longer than 1 year duration), and permanent AF (no attempts are planned for restoration of sinus rhythm) [3].

We found higher percent of paroxysmal AF in lower fibrosis and higher percent of persistent or permanent AF in higher degree of fibrosis. However, there was significant overlap in the degree of fibrosis between patients with different AF phenotypes. The phenotype did not accurately predict

the degree of atrial fibrosis [14, 22]. Moreover, we found that patients with lone AF (AF with no other cardiovascular disease condition) have the same burden of atrial fibrosis as those with non-lone AF [22, 23].

Left Atrial Fibrosis and Cerebrovascular Accident

AF patients have a higher risk of thromboembolic event compared to the general population [24]. The current scoring system (CHADS2 or CHADS2-VASC), based on clinical comorbidities (such as age, diabetes mellitus, congestive heart failure, etc.) has been shown to be modest [25, 26]. However, these are commonly used in current clinical practice.

A retrospective study by Daccarett et al. demonstrated that LA fibrosis by LGE is an independent risk factor for stroke [27]. Patients who experienced a prior stroke had a significantly higher percentage of LA fibrosis than those without history of a previous stroke (24.4 ± 12.4% vs 16.1 ± 9.8%, $p < 0.001$). Additionally, 53% of patients with the highest quartile of LA fibrosis (>21.1%) had experienced an ischemic stroke in comparison with 2.8% of patients with the lowest LA fibrosis quartile (LA fibrosis <8.5%).

Akoum and colleagues also demonstrated the higher incidence of LA appendage thrombus and spontaneous echo contrast in patient with higher degree of LA fibrosis [28]. Patients with atrial fibrosis of more than 20% were more likely to have a LAA thrombus (13.8% vs 3.3%, $p < 0.01$) and spontaneous echo contrast (17.2% vs 7.5%, $p = 0.04$) with odd ratio of 4.6 and 2.6, respectively. Hence, LA fibrosis from LGE helps separate the "true" low risk from "pseudo" low risk of stroke among patients with low CHADS2-VASC score. At our center, AF patients with a CHADS2-VASC score of 0 or 1 but with high LA fibrosis are treated with anticoagulation similar to a CHADS2-VASC score of 2 or higher.

Left Atrial Fibrosis and Recurrences After Ablation

RFA of atrial fibrillation is currently an accepted invasive management strategy for symptomatic patients, especially with those who failed antiarrhythmic drug therapy [29]. The success rate of RFA depends on patient characteristics and RFA strategies [30, 31]. Studies from our institution have shown that LA fibrosis from LGE is a strong independent predictor of arrhythmia recurrence after RFA [14, 22]. The Delayed-Enhancement MRI Determinant of Catheter Ablation of Atrial Fibrillation (DECAAF) study was a multicenter cohort study designed to evaluate the clinical utility of LA fibrosis from LGE [23]. This recently published DECAAF study demonstrated that for every 1% increases in atrial fibrosis, the hazard ratio of recurrence during 1 year was 1.06 (95% CI, 1.03–1.08; $P < 0.001$). When patients were divided into four groups based on the amount of LA fibrosis (group I, less than 10% of the atrial wall; group II, 10% or greater but less than 20%; group III, 20% or greater but less than 30%; and group IV, 30% or greater), unadjusted cumulative incidence of arrhythmia recurrence for groups I–IV were 15.3% (95% CI, 7.6%–29.6%), 35.8% (95% CI, 26.2%–47.6%), 45.9% (95% CI, 35.6%–57.5%), and 69.4% (95% CI, 48.6%–87.7%), respectively (Fig. 22.4). These results provide significant insight into the relationship between LA substrate (fibrosis) and the success of RFA.

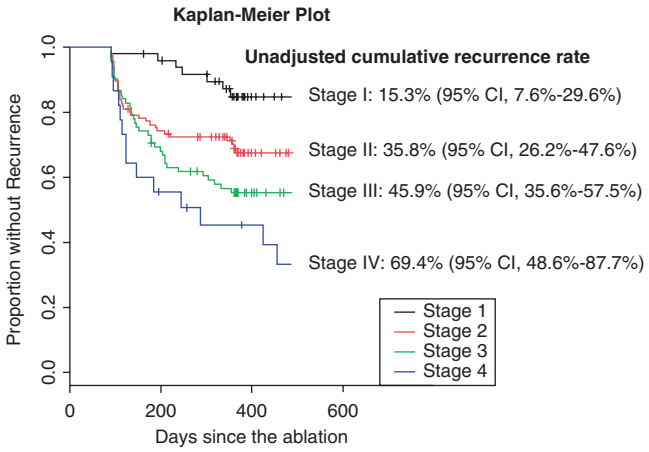

Fig. 22.4 Cumulative incidence of arrhythmia recurrence without covariate adjustment through day 565 after the ablation. Utah stage I, minimal fibrosis (<10%); Utah stage II, mild fibrosis (10–20%); Utah stage III, moderate fibrosis (20–30%); Utah stage IV, severe fibrosis (>30%)

Periprocedural Imaging

Structural Changes After AF Ablation

A reduction in LA size has been observed after RF ablation. Some studies have shown that reduction in LA size yields lower recurrence, and others found this phenomenon in both patients with and without AF recurrence [32, 33]. However, recent meta-analysis by Jeevanantham and colleagues demonstrated significant reduction in LA volume among recurrent-free patients compared to patients with recurrent AF after RFA [34]. Two possible explanations are reverse remodeling of LA wall and scar formation after AF ablation. However, the real explanation and clinical utility of this finding are unclear.

Staging of Atrial Fibrillation Using LGE MRI

The ability to quantify the amount of LA fibrosis has allowed us to establish a direct correlation between the degree of LA fibrosis and the success of AF management. We have

established a clinical staging system composed of four stages based on the amount of pre-ablation delayed enhancement (fibrosis) as a percentage of the volume of the left atrial wall. This clinical staging system includes four stages: Utah stage I (<10%), Utah stage II (10–20%), Utah stage III (20–30%), and Utah stage IV (>30%) (Fig. 22.5).

Those patients with minimal pre-ablation fibrosis (Utah stage I) did well, with conventional pulmonary vein isolation [22]. In the Utah stage 2, the number of PVs encircled by scar from ablation was found to be the most beneficial in reducing AF recurrence. These findings imply that pulmonary vein isolation is an appropriate ablation strategy for Utah stage I and II patients.

However, for Utah stages III and IV, pulmonary vein isolation alone is associated with a low success rate of ablation [14, 22, 23]. In the Utah stage III, the higher percent of left atrial scar at 3-month post-ablation was associated with a lower recurrence rate. In stage IV, which has the highest recurrence rate of AF after catheter ablation, neither LA scar after ablation nor PV encirclement reduced arrhythmia recurrence.

Our reports are in line with other publication where PV isolation is a reasonable approach in milder form of atrial fibrillation, whereas patients with more advanced AF are likely to have a better long-term outcome with more extensive ablation. Variable success rates have been reported with targeting areas of complex fractionated electrograms (CFAEs) [35], dominant frequency [36] adding linear lesions to PV circumferential isolation [37, 38], as well as disrupting ganglionated plexi connections to the atrium [39]. At the University of Utah, we proposed additional ablation in posterior and septal wall in patient with advanced fibrosis. We found that progressive increases in post-ablation posterior and septal wall scarring did reduce recurrence rates [40].

On the basis of this staging system, we have developed a comprehensive MRI-based AF management algorithm (Fig. 22.6), which helps us in triaging patients to AF ablation, as well as planning a corresponding ablation strategy and future anticoagulation strategy.

Assessment of Complication After RFA

Cardiac MRI after ablation can help us in assessing post-ablation atrial scar and detection of complications. In addition to intracardiac echocardiogram during procedure, we do perform LGE within 24 h after ablation to assess for any esophageal injury and pulmonary vein narrowing.

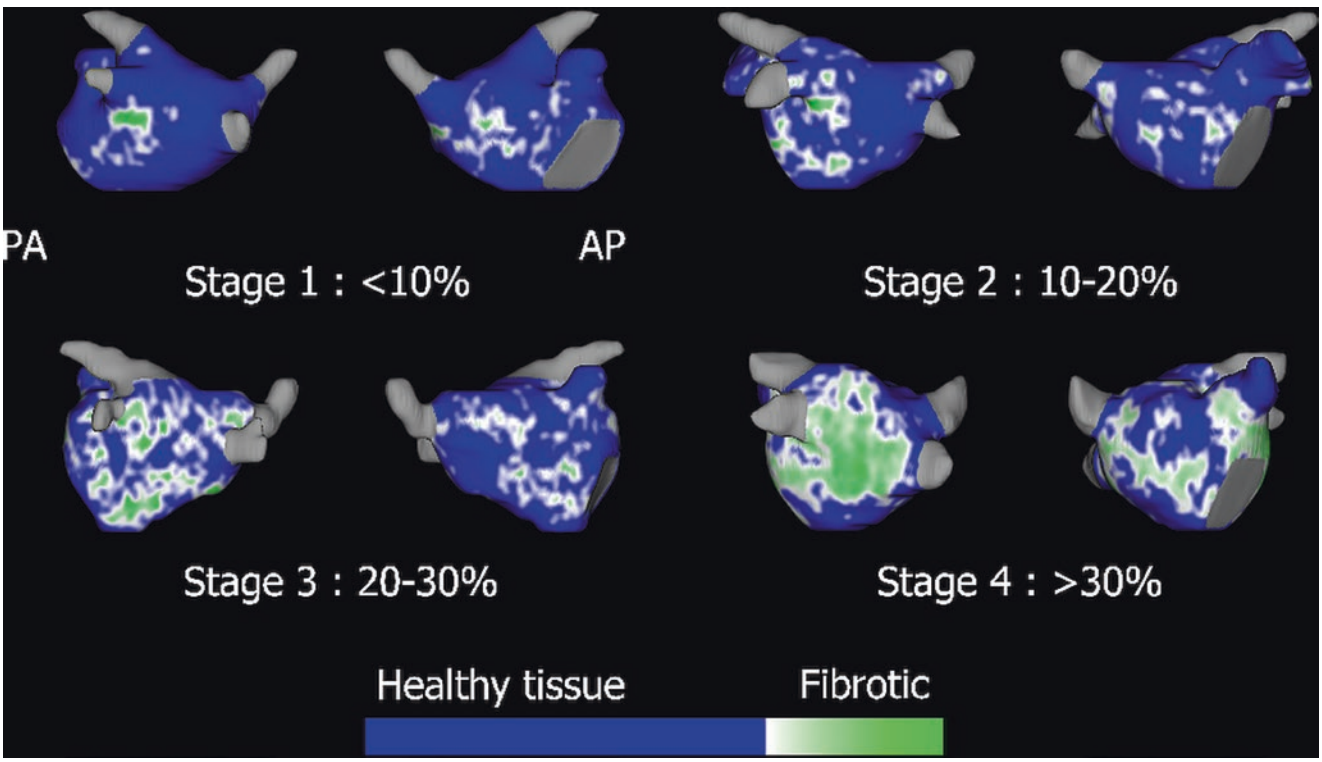

Fig. 22.5 Staging of LA fibrosis based on LGE. The LA fibrosis was calculated as a percentage of total LA surface area. Utah stage I has <10% fibrosis; Utah stage II has 10–20% fibrosis. Utah stage III has 20–30% fibrosis, and Utah stage IV has >30% fibrosis

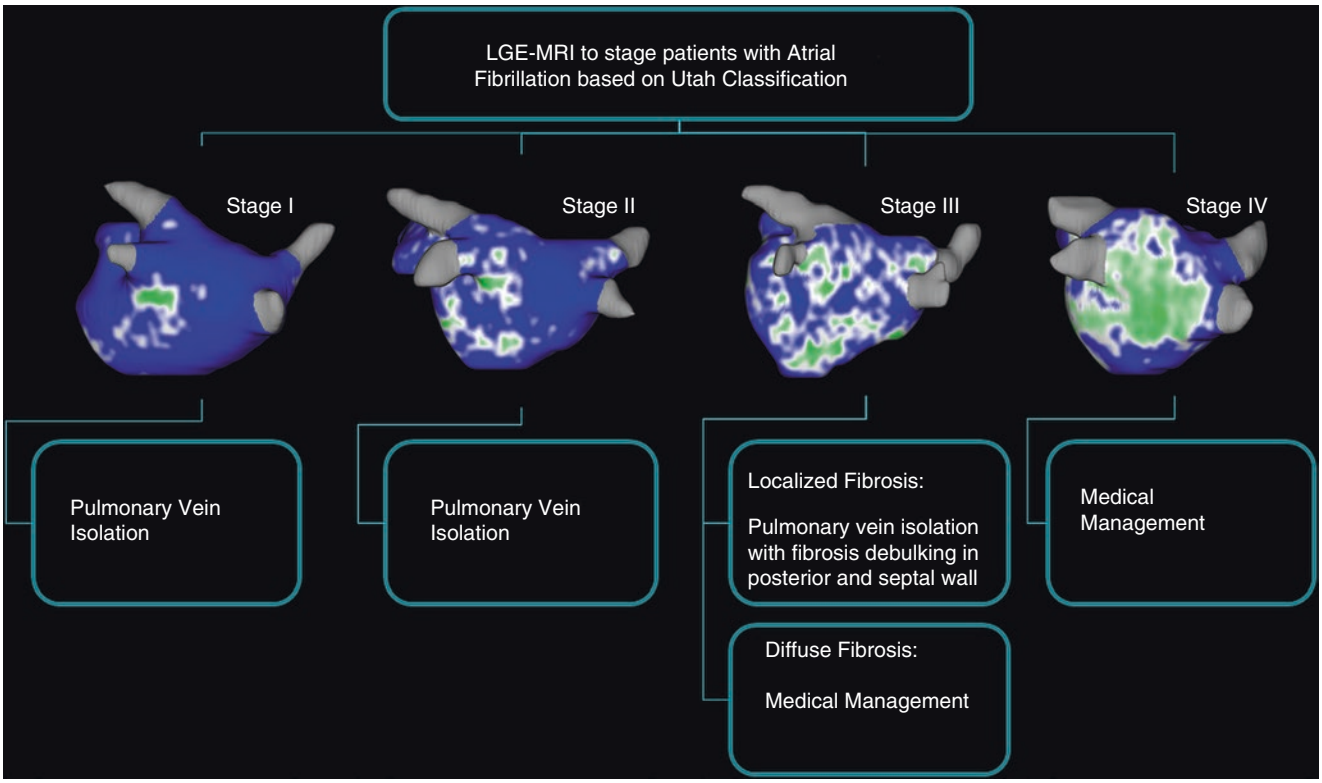

Fig. 22.6 Personalized management of atrial fibrillation based on LA fibrosis from LGE

Major complications occur in a small number of cases (6%), including procedure-related deaths, strokes, transient ischemic attacks, cardiac tamponade, and PV stenosis [41]. One of the two most feared complications after catheter ablation are pulmonary vein stenosis and atrial esophageal fistula. The incidence of PV stenosis has been reported to range from 1.5% to 42%, depending on the RFA technique used and the imaging modality used for assessment [42, 43]. The incidence has fallen with improvements in the technique; nevertheless, significant (> 50%) stenosis accounts for approximately 30% of major complications in the recent worldwide registry survey [41]. Symptoms of PV stenosis range from asymptomatic narrowing and persistent cough to significant hemoptysis and severe exertional dyspnea.

The severity of pulmonary vein stenosis is categorized according to anatomic severity by multi-detector computed tomography (MDCT), with mild stenosis defined as <50% luminal narrowing, moderate stenosis 50–69%, and severe stenosis ≥70% [44]. CMR is an attractive imaging technique which can offer both anatomical (severity of stenosis) and function information (pulmonary venous flow). Recently, Goo and colleagues demonstrated the feasibility of measuring pulmonary vein flow velocity by phase-contrast CMR [45]. However, CMR is currently not widely use in evaluation of PV stenosis, particularly given the higher spatial resolution of MDCT (evaluation of PV diameters) and the higher temporal resolution of echocardiography (velocity measurement).

Atrial esophageal fistula (AEF) is an uncommon yet serious complication of AF ablation. It results from injury to the esophagus during catheter ablation that occurs due to the close proximity of the esophagus to the posterior wall of the LA. Surveys on AF ablation have reported a 0.015–0.04% incidence of AEF post-ablation [41]. AEF is the second most common cause of mortality and accounts for 16% of cases of mortality after AF ablation. AEF typically presents between 2 and 6 weeks after catheter ablation. Common clinical features of AEF include dysphagia, nausea, heartburn, hematemesis or melena, high fever, sepsis, pericardial or pleural effusions, mediastinitis, and strokes. The reported mortality rate was more than 80%. Given the severity of this complication, utilizing noninvasive imaging for early detection of esophageal injury is an attractive strategy. In patient with clinical suspicion of AEF, upper gastrointestinal (UGI) endoscopy should be avoided due to risk of esophageal perforation and massive air embolism (due to air insufflation during endoscopy). Currently, computed tomography of the chest is the most common imaging modality used to evaluate patient with suspected AEF. The radiographic findings include pericardial air and effusion, intracardiac/intravascular air embolus, atrial and

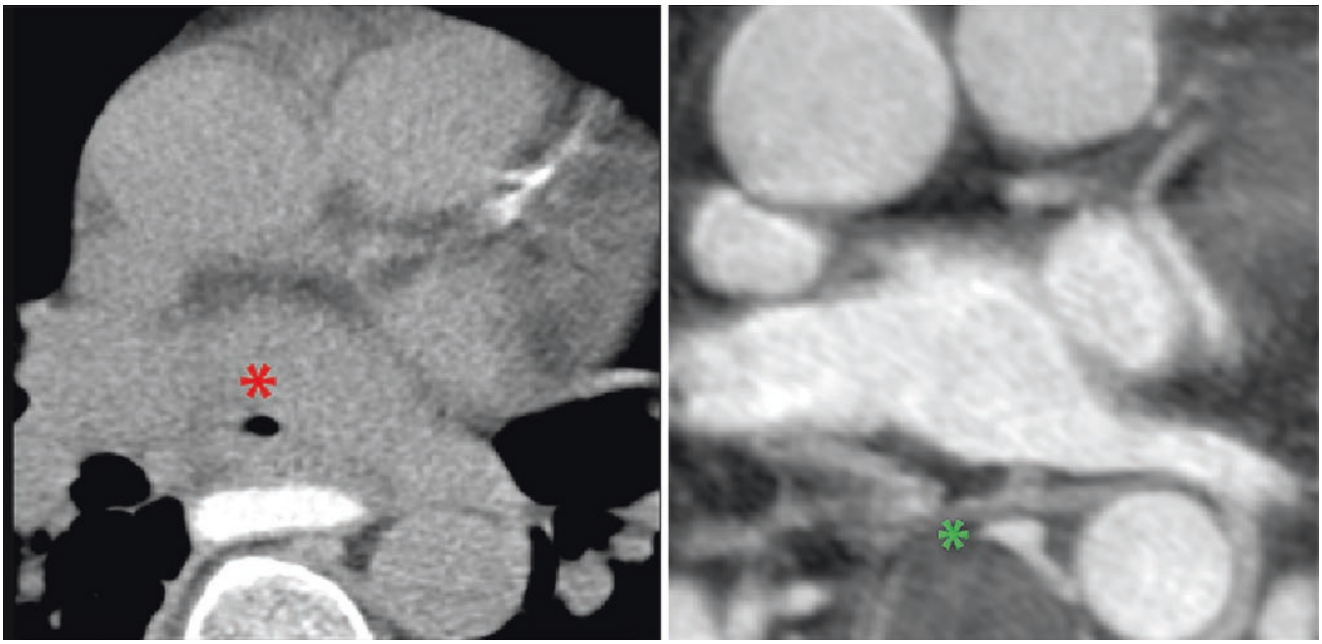

Fig. 22.7 Thoracic CT images demonstrate evidence of atrial esophageal fistula. The red mark denotes the air in the left atrial wall in thoracic CT scan with oral gastrografin contrast. The green mark on the right image denotes the erosion/perforation site of left atrial wall to esophagus, which was temporarily sealed

esophageal wall inflammation, channel/tract communicating atrial to esophagus, and intracardiac or intravascular clot and septic embolus (Fig. 22.7) [46].

Using UGI endoscopy to evaluate esophageal injury is not routinely performed in clinical practice. However, this is typically requested when the patient develops gastrointestinal symptoms but low suspicion for AEF. LGE is a noninvasive tool, and the ability to detect anterior esophageal enhancement has been evaluated. In a prospective study of patients undergoing AF ablation, 5 of 41 (12.2%) patients had anterior esophageal wall enhancement within 24 h of ablation [47]. Three of these 5 patients underwent MRI within 1 week of ablation, at which time the esophageal enhancement had resolved. There was no esophageal enhancement at 3 months after ablation. Three patients underwent upper esophageal endoscopy and were found to have esophageal erosions and/or ulcers adjacent to sites of RFA. Fortunately, repeat endoscopy in 1 week revealed complete resolution, and none of the patients developed AEF. On the contrary, a study by Meng and colleagues demonstrated that esophageal enhancement after catheter ablation is quite common (30%) and 74% of these enhancements were found at more than 30 days after AF ablation without evidence of AEF [48].

The post-ablation LGE is useful in our practice to identify those patients at risk of esophageal injury and PV stenosis. Patient with significant enhancement on anterior esophageal wall after AF ablation will undergo upper endoscopy to evaluate for esophageal erosion/ulcer.

Assessment of Lesion After RF Ablation

LA wall enhancement on T2-weighted (T2w) images was performed immediately after RF ablation, correlated with low-voltage areas (defined as <0.05 mV) on electroanatomical mapping. These areas signify the acute edema of LA wall post-RF ablation. However, the T2W enhancement area is larger than the enhancement by LGE MRI acutely post-AF ablation (Fig. 22.8) [49]. At 3 months after AF ablation, we found resolution of T2w enhancement, which signifies resolution of LA wall edema. The acute edema in acute phase after ablation does not predict the scar formation on LGE MRI at 3 months after ablation. This may partly explain the acute isolation of PV due to edema and late reconnection when edema resolved without scarring.

At 3 months after AF ablation, we perform repeat LGE for evaluation of LA scar. The scar quantifications were performed in similar fashion to pre-ablation LA fibrosis. However, scar after ablation was defined at three standard deviations above the normal tissue mean intensity [50]. This novel technique allows us to evaluate the circumferential scar around the pulmonary vein orifice (Fig. 22.9). The information from LA scar post-ablation allows us to predict the

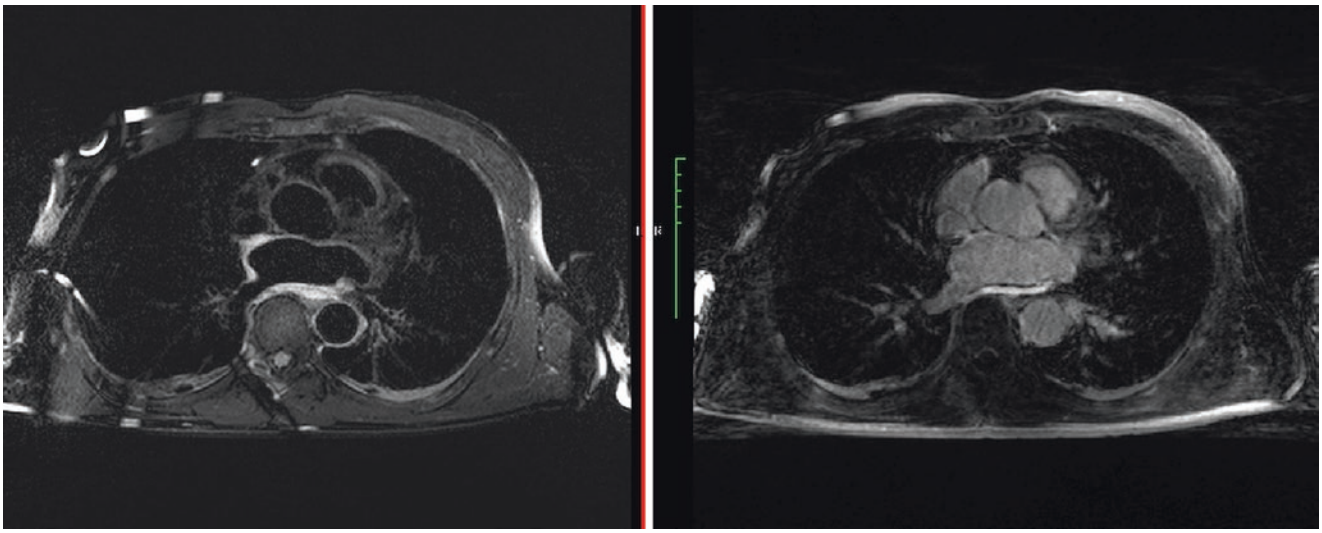

Fig. 22.8 T2W image (left) and LGE image (right) immediately after RFA. The area of enhancement after ablation was larger in T2W than LGE. The enhancement on T2W may represent acute edema, which will not transform into scar after RFA

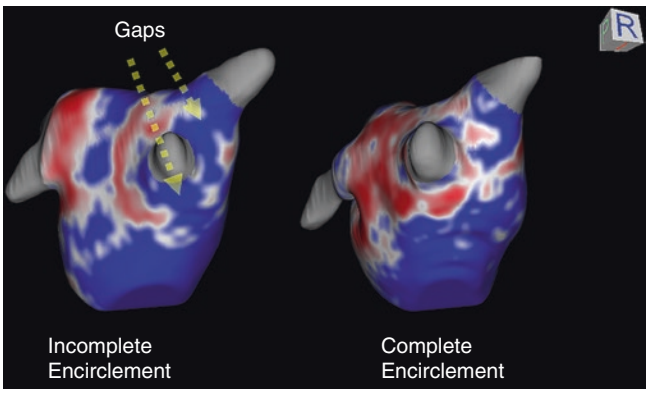

Fig. 22.9 Post-ablation LGE demonstrates the presence (left panel) and the absence (right panel) of gaps around the right pulmonary veins

recurrence after catheter ablation. As mentioned earlier, patients with minimal fibrosis are likely to respond to PV antral isolation, whereas advanced disease patients require additional ablation to generate more atrial scar tissue for a lower recurrence [32, 33].

Future Directions

Road to Real-Time MRI-Guided Catheter Ablation

Fluoroscopy is the standard technique in visualizing catheter location during ablation. However, there are limitations with fluoroscopy, such as radiation exposure risks and limited three-dimensional visualizations. Searching for a new imaging modality to overcome these limitations is in progress. MRI is a radiation-free modality with three-dimensional visualization. In addition, MRI can help characterize the tissue substrate prior to ablation and lesion formation after ablation. Ranjan and colleagues from our institution have demonstrated the feasibility of catheter visualization, safety, and intracardiac electrical signals recording in animal experiments [51]. The RF lesions were safely created in real-time MRI environment and were visualized in real time (with a T2w half-Fourier acquisition single-shot turbo spin-echo [HASTE] MRI sequence). The lesions visualized in T2w HASTE were confirmed with LGE MRI after ablation. Recent studies have shown the capability for real-time assessment of catheter mobility, signal recordings, and ability to deliver RF lesions [52, 53]. With these data, real-time MRI-guided ablation is the new frontier in cardiac electrophysiology.

References

1. Singer DE, Albers GW, Dalen JE, Go AS, Halperin JL, Manning WJ. Antithrombotic therapy in atrial fibrillation: the Seventh ACCP Conference on Antithrombotic and Thrombolytic Therapy. Chest. 2004;126(3 suppl):429S–56S.
2. January CT, Wann LS, Alpert JS, Calkins H, Cleveland JC Jr, Cigarroa JE, et al. 2014 AHA/ACC/HRS guideline for the management of patients with atrial fibrillation: a report of the American College of Cardiology/American Heart Association Task Force on Practice Guidelines and the Heart Rhythm Society. J Am Coll Cardiol. 2014;pii: S0735–1097(14):01740–9.
3. Calkins H, Brugada J, Packer DL, Cappato R, Chen SA, Crijns HJ, Heart Rhythm Society, European Heart Rhythm Association, European Cardiac Arrhythmia Society, American College of Cardiology, American Heart Association, Society of Thoracic Surgeons, et al. HRS/EHRA/ECAS expert consensus statement on catheter and surgical ablation of atrial fibrillation: recommenda-

tions for personnel, policy, procedures and follow-up. Europace. 2007;9:335–79.
4. Oakes RS, Badger TJ, Kholmovski EG, Akoum N, Burgon NS, Fish EN, et al. Detection and quantification of left atrial structural remodeling with delayed-enhancement magnetic resonance imaging in patients with atrial fibrillation. Circulation. 2009;119:1758–67.
5. Kato R, Lickfett L, Meininger G, Dickfeld T, Wu R, Juang G, et al. Pulmonary vein anatomy in patients undergoing catheter ablation of atrial fibrillation: lessons learned by use of magnetic resonance imaging. Circulation. 2003;107(15):2004–10.
6. Hauser TH, Yeon SB, McClennen S, et al. A method for the determination of proximal pulmonary vein size using contrast-enhanced magnetic resonance angiography. J Cardiovasc Magn Reson. 2004;6:927–36.
7. Hauser TH, Essebag V, Baldessin F, et al. Larger pulmonary vein crosssectional area is associated with recurrent atrial fibrillation after pulmonary vein isolation. Circulation. 2005;112:II–555.
8. Pappone C, Rosanio S, Augello G, et al. Mortality, morbidity, and quality of life after circumferential pulmonary vein ablation for atrial fibrillation: outcomes from a controlled nonrandomized long-term study. J Am Coll Cardiol. 2003;42:185–97.
9. Zahuranec DB, Mueller GC, Bach DS, et al. Pilot study of cardiac magnetic resonance imaging for detection of embolic source after ischemic stroke. J. Stroke Cerebrovasc Dis. 2012;21:794–800.
10. Mohrs OK, Nowak B, Petersen SE, et al. Thrombus detection in the left atrial appendage using contrast-enhanced MRI: a pilot study. AJR Am J Roentgenol. 2006;186:198–205.
11. Ohyama H, Hosomi N, Takahashi T, et al. Comparison of magnetic resonance imaging and transesophageal echocardiography in detection of thrombus in the left atrial appendage. Stroke. 2003;34:2436–9.
12. Rathi VK, Reddy ST, Anreddy S, et al. Contrast-enhanced CMR is equally effective as TEE in the evaluation of left atrial appendage thrombus in patients with atrial fibrillation undergoing pulmonary vein isolation procedure. Heart Rhythm. 2013;10:1021–7.
13. Stevens SM, Tung R, Rashid S, Gima J, Cote S, Pavez G, et al. Device artifact reduction for magnetic resonance imaging of patients with implantable cardioverter-defibrillators and ventricular tachycardia: late gadolinium enhancement correlation with electroanatomic mapping. Heart Rhythm. 2014;11(2):289–98.
14. McGann C, Akoum N, Patel A, Kholmovski E, Revelo P, Damal K, et al. Atrial fibrillation ablation outcome is predicted by left atrial remodeling on MRI. Circ Arrhythmia Electrophysiol. 2014;7(1):23–30.
15. Expert Panel on MR Safety, Kanal E, Barkovich AJ, Bell C, Borgstede JP, Bradley WG Jr, Froelich JW, et al. ACR guidance document on MR safe practices: 2013. J Magn Reson Imaging. 2013;37(3):501–30.
16. Spach MS, Boineau JP. Microfibrosis produces electrical load variations due to loss of side-to-side cell connections: a major mechanism of structural heart disease arrhythmias. Pacing Clin Electrophysiol. 1997;20:397–413.
17. Li D, Fareh S, Leung TK, Nattel S. Promotion of atrial fibrillation by heart failure in dogs: atrial remodeling of a different sort. Circulation. 1999;100:87–95.
18. Chen MC, Chang JP, Liu WH, Yang CH, Chen YL, Tsai TH, et al. Increased inflammatory cell infiltration in the atrial myocardium of patients with atrial fibrillation. Am J Cardiol. 2008;102:861–5.
19. Platonov PG, Mitrofanova LB, Orshanskaya V, Ho SY. Structural abnormalities in atrial walls are associated with presence and persistency of atrial fibrillation but not with age. J Am Coll Cardiol. 2011;58:2225–32.
20. Kainuma S, Masai T, Yoshitatsu M, Miyagawa S, Yamauchi T, Takeda K, et al. Advanced left-atrial fibrosis is associated with unsuccessful maze operation for valvular atrial fibrillation. Eur J Cardiothorac Surg. 2011;40:61–9.
21. Boldt A, Wetzel U, Lauschke J, Weigl J, Gummert J, Hindricks G, et al. Fibrosis in left atrial tissue of patients with atrial fibrillation with and without underlying mitral valve disease. Heart. 2004;90:400–5.
22. Akoum N, Daccarett M, McGann C, Segerson N, Vergara G, Kuppahally S, et al. Atrial fibrosis helps select the appropriate patient and strategy in catheter ablation of atrial fibrillation: a DE-MRI guided approach. J Cardiovasc Electrophysiol. 2011;22:16–22.
23. Marrouche NF, Wilber D, Hindricks G, Jais P, Akoum N, Marchlinski F, et al. Association of atrial tissue fibrosis identified by delayed enhancement MRI and atrial fibrillation catheter ablation: the DECAAF study. JAMA. 2014;31(5):498–506.
24. Dulli DA, Stanko H, Levine RL. Atrial fibrillation is associated with severe acute ischemic stroke. Neuroepidemiology. 2003;22(2):118–23.
25. Coppens M, Eikelboom JW, Hart RG, Yusuf S, Lip GY, Dorian P, et al. The CHA2DS2-VASc score identifies those patients with atrial fibrillation and a CHADS2 score of 1 who are unlikely to benefit from oral anticoagulant therapy. Eur Heart J. 2013;34(3):170–6.
26. Fang MC, Go AS, Chang Y, Borowsky L, Pomernacki NK, Singer DE. Comparison of risk stratification schemes to predict thromboembolism in people with nonvalvular atrial fibrillation. J Am Coll Cardiol. 2008;51(8):810–5.
27. Daccarett M, Badger TJ, Akoum N, et al. Association of left atrial fibrosis detected by delayed-enhancement magnetic resonance imaging and the risk of stroke in patients with atrial fibrillation. J Am Coll Cardiol. 2011;57:831–8.
28. Akoum N, Fernandez G, Wilson B, McGann C, Kholmovski E, Marrouche N. Association of atrial fibrosis quantified using LGE-MRI with atrial appendage thrombus and spontaneous contrast on transesophageal echocardiography in patients with atrial fibrillation. J Cardiovasc Electrophysiol. 2013;24:1104–9.
29. January CT, Wann LS, Alpert JS, Calkins H, Cleveland JC, Cigarroa JE, et al. 2014 AHA/ACC/HRS guideline for the management of patients with atrial fibrillation a report of the American College of Cardiology/American Heart Association Task Force on Practice Guidelines and the Heart Rhythm Society. J Am Coll Cardiol. 2014;130(23):2071–104.
30. Wilber DJ, Pappone C, Neuzil P, De Paola A, Marchlinski F, Natale A, et al. Comparison of antiarrhythmic drug therapy and radiofrequency catheter ablation in patients with paroxysmal atrial fibrillation: a randomized controlled trial. JAMA. 2010;303(4):333–40.
31. Oral H, Scharf C, Chugh A, Hall B, Cheung P, Good E, et al. Catheter ablation for paroxysmal atrial fibrillation. Circulation. 2003;108(19):2355–60.
32. Marsan NA, Tops LF, Holman ER, et al. Comparison of left atrial volumes and function by real-time three-dimensional echocardiography in patients having catheter ablation for atrial fibrillation with persistence of sinus rhythm versus recurrent atrial fibrillation three months later. Am J Cardiol. 2008;102:847–53.
33. Hof IE, Velthuis BK, Chaldoupi SM, et al. Pulmonary vein antrum isolation leads to a significant decrease of left atrial size. Europace. 2011;13(3):371–5.
34. Jeevanantham V, Ntim W, Navaneethan SD, et al. Meta-analysis of the effect of radio frequency catheter ablation on left atrial size, volumes and function in patients with atrial fibrillation. Am J Cardiol. 2011;105:1317–26.
35. Nademanee K, McKenzie J, Kosar E, Schwab M, Sunsaneewitayakul B, Vasavakul T, et al. A new approach for catheter ablation of atrial fibrillation: Mapping of the electrophysiologic substrate. J Am Coll Cardiol. 2004;43:2044–53.
36. Sanders P, Berenfeld O, Hocini M, Jais P, Vaidyanathan R, Hsu L, et al. Spectral analysis identifies sites of high frequency activity maintaining atrial fibrillation in humans. Circulation. 2005;112:789–97.

37. O'Neill M, Jais P, Takahashi Y, Jonsson A, Sacher F, Hocini M, et al. The stepwise ablation approach for chornic atrial fibrillation-evidence for acumulative effect. J Interv Card Electrophysiol. 2006;16:153–67.
38. Oral H, Scharf C, Chugh A, Hall B, Cheung P, Good E, et al. Catheter ablation for paroxysmal atrial fibrillation: Segmental pulmonary vein ostial ablation versus left atrial ablation. Circulation. 2003;108:2355–60.
39. Lu Z, Scherlag BJ, Lin J, Yu L, Guo J-H, Niu G, et al. Autonomic mechanism for initiation of rapid firing from atria and pulmonary veins: evidence by ablation of ganglionated plexi. Cardiovasc Res. 2009;84:245–52.
40. Segerson NM, Daccarett M, Badger TJ, Shabaan A, Akoum N, Fish EN, et al. Magnetic resonance imaging-confirmed ablative debulking of the left atrial posterior wall and septum for treatment of persistent atrial fibrillation: rationale and initial experience. J Cardiovasc Electrophysiol. 2010;21(2):126–32.
41. Cappato R, Calkins H, Chen SA, Davies W, Iesaka Y, Kalman J, et al. Updated worldwide survey on the methods, efficacy, and safety of catheter ablation for human atrial fibrillation. Circ Arrhythm Electrophysiol. 2010;3:32–8.
42. Cappato R, Calkins H, Chen SA, et al. Worldwide survey on the methods, efficacy, and safety of catheter ablation for human atrial fibrillation. Circulation. 2005;111:1100–5.
43. Saad EB, Marrouche NF, Saad CP, Ha E, Bash D, White RD, et al. Pulmonary vein stenosis after catheter ablation of atrial fibrillation: emergence of a new clinical syndrome. Ann Intern Med. 2003;138:634–8.
44. Baranowski B, Saliba W. Our approach to management of patients with pulmonary vein stenosis following AF ablation. J Cardiovasc Electrophysiol. 2011;22(3):364–7.
45. Goo HW, Al-Otay A, Grosse-Wortmann L, et al. Phase-contrast magnetic resonance quantification of normal pulmonary venous return. J Magn Reson Imaging. 2009;29:588–94.
46. Nair GM, Nery PB, Redpath CJ, Lam BK, Birnie DH. Atrioesophageal fistula in the era of atrial fibrillation ablation: a review. Can J Cardiol. 2014;30(4):388–95.
47. Badger TJ, Adjei-Poku YA, Burgon NS, et al. Initial experience of assessing esophageal tissue injury and recovery using delayedenhancement MRI after atrial fibrillation ablation. Circ Arrhythm Electrophysiol. 2009;2:620–5.
48. Meng J, Peters DC, Hsing JM, Chuang ML, Chan J, Fish A, et al. Late gadolinium enhancement of the esophagus is common on cardiac MR several months after pulmonary vein isolation: preliminary observations. Pacing Clin Electrophysiol. 2010;33(6):661–6.
49. Vergara GR, Marrouche NF. Tailored management of atrial fibrillation using a LGE-MRI based model: from the clinic to the electrophysiology laboratory. J Cardiovasc Electrophysiol. 2011;22:481–7.
50. McGann CJ, Kholmovski EG, Oakes RS, Blauer JJ, Daccarett M, Segerson N, et al. New magnetic resonance imaging-based method for defining the extent of left atrial wall injury after the ablation of atrial fibrillation. J Am Coll Cardiol. 2008;52:1263–71.
51. Ranjan R, Kholmovski EG, Blauer J, Vijayakumar S, Volland NA, Salama ME, et al. Identification and acute targeting of gaps in atrial ablation lesion sets using a real-time magnetic resonance imaging system. Circ Arrhythm Electrophysiol. 2012;5(6):1130–5.
52. Sommer P, Grothoff M, Eitel C, Gaspar T, Piorkowski C, et al. Feasibility of real-time magnetic resonance imaging-guided electrophysiology studies in humans. Europace. 2013;15(1):101–8.
53. Grothoff M, Piorkowski C, Eitel C, Gaspar T, Lehmkuhl L, Lücke C, et al. MR imaging-guided electrophysiological ablation studies in humans with passive catheter tracking: initial results. Radiology. 2014;271(3):695–702.

Interventional Cardiovascular MRI

23

Toby Rogers and Robert J. Lederman

Introduction

Interventional cardiovascular MRI (or "iCMR") is potentially revolutionary because of the exquisite tissue and blood imaging afforded to guide therapeutic procedures. By making small compromises in spatial or temporal resolution, and with little or no modifications to commercial high-performance MRI systems, images can be acquired and displayed almost instantaneously to operators. This may be useful simply to avoid ionizing radiation during conventional catheter-based procedures, especially in children. Perhaps more important, iCMR promises to enable more advanced procedures not otherwise possible without open surgical exposure.

X-ray fluoroscopy is widely available and is used to drive a wealth of catheter-based and minimally invasive cardiovascular and non-cardiovascular interventions. Other procedures are guided by external or invasive ultrasound (i.e., transesophageal or intravascular) or electromagnetic position mapping (*Carto, Biosense Webster; Ensite NavX, St Jude Medical*), alone or in tandem with X-ray. To change the primary image guidance modality away from X-ray would require a more favorable risk-benefit profile or would require applications not otherwise possible with X-ray. For certain applications, iCMR is likely to meet these requirements.

iCMR does not expose patients or operators to ionizing radiation. Children with congenital cardiovascular disease suffer excess risk of late malignancy after exposure to ionizing radiation [1]. They also are prone to multiple catheter-based treatments, subjecting them to higher cumulative radiation exposure. Cumulative exposure is also a risk to operators and staff [2]. Lead aprons worn during X-ray procedures are associated with career-threatening musculoskeletal injuries.

iCMR, by virtue of imaging soft tissue, blood spaces, and catheter devices simultaneously, may enable novel procedures. In preclinical experiments, iCMR has been shown to guide and track targeted cell delivery into or around myocardial infarctions, to guide atrial septal puncture, to drain pericardial effusions, and to obtain direct transthoracic access to the heart. iCMR is being developed in preclinical systems to guide cardiac valve repair and replacement, and extra-anatomic bypass, procedures that in the past would have required surgical exposure. In some settings, iCMR may provide a safety advantage over conventional image guidance, by revealing complications such as vascular perforation or rupture more rapidly and enabling more rapid treatment.

In recent years, iCMR in humans has become a clinical reality. Several institutions now perform MR-guided diagnostic right heart catheterization, and first-in-man MR-guided arrhythmia ablation and structural cardiac interventions have been performed recently. In this chapter, we discuss the technical challenges of iCMR and evaluate the potential solutions, describe how to equip an iCMR suite for clinical applications, and review the published preclinical and clinical experience to date.

Technical Issues

Pulse Sequences and Image Reconstruction

iCMR is possible because of the same technical advances that enable MRI of moving cardiac structures. Newer hardware with homogeneous magnetic fields and with rapidly switching magnetic gradients permit repetition times (TR) shorter than 3 ms. The most widely used pulse sequences are

T. Rogers
Cardiovascular, National Institutes of Health,
National Heart, Lung, and Blood Institute,
Bethesda, MD, USA
e-mail: toby.rogers@nih.gov

R. J. Lederman (✉)
Cardiovascular, Division of Intramural Research,
National Heart, Lung, and Blood Institute,
National Institutes of Health, Bethesda, MD, USA
e-mail: lederman@nih.gov

R. Y. Kwong et al. (eds.), *Cardiovascular Magnetic Resonance Imaging*, Contemporary Cardiology,
https://doi.org/10.1007/978-1-4939-8841-9_23

steady-state free precession (SSFP, also known as balanced fast field echo, trueFISP, and FIESTA), because of the relatively high signal-to-noise ratio (SNR) generated with short TRs. Gradient echo techniques, used especially to enhance magnetic susceptibility artifacts, can be equally fast but usually have inferior SNR.

During "interventional" MRI, pulse sequences are often adjusted interactively to change image contrast and to adjust the compromise between temporal and spatial resolution in favor of speed [3]. Compared with X-ray imaging, which typically uses 1024 × 1024 pixel images at 15 frames per second, a typical iCMR image will be 192 × 160 pixels at 10 frames per second. Because of enhanced tissue imaging, the relative information content in these small-matrix iCMR images is comparable to larger-matrix X-ray images.

We define "real-time" imaging as acquisition-to-display latency (or delay) of 250 ms or less, which is at the border of perceptibility by catheter operators and at a frame rate sufficient for the specific application, generally 5–15 frames/second. Imaging speed is adjusted through a combination of acquisition and post-processing techniques.

Undersampling refers to image creation with less-than-complete datasets. iCMR acquisitions can be undersampled further to increase temporal resolution, often combining multiple methods including interleaving echoes (analogous to alternating even and odd lines on older television sets), incomplete phase sampling of frequency space ("k-space"), and sampling of incomplete echoes. Alternative frequency space sampling trajectories also can employ undersampling. For example, frequency space can be sampled radially so that each echo intersects the center frequency [4], which are attractive because they intrinsically oversample the center of frequency space and undersample the outer frequencies. Others advocate "spiral" sampling of frequency space to combine advantages both of conventional rectilinear and radial sampling.

Parallel imaging techniques exploit the fact that differently located receiver coils each have different "perspectives." This is analogous to the enhanced imaging afforded by binoculars compared with monocular telescopes. Such techniques, bearing monikers such as SENSE and GRAPPA, require multiple hardware receiver channel systems, special receiver coils with reduced cross talk, and increased computational horsepower. In practice they readily increase frame rate two- to fourfold or more at an acceptable cost of image noise.

MRI Features Especially Useful for iCMR

Most commercial MRI systems provide rtMRI functionality using SSFP with interactive graphics slice prescription during continuous scanning. Additional functionality may be available using external computer workstations to control the scanner during iCMR procedures and display rtMR images.

Our labs have found several additional features to be valuable in preclinical and clinical iCMR. Perhaps most important is the ability independently to process signals from individual receiver channels, especially those attached to intravascular devices (see next section). Specifically, this permits signals from device channels, such as intravascular guidewires or endocardial injection needles, to be displayed in color (Fig. 23.1). This simple modification provides high user confidence in device location during rtMRI procedures. It has proven helpful also to be able to alter gain settings for each channel interactively, much as operators adjust gain on intravascular or transthoracic ultrasound devices.

Other features we have found useful include the ability to alter slice thickness or toggle on and off saturation pre-pulse to enhance the appearance of gadolinium-filled balloons and to highlight areas of gadolinium-enhanced myocardium. Image acceleration, such as with GRAPPA, is also toggled interactively. The interaction also can be automated. For example, investigators at Case Western Reserve University automatically reduce the field of view or increase temporal resolution during rapid device motion; the pictures may be fast but blurry during coarse device movements but slow and sharp during fine device positioning [6]. Similarly the field of view may be large during rapid movement or small during fine positioning.

Multiple slices acquired and displayed in rapid succession guide our investigational interventional procedures. Updates of individual slices can be paused or reactivated to speed the frame rate of other slices. This type of display also can be enhanced by interactive user point marking to identify important anatomic features or targets, the ability to make measurements online, and the ability to combine with prior roadmap images to make rapid before and after comparisons (Fig. 23.1).

iCMR operators have two general imaging strategies. For some applications, rtMRI is directed at target pathology, while devices are manipulated in or out of the desired target slice. Alternatively, the rtMRI slice can automatically track catheter movements and alter the slice prescription so as always to keep the desired catheter device in view while changing the view of the neighboring anatomy. Ideally, both imaging techniques should be available to the operator. We have found a "projection mode" feature useful during catheter manipulations within target slices. When parts of catheter devices move outside these selected slices, they appear "lost." By toggling projection mode (which switches to thick-slice or slice-less imaging akin to X-ray fluoroscopic projections), the catheter can be "found" and manipulated back into the target slice (Fig. 23.1).

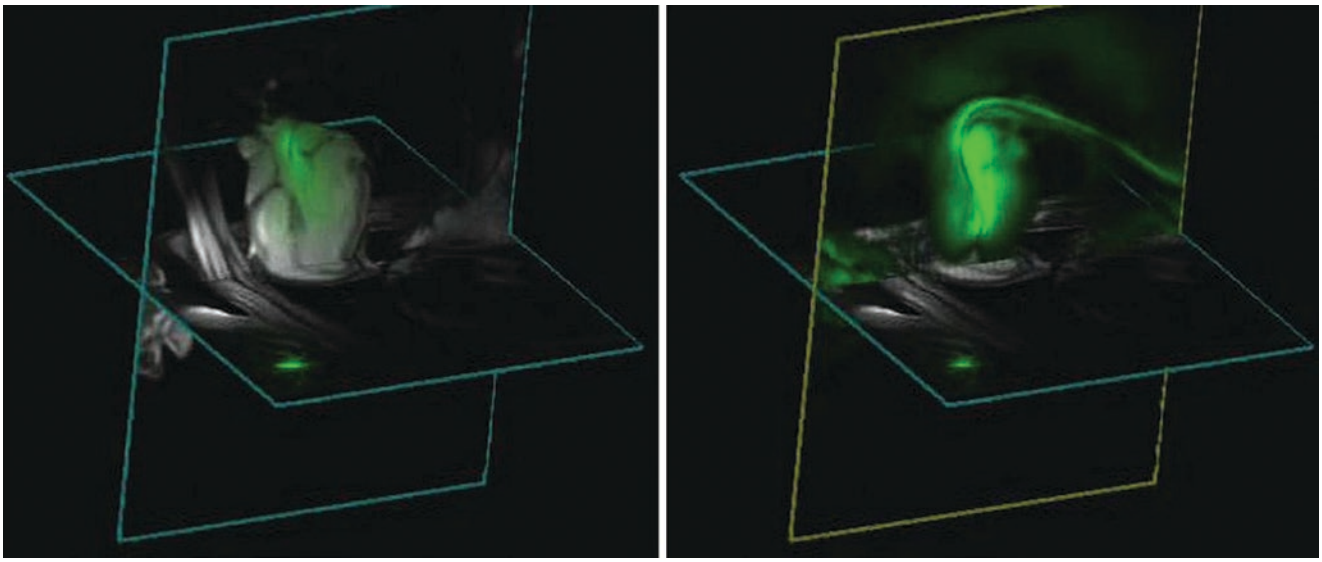

Fig. 23.1 Demonstration of multi-slice imaging. Two slices are acquired together and displayed in their true three-dimensional relationship. This also demonstrates the problem of out-of-plane catheters. On the left, the heart is visualized in multiple concurrent imaging planes, while a transaortic myocardial injection needle is manipulated. The guiding catheter is colored green. The distal end of the catheter is outside the selected imaging plane and is therefore not visible. On the right, "projection mode" is activated in the coronal view so that the entire length of the guiding catheter can be visualized. This functionality is possible with catheters incorporated "active" receiver coils [5]. (Adapted from Dick AJ, Guttman MA, Raman VK, Peters DC, Pessanha BS, Hill JM, et al. Magnetic resonance fluoroscopy allows targeted delivery of mesenchymal stem cells to infarct borders in swine. Circulation. 2003;108(23):2899–904, http://circ.ahajournals.org/content/108/23/2899, with permission from Wolters Kluwer Health)

Logistics and Safety: Assembling a Clinical Interventional MRI Suite

Constructing a clinical laboratory suitable for iCMR procedures is straightforward but requires a degree of customization [7, 8]. Once configured, the laboratory resembles conventional X-ray fluoroscopy suites (Fig. 23.2).

Infrastructure Requirements

All major system manufacturers provide turnkey installation of combined X-ray/MRI (XMR) systems consisting of single- or biplane X-ray fluoroscopy system, clinical 1.5–3 T MRI system, the capacity to transport patients rapidly and safely between the modalities, and X-ray- and radiofrequency-shielded doors that permit the two imaging systems to be used independently when they are not being used together. We believe XMR installations are both useful and cost-effective in providing adjunctive and bailout treatment environments. Moreover, the incremental cost over two separate labs is fairly low, consisting only of the barrier doors and the inter-modality patient transport system. As more experience is gained and the safety of iCMR is established, we anticipate that in the future an adjacent X-ray room will no longer be required.

For transfemoral arterial or transjugular venous access, the length of conventional 1.5 T MRI bores (approximately 150 cm) does not significantly interfere with catheter manipulations in adults. Shorter-bore (120 cm) 1.5 T MRI systems are commercially available and may reduce these obstacles but are certainly not a requirement. Shorter-bore MRI systems also may reduce patient anxiety and claustrophobia and may ease intra-procedural nursing care and observation.

One noteworthy logistical point: at present, transfemoral or transjugular access may best be obtained using X-ray or ultrasound guidance for backup. In a combined XMR system, arterial access is obtained under X-ray, and the patient is then transferred rapidly into the MRI system for further procedure conduct.

Communications

rtMRI is loud. Even in newer "acoustically shielded" systems, the acoustic noise is sufficiently loud that unassisted verbal communication is impossible and protective headsets are necessary to avoid occupational injury. Several commercial systems are now available, combining noise-suppression headsets, multiple channels, and wireless connectivity to facilitate movement around the MRI room (*Optoacoustics, Innovere*). Unless patients will always be under general

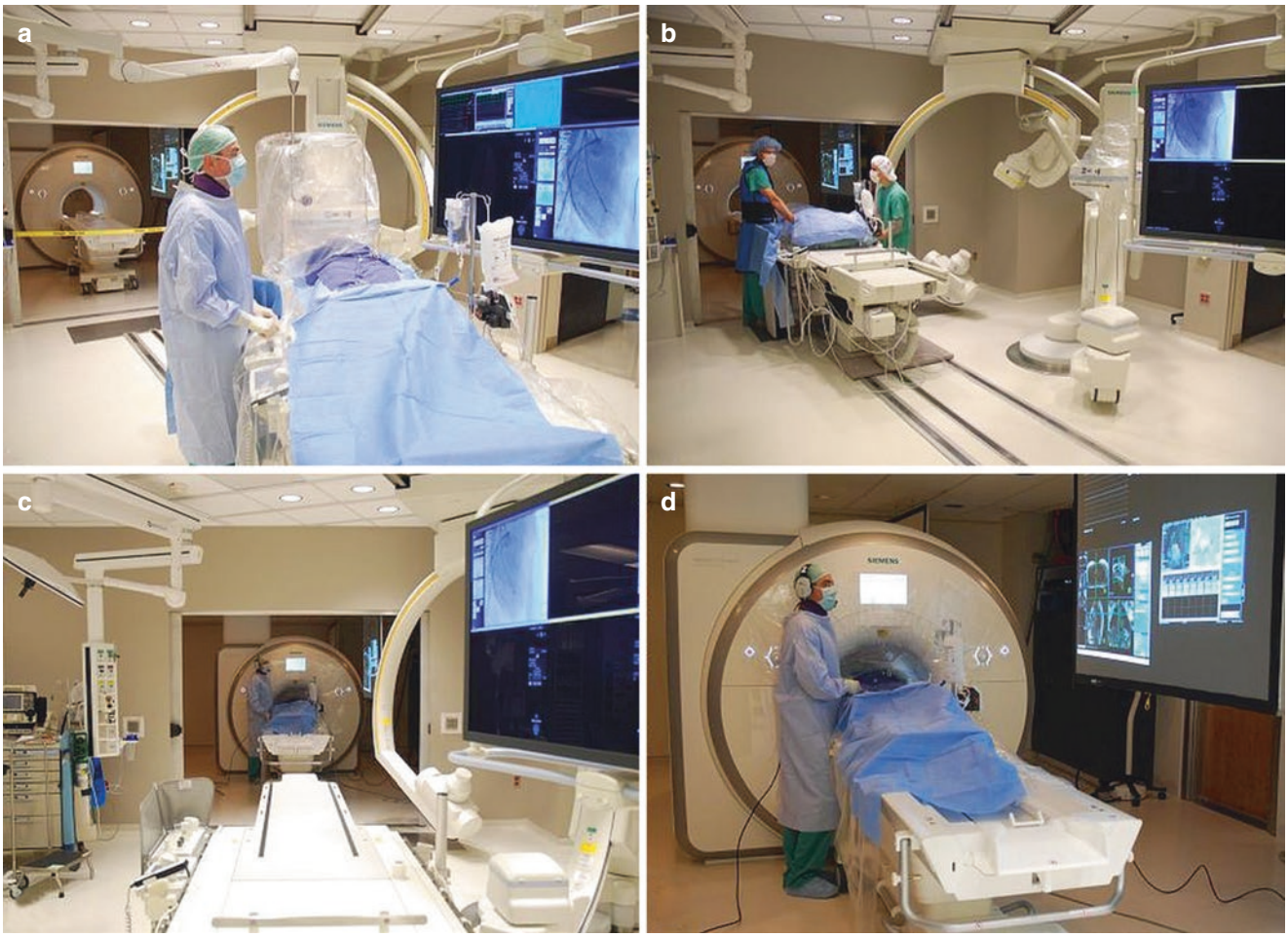

Fig. 23.2 iCMR suite: a view of the NIH XMR suite during a procedure. (**a**) Conventional X-ray fluoroscopy is used for coronary artery catheterization. (**b–c**) The patient is transferred to MRI on the transfer table. (**d**) Diagnostic right heart catheterization is performed using real-time MR guidance. The operators wear fiber-optic noise-suppression headsets with microphones and watch real-time MR images and hemodynamics projected from shielded projectors

anesthesia, multiple communication channels are valuable, as well as the ability for staff to switch between channels to address each other and/or the patient separately.

Video Display

At NIH, we customize a commercial rtMRI workstation, but similar systems are available (*Interventional Front End, Siemens; RTHawk, HeartVista*; *Cleartrace, MRI Intervention; iSuite, Philips*). We use multiple video displays: one for instantaneous hemodynamics, one mirroring the host computer for scanner control, and one for rtMRI display. Available display options include in-lab shielded LCD displays, either floor- or ceiling-mounted. Commercial LCD projectors can be shielded (*Gaven Industries*) against radiofrequency noise emissions, can be positioned inside the lab, and can project onto inexpensive aluminum-framed projector screens. Digital signals are transmitted into the MRI room through fiber-optic transmission lines passed through waveguides (large conductive cylinders installed across the radiofrequency shield that allow nonconductive materials to pass freely). Alternatively, projectors can project from outside the lab through waveguides onto the screen in the MRI room.

Sterility

Sterile procedure during iCMR is similar to other procedures. In our laboratories, before transfer from X-ray to MRI systems, we cover the sterile patient access site (usually groin or neck area) with large sterile drapes, especially to protect that site, while surface MRI coils are placed. We enclose surface coils in sterile plastic bags and interventional coil connectors in sterile plastic sheaths marketed to enclose

intravascular ultrasound connectors. Finally, we line the MRI bore and controls with adhesive clear plastic sterile drapes.

Safety, Patient Monitoring, and Emergency Evacuation

iCMR procedures require standard operating procedures that are an extension of those applied for standard noninvasive MRI procedures.

Suites need to be designed to minimize trips by "circulating" staff members across the RF barrier to gather devices. Opening the door, interrupting the RF barrier, usually interferes with the iCMR procedure by introducing excessive noise into images. This requires both circulating staff and disposable devices to be positioned inside the iCMR room.

Contingency plans must exist to avoid introducing ferrous "missiles" into the iCMR suite. As with standard noninvasive MRI, the risk is highest during emergencies. Defibrillator consoles or oxygen cylinders become missiles if inadvertently brought into the MRI room by emergency team members. As during standard MRI, contingency plans should be in place to rapidly evacuate the patient outside the field during emergencies. At NIH, we drill evacuations regularly and are able to move a patient out of the scanner, transfer to the adjacent X-ray suite, and defibrillate in under 1 min. We expect MR conditional defibrillators to become available in the near future, enabling "in-bore" therapy.

A great deal of biomechanical patient care equipment is commercially available for operation in the MRI suite, including patient monitoring equipment, intravenous fluid pumps, and mechanical ventilators. Such equipment still should be tested and *marked* as being safe for operation inside the high magnetic field. All other ferrous materials that are deemed essential must be tethered outside the high field line if they must remain inside the scanning room. Nitric oxide administration systems can be modified with extended plastic tubing that is passed through the waveguide.

MR-safe hemodynamic monitoring systems are available commercially (*Invivo, GE, Medrad*) and are sufficient for basic monitoring. However, there are currently no high-fidelity hemodynamic recording systems sold commercially. Custom systems have been built for research purposes using filters to correct for interference from the scanner and fiber-optic cables or wireless systems to transmit signals out of the room and using research acquisition hardware (*National Instruments*, *ADInstruments, Biopac*). A commercial system, which should integrate into conventional catheterization laboratory hemodynamic analysis systems (e.g., *Siemens Sensis, GE Mac-Lab*), is currently under development (*Pinmed*).

A surprisingly large number of lines are connected to the patient, and their management should be planned in advance. They are enumerated here for effect: (1) oxygen and other gases; (2) mechanical ventilation; (3) oximetric detector; (4) microphone; (5) headset; (6) multiple intravenous lines; (7) intra-arterial pressure transducer connectors; (8) interventional fluid manifold including contrast, flush, and waste lines; (9) urinary catheters; (10) electrocardiography leads for MRI and for bailout X-ray; (11) surface MRI coil connectors; and (12) intravascular MRI coil connectors. These should be arranged so that no inadvertent loops are formed of conductive materials and so that conductive materials are kept away from the wall of the MRI bore, both of which can contribute to heating. The lines also should be organized so that the patient can be evacuated rapidly without disrupting and disconnecting them.

Catheter Devices

X-ray fluoroscopic interventional devices are conspicuous because they attenuate X-ray photons. Most off-the-shelf devices are intrinsically conspicuous under X-ray; others incorporate heavy metals like barium or platinum. Catheter devices usually incorporate ferrous materials (such as wire braiding) to make them rigid and torque-resistant. By contrast, under MRI, structures are conspicuous because they contain or adjoin excited proton spins. Off-the-shelf catheter devices, designed for X-ray, usually distort the MR image because the ferrous materials destroy the local magnetic field. Devices rendered "MR-compatible" by having ferrous materials removed are also rendered invisible because they still don't contain water protons. Attempts to coat or fill catheter devices with gadolinium-type contrast agents have for the most part been unsuccessful, because not enough excited proton spins are able to interact with the gadolinium-type "relaxation" agent. Moreover, "MR-compatible" guidewire materials such as nitinol are electrically conductive, and, when long enough to be clinically useful, they are vulnerable to rapid heating from the MRI radio energy excitation, much as they would be inside a microwave oven. Table 23.1 and Fig. 23.3 provide an overview of general approaches to making catheter devices visible under MRI.

"Passive" Device Visualization

"Passive" catheter devices are the simplest and are visualized based on their intrinsic material properties. Most passive devices are visible because they do not contain water protons and therefore appear black using most MRI pulse sequences. Tracking dark devices can be challenging using MRI, because the darkness can be difficult to spot when it is diluted

Table 23.1 General approaches to make catheter devices conspicuous under MRI

Approach	Advantages	Disadvantages	Solutions	Examples
Passive devices: Catheter materials directly influences MR image	Simple and inexpensive View device by imaging device in tissue context Reduced technical and regulatory requirements	Visibility is reduced Susceptibility markers (steel, dysprosium) destroy nearby signal Conductive lines, if present, can heat	Can work in combination with active devices (e.g., passive balloon over active guidewire)	Gd-filled balloon [10–15] CO_2-filled balloon [16–18] Nitinol stent [13, 19–23] *Imricor* EP mapping and ablation system [24]
Active "profile" devices: Catheter incorporates an MRI receiver coil ("antenna") along much of its length and is imaged along with target tissue	View device by imaging device in tissue context Can use special MRI features: color-highlighting, projection mode, plane-tracking	Potential heating Less visible at tip than at shaft ("loopless" designs) "Profile" of devices is blurry compared with sharp profile of devices under X-ray or sharp "points" using active tracking devices	Detuning and decoupling can prevent heating Coils can enhance tip visibility	Surgi-Vision *Intercept* 0.030″ guidewire coil [7, 25, 26] NIH active 0.035″ guidewire with embedded temperature probe [27, 28]
Active "tracking-coil" devices: Catheter incorporates small MRI receiver coils that can be tracked with simple pulse sequences alternating with MRI pulse sequences	Points on device can be visualized rapidly and accurately Points can be tracked without imaging to increase speed or reduce absorbed RF Useful in automatic scan control (plane-tracking, etc.)	"Synthesized" points might deviate from "true" location on image Number of points is usually limited Requires "special" MRI pulse sequences, a minor modification	Can be combined with other approaches	MGH/GE EP mapping system [29, 30] *MRI Interventions* EP mapping and ablation system [31]

(or "volume-averaged") in a larger imaging slice. The dark spots can be enhanced by adding small amounts of metal to create "blooming" or magnetic susceptibility artifacts (Fig. 23.3a). These artifacts can make the passive device appear larger than the actual size and can even obscure surrounding tissue detail. Guidewires and catheters [32–34] have been made out of nonmetallic polymers (Fig. 23.3b), and clinical procedures have been conducted using polymer guidewires [35], passive CO_2-filled [16–18], or dilute gadolinium-filled balloon catheters [10].

"Active" Device Visualization

We prefer to use MRI catheter devices that are modified to incorporate MRI receiver coils or antennae. These so-called "active" catheter devices become highly visible when they are attached to the MRI scanner hardware because they accentuate nearby excited water protons. Early designs were intended for high-resolution tissue imaging or spectroscopy [36–42] of nearby tissue. In their simplest designs, the entire length or "profile" of active catheters is made conspicuous [27, 43–48]. In addition, these profile-design active catheters can help visualize the devices even if they move outside the selected scanning plane (Fig. 23.1). Profile-design active catheters generally are imaged along with target tissue and require no modification of imaging pulse sequences. Active catheter coils can be attached to separate receiver channels in the MRI system, analogous to separate audio channels in an audio system, and images deriving from catheters can be assigned colors that help to distinguish them from surrounding structures in 2D or 3D space [49] (Fig. 23.3c). When active guidewires are combined with passive catheters or balloons filled with dilute gadolinium MRI contrast, the pair becomes readily visible.

Another type of active catheter design, embedding tracking microcoils, is used to track individual points on the catheter during MRI [41, 50–52]. Tracking microcoil catheters require a slight modification of the MRI pulse sequences and a small number of intermittent nonselective excitations to localize the microcoils in space and calculate their position on the image. The microcoil location usually is depicted as a crosshair overlaid on the image (Fig. 23.3d, e). These tracking microcoil systems are simple and effective but unfortunately cannot depict the full length of catheter devices unless the catheter contains dozens of them.

Active catheter designs require conductive connections to the MRI scanner. These tend to heat if longer than 10–15 cm. MRI pulse sequence techniques can reduce the energy deposited per image and therefore heating [53], at an acceptable penalty in image quality. These include radial sampling, spiral sampling, and echo-planar imaging which use fewer excitation pulses and longer repetition times, variable flip angle sequences [54], and parallel imaging. Methods being developed to reduce specific absorption rate (SAR) at high fields, such as adaptive parallel transmission, may also prove helpful at lower fields to reduce heating during MRI-guided interventions [55].

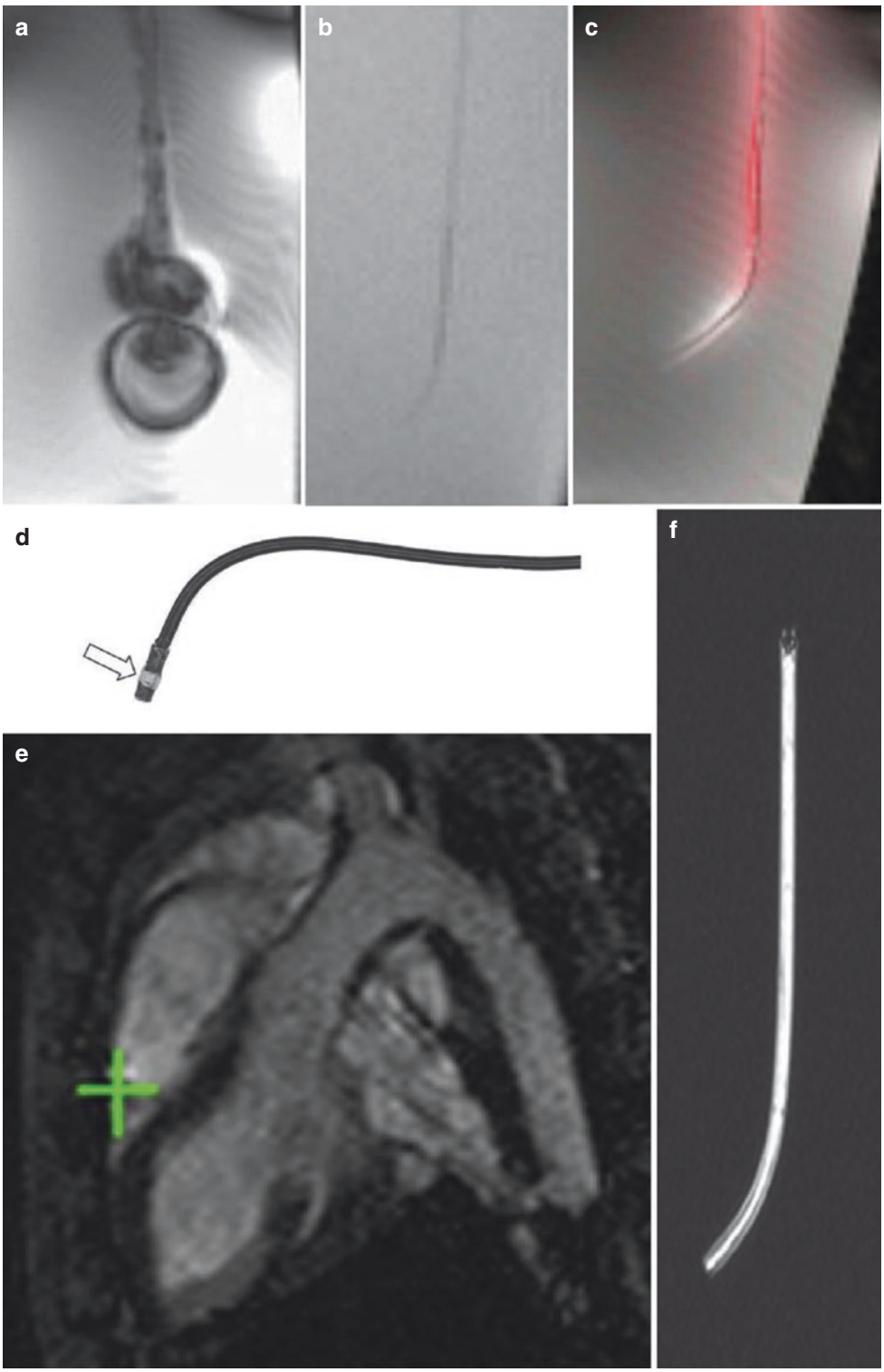

Fig. 23.3 Catheters: a comparison of representative catheter designs for iCMR. (**a**) Shows a traditional X-ray catheter, which incorporates stainless steel braid for strength. The steel distorts the MR image and has the potential to heat, as it would in a microwave oven. (**b**) Shows the same passive catheter without steel braids, rendering it nearly invisible even in vitro. (**c**) Shows the same catheter shape in an "active-profile" design, incorporating an MRI receiver coil to make it visible. (**d**) Shows a tracking microcoil design catheter incorporating a microcoil near the tip. The 3D position of the microcoil can be tracked rapidly and indicated using computer-synthesized crosshairs (green) as it is moved into the right ventricle of the animal shown in (**e**) (Courtesy of Michael. Bock, *DKFZ Heidelberg, Germany*). The rest of the catheter is not visible under MRI. (**f**) Shows a catheter incorporating a "wireless" inductively coupled receiver coil (Courtesy of Harald H. Quick, *University Essen, Germany*) that can be visualized as a bright signal using MRI [9]. (Reprinted from Lederman RJ. Cardiovascular interventional magnetic resonance imaging. Circulation. 2005;112(19):3009–17, http://circ.ahajournals.org/content/112/19/3009, with permission from Wolters Kluwer Health)

Several teams have developed circuitry for detuning or decoupling conductive transmission lines [56–60] or have developed alternative transmission lines such as fiber optics [61–64]. Using loopless antennae, existing interventional devices such as nitinol occluder delivery cables can be modified and tuned to indicate device deployment state (e.g., open versus closed) [65]. One profile-design, loopless active decoupled and detuned guidewire, the Surgi-Vision 0.030″ × 100 cm guidewire, briefly obtained US FDA marketing clearance for invasive intravascular MRI in humans [7, 25, 26]. The limitation of this device was that the receiver sensitivity fell to zero at the distal tip, which was difficult to visualize and insufficient to navigate vasculature under rtMRI. Improved designs have not yet been commercialized [48].

MR conditional guidewires would facilitate numerous interventions using otherwise intrinsically MR-safe devices (e.g., angioplasty balloons or non-braided catheters). To date polymeric guidewires do not afford the requisite mechanical properties (i.e., stiffness and torquability), but metallic (nonferromagnetic) guidewires risk heating. Our lab designed an alternative strategy to address the issue of device heating by embedding a fiber-optic temperature probe into a 0.035″ active guidewire with similar mechanical properties to commercial X-ray guidewires [27]. Heating was monitored continuously during in vivo use and was negligible under normal operating conditions. Importantly, the whole shaft is active, and the tip has a distinct signal which is critical when navigating the vasculature [28]. We plan to test this guidewire in human subjects once US FDA approval is granted.

Several teams have reported "wireless" active catheters or stents [66–69], which are inductively coupled with the MRI system (Fig. 23.3f). Theoretically these can be exploited to enhance later noninvasive imaging, for example, of restenosis or of captured thromboemboli.

Of note, multiple approaches to enhance device visibility can be combined. For example, an interventional MRI system could include an active-profiling guidewire that incorporates tracking microcoils near the tip to enhance distal visibility and a passive balloon incorporating passive platinum marker bands when deflated and filled with dilute gadolinium when inflated, used together to deliver an inductively coupled stent graft device.

The main barrier to further clinical translation of iCMR remains the limited commercial availability of clinical-grade active devices. Nevertheless, a wide range of prototype applications has been demonstrated in animals.

iCMR Applications

Certain applications lend themselves to iCMR development. Target anatomic structures that are relatively immobile or slow moving (such as peripheral arteries) are attractive because MR images can be updated slowly and therefore can have higher SNR or spatial resolution. Large or thick-walled structures (such as the heart or aorta) are attractive because they contain many proton spins and can be imaged with high SNR and contrast mechanisms might be available readily to distinguish them from neighboring structures. Structures that can be contained within a single imaging plane (such as straight segments of iliac arteries) can be imaged rapidly, compared with tortuous smaller structures such as coronary arteries, which are difficult to image in real time.

The myocardium is an attractive target despite its high degree of cardiac and respiratory motion because it is a large, thick-walled structure that is readily depicted (using SSFP MRI) in high contrast compared with the blood space. Even thin-walled structures, such as the myocardial atria, are visible with current rtMRI.

Coronary Artery Disease

The SNR of proton MRI is too low to provide temporal resolution (33–66 ms) at anywhere near the spatial resolution (200 μm) currently enjoyed by X-ray fluoroscopy operators conducting complex coronary interventions in heavily diseased, even occluded, coronary arteries using 0.014″ (0.35 mm) guidewires. Barring unforeseen technical breakthroughs, meaningful coronary artery interventions are not likely to be conducted using MRI.

That said, Spuentrup et al. [70] demonstrated navigation and delivery of passively visualized stainless steel stents in the coronary arteries of healthy swine. The devices and target proximal coronary arteries were readily visible using SSFP at 1.5 T despite cardiac motion and the small size of these structures. Nonetheless, we do not believe that coronary artery intervention is suited for iCMR, because the imaging is inferior and there is no clear benefit compared with X-ray fluoroscopy.

Peripheral Vascular Disease

The most straightforward iCMR applications, transluminal angioplasty [11, 12, 71–73] and stent deployment [13, 19, 20, 21, 74, 75], have been conducted in numerous animal models. Similarly, investigators have reported placement of vena cava filters [76–78] and even transcatheter visceral embolization of, for example, renal or hepatic parenchyma [79–81]. These are important proofs of concept toward clinical development. Indeed a few human examples of peripheral artery angioplasty and stenting have been reported. For the most part, these represent straightforward axial displacement of devices requiring little interactive image guidance.

iCMR also offers the convenience of using a single imaging modality to determine reference vessel size, whereas

X-ray-guided angioplasty requires adjunctive intravascular ultrasound to determine arterial wall characteristics (including media-to-media diameter). However, even in simple angioplasty and stenting, iCMR offers a potential safety advantage over conventional X-ray. Raval et al. [13] conducted iCMR-guided stenting of aortic coarctation in a pig model. Continuous imaging both of target pathology and devices immediately revealed catastrophic aortic rupture when deliberately oversized devices were employed. Early recognition offers the only opportunity effectively to treat this life-threatening complication.

Perhaps more compelling are applications that exploit the ability of MRI to visualize vascular spaces not conspicuous using X-ray. In a pig model of chronic total occlusion of peripheral arteries, Raval et al. [82] used iCMR to navigate a recanalizing guidewire. These trajectories cannot be determined using X-ray because the occluded lumen cannot fill with contrast. iCMR permitted the operators to traverse complex occlusions while remaining within the walls of the target operator. This can be especially important in recanalization of tortuous peripheral artery occlusions, such as those found in the pelvis.

Aortic aneurysm disease often entails complex tortuous three-dimensional structures that are difficult to visualize using projection X-ray. iCMR might provide a single-modality solution to procedure planning, device deployment, and anatomic and hemodynamic assessment of catheter-based (endograft) treatment of aortic aneurysm. In a simple pig model, Raman et al. [83] demonstrated all of the above steps using custom "active" stent graft devices. Endograft treatment under MRI restored a normal lumen contour and restored laminar flow. Moreover, MRI demonstrated device apposition to the target aortic wall and allowed interrogation for endoleak.

The team at University Hospital Essen has elegantly applied iCMR to guide the placement of stent grafts in an animal model of thoracic aortic dissection [84]. They used unmodified, passive stent graft devices. MRI clearly revealed the true and false lumens of the dissected aorta, guided stent graft deployment, and demonstrated stent graft obliteration of the false lumen. This was another excellent example of the intrinsic value of simultaneous tissue and device imaging using real-time MRI (Figs. 23.4 and 23.5).

Cardiac Catheterization and Structural Heart Interventions

The UCSF group [85] reported a comprehensive diagnostic cardiac catheterization procedure in a porcine model of atrial septal defect using iCMR. They used catheters containing tracking microcoils embedded near the tip. They were easily able to accomplish left and right heart catheterization including continuous intracavitary pressure monitoring and blood sampling. They also incorporated phase-contrast MRI into their procedures for the determination of shunt ratios. Other groups have reported rtMRI catheter manipulation using selective arteriography using, for example, tracking microcoil-based catheters for selective carotid artery catheterization [86], passive catheters over active guidewires for selective coronary arteriography [87], or active catheters for selective visceral artery catheterization [88] in swine.

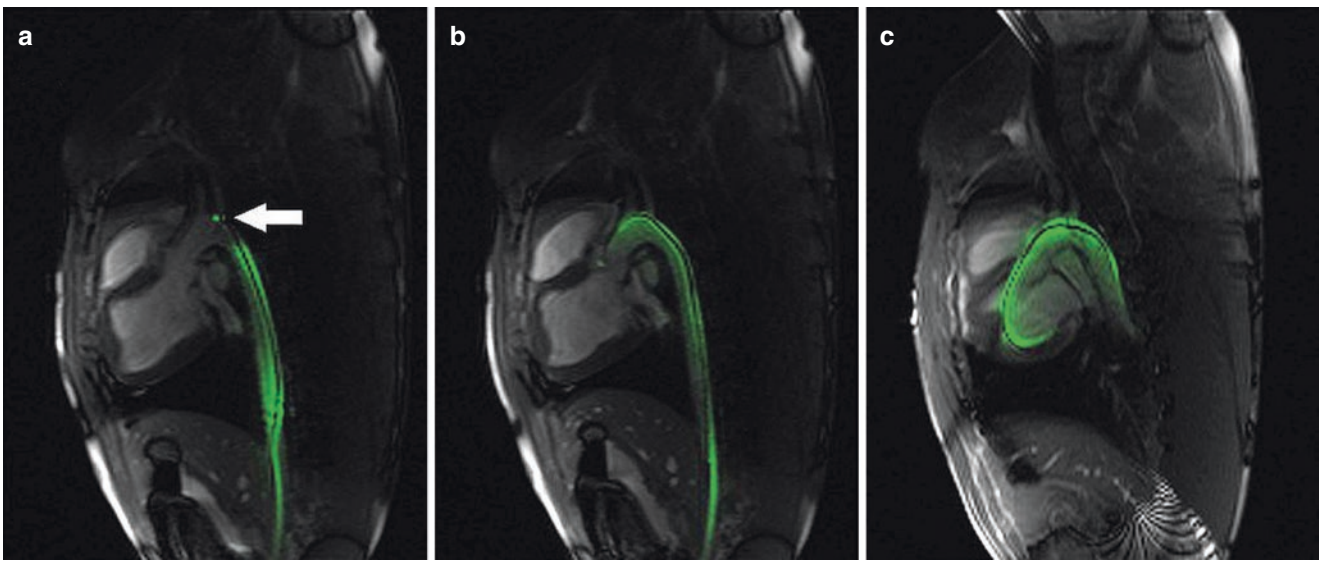

Fig. 23.4 NHLBI active guidewire: left heart catheterization in a pig using the NHLBI active iCMR guidewire. The whole shaft of the guidewire is active, and the tip has a separate and distinct signal (arrow). The guidewire is navigated to the (**a**) aortic arch and (**b**) aortic valve and (**c**) through the aortic valve into the left ventricle under real-time MR guidance

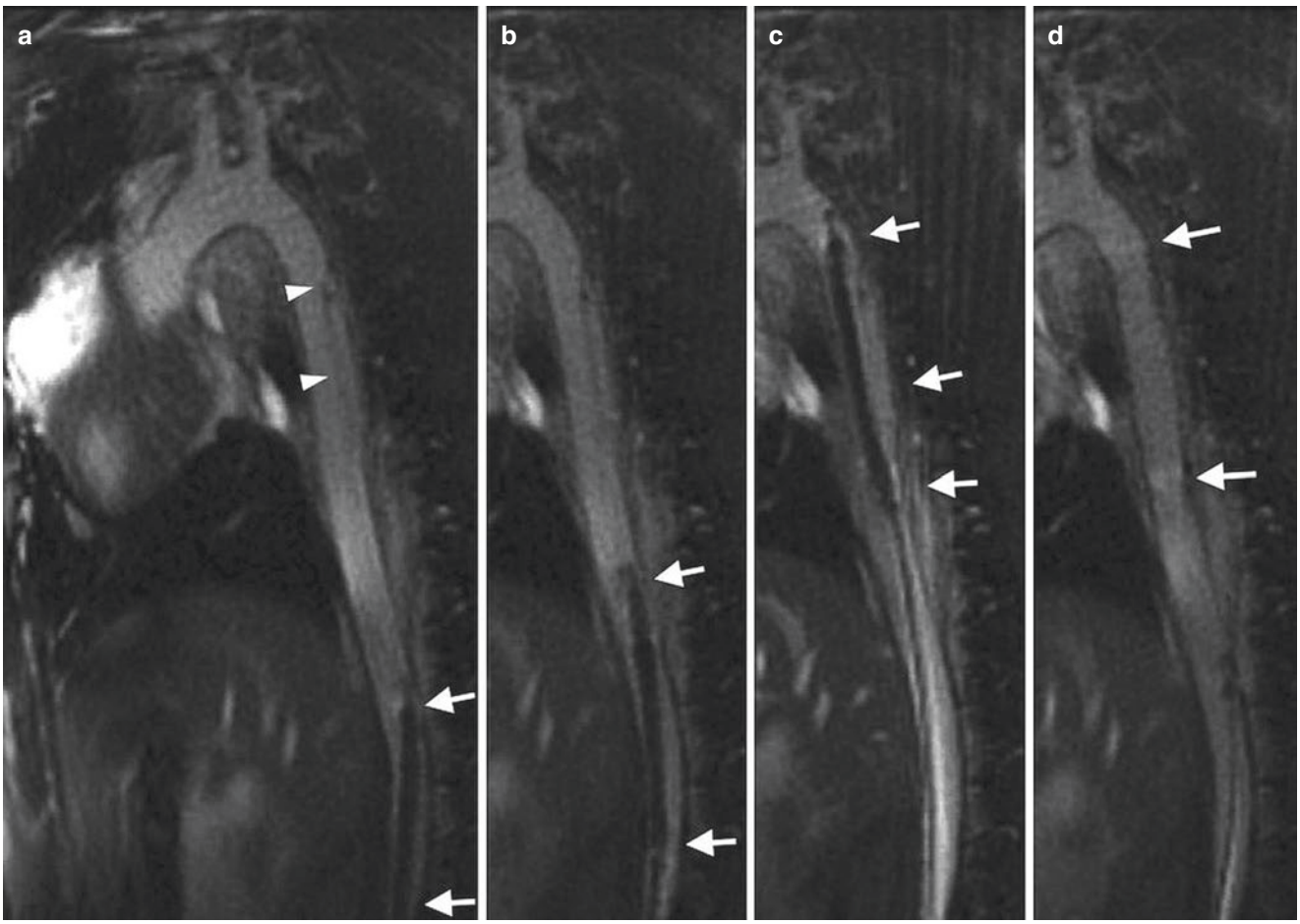

Fig. 23.5 Endograft treatment of thoracic aortic dissection in a pig model, using a commercially available passive device. (**a**) Baseline aortic dissection. The dissection is depicted with arrowheads. (**b**) The endograft is advanced retrograde from the iliac artery. The tip of the endograft (arrows) approaches the inferior aspect of the dissection, inside the true lumen. (**c**) The endograft is in final position before deployment. (**d**) Most of the false lumen is obliterated after endograft delivery. (Courtesy of Holger Eggebrecht, MD and Harald H. Quick, PhD, *University Hospital Essen, Germany*)

Several groups have deployed passively visualized nitinol occluder devices to treat porcine models of atrial septal defect [89] and thereafter to assess hemodynamics using phase-contrast MRI [90, 91].

Kuehne et al. [92] have reported preliminary experience deploying a passively visualized nitinol-based aortic valve prosthesis from a transfemoral approach in healthy swine. Theirs is a good demonstration of the value of combined tissue and device imaging for the precise placement of critical prosthetic devices.

Our lab [5, 93] and others [94–97] have used iCMR to deliver cells and other materials into specified targets in normal and infarcted animal hearts. We have found it particularly useful to interleave multiple slices during iCMR and to render them in 3D to represent their true geometric relationship. This technology provides "exposure" of the inside of the beating heart even better than does open-chest surgery. Targeting can be based on wall motion, late gadolinium enhancement (infarction), perfusion defects, strain maps, or any other contrast mechanism selected. When the injectate includes a contrast agent, real-time MRI can interactively depict the intramyocardial dispersion of the injected materials. This can be valuable for confirming successful delivery, for assuring confluence of treated volumes, and for avoiding inadvertently overlapping injections.

Cardiac Electrophysiology

Cardiac electrophysiology procedures are currently conducted using catheter techniques without compelling image guidance. Endocardial surface maps are generated using

electromagnetic mapping techniques, but these provide only "road maps" that do not account for respiratory and other dynamic changes. Most catheter-based ablation procedures are ultimately guided by multichannel intracardiac electrograms. Alternatively, ablation is conducted under direct surgical exposure [98]. iCMR might provide similar "exposure" for image-guided transcatheter ablation of cardiac arrhythmia and visualization of ablation lesions.

Several groups have performed preclinical catheter-tracking experiments using active catheters that acquire filtered local intracardiac electrograms [99] and have characterized ablated myocardium over time [100]. The team at Massachusetts General Hospital positioned electrophysiology catheters in an MRI system and overlaid these positions onto high-resolution cardiac images [29]. More recently, they performed left ventricular mapping in a porcine model of chronic infarction [30]. Others have used similar systems to ablate the cavo-tricuspid isthmus or pulmonary veins [24, 31, 101].

Extra-anatomic Communications

iCMR may even enable interventions outside normal lumen spaces. Arepally et al. [102] conducted image-guided puncture of the cardiac interatrial septum, a procedure usually conducted primarily using tactile feedback under X-ray. Our lab conducted similar septal puncture followed by balloon septostomy and MRI assessment of the resulting small intracardiac shunts [103]. While similar guidance is afforded by intracardiac or transesophageal ultrasound, these are important preclinical steps toward more elaborate procedures guided by MRI.

With the advent of transcatheter valvular interventions, alternative access routes to deliver large devices to the heart are required. iCMR facilitates development of novel approaches that are not feasible under X-ray guidance, for example, direct transthoracic access to the left ventricle through the cardiac apex [104] or right ventricle [105]. Ratnayaka et al. [106] demonstrated that a direct transthoracic approach could be used to close ventricular septal defects in an animal model (Fig. 23.6). An added advantage is the ability to monitor for and manage complications early, for example, pericardial effusion [107].

Using a unique double-doughnut MRI configuration containing an integrated flat-panel X-ray fluoroscopy system, Kee et al. have conducted preclinical [22] and clinical [108] transjugular intrahepatic portosystemic shunt (TIPS) procedures. Even in this proof-of-concept experiment, MRI reduced the number of transhepatic needle punctures compared with historical controls. Arepally et al. conducted even more adventurous preclinical experiments in creating a catheter-based mesocaval shunt outside the liver capsule [109]. Ratnayaka et al. recently created percutaneous bidirectional Glenn shunts in swine, connecting the superior vena cava and right pulmonary artery, using rtMRI guidance

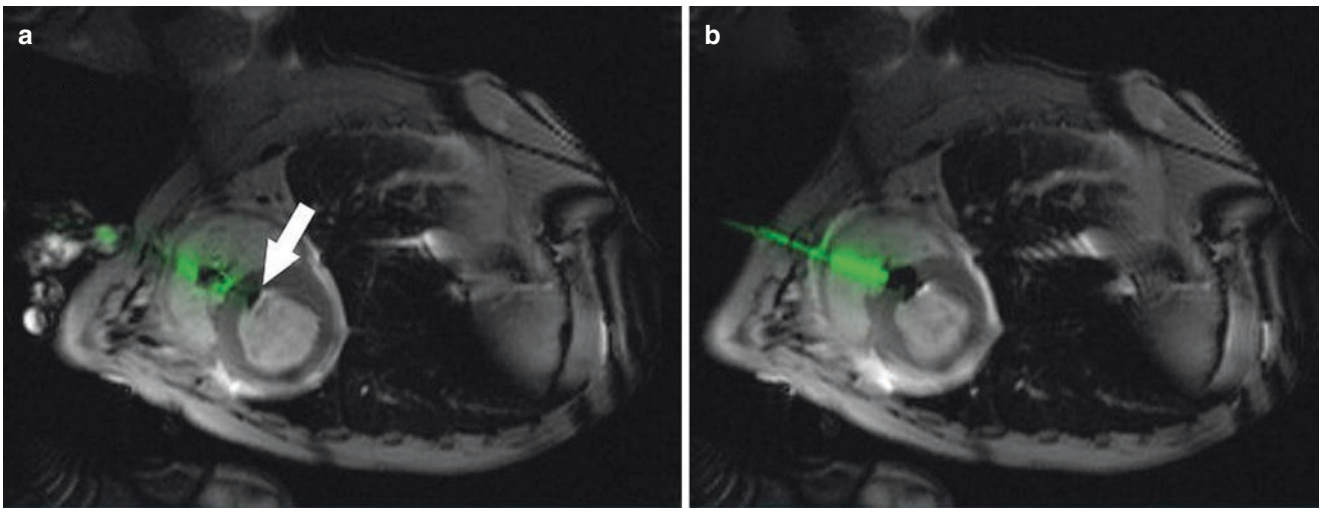

Fig. 23.6 iCMR direct transthoracic ventricular septal defect closure. The right ventricle is accessed directly through the chest wall using an MR "active" needle under real-time MR guidance. The ventricular septal defect (VSD) is crossed anterogradely and then closed using an Amplatz muscular VSD occluder. The delivery cable for the closure device is also active. (**a**) The left ventricular disk (arrow) is deployed and pulled back against the septum. (**b**) The right ventricular disk is then deployed and pushed forward against the septum to close the defect. The right ventricle free wall puncture is closed using an off-the-shelf vascular closure plug

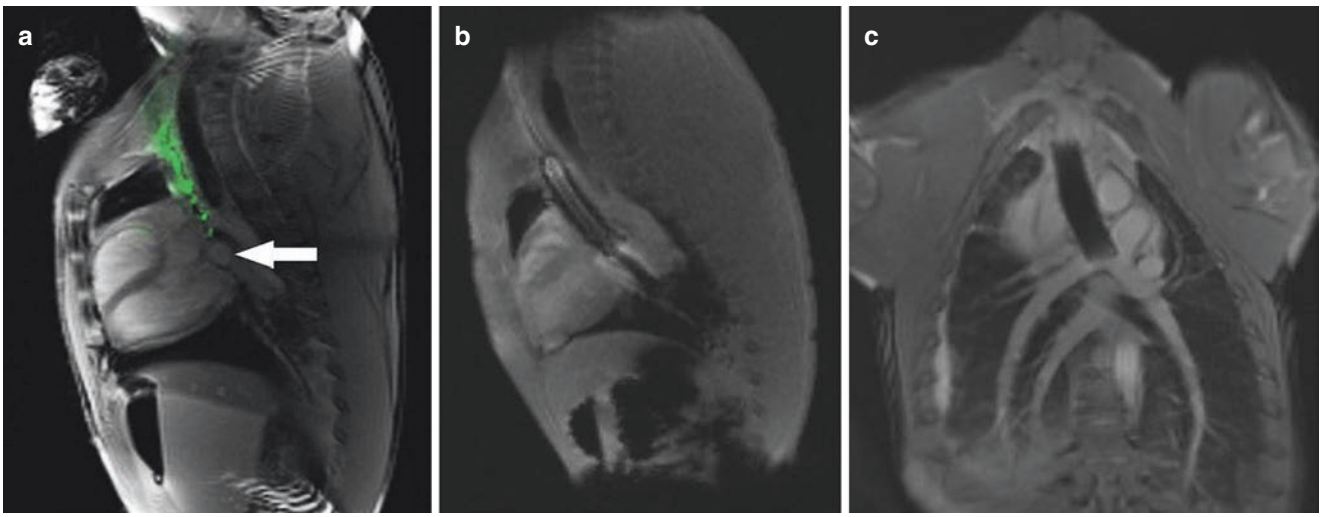

Fig. 23.7 iCMR percutaneous bidirectional Glenn shunt, Central venous access is obtained via the right internal jugular vein. (**a**) An active needle is used to puncture from the superior vena cava into the right pulmonary artery under real-time MR guidance (arrow). A guidewire is then positioned into the distal left pulmonary artery. (**b**) A covered stent is then deployed from the SVC into the right pulmonary artery. The stent balloon is filled with gadolinium. (**c**) The SVC and right pulmonary artery are now connected with a conduit (i.e., "Glenn" shunt)

and an "active" needle [106] (Fig. 23.7). This sort of extra-anatomic bypass, once made available to non-surgeons, has the potential to revolutionize mechanical revascularization.

Human iCMR Procedures

Diagnostic Cardiac Catheterization

Razavi et al. [17] at Kings College in London conducted the first diagnostic cardiac catheterization in children using a combined XMR environment. The same group conducted X-ray fused with MRI (XFM) procedures, in which prior MRI datasets were combined with real-time XRF to conduct therapeutic procedures. Kuehne et al. also conducted diagnostic cardiac catheterization procedures using passive catheter devices under rtMRI [18]. Three groups have reported invasive imaging of peripheral artery atheromata using profile-design active guidewire receiver coils [7, 25, 26]. In the report by Dick et al. [7], we concluded this guidewire design adds little to surface coils for diagnostic MRI of atherosclerosis but might have value in delivering interventional devices using iCMR. A team in Regensburg, Germany, conducted high-quality selective intra-arterial MR angiography [110] and reported preliminary revascularization procedures using passive devices in the iliac [23] and femoral [14] arteries. The Stanford team conducted iCMR-assisted TIPS procedures in patients [108].

At NIH [10] we perform MR-guided right heart catheterization using MR-safe catheters with gadolinium-filled balloons (Fig. 23.8). The procedure has been reclassified as a standard medical procedure in our hospital, and to date we have performed over 80 clinical cases in adults with a wide range of diseases, including pulmonary hypertension, heart failure, and intracardiac shunt. We have also opened an interventional MRI suite at the Children's National Medical Center in Washington DC to provide "radiation-free" catheterization to pediatric and adult patients with congenital heart disease.

Importantly, MR-guided catheterization promises to provide hemodynamic and functional information that X-ray fluoroscopy cannot [111]. Cardiac chamber volumes and function and large vessel dimensions can be assessed using cine imaging. In many diseases, for example, pulmonary hypertension or advanced heart failure and right ventricular mass, volume, and function have independent prognostic values [112, 113]. Phase-contrast MRI permits measurement of flow through major vessels (e.g., pulmonary arteries and aorta) and calculation of Qp and Qs. Muthurangu elegantly demonstrated that important hemodynamic parameters such as pulmonary vascular resistance [114] or pulmonary artery compliance [115] were more accurately assessed by combining MR phase-contrast-derived cardiac output and invasive pressure measurements, compared with traditional cath lab techniques (e.g., Fick or thermodilution), particularly during pulmonary vasoreactivity testing with high flow oxygen and inhaled nitric oxide.

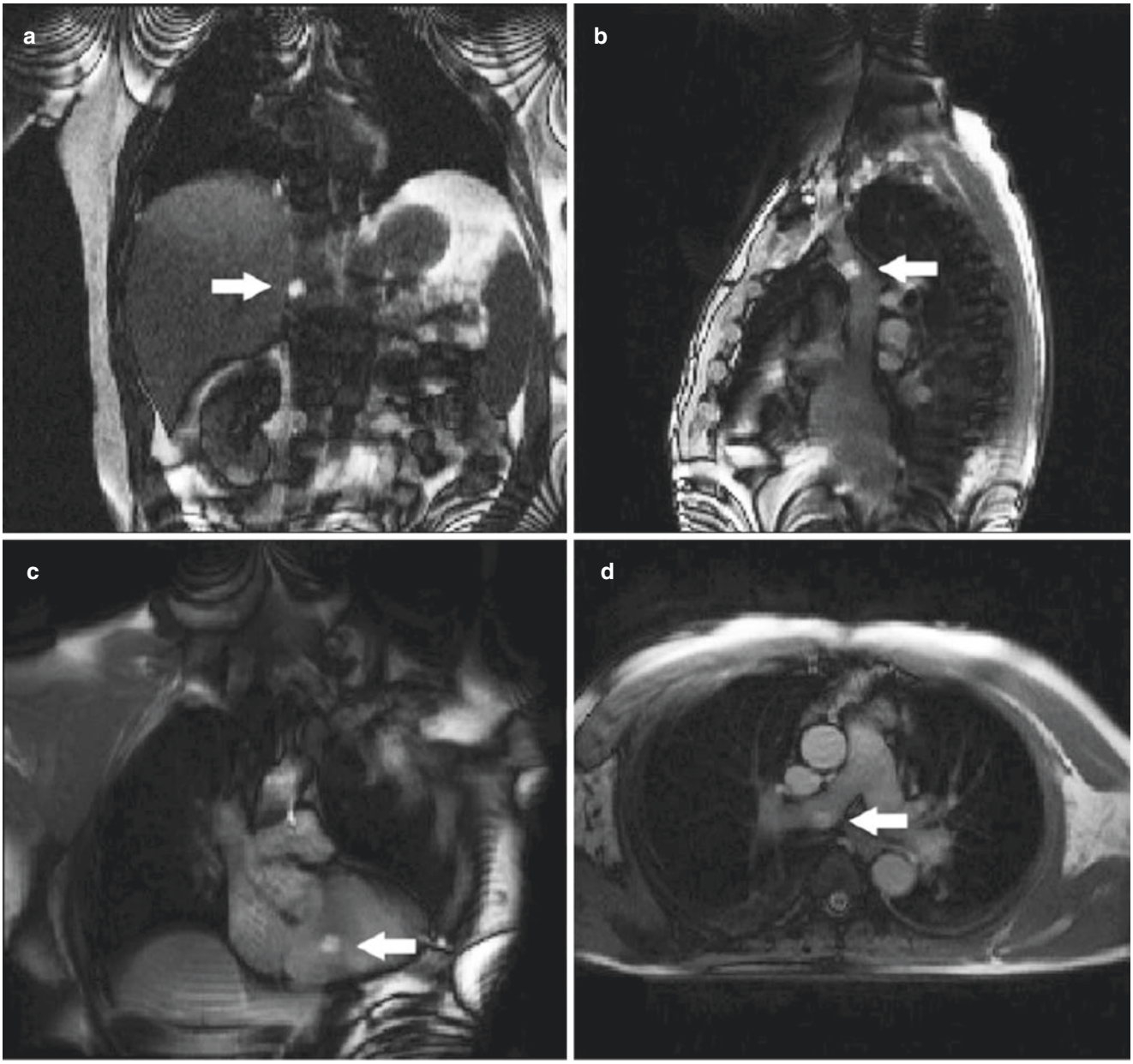

Fig. 23.8 MR right heart catheterization. The gadolinium-filled balloon wedge end-hole catheter is navigated through the right heart using real-time MR guidance. The balloon appears as a "white ball" on the images (arrows). Catheter tip positioned in the (**a**) inferior vena cava, (**b**) superior vena cava, (**c**) right ventricle, and (**d**) right pulmonary artery. At key positions, for example, the main pulmonary artery, simultaneous invasive pressures and MR phase-contrast flow measurements are acquired

By adding sequences such as lung perfusion to screen for chronic pulmonary thromboemboli, T1 mapping, or delayed contrast enhancement to screen for diffuse of regional myocardial fibrosis, a comprehensive "one-stop" cardiopulmonary assessment can be obtained [116, 117]. By repeating imaging and invasive hemodynamic measurements under different physiological provocations, for example, with exercise, saline challenge, or inhaled nitric oxide, iCMR catheterization could help unmask latent symptoms and pathology not apparent at rest and provide useful prognostic information [111, 118–120]. We now routinely perform functional imagi-ng, phase contrast to measure cardiac output, and invasive hemodynamic measurements at baseline and repeated with up to two physiological provocations in all patients, all within less than 2 h. We have also streamlined scanning protocols to eliminate the need for patient breath holding, using investigational real-time

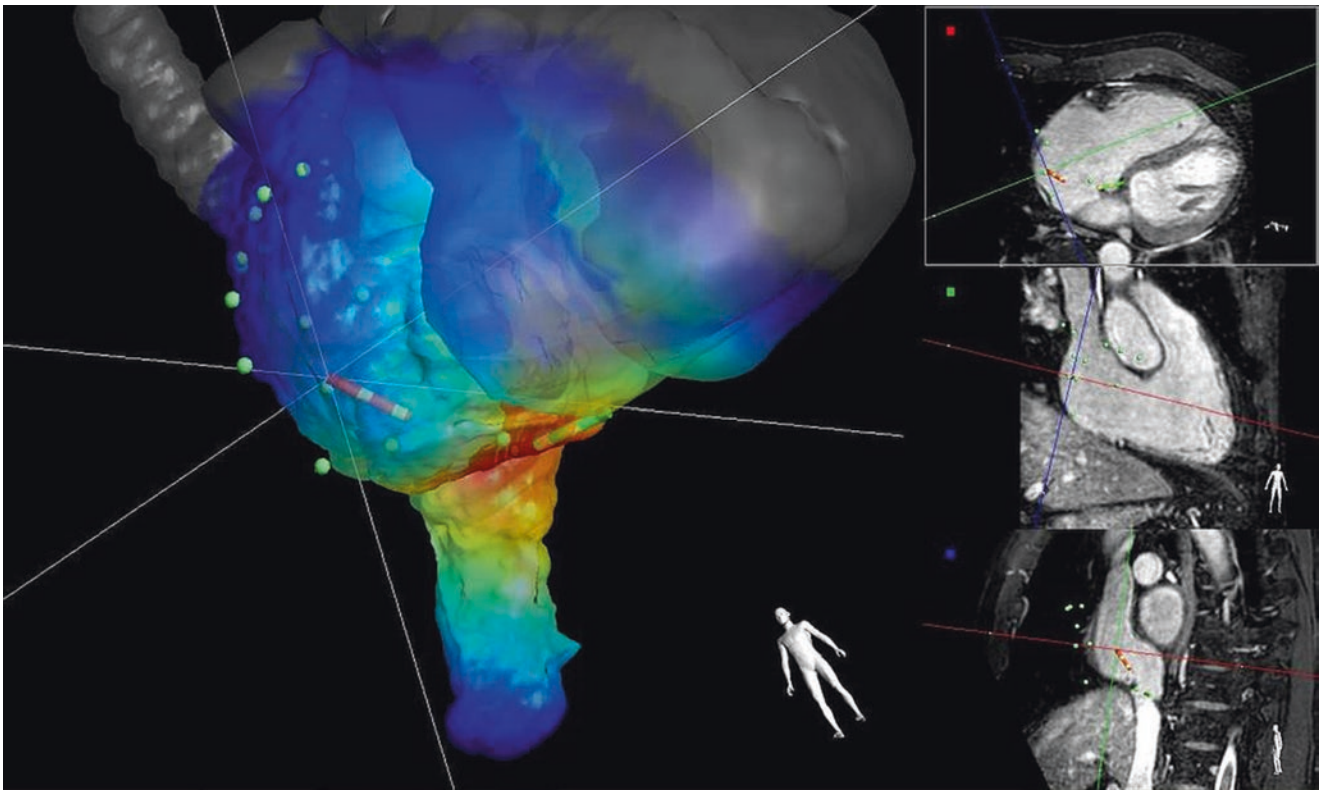

Fig. 23.9 Catheter ablation of typical right atrial flutter under MR guidance. The intracardiac electrogram is acquired at several locations with a first actively tracked catheter (red, Imricor Vision MR-EP catheter) while pacing with a second actively tracked catheter (green) located in the coronary sinus. The Interventional MR iSuite (Philips Research Hamburg) uses the position tracking data of the green catheter and corresponding activation time data to update a color-coded activation time map for each new mapped point. The colors represent the interpolation of previously acquired activation times on the right atrial endocardial shell. Red indicates early and blue late activation. The shell has been derived from the segmentation of a 3D cardiac scan acquired immediately before the intervention. (Courtesy of R. Rezavi, M. O'Neill, and T. Schaeffter, *King's College London, UK*; S. Weiss and S. Krueger, *Philips Research, Hamburg, Germany*; S. Wedan, G. Stenzel, T. Lloyd and D. Sunnarborg, *Imricor, Minnesota, US*)

sequences and free-breathing phase contrast with averaging [121, 122]. This is critical because many patients with advanced disease struggle to breath hold, particularly if they receive sedation for the catheterization procedure.

Structural Heart Interventions

Some structural iCMR procedures have already been performed in humans, including aortic coarctation angioplasty [123], femoral and popliteal artery angioplasty [14], and pulmonary valvuloplasty [35]. But widespread clinical adoption has been delayed by the unavailability of commercial MR-safe guidewires, catheters, and devices that meet the mechanical standards expected of conventional catheters and devices used in X-ray.

Cardiac Electrophysiology

Several manufacturers (*Imricor, MRI Interventions*) have developed MR conditional electrophysiology ablation systems and catheters, using passive or active tracking to navigate the cardiac chambers (Fig. 23.9). Using these systems, ablation of simple atrial arrhythmias has been reported in early human studies [124, 125] (Fig. 23.10). Extensive work is ongoing to optimize ablation lesion visualization, which has the potential to improve arrhythmia termination rates by enabling the operator to verify adequate ablation depth and continuity of ablation lines in real time [126–131]. There is evidence that procedural success defined by rates of arrhythmia recurrence after ablation correlates with the extent of late gadolinium enhancement [132].

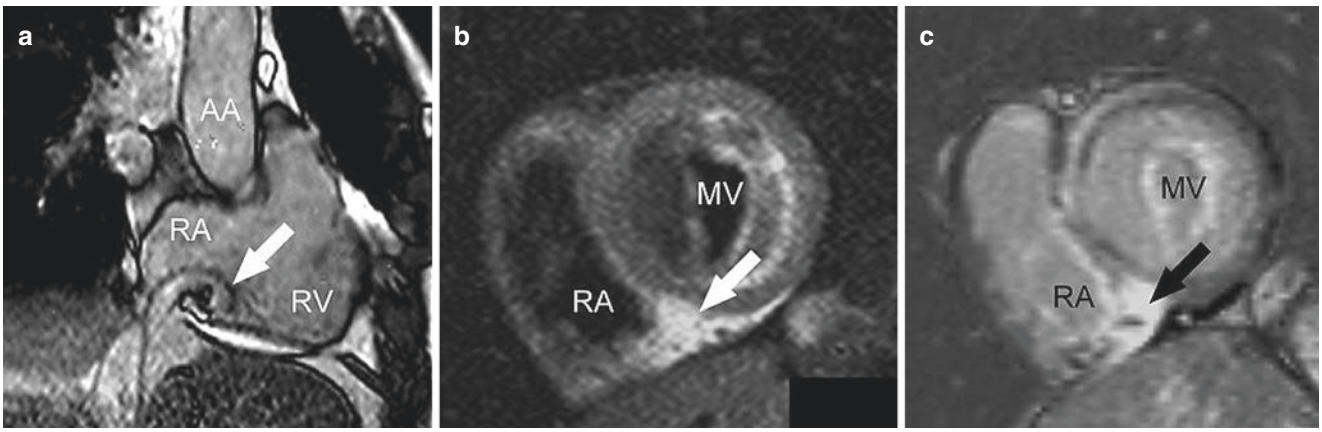

Fig. 23.10 Cavo-tricuspid isthmus ablation in a human subject. (**a**) The passively tracked tip of the ablation catheter is positioned above the cavo-tricuspid isthmus (arrow). Post-ablation T2-weighted (**b**) and late gadolinium enhancement (**c**) images of the cavo-tricuspid isthmus show the newly created ablation lesion (arrows). AA: ascending aorta; MV: mitral valve; RA: right atrium; RV: right ventricle. (Courtesy of M. Gutberlet, M. Grothoff and G. Hindricks, *University of Leipzig, Germany*)

Conclusion

Advocates promote the development of iCMR for the sake of reduction of radiation exposure to patients, especially young patients who are anticipated to require a large cumulative radiation exposure during diagnostic and therapeutic procedures; reduction of radiation exposure to operators and staff, who endure a large cumulative radiation exposure during their careers; and reduction of patient exposure to nephrotoxic iodinated contrast, which is important in patients with moderate-severe renal disease; and eliminating the requirement that staff wear heavy protective lead garments, which are associated with a high incidence of chronic musculoskeletal injury. Detractors argue that iCMR represents a costly and cumbersome alternative to procedures that otherwise are conducted rapidly and efficiently under X-ray guidance and occasionally enhanced with adjunctive ultrasound. Detractors also argue that despite any potential benefit, the large capital outlays and expected higher marginal cost of disposable (catheter) equipment are simply unjustifiable. These arguments are less tenable. Existing XMR facilities are constructed to permit each imaging system to be used independently of the other. The only incremental expense over separate angiography and MRI systems is the cost of the inter-modality transfer table and the barrier doors connecting the systems.

As described above, the chief obstacle to further development of iCMR is the limited availability of clinical-grade catheters and devices suitable for use in the MR environment. This in turn discourages wider deployment of XMR or iCMR systems. That said, clinical iCMR for simple diagnostic cardiac catheterization is feasible using existing technology and off-the-shelf catheters and is in routine clinical use in institutions in the United States and Europe. iCMR electrophysiology is expected to be an area of particular interest and technical development, now that MR conditional electrophysiology mapping and ablation systems are available and first-in-man arrhythmia ablation has been demonstrated.

However, iCMR may prove superior because using a single-modality, 3D anatomy, composition, function, and hemodynamics can be combined. iCMR can provide surgical-grade exposure to guide nonsurgical minimally invasive procedures and could enable completely new procedures to be developed. This has the potential to revolutionize the conduct of minimally invasive image-guided treatments.

Acknowledgment Supported by NIH Z01-HL005062.

References

1. Johnson JN, Hornik CP, Li JS, Benjamin DK Jr, Yoshizumi TT, Reiman RE, et al. Cumulative radiation exposure and cancer risk estimation in children with heart disease. Circulation. 2014;130(2):161–7.
2. Venneri L, Rossi F, Botto N, Andreassi MG, Salcone N, Emad A, et al. Cancer risk from professional exposure in staff working in cardiac catheterization laboratory: insights from the National Research Council's Biological Effects of Ionizing Radiation VII Report. Am Heart J. 2009;157(1):118–24.
3. Duerk JL, Butts K, Hwang KP, Lewin JS. Pulse sequences for interventional magnetic resonance imaging. Top Magn Reson Imaging. 2000;11(3):147–62.

4. Peters DC, FRKTMGWFBJEHKKVCAM. Undersampled projection reconstruction applied to MR angiography. Magn Reson Med. 2000;43(1):91–101.
5. Dick AJ, Guttman MA, Raman VK, Peters DC, Pessanha BS, Hill JM, et al. Magnetic resonance fluoroscopy allows targeted delivery of mesenchymal stem cells to infarct borders in swine. Circulation. 2003;108(23):2899–904.
6. Elgort DR, Wong EY, Hillenbrand CM, Wacker FK, Lewin JS, Duerk JL. Real-time catheter tracking and adaptive imaging. J Magn Reson Imaging. 2003;18(5):621–6.
7. Dick AJ, Raman VK, Raval AN, Guttman MA, Thompson RB, Ozturk C, et al. Invasive human magnetic resonance imaging during angioplasty: feasibility in a combined XMR suite. Catheter Cardiovasc Interv. 2005;64(3):265–74.
8. White MJ, Thornton JS, Hawkes DJ, Hill DL, Kitchen N, Mancini L, et al. Design, operation, and safety of single-room interventional MRI suites: practical experience from two centers. J Magn Reson Imaging. 2015;41(1):34–43.
9. Lederman RJ. Cardiovascular interventional magnetic resonance imaging. Circulation. 2005;112(19):3009–17.
10. Ratnayaka K, Faranesh AZ, Hansen MS, Stine AM, Halabi M, Barbash IM, et al. Real-time MRI-guided right heart catheterization in adults using passive catheters. Eur Heart J. 2013;34(5):380–9.
11. Godart F, Beregi JP, Nicol L, Occelli B, Vincentelli A, Daanen V, et al. MR-guided balloon angioplasty of stenosed aorta: in vivo evaluation using near-standard instruments and a passive tracking technique. J Magn Reson Imaging. 2000;12(4):639–44.
12. Omary RA, Frayne R, Unal O, Warner T, Korosec FR, Mistretta CA, et al. MR-guided angioplasty of renal artery stenosis in a pig model: a feasibility study. J Vasc Interv Radiol. 2000;11(3):373–81.
13. Raval AN, Telep JD, Guttman MA, Ozturk C, Jones M, Thompson RB, et al. Real-time magnetic resonance imaging-guided stenting of aortic coarctation with commercially available catheter devices in swine. Circulation. 2005;112(5):699–706.
14. Paetzel C, Zorger N, Bachthaler M, Hamer OW, Stehr A, Feuerbach S, et al. Magnetic resonance-guided percutaneous angioplasty of femoral and popliteal artery stenoses using real-time imaging and intra-arterial contrast-enhanced magnetic resonance angiography. Investig Radiol. 2005;40(5):257–62.
15. Paetzel C, Zorger N, Bachthaler M, Volk M, Seitz J, Herold T, et al. Feasibility of MR-guided angioplasty of femoral artery stenoses using real-time imaging and intraarterial contrast-enhanced MR angiography. RoFo: Fortschritte auf dem Gebiete der Rontgenstrahlen und der Nuklearmedizin. 2004;176(9):1232–6.
16. Miquel ME, Hegde S, Muthurangu V, Corcoran BJ, Keevil SF, Hill DL, et al. Visualization and tracking of an inflatable balloon catheter using SSFP in a flow phantom and in the heart and great vessels of patients. Magn Reson Med. 2004;51(5):988–95.
17. Razavi R, Hill DL, Keevil SF, Miquel ME, Muthurangu V, Hegde S, et al. Cardiac catheterisation guided by MRI in children and adults with congenital heart disease. Lancet. 2003;362(9399):1877–82.
18. Kuehne T, Yilmaz S, Schulze-Neick I, Wellnhofer E, Ewert P, Nagel E, et al. Magnetic resonance imaging guided catheterisation for assessment of pulmonary vascular resistance: in vivo validation and clinical application in patients with pulmonary hypertension. Heart. 2005;91(8):1064–9.
19. Buecker A, Neuerburg JM, Adam GB, Glowinski A, Schaeffter T, Rasche V, et al. Real-time MR fluoroscopy for MR-guided iliac artery stent placement. J Magn Reson Imaging. 2000;12(4):616–22.
20. Feng L, Dumoulin CL, Dashnaw S, Darrow RD, Delapaz RL, Bishop PL, et al. Feasibility of stent placement in carotid arteries with real-time MR imaging guidance in pigs. Radiology. 2005;234(2):558–62.
21. Kuehne T, Saeed M, Higgins CB, Gleason K, Krombach GA, Weber OM, et al. Endovascular stents in pulmonary valve and artery in swine: feasibility study of MR imaging-guided deployment and postinterventional assessment. Radiology. 2003;226(2):475–81.
22. Kee ST, Rhee JS, Butts K, Daniel B, Pauly J, Kerr A, et al. 1999 Gary J. Becker Young Investigator Award. MR-guided transjugular portosystemic shunt placement in a swine model. J Vasc Interv Radiol. 1999;10(5):529–35.
23. Manke C, Nitz WR, Djavidani B, Strotzer M, Lenhart M, Volk M, et al. MR imaging-guided stent placement in iliac arterial stenoses: a feasibility study. Radiology. 2001;219(2):527–34.
24. Ganesan AN, Selvanayagam JB, Mahajan R, Grover S, Nayyar S, Brooks AG, et al. Mapping and ablation of the pulmonary veins and cavo-tricuspid isthmus with a magnetic resonance imaging-compatible externally irrigated ablation catheter and integrated electrophysiology system. Circ Arrhythm Electrophysiol. 2012;5(6):1136–42.
25. Hofmann LV, Liddell RP, Eng J, Wasserman BA, Arepally A, Lee DS, et al. Human peripheral arteries: feasibility of transvenous intravascular MR Imaging of the arterial wall. Radiology. 2005;235(2):617–22.
26. Larose E, Yeghiazarians Y, Libby P, Yucel EK, Aikawa M, Kacher DF, et al. Characterization of human atherosclerotic plaques by intravascular magnetic resonance imaging. Circulation. 2005;112(15):2324–31.
27. Sonmez M, Saikus CE, Bell JA, Franson DN, Halabi M, Faranesh AZ, et al. MRI active guidewire with an embedded temperature probe and providing a distinct tip signal to enhance clinical safety. J Cardiovasc Magn Reson. 2012;14:38.
28. Kocaturk O, Kim AH, Saikus CE, Guttman MA, Faranesh AZ, Ozturk C, et al. Active two-channel 0.035″ guidewire for interventional cardiovascular MRI. J Magn Reson Imaging. 2009;30(2):461–5.
29. Reddy V, Malchano Z, Dukkipati S, Holmvang G, Schmidt E, Dumoulin C, et al. Interventional MRI: electroanatomical mapping using real-time MR tracking of a deflectable catheter [Abstract]. Heart Rhythm. 2005;2(15):S279–S80.
30. Dukkipati SR, Mallozzi R, Schmidt EJ, Holmvang G, d'Avila A, Guhde R, et al. Electroanatomic mapping of the left ventricle in a porcine model of chronic myocardial infarction with magnetic resonance-based catheter tracking. Circulation. 2008;118(8):853–62.
31. Vergara GR, Vijayakumar S, Kholmovski EG, Blauer JJ, Guttman MA, Gloschat C, et al. Real-time magnetic resonance imaging-guided radiofrequency atrial ablation and visualization of lesion formation at 3 Tesla. Heart Rhythm. 2011;8(2):295–303.
32. Bakker CJ, Hoogeveen RM, Weber J, van Vaals JJ, Viergever MA, Mali WP. Visualization of dedicated catheters using fast scanning techniques with potential for MR-guided vascular interventions. Magn Reson Med. 1996;36(6):816–20.
33. Bakker CJ, Bos C, Weinmann HJ. Passive tracking of catheters and guidewires by contrast-enhanced MR fluoroscopy. Magn Reson Med. 2001;45(1):17–23.
34. Buecker A, Spuentrup E, Schmitz-Rode T, Kinzel S, Pfeffer J, Hohl C, et al. Use of a nonmetallic guide wire for magnetic resonance-guided coronary artery catheterization. Investig Radiol. 2004;39(11):656–60.
35. Tzifa A, Krombach GA, Kramer N, Kruger S, Schutte A, von Walter M, et al. Magnetic resonance-guided cardiac interventions using magnetic resonance-compatible devices: a preclinical study and first-in-man congenital interventions. Circ Cardiovasc Interv. 2010;3(6):585–92. Epub 2010/11/26
36. Kantor HL, Briggs RW, Balaban RS. In vivo 31P nuclear magnetic resonance measurements in canine heart using a catheter-coil. Circ Res. 1984;55(2):261–6.
37. Martin AJ, Plewes DB, Henkelman RM. MR imaging of blood vessels with an intravascular coil. J Magn Reson Imaging. 1992;2(4):421–9.

38. Hurst GC, Hua J, Duerk JL, Cohen AM. Intravascular (catheter) NMR receiver probe: preliminary design analysis and application to canine iliofemoral imaging. Magn Reson Med. 1992;24(2):343–57.
39. Kandarpa K, Jakab P, Patz S, Schoen FJ, Jolesz FA. Prototype miniature endoluminal MR imaging catheter. J Vascul Interv Radio. 1993;4(3):419–27.
40. Atalar E, Bottomley PA, Ocali O, Correia LC, Kelemen MD, Lima JA, et al. High resolution intravascular MRI and MRS by using a catheter receiver coil. Magn Reson Med. 1996;36(4):596–605.
41. Hillenbrand CM, Elgort DR, Wong EY, Reykowski A, Wacker FK, Lewin JS, et al. Active device tracking and high-resolution intravascular MRI using a novel catheter-based, opposed-solenoid phased array coil. Magn Reson Med. 2004;51(4):668–75.
42. Worthley SG, Helft G, Fuster V, Fayad ZA, Shinnar M, Minkoff LA, et al. A novel nonobstructive intravascular MRI coil: in vivo imaging of experimental atherosclerosis. Arterioscler Thromb Vasc Biol. 2003;23(2):346–50.
43. Ladd ME, Erhart P, Debatin JF, Hofmann E, Boesiger P, von Schulthess GK, et al. Guidewire antennas for MR fluoroscopy. Magn Reson Med. 1997;37(6):891–7.
44. Ocali O, Atalar E. Intravascular magnetic resonance imaging using a loopless catheter antenna. Magn Reson Med. 1997;37(1):112–8.
45. Atalar E, Kraitchman DL, Carkhuff B, Lesho J, Ocali O, Solaiyappan M, et al. Catheter-tracking FOV MR fluoroscopy. Magn Reson Med. 1998;40(6):865–72.
46. Burl M, Coutts GA, Herlihy DJ, Hill-Cottingham R, Eastham JF, Hajnal JV, et al. Twisted-pair RF coil suitable for locating the track of a catheter. Magn Reson Med. 1999;41(3):636–8.
47. Rivas PA, Nayak KS, Scott GC, McConnell MV, Kerr AB, Nishimura DG, et al. In vivo real-time intravascular MRI. J Cardiosvas Magn Reson. 2002;4(2):223–32.
48. Susil RC, Yeung CJ, Atalar E. Intravascular extended sensitivity (IVES) MRI antennas. Magn Reson Med. 2003;50(2):383–90.
49. Guttman MA, Ozturk C, Raval AN, Raman VK, Dick AJ, DeSilva R, et al. Interventional cardiovascular procedures guided by real-time MR imaging: an interactive interface using multiple slices, adaptive projection modes and live 3D renderings. J Magn Reson Imaging. 2007;26(6):1429–35.
50. Dumoulin CL, Souza SP, Darrow RD. Real-time position monitoring of invasive devices using magnetic resonance. Magn Reson Med. 1993;29(3):411–5.
51. Leung DA, Debatin JF, Wildermuth S, McKinnon GC, Holtz D, Dumoulin CL, et al. Intravascular MR tracking catheter: preliminary experimental evaluation. Am J Roentgenol. 1995;164(5):1265–70.
52. Ladd ME, Zimmermann GG, McKinnon GC, von Schulthess GK, Dumoulin CL, Darrow RD, et al. Visualization of vascular guidewires using MR tracking. J Magn Reson Imaging. 1998;8(1):251–3.
53. Campbell-Washburn A, Rogers T, Xue H, Hansen MS, Lederman RJ, Faranesh AZ. Dual echo positive contrast bSSFP for real-time visualization of passive devices during MRI-guided cardiovascular catheterization. J Cardiovasc Magn Reson. 2014;16:88.
54. Srinivasan S, Ennis DB. Variable flip angle balanced steady-state free precession for lower SAR or higher contrast cardiac cine imaging. Magn Reson Med. 2014;71(3):1035–43.
55. Wu X, Akgun C, Vaughan JT, Andersen P, Strupp J, Ugurbil K, et al. Adapted RF pulse design for SAR reduction in parallel excitation with experimental verification at 9.4 T. J Magn Reson. 2010;205(1):161–70.
56. Ladd ME, Quick HH. Reduction of resonant RF heating in intravascular catheters using coaxial chokes. Magn Reson Med. 2000;43(4):615–9.
57. Lee C, McNamara C, Viohl I, inventors; Surgi-Vision, assignee. Connector and guidewire connectable thereto. United States patent 6,714,809. 2004.
58. Yeung CJ, Susil RC, Atalar E. RF safety of wires in interventional MRI: using a safety index. Magn Reson Med. 2002;47(1):187–93.
59. Serfaty JM, Yang X, Foo TK, Kumar A, Derbyshire A, Atalar E. MRI-guided coronary catheterization and PTCA: A feasibility study on a dog model. Magn Reson Med. 2003;49(2):258–63.
60. Weiss S, Vernickel P, Schaeffter T, Schultz V, Gleich B, editors. A safe transmission line for interventional devices. 5th International MRI Symposium; 2004; Boston
61. Wong EY, Zhang Q, Duerk JL, Lewin JS, Wendt M. An optical system for wireless detuning of parallel resonant circuits. J Magn Reson Imaging. 2000;12(4):632–8. Epub 2000/10/24
62. Konings MK, Bartels LW, van Swol CF, Bakker CJ. Development of an MR-safe tracking catheter with a laser-driven tip coil. J Magn Reson Imaging. 2001;13(1):131–5.
63. Eggers H, Weiss S, Boernert P, Boesiger P. Image-based tracking of optically detunable parallel resonant circuits. Magn Reson Med. 2003;49(6):1163–74.
64. Weiss S, Schaeffter T, Brinkert F, Kuhne T, Bücker A. Ein Verfahren zur sicheren Visualisierung und Lokalisierung von Kathetern fur MR-gefuhrte intravaskulare Prozeduren [An approach for safe visualization and localization of catheter during MR-guided intravascular procedures]. Z Med Phys. 2003;13(3):172–6.
65. Bell JA, Saikus CE, Ratnayaka K, Barbash IM, Faranesh AZ, Franson DN, et al. Active delivery cable tuned to device deployment state: enhanced visibility of nitinol occluders during preclinical interventional MRI. J Magn Reson Imaging. 2012;36(4):972–8.
66. Quick HH, Kuehl H, Kaiser G, Bosk S, Debatin JF, Ladd ME. Inductively coupled stent antennas in MRI. Magn Reson Med. 2002;48(5):781–90.
67. Kivelitz D, Wagner S, Schnorr J, Wetzler R, Busch M, Melzer A, et al. A vascular stent as an active component for locally enhanced magnetic resonance imaging: initial in vivo imaging results after catheter-guided placement in rabbits. Investig Radiol. 2003;38(3):147–52.
68. Kuehne T, Fahrig R, Butts K. Pair of resonant fiducial markers for localization of endovascular catheters at all catheter orientations. J Magn Reson Imaging. 2003;17(5):620–4.
69. Quick HH, Zenge MO, Kuehl H, Kaiser G, Aker S, Massing S, et al. Interventional magnetic resonance angiography with no strings attached: wireless active catheter visualization. Magn Reson Med. 2005;53(2):446–55.
70. Spuentrup E, Ruebben A, Schaeffter T, Manning WJ, Gunther RW, Buecker A. Magnetic resonance – guided coronary artery stent placement in a swine model. Circulation. 2002;105(7):874–9.
71. Wildermuth S, Dumoulin CL, Pfammatter T, Maier SE, Hofmann E, Debatin JF. MR-guided percutaneous angioplasty: assessment of tracking safety, catheter handling and functionality. Cardiovasc Intervent Radiol. 1998;21(5):404–10.
72. Yang X, Bolster BD Jr, Kraitchman DL, Atalar E. Intravascular MR-monitored balloon angioplasty: an in vivo feasibility study. J Vasc Interv Radiol. 1998;9(6):953–9.
73. Buecker A, Adam GB, Neuerburg JM, Kinzel S, Glowinski A, Schaeffter T, et al. Simultaneous real-time visualization of the catheter tip and vascular anatomy for MR-guided PTA of iliac arteries in an animal model. J Magn Reson Imaging. 2002;16(2):201–8.
74. Dion YM, Ben El Kadi H, Boudoux C, Gourdon J, Chakfe N, Traore A, et al. Endovascular procedures under near-real-time magnetic resonance imaging guidance: an experimental feasibility study. J Vasc Surg. 2000;32(5):1006–14.
75. Wacker FK, Hillenbrand C, Elgort DR, Zhang S, Duerk JL, Lewin JS. MR imaging-guided percutaneous angioplasty and stent placement in a swine model: comparison of open- and closed-bore scanners. Acad Radiol. 2005;12(9):1085.
76. Bartels LW, Bos C, van Der Weide R, Smits HF, Bakker CJ, Viergever MA. Placement of an inferior vena cava filter in a pig

guided by high-resolution MR fluoroscopy at 1.5 T. J Magn Reson Imaging. 2000;12(4):599–605.
77. Bücker A, Neuerburg JM, Adam GB, Glowinski A, Schaeffter T, Rasche V, et al. Real-time MR Guidance for inferior vena cava filter placement in an animal model. J Vasc Interv Radiol. 2001;12(6):753–6.
78. Frahm C, Gehl HB, Lorch H, Zwaan M, Drobnitzky M, Laub GA, et al. MR-guided placement of a temporary vena cava filter: technique and feasibility. J Magn Reson Imaging. 1998;8(1):105–9.
79. Bücker A, Neuerburg JM, Adam G, Glowinski A, van Vaals JJ, Gunther RW. MR-gesteuerte Spiralembolisation von Nierenarterien in einem Tiermodell [MR-guided coil embolisation of renal arteries in an animal model]. RoFo: Fortschritte auf dem Gebiete der Rontgenstrahlen und der Nuklearmedizin. 2003;175(2):271–4.
80. Fink C, Bock M, Umathum R, Volz S, Zuehlsdorff S, Grobholz R, et al. Renal embolization: feasibility of magnetic resonance-guidance using active catheter tracking and intraarterial magnetic resonance angiography. Investig Radiol. 2004;39(2):111–9.
81. Seppenwoolde JH, Bartels LW, van der Weide R, Nijsen JF, van het Schip AD, Bakker CJ. Fully MR-guided hepatic artery catheterization for selective drug delivery: a feasibility study in pigs. J Magn Reson Imaging. 2006;23(2):123–9. Epub 2005/12/24
82. Raval AN, Karmarkar PV, Guttman MA, Ozturk C, Sampath S, DeSilva R, et al. Real-time MRI-guided endovascular recanalization of chronic total arterial occlusion in a swine model. Circulation. 2006;113(8):1101–7.
83. Raman VK, Karmarkar PV, Guttman MA, Dick AJ, Peters DC, Ozturk C, et al. Real-time magnetic resonance-guided endovascular repair of experimental abdominal aortic aneurysm in swine. J Am Coll Cardiol. 2005;45(12):2069–77.
84. Eggebrecht H, Quick HH. [Personal Communication]. 2005.
85. Schalla S, Saeed M, Higgins CB, Martin A, Weber O, Moore P. Magnetic resonance – guided cardiac catheterization in a swine model of atrial septal defect. Circulation. 2003;108(15):1865–70.
86. Feng L, Dumoulin CL, Dashnaw S, Darrow RD, Guhde R, Delapaz RL, et al. Transfemoral catheterization of carotid arteries with real-time MR imaging guidance in pigs. Radiology. 2005;234(2):551–7.
87. Omary RA, Green JD, Schirf BE, Li Y, Finn JP, Li D. Real-time magnetic resonance imaging-guided coronary catheterization in swine. Circulation. 2003;107(21):2656–9.
88. Quick HH, Kuehl H, Kaiser G, Hornscheidt D, Mikolajczyk KP, Aker S, et al. Interventional MRA using actively visualized catheters, TrueFISP, and real-time image fusion. Magn Reson Med. 2003;49(1):129–37.
89. Buecker A, Spuentrup E, Grabitz R, Freudenthal F, Muehler EG, Schaeffter T, et al. Magnetic resonance-guided placement of atrial septal closure device in animal model of patent foramen ovale. Circulation. 2002;106(4):511–5.
90. Rickers C, Jerosch-Herold M, Hu X, Murthy N, Wang X, Kong H, et al. Magnetic resonance image-guided transcatheter closure of atrial septal defects. Circulation. 2003;107(1):132–8.
91. Schalla S, Saeed M, Higgins CB, Weber O, Martin A, Moore P. Balloon sizing and transcatheter closure of acute atrial septal defects guided by magnetic resonance fluoroscopy: assessment and validation in a large animal model. J Magn Reson Imaging. 2005;21(3):204–11.
92. Kuehne T, Yilmaz S, Meinus C, Moore P, Saeed M, Weber O, et al. Magnetic resonance imaging-guided transcatheter implantation of a prosthetic valve in aortic valve position: Feasibility study in swine. J Am Coll Cardiol. 2004;44(11):2247–9.
93. Lederman RJ, Guttman MA, Peters DC, Thompson RB, Sorger JM, Dick AJ, et al. Catheter-based endomyocardial injection with real-time magnetic resonance imaging. Circulation. 2002;105(11):1282–4.
94. Corti R, Badimon J, Mizsei G, Macaluso F, Lee M, Licato P, et al. Real time magnetic resonance guided endomyocardial local delivery. Heart. 2005;91(3):348–53.
95. Karmarkar PV, Kraitchman DL, Izbudak I, Hofmann LV, Amado LC, Fritzges D, et al. MR-trackable intramyocardial injection catheter. Magn Reson Med. 2004;51(6):1163–72.
96. Krombach GA, Pfeffer JG, Kinzel S, Katoh M, Gunther RW, Buecker A. MR-guided percutaneous intramyocardial injection with an MR-compatible catheter: feasibility and changes in T1 values after injection of extracellular contrast medium in pigs. Radiology. 2005;235(2):487–94.
97. Saeed M, Lee R, Martin A, Weber O, Krombach GA, Schalla S, et al. Transendocardial delivery of extracellular myocardial markers by using combination X-ray/MR fluoroscopic guidance: feasibility study in dogs. Radiology. 2004;231(3):689–96.
98. Hazel SJ, Paterson HS, Edwards JR, Maddern GJ. Surgical treatment of atrial fibrillation via energy ablation. Circulation. 2005;111(8):e103–6.
99. Susil RC, Yeung CJ, Halperin HR, Lardo AC, Atalar E. Multifunctional interventional devices for MRI: a combined electrophysiology/MRI catheter. Magn Reson Med. 2002;47(3):594–600.
100. Lardo AC, McVeigh ER, Jumrussirikul P, Berger RD, Calkins H, Lima J, et al. Visualization and temporal/spatial characterization of cardiac radiofrequency ablation lesions using magnetic resonance imaging. Circulation. 2000;102(6):698–705.
101. Hoffmann BA, Koops A, Rostock T, Mullerleile K, Steven D, Karst R, et al. Interactive real-time mapping and catheter ablation of the cavotricuspid isthmus guided by magnetic resonance imaging in a porcine model. Eur Heart J. 2010;31(4):450–6.
102. Arepally A, Karmarkar PV, Weiss C, Rodriguez ER, Lederman RJ, Atalar E. Magnetic resonance image-guided trans-septal puncture in a swine heart. J Magn Reson Imaging. 2005;21(4):463–7.
103. Raval AN, Karmarkar PV, Guttman MA, Ozturk C, DeSilva R, Wright VJ, et al. Real-time MRI guided atrial septal puncture and balloon septostomy in swine. Catheter Cardiovasc Interv. 2006;67(4):637–43.
104. Barbash IM, Saikus CE, Faranesh AZ, Ratnayaka K, Kocaturk O, Chen MY, et al. Direct percutaneous left ventricular access and port closure: pre-clinical feasibility. JACC Cardiovasc Intervent. 2011;4(12):1318–25.
105. Halabi M, Ratnayaka K, Faranesh AZ, Hansen MS, Barbash IM, Eckhaus MA, et al. Transthoracic delivery of large devices into the left ventricle through the right ventricle and interventricular septum: preclinical feasibility. J Cardiovasc Magn Reson. 2013;15(1):10.
106. Ratnayaka K, Saikus CE, Faranesh AZ, Bell JA, Barbash IM, Kocaturk O, et al. Closed-chest transthoracic magnetic resonance imaging-guided ventricular septal defect closure in swine. JACC Cardiovasc Intervent. 2011;4(12):1326–34.
107. Halabi M, Faranesh A, Schenke W, Wright V, Hansen M, Saikus C, et al. Real-time cardiovascular magnetic resonance subxiphoid pericardial access and pericardiocentesis using off-the-shelf devices in swine. J Cardiovasc Magn Reson. 2013;15(1):61.
108. Kee ST, Ganguly A, Daniel BL, Wen Z, Butts K, Shimikawa A, et al. MR-guided transjugular intrahepatic portosystemic shunt creation with use of a hybrid radiography/MR system. J Vasc Interv Radiol. 2005;16(2 Pt 1):227–34.
109. Arepally A, Kamarkar P, Weiss C, Atalar E. Percutaneous MR-guided transvascular access of the mesenteric venous system-study in a swine model [In Press]. Radiology. 2006;238(1):113–8.
110. Paetzel C, Zorger N, Seitz J, Volk M, Nitz WR, Herold T, et al. Intraarterial contrast material-enhanced magnetic resonance angiography of the aortoiliac system. J Vasc Interv Radiol. 2004;15(9):981–4.
111. Rogers T, Ratnayaka K, Lederman RJ. MRI catheterization in cardiopulmonary disease. Chest. 2014;145(1):30–6.

112. Di Salvo TG, Mathier M, Semigran MJ, Dec GW. Preserved right ventricular ejection fraction predicts exercise capacity and survival in advanced heart failure. J Am Coll Cardiol. 1995;25(5):1143–53.
113. Ghio S, Gavazzi A, Campana C, Inserra C, Klersy C, Sebastiani R, et al. Independent and additive prognostic value of right ventricular systolic function and pulmonary artery pressure in patients with chronic heart failure. J Am Coll Cardiol. 2001;37(1):183–8.
114. Muthurangu V, Taylor A, Andriantsimiavona R, Hegde S, Miquel ME, Tulloh R, et al. Novel method of quantifying pulmonary vascular resistance by use of simultaneous invasive pressure monitoring and phase-contrast magnetic resonance flow. Circulation. 2004;110(7):826–34.
115. Muthurangu V, Atkinson D, Sermesant M, Miquel ME, Hegde S, Johnson R, et al. Measurement of total pulmonary arterial compliance using invasive pressure monitoring and MR flow quantification during MR-guided cardiac catheterization. Am J Physiol Heart Circ Physiol. 2005;289(3):H1301–6.
116. Ohno Y, Hatabu H, Murase K, Higashino T, Nogami M, Yoshikawa T, et al. Primary pulmonary hypertension: 3D dynamic perfusion MRI for quantitative analysis of regional pulmonary perfusion. AJR Am J Roentgenol. 2007;188(1):48–56.
117. Ugander M, Oki AJ, Hsu LY, Kellman P, Greiser A, Aletras AH, et al. Extracellular volume imaging by magnetic resonance imaging provides insights into overt and sub-clinical myocardial pathology. Eur Heart J. 2012;33(10):1268–78.
118. Nishimura RA, Carabello BA. Hemodynamics in the cardiac catheterization laboratory of the 21st century. Circulation. 2012;125(17):2138–50.
119. Fujimoto N, Borlaug BA, Lewis GD, Hastings JL, Shafer KM, Bhella PS, et al. Hemodynamic responses to rapid saline loading: the impact of age, sex, and heart failure. Circulation. 2013;127(1):55–62.
120. Blumberg FC, Arzt M, Lange T, Schroll S, Pfeifer M, Wensel R. Impact of right ventricular reserve on exercise capacity and survival in patients with pulmonary hypertension. Eur J Heart Fail. 2013;15(7):771–5.
121. Xue H, Kellman P, Larocca G, Arai AE, Hansen MS. High spatial and temporal resolution retrospective cine cardiovascular magnetic resonance from shortened free breathing real-time acquisitions. J Cardiovasc Magn Reson. 2013;15:102.
122. Xue H, Inati S, Sorensen TS, Kellman P, Hansen MS. Distributed MRI reconstruction using gadgetron-based cloud computing. Magn Reson Med. 2015;73(3):1015–25
123. Krueger JJ, Ewert P, Yilmaz S, Gelernter D, Peters B, Pietzner K, et al. Magnetic resonance imaging-guided balloon angioplasty of coarctation of the aorta: a pilot study. Circulation. 2006;113(8):1093–100.
124. Eitel C, Piorkowski C, Hindricks G, Gutberlet M. Electrophysiology study guided by real-time magnetic resonance imaging. Eur Heart J. 2012;33(15):1975.
125. Grothoff M, Piorkowski C, Eitel C, Gaspar T, Lehmkuhl L, Lucke C, et al. MR imaging-guided electrophysiological ablation studies in humans with passive catheter tracking: initial results. Radiology. 2014;122671
126. Dickfeld T, Kato R, Zviman M, Lai S, Meininger G, Lardo AC, et al. Characterization of radiofrequency ablation lesions with gadolinium-enhanced cardiovascular magnetic resonance imaging. J Am Coll Cardiol. 2006;47(2):370–8.
127. Arujuna A, Karim R, Caulfield D, Knowles B, Rhode K, Schaeffter T, et al. Acute pulmonary vein isolation is achieved by a combination of reversible and irreversible atrial injury after catheter ablation: evidence from magnetic resonance imaging. Circulation: Arrhyth Electrophysiol. 2012;5(4):691–700.
128. Harrison JL, Jensen HK, Peel SA, Chiribiri A, Grøndal AK, Bloch LØ, et al. Cardiac magnetic resonance and electroanatomical mapping of acute and chronic atrial ablation injury: a histological validation study. Eur Heart J. 2014 Jun 7;35(22):1486–95.
129. Celik H, Ramanan V, Barry J, Ghate S, Leber V, Oduneye S, et al. Intrinsic contrast for characterization of acute radiofrequency ablation lesions. Circ Arrhythm Electrophysiol. 2014;7(4):718–27
130. Ranjan R, Kato R, Zviman MM, Dickfeld TM, Roguin A, Berger RD, et al. Gaps in the ablation line as a potential cause of recovery from electrical isolation and their visualization using MRI. Circ Arrhythm Electrophysiol. 2011;4(3):279–86.
131. Ranjan R, Kholmovski EG, Blauer J, Vijayakumar S, Volland NA, Salama ME, et al. Identification and acute targeting of gaps in atrial ablation lesion sets using a real-time magnetic resonance imaging system. Circ Arrhythm Electrophysiol. 2012;5(6):1130–5.
132. Peters DC, Wylie JV, Hauser TH, Nezafat R, Han Y, Woo JJ, et al. Recurrence of atrial fibrillation correlates with the extent of post-procedural late gadolinium enhancement: a pilot study. JACC Cardiovasc Imaging. 2009;2(3):308–16.

Targeted MR Imaging in Cardiovascular Disease

24

David E. Sosnovik and Peter Caravan

Magnetic resonance (MR) has been used largely to image gross anatomical features in the heart such as its dimensions, contractility, perfusion, and viability [1–3]. More recently, microstructural imaging techniques have been developed to assess the physical properties of individual cardiomyocytes and their three-dimensional arrangement in the heart [4–6]. Molecular MR interrogates the heart at yet another scale by providing noninvasive readouts of key cellular and molecular processes. In this chapter the development and application of molecular MR in the cardiovascular system will be reviewed.

The imaging of a molecular process requires three factors to be considered: (1) the nature and abundance of the target, (2) the properties of the ligand used to detect the target, and (3) the properties of the agent used to generate a detectable imaging signal. While cells can be successfully labeled ex vivo [7], with rare exceptions the imaging of intracellular targets in vivo cannot be reliably performed with MR. Molecular MR imaging agents have, therefore, largely been developed to image targets on the cell surface, in the extracellular matrix, or on the vessel wall [8–10].

Target Identification and Characterization

The ideal molecular target should be highly expressed, accessible, and specific for an underlying molecular process. Many targets in the cardiovascular system such as fibrin, collagen, elastin, and cell-free DNA fulfill these criteria and can be imaged with only minor modifications to clinically used gadolinium chelates [11–16]. Other targets such as apoptosis, angiogenesis, and adhesion molecules are expressed at far lower levels and require dedicated constructs with enhanced sensitivity to be developed [17–23].

Biological amplification of the ligand-target interaction can occur via several mechanisms and can further enhance sensitivity. The binding of a ligand to a receptor or to the cell surface frequently leads to internalization of the imaging agent, freeing the receptor or surface target for further binding. Internalization of an imaging agent often leads to its concentration in lysosomes, which further enhances the signal generated by most nanoparticles via an aggregation effect [24]. The binding of small gadolinium chelates to large proteins, such as albumin, can also drastically change their magnetic relaxation properties and enhance their sensitivity [25]. In an analogous fashion, the activation of an imaging agent by an enzyme can cause the agent to self-aggregate or bind to surrounding proteins, increasing the magnitude of the generated signal [26].

In addition to the characteristics of the target, the properties of the host tissue and environment are also important considerations. At the most basic level, the complete absence of any vascular supply, including collateral microchannels, can preclude the delivery of the agent to the intended target. The ability of the agent to cross the endothelial membrane is also of key importance when imaging interstitial or parenchymal targets. Few imaging agents, for instance, are able to reliably cross the blood-brain barrier. In the heart, the endothelial membrane is far more permeable, particularly after ischemic injury and even in the early stages of atherosclerosis [27]. The presence or absence of inflammation in a tissue is also a key factor. Inflammatory cells such as macrophages will phagocytose most nanoparticles, which can lead to their nonspecific accumulation. Conversely, this property can also be used to image inflammation in the myocardium or atherosclerotic plaque (Fig. 24.1) [28–34].

D. E. Sosnovik (✉) · P. Caravan
Massachusetts General Hospital, Harvard Medical School,
Martinos Center for Biomedical Imaging, Charlestown, MA, USA
e-mail: sosnovik@nmr.mgh.harvard.edu; caravan@nmr.mgh.harvard.edu

R. Y. Kwong et al. (eds.), *Cardiovascular Magnetic Resonance Imaging*, Contemporary Cardiology,
https://doi.org/10.1007/978-1-4939-8841-9_24

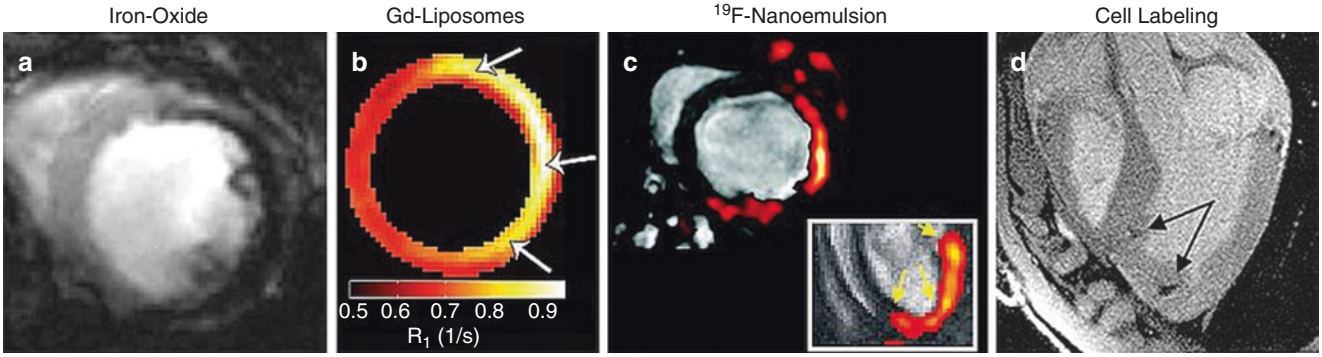

Fig. 24.1 Cell tracking in the heart with MR-detectable nanoparticles. (**a**–**c**) Labeling of inflammatory cells in vivo to detect myocardial inflammation and (**d**) ex vivo labeling to track injected stem cells. The labeling of inflammatory cells can be performed through the intravenous injection of (**a**) iron-oxide nanoparticles (Reprinted from Sosnovik et al. [28], http://circ.ahajournals.org/content/115/11/1384.long, with permission from Wolters Kluwer Health, Inc.), (**b**) gadolinium-labeled liposomes (Reprinted from Naresh et al. [29], with permission from Radiological Society of North America (RSNA®)), and (**c**) fluorine-containing nanoconstructs. T2*-weighted imaging of iron-oxide generates signal hypo-intensity, while R1 is increased by Gd-containing liposomes. The absence of any background fluorine signal (pseudo-colored red) requires proton MR images to be acquired for anatomical co-registration (Reprinted from Flogel et al. [30], http://circ.ahajournals.org/content/118/2/140.long, with permission from Wolters Kluwer Health, Inc.; Reprinted from Ye et al [31], http://circ.ahajournals.org/content/128/17/1878/tab-figures-data, with permission from Wolters Kluwer Health). (**d**) Ex vivo labeling of injected stem cells with an iron-oxide nanoparticle (Kraitchman et al. [7], http://circ.ahajournals.org/content/107/18/2290, with permission from Wolters Kluwer Health)

Imaging Agents and Platforms

Molecular MR imaging agents can de divided into those that modulate the proton signal and those using other nuclei such as ^{19}F (fluorine). The use of ^{19}F is appealing principally because of the absence of any background signal in the body. In addition, the polarization of fluorine is comparable to proton, and its Larmor frequency is close enough to that of protons to be detectable on conventional scanners, provided an appropriately tuned radio-frequency coil is used [35]. The major limitation of ^{19}F MRI, however, is its low sensitivity. Few targets are expressed at the levels needed to generate adequate signal from a targeted ^{19}F small molecule. Liposomes, however, can be loaded with large payloads of ^{19}F to improve sensitivity. The surface of the liposome can also be decorated with a ligand to a target on the endothelial surface, or if the endothelium is leaky a target just beneath its surface [36]. Alternatively, ^{19}F-containing liposomes and nano-emulsions can be used to detect monocytes and macrophages, since they accumulate in these inflammatory cells due to phagocytosis (Fig. 24.1) [30, 31]. This latter approach has been the most successful application of ^{19}F MRI to date and has been used to image inflammation in myocardial infarction, transplant rejection, atherosclerosis, and myocarditis [30, 31, 37–39]. The use of ^{19}F for molecular imaging, however, remains a preclinical research tool, and its potential for widespread clinical translation remains to be defined.

Molecular MRI of the proton signal can be performed with paramagnetic and superparamagnetic agents. Paramagnetic agents have largely been developed using the lanthanide metal ion gadolinium, although manganese-based probes have also been used [40–43]. Superparamagnetic imaging agents contain forms of iron oxide, which produce an extremely strong magnetic signal. These agents require the presence of an external field to be magnetized, but for superparamagnetic agents this effect saturates and reaches its maximum at a low field strength (approximately 0.5 Tesla), while paramagnetic agents continue to be magnetized with increasing field strength.

The strength of an imaging agent is determined by its relaxivity (r) in $mM^{-1}\ s^{-1}$, defined by the change in the relaxation rate (R, units s^{-1}) produced as a function of metal ion concentration (units mM or mmol/L). The longitudinal relaxivity (r1) of most small gadolinium chelates at 1.5 T is approximately 4–5 $mM^{-1}\ s^{-1}$. In contrast, the r2 of iron-oxide nanoparticles is over 80 $mM^{-1}\ s^{-1}$, and their r2* is substantially higher. The sensitivity of small gadolinium chelates is thus in the micromolar range, while that of superparamagnetic imaging agents is nanomolar.

Gadolinium-based agents are most frequently imaged with T1-weighted sequences. It is a misconception, however, to consider these agents as T1 agents and iron-oxide nanoparticles as T2 agents. The r2 of small gadolinium chelates at 1.5 T is very similar to their r1, approximately 4 $mM^{-1}\ s^{-1}$. If T2-weighted parameters are used, significant T2 contrast can be generated by gadolinium. The r1 of iron-oxide nanoparticles at clinical field strengths is actually three- to fourfold higher than the r1 of small gadolinium chelates. Therefore, if

T1-weighted parameters are used, these agents can be used to generate T1-based signal hyperintensity. The key parameter to consider when using a contrast agent is thus the r1/r2 ratio of the agent at a given field strength. When this ratio decreases, image parameters need to be adjusted to eliminate R_2 effects. For example, to generate T1-weighted images from iron-oxide nanoparticles or large gadolinium constructs, the TE has to be extremely short to avoid contamination from R2 effects. The development of ultrashort TE (UTE) sequences has made this extremely feasible [44].

The longitudinal and transverse relaxivities of imaging agents can respond very differently to changes in field strength, and imaging parameters must therefore be optimized for the r1/r2 ratio at that specific field. The r1/r2 of small gadolinium agents stays fairly stable between 1 and 3 Tesla. However, the r1 of albumin-bound Gd chelates, such as gadofosveset, decreases substantially with field [45]. Conversely, the r2 of these agents increases substantially at higher fields. The r2 of iron-oxide nanoparticles, such as ferumoxytol, plateaus around 0.5 Tesla, but their r1 decreases with field. Consequently, T1-weighted imaging of these agents at higher fields becomes progressively more difficult.

Since the transverse relaxivity (r2*) of superparamagnetic agents saturates at approximately 0.5 T, the sensitivity of these agents is already maximal at 1.5 T. The lower native R2* values of tissue at 1.5 T are a further advantage. It is a common misconception that high field strengths are required to image superparamagnetic iron-oxide imaging agents. Little is gained by moving to higher field strengths unless very high spatial resolution, for instance to image small animals, is required. Increasing the size of the iron-oxide particle, however, substantially increases its relaxivity. This effect has been used to create magnetic relaxation switches for in vitro diagnostics and magnetic microparticles with very high relaxivity [24, 46]. The size and high relaxivities of iron-oxide microparticles make them well suited to preclinical imaging of inflammatory cells and vascular targets [23, 47–49]. The potential of these agents to undergo successful clinical translation, however, is unclear. The large size of the iron-oxide core in these microparticles also makes them suited to a novel imaging technique known as magnetic particle imaging (MPI), discussed below. The properties of currently used molecular MR platforms, and their comparison with radiolabeled and optical imaging agents, is summarized in Table 24.1.

Table 24.1 Attributes of various modalities for molecular imaging in humans

	MRI	PET	Fluorescence
Sensitivity	+++	++++	++++
Resolution	+++	+	++++
Invasive	–	–	++++
Multispectral	++	–	++++
Intracellular imaging	–	++++	++
Activatable probes	+++	–	++++
Background signal problematic	–	++++	+++
Quantification	++	++++	++
Microscopy of agent	++	–	++++
Probe stability	++++	–	++++

Quantification and Reproducibility

One of the central appeals of molecular imaging lies in the potential to follow biological processes in the heart longitudinally. To do this accurately, imaging agents must be well suited to stable and reproducible synthesis, and the quantification of their uptake must be accurate. Traditionally, quantification in molecular imaging has been most readily performed with positron emission tomography (PET), which allows the absolute concentrations of a radiotracer to be derived. While more challenging, a similar degree of quantification is feasible with molecular MR.

The reproducible synthesis of imaging agents with stable properties including size, charge, surface potential, solubility, and relaxivity is guaranteed with discrete compounds such as small gadolinium chelates. Several generations of iron-oxide nanoparticles have been developed, and, while earlier generations were polydisperse, nanoparticle synthesis and characterization methods have become more robust, and current constructs are monodisperse with a very narrow size distribution [50]. The reproducible synthesis of liposomes, micelles, and other lipophilic agents is also feasible. The absence of radioactivity in molecular MR creates several advantages. Once synthesized, molecular MR agents are usually stable for months, allowing them to be synthesized in a single centralized location and stored remotely. This is not feasible with radiolabeled agents.

The development of highly accurate techniques to map T1, T2, and T2* in the myocardium has been of significant benefit to molecular MR. If the relaxivity of the agents is known, it is possible to calculate its concentration, with some caveats. Most targeted agents exist in tissue in a free and bound form. The relaxivity of the agent under both conditions must be known for its concentration to be determined. In addition, the tissue of interest must be imaged before the injection of the imaging agent to measure its native relaxation rate. The longitudinal relaxation rate (R1) after the injection of the agent is then given by: $R1_{post} = R1_{pre} + r1_F C_F + r1_B C_B$, where $r1_F$ is the longitudinal relaxivity of the free agent, $r1_B$ is the longitudinal relaxivity of the bound agent, and C_F and C_B are the free and bound concentrations of the agent, respectively. A similar equation can be formulated for the tranverse relaxation rate: $R2_{post} = R2_{pre} + r2_F C_F + r2_B C_B$. These two equations can then be used to derive C_F and C_B. The principal challenge of this

approach lies in the need to acquire a pair of relaxation maps both before and after the injection of the imaging agent.

Several novel forms of quantitative molecular imaging are currently underdevelopment and merit discussion. While positive (bright) contrast can be generated from superparamagnetic agents at clinical fields using T1 weighting, the r2* of these agent is far higher than their r1. Techniques to create bright contrast based on the r2* effects of iron oxides have thus been developed [51]. Most of these techniques exploit the ability of iron-oxide nanoparticles to create small subsidiary fields and shift the protons in their vicinity off-resonance. Selective excitation of the off-resonance spins, or alternatively suppression of the on-resonance spins, results in the generation of positive contrast only in the vicinity of the nanoparticles [34, 51–53]. Susceptibility-based approaches have also been developed [54]. While of significant value, off-resonance techniques remain vulnerable to susceptibility artifacts and may be less suited to longitudinal quantification than T1 and T2 mapping techniques [53].

Magnetic particle imaging (MPI) is an experimental technique, which has the potential to image single magnetic particles. The physical basis of MPI is beyond the scope of this chapter and has been reviewed in detail elsewhere [55]. In brief, the technique involves the dynamic movement (rastering) of a field-free point (FFP) across a field of view. Signal from iron-oxide particles is detected only at the FFP, allowing an image of particle distribution to be formed. One of the challenges of MPI, however, lies in the design of nanoparticles with properties optimized specifically for detection with this technique. The size of the iron-oxide core is of major importance in this regard, and this is not optimal for MPI in the current generation of approved nanoparticles.

Proton MRI has largely been used to image a single molecular target at any given time. Under very specific circumstances, when parameters can be chosen to balance the R1 and R2 effects of one agent, a second agent can be imaged simultaneously. This strategy has, for instance, been used to image apoptosis and necrosis with iron-oxide and Gd-based agents simultaneously [56]. A very promising approach to generate a multispectral signal within the proton pool has recently been described. Chemical exchange saturation transfer imaging (CEST) involves selective excitation of a specific chemical moiety at a known off-resonance frequency [57]. Under certain conditions, the exchange of protons between the excited off-resonance proton pool and the bulk water pool can occur, attenuating the magnetization of the main proton pool. A reduction in the signal in the main proton pool will occur only when radio-frequency excitation is performed at the correct off-resonance frequency. Paramagnetic agents that enhance the CEST effect have been developed and used in preclinical applications [58]. The challenge of CEST imaging in the heart lies in the need for an extremely good shim, allowing specific chemical moieties to be selectively excited. CEST contrast agents also require millimolar (mM) concentrations of exchangeable hydrogen atoms to be detectable making them at least two orders of magnitude less sensitive than relaxation agents. However recent reports suggest that molecular CEST imaging in the heart may be possible [59, 60].

The longitudinal relaxivity (r1) of small gadolinium chelates can change dramatically when they bind to large proteins, such as albumin.[45] The degree of this change shows a high degree of field dependence between 1 and 3 Tesla. This observation has led to the recent description of a new molecular imaging technique known as delta relaxation enhanced MR (DREMR) [61]. This technique involves cycling of the main (B0) magnetic field to image the agent under two field conditions, for example, 1.35 and 1.65 Tesla. The r1 of unbound agent at these field strengths is extremely similar, but the r1 of the albumin-bound agent changes significantly between 1.35 and 1.65 T [45]. Subtraction of the images acquired at the two field strengths thus provides a map of bound probe or albumin distribution. Further work will be needed to determine the utility of this approach for other targeted imaging agents.

Preclinical Imaging

A large number of imaging agents have been developed for preclinical MR imaging. These agents have highlighted the capabilities of molecular MR, its sensitivity for targets in the micromolar to low nanomolar range, and the value of integrating molecular and functional readouts [8–10].

Molecular MRI of targets in the myocardium has been performed with both small gadolinium chelates and iron-oxide nanoparticles (Fig. 24.2). Late gadolinium enhancement provides a very useful but nonspecific readout of myocardial injury. In contrast, molecular imaging agents are able to provide specific signatures of molecular events such as apoptosis, cell rupture, DNA release, myeloperoxidase activity, and collagen deposition [14, 16, 18, 56, 62, 63]. These signatures can be used to better characterize the response of the myocardium to acute injury and facilitate the development of cardioprotective strategies. Molecular readouts can also be used to better understand the inflammatory response of the myocardium to injury and identify new strategies to modulate it [28–31]. Infarct healing is followed by collagen deposition, which can be imaged specifically with a gadolinium chelate targeted to type 1 collagen [14]. The wash-in kinetics of this agent can also be used to measure myocardial perfusion [64].

The vascular endothelium is highly accessible to most molecular imaging agents, and numerous targets have been imaged in the preclinical setting (Fig. 24.3). These include oxidized LDL, vascular cell adhesion molecule 1

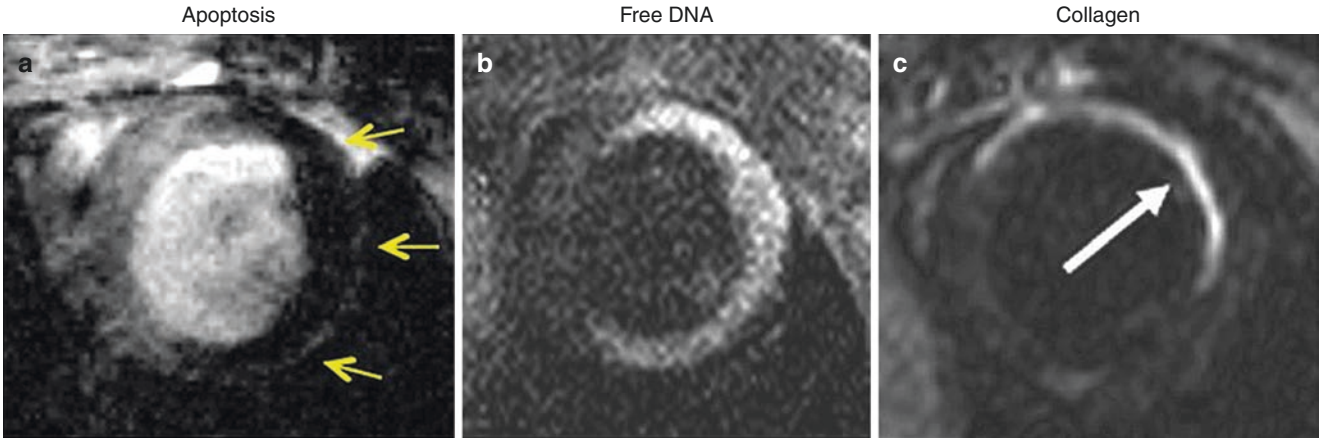

Fig. 24.2 Molecular MRI of cell injury and healing after ischemic injury. (**a**) Imaging of apoptosis with an annexin-labeled iron-oxide nanoparticle. Uptake of the probe by apoptotic cells produces signal hypo-intensity on T2*-weighted images (Reprinted from Sosnovik et al. [56], http://circimaging.ahajournals.org/content/2/6/460, with permission from Wolters Kluwer Heallth). (**b**) Detection of cell rupture and free-DNA release with a DNA-binding gadolinium chelate (Reprinted from Huang et al. [16], http://circimaging.ahajournals.org/content/circcvim/4/6/729.full.pdf, with permission from Wolters Kluwer Health). (**c**) Specific imaging of collagen deposition in an infarct scar using a collagen-targeted gadolinium chelate. When targeted Gd agents are used, unbound gadolinium is allowed to wash out of the blood pool completely, which appears dark (Reprinted from Helm et al. [14], with permission from Radiological Society of North America (RSNA®))

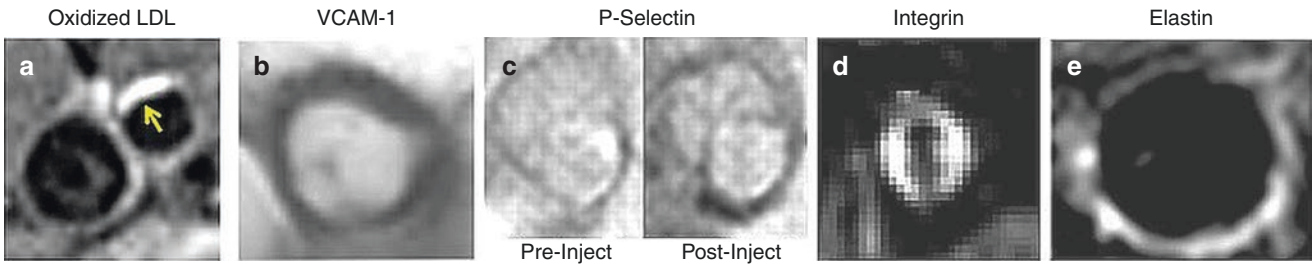

Fig. 24.3 Targeted imaging of biological processes involved in atherosclerosis and aneurysm formation. (**a**) Gd-containing immunomicelle targeted to oxidized LDL [66]. Probe uptake (arrow) is seen in an aortic plaque (Reprinted from Briley-Saebo et al. [66], http://circ.ahajournals.org/content/117/25/3206, with permission from Wolters Kluwer Health). (**b**) Iron-oxide nanoparticle labeled with a peptide to VCAM-1. Probe uptake in the aortic root, which is a site of early plaque formation in the ApoE−/− mouse, produces signal hypo-intensity (Reprinted from Nahrendorf et al. [22], http://circ.ahajournals.org/content/114/14/1504, with permission from Wolters Kluwer Health). (**c**) Iron-oxide microparticle targeted to both VCAM-1 and P-selectin. Uptake of the probe is again seen in the aortic root (Reprinted from McAteer et al. [23], http://atvb.ahajournals.org/content/32/6/1427.long, with permission from Wolters Kluwer Health). (**d**) Gd-containing liposomes targeted to the $\alpha_v B_3$ integrin involved in angiogenesis (Reprinted from Cai et al. [67], https://www.sciencedirect.com/science/article/pii/S1936878X1000344X?via%3Dihub with permission from Elsevier). (**e**) Small gadolinium chelate targeted to elastin. Uptake of the probe provides an important readout in aortic aneurysms (Reprinted from Botnar et al. [15], http://circimaging.ahajournals.org/content/7/4/679, with permission from Wolters Kluwer Health)

(VCAM-1), P-selectin, and the macrophage scavenger receptor [22, 23, 65, 66]. In addition, plaque angiogenesis has been imaged using integrin-targeted liposomes [20, 67]. Elastin in the vessel wall can also be imaged with a targeted small gadolinium chelate [15, 68]. Targeted liposomes can also be loaded with therapeutic moieties and used as delivery vehicles, with both diagnostic and therapeutic functions (theranostic). In the preclinical setting, anti-angiogenic and anti-inflammatory theranostics have been used with some success [69, 70].

Molecular MRI has also played an important role in the preclinical development of stem cell therapy. Initial work focused on the ex vivo labeling of stem cells to track their location after direct injection [7]. Cell labeling was performed with ferumoxides, iron-oxide microparticles, and ^{19}F nanoconstructs [7, 71–74]. MRI of labeled cells allowed the success of the local injection to be confirmed and provided important information on the location of the cells with respect to the infarct. The central limitation of all cell-labeling strategies, however, is that the label can persist in

nonliving cells. Alternative strategies, such as manganese-based MR and the use of MR-detectable reporter genes, such as ferritin, have thus been developed to image cell viability [42, 75].

Clinical Experience

Four molecular MR imaging agents have been used in cardiovascular imaging in humans to date: gadofosveset, ferumoxtran, ferumoxytol, and EP-2104R. The experience with these agents is reviewed below.

Gadofosveset

Small gadolinium chelates have a very brief intravascular phase. While improvements in gradient technology and pulse sequence design have reduced the need for intravascular imaging agents, these agents still facilitate the acquisition of angiograms with very high resolution. The concept of binding gadolinium (Gd) to albumin was initially demonstrated preclinically using an irreversible covalent bond. When bound to albumin, the relaxation frequency (also known as molecular tumbling rate) of Gd is drastically reduced, facilitating the transfer of energy between it and the excited proton pool [25]. Under normal circumstances, albumin remains in the intravascular space allowing covalent Gd-albumin constructs to have an extremely long circulatory half-life.

Translation of the Gd-albumin concept required a change from irreversible covalent binding to reversible noncovalent binding. Gadofosveset is a functionalized DTPA (diethylenetriamine-pentaacetic acid) chelate that binds reversibly to serum albumin. After injection, gadofosveset exists in the serum in a free form and an albumin-bound form, with the two forms in continuous exchange. Elimination of the free probe by renal excretion changes equilibrium conditions and results in the detachment of a portion of the bound probe from albumin until equilibrium is re-established, at which point the process recurs.

The clinical approval of gadofosveset has led to an interest in its application beyond angiography. One potential such application lies in the detection of vulnerable atherosclerotic plaques, which frequently demonstrate abnormal endothelial permeability [27, 76]. Angiogenesis in these plaques leads to a leaky capillary network and the accumulation of albumin in the extravascular space. Preclinical work and preliminary results in humans suggest that gadofosveset can detect the accumulation of albumin in leaky plaques and that this is associated with disease progression, plaque disruption, and symptoms [27, 76]. The kinetics of gadofosveset also raise the possibility of early imaging being performed to document luminal narrowing, followed by late imaging (30 min post injection) to detect plaque inflammation.

Ferumoxtran and Ferumoxytol

The first generations of iron-oxide nanoparticles were polydisperse and were rapidly cleared by the cells of the reticuloendothelial system [50]. Second generation agents, such as ferumoxtran, had more extensive dextran coats, were better fractionated, remained monodisperse in solution, and consequently had long circulation half-lives [50]. The long circulatory half-lives of these agents made them suited to the imaging of inflammation in the myocardium and vascular tree. The largest clinical experience with ferumoxtran has been in the imaging of neoplastic metastases to lymph nodes [77]. However, the agent was also used with significant success to image inflammation in carotid plaque in a trial of statin therapy [33]. The Atheroma trial involved serial imaging of plaque inflammation with T2*-weighted MR in patients on low- and high-dose atorvastatin. The anti-inflammatory effects of atorvastatin and the benefits of high-dose therapy were well visualized in the trial.

Myocardial inflammation occurs in several important contexts such as myocarditis, transplant rejection, and myocardial infarction. The utility of ferumoxtran in the imaging of myocardial macrophage infiltration was demonstrated in preclinical studies using a version of the probe in which the dextran side chains were cross-linked and animated (Fig. 24.1) [28]. The cross-linked iron-oxide (CLIO) probe could be easily labeled with a fluorochrome, allowing MRI to detect the agent in vivo and optical techniques to verify its cellular distribution. Within 24 h of ischemia, a dense macrophage infiltrate developed in the injured myocardium and could be robustly imaged with both T2* and off-resonance techniques [28, 53].

The clinical adoption of macrophage imaging with ferumoxtran was not possible due to the termination of the agent by the manufacturer. However, an analogous nanoparticle, approved for iron replacement therapy in patients with kidney disease, has been used with some success (Fig. 24.4). Ferumoxytol is extremely similar in size and relaxivity to ferumoxtran but has a carboxymethyl-dextran, rather than dextran, coat. This makes it slightly less avid for macrophages and monocytes than feromoxtran, but it is still taken up by these cells. Ferumoxytol has been successfully used to image atherosclerotic plaque inflammation in patients with aortic aneurysm [78]. Two clinical studies, to date, have also described the use of ferumoxytol to image the influx of inflammatory cells into a recent infarct [79, 80]. No major adverse events occurred in any of these

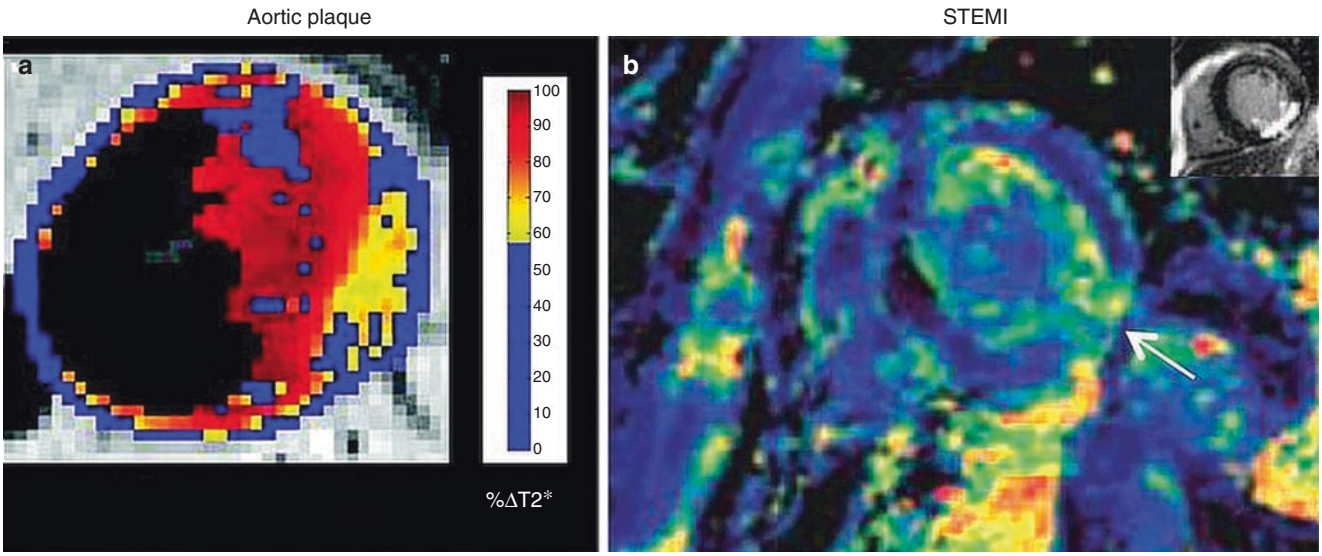

Fig. 24.4 Imaging of macrophage infiltration in humans with the long-circulating nanoparticle, ferumoxytol. (**a**) T2* difference map of an aortic aneurysm showing marked changes in T2* before and after ferumoxytol injection (Reprinted from Richards et al. [78], http://circimaging.ahajournals.org/content/4/3/274, with permission from Wolters Kluwer Health). (**b**) R2* map of a patient injected with ferumoxytol after an inferior STEMI (inset). R2* is significantly increased in the infarct after ferumoxytol injection (Reprinted from Alam et al. [79], http://circimaging.ahajournals.org/content/early/2012/08/08/CIRCIMAGING.112.974907, with permission from Wolters Kluwer Health)

studies after ferumoxytol injection, although serious anaphylaxis has been described in other settings. One of the challenges of using ferumoxytol to image monocyte infiltration lies in the need to distinguish the exogenous iron signal from any endogenous iron degradation products resulting from myocardial hemorrhage. This requires imaging to be performed before and after the injection of the agent, increasing cost and complexity. Nevertheless, the interest in this technique is high, and several clinical trials are currently ongoing.

Thrombus Imaging with EP-2104R

Molecular imaging of thrombus has been attempted with many approaches, some using platelets as the target of interest and others fibrin [11, 81, 82]. The majority of these agents have been used only in the preclinical setting. One agent, however, termed EP-2104R has completed phase 1–2 clinical trials and has been successfully used in over 50 patients to date (Fig. 24.5) [83, 84]. EP-2104R comprises four Gd-DOTA chelates appended to the C- and N-termini of an 11 amino acid peptide. This peptide was selected by phage display: first by performing a negative screen against fibrinogen, ensuring low levels of nonspecific background uptake in the blood, and then by positive selection against fibrin [11]. Fibrin is highly expressed in thrombi allowing it to be well detected with a small Gd chelate, and it is present in both acute and chronic thrombi.

Initial studies with EP-2104R were performed in animal models of acute and chronic thrombosis [12]. On the basis of this successful experience, clinical translation of the agent was performed in phase 1 and 2 clinical trials. No serious probe-associated adverse events occurred, and the agent successfully detected intracardiac, deep venous, and aortic and pulmonary thrombi [83, 84]. In addition to detecting known foci of thrombosis, EP-2104R imaging frequently identified hitherto unsuspected sources, such as aortic or intracardiac thrombus. One of the limitations of these first clinical studies lays in the heterogenous nature of the imaging protocols used. In the current era, it is most likely that T1 mapping would be used to detect the agent, but these sequences were not widely available at the time.

The technical performance of EP-2104R was excellent. However, the translation of the agent coincided with the height of the NSF scare, which limited enthusiasm for further commercial development. It should be noted, however, that the targeted nature of the agent allowed a far lower dose of Gd (0.016 mmol/kg) to be used. No changes in clotting times, platelet function or blood counts were seen with EP-2104R injection. The agent does not interfere with action of thrombolytics and can actually be used to monitor thrombolysis [85]. The vast majority of the injected agent is eliminated via renal excretion, and no cases of NSF have been

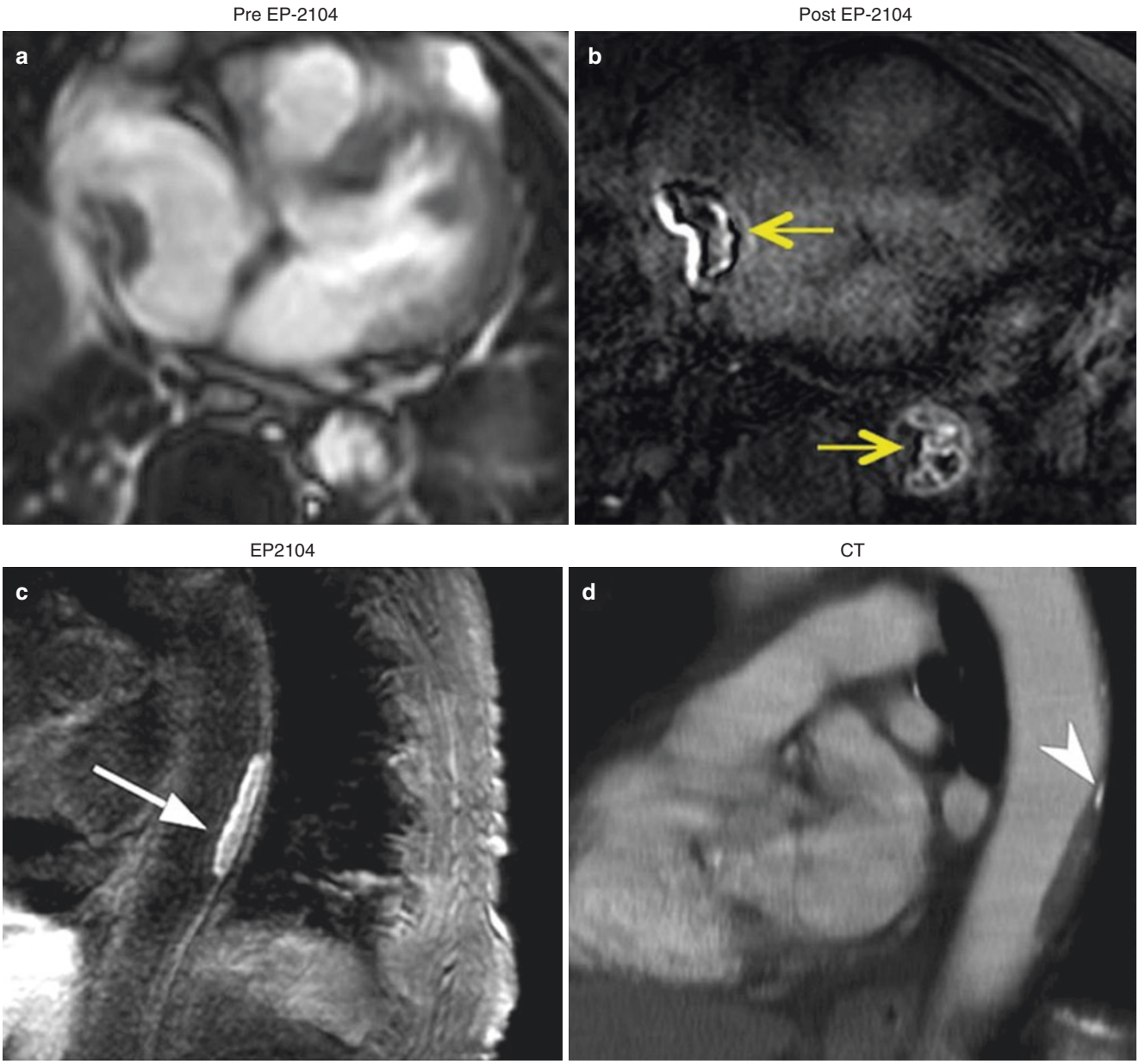

Fig. 24.5 Detection of thrombus in patients with a fibrin-targeted Gd probe. (**a**) Patient with a venous catheter in the right atrium with a surrounding filling defect (Reprinted by permission from Vymazal et al. [84], https://journals.lww.com/investigativeradiology/Abstract/2009/11000/Thrombus_Imaging_With_Fibrin_Specific.2.aspx, with permission from Wolters Kluwer Health). (**b**) Post EP-2104R injection, thrombus is clearly identified in the right atrium as well as in the descending thoracic aorta (Reprinted by permission from Vymazal, et al. [84], https://journals.lww.com/investigativeradiology/Abstract/2009/11000/Thrombus_Imaging_With_Fibrin_Specific.2.aspx, with permission from Wolters Kluwer Health). (**c**) Thrombus imaged in the descending thoracic aorta of a patient after EP-2104R injection (Reprinted by permission of Springer Nature, Spuentrup et al. [83]), and (**d**) corresponding CT scan (Reprinted by permission of Springer Nature, Spuentrup et al. [83])

reported in the 52 patients who received the probe. The experience with EP-2104R thus demonstrates that targeted Gd chelates can be used safely in humans. The agent also demonstrated the utility of molecular imaging of thrombus, as opposed to the detection of nonspecific filling defects with conventional imaging techniques. The potential for continued translation of EP-2104R, in an identical or similar form, is thus high.

Outlook

While significant challenges remain, several notable successes have occurred in the field of molecular MR over the last decade. Three agents have been used in clinical trials without adverse affects and with clear demonstration of efficacy. The ongoing refinement of T1 and T2 mapping techniques, as well as other quantitative approaches, will be of

significant benefit to molecular MR. The introduction of integrated PET-MR scanners has the potential to open up new possibilities in multimodality clinical molecular imaging, and integration with hyperpolarized MR could also present major synergies. Molecular MR has the potential to play a major role in facilitating the transition from empirical population-based therapy to targeted, individualized, and rationalized therapy in cardiovascular disease.

References

1. Osman NF, Kerwin WS, McVeigh ER, Prince JL. Cardiac motion tracking using CINE harmonic phase (HARP) magnetic resonance imaging. Magn Reson Med. 1999;42:1048–60.
2. Schwitter J, Wacker CM, van Rossum AC, Lombardi M, Al-Saadi N, Ahlstrom H, et al. MR-IMPACT: comparison of perfusion-cardiac magnetic resonance with single-photon emission computed tomography for the detection of coronary artery disease in a multicentre, multivendor, randomized trial. Eur Heart J. 2008;29:480–9.
3. Kim RJ, Wu E, Rafael A, Chen EL, Parker MA, Simonetti O, et al. The use of contrast-enhanced magnetic resonance imaging to identify reversible myocardial dysfunction. N Engl J Med. 2000;343:1445–53.
4. Sosnovik DE, Wang R, Dai G, Reese TG, Wedeen VJ. Diffusion MR tractography of the heart. J Cardiovasc Magn Reson. 2009;11:47.
5. Mekkaoui C, Huang S, Chen HH, Dai G, Reese TG, Kostis WJ, et al. Fiber architecture in remodeled myocardium revealed with a quantitative diffusion CMR tractography framework and histological validation. J Cardiovasc Magn Reson. 2012;14:70.
6. Sosnovik DE, Mekkaoui C, Huang S, Chen HH, Dai G, Stoeck CT, et al. Microstructural impact of ischemia and bone marrow-derived cell therapy revealed with diffusion tensor magnetic resonance imaging tractography of the heart in vivo. Circulation. 2014;129:1731–41.
7. Kraitchman DL, Heldman AW, Atalar E, Amado LC, Martin BJ, Pittenger MF, et al. In vivo magnetic resonance imaging of mesenchymal stem cells in myocardial infarction. Circulation. 2003;107:2290–3.
8. Sosnovik DE, Nahrendorf M, Weissleder R. Molecular magnetic resonance imaging in cardiovascular medicine. Circulation. 2007;115:2076–86.
9. Nahrendorf M, Sosnovik DE, French BA, Swirski FK, Bengel F, Sadeghi MM, et al. Multimodality cardiovascular molecular imaging, Part II. Circ Cardiovasc Imaging. 2009;2:56–70.
10. Leuschner F, Nahrendorf M. Molecular imaging of coronary atherosclerosis and myocardial infarction: considerations for the bench and perspectives for the clinic. Circ Res. 2011;108:593–606.
11. Overoye-Chan K, Koerner S, Looby RJ, Kolodziej AF, Zech SG, Deng Q, et al. EP-2104R: a fibrin-specific gadolinium-Based MRI contrast agent for detection of thrombus. J Am Chem Soc. 2008;130:6025–39.
12. Botnar RM, Buecker A, Wiethoff AJ, Parsons EC Jr, Katoh M, Katsimaglis G, et al. In vivo magnetic resonance imaging of coronary thrombosis using a fibrin-binding molecular magnetic resonance contrast agent. Circulation. 2004;110:1463–6.
13. Caravan P, Das B, Dumas S, Epstein FH, Helm PA, Jacques V, et al. Collagen-targeted MRI contrast agent for molecular imaging of fibrosis. Angew Chem Int Ed Engl. 2007;46:8171–3.
14. Helm PA, Caravan P, French BA, Jacques V, Shen L, Xu Y, et al. Postinfarction myocardial scarring in mice: molecular MR imaging with use of a collagen-targeting contrast agent. Radiology. 2008;247:788–96.
15. Botnar RM, Wiethoff AJ, Ebersberger U, Lacerda S, Blume U, Warley A, et al. In vivo assessment of aortic aneurysm wall integrity using elastin-specific molecular magnetic resonance imaging. Circ Cardiovasc Imaging. 2014;7:679–89.
16. Huang S, Chen HH, Yuan H, Dai G, Schuhle DT, Mekkaoui C, et al. Molecular MRI of acute necrosis with a novel DNA-binding gadolinium chelate: kinetics of cell death and clearance in infarcted myocardium. Circ Cardiovasc Imaging. 2011;4:729–37.
17. Schellenberger EA, Sosnovik D, Weissleder R, Josephson L. Magneto/optical annexin V, a multimodal protein. Bioconjug Chem. 2004;15:1062–7.
18. Sosnovik DE, Schellenberger EA, Nahrendorf M, Novikov MS, Matsui T, Dai G, et al. Magnetic resonance imaging of cardiomyocyte apoptosis with a novel magneto-optical nanoparticle. Magn Reson Med. 2005;54:718–24.
19. van Tilborg GA, Vucic E, Strijkers GJ, Cormode DP, Mani V, Skajaa T, et al. Annexin A5-functionalized bimodal nanoparticles for MRI and fluorescence imaging of atherosclerotic plaques. Bioconjug Chem. 2010;21:1794–803.
20. Winter PM, Morawski AM, Caruthers SD, Fuhrhop RW, Zhang H, Williams TA, et al. Molecular imaging of angiogenesis in early-stage atherosclerosis with alpha(v)beta3-integrin-targeted nanoparticles. Circulation. 2003;108:2270–4.
21. Oostendorp M, Douma K, Wagenaar A, Slenter JM, Hackeng TM, van Zandvoort MA, et al. Molecular magnetic resonance imaging of myocardial angiogenesis after acute myocardial infarction. Circulation. 2010;121:775–83.
22. Nahrendorf M, Jaffer FA, Kelly KA, Sosnovik DE, Aikawa E, Libby P, Weissleder R. Noninvasive vascular cell adhesion molecule-1 imaging identifies inflammatory activation of cells in atherosclerosis. Circulation. 2006;114:1504–11.
23. McAteer MA, Mankia K, Ruparelia N, Jefferson A, Nugent HB, Stork LA, et al. A leukocyte-mimetic magnetic resonance imaging contrast agent homes rapidly to activated endothelium and tracks with atherosclerotic lesion macrophage content. Arterioscler Thromb Vasc Biol. 2012;32:1427–35.
24. Perez JM, Josephson L, O'Loughlin T, Hogemann D, Weissleder R. Magnetic relaxation switches capable of sensing molecular interactions. Nat Biotechnol. 2002;20:816–20.
25. Caravan P, Cloutier NJ, Greenfield MT, McDermid SA, Dunham SU, Bulte JW, et al. The interaction of MS-325 with human serum albumin and its effect on proton relaxation rates. J Am Chem Soc. 2002;124:3152–62.
26. Chen JW, Pham W, Weissleder R, Bogdanov A Jr. Human myeloperoxidase: a potential target for molecular MR imaging in atherosclerosis. Magn Reson Med. 2004;52:1021–8.
27. Phinikaridou A, Andia ME, Protti A, Indermuehle A, Shah A, Smith A, et al. Noninvasive magnetic resonance imaging evaluation of endothelial permeability in murine atherosclerosis using an albumin-binding contrast agent. Circulation. 2012;126:707–19.
28. Sosnovik DE, Nahrendorf M, Deliolanis N, Novikov M, Aikawa E, Josephson L, et al. Fluorescence tomography and magnetic resonance imaging of myocardial macrophage infiltration in infarcted myocardium in vivo. Circulation. 2007;115:1384–91.
29. Naresh NK, Xu Y, Klibanov AL, Vandsburger MH, Meyer CH, Leor J, et al. Monocyte and/or macrophage infiltration of heart after myocardial infarction: MR imaging by using T1-shortening liposomes. Radiology. 2012;264:428–35.
30. Flogel U, Ding Z, Hardung H, Jander S, Reichmann G, Jacoby C, et al. In vivo monitoring of inflammation after cardiac and cerebral ischemia by fluorine magnetic resonance imaging. Circulation. 2008;118:140–8.
31. Ye YX, Basse-Lusebrink TC, Arias-Loza PA, Kocoski V, Kampf T, Gan Q, et al. Monitoring of monocyte recruitment in reperfused myocardial infarction with intramyocardial hemorrhage and microvascular obstruction by combined fluorine 19 and proton cardiac magnetic resonance imaging. Circulation. 2013;128:1878–88.

32. Jaffer FA, Nahrendorf M, Sosnovik D, Kelly KA, Aikawa E, Weissleder R. Cellular imaging of inflammation in atherosclerosis using magnetofluorescent nanomaterials. Mol Imaging. 2006;5:85–92.
33. Tang TY, Howarth SP, Miller SR, Graves MJ, Patterson AJ, et al. The ATHEROMA (Atorvastatin Therapy: Effects on Reduction of Macrophage Activity) study. Evaluation using ultrasmall superparamagnetic iron oxide-enhanced magnetic resonance imaging in carotid disease. J Am Coll Cardiol. 2009;53:2039–50.
34. Korosoglou G, Weiss RG, Kedziorek DA, Walczak P, Gilson WD, Schar M, Sosnovik DE, et al. Noninvasive detection of macrophage-rich atherosclerotic plaque in hyperlipidemic rabbits using "positive contrast" magnetic resonance imaging. J Am Coll Cardiol. 2008;52:483–91.
35. Caruthers SD, Neubauer AM, Hockett FD, Lamerichs R, Winter PM, Scott MJ, et al. In vitro demonstration using 19F magnetic resonance to augment molecular imaging with paramagnetic perfluorocarbon nanoparticles at 1.5 Tesla. Investig Radiol. 2006;41:305–12.
36. Waters EA, Chen J, Allen JS, Zhang H, Lanza GM, Wickline SA. Detection and quantification of angiogenesis in experimental valve disease with integrin-targeted nanoparticles and 19-fluorine MRI/MRS. J Cardiovasc Magn Reson. 2008;10:43.
37. van Heeswijk RB, De Blois J, Kania G, Gonzales C, Blyszczuk P, Stuber M, et al. Selective in vivo visualization of immune-cell infiltration in a mouse model of autoimmune myocarditis by fluorine-19 cardiac magnetic resonance. Circ Cardiovasc Imaging. 2013;6:277–84.
38. van Heeswijk RB, Pellegrin M, Flogel U, Gonzales C, Aubert JF, Mazzolai L, et al. Fluorine MR imaging of inflammation in atherosclerotic plaque in vivo. Radiology. 2015;275:421–9.
39. Hitchens TK, Ye Q, Eytan DF, Janjic JM, Ahrens ET, Ho C. 19F MRI detection of acute allograft rejection with in vivo perfluorocarbon labeling of immune cells. Magn Reson Med. 2011;65:1144–53.
40. Vandsburger MH, French BA, Kramer CM, Zhong X, Epstein FH. Displacement-encoded and manganese-enhanced cardiac MRI reveal that nNOS, not eNOS, plays a dominant role in modulating contraction and calcium influx in the mammalian heart. Am J Physiol Heart Circ Physiol. 2012;302:H412–9.
41. Jiang K, Li W, Li W, Jiao S, Castel L, Van Wagoner DR, Yu X. Rapid multislice T1 mapping of mouse myocardium: application to quantification of manganese uptake in alpha-Dystrobrevin knockout mice. Magn Reson Med. 2015;74:1370–9.
42. Dash R, Kim PJ, Matsuura Y, Ikeno F, Metzler S, Huang NF, et al. Manganese-enhanced magnetic resonance imaging enables in vivo confirmation of peri-infarct restoration following stem cell therapy in a porcine ischemia-reperfusion model. J Am Heart Assoc. 2015;4(7):1–15
43. Gale EM, Atanasova IP, Blasi F, Ay I, Caravan P. A manganese alternative to gadolinium for MRI contrast. J Am Chem Soc. 2015;137:15548–57.
44. Strobel K, Hoerr V, Schmid F, Wachsmuth L, Loffler B, Faber C. Early detection of lung inflammation: exploiting T1-effects of iron oxide particles using UTE MRI. Magn Reson Med. 2012;68:1924–31.
45. Boros E, Polasek M, Zhang Z, Caravan P. Gd(DOTAla): a single amino acid Gd-complex as a modular tool for high relaxivity MR contrast agent development. J Am Chem Soc. 2012;134:19858–68.
46. Taktak S, Sosnovik D, Cima MJ, Weissleder R, Josephson L. Multiparameter magnetic relaxation switch assays. Anal Chem. 2007;79:8863–9.
47. McAteer MA, Sibson NR, von Zur MC, Schneider JE, Lowe AS, Warrick N, et al. In vivo magnetic resonance imaging of acute brain inflammation using microparticles of iron oxide. Nat Med. 2007;13:1253–8.
48. Ye Q, Wu YL, Foley LM, Hitchens TK, Eytan DF, Shirwan H, Ho C. Longitudinal tracking of recipient macrophages in a rat chronic cardiac allograft rejection model with noninvasive magnetic resonance imaging using micrometer-sized paramagnetic iron oxide particles. Circulation. 2008;118:149–56.
49. von zur Muhlen C, von Elverfeldt D, Moeller JA, Choudhury RP, Paul D, et al. Magnetic resonance imaging contrast agent targeted toward activated platelets allows in vivo detection of thrombosis and monitoring of thrombolysis. Circulation. 2008;118:258–67.
50. Sosnovik DE, Nahrendorf M, Weissleder R. Magnetic nanoparticles for MR imaging: agents, techniques and cardiovascular applications. Basic Res Cardiol. 2008;103:122–30.
51. Cunningham CH, Arai T, Yang PC, McConnell MV, Pauly JM, Conolly SM. Positive contrast magnetic resonance imaging of cells labeled with magnetic nanoparticles. Magn Reson Med. 2005;53:999–1005.
52. Mani V, Briley-Saebo KC, Hyafil F, Fayad ZA. Feasibility of in vivo identification of endogenous ferritin with positive contrast MRI in rabbit carotid crush injury using GRASP. Magn Reson Med. 2006;56:1096–106.
53. Farrar CT, Dai G, Novikov M, Rosenzweig A, Weissleder R, Rosen BR, Sosnovik DE. Impact of field strength and iron oxide nanoparticle concentration on the linearity and diagnostic accuracy of off-resonance imaging. NMR Biomed. 2008;21:453–63.
54. Liu T, Spincemaille P, de Rochefort L, Wong R, Prince M, Wang Y. Unambiguous identification of superparamagnetic iron oxide particles through quantitative susceptibility mapping of the nonlinear response to magnetic fields. Magn Reson Imaging. 2010;28:1383–9.
55. Saritas EU, Goodwill PW, Croft LR, Konkle JJ, Lu K, Zheng B, Conolly SM. Magnetic particle imaging (MPI) for NMR and MRI researchers. J Magn Reson. 2013;229:116–26.
56. Sosnovik DE, Garanger E, Aikawa E, Nahrendorf M, Figuiredo JL, Dai G, et al. Molecular MRI of cardiomyocyte apoptosis with simultaneous delayed-enhancement MRI distinguishes apoptotic and necrotic myocytes in vivo: potential for midmyocardial salvage in acute ischemia. Circ Cardiovasc Imaging. 2009;2:460–7.
57. Liu G, Song X, Chan KW, McMahon MT. Nuts and bolts of chemical exchange saturation transfer MRI. NMR Biomed. 2013;26:810–28.
58. Ferrauto G, Delli Castelli D, Terreno E, Aime S. In vivo MRI visualization of different cell populations labeled with PARACEST agents. Magn Reson Med. 2013;69:1703–11.
59. Vandsburger M, Vandoorne K, Oren R, Leftin A, Mpofu S, Delli Castelli D, et al. Cardio-chemical exchange saturation transfer magnetic resonance imaging reveals molecular signatures of endogenous fibrosis and exogenous contrast media. Circ Cardiovasc Imaging. 2015;8(1):1–8
60. Haris M, Singh A, Cai K, Kogan F, McGarvey J, Debrosse C, Zsido GA, et al. A technique for in vivo mapping of myocardial creatine kinase metabolism. Nat Med. 2014;20:209–14.
61. Alford JK, Rutt BK, Scholl TJ, Handler WB, Chronik BA. Delta relaxation enhanced MR: improving activation-specificity of molecular probes through R1 dispersion imaging. Magn Reson Med. 2009;61:796–802.
62. Nahrendorf M, Sosnovik D, Chen JW, Panizzi P, Figueiredo JL, Aikawa E, et al. Activatable magnetic resonance imaging agent reports myeloperoxidase activity in healing infarcts and noninvasively detects the antiinflammatory effects of atorvastatin on ischemia-reperfusion injury. Circulation. 2008;117:1153–60.
63. Figge L, Appler F, Chen HH, Sosnovik DE, Schnorr J, Seitz O, et al. Direct coupling of annexin A5 to VSOP yields small, protein-covered nanoprobes for MR imaging of apoptosis. Contrast Media Mol Imaging. 2014;9:291–9.
64. Spuentrup E, Ruhl KM, Botnar RM, Wiethoff AJ, Buhl A, Jacques V, et al. Molecular magnetic resonance imaging of myocardial perfusion with EP-3600, a collagen-specific contrast agent: initial feasibility study in a swine model. Circulation. 2009;119:1768–75.

65. Amirbekian V, Lipinski MJ, Briley-Saebo KC, Amirbekian S, Aguinaldo JG, Weinreb DB, et al. Detecting and assessing macrophages in vivo to evaluate atherosclerosis noninvasively using molecular MRI. Proc Natl Acad Sci U S A. 2007;104:961–6.
66. Briley-Saebo KC, Shaw PX, Mulder WJ, Choi SH, Vucic E, Aguinaldo JG, et al. Targeted molecular probes for imaging atherosclerotic lesions with magnetic resonance using antibodies that recognize oxidation-specific epitopes. Circulation. 2008;117:3206–15.
67. Cai K, Caruthers SD, Huang W, Williams TA, Zhang H, Wickline SA, et al. MR molecular imaging of aortic angiogenesis. JACC Cardiovasc Imaging. 2010;3:824–32.
68. von Bary C, Makowski M, Preissel A, Keithahn A, Warley A, Spuentrup E, et al. MRI of coronary wall remodeling in a swine model of coronary injury using an elastin-binding contrast agent. Circ Cardiovasc Imaging. 2011;4:147–55.
69. Winter PM, Neubauer AM, Caruthers SD, Harris TD, Robertson JD, Williams TA, et al. Endothelial alpha(v)beta3 integrin-targeted fumagillin nanoparticles inhibit angiogenesis in atherosclerosis. Arterioscler Thromb Vasc Biol. 2006;26:2103–9.
70. Lobatto ME, Fayad ZA, Silvera S, Vucic E, Calcagno C, Mani V, et al. Multimodal clinical imaging to longitudinally assess a nanomedical anti-inflammatory treatment in experimental atherosclerosis. Mol Pharm. 2010;7:2020–9.
71. Hill JM, Dick AJ, Raman VK, Thompson RB, Yu ZX, Hinds KA, et al. Serial cardiac magnetic resonance imaging of injected mesenchymal stem cells. Circulation. 2003;108:1009–14.
72. Partlow KC, Chen J, Brant JA, Neubauer AM, Meyerrose TE, et al. 19F magnetic resonance imaging for stem/progenitor cell tracking with multiple unique perfluorocarbon nanobeacons. FASEB J. 2007;21:1647–54.
73. Amsalem Y, Mardor Y, Feinberg MS, Landa N, Miller L, Daniels D, et al. Iron-oxide labeling and outcome of transplanted mesenchymal stem cells in the infarcted myocardium. Circulation. 2007;116:I38–45.
74. Kraitchman DL, Tatsumi M, Gilson WD, Ishimori T, Kedziorek D, Walczak P, et al. Dynamic imaging of allogeneic mesenchymal stem cells trafficking to myocardial infarction. Circulation. 2005;112:1451–61.
75. Naumova AV, Reinecke H, Yarnykh V, Deem J, Yuan C, Murry CE. Ferritin overexpression for noninvasive magnetic resonance imaging-based tracking of stem cells transplanted into the heart. Mol Imaging. 2010;9:201–10.
76. Lobbes MB, Heeneman S, Passos VL, Welten R, Kwee RM, van der Geest RJ, et al. Gadofosveset-enhanced magnetic resonance imaging of human carotid atherosclerotic plaques: a proof-of-concept study. Investig Radiol. 2010;45:275–81.
77. Harisinghani MG, Barentsz J, Hahn PF, Deserno WM, Tabatabaei S, van de Kaa CH, et al. Noninvasive detection of clinically occult lymph-node metastases in prostate cancer. N Engl J Med. 2003;348:2491–9.
78. Richards JM, Semple SI, MacGillivray TJ, Gray C, Langrish JP, Williams M, et al. Abdominal aortic aneurysm growth predicted by uptake of ultrasmall superparamagnetic particles of iron oxide: a pilot study. Circ Cardiovasc Imaging. 2011;4:274–81.
79. Alam SR, Shah AS, Richards J, Lang NN, Barnes G, Joshi N, et al. Ultrasmall superparamagnetic particles of iron oxide in patients with acute myocardial infarction: early clinical experience. Circ Cardiovasc Imaging. 2012;5:559–65.
80. Yilmaz A, Dengler MA, van der Kuip H, Yildiz H, Rosch S, Klumpp S, et al. Imaging of myocardial infarction using ultrasmall superparamagnetic iron oxide nanoparticles: a human study using a multi-parametric cardiovascular magnetic resonance imaging approach. Eur Heart J. 2013;34:462–75.
81. Flacke S, Fischer S, Scott MJ, Fuhrhop RJ, Allen JS, McLean M, Winter P, et al. Novel MRI contrast agent for molecular imaging of fibrin: implications for detecting vulnerable plaques. Circulation. 2001;104:1280–5.
82. von Elverfeldt D, Meissner M, Peter K, Paul D, Meixner F, Neudorfer I, et al. An approach towards molecular imaging of activated platelets allows imaging of symptomatic human carotid plaques in a new model of a tissue flow chamber. Contrast Media Mol Imaging. 2012;7:204–13.
83. Spuentrup E, Botnar RM, Wiethoff AJ, Ibrahim T, Kelle S, Katoh M, et al. MR imaging of thrombi using EP-2104R, a fibrin-specific contrast agent: initial results in patients. Eur Radiol. 2008;18:1995–2005.
84. Vymazal J, Spuentrup E, Cardenas-Molina G, Wiethoff AJ, Hartmann MG, Caravan P, Parsons EC Jr. Thrombus imaging with fibrin-specific gadolinium-based MR contrast agent EP-2104R: results of a phase II clinical study of feasibility. Investig Radiol. 2009;44:697–704.
85. Ay I, Blasi F, Rietz TA, Rotile NJ, Kura S, Brownell AL, et al. In vivo molecular imaging of thrombosis and thrombolysis using a fibrin-binding positron emission tomographic probe. Circ Cardiovasc Imaging. 2014;7:697–705.

Cardiac T1 Mapping

25

Michael Jerosch-Herold and Ravi Teja Seethamraju

Introduction

In CMR the use of T1 mapping has grown rapidly over the last decade to meet the needs for myocardial phenotyping and the elucidation of myocardial pathology [1]. T1 mapping represents today an important complement to the CMR capabilities for assessment of ventricular function, and morphology, and has filled an important void for assessing myocardial tissue structure and tissue remodeling. Though some of the applications of myocardial T1 mapping, such as the detection of edema in acute myocardial infarction, are not new, T1 mapping offers more specific and accurate information [2], compared to traditional techniques like T1-weighted spin echo imaging.

T1 mapping brings together two concepts, namely, the measurement of the longitudinal relaxation time T1 as a marker of changes in tissue structure and composition and secondly, the technique of creating pixel-wise parametric maps, which encode computed T1 values to the underlying source images, so that the maps match the resolution of the source images [3]. Merging T1 measurements with parametric mapping has led to important advances in T1 imaging that are tailored to CMR such as the *mo*dified *L*ook-*L*ocker *i*maging technique (MOLLI). This chapter encompasses a review of the technical foundations of T1 mapping in the heart. From there we will proceed to applications of cardiac T1 mapping, such as the estimation of the extracellular volume fraction, which has seen an increasing use as a surrogate marker of interstitial remodeling and interstitial fibrosis.

M. Jerosch-Herold (✉)
Brigham and Women's Hospital, Harvard Medical School, Boston, MA, USA
e-mail: mjerosch-herold@bwh.harvard.edu

R. T. Seethamraju
Department of MR/R&D, Siemens Healthcare, Boston, MA, USA
e-mail: Ravi.Seethamraju@siemens-healthineers.com

T1 Relaxation Measurements

The measurement of the longitudinal relaxation time T1 is a well-established concept since the beginnings of nuclear magnetic resonance, though in its original form it amounts to a relatively time-consuming process. The nuclear spin magnetization is initially disturbed from its equilibrium state, e.g., in the form of a magnetization inversion with a 180 degree radio-frequency pulse. The recovery of the longitudinal magnetization (M_z) back to its equilibrium state is generally well described by an exponential function with a characteristic time constant that is labeled T1:

$$M_z = M_0 \cdot \left(1 - \eta \cdot \exp\left(-TI / T_1\right)\right), \qquad (25.1)$$

where η represents the magnetization inversion factor ($\eta = 2$ for an inversion; $\eta = 1$ for a saturation preparation), M_0 is the equilibrium magnetization, and TI is the time after inversion.

Determining the T_1 relaxation time requires sampling of the magnetization recovery at multiple times after magnetization inversion or saturation. For each signal sample, one has to create a transverse magnetization component during the magnetization recovery by applying a radio-frequency (RF) pulse, followed by a signal readout. Measuring or sampling the magnetization recovery therefore always entails disturbing the inversion recovery and yields a signal that is *proportional* to the longitudinal magnetization at that particular time after inversion (TI).

In MRI the standard for measuring T1 is based on an inversion recovery prepared spin echo (IR-SE) sequence, illustrated in Fig. 25.1: after inversion of the magnetization, a spin echo is produced at a predetermined time after the inversion (TI) to measure the state of the longitudinal magnetization. The process is repeated for a series of TI values, while assuring that the magnetization has recovered completely in between repetitions. If one uses a repetition time (TR) equivalent to approximately 5 × T1, then the condition

R. Y. Kwong et al. (eds.), *Cardiovascular Magnetic Resonance Imaging*, Contemporary Cardiology,
https://doi.org/10.1007/978-1-4939-8841-9_25

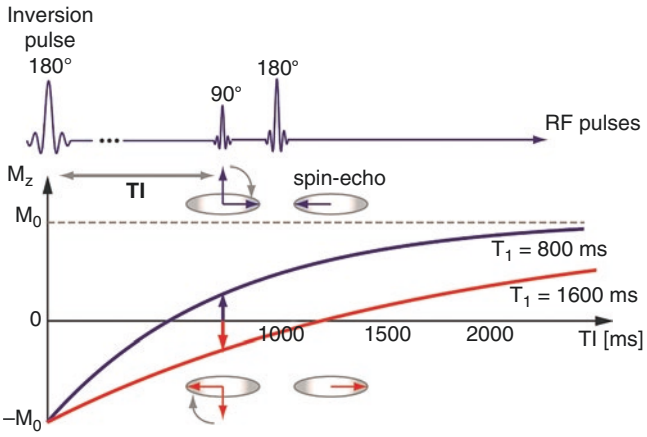

Fig. 25.1 The inversion recovery prepared spin echo technique illustrated in this figure is often used as reference standard for T1 measurements in phantoms. It consists of a magnetization inversion pulse, which is followed at a predetermined time after inversion (TI) by the generation of a spin echo with a 90°–180° pair of RF pulses. The amplitude of the resulting spin echo is proportional to the longitudinal magnetization at time TI. To measure T1 requires repeating the inversion and spin echo readout for a range of TI values. The magnetization has to be in its equilibrium state before application of the inversion pulse (i.e., fully recovered if there was a previous inversion and readout), which makes this a relatively slow technique for measuring T1. The time for repeating the inversion should be ~ 5× the expected T1 to assure complete magnetization recovery. The figure shows examples of inversion recoveries corresponding to a T1 = 800 ms (blue line) and T1 = 1600 ms (red line), with the latter value of T1 = 1600 ms corresponding approximately to the T1 of arterial blood at 3 Tesla

of complete magnetization recovery is met within (1–2*exp.(−5*T1/T1)) = 0.9865, i.e., within ~ 1%. The T1 of blood is approximately 1400 ms at 1.5 T, implying that the repetition time for an IR-SE-based T1 measurement would have to be on the order of 7 sec. In addition to the requirement to sample the inversion recovery for a series of TI values, one has to also use the same repetition time to perform all the phase-encoding steps in addition to the loop over the TI values, which makes this technique impractical for cardiac in vivo applications. It is mostly used today for in vitro, phantom-based validation of more advanced techniques.

Look-Locker Technique

Look and Locker introduced a faster method for measuring T1 that uses RF pulses with small flip angles to repeatedly sample the inversion recovery [4]. Each of these RF pulses disturbs at least slightly the magnetization recovery but preserves the exponential nature of the magnetization recovery. The curves of signal intensity versus TI from a Look-Locker acquisition give an exponential recovery constant, T1*, that is not equal to the T1 for an undisturbed inversion recovery – therefore the distinction between T1* and T1 is important. T1* is nevertheless related to the true T1, through a relation that involves the flip angle (α) and repetition time (*TR*) of the steady train of radio-frequency pulses that are applied for the signal readouts during the inversion recovery:

$$\frac{1}{T_1^*} = \frac{1}{T_1} - \frac{\ln\left(\cos\left(\alpha\right)\right)}{TR} \qquad (25.2)$$

As $\ln(\cos(\alpha)) < 0$ for any flip angle $\alpha < 90°$, one can deduce from the above equation that T_1* is shorter than T_1: the effect of the periodic α pulses is an apparent speedup of the magnetization recovery. The flip angles that are used for sampling of the longitudinal magnetization should be relatively small to avoid that T_1* becomes dominated by the effects of the periodic RF pulses – for this reason in Look-Locker acquisitions, one uses low-flip-angle gradient echo readouts. The above formula is seldom used in practice to estimate T1 from T1* because it requires that the flip angle be known, and simply using the flip angle specified in the user interface of the scanner is inadequate because it represents an approximate value – the actual flip angle may vary over the heart due to B_1 inhomogeneity. Instead, for Look-Locker sequences one fits the inversion recovery signal intensity (SI) curves to an equation of three unknown parameters (A, B, T1*):

$$\mathrm{SI} = A - B \cdot \exp\left(-TI / T_1^*\right) \qquad (25.3)$$

Here the parameter *A* represents the magnetization under the influence of the regular low-flip-angle readouts for long *TI* values ($\exp(-TI/T1^*) < <1$), while *B* corresponds to 2× the equilibrium magnetization (i.e., $2 \times M_0$ with the nomenclature of Eq. 25.1) in the case of an inversion preparation. It is important to note that the signal amplitude corresponding to the equilibrium magnetization M_0 (A_0) and *A* is not the same because of the periodic RF pulses for signal readout, and $A < A_0$. In fact, the ratio of *A/B* can be used to estimate the effect of the α pulses on the inversion recovery and calculate the true T1, under the assumption of perfect inversion efficiency:

$$T_1 = T_1^* \cdot \left(\frac{A}{B} - 1\right) \qquad (25.4)$$

The Look-Locker technique has been used for ECG-triggered T1 imaging in the heart. The implementation is illustrated in Fig. 25.2. Look-Locker T1 imaging results in a series of images for different TI values that fall into different cardiac phases. A location in the myocardium therefore changes position in the images for different TI values, rendering it difficult to generate parametric T1 maps. For Look-Locker imaging one employs a segmented acquisition,

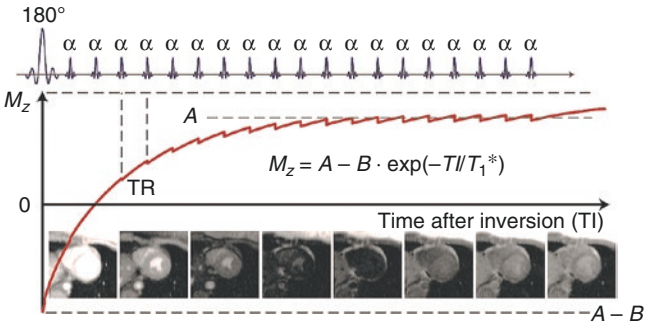

Fig. 25.2 The Look-Locker technique achieves a speedup in the sampling of the magnetization by performing a series of low-flip-angle readouts after an inversion pulse. The inversion recovery (red line) is perturbed by the train of RF pulses that are applied for the signal readouts at different TIs, though the inversion recovery is still well described by a single exponential with effective relaxation time constant T1*, if the undisturbed inversion recovery follows a single-exponential recovery with time constant T1. The T1 constant from the undisturbed recovery can be estimated from the measured T1*, and the signal amplitude parameters A and B in the equation in the figure under the assumption that the initial magnetization inversion is perfect - see above equation [4]

which has the advantage that the TI increments can be relatively small, and equal to the acquisition time for the k-space segments.

Modified Look-Locker Imaging (MOLLI)

In CMR the Look-Locker technique has been superseded by the so-called *modified* Look-Locker imaging (MOLLI) technique. With MOLLI, images corresponding to different TI values are all acquired during the same phase of the cardiac cycle. TIs are changed by altering the ECG trigger delay between R-wave and inversion pulse, which in turn changes the times between the inversion pulse and each image readout (i.e., TIs).

The basic building block of MOLLI, called a Look-Locker (LL) cycle, consists of an inversion pulse, after which a user-specified number of images are acquired, each during the same phase of a heartbeat, but with a different TI. The TI times from this cycle of image acquisitions have increments corresponding to the cardiac cycle duration. To sample the magnetization with smaller TI increments, one repeats such a LL cycle with a different trigger delay for the inversion pulse. The number of images that are acquired during each LL cycle can vary in a T1 measurement to meet the requirements for an optimal choice of TI values. Such an optimal choice depends on the expected range of T1, and in practice this meant that different MOLLI schemes were used for pre- and post-contrast T1 measurements. For shorter T1 values, one uses more and shorter Look-Locker cycles to sample the magnetization, and for longer expected T1s, it was important to use larger TI increments, and longer, but possibly fewer, Look-Locker cycles than for shorter T1's. Nevertheless, the use of different MOLLI schemes for pre- and post-contrast measurements has generally fallen out of favor and given way for the sake of expediency to the use of single MOLLI scheme for pre- and post-contrast T1 mapping in clinical studies.

Images are acquired in a single shot in MOLLI T1 imaging using a fast gradient echo image readout during balanced steady-state free precession (bSSFP). These single-shot image bSSFP readouts have to be rapid so that TI is reasonably well-defined. TI is defined as the time from the inversion pulse to the acquisition of the central k-space lines, but this represents an approximation which becomes increasingly poorer as the duration of the image acquisition (TA) becomes longer. Arguably, TI increments that are shorter than the image acquisition time (TA ≈ 150 ms) should not be used with MOLLI, and by the same token, the range of T1 values which can be accurately quantified with MOLLI has a lower limit above TA. MOLLI acquisitions use parallel imaging acceleration and partial Fourier encoding to shorten the image acquisition time.

A widely used MOLLI scheme for pre- and post-contrast T1 mapping is the 5-3-3 scheme, shown in Fig. 25.3, where the numbers refer to the duration of each LL cycle in multiples of a heartbeat duration. In addition it is customary to denote the duration of rest periods between LL cycles – to assure complete magnetization recovery before applying again an inversion pulse – by a number in brackets. For our 5-3-3 scheme, the complete specification including the rest periods would read: 5(3)3(3)3, where the rest periods in this case have a duration corresponding to three heartbeats after the first and second Look-Locker cycle. Specifying rest periods in multiples of a heartbeat has the disadvantage that the rest period varies in absolute time with heart rate and may be too short if the patient's heart rate is relatively high. Recent MOLLI implementations have therefore switched to a scheme where the rest periods are specified in seconds rather than heartbeats.

Shortened Modified Look-Locker (shMOLLI)

A shortened version of MOLLI, which is less demanding in terms of breath-holding duration, was introduced in 2000 by Piechnik et al. [5], using a MOLLI scheme of 5(2)1(1)1. The reader will note that the rest periods appear to be too short for longer T1 values, which would yield inaccurate T1 values if the standard approach of T1 fitting were to be used. A key component of shMOLLI is therefore a conditional processing algorithm that is applied to select the data points from the three Look-Locker cycles that are consistent with the estimated T1, without biasing the T1 estimate. This conditional processing involves an iterative process, where an initial estimate of T1, using all TIs, is used to determine if data from the

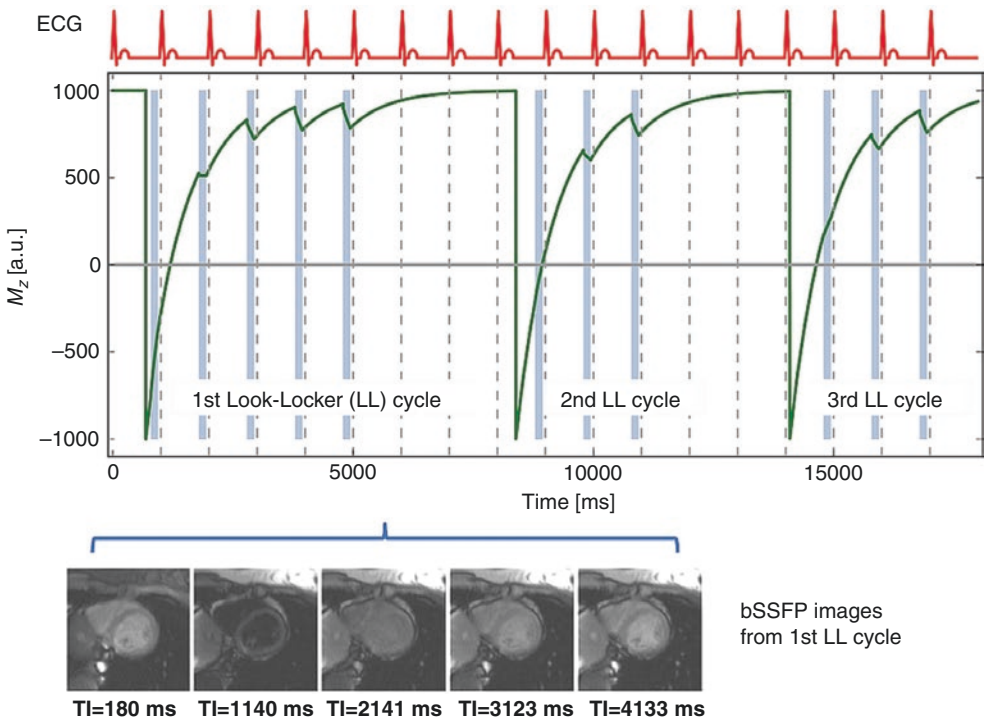

Fig. 25.3 The upper graph shows the time course of longitudinal magnetization (M_z) during a MOLLI 5(3)3(3)3 acquisition with TR/TE/flip angle = 3.0/1.5/25° and assuming T1 = 800 ms and T2 = 40 ms (green line). The light blue bars highlight the periods for the image readouts with a balanced steady-state free precession (bSSFP) technique. During the bSSFP readouts, the longitudinal magnetization is perturbed by the applied radio-frequency pulses, as can be seen from the green curve representing M_z. These perturbations are most noticeable during later parts of the inversion recovery. At the top is a schematic representation of the ECG signal, with an R-to-R interval duration of 1000 ms. The images at the bottom come from an equivalent MOLLI acquisition in a patient and show five images obtained during the first of the three Look-Locker cycles

last, or the last two Look-Locker cycles should be dropped from the T1 fit because the initial T1 is inconsistent with near complete relaxation recovery between Look-Locker cycles. For the full details on the conditional processing in shMOLLI, the reader is referred to the reference by Piechnik et al. [5].

T1 Imaging with SASHA and STONE

SASHA is a T1-mapping technique based on saturation recovery single-shot acquisition [6]. The use of a magnetization saturation pulse, instead of an inversion pulse, has the advantage that the state of the longitudinal magnetization *after* saturation is independent of its state beforehand, i.e., the previous history of the magnetization. SASHA therefore does not require rest periods between Look-Locker cycles if the saturation is perfect, which results in principle in T1 estimates that are independent of the patient's heart rate and shortened breath-hold durations. In its original implementation, the SASHA pulse sequence consists of ten single-shot bSSFP images acquired over consecutive heartbeats in end-diastole. The first image is acquired without magnetization preparation (equivalent to TI > >T1 with a saturation preparation). For the remaining images, the saturation pulse is applied with varying trigger delays, such that the time after saturation (TS) for the image acquisitions uniformly samples the saturation recovery over most of the RR interval.

The signal intensity (SI) saturation recovery in a SASHA measurement can be described by the following equation:

$$\mathrm{SI} = M_0 \cdot \left[1 - \eta_{\mathrm{apparent}} \cdot \exp\left(-TS / T_1\right)\right], \qquad (25.5)$$

where η_{apparent} represents the *apparent* saturation efficiency, and is one of the fit parameters. This apparent saturation efficiency reflects the actual efficiency (η_{act}, which equals 1 for a perfect saturation) of the saturation preparation but includes also effects of the SSFP single-shot readout on the measured signal, which involves T_1, T_2, and the flip angle. The apparent saturation efficiency, η_{apparent}, does therefore not equal 1, even when $\eta_{\mathrm{act}} = 1$.

SASHA has the distinction that after magnetization preparation, only a single image is acquired, while with MOLLI one acquires more than one image during at least one Look-Locker cycle of the MOLLI scheme. SASHA therefore gets closer to the ideal of sampling the longitudinal magnetization during a magnetization recovery without disturbance from a previous

readout. Accordingly, SASHA also dispenses with correcting the T1 obtained from a fit to equation [5], as is routinely done for MOLLI by using the transformation in equation [4].

The goal of perturbing a magnetization recovery with an image readout only once after a magnetization inversion could also be implemented with MOLLI but would result in long acquisition times. For multi-slice acquisitions, an acquisition scheme with single-image readouts per slice after each inversion pulse was combined with slice interleaving for what the creators termed slice-interleaved T1 ("STONE") [7]. With STONE, each Look-Locker cycle is still used for multiple image acquisitions, albeit for *different* slice locations, which eliminates the problem that the inversion recovery in any slice is perturbed before an image readout. The acquisition time for STONE is too long for breath-holding, but its original creators combined it with prospective slice tracking with a pencil-beam navigator to minimize motion perpendicular to the stack of image slices [7].

T1 Estimation

The images collected with a technique such as MOLLI provide samples of the magnetization recovery for pixel locations or myocardial segments and can be fit with a model equation such as [3] or [5], using a nonlinear least squares fitting algorithm. As the inversion recovery data are obtained from magnitude images, one of tasks is to restore the polarity of the recovery curves. This is often combined with the fitting itself, by iteratively determining the best TI interval for the zero crossing from the fit quality, as shown in Fig. 25.4**.**

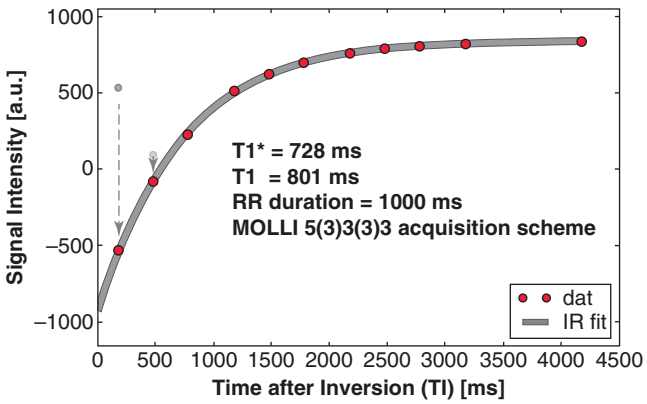

Fig. 25.4 Simulated data points shown as red dots were obtained from Bloch equation simulation for the inversion recovery during a MOLLI acquisition as shown in Fig. 25.3. The gray dots represent original magnitude data. The polarity of the inversion recovery is restored as part of the fitting to a mono-exponential recovery: $A - B \cdot \exp(TI/T_1^*)$. In this case the best fit was obtained by switching the sign of first two gray data points to the left. T1 was calculated from the best fit values for the parameters A, B, and T1*, using equation [4]. The true T1 in this simulated case was 800 ms and applying the approximation $T1 = (B/A - 1) \cdot T1^*$ gave in this case 801 ms, with a T1* of 728 ms obtained from the exponential fit

T1 estimates obtained from the Look-Locker, MOLLI, and SASHA techniques are known to suffer from potential error sources, such as B1 inhomogeneities and off-resonance offsets, T2 relaxation during balanced SSFP readouts, and imperfect inversion or saturation efficiency, among others. Most of these adverse effects on T1 estimation worsen with increasing field strength. Furthermore, even the k-space sampling trajectory used for the bSSFP readout can have a significant impact on T1 estimation.

For MOLLI, a standard approach to correct for the effects of repeated bSSFP readouts during the inversion recovery is to first calculate a T1* value by nonlinear least squares fitting to the model equation [3] and then estimating T1 with equation [4] and implicitly assuming perfect inversion efficiency. It should be noted that [4] represents an "empirical" correction, rather than being derived from first principles, as was originally done for [4] in the context of the Look-Locker technique. MOLLI, in contrast to Look-Locker, is characterized by intermittent undisturbed magnetization recoveries, with brief bSSFP readouts that can have a marked effect on the longitudinal magnetization recovery, as illustrated in Fig. 25.3. Any closed-form analytical expression, such as in equation [4], to calculate T1 from the T1* with MOLLI equation [4] is therefore merely an empirical approximation for such a relatively complex magnetization recovery, though equation [4] can still work surprisingly well, as can be seen from the example with Bloch simulations in Fig. 25.4**.**

It has been proposed that the fitting of the inversion recovery curves could instead use Bloch-equation-based simulated models of the inversion recovery, which could account for imperfections such as B_1 and B_0 inhomogeneities [8]. Such an approach would require obtaining additional images/data to characterize the B_1 and B_0 inhomongeneities [8] and is also computationally intensive. The latter drawback can be overcome by parallelization of the calculations using graphics processing units (GPU) [9]. As mentioned above, SASHA has the advantage that the magnetization recovery proceeds undisturbed up to the single bSSFP readout in each RR interval. Therefore the underlying model of the magnetization recovery is also simpler than for MOLLI, and imperfections in the bSSFP readout have only minor effects on the T1 estimate. The case for more complex Bloch-equation-based simulated models for T1 fitting would therefore only bring minor or insignificant benefits for SASHA measurements, compared to the simple model in equation [5].

Simulations based on the Bloch equations have also been used for the purpose of predicting the inversion efficiency based on the expected T1 and T2 values. A perfect inversion efficiency is assumed in many cases for the T1 estimation, like, e.g., in the use of equation [4], and deviations from perfect inversion efficiency result in an error in the T1 estimate. Mapping out the inversion efficiency in the heart is a challenging problem that could potentially slow down the clinical

workflow. The inversion efficiency can be measured more easily for stationary muscle tissue (e.g., in the calf muscle), and these "reference data" (assuming that T1 and T2 are similar) can be used to calculate the expected inversion efficiency for the heart. Cooper et al. have shown that accounting for the inversion efficiency in this manner can improve the T1 accuracy with MOLLI measurements [10]. If the inversion efficiency is known, then it is relatively straightforward to adapt equation [4] to include the saturation efficiency, which is expressed as a value $0 < \delta < 1$, where $\delta = 1$ represents a perfect inversion: $T1 = (B/A - 1)/\delta \cdot T_1{}^*$.

The inversion efficiency of adiabatic inversion pulses – the most common form of RF pulses used today for magnetization inversion in T1 mapping – depends in general on T1 and T2. This has prompted the search for adiabatic inversion pulses, where the inversion efficiency has a minimal dependence on the $T_{1,2}$ relaxation parameters, with the *tan/tanh* design representing in this sense an excellent choice [11]. With SASHA a deviation from perfect saturation efficiency can be shown analytically to have no effect on the estimated T1, which was borne out in practice [6]. Therefore the extra effort required for determining the inversion efficiency is most worthwhile for MOLLI and shMOLLI techniques with inversion preparation.

Magnetization Transfer

Magnetization transfer effects in myocardial tissue occur as a result of spin magnetization being exchanged with a "dark" pool of immobile spins, which by virtue of their broad resonance/short T2 relaxation times do not contribute directly to the detected signal. This dark pool of spins encompasses "bound" 1H nuclei in the intracellular space and in connective tissue, which can exchange with the pool of "free" 1H nuclei. The signal from the bound 1H nuclei cannot be directly observed with standard imaging sequences because of their extremely short T2 on the order of a ms, unless one uses imaging techniques with ultra-short echo times (UTE imaging) [12]. Nevertheless the exchange of spin magnetization between the "dark" pool of spins and mobile 1H nuclei has an effect on the latter, which, in the case of an inversion recovery sampled by periodic RF pulse excitations, results in an apparent shortening of T1 [13]. The magnetization transfer effect depends on the flip angle of the RF pulses in the bSSFP readout, as the pulses tend to partially saturate the pool of bound 1H nuclei. MOLLI and SASHA both use bSSFP image readouts, with a similar MT effect during the bSSFP readout in both cases. The MT effect on the apparent T1 is amplified with MOLLI, because the inversion recovery is in most instances perturbed by *multiple* bSSFP readouts during an inversion recovery in MOLLI, while SASHA uses only a *single* bSSFP for each saturation recovery [13]. The MT effects on T1 also depend on the type of RF pulse being used for magnetization inversion or saturation, though the incremental effect on T1 from MT effects showed only minor differences between different magnetization preparation schemes. While simulations have provided a relatively good understanding about MT effects on native myocardial T1, the effects of MT on post-contrast T1 measurements have not been investigated yet in detail.

Transcytolemmal Water Exchange

Gadolinium-based contrast agents are excluded from the intracellular space unless severe ischemia and infarction cause a breakdown of the cell membrane, with a concomitant loss of viability. Nevertheless, the presence of contrast agent in the extracellular space can have an indirect effect on the 1H magnetization in the intracellular space, and vice versa, through the exchange of water across the cell membranes. For most applications of post-contrast myocardial T1 mapping, it is assumed that the exchange of water across the transcytolemmal barrier is fast relative to the difference of "intrinsic" R1 in the intra- and extracellular spaces. ("Intrinsic" R1 refers here to the relaxation rate that would be observed in each space in the absence of any exchange, i.e. if the spaces are separated by an impermeable barrier.) In the limit of fast exchange, the relaxation rate of myocardial tissue is an average of the intrinsic R1s, with weighting factors that represent the fraction of mobile spins in each subspace. If we denote the extracellular volume fraction by ECV, then the tissue R_{1t} is given in the limit of *fast exchange* by:

$$R_{1t} \approx \mathrm{ECV} \cdot R_{1o} + (1 - \mathrm{ECV}) \cdot R_{1i}, \qquad (25.6)$$

where R_{1o} and R_{1i} are the intrinsic relaxation rates in the extracellular and intracellular spaces, respectively.

The difference of "intrinsic" R1's between intra- and extracellular spaces can be changed by introduction of a gadolinium-based contrast agent in the extracellular space. Therefore, the introduction of a contrast agent can shift the conditions for relaxation recovery from the fast-exchange limit to intermediate exchange rate conditions [14]. To a first approximation, an inversion recovery can then still be described by a single-exponential recovery model, but the dependence of the myocardial R_{1t} on the concentration of gadolinium in the extracellular plasma ceases to be linear [14]. This can be observed in the myocardium by plotting the R_{1t} against the R1 of blood (a good surrogate marker for the gadolinium concentration in blood) [15]. An example for a patient with aortic stenosis is shown in Fig. 25.5. The deviation from the linear dependence of R_{1t} in tissue on the R1 in blood becomes more pronounced as R1 in blood increases and with increasing intracellular lifetime (τ_{ic}).

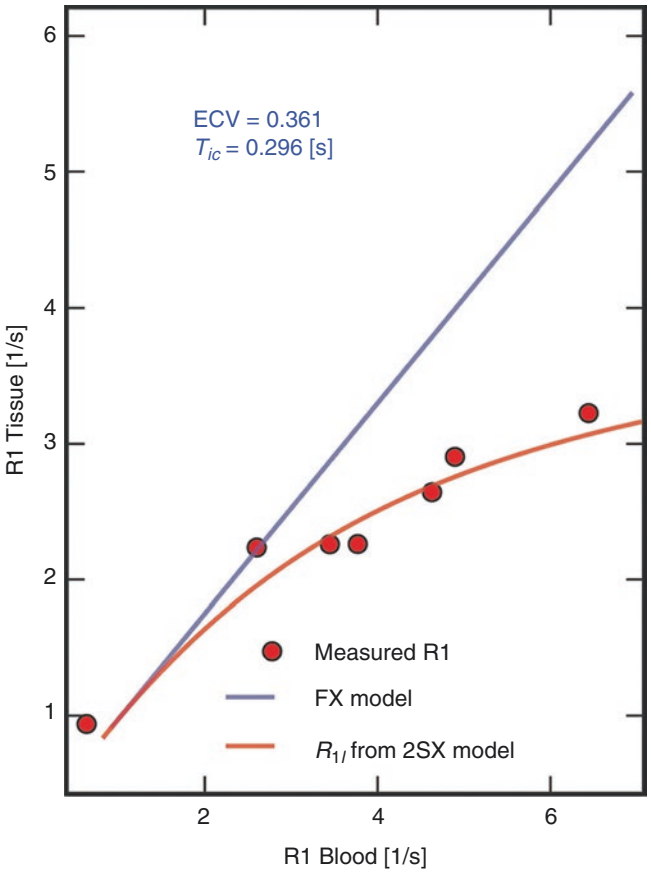

Fig. 25.5 Example of myocardial T1 measurements in patient with aortic stenosis. The blue line corresponds to the relationship between R1 in myocardial tissue and R1 in the blood pool under the assumption that the transcytolemmal exchange of water is in the fast-exchange (FX) limit. At higher contrast concentrations in blood (i.e., higher R1 values in blood), this assumption breaks down, as transcytolemmal exchange rate is no longer high compared to the difference of intrinsic R1 for the extra- and intracellular spaces. (For the plasma in the extracellular space, one can assume that R1 changes linearly with the R1 in blood) As one moves away from the fast-exchange limit (e.g., by giving more contrast), the rate of transcytolemmal exchange becomes effectively the bottleneck for myocardial T1 relaxation, and the R1 shows a sublinear dependence on R1 in blood. The red line was obtained from a fit of a 2-site water exchange model (2SX) to the measured R1 values, and the fit provides an estimate of the intracellular lifetime of water, a parameter that can be used to detect changes in cardiomyocyte diameter

The intracellular lifetime increases with cell size, and the effects of moving away from the fast-exchange limit are therefore most noticeable for post-contrast T1 measurements in cases of cardiomyocyte hypertrophy [16]. The effects of transcytolemmal water exchange can provide useful information on cardiomyocyte size, but can also be a bane, because the extracellular volume fraction can be underestimated if one does not take into account that the water exchange ceases to be sufficiently fast at higher contrast concentrations [15].

Accuracy Versus Precision in T1 Mapping

After the discussion of potentially confounding effects such as magnetization transfer, and transcytolemmal water exchange, it should not come as a surprise that the different techniques for T1 imaging or mapping perform differently in terms of accuracy and precision. Roujol et al. have performed detailed comparisons of MOLLI, shMOLLI, and SASHA [17]. They found that SASHA yields higher accuracy for T1 measurements than MOLLI, and shMOLLI, but its precision is lower than for MOLLI/shMOLLI. The lower accuracy of MOLLI and shMOLLI, compared to SASHA is partially a result of unintended effects like magnetization transfer, though arguably MT can provide an additional means for detecting pathological changes in myocardium. The lower precision of SASHA is a result of the reduced dynamic range that can be sampled during a magnetization recovery following a saturation pulse, compared to an inversion pulse. A smaller dynamic signal range increases the uncertainty in the parameter estimates when fitting the signal curves to a model equation for the magnetization recovery, which explains the lower precision of SASHA, compared to MOLLI and shMOLLI.

Accuracy and precision need to be traded off against each other when one makes a choice between MOLLI, shMOLLI, SASHA, and other T1-mapping techniques. In a clinical setting, where a CMR site has obtained reference data for healthy controls, higher T1 precision at the cost of lower accuracy may be a better trade-off, than higher T1 accuracy at the cost of lower precision. The detection of disease will depend on measuring precisely differences of T1 in patients with disease, compared to healthy controls, i.e., a more precise T1 estimation can increase diagnostic test accuracy.

Extracellular Volume (ECV) Fraction

Initial reports suggesting an increased uptake of contrast due to expansion of the extracellular space and buildup of interstitial fibrosis were based on post-contrast myocardial T1 imaging [18, 19]. The increased myocardial concentration of gadolinium contrast was reflected in a reduced T1 relaxation time. Myocardial T1 changes with the T1 of blood, and therefore the post-contrast myocardial T1 will depend on the injected contrast dosage, the delay between contrast injection and T1 measurement, the rate of clearance of contrast from blood, which relates to renal function, and other factors, such as magnetic field strength. In practice, it is difficult or impossible to control *all* of these factors.

The myocardial extracellular volume (ECV) fraction can be estimated from the ratio of changes of R1 (R1 = 1/T1) in myocardium and blood ($\Delta R1[\text{tissue}]/\Delta R1[\text{blood}]$).

This provides a marker of extracellular volume expansion that is independent of potential confounders like contrast agent dosage, field strength, and within certain limits the time delay between contrast injection and T1 measurement.

To describe the effect of a contrast agent on the 1H T1-relaxation, one uses the inverse of T1, the R1 relaxation rate (R1 = 1/T1), as R1 changes approximately linearly with contrast agent concentration in blood and tissue. At least in the limit of fast water exchange between the spaces with and without contrast agent (e.g., between blood plasma and red blood cells for a gadolinium-based contrast agent), the following relation between R1 and contrast agent concentration applies:

$$R_1 = R_{10} + r_1 \cdot [\mathrm{Gd}] \qquad (25.7)$$

R1 is the value measured for a voxel or region of interest in blood or tissue. Gadolinium-based contrast does not uniformly distribute within the voxel: in the case of blood, the contrast agent is excluded from the red blood cells. The R1 of blood can be expressed, with the blood hematocrit (Hct), and the Gadolinium contrast relaxivity (r_1) as:

$$R_1(\mathrm{blood}) = R_{10}(\mathrm{blood}) + r_1 \cdot [\mathrm{Gd}]_{\mathrm{plasma}} \cdot (1 - \mathrm{Hct}), \quad (25.8)$$

because conditions of fast 1H exchange between plasma and the water pool in red blood cells apply over the full range of Gd-dosages that are administered to patients. R_{10} (i.e., with a "0" subscript) refers to pre-contrast or "native" R1. In the case of myocardial tissue, the contrast agent is confined to the extracellular volume (ECV), and R1 of tissue can be expressed in the fast 1H exchange limit as:

$$R_1(\mathrm{tissue}) = R_{10}(\mathrm{tissue}) + r_1 \cdot [\mathrm{Gd}]_{\mathrm{EC}}\,\mathrm{ECV}, \qquad (25.9)$$

where ECV is the extracellular volume *fraction*. If one lets the contrast agent reach an equilibrium between blood and tissue ($[\mathrm{Gd}]_{\mathrm{EC}} = [\mathrm{Gd}]_{\mathrm{plasma}}$), then it becomes possible to derive from the R1 measurements an estimate of ECV, assuming that the blood hematocrit is known and that the relaxivity of the gadolinium contrast is the same in blood and tissue:

$$\frac{R_1(\mathrm{tissue}) - R_{10}(\mathrm{tissue})}{R_1(\mathrm{blood}) - R_{10}(\mathrm{blood})} = \frac{\Delta R_1(\mathrm{tissue})}{\Delta R_1(\mathrm{blood})} = \frac{\mathrm{ECV}}{(1 - \mathrm{Hct})} \equiv \lambda_{\mathrm{Gd}}$$

The ratio of R1 changes in tissue and blood is referred to as the myocardial partition coefficient for gadolinium (λ_{Gd}) [20, 21]. If one plots R1 measured in tissue, against R1 in blood, then λ_{Gd} corresponds to the slope of the least squares regression line fit to the measured R1 data – assuming that the fast water exchange limit applies for all data points.

After moving all measurable quantities to the left in the above equation, one obtains the following expression for ECV:

$$(1 - \mathrm{Hct}) \cdot \frac{\Delta R_1(\mathrm{tissue})}{\Delta R_1(\mathrm{blood})} = \lambda_{\mathrm{Gd}} \cdot (1 - \mathrm{Hct}) = \mathrm{ECV} \quad (25.10)$$

The derivation of the expression for ECV in [10] implicitly assumed that transcytolemmal water exchange was in the fast-exchange limit. This assumption is bound to break down with higher contrast dosages, and neglecting this may result in an underestimate of ECV [15]. The observed underestimate of ECV based on post-contrast T1 measurements within the first 10 min after contrast injection, compared to the use of later T1 measurements was previously interpreted as a sign that contrast concentrations in blood and tissue had not reached an equilibrium. This stands in contrast to tracer-kinetic simulations which indicate that T1 measurements can be performed as early as 3 min after injection except in situations of very low myocardial blood flow [22]. This suggests that the validity of assuming fast transcytolemmal exchange conditions for post-contrast T1 measurements, in particular early after contrast injection, needs to be carefully examined before estimating ECV.

Clinical Applications

The clinical applications of T1 mapping have focused on characterizing pathological alterations in myocardial tissue structure and composition in cardiomyopathies and acquired and congenital heart disease. The extracellular volume fraction (ECV) has been used as a surrogate marker for detecting the buildup of connective tissue through the associated expansion of the extracellular matrix in dilated and hypertrophic cardiomyopathies [23–25], aortic stenosis [26, 27], hypertensive heart disease [28], cardiotoxicity [29], and in ventricular remodeling after myocardial infarction [30]. Expansion of the extracellular volume fraction is also observed with infiltrative diseases such as cardiac amyloidosis [31–33]. Though post-contrast T1 measurements can be used for similar purposes as ECV, it should be noted that post-contrast T1 depends on multiple factors such as contrast dosage, time between contrast injection and T1 measurement, contrast agent clearance from the blood pool, and therefore renal function, all of which would have to be controlled for a sensitive detection of pathology. The ECV parameter has the distinct advantage of correcting for these factors, by including the changes of T1 in the blood pool between pre- and post-contrast states.

More recently, native T1 has received increasing attention for detecting myocardial pathology without requiring administration of a contrast agent. Native T1 is significantly longer with myocardial edema [34], in acute and chronic myocardial infarction [35, 36], and in cardiac amyloidosis [37, 38]. Figure 25.6 shows the correspondence between LGE and increased native T1 in a patient with a history of amphetamine abuse, where the T1 map was generated from motion-corrected MOLLI images. Whether native T1 is suitable for the detection of interstitial fibrosis, as shown for ECV, remains controversial. Therefore the use of gadolinium-based contrast in combination with pre- and post-contrast T1 measurements still offers benefits for tissue characterization.

Summary

The rapid pace of adoption of T1 mapping in CMR has prompted the publication in 2013 of a consensus statement from the Society for Cardiovascular Magnetic Resonance and the CMR Working Group of the European Society of Cardiology [1]. The fact that the findings from cardiac T1 mapping are dependent on a multitude of technical factors, as discussed in this chapter, has prompted the authors of the consensus statement to formulate recommendations for standardization of protocols and establishment of normative values, even if only done by CMR site. These recommendations are as pertinent today as at the time of publication. The fact that the authors did not make detailed technical recommendations reflects the fact that each technique, such as SASHA or MOLLI/shMOLLI, has specific advantages which cannot yet be combined in one sequence technique while giving rise to some systematic differences in T1 estimates.

Notwithstanding the current limitations and controversies, native T1 and ECV represent two new important biomarkers to detect myocardial pathology and improve diagnosis. There is a strong need to demonstrate that the findings from T1 mapping can be translated across sites, and first efforts involving T1 mapping, such as the HCMR trial [39], are currently underway.

Though concepts such as ECV quantification can also be implemented with other imaging modalities such as computed tomography [40], it is safe to say that CMR will play a leading role in advancing myocardial tissue characterization through T1 mapping and exploration of other contrast mechanisms such as magnetization transfer. Untangling different contrast mechanisms will likely remain a challenge, but this will not necessarily impede the detection of disease, assuming that normative values have been established with the same T1 mapping technique as used in patients.

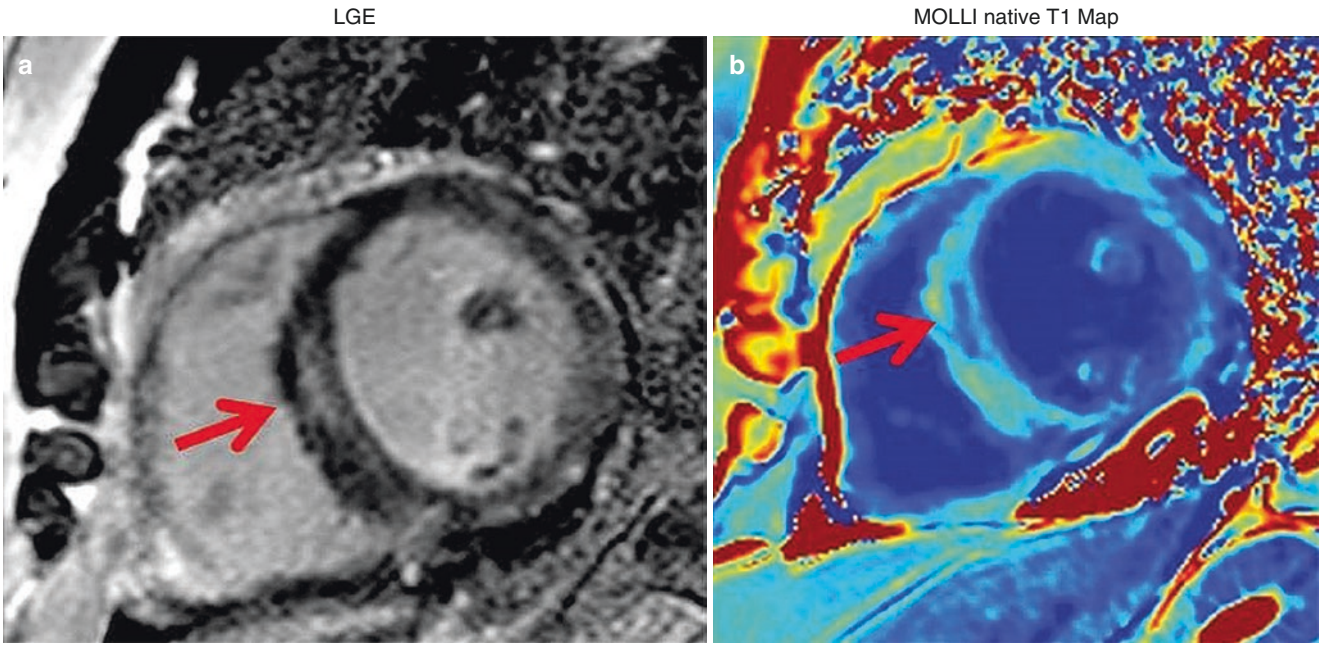

Fig. 25.6 In a male patient (Hx of amphetamine abuse) with nonischemic cardiomyopathy, the image of late gadolinium enhancement (LGE) in (**a**) provides evidence of diffuse fibrosis with a nonischemic pattern in the septum (red arrow) and the lateral and inferior wall segments. The map of native (i.e., pre-contrast) T1 in (**b**) shows a similarly sized area in the septum with increased T1 in the mid-septum, suggesting increased water content from edema. Studies in patients with acute myocardial infarction have also demonstrated a correspondence between LGE and native T1, suggesting that one can detect myocardial pathology without contrast administration by native T1 mapping

References

1. Moon JC, Messroghli DR, Kellman P, Piechnik SK, Robson MD, Ugander M, et al. Myocardial T1 mapping and extracellular volume quantification: a Society for Cardiovascular Magnetic Resonance (SCMR) and CMR Working Group of the European Society of Cardiology consensus statement. J Cardiovasc Magn Reson. 2013;15:92.
2. Ferreira VM, Piechnik SK, Dall'Armellina E, Karamitsos TD, Francis JM, Choudhury RP, et al. Non-contrast T1-mapping detects acute myocardial edema with high diagnostic accuracy: a comparison to T2-weighted cardiovascular magnetic resonance. J Cardiovasc Magn Reson. 2012;14:42.
3. Salerno M, Kramer CM. Advances in parametric mapping with CMR imaging. JACC Cardiovasc Imaging. 2013;6(7):806–22.
4. Look D, Locker D. Time saving in measurement of NMR and EPR relaxation times. Rev Sci Instrum. 1970;41:250–1.
5. Piechnik SK, Ferreira VM, Dall'Armellina E, Cochlin LE, Greiser A, Neubauer S, Robson MD. Shortened Modified Look-Locker Inversion recovery (ShMOLLI) for clinical myocardial T1-mapping at 1.5 and 3 T within a 9 heartbeat breathhold. J Cardiovasc Magn Reson. 2010;12:69.
6. Chow K, Flewitt JA, Green JD, Pagano JJ, Friedrich MG, Thompson RB. Saturation recovery single-shot acquisition (SASHA) for myocardial T(1) mapping. Magn Reson Med. 2014;71(6):2082–95.
7. Weingartner S, Roujol S, Akcakaya M, Basha TA, Nezafat R. Free-breathing multislice native myocardial T1 mapping using the slice-interleaved T1 (STONE) sequence. Magn Reson Med. 2014;74(1):115–24.
8. Marty B, Vignaud A, Greiser A, Robert B, de Sousa PL, Carlier PG. BLOCH equations-based reconstruction of myocardium T1 maps from modified look-locker inversion recovery sequence. PLoS One. 2015;10(5):e0126766.
9. Xanthis CG, Venetis IE, Chalkias AV, Aletras AH. MRISIMUL: a GPU-based parallel approach to MRI simulations. IEEE Trans Med Imaging. 2014;33(3):607–17.
10. Cooper MA, Nguyen TD, Spincemaille P, Prince MR, Weinsaft JW, Wang Y. How accurate is MOLLI T1 mapping in vivo? Validation by spin echo methods. PLoS One. 2014;9(9):e107327.
11. Kellman P, Herzka DA, Hansen MS. Adiabatic inversion pulses for myocardial T1 mapping. Magn Reson Med. 2014;71(4):1428–34.
12. de Jong S, Zwanenburg JJ, Visser F, der Nagel R, van Rijen HV, Vos MA, et al. Direct detection of myocardial fibrosis by MRI. J Mol Cell Cardiol. 2011;51(6):974–9.
13. Robson MD, Piechnik SK, Tunnicliffe EM, Neubauer S. T1 measurements in the human myocardium: the effects of magnetization transfer on the SASHA and MOLLI sequences. Magn Reson Med. 2013;70:664.
14. Landis CS, Li X, Telang FW, Molina PE, Palyka I, Vetek G, Springer CS Jr. Equilibrium transcytolemmal water-exchange kinetics in skeletal muscle in vivo. Magn Reson Med. 1999;42(3):467–78.
15. Coelho-Filho O, Mongeon F-P, Mitchell RM, Moreno H, Nadruz Junior W, Kwong RY, Jerosch-Herold M. The role of transcytolemmal water exchange in magnetic resonance measurements of diffuse myocardial fibrosis in hypertensive heart disease. Circ Cardiovasc Imaging. 2012.; in press
16. Coelho-Filho OR, Shah RV, Mitchell R, Neilan TG, Moreno H Jr, Simonson B, et al. Quantification of cardiomyocyte hypertrophy by cardiac magnetic resonance: implications for early cardiac remodeling. Circulation. 2013;128(11):1225–33.
17. Roujol S, Weingartner S, Foppa M, Chow K, Kawaji K, Ngo LH, et al. Accuracy, precision, and reproducibility of four T1 mapping sequences: a head-to-head comparison of MOLLI, ShMOLLI, SASHA, and SAPPHIRE. Radiology. 2014;272(3):683–9.
18. Sparrow P, Messroghli DR, Reid S, Ridgway JP, Bainbridge G, Sivananthan MU. Myocardial T1 mapping for detection of left ventricular myocardial fibrosis in chronic aortic regurgitation: pilot study. Am J Roentgenol. 2006;187(6):W630–5.
19. Iles L, Pfluger H, Phrommintikul A, Cherayath J, Aksit P, Gupta SN, et al. Evaluation of diffuse myocardial fibrosis in heart failure with cardiac magnetic resonance contrast-enhanced T1 mapping. J Am Coll Cardiol. 2008;52(19):1574–80.
20. Flacke SJ, Fischer SE, Lorenz CH. Measurement of the gadopentetate dimeglumine partition coefficient in human myocardium in vivo: normal distribution and elevation in acute and chronic infarction. Radiology. 2001;218(3):703–10.
21. Harris PA, Lorenz CH, Holburn GE, Overholser KA. Regional measurement of the Gd-DTPA tissue partition coefficient in canine myocardium. Magn Reson Med. 1997;38(4):541–5.
22. Jerosch-Herold M, Sheridan DC, Kushner JD, Nauman D, Burgess D, Dutton D, et al. Cardiac magnetic resonance imaging of myocardial contrast uptake and blood flow in patients affected with idiopathic or familial dilated cardiomyopathy. Am J Physiol-Heart Circ Physiol. 2008;295(3):H1234–42.
23. Ho CY, Abbasi SA, Neilan TG, Shah RV, Chen Y, Heydari B, et al. T1 measurements identify extracellular volume expansion in hypertrophic cardiomyopathy sarcomere mutation carriers with and without left ventricular hypertrophy. Circ Cardiovasc Imaging. 2013;6(3):415–22.
24. Moon JC, Reed E, Sheppard MN, Elkington AG, Ho SY, Burke M, et al. The histologic basis of late gadolinium enhancement cardiovascular magnetic resonance in hypertrophic cardiomyopathy. J Am Coll Cardiol. 2004;43(12):2260–4.
25. Puntmann VO, Voigt T, Chen Z, Mayr M, Karim R, Rhode K, et al. Native T1 mapping in differentiation of normal myocardium from diffuse disease in hypertrophic and dilated cardiomyopathy. JACC Cardiovasc Imaging. 2013;6(4):475–84.
26. Flett AS, Sado DM, Quarta G, Mirabel M, Pellerin D, Herrey AS, et al. Diffuse myocardial fibrosis in severe aortic stenosis: an equilibrium contrast cardiovascular magnetic resonance study. Eur Heart J Cardiovasc Imaging. 2012;13(10):819–26.
27. Lee SP, Lee W, Lee JM, Park EA, Kim HK, Kim YJ, Sohn DW. Assessment of diffuse myocardial fibrosis by using MR imaging in asymptomatic patients with aortic stenosis. Radiology. 2015;274(2):359–69.
28. Kuruvilla S, Janardhanan R, Antkowiak P, Keeley EC, Adenaw N, Brooks J, et al. Increased extracellular volume and altered mechanics are associated with LVH in hypertensive heart disease, not hypertension alone. JACC Cardiovasc Imaging. 2015;8(2):172–80.
29. Tham EB, Haykowsky MJ, Chow K, Spavor M, Kaneko S, Khoo NS, et al. Diffuse myocardial fibrosis by T1-mapping in children with subclinical anthracycline cardiotoxicity: relationship to exercise capacity, cumulative dose and remodeling. J Cardiovasc Magn Reson. 2013;15:48.
30. Carberry J, Carrick D, Haig C, Rauhalammi SM, Ahmed N, Mordi I, et al. Remote zone extracellular volume and left ventricular remodeling in survivors of ST-elevation myocardial infarction. Hypertension. 2016;68(2):385–91.
31. Bandula S, Banypersad SM, Sado D, Flett AS, Punwani S, Taylor SA, et al. Measurement of tissue interstitial volume in healthy patients and those with amyloidosis with equilibrium contrast-enhanced MR imaging. Radiology. 2013;268(3):858–64.
32. Banypersad SM, Sado DM, Flett AS, Gibbs SD, Pinney JH, Maestrini V, et al. Quantification of myocardial extracellular volume fraction in systemic AL amyloidosis: an equilibrium contrast cardiovascular magnetic resonance study. Circ Cardiovasc Imaging. 2013;6(1):34–9.

33. Campbell-Washburn AE, Price AN, Ellmerich S, Simons JP, Al-Shawi R, Kalber TL, et al. Monitoring systemic amyloidosis using MRI measurements of the extracellular volume fraction. Amyloid. 2013;20(2):93–8.
34. Ferreira VM, Piechnik SK, Dall'Armellina E, Karamitsos TD, Francis JM, Ntusi N, et al. Native T1-mapping detects the location, extent and patterns of acute myocarditis without the need for gadolinium contrast agents. J Cardiovasc Magn Reson. 2014;16:36.
35. Kali ACE, Sharif B, Kim YJ, Bi X, Spottiswoode B, Cokic I, et al. Native T1 mapping by 3-T CMR imaging for characterization of chronic myocardial infarctions. JACC Cardiovasc Imaging. 2015;8:1019–30.
36. Dall'Armellina E, Ferreira VM, Kharbanda RK, Prendergast B, Piechnik SK, Robson MD, et al. Diagnostic value of pre-contrast T1 mapping in acute and chronic myocardial infarction. JACC Cardiovasc Imaging. 2013;6(6):739–42.
37. Banypersad SM, Fontana M, Maestrini V, Sado DM, Captur G, Petrie A, et al. T1 mapping and survival in systemic light-chain amyloidosis. Eur Heart J. 2015;36(4):244–51.
38. Fontana M, Banypersad SM, Treibel TA, Maestrini V, Sado DM, White SK, et al. Native T1 mapping in transthyretin amyloidosis. JACC Cardiovasc Imaging. 2014;7(2):157–65.
39. Kramer CM, Appelbaum E, Desai MY, Desvigne-Nickens P, DiMarco JP, Friedrich MG, et al. Hypertrophic cardiomyopathy registry: the rationale and design of an international, observational study of hypertrophic cardiomyopathy. Am Heart J. 2015;170(2):223–30.
40. Nacif MS, Kawel N, Lee JJ, Chen X, Yao J, Zavodni A, et al. Interstitial myocardial fibrosis assessed as extracellular volume fraction with low-radiation-dose cardiac CT. Radiology. 2012;264(3):876–83.

Index

R. Y. Kwong et al. (eds.), *Cardiovascular Magnetic Resonance Imaging*, Contemporary Cardiology,
https://doi.org/10.1007/978-1-4939-8841-9